



Conference Proceedings of the 3rd European sCO2 Conference 2019



Location:
EDF Lab Paris-Saclay Research Centre
7 boulevard Gaspard Monge
91120 Palaiseau

Date: 19-20 September 2019



Conference Committee

Dieter Brillert, Universität Duisburg-Essen, Chair of Turbomachinery (conference chair)
Albannie Cagnac, EDF R&D, Fluid Dynamics, Power Generation and Environment Department
Uwe Gampe, Technische Universität Dresden, Chair of Thermal Power Machinery and Plants
Markus Haider, Technical University of Vienna, Institute for Energy Systems and Thermodynamics
Martin Rohde, Technical University of Delft, Department of Radiation Science & Technology
Jörg Starflinger, University of Stuttgart, Institute of Nuclear Technology and Energy Systems (IKE)
Giuseppe Bianchi, Institute of Energy Futures, Brunel University London
Andreas Werner, Technical University of Vienna, Institute for Energy Systems and Thermodynamics

Imprint

Conference Proceedings of the 3rd European sCO₂ Conference

ISSN 2510-7852

DOI 10.17185/dupublico/48871

URN: urn:nbn:de:hbz:464-20190925-112151-4

DuEPublico, Duisburg-Essen Publications Online
Universität Duisburg-Essen, D-45141 Essen
<https://duepublico.uni-duisburg-essen.de>

2019



This work may be used under a [Creative Commons Attribution 4.0 International](https://creativecommons.org/licenses/by/4.0/) license.

Agenda September 19th

09:00 – 09:15

Welcome and Introduction

Dieter Brillert (University of Duisburg-Essen / UDE) and Albannie Cagnac (Électricité de France / EDF)

09:15 – 09:45

EU commitment towards CO₂ emissions

Carmine Marzano and Roberto Passalacqua, European Commission

09:45 – 10:15

Coffee break

10:15 – 12:15

Heat Exchanger and Transfer (Session 1)

Chairman: Martin Rohde, TU Delft

Turbulence Modelling for Supercritical CO₂ Flows in a Vertical Tube

Otero Rodriguez, Gustavo Jose; González Portillo, Luis F.; Pecnik, Rene

Direct-Numerical Simulation of Flow and Heat Transfer within Channels of a Supercritical CO₂ Cooler

Laurien, Eckart; Pandey, Sandeep

Investigation of a Correlation Based Model for sCO₂ Compact Heat Exchangers

Hofer, Markus; Buck, Michael; Strätz, Marcel; Starflinger, Jörg

A Review of the Criteria for the Onset of Heat Transfer Deterioration with Supercritical CO₂ in Vertical Heated Single Circular Tubes

Theologou, Konstantinos; Mertz, Rainer; Laurien, Eckart; Starflinger, Jörg

10:15 – 12:15

Turbomachines and Power Systems (Session 2)

Chairman: Giuseppe Bianchi, Brunel University

Assessment of Performance and Costs of CO₂ Based Next Level Geothermal Power (NLGP) Systems

Glos, Stefan; Hansper, Jil; Grotkamp, Stefanie; Wechsung, Michael

Hybridization of a Small Modular Reactor with a Solar Power Plant using a Supercritical Carbon Dioxide Brayton Cycle

Tauveron, Nicolas; Pham, Quynh Trang; Alpy, Nicolas

Part-Load Operation of Coal Fired sCO₂ Power Plants

Dario, Alfani; Astolfi, Marco; Binotti, Marco; Macchi, Ennio; Silva, Paolo

Dynamic Modelling and Transient Analysis of a Molten Salt Heated Recompression Supercritical CO₂ Brayton Cycle

Zhou, Pan; Zhang, Jinyi; Le Moullec, Yann

12:15 – 13:15

Lunch

13:15 – 15:15

**sCO2 Experiments and Loops / Application of sCO2 Usage
(Session 3)** / Chairman: Stefan Glos, Siemens AG

Experimental Investigations and Simulations of the Control System in supercritical CO2 Loop

Vojacek, Ales; Melichar, Tomas; Doubek, Frantisek; Hajek, Petr; Hoppe, Timm

A Systematic Comparison of Supercritical CO2 Brayton Cycle Layouts for Concentrated Solar Power with a Focus on Thermal Energy Storage Utilization

Zhang, Jinyi; Le Moullec, Yann

Development and Power Generating Operation of the Supercritical Carbon Dioxide Power Cycle Experimental Test Loop in KIER

Cho, Junhyun; Shin, Hyunki; Cho, Jongjae; Choi, Bongsu; Roh, Chulwoo; Lee, Beomjoon; Lee, Gilbong; Ra, Ho-Sang; Baik, Young-Jin

Operational Experiences and Design of the sCO2-HeRo Loop

Hacks, Alexander Johannes; Freutel, Thomas; Strätz, Marcel; Vojacek, Ales; Hecker, Frieder; Starflinger, Jörg; Brillert, Dieter

13:15 – 15:15

Turbomachines and Power Systems (Session 4)

Chairman: Dieter Brillert, University Duisburg-Essen

Shouhang-EDF 10MWe Supercritical CO2 Cycle + CSP Demonstration Project

Le Moullec, Yann; Qi, Zhipeng; Zhang, Jinyi; Zhou, Pan; Yang, Zijiang; Wang, Xihua; Chen, Wenlong; Wang, Shuai

Machine Learning Based Design of a Supercritical CO2 Concentrating Solar Power Plant

Nabil, Tahar; Le Moullec, Yann; Le Coz, Adrien

Development of a Partial-admission Axial Turbine for a tens-kWe under Supercritical CO2 Condition

Cho, Jongjae; Shin, Hyunki; Cho, Junhyun; Choi, Bongsu; Baik, Young-Jin; Lee, Beomjoon; Roh, Chulwoo; Ra, Ho-Sang

15:45 – 17:15

Materials and sCO2 Mixtures (Session 5)

Chairman: Uwe Gampe, TU Dresden

Development and Application of INCONEL Alloy 740H in uSCO2 Power Systems

McCoy, Stephen A.; Baker, Brian A.; Gollihue, Ronald D.; deBarbadillo, John J.

Highly Efficient Plate-Fin Heat Exchanger (PFHE) Technical Development for s-CO2 Power Cycles

Tioual-Demange, Sarah; Bergin, Gaëtan; Mazet, Thierry

Practical Challenges and Failure Modes during Fabrication of Haynes 230 Micro-Pin Solar Receivers for High Temperature Supercritical Carbon Dioxide Operation

McNeff, Patrick S.; Paul, Brian K.; Dogan, Ömer N.; Rozman, Kyle; Kissick, Sean; Wang, Hailei; Drost, M. Kevin; Fronk, Brian M.

15:45 – 17:15

Turbomachines and Power Systems (Session 6)

Chairman: Alexander Hacks, University Duisburg-Essen

Modelling and Optimisation of Supercritical Carbon Dioxide Turbomachinery

van der Westhuizen, Ruan; van der Spuy, Johan; Groenwold, Albert; Dobson, Robert

Transient Response of Supercritical CO2 Axial Turbine for KAIST MMR

Son, In-woo; Heo, Jin Young; Oh, Bong Seong; Lee, Jeong Ik

Development and Testing of Dry Gas Seals for Turbomachinery in Multiphase CO2 Applications

Laxander, Armin; Fesl, Andreas; Hellmig, Benjamin;

Agenda September 20th

09:00 – 10:30

Materials and sCO₂ Mixtures (Session 7)

Chairman: Sebastian Unger, Helmholtz-Zentrum Dresden-Rossendorf

Supercritical Carbon Dioxide/Alternative Fluid Blends for Efficiency Upgrade of Solar Power Plant

Binotti, Marco; Di Marcoberardino, Gioele; Iora, Paolo; Invernizzi, Costante; Manzolini, Giampaolo

Accurate and Predictive Mixture Models Applied to Mixtures with CO₂

Jäger, Andreas; Mickoleit, Erik; Breilkopf, Cornelia

Effect of Impurities on Supercritical CO₂ Compatibility

Pint, Bruce A.; Unocic, Kinga A.; Keiser, James R.

10:15 – 12:15

Heat Exchanger and Transfer (Session 8)

Chairman: René Pecnik, TU Delft

Heat Transfer Characteristics of sCO₂ and Dynamic Simulation Model of sCO₂ Loop

Xiao, Gang; Xing, Kaixiang; Zhang, Jinyi; Le Moullec, Yann; Zhou, Pan; Yang, Tianfeng; Ni, Mingjiang; Cen, Kefa

Experimental Investigation of Heat Transfer and Pressure Drop in Tubes to Cool CO₂ Near the Critical Point

Wahl, Andreas; Mertz, Rainer; Eckart, Laurien; Starflinger, Jörg

Large Eddy Simulation of sCO₂ Flow with a Discontinuous Galerkin Method

Hennink, Aldo; Lathouwers, Danny; Rohde, Martin; Kloosterman, Jan Leen

10:30 – 11:00

Coffee break

11:00 – 12:00

Application of sCO₂ Usage (Session 9)

Chairman: Markus Haider, Technical University Vienna

Configuration of a Flexible and Efficient sCO₂ Cycle for Fossil Power Plant

Cagnac, Albannie; Mecheri, Mounir; Bedogni, Stefano

Modelling and Performance Analysis of a Supercritical CO₂ System for High Temperature Industrial Heat to Power Conversion at Off-Design Conditions

Marchionni, Matteo; Saravi, Samira Sayad; Bianchi, Giuseppe; Tassou, Savvas A.

11:00 – 12:00

sCO₂ Experiments and Loops (Session 10)

Chairman: Eckart Laurien, University Stuttgart

Experimental Testing of a 1MW sCO₂ Turbocompressor

Rapp, Logan Madacey; Stapp, David

Supercritical CO₂ Power Cycle Projects at gti

Macadam, Scott; Kutin, Michael; Follett, William W.; Subbaraman, Ganesan

12:00 – 12:30

Short Lunch

12:30 – 14:00

Application of sCO₂ Usage (Session 11)

Chairman: Andreas Werner, Technical University Vienna

Thermoeconomic Modeling and Analysis of sCO₂ Brayton Cycles

Penkuhn, Mathias; Tsatsaronis, George

Probabilistic Technique for Solving Computational Problem: Application of Ant Colony Optimization (ACO) to find the best sCO₂ Brayton Cycle Configuration

Mecheri, Mounir; Zhao, Qiao

Cooling System Cost and Performance Models for Economic sCO₂ Plant Optimization with Respect to Cold sCO₂ Temperature

Pidaparti, Sandeep R.; White, Charles W.; O'Connell, Andrew C.; Weiland, Nathan T.

12:30 – 13:30

sCO₂ Experiments and Loops (Session 12)

Chairman: Jörg Starflinger, University Stuttgart

Study of Autonomous Control System for S-CO₂ Power Cycle

Oh, Bong-Seong; Lee, Jeong Ik

Thermo-economic Heat Exchanger Optimization for Electro-Thermal Energy Storage based on Transcritical CO₂ Cycles

Sanz Garcia, Luis; Jacquemoud, Emmanuel; Jenny, Philipp

14:00 – 14:15

Closing Session

- Best paper award
- Announcement of the conference location and date for 2021

Papers

- Otero Rodriguez, Gustavo J.; González Portillo, Luis F.; Pecnik, Rene Page 12
 Turbulence modelling for supercritical CO2 Flows in a vertical tube
<https://doi.org/10.17185/dupublico/48872>
- Laurien, Eckart; Pandey, Sandeep Page 21
 Direct numerical simulation of flow and heat transfer within channels of a
 supercritical CO2 cooler
<https://doi.org/10.17185/dupublico/48873>
- Hofer, Markus; Buck, Michael; Strätz, Marcel; Starflinger, Jörg Page 30
 Investigation of a correlation based model for sCO2 compact heat exchangers
<https://doi.org/10.17185/dupublico/48874>
- Theologou, Konstantinos; Mertz, Rainer; Laurien, Eckart; Starflinger, Jörg Page 39
 An Assessment of the criteria for the onset of heat transfer deterioration with
 supercritical CO2 in vertical heated single circular tubes
<https://doi.org/10.17185/dupublico/48875>
- Glos, Stefan; Hansper, Jil; Grotkamp, Stefanie; Wechsung, Michael Page 49
 Assessment of performance and costs of CO2 based Next Level Geothermal
 Power (NLGP) systems
<https://doi.org/10.17185/dupublico/48876>
- Tauveron, Nicolas; Pham, Quynh Trang; Alpy, Nicolas Page 59
 Hybridization of a small modular reactor with a solar power plant using a
 Supercritical carbon dioxide Brayton cycle
<https://doi.org/10.17185/dupublico/48877>
- Dario, Alfani; Astolfi, Marco; Binotti, Marco; Macchi, Ennio; Silva, Paolo Page 68
 Part-load operation of coal fired sCO2 power plants
<https://doi.org/10.17185/dupublico/48897>
- Zhou, Pan; Zhang, Jinyi; Le Moullec, Yann Page 77
 Dynamic modeling and transient analysis of a molten salt heated recompression
 supercritical CO2 Brayton cycle
<https://doi.org/10.17185/dupublico/48879>
- Vojacek, Ales; Melichar, Tomas; Hájek, Petr; Doubek, Frantisek; Hoppe, Timm Page 89
 Experimental investigations and simulations of the control system in
 supercritical CO2 loop
<https://doi.org/10.17185/dupublico/48916>

- Zhang, Jinyi; Le Moulllec, Yann..... Page 105
A systematic comparison of supercritical CO₂ Brayton cycle layouts for concentrated solar power with a focus on thermal energy storage utilization
<https://doi.org/10.17185/dupublico/48904>
- Cho, Junhyun; Shin, Hyungki; Cho, Jongjae; Choi, Bongsu; Roh, Chulwoo; Page 116
Lee, Beomjoon; Lee, Gilbong; Ra, Ho-Sang; Baik, Young-Jin
Development and power generating operation of the supercritical carbon dioxide power cycle experimental test loop in KIER
<https://doi.org/10.17185/dupublico/48905>
- Hacks, Alexander Johannes; Freutel, Thomas; Strätz, Marcel; Vojacek, Ales; Page 125
Hecker, Frieder; Starflinger, Jörg; Brillert, Dieter
Operational experiences and design of the sCO₂-HeRo loop
<https://doi.org/10.17185/dupublico/48906>
- Le Moulllec, Yann; Qi, Zhipeng; Zhang, Jinyi; Zhou, Pan; Yang, Zijiang; Page 138
Wang, Xihua; Chen, Wenlong; Wang, Shuai
Shouhang-EDF 10MWe supercritical CO₂ cycle + CSP demonstration project
<https://doi.org/10.17185/dupublico/48884>
- Nabil, Tahar; Le Moulllec, Yann; Le Coz, Adrien Page 148
Machine learning based design of a supercritical CO₂ concentrating solar power plant
<https://doi.org/10.17185/dupublico/48885>
- Cho, Jongjae; Shin, Hyungki; Cho, Junhyun; Choi, Bongsu; Baik, Young-Jin;..... Page 158
Lee, Beomjoon; Roh, Chulwoo; Ra, Ho-Sang
Development of a partial-admission axial turbine for a tens-kWe under supercritical CO₂ condition
<https://doi.org/10.17185/dupublico/48887>
- McCoy, Stephen A.; Baker, Brian A.; Gollihue, Ronald D.; deBarbadillo, John J. Page 166
Development and application of INCONEL® alloy 740H in uSCO₂ power systems
<https://doi.org/10.17185/dupublico/48889>
- Tioual-Demange, Sarah; Bergin, Gaëtan; Mazet, Thierry..... Page 172
Highly efficient Plate-Fin Heat Exchanger (PFHE) technical development for s-CO₂ power cycles
<https://doi.org/10.17185/dupublico/48900>
- McNeff, Patrick S.; Paul, Brian K.; Dogan, Ömer; Rozman, Kyle; Kissick, Sean; Page 180
Wang, Hailei; Drost, M. Kevin; Fronk, Brian M.
Practical challenges and failure modes during fabrication of Haynes 230 Micro-Pin Solar Receivers for high temperature supercritical carbon dioxide applications
<https://doi.org/10.17185/dupublico/48901>
- Van Der Westhuizen, Ruan; Van Der Spuy, Johan; Groenwold, Albert; Dobson, Robert Page 190
Modelling and optimisation of supercritical carbon dioxide turbomachinery
<https://doi.org/10.17185/dupublico/48895>

- Son, In-woo; Heo, Jin Young; Oh, Bong Seong; Lee, Jeong Ik..... Page 201
 Transient response of supercritical CO₂ axial turbine for KAIST MMR
<https://doi.org/10.17185/dupublico/48896>
- Laxander, Armin; Fesl, Andreas; Hellmig, Benjamin Page 211
 Development and testing of dry gas seals for turbomachinery in multiphase
 CO₂ applications
<https://doi.org/10.17185/dupublico/48878>
- Binotti, Marco; Di Marcoberardino, Gioele; Iora, Paolo; Invernizzi, Costante Mario; Page 222
 Manzolini, Giampaolo
 Supercritical carbon dioxide/alternative fluids blends for efficiency upgrade
 of solar power plant
<https://doi.org/10.17185/dupublico/48892>
- Jäger, Andreas; Mickoleit, Erik; Breilkopf, Cornelia Page 230
 Accurate and predictive mixture models applied to mixtures with CO₂
<https://doi.org/10.17185/dupublico/48891>
- Pint, Bruce A.; Unocic, Kinga A.; Keiser, James R. Page 238
 Effect of impurities on supercritical CO₂ compatibility
<https://doi.org/10.17185/dupublico/48899>
- Xiao, Gang; Xing, Kaixiang; Zhang, Jinyi; Le Moullec, Yann; Zhou, Pan; Page 245
 Yang, Tianfeng; Ni, Mingjiang; Cen, Kefa
 Heat transfer characteristics of sCO₂ and dynamic simulation model of sCO₂ loop
<https://doi.org/10.17185/dupublico/48881>
- Wahl, Andreas; Mertz, Rainer; Eckart, Laurien; Jörg, Starflinger Page 255
 Experimental investigation of heat transfer and pressure drop in tubes
 to cool CO₂ near the critical point
<https://doi.org/10.17185/dupublico/48882>
- Hennink, Aldo; Lathouwers, Danny; Rohde, Martin; Kloosterman, Jan Leen Page 265
 Large Eddy Simulation of sCO₂ flow with a discontinuous Galerkin method
<https://doi.org/10.17185/dupublico/48883>
- Cagnac, Albannie; Mecheri, Mounir; Bedogni, Stefano Page 271
 Configuration of a flexible and efficient sCO₂ cycle for fossil power plant
<https://doi.org/10.17185/dupublico/48907>
- Marchionni, Matteo; Saravi, Samira Sayad; Bianchi, Giuseppe; Tassou, Savvas A. Page 281
 Modelling and performance analysis of a supercritical CO₂ system for high
 temperature industrial heat to power conversion at off-design conditions
<https://doi.org/10.17185/dupublico/48908>
- Rapp, Logan Madacey; Stapp, David Page 290
 Experimental testing of a 1MW sCO₂ Turbocompressor
<https://doi.org/10.17185/dupublico/48910>

- Macadam, Scott; Kutin, Michael Page 300
 Supercritical CO₂ power cycle projects at GTI
<https://doi.org/10.17185/dupublico/48911>
- Penkuhn, Mathias; Tsatsaronis, George Page 310
 Thermo-economic modeling and analysis of sCO₂ Brayton cycles
<https://doi.org/10.17185/dupublico/48909>
- Mecheri, Mounir; Zhao, Qiao Page 319
 Probabilistic technique for solving computational problem : application of
 Ant Colony Optimization (ACO) to find the best sCO₂ Brayton cycle configuration
<https://doi.org/10.17185/dupublico/48914>
- Pidaparti, Sandeep R.; White, Charles W.; O'Connell, Andrew C.; Weiland, Nathan T. Page 332
 Cooling system cost and performance models for economic sCO₂ plant optimization
 of cooling with respect to cold sCO₂ temperature
<https://doi.org/10.17185/dupublico/48915>
- Oh, Bong-Seong; Lee, Jeong Ik Page 345
 Study of autonomous control system for S-CO₂ power cycle
<https://doi.org/10.17185/dupublico/48913>
- Sanz Garcia, Luis; Jacquemoud, Emmanuel; Jenny, Philipp Page 353
 Thermo-economic heat exchanger optimization for Electro-Thermal
 Energy Storage based on transcritical CO₂ cycles
<https://doi.org/10.17185/dupublico/48917>

TURBULENCE MODELLING FOR SUPERCRITICAL CO₂ FLOWS IN A VERTICAL TUBE

Gustavo J. Otero R.*

Process and Energy Department Mechanical
Engineering Delft University of Technology
Delft, the Netherlands

Email: g.j.oterorodriguez@tudelft.nl

Luis F. González-Portillo

Grupo de Investigaciones Termoenergéticas (GIT)
Universidad Politécnica de Madrid
Madrid, Spain

Email: lf.gonzalez@upm.es

Rene Pecnik

Process and Energy Department
Mechanical Engineering Delft
University of Technology
Delft, the Netherlands
Email: r.pecnik@tudelft.nl

ABSTRACT

Standard eddy viscosity models are incapable of accounting for the effects of strong variation of thermophysical properties on turbulence of supercritical fluids [1], which can cause considerable inaccuracies in the prediction of the pressure drop, the heat transfer coefficient, and other quantities of interest for supercritical flows. In our previous research [2], we have developed consistent modifications for eddy viscosity models to make them more reliable for wall-bounded turbulent flow with sharp gradients in the thermophysical properties. In this paper, we implement these density-corrected turbulence models to our in-house Reynolds-Averaged Navier-Stokes (RANS) solver to simulate an upward heated turbulent pipe flow with CO₂ at supercritical pressure. The results show an improvement in the accuracy of the model for the force convection test cases. However, when heat transfer deterioration is present, the modified turbulence model is still not reliable. To investigate the cause of the inaccuracy, we introduced different methods to model the turbulent heat flux, by changing the constant value of the turbulent Prandtl number and using two different algebraic equations. As expected, the model for the turbulent Prandtl number considerably influences the overall simulation prediction. To better model heat transfer deterioration in an upward flow of a turbulent supercritical flow, a better approximation of the turbulent heat flux is necessary.

1. INTRODUCTION

Supercritical fluids — fluids above the critical pressure — have recently been considered for many engineering applications, in particular in the field of energy generation [3]. For instance, thermodynamics power cycles can use supercritical

fluids as the working fluid [4-5]. Moreover, renewable energy technologies, like solar energy and waste heat recovery, can benefit from the advantage of supercritical fluids [4, 6]. Other industrial processes with supercritical fluids include pharmaceutical processes or enhanced oil recovery [7]. All these applications require a comprehensive understanding of fluid dynamics and heat transfer of supercritical fluids to correctly design and model the system.

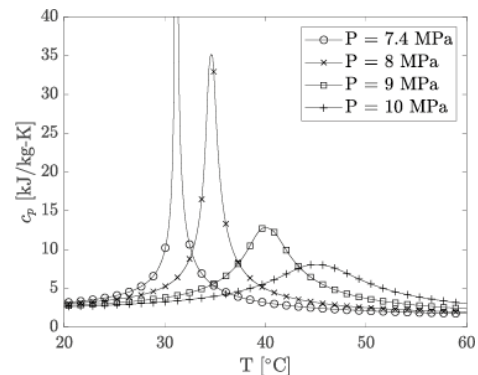


Figure 1. Variation of specific heat capacity as a function of temperature for constant pressure for CO₂

Supercritical fluids exhibit deviations from ideal thermodynamic behavior and do not have a recognizable phase change; the fluid transition from a liquid-like and gas-like phase occurs in a continuous manner. However, small changes in temperature and/or pressure in the supercritical region can lead to strong gradients on the thermophysical properties. For example, figure 1 shows the variation of the specific heat

capacity at constant pressure, c_p , as a function of temperature for CO₂ ($p_{cr} = 7.39$ MPa). The pseudo-critical temperature is the location where c_p has its peak at constant pressure. These abrupt variations of thermophysical properties of a supercritical fluid results in a flow behavior and a heat transfer which is different from an ideal gas flow [8].

In a heated upward flowing supercritical fluid, heat transfer deterioration may occur [9]. The sharp variation of thermophysical properties in the critical region and the effect of buoyancy influence turbulence, which could result in heat transfer deterioration [10].

Direct numerical simulations (DNS) have been performed to analyze the heat transfer to supercritical fluids in turbulent pipe flows [9,10]. But, these highly accurate simulations are limited to simple geometries and low Reynolds numbers due to the high computational cost needed. To bypass the computational cost, it is possible to solve the RANS equations coupled with eddy viscosity models. However, these models rely on a limited data, and their development is hampered by the lack of knowledge on supercritical fluids and heat transfer deterioration.

There are three challenges for modeling turbulence of an upward flowing supercritical fluid.

1. **Eddy viscosity:** an eddy viscosity model must properly account for variations in the thermophysical properties. Most models have been developed for incompressible flows and the effect of density on turbulence is not accounted for. We have proposed in our recent study [2] how eddy viscosity models can be modified to successfully account for this effect. The proposed modifications are generally applicable to any turbulence model and are based on analytic scaling arguments.
2. **Turbulent heat flux:** the model for the turbulent heat flux must account for variations in molecular Prandtl number across the boundary layer. Commonly, the turbulent heat flux is modelled using the analogy between turbulent momentum and heat flux by means of a turbulent Prandtl number (Pr_t). Several models have been developed and applied to ideal gas flows [11, 12]. It is known that in case of heat transfer deterioration, the definition of the turbulent Prandtl number is not applicable. The heat deterioration causes an inflection point in the streamwise velocity profile making $Pr_t \rightarrow \infty$ [10].
3. **Buoyancy production of turbulent kinetic energy:** the eddy viscosity model must account for the buoyancy production of turbulent kinetic energy (TKE). Also here, most of the models for the buoyancy production in the TKE equation assume the ideal gas law to relate density with temperature fluctuations [13]. Additional insight from DNS is required to develop accurate models to account for buoyancy effects.

This article investigates the accuracy of RANS turbulence model to predict heat transfer in a turbulent pipe flow with CO₂ at supercritical pressure. Three standard turbulence models, namely the Myong-Kasagi (MK) [14], Menter's $k - \omega$ SST [15], and Spallart-Allmaras (SA) [16] turbulence models are used to model the Reynolds stresses. The density modifications derived in our previous study [2] are included into the turbulence models to solve the system. Moreover, we investigate the influence of the turbulent Prandtl number on the heat transfer. Finally, two different algebraic models for the turbulent Prandtl number [11,12] are used to approximate the turbulent heat flux.

2. TEST CASE

2.1 Experimental data

In literature, experimental data is available to investigate turbulent heat transfer to supercritical fluids. For the present article, two data sources [17,18] are chosen to study the heat transfer deterioration of flows near the supercritical point. These studies experimented with CO₂ flowing upwards in a uniformly heated pipe at different conditions. The boundary conditions of these experiments are summarized in table 1. We will use the measured wall temperature to compare the simulations with the experiments; figure 2 shows the measured wall temperature from the selected experimental data.

The experiments of case 1, taken from Bae et al. [17], are shown in figure 2a. The case with the lowest heat flux ($q'' = 29.3$ kW/m²) is not affected by heat transfer deterioration; this can be seen by the smooth increase of wall temperature. For the experiment with the highest heat flux ($q'' = 48.8$ kW/m²), the larger wall temperature at the beginning of the measurements indicate heat transfer deterioration. Heat transfer deterioration decreases when the bulk temperature is close to the pseudo-critical value. For these experiments, the measurements are collected half a meter after the wall heating starts, thus no data is available at the inflow.

The experiments for case 2, reported by Kim et al. [18], show a more detailed quantification of the heat transfer deterioration. Figure 2b shows the wall temperature along the pipe. Heat transfer deterioration can be seen for a heat flux of 23 kW/m² and 30 kW/m² when the wall temperature crosses the pseudo-critical temperature. The wall temperature shows one or two steep peaks, characteristic of heat transfer deterioration.

2.2 Governing equations

In the present study, the RANS equations, written in cylindrical coordinates, are solved. To close the system of equations, an equation of state (EOS) is used to define the relation between density, pressure, temperature and internal energy. The multi-parameter equation of state of Kunz and Wagner [19] is used for CO₂.

Table 1. Experimental cases investigated, where p^* is the pressure, T_0^* is the inlet temperature, D^* is the pipe diameter, G^* is the mass flux and the accent “*” refers to a dimensional quantity. Re_0 and Pr_0 are the Reynolds and Prandtl number, respectively, at the inflow.

	p^* [MPa]	T_0^* [°C]	D^* [mm]	G^* [kg/(s m ²)]	q'' [kW/m ²]	Re_0 [-]	Pr_0 [-]
Case 1 [17]	8.12	5	6.32	400	29.3	2,500	2.14
	8.12	5	6.32	400	48.8	2,500	2.14
Case 2 [18]	8	15	7.8	314	20.0	29,000	2.3
	8	15	7.8	314	23.0	29,000	2.3
	8	15	7.8	314	30.0	29,000	2.3

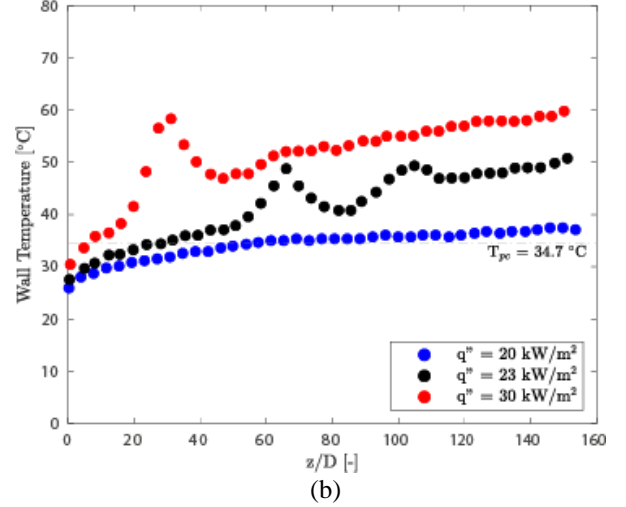
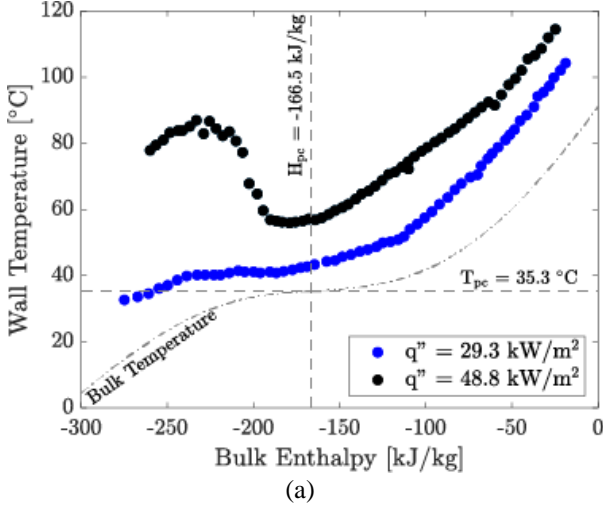


Figure 2. Wall temperature distribution as a function of the pipe stream-wise distance for two experimental set-up: (a) Bae et al [17] and (b) Kim et al. [18]. The bulk enthalpy can be seen as the pipe distance because a constant heat flux is introduced into the system. These figures were directly reproduced from the references [17,18]

The governing equations for momentum, in radial and stream-wise direction, and the energy can be expressed in their non-dimensional form (scaled by wall units), and assuming a two-dimensional steady-state axis-symmetric flow as:

- for momentum in stream-wise direction,
$$\frac{\partial \langle \rho \rangle \{u_z\}^2}{\partial z} + \frac{1}{r} \frac{\partial r \langle \rho \rangle \{u_z\} \{u_r\}}{\partial r} = - \frac{\partial \langle p \rangle}{\partial z} + \frac{\langle \rho \rangle}{Fr_0^2} + \frac{\partial}{\partial z} \left[\left(\frac{\langle \mu \rangle}{Re_\tau} + \mu_t \right) \left(2 \frac{\partial \{u_z\}}{\partial z} - \frac{2}{3} \nabla \cdot \{ \mathbf{u} \} \right) \right] + \frac{1}{r} \frac{\partial}{\partial r} \left[r \left(\frac{\langle \mu \rangle}{Re_\tau} + \mu_t \right) \left(\frac{\partial \{u_z\}}{\partial r} + \frac{\partial \{u_r\}}{\partial z} \right) \right],$$
- for momentum in radial direction,
$$\frac{1}{r} \left[\frac{\partial r \langle \rho \rangle \{u_z\} \{u_r\}}{\partial z} + \frac{\partial r \langle \rho \rangle \{u_r\}^2}{\partial r} \right] = - \frac{\partial \langle p \rangle}{\partial r} + \frac{1}{r} \frac{\partial}{\partial r} \left[r \left(\frac{\langle \mu \rangle}{Re_\tau} + \mu_t \right) \left(2 \frac{\partial \{u_r\}}{\partial r} - \frac{2}{3} \nabla \cdot \{ \mathbf{u} \} \right) \right] + \frac{\partial}{\partial z} \left[\left(\frac{\langle \mu \rangle}{Re_\tau} + \mu_t \right) \left(\frac{\partial \{u_z\}}{\partial r} + \frac{\partial \{u_r\}}{\partial z} \right) \right] - \frac{1}{r} \left(\frac{\langle \mu \rangle}{Re_\tau} + \mu_t \right) \left(2 \frac{\{u_r\}}{r} - \frac{2}{3} \nabla \cdot \{ \mathbf{u} \} \right),$$

- and energy,
$$\frac{\partial \langle \rho \rangle \{H\} \{u_z\}}{\partial z} + \frac{1}{r} \frac{\partial r \langle \rho \rangle \{H\} \{u_r\}}{\partial r} = \frac{1}{r} \frac{\partial}{\partial r} \left[r \left(\frac{\langle \lambda \rangle / Cp}{Re_\tau Pr} + \frac{\mu_t}{Pr_t} \right) \frac{\partial \{H\}}{\partial r} \right] + \frac{\partial}{\partial z} \left[\left(\frac{\langle \lambda \rangle / Cp}{Re_\tau Pr} + \frac{\mu_t}{Pr_t} \right) \frac{\partial \{H\}}{\partial z} \right],$$

where H is the specific enthalpy, u_z and u_r are the streamwise (axial) and radial velocity component, respectively. $\nabla \cdot \{ \mathbf{u} \}$ is the divergence of the velocity vector in cylindrical coordinates. The dimensionless parameters $Re_\tau = u_\tau \rho_w^* D^* / \mu_w^*$ and $Fr_0 = u_\tau / \sqrt{g^* D^*}$ are the friction Reynolds number and the Froude number, where $u_\tau = \sqrt{\tau_w / \rho_w^*}$ is the friction velocity. The Froude number takes into account the buoyancy effects with g^* the gravitational acceleration. In the RANS equations, we use the Reynolds decomposition for most of the quantities, defined as: $\phi = \langle \phi \rangle + \phi'$ with $\langle \phi' \rangle = 0$, and the Favre decomposition for the velocity and enthalpy, defined as: $\phi = \{ \phi \} + \phi''$ with $\langle \rho \rangle \{ \phi \} = \langle \rho \phi \rangle$, $\langle \rho \rangle \{ \phi'' \} = 0$, and $\langle \phi'' \rangle \neq 0$.

3. TURBULENCE MODELLING

The Reynolds shear stress and turbulent heat flux are modelled in the above equations by the Boussinesq

approximation ($\langle \rho u''_i u''_j \rangle = 2\mu_t \{S_{ij}\} - 2/3 \langle \rho \rangle k \delta_{ij}$) and the gradient diffusion hypothesis ($\langle \rho u''_i H'' \rangle = \mu_t / Pr_t \partial \{H\} / \partial x_i$), respectively, adding two extra unknowns to the system of equations: the eddy viscosity (μ_t) and the turbulent Prandtl number (Pr_t). In this section, we will discuss how these unknowns are modelled. Moreover, at the end of this section, we briefly discuss the model used for the buoyancy production of turbulence (G_k).

3.1 Turbulence modeling for heated flows with buoyancy

We apply standard (SA, SST, and MK) and variable density turbulence models. We use our recently derived variable density modifications to alter standard turbulence models [2]. In this section, we report how the density modifications for turbulence models are derived.

The semi-local scaling (SLS), as proposed by Huang *et al.* in 1995 [20], is based on the wall shear stress τ_w and on the local mean (instead of wall) values of the density and the viscosity to account for changes in viscous scales due to mean variations in the thermophysical properties. The aim of the SLS was to collapse turbulence statistics for compressible flows at high Mach numbers with those of incompressible flows. In the SLS framework, the friction velocity and viscous length scale are defined as $u_\tau^* = \sqrt{\tau_w / \langle \rho^* \rangle}$ and $\delta_v^* = \langle \mu^* \rangle / \langle \rho^* \rangle u_\tau^*$ respectively. Accordingly, the semi-local wall distance can be defined as $y^* = y / \delta_v^*$ and the semi-local Reynolds number as,

$$Re_\tau^* = \frac{u_\tau^* \langle \rho^* \rangle D^*}{\langle \mu^* \rangle} = \sqrt{\frac{\langle \rho^* \rangle \mu_w^*}{\rho_w^* \langle \mu^* \rangle}} Re_\tau,$$

where Re_τ and u_τ (both defined above), are the conventional friction Reynolds number and friction velocity based on viscous wall units. In general, any flow variable can be non-dimensionalized using wall-based units and semi-local units.

Instead of exclusively using the semi-local scaling to collapse turbulence statistics for compressible flows with different Mach numbers, Pecnik and Patel [21] extended the use of the scaling to derive an alternative form of the TKE equation for wall-bounded flows with a strong wall-normal variations of density and viscosity. Starting from the semi-locally scaled non-conservative form of the momentum equations, and with the assumption that the wall shear stress τ_w changes slowly in the stream-wise direction, the SLS TKE equation reads,

$$t_\tau^* \frac{\partial \hat{\rho} \hat{k}}{\partial t^*} + \frac{\partial \hat{\rho} \hat{k} \hat{u}_j}{\partial \hat{x}_j} = \hat{P}_k + \hat{G}_k - \hat{\rho} \hat{\varepsilon} + \frac{\partial}{\partial \hat{x}_j} \left[\left(\frac{\hat{\mu}}{Re_\tau} + \frac{\hat{\mu}_t}{\sigma_k} \right) \frac{\partial \hat{k}}{\partial \hat{x}_j} \right],$$

with \hat{P}_k as the turbulent production, \hat{G}_k as the buoyancy production, and $t_\tau^* = D^* / u_\tau^*$. For brevity with express the TKE equation with Cartesian notation; the derivation is equivalent in cylindrical coordinates. In the equation above, the semi-locally scaled quantities are denoted with the accent “^”, as $\hat{\phi}$. If this form of the TKE equation is used in conjunction with a turbulence model — MK and SST — the results for turbulent flows with large thermophysical property variations significantly

improve [21]. However, for general industrial applications with complex geometries, it is not feasible to solve the semi-locally scaled equations. The reason is that all turbulence variables would need to be rescaled every iteration step by quantities that depend on the wall friction at the closest wall and by local quantities of density and viscosity.

To overcome the dependence on the wall friction and local quantities, we convert the previous equation back to conventional scales, in particular to viscous wall units. The transformation from SLS quantities to locally-scaled, was performed to each term and after algebraic manipulation we end up with,

$$t_\tau \frac{\partial \langle \rho \rangle k}{\partial t} + \frac{\partial \langle \rho \rangle k \{u_j\}}{\partial x_j} = P_k + G_k - \langle \rho \rangle \varepsilon + \frac{1}{\sqrt{\langle \rho \rangle}} \frac{\partial}{\partial x_j} \left[\frac{1}{\sqrt{\langle \rho \rangle}} \left(\frac{\langle \mu \rangle}{Re_\tau} + \frac{\mu_t}{\sigma_k} \right) \frac{\partial \langle \rho \rangle k}{\partial x_j} \right].$$

If compared to the conventional model for the TKE, the derived equation shows only one major difference that lies in the diffusion term. The diffusion term that emerges from the semi-local scaling methodology is a function of $\langle \rho \rangle k$ (instead of k), while the diffusion coefficient and the overall diffusion term are divided by $\sqrt{\langle \rho \rangle}$.

In analogy to the modified TKE equation, we derived the modified transport equations for the turbulent dissipation ε , specific turbulent dissipation ω , and the eddy viscosity in the Spalart-Allmaras turbulence model ν_{SA} . An additional modification we implement, specifically for the MK model, is to replace the non-dimensional wall distance y^+ , and friction Reynolds number Re_τ , with their semi-local counterparts, namely the semi-locally scaled wall distance y^* , and the semi-local friction Reynolds number Re_τ^* . For more details on the derivation the reader is refer to [2].

3.2 Turbulent Prandtl number

The turbulent Prandtl number relates the turbulent shear stress with turbulent heat flux, including the velocity and temperature gradient in the wall-normal direction as,

$$Pr_t = \frac{\langle \rho u''_z u''_r \rangle \partial \langle T \rangle / \partial r}{\langle \rho T'' u''_r \rangle \partial \langle u \rangle / \partial r}.$$

In the current study, we have used three approximations of the turbulent Prandtl number. These relations were developed for a flow with constant thermophysical properties.

- The Reynolds analogy is the simplest model for the turbulent heat flux, in which the turbulent Prandtl number is assumed constant. It assumes a strong analogy between momentum and scalar transport. The turbulent Prandtl number of 0.7 to 1.0 represents most gases in the log-layer [11].
- Kays in 1994 [11] proposed an approximation of the turbulent Prandtl number as a function of the ratio of turbulent and molecular viscosity. The algebraic expression — similar to a mixing length model for the eddy viscosity — is given as:

$$Pr_t = \frac{1}{C_1 + C_2 \mu_\gamma - C_3 \mu_\gamma^2 [1 - \exp(-C_4 / \mu_\gamma)]},$$

where $\mu_\gamma = \mu_t / \langle \mu \rangle$ and the constants are $C_1 = 0.5882$, $C_2 = 0.228$, $C_3 = 0.0441$ and $C_4 = 5.165$.

- Irrenfried and Steiner [12] suggested an improvement of the turbulent Prandtl number by introducing an additional model parameter $\left(\gamma_{is} = \frac{1}{[\text{Pr}_{t,\infty} + 0.1\text{Pr}^{0.83}]} \right)$ that depends on the molecular Prandtl number. This correlation for turbulent Prandtl number reads

$$\frac{1}{\text{Pr}_t} = \frac{\gamma_{is} + C \text{Pe}_t \sqrt{2 \left(\frac{1}{\text{Pr}_{t,\infty}} - \text{Pr}_{t,\infty} \right)}}{-(C \text{Pe}_t)^2 \left[1 - \exp \left(-\frac{1}{C \text{Pe}_t} \sqrt{2 \left(\frac{1}{\text{Pr}_{t,\infty}} - \gamma_{is} \right)} \right) \right]}$$

where $C = 3.0$, and $\text{Pe}_t = (\mu_t / \langle \mu \rangle) \text{Pr}$ is the turbulent Peclet number. In the present study, we set $\text{Pr}_{t,\infty} = 1.0$.

3.3 Buoyancy production term

The buoyancy production term in the transport equation of the turbulent kinetic energy is defined as,

$$G_k = -\langle u_z'' \rangle \left(\frac{\partial \langle \rho \rangle}{\partial z} - \frac{\partial \langle \tau_{rz} \rangle}{\partial r} \right) \approx -\frac{\langle \rho \rangle}{Fr_0^2} \langle u_z'' \rangle.$$

The buoyancy production can be further simplified, using the Favre decomposition and relating the density fluctuation with the temperature fluctuations ($\langle \rho' u_z' \rangle = \beta_T \langle \rho u_z' T' \rangle$), as

$$G_k = -\frac{1}{Fr_0^2} \beta_T \langle \rho u_z' T' \rangle,$$

where the thermal expansion coefficient is defined as $\beta_T = -1 / \langle \rho \rangle (\partial \rho / \partial T)$. The closure of the $\langle \rho u_z' T' \rangle$ term is generally accomplished with simple gradient diffusion hypothesis. However in the present study, we have approximated the buoyancy production with the Generalized Gradient Diffusion Hypothesis (GGDH), because it includes the anisotropic turbulent diffusivity using the Reynolds shear stress [13]. Using the GGDH, the buoyancy production is modelled as

$$\langle \rho u_z' T' \rangle = -C_t T_\tau \left(\langle \rho u_z'' u_r'' \rangle \frac{\partial T}{\partial r} + \langle \rho u_z'' u_z'' \rangle \frac{\partial T}{\partial z} \right),$$

where C_t is a positive constant equal to 0.333. This model requires the turbulent time scale T_τ , which for a $k - \varepsilon$ and a $k - \omega$ model is given by $T_\tau = k / \varepsilon$ and $T_\tau = 1 / \omega$, respectively. For the Spallart-Allmaras model [16], buoyancy production is not taken into account.

4. CFD CALCULATIONS

4.1 Numerical setup

An in-house RANS code solves the governing equations — with a Poisson solver for the pressure correction — for momentum in radial and axial direction, enthalpy and turbulent scalars; the latter is dependent on the turbulence model. These equations are solved using a stagger space grid. A second-order central difference scheme and a Euler time integration scheme are used for the discretization in space and time, respectively. We used a maximum time step of 10^{-3} seconds. The diffusion terms in r-direction are treated implicitly, while the other terms are discretized explicitly.

The simulation setup consists of two parts as depicted in figure 3. First, an inflow generator is used to achieve a fully developed turbulent pipe flow. Periodic inlet and outlet boundaries and an isothermal flow are enforced to generate the inflow for the developing simulation. Afterwards, the fully developed profile is fed as the inlet boundary condition for the simulation of the developing pipe flow, which is uniformly heated from the wall.

The numerical domain of the pipe is axis-symmetric with a uniform discretization in the stream-wise direction ($N_z = 768$) and a non-uniform discretization in the wall-normal direction ($N_r = 192$). A hyperbolic tangent function is used to cluster the mesh points near the wall in order to ensure $y^+ < 1$ in the first mesh cell; no wall function is used. A grid convergence analysis was carried out for all the simulated cases to ensure mesh-independent results.

4.2 Results

This section of the paper reports the outcome of the RANS simulations of the upwards flowing CO_2 in the heated vertical pipe test cases. As mentioned in section 3, the compressible NS equations are coupled to three turbulence models — the MK, the SST, and the SA turbulence models. We assess the impact of including density corrections in these turbulence models on predicting the heat transfer. We refer to the turbulence models with the density modifications as MK- ρ , SST- ρ and SA- ρ .

4.2.1 Test case 1, Bae et al. [17]

The experiments from Bae et al. [17] are solved using the selected turbulence models with and without density modifications and the turbulent Prandtl number is approximated as $\text{Pr}_t = 0.9$.

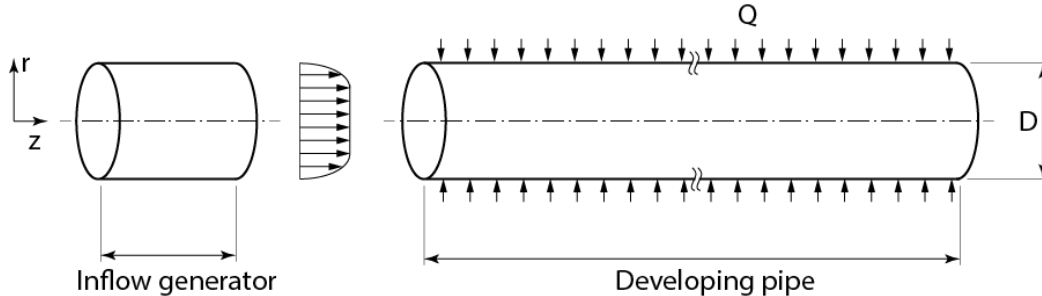


Figure 3. Numerical set-up for the CFD simulations

Most of the turbulence models accurately estimate the wall temperature for case 1 with a heat flux of 29.3 kW/m^2 , see figure 4a. One exception is the SST- ρ model, but as already mentioned in our previous study, Otero et al. [2], the density modifications have detrimental effects on this specific model. The standard MK model is another model that lacks accuracy when compared to the experiments. With the density modifications, the MK- ρ model improves considerably, resulting in a close match with the experimental data. The SA and SA- ρ both have a similar prediction; these models slightly overestimate the wall temperature below the pseudo-critical enthalpy. The SST model accurately matches the experimental values. For this particular experiment, the CFD simulations have sufficient accuracy with the exception of the MK and SST- ρ models. Therefore, we will not include these two models in the remainder of this article

For the experiment with a higher heat flux ($q'' = 48.8 \text{ kW/m}^2$), the results with all the turbulence models agree qualitatively with the experiments; the SST- ρ and MK models are not included. Moreover, none of the models are able to reproduce the wall temperature distribution quantitatively (see figure 4b). The SST model does not estimate any heat transfer deterioration, with the wall temperature below the measured values. The MK- ρ model overestimates the wall temperature until a bulk enthalpy of $\approx -40 \text{ kJ/kg}$, where a strong heat transfer deterioration is predicted. The SA models with and without density modifications qualitative predict the heat transfer deterioration but underestimating the wall temperature. Above the bulk enthalpy of -200 kJ/kg , all models are close to the experimental data, except the MK- ρ model.

4.2.2 Test case 2, Kim et al. [18]

For test case 2, we will focus only on the experiments from Kim et al. [18] with heat transfer deterioration; these experiments have a heat flux of 23 kW/m^2 and 30 kW/m^2 , see table 1. For these results, we approximate $Pr_t = 0.9$.

SA and SA- ρ are the only turbulence model able to reproduce heat transfer deterioration for the case 2 with a heat flux of 23 kW/m^2 , see figure 5a. The two peaks in wall temperature are represented qualitatively, but not at the exact location. The rest of models cannot predict heat transfer deterioration. For case 2, 23 kW/m^2 is the value of heat flux where heat transfer deterioration starts to occur, for example for 20 kW/m^2 no deterioration is observed in the experiments.

All the turbulence models can reproduce heat transfer deterioration for a heat flux of 30 kW/m^2 (see figure 5b). Consistent with the previous experiment, the SA models are capable of predicting the sudden increase in wall temperature but again at a wrong location. The largest wall temperature peak of the SST and MK- ρ models occurs upstream from the measured data. Moreover, the SA, SA- ρ , and MK- ρ overestimate the wall temperature at the peak, the SST model underestimates it. The wall temperature trends after this point differ among the models. The SA and SST models tend to a lower wall temperature as if

the heat transfer deterioration has been completed. Although overestimating the wall temperature, the MK- ρ model predicts qualitatively the wall temperature tendency with a steady increase in wall temperature at the outlet section of the pipe ($z/D > 80$).

The CFD simulation results from this second case for all four models are comparable to the inlet section of the high flux experiment of Bae et al. [17] (figure 4b). First, the SST model barely predicts heat transfer deterioration. Second, the SA and SA- ρ models predict the heat transfer deterioration earlier than observed in the experiments. Finally, the MK- ρ model follows the trend of the experiments qualitatively during the heat transfer deterioration. However, the performance of the turbulence model is not satisfactory. Therefore, we test different approximation of the turbulent Prandtl number with the expectation of a better approximation of the turbulent heat flux.

4.2.3 Turbulent heat transfer modelling:

In this section, we investigate different methods to model the turbulent heat transfer, more specifically the turbulent Prandtl number. We consider only Kim et al [18] experiments. We present the results for two RANS models: MK- ρ with an approximation of the turbulent Prandtl number: the Reynolds analogy ($Pr_t=0.9$) and two algebraic equations [11, 12], and SST with different constant values of the turbulent Prandtl number. The goal of this investigation is to evaluate the influence of the turbulent Prandtl model on the overall performance of the CFD simulation.

Both algebraic equations improve the prediction of the peaks for the wall temperature in the MK- ρ model, see figure 6a. Irrenfried's correlation predicts the second temperature peak. On the other hand, Kay's correlation estimates the first temperature peak accurately but predicts the second peak too early. Compared to the constant Prandtl number, the performance of the MK- ρ model is enhanced when coupled to algebraic equations for Pr_t . Still, compared to experimental data, the prediction of the turbulence model is not accurate.

The turbulent heat flux is inversely proportional to Pr_t ; the lower the Pr_t value is, the higher the turbulent heat flux. Figure 6b shows the results obtained with the SST model with four different constant values of turbulent Prandtl number: 0.4, 0.9, 1.0, and 1.4. The model with the lowest turbulent Prandtl number shows no trace of heat transfer deterioration. The buoyancy effect and heat transfer deterioration increase for higher turbulent Prandtl numbers. The value that better matches the measured data is $Pr_t = 1$, rather than the commonly used value of 0.9. These two constant Pr_t values give different wall temperature behavior, especially around the temperature peak. As expected, the turbulent Prandtl number considerably influences the prediction of the heat transfer deterioration. However, there is hardly any qualitative difference downstream for $z/D > 100$.

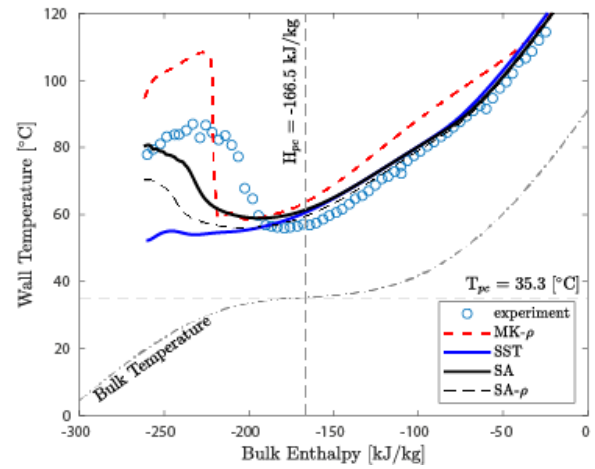
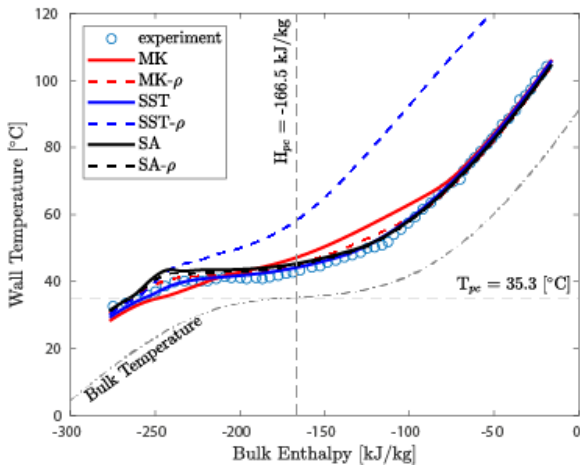


Figure 4. Wall temperature distribution as a function of the pipe stream-wise distance calculated with different RANS models (a) $q'' = 29.3 \text{ kW/m}^2$ and (b) $q'' = 48.8 \text{ kW/m}^2$ compared to experiments [17]

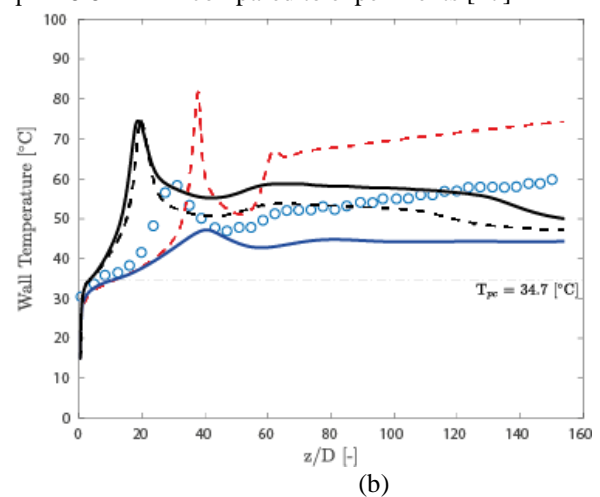
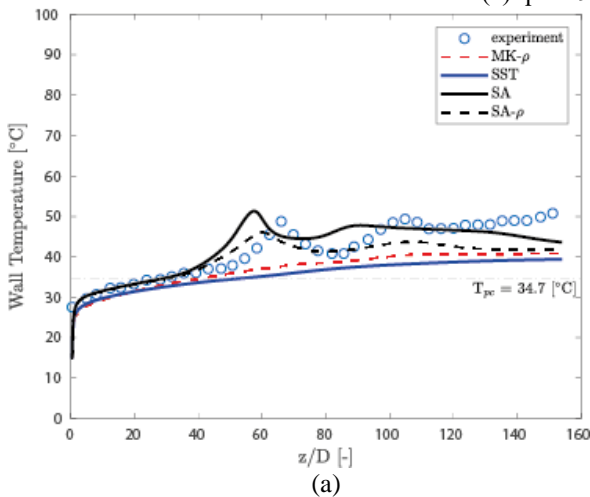


Figure 5. Wall temperature distribution as a function of the pipe stream-wise distance calculated with different RANS models (a) $q'' = 23 \text{ kW/m}^2$ and (b) $q'' = 30 \text{ kW/m}^2$ compared to experiments [18]

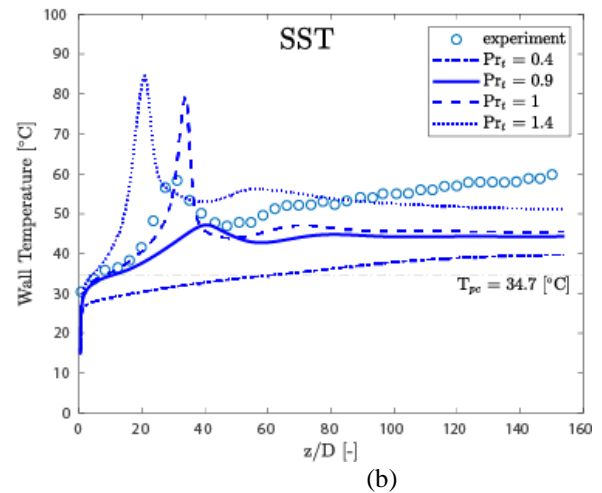
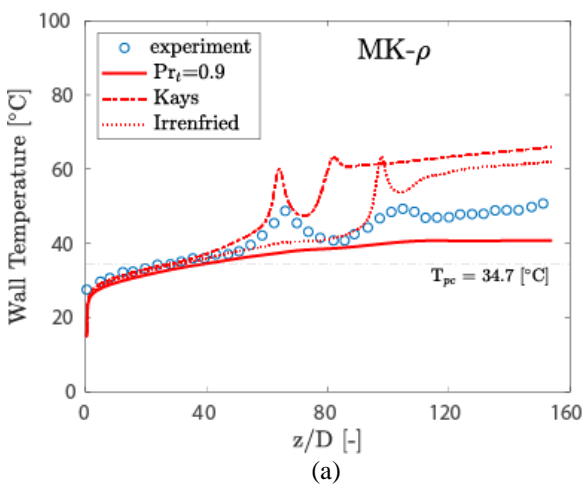


Figure 6. Wall temperature distribution as a function of the pipe stream-wise distance (a) $q'' = 23 \text{ kW/m}^2$ calculated with MK- ρ and (b) $q'' = 30 \text{ kW/m}^2$ calculated with SST compared to experiments [17, 18]

The turbulent Prandtl number approach is quantitatively unsuccessful when buoyancy effects cannot be neglected. Due to the influence of buoyancy and the development of heat deterioration, an inflection point develops in the streamwise velocity profile, but not in the temperature field [10, 22]. In such a case, Pr_t will tend to infinity (see definition in section 3.2). Therefore, for a better approximation of the heat transfer in a supercritical flow with heat transfer deterioration, the turbulent heat flux should be modelled with an alternative method, for example with the turbulent thermal diffusivity [13, 23].

5. CONCLUSION

This paper analyzes different models to predict the heat transfer of supercritical CO_2 flowing upwards in a pipe at conditions with and without heat transfer deterioration. The results are compared with experiments from literature.

Three different turbulent models with and without density correction — as proposed in our previous study [2] — are analyzed. Most of these turbulence models accurately predict heat transfer in the absence of heat transfer deterioration; the standard Myong and Kasagi and the modified Menter's $k - \omega$ SST models are the exceptions. However, heat transfer deterioration cannot be predicted by the investigated turbulence models. For this reason, we investigated the influence of the turbulent Prandtl number on the heat transfer for conditions when heat transfer deterioration occurs. Two different algebraic models for the turbulent Prandtl number are coupled with the turbulence models. The results obtained showed that the algebraic Prandtl number models — derived for constant property flows — gave encouraging results; they are able to quantify heat deterioration. However, the calculated wall temperature is quantitatively inaccurate. Future works will include models of the turbulent thermal diffusivity for the turbulent heat flux to predict the heat transfer of supercritical CO_2 flowing upwards in a pipe at conditions with heat transfer deterioration

NOMENCLATURE

ACRONYMS

DNS	Directed numerical simulation
EOS	Equation of State
MK	Myong-Kasagi (eddy viscosity model)
RANS	Reynolds-Averaged Navier-Stokes
SA	Spalart-Allmaras (eddy viscosity model)
SEV	Standard eddy viscosity model
SLS	Semi-local scaling
SST	Shear stress transport (eddy viscosity model)
TKE	Turbulent kinetic energy

SYMBOLS

c_p	specific heat at constant pressure
D	pipe diameter
Fr	Froude number
g	gravity
G	mass flux
G_k	Buoyancy production of turbulent kinetic energy

H	specific enthalpy
k	turbulent kinetic energy
N	number of discretization cells
p	pressure
Pe_t	turbulent Peclet number
P_k	Production of turbulent kinetic energy
Pr	Prandtl number
Pr_t	turbulent Prandtl number
q''	heat flux
r	wall-normal length
Re_τ	friction Reynolds number (locally scaled)
Re_τ^*	friction Reynolds number (semi-locally scaled)
S_{ij}	mean rate of strain tensor
T	temperature
T_τ	turbulent time scale
u	velocity
u_τ	friction velocity (locally scaled)
u_τ^*	friction velocity (semi-locally scaled)
y^+	Scaled wall distance (locally scaled)
y^*	Scaled wall all distance (semi-locally scaled)
z	stream-wise length

GREEK

β_T	thermal expansion coefficient
δ_{ij}	Kronecker delta ($\delta_{ij}=0$ if $i \neq j$ and $\delta_{ij}=1$ if $i = j$)
λ	thermal conductivity
ε	dissipation rate of k
ρ	density
τ	shear stress
μ	viscosity
μ_τ	eddy viscosity
σ_k	constant of the eddy viscosity model
ω	specific dissipation rate of k

SUBSCRIPTS

0	inflow
cr	critical
r	wall-normal direction
t	turbulent
w	wall
z	stream-wise direction

SUPERSCRIPTS/ACCENTS/OPERATORS

ϕ^*	dimensional quantity
ϕ	locally scaled quantity
$\hat{\phi}$	semi-locally scaled quantity
$\langle \phi \rangle$	Reynolds averaging
ϕ'	Reynolds fluctuation
$\{\phi\}$	Favre averaging
ϕ''	Favre fluctuation

ACKNOWLEDGEMENTS

The authors thank the Netherlands Organization for Scientific Research (NWO) who partially funded this research through the grant with project number 14711.

REFERENCES

- [1] He, W.S. Kim, J.H. Bae, Assessment of performance of turbulence models in predicting supercritical pressure heat transfer in a vertical tube, In *International Journal of Heat and Mass Transfer*, Volume 51, Issues 19–20, 2008, Pages 4659-4675.
- [2] G. J. Otero Rodriguez, A. Patel, R. Diez Sanhueza, and R. Pecnik, Turbulence modelling for flows with strong variations in thermo-physical properties. In *International Journal of Heat and Fluid Flow*, 73, 2018.
- [3] J. Dyreby, Modeling the supercritical Carbon Dioxide Brayton Cycle with Recompression, PhD Thesis, University of Wisconsin, Madison (2014).
- [4] L.F. González-Portillo, J. Muñoz-Antón, J.M. Martínez-Val, Thermodynamic mapping of power cycles working around the critical point, *Energy Convers. Manag.* 192 (2019) pp. 359-373.
- [5] Neises, T. and Turchi, C. A comparison of supercritical carbon dioxide power cycle configuration with an emphasis on CSP applications, *Energy Procedia* (2014), 49 1187-1196.
- [6] I. Pioro, S. Mokry, Heat Transfer to fluids at supercritical pressure, in A. Belmiloudi (Ed.), *Theoretical Analysis, Experimental Investigations and industrial systems*, IntechOpen, 2011, pp. 481-504.
- [7] Fages, Jacques, et al. "Particle generation for pharmaceutical applications using supercritical fluid technology." *Powder Technology* 141.3 (2004): 219-226.
- [8] J. D. Jackson, Supercritical heat transfer, in: *A-to-Z Guide to Thermo-dynamics, Heat and Mass transfer, and Fluids engineering*, Vol, V, Begellhouse, 1997.
- [9] J. H. Bae, J. Y. Yoo, and H. Choi. Direct numerical simulation of turbulent supercritical with heat transfer, *Journal of Physics of Fluids*, (April), 2005.
- [10] H. Nemati, A. Patel, B.J. Boersma, R. Pecnik, Mean statistics of a heated turbulent pipe flow at supercritical pressure, *International Journal of Heat and Mass transfer*, 83 (2015) 741-752.
- [11] W. M. Kays, Turbulent Prandtl number where are we? *Journal of Heat Transfer* 116 (2) (1994) 284-295.
- [12] C. Irrenfried, H. Steiner, DNS based analytical p-function model for RANS with heat transfer at high Prandtl numbers. *International Journal of Heat and Fluid flow*, 66 (2017) 217-255.
- [13] G. Zhang, H. Zhang, H. Gu, Y. Yang, X. Cheng, Experimental and numerical investigation of turbulent convective heat transfer deterioration of supercritical water in vertical tube, *Nuclear Engineering and Design* 248 (2012) 226-237.
- [14] N. Myong, H.K. and Kasagi. A new Approach to the Improvement of k-ε turbulence model for wall-bounded shear flows. *JSME*, 33(2), 1990.
- [15] F. R. Menter. Zonal Two Equation k-ω, Turbulence Models for Aerodynamic Flows. AIAA paper, page 2906, 1993. doi: 10.2514/6.1993-2906.
- [16] A. Spalart, S. Allmaras. A One-Equation Turbulence model. doi: 10.2514/6.1992-439.
- [17] Y.Y. Bae, H. Y. Kim, D. J. Kang, Forced and mixed convection heat transfer to supercritical CO₂ vertically flowing in a uniformly heated circular tubes. In *Experimental Thermal and Fluid Science*, 34 (8), 2010, pages 1295-1308.
- [18] J.K. Kim, H.K. Jeon, J. Y. Yoo, J.S. Lee, Experimental study on heat transfer characteristics of turbulent supercritical flow in vertical circular/ non-circular tubes, in the 11th International Topical Meeting on Nuclear Reactor Thermal-Hydraulics, 2005.
- [19] O. Kunz and W. Wagner. The gerg-2008 wide-range equation of state for natural gases and other mixtures: an expansion of gerg-2004. *Journal of chemical & engineering data*, 57(11): 3032-3091, 2012.
- [20] P. Huang, P. G., Coleman, G. N., Bradshaw. Compressible Turbulent channel flows, DNS results and modeling. *JFM*, (1995): 185-218, 1995.
- [21] A. Pecnik, R., Patel. Scaling and Modelling of turbulence in variable property channel, *Journal of fluid Mechanics* 2017.
- [22] H. Nemati. Direct Numerical Simulation of turbulent heat transfer to fluids at supercritical pressures (Doctoral dissertation), Retrieved from the library's database of the Delft University of Technology, 2016.
- [23] Kenjereš, S., S. B. Gunarjjo, and K. Hanjalić. "Contribution to elliptic relaxation modelling of turbulent natural and mixed convection." *International Journal of Heat and Fluid Flow* 26.4 (2005): 569-586.

DIRECT NUMERICAL SIMULATION OF FLOW AND HEAT TRANSFER WITHIN CHANNELS OF A SUPERCRITICAL CO₂ COOLER

Eckart Laurien*

Institute of Nuclear Technology and Energy Systems,
University of Stuttgart
Stuttgart, Germany
Email: Laurien@ike.uni-stuttgart.de

Sandeep Pandey

Institute of Nuclear Technology and Energy Systems,
University of Stuttgart
Stuttgart, Germany
Email: Pandey@ike.uni-stuttgart.de

ABSTRACT

The flow and heat transfer of supercritical CO₂ within representative channels of the cooler (condenser) of a proposed Brayton Cycle is investigated using Direct Numerical Simulation (DNS). The DNS method is based on the temporal and spatial integration of the fundamental conservation equations of motion and energy, the Navier Stokes Equations. Unlike other methods the DNS does not require a turbulence model, because all scales of the turbulence structures are numerically resolved on a very fine mesh. The method is limited to low Reynolds numbers and is therefore performed only for a low mass flux density of 53.87 kg/m²s. It requires the use of a High-Performance Computer Cray-XC 40. We have performed various DNS's of cooled circular pipes with a diameter of 2 mm and a length up to 60 diameters at 80 bars. The considered bulk temperature range between 69°C and 32°C is equivalent to the operational range of the cooler of the reference power cycle. The DNS wall-temperature data for two cases with different wall heat fluxes are smoothed and fitted with 3rd-order polynomials to constitute a practical prediction method for the wall heat flux at any given wall temperature based on interpolation. Under the assumption of a wall temperature of 25°C our results for the cooling wall heat flux are compared to existing empirical Nusselt correlations in order to demonstrate the differences of the various prediction methods. An attempt is made to scale our results to higher mass fluxes up to 2000 kg/m²s and the influence of buoyancy on this scaling method is discussed. Finally, the minimum required length of the cooler at a given wall temperature of 25°C is estimated using both the existing correlations as well as the present DNS-based prediction method. It is found, that predictions using these methods differ by up to a factor of two! None of the existing correlation agrees completely with our DNS results but a recommendation about the best correlation for future cooler design is given.

1 INTRODUCTION

1.1 MOTIVATION

Various efficient recuperative Brayton Cycles using supercritical carbon dioxide (sCO₂) as working fluid have been proposed by Dostal et al. [1]. Here, we use the version denoted as 'advanced design', in which the low-pressure part is at 7.7 MPa, which is only slightly above the critical pressure of 7.38 MPa. The cooler operates within a temperature range between 68.9°C (inlet) and 32°C (outlet) corresponding to an enthalpy-range between approximately 480 kJ/kg (inlet) and 300 kJ/kg (outlet). Under these conditions, the heat transfer within the individual channels of the cooler is difficult to predict and large uncertainties may arise. However, an accurate prediction of flow and heat transfer is important for the design and off-design characteristics of the cooler, because its outlet temperature influences directly the subsequent compressor.

1.2 LITERATURE STATE

In this enthalpy range the fluid properties T (temperature), ρ (density), c_p (specific heat capacity), and λ (heat conductivity) of sCO₂ undergo significant changes, **figs. 1-4** [2]

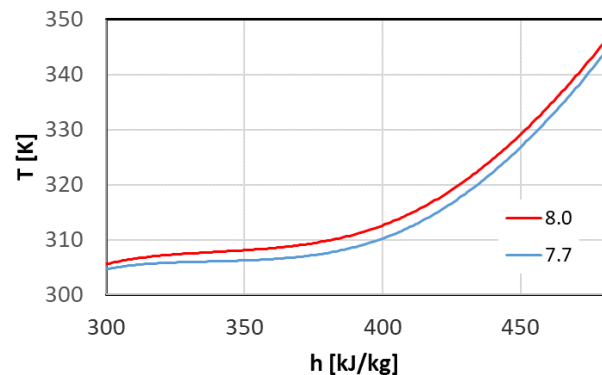


Figure 1: Temperature of sCO₂ vs. the enthalpy at two pressures in MPa.

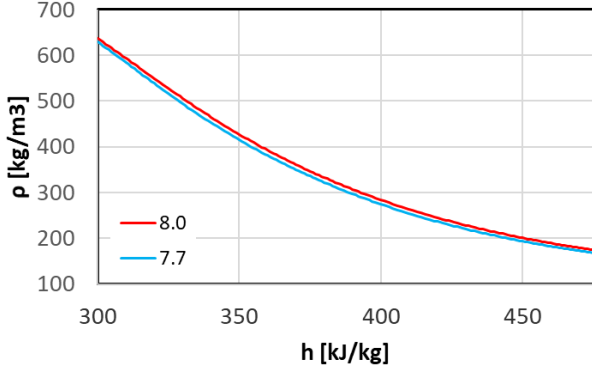


Figure 2: Same as figure 1 for the density.

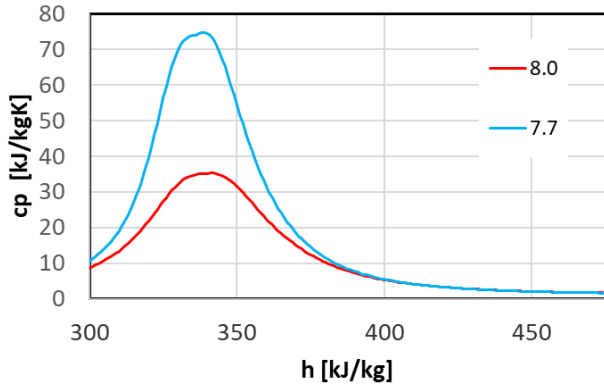


Figure 3: Same as figure 1 for the specific heat capacity.

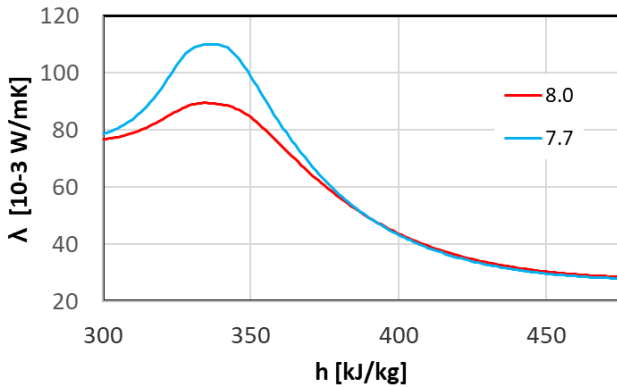


Figure 4: Same as figure 1 for the heat conductivity.

Due to the density increase the flow within the cooler channels of a compact heat exchanger experiences a drastical deceleration along the flow direction, which is from right to left in all figures throughout this paper. The turbulent heat transfer under these conditions is typically estimated or predicted by experimentally derived Nusselt correlations, which take the variable properties of sCO₂ but no buoyancy into account, see [3]. It is well known that significant deviations between the results of various correlations occur [4], leaving uncertainty about their accuracy and validity during design. However, with the Direct Numerical Simulation (DNS) a new powerful

investigation method of turbulent flows has recently become available to investigate and predict the turbulent heat transfer of sCO₂ [5-8]. It is based on the temporal and spacial numerical integration of the fundamental three-dimensional conservation equations of mass, momentum and energy, known as the Navier Stokes Equations. Unlike other numerical simulation methods the DNS does not require a turbulence model, because even the smallest scales of the turbulence structures are numerically resolved on a very fine mesh. This method is able to provide useful new information about the unsteady, turbulent velocity and temperature behaviour in a turbulent supercritical flow. Furthermore, it provides physically-based insight into the behavior of any flow quantity, which may be important in the design process.

1.2 AIM OF THIS WORK

In the present paper Direct Numerical Simulation is used to investigate the physical behaviour of flow turbulence in channels with a circular cross section under the cooler conditions of the present cycle. A practical interpolation method to predict the wall temperature for any given wall heat flux, or vice versa, is derived from our simulation. Its results are compared to empirical heat-transfer correlations. Thus, we aim to provide guidelines about the capabilities and uncertainties of existing heat transfer correlations for practical cooler design. Finally, the calculation of the minimum required length of the cooler under given wall-temperature conditions is taken as an example to demonstrate the uncertainties. A recommendation about correlations, which are feasible for further calculations, is given.

2 SIMULATION MODEL

Direct Numerical Simulation (DNS) is based on the numerical integration of the fundamental conservation equations of mass, momentum and energy (Navier-Stokes Equations, NSE) within a three-dimensional integration domain, representing the flow field. Due to the absence of a turbulence model, a turbulent flow can only be simulated if all turbulent length and time scales, i.e. the motion and development of both the large and the small turbulent eddies, are numerically resolved. This leads to fine numerical grids, here 14.7 million cells, and small timesteps of the simulation. From the unsteady simulation results, many interesting local flow quantities can be derived by 3D visualization and statistical postprocessing. We have employed the low Mach number Navier-Stokes equations, in which it is assumed that during the heat transfer at supercritical pressure, the compressibility effects due to acoustic interactions and pressure changes can be decoupled from thermal interactions.

In eq. (1) the time is t , the quantities x_i and u_i ($i,j=1,2,3$) are Cartesian coordinates and velocity components. As the properties, we have the viscosity $\mu(h)$, the density $\rho(h)$, and the thermal conductivity $\lambda(h)$. The local pressure is p , and the temperature $T(h)$, where h the specific enthalpy. The unit vector in axial direction e_{ax} can be 1 (upward flow), -1 (downward flow) or zero (no gravity), with $g = 9.81 \text{ kg/m}^2$. δ_{ij} is the Kronecker operator (1 for $i=j$ or 0 for $i \neq j$). The system represents the local,

instantaneous conservation of mass, momentum and enthalpy of a turbulent flow

$$\begin{aligned} \frac{\partial \rho}{\partial t} + \frac{\partial (\rho u_j)}{\partial x_j} &= 0 \\ \frac{\partial (\rho u_i)}{\partial t} + \frac{\partial (\rho u_i u_j)}{\partial x_j} &= \\ \rho g e_{ax} - \frac{\partial p}{\partial x_i} + \frac{\partial}{\partial x_j} \mu \left(\frac{\partial u_i}{\partial x_j} + \frac{\partial u_j}{\partial x_i} - \frac{2}{3} \delta_{ij} \frac{\partial u_k}{\partial x_k} \right) & \\ \frac{\partial (\rho h)}{\partial t} + \frac{\partial (\rho u_j h)}{\partial x_j} &= \frac{\partial}{\partial x_j} \lambda \frac{\partial T}{\partial x_j} \end{aligned} \quad (1)$$

The integration domain of our simulation model [9-10] is shown in **fig. 5**. It covers the region within a straight circular pipe with diameter $D=2\text{ mm}$ and length L up to $60D$. In this domain, the above NSE are integrated by the finite-volume method.

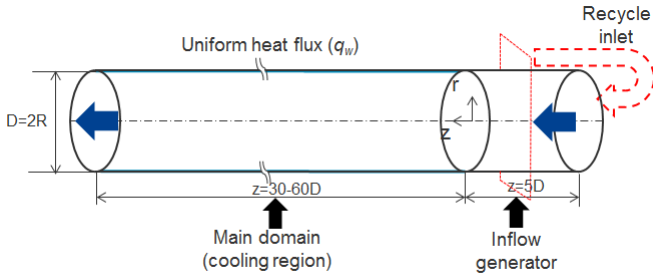


Figure 5: Integration domain and boundary conditions.

As boundary conditions, a flow of given mass flow rate G is imposed by adjusted pressure values at the flow inlet (right in **fig. 5**) and outlet (left). The pressure at the inlet is 8 MPa. The inlet temperature T_{in} is prescribed to fit cooler-relevant conditions. The wall is cooled with a given heat-flux density q_w , except within a short adiabatic inlet section to allow for the development of turbulence before cooling is applied. The fluid properties are determined locally as functions of the enthalpy h . As part of the NSE, gravity is defined such that the flow is either upward or downward, denoted as ‘mixed convection’. An artificial case without gravity is denoted as ‘forced’. Turbulence develops under the influence of shear, deceleration, and buoyancy. The processed data from these simulations are available online¹.

3.1 PHYSICAL INTERPRETATION OF RESULTS

We have investigated the physical aspects of turbulence development under wall-cooling conditions by an analysis of the small-scale flow structures [11-12]. The simulation results show the impaired heat transfer during downward flow and an enhanced heat transfer during the upward flow, contrary to the heating of sCO_2 [5-8]. In the downward flow, heat transfer is deteriorated initially but soon enough a heat transfer recovery was observed (see **fig. 6**). The main reason for deteriorated heat

transfer is the reduction in turbulence until $z=20D$ in the downward flow due to the adverse effects of the body force as a result of buoyancy as evident from **fig. 7**, which shows the instantaneous mass-flux streaks in the near wall region. The turbulent streaks were visualized by the deviation from their temporal average. The formation and breakdown of streaks can be observed in the inlet section ($z=0-5D$).

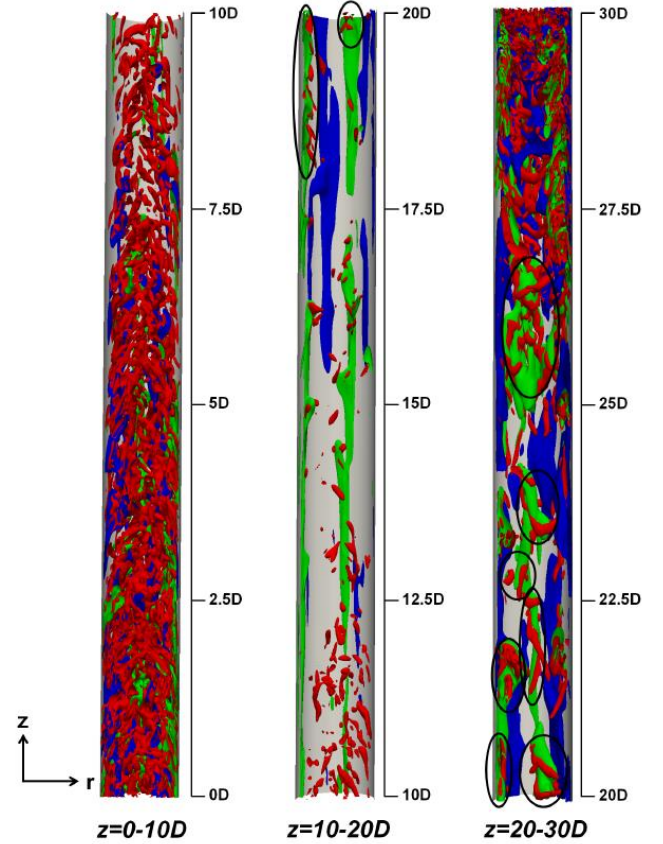


Figure 6: Iso-surfaces of streaks and vortex structure along the pipe for downward flow; blue: low speed streaks; green: high speed streaks; red: λ_2 vortex criterion.

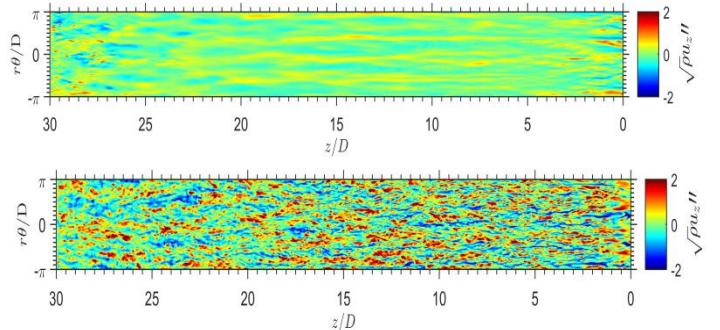


Figure 7: Visualization of the instantaneous streaks for downward (top figure) and upward (bottom figure) flow at a wall normal location unwrapped at $2r/D=0.95$ ($y^+=5.5$)

¹ At: <https://www.ike.uni-stuttgart.de/forschung/sco2/dns/>

In the first $5D$ section, streaks start stretching close to the wall and this elongation later spreads to the bulk region. Moreover, the intensity of the streaks decreases significantly. The low-speed streaks disappear from the flow in the deteriorated heat transfer regime ($z=10D-22D$). Additionally, the high-speed streaks elongate, particularly in the streamwise direction indicating ‘rod-like’-turbulence structures in the near-wall area for deteriorated heat transfer. The high-speed streaks become intense in their magnitude and ultimately start breaking down into smaller scales. The low speed streaks reappear after $z=22D$ and hinder the further growth of the high-speed streaks. Both high and low speed streaks are present in the recovery zone in the near-wall region.

Fig. 6 shows the iso-surfaces of low and high speed streaks along with the iso-surface of a vortex criterion (sometimes denoted as λ_2) to visualize these and other coherent turbulent structures. It starts reducing in the downstream direction and shifts away from the wall. The low-speed streaks are suppressed and the intensity of the coherent structure is reduced significantly. Moreover, high-speed streaks survive in the flow of the deteriorated heat transfer regime and are stretched in the streamwise direction in the near-wall region as observed earlier. After the reappearance of additional low-speed streaks at $z=15D$, the λ_2 vortex also starts increasing and interestingly the coherent structures are superimposed mainly on the high-speed streaks as highlighted with black circles.

Contrary to downward flow, the upward flow does not exhibit the elongated streaks in streamwise direction. Here, both low and high speed streaks remain in the flow throughout the pipe at all three depicted locations (refer **fig. 7**). Due to buoyancy and deceleration effects, the intensity of these streaks also increases in the streamwise direction. These streaks also widen in the circumferential direction as compared to downward flow. Both low and high streaks are more intense in the upward flow.

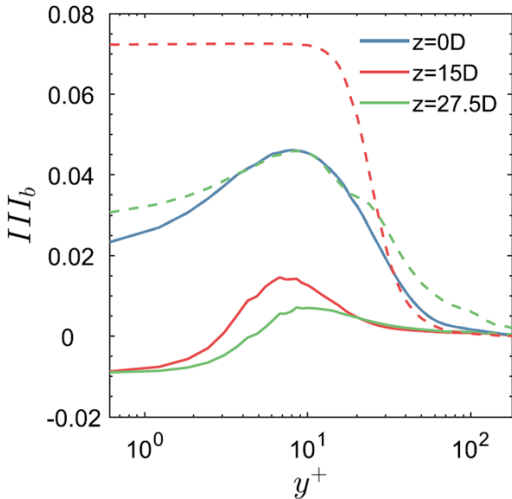


Figure 8: Radial distribution of III_b ; solid lines: upward flow and dashed line: downward flow

Figure 8 shows the third invariant of Reynolds stress anisotropy tensor ($III_b = b_{ij}b_{jk}b_{ki}/3$, where b_{ij} is the Reynolds stress anisotropy

tensor). It carries information about the nature of the anisotropy. In [10] we have presented it along the wall-normal direction at different streamwise locations in the ‘Lumley-Trirangle’. The third invariant has a negative value for the disk like structure (oblate structure) of turbulence and a positive value when the turbulence has the rod-like structure (prolate structure). In case of upward flow, third invariant becomes negative close to the wall and it indicates that turbulence structure is becoming disk-like in which only two principal stresses have significant magnitudes. Due to this disk-like feature, all turbulence structures are stretched in two directions and squeezed in the third direction. As expected, the downward flow has a completely different turbulence close to the wall compared to the upward flow. At $z = 15D$, the third invariant has a positive value which indicates, that turbulence became rod-like, i.e., elongated in one direction only. A transition back to the normal state can be seen at $z = 27.5D$ where the turbulence recovery was observed. The turbulent state remains anisotropic in the near-wall region, while only at the center of the pipe, turbulence becomes isotropic. This explains why the flow is difficult to model.

3.2 WALL QUANTITIES

In **figs. 9 and 10** the wall temperature of simulations with $G = 53.8 \text{ kg/m}^2\text{s}$ and $q_w=30.87 \text{ W/m}^2$ (denoted as low heat flux) or $q_w=61.74 \text{ W/m}^2$ (denoted as high heat flux) are presented for both upward and downward flow in the cooler range of the bulk enthalpie

$$h_b = h_{in} - \frac{q_w}{G} \frac{z}{D}, \quad (2)$$

where h_{in} is the enthalpy at the inlet position $z=0$, where the cooling begins. The bulk enthalpy represents at any axial position z the energy content in a flow.

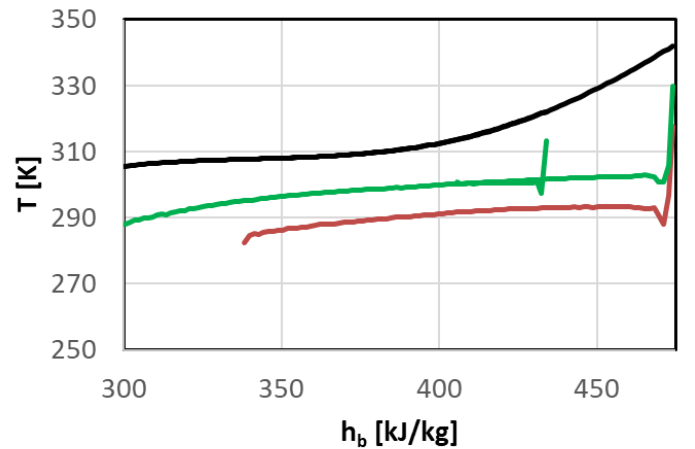


Figure 9: Upward flow with $G = 53.87 \text{ kg/m}^2\text{s}$. Bulk temperature (black) and wall temperature for low (green) and high wall heat flux (brown) vs. the enthalpy h .

For the low heat flux two simulations with different inlet temperatures 342 K~69°C and 322 K are presented, producing an overlap region, where the flow is not fully developed.

The heat transfer is enhanced by buoyancy in the upward flow case compared to the downward flow case due to the unstable thermal stratification (light below heavy fluid) and the associated turbulence production. The forced convection, no gravity, case for the same parameters is presented in fig. 11.

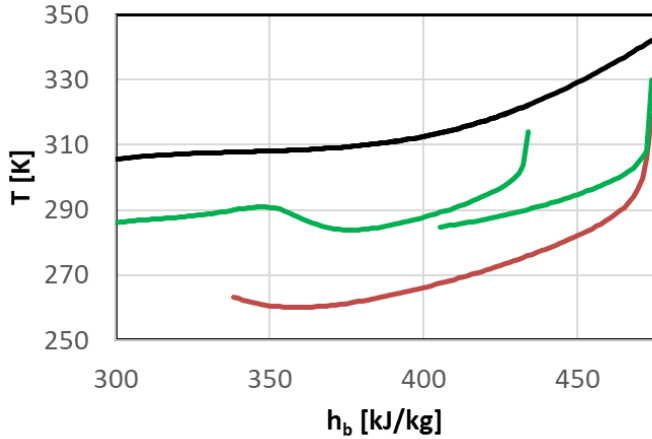


Figure 10: Same as the previous figure for downward flow.

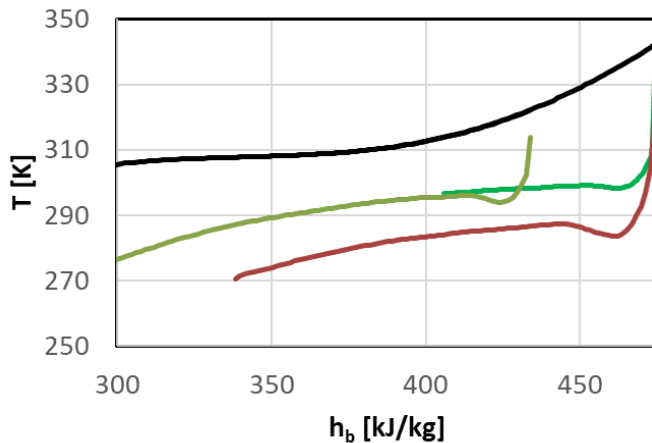


Figure 11: Same as the previous figure for the case without gravity (forced convection case).

This can be explained by the increased (liquid-like) viscosity near the wall when the larger heating is applied.

As a DNS result not only the wall temperature but also the wall shear stress is obtained, presented in fig. 12 for the forced convection case. It is interesting that for the high heat flux case the wall shear stress is larger than that for the small heat flux case.

The no-gravity case does not exist physically at this mass flux. However, for the purpose of extrapolation to higher mass fluxes it becomes relevant, see below. The small kink at the end of the DNS domain, also observed in fig. 9, is due to a low-range

upstream influence of the imperfect constant-pressure outflow boundary condition.

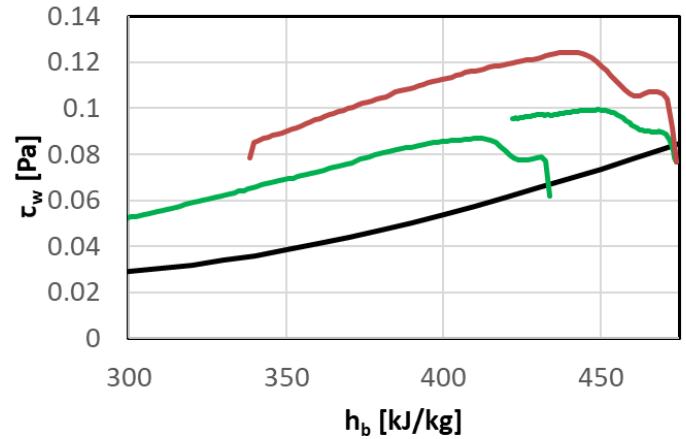


Figure 12: The wall shear stress for forced convection flow with $G = 53.87 \text{ kg/m}^2\text{s}$. For low (green) and high wall heat flux (brown) vs. the enthalpy h . The constant-property value is shown for comparison (black).

3.3 POLYNOMIAL APPROXIMATION

In order to make our DNS results applicable to engineering analysis, we have approximated their wall temperature by least-squares polynomial fits, see figs. 13-15. Strictly, a functional fit is only meaningful, if the flow can be treated locally, or in other words, regarded as ‘fully developed’. As this is not the case under some conditions, we have to make this assumption as an approximation! All regions in which we subjectively have classified the flow as non-fully developed have therefore been removed ‘by hand’ from our data before the polynomial fit was made. This leaves some gaps in the data, which were bridged by the polynomials.

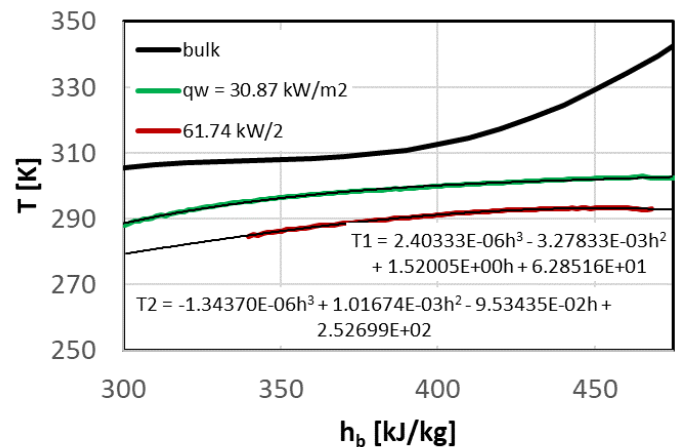


Figure 13: Polynomial fits of the wall temperature, upward flow.

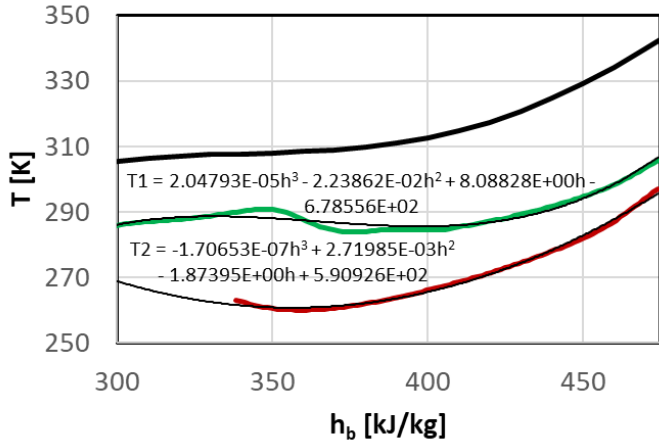


Figure 14: Same as the previous figure for downward flow.

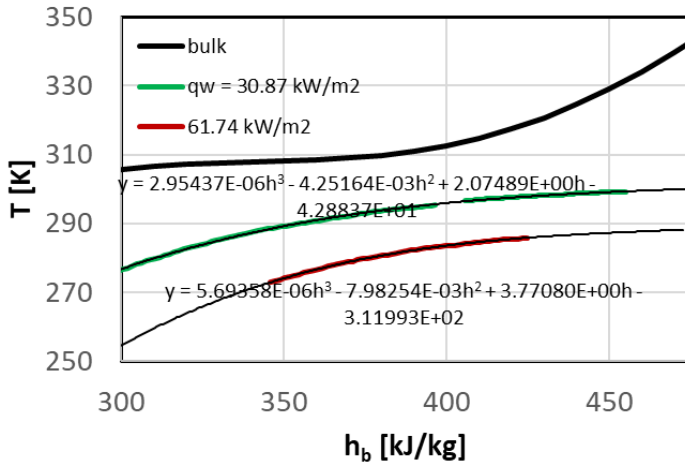


Figure 15: Same as the previous figure for flow without gravity influence (forced flow).

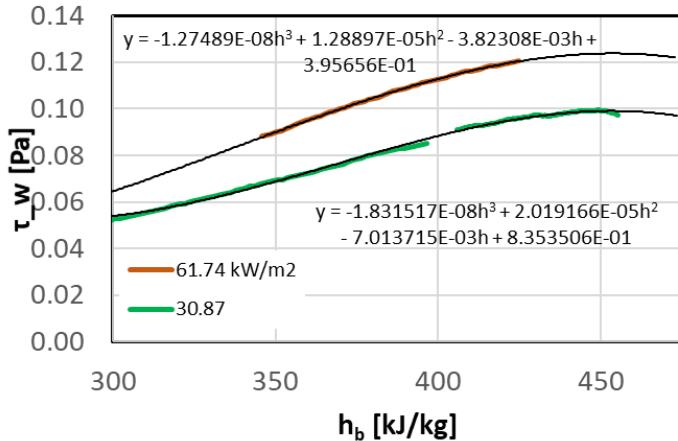


Figure 16: Polynomial fits of wall shear stress for forced flow.

At each enthalpy station, three values of the wall temperature are available: The bulk temperature corresponding

to no wall heating, and two temperatures for the two heating rates. From these data the wall heat flux for any given wall temperature can be obtained by piecewise linear interpolation. Extrapolation should be avoided.

In order to demonstrate, that this method is also feasible for the wall shear stress, we present the curve fits of **fig. 16** for the forced convection case. As the third data point the constant-property value of the wall shear stress can be used. However, in this paper the wall shear stress is not investigated further.

The range of validity of our method is:

- pipe diameter is 2 mm
- pressure is close to 80 bars
- mass flux density is $G = 53.78 \text{ kg/m}^2\text{s}$
- enthalpy is in the range between 300 and 480 kJ/kg

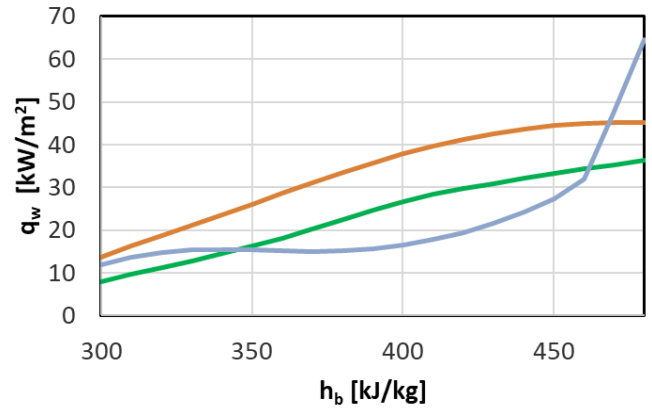


Figure 17: Wall heat flux obtained with our interpolation method at $G = 53.78 \text{ kg/m}^2\text{s}$ for an assumed wall temperature of 25°C , red: upward, blue: downward, green: forced flow

Next, this interpolation method is used for some practical calculations related to the cooler. Let us make the approximation, that the wall temperature of the (primary) sCO_2 -side of the cooler is $T_w = 25^\circ\text{C}$. We may regard our investigation as a limiting case, because this can in practice be achieved only approximately by a high mass flux of the secondary side with a fluid (e.g. water) of that temperature. With this assumption, the wall heat flux of a representative channel of the cooler can be determined by our interpolation method as a function of the enthalpy, see **fig. 17**.

From the figure it becomes obvious that the upward flow is favorable because leads to the highest heat flux over almost the entire enthalpy range due to buoyancy production of turbulence. However, this result has little practical value, because in practice the mass flux G will be much higher (up to $2000 \text{ kg/m}^2\text{s}$) and the influence of buoyancy may disappear with higher mass flux.

4.1 SCALING TO HIGHER MASS FLUX

We can expect that the effect of buoyancy decreases with higher mass flux. Therefore, the question must be investigated next, for which mass flux buoyancy can be neglected.

A buoyancy parameter

$$Bo^* = \frac{Gr^*}{Re^{3.425} Pr^{0.8}} \quad (3)$$

has been defined in [13] for gases on the basis of the Reynolds- und Grashof numbers

$$Re = \frac{GD}{\mu_b} \quad ; \quad Gr^* = \frac{g\beta_b \rho_b^2 q_w D^4}{\lambda_b \mu_b^2} \quad (4)$$

This parameter can be used as an indicator to determine whether buoyancy has an effect: buoyancy can be neglected if it is smaller than 10^{-6} [13]. This applies for our cooler channel cases with $G > 500 \text{ kg/m}^2\text{s}$ as shown in **fig. 18**. In the other cases buoyancy should be considered. With this information it becomes clear that the forced convection case is important for further consideration.

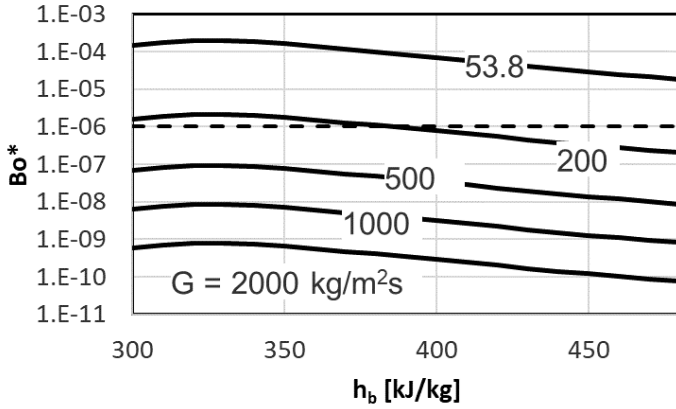


Figure 18: Buoyancy parameter Bo^* as a function of the bulk enthalpy for various mass-flux densities G under the assumption of $T_w = 25^\circ\text{C}$, - - - limiting value.

4.2 COMPARISON TO EMPIRICAL CORRELATIONS

In the following we will assume, that buoyancy has no effect. The heat transfer of such forced convection has been approximated with various empirical correlations given in [3], which are compared for $G = 53.78 \text{ kg/m}^2\text{s}$ in **fig. 19** with our forced convection case. None of the existing correlation agrees exactly with our DNS results but a recommendation, which correlation can be used for practical calculations is given as follows:

- Bringer and Smith gives good prediction for a low enthalpy range but underestimate it if $h > 350 \text{ kJ/kg}$,
- Pitla et al. overestimate the heat flux drastically, in the region $h > 400$,
- Krasnochekov et al. and Baskov et al. overestimate the heat flux drastically,
- Jackson's as well as Mokry-Poiro's correlation have been developed for wall heating but for cooling they underestimated the heat flux only slightly. They can be recommended for further use.

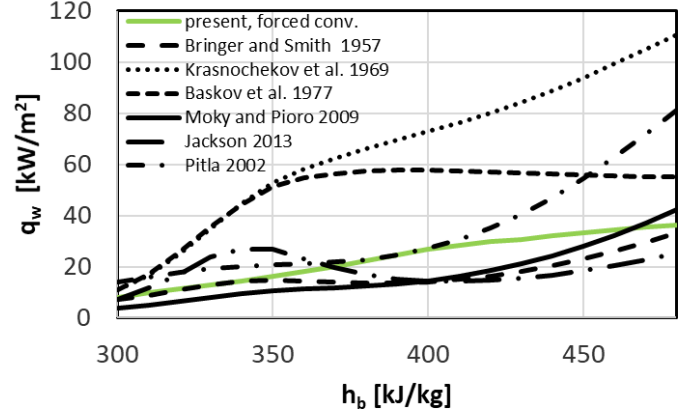


Figure 19: Wall heat flux at $G = 53.78 \text{ kg/m}^2\text{K}$ for various correlations and our DNS results for forced convection (green).

4.3 SCALING TO HIGHER MASS FLUX

A DNS for higher mass flux cannot be performed due to the extremely high numerical effort, that would be necessary. Therefore, we make an attempt to develop a scaling method. **Table 1** presents a list of the exponents used in the Nusselt correlations of the form

$$Nu_b = \frac{q_w D}{(T_b - T_w) \lambda_b} = C Re_b^n Pr_b^m \left(\frac{\rho_b}{\rho_w} \right)^p \left(\frac{\mu_b}{\mu_w} \right)^s \quad (5)$$

If the mass flux density G changes only the Reynolds number will change and all other quantities remain constant due to our assumption of a constant wall temperature. **Table 1** gives an overview of n used by the correlations given in [3]. Values are in the range $0.55 < n < 0.82$.

A scaling method relates two mass fluxes G_1 and G_2 to the two corresponding heat fluxes q_{w1} and q_{w2} using a power law with the exponent n

$$\frac{q_{w2}}{q_{w1}} = \left(\frac{G_2}{G_1} \right)^n \quad (6)$$

Table 1: The exponent n in the correlations given in [3]

Authors	year	n
Bringer & Smith	1957	0.77
Yoon et al.	2003	0.69
Son and Park	2006	0.55
Oh and Son	2010	0.7
Jackson	2002	0.82
Huai and Koyama	2007	0.8
Lee et al.	2013	0.56
Saltanov	2015	0.823
Simoies et al.	2008	0.8

As case 1 the above presented simulation case with $G = 53.78 \text{ kg/m}^2\text{s}$ is used. Case 2 is a case with an arbitrary higher heat and mass flux. No theoretical, value of n exists. In the following we use $n = 0.55$ and $n = 0.8$ in order to provide some guidelines. The same deviations as above are observed for high mass flux $G = 1000 \text{ kg/m}^2\text{s}$, **fig. 20**.

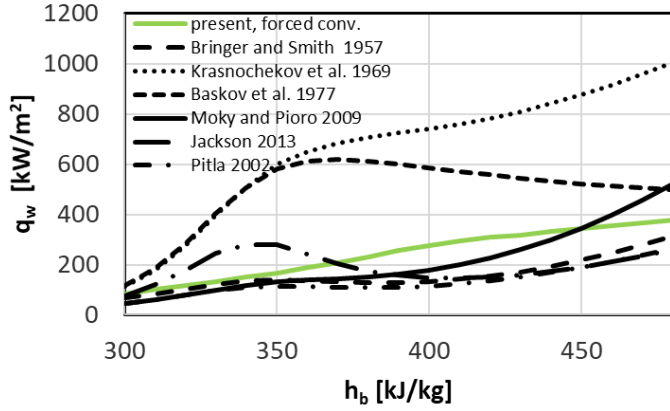


Figure 20: Wall heat flux at $G = 1000 \text{ kg/m}^2\text{s}$ (right), for various correlations and our DNS results, scaled with $n = 0.8$, for forced convection (green).

4.4 MINIMUM LENGTH OF THE COOLER

The minimum length L of the heat exchanger, which is at least necessary to the transfer the heat necessary to cool the CO_2 to the desired outlet temperature, is

$$L = \frac{G \cdot D}{4} \int_{h_{in}}^{h_{out}} \frac{1}{q_w} dh \quad (7)$$

Numerical values are presented in **fig. 21** calculated with various correlations and the present method as a function of G . Again, large deviations between the results appear.

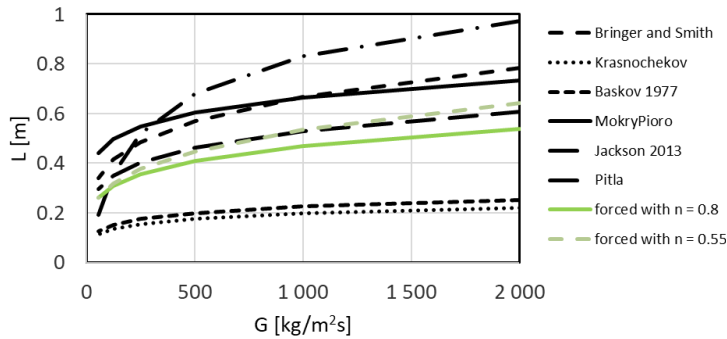


Figure 21: Minimum length L of the cooler calculated with correlations and our forced case with $n = 0.8$ and $n = 0.55$.

5. CONCLUSIONS

Direct numerical simulations have been performed to investigate the flow and heat transfer of supercritical CO_2 within representative channels of the cooler (condenser) of a proposed Brayton Cycle. The wall-temperature obtained from DNS for two cases with different wall heat fluxes are smoothed and fitted with a 3rd-order polynomials to constitute a practical prediction method for the wall heat flux at any given wall temperature based on interpolation. It is also found, that predictions of the minimum cooler length using the various methods differ by up to a factor of two! None of the existing correlation agrees completely with our DNS results but a recommendation, which correlation can be used for practical calculations is given.

NOMENCLATURE

C	-	constant in a correlation
c_p	kJ / kgK	specific heat capacity
g	m / s^2	gravity acceleration
G	$\text{kg} / \text{m}^2\text{s}$	mass flow density
Gr	-	Grashof number
D	m	pipe diameter
h	kJ / kg	specific enthalpy
L	m	minimum length of the cooler
n	-	exponent of Re in a correlation
Nu	-	Nusselt number
m	-	exponent in a correlation
p	Pa	pressure
Pr	-	Prandtl number
q_w	kW / m^2	wall heat flux
Re	-	Reynolds number
s	-	exponent in a correlation
t	s	time
T	K	temperature
u_i	m / s	velocity component
β	$1 / \text{K}$	thermal expansion coefficient
λ	W / mK	heat conductivity
μ	Pa s	dynamic viscosity
ρ	kg / m^3	density
τ_w	Pa	wall shear stress

Indices

ax	axial direction
b	bulk
in	inlet
pc	pseudo critical
w	wall

ACKNOWLEDGEMENTS

This work has been supported by the *Forschungsinstitut für Kerntechnik und Energiewandlung e.V., Stuttgart* and the *High-Performance Computer Center (HLRS) Stuttgart*.

REFERENCES

- [1] V. Dostal, M. Driscoll, and P.A. Hejzlar: Supercritical carbon dioxide cycle for next generation nuclear reactors, Tech. rep. MIT, 2004
- [2] E. Lemmon, M. Huber, and M. McLinden: NIST standard reference database 23: reference fluid thermodynamic and transport properties-REFPROP, version 9.1, 2013
- [3] L. F. Cabeza, A. de Garcia, A.I. Fernandez, and M.M. Farid: Supercritical CO₂ as heat transfer fluid: A review, *Applied Thermal Engineering* 125 (2017), 799-810
- [4] K. Brun, P. Friedman, and R. Dennis: Fundamentals and Applications of Supercritical Carbon Dioxide (sCO₂) Based Power Cycles, Elsevier, Cambridge, MA (2017)
- [5] J.H. Bae, J.Y. Yoo, and H. Choi: Direct numerical simulation of turbulent supercritical flows with heat transfer, *Phys. Fluids* 17 (10) (2005).
- [6] X. Chu, and E. Laurien, Direct numerical simulation of heated turbulent pipe flow at supercritical pressure, *J. Nucl. Eng. Radiat. Sci.* 2 (2016)
- [7] H. Nemati, A. Patel, B.J. Boersma, and R. Pecnik: Mean statistics of a heated turbulent pipe flow at supercritical pressure, *Int. J. Heat Mass Transfer* 83 (2015) 741–752
- [8] S. Pandey, X. Chu, and E. Laurien, and B. Weigand: On the Effect of Non-Uniform Body Force on Turbulence in a Channel Flow, under review.
- [9] S. Pandey, X. Chu and E. Laurien: Investigation of in-tube cooling of carbon dioxide at supercritical pressure by means of direct numerical simulation, *Int. Journal of Heat and Mass Transfer* 114, 944 – 957 (2017)
- [10] S. Pandey, E. Laurien, and X. Chu: Flow and Heat Transfer Characterization for Supercritical CO₂ During Heat Rejection, 2nd European CO₂ Conference, Essen, Germany, Aug. 30-31, 2018
- [11] S. Pandey, E. Laurien, and X. Chu: Development of direct numerical simulation database for supercritical carbon dioxide, 6th International Supercritical CO₂ Power Cycles Symposium, Pittsburgh, PA, March 27 - 29, 2018
- [12] S. Pandey, X. Chu, E. Laurien and B. Weigand: Turbulence modulation during heat rejection by a fluid at supercritical pressure, *Physics of Fluids* 30, 065105 (2018)
- [13] D.M. McEligot and J.D. Jackson: ‘Deterioration’ criteria for convective heat transfer in gas flow through non-circular ducts, *Nuclear Engineering and Design* 232 (2004), 327-333

INVESTIGATION OF A CORRELATION BASED MODEL FOR sCO₂ COMPACT HEAT EXCHANGERS

Markus Hofer*
University of Stuttgart
Stuttgart, Germany
markus.hofer@ike.uni-stuttgart.de

Michael Buck
University of Stuttgart
Stuttgart, Germany

Marcel Strätz
University of Stuttgart
Stuttgart, Germany

Jörg Starflinger
University of Stuttgart
Stuttgart, Germany

ABSTRACT

Motivated by the Fukushima accident, innovative heat removal systems for nuclear power plants are currently under investigation. One of them is the supercritical carbon dioxide (sCO₂) heat removal system, a closed Brayton cycle with sCO₂ as working fluid. ATHLET (Analysis of THERmal-hydraulics of LEaks and Transients) has been used to simulate the interaction of the heat removal system with the nuclear power plant. However, the component models need further development and validation.

In this paper, a general approach for the simulation of heat exchangers is applied to a compact heat exchanger (CHX), including the heat transfer and pressure drop correlations used in ATHLET. Based on stationary experiments of a two-plate CHX, dimensionless form loss coefficients for the sCO₂ inlet and outlet plenum are derived. In a second step, these coefficients are used as input values for a model, which solves the conservation equations for momentum and energy for a representative H₂O/sCO₂ channel pair. The results of the ATHLET simulations are in good agreement with the experiments. Compared to the mean values of the experiments, almost all simulated cases yield a deviation of less than 10 %, concerning transferred power and the pressure drop on the sCO₂-side.

INTRODUCTION

In case of a station blackout and loss of ultimate heat sink accident scenario in a boiling water reactor (BWR) or pressurized water reactor, the plant accident management strongly depends on the availability of electricity, e.g. provided by emergency diesel generators or external measures. If not available, core integrity will be violated, like in Fukushima Dachi. Such scenarios lead to the development of advanced decay heat removal systems. Since space is a limitation in existing power plants, the supercritical carbon-dioxide (sCO₂)

heat removal system “sCO₂-HeRo” was proposed [1], [2]. This system consists of a compact heat exchanger, a gas cooler, serving as the ultimate heat sink, and the turbomachinery, one compressor and a turbine mounted on one shaft. Since the turbine is generating more electricity than is used by the compressor and the electrical driven fans of the gas cooler, the system is self-propelling and self-sustaining. The excess electricity can even be used to support other accident measures. sCO₂ is selected as working fluid because of its favorable fluid properties, enabling the design of a very compact system. Moreover, sCO₂ is not combustible, non-toxic and commercially available. The design of a compact system is beneficial because it enables the reduction of material consumption and cost. In the case of the safety system, especially a compact CHX is necessary because the space in the containment of existing reactors is limited. Furthermore, for next generation power cycles reduced material consumption enables steeper transients during the operation.

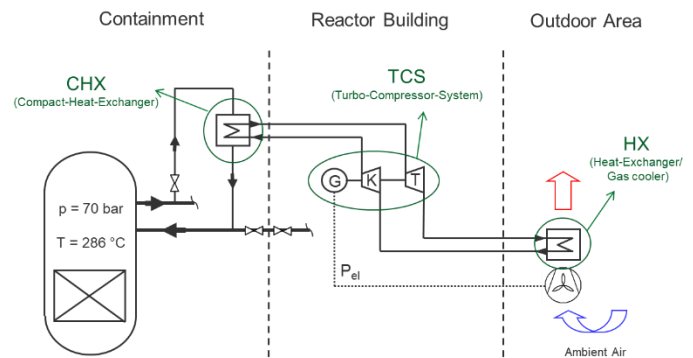


Figure 1: sCO₂ heat removal system attached to a BWR [1]

Figure 1 shows a scheme of the sCO₂-HeRo system attached to a BWR. In the case of an accident the valves, which connect

the CHX to the main steam line, open automatically. Driven by natural convection, the steam condenses in the primary side of the CHX and thereby heats the sCO₂ in the secondary side of the CHX. The pressurized and heated sCO₂ is expanded in the turbine, which drives the compressor and generates power for the fans of the gas cooler. After the turbine, the remaining heat of the sCO₂ is removed in the gas cooler to the ultimate heat sink. Finally, the sCO₂ is compressed and re-enters the CHX.

For the simulation of the thermo-hydraulic behavior of nuclear power plants, different system codes are used, e.g. CATHARE, RELAP, TRACE and ATHLET [3]. Because sCO₂ is considered as a working fluid for 4th generation reactor concepts as well as for the proposed heat removal system, work is in progress to extend these system codes for the simulation of sCO₂ power cycles [1], [4]–[6]. Venker investigated the feasibility of the sCO₂-HeRo approach in detail and implemented first extensions in the ATHLET code for the simulation of the heat removal system. Among other things, heat transfer and pressure drop correlations for sCO₂ were implemented and validated with experimental data. In the frame of the sCO₂-HeRo-project further reports and studies were published, including experiments with a two plate CHX [2], [7].

In this paper, these experimental results are used to investigate and validate a correlation-based approach to model a CHX. The extensions and first validations of the thermo-hydraulic system code ATHLET (Analysis of THERmal-hydraulics of LEaks and Transients) are summarized and discussed. Firstly, the experiments are briefly described and secondly, the modelling approach and the relevant correlations are explained in detail divided into a general, heat transfer and pressure drop section. Thirdly, the results are discussed in the same manner. In the end, the conclusion provides the most important findings and an outlook to future research activities.

EXPERIMENTS

The two-plate CHX test configuration consists of one H₂O and one sCO₂ plate, each with 15 rectangular channels. A detailed description of the set-up and the conducted experiments by using the SCARLETT test facility and a steam cycle at the IKE is given in [7]. The sCO₂ plate is schematically shown in Figure 2. The channel length is 150 mm and the length of each plenum is 13 mm, which results in a total inner length of 176 mm. The rectangular channels have a width of 2 mm and a height of 1 mm, which is also the height of both plenums. The inlet and outlet pipe of each plenum has an inner diameter of 10.2 mm and is attached perpendicular to the plate. For the H₂O side the geometries are the same. The heat transfer experiment with the CHX were performed in counter-current-flow configuration, so the H₂O and sCO₂ inlet are located at the opposite ends of the two-plate heat exchanger.

The experiments were carried out for three different sCO₂ inlet pressures, namely 9.5 MPa, 10 MPa and 11 MPa. For each inlet pressure, 12 measurements were conducted, mainly with a high H₂O mass flow rate and varying sCO₂ mass flow rates. The sCO₂ inlet temperature was between 38.8 °C and 39.6 °C and the H₂O inlet temperature between 284.8 °C and 285.6 °C. It is

assumed that the steam enters the CHX saturated, so the pressure is around 7 MPa.

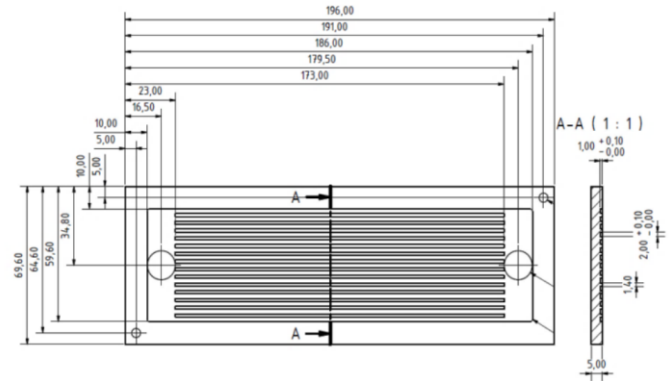


Figure 2: sCO₂ plate [7]

Case 5, which yielded the highest transferred power, is used as a reference in the results section to illustrate the simulation results. The parameters of case 5 are summarized in Table 1.

Table 1: Experimental values of case 5

	Inlet	Outlet
p_{sCO_2} in MPa	10.95	10.91
ϑ_{sCO_2} in °C	38.8	45.5
\dot{m}_{sCO_2} in g/s	36.5	
\dot{Q}_{sCO_2} in kW	1.15	
p_{H_2O} in MPa	7.03	7.02
ϑ_{H_2O} in °C	285.5	38.8
\dot{m}_{H_2O} in g/s	0.50	
\dot{Q}_{H_2O} in kW	1.30	

Deviations in the calculated transferred powers on the H₂O and sCO₂ side, which can be calculated from the experimental values of both sides, are caused by measurement uncertainties, heat losses and the fact that temperature and pressure are measured not directly at the inlet and outlet of the CHX. This also caused the equality of the sCO₂ inlet and the H₂O outlet temperature. Therefore, the simulated transferred power is compared against the mean of the experimental values.

MODELLING APPROACH

Since the CHX is only one component of the heat removal system and the interaction with the nuclear power plant will be analysed in the future the goal is to develop a fast and sufficiently accurate model. In ATHLET no specific CHX model exists. Therefore, the basic heat exchanger modelling approach was applied. Instead of modelling the entire heat exchanger, only a representative pair of channels is modelled and then scaled by the number of channels. Additionally, the pressure drop in each plenum is modeled by a form loss coefficient. In ATHLET a minimum pressure drop or gain caused by a change in the cross sectional flow area is already considered. However, the measured pressure loss is considerably higher due to the perpendicular attached tubes and the geometry of the plenum.

Therefore, additional form loss coefficients at the inlet and outlet junction of the heat exchanger are necessary. In the experiment, heat transfer also occurs in the plenum. However, due to the geometry of the plenum and the inlet effects, the amount of heat transferred in the plenum is relatively small. Therefore, the plenum is not modelled by an explicit subvolume but is reduced to a junction related pressure drop. Consequently, the length of the CHX in the simulation is equal to the channel length. In Figure 3, the nodalisation of the sCO₂ side is shown.

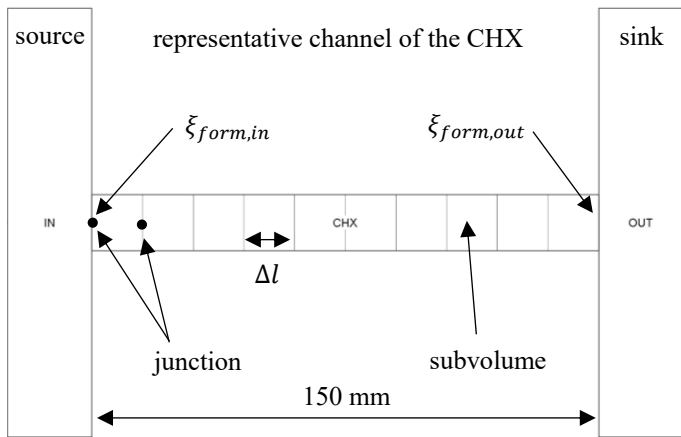


Figure 3: sCO₂ side nodalisation scheme

ATHLET distinguishes between circular channels and other geometries. Other geometries like rectangular channels geometry are characterized by flow area and hydraulic diameter. It is worth noting, that the heat transfer area can be selected independently from the channel geometry if a plate configuration is chosen. The heat transfer area of one subvolume is the product of the channel length and the plate width. The length of one subvolume is fixed by the chosen number of subvolumes but the plate width w and the plate thickness δ can be selected by the user. This plate object, as shown in Figure 4, is the connection between the sCO₂ and H₂O side. In ATHLET it also referred to as heat conduction object.

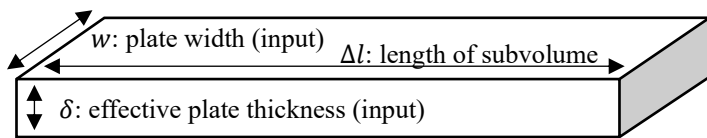


Figure 4: Plate heat conduction in ATHLET (single layer)

For this case, the appropriate plate width and the resulting heat transfer area can be selected by taking into account a few considerations. In the cross-sectional view, the width over which heat is transferred is the perimeter of the channel. However, the temperature distribution and the heat transfer are not uniform, especially for the two-plate configuration. The major part of the heat transfer occurs directly between the two channels, leading to the highest temperature difference in this region. On the opposite side of the plate, which is insulated against heat losses to the environment, the temperature difference and the

transferred power are much smaller. In Figure 5, the two-dimensional steady state temperature distribution calculated with a finite volume method inside the two-plate configuration is shown. It is assumed that the heat transfer for each channel is symmetrical. Therefore, the channel middle is located on the right border of the diagram and the middle between to channels on the left border. Since top and bottom are insulated, all boundaries are adiabatic. The symmetry assumption is only partly valid because the total number of channels is small. However, this simulation is sufficient to evaluate the effects of the non-uniform temperature distribution of this configuration. The highest temperature gradient can be observed directly between the channels. However, also the side walls and even the opposite wall contribute to the heat transfer. Therefore, the thermal resistance of the whole configuration should be considered.

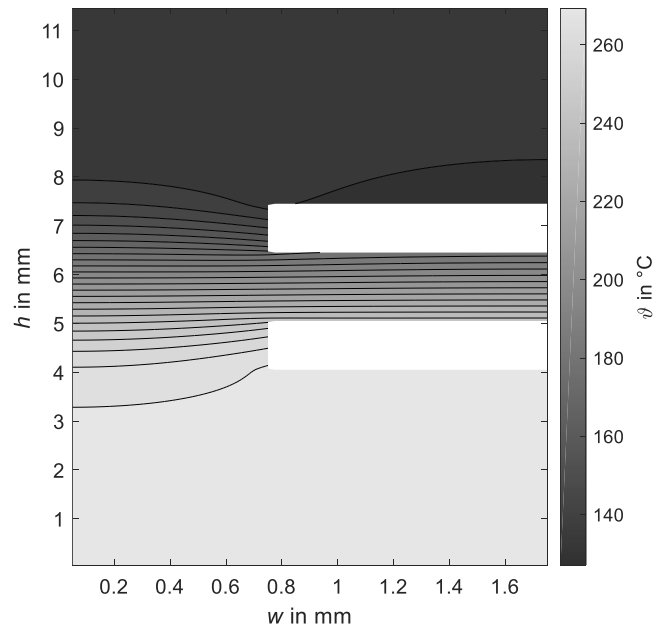


Figure 5: Temperature distribution between two half channels with adiabatic boundary conditions (not in scale)

Since the heat transfer is modelled by a simple single layer plate configuration in ATHLET, the correct thermal resistance must be specified by selecting adequate values for the plate width and thickness. As mentioned before the plate width should be the perimeter of the channel. When this parameter is fixed an effective plate thickness can be determined by comparing the thermal resistance of the simulated configuration to the simple plate configuration used in ATHLET. For the comparison the mean value of the heat transfer coefficient and the wall temperature along the channel length are calculated. Then the effective plate thickness can be determined by applying the mean values to both sides of the simple plate configuration. This calculation is conducted for various flow conditions inside the channels in order to evaluate if a constant value of δ is sufficient to describe the heat transfer characteristic of this configuration.

Graphically the effective plate thickness can be interpreted as a mean distance for the heat transfer between the two channels. The resulting value is always higher than the geometrical distance between the channels. Boundary effects like heat losses are not considered because they were assumed negligible.

Since the heat transfer coefficient is temperature dependent, its local value also varies along the channel perimeter in addition to the local value of the wall temperature. However, in ATHLET the heat transfer coefficient and the temperature difference are constant in one subvolume and, therefore, also along the channel perimeter. If these constant values are not equal to the mean values of the real configuration, then a correction factor C_{corr} is required in the equation of the transferred power \dot{Q} , given by

$$\dot{Q} = C_{corr} h A \Delta T. \quad (1)$$

Mathematically, the correction factor is the product of the correction factors of the heat transfer coefficient h and the temperature difference ΔT . The exact value of the factor depends on the set-up and on the conditions inside the channels. Its value can also be determined from the steady state heat conduction analysis. If the factor is constant, it can be included in the plate width calculation.

Heat transfer

The heat transfer coefficient h is calculated by using correlations on both sides. For the sCO₂ side, the heat transfer coefficient is calculated with the Gnielinski correlation [8], which is valid for Reynolds numbers between 2300 and 10⁶ and Prantl numbers from 0.6 to 2000. Reynolds, Prandtl and Nusselt number including the friction factor ξ can be calculated by

$$Re = \frac{\rho u d_h}{\eta}, \quad (2)$$

$$Pr = \frac{\eta c_p}{\lambda}, \quad (3)$$

$$Nu = \frac{\left(\frac{\xi}{8}\right)(Re-1000)Pr}{1+12.7\sqrt{\left(\frac{\xi}{8}\right)(Pr^{2/3}-1)}}, \quad (4)$$

$$\xi = (1.82 \log(Re) - 1.64)^{-2}. \quad (5)$$

For the proximity to the critical point, different modified correlations have been proposed. However, the best correlation must still be identified. Additionally, the conducted experiments are at least 2.1 MPa above the critical point. Moreover, the impact of a modified correlation on the overall heat transfer would be quite small, as it will be explained in the results section. Therefore, no further modified correlation was implemented on the sCO₂ side. On the H₂O side, two regimes occur, namely first film condensation and afterwards forced convection to the liquid. For the film condensation, the ATHLET correlations were improved and now the correlations given in [9], [10] are used.

The Nusselt number is calculated for the laminar and turbulent film taking into account the film Reynolds number

$$Re_f = \frac{\dot{m}_f}{\eta_f b} = \frac{(\rho u)_f (1-\varepsilon) d_h}{4\eta_f} = 0.25 Re (1-\varepsilon), \quad (6)$$

with the liquid film mass flow rate \dot{m}_f , the viscosity of the film η_f and the width of the cooling surface b . In this case, b is equal to the perimeter of the channel. Applying the common relation for the hydraulic diameter $d_h = 4A_c/U_c$, the equation can be transformed to the form implemented in ATHLET. However, it is important to note that the film Reynolds number differs by a factor of 0.25 and one minus the void fraction ε from the common definition of the Reynolds number used in ATHLET [11]. The film Reynolds number increases with increasing \dot{m}_f and decreasing ε . The correlation of the Nusselt number for the laminar film [9], [10], which dominates the heat transfer on the steam side, is given by

$$Nu_f = \frac{h_f \sqrt[3]{v_f/g}}{\lambda_f} = 0.693 \left(\frac{1-\rho_v/\rho_f}{Re_f} \right)^{1/3}. \quad (7)$$

The properties v_f , λ_f and ρ_f are determined at the film temperature, which is the average of the wall surface and fluid bulk temperature. To reduce the calculation effort, for ρ_f the density at liquid saturation is taken in ATHLET. The vapor bulk density ρ_v is calculated at the bulk temperature and g is the acceleration due to gravity. Equation 7 contains a factor $Re_f^{-1/3}$, which results in a decreasing Nusselt number for increasing \dot{m}_f , which is reasonable because the liquid film at the wall inhibits the heat transfer. The turbulent Nusselt equation is completely empirical and more complicated. In this region, the Nusselt number increases again with increasing Re_f . The laminar and turbulent equation are combined together, including a few correction factors. However, due to the small size of the channels, the heat transfer coefficient is dominated by the laminar equation.

The basic Nusselt correlation for laminar film condensation was derived analytically for steam condensing on a vertical plane and flowing down driven by gravity. Depending on the real configuration, different shear stress corrections can be applied. Since, the H₂O flows downward driven by gravity and a small circulation pump, the model for “vertical pipe, rectified flow” [9] is most applicable. However, the ATHLET CHX simulations yield the same velocity for the gas and liquid phase. Consequently, the relative velocity and the shear stress is zero and therefore the “uncorrected” equation is used. Additionally, the small size of the channels might affect the heat transfer. Since the exact contribution of small channels is unclear, the effect is neglected in this analysis for both, sCO₂ and H₂O.

The heat conduction through the plate is modeled as described in ATHLET Models and Methods [11]. The plate is modeled as a single layer and for the material properties, the built in functions of austenitic stainless steel are used. In the input the thickness of the plate must be specified. The thickness of the plate can be chosen equal to the direct distance between the

channels. However, a slightly higher value might be more realistic, because heat transfer occurs over the whole surface of the channel as mentioned before. Since the heat flow is perpendicular to the isotherms, the average conduction length is longer than the direct distance. The influence of the chosen thickness is analyzed in the results section in more detail.

Pressure drop

The occurring pressure drop on the sCO₂ side can be subdivided into the pressure drop of the inlet plenum, the channel pressure drop and the outlet plenum pressure drop. The pressure drop in the channel is derived from the Colebrook equation, which is recommended for normal pipes as well as for mini-channels [12]. The implicit correlation is approximated explicitly according to [11]. In order to calculate the channel pressure drop the wall roughness of the channel must be provided. The inlet and outlet plenum pressure drop can also be calculated with the equation used in ATHLET [11],

$$\Delta p_{plenum} = \xi_{form} \frac{\dot{m}^2}{2\rho}. \quad (8)$$

An appropriate value for the loss coefficient ξ_{form} must be given for the inlet and the outlet plenum. A single form loss is not sufficient for both plenums because the inlet and the outlet density are different depending on the amount of transferred heat. In order to determine the coefficients a single sCO₂ channel with constant heat input over the channel length was modelled in Matlab. The model solves the momentum conservation equation including the ATHLET correlations and determines the form loss coefficients by a best-fit method, minimizing the deviation between the experimental and simulated pressure drop. Instead of a constant heat input per channel length, it is also possible to implement the heat transfer and energy conservation equations to improve the best-fit method further. However, it was found that the first simple method provides good results, as shown in the results section.

RESULTS AND DISCUSSION

The correction factor for the transferred power given in Equation 1 and the effective thickness of the plate are determined by performing the two dimensional heat conduction calculations for various conditions covering the entire experimental range. For all simulated cases, the effective thickness is around 3.3 mm and the correction factor is around unity. The deviations are smaller than 6 % for both parameters. Therefore, no adaption of the plate width is necessary and it is chosen equal to the channel perimeter, which is 6 mm. The form loss coefficients for the inlet and outlet plenum, derived with Matlab, are 27.75 and 2.71, respectively. These coefficients must be divided by the square of channel cross sectional area for the use in equation 8 and in ATHLET. For the wall roughness of the channels, a value of 5 μm was selected. The influence of the number of subvolumes in the CHX was analyzed by varying the number between 5 and 40. An increasing number of subvolumes leads to a higher accuracy but also to a higher calculation effort. It was found that the calculation time increases almost linearly with the number of

subvolumes. Finally, 10 subvolumes were chosen because a further increase to 40 subvolumes changes the transferred power only by less than 2 %. Decreasing the number of subvolumes to 5 subvolumes leads to a unstable transient behavior. Consequently, 10 subvolumes yield a fast and accurate representation of the CHX.

Heat transfer

Figure 6 displays the deviation of the simulated transferred power from the experimental values. Only four cases deviate by more than 10 % from the experimental value. The maximum deviation is 11.7 %. All higher deviations occur at lower transferred powers where less experimental data are available. Moreover, all but one simulated value are in the interval which is defined by the transferred power for H₂O and sCO₂, derived from the experiments. In addition, the only value, which is located outside the interval, differs by less than 1 % from the mean experimental value. This is no contradiction because for this case the power calculated from the experimental values agree very well with each other. The difference between the power calculated from the experimental values for H₂O and sCO₂ can be explained by the experimental set-up and the measurement accuracy, as described in the experimental section. Altogether the simulation predicts the experimental values very well. Therefore, no further adaptations to the heat transfer correlations were considered here, as mentioned in the last section. The slight over-prediction of the transferred power might be related to the fact that heat losses were neglected in the simulations.

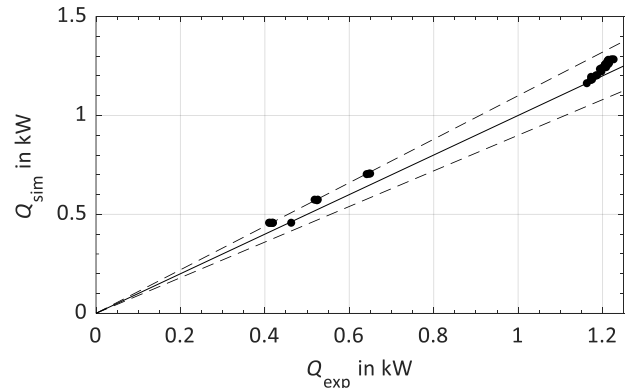


Figure 6: Simulated transferred power compared to the experimental values, in between the dashed lines the deviation is less than 10 %

In the following, case 5 of the experiments is discussed as an example. The boundary conditions for this case are given in the experimental section (Table 1). The simulated temperature profile of case 5 is shown in Figure 7. It includes the sCO₂ and H₂O bulk temperature and the wall temperature on both sides. The wall temperature, as well as the heat transfer coefficient and the transferred power are calculated per subvolume. Therefore, these values are plotted over the midpoint of each subvolume. On the left side of the diagram, the sCO₂ inlet and the H₂O outlet

are located. Due to the high heat capacity rate of sCO₂ compared to H₂O and the high overall heat transfer coefficient during the film condensation, the steam is condensed completely in the first third of the heat exchanger starting from the H₂O inlet. After the condensation forced convection cools down the water further. In ATHLET, the two regimes are connected with a cosine-shape interpolation. Therefore, the transition is smooth and does not cause numerical difficulties.

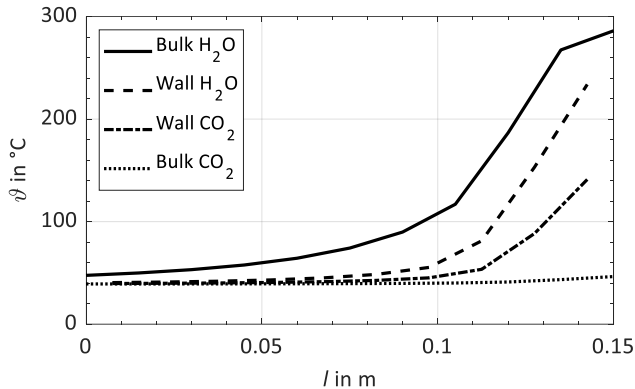


Figure 7: Simulated temperature profile in the CHX for case 5

The cosine-shape interpolation used in ATHLET is controlled by the void fraction, which is displayed in Figure 8. For a void fractions higher than zero and lower than 0.03 the two regimes are interpolated. From Figure 8 it is also visible that the steam quality drops below zero before the void fraction reaches zero. Therefore, at the end of the condensation process the steam is subcooled before it condenses completely. This effect is due to the ATHLET models which allow meta-stable states.

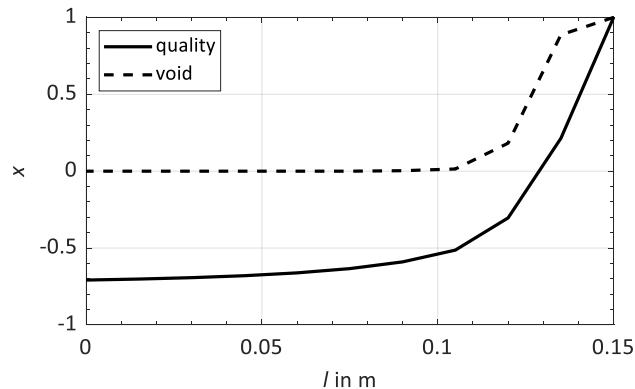


Figure 8: Steam quality and void fraction for case 5

During the film condensation the heat transfer coefficient on the H₂O side, displayed in Figure 9, is relatively high starting at 16 kW/m²K. The coefficient declines due to the increasing film thickness, which inhibits the heat transfer. The sCO₂ heat transfer coefficient is also relatively high with 4 kW/m²K at the sCO₂ outlet. However, compared to H₂O the coefficient is about two to four times lower during the condensation process. Therefore, the wall temperature is close to the H₂O temperature. After the condensation, the heat transfer coefficient of H₂O drops below

2 kW/m²K. As a result of the low H₂O side heat transfer coefficient, the wall temperature is close to the sCO₂ temperature in this section of the heat exchanger. Since the average of the wall temperature and sCO₂ bulk temperature, which is used for the calculation of the heat transfer coefficient, is close to the pseudo-critical temperature, the heat transfer coefficient of sCO₂ increases further. The peak in the heat transfer coefficient on the sCO₂ side is mainly caused by the peak of the specific heat capacity at the pseudo-critical point.

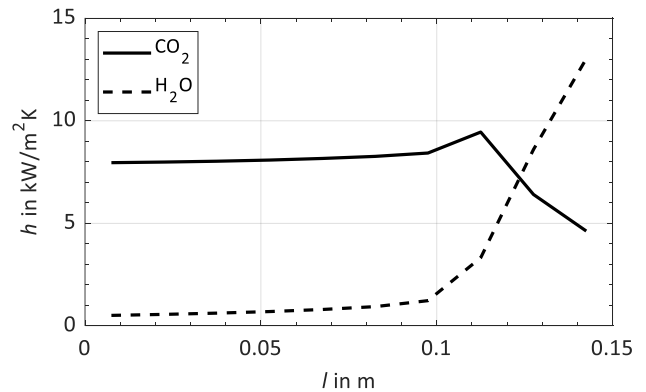


Figure 9: Simulated heat transfer coefficients for H₂O and sCO₂ for case 5

Close to the critical pressure and pseudo-critical temperature, improved correlations might provide the sCO₂ heat transfer coefficient with a higher accuracy. However, due to the low H₂O side heat transfer coefficient, the overall heat transfer coefficient and, therefore, the simulation results are affected scarcely. Thus, in this case no adaption of the heat transfer correlation is necessary. Summarizing, during the condensation, the sCO₂ side limits the overall heat transfer coefficient. After the condensation, the low heat transfer coefficient on the H₂O side strongly inhibits the heat transfer.

Because of these two facts, almost all the heat is transferred in the section where the condensation takes place. This is directly visible from the transferred power per channel length, shown in Figure 10. To maximize the transferred power, it is desirable to extend the condensation section. This can be achieved by a higher H₂O or a lower sCO₂ mass flow rate. In the current experimental set-up, the H₂O mass flow rate is restricted by the maximum electrical heating power of the evaporator with 1.6 kW. Moreover, the sCO₂ test facility introduces a lower bound on the sCO₂ mass flow rate. Furthermore, two additional effects prevent a higher total transferred power. Firstly, the Reynolds number is decreasing with decreasing sCO₂ mass flow rate and, therefore, the heat transfer coefficient on the sCO₂ side is also decreasing. Secondly, a lower sCO₂ mass flow rate leads to higher sCO₂ bulk temperatures. As a result, the average temperature, which is relevant for the determination of the heat transfer coefficient, also increases and departs from the pseudocritical temperature. This mainly decreases the specific heat capacity, which directly results in a decrease of the heat transfer coefficient.

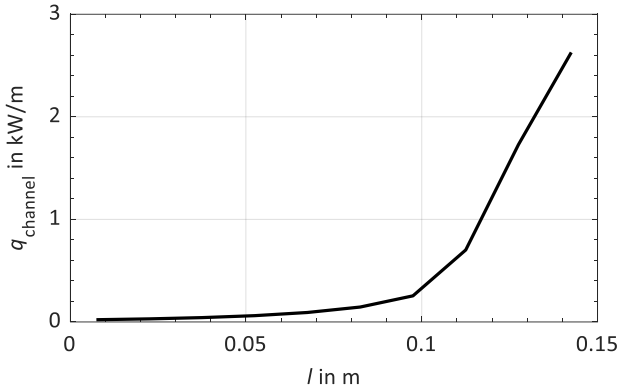


Figure 10: Simulated transferred power per channel length for case 5

Pressure drop

In Figure 11, the simulated and measured pressure drops on the sCO₂ side are compared. All but one case yield a deviation of less than 10 %. Therefore, it seems appropriate to model the pressure drop divided into channel, inlet and outlet pressure drop using the determined form loss coefficients, as described in the modelling section. The case with the lowest sCO₂ mass flow rate at a pressure of 11 MPa deviates by 17.4 %. For this case, the measurement might be erroneous because at low mass flow rates the control strategy of the SCARLETT test facility has lead to mass flow rate oscillations.

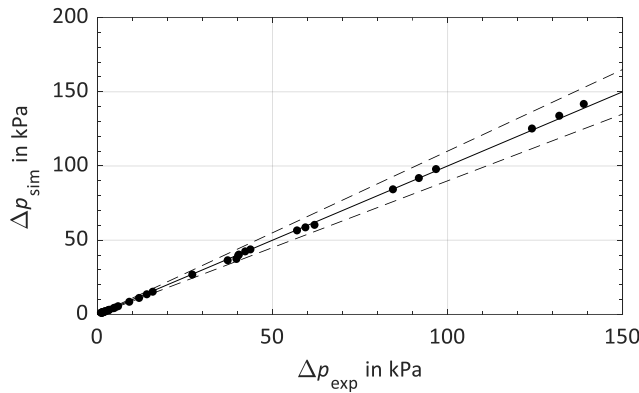


Figure 11: Simulated sCO₂ side pressure drop compared to the experimental values, in between the dashed lines the deviation is less than 10 %

In Figure 12 the sCO₂ side pressure drop of case 5 is shown. The total pressure drop of 42 kPa can be sub-divided into the inlet plenum, channel and outlet plenum pressure drop, 34 kPa, 5 kPa and 3 kPa, respectively. Probably, the perpendicular attached inlet and outlet pipes cause the high plenum pressure drops. Although, the main pressure drop can be attributed to the inlet plenum, it proved inadequate to model the pressure drop with just one form loss coefficient for the inlet plenum, because a higher sCO₂ outlet temperature yields a lower outlet density. This affects the plenum pressure drop defined in Equation 8. As

mentioned before, higher outlet temperatures occur for cases with a low sCO₂ and high H₂O mass flow rate.

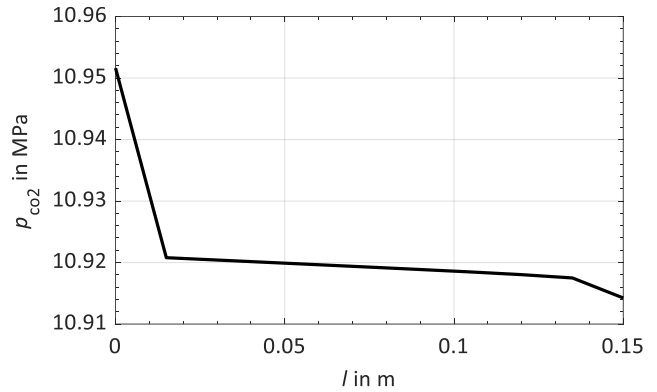


Figure 12: Simulated pressure profile for case 5

Mass flow rate variation

In order to show the influence of the H₂O and sCO₂ mass flow rates on the transferred power, a variation covering the experimental mass flow range was conducted. The results are provided in Figure 13. Over the whole range, the influence of the sCO₂ mass flow rate on the transferred power is almost negligible. Since the overall heat transfer coefficient during the condensation is high, the condensation of the steam takes up less than half of the heat exchanger length, for many cases even less than a quarter. The remaining length is more than sufficient to cool down the condensed steam independent of the sCO₂ mass flow rate. Only for very low sCO₂ and high H₂O mass flow rates the influence of the low Reynolds number on the sCO₂ side, which inhibits the heat transfer during the condensation and in the cool down phase, becomes visible. On the contrary, for high sCO₂ and H₂O mass flow rates, the investigated heat exchanger could transfer considerably more power and would still be able to condense and cool down the steam.

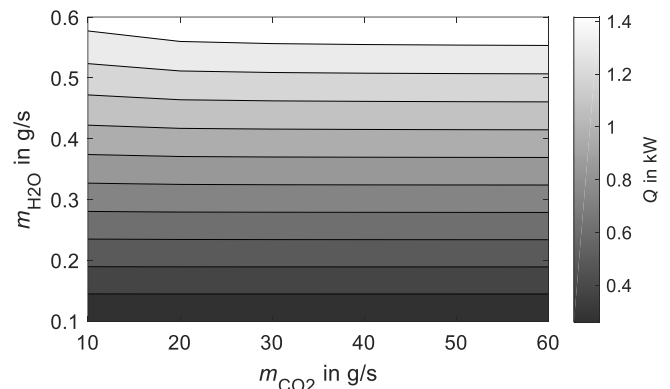


Figure 13: Influence of H₂O and sCO₂ mass flow rate on the transferred power for a sCO₂ inlet pressure of 11 MPa

CONCLUSION

In this study, a correlation based modelling approach for a sCO₂ compact heat exchanger (CHX) is investigated. Since no special CHX model exists in ATHLET, the general modelling

approach for co-current and counter-current flow arrangements is applied. Instead of modelling the whole heat exchanger, only one representative channel pair is modelled and the results are scaled with the number of channel pairs. The channels are divided in subvolumes and the local heat transfer coefficient and pressure drop are calculated with correlations. For sCO₂ the Gnielinski and the Coolebrook correlation are used.

In order to prove the validity of the modelling approach for the sCO₂/H₂O CHX, a model of a two-plate CHX is prepared in ATHLET and the simulation results are compared with experimental results. The form loss coefficients, which describe the inlet and outlet plenum pressure drop, are calculated with a best-fit method using a simple model for one sCO₂ channel. Additionally, the effective plate thickness is determined by a two dimensional steady state heat conduction calculation. For CHX with more plates and channels, e.g. for nuclear power plant applications, the effective plate thickness is considerably lower compared to the two-plate configuration.

In general, the results of the ATHLET simulations are in good agreement with the experimental values. Compared to the mean value of the experiments, almost all simulated cases yield a deviation of less than 10 % concerning the transferred power and the pressure drop on the sCO₂ side.

A closer evaluation reveals that most of the heat is transferred in the section of the heat exchanger, where steam condensation takes place. Since the heat transfer coefficient on the H₂O side is high during the condensation, the sCO₂ side, still being quite high, limits the overall heat transfer coefficient. After the condensation, the relation is inverted because the heat transfer coefficient of liquid H₂O is significantly lower for the investigated set-up. Considering the effective plate thickness, the influence of thermal resistance of the wall is almost negligible except for the small impact during the condensation phase. Moreover, an improved heat transfer correlation for sCO₂ for states close to the pseudocritical temperature would scarcely change the results because only downstream the condensation section, when the H₂O heat transfer coefficient is inhibiting the overall heat transfer phase, the temperature relevant for the determination of the heat transfer coefficient is close to the pseudocritical temperature. Future investigations will analyze this relation further. Finally, a variation of the H₂O and sCO₂ mass flow rate confirmed the minor impact of the sCO₂ mass flow rate. Furthermore, since less than half of the heat exchanger length is necessary for the condensation of the steam, the investigated CHX could transfer considerably more power or be shortened by 50%

In the future, more experiments will be analyzed to further validate the proposed approach. Moreover, cooling and cross-flow will be considered where either improved correlations or new models are necessary. After the model development and validation, the complete sCO₂-HeRo system, attached to a boiling or pressurized water reactor, will be simulated in ATHLET.

NOMENCLATURE

A	heat transfer area of heat exchanger (m ²)
A_c	channel cross sectional area / flow area (m ²)
b	width of the cooling surface (m)
C_{corr}	correction factor (-)
c_p	specific isobaric heat capacity (J/kgK)
d_h	hydraulic diameter (m)
h	heat transfer coefficient (W/m ² K)
l	length of heat exchanger (m)
\dot{m}	mass flow rate (kg/s)
Nu	Nusselt number (-)
p	pressure (MPa)
Pr	Prandtl number (-)
\dot{Q}	transferred power (W)
\dot{q}	transferred power per length (W/m)
Re	Reynolds number (-)
T	temperature (K)
u	velocity (m/s)
U_c	perimeter of one channel (m)
w	width of the plate (m)

Greek letters

δ	effective plate thickness (m)
Δl	length of one subvolume (m)
ε	void fraction (-)
η	dynamic viscosity (Pa/s)
ϑ	temperature (°C)
λ	thermal conductivity (W/mK)
ν	kinematic viscosity (m ² /s)
ξ_{form}	form loss coefficient of plenum (m ⁻⁴)
ρ	density (kg/m ³)

Subscripts

exp	experiment
f	film
s	simulation

Acronyms

BWR	boiling water reactor
CHX	compact heat exchanger
H ₂ O	water/steam
HeRo	heat removal system
sCO ₂	supercritical carbon dioxide

ACKNOWLEDGEMENTS

The presented work was funded by the German Ministry for Economic Affairs and Energy (BMWi. Project no. 1501557) on basis of a decision by the German Bundestag.

REFERENCES

- [1] J. Venker, “Development and Validation of Models for Simulation of Supercritical Carbon Dioxide Brayton Cycles and Application to Self-Propelling Heat Removal Systems in Boiling Water Reactors,” University of Stuttgart, IKE 2 – 156, 2015.
- [2] “sCO₂-HeRo.” [Online]. Available: <http://www.sco2-hero.eu/>. [Accessed: 19-Feb-2019].
- [3] D. Bestion, “System code models and capabilities,” in *THICKET*, 2008, pp. 81–106.
- [4] G. Mauger, N. Tauveron, F. Bentivoglio, and A. Ruby, “On the dynamic modeling of Brayton cycle power conversion systems with the CATHARE-3 code,” *Energy*, vol. 168, pp. 1002–1016, 2019.
- [5] L. Batet *et al.*, “Modelling of a supercritical CO₂ power cycle for nuclear fusion reactors using RELAP5–3D,” *Fusion Eng. Des.*, vol. 89, no. 4, pp. 354–359, Apr. 2014.
- [6] M. J. Hexemer, H. T. Hoang, K. D. Rahner, B. W. Siebert, and G. D. Wahl, “Integrated Systems Test (IST) Brayton Loop Transient Model Description and Initial Results,” in *S-CO₂ Power Cycle Symposium*, 2009, pp. 1–172.
- [7] M. R. Straetz, R. Mertz, and J. Starflinger, “Experimental investigation on the heat transfer between condensing steam and sCO₂ in a compact heat exchanger,” *2nd Eur. sCO₂ Conf. 2018*, Aug. 2018.
- [8] G. F. Hewitt, *Heat exchanger design handbook*. New York: Begell House, 1998.
- [9] P. von Böckh and T. Wetzels, *Wärmeübertragung: Grundlagen und Praxis*, 7th ed. Berlin: Springer, 2017.
- [10] R. Numrich and J. Müller, “J1 Filmkondensation reiner Dämpfe,” in *VDI-Wärmeatlas*, Berlin, Heidelberg: Springer Berlin Heidelberg, 2013, pp. 1011–1028.
- [11] H. Austregesilo *et al.*, “ATHLET Models and Methods,” Garching, 2016.
- [12] V. Dostal, M. J. Driscoll, and P. Hejzlar, “A Supercritical Carbon Dioxide Cycle for Next Generation Nuclear Reactors,” *Tech. Rep. MIT-ANP-TR-100*, pp. 1–317, 2004.

**AN ASSESSMENT OF THE CRITERIA FOR THE ONSET OF HEAT TRANSFER
DETERIORATION WITH SUPERCRITICAL CO₂ IN VERTICAL HEATED SINGLE
CIRCULAR TUBES**

Konstantinos Theologou*

Institute of Nuclear Technology and Energy Systems
(IKE), University of Stuttgart
Germany
Email: konstantinos.theologou@ike.uni-stuttgart.de

Rainer Mertz

Institute of Nuclear Technology and Energy Systems
(IKE), University of Stuttgart
Germany

Eckart Lauien

Institute of Nuclear Technology and Energy Systems
(IKE), University of Stuttgart
Germany

Jörg Starflinger

Institute of Nuclear Technology and Energy Systems
(IKE), University of Stuttgart
Germany

ABSTRACT

In the sCO₂-QA project (Qualification of analysis tools for the evaluation of residual heat-driven, self-sufficient system for decay heat removal) a residual heat-driven self-sufficient sCO₂-operated decay heat removal system is simulated with the German reactor code ATHLET (Analysis of thermal-hydraulics of leaks and transients). The decay heat removal system is a simple Brayton cycle consisting of a turbo compressor system located in the reactor building, a heat exchanger in the outdoor area and a compact-heat-exchanger in the containment. For a better understanding of the heat transfer characteristics of sCO₂ inside the compact heat exchanger and for the validation of ATHLET and other numerical codes experimental data are needed. The experimental results will be used for validation and/or improvement of heat transfer and pressure drop correlations in case of variable fluid properties.

All experiments were performed in the test facility SCARLETT (Supercritical Carbon Dioxide Loop at IKE Stuttgart) at the IKE (Institute of Nuclear Technology and Energy Systems), which provides sCO₂ under defined conditions. The heat transfer and pressure drop characteristics of carbon dioxide near the critical point were investigated in a vertical flow by basic heating experiments on two directly electrical heated circular tubes with the inner diameters of 4 and 8 mm and with a pressure of 7.75 MPa. Variations of the mass flux were chosen with 400 and 800 kg/m²s with a heat flux up to 110 kW/m².

In experiments with sCO₂ three different heat transfer mechanism (HTM) exist: The enhanced, the normal and the deteriorated heat transfer (DHT). In some applications e.g. for the operation of a supercritical pressure heat exchanger it is necessary to be able to predict the onset of DHT. In this publication, some of these criteria are presented and validated: One criterion based on the effect of flow acceleration, two criteria based on the effect of buoyancy and four more general criteria based on the heat flux to mass flux ratio.

INTRODUCTION

In the heat transfer of supercritical flows three different heat transfer mechanisms (HTM) can be observed: The normal heat transfer (NHT), the enhanced heat transfer (EHT) and the deteriorated heat transfer (DHT). In figure 1 the different mechanisms are exemplified for an upward flow in six new experiments with three different heat fluxes 30, 50, and 90 kW/m² and a mass flux between 800-1000 kg/m²s. Starting with the NHT regime (red) it can be seen that the inner wall temperature of the test tube depends solely on the local bulk fluid temperature has a nearly constant temperature difference to it. In contrast to NHT, the EHT (blue) shows a non-constant approximation of the inner wall temperature to the bulk temperature when the inner wall temperature exceeds the critical temperature. By increasing the heat flux at a constant mass flux, the course of the inner wall temperature deviates significantly from the course of the bulk fluid temperature. The inner wall temperature begins to rise after exceeding the critical

temperature and reaches a local peak. The occurrence of these temperature spike is here defined as DHT. In figure 1 a very flat temperature spike (yellow) can be seen. Some authors categorize only cases as DHT in which the spike is sharp but they do not give any quantitative definitions. The categorization as DHT in this publication includes the cases with broad peaks as well as with sharp peaks.

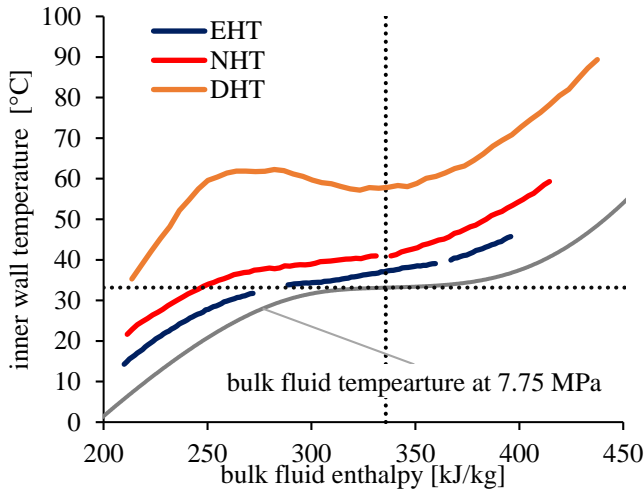


Figure 1: Heat transfer mechanism in a 4 mm with upward flow.

These mechanisms are due to the strongly variable fluid properties of sCO₂ near the critical point. The isobaric heat capacity reaches a maximum at the pseudocritical temperature while the density drops by ~300 kg/m³ in a temperature interval of ~5 °C, which is shown in Figure 2. The dynamic viscosity and the thermal conductivity, which also reach a peak value at pseudocritical temperature, can be seen in Figure 3. For plotting the graphs the NIST database REFPROP was used [1].

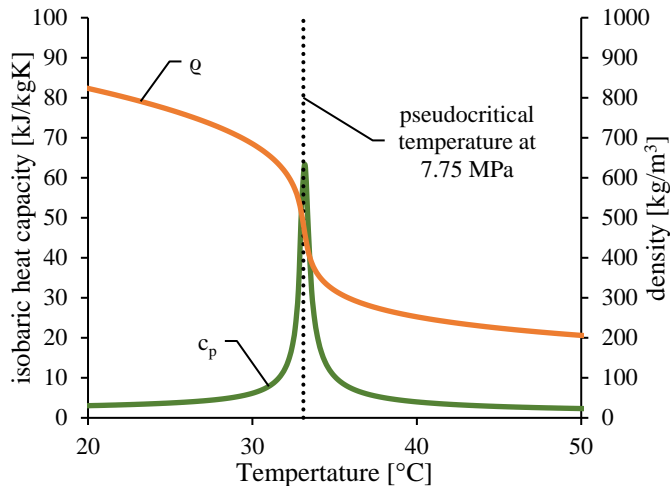


Figure 2: Heat capacity and density plotted over the temperature.

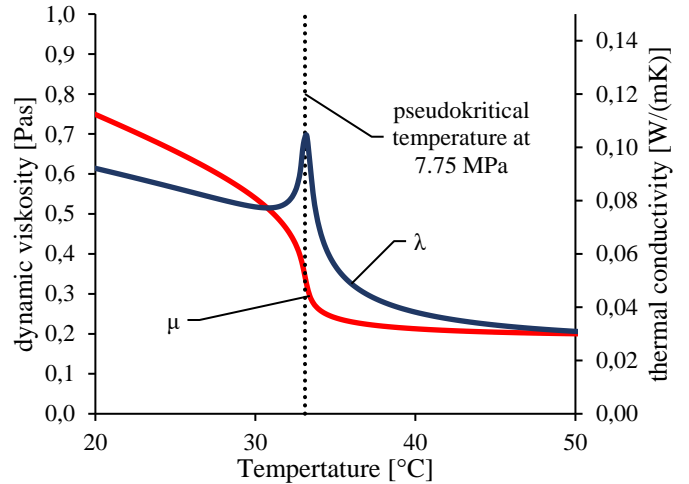


Figure 3: Dynamic viscosity and thermal conductivity plotted over the temperature.

This publication concentrates especially on the onset of DHT. The effects of the presents of DHT in a fully developed flow are well known and called the effects of buoyancy and flow acceleration. These have to be distinguished with the deterioration of the heat transfer based on thermal inflow effects. While heating up a tube the bulk fluid, its density decreases and the fluid expands which leads to a flow acceleration in flow direction. The radial difference of the fluid properties with a lower density in the near wall layer leads to the effect of buoyancy. Figure 4 illustrates the qualitative velocity profiles of an upward (left) and a downward flow (right). The forced convection shapes a parable like profile with a flat spike (red) while the natural convection shapes an M-shape profile (blue). In the case of a forced upward flow, the natural and forced convection have the same direction, thus the effect of buoyancy leads to higher velocities in the near wall layer and the resulting profile is also an M-shape. In this case, the differential velocity between the near wall layer and the bulk fluid decreases with the result of a lower heat transfer between these two regions. In the case of a forced downward flow the natural and the forced convection run in opposite directions with the result of increasing the turbulence which leads to a better heat transfer between the near wall layer and the bulk fluid [2]. Kurganov and Kapilny validated this velocity profiles experimentally [3].

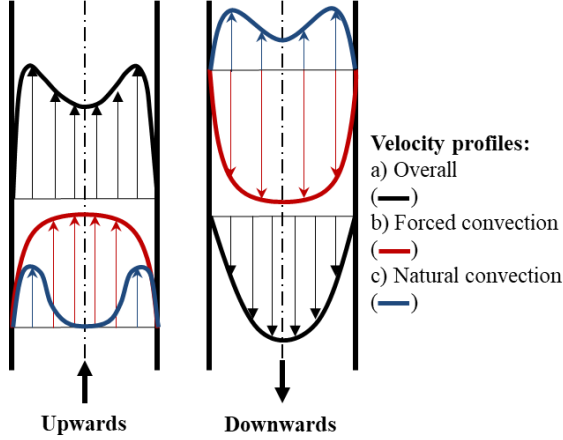


Figure 4: Velocity profiles of an upward and downward flow.

In case of deterioration of the heat transfer, wall temperatures can reach peak values after exceeding a critical heat flux, which can significantly affect the efficiency of a heat exchanger. It has to be considered that often sCO₂ is chosen as an experimental working fluid because of its critical point at a low temperature and pressure ($T_{cr}= 30.98$ °C and $p_{cr}= 7.38$ Mpa) in contrast to e.g. water ($T_{cr}= 373.85$ °C and $p_{cr}= 22.06$ Mpa). For this reason, early researches were already working on the development of criteria to avoid deterioration in heat transfer coefficient [4]. This criteria can enable manufacturer e.g. of supercritical pressure heat exchanger to develop operation guidelines and to specify limits of safe operation.

A good overview of some criteria for the onset of DHT is given by Löwenberg [2]. The first criterion from Petukhov et al. [5] is based on the effect of flow acceleration and predicts that the region of the NHT is determined by the ratio of the acceleration resistance, to the friction resistance which has to be smaller than 1-1.3.

$$\left(\frac{\xi_u}{\xi}\right)_{max} \leq 1 - 1.3 \quad (1)$$

$$\xi = \left(\frac{\rho_w}{\rho_b}\right)^{0.4} \left(1.82 \log\left(\frac{Re_b}{8}\right)\right)^2 \quad (2)$$

$$\xi_u \cong 8\dot{q}_b^+ \quad (3)$$

The friction resistance ξ can be calculated with the wall density ρ_w , the bulk density ρ_b and the Reynolds of the bulk Re_b .

For the acceleration resistance ξ_u the non-dimensional heat flux \dot{q}_b^+ is needed, which is discussed by McEligot and Jackson [6]:

$$\dot{q}_b^+ = \frac{\dot{q}\beta_b}{c_{p,b}G} \quad (4)$$

With the heat flux \dot{q} , the volumetric expansion coefficient β , the isobaric heat capacity c_p and the mass flux G . The criterion of Petukhov is valid for $Re_b < 2 * 10^4$ and will be investigated in this publication for higher Reynolds numbers.

The next criterion is based on the effect of buoyancy and is presented by Jackson et al. [7] and contains the area where the effect of buoyancy on heat transfer is less than 5 %.

$$\frac{\overline{Gr}_b}{Re_b^{2.7}} < 10^{-5} \quad (5)$$

$$\overline{Gr}_b = \frac{(\rho_b - \bar{\rho})g d_i^3}{\rho_b \nu_b^2} \quad (6)$$

$$\bar{\rho} = \frac{1}{T_w - T_b} \int_{T_b}^{T_w} \rho dT \quad (7)$$

The Grashof number \overline{Gr}_b based on density difference with the gravity g , the inner tube diameter d_i , the kinematic viscosity ν and the integrated density $\bar{\rho}$ which is approximated in Bae et al. [8] as:

$$\bar{\rho} \approx \begin{cases} \frac{\rho_w + \rho_b}{2} \\ \text{for } T_w < T_{pc} \text{ or } T_b > T_{pc} \\ \frac{[\rho_b(T_{pc} - T_b) + \rho_w(T_w - T_{pc})]}{T_w - T_b} \\ \text{for } T_b \leq T_{pc} \leq T_w \end{cases} \quad (8)$$

A formula for calculating the pseudocritical temperature T_{pc} is selected as follows:

$$T_{pc} = T_{cr} \left(1 + 1,3977 \left(\frac{p}{p_{cr}} - 1\right) - 0,37344 \left(\frac{p}{p_{cr}} - 1\right)^2 + 0,045 \left(\frac{p}{p_{cr}} - 1\right)^3\right) \quad (9)$$

With the temperature T in °C and the pressure p in bar. Another buoyancy based criterion for a fully-developed flow is given by McEligot and Jackson [6].

$$Bo^* = \frac{Gr^*}{Re_b^{3.425} Pr^{0.8}} > \sim 6 * 10^{-7} \quad (10)$$

$$Gr^* = \frac{g\beta_b \dot{q} d_i^4}{\lambda_b \nu_b^2} \quad (11)$$

With the Jackson buoyancy parameter Bo^* and the heat flux based Grashof number Gr^* .

In the literature there are also more general criteria to determine the onset of DHT based on a heat flux to mass flux ratio. Four of them are presented here, one for sCO₂ from Jeon et al. (eq. 13) and the others for water.

Yamagata et al. [9]:

$$\dot{q}_{cr} = 200G^{1.2} \quad (12)$$

Jeon et al. [10]:

$$\dot{q} > 0.2G^2 \quad (13)$$

Pioro et al. [11]:

$$\frac{\dot{q}}{G} \geq 400 \frac{J}{kg} \quad (14)$$

Styrovovich et al. [12]:

$$\frac{\dot{q}}{G} \geq 600 \frac{J}{kg} \quad (15)$$

To indicate the onset of DHT, a ratio between the experimental Nusselt number Nu_{exp} and a pure forced convection correlation is needed Nu_{fc} given e.g. by the modified Krasnoschekov & Protopopov correlation [8].

$$Nu_{fc} = 0.0183Re_b^{0.82}Pr_b^{0.4}\left(\frac{\rho_w}{\rho_b}\right)^{0.3}\left(\frac{\bar{c}_p}{c_{p,b}}\right)^n \quad (16)$$

$$\bar{c}_p = \frac{1}{T_w - T_b} \int_{T_b}^{T_w} c_p dT = \frac{i_w - i_b}{T_w - T_b} \quad (17)$$

$$n = \begin{cases} 0.4 & \text{for } T_b < T_w \leq T_{pc} \text{ or } 1.2T_{pc} \leq T_b < T_w \\ 0.4 + 0.2\left(\frac{T_w}{T_{pc}} - 1\right) & \text{for } T_b \leq T_{pc} < T_w \\ 0.4 + 0.2\left(\frac{T_w}{T_{pc}} - 1\right)\left[1 - 5\left(\frac{T_b}{T_{pc}} - 1\right)\right] & \text{for } T_{pc} < T_b \leq 1.2T_{pc} \text{ and } T_b < T_w \end{cases} \quad (18)$$

With the Prandtl number Pr and the specific enthalpy i .

EXPERIMENTAL SETUP

The experiments in this publication are carried out with the SCARLETT test facility at IKE, University of Stuttgart, for more details see Flaig et al. [13].

For diverse fundamental investigations of the heat transfer characteristics of sCO_2 near the critical point a new test rig was build up at IKE (Figure 5).

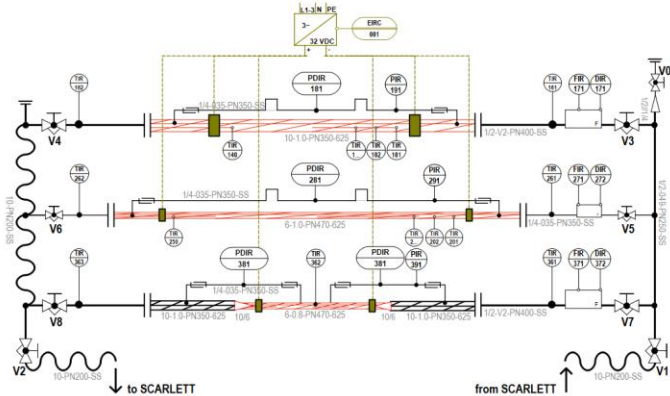


Figure 5: P&I Diagram of the test rig.

The test rig consists of three tubular test sections with different tube diameters. By bypassing between the three tubes the mass flow can be adjusted. It is variably mounted on a rack allowing for experiments with horizontal, upward and downward mass flows. The first and the second test section have the same structure, the only difference is the inner diameter of the used test tubes (4 mm and 8 mm). The third test section is used for investigations of pressure losses, not part of this publication. The test tubes are heated up directly with a DC power supply. To insulate the test rig electrically from the test tubes special insulating flanges are used. Before the sCO_2 passes the test tubes the mass flows and the bulk temperatures are measured. For

measuring the mass flow, Coriolis mass flow meter with an accuracy of $\pm 0.19\%$ of full scale is used. Figure 6 shows the dimensions of the test tubes with an inner diameter of 4 and 8 mm for the presented experiments.

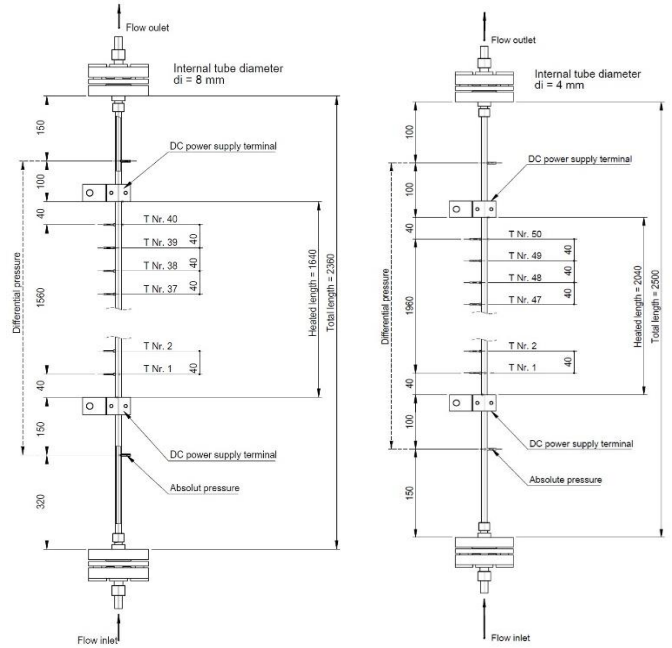


Figure 6: Dimensions of 1st (left) and 2nd (right) test section.

The total length of the first test tube is 2360 mm with a heated length of 1640 mm. The second test tube is 2500 mm long with a heated length of 2040 mm. Forty temperature sensors are tied with a temperature resistant yarn straight in 40 mm intervals on the outer surface of the first test tube and fifty sensors on the second test tube. The sensors are surface thin-film resistance temperature sensors (PT100) with an A-Class accuracy. The absolute pressure is measured in front of the heated area and the differential pressure is measured over the heated length. To measure the pressure inside the test tube without influencing the flow a 1 mm hole has been drilled into the tube wall. The accuracy of the differential and absolute pressure transmitters is $\pm 0.15\%$ of full scale. With the inner tube diameter d_i the hydraulic inflow length L_{hyd} of the fully developed flow has been calculated with the empirical formula of Herwig [14] for turbulent flow on the maximum expected Reynold number for the experiments.

$$\frac{L_{hyd}}{d_i} = 4.4Re_b^{\frac{1}{5}} \quad (19)$$

Alloy 625 was chosen for the tube material because of its high specific electrical resistance. The inner roughness of the 4 mm tube is $Ra = 0,549 \mu m$ and $Ra = 0,227 \mu m$ for the 8 mm tube. The applied electrical power heating up the test tubes is measured directly at the DC power supply terminals to avoid voltage losses in the over-dimensioned copper terminals. The monitoring accuracy of the DC power supply is given with $\pm 0.2\%$ of full scale.

DATA REDUCTION

The following table gives an overview of the experimental parameter of the presented experiments.

Table 1: Experimental parameter.

Parameter	Unit	Value
inner tube diameter	mm	4, 8
flow orientation	-	upward
inlet pressure	MPa	7.75
inlet temperature	°C	5, 30
mass flux	kg/m ² s	400, 800
heat flux	kW/m ²	10, 30, 50, 70, 90, 110
inlet Reynolds number	-	15000-60000

Twenty minute intervals with a 0.25 Hz recording frequency were selected for the data acquisition. In the next step, the arithmetic mean was calculated using approximately 300 values for each parameter. To ensure the reproducibility of the measurement each experiment was repeated at least twice to three times. All experiments start after having reached steady-state conditions.

Subsequently, a short overview of the governing equations to calculate the experimental Nusselt number is given. To verify an adiabatic state during the experiments, an energy balance of the measured thermal and electrical heat flow is calculated (Table 3). The National Institute of Science and Technology (NIST) database REFPROP provides the fluid properties [1].

$$|\dot{Q}_{el}| = |\dot{Q}_{th}| = \dot{Q} \quad (20)$$

$$\dot{Q}_{th} = \dot{m} * [i_{b,out}(T_{B,out}, p_{out}) - i_{b,in}(T_{B,in}, p_{in})] \quad (21)$$

$$\dot{Q}_{el} = P_{el} = U * I \quad (22)$$

With the transferred heat \dot{Q} , the mass flux \dot{m} , the specific enthalpy i , the electrical power P , the voltage U and the electrical current I .

The heat flux is calculated with the curved surface area of the inner surface $A_{i,sur}$ of the tube and the heated length with the assumption of an uniform heat generation by the direct electrical heating and the heated length L_h .

$$\dot{q} = \frac{\dot{Q}_{el}}{A_{i,sur}} = \frac{U * I}{\pi * d_i * L_h} \quad (23)$$

For the calculation of the bulk-temperature across the tube $T_{b,x}$ a linear approximation of the pressure losses is assumed.

$$T_{b,x} = f(i_{b,x}, p_x) \quad (24)$$

$$i_{b,x} = i_{b,in} + \left(\frac{L_x}{L_h}\right) * \frac{\dot{Q}_{el}}{\dot{m}} \quad (25)$$

With the mathematical heat conduction model of a circular tube with uniform heat generation an insulated outer surface and a cooled inner surface the inner wall temperature can be calculated with the measured outer wall temperature and the volumetric heat flux [15, p. 152]. The thermal conductivity of the tube-wall was also approximated linearly over the temperature.

$$T_{w,i} = T_{w,o} + \frac{q_v}{4\lambda_w} \left[\left(\frac{d_o}{2}\right)^2 - \left(\frac{d_i}{2}\right)^2 \right] - \frac{\dot{q}_v}{2\lambda_w} \left(\frac{d_o}{2}\right)^2 * \ln\left(\frac{d_o}{d_i}\right) \quad (26)$$

$$\dot{q}_v = \frac{\dot{Q}_{el}}{\frac{\pi}{4}(d_o^2 - d_i^2) * L_h} \quad (27)$$

With the volumetric heat flux \dot{q}_v , the thermal conductivity of Alloy 625 λ_w and the outer tube diameter d_o .

In the last step the heat transfer coefficient h can be calculated for each measured tube position.

$$h_x = \frac{\dot{q}}{T_{w,x} - T_{b,x}} \quad (28)$$

Consequently the experimental Nusselt number of the bulk fluid $Nu_{b,exp}$ can be calculated with the heat transfer coefficient and the thermal conductivity of the bulk fluid λ_b .

$$Nu_{b,exp,x} = \frac{h_x d_i}{\lambda_{b,x}} \quad (29)$$

The Reynolds number is calculated with the mass flow \dot{m} and the dynamic viscosity of bulk η_b .

$$Re_{b,x} = \frac{4\dot{m}}{\pi d_i \mu_b} \quad (30)$$

RESULTS

To validate the presented criteria for the onset of DHT three test series with overall thirteen experiments were carried out. The inner wall temperature profiles are plotted over the bulk enthalpy in Figure 7 – Figure 9. The first test series (Figure 7) consists of five experiments with the 4 mm test tube and a constant mass flux around 800 kg/m²s. The set heat fluxes were 30 (red), 50 (green), 70 (orange), 90 (brown) and 110 (yellow) kW/m². The next test series with the same test tube (Figure 8) were performed with a mass flux around 400 kg/m²s and with the heat fluxes of 10 (blue), 30 (red), 50 (green) and 70 (orange) kW/m². In test series three (Figure 9) the 8 mm tube was used to perform four experiments with a mass flux of 400 kg/m²s and the same variation of heat fluxes as in the second test series. The inlet bulk temperatures for the experiments are 5 °C with the exception of exp. 1.1 with 30 °C.

The first six to ten measuring points of the experiments with a higher heat flux (plotted in grey) were neglected for the further calculations to ensure a thermal fully developed flow, which represents inflow lengths around 50-100 diameters. These are typical values found in literature [16]. All experiments are categorized in three heat transfer regimes: EHT, NHT and DHT. For the categorization into the DHT regime, the criterion is a wall temperature peak reached before the bulk fluid passing the pseudocritical enthalpy. More details about the categorization can be read in the introduction of this publication.

The following diagrams (Figure 10-Figure 19) present the results for the validation of the criteria for the DHT onset and will be described below.

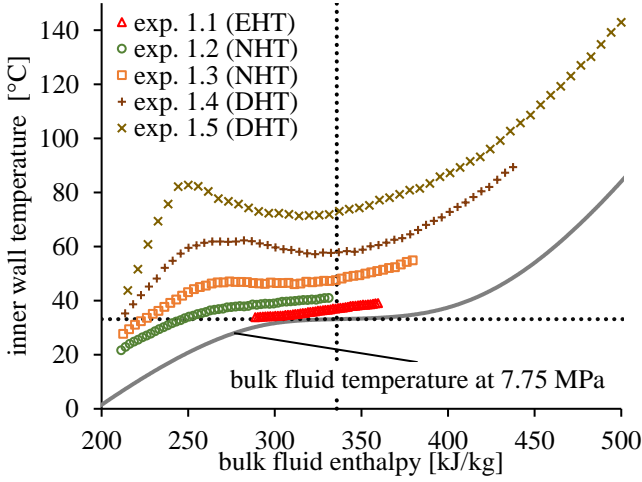


Figure 7: Inner wall temperature profile of the first test series.

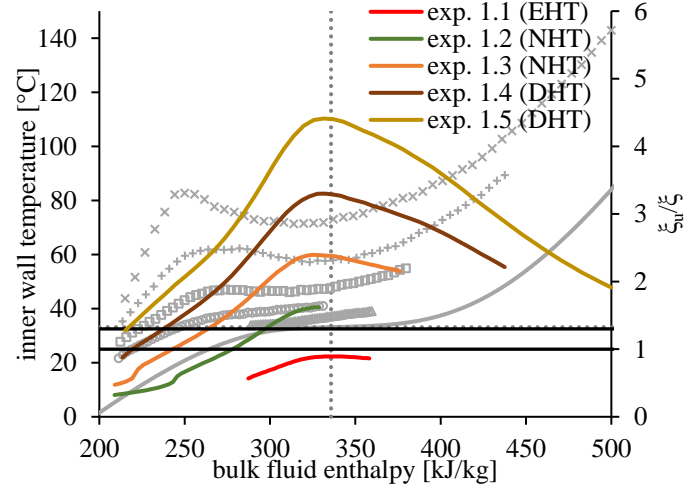


Figure 10: Petukhov's ξ_w/ξ_s -criterion for the first test series.

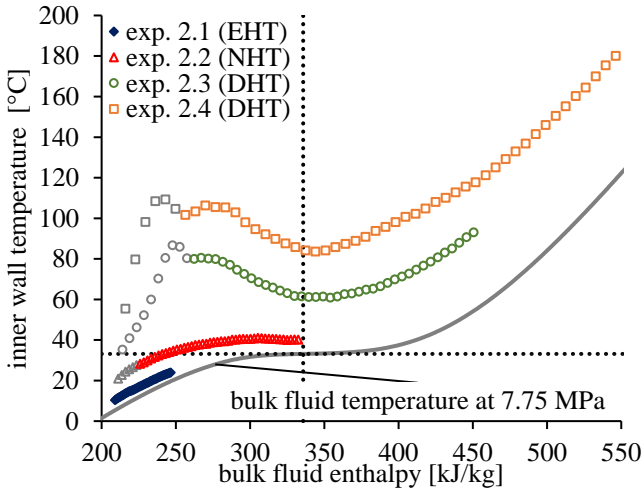


Figure 8: Inner wall temperature profile of the second test series.

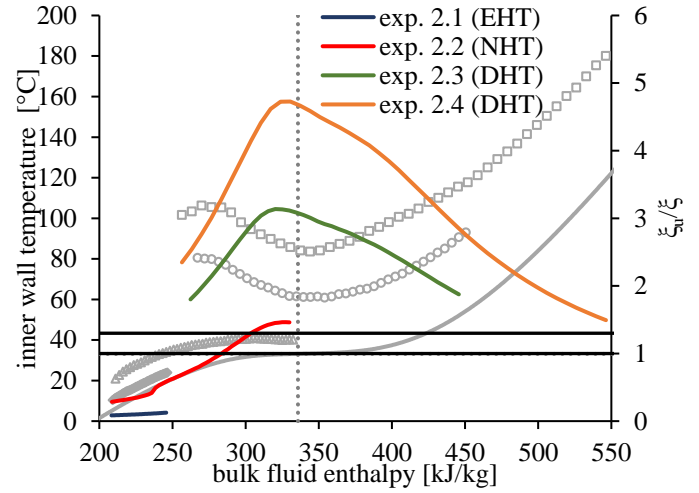


Figure 11: Petukhov's ξ_w/ξ_s -criterion for the second test series.

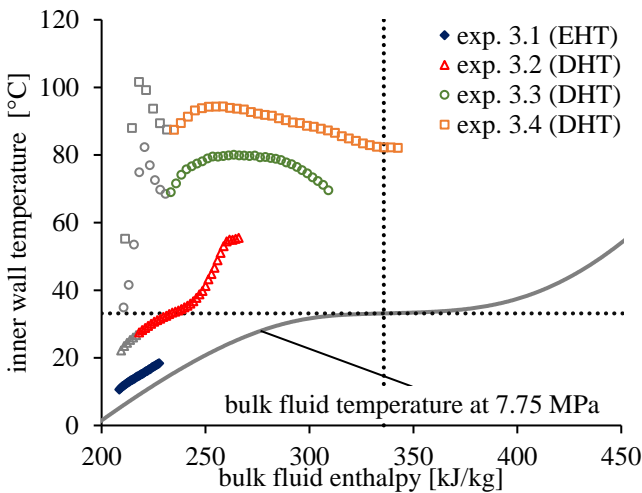


Figure 9: Inner wall temperature profile of the third test series.

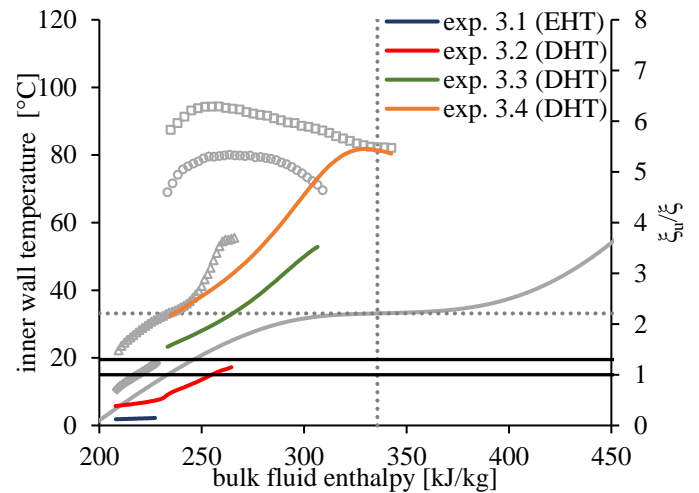


Figure 12: Petukhov's ξ_w/ξ_s -criterion for the third test series.

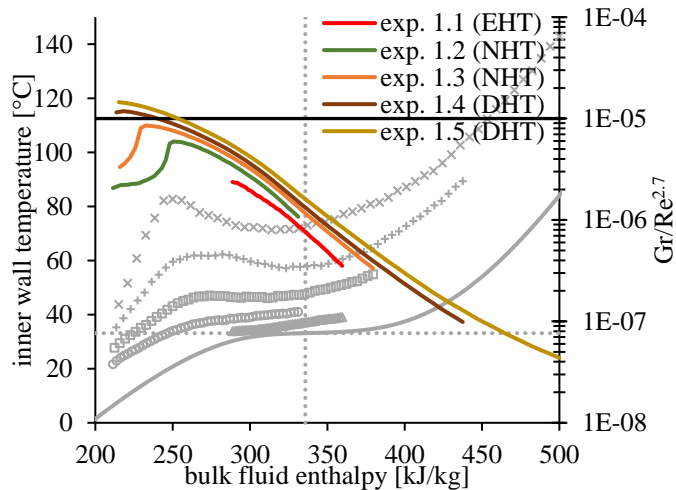


Figure 13: Jackson's $Gr/Re^{2.7}$ -criterion for the first test series.

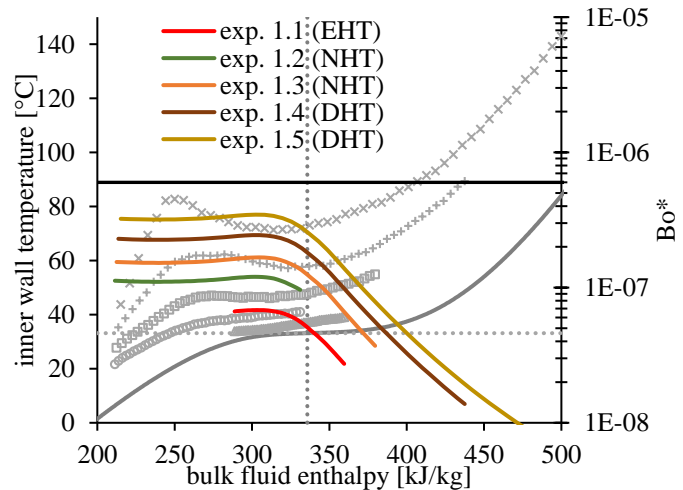


Figure 16: Jackson's Bo^* -criterion for the first test series.

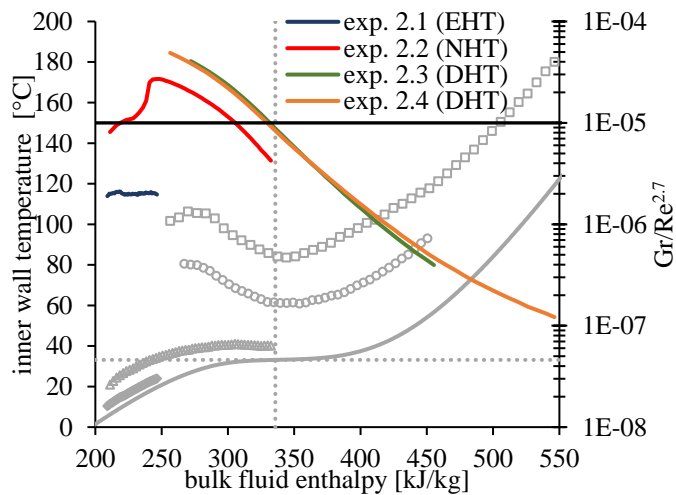


Figure 14: Jackson's $Gr/Re^{2.7}$ -criterion for the second test series.

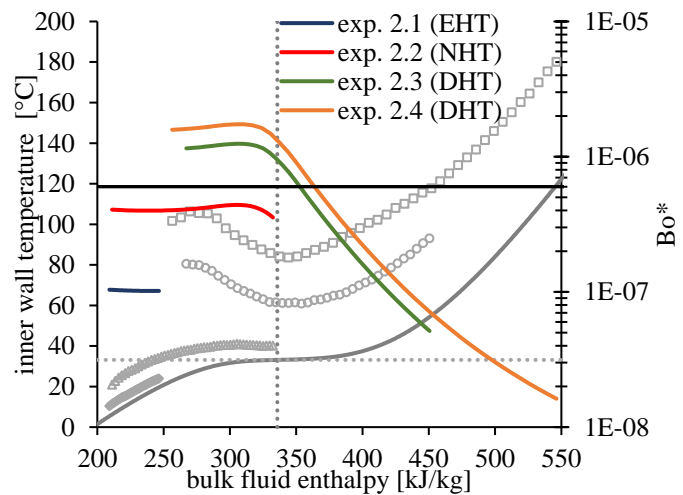


Figure 17: Jackson's Bo^* -criterion for the second test series.

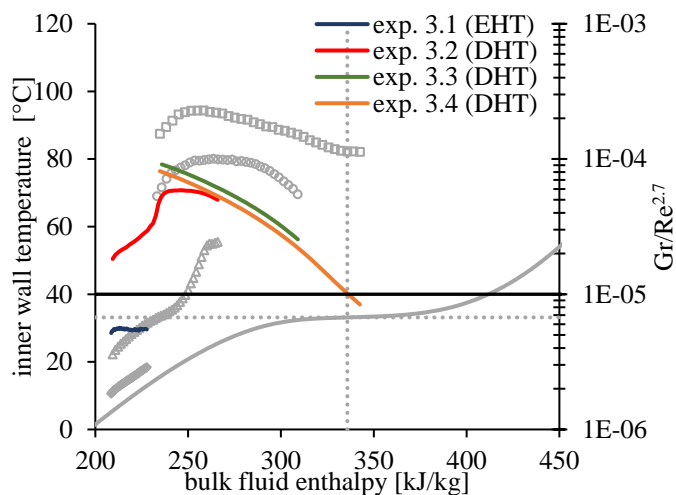


Figure 15: Jackson's $Gr/Re^{2.7}$ -criterion for the third test series.

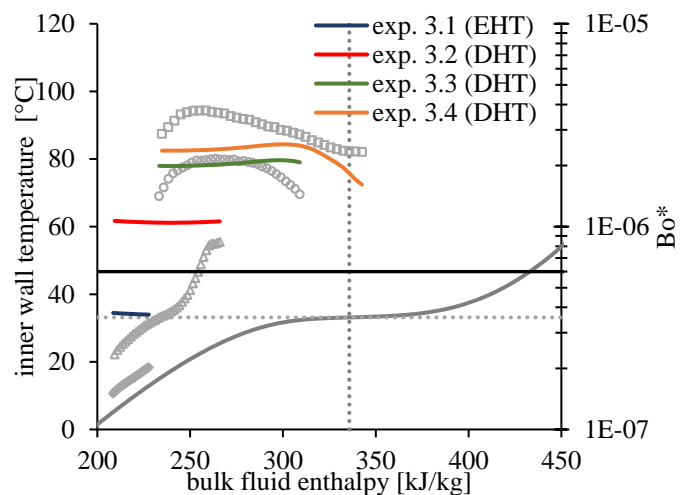


Figure 18: Jackson's Bo^* -criterion for the third test series.

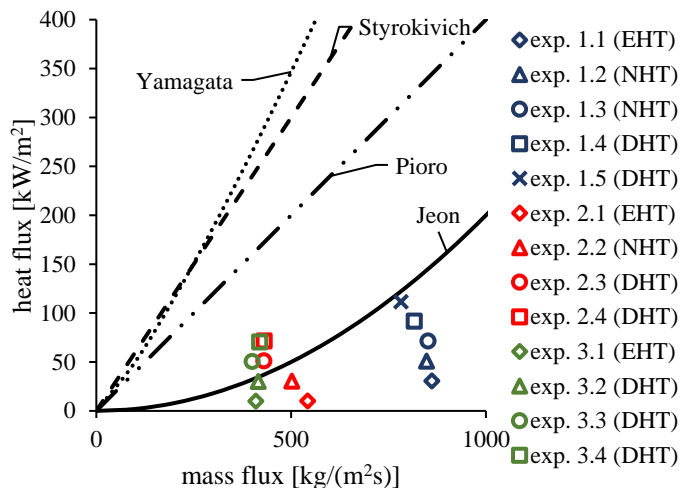


Figure 19: Validation of general criteria for the onset of DHT.

The Petukhov criterion, which is based on the effect of flow acceleration, shows a good agreement with the experimental results for the onset of DHT (see Figure 10-Figure 12) only three experiments disagree with the criterion (exp. 1.2, 1.3 and 2.2). The following two buoyancy based criteria from Jackson with the Grashof to Reynolds ratio (Figure 13-Figure 15) and the Buoyancy number (Figure 16-Figure 18) shows a good agreement with the experiments, too. It is remarkable that the criterion with the Grashof to Reynolds ratio gives the best information about the enthalpy, at which local onset and offset of DHT starts, see exp. 2.3 and 2.4. As shown in Löwenberg [2], the effect of flow acceleration is greater in small diameter tubes whereas the effect of buoyancy is greater in tubes with a bigger diameter. One possible reason that both criteria types, flow acceleration based and buoyancy based, show a good agreement can be that the chosen tube diameters are in a range where both effects have a similarly strong effect on the heat transfer.

Figure 19 shows the validation of the general criteria with heat flux to mass flux ratio. It can be seen that the criterion from Jean et al. [10] shows a consistency with the experiments. This was the only criterion, which was set up especially for sCO₂. The disagreement in exp. 1.4 and 1.5 is probably because of the low level of DHT. One reason for the deviance to the other criteria may be the different definitions of DHT as described in the introduction.

In Figure 20 to Figure 22 the ratio of the experimental Nusselt to the Nusselt for pure forced convection (see eq. 16) is plotted over the Buoyancy number. A ratio smaller than one is the regime of the mixed convection (black bold horizontal line in Figure 20 to Figure 22). It can be seen that the experimental values are located in the mixed convection region and by increasing the heat flux the effect of buoyancy is also increasing.

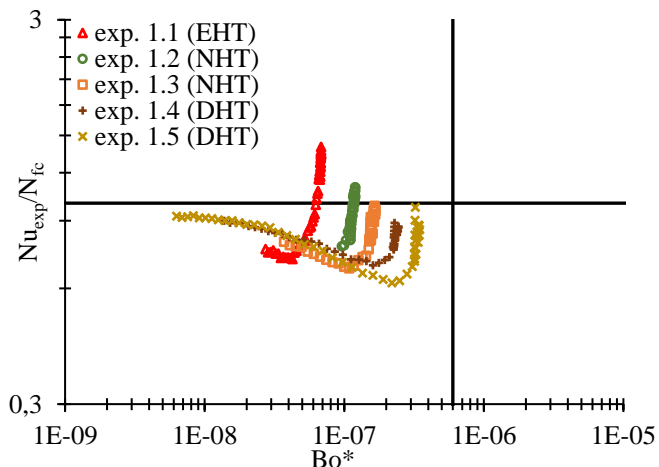


Figure 20: Effects of buoyancy on convective heat transfer for the first test series.

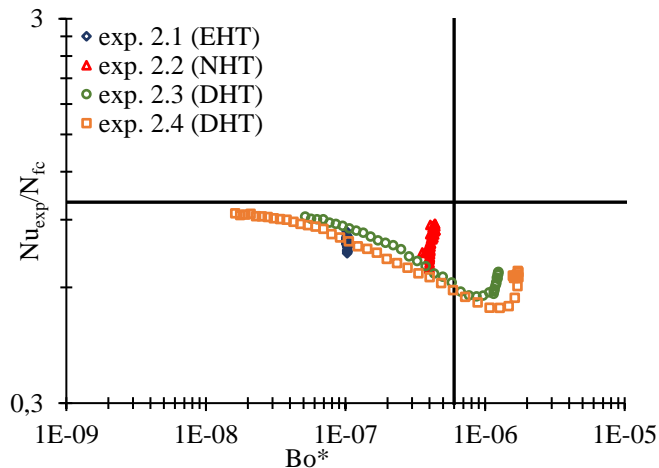


Figure 21: Effects of buoyancy on convective heat transfer for the second test series.

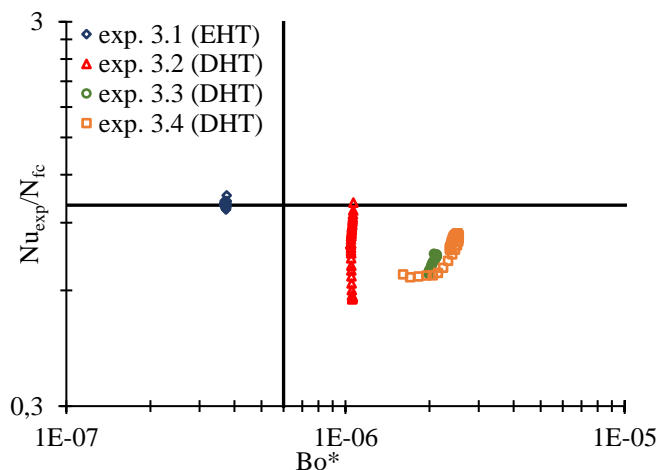


Figure 22: Effects of buoyancy on convective heat transfer for the third test series.

The next table (Table 2) shows a summary of the compliance of all presented criteria to the experiments.

Table 2: Validation of the presented criteria for the onset of DHT.

exp.	HTM	$\frac{\xi_w}{\xi}$	$\frac{Gr}{Re^{2.7}}$	Bo*	Ya.	St.	Pi.	Je.
1.1	EHT	O	O	O	X	X	X	O
1.2	NHT	X	O	O	X	X	X	O
1.3	NHT	X	O	O	X	X	X	O
1.4	DHT	O	O	X	X	X	X	X
1.5	DHT	O	O	X	X	X	X	X
2.1	EHT	O	O	O	X	X	X	O
2.2	NHT	X	X	O	X	X	X	O
2.3	DHT	O	O	O	X	X	X	O
2.4	DHT	O	O	O	X	X	X	O
3.1	EHT	O	O	O	X	X	X	O
3.2	DHT	O	O	O	X	X	X	O
3.3	DHT	O	O	O	X	X	X	O
3.4	DHT	O	O	O	X	X	X	O

O: in compliance with the experiments
X: not in compliance with the experiments

All experimental parameters can be seen in Table 3. The parameter in the last column is for the verification of adiabatic conditions.

Table 3: Experimental overview

exp.	$\frac{G}{[m^2 s]}$	$\frac{\dot{q}}{[kW/m^2]}$	p_{in} [MPa]	Δp [kPa]	$T_{b,in}$ [°C]	$1 - \left \frac{\dot{Q}_{th}}{\dot{Q}_{el}} \right $ [%]
1.1	861	31	7.78	26	30	1.6
1.2	849	51	7.72	42	5	8.1
1.3	852	71	7.70	35	5	5.4
1.4	816	92	7.79	41	5	0.3
1.5	782	112	7.76	64	5	0.5
2.1	543	10	7.71	57	5	4.0
2.2	502	31	7.69	17	5	12.6
2.3	431	51	7.70	7	5	2.0
2.4	431	71	7.69	8	5	3.9
3.1	410	10	7.78	36	5	4.1
3.2	416	30	7.78	28	5	0.7
3.3	400	50	7.78	78	5	3.0
3.4	420	70	7.77	71	5	6.8

CONCLUSION AND FUTURE WORK

Different criteria for the onset of DHT are presented and assessed against experiments carried out in the SCARLETT facility. One of these criteria is based on the effect of flow acceleration (Petukhov et al.), and the other two criteria are based on the effect of buoyancy (Jackson et al.). Furthermore, four other general criteria are used, which predict the onset of DHT through the ratio of heat flux to mass flux.

Validation of the presented criteria occurred through a series of experiments. Especially the Jackson's criterion showed a good

compliance with the local prediction of DHT. It is shown, that for a simpler assessment of the onset of this effect in sCO₂ the criterion of Jean et al. can be used.

NOMENCLATURE

A	: area, [m ²]
Bo	: buoyancy parameter, [-]
C_p	: specific heat, [J/(kg K)]
d	: diameter, [m]
g	: acceleration of gravity, [m/s ²]
G	: mass flux, [kg/(m ² s)]
Gr	: Grashof number, [-]
i	: specific enthalpy, [J/kg]
h	: heat transfer coefficient, [W/(m ² K)]
I	: current, [A]
L	: length, [m]
\dot{m}	: mass flow rate, [kg/s]
Nu	: Nusselt number, [-]
p	: pressure, [Pa] or [bar]
P	: electrical Power, [W]
Pr	: Prandtl number, [-]
\dot{Q}	: heat transfer rate, [W]
\dot{q}	: heat flux, [W/m ²]
\dot{q}_v	: volumetric heat flux, [W/m ³]
T	: Temperature, [°C] or [K]
Re	: Reynolds number, [-]
U	: voltage, [V]

Greek symbols

β	: volumetric expansion coefficient, [1/K]
λ	: thermal conductivity, [W/(m K)]
μ	: dynamic viscosity [Pa s]
ν	: kinematic viscosity, [m ² /s]
ξ	: friction resistance, [-]
ρ	: density, [kg/m ³]

Subscripts

b	: bulk fluid
cr	: fluid properties at critical point
el	: electric, calculated with el. power
exp	: experimental
fc	: forced convection
h	: heated length
hyd	: hydraulic length
i	: inner wall
in	: inlet bulk fluid conditions
max	: maximum
o	: outer wall
out	: outlet bulk fluid conditions
pc	: fluid properties at pseudocritical point
sur	: surface of tube
th	: thermal, calculated with bulk fluid
u	: acceleration resistance
w	: tube-wall
x	: local tube position

ACKNOWLEDGEMENTS

The presented work was funded by the German Federal Ministry for Economic Affairs and Energy (BMWi. Project no. 1501557) on basis of a decision by the German Bundestag.

REFERENCES

- [1] E. W. Lemmon, M. L. Huber, M. O. McLinden, *REFPROP*, NIST SRD 23, United States of America (2010).
- [2] M. F. Löwenberg, "Wärmeübergang von Wasser in vertikalen Rohrströmungen bei überkritischem Druck". Dissertation, Universität Stuttgart, Stuttgart (2007).
- [3] V. A. Kurganov; V. B. Ankudinov; A. G. Kaptilnyi, "Experimental study of velocity and temperature fields in an ascending flow of carbon dioxide at supercritical pressure in a heated vertical pipe", *HIGH TEMP* (1986).
- [4] B. S. Shiralkar and P. Griffith, "Deterioration in Heat Transfer to Fluids at Supercritical Pressure and High Heat Fluxes", *Journal of Heat Transfer* 1, pp. 27 (1969), (10.1115/1.3580115).
- [5] B. S. Petukhov; V. A. Kurganov; V. B. Ankudinov, "Heat transfer and flow resistance in the turbulent pipe flow of a fluid with near-critical state parameters", *Teplofizika Vysokikh Temperatur* (1983).
- [6] D. M. McEligot and J. D. Jackson, "'Deterioration' criteria for convective heat transfer in gas flow through non-circular ducts", *Nuclear Engineering and Design* 3, pp. 327–333 (2004), (10.1016/j.nucengdes.2004.05.004).
- [7] J. D. Jackson, "Fluid flow and convective heat transfer to fluids at supercritical pressure", *Nuclear Engineering and Design*, pp. 24–40 (2013), (10.1016/j.nucengdes.2012.09.040).
- [8] J. H. Bae; J. Y. Yoo; H. Choi, "Direct numerical simulation of turbulent supercritical flows with heat transfer", *Journal of Heat Transfer* 10, pp. 105104 (2005), (10.1063/1.2047588).
- [9] X. Cheng and T. Schulenberg, *Heat transfer at supercritical pressures. Literature review and application to an HPLWR*, FZKA 6609, Karlsruhe (2001).
- [10] H. Kim; Y. Y. Bae; H. Y. Kim; J. H. Song; B. H. Cho, "Experimental Investigation on the Heat Transfer Characteristics in a Vertical Upward Flow of Supercritical CO₂", *Proceedings of ICAPP*, pp. 372–381 (June 4-8, 2006).
- [11] I. L. Pioro; H. F. Khartabil; R. B. Duffey, "Heat transfer to supercritical fluids flowing in channels—empirical correlations (survey)", *Nuclear Engineering and Design*, 1-3, pp. 69–91 (2004), (10.1016/j.nucengdes.2003.10.010).
- [12] P. L. Kirillov and V. A. Grabezhnaya, "Heat Transfer at Supercritical Pressures and the Onset of Deterioration", *14th International Conference on Nuclear Engineering, Asme*, Volume 2, pp. 283-289 (2006), (10.1115/ICONE14-89274).
- [13] W. Flaig; R. Mertz; J. Starflinger, "Design, control procedure and start-up of the sCO₂ test facility SCARLETT", *DuEPublico, 2nd European sCO₂ Conference 2018, 2nd European sCO₂ Conference 2018, Essen, Germany*, pp. 1–11 (2018), (10.17185/duepublico/46081).
- [14] H. Herwig, *Strömungsmechanik*, Springer Fachmedien Wiesbaden, Wiesbaden (2016).
- [15] F. P. Incropera; D. P. DeWitt; T. L. Bergman; A. S. Lavine, *Principles of heat and mass transfer* 7. ed., Wiley, Singapore (2013).
- [16] H. S. Swenson; J. R. Carver; C. R. Kakarala, "Heat Transfer to Supercritical Water in Smooth-Bore Tubes", *Journal of Heat Transfer* 4, pp. 477 (1965), (10.1115/1.3689139).

2019-sCO₂.eu-109

Assessment of performance and costs of CO₂ based Next Level Geothermal Power (NLGP) systems

Stefan Glos*

Siemens AG, Gas and Power Division
Mülheim an der Ruhr, Germany
Email:Stefan.glos@siemens.com

Jil Hansper

Siemens AG, Gas and Power Division
Mülheim an der Ruhr, Germany

Stefanie Grotkamp

Siemens AG, Gas and Power Division
Mülheim an der Ruhr, Germany

Michael Wechsung

Siemens AG, Gas and Power Division
Mülheim an der Ruhr, Germany

ABSTRACT

Alternative power cycles based on supercritical carbon dioxide (sCO₂) are increasingly gaining in importance of scientific and industrial research in the energy sector. The applications for which this new technology is being discussed are mainly in the area of direct heated applications such as coal fired, concentrated solar power and indirect heated applications such as waste heat recovery and combined cycle power plants. Geothermal power generation based on supercritical carbon dioxide (sCO₂) is a topic of geophysical research and has been the object of numerous studies over the past years. In comparison to conventional hydrothermal power plants, such CO₂ based next level geothermal plume power plants (NLGP) systems exhibit several thermophysical advantages. Essentially, a more effective geothermal heat extraction and less need for auxiliary pumping power, due to a much stronger thermosiphon effect, compared to water-based geothermal energy extraction can be highlighted. In this paper a thermodynamic and energy conversion evaluation of NLGP systems is provided. The results are compared to conventional hydrothermal power cycles. The results of the thermodynamic calculations show that NLGP systems can supply significantly more electricity, compared to hydrothermal systems, particularly at "shallow" depths of 2-3 km and at low reservoir permeabilities. Based on the thermodynamic simulation calculations, initial turbine design considerations are discussed. Initial blade path calculations show a compact turbine layout for the CO₂ turbine. However, compared to fossil application the near critical expansion of a geothermal power plant leads to different design requirements. Initial cost estimations show that NLGP systems can generate electricity at competitive levelized costs of electricity (LCOE) at much lower resource temperatures than hydrothermal systems, thereby considerably expanding the geothermal resource base worldwide.

INTRODUCTION

Unlike to other renewable energies such as wind and solar energy, geothermal energy is available all year round and with virtually no fluctuations. The associated controllable and demand-oriented feed-in possibility is a great advantage of geothermal power plants. On the other hand, only a few regions on earth can be considered as locations for conventional geothermal power generation due to the required geological boundary conditions. Low temperature levels of the reservoirs that can be tapped at shallow depth prevent global economic use. Temperatures of around 100 °C make geothermal power generation using conventional methods based on a secondary Clausius Rankine or Organic Rankine cycle (ORC) unprofitable.

Against this background, the use of supercritical carbon dioxide (sCO₂) as an alternative energy-extraction medium from naturally permeable sedimentary-basin reservoirs and the use in direct and indirect geothermal power plant applications has been discussed in several publications. [1, 2, 3, 4]

The basic concept of a NLGP system, which is shown in Figure 1, can be outlined as follows: Waste CO₂ from one or several fossil fuel power plants, or other CO₂ emitters, is captured using Carbon Capture (CC) technologies. The captured CO₂ can be transported, for example through pipelines, to a NLGP site, where the CO₂ is injected into a geological CO₂ storage formation. In order to ensure economical operation of the CO₂ system, a high temperature of the CO₂ storage formation must be maintained, i.e. at least about 100°C. These geologic formations or reservoirs also need to have sufficient permeability of >10 mD (1 mD = 10⁻¹⁵ m²) and need to be overlain by a caprock of sufficiently low permeability of about <0.01 mD to enable efficient CO₂ injectivity into the reservoir through the injection well and to prevent CO₂ flow through the caprock, against which the CO₂ pools upwardly. In the reservoir, the CO₂ is geothermally heated and a portion is piped back to the surface power plant, where it

is expanded in a turbine, driving a generator, and hence producing electricity.

The temperature-dependent density variation of sCO₂ is large compared to water. In addition, supercritical CO₂ has a kinematic viscosity that is, under base-case NLGP conditions [1, 2, 3] of a reservoir at a depth of 2.5 km, under hydrostatic fluid pressure and a temperature of 100°C, about 25% the kinematic viscosity of water. In other words, under these conditions the mobility of sCO₂ is four times higher than that of water. Furthermore, the thermal expansibility of sCO₂ is much larger than that of water. The low kinematic viscosity and high thermal expansion coefficient of sCO₂ result in the formation of a strong thermosiphon, a physical effect which circulates a fluid without the necessity of a mechanical pump. Driven by this thermosiphon a Brayton cycle can be established, generating electricity, eliminating this particular parasitic power requirement of water-based geothermal systems.

In this paper a first technical and economic assessment of CO₂ based geothermal power plants is given. Initial performance calculations are presented and basic design considerations such as turbine design are carried out. The results are compared with conventional hydrothermal power plants (brine/ORC). Furthermore, an initial economic evaluation is presented based on LCOE calculations.

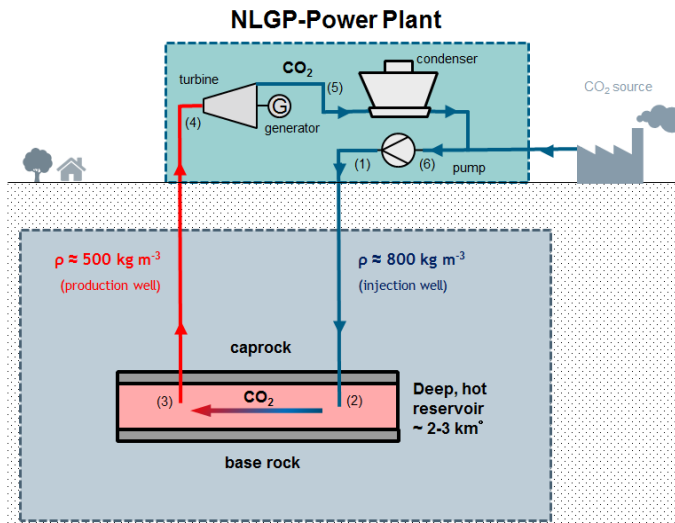


Figure 1: Exemplary illustration of a geothermal power cycle based on CO₂.

SIMULATION AND MODELING

The thermodynamic cycle simulations were carried out by an in-house simulation software and MS-Excel. Initial sCO₂ / ORC turbine design calculations were performed with internal design tools. The thermodynamic properties of CO₂, water and the ORC media were provided by the REFPROP (REFerence

fluid PROPERTIES) data base developed by the National Institute of Standards and Technology. [5]

The layout of a NLGP system according to figure 1 is comparatively simple. The related thermodynamic changes in the state of the CO₂ cycle are shown in the T-s diagram in figure 2. The power plant essentially consists of three main components:

- turbine (condition 4 to 5)
- condenser (5 to 6)
- optional pump (6 to 1)

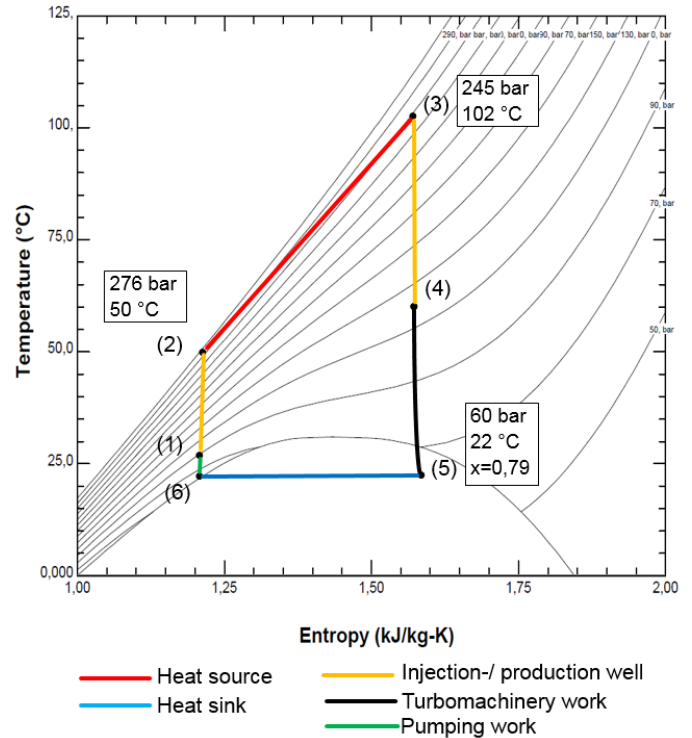


Figure 2: Exemplary illustration of a geothermal power cycle based on CO₂.

The CO₂ is injected into the subsurface in supercooled state (1). With increasing depth and thus increasing hydrostatic pressure, the temperature and pressure level increase until the CO₂ reaches supercritical state (2). The flow in the injection well is modeled as a vertical pipe considering the hydrostatic pressure according to equations 1 to 3. Based on the first law of thermodynamics and Bernoulli, the geodetic height difference z , the acceleration due to gravity g and the enthalpy of fluid h are used to determine the pressure change in the borehole. In addition, ζ represents the pressure loss coefficient and c the flow velocity of the fluid. Because the fluid density is pressure-dependent, an integration over the drilling length is necessary. For this purpose, the borehole is divided into 200 or rather 100 m long sub-segments where subscripts i and $i+1$ mark the beginning and the end of each element. The fluid density is considered to be constant within a segment.

$$(1) \quad \int_i^{i+1} \frac{dp}{\rho} = g \cdot z_{i,i+1} = h_{i+1} - h_i$$

$$(2) \quad \Delta p_{i,i+1} = g \cdot z_{i,i+1} \cdot \rho_i - \Delta p$$

$$(3) \quad \Delta p = \zeta \cdot \frac{\rho}{2} \cdot c^2$$

After compression in the injection well, the supercritical CO₂ is geothermally heated to reservoir temperature. The flow in the geologic reservoir is characterized by Darcy's law [2]. It combines the flow properties of a fluid with the properties of a porous medium and enables the calculation of a (fictitious) flow velocity in the reservoir in equation 4. Therefore, κ describes the permeability of the rock formation, μ the dynamic viscosity of the fluid, Δp_{Res} the pressure loss in the reservoir and L_{Res} the corresponding flow length. Assuming a constant mass flow, the pressure loss in the reservoir is thus determined by the geothermal mass flow \dot{m}_{geo} and the flow cross-section A_{Res} in the reservoir according to equation 5.

$$(4) \quad c_{Res} = \frac{\kappa}{\mu} \cdot \frac{\Delta p_{Res}}{L_{Res}}$$

$$(5) \quad \Delta p_{Res} = \frac{\mu}{\rho} \cdot \frac{L_{Res}}{A_{Res}} \cdot \frac{1}{\kappa} \cdot \dot{m}_{geo}$$

As fixed boundary conditions for the process simulation the reservoir temperature and hydrostatic pressure are defined at the bottom of the production well in state (3). Afterwards, the heated CO₂ flows through the production well to the surface, where it is used to generate electricity. The supercritical CO₂ expands in the turbine into the two-phase state region (5), is cooled in the condenser and converts to liquid state (6). Above-ground pumping, to state (1), enables a larger geothermal mass flow and thus increases the power plant output. Due to the so-called thermosiphon effect, which is induced by the variable density of CO₂, it is also possible to operate the system without additional pumps.

The storage formations suitable for NLGP systems are much larger than those used for conventional hydrothermal geothermal plants. Due to their size, systems with several production wells are possible, which increases the thermal output of the reservoir. The coordination number N determines the number of production wells. The coordination number $N = 1$ describes a 5-point system with an edge length of one kilometer consisting of one injection well and four production wells. The above-ground power plant is located centrally in the immediate vicinity of the injection well.

With an increased coordination number, the edge length and thus the number of injection and production wells increases in the manner shown in figure 3. This makes the system scalable.

The system size should be chosen depending on the boundary conditions of the reservoir and the economic efficiency.

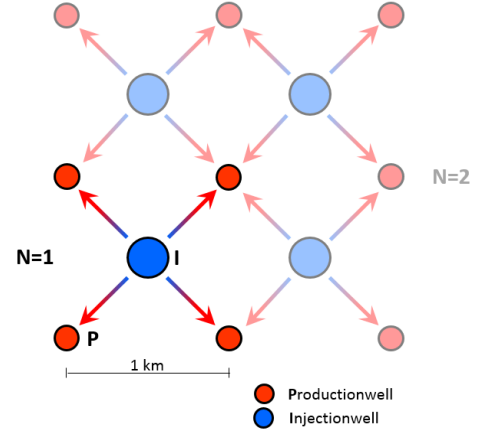


Figure 3: Hole pattern in relation to the coordination number N

THERMODYNAMIC EVALUATION

The cycle layout and reference conditions for the thermodynamic evaluation were chosen in accordance to Adams et al. [2] for a single 5-spot well pattern ($N=1$). The “base case” conditions, reflecting typical geologic reservoirs, are summarized in table 1. In opposite to Adams et al. [2] where R245fa was used as ORC-fluid medium, isobutane is used as the ORC-fluid medium in the presented investigation because of its lower environmental impact, lower costs, and as it is a common fluid in the considered temperature range.

Figure 4 summarizes the results of the thermodynamic analysis performed. The cumulative column represents the turbine power. Under reference conditions according to table 1 NLGP systems achieve a significant larger net power output (blue bars) compared to conventional, brine based (indirect) power plants.

Table 1: Summary of NLGP base case conditions

	NLGP Base Case
Coordination number N [-]	1(1km x1km)
Depth [m]	2500
Permeability [mD]	50
Temperature gradient [°C/km]	35
Well diameter [m]	0.41
Cooling Type	Wet Cooling tower
Heat Sink Temperature [°C]	15
Approach Temperature [°C]	7

The key factor for this result is the strong thermosiphon effect and lower pressure losses of the reservoir flow caused by the lower kinematic viscosity of sCO₂. On one hand the 4-times higher mobility of sCO₂, compared to water, leads to an approximate quadruplication of the CO₂ mass flowrate through

the turbine. On the other hand, the specific heat capacity

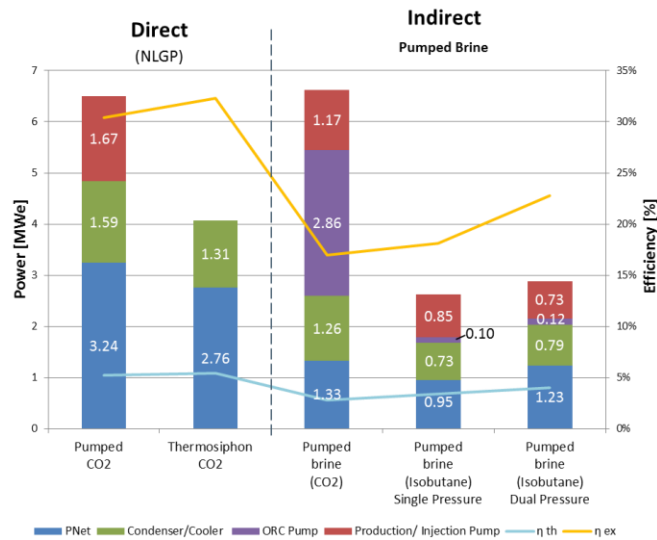


Figure 4: Comparison of the power output for different geothermal concepts (i.e. NLGP and indirect brine) at base case conditions.

of sCO_2 is approximately half, so that the transferred heat and thus the resulting net electric power output of the NLGP power plant, is approximate 2-3 times larger compared to conventional water-based (indirect) geothermal power plants. In addition, the direct conversion of the thermal energy in the turbine eliminates the exergy losses in a heat exchanger, so that the exergetic efficiency is higher than that of the indirect systems. In indirect systems, the isobutane-driven cycles achieve a higher net output. This can be explained by the high parasitic power losses in the secondary cycle when a gas, such as CO_2 , is compressed. By installing a dual-pressure ORC process, the efficiency of the brine case can be increased, which is also shown in figure 4. In this case, the geothermal heat is transferred at two different pressure levels to the working medium, which reduces the temperature differences between the fluids and thus the exergy losses in the heat exchanger. A larger amount of heat is thus extracted from the geothermal medium, which improves the thermal efficiency and decreases the reinjection temperature. The amount of heat absorbed in the reservoir is therefore correspondingly larger. Moreover, installing a dual-pressure process raises the complexity of the system. However, the efficiency and the net power output are still below the results of the NLGP cycle. In conclusion, the present thermodynamic analysis supports the results of Adam et al. [2].

Since geothermal power generation depends on the conditions of specific geological formation in the reservoirs the impact of reservoir depth and permeability was calculated in a next step which is outlined in four different combinations in figure 5.

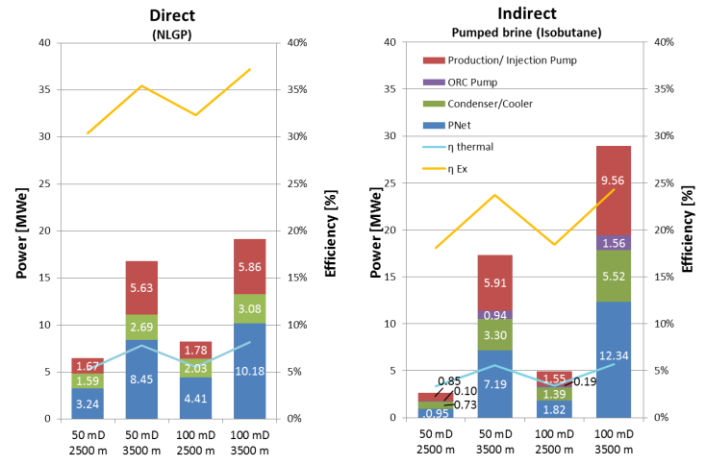


Figure 5: Illustration of the impact of different geologic conditions, (i.e. reservoir permeability and depth) on electric power output.

With increasing depth, the storage temperature and thus the temperature of the extracted geothermal fluid rise due to the geothermal temperature gradient. In both cycle types the turbine inlet temperature increases and thus the turbine power output. In addition, in the NLGP system, the higher reservoir temperature causes a larger difference in the average density between the injection and production wells, thereby enhancing the thermosiphon effect. Conversely, in the indirect cycle an increased reservoir temperature has an influence on the flow behaviour of the brine and thus on the pressure losses in the reservoir flow. The lower the dynamic viscosity of the geothermal medium, the lower the pressure losses in the reservoir flow. In contrast to the dynamic viscosity of CO_2 , that of brine is strongly dependent on the temperature. With increasing reservoir depth and temperature the dynamic viscosity of the brine decreases significantly. As a result, the pressure losses in the reservoir and thus the required pumping capacity of the geothermal pump decrease. This enables the extraction of a larger brine mass flow and thus larger component outputs. Overall, the increase in efficiency due to an increased reservoir depth can substantially be explained by the temperature elevation in the reservoir and its influence on the flow behavior of the brine. At increased permeability (with the same depth) the pressure losses in the reservoir, which need to be compensated, are lower. This results in a lower required pumping capacity and thus a higher net power output. For larger drilling depths and simultaneously enhanced permeability, the increase in performance is correspondingly greater.

In figure 6 the exergy transferred in the reservoir and the resulting net power are shown as a function of the mass flow for both the reference case and for changed reservoir conditions. The lower two plots in figure 6 show the corresponding exergy losses.

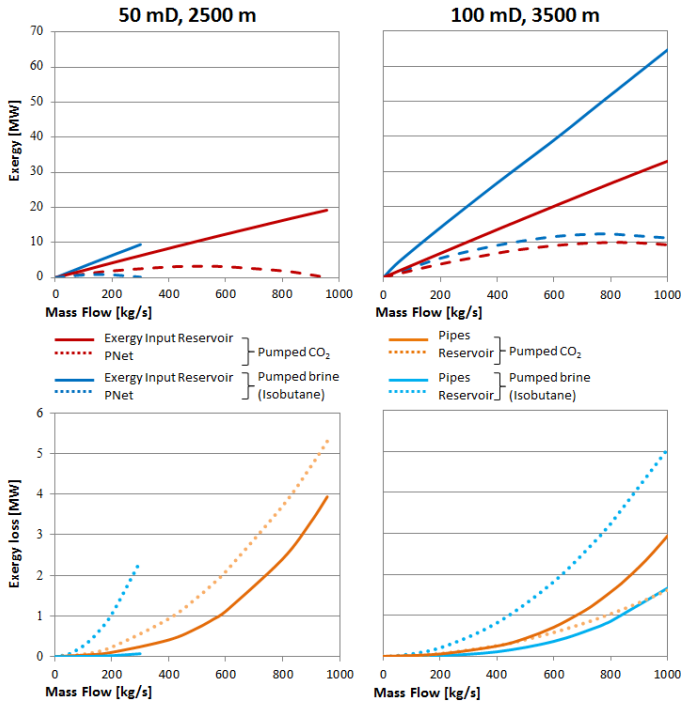


Figure 6: Comparison of exergy transfer and exergy losses for NLGP and brine based systems.

It is obvious that the amount of absorbed heat increases linearly for both studied reservoir cases. As the mass flow increases, the pressure losses in the pipes and in the reservoir also increase. The quadratic rise of the exergy losses deviates depending on the geothermal fluid. In the reference case, the limiting factor for the brine (isobutane) system is the pressure loss in the reservoir. For an increased permeability, i.e. 100 mD and reservoir depth of 3500 m, the pressure loss is reduced so significantly that the net output is even greater than that of the NLGP system. In this case the net output for both systems reaches a maximum at similar mass flow rates. Due to the higher isobaric heat capacity of brine, compared to CO₂, a larger amount of heat is transferred from the reservoir in the indirect hydrothermal system. Although the reservoir conditions are also of energetic advantage for the NLGP system, the high flow velocities of the CO₂ limit the net output. In contrast to the indirect system the pressure loss of the wells is the limiting factor for the NLGP system.

The evaluations indicate that the net power output strongly depends on the conditions of the reservoir and also confirm the results of Adams et al. [2]. In summary CO₂-based systems are advantageous to (indirect) brine-based systems for shallower depths and low permeabilities. The higher the reservoir permeability, the more the viscosity advantages of CO₂ become less important and the greater heat absorption capacity of the brine leads to a higher net output of conventional plants.

Analogous to conventional power plants, the ambient temperature or the site-specific boundary condition for recooling has a significant influence on the performance of the

power plant. The NLGP concept and the indirect plants with brine as geothermal fluid and isobutane are investigated regarding their sensitivity to changed ambient temperatures, i.e. the heat sink temperature. Figure 7 shows the analysis results. The middle column for 15 °C corresponds to the reference case.

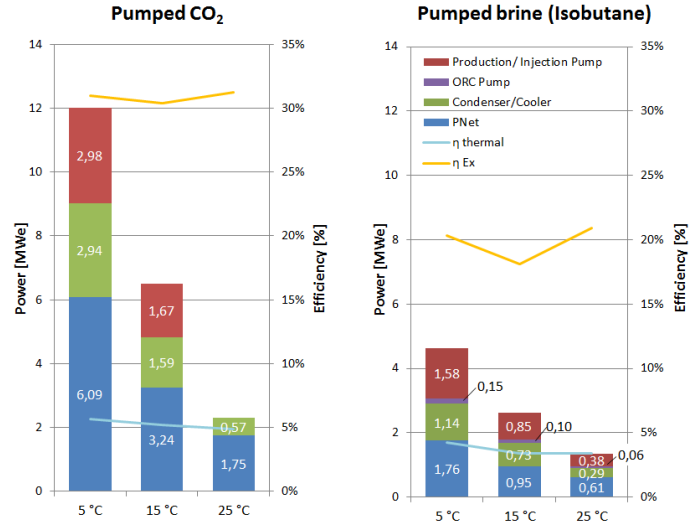


Figure 7: Impact of the ambient air (heat sink) temperature on the electric power output of NLGP and brine-based systems.

If the ambient air temperature is reduced from 25°C to 5°C, the output of the NLGP system is five times higher and the net output three times higher. The lower the ambient air temperatures, the lower is the injection temperature of the CO₂ and the higher is the averaged density of the fluid in the injection well. Under constant reservoir conditions, the difference in the average density between the injection and production well therefore increases, resulting in an enhanced thermosiphon effect at lower ambient air temperatures. Furthermore, the amount of heat absorbed in the reservoir increases with decreased injection temperature, which can also be seen in the larger parasitic load of the cooling system. In addition, with lower ambient air temperature both the condensing temperature and the condensing pressure decrease. This results in a lower turbine back pressure. The enthalpy difference and thus the power output of the turbine are accordingly higher.

At an ambient air temperature of 25°C, the entire process runs in the supercritical state area of CO₂. The additional use of a compressor cannot increase the net output due to the energy-intensive compression in the supercritical state. Powered entirely by the thermosiphon, the system still achieves a higher net output, compared to the brine-based systems, even at ambient temperatures of 25°C, under the given reservoir conditions. In contrast to the brine (isobutane) system, the dependence between density and fluid temperature of the CO₂ results in a higher sensitivity on ambient temperature changes of the NLGP system. However, for low ambient temperatures, e.g.

5 °C, NLGP systems can achieve an even greater net power output.

TURBINE DESIGN CONSIDERATIONS

Initial blade path calculation and design considerations were carried out with Siemens in-house software tools on the basis of the thermodynamic calculations described above. The pumped NLGP system and the brine (isobutane) system were investigated. For both applications highly efficient SST600 turbine modules were chosen consisting of reaction blades and turning at net frequency. Figure 8 shows the comparison of the CO₂ turbine and isobutane turbine for the base case. For both turbines enhance sealing systems have to be applied. However, due to the flammability of isobutane the leak tightness requirements will be significantly higher for the isobutane turbine. In table 2 the most relevant thermodynamic design conditions are listed for both turbines.

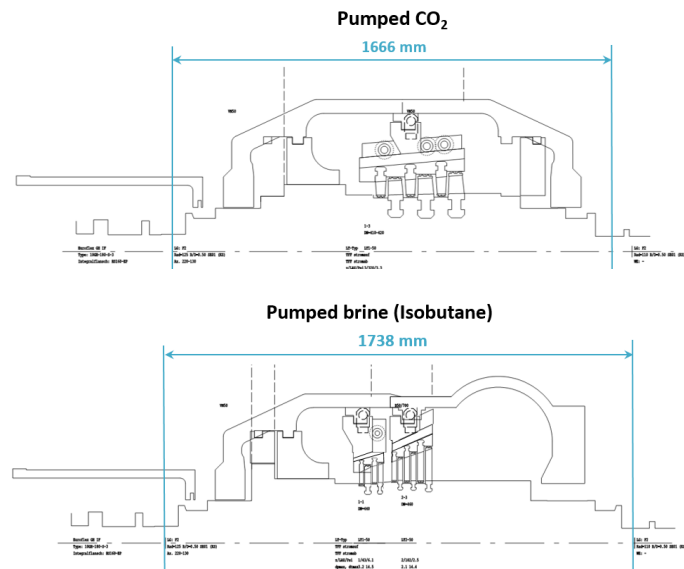


Figure 8: Scaled representation of the CO₂ turbine (top) and the isobutane turbine (bottom) of the reference case.

Table 2: Thermodynamic design conditions for the CO₂ and the ORC turbine are geothermal base case conditions

Value	Unit	CO ₂ turbine (~7MW)		Isobutan turbine (~3MW)	
p_{in} p_{out}	[bar]	118.9	61.3	10.1	3.3
T_{in} T_{out}	[°C]	60.0	22.9	66.6	34.8
\dot{m}	[kg/s]	514		74.4	
\dot{V}_{in} \dot{V}_{out}	[m ³ /s]	1.21	1.99	2.83	9.0
Δh	[kJ/kg]	14.6		39.8	
Δp	[bar]	57.6		6.8	

Because of the almost sixteen times higher density of the CO₂ the volume flow in the turbine inlet is less than half compared to the isobutane turbine even though the CO₂ mass flow is almost seven times larger. The near-critical expansion of

CO₂ results in a small density difference compared to isobutane, so that the increase in volume flow during the expansion is also low leading to a small widening of the flow path. Overall, blade path efficiencies for both turbines of approx. 91% can be achieved. Due the significant higher pressure differences the internal leakages of the CO₂ turbine will be higher compared to the ORC turbine resulting in a lower overall efficiency.

The large pressure difference with simultaneous low enthalpy drop in the CO₂ turbine leads to comparable large bending forces in the airfoils. As a result, an enlargement of the blade roots and the hub diameter is necessary to avoid impermissible stresses in the blade roots and airfoils, which is a significant difference compared to CO₂ turbines considered for fossil applications. To make this clear the expansion line of the CO₂ turbine for the NLGP was compared with the expansion lines of CO₂ turbines for waste heat recovery (CCPP) applications presented in [12], which is illustrated in figure 9 and in figure 10.

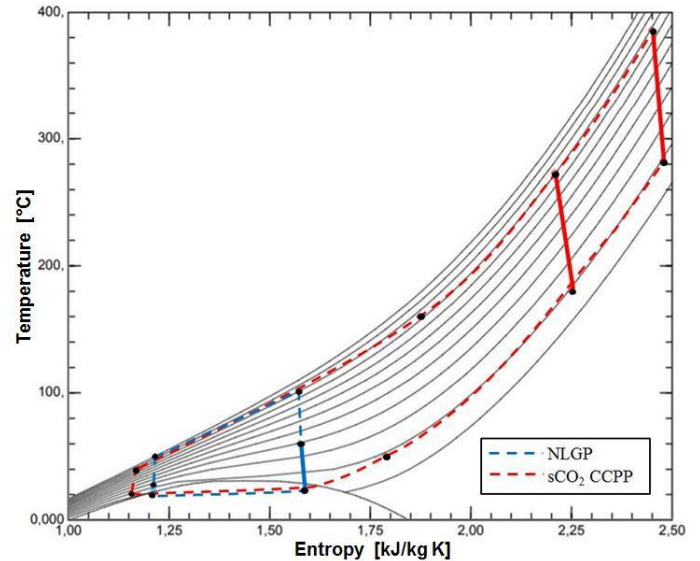


Figure 9: Comparison of the CO₂ expansion (bold lines) for geothermal power cycle and a fossil heat recovery application in a T-s-diagram.

It can be observed that the gradient $\Delta p/\Delta h$ is significant larger for the geothermal application which confirms the described design result for the NLGP turbine. Especially for large scaled applications with higher power output this can be a limiting factor so that optimized design concepts need to be developed. A low-speed operation mode for example could increase the number of stages and thus decrease the pressure drop across a single turbine stage.

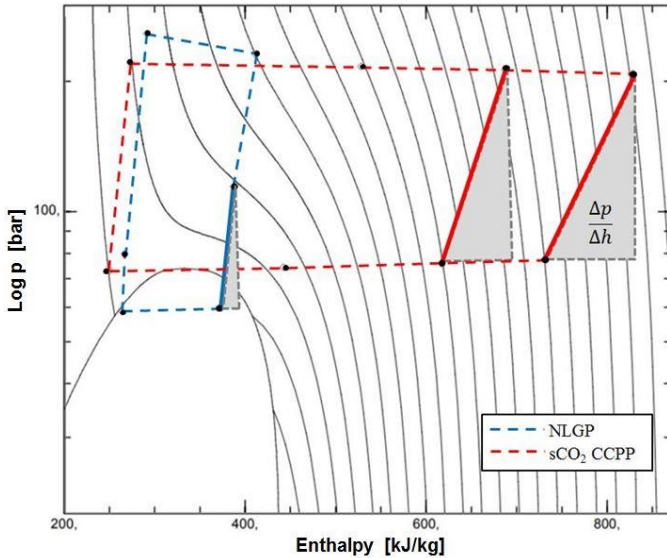


Figure 10: Comparison of the CO₂ expansion (bold lines) for geothermal power cycle (blue) and a fossil heat recovery application (red) in a log p-h-diagram.

The impact of varying reservoir conditions on the turbine design was investigated exemplarily for an increased permeability of 100 mD and a drilling depth of 3500 m. The resulting thermodynamic design conditions are summarized in Table 3.

Table 3: Thermodynamic design conditions for the CO₂ and the ORC turbine at modified geothermal conditions (3500m,100mD)

Value		Unit	CO ₂ turbine (~19 MW)		Isobutan turbine (~29 MW)	
p_{in}	p_{out}	[bar]	159.8	61.3	18.0	3.3
T_{in}	T_{out}	[°C]	86.6	22.9	97.4	41.4
\dot{m}		[kg/s]	820		531	
\dot{V}_{in}	\dot{V}_{out}	[m ³ /s]	1.93	3.62	10.92	66.93
Δh		[kJ/kg]	26.5		61.3	
Δp		[bar]	98.5		14.7	

Due to the changed process parameters, the mass flow in both turbines increases. The thermodynamic analysis shows that the geothermal mass flow of the brine (isobutane) system and thus the amount of heat absorbed in the reservoir is considerably larger under changed reservoir conditions. This leads to a seven times larger mass flow of isobutane to absorb the amount of geothermal energy. While the inlet volume flow of the isobutane turbine increases almost by a factor of 4, it is not even doubled in the CO₂ turbine. This will result in a significantly larger isobutane turbine for changed reservoir conditions due to the strong increase in volume flow in the isobutane cycle.

Geothermal power plants are characterised by high heat dissipation in the condenser and a low average thermodynamic temperature. Thus, the required heat exchanger surfaces are large and considerably increase the costs of the cooling system. Basic design calculations considering a shell-and-tube heat exchanger were carried out resulting in heat exchanger surfaces for the NLGP- and the (indirect) brine-based (isobutane in the secondary loop) system. Figure 11 illustrates the ratio of the respective heat exchanger surfaces depending on the different reservoir conditions.

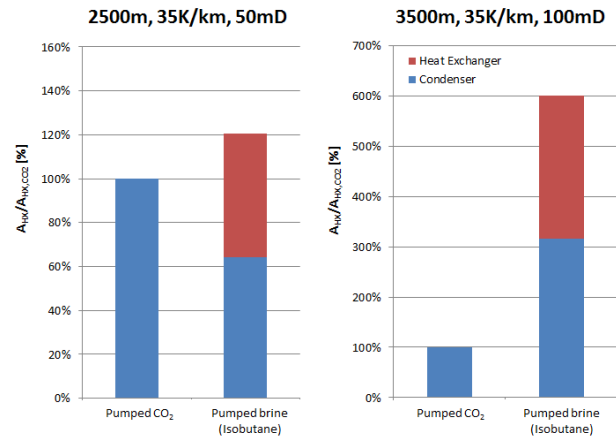


Figure 11: Comparison of heat exchanger surfaces for NLGP and brine based systems for different reservoir conditions (depth, geothermal gradient, permeability).

At base case conditions, the overall heat exchanger surface of the ORC system is approximately 20 % larger than that of the CO₂ plant. Although only half of the amount of thermal energy is transferred in the isobutane-condenser, it already represents more than 60% of the CO₂ condenser, which can be explained by the reduced heat transfer in the ORC condenser. In contrast to the NLGP system, the isobutane is superheated at the condenser inlet. In this gaseous state, the heat transfer is very low, leading to a large total heat exchange surface. Combined with the additional heat exchanger for the secondary cycle, the total required exchange surface of the brine (isobutane) system is larger.

For the modified reservoir conditions, i.e. 3500 m and 100 mD, the transferred exergy in the reservoir is approximately doubled for the (indirect) brine (isobutane) case, which can be seen in figure 5. Thus, the emitted heat in the condenser is even greater than that of the CO₂ plant. As a result, the overall required heat exchange surface is approximately six times larger.

Based on the initial design assumptions mentioned above, NLGP's surface power plant is less complex, has fewer and smaller components than the (indirect) ORC system. However, this economic advantage is partly compensated by the higher pressure level of the CO₂ cycle, which leads to greater wall

thicknesses of the components. To evaluate the different designs for the overall power plant, a detailed comparative design study would be the next step. However, a first generic economic assessment for NLGP based on LCOE calculations have been carried out, which is described next.

ECONOMIC EVALUATION

According to Bielicki et al. [6] the levelized costs of electricity (LCOE) for NLGP systems are decreasing when the power plant capacity is increasing from N=1 to higher coordination numbers until a minimum appears to be reached at N=5. Therefore, two N=5 cases were investigated for the economic evaluation.

In Table 4 the geologic properties of the reservoirs, the thermal boundary conditions of the power plants and the most relevant thermodynamic assumptions and characteristics for the two considered cases are given. They were chosen to represent typical conditions of reservoirs, which are common, where NLGP is feasible and geothermal systems are not economical. During the assumed operation lifetime of 25 years, no thermal depletion of the reservoirs was assumed.

Table 4: Boundary conditions of the two considered cases for the economic evaluation.

	Case 51 MW _e	Case 157 MW _e
Coordination number N [-]	5	5
Depth [m]	2500	3500
Permeability [mD]	50	100
Temperature gradient [°C/km]	35	35
Well diameter [m]	0.41	0.41
Cooling type	Wet cooling tower	Wet cooling tower
Ambient air heat sink temperature [°C]	15	15
Approach temperature [°C]	15	15
P gross [MW _e]	79	255
P net [MW _e]	51	157

The cost assessment is performed for a project with brownfield approach. This means, that an already developed well field with existing wells, which can be re-used as CO₂-injection wells, is assumed. This may be the case, for example, for carbon capture and storage (CCS) systems and for depleted gas or oil fields especially when CO₂ is injected for enhanced oil recovery (EOR) or enhanced gas recovery (EGR).

The NLGP energy system may be structured in two parts: the well field including surface piping, and the surface power plant. Beside well drilling as main cost driver, the wellfield costs include all efforts for wellfield completion e.g. costs for monitoring equipment. These costs can vary significantly due to project specific boundary conditions such as e.g. soil properties, available infrastructure and monitoring or regulative requirements. For the first cost assessment, estimates by

Flaming et al. are used [7]. They are based mainly on the detailed cost analysis for geologic CO₂ sequestration published by the United States Environmental Protection Agency, EPA (2008) [8], and well drilling estimates from the Geothermal Electricity Technology Evaluation Model (GETEM) [9].

Cost estimates for the CO₂ pipelines are also subject to a certain dispersion reflecting variations caused by the impact of specific terrain, land use, and population density. In the present investigation the costs for the 65 km surface piping are calculated on average with ca. 2.2 \$/(km m), including all necessary equipment, corrosion protection cost as well as all efforts e.g. for planning engineering and installation. Considering published data [8, 10] this approach is assumed to be conservative.

The estimated costs of the power island include all necessary systems, infrastructure, buildings, efforts for planning, engineering, commissioning etc. that are typically within the scope of a turnkey project. An additional 10% in costs is assumed for project development by the project owner. The power plant costs were derived by adjusting components for conventional power plants. Preliminary calculations, based on Siemens' product portfolio and in-house data show that the main cost drivers are related to the heat rejection, i.e. cooling tower, and gas cooler. Favourable cooling conditions, for example access to direct cooling at coastal or offshore locations, can therefore lead to significant cost reductions. In sum, the current cost estimates for the surface plant, including piping, are 300 M\$ (52 MW_e) and 480 M\$ (157 MW_e). Further cost optimization potentials, e.g. by improving the heat rejection systems, seem likely and need to be investigated.

To evaluate the economic competitiveness of a NLGP power plant, the LCOE can be compared. The LCOE are calculated based on assumptions and boundary conditions following Lazard's latest comparative LCOE analysis [11].

Table 5: Assumptions for LCOE calculation for the two example NLGP systems.

Capacity factor	90%
Operation lifetime	25 years
Project development/ construction time	1 year
Annual O&M cost	360 – 630 \$/kW
O&M cost escalation rate	2.25%
Equity rate	40%
Cost of equity	12%
Cost of debt before tax	8%
Debt payback period	Operation lifetime
Principal payment type	Levelized debt service
Combined tax rate	40%
Depreciation schedule	Modified accelerated cost recovery system (MACRS) 5-years

The capacity factor defines the assumed operational time of the power plant.

Operation and maintenance (O&M) cost for the wellfield and the surface power plant are for first calculations estimated in accordance with the assumptions used in GETEM [9] as a percentage of the capital costs. The resulting annual costs seem quite high, compared to experience with conventional power plants. Evaporated cooling water is considered with 1 \$/m³.

In sum, the O&M costs contribute up to 40% to the estimated LCOE. Therefore, more detailed cost investigations should be conducted in a next step to evaluate the differences between NLGP systems and geothermal power plants regarding O&M efforts.

Table 6 shows the resulting LCOE compared to Lazard's [11] results for some conventional and renewable technologies in 2018. No revenues or costs of CO₂ storage are included in this comparison. These will have to be considered in addition.

Given the presented boundary conditions and assumptions, Table 6 shows that a 52 MW_e NLGP power plant may be too small to reach competitiveness. In contrast, the calculated LCOE for the 157 MW_e example NLGP power plant is within the LCOE range that is typical for other baseload-capable power plants, such as coal, nuclear or solar-thermal towers, the latter with energy storage. It must be emphasized that the economic assessment strongly depends on the geologic properties of the reservoir. As the presented evaluation is not based on reservoirs which were selected especially for conditions optimal for NLGP, significant lower LCOE can be expected with the right reservoirs. These need to be identified in a next step. This aspect is confirmed in principle by Levy et al. [13] who have determined the LCOE of approximately 16 \$ ct /kWh for a 30 MW application (green field approach) for a Mexican reservoir with special geologic conditions.

Table 6: LCOE Comparison for various baseload-capable power plants

	Technology	LCOE [\$ ct/kWh]
Lazard (2018) [11]	Solar Thermal Tower with Energy Storage (110 -135 MW)	9 – 18
	Geothermal (20 -50 MW)	7 – 11
	Nuclear (2200 MW)	11 – 19
	Gas Combined Cycle (550 MW)	4 – 7
	Coal (600 MW)	6 – 14
NLGP (brownfield)	Case 52 MW	20
	Case 157 MW	12

SUMMARY & OUTLOOK

The thermodynamic evaluation show that CO₂-based geothermal power plants can produce significantly more output than conventional (indirect) hydrothermal systems, particularly at "shallow" depths of 2-3 km and low reservoir permeabilities. Higher reservoir temperatures, e.g. due to greater reservoir depth, reduce the kinematic viscosity of the brine and thus the pressure losses occurring in the reservoir. The greater the reservoir permeability and the higher the reservoir temperature, the greater the energetic advantage of indirect brine systems with a secondary ORC (isobutane) process.

While the variable density of the CO₂ leads to a higher performance for relatively shallow reservoir depths, due to the thermosiphon effect, this property also results in a greater sensitivity of NLGP systems to cooling conditions, compared to brine-based geothermal systems, where low ambient air heat rejection temperatures are particularly advantageous for NLGP systems.

Initial design considerations showed a compact turbomachinery layout leading to a more compact design compared to brine/ORC systems especially for larger power output. Due to the expansion close to the critical point some different design requirements compared to fossil application needs to be considered. Thus, optimized designs are necessary which needs to be elaborated in the next future.

The calculated LCOEs for the example cases show, that with suitable geologic properties, NLGP systems can generate electricity at competitive costs, when a brownfield approach is used. Reservoirs with more beneficial geologic boundary conditions will lead to a further significant reduction of LCOEs. Thus, suitable locations need to be identified; enhanced cost analyses should be carried out, to determine the boundary conditions for competitive NLGP systems even with greenfield approach.

Including the costs of CO₂-emissions and the economic benefits of providing CO₂ storage in the cost comparison can lead to a further shift in favour of NLGP systems.

NOMENCLATURE

<i>CC</i>	Carbon Capture
<i>CCS</i>	Carbon capture and storage
<i>CCPP</i>	Combined cycle power plant
<i>EGR</i>	Enhanced gas recovery
<i>EOR</i>	Enhanced oil recovery
<i>GETEM</i>	Geothermal Electricity Technology Evaluation Model
<i>Geo</i>	geologic
<i>h</i>	Enthalpy [kJ/kg]
<i>LCOE</i>	Levelized costs of electricity
<i>m</i>	Mass flow [kg/s]
<i>mD</i>	millidarcy
<i>N</i>	Coordination number
<i>NLGP</i>	Next Level geothermal Power Plant
<i>ORC</i>	Organic Rankine cycle
<i>O&M</i>	Operation and maintenance

p	Pressure [bar]
P	Power output [MW]
ref	Reference
<i>REFPROP</i>	REFerence fluid PROPERTIES
<i>Res</i>	<i>geologic reservoir</i>
sCO_2	Supercritical Carbon Dioxide
T	Temperature [°C or K]
T_m	Mean Temperature [°C or K]
TTD	Terminal Temperature Difference [K]
\dot{V}	Volume flow [m ³ /s]
w/s	Water/Steam
x	Steam quality [-]
Δ	Difference
η	Efficiency [%]
κ	Permeability
μ	Dynamic viscosity
ζ	Pressure loss coefficient
ρ	Density [kg/m ³]

REFERENCES

- [1] Randolph, J.B., and M.O. Saar: Combining geothermal energy capture with geologic carbon dioxide sequestration, *Geophysical Research Letters*, doi.org/10.1029/2011GL047265, 38, L10401, 2011.
- [2] Adams, B.M., Kuehn, T.H., Bielicki, J.M., Randolph, J.B., & Saar, M.O.: A comparison of electric power output of CO₂ Plume Geothermal (NLGP) and brine geothermal systems for varying reservoir conditions, *Applied Energy* 140, 265-377 (2015).
- [3] Adams, B.M., T.H. Kuehn, J.M. Bielicki, J.B. Randolph, and M.O. Saar, On the importance of the thermosiphon effect in NLGP (CO₂ Plume Geothermal) power systems, *Energy* (2014).
- [4] Garapati, N., J.B. Randolph, and M.O. Saar, Brine displacement by CO₂, energy extraction rates, and lifespan of a CO₂-limited CO₂ Plume Geothermal (NLGP) system with a horizontal production well, *Geothermics*, doi.org/10.1016/j.geothermics.2015.02.005, 55:182–194, 2015.
- [5] Lemmen, E.W., Huber, M.L., McLinden M.O.: NIST Reference Fluid Thermodynamic and Transport Properties—REFPROP Version 9.1 (2013).
- [6] Bielicki, J.N., Adams, B.M., Choi, H., Jamiyansuren, B., Saar, M.O., Taff, S.J., Buscheck, T.A., Ogland-Hand, J.D.: Sedimentary Basin Geothermal Resource for Cost-Effective Generation of Renewable Electricity from Sequestered Carbon Dioxide, *Proceedings, 41st Workshop on Geothermal Reservoir Engineering Stanford University, Stanford, California* (2016).
- [7] Fleming, M.R., Adams, B.M., Kuehn, T.H., Bielicki, J.M., and Saar, M.O. (in preparation). The Generation, Storage, and Operation of CO₂-Plume Geothermal Energy Storage (NLGPES) in a Low-Temperature Sedimentary Reservoir. *Applied Energy*.
- [8] EPA (United States Environmental Protection Agency): Geologic CO₂ Sequestration Technology and Cost Analysis, *Technical support document* (2008).
- [9] Mines, G.: GETEM User Manual, retrieved from <https://www.energy.gov> (2016).
- [10] Dubois, M.K., McFarland, D., Bidgoli, T.S.: CO₂ Pipeline Cost Analysis Utilizing a Modified FE/NETL CO₂ Transport Cost Model Tool. *2017 Mastering the Subsurface Through Technology Innovation, Partnerships and Collaboration: Carbon Storage and Oil and Natural Gas Technologies Review Meeting, Pittsburgh* (2017).
- [11] Lazard: Lazard’s Levelized Cost of Energy Analysis – Version 12.0, retrieved from <https://www.lazard.com> (2018).
- [12] Glos, S., Schlehner, D.; Wechsung, M.; Wagner, R.; Heidenhof, A. (2018). Evaluation of sCO₂ power cycles for direct and waste heat applications, *2nd European sCO₂ Conference 2018*
- [13] Levyy E.K., Wang, X., Pan, C., Romero, C.E., Maya, C. E.: Use of hot supercritical CO₂ produced from a geothermal reservoir to generate electric power in a gas turbine power generation system, *Journal of CO₂ Utilization* 23 (2018) 20-28

HYBRIDIZATION OF A SMALL MODULAR REACTOR WITH A SOLAR POWER PLANT USING A SUPERCRITICAL CARBON DIOXIDE BRAYTON CYCLE

N. TAUVERON*
CEA-LITEN
Grenoble, France
nicolas.tauveron@cea.fr

Q. T. Pham
CEA-LITEN
Grenoble, France

N. Alpy
CEA-DEN
Saint-Paul-lez-Durance, France

ABSTRACT

Co-existence of nuclear-renewable energies in a single hybrid power plant is considered as a possibly efficient and flexible option to significantly reduce environmental impacts due to combination of two climate-friendly decarbonized energy sources. The concept refers to an innovative system, which locally balances the fluctuating renewable energy source such as solar, by the steady base load nuclear output, thereby smoothening the energy production. This hybrid system also features a thermal energy storage (TES) and the whole combination allows accommodating the daily and seasonally varying electrical grid demand (which specification is likely to sharpen with the increased penetration of renewables energies). In the literature, many works address hybridization of solar and fossil thermal sources or solar and other renewable sources, such as geothermal or biomass. Several concepts of hybridization of nuclear and fossil thermal sources have been also investigated. On the other hand, few works have been reported on hybridization of a solar power plant with a small modular nuclear reactor (SMR). In such a system, the proven pressurized water reactor technology is usually considered and a steam Rankine cycle is used as the power conversion system, the operating pressure being lowered compared to conventional PWRs.

Inline, the current preliminary work investigates integration of a SMR with a concentrated solar power plant (CSP) equipped with a TES. However, a supercritical CO₂ Brayton cycle is originally applied for power generation. The nuclear energy loop transfers heat to the thermodynamic cycle and the solar heat allows upgrading the turbine inlet temperature. Implementation of the TES enables continuous scO₂ heating and thereby non-stop plant operation. The proposed high temperature hybrid configuration is aimed at benefiting from the technological advances as regards key components such as heat exchangers and gas turbines so that high performances are considered along the plant thermal efficiency optimization process. An alternative option based on hybridization of a SMR, a low temperature solar power plant, an absorption chiller and a cold energy storage, is also investigated.

1. INTRODUCTION

Solar energy has become a trending topic when talking about renewables. However large-scale integration of solar energy into the electric grid presents some major technical challenges. As an intermittent energy source, solar energy requires either energy storage or fuel-based backup power so that it can provide dispatchable and reliable power. Concentrated solar power (CSP) offers specific benefits as a renewable energy source due to the ability to readily incorporate energy storage. CSP concentrates sunlight by a number of mirrors and uses the heat collected from sun's radiation to heat up a working fluid (oil, molten salt ...). The heated fluid can then be used with conventional power generation equipment (i.e., turbines, generators, etc.) to produce electricity. Current CSP power plants consist in three parts including the solar field, the thermal energy storage (TES) subsystem and the power block. TES is considered as the key part of the CSP because such subsystem provides not only dispatchable electricity but also stability to the electricity network in case of high fraction of renewable production or intermittency due to weather conditions. In other words, TES allows CSP achieving higher capacity factor. Besides, CSP is also advantageous because of its amenability to hybridization with other energy sources in order to reduce capital costs by sharing equipment as well as to enhance the energy dispatchability and reliability. Moreover, co-generation of solar energy and another energy source in a hybrid power plant might bring opportunity for more flexible operation by alternating between energy sources, which can lead to improved overall efficiency through synergy of the different energy sources.

Hybridization of solar energy with other energy source has been studied intensively in the literature. A review on the studies and published papers concerning conventional and non-conventional hybrid solar-thermal power plants since 1970s was carried out by (Ref. 1). Moreover, the technical and economic advantages as well as the issues of the technology was also described and analyzed by (Ref. 2). The work of Jamel et al. pointed out that hybridization of existing fossil fuel power

* corresponding author(s)

plants (i.e. steam-cycle power plants, combined-cycle power plants and gas-turbine power plants) with solar energy is one potential option to overcome the rapid depletion of fossil fuel reserves and their environmental effects while generating stable and reliable electricity. More interestingly, co-generation of CSP with other fossil and renewable power generation also allows reducing solar plant capital costs due to joint use of common equipment by hybridization (Ref. 1, 3, 4). Up to now, several integrated CSP-coal or CSP-natural gas hybrid power plants are under construction or already in operation.

In addition to fossil fuel like gas and coal, hybridization of CSP with other energy source like biofuels, geothermal, photovoltaics and wind, has been also of interest. Recently, Powel and Rashid published a review article in which they summarized the findings from the previous works conducted in the last ten years in which various energy sources were hybridized with CSP (Ref. 5). The article also provides an overview of the possible hybrid configurations, with advantages and disadvantages discussed.

Some publications could be found in the literature concerning a hybrid concept of a nuclear power plant with a thermal energy storage. The aims were to increase the nuclear power plant flexibility by employing the thermal storage system in an energy grid containing high contribution of renewable energy sources such as solar and wind (Ref. 6, 7, 8, 9). It is known that the existing nuclear power plants generate constant base load power and are most economic when operated at constant power levels. In other words, it is needed to run the nuclear power plants as many hours annually as possible to maintain a high capacity factor.

While many combinations of solar with another source of energy have been proposed and put into practice, integration of solar energy with nuclear energy has not been yet investigated widely. Ruth et al. introduced a potential concept of nuclear-renewable hybrid energy systems (Ref. 10). According to the authors, integrating nuclear and renewable energies in a single hybrid energy system allows balancing the fluctuating solar/wind-generated electricity by a portion of nuclear-generated electricity to response the power demand. If the demand is low, the excess nuclear heat is stored in the thermal energy storage for later use. Furthermore, such a hybrid system could not only provide secure and reliable power corresponding to the greatly increasing variability of the electric demand but also provide affordable and low carbon energy.

A conceptual design of solar-nuclear hybrid power plant including a nuclear energy loop, a solar energy loop and electrical generation loop was demonstrated by Sakadjlan et al. in their pattern published in 2015 (Ref. 11). Recently in 2016 and 2017, Popov et Borissova proposed innovative configurations of hybrid nuclear-solar power plant systems (Ref. 12, 13, 14). They are described and commented in next section. Due to the shortage of strong solar-nuclear hybrid power plant concept in the literature, the above introduced work will be taken as the reference case.

Moreover, the current work also suggests an integration of a small modular reactor and a concentrated solar power plant equipped with a thermal energy storage in which supercritical CO₂ Brayton cycle is adopted for power generation. Evaluation of plant's performance between a coupled nuclear-solar power plant and an ordinary nuclear power plant is reported and advantages/disadvantages of utilization of SCO₂ Brayton cycle instead of classical steam Rankine cycle in such innovative hybrid system is also discussed. An alternative option based on hybridization of a SMR, a low temperature solar power plant, an absorption chiller and a cold energy storage, is finally investigated.

2. NUCLEAR-SOLAR HYBRIDIZATION USING RANKINE CYCLE

The nuclear power generation at large scale has been commercialized since several decades. Up to now, of all the traditional energy sources, nuclear appears to be the only candidate which can offer abundant and cheap power without emission of greenhouse gas. Despite of the amazingly increasing development and penetration of renewable energies, typically solar and wind, nuclear still takes an important role in generating clean electricity in the power industry. However, since the initial investment to construct a large nuclear power plant is costly, the licensing procedure and erection time are long, most developing countries which do not have experience of building nuclear power plants or countries with small grid size cannot easily afford. Such conditions initialized new projects on small and medium nuclear reactors. Since the years of 2000s, there has been a growing interest for the development and deployment of small and medium size nuclear power plants to meet the expanding need for clean and sustainable power in a broader range of energy markets. A small modular reactor (SMR) is characterized by its small power capacity (less than 300 MWe) and involves small and modularized components. SMR is substantially factory manufactured and installed in the the plant rather than stick-built on the site. Such small size also allows a significant reduction of construction period. Because of its small and modular characteristics, the SMRs are expected to be more flexible and adaptable for integration with other energy sources (like solar or wind) in a hybrid power plant.

Nowadays, more and more attention is given to SMR research and development in all nuclear nations around the world. Various technologies have been selected for the designs of SMR. The majority of operating, under-construction or design conceptual SMRs are based on classical PWR nuclear power plant technologies using water coolant; whereas, some other SMRs take the advanced technologies of 4th generation of fast neutron reactors employing metal, molten salt or gas as coolant. Moreover, there exist also SMRs designed based on nuclear propulsion technology such as submarine, aircraft carrier, icebreaker and barge (Ref. 15). In the studies taken as references (Ref. 12, 13, 14), SMR design values were derived from Nuscale project and are summarized in Table 1.

Table 1: Design parameters of SMR plant (from Ref 13, 16)

Reactor core thermal power	159933 kWt
Turbine inlet temperature	255 °C
Turbine inlet pressure	31 bar
Steam flow	71.3 kg/s
Feedwater temperature	149 °C
Condenser pressure	0.085 bar
Net electric power	~ 43911 kWe
Thermal efficiency	27.45%

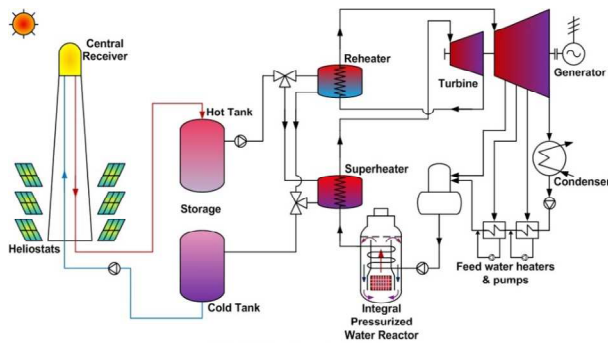


Figure 1: configuration of SMR - Solar tower hybrid power plant (extract from Ref. 13)

Three different solar power plant technologies including the solar photovoltaics (PV), solar tower and parabolic troughs have been selected for coupling with a small modular nuclear reactor (SMR) and a thermal energy storage (TES). For clarity reasons only solar tower case is described in detail hereafter. Similarly to the solar-nuclear hybridization presented by (Ref. 11), the wide spread Pressurized Water Reactor type has also been taken as the reference nuclear power plant and Rankine cycle is also coupled in the power block. Heat from solar field is also used for superheating and reheating the steam at the inlet of turbine stages which results in significant improvement of plant thermal efficiency. The most promising configuration is shown in Figure 1. The introduced hybrid power plant consists of four main parts, which are solar field, thermal storage, SMR and power block. Two-tanks molten salt thermal energy storage is equipped to the solar field and SMR acts as a steam generator. The nuclear steam is superheated by the exchanged heat with the hot molten salt circulating in the solar field before it enters high pressure turbine. Reheat is also carried out prior to steam expansion in the low turbine stages.

Calculations with Thermoflex were carried out by Popov and Borisova to evaluate the performance of hybrid plant and to compare to that of the SMR plant alone. In our study, we use another simulation tool, named as Engineering Equation Solver (Ref. 17), to assess the hybrid plant performance. Calculation results provided by EES are given in Table 2 and they are in good agreement with Thermoflex results. As clearly seen, hybridization of SMR to solar power plant enhances

significantly the plant efficiency in comparison to that of the nuclear power plant. Enhancement of 10 points has been obtained for the hybrid plant.

Table 2: Performance comparison of hybrid power plant to nuclear alone power plant

Plant parameters	SMR alone	SMR + CSP + TES
Turbine inlet temperature [°C]	255	555
Turbine inlet pressure [bar]	31	30.4
Net electric power [MWe]	44	92
Net electric efficiency [%]	27.45	37.47

3. NUCLEAR-SOLAR HYBRIDIZATION AT HIGH TEMPERATURE USING SCO₂ CYCLE

The steam-Rankine cycle was the most suitable power conversion system for a conventional water cooled nuclear reactor for more than 60 years. It has demonstrated a good efficiency and system reliability when the reactor operating temperature is below 350°C. To improve the economy and safety of nuclear reactor systems, two distinct research trends in the nuclear technology are considered. One trend focuses on the small modular reactor (SMR) development as previously mentioned. The other trend concerns the design and development of advanced nuclear reactor concepts for next nuclear reactor generation (Gen IV nuclear reactor). Since the early 2000s, more and more attentions on Gen-IV reactor systems are recorded. The working temperature of the advanced nuclear reactor goes far beyond that of existing water cooled reactor. The aim of increasing the operating temperature over 500°C is to achieve higher efficiency than in the past. Various concepts of Gen-IV reactor systems have been proposed and studied using different coolants such as helium, sodium, lead, molten salt and gas. In such situation, the supercritical carbon dioxide (SCO₂) Brayton cycle has been widely considered as a favorable candidate for being employed in the next generation nuclear reactor power conversion systems. Previous analyses of SCO₂ Brayton power cycle have demonstrated that the cycle shows better efficiency and has many advantages compared to the traditional Rankine cycle (Ref. 18, 19, 20, 21, 22).

In our project, the possibility to employ SCO₂ Brayton cycle for a nuclear-solar hybrid power plant will be investigated. Various Brayton cycle layouts will be applied for the power block of a nuclear-solar power plant (NSPP) coupling a small modular nuclear reactor (SMR) with a concentrated solar power plant (CSP). Similarly to the cited NSPP configuration proposed by Popov et Borisova, the CSP with thermal energy storage (TES) is located at the outlet of the SMR. The heat from CSP serves for heating up the SCO₂ temperature before it enters the turbine. The percentage of solar heat contribution is increasing from 0 to 100% and the corresponding hybrid plant efficiency is calculated respectively using EES.

Following conditions and component parameters:

- The maximum pressure in the SCO2 loop is $P_{max} = 20\text{MPa}$ (other values of P_{max} were considered but not presented in this paper)
- The minimum temperature is the temperature at the outlet of precooler $T_{min} = 27^\circ\text{C}$ (condensing mode)
- Turbine efficiency: $E_{turbine} = 93\%$
- Compressor efficiency: $E_{compressor} = 89\%$
- Effectiveness of recuperators: $E_{recuperator} = 95\%$

These are taken from (Ref. 23) in which the author investigated different cycle layouts for coupling of SCO2 Brayton cycle with a SMR or a sodium-cooled fast reactor within a wide range of turbine inlet temperature, from 250°C to 850°C . Parametric calculations were carried out aiming at optimizing the working conditions at a given inlet turbine condition (temperature and pressure) including the outlet pressure of the turbine, the split ratio (for recompression layout), the outlet temperature of the condenser. In our study, we firstly applied the model from Ref. 23 and carried out the calculations of SCO2 Brayton cycle for a SMR with our tool EES. A good agreement has been obtained between the two calculation tools.

Then, the model is used for calculations with the currently considered NSPP to evaluate the performance of the hybrid plant with SCO2 cycle and compare it to the previously case when Rankine cycle is employed for NSPP as shown in (Ref. 13). The heat output from the SMR and the CSP are taken as those from the reference case (i.e. $Q_{SMR} = 160\text{MWt}$ and $Q_{CSP} = 86\text{MWt}$). Additionally, following criteria from the NSPP given by (Ref. 13) are taken:

- The inlet and outlet temperatures of the SCO2 loop passing through the steam-SCO2 heat exchanger cannot be greater than those of the steam cycle, i.e. $T_{OHX} \leq T_{out,SMR} = 255^\circ\text{C}$, $T_{IHX} \leq T_{in,SMR} = 149^\circ\text{C}$
- Maximum temperature in the SCO2 loop cannot be greater than the maximum temperature provided by the solar loop $T_{max} \leq 555^\circ\text{C}$

Recompression SCO2 Brayton cycle is examined, as illustrated in Figure 2, using a similar methodology. However the efficiency of hybrid power plant is much less than that of the nuclear power plant. In fact, in the reference hybridization of SMR-CSP-TES with a steam Rankine cycle presented by (Ref. 13), the maximum temperature in the steam can achieve 555°C which is 300°C greater than the temperature at the outlet of SMR (255°C) and is $\sim 400^\circ\text{C}$ greater than the inlet temperature of SMR (149°C). Such large temperature difference is essential to bring significant efficiency enhancement for the hybrid plant. Unfortunately, with a SCO2 recompression cycle, the temperature difference between the hot and the cold sides (hot side refers to the outlet of the heat exchanger and cold side

refers to the inlet of the heat exchanger) is more limited. The following Table 3 provides the optimal temperature difference obtained by a recompression cycle at 20MPa when hot temperature is varied from 240 to 555°C . It is seen that the recompression SCO2 Brayton cycle is only efficient in a limited range of temperature.

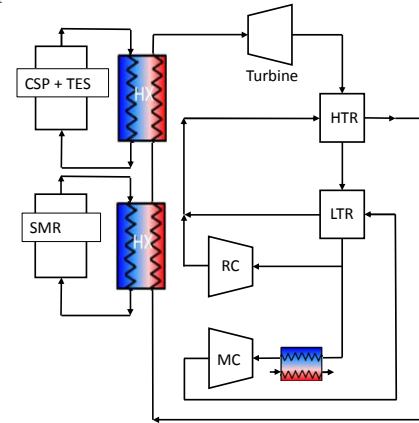


Figure 2: Recompression layout of SCO2 Brayton cycle for NSPP.

It can be noticed that temperatures appearing in the second line of Table 3, correspond actually to the coupling case of the SCO2 recompression cycle to the currently considered SMR. Considering additionally that the temperature getting out from the lower heat exchanger of Figure 2, i.e. 255°C , is also the temperature entering the upper heat exchanger (with solar cycle), according to the fourth line in Table 3, the corresponding outlet temperature of the upper heat exchanger should be 399°C in the optimal case. However, with the provided solar heat from CSP, the SCO2 temperature only increases up to 320°C max which is far away from the optimal value. Therefore, a low plant efficiency is observed for this hybrid using recompression SCO2 cycle.

Table 3: Optimal calculation for recompression SCO2 cycle at 20MPa with varying temperature range

P_{min} MPa	Split ratio	T_{OHX} $^\circ\text{C}$	T_{IHX} $^\circ\text{C}$	ΔT $^\circ\text{C}$	Efficiency (%)
8.235	0.684	240	139	101	27.96
8.2338	0.684	255	149	106	29.46
7.779	0.624	380	240	120	39.4
7.779	0.625	399	255	144	40.56
7.791	0.624	405	260	155	40.92
7	0.589	555	380	175	49.08

Other layouts SCO2 Brayton cycle have been also considered but none of them provides interesting findings on the advantage of employing SCO2 Brayton cycle for improvement of NSPP plant's performance.

In the following paragraph, a cascaded configuration employing three recompression SCO2 Brayton cycle at different temperature ranges is introduced (Figure 3). As above

explained, the direct employment of recompression SCO2 Brayton cycle could not help improving the hybrid plant due to the limitation of temperature difference between the inlet and outlet of heat exchanger. In the below configuration, SCO2 is heated up gradually in three steps. The temperature ranges in each stage are optimized to obtain maximum overall hybrid power plant.

The overall efficiency for the currently considered hybrid NSPP with the proposed cascaded configuration containing three recompression SCO2 Brayton cycles is 38.81%. About 11 points increase of plant efficiency is achieved in comparison to when the NPP is alone and simple layout SCO2 Brayton cycle is used. For the case when the recompression layout is utilized for an alone NPP, more than 9 points of plant efficiency enhancement is obtained due to hybridization with the CSP.

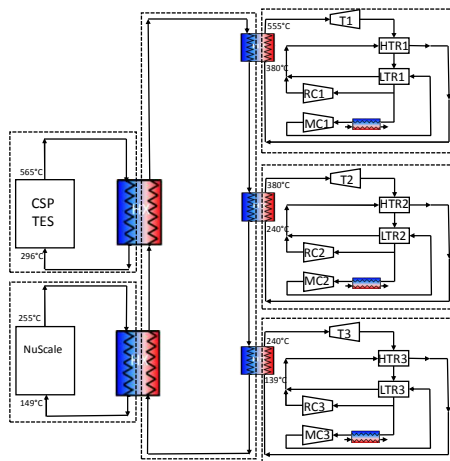


Figure 3: Cascaded layout of three recompression SCO2 Brayton cycle for NSPP.

It is seen that for a nuclear power plant, SCO2 Brayton cycle shows better plant efficiency than the Rankine cycle. About 2 points of increase in SMR plant efficiency could be obtained by replacing the Rankine cycle by recompression SCO2 Brayton cycle (29.46% vs 27.45%). Moreover, when being integrated with the solar tower power plant (NSPP case), the application of SCO2 recompression cycle with cascaded configuration shows competitive plant efficiency to Rankine cycle (38.81% for SCO2 cycle and 37.47% for Rankine cycle). This result is obtained by using certain hypothesis concerning the efficiencies of the cycle components (turbine, compressor, recuperators) as well as other assumptions for maximum pressure temperature and minimum temperature of the cycles. A sensibility study on those parameters would be of interest to investigate the effects of them on the plant efficiency. Additionally, it should be highlighted that beside the advantage in cycle efficiency, other factors should be considered including the size and cost of components (especially the turbomachinery).

Table 4: Efficiency of three cascaded recompression SCO2 Brayton cycles for NSPP

Loop	Imposed parameters	Optimised parameters	Loop efficiency
Upper	Pmax = 20MPa Tmin = 27°C TOHX= 555°C	Pmin = 7 MPa TIHX=380°C Split ratio = 0.5891	49.08 %
Middle	Pmax = 20MPa Tmin = 27°C TOHX= 380°C	Pmin=7.78MPa TIHX = 240°C Split ratio= 0.6264	39.4%
Bottom	Pmax = 20MPa Tmin = 27°C TOHX= 240°C	Pmin=7.78MPa TIHX = 138.7°C Split ratio = 0.6838	27.96%

These aspects are not covered in the framework of our paper but have been shown in the literature are much more favorable for SCO2 Brayton cycles than for Rankine cycle. Therefore, it is convincing that the application of SCO2 Brayton cycle for the nuclear-solar hybrid power plant instead of using the classical Rankine cycle has high potential and further research should be considered in the future to make the concept feasible.

4. NUCLEAR-SOLAR HYBRIDIZATION AT LOW TEMPERATURE USING SCO2 CYCLE

As mentioned previously, two nuclear-solar hybrid power plant configurations are proposed in the current work. The above section presents the so-called high temperature hybrid plant configuration. As discussed, at operating temperature up to 600°C and utilization of sCO2 Brayton loop for the power conversion, the high temperature nuclear-solar hybridization provides interesting benefits, including an attractive thermal efficiency in comparison to the system employing Rankine steam cycle. Moreover, it has several other advantages over water cycles (i.e. more compact, lower water consumption ...). However, the solar power plant as well as the thermal energy system operating at high temperature can be expensive (Ref. 13). Also, the use of such high temperature systems (i.e. molten salt) can have some constraints for our application (220°C freezing point; proximity of nuclear reactor). Therefore, we are investigating an alternative nuclear-solar hybrid power plant which does not employ high temperature solar power technology or high temperature heat storage. In this section, the second hybrid configuration will be introduced, called low temperature nuclear-solar hybridization, representing an electrical production system based on a nuclear-solar coupled heat source at lower range of operating temperature, i.e. less than 300°C. More precisely, the low temperature hybridization idea is based on the use of low temperature technologies of the solar thermal collectors (Ref. 24) and thermal energy storage (Ref. 25) allowing operation at a wide but lower range of temperature, in between 100°C to 300°C instead of 600°C. Moreover the constraint to keep a low temperature under 27°C

for the heat sink can be a real challenge and this issue is coped with the low temperature concept.

The heart of the architecture lies in the position of the solar heat source in the hybrid system. In the high temperature case, the solar source locates downstream of the nuclear heat source, serving for superheating the SCO₂ flow out going from the nuclear-SCO₂ heat exchanger so that the SCO₂ enters the turbine at higher temperature, resulting in significant enhancement of the thermal efficiency of the hybrid power plant. In the current low temperature hybridization, the heat from the solar field will be used to preheat the SCO₂ in the power conversion cycle before it enters the nuclear-SCO₂ heat exchanger then the turbine. This aims also at improving the overall efficiency of the hybrid power system. In addition, the proposed configuration makes the hybrid system flexible. Indeed, one part of the solar heat serves for direct generation of electricity through a SCO₂ Brayton loop as described. The other part of the solar heat could be used to feed an absorption chiller which in turn will produce cold water for cooling down the SCO₂ at the inlet of the compressor. This allows the power block operating in a condensing mode for which the inlet temperature to the compressor could be lowered compare to ambient temperature. Such cooling process helps reducing the work required by the compressor, hence, increasing the total net work done by the system as well as its thermal efficiency. The working principle of the low temperature solar-hybrid power plant is described hereafter.

The hybrid system is composed of a molten salt cycle (solar heat source), a nuclear heat source and a SCO₂ cycle (Figure 4). The SCO₂ first receives one part of the available solar heat and is preheated (state 10) before entering the second heat exchanger in which it is heated again by the heat from the nuclear steam cycle (state 11). Then, the heated SCO₂ arrives at the turbine inlet (state 1). SCO₂ flow is expanded in a turbine connected to an electricity generator (state 2). Then, in order to increase the efficiency of the cycle, SCO₂ exchanges heat to the high temperature recuperator (HTR, state 3), then to the low temperature recuperator (LTR, state 4). In case of the SCO₂ Brayton recompression layout as shown in Figure 4, at state 4, the SCO₂ flow is split by a factor X named split ratio. One part of the SCO₂ flow passes successively through two stages of cooling (state 4 up to state 5). The flow is first cooled down to ambient temperature due to connection to an external cooling source. Then, it passes through another precooler in which the heat from SCO₂ is exchanged to a cold liquid source. Hence, SCO₂ becomes cooler. Such cold liquid source is produced by an absorption chiller which is fed by a part of the available solar heat. The sCO₂ is then compressed in a compressor (MC) to the state 6. The compressed fluid is heated by the recuperated heat from the LTR (state 8). The other part of SCO₂ flows extracted from the main flow does not pass through the recuperator but directly enters the recompression compressor in which it is compressed and gets out at state 7. This outgoing flow reintegrates to the main flow at state 9 before entering to the

high temperature recuperator in which the SCO₂ is heated up again before returning to the solar-SCO₂ heat exchanger (state 10) and the cycle continues.

It is noted that according to the currently presented hybrid configuration, depending on the electric demand, the partition of the solar heat serving for SCO₂ cycle for generating electricity and for feeding the absorption machine can be adjusted. Also, the cold liquid produced by the absorption machine can be used directly for SCO₂ cooling or in case of excess, it will be stored in the cold storage for other applications.

Figure 4 provides the schematic diagram of the proposed low temperature nuclear-solar hybrid plant with details of the components existing in the solar field (solar thermal collectors and the two molten-salt tanks of the thermal energy storage system) as well as the absorption chiller (composed of a generator, an absorber, an evaporator and a condenser) with the cold liquid storage (with two storage tanks). Absorption chiller technology can be either H₂O-LiBr type or NH₃-H₂O type (as in Figure 4). In the current study, NH₃-H₂O is preferred as lower temperatures can be obtained.

As done for the high temperature hybrid plant, static calculations with EES have been performed to evaluate the thermodynamic performance of the low temperature hybrid plant. Similar SMR is employed with nuclear thermal heat output of 160 MWt. The solar field with heliostats are now replaced by the solar thermal collectors operating at low temperature (less than 150°C). An adaptive thermal energy storage will be equipped (ex. steam, oil ...). However, the thermal capacity of the solar field is assumed to be the one given by (Ref.13) ($Q_{\text{solar}} = 86 \text{ MWt}$). Pressure drop is neglected. Assumptions for efficiencies of the components in the SCO₂ cycle (turbine, recuperators, and compressors) are the same as in the section 3.1 while the coefficient of performance (COP) of the chiller is supposed to be 0.6.

The temperatures at the cold and hot legs of the nuclear-SCO₂ heat exchanger are maintained at the inlet and outlet temperature of the reference SMR (i.e. $T_{\text{IHX}} = 149^\circ\text{C}$ at state 11, $T_{\text{OHX}} = 255^\circ\text{C}$ at state 1). The inlet turbine pressure (also called as the maximum pressure) is imposed at 20 MPa. The SCO₂ flow is supposed to be cooled down to 5°C before entering the main compressor (i.e. the temperature of the cold liquid produced by the absorption chiller is assumed as 5°C, as an example). The inlet temperature to the solar-SCO₂ heat exchanger (state 10) varies corresponding to varying participation of solar heat for SCO₂ preheating. The parameters to be calculated include the inlet compressor pressure, the split ratio, the repartition between the solar heat serving for SCO₂ preheating and the one consumed by the chiller to produce cold liquid at 5°C, the optimized output power as well as the overall thermal efficiency of the hybrid power system.

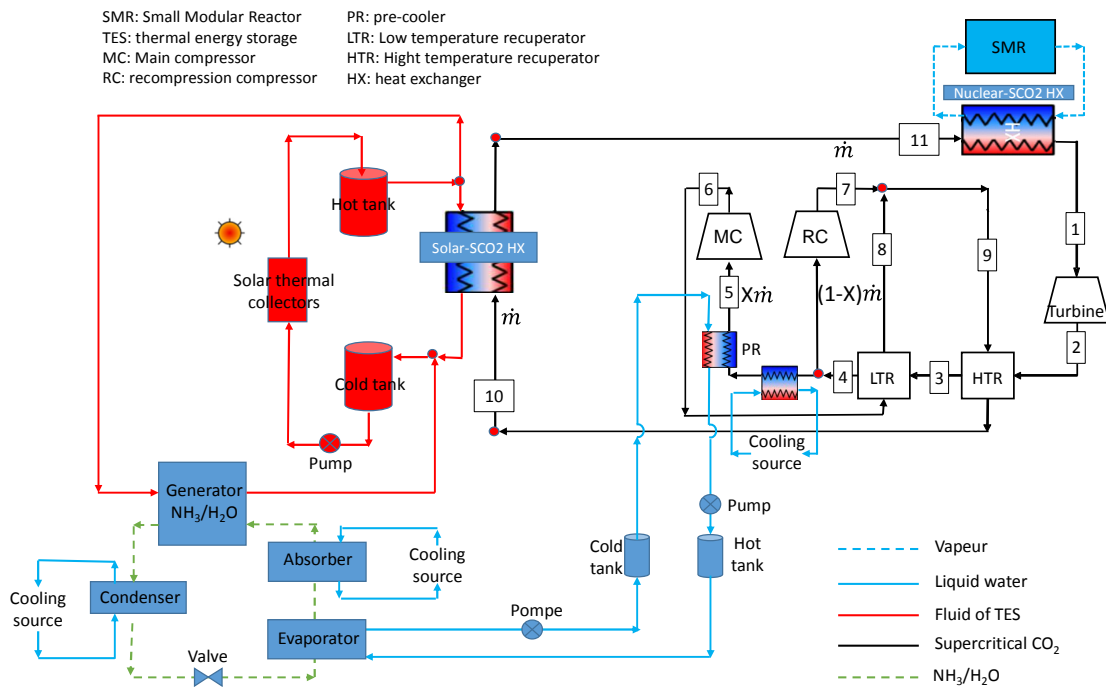


Figure 4: Schematic diagram with detailed components of solar field with thermal energy storage and absorption chiller with cold liquid storage.

In the following, Figure 5 and Figure 6 exhibit the net output power obtained for the currently studied nuclear-solar hybrid power plant as a function of the percentage solar heat serving directly for SCO₂ preheating, respectively. It is seen that the participation of solar heat for preheating SCO₂ before entering the nuclear-SCO₂ heat exchanger reveals better performance in comparison to the non-preheating case. Indeed, up to 18% of power enhancement could be produced at the output of the generator, corresponding to about 2 points improvement of the plant efficiency.

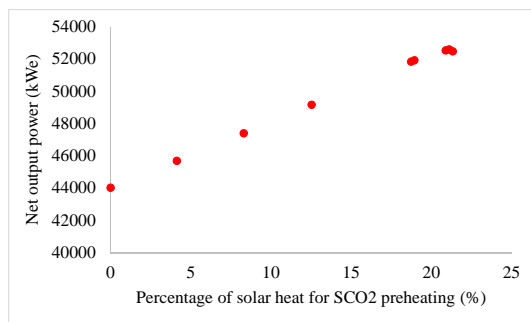


Figure 5: Net power output obtained by the low-temperature hybrid plant

It is noted that the ambient temperature is quite high compared to low temperature of the cycle (27°C vs 5°C), leading to a high demand of cold liquid for the SCO₂ cooling process (from 27°C to the inlet compressor temperature of 5°C). Therefore, the main part of the available solar heat is consumed by the absorption chiller for cold liquid production. Only about 20% of the solar heat will serve for preheating in the SCO₂ cycle. By contrast, if reference temperature was lower or cold liquid temperature higher, the cold liquid requirement for SCO₂ cooling would be much less and as a result a higher part of the solar heat could be used for SCO₂ preheating.

It is observed that in terms of thermal efficiency, the low-temperature hybrid plant is not as attractive as the high-temperature one. However, with such configuration, low temperature technologies for solar power plant could be employed, making the idea potentially competitive thanks to cost reduction trends for low-temperature heat generation CAPEX (Ref. 24). Furthermore use of low-temperature heat storage can be interesting due to low energy capacity cost (Ref. 25).

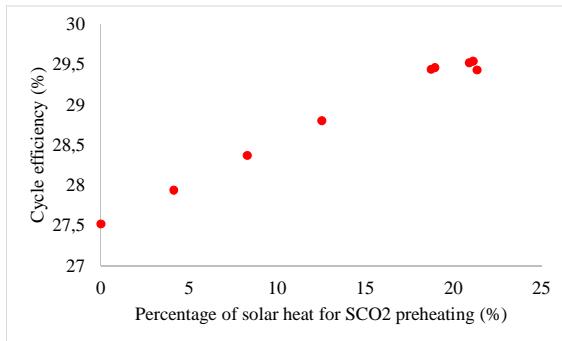


Figure 6: Thermal efficiency obtained by the low-temperature hybrid plant

CONCLUSIONS

Both nuclear and solar can provide significant contribution to provide clean and sustainable electricity to the power industry. Nuclear power plants generally provide constant base load power while solar energy is intermittent. Balancing fluctuating solar with nuclear energy is considered as the solution for the current and future energy systems, in order to improve the viability of the nuclear power plant in an electricity grid containing a significant fraction of renewable (solar and wind) energy sources. A literature survey has been carried out and showed that there exist only few works on the design and development of nuclear-solar hybrid power plants. The paper reviews and provides a detailed analysis of hybrid small nuclear reactor – solar tower power plant equipped by a TES, recently available in the literature.

The paper investigates the potential application of the SCO₂ Brayton cycle instead of a Rankine cycle in the power block of the hybrid plant; nuclear and solar heat were chosen to be identical with the reference concept plant, without any attempt of optimization. Two conceptual architectures for the nuclear-solar hybrid power plant employing SCO₂ Brayton cycle have been proposed for different conditions of operating temperatures. The high temperature hybrid power plant takes benefit from the solar heat to heat up the SCO₂ at the outlet of the SMR, allowing an important increase of inlet turbine temperature, leading to improvement of the cycle's thermal efficiency. Such high temperature hybrid configuration involves three SCO₂ loops according to recompression layouts, allowing a gradual increase of SCO₂ temperature from about 150°C up to 555°C. This hybrid power plant reveals a better thermodynamic performance in comparison to the case when the SMR is alone. An increase of up to 11 points can be obtained due to hybridization. Moreover, the idea of SCO₂ Brayton cycle seems to be really competitive to the classical Rankine one thanks to its advantageous characteristics such as the compactness and the friendliness to the environment.

Despite many advantages of the high temperature hybrid power plant configuration, it can be interesting to propose a low temperature alternative. This configuration will be based on low-temperature solar heat generation technology currently developed for industrial processes and district heating and low-temperature heat storage. The low temperature hybrid power concept consists in a plant in which the solar heat is consumed for two purposes, first to preheat the SCO₂ before it returns to the nuclear-SCO₂ heat exchanger and second to feed an absorption chiller in order to produce cold liquid which serves for precooling the SCO₂ at the inlet of the main compressor. In terms of thermodynamic performance, due to hybridization, 2 points of efficiency enhancement could be obtained by such hybrid system. More interestingly, the architecture allows utilization of low temperature technologies for solar field as well as for the TES system.

ACKNOWLEDGEMENTS

This study was supported by CEA transverse NTE program. The authors acknowledge Professor Popov at Nuclear Engineering Department, Technical University of Sofia, Bulgaria for his kind answers to our questions concerning his paper on the nuclear-solar hybrid power plant.

REFERENCES

1. M.S. JAMEL, A. ABD. RAHMAN, A.H. SHAMSUDDIN, "Advances in the integration of solar thermal energy with conventional and non-conventional power plants", 20, 71-81, 2013
2. T.A. WILLIAM, M.S. BOHN, H.W. PRICE, "Solar thermal electric hybridization issues", International solar energy conference, ASME, Maui, Hawaii, March 19-24, 1995
3. X. ZHAI, Y.J. DAI, R.Z. WANG, "Energy and exergy analyses on a novel hybrid solar heating, cooling and power generation", Applied Energy, 86 (9), 1395-1404, 2009
4. E. HU, Y.P. YANG, A. NISHIMURA, F.YILMAZ, A. KOUZANI, "Solar thermal aided power generation", Applied Energy, 87 (9), 2881-2885, 2010
5. K.M. POWEL, K. RASHID, K. ELLINGWOOD, J. TUTTLE, B.D. IVERSON, "Hybrid concentrated solar thermal power systems: A review", Renewable and Sustainable Energy Reviews, 80, 215-237, 2017
6. C.FORBERG, "Hybrid systems to address seasonal mismatches between electricity production and demand in nuclear renewable electrical grids", Energy Policy, 62, 333-341, 2013
7. S. A. ALAMERI, J.C. KING, "A coupled nuclear reactor thermal energy storage system for enhance load following operation", International Nuclear Atlantic Conference INAC, Recife, PE, Brazil, 24-29 November, 2013
8. P. DENHOLM, J.C. KING, C.F. KUTCHER, P. P. H. WILSON, "Decarbonizing the electric sector: Combining renewable and nuclear energy using thermal storage", Energy Policy, 44, 301-311, 2012
9. J. EDWARDS, H. BINDRA, P. SABHARWALL, "Exergy analysis of thermal energy storage options with nuclear power plants", Annals of Nuclear Energy, 96, 104-111, 2016.

10. M. RUTH, O.R. ZINAMAN, M.ANTKOZIAK,, R.D. BOARDMAN, R.S. CHERRY, M.D. BAZILIAN, “Nuclear-renewable hybrid energy systems: opportunities, interconnections, and needs”, *Energy Conversion Management*, 78, 684-94, 2014.
11. B.B. SAKADJLAN, W.A. ARNOLD, D.L. KRAFT, Solar-Nuclear hybrid power plant, US Patent, No. US2015/0096299 A1, 2015.
12. D. POPOV, A. BORISOVA, “An option for the integration of solar photovoltaics into small nuclear power plant with thermal energy storage”, *Sustainable Energy Technologies and Assessments*, 18,119-126, 2016
13. D. POPOV, A. BORISOVA, “Innovative configuration of a hybrid nuclear-solar tower power plant”, *Energy*, 125, 736-746, 2017
14. D. POPOV, A. BORISOVA, “Innovative configuration of a hybrid nuclear-parabolic trough solar power plant”, *International Journal of sustainable energy*, 1-24, 2017
15. H.J. YOON, Y. Ahn, J.I. Lee, Y. Addad, “Potential advantages of coupling supercritical CO2 Brayton cycle to water cooled small and medium size reactor”, *Nuclear Engineering and Design*, 245, 223-232, 2012
16. <http://www.nuscalepower.com/smr-benefits/small>
17. S.A. Klein, *Engineering Equation Solver, F-Chart Software*, Middleton, WI, 2010.
18. G. ANGELINO, “Real gas effects in carbon dioxide cycles”, *ASME paper*, 69, 103.
19. N.B. DESAI, S. BANDYOPADHYAY, J.K. NAYAK, R. BANERJEE, S.B. KEDARE, “Simulation of 1MWe Solar Thermal Power Plant”, *Energy Procedia*, 57, 507-516, 2014
20. V. DOSTAL, “A supercritical carbon dioxide cycle for next generation nuclear reactors”, *Massachusetts Institutes of Technology, Department of Nuclear Engineering*, 2004
21. V. DOSTAL, P. HEJZLAR, M.J. DRISCOLL, “High performance supercritical carbon dioxide cycle for next generation nuclear reactors”, *Nuclear Technology*, 154, 265-282, 2006
22. V. DOSTAL, P. HEJZLAR, M.J. DRISCOLL, “The supercritical carbon dioxide power cycle: comparison to other advanced power cycles”, *Nuclear Technology*, 150, 283-301, 2006
23. H.S. PHAM, N. ALPY, J.H. FERRASSE, O. BOUTIN, J. QUENAUT, M. TOTHILL, D. HAUBENSACK, M. SAEZ, «Mapping of the Thermodynamic performance of the supercritical CO2 cycle and optimization for a small modular reactor and a sodium cooled fast reactor”, *Energy*, 87, 412-424, 2015.
24. O. HOOGLAND, E. VEENSTRA, P. TORRES, I. IPARRAGUIRRE TORRES, H. KUITTINEN “Study on impacts of EU actions supporting the development of renewable energy technologies”, Ref: 2017/RTD/SC/PP-05441-2017, 2018.
25. H. BINDRA, S. REVANKAR “Storage and Hybridization of Nuclear Energy, Techno-economic Integration of Renewable and Nuclear Energy”, Elsevier, 2019.

PART-LOAD OPERATION OF COAL FIRED sCO₂ POWER PLANTS

Dario Alfani*

Politecnico di Milano
Milano, Italy

Email: dario.alfani@polimi.it

Marco Astolfi

Politecnico di Milano
Milano, Italy

Marco Binotti

Politecnico di Milano
Milano, Italy

Ennio Macchi

Politecnico di Milano
Milano, Italy

Paolo Silva

Politecnico di Milano
Milano, Italy

ABSTRACT

The present work deals with the study of the part-load performance and operating strategies of a coal fired sCO₂ power plant. In sCO₂ cycles the compression phase generally starts very close to the fluid critical point in a region characterized by significant real gas effects, so that depressurization, that is the typical operating strategy adopted for closed gas cycles, may not be the optimal one. In fact, a significant variation of fluid thermodynamic properties along the compression will occur with a probable penalization on the overall plant efficiency. A recuperative recompressed cycle with High Temperature Recuperator (HTR) achieving a cycle efficiency of 41.92% is designed and part-load performances of the overall power plant are analyzed also taking into account the boiler off-design behavior. Different operating strategies are investigated considering the combinations of component features such as rotational speed and variable geometry at the inlet of turbomachinery, fan speed on the heat rejection unit, variation of the fluid inventory. The best operating strategy energy-wise is finally proposed, providing a numerical estimation of the off-design overall plant performance and highlighting some design criteria for boiler and turbomachinery.

INTRODUCTION

Supercritical CO₂ cycles for power generation are gaining a large interest from industry, institutions and academia as demonstrated by the large amount of investments, founded projects and research papers. This attention is motivated by the potential of sCO₂ technology of replacing conventional steam plants in a number of applications and likely playing a relevant role in the future energy scenario. The H2020 sCO₂-Flex [1] project is studying the possible application of sCO₂ cycles in coal fired power plants in order to enhance their flexibility and ease the integration with non-dispatchable renewable energy sources

such as wind and solar. Main advantages of sCO₂ power plants with respect to USC technology are: (i) potential higher efficiency, (ii) compactness of the turbomachinery, (iii) no need of water treatment, deaerator, vacuum pump, etc., (iv) high performance at part-load and (v) fast transients. The first two figures have been numerically evaluated in different independent studies while the assessment of flexibility still lacks deep investigation. This study focuses on the part-load performance and control strategies for a sCO₂ cycle used as power cycle in a coal-fired power plant. Differently from closed Joule-Brayton cycles using for example He and N₂ that operate in the ideal gas region, in sCO₂ power cycles the main compressor is generally designed to operate very close to the fluid critical point in a region characterized by marked real gas effects (i.e. a region where the gas has a compressibility factor Z significantly lower than 1) [2]. For these plants, cycle depressurization at partial load may involve a significant variation of fluid properties along compression with an efficiency penalization that may jeopardize also the overall plant performance. The optimization of the part-load operation of sCO₂ power plants is scarcely studied in literature and the main unknowns regard the design and the operation of turbomachinery. Different operating strategies are investigated in this work for a recuperative recompressed cycle configuration selected within the sCO₂-Flex project and considering the combinations of component features: (i) turbine and compressor (fixed/variable velocity, with or without variable geometry), (ii) heat rejection unit (fixed/variable fan speed), (iii) fluid inventory (variable/fixed). For each design combination, the best operating strategy in terms of system efficiency is proposed, providing a numerical estimation of the part-load performance attainable with sCO₂ power plants and highlighting suggested design criteria for the turbomachinery.

METHODOLOGY AND CYCLE LAYOUT

Due to the large number of possible applications for sCO₂ cycles, more than 50 different sCO₂ cycle layouts have been proposed in literature [3]. The use of a sCO₂ cycle as power cycle for coal-fired power plants is being investigated within the sCO₂-Flex project which has identified 21 promising cycles for this specific application. Typically, sCO₂ cycles are strongly regenerative, limiting the temperature variation across the primary heat exchanger: this feature allows achieving high cycle efficiencies, but does not ease the coupling with a boiler in which it is necessary to cool down as much as possible the hot flue gases. Combustion air preheating by means of a Ljungström heat exchanger can mitigate this problem, but a compromise between cycle and boiler efficiency is required. After a preliminary analysis, the sCO₂-Flex consortium has identified three cycles as the most suitable ones for the selected application. The selection was made considering i) the cycle performance, ii) the boiler integration and performance and iii) the system simplicity. In this study a recuperative recompressed cycle with High Temperature Recuperator (HTR) bypass is considered. The cycle layout is reported in Fig. 1.

This cycle is the simplest among the three cycles selected within the sCO₂-Flex project [4] and guarantees effective flue gas cooling thanks to the CO₂ stream that bypasses the HTR and is heated up in the boiler. The presence of the secondary compressor allows a good balance of the heat capacities of the cold and hot CO₂ streams in the Low Temperature Recuperator (LTR), reducing the irreversibilities related to the heat exchange and thus boosting the cycle efficiency.

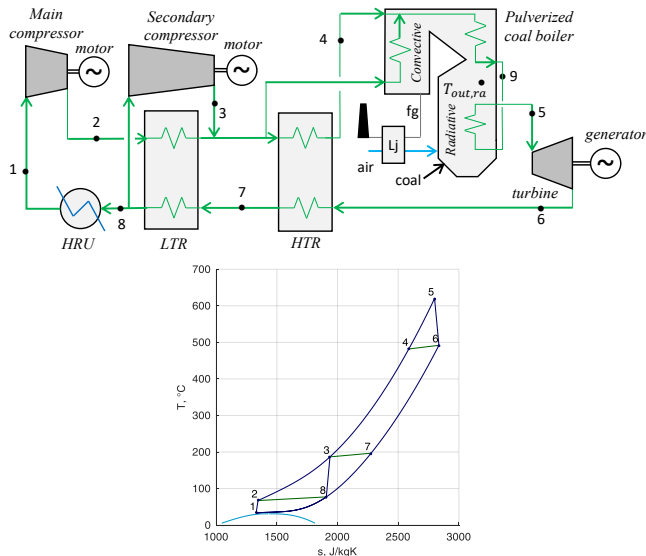


Figure 1: (top) schematic plant layout and (bottom) T-s diagram of the recompressed cycle with HTR bypass.

The numerical model adopted within sCO₂-Flex and used in this work for the simulation of the coal-fired sCO₂ power plant has been developed in MATLAB® [5] and adopts REFPROP 9.1 database [6] for the calculation of thermodynamic properties of CO₂. The code is able to solve mass and energy balances, to

compute the cycle thermodynamic performances and to evaluate the main components design parameters for several cycle configurations.

Once the design is performed, the obtained results (e.g. heat exchanger surfaces and volumes) are used as input data for the part-load simulation. The different part-load operating strategies are compared in terms of system efficiency and turbomachinery operating conditions, neglecting in this phase of the study the variation of the turbomachinery efficiency.

CYCLE THERMODYNAMIC DESIGN

The analysis in the present study is carried out for a power plant having a gross cycle electric power output (\dot{W}_{gross}) of 100 MW_{el}. Cycle maximum temperature and pressure are set to 620°C and 250 bar respectively, according to the current values used for Ultra Super Critical (USC) boilers. Turbine efficiency and compressor efficiencies were evaluated with a preliminary sizing in [7]. In order to ease the replicability of the system in different sites an air-cooled heat rejection unit is considered. The minimum cycle temperature is fixed to 33°C, while the minimum cycle pressure is optimized in order to maximise the cycle efficiency. As further assumption, the same temperature is assumed for the high-pressure CO₂ stream exiting the LTR and for the CO₂ stream exiting the secondary compressor, thus guaranteeing no mixing losses. Similarly, the high-pressure CO₂ exiting the HTR and the bypass CO₂ stream are isothermally mixed. All the main assumptions for the cycle design are summarized in Table 1.

Table 1: Main assumptions for the cycle design

Cycle assumptions	
Cycle design gross electric power \dot{W}_{gross} , MW	100
Maximum cycle temperature T_5 , °C	620
Maximum cycle pressure p_2 , bar	250
Minimum cycle temperature T_1 , °C	33
Turbine isentropic efficiency, η_{turb}	84.3 % *
Main compressor isentropic efficiency, η_{comp1}	82.2 % *
Second. compressor isentropic efficiency η_{comp2}	82.4 % *
Generator/motor efficiency $\eta_{me,t} / \eta_{me,c}$	96.4 %
LTR pinch point ΔT_{LTR} , °C	10
HTR pinch point ΔT_{HTR} , °C	10
HRU CO ₂ ($\Delta p/p_{in}$)	0.5 %
Recuperator hot side ($\Delta p/p_{in}$)	0.5 %
Recuperator cold side ($\Delta p/p_{in}$)	0.5 %
HRU electric cons. per MW of heat rejected ξ	0.0085

*The reported turbomachinery efficiency value is just indicative.

Cycle thermodynamic efficiency (η_{cycle}) is calculated considering the turbine and compressors work, the mechanical and electric efficiencies of generator ($\eta_{me,t}$) and motors ($\eta_{me,c}$) and the heat rejection auxiliaries consumption.

$$\eta_{cycle} = \frac{\dot{W}_{net}}{\dot{Q}_{in,cycle}} = \frac{\dot{W}_t - \dot{W}_{c1} - \dot{W}_{c2} - \dot{W}_{HRU,aux}}{\dot{Q}_{in,cycle}} \quad (1)$$

$$= \frac{\left[\Delta h_{5-6} \eta_{me,t} - SR \frac{\Delta h_{1-2}}{\eta_{me,c}} - (1 - SR) \frac{\Delta h_{3-8}}{\eta_{me,c}} - SR \xi \Delta h_{8-1} \right]}{\Delta h_{4-5} + BR \Delta h_{3-4}}$$

BOILER THERMODYNAMIC DESIGN

The boiler is fuelled with BILINA HP1 coal, whose ash-free chemical composition on a molar basis is C: 37.85%, H: 34.81%, O: 9.16%, N: 0.40%, S: 0.25%, H₂O: 17.53% with a Lower Heating Value (LHV) equal to 16.9 MJ/kg. Closed system coal drying is assumed, thus evaporated water enters the boiler together with coal and flue gas composition corresponds to coal as received. The excess of air with respect to the stoichiometric value is assumed equal to 20% in order to guarantee complete combustion and to limit boiler stack losses. The stack temperature has been limited to 130°C in order to avoid acid condenses in the flue gases, mainly caused by the combination of sulfur trioxide (SO₃) present in the flue gases with moisture to form sulfuric acid (H₂SO₄). The adiabatic flame temperature is computed for simplicity without considering air staging, as this has secondary impact on the overall boiler energy balance.

The heat exchangers layout in the boiler is preliminary and considers two different boiler zones:

- A high temperature radiative zone where the main heat exchange mechanism is the radiation due to the presence of the flame and the high temperature of the flue gases. This zone includes the high temperature section of the Primary Heat Exchanger (HT-PHE) and the flue gases are cooled down to 1200°C [8].
- An intermediate-low temperature radiative-convective zone in which both radiation and convection are considered. In this zone the low temperature section of the Primary Heat Exchanger (LT-PHE) and the HTR bypass heat exchanger (HTRB) are considered.

Table 2: Main assumptions for the boiler thermodynamic design

Boiler assumptions	
Ambient temperature, °C	20
Minimum allowable stack temperature T_{stack} , °C	130
Minimum allowable boiler pinch point $\Delta T_{pp,boiler}$, °C	50
Minimum allowable Ljungström pinch point $\Delta T_{pp,Lj}$, °C	30
Boiler CO ₂ side Δp_{boiler} , bar	2.5
Excess of air	20%
Flue gas temperature at the radiative zone exit, $T_{out,rad}$, °C	1200
Maximum air temperature at LJ outlet, $T_{LJ,max}$, °C	350

Boiler efficiency (η_{boiler}) is calculated considering the heat loss with the flue gases at the stack, thus neglecting heat losses from boiler walls to the environment:

$$\eta_{boiler} = \frac{\dot{Q}_{in,cycle}}{\dot{Q}_{LHV}} = 1 - \frac{\int_{T_{amb}}^{T_{stack}} \dot{m}_{fg} c_{p,fg}(T) dT}{\dot{m}_{fuel} LHV_{fuel}} \quad (2)$$

The plant overall efficiency (η_{plant}) is calculated as the product between cycle efficiency and boiler efficiency:

$$\eta_{plant} = \eta_{cycle} \eta_{boiler} = \frac{\dot{W}_{net}}{\dot{Q}_{LHV}} \quad (3)$$

HEAT EXCHANGERS SIZING

The detailed design of the heat exchangers is performed according to the thermodynamic design of the cycle and of the boiler, assuming the pressure drops provided in Table 1 as target.

As widely suggested in literature [9][10][11], Printed Circuit Heat Exchangers (PCHE) are considered for the LTR and HTR and their sizing is made in accordance with the work developed by Dostal [9] and with a set of hypotheses already used in previous works [4][12]. The recuperators are discretized in 50 sections and for each segment the overall heat transfer coefficient, the required heat transfer area, metal and sCO₂ volumes are obtained.

The primary heat exchanger is designed as a two-pass heat exchanger. The radiative high temperature section (HT-PHE) is considered as a membrane wall heat exchanger while the convective-radiative intermediate temperature section (LT-PHE) is assumed as counter flow tubular heat exchanger. The HTRB heat exchanger is assumed as a counter flow tubular heat exchanger as well. The value of the radiative heat flux on the membrane walls is computed through a series of Thermoflex [8] simulations of the radiant boiler component and its value is assumed equal to 117 kW/m².

Both tubular heat exchangers in the boiler (LT-PHE and HTRB) are discretized in 50 steps, each one exchanging the same amount of heat. The internal heat transfer coefficient is computed with the Dittus-Boelter correlation [13], while the external heat transfer coefficient is computed as the sum of a convective and a radiative contribution, both estimated through correlation obtained from Thermoflex as function of the flue gases velocity and temperature[8], [12].

The overall heat transfer coefficient referred to the internal area for the j -th step $U_{in,j}$ is then obtained as:

$$U_{in,j} = \left(\frac{1}{htc_{CO_2,j}} + \frac{d_{in} \ln \left(\frac{d_{ex}}{d_{in}} \right)}{2k_t} + \frac{\frac{A_{in,j}}{A_{ex,j}}}{(htc_{FG,rad} + htc_{FG,conv})} \right)^{-1} \quad (4)$$

The internal heat transfer area of each heat exchanger in the radiative-convective section is finally computed as:

$$A_{in} = \sum_{j=1}^{50} \frac{\dot{Q}_j}{U_{in,j} \Delta T_{m,j}} \quad (5)$$

The heat rejection unit heat exchange area is predicted with LU-VE proprietary correlations [14] computing the heat transfer coefficients, the pressure drops and the overall heat exchanger area.

Finally, the Ljungström air preheater, given its effectiveness from the thermodynamic design, is sized with Thermoflex.

The main geometrical assumptions for the different heat exchangers design are reported in Table 3.

Table 3: Main assumptions for the different heat exchangers design

PCHE	
Thickness of plate, mm	1.5
Diameter of semi-circular channel, mm	2
Thickness of wall between channels, mm	0.4
Heat exchanger material	INCOLOY 800
HT-PHE	
Tube internal diameter, mm	20
Ratio of tube pitch to external diameter	1.45
Tube and membrane material	INCONEL 617
HTRB and LT-PHE	
Tube internal diameter, mm	40
Ratio of tube pitch to external diameter	1.2
Ratio of transverse tube pitch to ext. diameter	10
Tube material	INCONEL 617

DESIGN RESULTS

The results of the thermodynamic design of the system are reported in Table 5. The obtained net cycle efficiency is 41.92%, while the boiler efficiency is 94.37%; combining these two contributions an overall efficiency of 39.56% is achieved. All the main thermodynamic properties of the cycle streams are reported in Table 4.

Table 4: Thermodynamic streams of the sCO₂ cycle

Point	Temp. (°C)	Press. (bar)	Density (kg/m ³)	Enthalpy (kJ/kg)	Entropy (kJ/kgK)
1	33	81.18	632.40	301.77	1.33
2	67.13	250	751.30	330.74	1.34
3	186.68	248.75	343.45	563.33	1.94
4	481.88	247.51	167.71	946.82	2.59
5	620	245.51	138.39	1120.15	2.80
6	491.88	82.41	56.60	974.91	2.84
7	196.68	81.99	99.65	635.15	2.28
8	77.13	81.58	168.38	485.70	1.91
9	531.14	246.80	155.81	1008.4	2.67

As it is possible to notice from Figure 2, which depicts the boiler T-Q diagram, the optimal boiler design presents values of pinch point temperature differences at the main HX sections higher than the minimum achievable technical value. This fact is due to the limitation imposed to the stack temperature and to the combustion air preheating temperature.

Thus, as it is possible to notice from Table 5 that, in order to maximize the boiler efficiency, stack temperature is pushed down by the optimizer to its lower bound value, while at the

same time the air combustion temperature at Ljungstrom HX exit is pushed to its upper bound value.

Table 5: Main results of the boiler and cycle design.

Boiler and cycle optimized results	
CO ₂ mass flow at turbine inlet, kg/s	1087.12
CO ₂ mass flow at HRU, kg/s	698.53
CO ₂ mass flow at HTR bypass, kg/s	123.95
Split ratio SR	0.643
Bypass ratio BR	0.114
Minimum cycle pressure p_1 , bar	81.18
Coal mass flow rate, kg/s	14.80
Air mass flow rate, kg/s	98.22
Flue gases mass flow rate, kg/s	111.65
Adiabatic flame temperature, °C	1980.96
Flue gases stack temperature, °C	130
Optimal boiler pinch point $\Delta T_{pp,boiler}$, °C	209.25
Ljungström pinch point $\Delta T_{pp,Lj}$, °C	45.93
Turbine electric power, MW _{el}	152.27
Main compressor electric power, MW _{el}	20.98
Secondary compressor electric power, MW _{el}	31.28
Heat rejection auxiliaries consumption, MW _{el}	1.09
Cycle efficiency	41.92%
Boiler efficiency	94.37%
Overall efficiency	39.56%

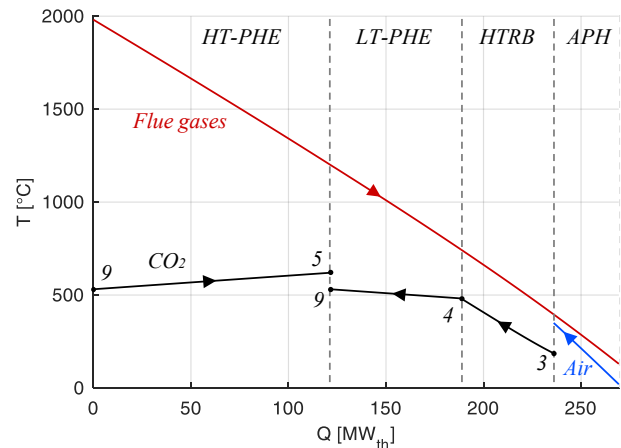


Figure 2: Boiler T-Q (temperature vs. thermal power exchanged) diagram.

Table 6 reports the main results of the HX design showing how the two recuperators require large overall heat exchange areas due to the small ΔT_{LTR} and ΔT_{HTR} selected.

Table 6: Main results of the heat exchangers design

Parameter	HRU	LTR	HTR	HT-PHE	LT-PHE	HTRB
Heat duty, MW	188.4	162.4	369.3	121.5	66.9	47.5
Hot side heat transfer coefficient, W/m ² K	4880.7	4398.9	3682.7	-	105.7	84.7
Cold side heat transfer coefficient, W/m ² K	75.8	4503.5	3717.4	-	3419.6	4247.1
Global heat transfer coefficient, W/m ² K	53.4	2039.5	1737.6	80.2	98.2	80.3
Internal heat transfer surface, m ²	8912	6898.7	14345.5	1595	1203	1876
HX metal mass, kg	70316	43258	89953	77331	73573	113787

PART LOAD OPERATION

The analysis of the system at part load is performed assuming a reduction of the fuel input and a proportional reduction of the combustion air to keep the air-to-fuel ratio constant and to guarantee an effective combustion also in off-design conditions. For the considered preliminary analysis, a constant ambient air temperature and a constant compressor inlet temperature are assumed as well, since the focus of the work is on the different operating strategies available for an active part-load control. As in design conditions, an isothermal mixing at the high pressure exit of the LTR and HTR is imposed by properly varying the split fraction to the secondary compressor and the one to the HTR bypass. The maximum sCO₂ temperature (T_5) is kept constant in order to simplify the analysis and avoid metal overheating in the furnace. The pressure drops in each heat exchanger section at part-load are corrected with respect to the design value through the following correlation:

$$\Delta p = \Delta p_{design} \left(\frac{\rho_{design}}{\rho} \right) \left(\frac{\dot{m}}{\dot{m}_{design}} \right)^2 \quad (6)$$

The heat transfer coefficients at part load operation on the CO₂ side for LTR, HTR, HTRB and LT-PHE and on the flue gas side for HTRB and LT-PHE are computed with a simplified approach as function of the ratio between the mass flow rate in off-design conditions and the mass flow rate in nominal operation:

$$ht_{CO_2} = ht_{CO_2,design} \left(\frac{\dot{m}_{CO_2}}{\dot{m}_{CO_2,design}} \right)^{0.8} \quad (7)$$

$$ht_{FG} = ht_{FG,design} \left(\frac{\dot{m}_{FG}}{\dot{m}_{FG,design}} \right)^{0.6} \quad (8)$$

The different exponents on the mass flow ratios for CO₂ and flue gases depends on the different correlations used for the calculation of the convective heat transfer coefficients [13].

In the HT-PHE, being the radiation the main heat exchange mechanism, the equivalent overall heat transfer coefficient U_{ra} computed in nominal conditions (see

Table 6) is kept constant independently from the load as the variation of the adiabatic flame temperature is limited.

Finally, for the HRU, it has been preferred to adopt ad hoc correlations due to the proximity of the CO₂ thermodynamic conditions to the critical point [15].

Heat rejection unit fan consumption is calculated with reference to the nominal value and adopting an exponential function as reported:

$$\dot{W}_{HRU,aux} = \dot{W}_{HRU,aux,design} \left(\frac{\dot{m}_{air}}{\dot{m}_{air,design}} \right)^{2.78} \quad (9)$$

Different options are available for the part-load control of the cycle, depending on the turbomachinery features: compressors and turbine may be equipped with Variable Inlet Guide Vanes (VIGV) and may be able to vary their rotational speed. Moreover, a further option available in closed gas cycles is related to the possibility of varying the working fluid inventory thus changing the operating pressure of the system. In the present work different options are considered for the sCO₂ turbine and their effect on cycle performance and compressors operating points are investigated. The turbine is assumed to operate in choked flow conditions, thus the following correlation holds:

$$\frac{\dot{m}_5 \sqrt{T_5}}{p_5 A_{in,turb}} = \frac{\dot{m}_{5,design} \sqrt{T_{5,design}}}{p_{5,design} A_{in,turb,design}} \quad (10)$$

For simplicity, no variation on turbomachinery efficiency is considered. The following cases are identified:

- CASE 1: Turbine in sliding pressure and fixed minimum cycle pressure;
- CASE 2: Turbine in sliding pressure and optimized variable minimum cycle pressure;
- CASE 3: Turbine with partial admission and fixed minimum cycle pressure.

RESULTS

CASE 1: Turbine in sliding pressure and fixed minimum cycle pressure.

Figure 3, left depicts the trend of cycle efficiency, boiler efficiency and the plant efficiency. The cycle efficiency tends to remain constant for a wide range of fuel input as the negative effect related to the reduced compression ratio with consequent reduction of the net specific power output of the cycle is compensated by the increased heat exchangers effectiveness. In fact, at part load the heat exchangers are oversized with respect to their duty and thus perform in a more effective way as it is possible to see from the boiler efficiency trend. For coal mass flow rates below 60% of the nominal value cycle efficiency drops due to the excessive decrease in the pressure ratio of the cycle. Furthermore, the strong reduction of the CO₂ mass flow rates penalizes the HX heat transfer coefficients limiting the internal heat regeneration of the cycle.

Figure 3, right reports the trends of the adiabatic flame temperature and flue gases stack temperature: as the coal mass flow rate is reduced and the CO₂ is able to cool down the flue gases in a more efficient manner, the heat available for air preheating decrease thus limiting the combustion air temperature and consequently the adiabatic flames temperature. At very low loads these effects are limited by the strong penalization of the HXs heat transfer coefficients due to the reduced mass flow rates.

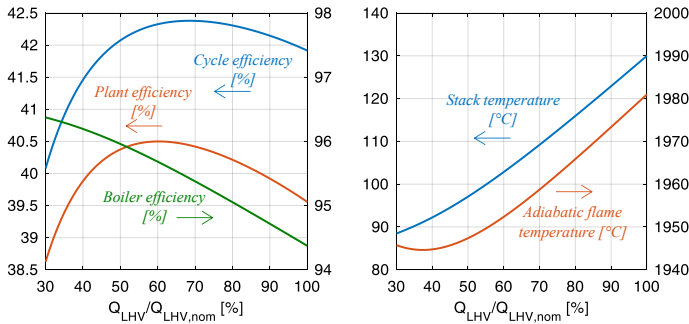


Figure 3: (left) Trends of the cycle efficiency, boiler efficiency and plant efficiency as function of the boiler heat input and (right) stack and adiabatic flame temperature as function of the fuel input for CASE 1.

CASE 2: Turbine in sliding pressure and optimized variable minimum cycle pressure.

The previous analysis strongly highlights how at lower loads could be beneficial to increase the cycle pressure ratio in order to limit the penalization on cycle efficiency and power plant net power output. This kind of regulation can be obtained with different compressor features: a possibility is the adoption of VIGV at compressors inlet and/or to employ electrical motors equipped with frequency converters to vary the rotational speed of the turbomachines.

A sensitivity analysis is carried out decreasing the minimum cycle pressure (equal to 81.18 bar in design conditions) with a step of 1 bar with respect to the nominal one in order to have six different scenarios. Figure 4 depicts the trend of the plant efficiency: it is possible to note that optimal minimum pressure decreases with the fuel input thanks to the increased pressure ratio leading to a higher net specific power output. Acting properly on the cycle minimum pressure allows in the case of 30% coal mass flow rate to slightly increase the efficiency from a value equal to 38.62% up to a value of 39.35%.

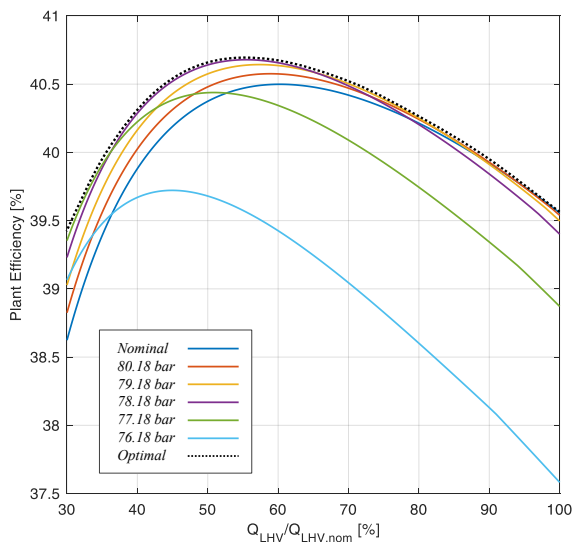


Figure 4: Trends of the plant efficiency as function of the fuel input for different minimum cycle pressures (CASE 2).

Figure 5 and Figure 6 report the main and the secondary compressor operating points as function of the fuel input for CASE 1 and CASE 2 on a dimensionless $\Delta h-\dot{V}$ chart. The white areas on the charts show the operating region for the two compressors equipped with VIGV and variable speed (60%/105%) according to a preliminary design performed within the sCO₂-Flex project: line on the top-left represents the surge limit, while line on the bottom-right represents the choke limit. In CASE 1, at minimum fuel input (30%) the main compressor operating point falls out of the operative region crossing the surge limit line while in CASE 2 this is avoided. In fact, decreasing the minimum pressure with the load allows to walk off the critical point limiting the reduction of the volumetric flow (the compressibility factor at the compressor inlet and the SR increase) not incurring in any issue related to choking or surge. The operating points of the secondary compressor reported in Figure 6 do not show particular criticalities and do not impose further constraints to the operation of the system. Differently from the primary compressor, the secondary compressor at minimum fuel input and for reduced minimum pressure experiences a reduction of the inlet volumetric flow mainly due to the reduction of its mass flow rate, proportional to (1-SR). One further degree of freedom not investigated in this work is related to the possibility of varying the split ratio SR removing the isothermal mixing constraint and thus act both on the main and secondary compressor volumetric flows. It is important to underline once again that a more detailed investigation considering also the variation of turbomachinery isentropic efficiency is necessary to evaluate the best operating strategy at part load.

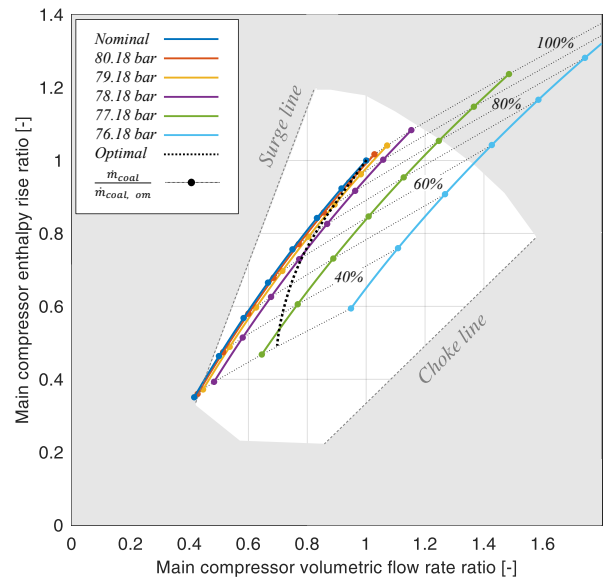


Figure 5: Main compressor operating points for the fixed minimum cycle pressure equal to the nominal value (CASE 1) and for variable minimum pressure case (CASE 2) as function of the fuel input. The white area in the figure represents the operating region for the main compressor with VIGV and variable rotating speed.

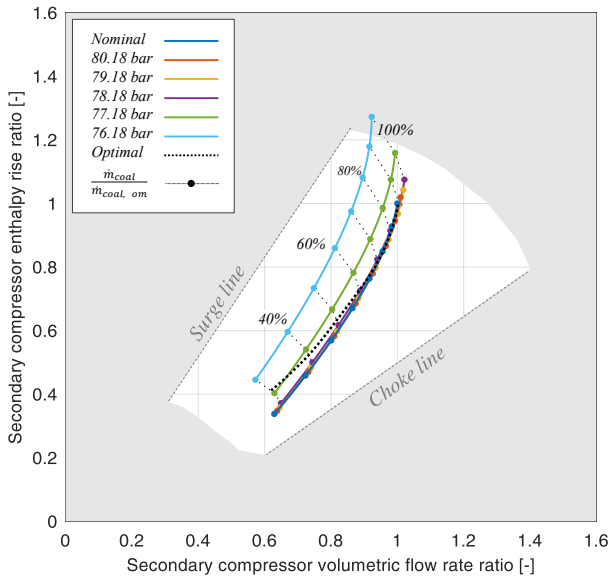


Figure 6: Secondary compressor operating points for the fixed minimum cycle pressure equal to the nominal value (CASE 1) and for variable minimum pressure case (CASE 2) as function of the fuel input. The white area in the figure represents the operating region for the main compressor with VIGV and variable rotating speed.

CASE 3: Turbine with partial admission and fixed minimum cycle pressure.

A further possibility in order to control part-load operation of sCO₂ power plants is to provide the turbine by Inlet Guide Vanes (IGV) or a partial admission arc in order to control the cycle maximum pressure. The choice between the two technologies generally depends mainly on the size and the type of the component (radial centripetal vs axial turbine) and on its maximum operating temperature, factors that can significantly limit the adoption of these technologies due to the high thermomechanical stresses. The analysis is repeated only for the nominal value of the cycle minimum pressure assuming a fixed value of the maximum cycle pressure, but the analysis can be extended combining the contribution of the different control strategies. Figure 7 shows how the plant efficiency for CASE 3 increases thanks to the improved effectiveness of the heat exchangers. At 30% of the fuel input the plant efficiency achieves 41.76%, 2.41 percentage points more than CASE 2. However, a severe drawback of this control strategy is related to the compressors operating point (see Figure 8): already at 80-90% of the coal fuel input the operating point of the compressors moves towards the surge zone, crossing it for a value around the 75% of the load. This fact not only limits significantly the initial hypothesis on constant turbomachinery efficiency, but it makes impossible to adopt this strategy in order to control the plant at partial loads.

A possible solution is the use of more compressors in parallel that can be switched off as the load is reduced. It is

important to underline anyhow that smaller compressors may be characterized by lower performance and higher total costs. Another solution is related to the selection of a different design point of the compressor. Finally, as for the sliding pressure case, a variation of the minimum cycle pressure can positively influence the volumetric flow at the compressor inlet.

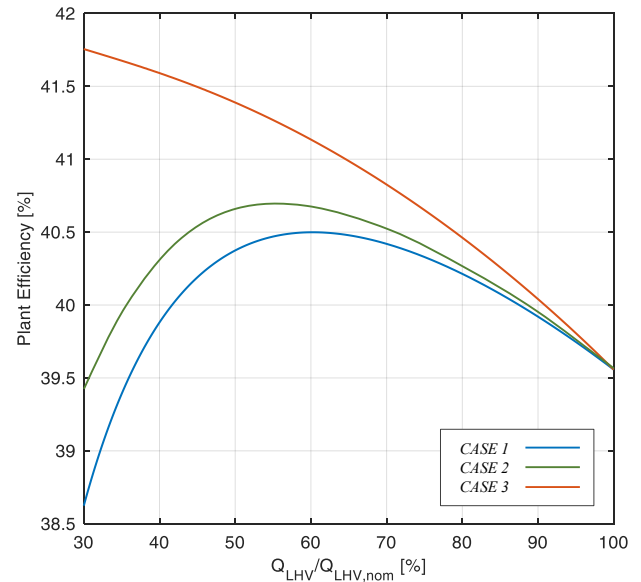


Figure 7: Variation of plant efficiency with the fuel input for the three different investigated strategies

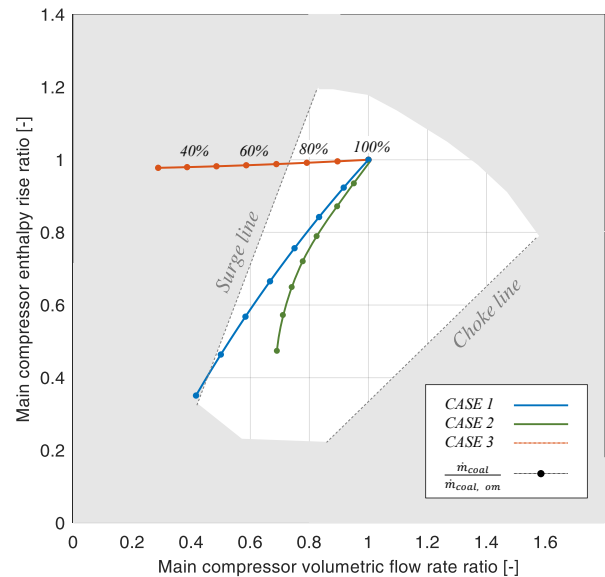


Figure 8: Main compressor operating points for CASE 1, CASE 2 and CASE 3 as function of the fuel input. The white area in the figure represents the operating region for the main compressor with VIGV and variable rotating speed.

CONSIDERATIONS ON CO₂ INVENTORY

From the design of each heat exchanger and assuming reasonable piping length between the different components the inventory of CO₂ was computed in nominal conditions and at part load for the three different studied cases. The results reported in Figure 9 show how the CO₂ inventory variation is very limited if fixed pressures are assumed (CASE 3), while it can vary significantly if a sliding pressure at the turbine inlet is considered. CASE 3 scenario would thus imply smaller volumes required to store the excess CO₂ during part load operation.

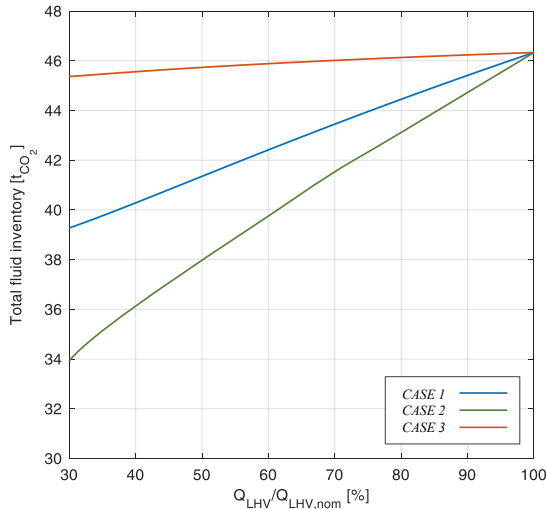


Figure 9: variation of CO₂ inventory within the system with the fuel input for the three different investigated strategies

CONCLUSIONS AND FUTURE WORKS

In the present work, the study of a recuperative recompressed sCO₂ cycle with HTR by-pass as power cycle for a coal-fired power plant was performed. The achieved cycle efficiency is 41.92% and the overall plant efficiency is of about 39.56%. Once a preliminary design of all the main heat exchangers was performed, different part load operating strategies were compared in order to identify their impact on the plant efficiency and on the operating points of the main and secondary compressor. From the overall plant efficiency point of view keeping the same turbine inlet pressure at part load (thanks to IGV or partial arc admission) guarantees the best performance with an increase of plant efficiency at part load of 2.2 points percent thanks to the increased recuperators efficiency. This operating strategy guarantees also a limited CO₂ inventory variation, but on the other hand cannot be pursued with a single main compressor but requires more compressors in parallel. If the turbine works with sliding pressure the plant efficiency slightly increases down to 50% of the fuel input and then decreases and the CO₂ inventory changes significantly. With this operating strategy the optimization of the minimum cycle pressure has limited impact on the plant efficiency (0.7 points percent more at 30% of the fuel input) but can ease the operation of the main compressor. Future development of this work will

include the study of the impact of the turbomachinery efficiency variation with the operating conditions and will investigate further operational degrees of freedom such as variation of the split ratio or of the HTR bypass ratio.

NOMENCLATURE

Symbols

A	Area (m ²)
c _p	Specific Heat Capacity (J/kg-K)
h	Enthalpy (J/kg-K)
htc	Heat Transfer Coefficient (W/m ² -K)
k _t	Thermal Conductivity (W/mK)
\dot{m}	Mass Flow Rate (kg/s)
\dot{Q}	Thermal Power (W)
T	Temperature (°C)
U	Overall heat transfer coefficient (W/m ² -K)
\dot{W}	Power (W)
η	Efficiency (%)
ξ	Specific HRU Elec. Consumption (W _{el} / W _{th})
Z	Compressibility factor

Acronyms

APH	Air Preheater
BR	Bypass Ratio
HRU	Heat Rejection Unit
HTR	High Temperature Recuperator
HTRB	High Temperature Recuperator Bypass
HT-PHE	High Temperature Primary Heat Exchanger
HX	Heat Exchanger
LHV	Lower Heating Value
LTR	Low Temperature Recuperator
LT-PHE	Low Temperature Primary Heat Exchanger
PCHE	Printed Circuit Heat Exchanger
SCO ₂	Supercritical CO ₂
SR	Split Ratio
USC	Ultra Super Critical
VIGV	Variable Inlet Guide Vanes

ACKNOWLEDGEMENTS

The sCO₂-flex project has received funding from the European Union's Horizon 2020 research and innovation programme under grant agreement N° 764690.

BHGE - Nuovo Pignone has provided preliminary turbomachinery information and parameters

REFERENCES

- [1] “SCO2-flex.” [Online]. Available: <http://www.sco2-flex.eu/>.
- [2] G. Angelino, “Real gas effects in carbon dioxide cycles,” in *International Gas Turbine Conference & products Show, Cleveland, Ohio - March 10-13, 1969*, 1969, no. ASME Paper No. 69-GT-102.
- [3] F. Crespi, G. Gavagnin, D. Sánchez, and G. S. Martínez, “Supercritical carbon dioxide cycles for power generation: A review,” *Appl. Energy*, vol. 195, pp. 152–183, 2017.
- [4] D. Alfani, M. Astolfi, M. Binotti, S. Campanari, and P. Silva, “D5.1 - Report on the nominal design of different plant configurations and sensitivity analysis on main design parameters.” 2019.
- [5] Mathworks, “Matlab tool.” Mathworks, 2017.
- [6] E. Lemmon, M. Huber, and M. McLinden, “NIST standard reference database 23: reference thermodynamic and transport properties-REFPROP.” National Institute of Standards and Technology, Gaithersburg, 2013.
- [7] M. Mecheri and S. Bedogni, “D1.3 - Report on the selected cycle architecture.” 2018.
- [8] “Thermoflow.” 2016.
- [9] V. Dostal, M. J. Driscoll, and P. Hejzlar, “Advanced Nuclear Power Technology Program A Supercritical Carbon Dioxide Cycle for Next Generation Nuclear Reactors,” 2004.
- [10] M. . Carlson, A. . Kruizenga, C. Schalansky, and D. F. Fleming, “Sandia progress on advanced heat exchangers for sCO2 Brayton cycles,” in *The 4th International Symposium*, 2014.
- [11] G. O. Musgrove, R. Le Pierres, and J. Nash, “Heat Exchangers for Supercritical CO2 Power Cycle Applications,” in *The 4th International Symposium for Supercritical CO2 Power Cycles*, 2014.
- [12] D. Alfani, M. Astolfi, M. Binotti, S. Campanari, F. Casella, and P. Silva, “Multi objective optimization of flexible supercritical CO2 coal-fired power plant,” in *ASME Turbo Expo 2019: Turbomachinery technical conference and exhibition*, 2019.
- [13] T. L. Bergman and F. P. Incropera, *Fundamentals of heat and mass transfer*. Wiley, 2011.
- [14] “LU-VE S.p.A. - Heat Exchangers for refrigeration and air conditioning.” [Online]. Available: <https://www.luve.it/>. [Accessed: 30-Apr-2019].
- [15] “Private communication with LU.VE.” 2016.

DYNAMIC MODELING AND TRANSIENT ANALYSIS OF A MOLTEN SALT HEATED RECOMPRESSION SUPERCRITICAL CO₂ BRAYTON CYCLE

Pan ZHOU*
EDF R&D China
Beijing, China
Email: Pan.zhou@edf.fr

Jinyi ZHANG
EDF R&D China
Beijing, China

Yann LE MOULLEC
EDF R&D China
Beijing, China

ABSTRACT

Supercritical CO₂ power generation cycle is a promising power generation technology with a high potential to reach high thermal efficiency and high flexibility. In this work, a recompression cycle with intercooling and preheating is selected for the application of supercritical CO₂ cycle in concentrated solar power. Given the design boundary conditions, all the equipment are designed and optimized by in-house code, which gives a preliminary geometry for the equipment. The calculated geometries are then integrated into dynamic modules to simulate the off-design behaviors of equipment. Based on the developed equipment dynamic modules, a dynamic physical model of selected cycle is built in Modelica language implemented in Dymola. Part load transient scenarios are defined with technical constraints, such as minimum main compressor inlet temperature and minimum molten salt outlet temperature. With these key scenarios defined and constraints integrated into the model, sensitivity analyses are carried out to understand system dynamics. Global operation and control strategies for system protection, regulation and performance optimization are proposed and designed within MATLAB&SIMULINK to satisfy the pre-defined performance criteria. Finally, scenario simulations are done with the proposed control strategy and tuned control parameters to justify its feasibility.

INTRODUCTION

Supercritical CO₂ (sCO₂) cycle has drawn much attention for power generation industry in recent years. Compared to water steam Rankine cycle, it has advantages of simpler cycle layout, more compact turbo-machineries and high potential to reach higher efficiency. In the meantime, CO₂ is inexpensive, dense and less corrosive than water at same high temperature, with an easily reachable critical point at 30.98 °C and 73.8 bar. sCO₂ power cycles could be applied to various potential heat source including nuclear power, coal-fired power, waste heat recovery and renewable energy sources such as concentrated solar power (CSP) and fuel cells [1].

CSP can provide carbon free and renewable energy to meet the energy demand. With integration of thermal storage system, CSP can decouple the solar-to-thermal and thermal-to-electric conversion regardless of the weather condition. However, the Levelized Cost of Electricity (LCOE) of CSP is still non-competitive (120\$/MWh, average by 2020, reported in IRENA). Compared with the water steam Rankine cycle utilized in the existing CSP industry, sCO₂ cycles coupled with high temperature solar receivers and thermal storage are considered to be a solution to increase cycle efficiency and system flexibility, then to reduce the LCOE of CSP [2].

Dynamic modelling is a useful and efficient tool to help verify the equipment and to develop or optimize the control strategy of the power cycle. Yan [3] has carried out dynamic analysis and control system design for a nuclear gas turbine power plant, in which utilization of inventory control and by pass control is recommended respectively for keeping cycle efficiency and providing fast load regulation. Moiseyev *et al.* [4] has developed a detailed dynamic model for a recompression sCO₂ Brayton cycle and has studied the cycle automatic control including inventory control, flow split control and etc. In the thesis of Carstens [5], a dynamic model for a sCO₂ recompression cycle of 600 MWth has been developed and part load simulation has been carried out with designed PID controllers.

In this work, pre-design of a 10 MWe recompression with intercooling and preheating sCO₂ Brayton cycle for CSP using molten salt as heat transfer fluid has been carried out and a dynamic model has been developed in Dymola with Modelica language. This cycle was designed for Shouhang – EDF demonstration project signed in 2018, with the objective of retrofit the Shouhang 10MWe CSP plant with sCO₂ Brayton cycle before the end of 2020. Transient analysis, temperature control and part load control have been carried out to analyze the dynamic behavior of the model and to study different control strategy for cycle part load.

SYSTEM CONFIGURATION

The cycle studied in this work is a recompression cycle with intercooling and preheating, which is designed for a net power output of 10MWe and is optimized to work with molten salt between 530 °C and 290 °C. The cycle layout is presented in Figure 1 with main part-load control systems. Auxiliary

Table 1 Key parameters of 10 MWe sCO₂ Brayton cycle

Parameter	Unit	Value
Turbine inlet temperature	°C	467.6
Turbine inlet pressure	bar	250
Turbine mass flow rate	kg/s	137.7
MC inlet temperature	°C	35
MC inlet pressure	bar	106.3
Recompression split ratio	-	27.74%
Molten salt inlet temperature	°C	530
Turbine power	MWe	16.1
Main compressor power	MWe	2.4
LTR heat exchanged	MW	20.8
HTR heat exchanged	MW	26.5
Net power output	MW	10

compressor (AC) is for recompression. The intercooling aims at minimizing the compressor work by cooling the sCO₂ fluid, which increases the density of sCO₂ [1]. On the other hand, the preheating helps increasing the utilization of molten salt while maintaining a high efficiency. The minimum cycle temperature and pressure are selected to be 35 °C and 82.1bar for the consideration of the sharp variations of sCO₂ properties near its critical point. Detailed cycle parameters are presented in Table 1, which are optimized statically to achieve the highest output power.

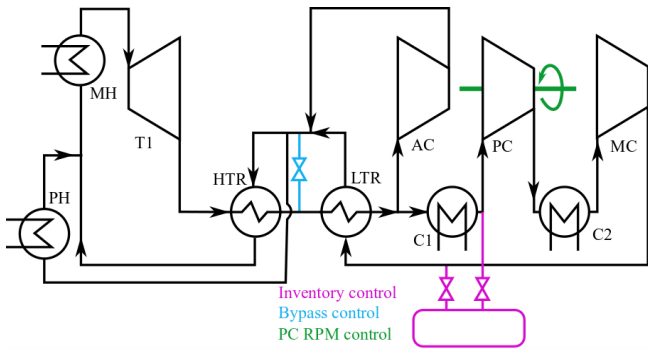


Figure 1 System configuration of 10MWe Recompression intercooling and preheating sCO₂ Brayton cycle

Molten salt/CO₂ heater, as the primary heater, is used to avoid the high challenge from high-pressure receiver design and to keep the advantage of full decoupling between sunshine and power generation. For the cooling, air cooler is used but with an indirect scheme: CO₂ is cooled by water that circulates in a closed loop while water is cooled by air cooler. Therefore, there will be no challenge on the resource of water on site. Figure 25 presents the yearly temperature in Dunhuang. In the hottest day, the maximum temperature is 38 °C which will be a challenge to the cooling system. However, it could be observed that the daily

temperature difference is very high in Dunhuang, which is an ideal case for cold storage to guarantee the operation of cooler. CO₂ inventory system is also implemented as one of the main measures for load control, and it serves also as the main storage system during system startup and shutdown. The charge point is set before the inlet of the pre-compressor (PC, compressor located before the main compressor of the cycle) as the pressure at this point is the lowest in the cycle. In the same way, the discharge point is designed after the main compressor where the pressure is highest in the cycle. PC is designed to work at variable speeds, as another measure for load regulation.

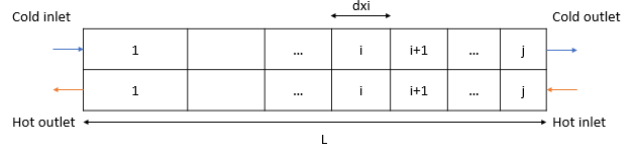


Figure 2 Inhomogeneous discretization of PCHE

PRE-DESIGN OF EQUIPMENT

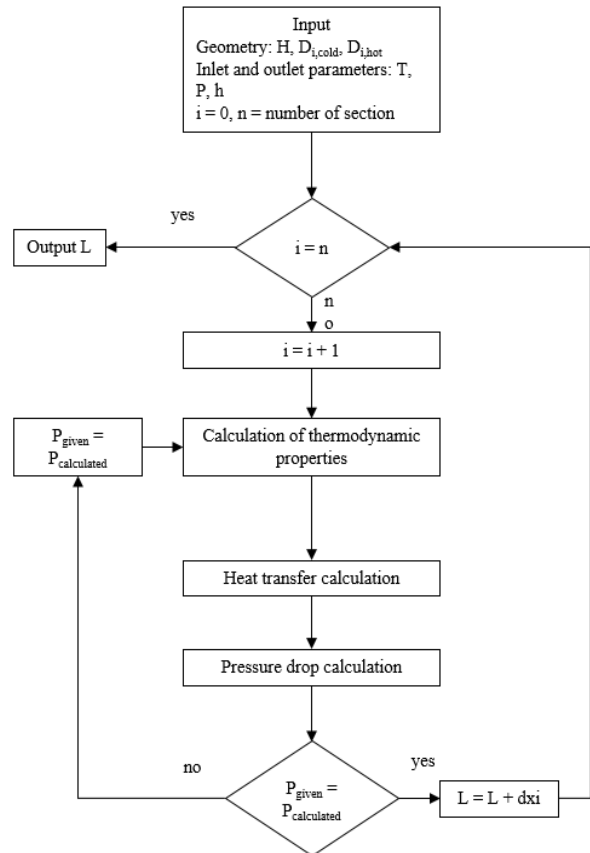


Figure 3 Algorithm of heat exchanger pre-design tool

To establish the dynamic model, it is necessary to define the geometry of every component in the cycle. Therefore, pre-design is carried out for each component in excel.

1. Heat exchangers

Since they are used in most sCO₂ Brayton cycles, including those in SNL and Echogen [6], Printed circuit heat exchangers

(PCHE), with straight channel have been chosen in this work to represent the two recuperators of the cycle. The pre-design tool for PCHE utilizes inhomogeneous discretization method as showed in figure 2, which means that the heat exchanged for each section remains constant.

Study has been done to choose an appropriate number of sections (Ns) for pre-design. It was found that for $N_s > 20$, the design parameter given by the tool remains stable. As a result, 20 has been chosen for the number of section in the calculation of pre-design. The model considers a 1-D thermal conduction and the global heat transfer equation is presented below and the signification of parameter is listed in chapter nomenclature.

$$\frac{1}{K_i S_{min,i}} = \frac{1}{h c_{cold,i} \times S_{cold,i}} + \frac{1}{h c_{hot,i} \times S_{hot,i}} + \frac{e}{\lambda S_{min,i}}$$

$$S_{min,i} = \text{Min}(S_{hot,i}, S_{cold,i})$$

Figure 3 represents the algorithm of geometry calculation for the pre-design tool. This algorithm calculates the length of PCHE by importing the height H of PCHE, hot and cold side channel diameter $D_{i,hot}$ and $D_{i,cold}$ and inlet and outlet thermodynamic properties temperature T, enthalpy h and pressure P. Calculation begins from the section one (counted from cold side). In each section, the thermodynamic properties are calculated by NIST REFPROP and then followed by heat transfer and pressure drop calculations. Gnielinski's correlation [7] is used to determine the heat transfer coefficient, listed in Table 3. The pressure of each section is supposed to be constant in the calculation and it was corrected after the calculation of pressure drop. The Darcy factor is determined by Haaland's correlation [8].

Table 2 Geometry of heat exchanger determined by pre-design tool.

	LTR	HTR	C1	C2	PH	HI
Length (m)	0.93	0.88	27.2	12.5	11.8	11.8
Height (m)	1.53	2.16	-	-	-	-
D_{cold} (mm)	0.82	0.85	750	640	522	761
D_{hot} (mm)	1.50	1.41	0.03	0.03	0.03	0.03
U ($W/m^2/K$)	1679	1233	1047	1502	540	501

With this algorithm to calculate the length of heat exchanger, the pre-design tool minimizes the estimated price by varying the channel diameter of both sides and height of the PCHE. As for the optimization constraints, pressure drop for both sides was set to be 1 bar which is fixed for the cycle design and the minimum channel diameter is set to be 0.5 mm.

The heater and cooler utilized in the cycle are Shell and Tube heat exchangers (STHX). The pre-design process of STHX is similar with that of PCHE except for the calculation of pressure drop which is different for tube and shell sides. The calculation of pressure drop in both sides followed the correlations described in Kakaç's book [9]. Table 2 represents the result of heat exchanger pre-design. For STHX, cold side diameter represents shell internal diameter.

2. Turbomachinery

For turbo-machinery, predesign of centrifugal compressor and radial turbine of single stage has been carried out. In general, the preliminary design of turbomachinery consists of rotor calculation, stator calculation and performance estimation which includes different types of losses. In this work, a one-dimensional meanline design approach described by Ventura et al. [10] was applied for the pre-design of radial turbine. Oh et al [11] published an optimum set of empirical loss models for the performance estimation of centrifugal compressor. Expected isentropic efficiencies of compressor and turbine are 80% and 85% respectively.

With the help of these two approaches, geometry of turbomachinery was obtained, which was used for the off-design. Off-design generates curves of correlation between efficiency η and mass flow rate Q and also correlation between pressure ratio PR and mass flow rate Q for each rotation speed.

In dynamic model, it is preferred to introduce the performance curves to represent the dynamic behavior of turbomachinery for simplicity of dynamic model. However, the general performance curves are charts with 5 dimensions representing inlet temperature, inlet pressure, mass flow rate, rotation speed and efficiency or pressure ratio respectively, which still increases the complexity of the dynamic model. As a result, the 5-D performance curves were nondimensionalized into a 2-D chart according to the approach described in the thesis of M. Dyreby [12]. Those 2-D charts represent the relation between modified flow coefficient ϕ^* and modified efficiency η^* or modified head coefficient ψ_i^* , which are showed below:

$$\phi^* = \frac{Q}{\rho U D^2} \left(\frac{N}{N_{design}} \right)^x$$

$$\psi_i^* = \frac{\Delta h_i}{U^2} \left(\frac{N_{design}}{N} \right)^y$$

$$\eta^* = \eta \left(\frac{N_{design}}{N} \right)^z$$

The values of x, y and z are chosen according to the case studied and to the result of nondimensionalization. N represents the rotation speed. N_{design} is the designed rotation speed. D is the impeller diameter and U is the impeller tip speed.

DYNAMIC MODELING

The dynamic physical model of this cycle is developed with Modelica language implemented in Dymola. Modelica is an equational and object-oriented modeling language, whose compilers translate the equational models to imperative program such as C++ to generate executable code [13]. The simulation software platform Dymola is a simulation and modeling tool for large and complex system, composed of component models, in domains within automotive, aerospace, energy and other applications.

In this work, a complete system model has been developed in Dymola, which is composed of several component models such as turbomachinery, heat exchanger and other models. The

models were developed based on user-defined components and ThermoSysPro – a library of component models which is used for simulation and modeling of power plants, developed by El Hefni [13]. Each component is developed and then validated before being integrated into the full system.

The thermodynamic properties of CO₂ are calculated by REFPROP integrated in Dymola. As all the components in the system operate in supercritical phase, they are modeled as pure phase modules. For simplification, sCO₂ is separately cooled by water in Cooler 1 and 2 because the air cooler is not modelled in the system. In cycle pre-design, the pressure drop of valves was not considered but in dynamic model, the valve models brought certain pressure drop, which made a slight difference on the parameters between designed cycle and dynamic model. However, this difference should not have major impact on the dynamic behavior of the system.

1. Mass, Energy and Momentum Balance

The mass, energy and momentum conservation are fundamental laws that represent the thermal-hydraulic behavior of a fluid. Generally, a zero-dimension approach is used for thermal process modeling. As a result, the following three equations are used in the dynamic modeling:

$$V \cdot \left(\frac{\partial \rho}{\partial p} \frac{\partial p}{\partial t} + \frac{\partial \rho}{\partial h} \frac{\partial h}{\partial t} \right) = \sum \dot{Q}_{in,i} - \sum \dot{Q}_{out,i}$$

$$V \left(\left(h \frac{\partial \rho}{\partial p} - 1 \right) \frac{\partial p}{\partial t} + \left(h \frac{\partial \rho}{\partial h} + \rho \right) \frac{\partial h}{\partial t} \right) = \sum \dot{Q}_{in,i} \cdot h_{in,i} - \sum \dot{Q}_{out,i} \cdot h_{out,i}$$

$$L \frac{dQ}{dt} = A \cdot (p_{in} - p_{out} - \Delta p)$$

Q represents mass flow rate, h represents specific enthalpy and p represents pressure. Subscript in and out mean component inlet and outlet properties, all the properties without subscript means the medium volume average property in the component.

2. Heat exchanger models

Figure 4 represents the configuration of user-defined PCHE model in Dymola which consists of three parts: cold side tube, hot side tube and heat transfer wall. Applying the geometry given by pre-design, the tube model simulates pressure drop and heat transfer process which is considered to be the same in each parallel channel and a 1-D thermal conduction was considered in this model.

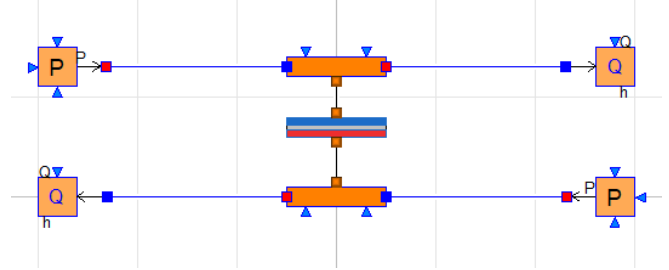


Figure 4 Configuration of user-defined PCHE model in Dymola

Table 3 summarizes the correlations used in the calculation of heat transfer coefficient and pressure drop for PCHE and STHX. Unlike inhomogeneous discretization used in pre-design, homogeneous discretization is applied in the dynamic model in order to decrease the number of equations to be solved, as well as to decrease the simulation time of the model. The heat transfer wall represents a series of thermal resistances between cold fluid and hot fluid.

The study of the influence of the number of sections (Ns) on the precision of the dynamic model compared to predesign is carried out to find a trade-off between precision and complexity of the model. The relative difference between achieved duty of dynamic model and target duty represents the precision of the model. The model is firstly verified at steady-state by comparing the heat transfer and pressure drop results with the target values and then several scripts are carried out to check the dynamic behavior of the model.

Table 3 Correlations for heat transfer coefficient and pressure drop calculation of PCHE and Shell & Tube heat exchanger.

	Heat Transfer	Pressure drop
PCHE	Laminar [3]: $Nu = 4.089$	Laminar [3]: $f = 63.2/Re$
	Transitional: linear interpolation between laminar and turbulent flow	Transitional: linear interpolation between laminar and turbulent flow
	Turbulent: Gnielinski [3] $Nu = \frac{\left(\frac{f_D}{8}\right) \times (Re - 1000) \times Pr}{1 + 12.7 \times \sqrt{\frac{f_D}{8}} \times (Pr^{\frac{2}{3}} - 1)} = \frac{h_i \times d_i}{k_t} \text{ for } Re > 10^4$ $f_D = 4 \times (1.58 \ln Re - 3.28)^{-2}$	Turbulent: Chen (1979) [3] $f = \left(3.48 - 1.7372 \ln \left(2\epsilon - \frac{16.2426 \ln A}{Re} \right) \right)^{-2}$ $A = \left(\frac{(2\epsilon)^{1.1098}}{6.0983} + \frac{7.149}{Re} \right)^{0.8981}$
Shell & Tube	Same as turbulent regime of PCHE	

3. Turbomachinery

For each dynamic model of turbomachinery, two 2-D charts obtained from pre-design were integrated:

$$\eta^* = f(\phi^*)$$
$$\psi_i^* = f(\phi^*)$$

The rotation speed of turbomachinery is given by user, which could be fixed or variable. Other parameters are calculated according to the two equations above and the inlet and outlet conditions of turbomachinery model.

TEMPERATURE CONTROL LOOPS

In this work, four basic Proportional-Integral-Derivative (PID) controllers are integrated in the system to ensure that the turbomachinery is in the safe operation region and that the molten salt is beyond its freezing point.

PID controllers were designed in Matlab PID tuner. As design constraints, the phase margin and gain margin are set to be respectively higher than 60 deg and 60 dB. A maximum overshoot of 5% was allowed in order to satisfy the demand of rising time and oscillation was not accepted.

PID controllers of main compressor inlet temperature (MCIT) and Pre-compressor inlet temperature (PCIT) are integrated in the cooling system. They respectively control the inlet temperature of MC and PC to 35 °C by manipulating the mass flow rate of cooling water in C1 and C2 in case of sharp properties variation of sCO₂ near the critical point, which could influence the operation of the compressors. These two controllers are important for system part-load during which MCIT and PCIT variation commonly occurs. As mentioned before, the cooling system is designed to be an air cooler which cool down the water for the cooling of sCO₂ fluid. Although the air cooler was not integrated in the dynamic system, its effect on cooling water temperature cannot be ignored. If the air temperature decreases, e.g. due to the diurnal temperature difference, the cooling water temperature will drop, which leads to the variation of MCIT and PCIT and also to the system efficiency and power output.

Molten salt outlet temperature (MSOT) is controlled to 290 °C by acting on the molten salt mass flow rate to avoid the molten salt freezing and overheating of cold storage tank. To control Turbine inlet temperature (TIT), the manipulated variable should be the openness of the valve that connects MC outlet and turbine inlet. In order to simplify the dynamic model, mass flow rate of the fluid through the valve was selected to be the manipulated variable. TIT is controlled not to exceed its operation temperature, namely 467.6 °C. These two controllers avoid overheat of TIT and prevent the freezing of molten salt, which could block the molten salt pipe. These two controllers are also important during system part-load. Moreover, the molten salt inlet temperature could be not stable because it is sensible to the solar irradiation and molten salt control which depends on real time weather and it also has influence on TIT.

PART LOAD CONTROL STRATEGY

Part load control is significant in power plant as the output power should satisfy the demand of grid. Several control

strategies have been proposed for the automatic control of gas turbine power plant which could be integrated in the sCO₂ Brayton cycle. Inventory control is an efficient control method for part load as the overall cycle efficiency is nearly constant during the control process [3]. Bypass control is preferable for rapid load control demand although it is less efficient than inventory control [3].

In this work, three control methods were separately integrated in the dynamic model and the study of their performance was carried out: inventory control, bypass control and variable PC rotation speed control. PID controllers have been designed in Matlab and then integrated in dynamic model.

1. Inventory control

Inventory control uses two tanks of CO₂, and is able to manipulate fluid injection and releasing in the system to achieve part load operation of system. First tank is directly connected to injection and release points, which is at around 100 bar and 35 °C. The pressure of this tank is maintained by a compressor which connect these two tanks. The injection and release is achieved by manipulating the openness of corresponding valves. The released sCO₂ will be cooled before enter the first tank. The charge and discharge of CO₂ in the cycle can be carried out at different points of the cycle. It is typically preferred to inject at low pressure points, e.g. inlet of PC and to release at high pressure points, e.g. outlet of MC. In this work, the charge point is selected to be at PC inlet with a sCO₂ tank of 160 bar and 35 °C and the cycle discharges at MC outlet to a tank at 83 bar. These two tanks are designed to maintain constant pressure during inventory charging and discharging. During discharge, the valve between MC downstream and discharge point is opened, the mass flow rate and pressure of the whole cycle decrease which leads to the drop of load.

Inventory control is to control the load of the system by manipulating the mass flow rate of the fluid through charge or discharge valve as showed in Figure 1. As the system temperature is changed during part load, the MCIT and PCIT should be controlled at 35 °C to avoid transcritical phenomena and instability of compressor operation. Moreover, TIT and MSOT controller should be integrated in the system. The rotation speed of turbomachinery is kept constant during inventory control. In addition, the inlet pressure of PC should be monitored in case of reaching critical pressure.

2. HTR & Heater & Turbine Bypass Control

By pass control achieves part load by venting fluid from LTR cold outlet to LTR hot inlet so that HTR, heaters and turbine are bypassed as showed in Figure 1. Turbine output power will therefore decrease which leads to the drop of load.

During the bypass control, the load is controlled by manipulating the mass flow rate through the bypass valve. Similarly to inventory control, elementary controllers of MCIT, PCIT, TIT and MSOT should be integrated.

3. Variable PC rotation speed control

In this work, PC is designed to be in a separated shaft in order to help performing the start-up, shut down and part load of the cycle. Once the rotation speed of PC decreases, the mass flow rate and pressure ratio of the turbomachinery will decrease, which leads to the drop of load. However, the achievable load variation of this method is limited. For this method, there is no charge or discharge point in the cycle. Therefore, the total mass of CO₂ in the cycle will keep constant and the mass flow rate of CO₂ in the cycle will not have big variation. The distribution of pressure in the cycle will keep stable. As a result, the load will not much vary. On the other hand, this method could be combined with inventory control which has injection and releasing point in the cycle.

RESULTS AND DISCUSSION

1. Inventory control

In this work, scenario of discharge to 70% load with inventory control has been carried out for the system without and with elementary PID controllers so that the effect of elementary controllers (basic loop control) can be discussed.

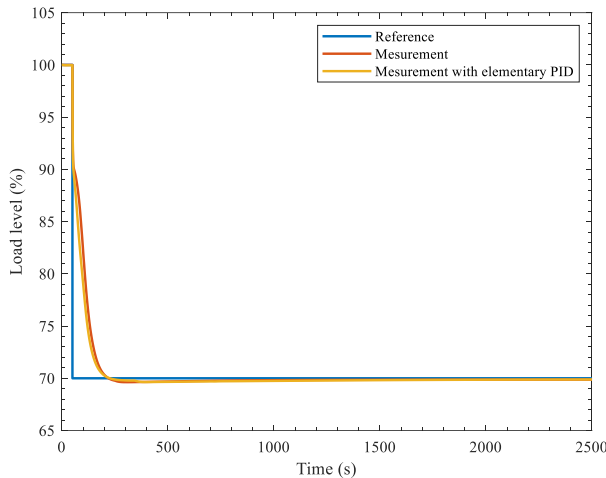


Figure 5 Load level during discharge

Without elementary controllers, the controller for inventory control reacts immediately when a step reference signal is sent as showed in Figure 5. The load of system decreases and reaches the reference value after an overshoot of 0.9%. Figure 6 represents the variation of cycle net efficiency during the discharge. It can be observed that the efficiency decreases from 35.67% to 31.74% and then rises to 33.39%: a drop of 2.3% for efficiency which is higher than the same case for an ultra-supercritical Rankine cycle. At the beginning, reduction of efficiency is mainly caused by the initial decrease of TIT and the turbine inlet pressure as showed in Figures 7 and 8. Moreover, it can be observed in Figure 9 that the LTR hot side pinch increases 5 °C, which is another cause for the decrease of efficiency. From figure 26 it can be observed that compared to 100% load, heat transfer efficiency decreased at 70% load so that LTR pinch increases. Then, TIT increases because the mass flow

rate of molten salt is kept constant but the mass flow rate of sCO₂ in cycle decreases, which yields a slow increase of efficiency.

It should be noted that the cycle minimum pressure decreased to 70.5 bar which is below the critical pressure. Action needs to be taken to avoid this situation. A constraint could be added in the controller: when the PC outlet pressure is lower than a predefined safe pressure (e.g. 74bar), no intervention is applied to inventory control.

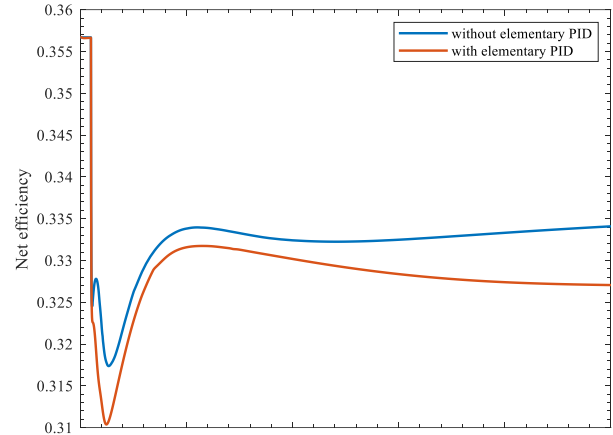


Figure 6 Cycle net efficiency during discharge

As for the cooling system, it can be observed in Figure 11 that without elementary PID controller, PCIT decreases from 35 °C to 29 °C because the mass flow rate of cooling water is kept constant. However, MCIT decreases at the beginning, rises then to 37 °C and finally decreases slowly to 36 °C as showed in Figure 12. The drop at the beginning should be caused by the decrease of PC inlet temperature and sCO₂ mass flow rate. However, when the mass flow rate of sCO₂ decreases, according to the performance map of the compressor, the efficiency of PC decreases so that PC outlet temperature increases which leads to the increase of MCIT. From the discussion above, it can be concluded that it is important to add elementary PID controllers for TIT, MSOT, PCIT and MCIT.

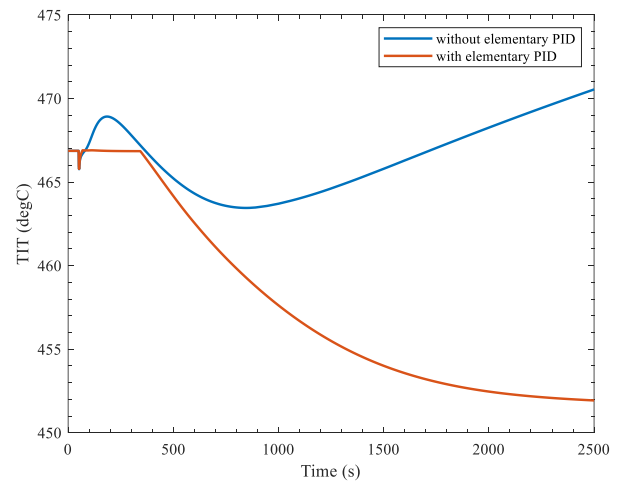


Figure 7 TIT during discharge

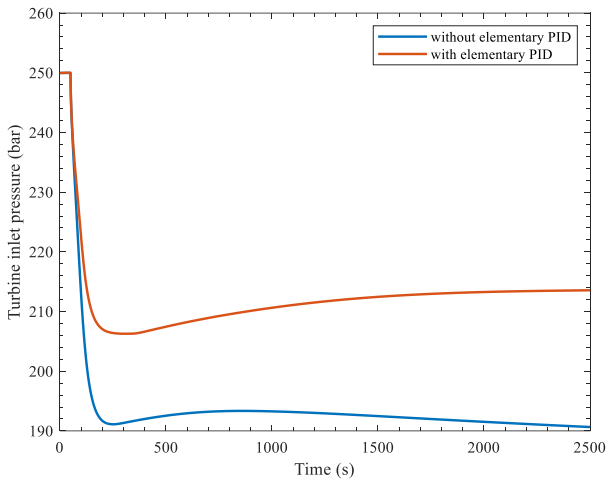


Figure 8 Turbine inlet pressure during discharge

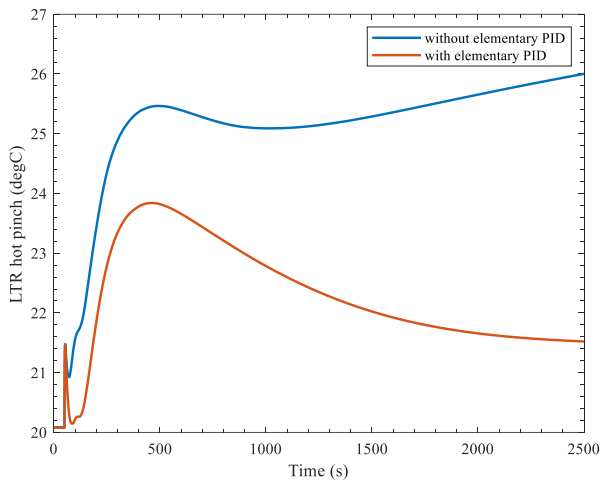


Figure 9 LTR hot side pinch during discharge

With elementary controllers, it can be observed in Figures 7, 10 and 11 that TIT, MSOT and PCIT are controlled in their reference region. However, MCIT increases to 38.5 °C, instead of 35 °C, as showed in Figure 12. As stated in the last section, MCIT is controlled by manipulating the mass flow rate of C2 cooling water. It should be noted that there is a limit for augmentation of mass flow rate of cooling water because when it becomes too big, the water pressure drop will increase. In this scenario, the pressure drop already reached its highest value and the maximum allowed mass flow rate cannot satisfy the cooling of MCIT. As a result, the control of MCIT could not be achieved only by manipulating the mass flow rate of cooling water. In reality, the water is cooled by an aircooler. It is possible to act on the velocity of air in aircooler to manipulate the temperature of cooling water. And it can be observed in Figures 7 and 10 that with current TIT and MSOT controllers, TIT decreases while MSOT is kept constant at 290 °C because MS mass flow rate is

reduced to help keep MSOT at 290 °C and there is no solution to increase TIT.

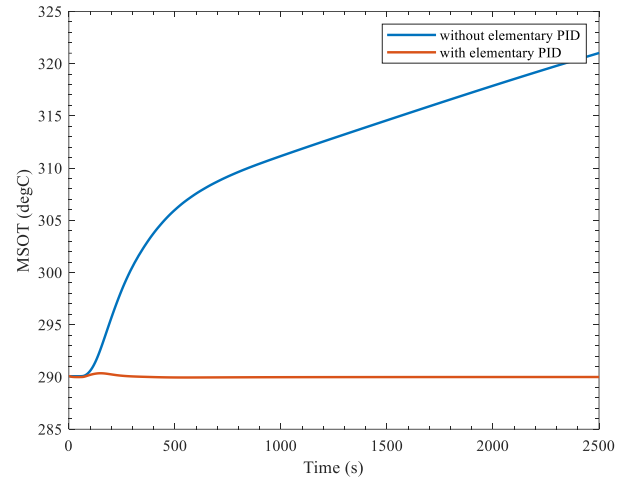


Figure 10 MSOT during discharge

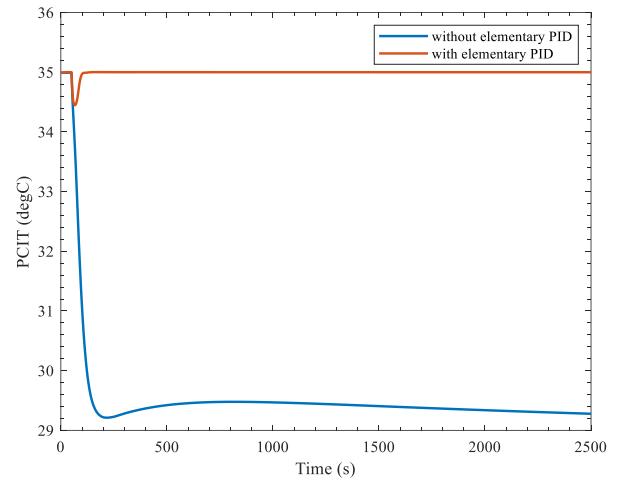


Figure 11 PCIT during discharge

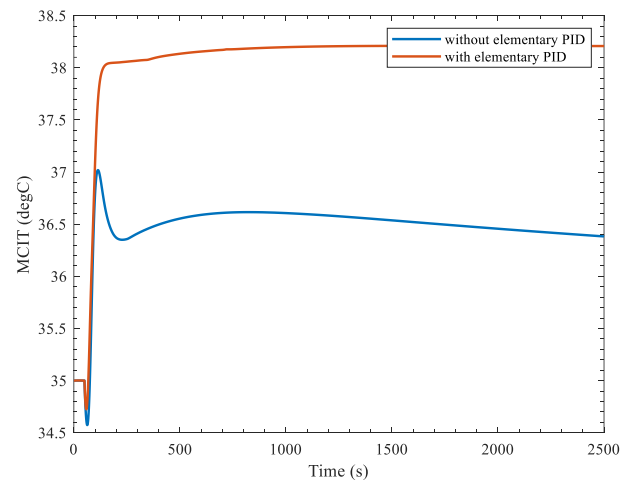


Figure 12 MCIT during discharge

As showed in Figure 6, the cycle net efficiency decreased to lower value with elementary PID controller. It is mainly caused by the decrease of TIT since the mass flow rate of MS decreased to keep MSOT at 290 °C. When the load decreased to 70%, the difference of cycle efficiency between scenario without and with elementary PID is 0.22%.

2. Bypass control

In this work, a scenario of discharge to 70% load with bypass control is carried out for the system and the effect of elementary controllers (basic loop control) is discussed.

Without elementary controllers, the bypass controller reacts extremely fast when a step signal of part load is sent as showed in Figure 13. However, it can be observed in Figure 14 that the cycle net efficiency drops from 35.66% to 26.34% because of the decrease in turbine inlet flow, which causes a decrease in output power. This leads to the continuous rise of TIT as showed in Figure 18. Bypass control has no significant influence on MCIT and PCIT which increases to 36 °C as showed in Figures 19 and 20.

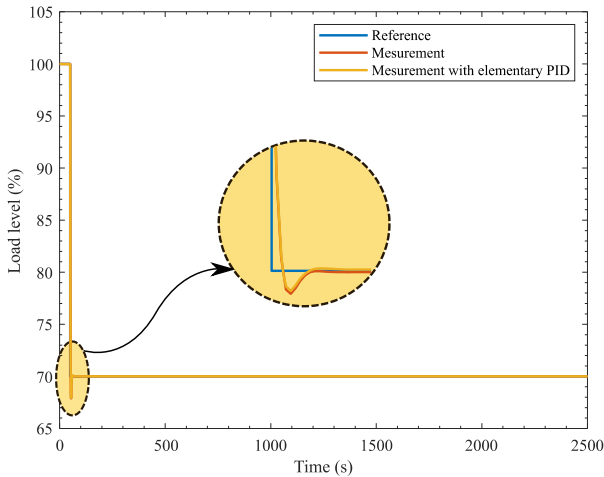


Figure 13 Load level during bypass control

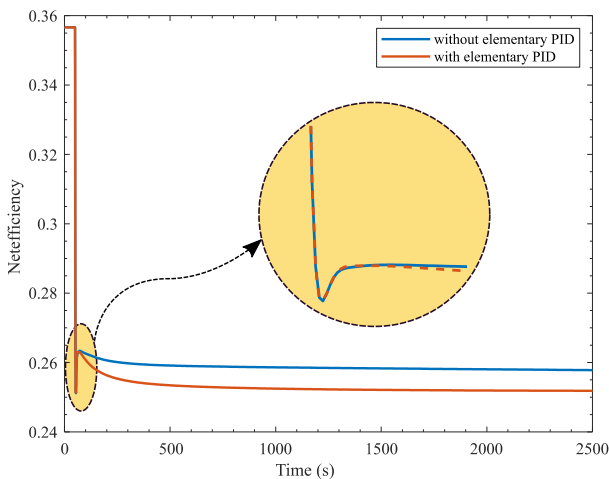


Figure 14 Efficiency during bypass control

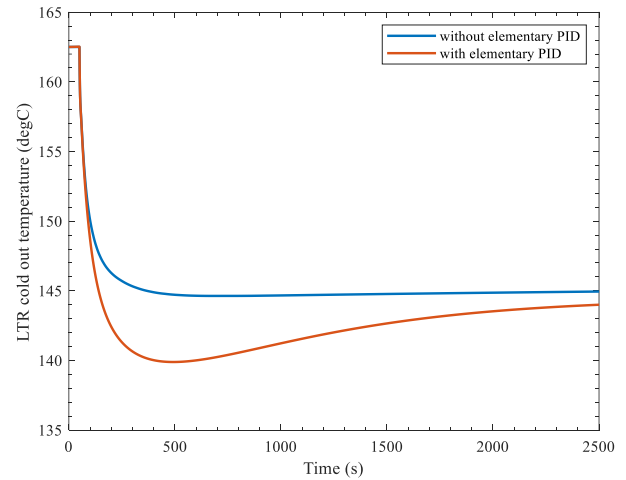


Figure 15 LTR cold outlet temperature during bypass control

After adding elementary controllers, TIT, MSOT PCIT and MCIT have been well controlled.

However, bypass control brings challenge to PCHE. As showed in Figure 15, for a step response of part load, LTR cold outlet temperature drops from 162 °C to 150 °C in 40s in the beginning, which produces a large thermal stress of PCHE. Constraint needs to be added to the by-pass controller to avoid large thermal stress of PCHE. Reasonable ramp signal of load could be taken to slow down the drop of PCHE temperatures.

3. Variable PC rotation speed

Same part load scenario as the control strategy before has been carried out for the variable PC rotation speed control. However, limit on the variation of PC rotation speed restricted the level of part load. In this study, the design rotation speed of PC is 9500 RPM. Besides, the dynamic model could achieve a step of PC rotation speed from 9500 to 5000 RPM. As a result, scenarios of load decreasing from 100% to 90% without elementary control have been carried out for variable PC rotation speed control.

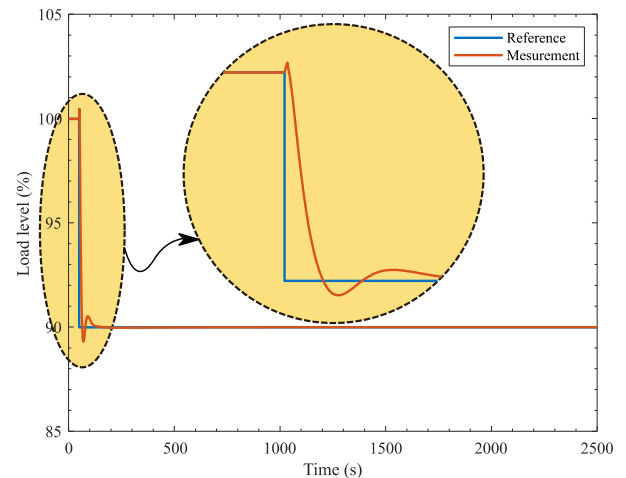


Figure 16 Load level during part load without elementary PID

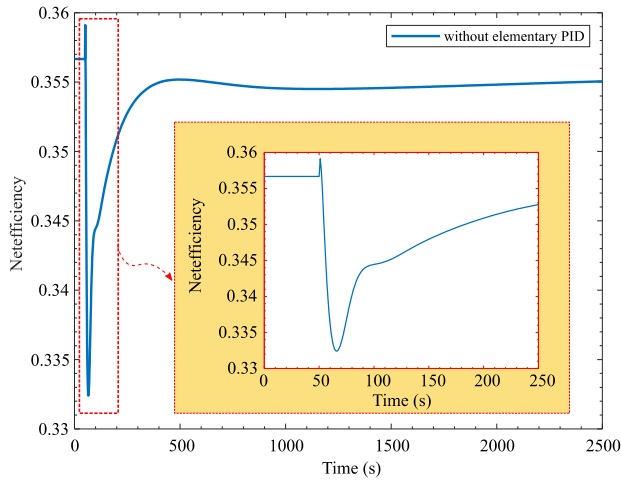


Figure 17 Cycle Efficiency during part load without elementary PID

As showed in Figure 16, the load level decreases with the step reference and reaches 90% in a short time after an overshoot caused by the PID controller. The cycle efficiency decreases of 0.004% for load from 100% to 90%, which is smaller than 0.8% for inventory control and 3.22% for bypass control at same load level decrease. As showed in Figures 21 and 22, TIT and MSOT had the same variations as during inventory control. For the cooling part, both MCIT and PCIT decrease, especially MCIT that reaches the CO₂ critical temperature as showed in Figures 23 and 24. Therefore, elementary controllers need to be integrated for this control strategy.

4. Discussion

Three control methods for part load have been tested in this work. Inventory control could maintain the cycle efficiency within a certain range during part load but it is risky to realize a huge discharge flow because the minimum pressure of the cycle could go below the critical pressure. Moreover, the controllers for MCIT and PCIT are important for the proper operation of the compressors. Bypass control has the advantage of fast load but the cycle efficiency would have a significant drop and the gradient of temperature of PCHE should be monitored in case of high thermal stress. Variable PC rotation speed control can better keep the cycle efficiency than inventory control but it has its limit on the achievable load level and elementary controllers need to be integrated. It should be noted that the variable PC rotation speed control could be replaced by an inlet guide valve (IGV) at industrial scale.

It is possible to combine these three control methods to find an appropriate control strategy according to part load demand. For example, for part load from 100% to 50%, inventory control and bypass control could be combined to find a trade-off between load decreasing speed and cycle net efficiency [14]. Besides, bypass control and variable PC rotation speed control could be combined to achieve small load decline range.

CONCLUSION

In this work, a dynamic model has been developed for a 10MWe sCO₂ Brayton cycle with detailed equipment pre-design and off-design. Fundamental physical laws and models found in open literature are utilized to develop main sub-models such as heat exchangers and turbomachinery. Although simplification has been done to reduce the complexity of the dynamic model, it remains a highly non-linear system of equations, with nearly 5000 equations. In particular, the sharp variations of sCO₂ properties near its critical point significantly slows down the resolution of this dynamic system.

Based on the dynamic model, three methods for achieving part load of system have been discussed, each with its own benefits and shortcomings. Inventory control could keep cycle efficiency but strict elementary controllers need to be integrated to guarantee the safe operation of turbomachinery and molten salt. Bypass control could achieve fast load, but will lose cycle efficiency. Variable PC rotation speed control could better maintain the cycle efficiency but is limited by its operation range. It can thus be concluded that elementary control of cooling and heating system is extremely important, as it impacts the actual performance of the cycle in operation. In this work, it is found that MCIT and PCIT could not be perfectly controlled by manipulating only the mass flow rate of cooling water because of huge water pressure drop engaged by the increasing mass flow rate. Additional measure should be taken to guarantee the safe operation of compressors. For example, the design of cooler could be modified for larger pressure drop. Moreover, the aircooler model could be integrated in the system so that besides water mass flow rate, the air velocity could be another manipulated variable. As for the heating system, a solution for increasing TIT should be found to avoid the possible reduction of TIT during inventory control. Although TIT and MSOT controllers are designed separately, they have influence on each other's behavior. As a result, it is necessary to design a better control strategy for these two parameters.

Finally, with these three part load methods, possible combination could be made for different part load scenarios according to their advantages. Normally, by-pass control could be selected for a fast and short-term part-load demand. However, if a long-term part-load is requested, by-pass control and inventory control could be combined: by-pass control is responsible for fast load regulation at the beginning and when the load reaches the desired value, the by-pass control could be replaced by inventory control to recover the cycle efficiency. In addition, variable PC rotation speed control and inventory control could be combined for faster and efficient part load control as discussed in previous paragraph. These possible combinations will be studied in the future work.

NOMENCLATURE

Symbols	
p	Pressure (MPa)
Q	Mass flow rate (kg/s)
T	Temperature (°C)
hc	Heat transfer coefficient (W/m ² /K)
S	Heat exchange Surface (m ²)

K	Global heat transfer coefficient ($W/m^2/K$)
f_D	Darcy factor
f	Fanning factor
e	Thickness of heat exchanger wall
Greek symbols	
η	Efficiency
ϕ	Flow coefficient
ψ	Head coefficient
λ	Conductivity
Abbreviations	
AC	Auxiliary compressor
C1	Cooler 1
C2	Cooler 2
CO ₂	Carbon dioxide
CSP	Concentrated solar power
HTR	High temperature recuperator
IC	Intercooling
LTR	Low-temperature recuperator
MC	Main compressor
MH	Main heater
MS	Molten salt
PC	Pre-compression / pre-compressor
PCHE	Printed circuit heat exchanger
PH	Preheating / preheater
RC	Recompression
SCO ₂	Supercritical CO ₂
STHX	Shell and tube heat exchanger
TIT	Turbine inlet temperature
Subscripts/superscripts	
cold	cold side flow of heat exchanger
hot	hot side flow of heat exchanger
in	inlet flow
out	outlet flow
*	modified

REFERENCES

- [1] Y. Ahn, S. Jun Bae, M. Kim, S. Kuk Cho, S. Baik, J. Ik Lee and J. Eun Cha, "Review of Supercritical CO₂ power cycle technology and current status of research and development," *Nuclear Engineering and Technology*, pp. 1-15, 2015.
- [2] M. Binotti, M. Astolfi, S. Campanari, G. Manzolini and S. Paolo, "Preliminary assessment of sCO₂ power cycles for application to CSP solar tower plants," *Energy Procedia*, vol. 105, pp. 1116-1122, 2017.
- [3] X. Yan, "Dynamic Analysis and Control System Design for an Advanced Nuclear Gas Turbine Power Plant," Massachusetts Institute of Technology, 1990.
- [4] A. Moiseyev, K. Kulesza and J. Sienicki, "Control System Options and Strategies for Supercritical CO₂ cycles," Argonne National Laboratory, 2006.
- [5] N. A. Carstens, "Control Strategies for Supercritical Carbon Dioxide Power Conversion Systems," Massachusetts Institute of Technology, 2007.
- [6] M. Carlson, A. Kruijenga, C. Schalansky and D. Fleming, "Sandia Progress On Advanced Heat Exchangers For sCO₂ Brayton Cycles," in *The 4th International Symposium - Supercritical CO₂ Power Cycles*, Pittsburgh, 2014.
- [7] J. Hesselgreaves, *Compact Heat Exchangers*, Pergamon, 2001.
- [8] H. L. I. John and H. L. V. John, *A Heat Transfer Textbook*, Phlogiston Press., 2018.
- [9] S. Kakaç, H. Liu and A. Pramuanjaroenkij, *HEAT EXCHANGERS*, CRC Press, 2012.
- [10] A. V. Carlos, A. J. Peter, S. R. Andrew, P.-R. Paul and S. Emilie, "Preliminary design and performance estimation of radial inflow turbines: an automated approach," *Journal of Fluids Engineering*, vol. 134, pp. 031102 1-13, 2012.
- [11] H. Oh, E. Yoon and M. Chung, "An optimum set of loss models for performance prediction of centrifugal compressors," *Proceeding of the Institution of Mechanical and Engineer*, vol. 211, 1997.
- [12] J. D. John, "Modeling the Supercritical Carbon Dioxide Brayton Cycle with Recompression," 2014.
- [13] E. H. Baligh and B. Daniel, *Modeling and Simulation of Thermal Power Plants with ThermoSysPro*, Springer, 2018.
- [14] J. Zhang, Z. Yang and Y. Le Moullec, "Dynamic modelling and transient analysis of a molten salt heated recompression supercritical CO₂ Brayton cycle," in *The 6th International Supercritical CO₂ Power Cycles Symposium*, Pittsburgh, 2018.

ANNEX A: FIGURES FOR DIFFERENT CONTROL STRATEGY

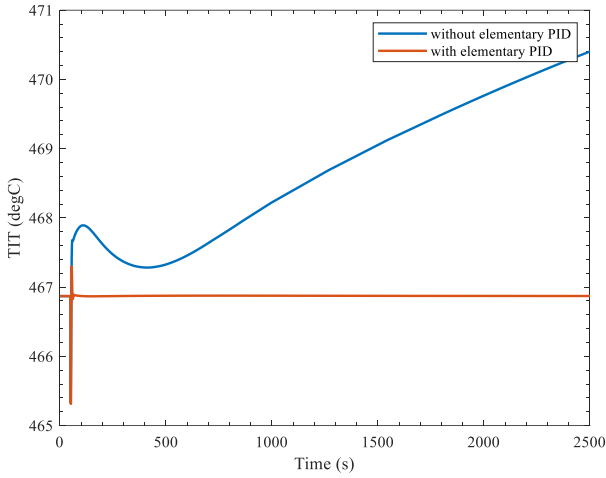


Figure 18 TIT during bypass control

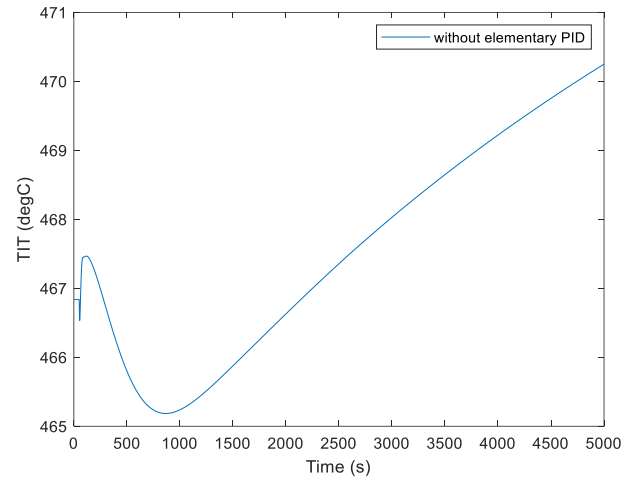


Figure 21 TIT during part load by variable PC rotation speed

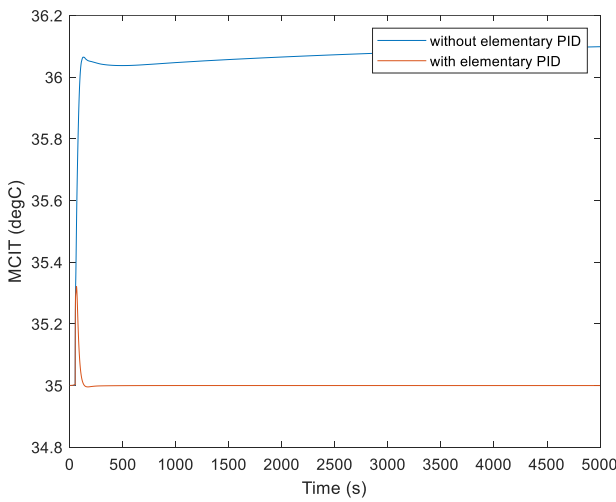


Figure 19 MCIT during bypass control

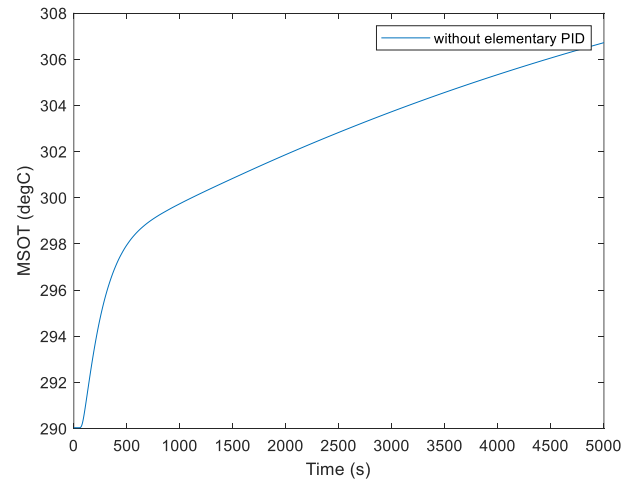


Figure 22 MSOT during part load by variable PC rotation speed

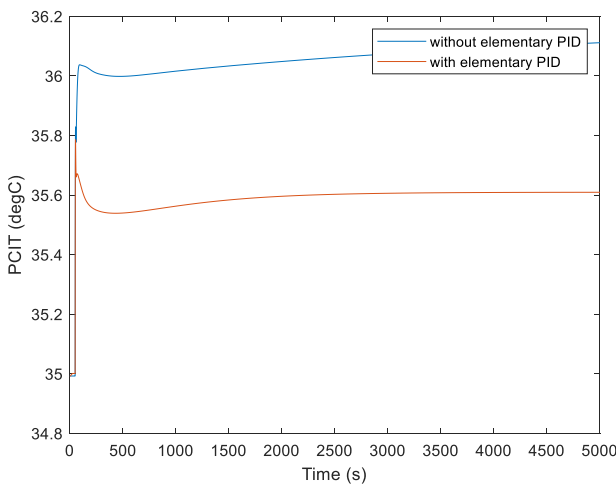


Figure 20 PCIT during bypass control

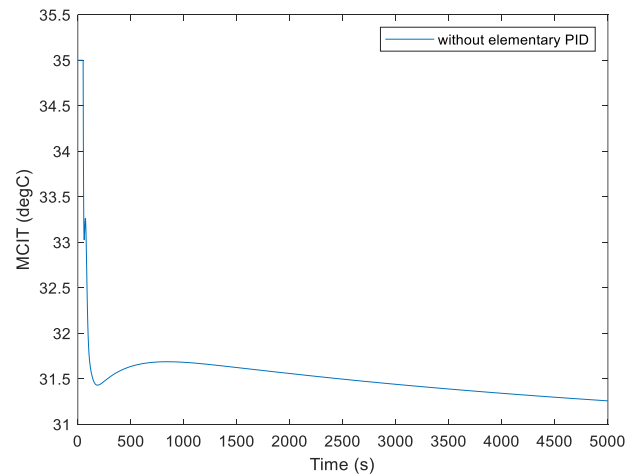


Figure 23 MCIT during part load by variable PC rotation speed

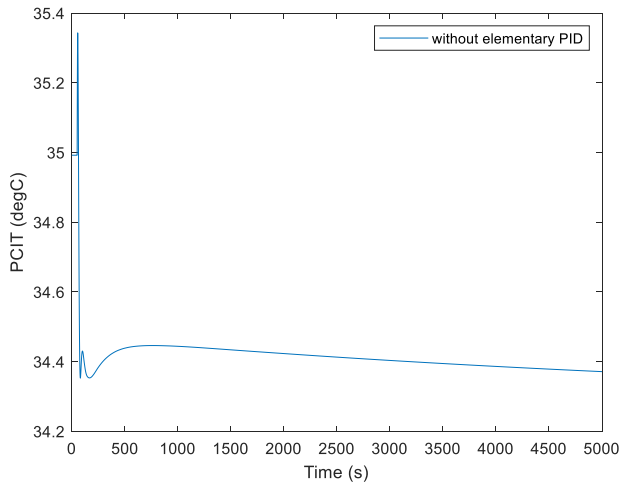


Figure 24 PCIT during part load by variable PC rotation speed

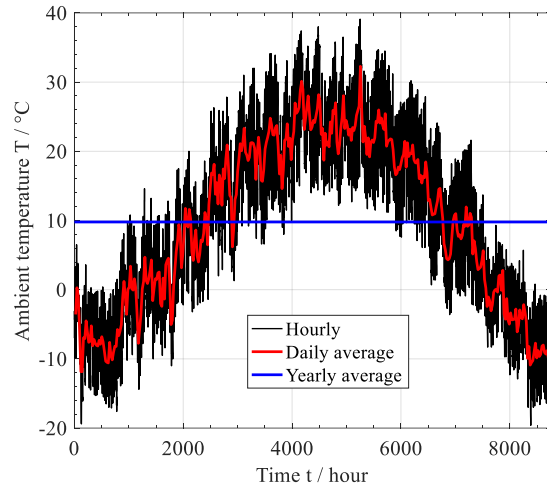


Figure 25 Yearly temperature distribution in Dunhuang

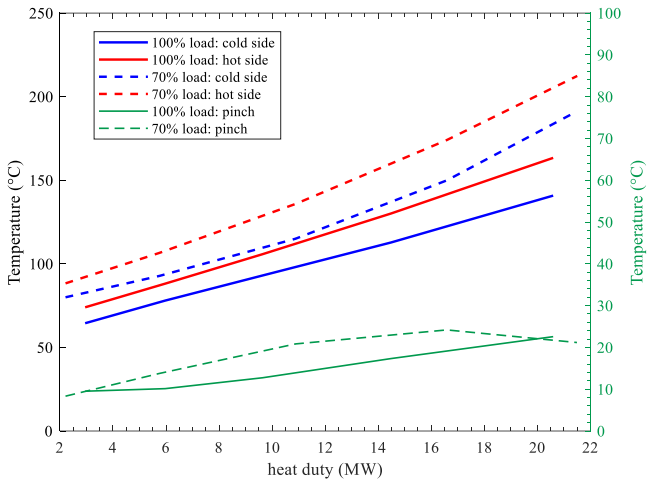


Figure 26 Temperature - Heat duty diagram (left axes) and LTR pinch (right axes)

EXPERIMENTAL INVESTIGATIONS AND SIMULATIONS OF THE CONTROL SYSTEM IN SUPERCRITICAL CO₂ LOOP

Ales Vojacek*
Research Centre Řež
Řež, Czech Republic
ales.vojacek@cvrez.cz

Tomas Melichar
Research Centre Řež
Řež, Czech Republic

Petr Hajek
Research Centre Řež
Řež, Czech Republic

Frantisek Doubek
Research Centre Řež
Řež, Czech Republic

Timm Hoppe
XRG Simulation GmbH
Hamburg, Germany

ABSTRACT

An efficient instrumentation and control system (I&C), which is adaptable to loads variations (temperature, pressure, mass flow), is essential for design of power units working with supercritical CO₂ (sCO₂) to ensure high sCO₂ cycle performance with quick response. Hence, sophisticated model-based control system design, supported by dynamic system-level modelling, simulations, and experimental verification is needed. This technical paper presents experimental tests and numerical simulations of the control system of the experimental supercritical CO₂ loop at Research Centre Rez (CVR), Czech Republic. The measurements covered testing of temperature, pressure and mass flow controllers. Set-up of the controllers and dynamic response of the system are investigated for several transient scenarios in supercritical and subcritical pressures including transition of the pseudocritical region. The experimental set-up along with the boundary conditions are described in detail, hence the gained data set can be used for benchmarking of system thermal hydraulic codes. Such a benchmarking was performed with the open source Modelica-based code ClaRa using the simulation environment DYMOLA 2019.

INTRODUCTION

The power cycle using sCO₂ is an innovative concept which is a competitive alternative to the dominated steam Rankine cycle, gas Brayton cycle or their combination. The sCO₂ cycles have a clear potential to attain comparable or even higher cycle efficiencies than conventional steam Rankine/ or Brayton gas cycles [1], [2]. The sCO₂ combine many advantages of both the steam Rankine cycle (minimizing the power requirement for compressing the working fluid + heat rejection at low temperatures) and Brayton gas cycle (small

size, modular design, fast built units). It also achieves a high degree of thermal recuperation as both Brayton and Rankine cycles. The research activities on sCO₂ power plants are progressively increasing during the last decades and there is a growing interest in the worldwide sCO₂ events as well. It certainly shows a significant market potential. A report by Sandia Nat. Lab. [3] claims the prospective is to bring the sCO₂ cycle to technical readiness level 6 (till 2020) paving the way to demonstration projects (from 2020) and to commercialization (from 2025). The outlook is in line with the testimony of currently running sCO₂ projects in Europe, e.g. sCO₂-Flex [4].

A number of investigators have carried out extensive experimental tests and analyses of sCO₂. However, their work is rather limited to the component behavior studies, i.e. heat transfer and pressure drop models in heaters/coolers/heat exchangers [5], [6], [7]. An exhaustive literature survey on research in supercritical heat transfer is reported in [8]. Very few data can be found on operation and analysis of compressors and turbines [1], [9]-[13]. This is due to the fact that first prototypes of turbomachines are being just built. What is missing is simulation tool which is validated on models of the system level (component interaction) on both steady states and dynamic transients including control system interactions.

The main objective of this work is to provide evidence that the open source Modelica-based code ClaRa [14] is suitable for modeling steady states and transient scenarios along with Proportional Integral Derivative (PID) controllers' actions and their tuning in sCO₂ environment. For this purpose, CVR has performed number of experimental tests in the sCO₂ facility, located in CVR in the Czech Republic. As a part of experimental campaign, three steady states were selected (covering different temperature levels and pressures) in order to benchmark the numerical model at first place. A set of relevant parameters are given later in the text along with a detailed description of the experimental facility (loop geometry, nominal

pressures, temperatures, heating power and mass flow rate, etc.) to allow preparation of the computational models.

Once the numerical model was cross-checked, the tuning procedure of the PID controllers was performed. There are number of different control loops in the sCO₂ loop at CVR. However, as the control mode is most often associated with temperature, hence the temperature controller at the outlet of the heater 2 (H2) was selected to be subject of this work. Many various tuning methods have been proposed from 1942 up to now for gaining better and more acceptable control system response based on our desirable control objectives such as percent of overshoot, integral of absolute value of the error, settling time, manipulated variable behavior and etc. One of the most common PID controller tuning technique used in industry was consolidated and evaluated both from experimental data as well as from the numerical model. The tuning method chosen was the Cohen-Coon method [15] where process dynamics is based on a first order plus deadtime model. The tuning settings was calculated using the Cohen-Coon rules [16] and implemented in both real and Modelica controller. Afterwards, several tests were carried out in order to ensure the response is in line with the overall control objective of the loop.

Above mentioned procedure was conducted for a specific thermal hydraulic condition (pressure, temperature) in the sCO₂ experimental loop. For linear processes, where the process characteristics do not change significantly with time or load conditions, then using the set fixed PID parameters will probably be sufficient to ensure effective control. In the case of non-linear processes, however, being limited to a single set of fixed parameters can become problematic. One would need to set the parameters for the worst case, i.e. giving a very low gain, not to cause instabilities in higher gain conditions. In order to find the best overall response, independent sets of PID parameters are needed. Hence, numbers of tests with different conditions were executed with numerical models and different PID sets were derived. Finally, the new sets were implemented in the numerical model and checked for improvements in the control of a process.

The presented results in this paper will benefit to researchers, designers, software engineers, thermal hydraulic specialists, and operators of sCO₂ energy systems through the shared measured data in a unique sCO₂ facility.

DESCRIPTION OF THE LOOP AND GEOMETRY SPECIFICATIONS

The sCO₂ experimental loop at CVR was constructed within SUSEN (Sustainable Energy) project in 2017. This unique facility enables component testing of sCO₂ Brayton cycle such as compressor, turbine, HX, valves and to study key aspects of the cycle (heat transfer, erosion, corrosion etc.) with wide range of parameters: temperature up to 550°C, pressure up to 30 MPa and mass flow rate up to 0.35 kg/s. The loop is designed to represent sCO₂ Brayton cycle behavior.

Although the sCO₂ loop characteristics are not prototypical of the foreseen sCO₂ power plant, the experiments

on this simplified facility is sufficient to assess the capability of the numerical codes to deal with the thermal-hydraulic behavior of the sCO₂ loop. One of the adaptation of the loop is that a radial compressor expected on the prospective sCO₂ power plant is substituted by a piston type pump. In addition, a turbine is replaced by a reduction valve.

Annex A shows the piping and instrumentation diagram (PID) of the loop. The primary circuit is marked in thick red and it consists of following main components:

- The piston-type main pump (MP), which circulates sCO₂ through the circuit with the variable speed drive for the flow rate control.
- The high and low temperature regenerative heat exchangers (HTR HX/LTR HX), which recuperate the heat, hence reduce the heating and cooling power.
- The 4 electric heaters (H1/1, H1/2, H2, H3), which have in total a maximum power of 110 kW and raise the temperature of sCO₂ to the desired test section (TS) inlet temperature up to 550°C.
- The reduction valve which consists of series of orifices to reduce the pressure and together with oil (Marlotherm SH) cooler (CH2) represent a turbine.
- The water cooler (CH1) cools down the sCO₂ at the inlet of the MP by water cooling circuit. The secondary water cooling circuit is cooled by tertiary water cooling circuit. PI&D of the sCO₂ loop does not depict tertiary water cooling circuit for simplification matter of the benchmark exercise. The complete sets of boundary conditions are defined for the secondary water cooling circuit allowing this reduced approach.
- Air driven filling (reciprocating) compressor (gas booster station) which pumps the sCO₂ from the CO₂ bottles and also controls the operating pressure.
- Exhaust system for the excess amount of sCO₂

The P&ID of the sCO₂ loop contains all installed key measurement devices, such as a mass flow meter, Pt-100 sensors, thermocouples, pressure sensors and wattmeters. The nomenclature of the measurement devices respects the KKS identification system for power plants.

The uncertainties provided by the measurement devices, transducer, input card, and control system are summarized in Annex B. The errors correspond to calibration certificates and manufacturer's instructions.

Just for a matter of clarity, the zig-zag line at the P&ID stands for the oil cooler CH2 and connected pipeline. This line was closed during testing campaign since it was not needed to have extra cooling power in oil cooling circuit.

The main operating parameters of the primary circuit are shown in Table 1.

Table 1: The main operating parameters of the sCO₂ primary loop.

Maximum operation pressure	25 MPa
Maximum pressure	30 MPa
Maximum operation	550°C

temperature	
Maximum temperature in HTR	450°C
Maximum temperature in LTR	300°C
Nominal mass flow	0.35 kg/s

The sCO₂ loop layout is depicted in Figure 1 and the top view of the built facility is shown in Figure 2.

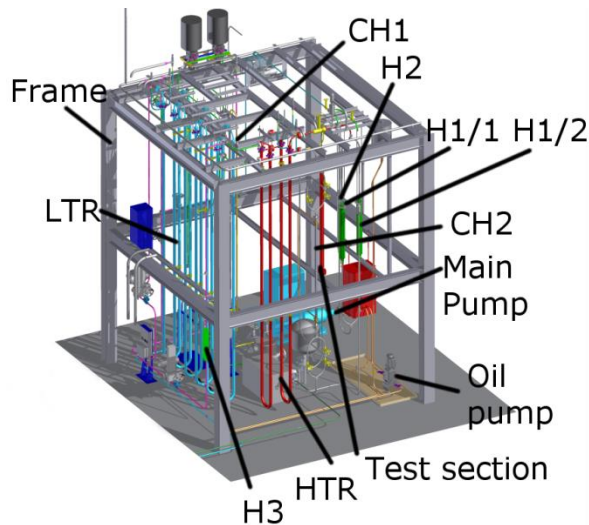


Figure 1: 3D CAD model of the sCO₂ loop.

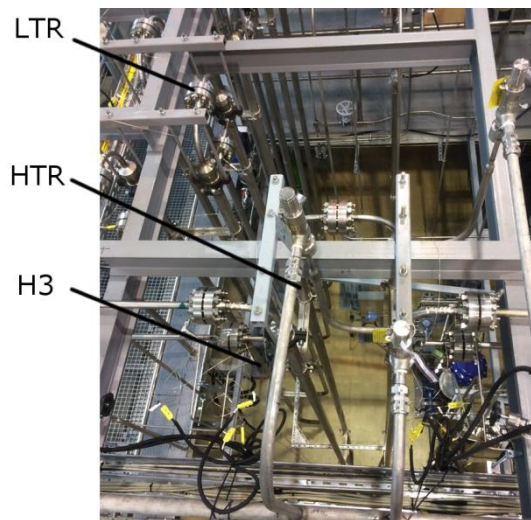


Figure 2: A view from the top on the built sCO₂ loop.

Table 2 summarizes parameters of the MP and the schematic cross-section of the MP is shown in Figure 3.

Table 2: Parameters of the main pump.

Device	Main Pump - PAX-3-30-18-250-YC-CRYO-drive 9/FM
Nominal inlet pressure	12.5 MPa
Nominal outlet pressure	25 MPa

Maximal outlet pressure	30 MPa
Nominal inlet temperature	25°C
Maximum inlet temperature	50°C
Nominal isentropic efficiency	0.7
Rotational speed (manufacturer data)	250÷1460 rpm
Volumetric flowrate (manufacturer data)	5÷30 l/min.
Rotational speed -> Volumetric flowrate (measurement data)	555 rpm -> 9.8 l/min 935 rpm -> 16.7 l/min

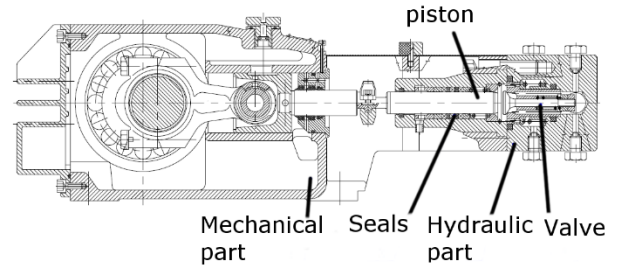


Figure 3: Cross-section of main pump.

In Table 3, the main parameters of the filling compressor are listed.

Table 3: Parameters of the filling compressor.

Device	Filling compressor - DLE5-15-GG-C
Nominal inlet pressure of CO ₂	0.5 MPa
Nominal outlet pressure	6.5 MPa
Maximum outlet pressure	30 MPa
Nominal flowrate	15 standard litre per minute
Nominal air pressure	0.6 MPa

Geometric parameters of the heat exchanging components of the sCO₂ loop needed for preparation of the model are described in

Annex C. The parameters needed for the model settings such as pipe diameters and lengths, layouts of heat exchangers and heaters and materials are listed for each component according to PI&D scheme in the Annex A.

The geometry of HTR heat exchangers is demonstrated in Figure 4. It is a counter-current shell and tube heat exchanger and it concludes of 2 U-tube modules. The LTR heat exchanger is of a same type and it includes 6 U-tube modules.

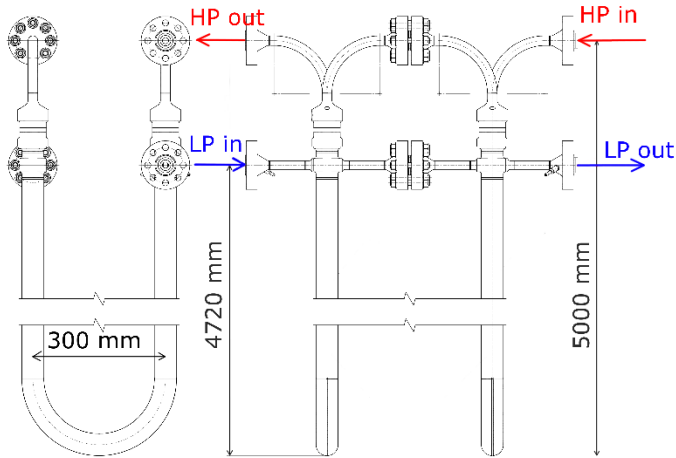


Figure 4: HTR heat exchanger.

The geometry of the tube plate LTR/HTR heat exchanger of inserted in a shell is displayed in Figure 5.

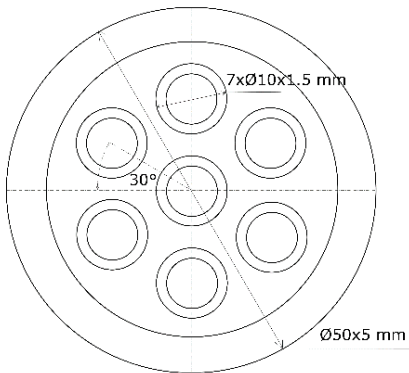


Figure 5: LTR/HTR heat exchanger tube plate in a shell.

The cross cut of electrical heater rod of H1/1, H1/2, H2 and H3 is shown in Figure 6.

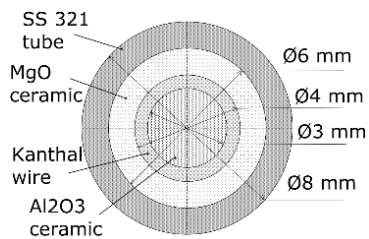


Figure 6: Electrical heater rod cross cut.

The cross cut of electrical heaters of H1/1, H1/2 H3 are shown in Figure 7 and H2 in Figure 8. All heaters are equipped with guiding tube $\text{Ø} 36 \times 2 \text{ mm}$ which directs the flow around the electrical heater rods. This tube is plugged on both ends.

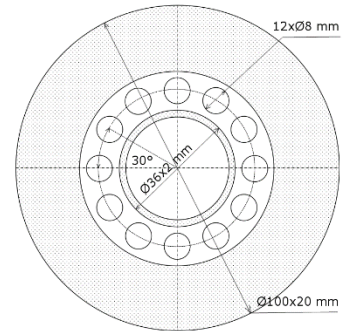


Figure 7: Electrical heater H1/1, H1/2 and H3 cross cut.

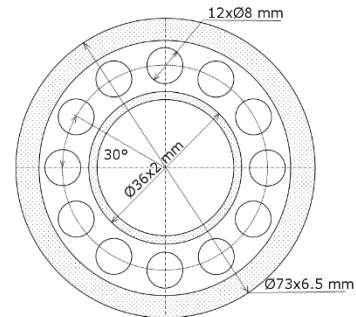


Figure 8: Electrical heater H2 cross cut.

The electrical heater H3 with nominal power 20 kW is positioned at the bypass of the LTR in order to simulate the behavior of a recompression cycle.

The pressure loss coefficients of the valves related to cross-section areas of corresponding pipelines (inner diameter 14 mm) are listed in Table 4.

Table 4: Pressure loss coefficient of the fully-open valves

Valve type	Pressure loss coefficient [-]
Reduction valve (characteristic in Table 5)	827
Control valves (linear characteristic)	14
Closing valves ("hot" part of the loop)	12
Closing valves ("cold" part of the loop)	4

The reduction valve characteristic Opening versus K_v/K_{vs} of the reduction valve is displayed in Table 5. Averaged values of K_v/K_{vs} from all measured data covering temperature range $50^\circ\text{C} \div 450^\circ\text{C}$ are given (no data from manufacturer are available).

Table 5: Characteristic of the of the reduction valve.

Opening [%]	K_v/K_{vs} [-]
0	0.09
40.5	0.45
45	0.52
50	0.59
55	0.65
60	0.70
65	0.74

70	0.79
75	0.85
80	0.90
85	0.92
90	0.95
95	0.97
100	1.00

The geometric parameters of pipelines according to the PI&D scheme are summarized in Annex D including the pipe diameters and lengths. Parameters of bends are also mentioned to allow modelling of local pressure losses.

The “hot” parts (from inlet to heater H3 and inlet of high pressure LTR to outlet of low pressure LTR) of the loop are insulated with rock wool Orstech DP 100. Thermal conductivity of the insulation material depending on temperature can be found here [17]. The test section and heaters are insulated with 0.14 m thickness and the rest with 0.1 m. is shown in Table 8. The insulation on the RV (of length of approximately 0.5 m) is not installed.

In Annex E, locations of measurement sensors corresponding to the loop layout are listed. The positions of the sensors have to be taken into account in the computational models as well. The table includes all needed sensors of temperature, pressure, mass-flow rate, heating powers and pump speed. Apart from this, positions of valves are also mentioned. Layout of the sensors can be also seen in the PID diagram.

STEADY-STATES BENCHMARK

As a part of the CVR sCO₂ loop experimental program for benchmark on thermal hydraulic code, several steady states were achieved. In order to tune the numerical models, 3 selected steady states (covering different temperature levels and pressures) with set of relevant parameters are shown in Annex F along with the results from calculation performed Modelica-based code ClaRa. The simulated results show fair agreement, demonstrating reasonable accuracy of the simulation tool. There are maximum 2.5 K/0.2 MPa/0.6 kW temperature/pressure/heating power errors respectively.

DESIGN OF A NUMERICAL MODEL IN THE CLARA LIBRARY

The performance of the sCO₂ loop CVR is simulated with a numerical model, developed in the Modelica language within Dymola environment, using the free ClaRa library.

Modelica

Modelica is a specialized object-oriented equation-based language for physical modelling. Nowadays it is widely used in industry and research for object oriented modelling and transient simulation of cyber physical systems. It is designed for simulation of complex multi-domain systems, e.g., systems containing mechanical, electrical, electronic, hydraulic,

thermal, control, electric power or process-oriented subcomponents [18]. The Modelica language is based on equations and thus, on the contrary to the block-oriented languages (e.g. Simulink), the exact computational strategy is left to the tool itself in the compilation phase. This approach allows us to combine components (predefined or custom-built) using connectors and leave the derivation of computation causality to the machines [19]. From the authors’ experience, this not only significantly saves time, but helps to avoid a number of mistakes and enables component reuse. For these features, Modelica is widely used in industry and research for modelling and simulation of cyber physical systems.

Dymola Environment

Several environments for the Modelica language exist. For current analysis, the Dymola (version 2019, Dassault Systemes, Paris, France) has been chosen for its compatibility with the ClaRa library.

ClaRa library

To simplify the modelling process and to avoid development of components from scratch, a number of free as well as commercial Modelica libraries are available. For this study the ClaRa library was used [14] (Clasius-Rankine cycles), designed for modelling transient thermal behaviour of power plants and power systems. The ClaRa was primarily developed for the water-steam cycle and the gas path of coal dust fired boilers and heat recovery steam generators. However, with the implemented physical property models of nearly each substances used in industry today derived from the NIST database, the utilization is large. ClaRa features many benefits for the user. One of them is that it is easy enhance the code, hence creating your own models according to your requirement which perfectly meets your needs.

Several modifications had to be made to enable to model sCO₂ loop CVR with ClaRa. Hence, the original source code has been extended, particularly for the shell part of the model of shell and tube heat exchanger (STHX), a model of heating rod elements and PID controllers. The extension of the model of shell part was based on the existing tube pipe model. Geometry as well as corresponding replaceable models of heat transfer and pressure drops were created to allow compatibility with the new shell model. As for the model of heating rod elements, it was based on existing wall structure and a heating source term was incorporated into the heating equation. The models of PID controllers were enhanced to enable changes of PID settings during calculations.

TUNING OF PID CONTROLLERS INTRODUCTION

For purpose of control and monitoring the sCO₂ loop CVR, there is applied I&C with two independent operation workstations. The I&C manage measurements, signalization, control and adjusting of parameters and protect the technology through implemented series of safe functions in case of abnormal conditions. Further, it keeps all data archived. The I&C is built on integrated control system environment ABB

FREELANCE with ABB – AC900F control units and S800 I/O [21] modules directly attached on terminal units (for binary signals) and Siemens ET200M (for analog signals) [22].

Accurate control is critical to every process. As a means of ensuring that tasks such as production, distribution and treatment processes are carried out under the right conditions for the right amount of time and in the right quantities, control devices form a crucial part of virtually every industrial process. Currently the PID algorithm is the most popular feedback controller used in industry. Having a three term functionality that deals with transient and steady-state responses, the PID controller offers a simple, inexpensive, yet robust algorithm that can provide excellent performance, despite the varied dynamic characteristics of the process or plant being controlled [23]. To get the best out of the PID controllers, many tuning techniques have been developed over the past several decades. The very first techniques are dated to 1942 when Ziegler and Nichols published their paper. They have come with a closed-loop and open-loop method. The principles of these methods still provide the foundation of many of the auto tune algorithms used in many modern industrial applications. Despite its simplicity, the Ziegler Nichols closed loop method can take a long time to perform and also has the potential to create uncontrolled oscillations, which affects control stability. Eleven years after Ziegler and Nichols published their findings, in 1953, Cohen and Coon published a new tuning method. Like the Ziegler-Nichols open loop rules, the Cohen-Coon rules aim for a quarter-amplitude damping response. The Cohen-Coon tuning rules are suited to a wider variety of processes than the Ziegler-Nichols tuning rules. The Ziegler-Nichols rules work well only on processes where the dead time is less than half the length of the time constant. The Cohen-Coon tuning rules work well on processes where the dead time is less than two times the length of the time constant (and it can be stretched even further if required) [16]. Hence, the Cohen-Coon method has been used in this paper.

It is often forgotten or simply not known that different tuning rules were developed for different versions of the PID controller algorithm. The engineer responsible for tuning a control loop must be aware of the form of the algorithm used for the PID controller. The main PID structures (Interactive, Non-interactive and parallel) are very well described in [16]. The Cohen-Coon rule, used in this paper, utilizes the Non-interactive algorithm. The algorithm is described in equation (1).

$$CO = K_c \cdot \left(e(t) + \frac{1}{T_i} \int e(t) dt + T_d \frac{de(t)}{dt} \right) \quad (1)$$

The Cohen-Coon tuning rule uses three process characteristics: process gain (GP), dead time (td), and time constant (Tau). These are determined by doing a step test and analyzing the results. In order to derive these characteristics, the PID controller which is subject of the tuning needs to be in manual and the system has to be stabilized. A step change in the controller output (CO) is introduced and after the process variable (PV) stabilizes at a new value, the characteristics can be determined according to Figure 9. The size of this step

should be large enough that the process variable moves well clear of the process noise/disturbance level.

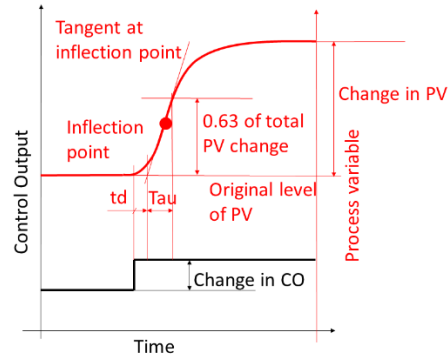


Figure 9: Schematic figure of Cohen-Coon characteristics. Calculation of new tuning settings using the Cohen-Coon tuning rule is described in Table 6.

Table 6: Cohen-Coon rule [16].

	K_c	T_i	T_d
P controller	$\frac{1.03}{GP} \left(\frac{Tau}{td} + 0.34 \right)$		
PI controller	$\frac{0.9}{GP} \left(\frac{Tau}{td} + 0.092 \right)$	$3.33td \left(\frac{Tau + 0.092td}{Tau + 2.22td} \right)$	
PD controller	$\frac{1.24}{GP} \left(\frac{Tau}{td} + 0.129 \right)$		$0.27td \left(\frac{Tau - 0.324td}{Tau + 0.129td} \right)$
PID controller	$\frac{1.35}{GP} \left(\frac{Tau}{td} + 0.185 \right)$	$2.5td \left(\frac{Tau + 0.185td}{Tau + 0.611td} \right)$	$0.37td \left(\frac{Tau}{Tau + 0.185td} \right)$

One has to be careful when calculating the process gain GP according to equation (2), since normalized values needs to be implemented, i.e. the total change obtained in PV has to be converted to a percentage of the span of the measuring device. Similarly to the change of CO in percentage.

$$GP = \frac{\text{change in PV} [\%]}{\text{change in CO} [\%]} \quad (2)$$

TUNING OF PID CONTROLLERS AND COMPARISON WITH MEASURED DATA

There are number of different control loops in the sCO₂ loop at CVR. However, as the control mode is most often associated with temperature, hence the temperature controller at the outlet of the heater 2 (H2) was selected to be subject of this work.

As described in previous chapter, the Cohen-Coon method is used in this paper to determined PID controller constant. Two step changes in the heater 2 (H2) during a stabilized system were introduced and process variable (T_CO₂H₂out - 1LKD40CT004) curves have been generated.

Step-up

Firstly, a sudden step-up increase in H2 power output (from initial 6.2 kW to final 10.9 kW) was initiated at stable system. The response curve of the process variable (temperature outlet from H2) is shown in Figure 10.

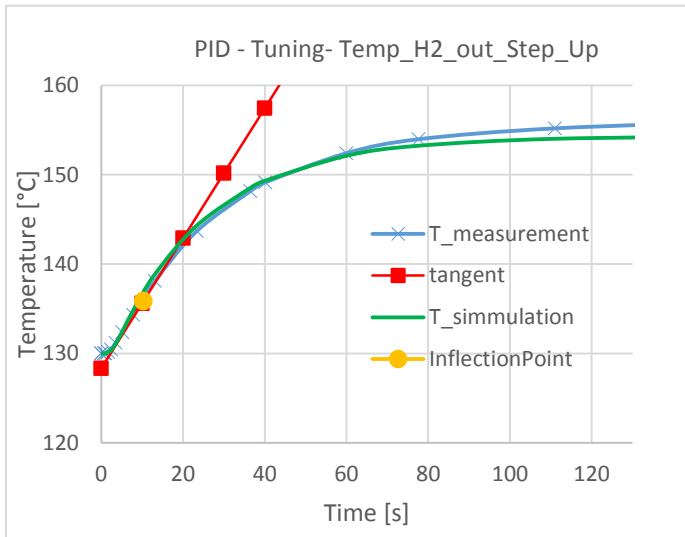


Figure 10: Response curve of temperature outlet from H2 during step-up test.

Step-down

In order to verify the first test, second step test was conducted after the stabilization of parameters in the system. A sudden step-down decrease in H2 power output (from initial 10.9 kW to final 6.6 kW) was initiated at stable system. The response curve of the process variable (temperature outlet from H2) is shown in Figure 11.

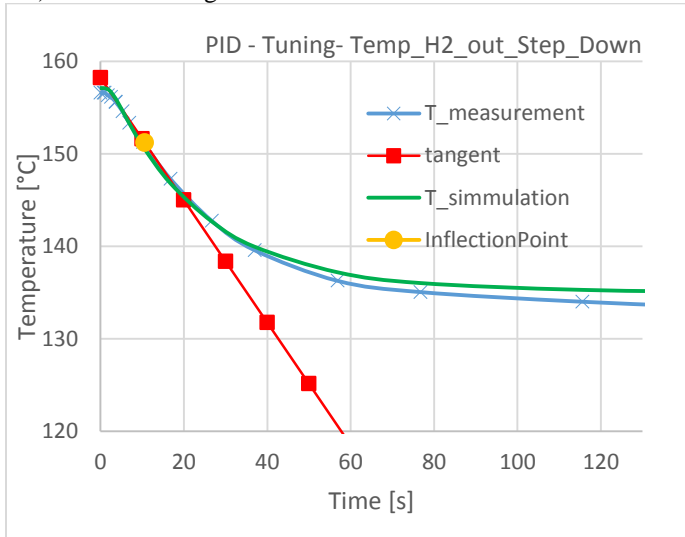


Figure 11: Response curve of temperature outlet from H2 during step-down.

In both cases, the simulated results from the ClaRa model follows the measured values of the process variable very well. The total maximum error calculated from absolute temperatures in Kelvins, does not exceeds 0.5 %.

Table 7 summarizes the PID tuning settings from both tests including the settings derived from simulations. Note that calculated controller gain (Kc) is according to recommendation [16] divided the by two to reduce overshoot and improve

stability. For clarity, the process gain (GP) was calculated as follows (the step-up experimental values are shown):

$$GP = \frac{\frac{\text{change in PV [K]}}{\text{range of PV [K]}}}{\frac{\text{change in CO [kW]}}{\text{range of CO [kW]}}} = \frac{\frac{155.3 - 130}{600 - 0}}{\frac{10.9 - 6.2}{30 - 0}} = 0.27 \quad (3)$$

Table 7: PID tuning settings for measured and simulated data

	Kc	Ti	Td
Step-up test – measured	29.14	5.60	0.85
Step-down test - measured	26.79	5.97	0.90
Average - measured	27.96	5.79	0.88
Step-up test – simulated	26.79	5.35	0.81
Step-down test - simulated	26.33	5.24	0.79
Average - simulated	26.56	5.30	0.80

The PID constants obtained from both experimental tests are in very good agreement. The discrepancy of the PID sets derived from simulations and experiment is within 10%. One of the possible explanation for error results from the fact that the dead time for both test cases are relatively small (around 2.2 s), hence even a small error (of few tenths of seconds) in determination the dead time from the tangent line at inflection point can lead to significant inaccuracy in the PID constants.

In order to provide complete data for benchmark exercises, all relevant parameters of the sCO₂ loop CVR at steady state conditions, prior to the step changes, are summarized in ANNEX G. In addition, the simulated results are shown, providing further evidence about the capability of the numerical code capturing the measured values.

TUNING OF PID CONTROLLERS FOR MULTIPLE PROCESS CONDITIONS

Fluid properties of the sCO₂ near the critical point experiences highly non-linear variations. This is one of the key enabling features for the sCO₂, however on the other hand, it presents challenges for modeling, and exhibits unique behavior during transients which greatly complicate the control of the system. To demonstrate that series of response curves with different conditions (pressure 10 MPa ÷ 20 MPa, temperature 30 °C ÷ 400 °C) were simulated and tuning constants of the PID controller were derived using Cohen-Coon method for each case. Once again, the temperature outlet from heater H2 was selected as a process variable. Notice that the parametric values of pressures stated here are meant to be pressures at the heater H2 where the response test took place, i.e. high pressure side of the loop (from outlet of the main circulation pump to reduction valve). Further, mass flow rate through the sCO₂ loop was kept constant at 0.13 kg/s and so do the low pressure values (7.65 MPa) to maintain a core of similarity with the PID tuning in the previous chapter. Hence, 10 MPa at the high pressure side was the minimum value for a given low pressure 7.65 MPa taking into account the pressure losses through the loop.

The resulted tuned controller gains (Kc) for different conditions in the sCO₂ loop are plotted in Figure 12. Since the

integral and derivative time constants did not varied significantly and stayed in a relatively small range ($T_i = 4 \text{ s} \div 6 \text{ s}$ and $T_d = 0.6 \text{ s} \div 1 \text{ s}$), they are not shown here explicitly. From the Figure 12 it can be observed that the controller gains follow the behavior of heat capacity. The specific heat capacity (cp) is peaking at so called pseudo-critical temperatures and similarly the controller gains. This effect is growing closer it gets to the critical pressure. The behavior of controller gains can be explained as follows. Where the cp is higher, there the PID controller needs higher gain in order to have sufficiently fast response. On the other hand, where cp is smaller, there the PID controller needs lower gain not to cause oscillations. Note that controller gains are gain divided the by two to reduce overshoot and improve stability.

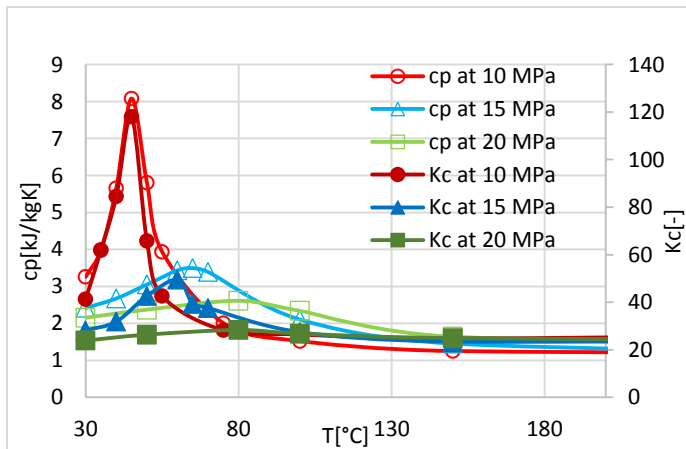


Figure 12: Calculated values of controller gains and specific heat capacities at different pressures and temperatures.

Once the new sets of PID controller were derived, they were tested on several examples. Following figures Figure 13, Figure 14 and Figure 15 shows the behavior of PID controller of the temperature outlet from H2 during the step change of set point. For demonstration, two extreme PID sets were chosen together with manually tuned constants. One extreme case represents the parameters tuned for the highest cp approx. $8 \text{ kJ}\cdot\text{kg}^{-1}\cdot\text{K}^{-1}$ ($K_c=118$, $T_i=3.7 \text{ s}$, $T_d=0.6 \text{ s}$) and the other for the lowest cp approx. $1 \text{ kJ}\cdot\text{kg}^{-1}\cdot\text{K}^{-1}$ ($K_c=25$, $T_i=5 \text{ s}$, $T_d=1 \text{ s}$). Both were derived from previous calculation tuned by Cohen-Coon method. For the manually tuned PID following constants were used ($K_c=25$, $T_i=20 \text{ s}$, $T_d=1 \text{ s}$), i.e. the setting was the same as for the case with the lowest cp , only the integral time constant quadrupled.

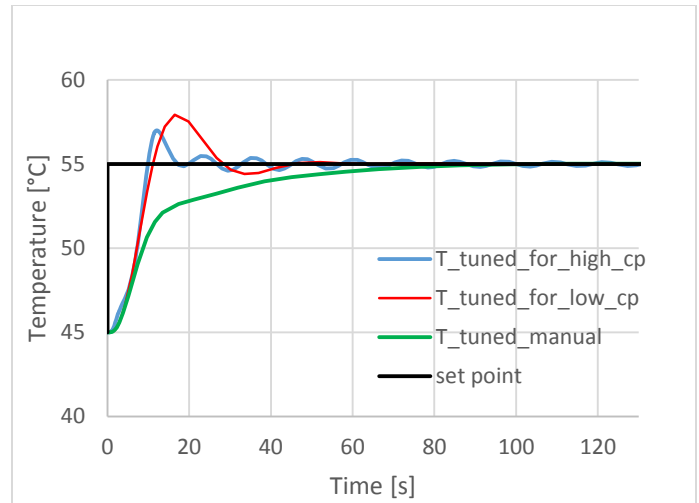


Figure 13: Outlet temperatures of H2 at 10MPa controlled by PID with different settings (set point at 45°C).

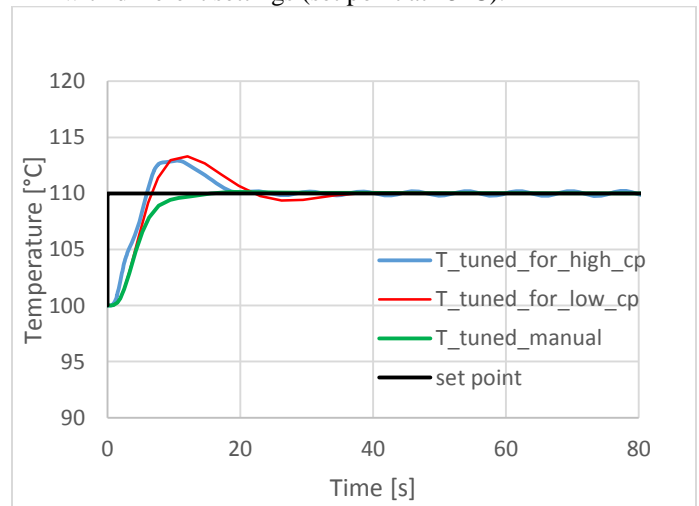


Figure 14: Outlet temperatures of H2 at 10MPa controlled by PID with different settings (set point at 100°C).

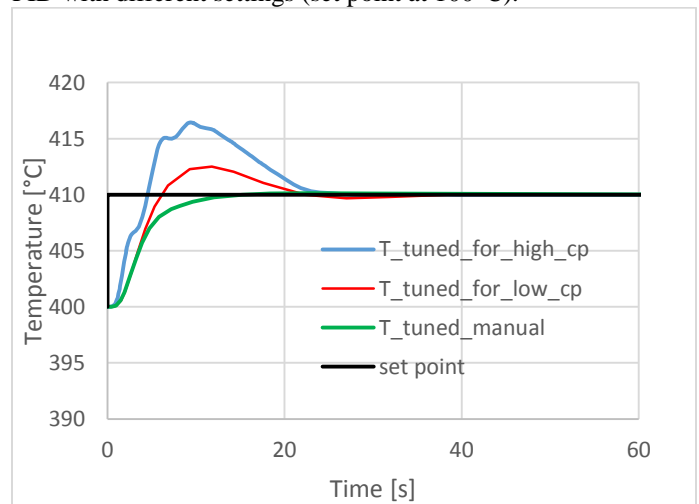


Figure 15: Outlet temperatures of H2 at 10MPa controlled by PID with different settings (set point at 400°C).

It can be observed that the process variable, controlled by PID with settings tuned for high cp, exhibits comparatively high overshoots and instabilities, especially for the higher temperatures test cases (above 100°C). Improvement can be seen for the low cp tuning. It still exhibits quite high overshoots, however the oscillations were significantly reduced. The manually tuned controller behaves well for all 3 tested temperatures. It shows no overshoots, no oscillations, only for the test at 45°C, time for the process variable to settle is quite long (100 s) and it could be improve by increasing the controller gain.

CONCLUSION

The paper shows a comprehensive insight into the experimental investigations and simulations of the sCO₂ loop in CVR. Rather than focusing on separate component behavior, this study aims on a system level (component interaction) for both steady states and dynamic transients including control system interactions and PID tuning techniques. Particularly, this paper contains valuable experimental data of the sCO₂ loop and their comparison with simulations.

The first part of the paper presents the sCO₂ loop, and shows its configuration and specifications. This includes the design parameters of all main components as well as the P&I diagram with measurements and their positions in the system and the piping. Altogether three sets of measured steady states data are outlined and together with detail description of the loop it gives necessary information for performing the benchmark exercise on numerical codes. Such a benchmark was performed with the open source Modelica-based code ClaRa using the simulation environment DYMOLA 2019. The simulated results show fair agreement with measured data, demonstrating reasonable accuracy of the simulation tool. There are maximum 2.5 K/0.2 MPa/0.6 kW temperature/pressure/heating power errors respectively. Further measurements and simulations were carried out, particularly transients, however it is out of the page limit for the paper. Hence, the results of these analyses will be published somewhere else.

Once the numerical model on steady states was validated, the transient tests covering the tuning procedure of the PID controllers were performed. The scope of the study is to give a first approximation of tuning parameters of such a system. For this purpose, one of the most utilized tuning technique, the Cohen-Coon (C-C) method, was deployed. The temperature controller at the outlet of the heater 2 (H2) was selected to be subject of this work. A sudden step-up/step-down increase/decrease in H2 power output respectively at a given condition was executed. The response temperature curves were analyzed and PID constants for the controller were calculated. The PID constants obtained from both experimental tests are in very good agreement. The discrepancy of the PID sets derived from simulations and experiment is within 10%.

For the sake of highly non-linear behavior of sCO₂, series of response curves with different conditions (pressure 10 MPa

÷ 20 MPa, temperature 30 °C ÷ 400 °C) were simulated in order to find the optimum PID settings for all prospective conditions for sCO₂ loop in CVR. It was observed that the resulted controller gains follow behavior of the specific heat capacity, hence they were peaking at the pseudocritical points. This naturally intensifies closer it gets to the supercritical pressure. Hence, near the pseudocritical temperatures and supercritical pressures the PID would need to be given various customized sets of constants for particular conditions. Far from the pseudocritical temperatures, single PID setting should be sufficient.

Once the new sets of PID controller were derived, they were tested on several examples. It has been found that the tuned PID constants according to C-C method exhibits relatively high overshoots. It is due to the fact that different tuning techniques gives preferences to fast response prior to stable behavior. The results from the paper indicates that C-C method prefers fast response. Hence, if one would like to use sole set of PID for all different conditions then it is recommended to use the settings tuned for lower values of cp, i.e. with lower controller gain. Otherwise, the system might oscillates in low cp regions. One has to understand that derived PID constants according to C-C method are just first approximations and further manual tuning are inevitable. In this paper the manually tuned parameters were based on the C-C tuning setting for low cp case and only the integral time constant was quadrupled. With this PID setting the performance of the controller was very much improved with practically representative actions.

Further investigations are planed including deployment of several other tuning techniques in order to improve predictions of the PID settings. In addition, other control loops of the sCO₂ experimental facility in CVR, i.e. mass flow through the cycle driven by circulation pump with frequency convertor or pressure in the system driven by reduction valve etc., are prospective to be tested.

NOMENCLATURE

cp	Specific heat capacity, J·kg ⁻¹ ·K ⁻¹
D	Diameter, m
e(t)	Error (Set point – Process variable)
H	Enthalpy, J·kg ⁻¹
K _c	Controller gain
K _v	Flow coefficient of the valve, m ³ ·h ⁻¹
K _{vs}	K _v at a fully-open valve position, m ³ ·h ⁻¹
L	Length, m
\dot{m}	Mass flow, kg·s ⁻¹
p	Pressure, Pa
P	Power, W
T	Temperature, K
T _i	Integral time constant
T _d	Derivative time constant
ρ	Density, kg·m ⁻³

ACRONYMS

C-C	Cohen-Coon
CH1	Water cooler
CH2	Oil cooler
CO	Control output signal of PID controller
GP	Process gain
H1/1	Electric heater
H1/2	Electric heaters
H2	Electric heaters
H3	Electric heaters
HP	High pressure
HTR	High temperature regenerative heat exchanger
I&C	Instrumentation and control system
KKS	Identification system for power plants
LP	Low pressure
LTR	Low temperature regenerative heat exchanger
MP	Main pump
PID	Proportional Integral Derivative
P&ID	Piping and instrumentation diagram
PV	Process value
RV	Reduction valve
sCO ₂	Supercritical CO ₂
td	Dead time (time difference between the change in CO and the intersection of the tangential line and the original PV level)
Tau	Time constant (time difference between intersection at the end of dead time, and the PV reaching 63% of its total change)
STHX	Shell and tube heat exchanger

ACKNOWLEDGEMENTS

This paper has been conducted within the sCO₂-Flex project which has received funding from the European Union's Horizon 2020 research and innovation programme under grant agreement N° 764690.



REFERENCES

- [1] DOSTAL V.: A supercritical carbon dioxide cycle for next generation nuclear reactors [Ph.D. thesis]. Department of Nuclear Engineering, Massachusetts Institute of Technology (MIT); 2004.
- [2] BRUN K.; FRIEDMAN P.; DENNIS R.: Fundamentals and Applications of Supercritical Carbon Dioxide (SCO₂) Based Power Cycles. 1st edition, Elsevier Science & Technology, 2017.
- [3] MENDEZ, C.M., ROCHAU G.: sCO₂ Brayton Cycle: Roadmap to sCO₂ Power Cycles NE Commercial Applications, SANDIA REPORT, SAND2018-6187, Printed June 2018, Albuquerque, New Mexico.
- [4] CAGNAC, A., 2018, "The supercritical co₂ cycle for flexible & sustainable support to the electricity system (sco₂-flex)," Electricité de France, Avenue de Wagram 22, 75008, Paris 08, Accessed Apr. 4, 2019, <http://www.sco2-flex.eu/>.
- [5] BRINGER, R.P.; SMITH, J.M.: Heat transfer in the critical region. *AIChE J.* 3 (1), 49–55, 1957.
- [6] PETUKHOV, B.S.; KRASNOSCHEKOV, E.A.; PROTOPOPOV, V.S.: An investigation of heat transfer to fluids flowing in pipes under supercritical conditions. In: *International Developments in Heat Transfer: Papers presented at the 1961 International Heat Transfer Conference, ASME, University of Colorado, Boulder, Colorado, USA, 8–12 January, Part III, Paper 67, pp. 569–578, 1961.*
- [7] DUFFEY, R.B.; PIORO, I.L.: Experimental heat transfer of supercritical carbon dioxide flowing inside channels (survey), *Nuclear Engineering and Design* 235 (2005) 913–924.
- [8] VOJACEK, A. ET AL.: Challenges in supercritical CO₂ power cycle technology and first operational experience at CVR, 2nd European sCO₂ Conference, Duisburg-Essen, August 2018, DOI: 10.17185/dupublico/46075.
- [9] WRIGHT, S.A. ET AL.: Operation and Analysis of a Supercritical CO₂ Brayton Cycle, SAND2010-0171, Albuquerque, New Mexico, Sep. 2010.
- [10] UTAMURA, M. ET AL.: Demonstration of supercritical CO₂ closed regenerative brayton cycle in a bench scale experiment. *Proceedings of ASME Turbo Expo 2012, June 11-15, 2012, Copenhagen, Denmark, GT2012-68697.*
- [11] HACKS A. J.; VOJACEK A.; DOHMEN H. J.; BRILLERT D.: Experimental Investigation of the sCO₂-HeRo Compressor. 2018-sCO₂.eu-115, 2nd European supercritical CO₂ Conference, August, 2018.
- [12] AHN, Y. ET AL.: Design consideration of supercritical CO₂ power cycle integral experiment loop, *Energy* 86 (2015) 115-127.
- [13] CHO, J. ET AL.: Research on the development of a small-scale supercritical carbon dioxide power cycle experimental test loop, *The 5th International Symposium - Supercritical CO₂ Power Cycles, March 28-31, 2016, San Antonio, Texas.*
- [14] NIELSEN, L.: TLK-Thermo GmbH, "Dyncap/Dynstart | ClaRa – Simulation of Clausius-Rankine cycles | TLK-Thermo GmbH, Braunschweig | XRG Simulation GmbH, Hamburg | Institut für Thermofluidodynamik (TUHH), Hamburg | Institut für Energietechnik (TUHH), Hamburg." [Online]. Available: <https://www.claralib.com/>. [Accessed: 4-Apr-2019].
- [15] COHEN, G. H.; G. A. COON (1953): "Theoretical consideration of retarded control." *Trans. ASME*, 75, pp. 827-834.
- [16] SMUTS, J.F.: Control notes – Reflection of a process control practitioner. [Online]. Available: <http://blog.opticontrols.com>. [Accessed: 4-Apr-2019].
- [17] Division Isover, Saint-Gobain Construction Products CZ a.s., Masarykova 197, 517 50 Častolovice. [Online].

Available: <https://www.isover.cz/en/products/orstech-dp-100>. .
[Accessed: 4-Apr-2019].

[18] CASELLA F.; LEVA, A.: “Modelling of thermo-hydraulic power generation processes using Modelica,” *Math. Comput. Model. Dyn. Syst.*, vol. 12, no. 1, pp. 19–33, Feb. 2006.

[19] KOFRANEK, J. ET. AL.: “Causal or acausal modeling: labour for humans or labour for machines,” in *Technical Computing Prague*, 2008, pp. 1–16.

[20] NIST Reference Fluid Thermodynamic and Transport Properties Database (REFPROP): Version 10.

[21] Ulrich Spiesshofer, ABB Asea Brown Boveri Ltd, Affolternstrasse 44, 8050 Zurich, Switzerland Available: <https://new.abb.com/control-systems/essential-automation/freelance>. [Accessed: 4-Apr-2019].

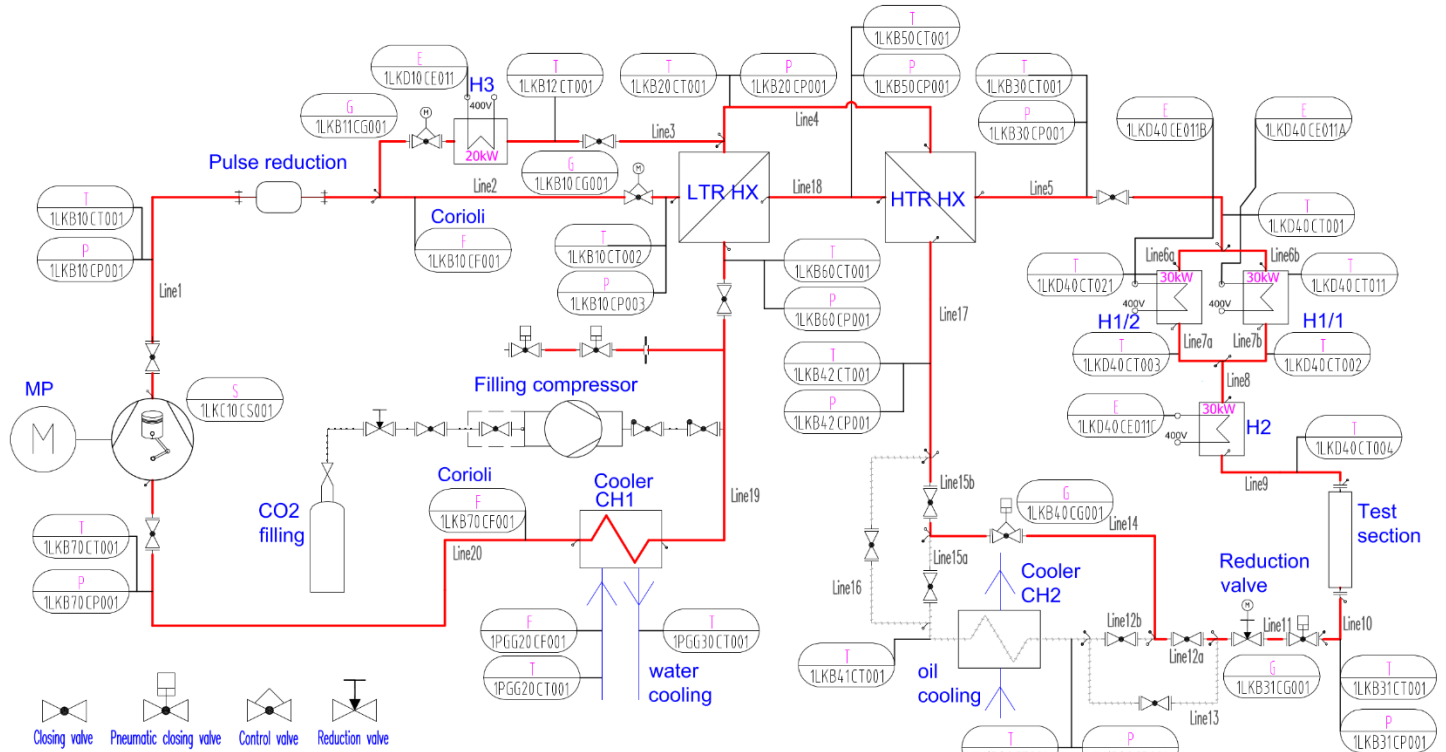
[22] Siemens Aktiengesellschaft Werner-von-Siemens-Straße 1, 80333 Munich, Germany Available: <https://w3.siemens.com/mcms/distributed-io/en/ip20-systems/et200m/interface-modules/pages/default.aspx>. [Accessed: 4-Apr-2019].

[23] LI, Y.; ANG, K.H.; CHONG, G.C.Y. (2006) PID control system analysis and design. *IEEE Control Systems Magazine* 26(1):pp. 32-41.

[24] ZIEGLER, J. G.; NICHOLS, N.B.: “Optimum Settings for Automatic Controllers,” *Transactions of the ASME*, Vol. 64, 1942, pp. 759-768.

ANNEX A

PIPING AND INSTRUMENTATION DIAGRAM (P&ID) OF THE SCO₂ LOOP, CVR



ANNEX B

UNCERTAINTY OF THE MEASUREMENT DEVICES IN SCO₂ LOOP, CVR

Variable	Range	Unit	Description	Device error	Transducer error	Input card error	Control system error	Total error
\dot{m}_{CO_2}	0 - 0.7	kg/s	mass flow rate 1LKB10CF001, 1LKB70CF00 1Rheonik (RHM12)	0.15 % from 1.66 kg/s	Rawet - PX310S	Siemens SM 331	ABB frealence	+/- 0.007 kg/s
					0.1 % from range	0.4 % from range	0.1 % from range	
T_{SCO_2}	0 - 600	°C	TC (type K) T_{SCO_2} , Omega	+/- 0.5 K for (0÷100°C) +/- 0.6 K for 300°C +/- 1.4 K for 500°C	Rawet - PX310S	Siemens SM 331	ABB frealence	+/- 4.1 K for (0÷100°C) +/- 4.2 K for 300°C +/- 5 K for 500°C
					0.1 % from range	0.4 % from range	0.1 % from range	
$p_{\text{SCO}_2\text{-LP}}$	0 - 15	MPa	sCO ₂ pressures at low pressure side of	0.15 % from range	Rawet - PX310S	Siemens SM 331	ABB frealence	+/- 0.11 MPa

			the loop, GE (UNIK 5000)		0.1 % from range	0.4 % from range	0.1 % from range	
p _{sCO2_HP}	0 - 30	MPa	sCO ₂ pressures at high pressure side of the loop, GE (UNIK 5000)	0.15 % from range	Rawet - PX310S	Siemens SM 331	ABB freelance	+/- 0.23 MPa
					0.1 % from range	0.4 % from range	0.1 % from range	
P _{H1/1-2} P _{H2,3}	0 - 30	kW	electric power of heaters, MT Brno	0.75 % from range	Rawet - PX310S	Siemens SM 331	ABB freelance	+/- 0.4 kW
					0.1 % from range	0.4 % from range	0.1 % from range	
T _{water}	0 - 120	°C	water temperature of the cooling circuit, JSP (Pt 100)	0.15K+0.2 % from range	Rawet - PX310S	Siemens SM 331	ABB freelance	+/- 1.1 K
					0.1 % from range	0.4 % from range	0.1 % from range	
m _{water}	0 – 3.8	kg/s	water mass flow rate of the cooling circuit, turbine flowmeter, Hoffer	1.1 % from range	-	-	ABB freelance	+/- 0.046 kg/s
					-	-	0.1 % from range	

ANNEX C

UNCERTAINTY OF THE MEASUREMENT DEVICES IN SCO2 LOOP, CVR

Component	Geometry
HTR + LTR (counter-flow shell and tube-type from SS 321)	Length of HTR = 20 m (2 x U-tube vertical), 3 x 2 = 6 high pressure flanges Ø 110 mm (height 25 mm) and the same 6 low pressure flanges Length of LTR = 60 m (6 x U-tube vertical), 7 x 2 = 14 high pressure flanges Ø 110 mm (height 25 mm) and the same 14 low pressure flanges Number of internal tubes = 7, Internal tube Ø 10 x 1.5 mm, Shell Ø 50 x 5 mm.
H1/1 + H1/2 (30 + 30 kW) (from SS 321)	Length = 0.95 m, Number of heating rods = 2 x 6, Diameter of a heating rod Ø 8 mm (cladding tube Ø 8 x 1 mm SS 321, ceramic (MgO) filling Ø 6 x 1 mm, ceramic (Al ₂ O ₃) filling Ø 4 x 1.75 mm, Ø 0.5 mm wire Kanthal alloy (FeCrAl)), Shell Ø 100 x 20 mm, guiding tube Ø 36 x 2 mm with plugs on both ends
H2 (30 kW) (from Inconel 625)	Length = 0.95 m, Number of heating rods = 2 x 6, Diameter of a heating rod 8 mm (ceramic filling and wire as in H1/1 + H1/2), Shell Ø 73 x 6.5 mm, 2 x 1 = 2 flanges Ø 110 mm (height 25 mm), guiding tube Ø 36 x 2 mm with plugs on both ends
H3 (20 kW) (from SS 321)	Length = 0.75 m, Number of heating rods = 2 x 6, Diameter of a heating rod Ø 8 mm (ceramic filling and wire as in H1/1 + H1/2), Shell Ø 100 x 20 mm, guiding tube Ø 36 x 2 mm with plugs on both ends
CH1 (counter-flow shell and tube-type from SS)	Length = 7.5 m, Number of internal tubes = 7, Internal tube Ø 10 x 1.5 mm, Shell Ø 43 x 1.5 mm
CH2 (counter-flow shell and tube-type from Inconel 625 (CO ₂ side)/SS 321 (oil side))	Length = 1.8 m, Number of internal tubes = 7, Internal tube Ø 10 x 1.5 mm, Shell Ø 43 x 1.5 mm, 2 x 2 = 4 high flanges Ø 110 mm (height 25 mm)
TS (from Inconel 625)	Length = 2 m, Shell Ø 73 x 6.5 mm, 2 x 2 = 4 high flanges Ø 140 mm (height 26 mm)
Reduction valve (from SS 321)	Body weight 125 kg, Length = 0.5 m
Control valves (3x) (from SS 321)	Body weight 5 kg, Length = 0.3 m (each)
Closing valves	Body weight 1 kg, Length = 0.3 m

*("hot" part of the loop) (from SS 321)	(each)
Closing valves **("cold" part of the loop) (from SS 321)	Body weight 5 kg, Length = 0.3 m (each)

* The "hot" part of the loop is from inlet of heater H3 and inlet of high pressure LTR to outlet of low pressure LTR.

** The "cold" part is the rest of the loop (from outlet of low pressure LTR to inlet to heater H3 and inlet of high pressure LTR.

ANNEX D

PIPELINE GEOMETRY OF THE SCO₂ LOOP

Line 1	Pipeline from MP to T-junction LTR by-pass	Length = 2.6 m, 1x90° Bend, Tube Ø 22 x 4 mm
Line 2	Pipeline from T-junction LTR by-pass to LTR	Length = 6.8 m, 6x90° Bend, Tube Ø 22 x 4 mm
Line 3	LTR by-pass	Length = 7.6 m, 2x90° Bend, Tube Ø 22 x 4 mm
Line 4	Pipeline from outlet of high pressure LTR to inlet of high pressure HTR	Length = 0.7 m, 2x90° Bend, Tube Ø 22 x 4 mm
Line 5	Pipeline from outlet of high pressure HTR to T-junction at the inlet of H1/1 and H1/2	Length = 1 m, 1x90° Bend, Tube Ø 22 x 4 mm
Line 6a/6b	2 identical pipelines from T-junction at the inlet of H1/1 and H1/2 to H1/1 and H1/2	Length = 1.4 m, 1x60° Bend, Tube Ø 22 x 4 mm
Line 7a/7b	2 identical pipelines from H1/1 and H1/2 to T-junction at the outlet of H1/1 and H1/2	Length = 1.5 m, 1x60° Bend, Tube Ø 22 x 4 mm
Line 8	Pipeline from T-junction outlet of H1/1 and H1/2 to H2	Length = 1.9 m, 2x90° Bend, Tube Ø 22 x 4 mm
Line 9	Pipeline from H2 to test section	Length = 2 m, 2x90° Bend, Tube Ø 22 x 4 mm
Line 10	Pipeline from test section to reduction valve	Length = 1.9 m, 1x90° Bend, Tube Ø 22 x 4 mm
Line 11	Pipeline from reduction valve to T-junction of line 12a/13	Length = 8.4 m, 8x90° Bend, Tube Ø 20 x 3 mm
Line 12a	Pipeline from T-junction of line 12a/13 to T-junction CH2 by-pass (inlet of CH2 by-pass)	Length = 0.4 m, 1x60° Bend, Tube Ø 20 x 3 mm
Line 12b	Pipeline from T-junction CH2 by-pass (inlet of CH2 by-pass) to T-junction of line 12b/13	Length = 0.4 m, 1x60° Bend, Tube Ø 20 x 3 mm
Line 13	Pipeline from T-junction of line 12a/13 to T-junction of line 12b/13 to	Length = 0.9 m, 2x60° Bend, Tube Ø 20 x 3 mm
Line 14	Pipeline CH2 by-pass	Length = 5.5 m, 4x90° Bend, Tube Ø 20 x 3 mm
Line 15a	Pipeline from T-junction of line 15a/16 to T-junction CH2 by-pass (outlet of CH2 by-pass)	Length = 0.4 m, 1x60° Bend, Tube Ø 20 x 3 mm
Line 15b	Pipeline from T-junction CH2 by-pass (outlet of CH2 by-pass) to T-junction of line 15b/16	Length = 0.4 m, 1x60° Bend, Tube Ø 20 x 3 mm
Line 16	Pipeline from T-junction of line 15a/16 to T-junction of line 15b/16	Length = 0.9 m, 2x60° Bend, Tube Ø 20 x 3 mm
Line 17	Pipeline from T-junction of line 15b/16 to inlet of low pressure HTR	Length = 0.8 m, 1x90° Bend, Tube Ø 20 x 3 mm
Line 18	Pipeline from outlet of low pressure HTR to inlet of low pressure LTR	Length = 0.7 m, 2x90° Bend, Tube Ø 22 x 4 mm
Line 19	Pipeline from outlet of low pressure LTR to CH1	Length = 1.8 m, 2x90° Bend, Tube Ø 20 x 3 mm
Line 20	Pipeline from CH1 to MP	Length = 4.4 m, 7x90° Bend, Tube Ø 20 x 3 mm

ANNEX E

POSITION OF THE MEASUREMENT SENSORS

Measurement type	Position	Pipeline
m_CO2_MP (1LKB70CF001)	3.9 m prior to MP inlet	line 20
m_CO2_LTR (1LKB10CF001)	1.6 m from MP outlet	line 1
rotational speed_MP (1LKC10CS001)	MP	line 1
power_H1/1 (1LKD40CE011A)	H1/1	line 6b,7b
power_H1/2 (1LKD40CE011B)	H1/2	line 6a,7a
power_H2 (1LKD40CE011C)	H2	line 8,9
power_H3 (1LKD10CE011)	H3	line 3
p_CO2_MP_in (1LKB70CP001)	3.4 m prior to MP inlet	line 20
T_CO2_MP_in (1LKB70CT001)	5.1 m prior to MP inlet	line 20
p_CO2_MP_out (1LKB10CP001)	1.6 m from MP outlet	line 1
T_CO2_MP_out (1LKB10CT001)	1.6 m from MP outlet	line 1
position_valve_LTR_in (1LKB10CG001)	control valve LTR inlet	line 2
position_valve_LTR_by-pass (1LKB11CG001)	control valve LTR by-pass	line 3
T_by-pass LTR (1LKB12CT001)	0.8 m from H3 outlet	line 3
p_CO2_LTR_p_high_side_in (1LKB10CP003)	LTR high pressure inlet	line 2
T_CO2_LTR_p_high_side_in (1LKB10CT002)	LTR high pressure inlet	line 2
p_CO2_LTR_p_high_side_out (1LKB20CP001)	HTR high pressure inlet	line 4
T_CO2_LTR_p_high_side_out (1LKB20CT001)	HTR high pressure inlet	line 4
T_CO2_HTR_p_high_side_out (1LKB30CT001)	HTR high pressure outlet	line 5
p_CO2_HTR_p_high_side_out (1LKB30CP001)	HTR high pressure outlet	line 5
T_CO2_H1/1_H1/2_in (1LKD40CT001)	H1/1, H1/2 inlet (T-junction)	line 5
T_CO2_H1/1_out (1LKD40CT002)	H1/1, H1/2 outlet (T-junction)	line 7b
T_CO2_H1/2_out (1LKD40CT003)	H1/1, H1/2 outlet (T-junction)	line 7a
T_CO2_H2_out (1LKD40CT004)	1.2 m from H2 outlet	line 9
p_CO2_RV_in (1LKB31CP001)	TS outlet	line 10

T_CO2_RV_in (1LKB31CT001)	TS outlet	line 10
position of RV (1LKB31CG001)	RV	line 11
position_valve_CH2_by-pass (1LKB40CG001)	control valve CH2 by-pass	line 14
p_CO2_HTR_p_low_side_in (1LKB42CP001)	HTR low pressure inlet	line 17
T_CO2_HTR_p_low_side_in (1LKB42CT001)	HTR low pressure inlet	line 17
p_CO2_HTR_p_low_side_out (1LKB50CP001)	HTR low pressure outlet	line 18
T_CO2_HTR_p_low_side_out (1LKB50CT001)	HTR low pressure outlet	line 18
p_CO2_LTR_p_low_side_out (1LKB60CP001)	LTR low pressure outlet	line 19
T_CO2_LTR_p_low_side_out (1LKB60CT001)	LTR low pressure outlet	line 19
m_H2O_CH1 (1PGG20CF001)	1.4 m prior to CH1 inlet	water circuit
T_H2O_CH1_in (1PGG20CT001)	CH1 inlet	water circuit
T_H2O_CH1_out (1PGG30CT001)	CH1 outlet	water circuit

ANNEX F
MEASURED AND CALCULATED STEADY STATE PARAMETERS

parameter	Unit	5_meass	5_sim	error_abs	37_meass	37_sim	error_abs	61_meass	61_sim	error_abs
m_CO2_MP (1LKB70CF001)	kg/s	0.227	0.225	0.0	0.187	0.188	0.0	0.198	0.198	0.0
m_CO2_LTR (1LKB10CF001)	kg/s	0.227	0.225	0.0	0.187	0.188	0.0	0.198	0.198	0.0
power_H1/1 (1LKD40CE011A)	kW	0.806	0.959	-0.2	6.539	6.731	-0.2	3.077	2.676	0.4
power_H1/2 (1LKD40CE011B)	kW	0.932	0.959	0.0	6.688	6.731	0.0	3.190	2.676	0.5
power_H2 (1LKD40CE011C)	kW	26.865	27.452	-0.6	17.634	17.672	0.0	28.075	28.022	0.1
power_H3 (1LKD10CE011)	kW	0.000	0.000	0.0	0.000	0.000	0.0	0.000	0.000	0.0
p_CO2_MP_in (1LKB70CP001)	MPa	8.821	8.841	0.0	7.502	7.529	0.0	7.968	7.989	0.0
T_CO2_MP_in (1LKB70CT001)	°C	21.259	21.172	0.1	19.267	19.291	0.0	16.913	16.916	0.0
p_CO2_MP_out (1LKB10CP001)	MPa	19.820	19.997	-0.2	20.591	20.806	-0.2	19.920	20.177	-0.3
T_CO2_MP_out (1LKB10CT001)	°C	33.980	35.394	-1.4	38.708	36.335	2.4	30.709	31.384	-0.7
position_valve_LTR_in (1LKB10CG001)	%	100.000	100.000	0.0	100.000	100.000	0.0	100.000	100.000	0.0
position_valve_LTR_by-pass (1LKB11CG001)	%	0.000	0.000	0.0	0.000	0.000	0.0	0.000	0.000	0.0
p_CO2_LTR_p_high_side_in (1LKB10CP003)	MPa	19.828	19.944	-0.1	20.624	20.767	-0.1	19.944	20.136	-0.2
T_CO2_LTR_p_high_side_in (1LKB10CT002)	°C	32.697	35.059	-2.4	36.755	35.920	0.8	29.060	31.102	-2.0
T_CO2_HTR_p_high_side_out (1LKB30CT001)	°C	70.975	71.993	-1.0	208.699	206.823	1.9	342.986	343.688	-0.7
p_CO2_HTR_p_high_side_out (1LKB30CP001)	MPa	19.670	19.794	-0.1	20.506	20.655	-0.1	19.808	19.994	-0.2
T_CO2_H1/1_H1/2_in (1LKD40CT001)	°C	71.363	71.945	-0.6	209.193	206.702	2.5	344.299	343.570	0.7
T_CO2_H1/1_out (1LKD40CT002)	°C	75.001	75.000	0.0	259.999	260.000	0.0	365.060	365.000	0.1
T_CO2_H1/2_out (1LKD40CT003)	°C	74.996	75.000	0.0	259.989	260.000	0.0	365.055	365.000	0.1
T_CO2_H2_out (1LKD40CT004)	°C	122.019	123.820	-1.8	328.064	329.504	-1.4	470.081	472.544	-2.5
p_CO2_RV_in (1LKB31CP001)	MPa	19.697	19.700	0.0	20.508	20.510	0.0	19.768	19.770	0.0
T_CO2_RV_in (1LKB31CT001)	°C	123.183	123.471	-0.3	328.633	328.275	0.4	470.068	470.686	-0.6
position of RV (1LKB31CG001)	%	63.000	63.000	0.0	57.000	57.000	0.0	60.000	60.000	0.0
position_valve_CH2_by-pass (1LKB40CG001)	%	100.000	100.000	0.0	100.000	100.000	0.0	100.000	100.000	0.0
p_CO2_HTR_p_low_side_in (1LKB42CP001)	MPa	9.270	9.050	0.2	7.939	7.705	0.2	8.436	8.171	0.3
T_CO2_HTR_p_low_side_in	°C	77.759	77.781	0.0	300.213	300.189	0.0	447.576	447.592	0.0

(1LKB42CT001)										
p_CO2_LTR_p_low_side_out (1LKB60CP001)	MPa	8.877	8.894	0.0	7.562	7.574	0.0	8.020	8.032	0.0
T_CO2_LTR_p_low_side_out (1LKB60CT001)	°C	42.177	43.981	-1.8	39.155	39.484	-0.3	37.825	39.390	-1.6

*Note that all pressures are gauge pressures.

ANNEX G MEASURED AND CALCULATED STEADY STATE PARAMETERS

parameter	Unit	step-Up_meas	step-Up	error_abs	step-Down_meas	step-Down	error_abs
m_CO2_MP (1LKB70CF001)	kg/s	0.001	0.000	0.0	0.001	0.132	-0.1
m_CO2_LTR (1LKB10CF001)	kg/s	0.131	0.132	0.0	0.131	0.132	0.0
power_H1/1 (1LKD40CE011A)	kW	3.116	3.821	-0.7	1.295	2.123	-0.8
power_H1/2 (1LKD40CE011B)	kW	3.169	3.821	-0.7	1.373	2.123	-0.7
power_H2 (1LKD40CE011C)	kW	6.206	6.128	0.1	10.901	11.200	-0.3
power_H3 (1LKD10CE011)	kW	15.381	14.131	1.2	14.705	13.247	1.5
p_CO2_MP_in (1LKB70CP001)	MPa	7.581	7.533	0.0	7.493	7.433	0.1
T_CO2_MP_in (1LKB70CT001)	°C	16.152	16.047	0.1	16.236	16.047	0.2
p_CO2_MP_out (1LKB10CP001)	MPa	10.346	10.457	-0.1	10.465	10.723	-0.3
T_CO2_MP_out (1LKB10CT001)	°C	17.663	19.454	-1.8	17.947	19.889	-1.9
position_valve_LTR_in (1LKB10CG001)	%	0.000	1.000	-1.0	0.000	1.000	-1.0
position_valve_LTR_by-pass (1LKB11CG001)	%	100.000	100.000	0.0	100.000	100.000	0.0
T_by-pass LTR (1LKB12CT001)	°C	44.978	45.000	0.0	45.000	45.000	0.0
p_CO2_LTR_p_high_side_in (1LKB10CP003)	MPa	10.359	10.416	-0.1	10.476	10.683	-0.2
T_CO2_HTR_p_high_side_out (1LKB30CT001)	°C	73.478	69.844	3.6	87.678	82.396	5.3
p_CO2_HTR_p_high_side_out (1LKB30CP001)	MPa	10.326	10.396	-0.1	10.450	10.662	-0.2
T_CO2_H1/1_H1/2_in (1LKD40CT001)	°C	73.506	69.684	3.8	87.697	82.229	5.5
T_CO2_H1/1_out (1LKD40CT002)	°C	100.030	100.000	0.0	100.015	100.002	0.0
T_CO2_H1/2_out (1LKD40CT003)	°C	100.032	100.000	0.0	100.009	100.002	0.0
T_CO2_H2_out (1LKD40CT004)	°C	130.007	130.000	0.0	156.473	157.108	-0.6
p_CO2_RV_in (1LKB31CP001)	MPa	10.333	10.320	0.0	10.453	10.579	-0.1
T_CO2_RV_in (1LKB31CT001)	°C	131.158	129.322	1.8	157.165	156.287	0.9
position of RV (1LKB31CG001)	%	100.029	100.029	0.0	100.029	100.029	0.0
position_valve_CH2_by-pass (1LKB40CG001)	%	99.337	99.337	0.0	99.617	99.617	0.0
p_CO2_HTR_p_low_side_in (1LKB42CP001)	MPa	7.768	7.649	0.1	7.684	7.549	0.1
T_CO2_HTR_p_low_side_in (1LKB42CT001)	°C	116.219	114.154	2.1	142.026	139.466	2.6
p_CO2_LTR_p_low_side_out (1LKB60CP001)	MPa	7.597	7.557	0.0	7.509	7.458	0.1
T_CO2_LTR_p_low_side_out (1LKB60CT001)	°C	43.855	43.218	0.6	43.919	43.302	0.6

*Note that all pressures are gauge pressures.

A SYSTEMATIC COMPARISON OF SUPERCRITICAL CO₂ BRAYTON CYCLE LAYOUTS FOR CONCENTRATED SOLAR POWER WITH A FOCUS ON THERMAL ENERGY STORAGE UTILIZATION

Jinyi Zhang*
EDF R&D China
Beijing, China
Email: Jinyi.zhang@edf.fr

Yann Le Moullec
EDF R&D China
Beijing, China

ABSTRACT

Supercritical CO₂ cycle, due to its potential to reach high thermal efficiency and high flexibility, is a promising approach to increase the competitiveness of concentrated solar power. By taking into account thermal energy storage utilization, this paper provides a meaningful comparison of different supercritical CO₂ cycles for application in concentrated solar power. Regenerative, recompression, pre-compression and partial cooling cycles are considered as four fundamental cycles. By combining these fundamental cycles with intercooling, preheating and reheating, it results in a wide range of cycle candidates for comparison and analysis. Each cycle is modeled and optimized with the objective to maximize the specific power output for different thermal energy storage utilization. The results show that, with a high thermal energy storage utilization, in order to maximize the cycle efficiency, it is not optimal for most of the studied cycle to reach its upper limit of temperature. Besides, with the thermal storage utilization as a constraint for optimization, intercooling, preheating and reheating show different efficiency enhancement behavior on different region of thermal energy storage utilization.

INTRODUCTION

In recent years, facing the worldwide environmental challenge and the scarcity of fossil fuels in some regions of the world, renewable energy is gaining more and more importance in the development portfolio of energy industry. Solar and wind energy are two major renewable energy solutions which attract most of the attentions, however, the highly uncontrollable variability of solar irradiation and wind bring huge challenges for the electric power grid to match the instantaneous energy demand and production. As a result, the renewables are suffering serious curtailment, e.g. in 2016, the curtailment of wind and solar PV energy reached 57.3 TWh in China [1]. In addition, the highly uncontrollable variability of solar irradiation and wind also limits the highest share of renewable energy that can be integrated into the power system in the future. Concentrated

solar power (CSP), which can reach a high solar energy utilization efficiency and operate with low-cost thermal energy storage (TES), e.g. the commercially utilized molten salt, namely Solar Salt (60 wt% NaNO₃ and 40 wt% KNO₃), is a grid-friendly renewable solution. Because CSP, if equipped with enough TES, is able to completely decouple the solar-thermal and thermal-electricity conversions, achieving continuous production and regulating the power output depending on the grid demand, regardless of the weather conditions.

However, CSP's high cost, 120 \$/MWh in average in 2020 reported by International Renewable Energy Agency (IRENA), makes it difficult for long-term deployment. In order to increase its competitiveness compared to other renewable solutions with storage, in addition to the efforts done to reduce the capital cost, there are two main technology development paths: one is to increase the solar-thermal efficiency by optimizing solar collector efficiency, the other is to increase the thermal-electricity efficiency by increasing the thermal storage temperature or the power generation cycle efficiency. Supercritical CO₂ (SCO₂) power generation cycle is identified as a promising technology with high potential in the second path to increase the thermal-electric efficiency and reduce the capital cost due to simpler layout and more compact turbo-machinery [2–6].

Besides, CO₂ also exhibits many attracting characteristics as a heat transfer fluid [7–9]: It is abundant, inexpensive, non-toxic and it has a easily-achievable critical point (30.98 °C, 7.38 MPa). It also shows a good thermal stability up to 1500 °C and no freezing problem down to -55 °C. Gas Brayton cycle operating with SCO₂ benefits from the real gas behavior of CO₂ in the vicinity of the Andrews curve, which leads to the reduction of specific volume and therefore of the compression work in the cycle. More reduction of compression work is achieved when CO₂ is compressed closer to its critical point, as the fluid becomes more incompressible. This mechanical effect, i.e. the significant reduction of compression work, results in a significant thermal efficiency improvement of SCO₂ Brayton

cycle compared to other working fluid for Brayton cycle, e.g. helium or air [10]. As the SCO₂ cycle operates with high pressure and small pressure ratio, the fluid remains dense throughout the entire system, as a result, the volume of turbo-machineries is significantly reduced, ~90% smaller than water steam turbine [10]. The fact that replacing water by CO₂ in the power block simplifies significantly the operation of CSP plants which are mostly located in the droughty areas.

Feher is one of the first authors who proposed CO₂ as a heat transfer fluid for power generation cycle and pointed out the pinch problems of recuperator in a regenerative cycle [7]. Anglino performed one of the earliest and the most detailed investigation of SCO₂ cycles and introduced novel cycle configurations such as recompression, pre-compression and partial cooling, to overcome the internal irreversibility problem in the recuperator then to improve the cycle performance [8,11,12]. Dostal, based mainly on the cycle configurations proposed by Anglino, further introduced intercooling and reheating, carried out a comprehensive study on SCO₂ cycles for application to advanced nuclear reactors and concluded that recompression cycle yielded the highest efficiency while remaining simple.

With the development of CSP, more and more studies have been focusing on the integration of CSP and SCO₂ cycle. Yamaguchi proposed SCO₂ Rankine cycle for solar thermal power generation and built an experimental loop to study the characteristics of SCO₂ cycle coupled with solar energy [13–15], but no cycle selection or optimization has been done. Turchi did some dedicated study on SCO₂ cycles for CSP [2–6,16] and concluded that partial cooling cycle outperformed the recompression cycle and pointed out that the importance of larger temperature differential across the primary heat exchanger for more cost efficient thermal energy storage (TES) systems and possible more thermally efficient receivers [16]. Many studies have also been done for the application of SCO₂ cycles in coal-fired power (CFP) [17–19] and waste heat recovery (WHR) [20–22]. Because CFP needs to recover as much as possible the combustion heat to maximize the boiler efficiency and WHR needs to recover the low-grade heat to maximize the net power output from the bottoming cycle, SCO₂ cycles with preheating are firstly proposed for these applications, in order to achieve a larger temperature differential utilization of heat source [17,21]

More studies are also found in recent years to analyze different SCO₂ cycles for application in CSP [23–29]. However, most of the current cycle studies for CSP have been focusing on the comparison or optimization of cycle in terms of thermal efficiency or overall plant efficiency, which resulted in poor utilization of thermal storage potential. However, for CSP plant, due to the fact that TES system represents ~20% of the total plant investment, it requires that the potential of thermal storage medium should be efficiently exploited in order to reach a more cost-efficient design of TES system. In the meantime, the cycle thermal efficiency should be kept as high as possible to minimize the levelized cost of electricity (LCOE). In order to take these two factors together into account, the electric power generated from a specific amount of thermal storage, which is equivalent

to the product of thermal storage utilization ratio and cycle thermal efficiency, is selected as a cycle performance criterion in this study. Besides, thermal storage utilization ratio, as a function of cold-side temperature and hot-side temperature, is the juncture among the three main subsystems of CSP, i.e. solar field, TES and power block. It influences directly the thermal-electrical efficiency of power block, solar-thermal efficiency and the size of TES system. Therefore, it is an important indicator for the integration of SCO₂ with CSP and a better understanding on its impact on the performance could provide a clearer guideline on the selection of SCO₂ cycle for application in CSP.

This paper aims to provide a meaningful comparison of different SCO₂ cycles for application in CSP with Solar Salt, by taking into account the TES utilization. Regenerative, recompression, pre-compression and partial cooling cycle are considered as four fundamental cycles. By combining these fundamental cycles with several cycle characteristics such as intercooling, preheating and reheating, it results in a wide range of cycle candidates for comparison and analysis in this paper.

SCO₂ CYCLES

Regenerative (RG) cycle is the simplest cycle that is able to achieve an acceptable performance, but due to the pinch-point problem in the recuperator, its potential to reach a high thermal efficiency is limited. Most of the complex SCO₂ cycles are derived from RG cycle, therefore, it is considered as a reference for cycle analysis and comparison. Regenerative cycle with recompression, i.e. recompression (RC) cycle, solves the pinch-point problem by splitting part of the hot-side outlet flow of the recuperator. One part of the flow passes the cooler, the main compressor and recuperator, while the other part of flow enters directly into an auxiliary compressor. These two flows join later at the cold-side outlet of recuperator. As a result, RC cycle achieves higher thermal efficiency compared to RG cycle. Pre-compression (PC) cycle introduces another approach to reduce the effect of the pinch-point problem. It reduces the heat capacity difference between low-pressure and high-pressure flows by increasing the pressure of the low-pressure flow. Partial cooling (PartC) cycle is similar to RC cycle except that the recuperator hot-side outlet flow is cooled down and compressed to a higher pressure before splitting into two flows. These 4 cycles are the most fundamental SCO₂ cycles for analysis.

Besides, there are several cycle characteristics that can be combined with these fundamental cycles: (1) Intercooling (IC) between stages of compressor is a classical approach to reduce the compressor work then to improve cycle efficiency; (2) Pre-heating (PH) means to split a part of the recuperator cold-side outlet flow and make it heated by the low-grade heat of heat

Table 1
Fundamental SCO₂ cycles with their derivatives

Fundamental	+ IC	+ PH	+ RH
RG	RG-IC	RG-PH	RG-RH
RC	RC-IC	RC-PH	RC-RH
PC	PC-IC	PC-PH	PC-RH
PartC	PartC-IC	PartC-PH	PartC-RH

Table 2

Modelling hypotheses for performance preliminary assessment

Parameters	Unit	Value
Maximum molten salt temperature, T_{max}^{MS}	°C	565
Minimum molten salt temperature, T_{min}^{MS}	°C	290
Maximum pressure, p_{max}	MPa	25
Main compressor inlet temperature, T_{MCI}	°C	35
Pre-compressor inlet temperature, T_{PCI}	°C	35
Compressor isentropic efficiency, η_{comp}	%	89
Turbine isentropic efficiency, η_{tb}	%	93
Molten salt/CO ₂ heat exchanger minimum internal pinch, $\Delta T_{min}^{MS/CO_2}$	°C	5
CO ₂ /CO ₂ heat exchanger minimum internal pinch, $\Delta T_{min}^{CO_2/CO_2}$	°C	5
Molten salt /CO ₂ heat exchanger pressure drop (CO ₂ side), $\Delta p^{MS/CO_2}$	MPa	0.1
CO ₂ /CO ₂ heat exchanger pressure drop, $\Delta p^{CO_2/CO_2}$	MPa	0.1

source in the pre-heater before entering into the next recuperator (if any) or the main heater. (3) Reheating (RH) between high-pressure and low-pressure turbine is another classical approach to improve the cycle efficiency. These four fundamental cycles combined with IC, PH and RH, result in sixteen cycles as shown in Table 1. All the cycle layouts are shown in Annex A.

DESIGN BOUNDARY CONDITIONS AND HYPOTHESIS

This paper aims to present the SCO₂ cycle study for the current high-temperature CSP technology, i.e. Solar Salt tower technology. Therefore, Solar Salt's physical property and operation temperature range 290 °C and 565 °C is used to define the TES system, which serves as the design boundary condition for power block since TES system is the only interface between solar field and power block. The key hypothesis for cycle modeling and calculation is listed in Table 2.

MODELING AND STUDY APPROACH

1. Equipment Model

All the equipment model used in the cycle performance analysis is zero-dimension model based on energy balance equation. For cycle analysis, three types of equipment are needed: turbine, compressor and heat exchanger. Table 3 shows the governing equations used for them.

Table 3

Governing equations for main equipment

Equipment	Governing equations
Turbine	$W = \dot{m} \cdot (h_{in} - h_{out})$ $\eta_{turbine} = (h_{in} - h_{out}) / (h_{in} - h_{out, is})$
Compressor	$W = \dot{m} \cdot (h_{out} - h_{in})$ $\eta_{compressor} = (h_{out, is} - h_{in}) / (h_{out} - h_{in})$
Heat exchanger	$Q = \dot{m} \cdot (h_{out} - h_{in})$

For the heat exchanger model, in order to avoid internal pinch problem, discretized analysis is done for all the heat exchangers in the cycle. This analysis assumes that all the heat exchangers are counter-flow type. It gives the temperature distribution along the flow path, which helps to detect pinch problem and to keep the minimum pinch respect the pinch constraint in Table 2.

2. TES utilization

The TES utilization τ is defined as a ratio between utilized temperature range and allowed operation temperature range of the TES medium:

$$\tau = \frac{T_{upper}^{MS} - T_{lower}^{MS}}{T_{max}^{MS} - T_{min}^{MS}}$$

The allowed TES operation temperature range is defined based on the physical property of TES medium. For the commercially available Solar Salt currently used in CSP power plant, the allowed TES operation temperature range is between 290 °C and 565 °C. Therefore, if in a certain TES design, the Solar Salt leaves the hot storage tank at 500 °C and enters the cold storage tank at 300 °C, the TES utilization ratio, based on the definition above, is $(500 \text{ °C} - 300 \text{ °C}) / (565 \text{ °C} - 290 \text{ °C}) = 72.73\%$. TES utilization ratio could also be defined based on enthalpy, with no major impact on the conclusions obtained in this study.

3. Specific Power Output

The specific power output w is defined as the power output that could be generated from a specific mass of thermal storage:

$$w = \frac{P \cdot t_{storage}}{m_{storage}}$$

Where $m_{storage}$ is TES storage molten salt amount in mass, $t_{storage}$ is TES storage hour, P is cycle net power.

4. Efficiency

The efficiency η definition here does not take into account the auxiliary consumption or mechanical losses in the turbo-machineries:

$$\eta = \frac{\sum W_{turbine} - \sum W_{compressor}}{\sum Q_{in}}$$

Where $W_{turbine}$ is the turbine output power, $W_{compressor}$ is the compressor power consumption, Q_{in} is the heat duty of molten salt/CO₂ heat exchanger.

5. Cycle optimization

The algorithm used for cycle optimization is generalized reduced gradient method, together with stochastic initialization in order to avoid local optimum problem. For cycle optimization, the objective is to maximize the specific power output w while keeping the required TES utilization. The variables \vec{X} to be optimized are summarized in Table 4.

Then the optimization problem can be expressed as:

Table 4

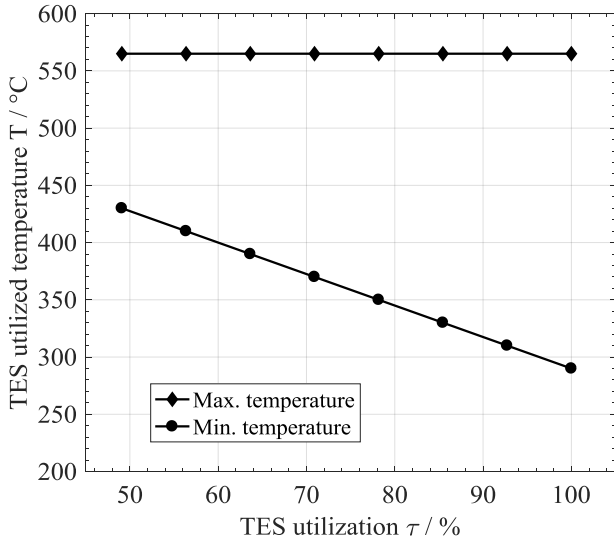
Governing equations for main equipment

Cycle	Variables to be optimized \vec{X} + (T_{upper}^{MS} , $T_{tb,inv}$, $T_{LTR,hot,out}$, p_{lower} , p_{upper} , \dot{m})
RG	-
RG-IC	p_{IC}
RG-PH	$\tau_{PH,split}$, $T_{HTR,hot,out}$
RG-RH	$\tau_{RH,split}^{MS}$, T_{RH} , p_{RH}
RC	$\tau_{RC,split}$, $T_{HTR,hot,out}$
RC-IC	$\tau_{RC,split}$, $T_{HTR,hot,out}$, p_{IC}
RC-PH	$\tau_{PH,split}$, $T_{HTR,hot,out}$, $\tau_{PH,split}$
RC-RH	$\tau_{RC,split}$, $T_{HTR,hot,out}$, $\tau_{RH,split}^{MS}$, p_{RH} , T_{RH}
PC	$T_{HTR,hot,out}$, CR_{PC}
PC-IC	$T_{HTR,hot,out}$, CR_{PC} , p_{IC}
PC-PH	$T_{HTR,hot,out}$, CR_{PC} , $\tau_{PH,split}$
PC-RH	$T_{HTR,hot,out}$, CR_{PC} , $\tau_{RH,split}^{MS}$, p_{RH} , T_{RH}
PartC	CR_{PC} , $\tau_{PC,out,split}$, $T_{HTR,hot,out}$
PartC-IC	CR_{PC} , $\tau_{PC,out,split}$, $T_{HTR,hot,out}$, p_{IC}
PartC-PH	CR_{PC} , $\tau_{PC,out,split}$, $T_{HTR,hot,out}$, $\tau_{PH,split}$
PartC-RH	CR_{PC} , $\tau_{PC,out,split}$, $T_{HTR,hot,out}$, $\tau_{RH,split}^{MS}$, p_{RH} , T_{RH}

$$Max. w(\vec{X})$$

Subject to

$$\left\{ \begin{array}{l} T_{upper}^{MS} \leq T_{max}^{MS} \\ T_{lower}^{MS} \geq T_{min}^{MS} \\ \tau_{TES} = \tau_{given} \\ \forall x \in \text{heat exchanger}, \Delta T_x \geq \Delta T_{min} \\ p_{upper} \leq p_{max} \\ \forall \tau, 1 \geq \tau \geq 0 \\ \forall CR, CR \geq 1 \end{array} \right.$$

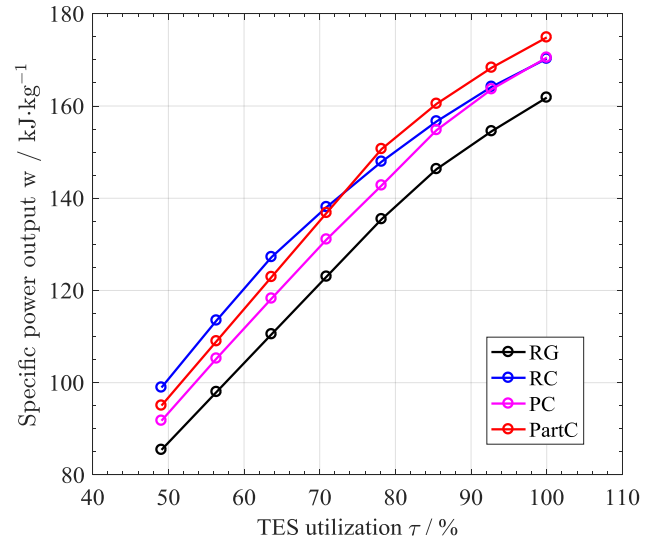
**Figure 1:** Effect of TES utilization on optimized TES utilized temperature range**RESULT AND DISCUSSION**

The optimization is done case by case and each optimization case is defined by cycle layout and TES utilization. The objective of optimization for every case is to maximize the power output from a specific amount of TES medium.

Figure 1 shows the final TES utilized temperature range given by the optimization for all the studied cases. The optimization results show that, for every cycle layout and every TES utilization, the maximum utilized temperature is always equal to the maximum allowable temperature, i.e. 565 °C for Solar Salt. This is not a surprising result, because for a thermodynamic cycle which transforms thermal energy into mechanical energy, it is always more favorable to use high-grade heat in order to maximize the cycle efficiency. Besides, high-temperature molten salt has a higher specific heat capacity than that of low-temperature molten salt. This is another reason that it is more advantageous to use high temperature molten salt in order to maximize the power output from molten salt.

Figure 2 shows that, for the fundamental cycles, the specific power output decreases monotonically when TES utilization decreases. The specific power output reaches its maximum at 100% TES utilization. Considering that the power output is the product of cycle efficiency and thermal power input into the cycle, the results means that the cycle efficiency gain due to lower TES utilization and higher grade of heat from TES is not sufficient to compensate the loss of TES utilization potential. A higher TES utilization results in a smaller TES system but a lower cycle efficiency of power block, which leads to a bigger solar field. The TES utilization is also closely related to the solar receiver efficiency which has an important impact on solar field. Therefore, TES utilization is an important factor to be optimized when integrating SCO_2 cycle with CSP.

Figure 3 shows the evolution of optimized cycle efficiency with respect to the TES utilization. With the decrease of TES utilization, for each cycle, the cycle efficiency increases

**Figure 2:** Effect of TES utilization on specific power output

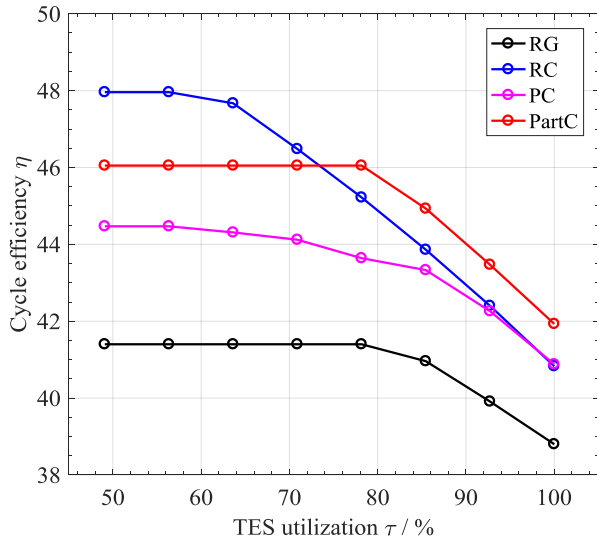


Figure 3: Effect of TES utilization on cycle efficiency for fundamental cycles

monotonically, mainly due to higher TIT temperature resulting from higher average heat source temperature. However, in general, except for reheating cycles, this trend could not be continued when it reaches its efficiency limit. The existence of this limit mainly comes from the fact that the TIT temperature could not be further increased any more when it reaches the temperature limit set by the heat source maximum temperature and the minimum pinch temperature allowed in the heat exchanger between heat source and CO₂. For reheating cycles, there are two turbines, one high-pressure turbine and one low-pressure turbine, with the same mass flow rate. As a result, there are two TITs to be maximized to the temperature limit, which leads to higher requirement on the heat source quality.

Table 5

Comparison between RG-FO and RG-PO cases (All extensive values are expressed as a ratio to that of RG-FO case)

		RG-FO	RG-PO
TIT	°C	504.23	560.00
TOT	°C	374.63	407.60
Pressure ratio	-	3.06	3.58
Cycle min. pressure	Bar	81.74	69.75
MCOT	°C	78.43	135.76
LTR UA	kW/°C	1.00	0.16
MH UA	kW/°C	1.00	4.47
Cooler UA	kW/°C	1.00	1.12
LTR heat duty	MW	1.00	0.52
MC work	MW	1.00	1.56
Turbine work	MW	1.00	0.97
MH heat duty	MW	1.00	1.00
Efficiency	%	38.80	31.30

Alternatively speaking, the efficiency limit of reheating cycle comes with a much lower TES utilization.

It is interesting to observe in Figure 4 that for high TES utilization level, TIT does not reach its upper limit to have the best cycle efficiency. Alternatively speaking, if TIT is set to its upper limit for high TES utilization, the cycle efficiency cannot reach its optimum. In order to keep TIT to its upper limit and reach a high TES utilization level, based on the general recuperation cycle layout, it requires the turbine to have a larger expansion ratio, then to have a larger temperature reduction through the turbine in order to have a better match with the TES low-end temperature. This makes the compressors have a higher compressor ratio and brings an extra constraint on the optimization of compressor operation condition, which results in higher compression energy consumption, and consequently, lower efficiency.

For RG cycle, a comparison for 100% TES utilization is shown in Table 5 between the full optimization case (RG-FO) and the partial optimization case (RG-PO). In the FO case, all the variables in Table 4 are optimized by the solver, but in the

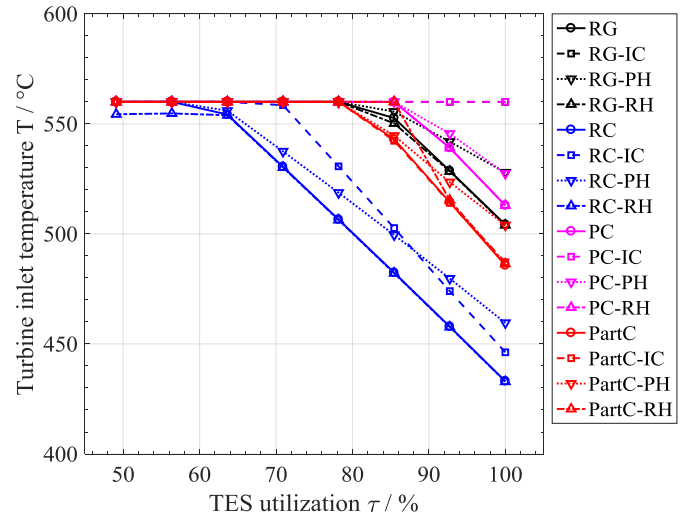


Figure 4: Effect of TES utilization on turbine inlet temperature

PO case, all are optimized except for TIT and TIT is set to be equal to the upper limit, i.e. 560 °C in this study. The final PO result shows that the cycle minimum pressure is optimized to be 69.75 bar. As a consequence, the main compressor has a higher compressor ratio of 3.58 and 56% higher compression work. This is the main reason that even with a higher TIT, the efficiency is only 31.30%, much lower than the FO case where the efficiency is 38.80%.

Among the four fundamental cycles, RG cycle, as the reference cycle, gives the lowest efficiency in the studied TES utilization range. RG gives efficiency of 38.80% at 100% TES utilization and the efficiency increases with the decrease of TES utilization and finally reach the highest efficiency of 41.40%. With pre-compression to solve the pinch problem in the recuperator, compared to RG cycle, PC cycle improves

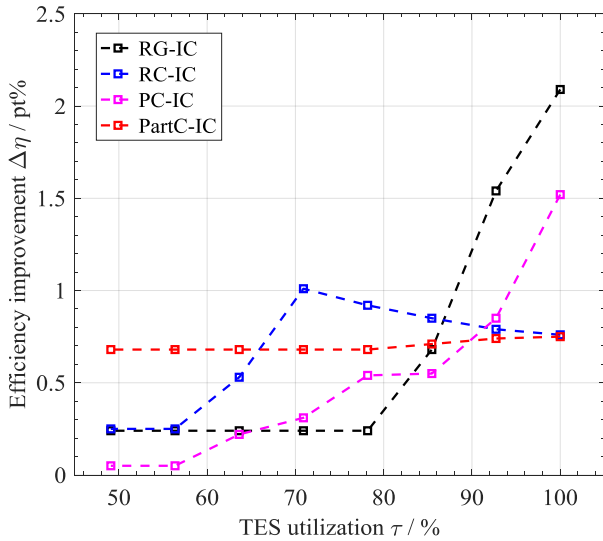


Figure 5: Effect of TES utilization on intercooling efficiency improvement effectiveness

significantly the efficiency, compared to RG cycle, +2 pt% at 100% TES utilization and +3 pt% at 49% TES utilization. RC cycle deals with the pinch problem by flow splitting. Comparing the optimization result of PC and RC cycle given in Figure 3, it is clear that flow splitting in RC cycle, in general, is a more efficient way to deal with this problem, which helps the cycle to recuperate better the exhaust heat from turbine outlet flow, especially in the region of low TES utilization. At 49% TES utilization, RC reaches the highest efficiency of 47.96%, +3.5% higher than PC cycle. PartC cycle outperforms the other three fundamental cycles in the region of high TES utilization. Compared to RC cycle, the efficiency improvement mainly comes from the fact that extra cooling at the outlet of low-temperature recuperator helps to increase the TIT while keeping the TES utilization at a high level. But high TIT and high TES utilization leads to a high compression ratio, which makes the cycle minimum pressure close to 60 bar.

This low pressure could make the operation of compressor very difficult. However, this extra cooling becomes a constraint for exhaust heat recuperation when TES utilization ratio is below 73%, therefore, RC cycle efficiency becomes higher than that of PartC cycle. When reaching the region of convergence, PartC achieves its highest efficiency of 46.05%, near -2% lower than RC cycle efficiency at convergence.

As shown by Figure 5, combining IC with the fundamental cycles could generally improve efficiency, especially at the high TES utilization region, because intercooling helps to reduce compressor outlet temperature, then better use the low-grade heat from heat source. In the meantime, as shown in Figure 4, it helps to reach a higher TIT with the same TES utilization. At the low TES utilization region, IC also helps on the efficiency improvement but less evidently. Since the intercooling is done on the compressor that operates on the whole flow for RG cycle and PC cycle, IC helps more significantly to increase the

efficiency, by +2.09 pt% at 100% TES utilization for RG cycle and by +1.52 pt% for PC cycle. For RC cycle, the highest IC improvement occurs at 71% TES utilization, near +1 pt%. The impact of IC on PartC cycle is almost constant for the studied range of TES utilization, with a maximum efficiency improvement of +0.75 pt% at 100% TES utilization.

As shown by Figure 6, combining PH with the fundamental cycles could improve efficiency, but only at the high TES utilization region. Because PH is designed to split part of the low-temperature flow during recuperation to recover the low-grade heat from heat source, it is not surprising that it could achieve a higher efficiency at high TES utilization. At low TES utilization, there is no lower grade heat that could match the temperature profile during recuperation, therefore, PH is not useful any more. PH helps significantly RC cycle to improve efficiency because RC cycle is not adapted to utilize low-grade heat. PartC cycle, with extra cooling before compression, compared to PartC cycle, could behave better with low-grade heat, therefore, the impact of PH on PartC is less evident. PH, with the flow splitting between recuperator, provide an

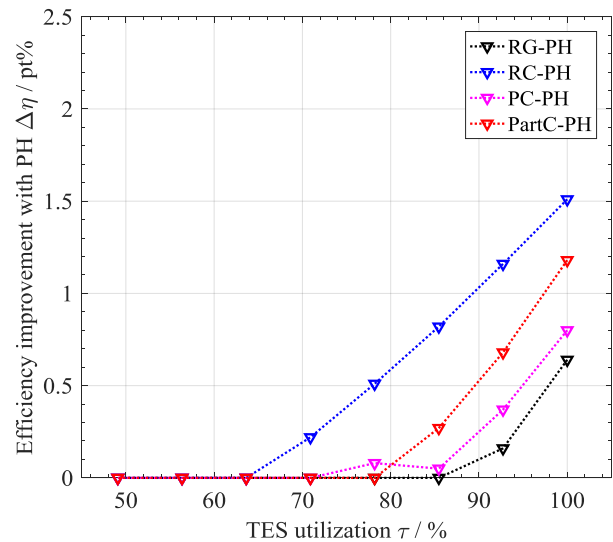


Figure 6: Effect of TES utilization on intercooling efficiency improvement effectiveness

additional approach for PC and RG cycle to improve the recuperation, therefore, improvement is also observed for these cycles.

As shown by Figure 7, combining RH with the fundamental cycles could improve efficiency, but only at the low TES utilization region, which is opposite to the effect of IC and PH. For RH, the molten salt flow is divided into two parts to heat the whole CO₂ flow at different locations. At high TES utilization, without additional measure, any effort to divide the molten salt into two is difficult for efficiency improvement because this leads to mismatch between the mass flow of molten salt and that of CO₂. With this mismatch, a higher CO₂ inlet temperature or a smaller CO₂ mass flow is required in order to achieve a better

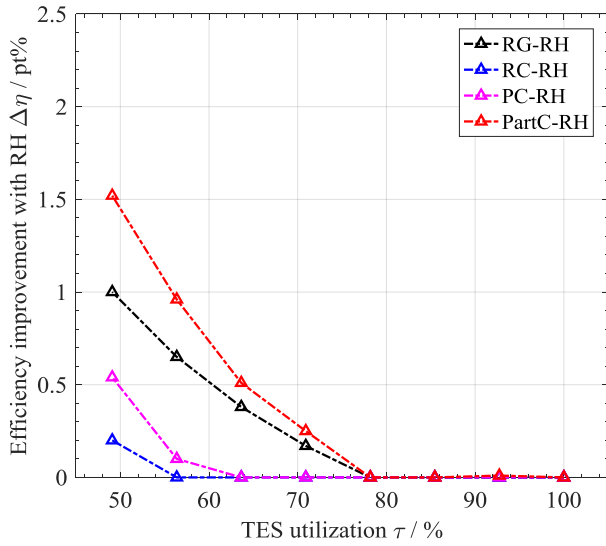


Figure 7: Effect of TES utilization on reheating efficiency improvement effectiveness

main heater effectiveness. In the first case where a higher main heater inlet temperature is required, it is necessary to have a high TOT, which has a negative impact on turbine power output then leads to efficiency loss. Besides, this is also limited by the high TES utilization requirement. In the second case where CO_2 mass flow should be reduced, in general, in order to still keep power output at a high level, it is necessary to reach a high cycle pressure ratio. Finally, the optimization is a balance between efficiency gain due to reheating and efficiency loss due to the necessity to keep a high TOT and a high pressure ratio. According to the results, the efficiency gain due to reheating dominates the trends when TES utilization is lower than 80%. Therefore, generally, RH is a measure to better use the high-grade heat when available. PartC cycle, due to the existence of extra cooling, it achieves a high cycle pressure ratio and a smaller CO_2 mass flow rate, then it is able to implement RH in an effective way and it helps the most for PartC cycle, because PartC cycle provides a more suitable structure to match the requirement of RH. RC cycle is more suitable for high-grade heat source. Because by flow splitting, it could achieve very effective recuperation of turbine exhaust heat, it tends to reach the highest possible main heater CO_2 inlet temperature. But for high TES utilization, this trend is limited by the molten salt outlet temperature. RH intensifies the same trends as RC cycle, with the constraint of TES utilization, it is not useful until very low TES utilization. According to the result, when TES utilization becomes smaller than 56%, RH becomes effective to the efficiency improvement. RG cycle is the basic cycle with poor recuperation and poor efficiency. Due to the poor recuperation, the main heater inlet temperature cannot be heated to the limit set by the turbine outlet temperature and pinch, therefore, there is still efficiency improvement margin for RH to be effective in RG cycle. In terms of recuperation effectiveness, PC cycle is

between RG and RC cycle, therefore, in average, the impact of RH on PC is between these two cycles.

Among all the cycle studies, as shown by Figure 8, for TES utilization between 100% and 93%, i.e. molten salt exhaust temperature between 290 °C and 310 °C, PartC-PH gives the highest efficiency from 43.11% to 44.16%. For TES utilization between 93% and 75%, i.e. molten salt exhaust temperature between 310 °C and 359 °C, PartC-IC gives the highest efficiency from 44.16% to 46.73%. For TES utilization between 75% and 49%, i.e. molten salt exhaust temperature between 359 °C and 430 °C, RC-IC gives the highest efficiency from 46.73% to 48.21%. For TES utilization below 49%, it is observed that RC-RH cycle efficiency continues to increase with the decrease of TES utilization. When TES utilization reaches approximately 45%, the RC-RH starts to outperform all the other cycles. Solar Salt is allowed to operate between 565 °C and 290 °C, but with less than 50% TES utilization, only half of the thermal storage potential is used, which means, compared to full utilization, TES system needs two times molten salt, much bigger molten salt storage tank and auxiliary systems, as a result, much larger investment. In this case, even with a higher cycle efficiency, there is no guarantee that it will be an optimal cycle for CSP project.

CONCLUSION

In this study, four fundamental SCO_2 cycles, together with twelve cycle derivatives are modeled, optimized and compared in the context of integrating SCO_2 cycle with high-temperature CSP technology which is currently available for industry, i.e. CSP with Solar Salt tower. Based on this comparison, the study focuses on understanding the cycle performance behaviors with different TES utilization. Main conclusions are drawn as follows:

- 1) It is always more favorable to use higher-temperature molten salt when available.
- 2) Lower TES utilization, i.e. higher molten salt exhaust temperature, helps to reach higher cycle thermal efficiency, but at the cost of reducing specific power output of thermal storage system. Alternatively speaking, with lower TES utilization, for the same size of thermal storage system, it can only produce less electricity, even with a higher cycle efficiency.
- 3) For high TES utilization, it is not always optimal for TIT to reach its upper temperature limit set by the maximum molten salt temperature.
- 4) Intercooling can help to improve cycle efficiency, and in general, it is more effective at high TES utilization.
- 5) Preheating can help to improve cycle efficiency, but only at high TES utilization. For the considered cycles in this study, when TES utilization is lower than 64%, preheating could not help any more for efficiency improvement.
- 6) Reheating can help to improve cycle efficiency, but only at low TES utilization. For PartC cycle and RG cycle, it starts to be effective when TES utilization is lower than 78%. For PC cycle, it starts to be effective

when TES utilization is lower than 64%. For RC cycle, it starts to be effective when TES utilization is lower than 56%.

- 7) Among all the considered cycles, in terms of efficiency, PartC-PH cycle is optimal for TES utilization between 100% and 93%; ParC-IC cycle is optimal for TES utilization between 93% and 75%; RC-IC cycle is optimal for TES utilization between 75% and 49%.

In a conclusion, TES utilization is an important factor when integrating SCO₂ cycle with CSP, because it serves as the key interface parameter between solar field, TES and power block. As shown by this study, it has an important impact on the selection of SCO₂ cycle for CSP. It is also evident that TES utilization, together with other key parameters such as storage hour and design net power output, directly determine the size of TES system. In the meanwhile, TES utilization influences directly the receiver thermal loss and indirectly the size of solar field via thermal cycle efficiency. Therefore, keeping TES utilization as a factor to be optimized, a global study that takes solar field and TES system into account should be further done to analyze the performance of SCO₂ cycle.

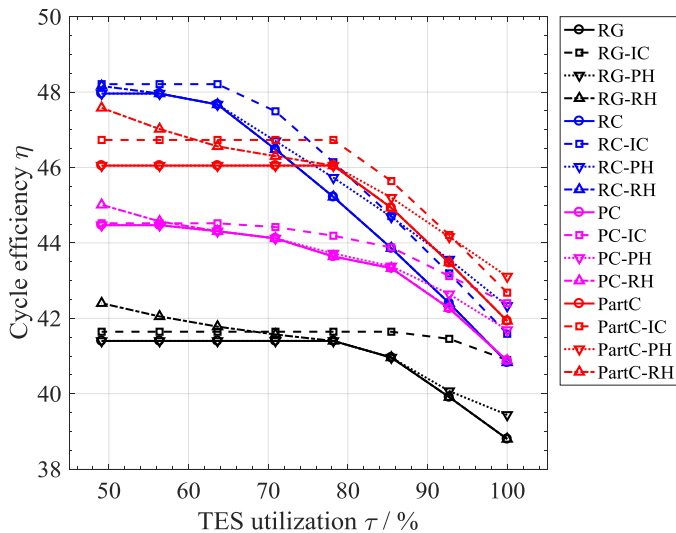


Figure 8: Effect of TES utilization on reheating efficiency improvement effectiveness

NOMENCLATURE

Symbols	
CR	compression ratio
P	power (MW)
p	pressure (MPa)
Q	heat duty (MW)
T	temperature (°C)
W	turbine/compressor work (MW)
Greek symbols	
η	efficiency

τ	split ratio
Abbreviations	
AC	auxiliary compressor
C	cooler
CO ₂	Carbon dioxide
CSP	concentrated solar power
FO	full optimization
HTR	high temperature recuperator
IC	intercooling
LCOE	Levelized cost of electricity
LTR	low-temperature recuperator
MC	main compressor
MH	main heater
PartC	partial cooling
PC	pre-compression / pre-compressor
PH	Preheating / preheater
PO	partial optimization
RC	recompression
RG	regenerative
RH	reheating
SCO ₂	supercritical CO ₂
TES	thermal energy storage
TIT	turbine inlet temperature
TOT	turbine outlet temperature
Subscripts/superscripts	
cold	cold side flow of heat exchanger
Hot	hot side flow of heat exchanger
in	inlet flow
MS	molten salt
out	outlet flow
split	flow split
tb	turbine

REFERENCES

- [1] Liu S, Bie Z, Lin J, Wang X. Curtailment of renewable energy in Northwest China and market-based solutions. *Energy Policy* 2018;123:494–502. doi:10.1016/j.enpol.2018.09.007.
- [2] Turchi CS. Supercritical CO₂ for Application in Concentrating Solar Power Systems. *Supercrit. CO₂ power cycle Symp.* Troy, New York, 2009.
- [3] Glatzmaier GC, Turchi CS. Supercritical CO₂ as a Heat Transfer and Power Cycle Fluid for CSP Systems. *ASME Int. Conf. energy Sustain.* San Fr., 2009. doi:10.1115/es2009-90332.
- [4] Ma Z, Turchi CS. Advanced Supercritical Carbon Dioxide Power Cycle Configurations for Use in Concentrating Solar Power Systems. *Supercrit. CO₂ power cycle Symp.* Boulder, Color., 2011.
- [5] Turchi CS, Ma Z, Dyreby J. Supercritical Carbon Dioxide Power Cycle Configurations for Use in Concentrating Solar Power Systems. *ASME Turbo Expo, Copenhagen, Denmark, 2012.* doi:10.1115/GT2012-68932.
- [6] Neises T, Turchi CS. Supercritical carbon dioxide power cycle design and configuration optimization to minimize levelized cost of energy of molten salt power

- towers operating at 650°C. *Sol Energy* 2019;181:27–36. doi:10.1016/j.solener.2019.01.078.
- [7] Feher EG. The supercritical thermodynamic power cycle. *Energy Convers* 1968;8:85–90. doi:10.1016/0013-7480(68)90105-8.
- [8] Angelino G. Real Gas Effects in Carbon Dioxide Cycles. ASME Gas turbine Conf. Prod. show, Cleveland, Ohio, 1969. doi:10.1115/69-gt-102.
- [9] Ahn Y, Bae SJ, Kim M, Cho SK, Baik S, Lee JI, et al. Review of supercritical CO₂ power cycle technology and current status of research and development. *Nucl Eng Technol* 2015;47:647–61. doi:10.1016/j.net.2015.06.009.
- [10] Dostal V. A Supercritical Carbon Dioxide Cycle for Next Generation Nuclear Reactors. Massachusetts Institute of Technology, 2004.
- [11] Angelino G. Perspectives for the Liquid Phase Compression Gas Turbine. *J Eng Gas Turbines Power* 1967;89:229–36. doi:10.1115/1.3616657.
- [12] Angelino G. Carbon dioxide condensation cycles for power production. *J Eng Gas Turbines Power* 1968;90:287–95. doi:10.1115/1.3609190.
- [13] Yamaguchi H, Zhang XR, Fujima K, Enomoto M, Sawada N. Solar energy powered Rankine cycle using supercritical CO₂. *Appl Therm Eng* 2006;26:2345–54. doi:10.1016/j.applthermaleng.2006.02.029.
- [14] Zhang XR, Yamaguchi H, Uneno D. Experimental study on the performance of solar Rankine system using supercritical CO₂. *Renew Energy* 2007;32:2617. doi:10.1016/j.renene.2007.01.003.
- [15] Zhang XR, Yamaguchi H. An experimental study on evacuated tube solar collector using supercritical CO₂. *Appl Therm Eng* 2008;28:1225–33. doi:10.1016/j.applthermaleng.2007.07.013.
- [16] Neises T, Turchi CS. A comparison of supercritical carbon dioxide power cycle configurations with an emphasis on CSP applications. *Energy Procedia* 2013;49:1187–96. doi:10.1016/j.egypro.2014.03.128.
- [17] Le Moullec Y. Conceptual study of a high efficiency coal-fired power plant with CO₂ capture using a supercritical CO₂ Brayton cycle. *Energy* 2013;49:32–46. doi:10.1016/j.energy.2012.10.022.
- [18] Mecheri M, Le Moullec Y. Supercritical CO₂ Brayton cycles for coal-fired power plants. *Energy* 2016;103:758–71. doi:10.1016/j.energy.2016.02.111.
- [19] Xu J, Sun E, Li M, Liu H, Zhu B. Key issues and solution strategies for supercritical carbon dioxide coal fired power plant. *Energy* 2018;157:227–46. doi:10.1016/j.energy.2018.05.162.
- [20] Lehar MA, Michelassi V. System and method for recovery of waste heat from dual heat sources. U.S. Patent No. 9038391, 2012.
- [21] Timothy J. Held. Supercritical CO₂ cycles for gas turbine combined power plants. Power Gener. Int. Las Vegas, Nevada, 2014.
- [22] Huck P, Freund S, Lehar M, Peter M. Performance comparison of supercritical CO₂ versus steam bottoming cycles for gas turbine combined cycle applications. 5th Int Symp - SCO₂ Power Cycles2 2016. doi:10.1017/CBO9781107415324.004.
- [23] Chacartegui R, Muñoz De Escalona JM, Sánchez D, Monje B, Sánchez T. Alternative cycles based on carbon dioxide for central receiver solar power plants. *Appl. Therm. Eng.*, 2011. doi:10.1016/j.applthermaleng.2010.11.008.
- [24] Dunham MT, Iverson BD. High-efficiency thermodynamic power cycles for concentrated solar power systems. *Renew Sustain Energy Rev* 2014;30:758–70. doi:10.1016/j.rser.2013.11.010.
- [25] Cheang VT, Hedderwick RA, McGregor C. Benchmarking supercritical carbon dioxide cycles against steam Rankine cycles for Concentrated Solar Power. *Sol Energy* 2015;113:199–211. doi:10.1016/j.solener.2014.12.016.
- [26] Al-Sulaiman FA, Atif M. Performance comparison of different supercritical carbon dioxide Brayton cycles integrated with a solar power tower. *Energy* 2015;82:61–71. doi:10.1016/j.energy.2014.12.070.
- [27] Wang K, He YL, Zhu HH. Integration between supercritical CO₂ Brayton cycles and molten salt solar power towers: A review and a comprehensive comparison of different cycle layouts. *Appl Energy* 2017;195:819–36. doi:10.1016/j.apenergy.2017.03.099.
- [28] Wang K, Li MJ, Guo JQ, Li P, Liu Z Bin. A systematic comparison of different S-CO₂ Brayton cycle layouts based on multi-objective optimization for applications in solar power tower plants. *Appl Energy* 2018;212:109–21. doi:10.1016/j.apenergy.2017.12.031.
- [29] Guo J-Q, Li M-J, Xu J-L. Performance comparison of SPT systems integrated with various supercritical CO₂-based mixture Brayton cycles based on multi-objective optimization. *Energy Procedia* 2019;158:1823–8. doi:10.1016/j.egypro.2019.01.427.

ANNEX A

FUNDAMENTAL SCO_2 CYCLES AND THEIR DERIVATIVES

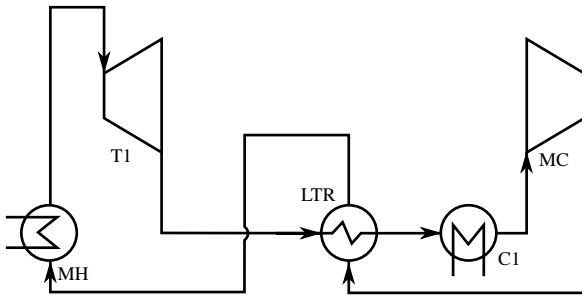


Figure 9: Regenerative (RG) cycle

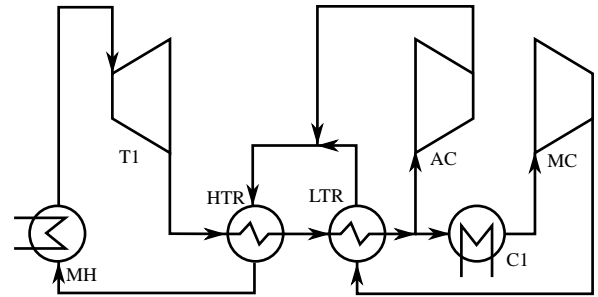


Figure 13: Recompression (RC) cycle

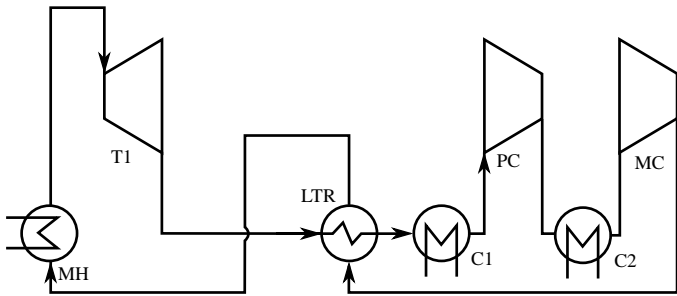


Figure 10: Regenerative (RG) cycle with intercooling (IC)

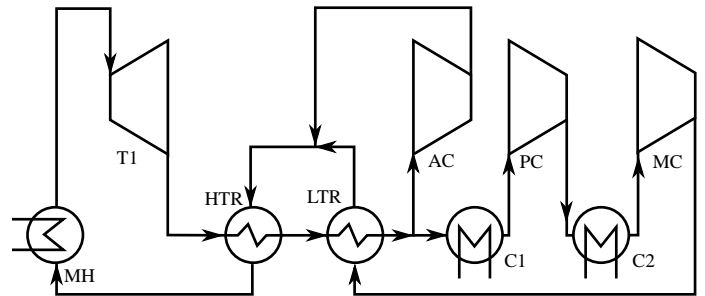


Figure 14: Recompression (RC) cycle with intercooling (IC)

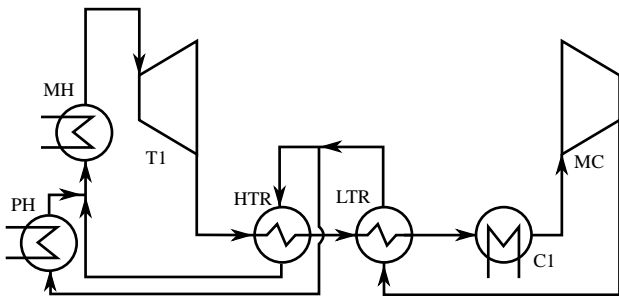


Figure 11: Regenerative (RG) cycle with preheating (PH)

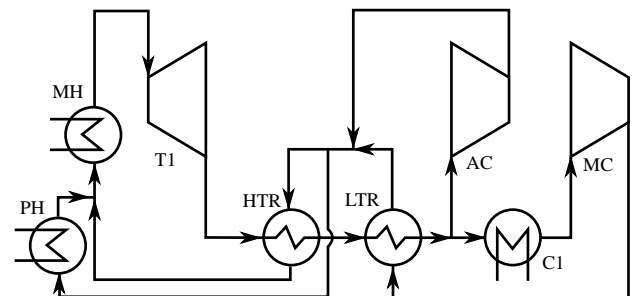


Figure 15: Recompression (RC) cycle with preheating (PH)

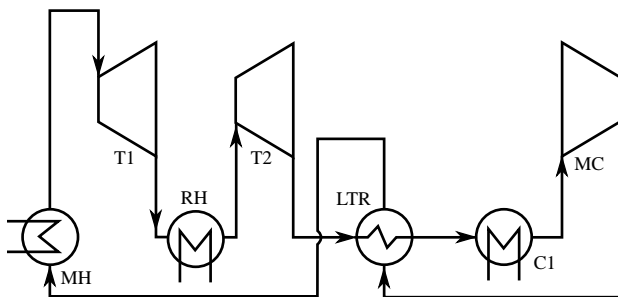


Figure 12: Regenerative (RG) cycle with reheating (RH)

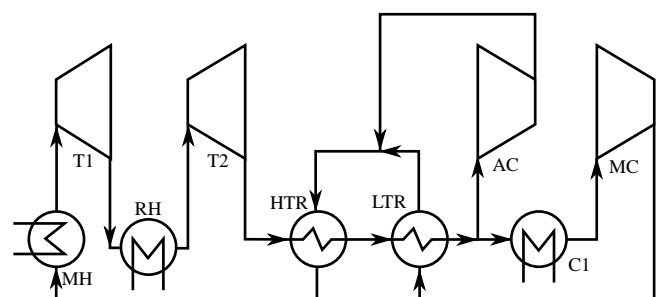


Figure 16: Recompression (RC) cycle with reheating (RH)

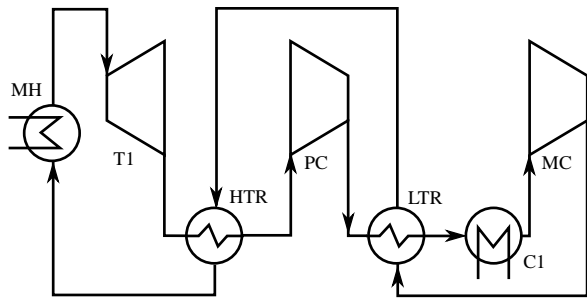


Figure 17: Pre-compression (PC) cycle

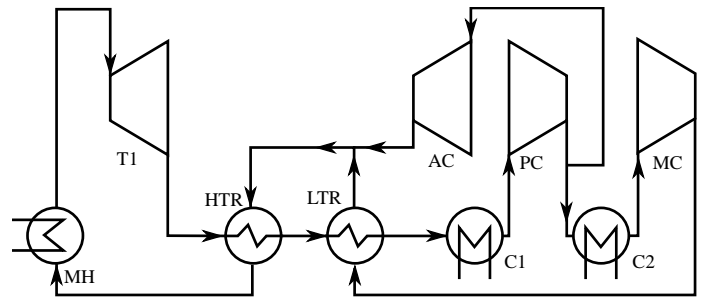


Figure 21: Partial cooling (PartC) cycle

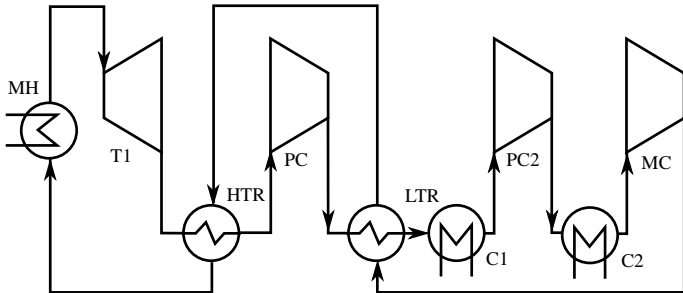


Figure 18: Pre-compression (PC) cycle with intercooling (IC)

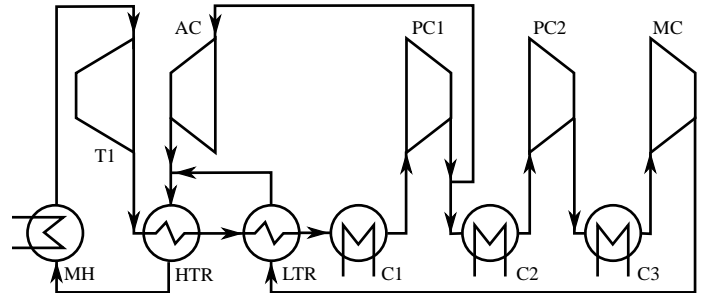


Figure 22: Partial cooling (PartC) cycle with intercooling (IC)

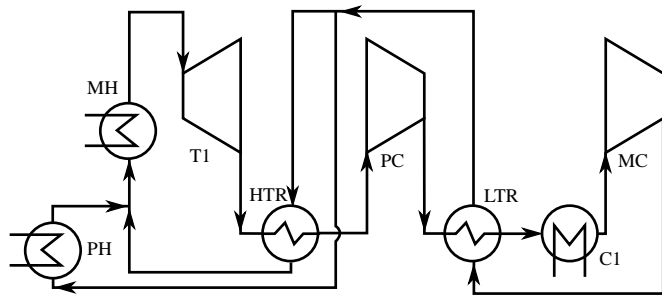


Figure 19: Pre-compression (PC) cycle with preheating (PH)

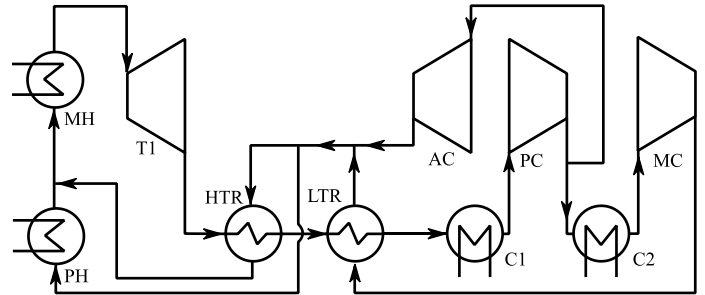


Figure 23: Partial cooling (PartC) cycle with preheating (PH)

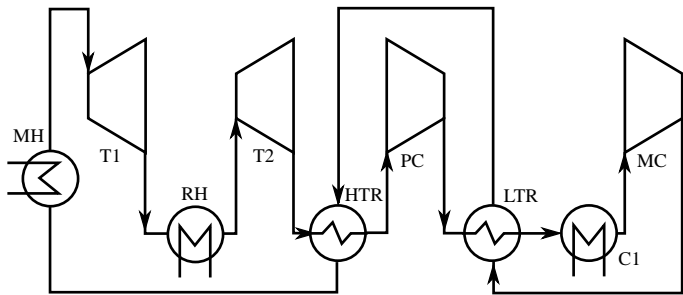


Figure 20: Pre-compression (PC) cycle with reheating (RH)

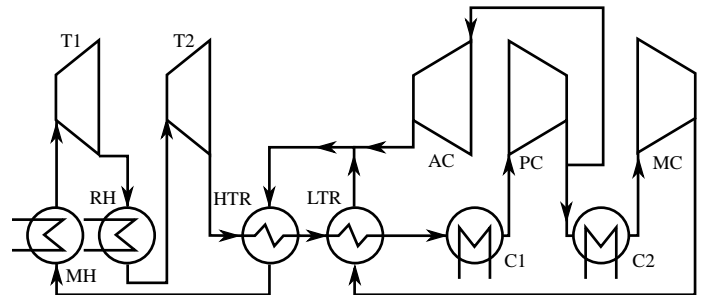


Figure 24: Partial cooling (PartC) cycle with reheating (RH)

DEVELOPMENT AND POWER GENERATING OPERATION OF THE SUPERCRITICAL CARBON DIOXIDE POWER CYCLE EXPERIMENTAL TEST LOOP IN KIER

Junhyun Cho*
Korea Institute of Energy
Research
Daejeon, South Korea
jhcho@kier.re.kr

Hyungki Shin
Korea Institute of Energy
Research
Daejeon, South Korea

Jongjae Cho
Korea Institute of Energy
Research
Daejeon, South Korea

Bongsu Choi
Korea Institute of Energy
Research Daejeon, South
Korea

Chulwoo Roh
Korea Institute of
Energy Research
Daejeon, South
Korea

Beomjoon Lee
Korea Institute of
Energy Research
Daejeon, South
Korea

Gilbong Lee
Korea Institute of
Energy Research
Daejeon, South
Korea

Ho-Sang Ra
Korea Institute of
Energy Research
Daejeon, South
Korea

Young-Jin Baik
Korea Institute of
Energy Research
Daejeon, South
Korea

ABSTRACT

Korea Institute of Energy Research Institute (KIER) develops three supercritical carbon dioxide power cycle (S-CO₂) experimental test loops: kWe, tens of kWe and hundreds of kWe class. First, a 4.5 kWe single radial-type turbo-generator with a labyrinth seal and an angular contact ball bearing was developed to operate a simple recuperated transcritical cycle. A 86 We of electric power was obtained during 30 minutes under a 320°C of turbine inlet condition. Second, a 60 kWe single stage axial impulse-type turbo-generator with a conventional carbon floating ring seal and oil-lubricated tilting-bearings was developed. A 10 kW of electric power was obtained during 4.2 hours by operating on the simple transcritical cycle using a liquid CO₂ pump. A 212°C of temperature and 123 bar of pressure were maintained at the turbine inlet. A continuous closed loop was successfully operated by adding a leakage make-up loop. Third, a 120 kWe dual Brayton test loop for a 500°C and a 130 bar of turbine inlet conditions is now being developed. A flue-gas heater, a centrifugal compressor with a dry gas seal and two recuperators were developed, now, these components are being commissioned respectively.

INTRODUCTION

Researchers have studied the supercritical CO₂ (S-CO₂) cycle as a promising power cycle technology that has benefits of improved thermal efficiency, reduction in size, LCOE (Levelized cost of electricity), water use, quick response time, and various conventional and renewable heat sources applications. USA is now constructing a 10 MWe indirect S-

CO₂ pilot plant operated by GTI, Southwest Research Institute (SwRI) and GE Global Research with support from U.S. Department of Energy/National Energy Technology Laboratory (U.S. DOE/NETL) [1]. The Southwest Research Institute and GE Global Research have been designing a 10 MWe S-CO₂ turbo-expander as a Sunshot program which 700°C turbine inlet temperature and are commissioning it at a 1 MWe testing facility [2]. Naval Nuclear Laboratory previously Bechtel Marine Propulsion Co. has developed a 100 kWe test loop for marine application and is testing a dynamic performance of the component and the cycle [3]. Peregrine Turbine Technologies has developed a 1 MWe S-CO₂ turbopump and is testing the device on the test loop facility of the Sandia National Laboratory [4]. Echogen has developed and tested an 8 MW S-CO₂ system and now is developing a 1.3 MWe leak-free S-CO₂ system [5].

A direct-fired S-CO₂ cycle as known as Allam cycle, NetPower collaborated with Toshiba is now commissioning a 50 MWth demo plant [6]. KEPCO (Korea Electric Power Corporation) with Hanhwa Power system have started project to develop 10 MWe-class direct-fired S-CO₂ system [7].

The Korea Institute of Energy Research (KIER) is operating two lab-scale S-CO₂ experimental test loops which are 500°C-kWe-class and 200°C-tens of kWe-class and is now constructing the final 500°C-hundreds of kWe-class test loop consists of two axial-type turbines for distributed power source applications. In 2017, preliminary electricity generation tests of both test loops were successful. A 287 We electricity was obtained from kWe-class radial type turbo-generator under 400°C/112bar turbine inlet conditions. A 10 kWe electricity

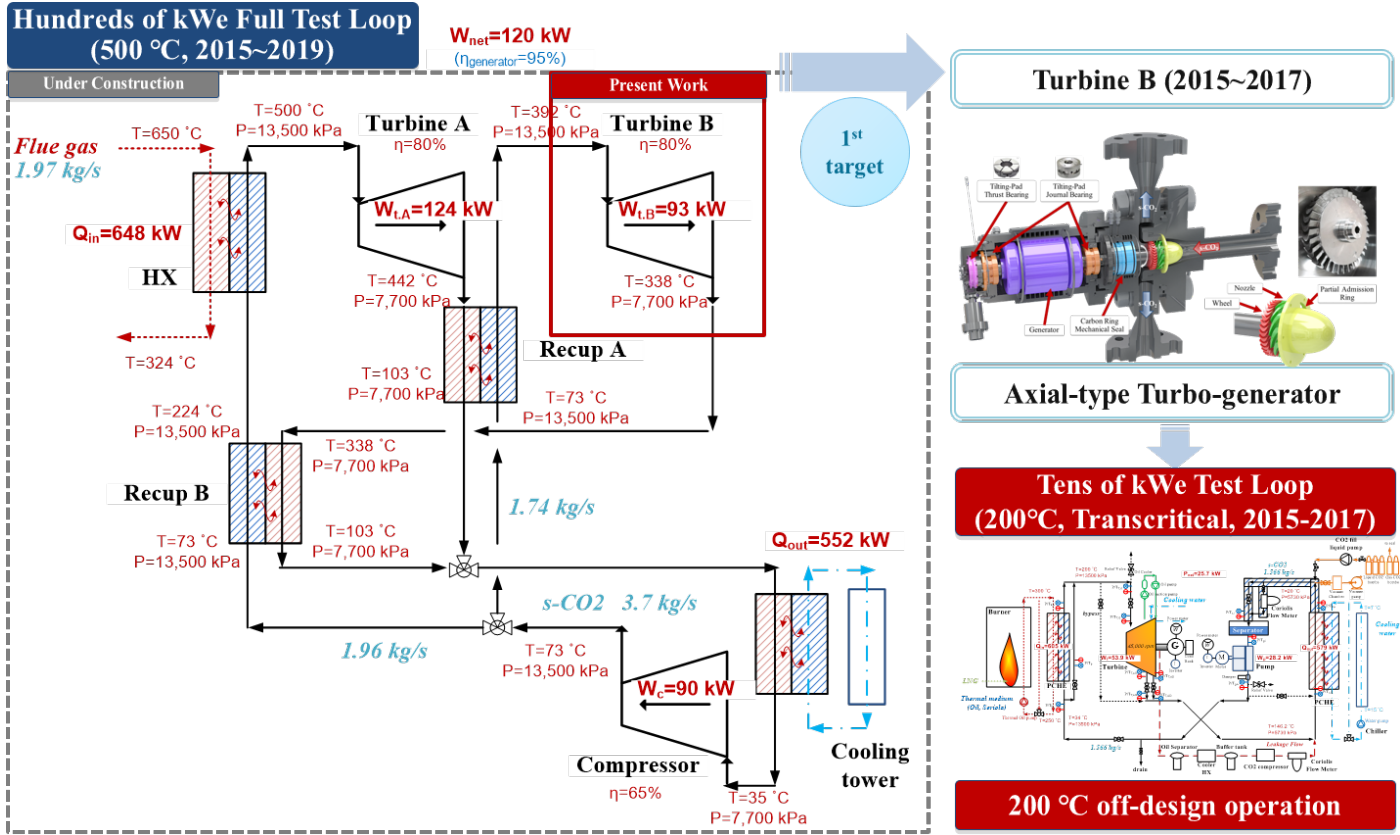


Figure 1: KIER hundreds kWe-class S-CO₂ dual Brayton cycle test loop and construction strategy [8]

was obtained from tens of kWe-class axial type turbo-generator under 205°C/100bar [8].

In this paper, first, the target final 500°C-hundreds of kWe-class test loop cycle configuration and development strategy are presented. After that, continuous power generating operation results of tens of kWe-class transcritical cycle with an axial-type turbo-generator for 200°C turbine inlet temperature is described. Then, continuous power generating operation results of a kWe-class transcritical cycle with a radial-type turbo-generator for 500°C turbine inlet temperature are presented. Finally, back to the first, development of key components for the final test loop are described.

HUNDREDS OF KWE-CLASS TEST LOOP (FULL CYCLE)

KIER designed a hundreds kWe-class test loop with a turbine inlet temperature of 500°C, as described on the left of Fig. 1. This cycle consists of two turbines, one compressor, two recuperators, and a flue-gas heater.

In case of fuel-fired heat source such as a biomass, waste heat recovery and a bottoming cycle which the heat of the wide temperature range of the heat source has to be utilized, higher power of the cycle is preferred rather than the cycle efficiency. In this study, as shown in Fig.1, the cascade-type Brayton cycle

is designed with two turbines described as a turbine A and B. To design and manufacture realistic components under limited budget, mass flow rate of the cycle which determines capacity of each component is determined as a 3.7 kg/s for the sake of manufacturable compressor impeller blade height and operable rotating speed limited by a bearing and a seal.

The maximum cycle pressure/temperature was determined as 135 bar/500°C, which is a similar level to the world’s optimal operating conditions, as reported by the Sandia National Laboratory. The efficiency of the compressor and two turbines are determined to 65% and 80% respectively which are realistic values from previous researches. Detailed descriptions of the cycle are presented in our reference [11]

Because a great deal of cost and time is required to construct a full cycle test loop, as a phased approach, a relatively low-temperature turbine with an inlet temperature of 392°C, described as turbine B in the schematic, was designed and manufactured as an axial impulse-type turbo-generator, as illustrated on the right of Fig. 1. In order to drive this turbine, a tens of kWe-class transcritical test loop was developed using existing 300°C-class heat source and pumping facilities. Because our heat source temperature is limited to 300°C, the turbine was tested at an inlet temperature of 200°C, which is the off-design condition. During construction of the entire test

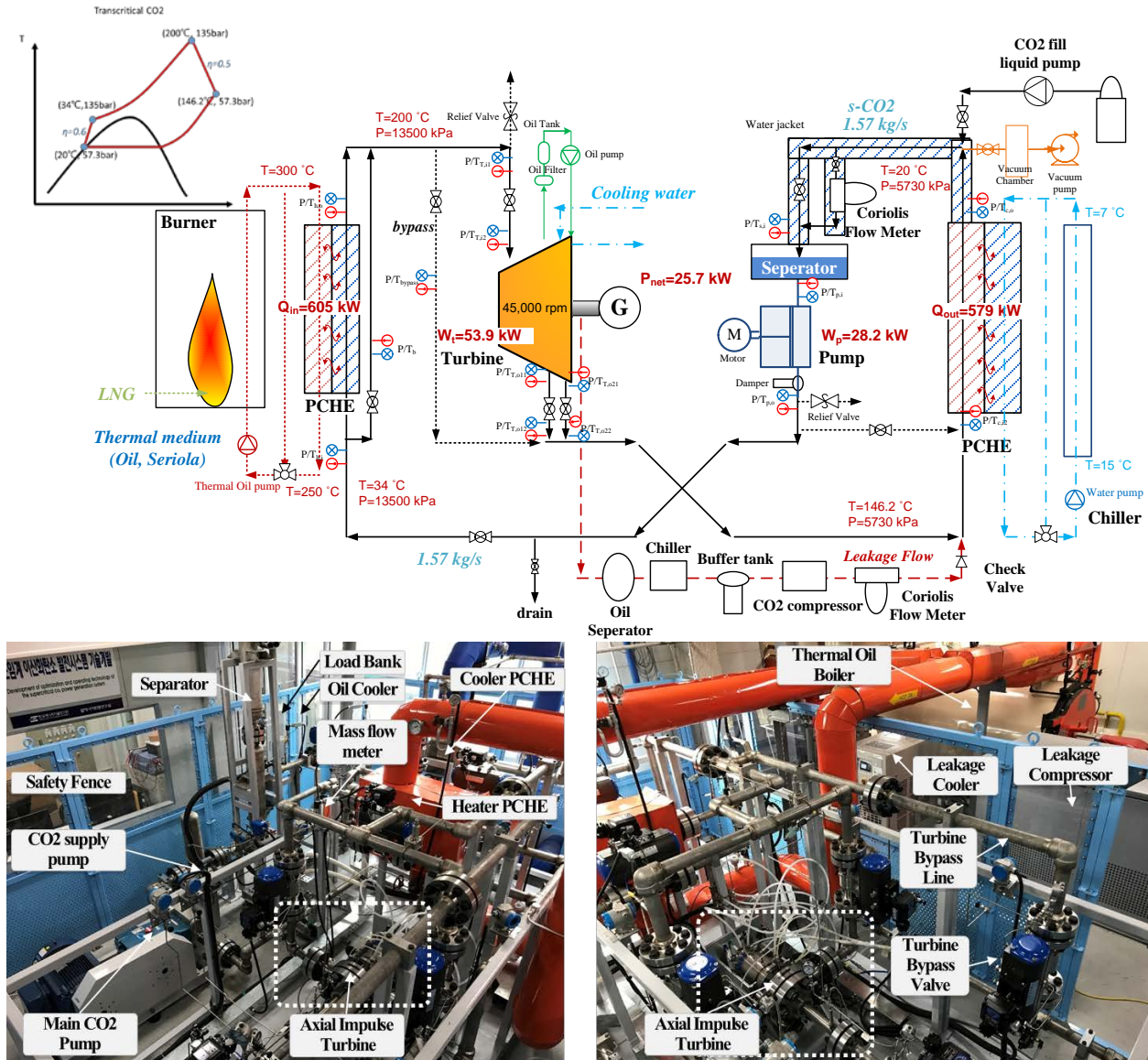


Figure 2: A Transcritical supercritical CO₂ power cycle test loop [8]

loop, by operating this turbine B, we could determine the cycle characteristics and improve the design of the test loop, including the axial turbo-generator and its components such as bearings, seals, rotordynamics and leakage management. After preliminary power generating operation implemented in 2017 [8], in this study, the design of test loop and turbo-generator is reviewed and continuous operation results are presented.

AXIAL-TYPE TURBO-GENERATOR (TURBINE B)

In order to overcome reported gas-foil bearing failure problems of the radial-type turbine induced by high rotational speed and axial force [9], an axial-type impulse turbine and partial admission nozzle was designed and manufactured to reduce axial force and the rotational speed by up to 45,000 RPM. A carbon ring-type mechanical seal and conventional oil-

lubricated tilting-pad journal and thrust bearings were used. A mean diameter of turbine wheel was 73 mm and the blade height was 8.36 mm. A 60 kWe permanent magnet (PM) generator type was also designed. Using an axial-type turbine with a mechanical seal similar to the dry-gas -seal and oil-lubricated bearings, the design is meaningful as it can be applied to further MW-scale turbo-generator designs. Details were described in our other reference [10].

TENS OF KWE-CLASS TRANSCRITICAL TEST LOOP FOR DRIVING AXIAL-TYPE TURBO-GENERATOR AT 200°C

As the first step to developing an S-CO₂ power cycle, a transcritical S-CO₂ power cycle was constructed at the turbine

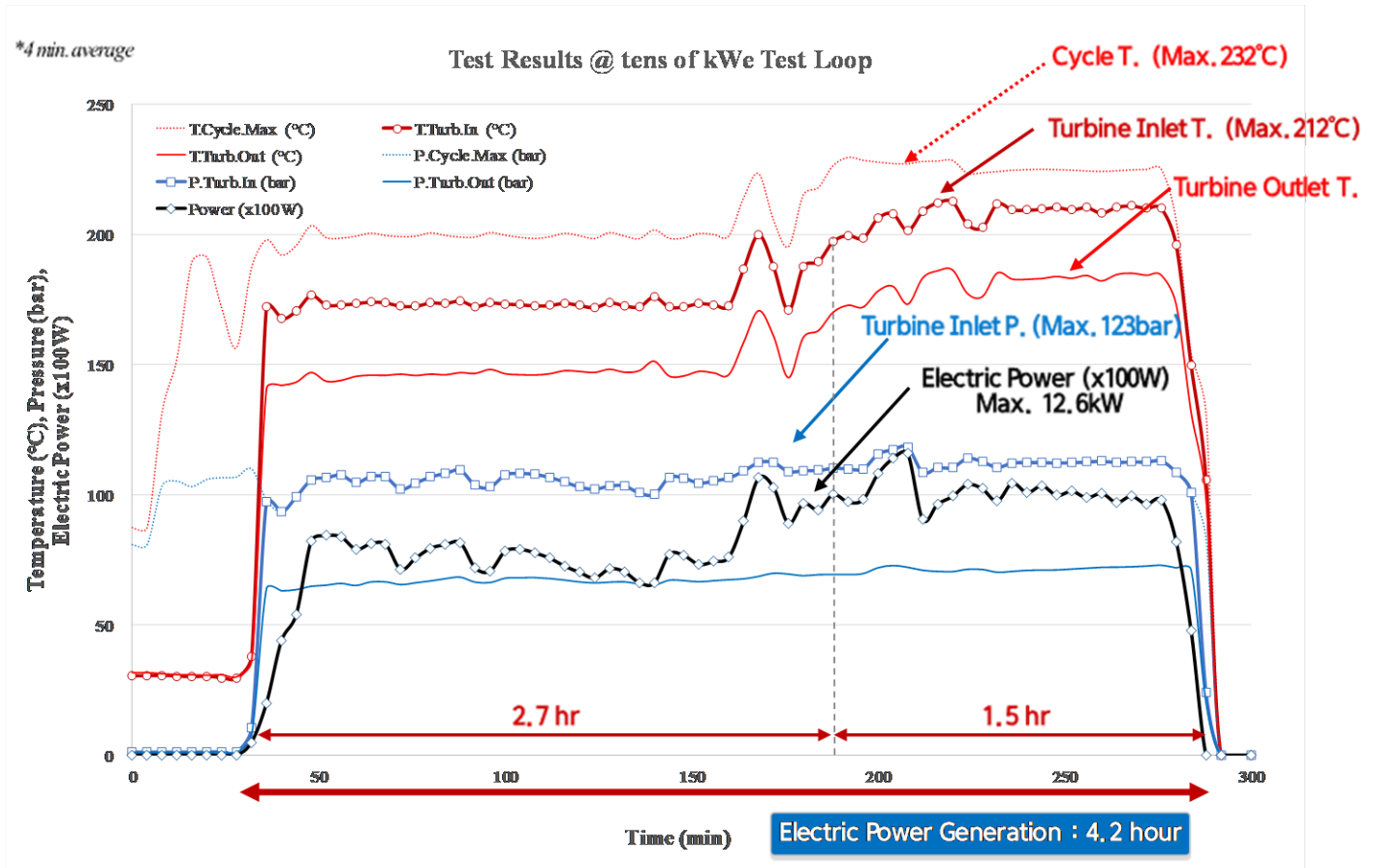


Figure 3: A 4.2 hours continuous power generating operation result [11]

inlet at 200°C in one step. For this purpose, the turbo-generator originally designed and manufactured under the target condition of 392°C is operated for off-design operation at 200°C. An un-recuperated transcritical cycle test loop neglecting the cycle efficiency was designed and fabricated, as illustrated in Fig. 2.

The maximum temperature was 200°C as the first step target, which is a relatively mild condition for the system. Liquid CO₂ at 20°C, 57 bar, and 1.57 kg/s was pressurized into a supercritical state at 135 bar using a plunger-type reciprocating liquid CO₂ pump (Catpumps, USA) with an inverter-controlled electric motor in order to test the various flow conditions. An LNG-fired thermal oil boiler heated the CO₂ to 200°C through a printed circuit heat exchanger (PCHE), and after driving the turbine the CO₂ was cooled through the PCHE.

In order to use a technically stable oil-lubricated bearing, a floating carbon ring type mechanical seal was installed in the turbo-generator, which inevitably leads to turbine leakage flow. In the current turbo-generator design, a 2 to 3% leakage flow was estimated; therefore, the leakage management system was constructed to re-inject CO₂ into the system. An oil separator, cooler, and buffer tank were constructed for cooling the hot leakage flow and removing incoming bearing oil. A three-stage

reciprocating oil-free-type CO₂ compressor was constructed for pressurizing up to 80 bar in order to recharge the atmospheric leakage flow into the main loop. The leakage flow amount was measured with a Coriolis mass flow meter. Also, details of test loops are described in our reference [8, 11].

CONTINUOUS POWER GENERATING OPERATION RESULTS (AXIAL TURBO-GENERATOR, TURBINE B)

For the operation of the cycle and turbo-generator, the test loop was assembled, and the leakage and hydraulic pressure test were carried out using nitrogen. Thereafter, each component, such as auxiliary equipment for turbine driving, a main pump, boiler, chiller, leakage management system, CO₂ supply system, control, and measurement. A vacuum pump was used to remove all air in the test loop, and the vacuum level was approximately 1.33 Pa. Following this, CO₂ was filled into the system. The amount of working fluid in the closed cycle was an important factor in the system operation. The CO₂ filling mass in the system was determined while monitoring the temperature and pressure through the preliminary operation.

After operating the system through the turbine bypass valve and confirming the S-CO₂ cycle configuration, the turbine inlet and outlet valves were opened and the bypass valve was closed, allowing S-CO₂ to drive the turbine. The

operation procedure and strategy for bearing oil lubrication, the mechanical seal barrier gas supply, turbine leakage re-injection system, and inverter driving start were developed and operated. As a result of the high operating pressure of above 57 bar, a high axial force occurred at the thrust bearing. In order to overcome the maximum static friction force of the bearing at the start, before the turbine valves opened, the turbo-generator was driven by the inverter at 30,000 RPM. [8]

Figure 3 displays the continuous experimental results of the electric power production operation. The turbine output was adjusted by controlling the main CO₂ pump speed, boiler heating temperature, re-injection/make-up amount of CO₂ and load of the load bank. An average of 10 kWe of electric power (Max. 12.6 kWe), measured by the power meter, was obtained at a maximum turbine inlet temperature of 212°C and pressure of 123 bar, and the continuous operation time of the turbine power production was 4.2 hours. Our target was 2 hours. From the start operation, the temperature of the turbine inlet is maintained below 200°C for safe continuous operation to check all parameters of the test loop. Vibration level of the rotor was stable, pressure and temperature conditions at each part of the test loop were well controlled. The temperature of the bearing was stable under 60°C.

The turbine leakage from the seal was larger than the estimation at the start before heat-up, as the turbine body was heated up leakage flow decreases. Because the turbine B was designed at the temperature of 392°C, the leakage flow passage was designed suitable for original operating conditions. So, leakage mass flow rate was inevitably larger than the design value at relatively low temperature condition in this test. Also, the mass flow rate of the leakage compressor was designed at the conditions of 392°C operation that leakage flow was estimated as a 2-3% of the main stream, so in this low temperature off-design operation, the mass flow rate exceeded over capacity of the leakage compressor. Therefore, the back pressure was increased up to 8 bar at the mechanical seal flow passage, so injection pressure of the barrier CO₂ gas from the gas tank was increased to above 9 bar. In addition, bypass line was installed between the turbine leakage outlet and the leakage compressor inlet to throw away the excess leakage flow from the seal. So, the charging mass in the test loop was slightly decreased during operation. Therefore, the CO₂ was continuously refilled using a filling liquid pump from the liquid CO₂ tank.

After 2.7 hours operation without any problems, the turbine inlet temperature was increased above 200°C which is operating goal of the Transcritical cycle test loop. After additional 1.5 hours operation, test was normally shut-down for the next step operation.

In Fig. 3, low frequency oscillations of pressures and temperatures were because of slow response of a thermal oil boiler temperature on/off control. And oscillations of the leakage flow from the seal as a temperature change induced charging mass in the system, so pressure of the turbine inlet was oscillated. Therefore, amount of the driving air of the

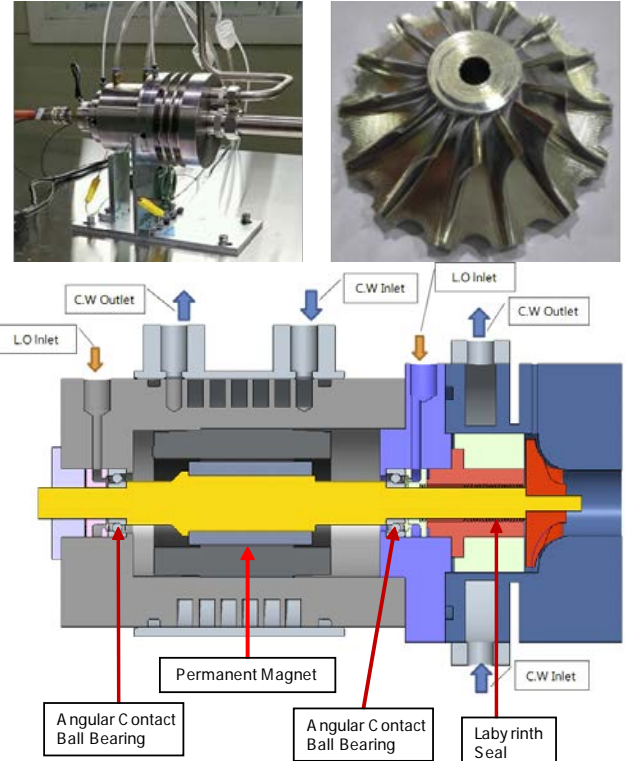


Figure 4: A kW-class radial turbo-generator for 500°C inlet condition [8]

filling pump was continuously controlled by using a control valve opening level in order to adjust amount of the charging mass.

Although these experimental results are not perfect for the design conditions, it is important to note that the objective of this project was not to demonstrate the efficiency benefits of S-CO₂ power cycles. Rather, the objective of the project was to develop an S-CO₂ power generation system with an axial-type turbine resolving bearing failure problems reported by other research groups by applying turbomachinery technology applicable to a commercial plant. Through continuous operating results during 4.2 hours, it was shown that robust and stable operation and control was possible [11].

In addition, it was the first operating results of S-CO₂ test loop with a re-injection system to compensate the turbine leakage from the mechanical seal. To configure make-up system, a barrier gas to the floating carbon ring seal was supplied from pure CO₂ gas tank, a 3-stage oil-free reciprocating CO₂ compressor, a reservoir, an oil separator and a cooling system were installed. In addition, operating strategy was developed according to turbine operating procedure. These caused additional costs and power loss which affect total plant efficiency and LCOE. It is inevitable and important technical issue in the S-CO₂ system. From these lessons learned, a novel CO₂ leakage re-injection strategy studies by using an ejector cycle and a heat pump cycle were done and presented in the our references [12, 13]

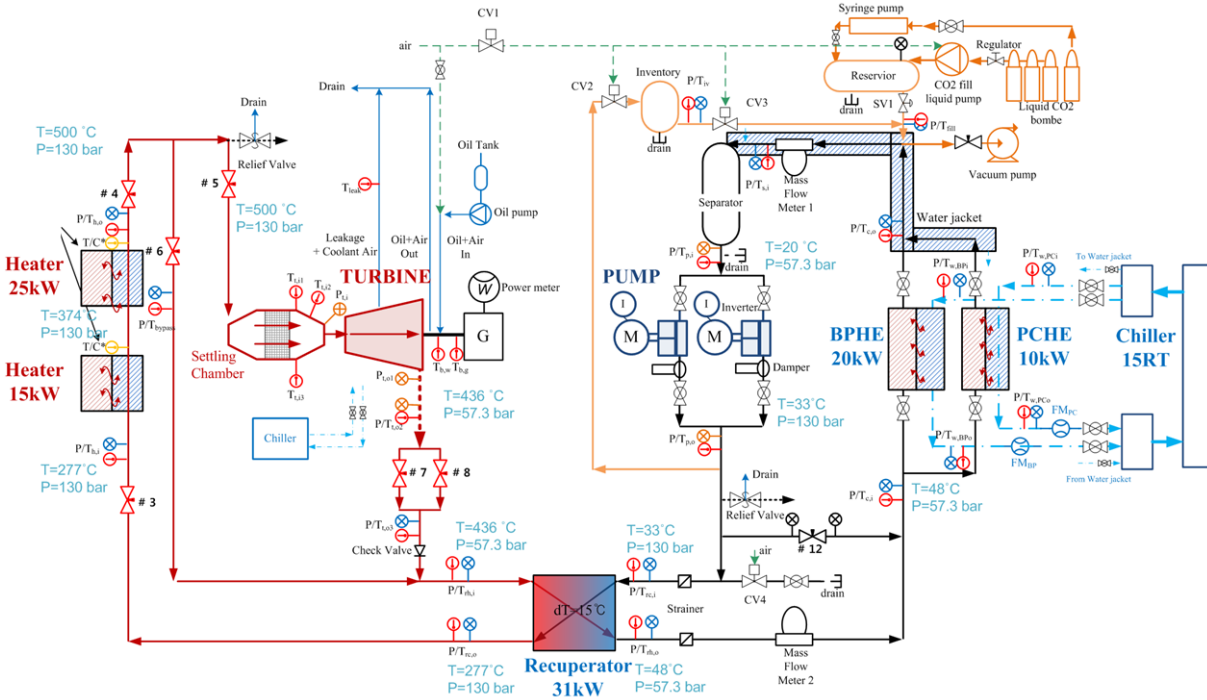


Figure 5: Schematic of kWe-class sCO₂ transcritical cycle test loop [8]

KWE-CLASS TRANSCRITICAL TEST LOOP FOR DRIVING RADIAL-TYPE TURBO-GENERATOR AT 500°C

As a two-track development strategy, in order to experience 500°C of supercritical carbon dioxide condition before development of the final test loop, a small kWe-class radial turbo-generator and its test loop assembled by tube fittings were developed and operated.

Figure 4 shows a 4.5 kWe-class radial type turbo-generator and Figure 5 shows its test loop for 500°C turbine inlet condition. From development experience of the small-scale radial turbo-generator during 2014-2016, the first design criteria was to reduce the rotational speed of the turbine under extremely small mass flow rate condition. Therefore, a 1/10 partial admission nozzle was designed. A target rotational speed was 120,000 RPM. In addition, in order to reduce axial force,

the scalloped geometry was applied to the turbine wheel. Most challenging work was thermal design induced by high inlet temperature at high pressure. In order to cool the rotor, cooling block was installed just after the turbine wheel. As a result, the length of the rotor increased, so the rotordynamics was difficult. To overcome challenging rotor instability, bearing stiffness and damping were sophisticatedly considered. Because of small diameter and high speed of the rotor, the labyrinth seal and the conventional oil-lubricated angular contact ball bearings were used. [8]

In Fig.5, a simple recuperated transcritical test loop configuration is described. The main components are two pumps, a turbo-generator, two immersion type of electric heaters, a printed circuit heat exchanger (PCHE) type recuperator, a settling chamber, a chiller, and pressure vessels. The two liquid pumps pressurized liquid CO₂ into supercritical state. The supercritical CO₂ flows through the recuperator and

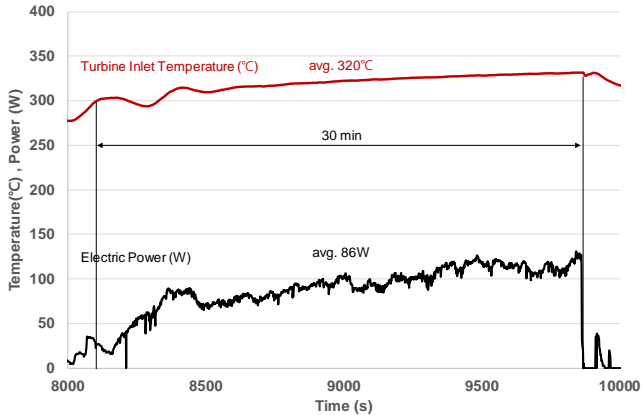


Figure 6: Power generation of the kWe-class sCO₂ test loop

is heated by the residual heat of turbine outlet flow. In the two electric heater, CO₂ is more heated until the turbine inlet condition is reached and then, its flow characteristic becomes uniform at the settling chamber. Next, the heated sCO₂ drives the turbo-generator by the expansion work and the generated power is measured with a power meter. In the turbine outlet, because the supercritical CO₂ still has a large amount of energy, it is cooled down at the recuperator. In the cooler PCHE, it is cooled to make a pump inlet condition which is equal to the minimum temperature of the cycle. A separator is used to divide two phase CO₂ into liquid and gas because pump can pressurize the liquid CO₂ only. A reservoir and an inventory are used to control the filling amount of CO₂ in the test loop. [8]

CONTINUOUS POWER GENERATING OPERATION RESULTS (RADIAL TURBO-GENERATOR)

A preliminary test at the 300°C is first performed prior to a test at 500°C. Test results are shown in Fig. 6. An electric power is generated for 30 min and its average is measured as 86 W at an average turbine inlet temperature of 320°C. The fluctuation of the power results from the leak of the turbo-generator and variability of a heater control system. When the 10% amount (7 g/s) of main mass flow rate (70 g/s) CO₂ leaks through the turbo-generator, the filling amount of CO₂ in the system is decreased. Therefore, the filling pumps starts to operate and then, make-up CO₂ is injected into the test loop. In this process, the filling amount continue to change and the turbine inlet conditions such as pressure and temperature are changed together. In addition, slow response of the electric heater also affects to the variation. In the future work, a test will be performed at the maximum temperature of 500°C with the kWe-class test loop. In addition, based on the experience of tens of kWe-class and a kWe-class test loops, the final test loop will be manufactured and operational in November 2019.

DEVELOPMENT OF HUNDREDS OF KWE TEST LOOP (CONSTRUCTION)

Back to our final target test loop described in Fig.1, Figure 7 shows main components of the test loop. First, a 90 kW centrifugal type compressor with a mass flow rate of 3.7 kg/s was developed by our research group collaborated with domestic research institute and domestic vendor. A 77 bar of compressor inlet pressure condition was determined for the sake of stable operation at the slightly far from the critical point of carbon dioxide. A 135 bar of compressor outlet pressure was determined to similar level of Sandia National Lab's test loop target. A compression ratio of 1.7 and a rotational speed of 70,000 RPM compressor was designed. The diameter of the compressor impeller is 43.6 mm, and the efficiency was estimated by a CFD analysis as 79.3%. Using a dry gas seal (DGS) which is well known as the best low leakage conventional seal technology and high speed oil-lubricating tilting-pad bearings compressor layout was designed and rotordynamics analysis was performed.

In particular, in order to reduce leakage though the compressor at high pressure, high axial force and high speed condition, the DGS and DGS control system that supplementary CO₂ and N₂ supply equipment were designed. A CO₂ booster and a CO₂ electric heater were added in this DGS control system to maintain dry condition of the CO₂ at the seal face. Because of Joule-Tomson effect at the seal face, CO₂ can be iced due to large pressure decrease and it could occur seal failure. Also in order to reduce axial force imposed on the compressor, the DGS part was designed and modified according to compressor layout design. Leakage was estimated to be 0.1 to 0.2% of main mass flow rate. Using a high-speed coupling and a high-speed driving motor supplied by domestic vendor, the compressor is now on the commissioning process. After component level test on the compressor test-rig, performance curves will be obtained and then the compressor will be assembled to the final test loop.

A 500°C-class turbine described as turbine A in Fig. 1 was designed as an axial-type turbo-generator as shown in Fig. 7. A capacity of turbine power was 110 kW, a wheel mean diameter was 52.7 mm and a rotational speed was 70,000 RPM. As similar to the turbine B, oil-lubricated tilting-pad journal and thrust bearings and a floating carbon ring-type mechanical seal were used. A 56% of partial admission nozzle was also designed. To reduce axial force imposed to the thrust bearings, a balancing piston was designed between two journal bearings. A compressed air of 6 bar from utility air compressor would be supplied to the back face of the balancing piston to compensate axial force. A pressure of air is controlled by sensing axial force measured by a load cell installed at the end of the shaft. To reduce length of the shaft for better rotordynamics, the balancing piston and a high speed generator stator were designed to have short length as possible.

KIER 2019 Targets : 500°C/130bar, >50kWe, 2 hrs of continuous running)

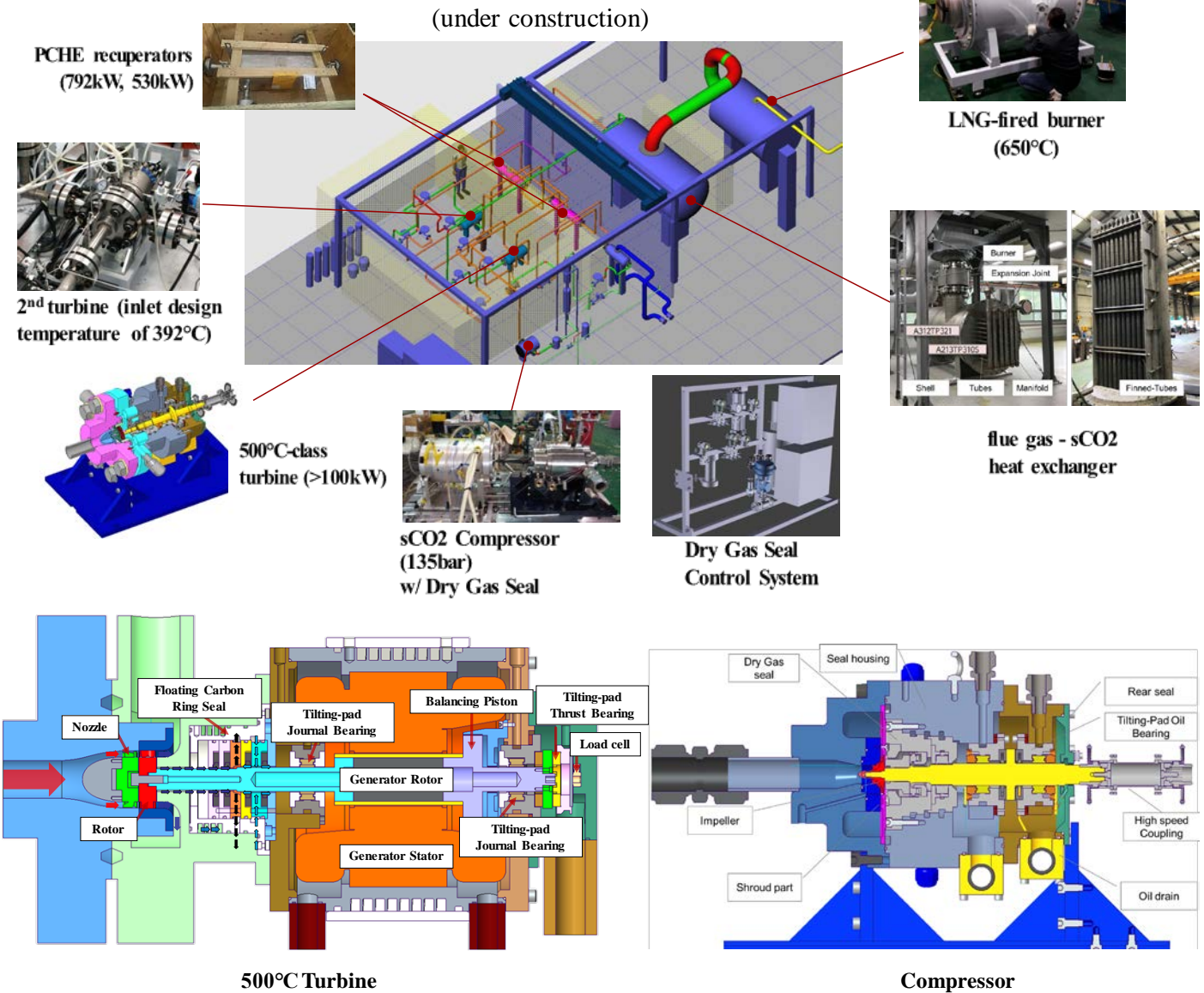


Figure 7: The final hundreds of kWe-class sCO₂ cycle test loop

To generate 500°C supercritical carbon dioxide at 135bar condition, a LNG-fired flue gas heater was designed and manufactured by domestic vendor. It consists of a burner and a shell-and-finned tube type heat exchanger. A capacity of the burner and the heat exchanger were 1,500,000 kcal/hr and 648 kW respectively. A 650°C of hot gas is generated in the burner by mixing with a cool air using a blower. A 5 kPa of supply pressure and a 6,000 Nm³/hr flow rate conditions were satisfied. The heat exchanger was fabricated with the A312TP321 shell and A213TP310S seamless tubes. The outer diameter of the tube was 42.7 mm and the thickness was 9 mm. Finned tubes were assembled to the manifold and 2500 class of

3 inches ANSI flanges were welded. In order to mitigate thermal expansion of the burner and the heat exchanger estimated as a 15 mm, a high temperature expansion joint was fabricated with A312TP321 by domestic vendor. Now 350°C flue-gas was generated to heat S-CO₂ up to 120 °C by preliminary combustion test.

Two PCHE recuperators and one PCHE cooler were designed and fabricated by VPE(USA). A pressure drop conditions for all nozzles were 0.3 bar and the material was SS316L. Strainers were included at the flanges. High pressure/temperature globe type control valves were also designed and fabricated by domestic vendor to configure

operating strategy such as bypass operation, compressor operation and turbine operations. A 2 inches ANSI 2500 class flanges were fabricated. Simultaneously, piping design and preliminary piping stress analysis were performed including all major devices, supports and control valves as following ASME B31.1 standard.

Now, we are commissioning each components, designing and fabricating other components, after that, preliminary operation results will be obtained on November, 2019. [11]

CONCLUSIONS

A hundreds of kWe-class S-CO₂ test loop with a 500°C turbine inlet temperature condition was developed and partially fabricated. Two axial-type turbo-generators, one centrifugal-type compressor, two PCHE recuperators, one flue gas heater and one PCHE cooler were designed. As a step-by-step approach, the low temperature turbine which inlet temperature of 392°C was designed and manufactured with a carbon floating mechanical seal and an oil-lubricating tilting-pad bearing which are suitable technologies for a commercial large-scale plant. To drive this turbine, existing test facilities were used. A 4.2 hrs continuous electricity generating operation test was conducted at 200°C off-design condition. Turbine leakage flow was re-injected to the system by using a leakage compressor. It shows additional technical issue of the S-CO₂ system.

In addition, a small kW-class radial turbo-generator and its transcritical test loop which operates at 500°C was developed and operated to investigate characteristic of S-CO₂ components at the high temperature condition. A 30 mins of continuous power generation was succeeded over 300°C turbine inlet temperature condition. Because of thermal design of the rotor, a shaft has to be long, it causes rotordynamics problems. It would be improved after modifying rotordynamics of the high speed turbo-generator.

Finally, a centrifugal type compressor with a dry gas seal and a tilting-pad bearings and an axial type turbo-generator with a balancing piston, floating carbon ring seal and a tilting-pad bearings were developed for the final test loop. A LNG-fired flue gas heater with a shell-and-finned tube heat exchanger that generate 500°C S-CO₂ was also designed and preliminarily tested. Other parts such as recuperator, cooler and piping systems were also designed and partially manufactured. It is expected to operate entire test loop in end of 2019.

ACKNOWLEDGMENTS

This work was conducted under the framework of the Research and Development Program of the Korea Institute of Energy Research (KIER) (B9-2432).

REFERENCES

[1] Vann Bush, Keynote-GTI STEP forward on sCO₂ power, The 6th International Supercritical CO₂ Power Cycles Symposium, March 27 - 29, 2018, Pittsburgh, Pennsylvania

[2] Jeffrey Moore, Commissioning of a 1 MWe Supercritical CO₂ Test Loop, The 6th International Supercritical CO₂ Power Cycles Symposium, March 27 - 29, 2018, Pittsburgh, Pennsylvania

[3] Lewis J, Clementoni EM, Cox T. Effect of Compressor Inlet Temperature on Cycle Performance for a Supercritical Carbon Dioxide Brayton Cycle. The 6th International Supercritical CO₂ Power Cycles Symposium, March 27 - 29, 2018, Pittsburgh, Pennsylvania

[4] David S. Stapp, SCO₂ Turbomachinery Developments, The 6th International Supercritical CO₂ Power Cycles Symposium, March 27 - 29, 2018, Pittsburgh, Pennsylvania

[5] Jason D. Miller, Test Results of a 1.5MW High Speed Motor-Generator in a Pressurized CO₂ Environment, The 6th International Supercritical CO₂ Power Cycles Symposium, March 27 - 29, 2018, Pittsburgh, Pennsylvania

[6] David Freed, A Gas Turbine-driven, Integrally Gear Compressor solution: Enabling the Carbon Capture of the sCO₂ Allam Cycle Power Plant. The 6th International Supercritical CO₂ Power Cycles Symposium, March 27 - 29, 2018, Pittsburgh, Pennsylvania

[7] Jang SH, Keynote presentation, The 6th International Supercritical CO₂ Power Cycles Symposium, March 27 - 29, 2018, Pittsburgh, Pennsylvania

[8] Cho J, Shin H, Cho J, Ra H-S, Roh C, Lee B, Lee G, Choi B, Baik Y-J. Preliminary Power Generating Operation of the Supercritical Carbon Dioxide Power Cycle Experimental Test Loop with a Turbo-generator. The 6th International Supercritical CO₂ Power Cycles Symposium, March 27 - 29, 2018, Pittsburgh, Pennsylvania

[9] Thomas C, Steven W, James P, Darryn F, Gary R, Robert F. Performance Characteristics of an Operating Supercritical CO₂ Brayton Cycle, Journal of Engineering for Gas Turbines and Power, Vol. 134, 2012, 11703-1

[10] Cho J, Shin H, Cho J, Baik Y-J, Choi B, Roh C, Ra H-S, Kang Y, Huh J. Design, Flow simulation and performance test for partial admission axial turbine on supercritical CO₂ condition. Proceedings of ASME Turbo Expo 2018: Turbomachinery Technical Conference and Exposition, GT2018-76508, June 11 - 15, 2018, Oslo, Norway

[11] Choi B, Cho J, Shin H, Cho J, Roh C, Lee B, Lee G, Ra H-S, Baik Y-J. DEVELOPMENT OF A HUNDREDS OF KWE-CLASS SUPERCRITICAL CARBON DIOXIDE POWER CYCLE TEST LOOP IN KIER, Proceedings of ASME Turbo Expo 2019: Turbomachinery Technical Conference and Exposition GT2019 June 17-21, 2019, Phoenix, Arizona USA

[12] Muhammad HA, Lee G, Cho J, Bhatti UH, Baik Y-J, Lee B, Design and optimization of CO₂ pressurization system integrated with a supercritical CO₂ power cycle for the CO₂ capture and storage system, Energy Conversion and Management, 195, 2019, pp.609-619

[13] Muhammad HA, Lee B, Lee B, Cho J, Baik Y-J, Investigation of leakage reinjection system for supercritical CO₂ powercycle using heat pump, Renewable Energy, 144, 2019, pp.97-106

OPERATIONAL EXPERIENCES AND DESIGN OF THE sCO₂-HERO LOOP

Alexander J. Hacks*

Chair of Turbomachinery
University Duisburg-Essen
Duisburg, Germany
Alexander.Hacks@uni-due.de

Thomas Freutel

Kraftwerks-Simulator-Gesellschaft mbH (KSG)
Essen, Germany

Marcel Strätz

University of Stuttgart
Stuttgart, Germany

Ales Vojacek

Research Centre Řež
Řež, Czech Republic

Frieder Hecker

Gesellschaft für Simulatorschulung mbH (GfS)
Essen, Germany

Joerg Starflinger

University of Stuttgart
Stuttgart, Germany

Dieter Brillert

Chair of Turbomachinery
University Duisburg-Essen
Duisburg, Germany

ABSTRACT

Due to its fluid properties at certain temperature and pressure, supercritical CO₂ (sCO₂) allows to build compact power cycles for certain applications. This characteristic of sCO₂ is utilized in the sCO₂-HeRo project to design a compact heat removal system as a simple Joule cycle. This paper presents the experiences and one set of measurements from these initial tests together with a description of the start-up and control strategy and procedure. The control and operation capabilities of the sCO₂-HeRo loop during filling and circulation operation are qualitatively compared to those of the other two sCO₂ loops (SCARLETT and SUSEN) employed within the project. The consequences of using different components in the loops on the operation are analyzed. It is pointed out that employing a filling compressor to add high-pressure CO₂ gives great operation flexibility while the use of piston accumulators may be used to stabilize cycle pressure and increase filling speed. Furthermore, if sCO₂ is only required in the test section, a transcritical cycle may be used, offering faster filling and simpler control. Additionally, the paper describes the sCO₂-HeRo cycle's design parameters, including detailed geometrical information and performance parameters of the assembled components required for the simulation of the loop. These may be used together with future measurement results for the validation of simulations.

INTRODUCTION

The system developed within the EU funded sCO₂-HeRo project will raise nuclear reactor safety to a higher level. In case of a combined Station Blackout (SBO) and Loss of Ultimate

Heat Sink (LUHS) accident scenario, it transfers the decay heat to a secondary ultimate heat sink, e.g. the ambient air (Benra et al. [1]). Due to its compactness, it can be retrofitted to existing nuclear power plants. Within the sCO₂-HeRo project, a small-size sCO₂ demonstrator cycle was developed and constructed at the PWR glass model at the Simulator Centre of KSG/GfS in Essen. The PWR glass model allows to simulate and visualize different accident scenarios. While the single components were already tested, the coupling of the sCO₂-HeRo cycle to the glass model allows to experimentally examine the function of the sCO₂-HeRo system in total and its interaction with the PWR cycle. Main objective of the system test is to proof the heat extraction from the core and to validate the operation strategy of the system. Thus, by completing the system integration tests, the system is brought to Technology Readiness Level 4 (TRL 4). The measurement results will further be used for code validation.

The presented paper describes two aspects. The first being the operation experiences made at the sCO₂-HeRo loop and its comparison with the SCARLETT and SUSEN loop. These loops were used for component testing within the sCO₂-HeRo project. The focus of the comparison lies on the filling and circulation of CO₂, revealing the influence of the different cycle layouts on cycle operation within these operating phases. To give a deeper understanding of the whole sCO₂-HeRo cycle, the second aspect of the paper is the detailed description of the loop itself. This contains the piping and instrumentation diagram (P&I), the main components, the measurement equipment and the cycle dimensions and thus allows to use future measurement results for code (cycle simulation) validation.

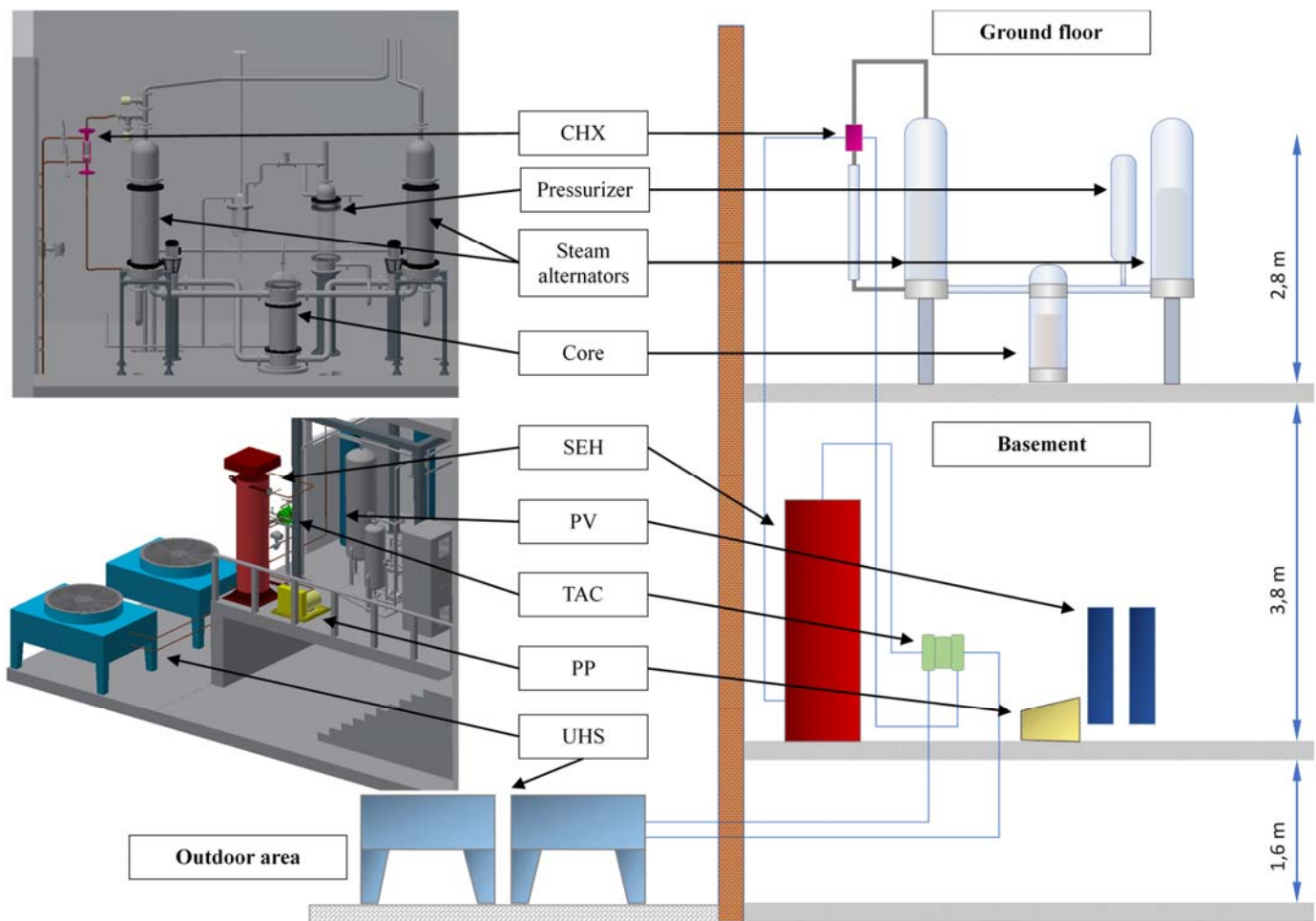


Figure 1: CAD-Drawing and component position of the sCO₂-HeRo cycle

GENERAL CYCLE FUNCTION AND LAYOUT

This paragraph gives a generalized description of sCO₂-HeRo cycle function and layout. The sCO₂-HeRo cycle is attached to the glass model according to the scheme in Fig. 8 in Annex A (Strätz et al. [8]) with the components depicted in Fig. 1. Here, in the 3D-CAD model on the left, the components of the glass model are colored in gray and the components of the sCO₂-HeRo cycle are marked with different colors. The height scheme on the right indicates the positions of the components on the three levels: the ground floor, the basement and the outdoor area. The corresponding detailed description of all components and their arrangement is provided in the second part of the paper.

In case of postulated accident scenario with sCO₂-HeRo operation, valve 1, connecting the steam generator of the glass model to the heat sink, is closed and valve 2 opens establishing a natural circulation driven cooling loop on the steam side of the PWR glass model. Driven by natural convection, the steam flows

upwards into the compact heat exchanger (CHX, pink), where the heat is transferred to the sCO₂ side by condensation heat transfer. The condensate can be observed in a glass tube depicted in shaded blue below the CHX in Fig. 1. Through this tube it flows downwards driven by gravity and re-enters the steam generator through the feedwater line, which results in continuous heat removal from the primary circuit via the u-tubes. In the sCO₂-HeRo loop downstream of the CHX a slave electrical heater (SEH, red) is installed in the basement. It provides predetermined inlet conditions to the turbine and enables transient experiments and operation of the sCO₂-HeRo loop in off-design conditions. Such flexible conditions allow for operation of the sCO₂-cycle close to operation boundaries without any negative feedback effect to the glass model. Downstream of the SEH, the turbine of the turbomachine (TAC, green), which consists of turbine, alternator and compressor, expands the sCO₂. It then flows outside into the gas coolers of the ultimate heat sink (UHS, light blue), from which it is

delivered to the CHX by the compressor. In the design point of the system the turbine provides more power than required for the compression leading to a self-sustaining system with excess electricity at the alternator. In the nuclear power plant, this electricity will be used for the electrical driven fans of the UHS and for different kinds of auxiliary devices. Additional to the previously mentioned components, Fig. 1 also contains the piston pump (PP, yellow) for circulation and leakage feedback and the pressure vessels, designed as piston accumulators, for the start-up procedure and compensating fluid expansion (PV, dark blue).

OPERATIONAL EXPERIENCES

This section describes the filling and circulation procedure of the sCO₂-HeRo cycle as well as of the two other cycles SCARLETT (Flaig et al. [3]) and SUSEN (Vojacek et al. [10]) which were used in the sCO₂-HeRo project for component tests. The cycles are constructed for different purposes and thus have different layouts and operation strategies. Their influence on the overall procedure is analyzed.

FILLING AND CIRCULATION PROCEDURE - sCO₂-HERO

The sCO₂-HeRo cycle was particularly designed for the system tests and consists of numerous components. Those important for the filling and circulation operation, are depicted in Fig. 2 which represents a simplification of the detailed piping and instrumentation (P&I) diagram shown in Fig. 9 in Annex B. Additional to the main components, it includes the pipe numbers (squares) and measurement numbers (circles) according to Table 3 and Table 1 respectively. The TAC is not included because it is bypassed in the circulation operation.

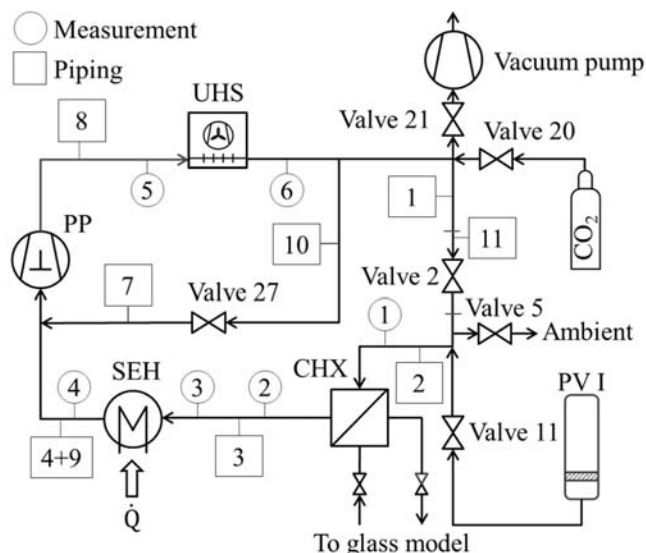


Figure 2: P&I diagram - sCO₂-HeRo circulation loop

The filling procedure starts with the evacuation of the loop using the vacuum pump until a pressure of less than 0.1 bar absolute is reached. Holding the vacuum without running the vacuum pump reveals possible leakages. After evacuating the cycle, it is filled with gaseous CO₂ from the bottle. To drive the CO₂ into the cycle, the bottle is heated maintaining a driving pressure difference. The evaporation enthalpy of the CO₂ and the heating power induced to the CO₂ determine the filling speed. Valve 21 needs to be opened before evacuation and closed thereafter. Otherwise starting of the filling procedure by opening valve 20 leads to an increase of the pressure in the glass model, which uses the same vacuum pump as the sCO₂ cycle. With the cycle having a volume of about 200 l without the two PV, different masses of CO₂ need to be filled to the cycle depending on the desired operation conditions. First subcritical gaseous tests required about 23 kg of CO₂ while about 30 kg will be required for initial tests with sCO₂ (without PV). After filling, the cycle volume was recalculated from the CO₂ conditions and filled mass of CO₂. A comparison to the sum of volumes of the single components and piping showed good agreement, validating the volumetric cycle model. The unavoidable leakage rate (e.g. through packing glands of the valves) can be determined as long as the CO₂ is completely gaseous. In the sCO₂-HeRo, it is determined to be around 5 mg/s at 40 bar and 20 °C which is related to the number of valves and connections and equivalent to a bore of a diameter of 20 μm. Note that the sealing of the PP leads to a quite large leakage rate and thus it is disconnected from the cycle in standby. Another option for filling, used to reach supercritical pressure, is to fill CO₂ directly to the PV while the valve towards the loop (valve 11) is closed. To do so the “zero-pressure” of the PV is initially set below the saturation pressure of CO₂, which lies at approximately 57 bar at 20°C ambient temperature. The pressure value determines the mass of CO₂ that is filled before reaching stationary conditions in the PV. Raising the nitrogen pressure to the desired value determines the CO₂ pressure making it liquid. This is easily possible as nitrogen in gas bottles is stored at much higher pressure as the maximum cycle pressure. It is noted that this procedure could also be applied during cycle operation. However, the required automated control and filling unit at the PV is currently not installed.

To start the circulation operation, the loop is filled up with the mass of CO₂ to reach the desired operating conditions. PV I can be employed to balance the pressure before the CHX and PP. As it is held at room temperature it may take a huge amount of CO₂. When filling of the cycle is finished, the cycle reaches steady state conditions after a certain amount of time. At this standby condition, the PP is started. If the standby condition lies within the 2-Phase region, the SEH must be turned on prior to the PP to evaporate liquid CO₂ in the SEH as the PP is designed for single phase gaseous CO₂. Considering the arrangement of the components in Fig. 1, it is evident that except for the little amount of liquid CO₂ that deposits in the SEH all liquid CO₂ will be in the UHS. This leads to two restrictions when the cycle is started. First, valve 27 may not be opened from the beginning if

the standby conditions lead to liquid CO₂ in the UHS. Note that the temperature and thus the CO₂ conditions in the UHS depend upon the ambient temperature outside, which can be well below room temperature. Secondly, the heating power in the SEH directly after starting the PP must be sufficiently high to evaporate all liquid CO₂ coming from the UHS to avoid phase change of the CO₂ at the PP. In operation the cycle pressure is determined by PV I if valve 11 is opened. Since the volume of PV I is large, low deviations from the pre-set pressure are expected. If valve 11 is closed, there is no pressure balancing device anymore, and the pressure depends only on the filled mass of CO₂ and the temperature levels within the cycle. However, the pressure in the cycle can be reduced by releasing CO₂ via the blow off valve 5 to the ambient air (Fig. 2).

Table 1 contains the measurement results of one “cold” circulation run. During this circulation run the PP operated at full flow rate (valve 27 closed) and the heating power of the SEH was 0 kW while some heat was transferred via the CHX. Furthermore, valve 2 was fully opened while valve 11 and 27 were closed. Note that the CO₂ was cooled in the SEH because it did not reach steady state conditions due to its large thermal inertia. These measurements prove the heat transfer in the CHX and are used to validate calculated pressure losses.

Table 1: Measurements for subcritical circulating operation

Measurement position	p / bar	T / °C	\dot{m} / $\frac{\text{kg}}{\text{s}}$
1	44.4	15.0	0.2
2	43.8	44.3	
3	43.0	43.7	
4	42.7	22.7	
5	48.7	34.3	
6	48.4	20.1	

FILLING AND CIRCULATION PROCEDURE - SCARLETT

Figure 3 shows a simplified P&I diagram of the sCO₂ SCARLETT (Supercritical Carbon Dioxide Loop at IKE Stuttgart) loop at the Institute of Nuclear Technology and Energy Systems (IKE), Stuttgart, Germany (Flaig et al. [3]).

At the start, the SCARLETT loop is evacuated by the vacuum pump and filling unit, shown on the left side in Fig. 3. Valve 1 and valve 2 are opened, valve 3 remains closed and the vacuum pump is switched on. During the evacuation it must be guaranteed that all valves in the cycle are opened to ensure that the entire loop is evacuated. The process is monitored by pressure gauges, and it is stopped after a few hours of operation until the pressure stabilizes at a value of less than 0.05 bar. Afterwards, valves 1 and 2 are closed. In the following, a CO₂

gas bottle is connected to the filling unit, and valve 2 and 3 are opened. Gaseous CO₂ is filled into the loop until a pressure of about 7 bar is reached. After closing valve 2 and 3 the CO₂ gas bottle is replaced by a CO₂ dip tube bottle which delivers liquid CO₂ through valve 2 and 3 into the storage vessel with a volume of about 120 l until a mass of about 40 kg is reached. Afterwards, valve 2 and 3 are closed, and the cycle is ready for operation. Due to saturation conditions, there is a pressure of about 57 bar (20 °C) in the entire facility, and gaseous as well as liquid CO₂ exists in the storage vessel.

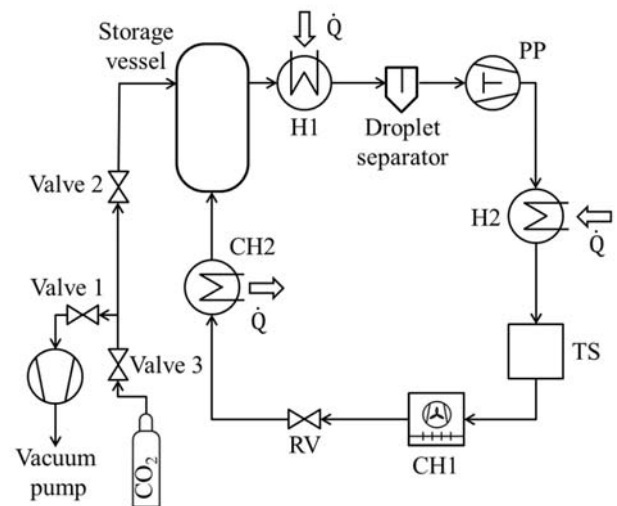


Figure 3: Simplified P&I diagram - SCARLETT loop

Before starting operation, auxiliary devices like cryostats, measurement data acquisition and the control system are switched on. At the beginning of the operation, the evaporator (H1) heats the CO₂ until a temperature difference of about 5 °C is reached between the CO₂ in the storage vessel and the CO₂ at the outlet of H1. Reaching this point, the reduction valve (RV) is closed and the piston compressor (PP) is switched on, leading to a flow of liquid CO₂ from the storage vessel through the electrical heated H1 where it is evaporated and superheated. The heating power is controlled and adjusted to ensure a CO₂ superheating of about 15 °C. After leaving the droplet separator, in which remaining liquid CO₂ droplets are separated from the flow, it enters the compressor (PP). There, the CO₂ is compressed and simultaneously compression heated, leading to a pressure increase at the high-pressure side of the SCARLETT loop. In the following, the conditioner (H2), the gas coolers (CH1) and the condenser (CH2) are switched on for the conditioning of the sCO₂. After reaching a defined pressure of about 40 bar on the high-pressure side of the loop, the RV automatically increases or decreases the opening degree, controlled by the control system. In CH2 the CO₂ is completely condensed before it re-enters the storage vessel. The start-up procedure is finished when a sCO₂ pressure of 80 bar and a mass flow rate of about 60 g/s is provided at the inlet of the test section (TS), when a constant superheating of about 15 °C is reached and when both controllers, the pressure and mass flow controller, are in

operation. These controllers are used for adjusting the opening degree of the RV, the revolution speed of the PP and the cooling- or heating power of the conditioning units, leading to steady state conditions at the inlet of the TS. For all experiments to be carried out in the modular TS attached to SCARLETT, these values are the stable initial conditions which can be modified for different purposes, e.g. heating or cooling experiments.

FILLING AND CIRCULATION PROCEDURE - SUSEN

The P&I diagram of the sCO₂ SUSEN loop at CVR is described in Fig. 4. The very first procedure necessary before starting-up the loop is vacuuming by means of a vacuum pump to get rid of the moisture (vacuum drying) and non-condensable gases like air. In order to intensify the cleaning technique, CO₂ is let into the loop. The desired purity is checked by sampling.

The next process is the filling. To fill the loop with the required mass to achieve operating conditions, CO₂ vapor from a standard 50 l pressurized bottle with pure CO₂ (4.5 – 99.995%), where 2 phase CO₂ is stored, is introduced just before the water cooler CH1. Hot air might be used to heat up the bottle to speed up the filling. The weight of the bottle is measured to know how much CO₂ goes into the loop. As the pressure in the system rises and approaches the pressure in the bottle, the process slows down. Hence, an air driven reciprocating filling compressor (FC) is used to speed up the filling. When a fixed mass based on model predictions gets near the normal operating mass (in our case around 40 kg of CO₂ for total cycle volume of about 95 l), the main circulation piston pump (PP) can start circulating the CO₂ content around. To increase the pressure in the system, the heaters are switched on. The maximum limit of 50 K/h temperature increase is controlled. As the system heats up and pressure rises, the mass flow rate increases as the density at the inlet to the PP increases. If further mass adjustments are needed to reach the desired parameters, the FC is used to fill the CO₂ to the loop. Reducing the pressure can be performed through opening the bleeding valves (BV) with orifices installed in the pipe. For setting the inlet temperature to the PP, the frequency of the water pump is adjusted to control the water flow rate through the CH1 cooler. The operation of the loop is controlled by the main pump speed drive. Flow rate of sCO₂ is measured with a Coriolis flow meter. It is possible to adjust the flow rate through the low temperature recuperator (LTR) by-pass so to simulate a recompression cycle, as well as to adapt flow rate through the CH2 (simulating the turbine heat power release). The loop is divided into the low- and high-pressure part. The separation is performed by the reduction valve. The pressure in both parts is adjusted by the opening position of the valve.

To protect the loop against over pressure several pressure relief valves are installed at positions, where increase of pressure might occur. These are e.g. the heating parts equipped with closing valves both at the inlet and outlet as well as the pump.

The shut-down procedure is performed through the heating power control. The 50 K/h temperature change should be satisfied to bring the loop to the cold state (20°C). If there is a

need for repair, the necessary part or the whole loop is evacuated through the release valves and system of orifices to slow down the pressure change.

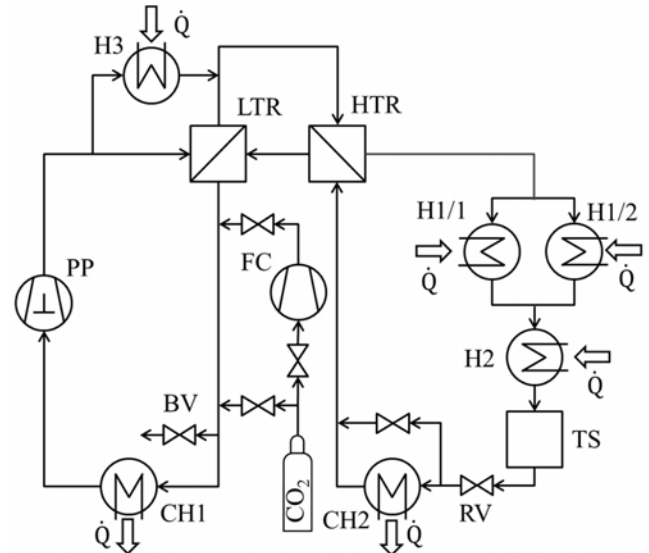


Figure 4: P&I diagram – SUSEN loop

COMPARISON

The described loops are substantially different regarding the components with effect on the operation strategy. Two aspects related to the filling and first circulation operation of the sCO₂-HeRo cycle are compared to each other hereafter.

The first operation aspect is the filling of the loop. As described in the previous section filling of all loops starts by evacuating the loop to pressures below 0.1 bar. After that, the loop is filled from the bottle up to a certain pressure limit determined by the saturation pressure. The SCARLETT loop employs, different from the other two, dip tube bottles to fill liquid CO₂ to a storage tank. Compared to conventional gas bottles, this enables the filling of a higher CO₂ mass. SUSEN and sCO₂-HeRo fill gaseous CO₂ directly into the loop which opens the possibility of heating up the gas bottle. The SUSEN loop allows to increase the pressure to over the saturation pressure of CO₂ by using the FC while the sCO₂-HeRo loop applies the PV. Note that in this way the storage unit in the SUSEN cycle are the gas bottles which are only connected to the FC and disconnected from the cycle itself. Therefore, they do not contribute to the cycle volume. The SCARLETT loop supplies the test section with sCO₂ by compressing the gas leaving the evaporator downstream of the storage vessel. The storage vessel itself is always subcritical. Thus, the SCARLETT loop is strictly speaking transcritical, and no additional filling over the saturation pressure is required. It can be concluded that the filling of the SCARLETT loop is the quickest because of its it transcritical operation requiring only saturation pressure in the storage vessel. The filling of the entirely supercritical loops SUSEN and sCO₂-HeRo may require (related to the desired

operation conditions) to add more CO₂ after saturation conditions are reached. Applying the prefilled PV in the sCO₂-HeRo cycle allows to increase the pressure quicker than using the FC. However, as the vessel is primarily meant to stabilize the pressure in the cycle, the connection valve must be open after filling. Therefore, only one pressure can be set by the PV determined by careful calculation while the FC allows to set any pressure independently and is thus more flexible.

The second aspect is the dynamic setting of operation conditions in the desired test section. SCARLETT compresses the CO₂ coming from the subcritical storage vessel at stable saturation pressure with the compressor before conditioning it to the desired temperature. Pressure and temperature in the test section can be freely set by the compressor speed, the expansion valve position and the conditioning power. It is limited only by the mass in the storage vessel because increased mean density or volume of the test specimen in the sCO₂ section requires additional mass to be fed. In the SUSEN loop the conditions are set, applying the release valves or FC respectively. This allows operation independent of filling conditions. The sCO₂-HeRo cycle allows only one preset pressure, which relates to the selected pressure in the PV, determined by the initial filling mass of CO₂ and the preset N₂ pressure in the other chamber. The sCO₂-HeRo has a release valve (valve 5), too. However, the pressure in the cycle does not change significantly as long as the PV are connected because the CO₂ mass within the PV is large and a change of pressure relates only to the movement of the piston and thus decrease of the N₂ pressure. Subsequent increase of pressure is then no longer possible because there is currently no possibility to add N₂ to the PV during cycle operation. Even with such an apparatus, the amount of CO₂ in the PV is lower after pressure reduction and increasing the N₂ pressure will only increase the cycle pressure as long as the piston in the PV does not reach the lower limit and the CO₂ part is empty. Thus, it is not possible to do large pressure variations multiple times even if the N₂ pressure is regulated during operation.

SCO₂-HERO DESIGN SPECIFICATIONS

Following on the already introduced 3D-CAD in Fig. 1, the sCO₂-HeRo cycle is introduced in more detail, allowing to reproduce the cycle model. This includes the complete P&I diagram, showing the arrangement of the components, the specifications of each component as well as those of the piping and measurement instruments.

PIPING AND INSTRUMENTATION DIAGRAM

The P&I diagram in Fig. 9 in Annex B represents the base of the cycle model. It includes the components of the main sCO₂-HeRo system, components for start-up procedures, as well as the measurements at each location. Furthermore, it can be divided into 8 sections which are described in the following.

Section 1 is marked with red (high pressure) and blue (low pressure) pipes and depicts the components of the main sCO₂-HeRo cycle, like the compressor, CHX, SEH, turbine and UHS.

Furthermore, temperature (T), pressure (p), density (ρ), load (M), revolution (n), vibration (f), voltage (U), current (I) and mass flow rate (F) measurement devices as well as different kind of valves are installed.

The region marked with number 2 shows the TAC system with the frequency converter as well as the PP. The TAC is the heart of the cycle as it is the component inducing the flow and thus transporting the decay heat from the core via the CHX to the UHS. Furthermore, the turbine produces the driving force for the compressor and for the alternator from the decay heat. Therefore, it makes the system self-sustaining. The frequency converter controls the mechanical load, the revolution speed, the excess electricity and the temperature at the alternator. To reduce friction losses at the alternator and to prevent any kind of damage in the bearings of the TAC, the PP independently reduces the pressure at the alternator and bearings by drawing a defined CO₂ leakage flow from the housing of the TAC (Fig. 5). The leakage flow and pressure are adjusted by recirculating a part of the flow rate of the PP. Another purpose of the PP is the circulation of CO₂ in the cycle when the TAC is not used.

The SEH (in section 3) is required because the heat provided by the glass model via the CHX is insufficient to operate the sCO₂-cycle at conditions of nuclear power plants. The heat input into the sCO₂ is either realized as a constant electrical heating power or via a master slave control. Thus, the SEH allows a decoupling of the sCO₂-HeRo cycle from the PWR glass model cycle for certain test cases because its heating power is sufficient to operate the sCO₂ cycle without the CHX. On the other hand, in the master slave configuration, the heating power is adjusted according to the heat input from the compact heat exchanger.

The UHS is numbered with 4 in Fig. 9. Since the heat removal to the UHS is supported by electrical driven fans, voltage and current values can be adjusted and monitored to regulate the air flow and thus cooling power.

Section 5 shows the CHX. Measurement devices for measuring the pressure and temperature at the inlet and outlet of the CHX as well as for measuring the steam mass flow rate at the inlet of the CHX are installed. The two needle valves on the steam side of the CHX at the inlet and outlet are used for connecting or disconnecting the CHX from the glass model and regulating the steam flow.

The two PV are in Section 6. They are required for the sCO₂-HeRo cycle to be able to start via a pressure surge. Additionally, PV II has the function of maintaining a constant compressor inlet pressure. It is assumed that in case of a start-up procedure valves 2, 4, 15, 25, 28 and 29 are open. Then, valve 11 at the bottom of PV I will be opened, and due to the adjusted pressure difference between the main cycle and PV I, the inventory is forced to flow into the sCO₂-HeRo cycle. With valve 6 closed, it is heated up in the CHX and SEH before entering the turbine, where it forces the shaft to start rotating. Following on the expansion in the turbine, it flows through the

UHS and through in the lower chamber of PV II. After reaching the breakeven point, when the compressor outlet pressure exceeds the pressure in PV I and the turbine provides more power than needed for the compressor, the start-up procedure is finished by closing the compressor bypass valve 2 to open valve 6. Then, the sCO₂-HeRo system is self-sustaining closed loop operation.

Before the entire sCO₂-HeRo cycle can start operation, it has to be evacuated and filled with CO₂. The vacuum pump unit for evacuation is numbered with 8 while the filling-unit consisting of a heated gas bottle and a valve is in section 7.

COMPONENT SPECIFICATIONS

The specifications of the components in the cycle, given in this section, define the capabilities of the sCO₂-HeRo cycle. For reasons of limited length of the paper, only the main parameters are given. More detailed information regarding design and testing of the components can be found in the referenced papers.

TAC: The TAC was designed and manufactured by the Chair of Turbomachinery at the University of Duisburg-Essen and consists of a radial compressor with an outer impeller diameter of 40 mm and a radial turbine with an outer impeller diameter of 66 mm. Both impellers are mounted to opposite sides of one shaft. The shaft also includes the alternator in the middle and the bearings in between the alternator and the impellers (Fig. 5). All components are in one hermetic casing which is designed for a maximum pressure of 130 bar. The design rotating speed of the TAC is 50,000 rpm with a design electric power of about 7 kW. For monitoring the bearing temperatures and the vibration of the shaft, four temperature and three vibration measurement devices are installed. For more information on design of the TAC, please refer to Hacks et al. [4]. They describe the design procedure in detail and published the whole compressor geometry while Hacks et al. [5] present the first compressor performance tests and validation of the compressor performance map.

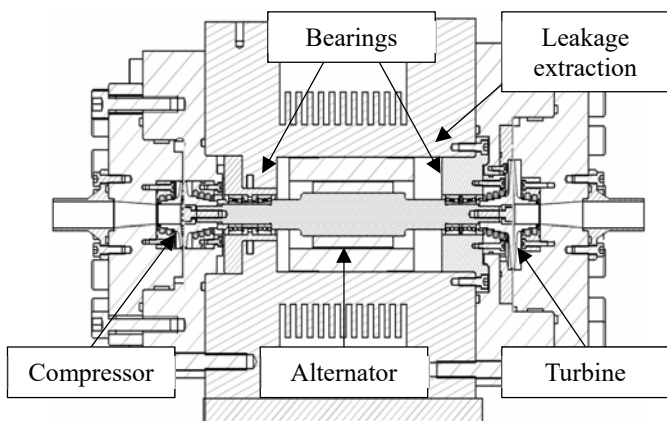


Figure 5: sCO₂-HeRo TAC [4]

CHX: The CHX was designed and manufactured by the Institute of Nuclear Technology and Energy Systems (IKE) at the University of Stuttgart. The inlet conditions for the design of the

CHX were derived from experimental investigations at the glass model and from sCO₂-HeRo cycle calculations. In the design point of the system, sCO₂ enters the CHX with a temperature of 46.8 °C, a pressure of 117.5 bar and a mass flow rate of 0.65 kg/s. A steam condensing power of 6 kW was calculated according to a steam temperature of 70.3 °C, a steam pressure of 0.32 bar and a steam mass flow rate of 2.6 g/s at the inlet of the CHX (Strätz et al. [8]).



Figure 6: Components of a compact heat exchanger with milled channels

In the following, the design of the CHX was determined under consideration of given boundary conditions, received data from single effect experiments as well as from numerical analysis. Straetz et al. [9] give a description of the single effect experiments. The counter current flow between condensing steam and sCO₂ was applied because it provides the highest heat transfer capacity per surface area. The steam plate was designed with 15 straight rectangular channels with a channel width of 2 mm and a channel height of 1 mm. The wall thickness between two channels is 1.4 mm and the plate thickness is 2.4 mm. The sCO₂ plate with 15 rectangular channels, a channel width of 2 mm, a channel height of 1 mm, a wall thickness of 1.4 mm and a plate thickness of 2.4 mm is quite similar. The “Z Shape” of the sCO₂ channels is necessary to connect two of the four plenums with the steam side and two of the four plenums with the sCO₂ side - under consideration of a stacked CHX (Fig. 6) with more than one plate on each side. The effective channel length for sCO₂ is 150 mm, which is the straight length of the middle part of the channels. The entire amount of plates for the CHX is 28, with respect to a necessary transferred heat power of 6 kW and a maximum allowed sCO₂ pressure drop of 0.5 bar. In addition, 14 plates with 15 channels per plate results in 210 channels on each side of the compact heat exchanger.

SEH: The SEH was bought from Elmess Thermo System Technik and is of the type HK with a maximum electrical heating power of 240 kW. The internal DN50 piping is manufactured as a coil with an outer diameter of 590 mm and height of 2,000 mm. The internal volume is about 110 l and the maximum allowed pressure is 155 bar. A protection device monitors the temperature of the heating elements and protects them against overheating by shutdown. A controller was implemented, which is regulating the heating power according to the measured outlet temperature. The heating power is calculated from squared effective voltage of the phase angle control.

UHS: The supercritical CO₂ in the sCO₂-HeRo system is cooled by means of air, hence providing heat sink to ambient for an unlimited period of time. The UHS consist of two parallel units designed as air cooled sCO₂ finned-tube with the design parameters shown in Table 2. The two units are of the type GGHV CD 090.1QF/11E-31 delivered by Güntner GmbH & Co. KG. The internals of sink UHS include stainless steel AISI 304 tubes in staggered arrangement with rectangular aluminum fins (metal sheet). The arrangement is such that the flow on the sCO₂ side is purely horizontal (except the inclined bends placed outside the air flow) while on the air side the flow is completely vertical. An illustrative scheme is shown in Fig. 7. Vojacek et al. [11] show a conceptual design drawing of one unit of the UHS. With an overall size of about 1.6 m in length 2.2 m in width and a height of 1.4 m each single unit features an overall heat transfer area of 361 m² and a total internal volume of 40 l including headers. More details of the geometry of the UHS are as follows. Number of tubes = 8, number of rows in depth = 6, tube diameter Ø 12 mm x 0.7 mm, number of passes = 5.5, length of one tube = 46.2 m (1.4 x 6 x 5.5 = 46.2 m), thickness of fin = 0.5 mm, pitch between the fins = 2.4 mm, staggered arrangement, pitch of tubes perpendicular to the air flow direction = 50 mm, pitch of tubes above each other from the air flow sense = 25 mm and pitch of tubes behind each other (diagonal) from the air flow sense = 35 mm. The performance of one unit of the UHS was determined in performance test within the SUSEN-loop at CVR by Vojacek et al. [11]. They describe the test procedure and the measured cooling performance as well as internal pressure losses in detail.



Figure 7: Illustrative picture of the internals of sink UHS including tubes with rectangular fins [2]

Table 2: Design parameters of one UHS unit [11]

Pressure of sCO ₂ inlet to sink UHS	78.3 bar
Temperature of sCO ₂ outlet of sink UHS	33 °C
Temperature of sCO ₂ inlet to sink UHS	166 °C
Mass flowrate of sCO ₂	0.325 kg/s
Thermal power of sink UHS	92.5 kW
Temperature of air inlet to sink UHS	25 °C
Temperature of air outlet of sink UHS	50 °C
Volumetric flowrate of air outlet	12500 m ³ /h
Electric power of EC fans	0.33 kW

PP: The piston pump is of the type P72/225-80 III and supplied by Speck-Triplex-Pumpen GmbH & Co. KG. It has a design power of 3.8 kW at a flow rate of 120 l/min. Since it runs at a fixed speed of 260 rpm, the flow rate is adjusted by using a re-circulation of the flow via pipe 10, which is adjusted by valve 27 (Fig. 9). Its maximum pressure is 80 bar. Furthermore, it is designed for gaseous CO₂ and phase changes at the PP are prohibited.

PV: The two piston accumulators are supplied by Roth Hydraulics GmbH. The product number is AK 100-220-36. They have a nominal volume of 100 l of CO₂ each, with a design pressure of 220 bar. A piston accumulator consists of two chambers inside a cylinder, separated from each other by a sliding piston with here 360 mm diameter. Two piston accumulators are attached to the sCO₂-HeRo loop, one for the high-pressure part and one for the low-pressure part. The CO₂ conditions in the lower chamber of PV I and PV II are measured with pressure gauges and Pt100. The upper chamber is filled with nitrogen with high quality. This gas works as a cushion for the mostly incompressible hydraulic fluid in the lower chamber, in this case liquid carbon dioxide. Working pressure is defined by filling the nitrogen chamber with “zero pressure”, with an empty liquid chamber. By filling up the liquid chamber with fluid, the pressure of the nitrogen cushion will increase. Hence, only a fraction of the nominal volume will be used. A pressure increase from a setpoint of 70 bar by 10 bar will occur from 9.1 l liquid CO₂ at adiabatic conditions. On isothermal conditions with very slow changes in pressure, the same increase will be caused by 13.6 l liquid, starting empty at 70 bars and 20 °C. Because of this stiff characteristic, the accumulators will be used as mere buffers for temperature related expansion and for pushing the turbine for startup, but not as storage tanks for the coolant volume of the sCO₂-HeRo loop.

Piping: The seamless piping is made of stainless steel of alloy-316 (1.4435). The 316 alloy is resistant in corrosive environments. The vendor Swagelok limits the pressure for ¾ inch pipes (catalogue number SS-T12-S-065-6ME, outer diameter 19 mm, with 1.6 mm thickness) to 227.5 bar (3300 psig) for a normal temperature range and 218 bar for higher

temperatures up to 204 °C, which is well above the maximum operational pressure of 130 bar of the loop. The cross-sectional area of a typical pipe is slightly below 2 cm². Hence, with an estimated mass flow \dot{m} of 0.65 kg/s and a minimum density ρ of about 100 kg/m³ after the turbine a maximum flow velocity of $w=32$ m/s is to be expected. Using a Moody chart (Moody, L.F. [6]) a Darcy-Weisbach friction factor of $\lambda=0.015$ results for a wide range of Reynold's numbers with an estimated roughness of 5 μ m. Hence, for each meter pipe length L the dimensionless loss factor ζ can be estimated to be 0.94 resulting in a pressure loss of 0.5 bar/m. Thus, a pipe length of about 4.5 m between turbine exhaust and UHS-branching line will lead to a loss of about 2.3 bar. Losses by a check valve in this line are to be considered separately and are assumed to be in the same order of magnitude. Hence, pipe size is assumed to be sufficient. In other lines, because of lower flow velocity, only fractions of this pressure loss should be expected. The piping includes bends with large radii to avoid additional pressure losses, typically adding a loss factor ζ of about 0.13 for a 90° bend (Martin et al. [6]). Table 3 shows the different pipe lengths and number of bends in the cycle. Note that in pipe number 1 and 5 the flow is divided because of the two parallel UHS units. The pipe length is reduced accordingly to compensate the lower flow rate. Further, the pipes are not insulated.

Table 3: Piping parameters

Pipe-No.	Length / m	No. of 45° bends	No. of 90° bends	No. of elbows
1	6.6	0	10	0
2	6.6	5	1	1
3	9	1	6	0
4	1.8	0	4	0
5	4.5	0	7	0
6	1.6	0	2	1
7	2.0	1	3	1
8	1.8	0	3	0
9	3.2	0	4	0
10	1.1	1	0	0
11	0.4	0	0	2

Fittings: Pipe junctions and branches are done by fittings of Swagelok. All parts are made from alloy 316 steel. Welding was avoided, so parts can be easily remounted and mounted. As long as there is no “knee” in the pipe junction, there should be only negligible pressure loss. A knee with a sharp 90° turn can contribute a loss factor ζ of up to 1.3 (Martin et al. [6]). Fittings allow a maximum operational pressure to 200 bar.

Valves: Because of the fittings' compatibility, the four different kinds of valves were ordered mostly from Swagelok.

1. Ball valves with the product number SS-65TS12 with straight flow line to avoid losses are made from stainless steel of 316 type and PTFE seats. To avoid pressure hammers, these valves are mostly operated manually, e.g. to isolate components, like the piston pump. The use is limited for combination with Swagelok fittings below 190 °C because of fluoride rubber materials used for tightness.
2. Needle valves (SS18-RS12) are used to control the flow and offer the option to be equipped with a motoric drive. The flow direction within the needle valve will be changed by more than 90° twice, and an orifice narrows the flow path, so losses will be inevitable. In the used valves, the orifice's diameter is 9.5 mm, the Cv-Value is 1.8 (Kv = 1.56). With a flow of 0.65 kg/s at density about 500 kg/m³ (after compressor), a pressure loss of about 4.3 bar is to be expected at valve 4 (Fig. 9). On the other hand, because of closure time, pressure hammers will be avoided.
3. Check Valves (SS-CHS12-1/3) are used to avoid backflow to compressor or turbine during start-up with the PV or circulating medium with the PP. Because of materials used in the fittings, temperature is limited to 190 °C.
4. Safety relieve valves are employed to ensure limited pressure in the cycle of maximally 130 bar in the high and 113 bar in the lower pressure part.

Pressure sensors: Industrial quality ceramic membrane pressure sensors are used, adapted to the different temperature ranges and a pressure from 0 to 160 bar. Position of pressure transformers is nearby a temperature measuring, so the state of the coolant can be followed from pT-characteristics, especially in the supercritical and single-phase regions. Precision is given as +/- 0.5 % of full range, meaning +/- 0.8 bar deviation from linear behavior. Additionally, a temperature dependence of the signal must be taken into account, with no data available for the transmitters used. Typically, deviations can be about 0.3% full range (+/- 0.5 bar) for each 10 K temperature difference, even in the range of temperature compensation. Last but not least, the stability or reproducibility of the signal has to be taken into consideration, some kind of hysteresis or statistical error, which is typically in the order of 0.05 % (about +/-0.1 bar) of full range. Thoroughly measuring and numerically calibrating the different transmitters can be used to compensate non-linear effects and temperature influence. Statistical error can be estimated by repeated measuring under comparable conditions.

Temperature sensors: Temperature sensors are Pt100 resistor thermometers with Class A specification, manufactured by Electronic Sensors. This demands deviations less than 0.35 °C up to 100 °C and 0.55 °C in the range up to 200 °C. Temperature sensors for TAC bearings are type K thermocouples. There is no special necessity to precision, fast indication is needed to protect the TAC.

Flow meters: Two Coriolis type flow meters are used, PromassFP (CNGmass DCI) from Endress&Hauser. In industry, these transmitters are designed for the use with natural gas. A mass flow between 0-1.33 kg/s can be measured in the DN15

lines. By measuring principle from phase shift between oscillations in between the two branches of the device, mass flow is measured independently from density. The flow meters are also used to measure the density, which is especially important at the compressor inlet, which is close to the critical point, because determining the fluid properties via REFPROP is less prone to density uncertainties than temperature uncertainties. Precision relies on calibration. Deviation from calibrated values is given with 0.5 %.

Control and electrical power supply: Control of components is done by SIEMENS S7 Control Technology, with PCS7 as surface to operate and monitor. It was included to the existing parts operating the glass model. Heater control is done by JUMO phase angle control, fitted to the S7 Environment. Monitoring of CO₂ concentration and subsequent ventilation is independently realized. Shutdown of electrical power supply as protective action will be hard wired. Same is valid for overheating protection of the SEH. The electrical power for SEH can be shut off independently from other components, thus allowing operation of the sCO₂-HeRo loop for commissioning purpose or tests. Because components are located outside the building, common grounding was thoroughly done to avoid differences in electrical potential.

COMMISSIONING AND SAFETY

Several safety features have been employed to safely operate the sCO₂-HeRo cycle. The safety concept is checked and approved by the TÜV according to the present guidelines. First of all, access to the rooms containing the components is restricted. These rooms will not be entered in principle once a certain pressure and temperature margin is exceeded. Additionally, the rooms are equipped with CO₂ detection systems and ventilation systems, which detect leakages and warns the personnel in case the CO₂ concentration in the room gets too high. The ventilation helps to reduce the concentration quickly. Furthermore, pressure relieve valves provide safety against overpressure and fail-safe safety measures against overheating of the SEH and the motor/bearings of the TAC prevent severe machine damage in case of control failure. Additionally, the vibration of the TAC is monitored and special fast acting pneumatic driven ball valve, protects the TAC from overspeed, bypassing the flow to the heat sink immediately.

CONCLUSION

The paper describes the general operation of the sCO₂-HeRo cycle for filling and circulation procedures. These procedures are qualitatively compared with the operation of the other sCO₂-cycles within the sCO₂-HeRo project, namely the SCARLETT and SUSEN loop. These cycles show significantly different layouts in terms of used components. It is pointed out that filling of a transcritical cycle with a large storage vessel such as the SCARLETT loop is possible using CO₂ bottles only. The use of dip-tube bottles may allow filling in more mass more quickly. In addition, the size of the storage vessel determines the

range of operation conditions within the test section due to the different mean density in the loop. Furthermore, due to saturation pressure in the vessel, it provides stable compressor inlet pressure simplifying the control of the conditions in the test section. The SUSEN and sCO₂-HeRo loop apply standard CO₂ gas bottles to fill the loop. As they operate entirely in the supercritical regime, adding additional CO₂ after filling from the bottle may be required. Different approaches are the use of a FC in the SUSEN loop and PV with adjustable pressure in the sCO₂-HeRo loop. It can be concluded that the change of operation conditions by control of the CO₂ mass in the cycle is more flexible applying a FC, but the PV are faster. Generally, it can be concluded that each cycle must be designed according to the according needs, and the given examples help to select a suitable approach. A first set of measurements is given in this paper, representing a simple circulation of yet subcritical, gaseous CO₂, allowing a first validation of pressure losses. Further measurements will be carried out and published in the near future including stationary and transient test cases.

The second part of the paper gives a comprehensive overview of the sCO₂-HeRo cycle configuration and specifications. This includes the design parameters of all main components, number and types of valves, the piping as well as measurement equipment. The P&I diagram and the height scheme present the position of all components. The referenced papers give more sophisticated information and a deeper insight in the design and testing of the components TAC, CHX and UHS.

NOMENCLATURE

D	Diameter
L	Length
\dot{m}	Mass flow
p	Pressure
\dot{Q}	Heat flow
T	Temperature
w	Flow velocity
ζ	Loss factor
η_{is}	Isentropic efficiency
λ	Darcy-Weisbach friction factor
π	Pressure ratio (total to static)
ρ	Density

ABBREVIATIONS

BV	Bleeding valve
CH	Cooler
CHX	Compact heat exchanger
F	(Mass-)Flow measurement

FC	Filling compressor
H	Heater
HTR	High temperature recuperator
LTR	Low temperature recuperator
LUHS	Loss of ultimate heat sink
p	Pressure measurement
P&I	Piping and instrumentation diagram
PP	Piston pump
PV	Pressure vessel (piston accumulator)
PWR	Pressurized water reactor
RV	Reduction valve
SBO	Station black out
sCO ₂	Supercritical CO ₂
SEH	Slave electrical heater
T	Temperature measurement
TS	Test section
TAC	Turbomachine (turbine, alternator, compressor)
UHS	Ultimate heat sink
ρ	Density measurement

ACKNOWLEDGEMENTS

This project has received funding from the European research and training programme 2014 – 2018 under grant agreement No 662116, 764690 and 847606.



REFERENCES

- [1] Benra, F.-K., Brillert, D., Frybort, O., Hajek, P., Rohde, M., Schuster, S., Seewald, M. & Starflinger, J. (2016). A supercritical CO₂ low temperature Brayton-cycle for residual heat removal. *The 5th International Symposium - Supercritical CO₂ Power Cycles*, San Antonio, Texas, USA
- [2] GFHC - Güntner Fluid Cooler, [Online]. Available: https://www.guentner.eu/fileadmin/literature/europe/condenser_s_drycoolers/GFHC/Guentner_GCHC_GCVC_GGHC_GGVC_GFHC_GFVC_Info_EN.pdf. [Accessed: 1-Oct-2018]
- [3] Flaig W., Mertz R., Starflinger J. (2018). Setup of the Supercritical CO₂ Test Facility SCARLETT for Basic Experimental Investigations of a Compact Heat Exchanger for an Innovative Decay Heat Removal System. *Journal of Nuclear Engineering and Radiation Science*, 4(031004-1).
- [4] Hacks, A. J., Schuster, S., Dohmen H. J., Benra F.-K., Brillert D. (2018). Turbomachine Design for Supercritical Carbon Dioxide within the sCO₂-HeRo.eu Project. *Journal of Engineering for Gas Turbines and Power*, 140(12)
- [5] Hacks A. J., Vojacek A., Dohmen H. J., Brillert D. (2018). Experimental Investigation of the sCO₂-HeRo Compressor. *2nd European supercritical CO₂ Conference*, Essen, Germany
- [6] Martin, H., Gnielinski, V., Mewes, D., Steiner, D., Stephan, K., Schaber, K., ... & Kabelac, S. (2002). VDI Wärmeatlas: Berechnungsblätter für den Wärmeübergang. *Verein Deutscher Ingenieure*
- [7] Moody, L.F. (1944) "Friction factors for pipe flow", *Transactions of the ASME* 66(8), 671-684
- [8] Strätz, M., Starflinger, J., Mertz, R., Seewald, M., Schuster, S., Brillert, D. (2017). Cycle calculations of a small – scale heat removal system with supercritical CO₂ as working fluid. *Proceedings of the 14th International Conference on Nuclear Engineering*, ICONE25, Shanghai, China
- [9] Strätz, M., Mertz, R., Starflinger, J. (2018). Design of a compact heat exchanger and heat transfer investigation of a scaled down sCO₂-HeRo system. *Proceedings of the International Congress on Advances in Nuclear Power Plants (ICAPP)*, Charlotte, USA.
- [10] Vojacek, A., Hacks, A. J., Melichar, T., Frybort, O. & Hajek, P. (2018). "Challenges in supercritical CO₂ power cycle technology and first operational experience at CVR. *2nd European supercritical CO₂ Conference*, Essen, Germany
- [11] Vojacek A., Dostal V., Goettelt F., Rohde M., Melichar T. (2019). Performance Test of the Air-Cooled Finned-Tube Supercritical CO₂ Sink Heat Exchanger. *Journal of Thermal Science and Engineering Applications*, 11(6)

SCHEME OF THE GLASS MODEL WITH SCO₂-HERO

Figure 8 shows a schematic sketch of the sCO₂ cycle with the interface to the PWR glass model and valves important for operation in the glass model. Here, the CHX at the interface is denoted with PCHE in Fig. 8 and valve 2 is actually realized by two valves (valve 32 and 33, see Fig. 9) in order to completely disconnect it from the original glass model.

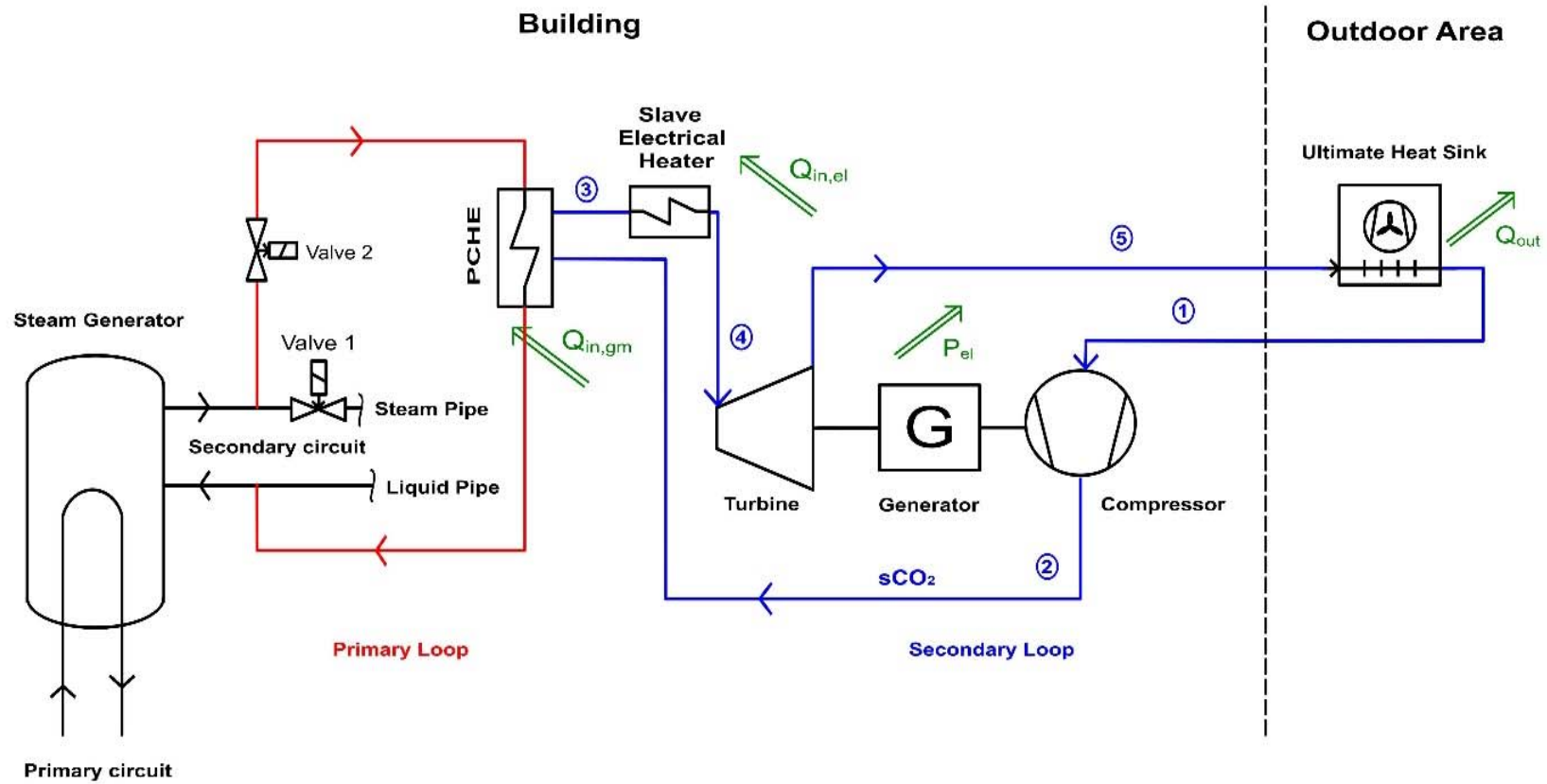


Figure 8: Scheme of the glass model with sCO₂-HeRo [8]

ANNEX B

P&I DIAGRAM OF THE SCO₂-HERO CYCLE

Figure 9 shows the P&I diagram of the sCO₂-HeRo cycle only. The connection to the PWR glass model, schematically presented in Fig. 8, is realized by the steam pipes in section 5.

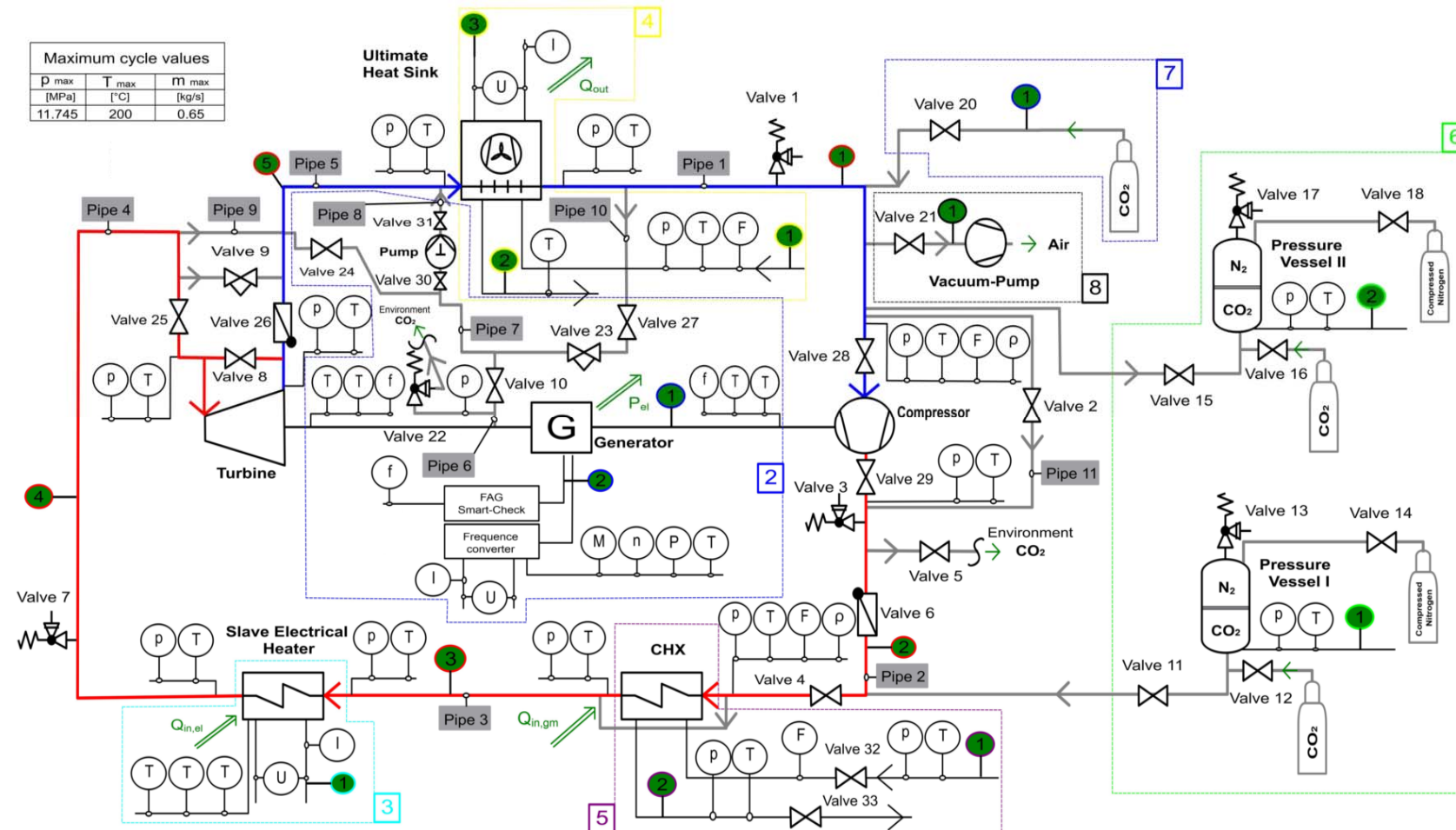


Figure 9: P&I diagram of the sCO₂-HeRo cycle

**SHOUHANG-EDF
10MWE SUPERCRITICAL CO₂ CYCLE + CSP DEMONSTRATION PROJECT**

Yann Le Moullec
EDF R&D China
Beijing, China

Jinyi Zhang*
EDF R&D China
Beijing, China
Email: Jinyi.zhang@edf.fr

Zijiang Yang
EDF R&D China
Beijing, China

Wenlong Chen
Shouhang IHW
Beijing, China

Zhipeng Qi
Shouhang IHW
Beijing, China

Pan Zhou
EDF R&D China
Beijing, China

Xihua Wang
Shouhang IHW
Beijing, China

Shuai Wang
Shouhang IHW
Beijing, China

ABSTRACT

Supercritical CO₂ power cycle, due to its potential to reach high thermal efficiency and high flexibility, is a promising approach to increase the competitiveness of concentrated solar power. Shouhang and EDF signed a collaboration contract in May 2018, with the objective to retrofit Shouhang's 10MWe concentrated solar power plant with a 10MWe supercritical CO₂ power cycle before the end of 2020. As the first industrial scale application of supercritical CO₂ cycle on solar thermal power plant in the world, this project aims to demonstrate several key technical aspects, including optimal cycle design for concentrated solar power, equipment design and operation, system operation and control. In addition to all the technical aspects related to supercritical CO₂ cycle, high-temperature molten salt and cold storage are also novel concepts to be investigated during this project. The 10MWe supercritical CO₂ cycle to be demonstrated is designed to work with the current existing solar field and thermal storage field. As a good compromise of demonstration interest for future commercial project, salt utilization, cost, complexity and efficiency, recompression cycle with intercooling and preheating is selected. In this paper, project concept and system design are presented, as well as the recent progress. Technical considerations on overall selection of technology path, equipment and system design, especially the problem related to the integration of SCO₂ cycle with CSP, are also addressed.

INTRODUCTION

In recent years, facing the worldwide environmental challenge and the scarcity of fossil fuels in some regions of the world, renewable energy is gaining more and more importance in the development portfolio of energy industry. Solar and wind energy are two major renewable energy solutions which attract most of the attention, however, the highly uncontrollable variability of solar irradiation and wind brings huge challenges for the electric power grid to match the instantaneous energy demand and production. As a result, the renewables are suffering serious curtailment, e.g. in 2016, the curtailment of wind and solar PV energy reached 57.3TWh in China [1]. In addition, the highly uncontrollable variability of solar irradiation and wind also limits the highest share of renewable energy that can be integrated into the power system in the future. Concentrated solar power (CSP), which can reach a high solar energy utilization efficiency and operate with low-cost thermal energy storage (TES), e.g. the commercially utilized solar molten salt (60 wt% NaNO₃ and 40 wt% KNO₃), is a grid-friendly renewable solution. Because CSP, if equipped with enough TES, is able to completely decouple the solar-thermal and thermal-electricity conversions, then achieving continuous production and regulating the power output depending on the grid demand, regardless of the weather conditions.

However, CSP's high cost, 120\$/₂₀₁₆/MWh in average in 2020 reported by IRENA, makes it difficult for long-term

deployment. In order to increase its competitiveness compared to other renewable solutions with storage, i.e. photovoltaic with battery, in addition to the efforts done to reduce the capital cost, there are two main technology development paths: one is to increase the solar-thermal efficiency by optimizing solar collector efficiency, the other is to increase the thermal-electricity efficiency by increasing the thermal storage temperature or power generation cycle efficiency. Supercritical CO₂ (SCO₂) power generation cycle is identified as a promising technology with high potential in the second path to increase the overall thermal-electric efficiency and reduce the capital cost due to simpler layout, more compact turbo-machinery and possibly higher flexibility during startup and shutdown [2–6].

Besides, CO₂ also exhibits many attracting characteristics as a heat transfer fluid [8–10]: it is abundant, inexpensive, non-toxic and less corrosive compared to water at the same high temperature with easily-achievable critical point (30.98 °C, 7.38 MPa). It shows also a good thermal stability up to 1500 °C and no freezing problem down to -55 °C. Gas Brayton cycle operating with SCO₂ benefits from the real gas behavior of CO₂ in the vicinity of the Andrews curve, which leads to the reduction of specific volume and therefore of the compression work in the cycle. More reduction of compression work is achieved when CO₂ is compressed closer to its critical point, as the fluid becomes more incompressible. This mechanical effect, i.e. the significant reduction of compression work, results in a significant thermal efficiency improvement of SCO₂ Brayton cycle compared to other working fluid for Brayton cycle, e.g. helium or air [7]. Compared to Helium Brayton cycle, SCO₂ cycle needs a much lower turbine inlet temperature to achieve the same efficiency [7], which brings less challenge for the heat sources, especially for CSP. As the SCO₂ cycle operates with high pressure and small pressure ratio, the fluid remains dense throughout the entire system, as a result, the volume of turbo-machineries is significantly reduced (Without considering the giant condenser after the water steam turbine, the volume of the SCO₂ turbine designed for this 10MWe project is only ~6% of that of the currently onsite 10MWe water steam turbine.). Replacing water by CO₂ in the power block also simplifies significantly the operation of CSP plants which are mostly located in the droughty areas.

Due to its potential to reach high efficiency and high flexibility with compactness and simplicity, in recent years, there are more and more efforts from academies and industries, with the support of government funding, to build test facilities from kW-scale to MW-scale, in order to better understand the system, investigate possible technical problems and discover feasible solutions to deal with the underlying challenges. Here is a summary of important projects which already built a test facility or is building one: (1) In 2010, Bettis Atomic Power Laboratory and Knolls Atomic Power Laboratory, under the support of Naval Reactor Program, completed the installation of a 100kW / 300 °C / 16.5MPa simple recuperated closed-loop SCO₂ cycle with a two shaft design: a turbine driven compressor and a turbine driven generator [11–13]; (2) In 2012, Sandia National Lab completed the installation of a 250kW / 540 °C / 13.5MPa

Table 1

Key design parameters of Shouhang Dunhuang 10MWe CSP plant

Parameters	Value
Location	Dunhuang, Gansu, China
Design net power (MWe)	10
Annual power generation (GWh) ^{Year 2017}	10.67
Thermal storage hour (h)	15
Storage medium	Solar Salt
Molten salt amount (ton)	5800
Design max. MS temperature (°C)	565
Design min. MS temperature (°C)	290
Tower height (m)	138
Heliostat amount (#)	1525
Heliostat surface (m ²)	115.5
Total reflective surface (m ²)	176138
Cooler	Air cooler

SCO₂ closed-loop recompression cycle with two turbo-alternator-compressors, one gas chiller of type printed circuit heat exchanger (PCHE), two recuperator of type printed circuit heat exchanger and six heater of type shell and tube heat exchanger [14]; (3) In 2012, Southwest Research Institute, with the support of Sunshot Program and its industrial partners, launched a SCO₂ project to design a high temperature and high efficiency SCO₂ turbine and to build a 1MWe test loop to test the turbine at off-design conditions, i.e. at 1MWe scale. The high-temperature testing of turbine at reduced flow has been finished recently[15,16]. (4) In 2015, Nuclear Power Institute of China (NPIC) started the design and construction of 1MWe SCO₂ simple recuperated test loop [17]. (5) In 2016, Xi'an Thermal Power Research Institute (TPRI) started the design and construction of a natural gas fired 5MWe / 600 °C / 20MPa SCO₂ recompression cycle with preheating and reheating [18,19].



Figure 1. Shouhang Dunhuang 10MWe CSP plant

With all the research done before by the academies and industries, Shouhang and EDF, in May 2018, signed a collaboration contract to retrofit Shouhang's 10MWe CSP plant with a SCO₂ power cycle, in order to push its technical readiness to a higher level, then to assess its technical and economic feasibility in large-scale commercial projects. The objective of

this demonstration project is to build a 10MWe closed-loop SCO_2 cycle adapted to the heat source characteristic of CSP. In the scope of this project, some key technical aspects that are critical for the future commercial application of SCO_2 cycle in CSP will be investigated: (1) Optimal SCO_2 cycle design for CSP; (2) 15MWe-scale high-temperature and high-efficiency turbine design and operation; (3) Near-critical point compressor design and operation; (4) 40MW-scale compact heat exchanger design and operation; (5) Near-critical CO_2 cooler design and operation; (6) 30MW-scale molten salt/ CO_2 heat exchanger design and operation; (7) High-temperature ($>620^\circ\text{C}$) heat transfer fluid selection; (8) High temperature ($>620^\circ\text{C}$) thermal energy storage system design and operation; (9) High temperature ($>620^\circ\text{C}$) electrical heater; (10) System operation and control; (11) System flexibility analysis; (12) Material test for SCO_2 , molten salt and high-temperature heat transfer fluid; (13) Cold storage. This paper aims to give an overview of project concept. System design and technical considerations behind are presented and discussed.

SHOUHANG DUNHUANG 10MWE CSP PLANT

The 10MWe CSP plant to be retrofitted is located in Dunhuang, Gansu Province, North-West of China, which started operation since 2016. This is a solar thermal power plant operated with molten salt tower, 15h two-tank molten salt storage, a 10MWe water steam Rankine cycle and a 20MW air cooler. With the design scale of thermal storage, it could provide enough heat to realize 24-hour continuous operation. More information is given in Table 1.

SCO_2 + CSP DEMO SYSTEM DESIGN

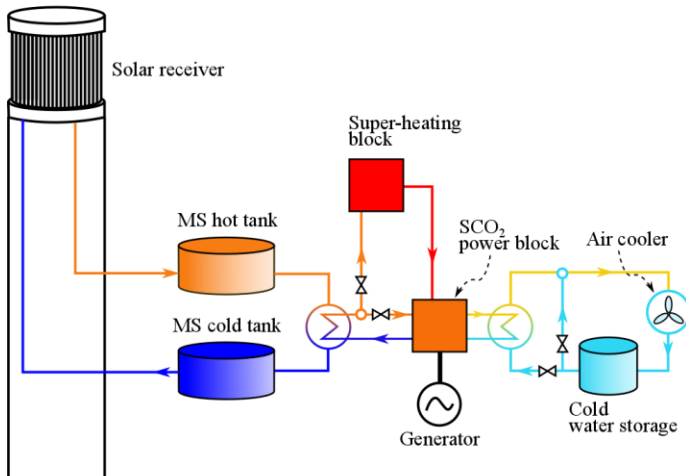


Figure 2. Demonstration system concept

The demonstration system design concept is shown in Figure 2. It consists of heliostat field, solar tower and receiver, thermal energy storage system with one hot tank and one cold tank, SCO_2 power block, superheating block, cooling system with cold storage. The demonstration project keeps the current existing

Table 2

Main design boundary conditions and hypotheses for preliminary performance assessment of demonstration project

Parameters	Value
SCO_2 cycle net power (MWe)	10
Molten salt maximum temperature ($^\circ\text{C}$)	530
Molten salt exhaust temperature ($^\circ\text{C}$)	>290
Design molten salt mass flow rate (kg/s)	80
Compressor isentropic efficiency (%)	80
Turbine isentropic efficiency (%)	85
Heat exchanger min. pinch temperature ($^\circ\text{C}$)	10
Heat exchanger pressure drop (bar)	1
Max. CO_2 pressure (bar)	250
Min. CO_2 temperature ($^\circ\text{C}$)	35

solar field and thermal energy storage system with minor modification on the instrumentation, piping and pumping system of TES system.

A SCO_2 power block is built in parallel with the current water steam Rankine cycle. Since the water steam Rankine cycle is kept, it is possible to use the electricity generated by it to help the startup of SCO_2 cycle. One of the demonstration project objectives is to investigate high-temperature operation of SCO_2 turbine ($\geq 620^\circ\text{C}$), but using the current existing molten salt system, the maximum temperature that can be achieved is 565°C , which is not enough for high-temperature turbine operation, therefore, a super-heating block is added after the main heater between current molten salt and CO_2 to heat CO_2 temperature to the desired temperature. With extra heating, it is expensive to operate in long-term, as a result, the high-temperature operation mode is kept only for research purpose. During normal operation, the only heat source comes from the current solar field and TES system.

The cooling system is an indirect water cooling system with atmosphere as the final heat sink. SCO_2 cycle is sensitive to the fluctuation of cycle minimum temperature, especially for the near-critical compressor operation. The indirect cooling is selected to attenuate the fluctuation of local air temperature through the intermediate cooling water cycle. With this indirect cooling design, it is also possible to integrate cold storage into it, which can be beneficial to stabilize cycle operation and achieve higher overall efficiency.

SCO_2 POWER BLOCK DESIGN BOUNDARIES

The supercritical CO_2 cycle to be demonstrated is designed to operate with the existing solar field and thermal storage system in a commercial project. Therefore, there are more constraints to be respected during the SCO_2 system design phase:

- 1) Design net power output to be 10MWe: The retrofitting will be done in a commercial project to replace the original water steam Rankine cycle, therefore, according to the local regulation, the design power output cannot be modified.
- 2) Molten salt exhaust temperature to be lower than 320°C : The cold storage tank is design to operate with molten salt at 290°C , in order to avoid any technical risk regarding

Table 3

Summary of considered cycles

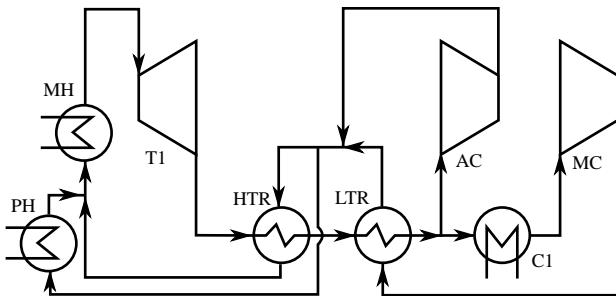
Cycle	Max .T	Min. P	CO ₂ flow	Split ratio	Power	Eff.	MS Outlet T ⁺	HX UA (100% = 4857 kW/ °C)*	Complexity (Nbr. Turbomachinery)
	°C	bar	Kg/s	%	MWe	%	°C	%	
RG-IC	520	68.5	96.2	-	10.06	34.6	290	100.00	3
RC-IC	438	82.6	145.9	31.67	9.95	34.2	290	107.47	4
RC-IC	470	82.0	126.5	33.04	9.33	36.6	320	98.68	4
RC-PH	439	87.1	162.94	34.17	10.01	34.4	290	133.05	3
RC-DPH	464	86.9	141.8	24.92	10.18	34.9	290	100.29	3
RC-IC-PH	468	82.1	137.7	27.74	10.35	35.6	290	113.87	4
PartC-PH	485	72.3	122.0	41.32	10.40	35.8	290	101.00	4

*100% means UA=4857 kW/ °C, higher than 100% means the heat exchanger needs more UA

* The available molten salt temperature utilization range for this project is 290 °C ~ 530 °C. To maximize the overall power output, the result shows that the molten salt will always be 100% utilized, i.e. between 290 °C and 530 °C.

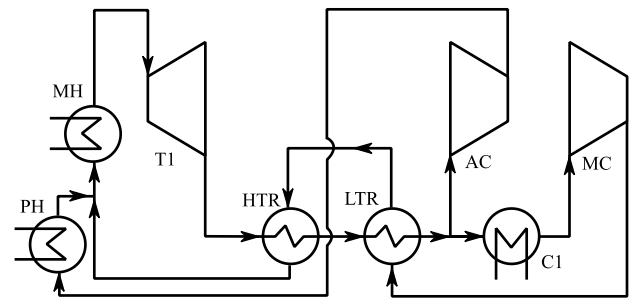
cold tank cooling and thermal expansion, after consulting the design team of thermal storage system, 320 °C is selected as the upper limit for molten salt exhaust temperature.

- 3) Molten salt inlet temperature for main heater to be 530 °C: The original design molten salt maximum operation temperature is 565 °C, but due to the complexity of solar field control and high variation of weather conditions, the maximum molten salt achieved is mostly 530 °C.
- 4) Dry cooling: The 10MWe CSP plant locates in one of the most water-deficient area in China, therefore, any cooling system with high need or high consumption of water is strictly prohibited. Only dry cooling is allowed in this region.

**Figure 3.** RC-PH: recompression cycle with preheating

As a demonstration project, it is important to demonstrate performance but in the meanwhile, the risk should be well controlled. Higher cycle pressure can help to improve cycle efficiency, but it brings also high risk for the design and operation of turbine. For ultra-supercritical water steam cycle, a 30MPa high-pressure turbine design is already achieved and commercialized, but for SCO₂, a less mature technology, a 5MPa margin is taken to reduce the risk of less of experience. 35 °C is selected as the design minimum cycle temperature in order to

keep a safe margin with the critical temperature of 31.10 °C. For the efficiency of turbo-machineries, 89% and 93% is expected for compressor and turbine when the technology becomes mature, but at the current stage, a 9% margin is taken as a first estimation due to lack of experience for most of the suppliers. Compared to turbo-machineries, there are more effective and comparable reference for heat exchanger, but considering the cost, 10 °C / 1bar is selected as the minimum pinch temperature and maximum pressure drop for the main heat exchanger in the cycle. The main design boundary conditions are summarized in Table 2.

**Figure 4.** RC-DPH: recompression cycle with direct preheating

SCO₂ CYCLE DESIGN

For the selection of SCO₂ cycle, as a SCO₂ demonstration project to prepare for the commercialization of SCO₂ in CSP, the selected cycle layout should be optimized for CSP application, or at least able to demonstrate all the key cycle configurations. In the meantime, the complexity should be moderate in order to control the project risk well. Cost is also an important factor to be considered. Therefore, all the reheating cycles are not considered due to an extra turbine increases significantly the cost and has no direct benefit in terms of new technology demonstration. Two different approaches are adopted for cycle

selection: one based on expertise and the other based on a SCO_2 cycle superstructure developed by Zhao Qiao in EDF R&D [20].

In order to achieve a good compromise of demonstration interest for future commercial project, salt utilization, cost, complexity and efficiency, a wide range of cycles are studied, six among them are presented in this paper:

- 1) Regenerative with intercooling (RG-IC)
- 2) Recompression with intercooling (RC-IC)
- 3) Recompression with preheating (RC-PH)
- 4) Recompression with direct preheating (RC-DPH)
- 5) Recompression with intercooling and preheating (RC-IC-PH)
- 6) Partial cooling and direct preheating (PartC-PH)

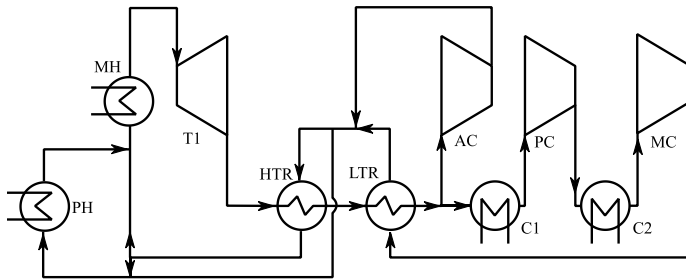


Figure 5. RC-IC-PH: recompression cycle with intercooling and preheating

With the cycle power output as the final optimization objective function (Details on the optimization can be found in another study of the author [21]), these 6 cycles are modeled and optimized within the imposed boundary conditions by this project. The key parameters after optimization for each studied cycle is shown in Table 3. The final results show that SCO_2 cycles tend to use 100% of the molten salt available to maximize the power output. RG-IC offers a very good performance especially considering its simplicity and underlined lower risk for development and low cost. However, due to its incapability to solve the pinch problem in the recuperator, RG-IC could not achieve a high efficiency which would be interesting enough for the future commercial project. Therefore, RG-IC is not selected for this project which is dedicated to demonstrate an optimal cycle for CSP. Within the constraint imposed, especially the one that limits molten salt outlet temperature to be lower than 320 °C, RC-IC cycle could possibly reach a higher efficiency of 36.6% with MS exhaust temperature of 320 °C, but it produces less power. Preheating, in this case, helps to improve slightly the efficiency at the cost of 30% more heat exchanger. A different way to implement preheating, called “Direct preheating”, can improve further the efficiency and with smaller heat exchanger, by using only one recuperator in the cycle and make the recompression flow go directly into the preheater. The better performance of “Direct preheating” mainly comes from the hypothesis made for the performance evaluation, because with only one recuperator, it helps to save compression work. The difference between PH and DPH is shown by Figure 3 and Figure

4. RC-IC-PH and PartC-PH cycles give very similar performance, with a higher efficiency than the others. However, PartC-PH cycle is a trans-critical which will bring big challenge to the design and operation of compressor. Therefore, RC-IC-PH cycle is finally selected for the implementation, even with a 14% bigger heat exchanger.

In the RC-IC-PH cycle, with the demonstration boundary conditions imposed, the CO_2 flow is heated to 468 °C by 530 °C molten salt in the main heater, then is discharged in the turbine from 250 bar to 85 bar. The hot outlet flow of turbine goes through the recuperators to transfer the remaining thermal energy into the cold CO_2 flow on the other cycle of cycle, then is split into two parts. One flow, ~72% of total flow, goes into the pre-cooler to be cooled to 35 °C, pre-compressed to 107 bar then re-cooled to 35 °C for the final compression to 250 bar, the high pressure flow then enters the LTR to recuperate the thermal energy of turbine outlet flow. The other flow, ~28% of the total flow, goes into the auxiliary compressor to be compressed directly to 250bar, then mixed with LTR cold outlet flow. Before entering HTR, one part of flow, ~30%, is re-split into the preheater to be heated by the low-temperature molten salt which comes from the outlet of main heater, the other part goes into HTR to be heated by hot turbine outlet CO_2 flow. These two flow mix before the main heater, and are then heated to the maximum temperature before entering turbine. This cycle achieves 35.6% of cycle net efficiency and 100% utilization of molten salt, which brings no significant modification to the operation of storage system and solar system. It produces 10.35MWe as the gross power with maximal temperature and pressure of 468 °C and 250.0bar, minimum temperature and pressure of 35.0 °C and 82.1 bar, recompression split ratio of 27.74%. A summary of turbomachinery parameters and heat exchanger parameters is given in Table 4 and Table 5.

Table 4
Summary of turbomachinery parameters

	<i>Turbine</i>	<i>PC</i>	<i>MC</i>	<i>AC</i>
Power (MW)	16.1	0.6	2.4	2.8
Inlet T (°C)	468	35	35	68
Inlet p (bar)	250	82	106	83
CR	2.9	1.3	2.4	3.0
Mass flow rate (kg/s)	137.7	99.5	99.5	38.2

Table 5
Summary of heat exchanger parameters

	LTR	HTR	PH	MH	C1	C2
Heat duty (MW)	20.8	26.5	7.5	21.6	14.5	4.2
Average LMTD (°C)	15.5	18.9	25.4	36.5	15.3	10.6
UA (kW/K)	1488	1468	339	745	1094	396
Effectiveness (%)	88.6	89.1	90.6	91.5	70.6	57.9

SUPERHEATING SUBSYSTEM

SCO₂ cycle starts to show advantage compared to water steam Rankine cycle when the cycle maximal temperature reaches around 550 °C (This temperature depends on the design of SCO₂ and water steam cycle). Even with the current molten salt, when turbine and compressor design and manufacturing become mature, i.e. compressor efficiency reaches 89% and turbine efficiency reaches 93%, it is also possible for a SCO₂ cycle without reheating of 500 °C / 30 MPa to reach the same level of cycle net efficiency as a water steam cycle (around 45.3%) at the cost of around 4% loss of molten salt storage potential. Considering SCO₂ has the potential to save power block cost, increase significantly flexibility and reduce parasitic energy consumption, it remains a strong competitor of water steam cycle at this temperature level. However, in order to be able to fully demonstrate the feasibility of SCO₂ cycle for the future generation of CSP technology with higher temperature thermal storage medium in the scope of this project, it is necessary to raise the SCO₂ cycle temperature to a higher temperature, at least beyond 620 °C.

Yet, with today's solar system and solar salt in Dunhuang plant, the molten salt can only be raised to 565 °C at most, which is not enough compared to the desired temperature. Therefore, a superheating system is considered. To realize the superheating block, seven options have been preliminarily reviewed: three options with direct heating of CO₂ and four options with indirect heating of CO₂, with an intermediate heat transfer fluid (HTF):

- 1) Direct heating by gas combustion: CO₂ enters a natural gas boiler at a temperature around 500 °C and leaves at 620 °C. Considering the SCO₂ gas boiler has been used in TPRI's 5 MWe project, there is no significant technical barrier to overcome. However, with a high inlet flow temperature of around 500 °C, the efficiency of gas boiler is very low. It is possible to redesign the boiler to make use of the low-grade heat of flue gas, but this increases significantly the system complexity with no interest for the future CSP application. In the meantime, natural gas is expensive.
- 2) Direct electrical heating supplied by a PV solar farm: CSP with PV is a commercially interesting concept to be demonstrated. After evaluation with self-developed dynamic model, a 5MWe solar PV farm is needed to generate enough electricity for superheating, which implies a large amount of supplementary investment. In addition, the policy complexity of coupling a commercial PV project with a demonstration project also brings huge challenge to make this PV farm profitable. Another reason is that the instability of PV electricity production may make the experimental plan unpredictable or high additional cost from the purchase of electricity from the grid.
- 3) Direct electrical heating supplied by auto-consumption: This approach could be implemented if the high temperature operation mode is not too often and for research use only. Nevertheless, electric heater that is able

to withstand very high pressure (200~300bar) are expensive.

- 4) High temperature heat transfer fluid in the receiver and storage: This approach has been seriously considered as the receiver design of the demonstrator is able to withstand up to 900 °C. But the molten salt and the storage system is not able to withstand a temperature up to 620 °C. New heat transfer fluid and new storage tank can be implemented but only after a dedicated material corrosion test on the new heat transfer fluid. Besides, the investment is very high.
- 5) High temperature heat transfer fluid heated by electrical heating from auto-consumption or PV farm: To simplify the electrical heater design and cut its cost down, the use of indirect heating is considered. Besides, this option allows the demonstration of high-temperature HTF / CO₂ heat exchanger, high-temperature HTF electric heater and the high-temperature HTF operation, which is useful for the design of future-generation of CSP. This option will be prioritized for this conceptual design.
- 6) High temperature heat transfer fluid heated by gas combustion: This option reduces some potential difficulties in the design of the gas heater and allow the demonstration of a HTF/CO₂ superheater, but it has the same problem as mentioned in option 1.
- 7) High temperature heat transfer fluid heated by gas engine exhaust: This option aims to mitigate the fuel cost of gas heating by the cogeneration of electricity and high temperature HTF but today there is no available gas engine or gas turbine with an exhaust gas temperature above 650 °C at the required scale. Moreover, it is very unlikely that this option could contribute to reduce lifetime cost of the demonstration.

Based on this review and analysis, option 5 (indirect electrical heating) will be considered as main solution, mainly due to its long-term interest for future generation of CSP. Technical and economical assessment of this option is ongoing. If it is not validated at the current phase or classified as high risk, a smaller scale high-temperature HTF operation loop will be built for material test and loop operation study. In the meantime, option 1 and option 3 are taken as backup solution if no technically and economically feasible HTF is found.

Several promising candidates for HTF under discussion now are Chloride salts (ClMgNaK and ClZnNaK), Nitrate Salt, sodium and low melting point glass.

COOLING SYSTEM WITH COLD STORAGE

Dunhuang, located in North-West region of China, belongs to temperature continental climate zone, whose main temperature characteristics is the large annual mean temperature difference. As indicated by Figure 6, Dunhuang has an annual temperature difference of 58.7 °C and an annual mean temperature of 9.78 °C. Besides, the daily temperature difference is also very high: even during the hottest day when the daily highest temperature is 38 °C, the minimum temperature can be as low as 17 °C. This kind of annual temperature distribution

makes it an ideal case to test cold storage. Figure 7 shows the average daily temperature for every month in Dunhuang. It can be observed that even during the hottest months, i.e. June, July and August, there are only 9 hours per day when ambient temperature is higher than 25 °C. For the rest 15 hours, the ambient temperature is lower than 25 °C with an average temperature of 20 °C and a minimum temperature of 16 °C. Based on this daily temperature difference, together with proper sizing and operation of air cooler, there can be sufficient cooling source to maintain the SCO₂ cycle operated with the highest efficiency during a whole day.

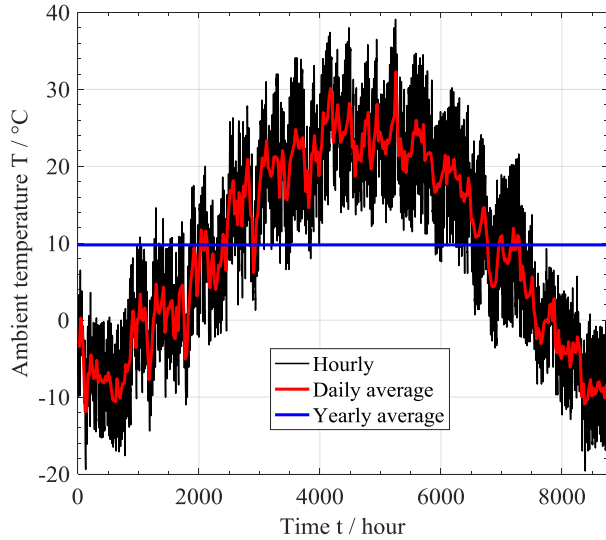


Figure 6. Yearly temperature distribution in Dunhuang

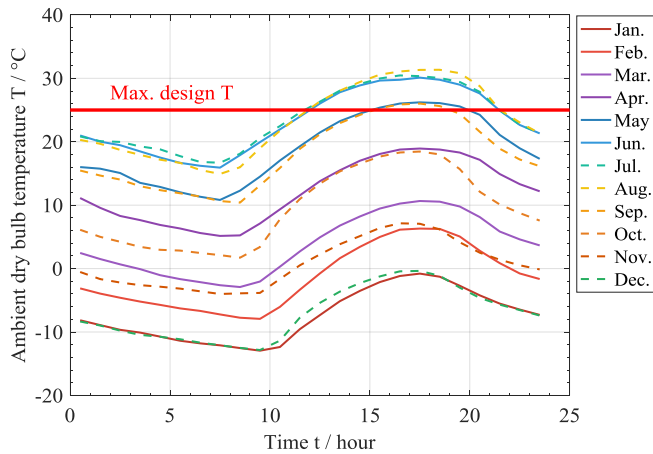


Figure 7. Daily temperature profile in Dunhuang

A simplified dynamic model is build for the cooling system with the objective to conduct a preliminary performance assessment. The model consists of the following key modules:

- Air cooler: the air cooler is modeled assuming that there is an ideal controller to reduce the cooling water temperature to the desired temperature level which is the real time air temperature – design air cooler pinch.

- A water/CO₂ heat exchanger: it is modeled in detail to give a precise estimation on the cooling water flow required to cool down the CO₂ flow to the design temperature before entering compressors, when the temperature of cooling water changes due to ambient temperature variation. For more modeling details, you can refer to another paper presented by EDF R&D China on dynamic modeling and control system design.
- Cold storage water tank: it is modeled as a perfectly stirred reactor.

The main operation logics of cooling system are:

- The air cooler is operated at full load whenever the ambient temperature is below design ambient temperature. Otherwise, it is stopped.
- The cold storage is discharged whenever the cooling water is needed, at the required flow rate.

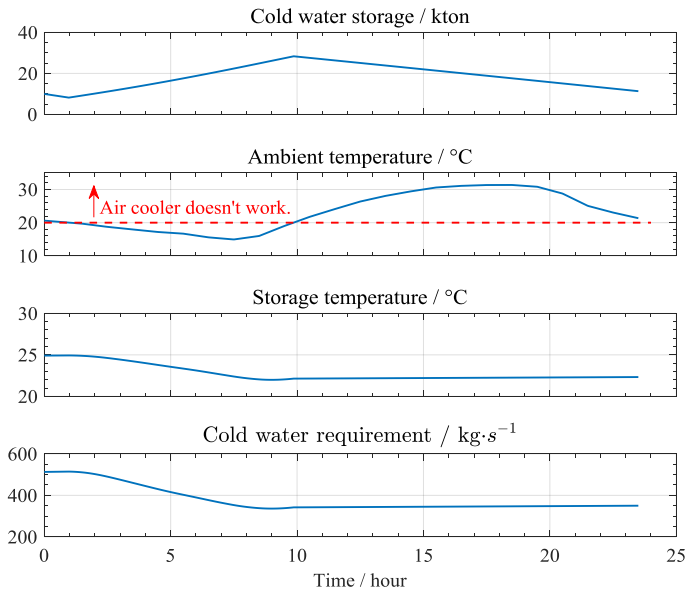


Figure 8. 24-hour continuous full-load operation during a typical day in August, with air-CO₂ pinch of 15 °C, initial storage water temperature of 25 °C, an oversized air cooler, two times capacity than that required during cycle full load: (1) Evolution of cold water storage amount; (2) Evolution of ambient temperature; (3) Evolution of cold water storage temperature; (4) Evolution of required cold water for SCO₂ system.

For the selected demonstration cycle, given a constant 5 °C temperature pinch for air cooler and 10 °C pinch for the CO₂ cooler, the maximum design ambient temperature is 20 °C. Therefore, the air cooler is set to operate only when ambient temperature is below 20 °C. The dynamic model created is used to simulate a 24-hour full-load continuous cycle operation in a day with a typical daily temperature profile in August, which represents the typical temperature profile that one of the hottest month would have. Figure 8 shows the transient behavior of cold storage during the day with an oversized air-cooler capacity, two times capacity than that required during cycle full load. The cold storage tank is initiated with 10k tons 25 °C water. At the beginning of the day, the ambient temperature is higher than the

design temperature, air cooler does not work at the moment, then a slight decrease is observed. But later, the ambient temperature decreases below 20 °C. It creates a perfect heat sink for air cooler, therefore air cooler is controlled to work at full load, generates two times than necessary cold water, resulting in an accumulation of cold water in the storage tank. The storage is used later during the day when ambient temperature is much higher than the design temperature. Finally, with the over-sized air cooler, at the end of day, there is still enough water storage for the next-day operation even with a hot weather like this day. Air cooler only works 42% of a day while the cycle operate at full time and full load, with no impact from hot ambient temperature on the cycle operation and efficiency. The peak storage is reached when the temperature starts to exceed the design criterion. During the day, due to the lower ambient temperature region, the storage water temperature decreases monotonically until the moment when air cooler does not work any more. This trend helps a lot to reduce the consumption of cold storage because with a lower cold temperature, a lower mass flow rate is sufficient to achieved the same cooling requirement.

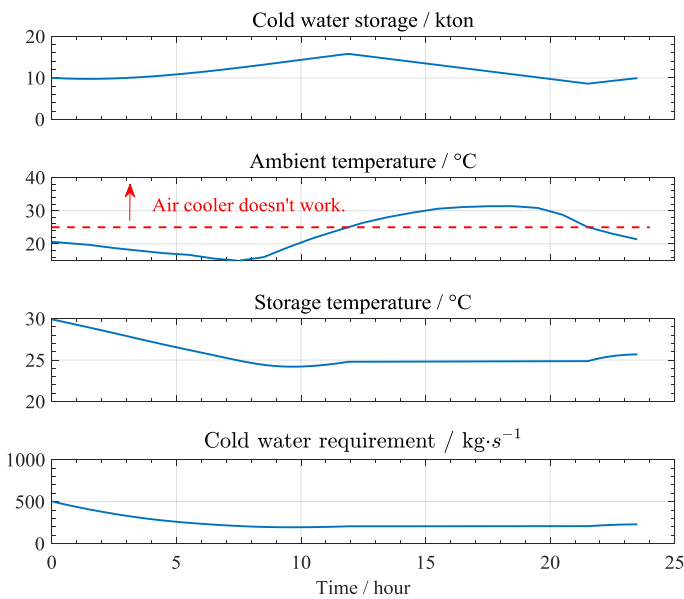


Figure 9. 24-hour continuous full-load operation during a typical day in August, with air-CO₂ pinch of 10 °C, initial storage water temperature of 30 °C, an sub-sized air cooler, 80% capacity than that required during cycle full load: (1) Evolution of cold water storage amount; (2) Evolution of ambient temperature; (3) Evolution of cold water storage temperature; (4) Evolution of required cold water for SCO₂ system.

If the air/CO₂ temperature pinch is reduced to 10 °C, 5 °C for air/water and 5 °C for water/CO₂, as shown by Figure 9, the peak storage is significantly reduced to 160k ton, meaning that the storage could be reduced as well as the initial investment. In the meantime, the air cooler allowed operation time is increased from 8 hours to 12 hours, therefore, the air cooler capacity is reduced to 80% of that required at cycle full load. This further reduce the cost of air cooler, even compared to the case with no cold storage. Besides, it should be emphasized that this is the

operation during the hottest day with no deep optimization on the control of storage. If more efforts could be done, there is still space for further optimization.

Alternatively, by taking into account the possibility to implement cold storage, the design minimum temperature could be reduced to further increase the cycle design efficiency, even a SCO₂ Rankine cycle could be considered. For a recompression cycle with intercooling and preheating, given the mature technology hypothesis (turbine efficiency 93%, compressor efficiency 89%, 5 °C pinch and 1 bar pressure drop for heat exchangers), Figure 10 underlines the benefit of reducing cycle minimum temperature. In this case, when cycle minimum temperature is reduced by 5 °C, efficiency is increased by +1.34pt%. Considering the significant efficiency improvement potential and the daily electricity price variation, it could also be economically feasible to implement extra cooling facility with cold storage. Detailed techno-economic analysis will be done further evaluate its feasibility and benefit.

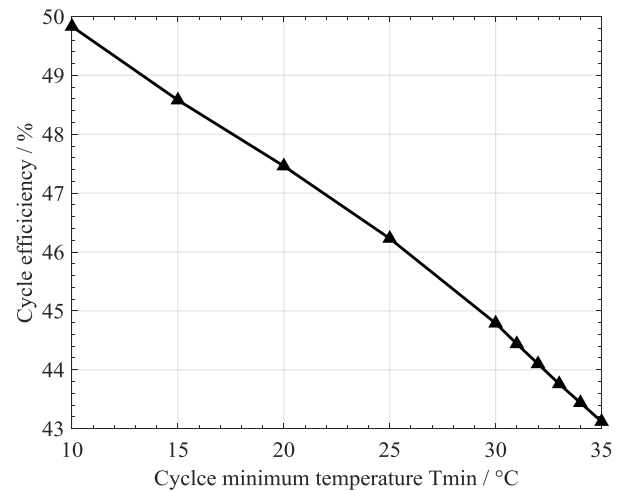


Figure 10. Variation of cycle efficiency with respect to cycle minimum temperature for a recompression SCO₂ cycle with intercooling and preheating, which operates with molten salt between 565 °C and 290 °C, turbine efficiency of 93%, compressor efficiency of 89%, heat exchanger pinch of 5 °C and heat exchanger pressure drop of 1 bar

During winter, as shown by Figure 7, the maximum daily temperature is only 0 °C. Freezing may bring problems to the operation. Therefore, necessary insulation or putting the main piping underground are considered to prevent the freezing risk. Base the experience of thermal power plant operated in the same region, these measures should be enough to solve this issue.

CONCLUSION

In this paper, the Shouhang-EDF SCO₂ demonstration project is presented, in terms of overall system design, key technical path selection and consideration. The main conclusions are as follows:

- 1) As an industrial scale SCO₂ project integrated with a commercial CSP plant, it is able to demonstrate equipment design, system design and operation that could be scaled up to large industrial application of SCO₂ cycle.

- 2) Superheating solutions are now under investigation. It will be implemented in the second phase of project, but during the design in the first phase, all the necessary space and connections are kept for the further implementation of superheating block. Besides, in the first phase, material test will be done for high-temperature heat transfer fluid, and a small test loop for high-temperature heat transfer fluid is under discussion.
- 3) The climate in Dunhuang makes it an ideal place to implement cold storage in order to achieve better overall efficiency. The detailed investigation is ongoing to find the optimal design by taking into account the power plant operation and cost.
- 4) The SCO_2 RC-IC-PH cycle is selected for the final implementation as a compromise demonstration interest for future commercial project, salt utilization, cost, complexity and efficiency. It achieves a net efficiency of 35.6%.

The conceptual design and the first-round discussion with possible suppliers are finished. The second round discussion will be closed before the end of May, 2019, when a short list of suppliers will be determined for the following detailed discussion. In parallel, the basic design is ongoing, cooperating with design institute. The final determination of key equipment supplier will be fixed before June, 2019. Because after the clear definition of project scope, the project is progressing aggressively recently, it is expected to have more to discuss during the conference in September.

NOMENCLATURE

<i>Symbols</i>	
A	Heat exchanger area (m^2)
P	power (MW)
p	pressure (bar)
T	temperature ($^\circ\text{C}$)
U	Heat exchange coefficient ($\text{W}/\text{m}^2/\text{K}$)
<i>Abbreviations</i>	
AC	auxiliary compressor
C	cooler
CO_2	carbon dioxide
CR	Compression ratio
CSP	concentrated solar power
HTF	heat transfer fluid
HTR	high temperature recuperator
HX	Heat exchanger
IC	intercooling
LCOE	levelized cost of electricity
LMTD	log mean temperature difference
LTR	low-temperature recuperator
MC	main compressor
MH	main heater
MS	Molten salt
PartC	partial cooling
PC	pre-compression / pre-compressor
PCHE	Printed circuit heat exchanger

PH	Preheating / preheater
PV	Photovoltaic
RC	recompression
RG	regenerative
RH	reheating
SCO_2	supercritical CO_2
TES	thermal energy storage

REFERENCE

- [1] Liu S, Bie Z, Lin J, Wang X. Curtailment of renewable energy in Northwest China and market-based solutions. *Energy Policy* 2018;123:494–502. doi:10.1016/j.enpol.2018.09.007.
- [2] Turchi CS. Supercritical CO_2 for Application in Concentrating Solar Power Systems. *Supercrit. CO_2 power cycle Symp.* Troy, New York, 2009.
- [3] Glatzmaier GC, Turchi CS. Supercritical CO_2 as a Heat Transfer and Power Cycle Fluid for CSP Systems. *ASME Int. Conf. energy Sustain.* San Fr., 2009. doi:10.1115/es2009-90332.
- [4] Ma Z, Turchi CS. Advanced Supercritical Carbon Dioxide Power Cycle Configurations for Use in Concentrating Solar Power Systems. *Supercrit. CO_2 power cycle Symp.* Boulder, Color., 2011.
- [5] Turchi CS, Ma Z, Dyreby J. Supercritical Carbon Dioxide Power Cycle Configurations for Use in Concentrating Solar Power Systems. *ASME Turbo Expo,* Copenhagen, Denmark, 2012. doi:10.1115/GT2012-68932.
- [6] Neises T, Turchi CS. Supercritical carbon dioxide power cycle design and configuration optimization to minimize levelized cost of energy of molten salt power towers operating at 650°C . *Sol Energy* 2019;181:27–36. doi:10.1016/j.solener.2019.01.078.
- [7] Dostal V. A Supercritical Carbon Dioxide Cycle for Next Generation Nuclear Reactors. *Massachusetts Institute of Technology*, 2004.
- [8] Feher EG. The supercritical thermodynamic power cycle. *Energy Convers* 1968;8:85–90. doi:10.1016/0013-7480(68)90105-8.
- [9] Angelino G. Real Gas Effects in Carbon Dioxide Cycles. *ASME Gas turbine Conf. Prod. show*, Cleveland, Ohio, 1969. doi:10.1115/69-gt-102.
- [10] Ahn Y, Bae SJ, Kim M, Cho SK, Baik S, Lee JI, et al. Review of supercritical CO_2 power cycle technology and current status of research and development. *Nucl Eng Technol* 2015;47:647–61. doi:10.1016/j.net.2015.06.009.
- [11] Ashcroft JA, Kimball KJ, Corcoran MR. Overview of Naval Reactors Program Development of the Supercritical Carbon Dioxide Brayton System. *Supercrit. CO_2 power cycle Symp.* Troy, Now York, 2009.
- [12] Kimball KJ, Clementoni EM. Supercritical Carbon Dioxide Brayton Power Cycle Development Overview. *ASME Turbo Expo*, Copenhagen, Denmark, 2012.

- [13] Clementoni EM, Cox TL, Sprague CP. Startup and Operation of a Supercritical Carbon Dioxide Brayton Cycle. *J Eng Gas Turbines Power* 2014. doi:10.1115/1.4026539.
- [14] Pasch J, Conboy T, Fleming D, Rochau G. Supercritical CO2 recompression Brayton cycle: completed assembly description. California: 2012.
- [15] Moore J, Brun K, Evans N, Chiranjeev Kalra. Development of 1 MWe supercritical CO2 test loop. ASME Turbo Expo, Montr. Quebec, Canada, 2015.
- [16] Moore JJ, Cich S, Towler M, Allison T, Wade J, Hofer D. Commissioning of a 1 MWe supercritical CO2 test loop. Supercrit. CO2 power cycle Symp. Pittsburgh, Pennsylvania, 2018.
- [17] Wang J, Huang Y, Zang J, Liu G. Recent Research Progress on Supercritical Carbon Dioxide Power Cycle in China. ASME Turbo Expo, Montréal, Canada, 2015. doi:10.1115/gt2015-43938.
- [18] Li H, Zhang Y, Gao W, Yao M. Preliminary design study on a Multi-Megawatts Fossil-based Supercritical CO2 Recompression and Reheat Integral Test Facility. Supercrit. CO2 power cycle Symp. San Antonio, Texas, 2016.
- [19] Li H, Zhang Y, Yao M, Yang Y, Han W, Bai W. Design assessment of a 5 MW fossil-fired supercritical CO2 power cycle pilot loop. *Energy* 2019;174:792–804. doi:10.1016/j.energy.2019.02.178.
- [20] Zhao Q, Mecheri M, Neveux T, Privat T, Jaubert NJ. Superstructure optimization of supercritical CO2 Brayton cycle by MINLP approach. Supercrit. CO2 power cycle Symp. Pittsburgh, Pennsylvania, 2018.
- [21] Zhang J, Le Moullec Y. A systematic comparison of supercritical CO2 Brayton cycle layouts for concentrated solar power with a focus on thermal energy storage utilization. Eur. Conf. Supercrit. CO2 power Syst. Paris, Fr. (NOT Publ. YET), 2019.

MACHINE LEARNING BASED DESIGN OF A SUPERCRITICAL CO₂ CONCENTRATING SOLAR POWER PLANT

Tahar Nabil*
EDF R&D China Center
Beijing, China
Email: tahar-t.nabil@edf.fr

Yann Le Moullec
EDF R&D China Center
Beijing, China

Adrien Le Coz
EDF R&D China Center
Beijing, China

ABSTRACT

Replacing steam water by supercritical CO₂ is a promising track for increasing the thermal efficiency of concentrating solar power plants, likely to facilitate the development of this industry. Adopting this new working fluid requires first a careful optimal design of the power cycle. In this work, we propose a novel, fully data-driven approach to address this task. Unlike state-of-the-art methods, which rely on some expert knowledge and an intrinsically limited search space, our method freely explores the solution space in an unconstrained and efficient manner. We revisit cycle design and formulate this problem as a machine learning task consisting in training a statistical generator. Starting from a limited number of random power cycle layouts, we are able to train a model, namely a recurrent neural network, from which new layouts can be sampled. These new configurations are thermodynamically valid, i.e. they do correspond to cycles from which a thermal efficiency can be computed. Besides, we show how to transform the model to bias the samples towards regions of both high thermal efficiency and net shaft power. The final model is efficient, with at least 86% of the newly created layouts outperforming a target specification of 30% thermal efficiency and 10MW net shaft power. Numerical experiments finally prove that the method successfully generates a large pool of good cycles that compare favourably with standard expert designs, suggesting thus that machine learning can challenge expert knowledge in process synthesis problems.

INTRODUCTION

Improving the thermal-to-electric conversion efficiency of thermal power plants is an active field of research, because of the pressing need for reducing the carbon dioxide (CO₂) emissions released by the power industry. Whereas most thermal plants, whether they are nuclear, fossil or concentrating solar power (CSP) plants, are based on a steam cycle, closed-loop Brayton cycles using supercritical carbon dioxide (SCO₂) as a working fluid are now being investigated [1–4]. Compared to steam, SCO₂ is thought to

bring cost and environmental impact reduction as a result of an increased efficiency, a more compact turbomachinery, and a simpler configuration of the power block. These desirable properties stem from the high-density and strongly non-linear behaviour of carbon dioxide near its easily reachable critical point, at 30.98°C and 73.8bar. In particular, the compression work for CO₂ cycles near the critical point is greatly reduced compared to other working fluids [1]. Looking more specifically at CSP cycles, advantageously replacing steam by SCO₂ could thus further foster the development of this emerging industry. Indeed, while CSP coupled with thermal energy storage is able to handle the intrinsic variability of the solar radiation by decoupling the solar-to-thermal and thermal-to-electric conversions, its cost remains high - typically from 60 to around 100 \$/MW in the near future according to the International Renewable Energy Agency (IRENA). By improving the thermal-to-electric efficiency of the power cycle, SCO₂ could help lowering the cost of CSP. However, while the techno-economic performances of the steam cycle for CSP are well understood, SCO₂ cycles remain largely theoretical objects whose layout and parameter optimization should be further examined. How then to synthesize a highly efficient SCO₂ power cycle for CSP application?

This task, called process design, is a complex parametric optimization problem. Expert methods were first developed: some cycle layouts are selected using domain knowledge, and the free parameters of each layout are then optimized with respect to some criteria, for instance energy efficiency [5], exergy efficiency [6] or cost and performance trade-off [7]. Typical layouts are the regenerative, recompression, intercooling, pre-heating cycles, etc. [8]. This strategy fails nevertheless to design power cycles automatically, and do not enable the comparison of many configurations, such that more relevant ones could be missed.

Optimization-based approaches have thus emerged, to extend expert designs. They usually rely on a superstructure which contains a combinatorial number of layout alternatives. For instance, the superstructure in [9] involves 1152 layouts of a SCO₂ coal-

* corresponding author

fired power plant. Superstructure optimization is a mixed-integer nonlinear programming problem, where the best cycle configuration and its corresponding best design parameters are found simultaneously [9, 10]. Although the solver converges towards an optimal configuration *within* the superstructure, the optimization-based approach suffers from the same limitation as the expert design. Even if larger, the search space remains intrinsically limited by the current state-of-the-art knowledge since the superstructure is drawn by an expert. Potentially relevant solutions *outside* the superstructure are therefore also left out. Besides, defining a comprehensive superstructure is a complex error-prone task.

Consequently, optimization-based yet superstructure-free synthesis approaches are currently searched for in order to better explore the solution space. In this regard, see for instance the use of evolutionary algorithms applied to a population of power cycles in [11, 12]. Such algorithms usually iterate through three main steps:

1. generate new power cycles;
2. evaluate their fitness (e.g. their thermal efficiency);
3. learn from the previous steps to search for better cycles.

Step 1 focuses on proposing new power cycle layouts. In [11–13], this is achieved by carefully choosing the mutation operator of the evolutionary algorithm. Step 2 requires solving a generally nonlinear optimization problem for every fitness computation. Finally, step 3 may take several forms, e.g. selection rules in evolutionary algorithms [11–13]. A distinguishing feature of the new methodology is thus its *genericity*, with little to no application-specific knowledge. Another feature is the *data-driven* approach, by evaluating the fitness of successive sets of possible candidates, until the algorithm converges towards a pool of good power cycles with high fitness. Because these already existing data-driven contributions require either further validation on the complex power plant design problem [13] or a non-negligible expert knowledge for designing the mutation operator [11], we identify the need for exploring new fully data-driven approaches going beyond evolutionary algorithms.

Study objectives

Our main purpose is to propose a new data-driven process synthesis method able to challenge expert designs. The method should freely and efficiently explore the search space, in order to produce a large set of *good* power cycles and look for solutions experts could have missed. The recent advances of deep learning [14] suggest to formulate this machine learning problem as a generative statistical task. This means that, given a predefined set of power cycles, we aim at estimating a statistical model from which we can sample new power cycles, close but distinct from the initial set. As a first step, we investigate whether a state-of-the-art deep learning model, namely the recurrent neural network, is able to fulfill this task by generating new layouts that are all thermodynamically valid, i.e. that correspond to actual power cycles whose thermal efficiency can be assessed (regardless of its actual value). The second objective is then to derive a statistical generator that

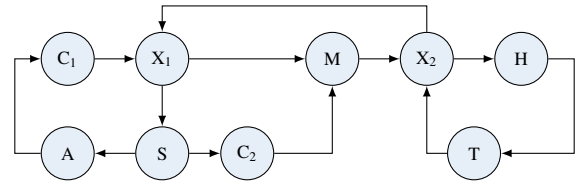


Figure 1: Graph representing the recompression SCO₂ power cycle. T: turbine, C: compressor, A: cooler, H: heater, X: heat exchanger with cold (resp. hot) stream flowing horizontally (resp. vertically), S: splitter, M: mixer.

not only produces new, thermodynamically valid, layouts, but also concentrates specifically on highly efficient designs. We will use transfer learning, i.e. adjust the parameters of the statistical model trained during the first step, to derive this specialized model.

We focus here on SCO₂ CSP power cycles, with heat transferred from molten salt (60 wt% NaNO₃ and 40 wt% KNO₃), and solar tower technology. Yet, the methodology applies equivalently to any other power cycle. Before describing in more details the models and results obtained in this work, the next section introduces the data representation and available dataset.

DATASET

1. Representing power cycles

Graph representation

In this paper, a supercritical carbon dioxide power cycle is represented by a directed graph. The components of the cycle are the elementary units that may be part of any power cycle, namely a heater (molten salt-CO₂ heat exchanger), a turbine, a compressor, a cooler, a CO₂-CO₂ heat exchanger, and 2-branch splitters and mixers. They are converted into the vertices of the graph, whereas CO₂ flowing from component A to component B is equivalent to a directed edge between the corresponding nodes. Without further input, the graph only informs about the topology (layout) of the cycle, and not about its thermal state. As an example, see the recompression cycle depicted in Figure 1.

String representation

We introduce furthermore a string representation of a power cycle, and state that a power cycle may be uniquely represented by a *word*, i.e. an ordered sequence of letters. Consider indeed the alphabet $\mathcal{A} = \{T, C, H, A, a, b, c, d, 1, 2, 3, 4, 5, -1, -2, -3, -4, -5\}$, where script-size letters a, b, etc. denote semi-heat-exchangers, a positive integer denotes a mixer and its opposite value the corresponding splitter, while T, C, H, A are as in Figure 1. The alphabet \mathcal{A} is given in its (arbitrarily defined) lexicographic order. A power cycle graph is then translated into a word as follows:

1. start from an empty string, select the unit ranked first in lexicographic order, i.e. a turbine, and append the corresponding letter to the string. The word reads thus T. In case of multiple



Figure 2: Examples of thermodynamically infeasible (left, fluid heating itself) or unsuitable (right, shared inlet conditions) heat exchanger designs, and corresponding words with spelling mistakes.

turbines, select the one whose successor appears first in \mathcal{A} .
Example: for a cycle including two turbines, one followed by a heat exchanger, the other by a heater, choose then the latter one, since H comes before a in \mathcal{A} .

2. "follow the flow": move to the unique successor of the turbine, append its associated letter to the word, and iterate until the successor of the current component is the initial turbine.

A few special rules are added to guarantee the uniqueness of the word. (i) Every heat exchanger in the cycle appears twice in the word, for it has two sides. These two sides are denoted by the same letter, e.g. a, meaning that they belong to the same exchanger - it is not necessary to distinguish between cold and hot. (ii) 2-branch splitters and mixers always come in pairs, one pair should be denoted by a single index in absolute value (e.g. a pair $(-1, 1)$). (iii) The first encountered heat exchanger should be denoted a, the second b, etc. i.e. the numbering respects the standard lexicographic order. Similarly for pairs of splitters/mixers. (iv) Assume the current component is a splitter. Because it has two successors instead of one, the "follow the flow" rule is complemented as follows:

- append its letter (say e.g. -1) to the word;
- explore the first branch in lexicographic order, follow the flow and augment the word, until the associated mixer 1 is met;
- if the mixer has been seen before, i.e. 1 appears now twice in the word, then continue the exploration forward, i.e. move to the unique successor of the mixer 1;
- otherwise, return to the root splitter -1 , augment the word by following the flow in the other branch until mixer 1 is met. Mixer 1 appears now twice in the word, so the exploration continues forward from 1.

A splitter appears thus exactly once in the word, its corresponding mixer exactly twice. *Example:* the word equivalent to the recompression cycle in Figure 1 is Tab-1C1ACb1aH.

The benefits of using words lie in the uniqueness and compactness of the representation. Because of the specific properties of a power cycle, the lexicographic order defined on \mathcal{A} and these simple spelling rules, there is indeed a one-to-one bijection between graphs and words. Hence, the finite alphabet \mathcal{A} and the rules defined in this section form a *language* for describing power cycle layouts. This formal grammar is built in analogy to the SMILES format for representing molecular structures [15].

Table 1: Supercritical CO₂ CSP plant design constraints.

Symbol - description	Value
T_{max} - maximum operating temperature	560 °C
T_{min} - minimum operating temperature	35 °C
P_{max} - maximum operating pressure	250 bar
dp_c - pressure drop (cooler)	0.5 bar
dp_{hx} - pressure drop (heater, exchanger)	1 bar
ΔT - temperature pinch (heat exchanger)	5 K
η_c - isentropic efficiency (compressor)	0.89
η_t - isentropic efficiency (turbine)	0.93
\dot{m} - molten salt mass flow	80 kg/s
T_1 - molten salt minimum temperature	290 °C
T_2 - molten salt maximum temperature	565 °C

2. Available data

In order to assume the least possible expert knowledge in the course of process design, the initial database consists of a set of random cycles. More precisely, building on the graph representation, each cycle is obtained firstly by creating a closed graph containing the minimal set of units, i.e. turbine, cooler, compressor and heater. Then, a random number of random components are inserted in the cycle at random locations, with equal probabilities. Finally, graphs that are thermodynamically infeasible are discarded. To do so, they are first converted into words. Then, a set of hand-designed rules are established in order to link invalid power cycles to invalid sequences of letters. Indeed, the link between graph structure and thermodynamic feasibility can easily be spotted by using the equivalent string representation. *Example:* Figure 2 shows some sequences of letters that yield unsuitable cycles. For instance, words including the pattern " $..aa..$ " are rejected, because they correspond to cycles having an exchanger whose outlet stream of the first half is used as input to the second half. Similarly the pattern " $..-1a..-1a...$ " is unsuitable, since it means that the exchanger a has two inlet streams at the exact same thermodynamic conditions (coming from the same source, the splitter -1). These two rules, and additional ones omitted here for sake of brevity, are enough to assess the validity of a word.

Fitness evaluation

A labeled dataset is obtained by maximizing a user-defined fitness function, chosen here to be the product $\mathcal{P} \times \eta$ of the net shaft power output $\mathcal{P} = (|P_t| - |P_c|)$ in MW and the thermal efficiency $\eta = \mathcal{P}/Q_{abs}$ in %, where P_t is the power generated by all the turbines of the cycle, P_c the power consumed by all the compressors and Q_{abs} the total heat transferred to the working fluid in molten salt/CO₂ heat exchangers. Each power cycle configuration is subjected to the same set of design constraints, representative of the expected technology advancement for developing a 10MW SCO₂ CSP plant with solar salt (60 wt% NaNO₃ and 40 wt% KNO₃) tower technology, and summarized in Table 1.

The free parameters are the target temperatures of the heaters

and coolers, the pressure ratios of the turbomachinery as well as the mass fraction of the splitters. The static equations leading to η may be found in any thermodynamics textbook, e.g. [16].

This problem is implemented in Python, with thermodynamic fluid properties computed by the CoolProp library [17]. NetworkX [18] is used to handle graph data, with the thermodynamic state of each component stored as node attribute. The nonlinear optimization task is solved by a Particle Swarm Optimizer (PSO, [19]) with 100 randomly initialized particles. The best particle after convergence of the PSO is then used as initialization of a simplex algorithm (Nelder-Mead algorithm, [20]).

METHODS

Given the dataset described in the previous section, we are now ready to formulate our machine learning task. Starting from a collection \mathcal{D}_0 of power cycle layouts, the first step towards data-driven process design is to learn a statistical model able to sample from the unknown distribution underlying \mathcal{D}_0 , i.e. able to produce new power cycle layouts, representative but distinct from the cycles in \mathcal{D}_0 . Using the string representation, the model should thus generate new valid words. By *valid word*, we mean a sequence of letters in the alphabet \mathcal{A} that can be converted into a power cycle from which a thermal efficiency actually can be computed. *Example*: Tab-1C1ACb1aH (recompression cycle) and TaACaH (regenerative Brayton cycle) are valid sequences, but TAH (no compressor C in the cycle) and TaaACH (infeasible heat exchanger) are not. The purpose is therefore to learn “the language of power cycles”, we refer to this task as the *language, or spelling, learning*.

The second task consists then into specializing the statistical model such that it generates only power cycles with certain desired properties, for instance a high thermal efficiency.

1. Recurrent neural networks

The statistical generative model is chosen to be a recurrent neural network (RNN), a class of neural networks that allows feedback to handle sequential data [21]. RNNs are used e.g. in natural language processing, to automatically generate meaningful sequences of words, i.e. sentences [22]. Power cycles are also sequential data, being ordered sequences of units represented by letters in \mathcal{A} . The inputs of our RNN will be sequences of fixed-size vectors, where each unit is converted into a unique vector by adopting one-hot encoding: to the i^{th} letter of \mathcal{A} corresponds a vector of size $|\mathcal{A}|$, whose entries are 0's, except the i^{th} one set to 1. A power cycle is thus a sequence of one-hot vectors. RNNs are attractive models since they allow for persistency of the information, i.e. memory, and can deal with correlations between data points close in the sequence. Besides, they can handle inputs of variable dimension, i.e. power cycles with a variable number of units.

Assuming that it operates over vectors $x^{(t)}_{t=1}^N$, with index t referring to the order of appearance in a sequence, a RNN is a N -layer neural network, with the concept of memory of the network translated by introducing the notion of a cell. At a given step t , the $cell_t$ is the result of the previous $cell_{t-1}$ and the current input $x^{(t)}$. The content of $cell_t$ determines then both the output at the current

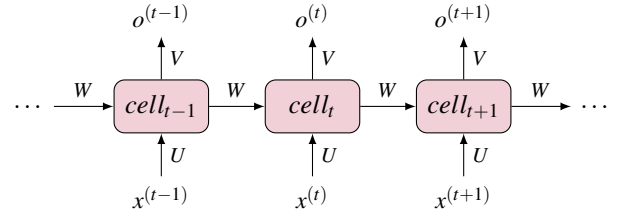


Figure 3: Unfolded recurrent neural network representation.

step and the next state of $cell_{t+1}$, as shown in Figure 3. Let vector h_t denote the hidden state of $cell_t$, h_t encapsulates the memory of the network. We have $h_t = \sigma(Ux^{(t)} + Wh_{t-1})$, with σ a nonlinear function, e.g. the sigmoid $\sigma: \mathbb{R} \ni x \mapsto 1/(1 + \exp(-x)) \in (0, 1)$. The output at step t is $o^{(t)} = f(Vh_t)$, with f a given function. For instance, if $f = \text{softmax}$, the vector $o^{(t)}$ is then a probability distribution across \mathcal{A} for the next item $X^{(t+1)}$ in the sequence. The weight matrices U, V, W are shared across time: the same task is performed at each step, only with different inputs.

Long short-term memory A major shortcoming of conventional RNN is their poor ability to catch long-term dependencies in the data, failing to account for close relations between $x^{(t)}$ and $x^{(t')}$ for $t' \gg t$. Long short-term memory (LSTM) networks, a subclass of RNNs, were thus introduced to address this issue [23]. They share the structure depicted in Figure 3, except that the design of the cell is modified: LSTM cells have four layers, against one for RNNs. These four layers interact in order to remove or add information to the cell state. See [23] for further information on the detailed structure of LSTMs.

Generative net Consider a RNN whose output $o^{(t)}$ is the probability distribution of the next input $x^{(t+1)}$: $o^{(t)} = P(x^{(t+1)} | x^{(1)}, \dots, x^{(t)})$. For instance, here, the RNN computes the probability of the i^{th} component of a cycle given the first $i-1$ units. Suppose, by convention, that any word starts with a GO token and ends with an EOS (end of sequence) token. Then, once the RNN is trained, it can be used to generate new sequences: start with a GO token, sample the next element in the sequence from the output $P(x^{(t+1)} | x^{(1)}, \dots, x^{(t)}) = P(x^{(2)} | x^{(1)})$, and iterate until an EOS token is sampled. Hence, sequences of variable length may be generated.

2. Language learning from few data

In practice, training RNNs requires large amounts of diversified data, which we do not have. We proceed thus to data augmentation and suggest to use RNNs alternatively in training and generative modes in order to enlarge an initial set \mathcal{D}_0 of random cycles.

1. Set index $k = 0$.
2. Use the cycles in \mathcal{D}_k to train a RNN model.
3. Use the model learned in 2. to generate new cycles, filter out the invalid cycles, append the remaining ones to \mathcal{D}_k , forming a new, augmented, dataset \mathcal{D}_{k+1} .

4. $k \leftarrow k + 1$, return to 2. until a maximum number of iterations is reached.

For the procedure to be relevant, we use the rules described in the Dataset section to automatically filter out invalid words. The rules are applied at step 3 of the procedure, and not during step 2: the trained model is merely told what to imitate (the input data), not what to avoid. Observe also that the RNN trained from \mathcal{D}_{k+1} is not a finetuned version of the RNN trained from \mathcal{D}_k , since its parameters are randomly initialized. Each model is trained from a database of increasing size, such that after a few iterations, the RNN should be able to mostly generate valid power cycles.

3. Finetuning

For the purpose of power cycle design, the actual machine learning task we aim at is to generate *highly efficient* cycles, not merely power cycles. Here, we want power cycles with fitness $\mathcal{P} \times \eta > \delta$, for a predefined threshold δ . Because the number of cycles in \mathcal{D}_0 meeting this criterion is very small, training a RNN directly from this subset would produce an overfitted model. Instead, the desired model is achieved by a process called transfer learning, or finetuning. Firstly, a RNN is trained to generate thermodynamically valid layouts, regardless of their fitness value. This language model, denoted \mathcal{M}_1 , is obtained following the methodology described in the previous section. \mathcal{M}_1 is then re-trained on a smaller subset of cycles sharing the property $\mathcal{P} \times \eta > \delta$, yielding a new model \mathcal{M}_2 with the same RNN architecture but different parameters. \mathcal{M}_1 learns thus general features of power cycles; this knowledge is stored in its parameters after training. Although \mathcal{M}_2 is trained on a different dataset, its parameters are initialized to the values obtained by \mathcal{M}_1 . In this manner, knowledge (about how to draw a thermodynamically valid layout) is transferred to the second model (specialized in generating highly efficient power cycles).

In the end, new layouts are sampled from the finetuned model. We emphasize the fact that this deep learning method does not provide any guarantee regarding its convergence towards the "best" layout. Its interest lies rather in its ability to create large sets of data, hopefully meaningful for the process engineer. We say thus that the exploration of the space of power cycles is efficient if the new cycles do have their fitness above the predefined threshold δ .

RESULTS AND DISCUSSION

1. Experimental settings

The purpose of the numerical experiments is two fold. Starting from a small database of power cycles layouts, the first step consists in generating virtually infinitely many new, distinct, power cycles - regardless of their thermal efficiency. The second task is more specific: we want to generate power cycles whose layout guarantees a minimum level of thermal performance of the cycle. The first task is achieved by (i) training a RNN on the initial, random, database, (ii) using this model in generative mode, to produce new cycles (iii) append valid new cycles to the initial database, and (iv) iterate until the training set has sufficiently grown and the

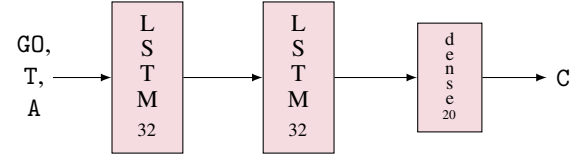


Figure 4: Structure of the RNN model for generating new power cycles. In training mode, the model learns to predict the component (compressor C) that comes next given the beginning of the cycle (GO token, turbine T, cooler A).

learned model has reached a good success rate in generation mode. In this case study, we train the RNN to predict the next letter given the first part of a word (sequence-to-one model). Hence, to every power cycle w of length n in the training set correspond $n - 1$ pairs of input-output data for the RNN. These pairs are formed by the one-hot sequences of the first i letters of w as input, and the one-hot representation of the $i + 1^{th}$ letter as output, for $i = 1, \dots, n - 1$.

The architecture of the RNN model is displayed in Figure 4. It has 3 stacked layers, two LSTM layers, each with a hidden state vector of size 32, and a dense output layer with softmax activation. The softmax function normalizes the dense layer output in order to form a probability distribution over the alphabet \mathcal{A} . The dense layer comprises thus 20 units, corresponding to the size of the alphabet \mathcal{A} , including GO and EOS tokens. In total, the model contains 15,764 parameters to tune. The training is performed using Keras [24], by minimizing the categorical cross-entropy using the Adam optimizer (see [14, 24]), keeping 15% of the training set for validation. In generation mode, we sample letters, i.e. power cycle components, from the distribution given by the softmax activation function. All computations are carried out on Python 3.6.

The second part of the study is carried-out by finetuning the RNN model obtained previously. In particular, the architecture of the RNN model displayed in Figure 4 is kept unchanged, and so are the cost function, optimizer and training/validation ratio.

2. Learning the structure of a power cycle

Data augmentation The training process is initialized with a set \mathcal{D}_0 made of 450 distinct valid words randomly generated. In this case study, the words in \mathcal{D}_0 all contain at most one heat exchanger as well as at most one pair of splitter/mixer. 10 iterations of the procedure described in the previous section yield 53,959 unique words that can be converted into valid power cycles, with learning curve depicted in Figure 5. Thus, even if the initial dataset is very small, the iterative procedure succeeds in growing a dataset to a more reasonable size, along with an accurate model.

Although the alphabet \mathcal{A} allows for up to 5 heat exchangers and 5 pairs of splitter/mixer, the generated words are all according to the initial dataset \mathcal{D}_0 , i.e. with at most one of each of these two components. This illustrates a limitation of our data augmentation method: RNN are not able to go beyond the initial dataset, regardless of the alphabet, and cannot suggest for instance to use more heat exchangers. Hence, the shape of \mathcal{D}_0 strongly determines the

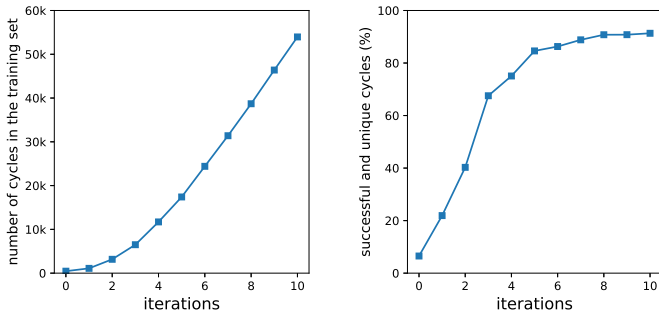


Figure 5: (Left) Number of power cycles in the training sets \mathcal{D}_k and (right) proportion of valid and unique cycles generated by the RNN trained on \mathcal{D}_k .

kind of layouts produced afterwards by the RNN.

Language model Starting from the 53,959 distinct power cycles, of which 15% are kept for validation, we trained then another RNN model, denoted \mathcal{M}_1 , with randomly initialized weights, and generated 100,000 words. Out of these 100k words, there are 93.1% valid words that can be converted into power cycles, out of which 87% are unique, of which 86% are new cycles. \mathcal{M}_1 is thus able to generate a large number of new layouts, and thereby to explore the space of SCO_2 cycles, within the boundaries set by \mathcal{D}_0 (e.g. no more than one heat exchanger). It has learned the language of power cycles, in the sense that 93.1% of the sequence of letters it generates do correspond to a power cycle layout from which a thermal efficiency can be computed. These statistics compare well with state-of-the-art RNN generative models trained on another problem, namely *de novo* drug design. See for instance the RNN in [25], which generates 94% valid words, out of which 90% are new. These results are all the more encouraging given that RNNs in drug design are trained on datasets of typically 10^5 to 10^6 samples, whereas our training set scales in 10^4 .

In order to assess whether the power cycles generated by \mathcal{M}_1 are functionally similar to the original, random, database, we estimated the optimal shaft power \mathcal{P} and thermal efficiency η for approximately 10,000 cycles in each one of the two collections, where the optimal design is obtained by maximizing the product $\mathcal{P} \times \eta$. This yields the normalized distributions drawn in Figure 6. The rather close agreement between the two distributions proves that \mathcal{M}_1 has successfully learned how to produce large sets of new power cycles, at the same time similar (in performances) and distinct (in layouts) from the original samples.

Figure 6 also underlines the need for finetuning, as it can be observed that a large share (43%) of the cycles generated by \mathcal{M}_1 actually consume more power than they are able to produce, and only a small proportion (less than 4%) have a reasonably good efficiency (greater than 30%). Again, RNN is intrinsically limited to its training set, and cannot improve it. However, this illustrates by contrast a key benefit of RNNs compared to random generators: while a random generator is bound to produce cycles all sampled

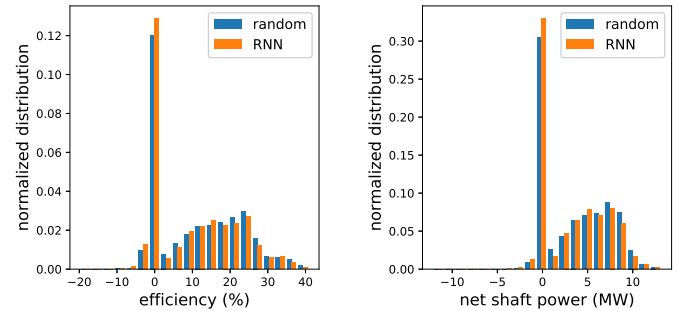


Figure 6: Distributions of the optimal efficiency (left) and net shaft power (right) achieved respectively for 11,744 cycles randomly generated (blue) and 9,116 cycles sampled by model \mathcal{M}_1 (orange).

from the distribution in Figure 6, RNN parameters can be subsequently modified to shift the distribution towards regions of higher values of η and \mathcal{P} . Hence the need for finetuning, to efficiently guide the exploration of the search space, addressed next.

3. Finetuned model

Targeting the design of a 10 MW CSP plant, we applied finetuning to produce cycles with $\mathcal{P} \times \eta > 300$, i.e. we aimed to generate cycles at least equivalent to a theoretical cycle with 30% efficiency and 10MW net shaft power output (all the heat available from molten salt is absorbed by the theoretical cycle).

\mathcal{M}_1 is finetuned into \mathcal{M}_2 on a dataset containing 457 samples (15% kept for validation) with fitness $\mathcal{P} \times \eta > 300$. Because it is a small scale database, we adopt a training procedure similar to the first step. At each iteration, the model is finetuned for 5 epochs, with 5,000 cycles generated at each epoch. Nevertheless, the computational cost of evaluating the fitness of these 25,000 cycles, i.e. of solving a nonlinear optimization problem, is too heavy. To circumvent this issue, we trained a classifier on a separate database, prior to the finetuning. The task of the classifier is to assign every cycle in either one of two classes, namely $\mathcal{P} \times \eta > 300$ (positive class) or $\mathcal{P} \times \eta \leq 300$ (negative class). The prediction is formed based on the cycle layout only, and is not helped by any thermodynamic computation. At each iteration, the classifier replaces thus the fitness evaluation step, avoiding to solve the optimization problem. The outcome of the iterations is a pool of cycles predicted to be positive by the classifier. Using the classifier, fitness evaluation is replaced by fitness prediction. Actual fitness evaluation occurs then only when the iterations stop, in order to provide the actual designs of these good cycles.

Here, the classifier combines a LSTM layer with 32 hidden units and a 1-unit dense output layer with sigmoid activation. The training set contains 11,359 samples, of which 44% are positive. The performances of the classifier on a 1,000-sample test set are: 98% in accuracy (total error rate), 97% recall (fraction of true positive cycles that the classifier also predicts to be positive) and 98% in precision (fraction of predicted positive cycles that actually are positive). Although an important contribution of this work, the

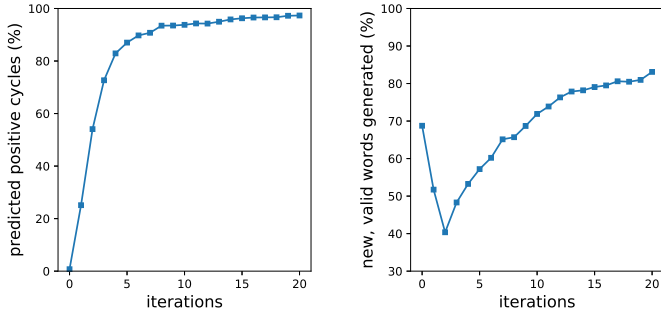


Figure 7: (Left) Fraction of valid generated cycles that are predicted to be positive ($\mathcal{P} \times \eta > 300$) and (right) fraction of the generated cycles that are both new and valid, during the course of the training of the finetuned model \mathcal{M}_2 .

solution of this complex problem is not further described, for sake of brevity.

The training procedure results in 25,000 cycles per iteration, out of which those that have not been seen during previous iterations and that are predicted to be positive by the classifier form then the new training set for the next iteration of finetuning. The learning curve showing the performances of the finetuned RNN \mathcal{M}_2 at each iteration is displayed in Figure 7 (left). Similarly to the results in Figure 5, \mathcal{M}_2 is quickly able to generate a large proportion of cycles which will be detected as positive by the classifier - hence most likely with $P \times \eta > 300$. After a few iterations where the model loses some information acquired before finetuning, the final model generates almost only valid words not included in the training set, as shown in Figure 7 (right).

In total, 307,165 cycles have been predicted to be positive and valid during the finetuning process of the RNN. We proceeded then to the actual optimization of the fitness function $\mathcal{P} \times \eta$ of 17,212 cycles randomly selected in this set, in order to study their thermal performances. Figure 8 confirms the effectiveness of the finetuning: compared to the map obtained without finetuning (model \mathcal{M}_1 , Figure 8, left), the cycles generated by \mathcal{M}_2 are almost all located towards region of higher values of $\mathcal{P} \times \eta$, beyond the boundary $\mathcal{P} \times \eta = 300$ (Figure 8, right). 86% of the 17,212 cycles actually are above the threshold $\mathcal{P} \times \eta > 300$, which is less than the precision of the classifier (98%). This difference might partially be explained by the fact that the optimizer only converges towards a local minimum, with no guarantee of reaching the absolute best value. Besides, predicting the fitness based on the layout information is a complex task. In particular, cycles on either sides of the boundary $\mathcal{P} \times \eta = 300$ might not be significantly structurally different from each other - observe that the negative cycles are mostly located close to the border (94% of the cycles are such that $\mathcal{P} \times \eta > 250$). On the other hand, without finetuning, less than 4% of the cycles are above the threshold. These results demonstrate how a finetuned RNN model can efficiently explore the search space and generate thousands of “good” power cycles.

By choosing the product $\mathcal{P} \times \eta$ as fitness function, we want

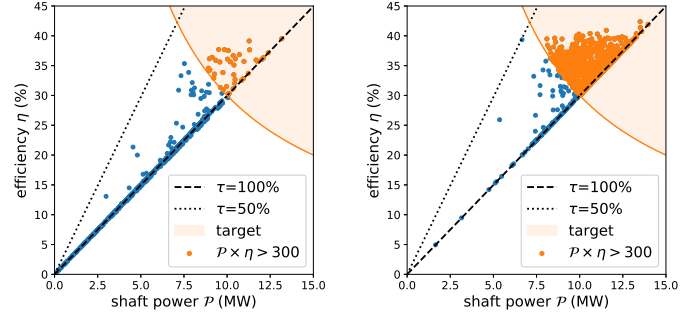


Figure 8: Performances (\mathcal{P}, η) of 1000 cycles sampled from \mathcal{M}_1 (left, no finetuning) or \mathcal{M}_2 (right, finetuning). Cycles on the main diagonal have full salt use rate $\tau = 100\%$ and maximum amount of heat transferred from molten salt to the cycle ($\eta = \mathcal{P}/Q_{abs}$).

to promote the design of cycles with both high efficiencies and high net power input. Unsurprisingly, this results in a majority of cycles with high salt use rate, where the salt use rate, or thermal energy storage (TES), τ , is the ratio $\tau = (T_2^* - T_1^*) / (T_2 - T_1)$, with T_1, T_2 the maximum temperature range allowed for the molten salt, as in Table 1, and T_2^*, T_1^* the effective temperature range of the molten salt achieved by the optimal design. With $\tau = 100\%$, the maximum amount of heat Q_{abs}^{max} is transferred from molten salts to the power cycle. Since $\eta = \mathcal{P}/Q_{abs}$, this means that for a fixed target power output \mathcal{P} , any cycle must have $\eta \geq \mathcal{P}/Q_{abs}^{max}$ - hence the shape of Figure 8, with every point above the dashed line $\tau = 100\%$. 63% of the tested cycles are such that $\tau > 0.9$. For other layouts, however, the best design finds a trade-off characterized by $0.6 \leq \tau \leq 0.9$. Figure 9 sheds light on this trade-off. In general, cycles with higher TES τ will produce more power \mathcal{P} . On the contrary, the efficiency η tends to increase with lower values of τ , consistently with the definitions of η and τ : smaller values of τ mean less heat Q_{abs} provided to the cycle, hence larger values of η . Besides, this trade-off has economical consequences. Indeed, having high TES τ enables to reduce the size of the storage system. On the other hand, lower values of η come with bigger solar fields, for a given target power \mathcal{P} . Hence, the criterion $\mathcal{P} \times \eta$ gives

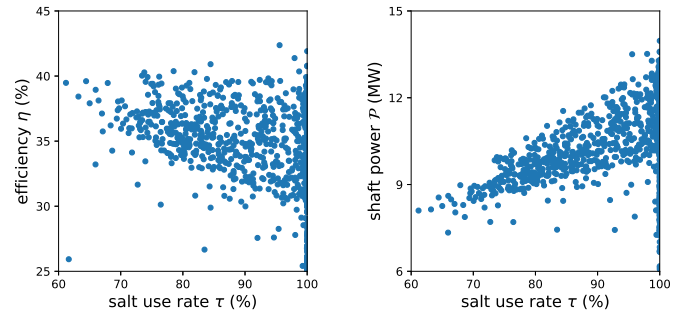


Figure 9: 1000 cycles in (left) the (τ, η) plane and (right) the (τ, \mathcal{P}) plane, sampled from the RNN model after finetuning.

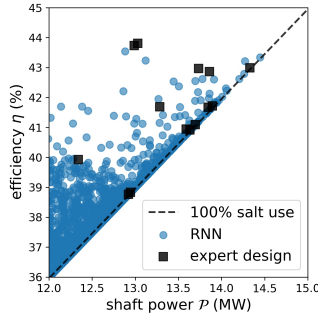


Figure 10: Best performances \mathcal{P} , η obtained by the finetuned a RNN model \mathcal{M}_2 (blue circles) or by expert design (black squares)

a preview of what techno-economic design could result in. The best cycles in Figure 9 are those able to reach high TES while maintaining an elevated thermal efficiency, thereby decreasing the cost of both the storage system and the solar field.

Furthermore, observe that the generated cycles all have at most one heat exchanger, whereas it is well known that splitting the heat exchanger in two, respectively for the low and high temperature recuperations may help improving the thermal efficiency. Hence, most expert designs include one or two heat exchangers. Typical expert SCO_2 cycles, not described extensively here for sake of brevity are the Regenerative (RG, TaACaH), Recompression (RC, Tab-1C1ACb1aH), Pre-compression (PC, TaCbACbaH) and Partial cooling (PartC, TabAC-1C1ACb1aH). These fundamental cycles may be combined with standard improvement strategies, such as Intercooling (IC), Pre-heating (PH) and Reheating (RH). We compared the best designs achieved for these 16 state-of-the-art cycles (from RG-IC, RG,PH,... to PartC-RH), obtained by maximizing the same fitness function $\mathcal{P} \times \eta$, to those obtained with our method. It can be seen from Figure 10 that the best cycles sampled from the RNN model \mathcal{M}_2 perform equally well in the sense of the criterion $\mathcal{P} \times \eta$, and even slightly better for some of them, than the expert cycles. Although \mathcal{M}_2 was not trained with any *a priori* knowledge on the meaningful ordering of the components (the initial dataset \mathcal{D}_0 is random), it succeeds thus in challenging state-of-the-art expert designs.

From a more qualitative standpoint, the best layouts found in this case study are the words TaACAC-1CH1ACa1H and TaAC-1CH1ACACaH1, respectively with $\mathcal{P}, \eta, \tau = 43.3\%, 14.4\text{ MW}, 100\%$ and $\mathcal{P}, \eta, \tau = 43.2\%, 14.3\text{ MW}, 99\%$. Since these two words almost are the same, it means that both cycles are structurally very similar. See Figure 11 for a graph representation of TaACAC-1CH1ACa1H and TaAC-1CH1ACACaH1, confirming the closeness of these two cycles. In this experiment, the data-driven method slightly improves the expert design, in terms of best fitness function $\mathcal{P} \times \eta$. Yet, several findings are worth mentioning and show how relevant machine learning design is for cycle design. First of all, the best cycles displayed in Figure 11 actually both are a combination of PartC and IC, plus PH for TaACAC-1CH1ACa1H. This proves that the method

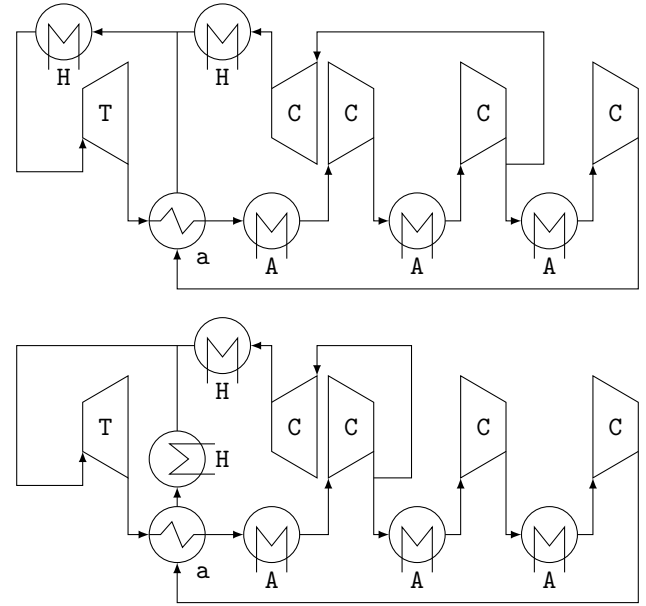


Figure 11: Layouts of the best cycles generated by the RNN, (above) TaACAC-1CH1ACa1H ($\eta = 43.3\%$, $\mathcal{P} = 14.4\text{ MW}$) and (below) TaAC-1CH1ACACaH1 ($\eta = 43.2\%$, $\mathcal{P} = 14.3\text{ MW}$).

described in this work has gained physical insights despite being conceived without domain knowledge. The concepts of partial cooling, intercooling and preheating stand out, which is a valuable information for designing cycles with other constraints. On the other hand, \mathcal{M}_2 adds some creativity, observed for instance in the original heating scheme of TaAC-1CH1ACACaH1 (see Figure 11, below). Besides, the main advantage of machine learning based design is that it can provide a whole population of (virtually infinitely many) *very good* cycles. Hence, the designer is able to pick a cycle that corresponds more closely to the constraints of a given project while maintaining equivalent level of performances. This profusion might be even more interesting when considering the techno-economic design.

Although computation time is not necessarily critical when dealing with power cycle design, our method suffers from a heavy computational cost. Because it is data intensive, the difficulty lies in the evaluation of the fitness function of a huge number of different power cycles. This limitation was also identified in other data-driven approaches, e.g. [11]. The numerical challenge varies with the layout of the cycle, with layouts containing at most one heat exchanger being more straightforward to simulate. The median of the 17,212 cycles sampled from the finetuned RNN is typically around one minute on one core of a 2.70 GHz, 16 GB-RAM laptop. Finding ways to efficiently solve the non-linear maximization of $\mathcal{P} \times \eta$ could thus increase the pace of exploration of the solution space.

CONCLUSION

This study aimed at revisiting power cycle design, with application to supercritical CO_2 CSP cycles, by adopting a data-driven

approach. Starting from a small set of random power cycle layouts, we used recent deep-learning techniques to train statistical models able

1. to imitate the initial database by generating new power cycles with similar structure and thermal properties (model \mathcal{M}_1);
2. to improve the initial database by producing specialized power cycles, all with a high thermal-to-electric efficiency and high net shaft power (model \mathcal{M}_2).

The main achievement is thus that the finetuned model \mathcal{M}_2 can produce large sets of distinct power cycles sharing good thermal properties. This could prove valuable to find a layout that suits best the peculiar constraints of a given project. Expert knowledge on power cycle design was not used at any step in the training of the deep learning model. In particular, the initial dataset \mathcal{D}_0 was randomly created, with no help of any domain expert. Yet, the successful cycles found in our experiments exhibit well-known patterns. For instance, partial cooling, intercooling and preheating schemes are included in the best layouts. The definition of the initial database is key to the process, because the model simply learns to imitate the cycles that belong to the training set. For the sake of demonstration, we chose here the most unfavourable setting by starting from a database with a limited number of power cycles, created at random. However, the constraint of randomness can be relaxed, by including expert layouts in \mathcal{D}_0 . Beyond the few cycles discussed here (RG, RC, etc.), we can exploit already proposed superstructures to list many alternatives. Using the string representation of power cycles introduced in this article, it is easy to see for instance that the superstructure in [9] with 1152 configurations actually contains 450 unique cycles that can be added to \mathcal{D}_0 .

In any case, it is to be noted that the definition of \mathcal{D}_0 is key to the process, because it will shape the distribution of the statistical model. In particular, the ratio of expert to random layouts in \mathcal{D}_0 controls the amount of expert knowledge transmitted directly to the model. If much greater than 1, the RNN language model \mathcal{M}_1 will most likely learn to infer the best concepts from those provided by the expert. On the contrary, if it tends to 0, as in this work, \mathcal{M}_1 will promote the best concepts from scratch - at the expense of more "waste" at the beginning of the training.

This preliminary study on machine learning based design of power cycle may be extended in several ways. One line of work consists in improving the fitness evaluation step, in terms both of convergence of the optimizer and efficiency of the solver used to perform the static simulation of the cycles. This would alleviate the computational cost of this expensive step, thereby opening the way to allow for more complex cycles to be included in the original database, e.g. with more than one heat exchanger.

Another promising extension is to proceed to the techno-economic design of SCO_2 cycles for industrial scale applications. This difficult task could indeed benefit from the large pool of thermodynamically similar but structurally different cycles generated by the RNN to lower the energy price of CSP.

Finally, let us mention that this work has enabled the creation of large datasets. They could be exploited to test alternative gen-

erative statistical models, such as the variational autoencoder [26], as well as more sophisticated finetuning strategies, for instance within reinforcement learning framework [25].

NOMENCLATURE

Acronyms

CO ₂	carbon dioxide
CSP	concentrating solar power
IC	intercooling
KNO ₃	potassium nitrate
LSTM	long-short term memory
MS	molten salt
NaNO ₃	sodium nitrate
PSO	particle swarm optimizer
PartC	partial cooling
PC	pre-compression
RC	recompression
RG	regenerative
RH	reheating
RNN	recurrent neural network
SCO ₂	supercritical carbon dioxide
TES	thermal energy storage

Symbols

-1, -2, ...	tokens representing splitters
1, 2, ...	tokens representing mixers
\mathcal{A}	alphabet of power cycle components
A	token representing a cooler
C	token representing a heat exchanger
\mathcal{D}_0	collection of randomly generated cycles
\mathcal{D}_k	collection of cycles sampled from the RNN
H	token representing a heater
\mathcal{M}_1	RNN trained on a large dataset (language model)
\mathcal{M}_2	finetuned RNN model (specialized model)
\mathcal{P}	net shaft power output (MW)
P_c	compressor work (MW)
P_t	turbine work (MW)
Q_{abs}	heat duty (MW)
T	token representing a turbine
T_1	minimum allowed MS temperature (°C)
T_1^*	actual minimum MS temperature (°C)
T_2	maximum allowed MS temperature (°C)
T_2^*	actual maximum MS temperature (°C)
U, V, W	parameter matrices of a RNN
a, b, ...	tokens representing a heat exchanger
h	hidden state of a RNN
o	output vector of a RNN
x	input vector of a RNN

Greek symbols

δ	threshold for the fitness function
η	thermal-to-electric efficiency (%)
σ	activation function in a neural network
τ	salt use rate

REFERENCES

- [1] V. Dostal, P. Hejzlar, and M. J. Driscoll, "High-performance supercritical carbon dioxide cycle for next-generation nuclear reactors," *Nuclear Technology*, vol. 154, no. 3, pp. 265–282, 2006.
- [2] Y. Le Moulec, "Conceptual study of a high efficiency coal-fired power plant with CO₂ capture using a supercritical CO₂ brayton cycle," *Energy*, vol. 49, pp. 32–46, 2013.
- [3] M. Mecheri and Y. Le Moulec, "Supercritical CO₂ brayton cycles for coal-fired power plants," *Energy*, vol. 103, pp. 758–771, 2016.
- [4] T. Neises and C. Turchi, "A comparison of supercritical carbon dioxide power cycle configurations with an emphasis on CSP applications," *Energy Procedia*, vol. 49, pp. 1187–1196, 2014.
- [5] F. A. Al-Sulaiman and M. Atif, "Performance comparison of different supercritical carbon dioxide brayton cycles integrated with a solar power tower," *Energy*, vol. 82, pp. 61–71, 2015.
- [6] J. Wang, Z. Sun, Y. Dai, and S. Ma, "Parametric optimization design for supercritical CO₂ power cycle using genetic algorithm and artificial neural network," *Applied Energy*, vol. 87, no. 4, pp. 1317–1324, 2010.
- [7] V. T. Cheang, R. A. Hedderwick, and C. McGregor, "Benchmarking supercritical carbon dioxide cycles against steam Rankine cycles for concentrated solar power," *Solar Energy*, vol. 113, pp. 199–211, 2015.
- [8] Y. Ahn, S. J. Bae, M. Kim, S. K. Cho, S. Baik, J. I. Lee, and J. E. Cha, "Review of supercritical CO₂ power cycle technology and current status of research and development," *Nuclear Engineering and Technology*, vol. 47, no. 6, pp. 647–661, 2015.
- [9] Q. Zhao, "Conception and optimization of supercritical CO₂ brayton cycles for coal-fired power plant application," Ph.D. dissertation, Université de Lorraine, 2018.
- [10] L. Wang, Y. Yang, C. Dong, T. Morosuk, and G. Tsatsaronis, "Parametric optimization of supercritical coal-fired power plants by minlp and differential evolution," *Energy Conversion and Management*, vol. 85, pp. 828–838, 2014.
- [11] L. Wang, P. Voll, M. Lampe, Y. Yang, and A. Bardow, "Superstructure-free synthesis and optimization of thermal power plants," *Energy*, vol. 91, pp. 700–711, 2015.
- [12] L. Wang, M. Lampe, P. Voll, Y. Yang, and A. Bardow, "Multi-objective superstructure-free synthesis and optimization of thermal power plants," *Energy*, vol. 116, pp. 1104–1116, 2016.
- [13] T. Neveux, "Ab-initio process synthesis using evolutionary programming," *Chemical Engineering Science*, 2018.
- [14] I. Goodfellow, Y. Bengio, and A. Courville, *Deep learning*. MIT press Cambridge, 2016, vol. 1.
- [15] "Smiles," <http://www.daylight.com/dayhtml/doc/theory/theory.smiles.html>, accessed: 2018-11-23.
- [16] M. Moran, H. Shapiro, D. Boettner, and M. Bailey, *Fundamentals of engineering thermodynamics*. John Wiley & Sons, 2010.
- [17] I. H. Bell, J. Wronski, S. Quoilin, and V. Lemort, "Pure and pseudo-pure fluid thermophysical property evaluation and the open-source thermophysical property library coolprop," *Industrial & Engineering Chemistry Research*, vol. 53, no. 6, pp. 2498–2508, 2014.
- [18] A. A. Hagberg, D. A. Schult, and P. J. Swart, "Exploring network structure, dynamics, and function using networkx," in *Proceedings of the 7th Python in Science Conference (SciPy2008)*, G. Varoquaux, T. Vaught, and J. Millman, Eds., 2008, pp. 11–15.
- [19] R. Eberhart and J. Kennedy, "A new optimizer using particle swarm theory," in *Proc. 6th Int. Symp. Micro Mach. Human Sci. (MHS95)*. IEEE, 1995, pp. 39–43.
- [20] J. A. Nelder and R. Mead, "A simplex method for function minimization," *The computer journal*, vol. 7, no. 4, pp. 308–313, 1965.
- [21] D. E. Rumelhart, G. E. Hinton, and R. J. Williams, "Learning representations by back-propagating errors," *Nature*, vol. 323, no. 6088, p. 533, 1986.
- [22] K. Cho, B. Van Merriënboer, C. Gulcehre, D. Bahdanau, F. Bougares, H. Schwenk, and Y. Bengio, "Learning phrase representations using rnn encoder-decoder for statistical machine translation," *arXiv preprint arXiv:1406.1078*, 2014.
- [23] S. Hochreiter and J. Schmidhuber, "Long short-term memory," *Neural computation*, vol. 9, no. 8, pp. 1735–1780, 1997.
- [24] F. Chollet *et al.*, "Keras," <https://keras.io>, 2015.
- [25] M. Olivecrona, T. Blaschke, O. Engkvist, and H. Chen, "Molecular de-novo design through deep reinforcement learning," *Journal of cheminformatics*, vol. 9, no. 1, p. 48, 2017.
- [26] R. Gómez-Bombarelli, J. N. Wei, D. Duvenaud, J. M. Hernández-Lobato, B. Sánchez-Lengeling, D. Sheberla, J. Aguilera-Iparraguirre, T. D. Hirzel, R. P. Adams, and A. Aspuru-Guzik, "Automatic chemical design using a data-driven continuous representation of molecules," *ACS central science*, vol. 4, no. 2, pp. 268–276, 2018.

DEVELOPMENT OF A PARTIAL-ADMISSION AXIAL TURBINE FOR A TENS-KWE UNDER SUPERCRITICAL CO₂ CONDITION

Jongjae Cho*
Korea Institute of Energy
Research
Daejeon, South Korea
Email:jjcturbine@kier.re.kr

Hyunki Shin
Korea Institute of Energy
Research
Daejeon, South Korea

Junhyun Cho
Korea Institute of Energy
Research
Daejeon, South Korea

Bongsu Choi
Korea Institute of Energy
Research
Daejeon, South Korea

Beomjoon Lee
Korea Institute of Energy
Research
Daejeon, South Korea

Chulwoo Roh
Korea Institute of Energy
Research
Daejeon, South Korea

Ho-Sang Ra
Korea Institute of Energy
Research
Daejeon, South Korea

Young-Jin Baik
Korea Institute of Energy
Research
Daejeon, South Korea

ABSTRACT

The development of a tens-kWe turbo generator that uses supercritical carbon dioxide (sCO₂) cycle technology at the lab scale is described herein. The design concept for the turbo-generator involves using commercially available components to reduce the developmental time and to increase the reliability of the machine. The developed supercritical partial-admission CO₂ turbine has a single-stage axial-type design with a 73-mm rotor mean diameter. The design of the sCO₂ turbine uses impulse and partial admission. The design concept can reduce the axial force and rotational speed, and also secure the processability of the turbine. We simulated the flow of the designed sCO₂ turbine. To increase the simulation accuracy, a real gas property table is coupled with the CFD solver. The turbine performance test apparatus and test results are described; then, the turbine is continuously operated for 4 hours 12 minutes. The maximum turbine power is 22.9 kW, and the maximum electric power is 12.6 kWe.

INTRODUCTION

The supercritical carbon dioxide (sCO₂) power cycle is gaining increasing attention as a technology that can potentially replace the conventional power cycle. One of the major advantages of the sCO₂ power cycle is that it reduces the turbomachinery size because of the high density of the supercritical phase [1]. The power cycles of sCO₂ have the potential to attain significantly higher cycle efficiencies compared with a conventional steam Rankine cycle [2]. High cycle efficiency will automatically lead to low fuel cost and low water usage; for fossil fuel heat sources, it will lead to low greenhouse gas emissions.

Furthermore, the sCO₂ cycles operate at high pressures throughout the cycle, thereby generating a high-density

working fluid. Owing to this, equipment size and plant footprint are reduced, thereby reducing the capital cost [2].

Numerous studies have been conducted on the sCO₂ cycle and the essential components of this cycle. Table 1 summarizes the specifications for sCO₂ power turbines derived from various studies. Sandia National Lab (SNL) developed a 250-kWe sCO₂ power generation test loop [3-5]. Bechtel Marine Propulsion Corporation (BMPC) developed a 100-kWe sCO₂ Brayton cycle integrated systems test loop [7-9]. Tokyo Institute of Technology (TIT) developed a 10-kWe sCO₂ power generation test loop [10]. Southwest Research Institute (SwRI) and GE Global Research have been designing a 10-MWe sCO₂ turbo-expander; they are also building a 1-MWe test facility to test the design with a reduced capacity [11]. Echogen developed an 8-MWe sCO₂ power generation system for waste heat recovery, and this system has generated 2.4 MWe of power [12].

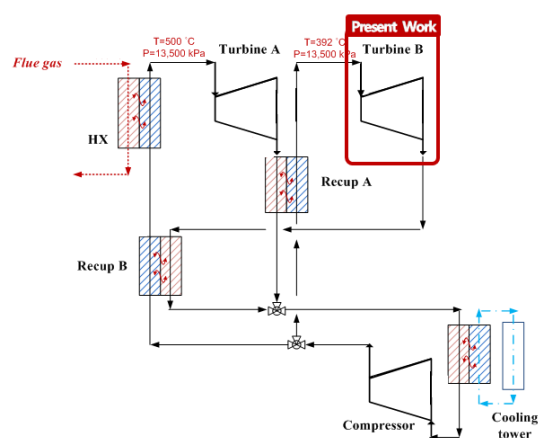


Figure 1: KIER sCO₂ dual-cycle loop

* corresponding author(s)

Table 1: Specifications for sCO₂ power turbines

	KIER (South Korea)	SNL (USA) [3-5]	BMPC (USA) [7-9]	TIT (JAPAN) [10]	SwRI/GE (USA) [11]	Echogen (USA) [12]
Capacity (kWe)	93	250	100	10	1000	8000
Turbine	Axial	Radial	Radial	Radial	Axial	Radial
Bearing	Tilting pad	Gas foil journal	Gas foil journal	Gas foil journal	Tilting pad	Tilting Pad
Power generation (kWe/°C/bar)	12.6/216/123	15/477/105	40/282/141	0.11/260/105	-/700/250	2350/275/-

Since 2013, the Korea Institute of Energy Research (KIER) has been studying the sCO₂ power cycle to develop test loops. The first test loop developed at KIER was a 10-kWe-class simple unrecuperated Brayton power cycle. The loop was designed to test the feasibility of sCO₂ systems and to develop feasible designs for small-scale sCO₂ systems. In the preliminary test, the test loop was successfully operated [13-14]. The second test loop was developed in 2014 for analyzing the cycle characteristics and investigating the cycle operation data. Owing to the heat source limitations, a radial power turbine with partial admission and a sub-kWe capacity was designed. In 2016, the turbine was driven successfully on the test loop, and the maximum turbine power was 670 We [15].

A dual-cycle loop suitable for recovering waste heat is being developed at KIER. The cycle comprises two turbines, one compressor, two recuperators, a combustion heat source heater, and a cooler. Fig. 1 shows the cycle loop. The Turbine A design will be accomplished in 2019. Turbine “B” was developed first to reduce the developmental costs and time. The components of the previous 10-kWe-class test loop were upgraded for using them in a turbo generator. Turbine “B”, shown in Fig. 1, was designed as an axial-type impulse turbine. The test-loop facility has been designed and manufactured for developing Turbine “B” at KIER.

This study presents and discusses the numerical simulation and test results on the cycle loop for the Turbine “B”.

TURBINE AERODYNAMIC DESIGN

sCO₂ has a small volumetric flow rate and a small turbine size with a high rotational speed. In addition, the high inlet pressure creates a high axial force. Owing to these characteristics, it is difficult to choose the bearing, and a high possibility for bearing failure is involved. To solve these problems and ensure robust operations, tilting-pad bearings were used although it would reduce the efficiency. A tilting-pad bearing design has a relatively large mechanical loss and low operating speed than a ball bearing; however, it has a robust bearing and can resist the high axial and radial forces. To use this bearing, the turbine operation speed was restricted and a high loss was permitted. We chose an axial impulse turbine to reduce the axial force. Fig. 2 [16] shows that the axial turbine and the tilting-pad bearing are appropriate for developing a

Megawatt-class engine. Our component and technology choices were aimed toward developing the know-how and technology for the Megawatt class.

Tilting-pad bearings cannot constitute the hermetic layout of the turbine, and a seal is required to prevent CO₂ leakage. Thus, the basic layout of the turbo generator was the turbine-seal-generator. To reduce the leakage level to <2%, carbon ring seals were selected and placed between the turbine and the bearing. This tilting-pad bearing restricted the rotational speed to <45,000 rpm under the normal operation conditions. However, the turbine inlet condition demands over 100,000 rpm as the operating speed in the optimal design. Table 2 displays the design condition for Turbine “B”. The total temperature of the turbine inlet was 392°C, the total inlet pressure was 135 bar, and the specific work was 53.08 kJ/kg.

In the preliminary design of the turbine, the low rotational speed reduced the blade height more than the high rotational speed. In addition, the minimum gap between the rotor passages was over 2.5 mm for the five-axis computer numerical control (CNC) machining. Designing an adequately sized turbine for CNC machining and for good performance under rotational speed and mass flow rate constraints is difficult. Table 3 displays the design results. The rotor mean diameter of the turbine is 73 mm. The turbine efficiency of the design point was 86.1% without the rotor tip clearance. The specific work was predicted as 57.07 kJ/kg. The clearance/span ratio (3.6%) of the turbine was selected by considering the turbine performance, manufacturability, and allowable assembly tolerances.

TM Feature	Power (MWe)						
	0,3	1,0	3,0	10	30	100	300
TM Speed/Size	75,000 / 5 cm		30,000 / 14 cm		10,000 / 40cm		3600 / 1.2 m
Turbine type	Single stage	Radial		multi stage			
			single stage	Axial	multi stage		
	Single stage	Radial		multi stage			
Bearings				single stage	Axial	multi stage	
Seals							

Figure 2: Component and technology options for sCO₂ systems [16]

Table 2: Turbine “B” design conditions

Specific work	kJ/kg	53.08
Inlet total pressure	bar	135
Inlet total temperature	°C	392
Pressure ratio (PR_{TT})	-	1.75
Rotational speed	rpm	under 45,000

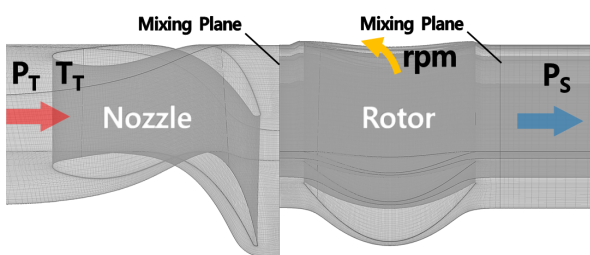
Table 3: Turbine “B” preliminary design results

Nozzle vane height	mm	8.36
Rotor blade height	mm	8.36
Rotor mean diameter	mm	73
Rotational speed	rpm	45,000
Partial-admission ratio	%	100
Specific work	kJ/kg	57.07
Efficiency (η_{TT}) *	%	86.1

* without rotor tip clearance

NUMERICAL ANALYSIS

Based on the preliminary design results, a numerical analysis was performed to determine the final design of the turbine using the commercial computational fluid dynamic (CFD) solver ANSYS CFX [17]. We also used the Reynolds-averaged Navier–Stokes two-equation model: the $k-\omega$ shear stress transport of Menter [18]; wall functions were also applied. For the analysis, we resolved the boundary layer to an approximate average y^+ value of 3. The total mesh size was set to approximately 6.1 million.

**Figure 3:** Numerical domain and mesh

The inlet boundary condition was defined by the total pressure and temperature. The outlet boundary condition was defined by the static pressure. At the wall boundary condition, non-slip and adiabatic wall boundary conditions were applied. A mixing-plane model was defined between the interface of the stationary and rotating zones. CFD analysis was performed under conditions of full admission because of the computational cost. Fig. 3 shows the numerical domain and the

boundary conditions of Turbine “B”. The CFD was performed based on real gas characteristics using the NIST REFPROP software.

Fig. 4 shows the performance maps of the turbine with the full admission condition for efficiency and the mass flow rate based on the rotational speed. The efficiency (η_{TT}) on the design point (PR_{TT} 1.75, N/N_{DP} 1.0) is 78.5%. A peak efficiency of 80% was achieved at the design rotational speed (N/N_{DP} 1.0). As the rotational speed increased, the efficiency decreased in accordance with the decrease in pressure ratio. The turbine flow was choked at the nozzle near the design pressure ratio (PR_{TT} 1.75). Fig. 5 shows the Mach number contours based on the pressure ratio at the design rotational speed (45,000 rpm). Above the design pressure, the flow was choked at the nozzle throat. At PR_{TT} 3.0, the flow was also choked at the rotor passage.

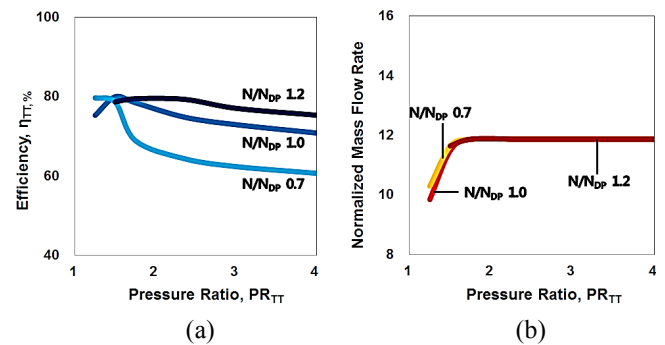
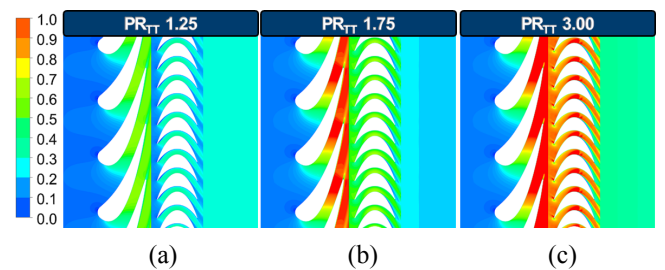
**Figure 4:** Performance maps predicted by CFD showing (a) efficiency and (b) mass flow rate**Figure 5:** Mach number contours of each pressure ratio at 50% span efficiency at the design rotational speeds of (a) PR_{TT} 1.25, (b) PR_{TT} 1.75, and (c) PR_{TT} 3.00

Fig. 6 shows a schematic view of axial thrust force and the surface pressure contours at the design point. Fig. 7 is the graph for the area-weighted average surface pressure and the force according to the rotor radius, as shown in Figs. 6 and 7. Near the rotor hub region, the surface pressure at the back-face is higher than that in the front-face. However, the area of the back-face of the rotor is smaller than the front-face because of the shaft. Therefore, an axial force acts from the front-face of

the rotor to its back-face. The axial force generated by the CFD was approximately 5.8 kN at the full admission condition.

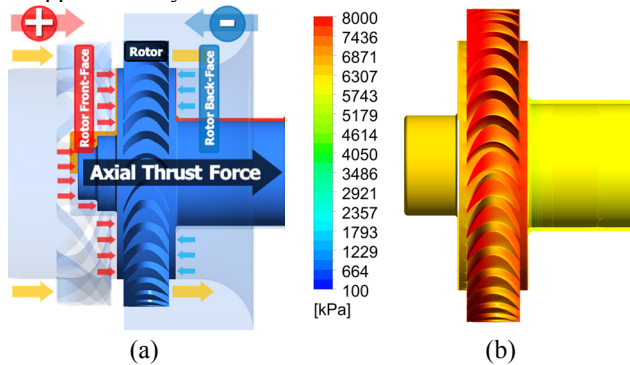


Figure 6: Schematic view of axial thrust force (a) and surface pressure contours at the design point (b)

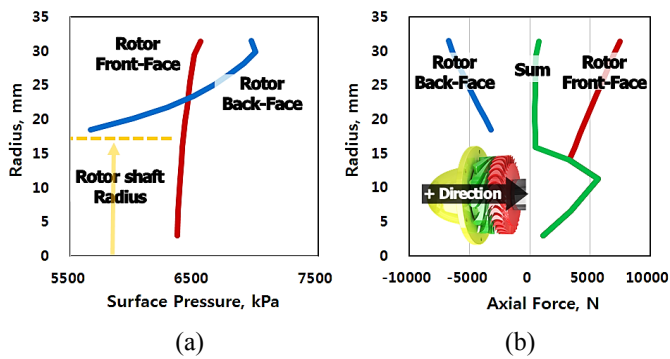


Figure 7: Area-weighted average (a) surface pressure and (b) axial force at the design point

TURBINE ASSEMBLY

Fig. 8 shows the designed turbine geometry, manufactured nozzle, and rotor. The turbine tests were conducted under 16.7% partial-admission condition because the burner had limited capacity. A partial-admission plate was installed, as shown in Fig. 8. Two principal types of losses, such as pumping losses and driving-fluid losses, occur with partial admission. The performance based on the partial admission was corrected using the performance test results of a reference [19] because the turbine had a full-admission design.

A configuration of KIER’s turbo generator was used to separate the turbine part and the generator part using a mechanical seal and applying tilting-pad bearings. In this turbine-generator layout, the turbine exerted a large amount of axial force on the axis. The axial force could not be canceled because of the absence of a compressor. Thus, a tilting-pad thrust bearing was adopted to resist the axial force. Fig. 9 shows a layout of the turbo generator.

Fig. 10 shows the flow diagram of the turbine, as well as the oil supply lines for lubricating the tilting-pad bearings and the coolant lines for cooling the generator and turbine. When

the test was prepared, an unacceptable amount of flow leakage occurred despite applying the carbon ring seal because of high-pressure operating conditions. This leakage required a leakage management system. The leakage management system, which used a reciprocating CO₂ compressor to re-inject the leak flow into the main test loop, was developed at KIER. A barrier gas was used to control the leakage flow, and the leakage flow and the barrier gas were re-injected into the main test loop using the leakage management system.



Figure 8: Manufactured rotor and nozzle of Turbine “B”

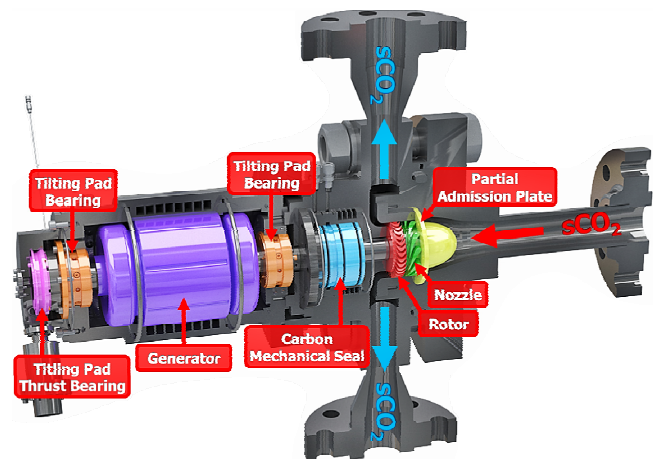


Figure 9: Layout of a turbo generator with Turbine “B”

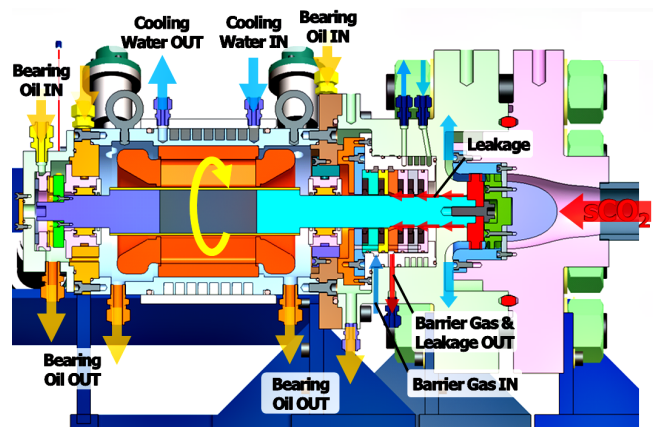


Figure 10: Flow diagram of the system with Turbine “B”

PERFORMANCE TEST FACILITY

The test loop was built by modifying the previous 10-kW cycle built by KIER researchers to test the performance of Turbine B before developing the sCO₂ dual cycle shown in Fig. 1. As shown in Fig. 11, the test loop comprised a turbo generator, a liquid CO₂ pump, a PCHE heater, a PCHE cooler, a burner, a separator, and a leakage management system. Fig. 12 shows the turbo generator assembly in the test loop. Fig. 13 shows a test-loop facility to drive the axial turbo generator with Turbine “B”. Using a test-loop control system, we conducted tests to control the valves, pump, and burner. The test data, such as the temperature, pressure, mass flow rate, electric power, rotational speed, and vibration, were obtained using a data measurement system.

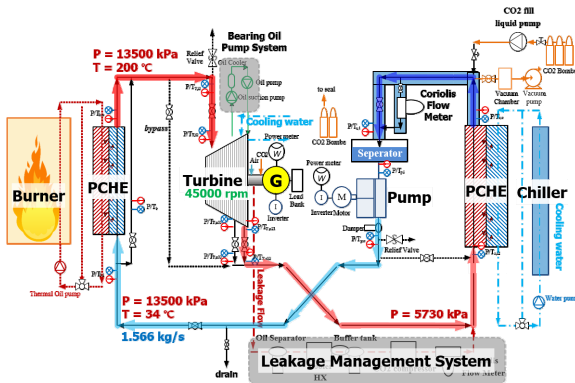


Figure 11: sCO₂ test loop of Turbine “B”

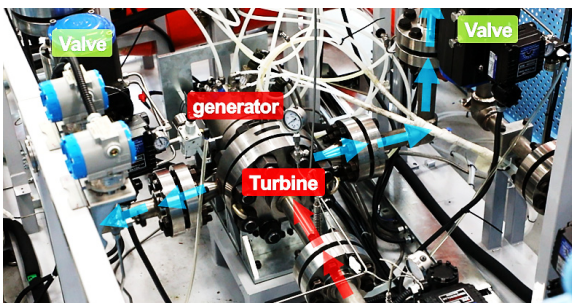


Figure 12: Turbo generator assembly with Turbine “B”

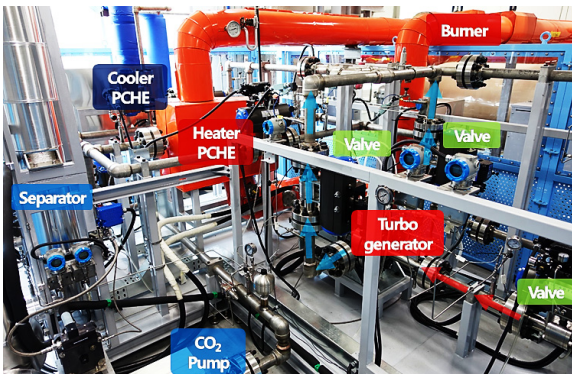


Figure 13: KIER sCO₂ test-loop facility for Turbine “B”

PERFORMANCE TEST

Turbine B was tested with the inlet temperature of 200°C and 16.7% partial admission because of limited burner and pump capacities. The test condition was the off-design condition. The test condition is shown in Table 4.

Table 4: Test conditions for Turbine “B” on the test-loop cycle

Inlet total pressure	bar	135
Inlet total temperature	°C	200
Pressure ratio (PR _{TT})	-	2.36
Rotational speed	rpm	under 45,000
Partial-admission ratio	%	16.7

Based on a previous cycle test research, the procedure for operating the test-loop cycle was modified to make it acceptable to this cycle [15]. The turbine performance test was performed after satisfying the cycle conditions for the test using the turbine bypass loop. When the cycle conditions were satisfied, the inlet and outlet valves of the turbine were opened to measure the data related to the turbine performance. The initial startup of the turbine was performed by converting the generator into a motor. When the turbine operated smoothly, the motor functioned as a generator and produced electric power.

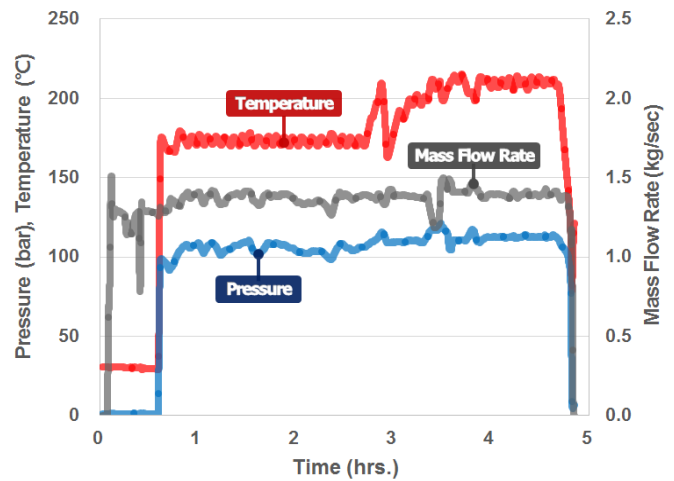


Figure 14: Pressure, temperature and mass flow rate at turbine inlet according to time lapse

Fig. 14 plots the pressure, temperature, and mass flow rate data at the turbine inlet measured via the performance test of Turbine “B” in the test-loop cycle. The maximum inlet pressure of the turbine obtained through the test was 122.8 bar, and the maximum temperature was 215.7 °C. The turbine test was not performed the target test conditions because of several problems in the turbo generator assembly and the test facility.

In addition, it was not easy to keep the inlet and outlet conditions of the turbine constant under the desired conditions because the test loop was a Rankine cycle, and the leakage management system was additionally installed.

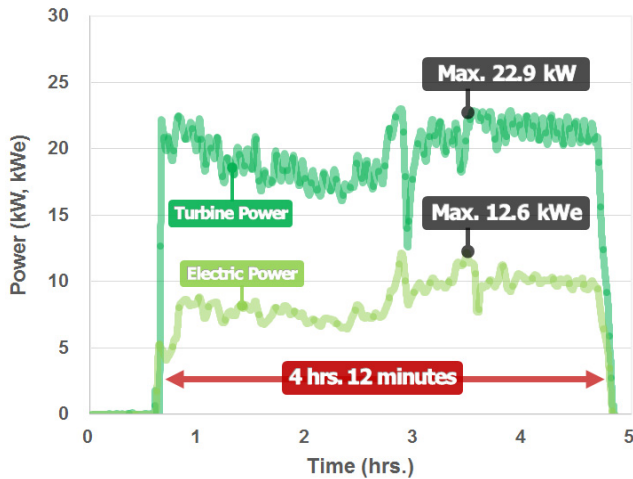


Figure 15: Generated turbine power and electric power according to time lapse

Fig. 15 shows the generated turbine power and electric power of the turbo generator over time. The turbine was continuously operated for 4 hrs. 12 minutes to produce power. The maximum turbine power was 22.9 kW, and the maximum electric power was 12.6 kWe. However, the turbine power and electric power values fluctuated substantially because it was difficult to keep the turbine inlet and outlet conditions constant. As mentioned above, a tilting-pad bearing has a relatively large mechanical loss compared with other common bearings. Therefore, the turbine power and electric power data have a relatively large difference.

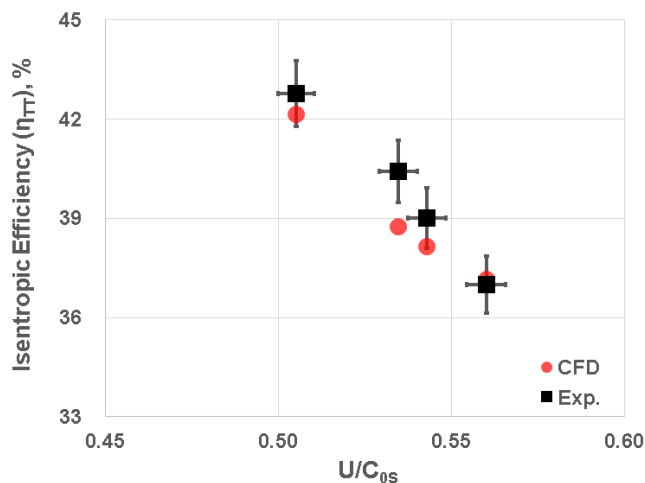


Figure 16: Comparison CFD and experimental results for isentropic efficiency according to spouting velocity ratio

Fig. 16 shows comparison the experimental results with the CFD results for the isentropic efficiency according to the spouting velocity ratio (U/C_{0s}) at several test conditions. The uncertainty for the spouting velocity ratio is $\pm 1.02\%$ and the uncertainty for the efficiency is $\pm 2.34\%$ [20]. For comparative conditions, most CFD results are within the uncertainty of the test, and the maximum error within the comparison condition is 4.1%. Therefore, the CFD results for the experimental cases are in good agreement with the test results.

Fig. 17 shows the estimated full admission efficiency for each test case. Based on the CFD results for performance with partial admission ratios, the correlation for estimated full admission performance was derived. The correlation is a function of U/C_{0s} and partial admission ratio. The estimated isentropic efficiency for full admission at U/C_{0s} of 0.51 is about 76.3%.

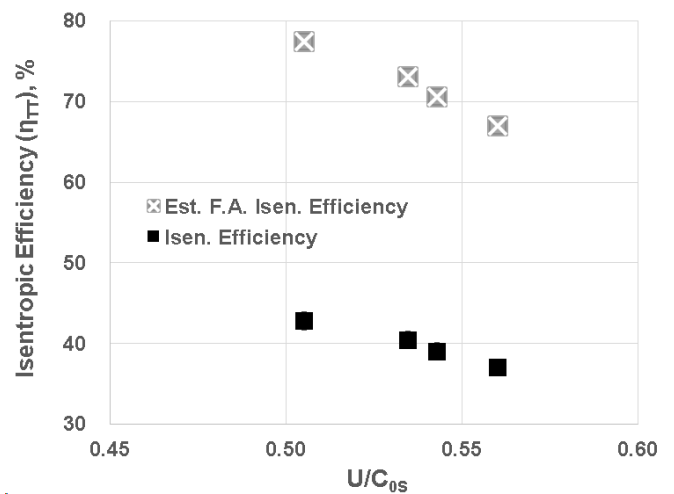


Figure 17: Estimated full admission efficiency for each test cases

SUMMARY AND FUTURE WORK

A turbine for use in the KIER dual $s\text{CO}_2$ cycle for the recovery of waste heat was developed. To incorporate the technology applicable to the Megawatt class, axial turbine and tilting-pad bearings were used to develop a turbine. We performed the preliminary design of the turbine and verified the performance and design based on the preliminary design results using numerical analysis. Then, the test-loop facility for the turbine performance test was designed and fabricated.

The turbine maximum inlet pressure in the test was 122.8 bar, and the maximum temperature was 215.7 °C. The turbine was operated continuously for 4 hrs. 12 minutes to produce electricity. The maximum turbine power was 22.9 kW, and the maximum electric power was 12.6 kWe. Based on the experimental results, the CFD results were verified and the results confirmed that the CFD results were in good agreement with the test results.

The problems (large mechanical losses, not maintained steady test conditions, low data sampling rate, etc.) were encountered during the test and developmental processes. We plan to revise and improve the test facility and turbine with upgrading a DAQ system, installing a dynamometer system and a balancing piston, modification of the oil system. In addition, we have a plan to test the turbine inlet temperature up to 500 °C by the end of 2019 through improved test equipment.

NOMENCLATURE

C	velocity	
c	chord	
ks	equivalent grain	sand
h	height	
m	mass flow rate	
N	rotational speed	
PR	pressure ratio	
P	pressure	
Pw	power	
U	rotational speed	
T	temperature	
η	efficiency	

SUBSCRIPTS

DP	design point
S	static
0S	isentropic
T	total
TC	tip clearance
TT	total to total

ACKNOWLEDGEMENTS

This work was conducted under the framework of Research and Development Program of the Korea Institute of Energy Research (KIER) (B9-2432, B9-2461).

REFERENCES

[1] Wright, S. A., Conboy, T M. and Rochau, G. E. (2011). Overview of Supercritical CO2 Power Cycle Development at Sandia National Laboratories. University Turbine Systems Research Workshop.

[2] Brun, K., Friedman, P., Dennis, R. (2017). Fundamentals and Applications of Supercritical Carbon Dioxide (SCO2) Based Power Cycles. Woodhead Publishing, Oxford, pp. 1~21.

[3] Wright, S. A., Radel, R. F., Vernon, M. E., Rochau, G. E., Pickard, P. S., (2010). Operation and analysis of a supercritical CO2 Brayton cycle. SANDIA REPORT 2010, SAND2010-0171.

[4] Pasch, J., Conboy, T., Fleming, D., Rochau, G. (2012). Supercritical CO2 recompression Brayton cycle: completed assembly description. SANDIA REPORT 2012, SAND2012-9546.

[5] Conboy, T., Wright, S. A., Pasch, J., Fleming, D., Rochau, G., Fuller, R. (2012). Performance characteristics of an operating supercritical CO2 Brayton cycle. Journal of Engineering for Gas Turbines and Power, 134(111703), pp. 1-12.

[6] Conboy, T., Pasch, J., Fleming, D. (2013). Control of a supercritical CO2 recompression Brayton cycle demonstration Loop. Journal of Engineering for Gas Turbines and Power, 135(111701), pp. 1-12.

[7] Clementoni, E. M., Cox, T. L. (2014). Steady-state power operation of a supercritical CO2 Brayton cycle. Proceedings of ASME Turbo Expo 2014, Dusseldorf, Germany, June 16-20 2014, GT2014-25336.

[8] Clementoni, E. M., Cox, T. L. (2014). Practical aspects of supercritical CO2 Brayton system testing. Proceedings of the 4th International Symposium-Supercritical CO2 Power Cycles, Pittsburgh, Pennsylvania, September 9-10.

[9] Clementoni, E. M., Cox, T. L. (2014). Steady-state power operation of a supercritical CO2 Brayton cycle. Proceedings of the 4th International Symposium-Supercritical CO2 Power Cycles, Pittsburgh, Pennsylvania, September 9-10.

[10] Utamura, M., Hasuike, H., Ogawa, K., Yamamoto, T., Fukushima, T., Watanabe, T., Himeno, T. (2012). Demonstration of supercritical CO2 closed regenerative Brayton cycle in a bench scale experiment. Proceedings of ASME Turbo Expo 2012, Copenhagen, Denmark, June 11-15, GT2012-68697.

[11] Moore, J., Brun, K., Evans, N., Bueno, P., Kalra, C. (2014). Development of a 1 MWe supercritical CO2 Brayton cycle test loop. The 4th international symposium-Supercritical CO2 power cycles, September 9-10, Pittsburgh, Pennsylvania.

[12] Held, T.J. (2014). Initial test results of a megawatt-class supercritical CO2 heat engine. The 4th international symposium-Supercritical CO2 power cycles, September 9-10, Pittsburgh, Pennsylvania.

[13] Cho, J., Choi, M., Baik, Y., Lee, G., Ra, H., Kim, B., Kim, M. (2016). Development of the turbomachinery for the supercritical CO2 power cycle. International Journal of Energy Research 2016, 40(587-99).

[14] Cho, J., Shin, H., Ra, H., Lee, G., Roh, C., Lee, B., Baik, Y. (2016). Development of the supercritical carbon dioxide power cycle experimental loop in KIER. Proceedings of ASME Turbo Expo 2016, Seoul, South Korea, June 13-17, GT2016-57460.

[15] Shin, H., Cho, J., Baik, Y-J., Cho, J., Roh, C., Ra, H-S., Kang, Y., Huh, J. (2017). Partial admission, axial impulse type turbine design and partial admission radial turbine test for

SCO₂ cycle. Proceedings of ASME Turbo Expo 2017: Turbomachinery Technical Conference and Exposition, GT2017-64369, June 26-30, 2017, Charlotte NC.

[16] Fleming, D., Conboy, T., Pash, J., Rochau, G., Fuller, R., Holschuh, T., Wright, S. (2013). Scaling considerations for a multi-megawatt class supercritical CO₂ Brayton cycle and commercialization. Sandia National Laboratories, Albuquerque, NM.

[17] ANSYS® (2017). ANSYS CFX User Guide, Release 18.1. ANSYS, Inc.

[18] Menter, F. (1994). Two-equation eddy-viscosity turbulence model for engineering applications. *AIAA Journal*, 32(8), pp. 1598-1605.

[19] Kohl, R., Herzig, H. and Whitney, W. (1949). Effects of partial admission performance of a gas turbine. NACA Technical Note, No. 1807, Lewis Flight Propulsion Laboratory.

[20] Coleman, H.W., and Steele, W.G. (1999). *Experimentation and uncertainty analysis for engineers*, 2nd Ed., John Wiley & Sons, New York

DEVELOPMENT AND APPLICATION OF INCONEL® ALLOY 740H IN USCO₂ POWER SYSTEMS

Stephen A McCoy*

PCC Metals Group
Hereford, UK

Email: smccoy@specialmetals.com

Brian A Baker

Special Metals Corporation
Huntington, USA

Ronald D Gollihue

Special Metals Corporation
Huntington, USA

John J deBarbadillo

Special Metals Corporation
Huntington, USA

ABSTRACT

Nickel-base alloys are required for many of the high pressure components in advanced ultra-supercritical steam and CO₂ power systems operating at temperatures and pressures exceeding 650°C and 25 MPa. Age-hardened alloys offer a distinct advantage over traditional solid solution strengthened Nickel alloys and stainless steels by virtue of their significantly higher creep strength. This makes it possible to reduce wall thickness and thereby minimize total construction cost. INCONEL® alloy 740H (UNS N07740) is an age-hardened alloy that was developed and extensively characterized for advanced ultra-supercritical steam boilers. Extensive material testing led to ASME Code Case 2702 covering UNS N07740. Alloy 740H is the first age-hardened nickel-base alloy permitted for welded construction for use in the creep limited temperature regime. More recent development work on the alloy has focused on applications for supercritical CO₂ systems. Various laboratories have reported on oxidation properties of the alloy under simulated operating conditions. This paper reviews the mechanical and corrosion properties of the candidate materials and focuses on the manufacturing and properties of piping products that are being applied for the various advanced ultra-supercritical steam and supercritical CO₂ projects now planned or underway. As many of the structures are constructed by welding, a review of welding practices is presented, including dissimilar welds and their properties.

INTRODUCTION

Many of the planned advanced sCO₂ energy conversion systems are projected to operate at temperatures above 700°C. This is above the temperature capability of ferritic stainless steel and austenitic steels that have greatly reduced strength that would require impractical wall thickness

to contain high pressure fluids. Solid solution strengthened nickel-base alloys such as 800HT, 230 and 617 have been used successfully in chemical process, energy and aerospace industries for many years; however, at the high pressures projected for many applications, impractically thick walls would be required for these materials as well [1]. For this reason, high strength age hardened alloys were evaluated for service, initially in a succession of European programs, then the US Advanced - Ultra Supercritical (A-USC) Consortium and then by advanced energy programs around the world. Alloy 740 (UNS N07740) was specifically developed under the THERMIE program for boiler tube for coal fired power plants [2]. The alloy featured high strength, sufficient ductility for fabrication into tube, weldability and resistance to oxidation and coal ash corrosion. Later the US program considered it for use in headers and reheat pipes. For this application better microstructure stability and heavy section weldability was needed. The alloy composition was subsequently optimized to improve these properties [3]. The optimized alloy, called 740H, fell within the original broad alloy definition. The composition of the optimized alloy is shown in Table 1.

During the period from 2002-2010 the US A-USC consortium conducted an extensive evaluation of mechanical properties and fabricability. This work has been documented in numerous technical publications [4-6] and culminated in submission of a data package that led to the ASME Code case 2702 [7]. Alloy 740H is the first age-hardened alloy to be accepted for fabrication of pressurized equipment. The advantage for alloy 740H in the temperature range of current

TABLE I. MAXIMUM, MINIMUM AND NOMINAL OF PRIMARY COMPOSITIONAL ELEMENTS OF ALLOY 740H.

Max/Min/Nominal	Ni	Fe	Cr	Co	Mo
Max	Bal	3.0	25.5	22	2.0
Min	Bal	---	23.5	15	---
Nominal	Bsl	0.25	24.5	20	0.5
Max/Min/Nominal	Al	Ti	Nb	Si	C
Max	2.0	2.5	2.5	1.0	0.08
Min	0.2	0.5	0.5	---	0.01
Nominal	1.4	1.4	1.5	0.15	0.03

interest for advanced power plants is shown in Figure 1 (values for alloys 617 and 800HT from ASME BPVC Section II, Materials, Part D, Properties, Table 1B; values for alloy 740H from ASME code case 2702). The rules of the current code as they apply to fabrication of complex systems will be discussed in this paper. Following Code approval, Special Metals working with consortium members, suppliers and selected fabricators began an extensive program to determine the limits of mill product dimensions, manufacture of fittings, and welding using a variety of processes, materials and configurations. This work has been reported in numerous venues [8-9].

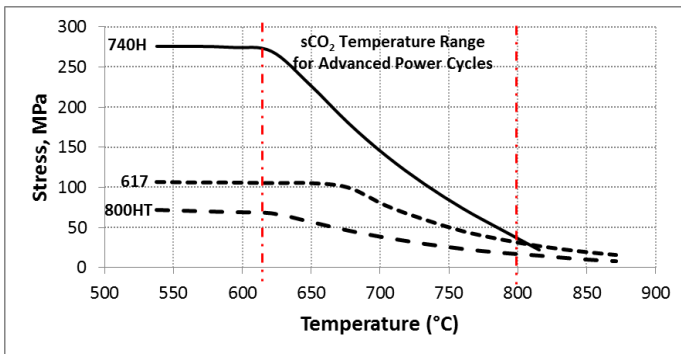


FIGURE 1. ASME MAXIMUM ALLOWABLE STRESS FOR ALLOYS 740H, 617 AND 800HT.

Age-hardened alloys have characteristics that are very desirable for power plant use. They are relatively soft and formable in the solution treated condition. In this condition they can be rolled and drawn to form sheet and tube, and tube can be cold formed by bending. Subsequently the components are again solution treated and aged. Direct aging of cold formed parts is restricted due to a loss of creep strength. Alloys of this type can be welded successfully although strict protocols must be followed and high energy processes cannot be used. Concerns about use of age-hardened alloys in this application include long time microstructure stability (> 100,000 h. at temperature), impact

toughness, creep, creep-fatigue, over temperature damage tolerance and strain-aging and stress relaxation cracking of welds. Understanding of the issues is being developed through continued laboratory work, component manufacture, and in-plant test loops and pilot plants. The following discussion presents recent developments using alloy 740H.

Although alloy 740H was developed under A-USC programs, in recent years it has been considered for sCO₂ service as well. Although A-USC in-plant test loops to gain fabrication and operating experience have been installed [10] to date a full operating system has not yet been constructed. In the interim sCO₂ programs have advanced including Sunshot [11] and Supercritical Transformational Electric Power (STEP) [12].

RESULTS AND DISCUSSION

Mechanical properties

Tube and pipe are the primary product forms used in advanced energy systems and hence have been the focus of much of the development work. Although there is no clear distinction in codes between tube and pipe on the basis of fabrication methods, for this paper tube will be defined as extruded, cold worked annealed and aged product whereas pipe is defined as extruded and directly annealed and aged. While there is considerable size overlap between the two products, tube tends to lie at smaller diameters and thinner wall product. There also is an inherent grain size difference between tube and pipe with tube having a much wider possible range of ASTM #3-8. In the case of pipe the grain size may be ASTM #1-5 depending on pipe size. Grain size in as extruded pipe can be more difficult to refine due to the relatively high temperatures required for the extrusion operation. Generally alloy 740H will be producible over the standard range of nickel alloys. Tube has been produced by both drawing, pilgering and roll forming processes. Pipe has all been produced by extrusion on presses at Special Metals (Huntington, WV and Hereford, UK) and Wyman-Gordon (Houston, TX and Livingston, UK)

TABLE 2. TYPICAL ROOM TEMPERATURE MECHANICAL PROPERTIES FOR VARIOUS SOLUTION ANNEALED AND AGED PRODUCT FORMS OF ALLOY 740H.

Product Form	0.2% PS MPa	TS, MPa	El. %
Pipe	728 - 741	1083 - 1094	31 - 34
Tube	731 - 769	1153 - 1174	33- 42
ASME 2702	620 min.	1035 min.	El. 20 % min

Mechanical properties have been extensively evaluated and documented in the literature (3-7, 10). Generally additional production has confirmed the data used in the data package submitted for ASME code approval. The ASME specified heat treatment for 740H is a solution anneal at (1100°C) (2010°F) minimum and aging at 760-816°C (1400-1500°F).

Microstructure and stability

Many superalloys undergo microstructural changes if they are held for long periods of time at elevated temperatures. These changes may include formation of complex carbides, growth of γ' and the formation of a variety of topological close-packed (TCP) phases including Laves and sigma. These phases may form undesirable morphologies that reduce ductility and toughness. In the application of superalloys for power plant use it is necessary to demonstrate that they will be stable for the design lifetime of the plant. To evaluate the microstructural stability of 740H, material obtained from commercially produced pipe was exposed stress-free for times up to 10,000 h at 700°C (1292°F), 750°C (1382°F) and 800°C (1472°F). Longitudinal Charpy V-notch impact tests were conducted and the microstructure was analyzed in detail. The results of this investigation reported by deBarbadillo [13], are shown below in Figure 2. This high temperature exposure study demonstrate the material shows some loss of ductility as carbides form on the grain boundaries, however the material retains an adequate level of impact strength after 10,000hrs.

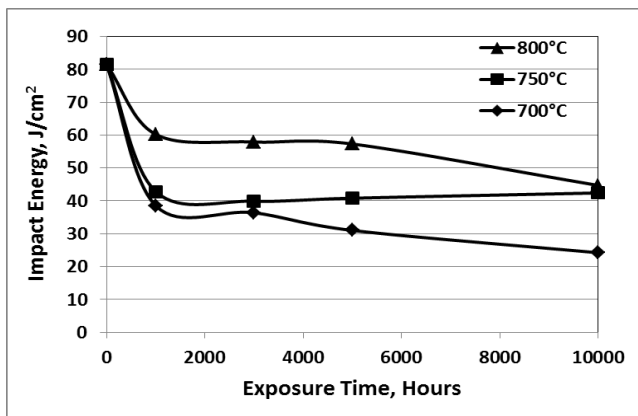


FIGURE 2. CHARPY IMPACT TOUGHNESS AFTER HIGH TEMPERATURE EXPOSURE FOR TIMES UP TO 10,000 HOURS

A representative scanning electron micrograph (SEM) of material in the as heat treated condition is shown in Figure 3. The grain interiors show a uniform fine γ' precipitate. The grain boundaries are almost completely covered with $M_{23}C_6$ and

coarse γ' . Material exposed for 5,000 h at 750°C (1382°F) is shown in Figure 4. Note that the γ' has grown significantly, but it continues to maintain a generally cubic morphology. Larger chunky γ' decorates the grain boundaries. Most of the remaining grain boundary area is covered by $M_{23}C_6$ carbide. No evidence of η or G phase. Sigma phase is predicted by Thermo-Calc to form at 650°C (1202°F) in this alloy at very long exposure times, but to date, it has not been reported. Creep deformation sometimes accelerates microstructural changes by providing enhanced diffusion and nucleation sites. Based on limited observations this does not seem to be the case for 740H. Figure 5 shows the structure near the fracture surface of a specimen tested at 750°C (1382°F) with an initial applied stress of 280 MPa (40.6 ksi) that broke in 1087.4 h. The structure is similar to the starting structure, but a chain of grain boundary voids is visible. Test bar fracture occurs by linking of these voids. There was no sign of a precipitate-free zone adjacent to the grain boundary although this feature has been observed in welds of 740H.

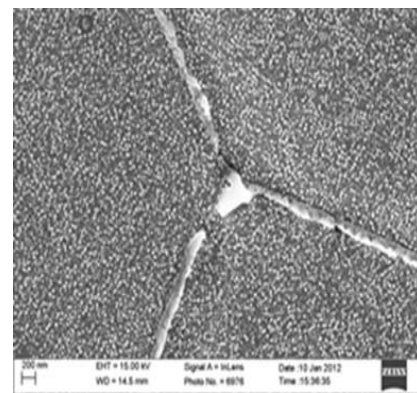


FIGURE 3. SEM MICROGRAPH SHOWING SOLUTION ANNEALED AND AGED MATERIAL

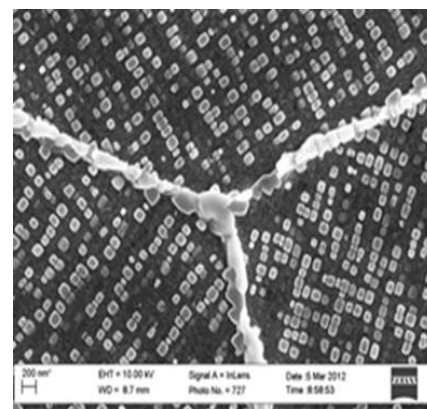


FIGURE 4. SEM MICROGRAPH SHOWING SOLUTION ANNEALED AND AGED MATERIAL AFTER 5000HRS EXPOSURE AT 750C

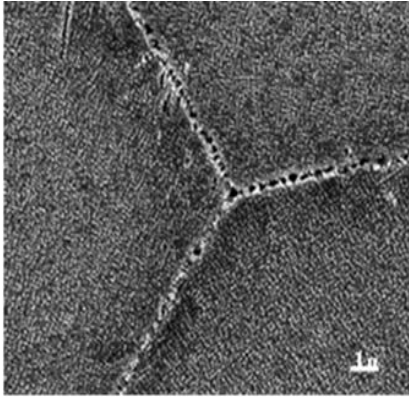


FIGURE 5. SEM MICROGRAPH SHOWING REGION NEAR FRACTURE FACE OF A CREEP RUPTURE SPECIMEN FAILED AT 1087.4 H AT 750C AND 280 MPA



FIGURE 6. HEAVY WALL 740H PIPE EXTRUSION.

Corrosion in supercritical carbon dioxide

The Brayton cycle system, using supercritical carbon dioxide as the working fluid, is being used and developed for use in various power generation systems, including nuclear, solar, and fossil/biofuel. This system provides a means of achieving very high levels of efficiency when compared with using a steam power cycle. The University of Wisconsin-Madison has devised an apparatus to evaluate the corrosion behavior of metal samples in high high-pressure carbon dioxide at temperatures up to 650°C (1202°F) [14]. The results indicate that 740H has a very low rate of mass gain at temperatures up to 650°C. More recent work by Kung et al at EPRI at 700°C and 200 bar on alloy 740H has shown only very thin oxide scales of 1 μm develop after exposures of up to 5000 hours in CO₂ containing 3.6% vol O₂ and 5.3% vol H₂O [15].

Manufacturing Demonstration

Tube has been made in alloy 740H by extruding billet, cut from forged bar, to tube shell and cold working to size using multiple cold work and anneal cycles. This tube process is similar to that used for other “hard” alloys such as 625 and 718.

Large pipe of 740H sections have been extruded at Wyman-Gordon Houston TX. This 378 mm OD x 88 mm W x 10.5 m L pipe is shown in Fig 6. A 762 mm diameter VIM/VAR Ingot was used for this extrusion. VAR was selected as the remelt step in order to minimize the risk of solidification segregation. Excellent chemistry uniformity and microstructure was obtained. The detail for this work has been reported previously [13].

Welding

Fusion welding is an essential joining method for power plant construction. Welding studies on alloy 740H showed that it could be readily welded by GTAW and GMAW processes with good operability, tensile and bend properties. Successful girth welds were made on superheater tubes. Alloy 740H has excellent resistance to liquation cracking while retaining the operability characteristics of the original alloy. An SMAW electrode is not currently available for alloy 740H due to the difficulty of transferring Al and Ti through the flux. Alloy 263 fluxes have been developed and it is expected that SMAW capability will be adopted into the ASME code case 2702.

Process parameters have been optimized by making butt welds on restrained 75 mm (3 in) thick plates and these parameters were then used to make circumferential welds on 378 mm (14.9) OD x 88 mm (3.46 in) wall extruded, solution annealed and aged pipe. The welds were made using a hot-wire narrow-groove GTAW process with a fixed torch and rotating work piece. Argon-25% He was used as the shielding gas for the matching composition filler wire. Welds were made with 5, 2, and 1 degree beveled V-grooves with a 1.57 mm (0.062 in) land. A cross-section of a weld with a 1 degree bevel is shown in Figure 7. Note that the entire weld of 33 passes is one bead wide. The full pipe section was aged per ASME code requirement for 5 h at 800°C (1472°F) using a ceramic tile heating blanket. This method is commonly used for post-weld heat-treatment of field welds. No fissures, porosity or cracking were detected with ultra-sonic, radiographic or microscopic examination. Details of microstructure and weld qualification properties have been previously been reported [16]. Key requirements for successful heavy section 740H welds are 1) use of proper shielding gas, 2) careful management of heat input and inter-pass temperature, 3) maintenance of correct bead geometry, and 4) frequent removal of residual surface oxides.



FIGURE 7. MACROGRAPH OF 88MM THICK PIPE SECTION WELDED WITH HOT WIRE-GTAW.



FIGURE 9. WELDING TRIAL DEMONSTRATING PIPE JOINT BETWEEN 316H, 740H AND P92.



FIGURE 8. SIMULATED FABRICATION OF A HEAVY WALL PIPE HEADER.

Once it was determined that sound welds could be made in heavy-wall pipe, a full scale header section was fabricated. For this simulated header, the nipples were inserted in predrilled holes and GTAW welded on the inside with a special rotary torch. The external welds were made manually by GTAW. This prototype header section is shown in Figure 8.

The alloy 740H will need to be joined to ferritic steels, austenitic stainless steel and other nickel alloys in various parts of the heaters, recuperators or to the turbine Work by several fabricators is underway to evaluate dissimilar metal welds. Work by Moody et al [17] and Baker et al [18] showed the development alloy 740H pipe welds to 316H and P92 steels. Restrained, V-groove plate welds were made using GTAW (FM 82, P87 and 617) and SMAW (WE 182 and P87). The 740H was in the aged condition and welds were stress relieved for 4 h at 775°C. All combinations produced sound welds and all except SMAW with WE P87 passed ASME tensile and bend qualification requirements with failure in the steel base metal. Creep, stress relaxation and fatigue tests were used to generate data for an FEA analysis of the high temperature joint design.

NOMENCLATURE

A-USC = Advanced-Ultrasupercritical

EPRI = Electric Power Research Institute

ASME = American Society of Mechanical Engineers

ASTM = American Society for Testing and Materials

GTAW = Gas Tungsten Arc Welding

GMAW = Gas Metal Arc Welding

SMAW = Shielded Metal Arc Welding

UNS = Unified Numbering System

VIM = Vacuum Induction Melting

VAR = Vacuum Arc Remelting

ESR = Electro-slag Remelting

OD = Outside Diameter

ID = Inside diameter

ACKNOWLEDGEMENTS

The authors are grateful for technical advice received from Babcock & Wilcox, Doosan Power and EPRI.

REFERENCES

- [1] J.P. Shingledecker, et al., "U.S. Program on Advanced Ultrasupercritical Power Plant Materials – The Economy of Using Advanced Materials", *IEA Clean Coal Technology Workshop: Advanced Ultrasupercritical Coal-fired Power Plants*, Vienna, Austria, 19-20 September, 2012.
- [2] B.A. Baker and G.D. Smith, "Corrosion Resistance of Alloy 740 as Superheater Tubing in Coal-fired Ultra-supercritical Boilers", *NACE Corrosion 2004*, NACE Int., Houston, TX, Paper No. 04526.
- [3] B.A. Baker, and R.D. Gollihue, "Optimization of INCONEL alloy 740 for Advanced Ultra-supercritical Boilers", *6th Int. Conf.: Advances in Materials Technology for Fossil Power Plants*, eds. Gandy, Shingledecker and Viswanathan, ASM Int., Materials Park, OH, 2010, 96-109
- [4] P.F. Tortorelli, et al., "Creep-Rupture Behavior of Precipitation Strengthened Ni Base Alloys Under Advanced Ultrasupercritical Steam Conditions", *7th Int. Conf.: Advancements in Materials Technology for Fossil Power Plants*, eds. Gandy and Shingledecker, ASM Int., Materials Park, OH, 2013, 131-142.
- [5] J.J. deBarbadillo, "INCONEL alloy 740H", *Materials for Ultra-Supercritical and Advanced Ultra-Supercritical Power Plants*, ed. A. Di Gianfrancesco, Elsevier, London, 2017, 469-506.
- [6] R. Viswanathan, et al., "Boiler Materials for Ultrasupercritical Coal Power Plants", US DOE No. DE-FG26-01NT41175, Feb. 15, 2006, p. 54.
- [7] ASME, "Case 2702 Seamless Ni-25Cr-20Co Material, Section 1, Cases of the ASME Boiler and Pressure Vessel Code, BPV-Supp. 7 2011, American Society of Mechanical Engineers.
- [8] B.A. Baker et al., "Manufacturing Demonstration of INCONEL alloy 740H for A-USC Boilers", *7th Int. Conf.: Advances in Materials Technology for Fossil Power Plants*, eds. Gandy and Shingledecker, ASM Int., Materials Park, OH, 2013, 215-229.
- [9] B.A. Baker, R.D. Gollihue, and J.J. deBarbadillo, "Fabrication and Heat Treatment of Weld Joints in INCONEL Alloy 740H Superalloy Steam Header Pipe and Superheater Tubing", *Proc. 10th Int. Conf.: Welding and Repair Technology for Power Plants*, EPRI, Marco Island, FL, 2012.
- [10] J. Shingledecker, R. Purgert and P. Rawls, "Current Status of U.S. DOE/OCDO A-USC Materials Technology Research and Development Program", *7th Int. Conf.: Advances in Materials Technology for Fossil Power Plants*, eds. Gandy and Shingledecker, ASM Int., Materials Park, OH, 2013, 41-52.
- [11] J. Moore, "Development of a High Efficiency Hot Gas Turbo-Expander and Low Cost Heat Exchangers for Optimized CSP Supercritical CO₂ Operation", DOE EERE STEP CSP Subprogram, Award DE-EE0005804, Quarterly Report, Dec. 15, 2016.
- [12] S. Macadam, "Supercritical Carbon Dioxide Pilot Plant Testing Facility Project", 2017 University Turbine Systems Research Project Review Meeting, DOE/NETL, Pittsburgh, PA, Nov. 1-2, 2017
- [13] de Barbadillo, J.J., Baker, B.A., and Gollihue, R.D., "Age-Hardened Nickel-base Alloys for Advanced Energy Applications, 8th International Symposium on Superalloy 718 and Derivatives, Pittsburgh PA, Sept. 28-Oct. 1, 2014
- [14] Sridharan, K., "Corrosion in supercritical Carbon Dioxide: Materials, Environmental Purity, Surface Treatments and Flow Issues," U. S. DOE Report 10-872, December 10, 2013, p. 205.
- [15] S. Kung et al, "Characterisation of oxide scale structures on alloys exposed to open-fired sCO₂ power cycles", 6th International supercritical CO₂ power cycles symposium, March 27 – 29, Pittsburgh, PA, USA
- [16] Siefert, J.A., Tanzosh, J.M., and Ramirez, "Weldability of INCONEL alloy 740H", *Proceedings: Sixth International Conference in Advances in Materials Technology for Fossil Power Plants*, Santa Fe, NM, Aug. 31 – Sept 3, 2010, 1045-1066.
- [17] P. Moody, et al., "Application of INCONEL Alloy 740H to Pipe Transition Joints in Advanced Power Plant", *8th Int. Conf.: Advances in Materials Technology for Fossil Power Plants*, eds. Parker, Shingledecker, and Siefert, ASM Int., Materials Park, OH, 2016, 161-168.
- [18] B.A. Baker, R.D. Gollihue and J.J. deBarbadillo, "Dissimilar Metal Welding of Alloy 740H", *11th Int. Conf.: Welding and Repair Technology for Power Plants*, EPRI, Naples, FL, 2014.

HIGHLY EFFICIENT PLATE-FIN HEAT EXCHANGER (PFHE) TECHNICAL DEVELOPMENT FOR S-CO₂ POWER CYCLES

Sarah TIOUAL-DEMANGE*
Fives Cryo
Golbey, FRANCE
sarah.tioual-demange@fivesgroup.com

Gaëtan BERGIN
Fives Cryo
Golbey, FRANCE

Thierry MAZET
Fives Cryo
Golbey, FRANCE

ABSTRACT

Among all the equipments required for advanced Brayton cycles using supercritical CO₂ (s-CO₂), heat exchangers are clearly key components. Fives Cryo, with its expertise in thermal-hydraulic design and brazing fabrication is developing a compact, and highly efficient heat exchangers for s-CO₂ power cycles, thanks to their heat exchange capability with low pinch and high available flow sections. The aim of the development of this specific heat exchanger technology is to achieve an elevated degree of regeneration with recuperators at low and high temperatures. Plate-Fin Heat Exchanger (PFHE) is then a seductive solution to meet the desired thermal duty with low pressure drop leading to a reduction in size and capital cost. The enhancement of the mechanical integrity of PFHE equipment would lead to compete with, and even outweigh, Printed Circuit Heat Exchangers (PCHE) technology.

s-CO₂ Cycle conditions expose heat exchangers to severe conditions up to 500 °C and 250 bar. Base material selection is essential, and for cost reasons, it is important to keep affordable heat-resistant austenitic stainless steel grades, much cheaper than a nickel-based alloy. Another advantage of high compactness of PFHE is the diminution of the amount of material used in the heat exchanger fabrication, decreasing even more its cost. The challenge presented here is to qualify PFHE, especially its mechanical resistance, at cycle operating conditions. To reach the requirements, several fabrication fields were explored.

One critical point is the design of the fins. As secondary surface they permit the maximization of heat transfer at a low pressure drop. At the same time mechanical strength has to be guaranteed. To withstand high pressure, fins thickness has to be significant, which makes the implementation complicated. Efforts were dedicated to successfully obtain an optimal shape. Forming of fins was therefore improved compared to conventional techniques. Important work was undertaken to define industrial settings to flatten the top of the fins leading to a maximum contact between the brazing alloy and the fins. Consequently brazed joints quantity is minimized inducing a diminution of the presence of eutectic phase, which is structurally brittle and limits the mechanical strength of the construction.

A detailed metallurgical study brings other elements leading to the prevention of premature rupture of the brazed structure. The idea is to determine an optimized solidification path and to identify a temperature range and holding time where the brazed joint is almost free of eutectic phase during the assembly process in the vacuum furnace.

INTRODUCTION

The Brayton cycle is the working principle of gas turbine engines. It can be a closed or open cycle. For classical open Brayton cycles, the working fluid from the compressor is injected into a combustion chamber where the high pressure fluid is mixed with fuel. In this case, the fluid is generally air. Closed Brayton cycles replace the combustion chamber with two heat exchangers following the compressor and the turbine. The working fluid in this

case is recycled continuously. The heat exchanger following the compressor, enhance the energy of the working fluid in order to activate the turbine, goes through the second heat exchanger which cool it to restore its initial conditions to go back into the compressor ([1], [2]). The working principle of the closed Brayton cycle shows the importance of heat exchangers in the thermodynamic process. These equipments need to be compact and able to be operated under severe mechanical and environmental constraints.

For Brayton cycles applications using supercritical CO₂, PCHE technology is mostly used thanks to its design capabilities: PCHE can be used for very high pressure and temperature conditions, compared to classical FPHE ([3], [4], [5]). Nevertheless, according to their important compactness and their economic interest, if the mechanical properties of FPHE and its integrity could be improved to reach PCHE performances, it would be the perfect choice in this field, since PCHE is a very expensive equipment, due to its important material density and the diffusion bonding assembly technique. Our work presented in this paper is achieved in the framework of this goal.

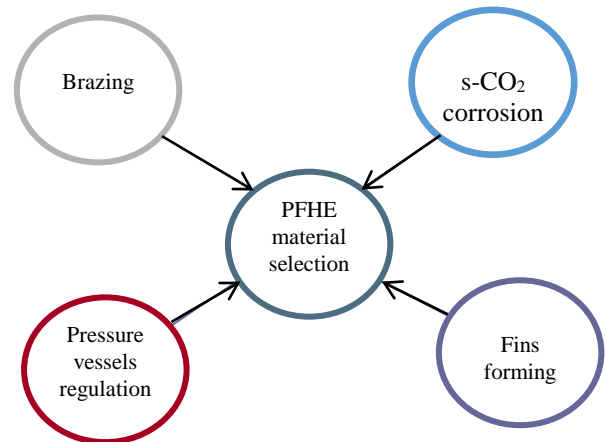
At Fives Cryo, we have a good knowledge in designing and manufacturing brazed PFHEs, which help us developing very efficient heat exchangers, in order to meet the requirements needed for s-CO₂ power cycles as part of the s-CO₂-flex European project. Recuperators are therefore developed, which should operate under pressures up to 250 bars and temperatures of about 500°C, in a s-CO₂ corrosive environment, due to its impurities content (water, oxygen ...). PFHE can be made with quite large channels compared to PCHE, which permit to reach moderate pressure drop. The main objectives of the development are to propose a heat exchanger based on that technology that meets several requirements while increasing the cycle's efficiency. Quite a few aspects were investigated and among them to perform the design, the manufacturing, and to test it under the defined conditions.

The main tasks to consider are thus:

- to define appropriate materials for contact with high temperature impure s-CO₂ on the basis of corrosion tests,
- to achieve mechanical tests to satisfy operating conditions,

- to design and manufacture the heat exchanger by brazing and welding
- Finally, to confirm thermal and hydraulic performances of the heat exchanger.

The diagram below summarizes these tasks.



This paper mainly focuses on the work performed in the frame of manufacturing a plate-fin design that can withstand high-temperature and high temperature conditions and also survives in corrosion environment. The technical challenge is to determine a suitable configuration for all the constraints imposed by this process.

MATERIAL SELECTION

Depending on material interaction with CO₂ stream and available information on impurities content such as oxygen or water that affect corrosion rates, some candidate alloys cannot be employed. Brazing as an assembly technique has also to be evaluated on potential reaction rates with the circulating working fluid in the cycle. Little information is available, especially in supercritical conditions thus, corrosion data results are needed.

Furthermore, corrosion consideration has to be done in accordance with suitable mechanical strength. A selection of materials has to be discarded as they are not permitted to be employed at a level of 500 °C according to the boilers and pressure vessels regulation. Other concerns mainly deal with fins formability, and capacity of the alloy to be assembled by brazing and welding.

Consequently, a shortlist of 3 different alloys was established: were selected, an austenitic stainless steel alloy compatible with brazing/welding conditions and aluminized in order to improve its corrosion resistance; a nickel-based alloy, which is certainly the more convenient choice for high corrosion resistance in drastic conditions and high mechanical resistance but presents the higher cost ; and a coated carbon steel alloy, which is a very innovative solution and could be very interesting economically and mechanically, but it needs to be validated for industrial use. The testing of these materials is still carried out by external contributors to the project, at s-CO₂ cycle's maximum temperature (500°C), hence, the results will not be included in the present paper.

This material selection clearly impacts the design of PFHE which is the result of a compromise but it should keep an advantage of high recuperation capacity at a moderate cost.

Despite the current lack of information on the corrosion resistance of the selected materials, we will relate in the sequel of this paper, the work achieved to enhance the mechanical resistance of PFHE assembly.

MECHANICAL RESISTANCE

An overview of basic elements necessary for the construction of a Plate-Fin Heat Exchanger can be seen on **Figure 1**, where the 3 flows are modeled by green, blue and red colors to illustrate the capability of this technology to withstand multiple flows. For s-CO₂ cycles, only 2 fluids are circulating for heat exchange.

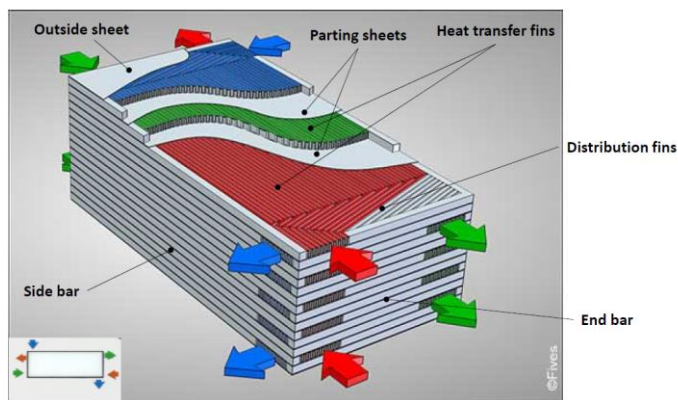


Figure 1: Example of a standard design of a Plate- Fin Heat Exchanger (PFHE) manufactured at Fives Cryo.

It consists of multiple layers of corrugated metal fins, separated by plates and closed with bars at the edges. The structure is joined together by brazing (**Figure 2**). The fluids circulate in the different layers thanks to headers welded on the collecting areas.

In the light of the project, PFHE have to be qualified considering that this heat exchanger technology is not known as the best solution for s-CO₂ Brayton cycles due to the maximum temperature and pressure limitations. PCHE (Printed Circuit Heat Exchanger) is preferred regarding its structural characteristics ([3], [4], [5]): it is manufactured with a succession of printed plates. It can handle very high mechanical constraints at the cost of higher pressure drop and economical cost compared to PFHE. The differences between these two technologies are described in **Figure 2** below.

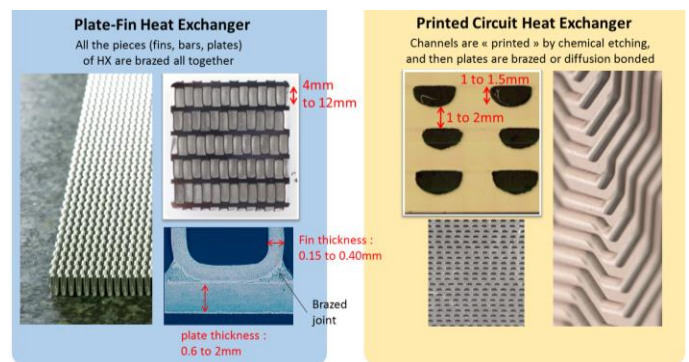


Figure 2: Comparison of two compact heat exchangers: PFHE versus PCHE

Forming process of the fins

In order to understand the mechanical design of a PFHE, it is important to clarify how Fives Cryo proceeds to form the fins:

We manufacture our own fin dies, according to defined fin geometry, and we install them on a hydraulic fin press machines. Fins are obtained by successive bending of flat sheets.

The continuous challenge is to control the deformation of the material to give the desired shape to the material.

Brazing process

Fins parts are then cleaned in order to remove the grease of the stamping machines or any dirt that could affect the quality of the brazing procedure.

The parting sheets are recovered by a specific amount of Ni based brazing filler metal. The melting point of this filler metal is slightly lower than the stainless steel (the filler metal liquidus is below the solidus of the base metal), which will ensure the stiffness of the assembly when it solidifies.

The different elements constituting the heat exchanger (fins, bars, parting sheets and external plates) are then stacked according to detailed sketches.

After the stacking of all these elements, the assembly is compressed via a specific tool, in order to prevent any movement or displacement of the stacked elements which may compromise the integrity of the exchanger.

The brazing occurs in a vacuum furnace. A confidential specific cycle is applied, and the evolution of the temperature in the matrix is monitored via thermocouples. This step is very important to ensure a homogeneous heating of the assembly.

The manufacturing of such equipments is submitted to the requirements of pressure vessels codes, among them the ASME (American Standards of Mechanical Engineers) code.

Validation of mechanical strength is mandatory to authorize the equipment and to operate the heat exchanger at temperature and pressure imposed by the specifications. This is particularly recommended to perform bursting tests on representative brazed samples (see on **Figure 3**). As the assembly technique should not be the weak point of the structure, the rupture should occur in the fins which are formed from the base material selected.

The bursting tests allows to validate the ability of the fins to resist the actual applied pressure to the heat exchanger, applying a safety factor.

According to the regulation, we need to determine a Maximum Allowable Working Pressure (MAWP) via an approved method by the code.

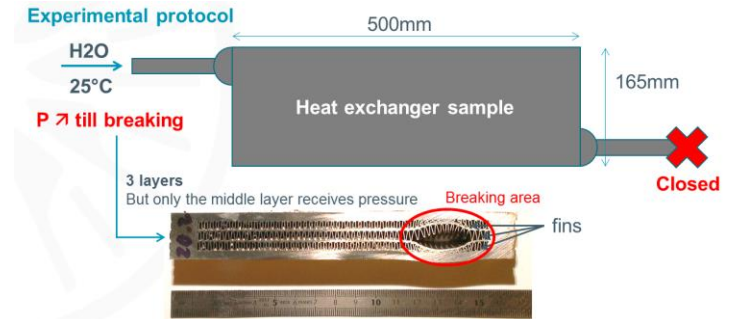


Figure 3: example of a burst brazed sample

The bursting test (**Figure 3**) consists of manufacturing a triple layer prototype of PFHE, which will be tested under pressurized water flowing in the middle layer (the top and bottom layers are dummies). The rupture should happen in the legs of the fins (base material). Otherwise, if it occurs in the brazed joint, the test fails.

The obtained bursting pressure is then converted to a MAWP via formulas given by the applicable pressure vessels code. This MAWP will determine the limit of the design pressure of the equipment at design temperature. A safety factor is then applied: for example, considering the ASME code, the MAWP strongly depends on the operating temperature. In fact, the bursting pressure is converted first into a maximum allowable working pressure at ambient temperature (which is the bursting test temperature), and then, to a maximum allowable working pressure at the operating temperature (which is equal to 500°C for our s-CO₂ cycle), according to the following formulas:

$$MAWP = P \frac{S}{S_2}$$

$$P = \frac{B}{4} \times \frac{S_{\mu}}{S_{\mu avg}}$$

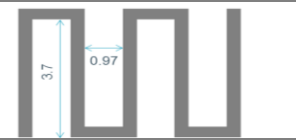
Where P is the maximum allowable working pressure at the design temperature; S the maximum allowable stress value at the design temperature, but not exceed S₂, which is the maximum allowable stress value for the material used in the test at test temperature; B the bursting test pressure, S_μ the specified minimum tensile strength at

room temperature; and $S_{\mu avg}$ the average actual tensile strength of test specimens at room temperature.

One aim of the work undertaken here is to successfully design a PFHE matrix compatible with $s\text{-CO}_2$ Flex cycle conditions and competitive with PCHE.

Two types of heat exchangers are required for the cycle: a low temperature recuperator (LTR) and a high temperature recuperator (HTR). One stream is circulating in these heat exchangers at a high pressure close to 250 bars. The focus of the present study is the development of a HTR, which can be operated at $s\text{-CO}_2$ cycle conditions. A dedicated fin with preliminary characteristics is proposed (see **Table 1** below for geometry description). The geometry was evaluated to conform to design conditions, as material mechanical strength is varying with temperature.

Table 1: Geometrical description of the fins

HT-HP Fin characteristics	
Thickness (mm)	0.3
Height (mm)	4
FPM (Fin Per meter)	787.4
Geometry	

A 316 stainless steel grade is used to manufacture brazed samples and fins in particular. This material has normalized mechanical characteristics.

According to the ASME code, a value of approximately 1500 bar would be necessary to achieve at the bursting tests for qualifying this assembly for a use at 500°C at 250 bar.

First tests results indicated that a bursting pressure of 800 bar were reached. This value is low compared to the required one. Furthermore, the rupture occurred in the brazed joint (**Figure 4**) and not in the fins legs, this does not validate the test.

Intrinsically, this structure should resist at a higher level of mechanical stress. The analysis of the location of the rupture (**Figure 4**) revealed that the brazed zone is composed of a brittle phase and a ductile one. The ductile phase is located on the top of the fins only, which is not sufficient to preserve the mechanical properties of the

entire brazed joint. The microstructure in this area has to contain as little fragile phase as possible, in order not to be mechanically limiting.

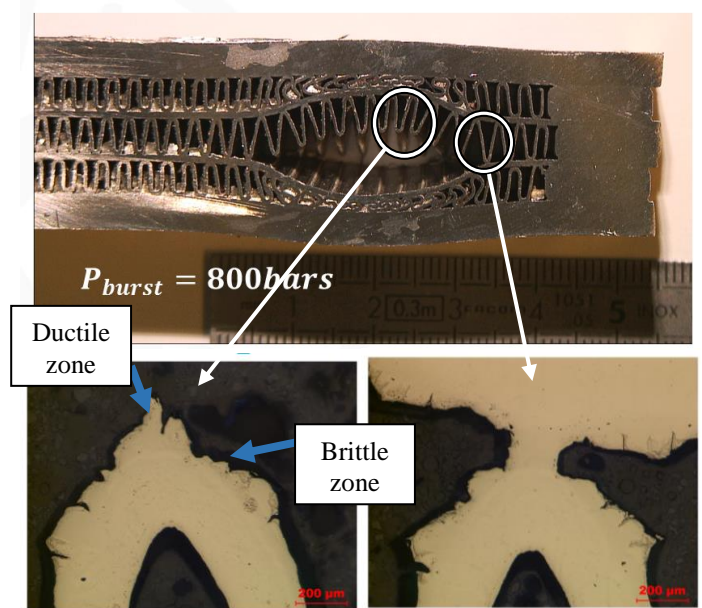


Figure 3: Fins rupture area, showing the presence of a ductile zone and a fragile brittle zone in the filler metal.

A metallurgical study was carried out to better understand what the root cause of this weakness is. It revealed that the origin of the premature rupture is the formation of a eutectic brittle phase (**Figure 5**), which influences highly the mechanical resistance of the assembly.

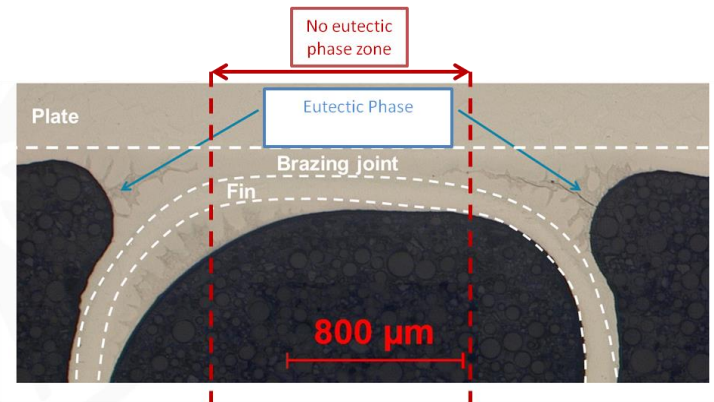


Figure 4: Micrograph images of the brazed region between fins and the plate, showing the presence of a eutectic phase on the edge of the brazed joint

In order to reduce the area of the eutectic phase and increase the mechanical properties of the brazed joint, it is possible to consider the following options:

- To optimize the fins' geometry by forming a flat top and get a square overall shape and thus limiting the amount of brazing in this critical area (**Figure 6**),
- To improve the brazing cycle to lead to a homogenization of the microstructure.

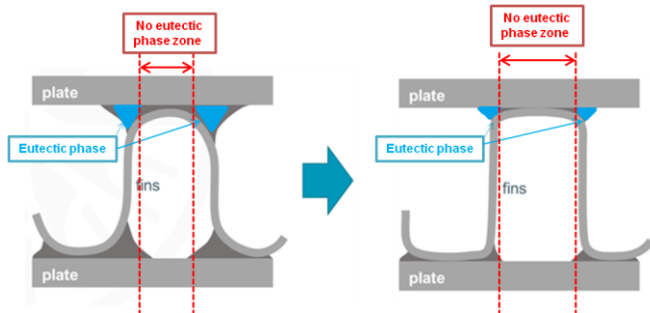


Figure 5: Schematic representation of the geometric enhancement of the fins with circular and square shape

Optimization of the fins geometry

Fins are obtained from flat sheets by successive bending thanks to fin stamping presses used in conjunction with fin dies. These tools are designed for deformation and this deformation application gives the desired shape to the material.

In order to reduce the amount of the brittle phase in the brazed joint, the geometry of our stamping machine tools was adapted, to flatten as much as possible the top of the fins (**Figure 7**). A proprietary system was developed to do so.

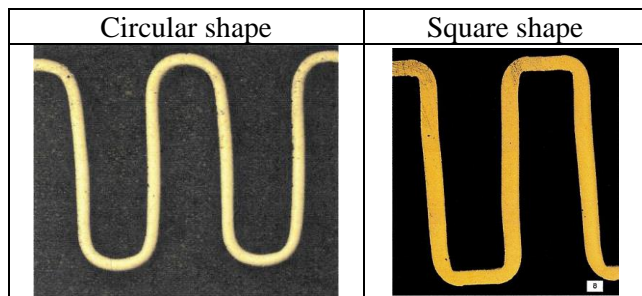


Figure 6: Micrograph images of the fins before and after the shape modification

The bursting tests realized on brazed samples assembled with these new fins showed an important increase in the

mechanical strength of the brazed structure. Indeed the bursting pressure reached was 1200 bars, and the rupture occurred in the base metal that time (**Figure 8**).

Analyzing intimately the rupture, it can be observed that it started at the fins radius. This area is clearly thinned by 15% compared to the initial thickness of the strip coil due to the forming process.

The challenge is to counter this thickness reduction, which will lead to a higher mechanical strength, by working on the shape of the stamping machine tool. Another way is to change the base metal with a material having higher mechanical properties. For the last option, it is mandatory to find a compromise between the material strength and its stamping ability to form suitable fins.



Figure 7: View of the rupture location of a brazed sample composed of "square"-shaped fins

Understanding of the solidification kinetics during the brazing cycle

A study is carried out focusing on transient liquid phase bonding (TLP) joining the austenitic stainless steel base metal using a nickel based brazing alloy.

The aim is to characterize the filler alloy and the joints bonded by TLP, in order to better understand the solidification path and improve the brazing cycle and assembly quality.

The process of TLP bonding consists on inserting a layer composed of a melting point depressant alloying element between the base metal layers. The melting of this interlayer at the brazing temperature results of joining the structure.

An isothermal holding time at this temperature permits the melting depressant element to diffuse into the base

metal, which will modify the liquidus [6] and results in isothermal solidification (**Figure 9**).

For some cases, the isothermal solidification is incomplete: some of the liquid phase remains, solidifies while cooling, which leads to the formation of a eutectic brittle phases in the joints.

Long isothermal holding can prevent the appearance of these brittle phases, but has also a negative impact on the corrosion resistance of the base material due to sensitization by chromium depletion. In fact, in austenitic stainless steels, chromium carbide precipitates at grain boundaries: this phenomenon is called intergranular corrosion [7].

Long isothermal holding is also not economical from an industrial point of view and very time consuming.

All these points bring the high issues to determine the minimum time required to complete the isothermal solidification.

316 stainless steel specimens were prepared from 4 mm thick plate. The mating surfaces of the plates were mechanically ground to remove surface oxide layer, and the filler metal was applied. The plates were put in contact, and compressed with a stainless steel tool. TLP bonding was operated in a primary vacuum furnace at 1180°C, and then quenched in water. The thermal cycle details and the measurements techniques are explained in [8].

The phases formed in the filler metal after brazing, at the equilibrium were identified via measures of chemical compositions using EDX (energy dispersive X-ray spectrometry). The results details of these measurements will not be disclosed in this paper, due to some confidentiality issues. The identified phases are an austenitic solid solution and two silicides (which will be designated as phase A and phase B on **Figure 10**).

This permits to identify diffusion controlled aspects of the isothermal solidification. An investigation is in progress to determine an empirical formula. The aim is to estimate the necessary time for the completion of the isothermal solidification, based on the diffusion parameters. This will help to define a convenient brazing cycle leading to keep fair properties of the material regarding corrosion issues as explained before.

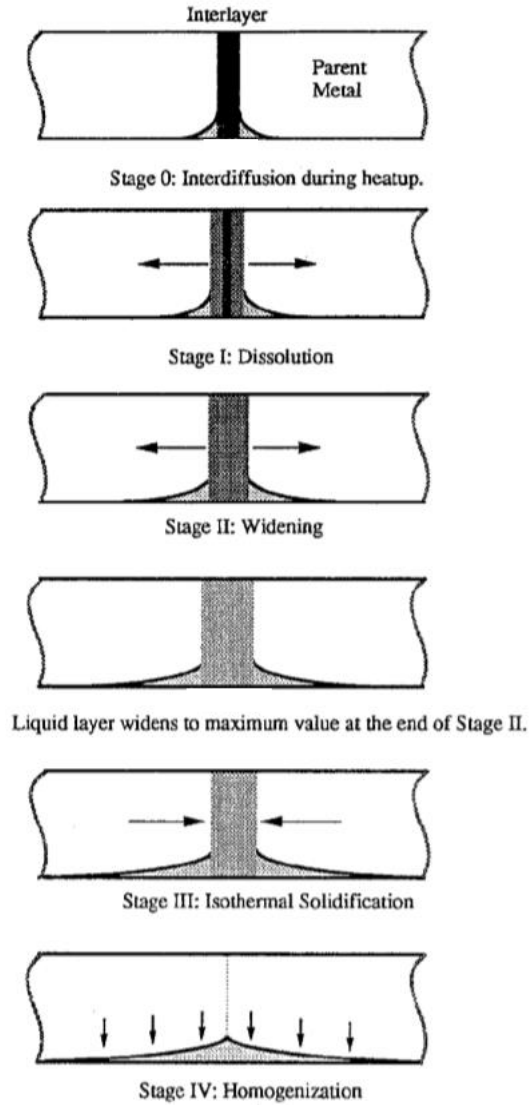


Figure 8: Stages of TLP bonding. The concentration of the melting point depressant is evidenced by the grey shading and the movement of the solid-liquid interface by the arrows [6]

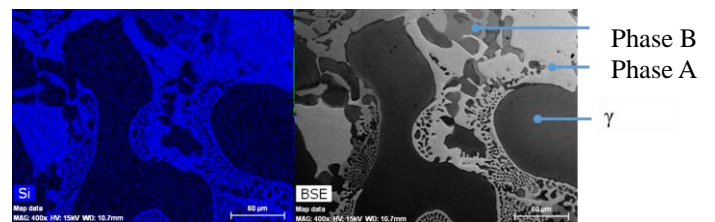


Figure 10: Si EDX and BSE (Back-scatter detector) maps of a solidified microstructure of the filler metal

CONCLUSION

The s-CO₂ flex project aim is to develop and validate a Brayton cycle using supercritical CO₂ which will help to adapt fossil fuel power plants to integrate renewable energy sources.

Because of the nature of this working fluid, severe operating conditions are possible. In particular heat exchangers are confronted to a high level of temperature and pressure.

Usually, PCHE technology is the prior choice for this application thanks to its mechanical integrity and its thermal and hydraulic performances, but PFHE developed at Fives Cryo could be a better candidate for s-CO₂ Brayton cycle applications with its high degree of compactness at a moderate cost, if its mechanical and corrosion resistance are improved to bring internal structure at an opportune level.

To that end, a specific development is performed: in the frame of s-CO₂ flex project, Fives Cryo develops the manufacturing of both recuperators of the cycle (LTR & HTR), which are stainless steel heat exchangers, centering on following topics:

- selection of a material with high mechanical properties resistant to corrosion against impure supercritical CO₂ and validation by means of corrosion tests under real cycle conditions,
- extension of the mechanical strength of the PFHE structure to meet the process requirements, by developing new “square”-shaped fins. This modified geometry reduces the brittle phase presence in the brazed joint hence enhancing the solidity of the assembly,
- understanding of the solidification kinetics during the brazing cycle and determining of the most appropriate cycle parameters to get brazed joints as free as possible from brittle phases, while preserving the mechanical strength and the corrosion resistance of the base metal.

Currently, much progress has been made on the second and last topics. There is a fair confidence to succeed qualifying PFHE technology to be part of future s-CO₂ Brayton cycles in power plants.

ACKNOWLEDGEMENTS

The authors would like to thank the European Union’s Horizon 2020 research and innovation program for financial support to conduct this research.

REFERENCES

- [1] M. E. Siddiqui and K.H. Almitani. (2018). Energy Analysis of the S-CO₂ Brayton Cycle with Improved Heat Regeneration. Saudi Arabia, Jeddah.
- [2] K. R. Zada, R. Kim, A. Wildberger and C. P. Schalansky. (2018). Analysis of Supercritical CO₂ Brayton Cycle Recuperative Heat Exchanger Size and Capital Cost with Variation of Layout Design. USA, Pennsylvania, Pittsburgh.
- [3] D. Ranjan, B. Robinson and M. Carlson. Fundamental Study of Key Issues Related to Advanced S-CO₂ Brayton Cycle: Prototypic HX Development and Cavitation. NEUP U.S. Department of Energy. USA.
- [4] D. Shiferaw, J. Montero Carrero, R. Le Pierres. (2016). Economic Analysis of SCO₂ Cycles with PCHE Recuperator Design Optimisation. USA, Texas, San Antonio.
- [5] I. Jentz, M. Anderson and X. Sun. (2015). Modeling the Mechanical Integrity of Airfoil Printed Circuit Heat Exchangers. USA. Chicago
- [6] W. D. MacDonald and T. W. Eagar. (1992). Transient Liquid Phase Bonding. USA, Massachusetts.
- [7] S. Tokita, T. Yokoyama, H. Kokawa, Y.S. Sato and H.T. Fujii. (2013). Friction Stir Welding of Grain Boundary Engineered 304 Austenitic Stainless Steel. Japan, Osaka.
- [8] S. Guernaoui, B. Rouat, J. Zollinger and H. Combeau. (2019). Proceedings of 12th International Conference on Brazing, High Temperature Brazing and Diffusion Bonding. Germany, Aachen

**PRACTICAL CHALLENGES AND FAILURE MODES DURING FABRICATION OF
HAYNES 230 MICRO-PIN SOLAR RECEIVERS FOR HIGH TEMPERATURE
SUPERCRITICAL CARBON DIOXIDE OPERATION**

Patrick S. McNeff
Oregon State University
Corvallis, OR, USA

Brian K. Paul
Oregon State University
Corvallis, OR, USA

Ömer N. Doğan
National Energy
Technology Laboratory
Albany, OR, USA

Kyle A. Rozman
Leidos Research Support Team
Pittsburgh, PA, USA

Sean Kissick
Oregon State University
Corvallis, OR, USA

Hailei Wang
Utah State University
Logan, UT, USA

M. Kevin Drost
Oregon State University
Corvallis, OR, USA

Brian M. Fronk*
Oregon State University
Corvallis, OR, USA

Brian.Fronk@oregonstate.edu

ABSTRACT

Printed circuit heat exchangers (PCHX) fabricated from high nickel alloys have shown promise as primary heat exchangers, recuperators, and solar receivers for high temperature and pressure supercritical carbon dioxide power cycles. There are numerous challenges in fabricating these devices including forming channel features, joining via diffusion or transient liquid phase bonding, and brazing/welding of headers. Commercial entities are understandably hesitant to share proprietary best practices, and both commercial and non-commercial entities working on these components tend not to publically share failures and mistakes. However, sharing of this information could prevent similar costly errors and further the understanding of the coupled manufacturing, materials and mechanics issues in creating these components.

Thus, in this paper, we document the challenges, failures, and mitigation methods uncovered in fabrication of prototype micro-pin based solar thermal receivers constructed of Haynes 230 and fabricated through a combination of photochemical machining (PCM), wire electrical discharge machining (EDM), transient liquid phase (TLP) bonding, vacuum brazing, and gas tungsten arc welding (GTAW). The receiver is designed to absorb concentrated solar fluxes greater than 140 W cm⁻², while heating supercritical carbon dioxide from 550 °C to 720 °C at a pressure of 20 MPa to 25 MPa. The prototype receiver consists of a thin (~450 μm), Haynes 230 coversheet bonded to a 15 cm × 15 cm Haynes 230 micro-pin plate. The pieces are joined using a TLP bonding process with a nickel-phosphorus interlayer. Prior to bonding, micro-pins with height ~150 μm and diameter 300 μm are fabricated using PCM in the plate, and through slot features are made using wire EDM. Finally, flow headers are joined to the microchannel plate through a combination of vacuum brazing and GTAW.

During hydrostatic proof testing, the prototype device failed when the coversheet delaminated from the pin array at a pressure of 290 bar. A failure analysis including scanning electron microscopy (SEM) to view failure sites and energy-dispersive X-ray spectroscopy (EDS) to evaluate elemental analysis of the failed areas was conducted. The failure modes can be broadly categorized as (1) failures potentially relating to reliquification of the transient liquid phase bonds between the micro-pins plate and coversheet during post-processing, (2) failures related to manufacturing defects, and (3) failures attributed to design.

INTRODUCTION

The United State Department of Energy (DOE) has identified supercritical carbon dioxide (sCO₂) Brayton cycles with turbine inlet temperatures >720 °C as the most promising power cycle for next generation concentrated solar thermal power (CSP) systems [1]. In these systems, a field of two-axis tracking heliostats concentrate solar radiation on to a receiver located atop a central tower. The concentrated thermal energy is then transferred to the sCO₂ power system or to thermal storage through a circulating gas, liquid molten salt, or through solid particles [1].

In ongoing work by the authors, we are developing a solar receiver technology that uses concentrated solar flux greater than 140 W cm⁻² to heat sCO₂ from an inlet temperature of 550 °C to an outlet of 720 °C at an operating pressure of > 20 MPa. The receiver must have an efficiency greater than 90%, meaning that for every 1 MW of concentrated solar flux incident on the surface, 900 kW of energy is transferred into the sCO₂. This efficiency is inclusive of optical reflection losses, reradiation losses, and convective losses from the receiver surface. Gas based solar receivers (air, helium, etc.) are typically constructed of multiple tubes in parallel/circuited flow arrangement to

* corresponding author(s)

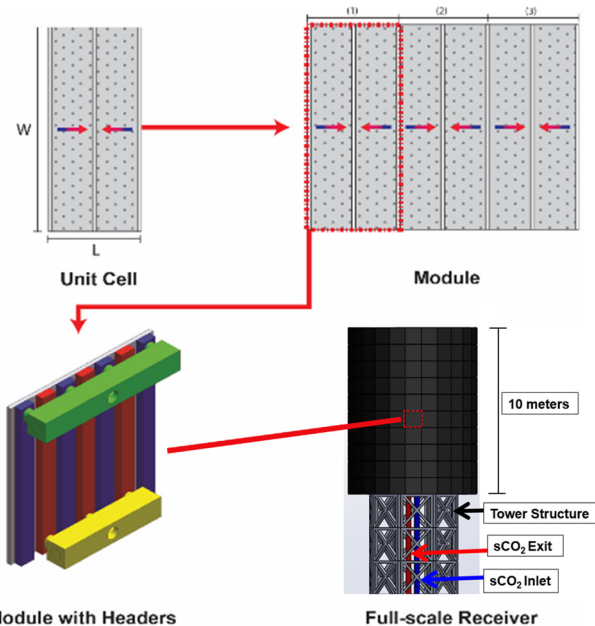


Figure 1: Conceptual schematic of numbering-up concept.

minimize pressure drops. However, the gas-side convective heat transfer coefficient is relatively low, resulting in high receiver surface temperature and unacceptable thermal losses [2]–[4]. Furthermore, using high pressure $s\text{CO}_2$ in a tubular receiver would require thick walled tubes, further increasing thermal resistance and surface temperature.

Thus, we have pursued a micro-pin ($D_H \sim 300 \mu\text{m}$) concept to meet the challenges of high temperature/pressure operation and the need for extremely high gas-side convective heat transfer coefficients. Micro-pins were chosen over microchannels as they are more resistance to plugging and provide better flow distribution. A blocked microchannel could result in local overheating and failure of the device.

This technology allows incident fluxes greater than 140 W cm^{-2} with efficiency $> 90\%$, and the use of very thin walls to contain the pressures. Figure 1 shows a conceptual schematic of how micro-pin based receivers could be numbered-up to multi-MW central receivers. Here, multiple-parallel unit-cells are fabricated into modules ($\sim 1 \text{ m} \times 1 \text{ m}$), which are then arranged into a central receiver and plumbed in parallel. Supercritical CO_2 from the main receiver riser is split into each module, and then further subdivided into each unit-cell where it is heated, recombined in the outlet headers and sent back to the power cycle/thermal storage. This approach minimizes parasitic pressure drop of the $s\text{CO}_2$ [5], enables the possibility of zoned flow control within the receiver to maximize annualized performance [6], and allows for the realization of economies of scale in the manufacturing of the individual modules.

The goal of our ongoing work is to demonstrate the ability to fabricate and test a scaled prototype ($15 \text{ cm} \times 15 \text{ cm}$, approximately 15 kW of thermal input) in a concentrated solar

dish. The prototype consists of multiple unit-cells and is designed to heat $s\text{CO}_2$ to temperatures of $720 \text{ }^\circ\text{C}$ using concentrated solar flux. Materials, mechanical, and thermal computational and experimental studies [5], [7]–[11] were used to specify designs and fabrication techniques that would meet the performance targets and survive the extreme conditions. This paper describes the challenges, failure modes, and opportunities for improvements from the initial attempt to synthesize these separate effects investigations into the design and fabrication of a prototype unit.

RECEIVER MATERIAL AND DESIGN

To survive the extreme operating conditions, only nickel-based solid-solution-strengthened and precipitation-strengthened superalloys were considered. After considering (a) the availability of material in the required form factor (sheet, plate, and bar), (b) the corrosion resistance with $s\text{CO}_2$ at temperature and pressure, (c) the ease of fabricating micro features, and (d) our experience with diffusion and transient-liquid phase bonding of the materials, we selected Haynes 230, a solid-solution-strengthened alloy. First, although Haynes 230 is primarily a solid-solution-strengthened alloy, it contains high volume fraction of M_6C phase, which is instrumental in stabilizing matrix grain size at high bonding temperatures. Haynes 230 is known as one of the most grain-growth-resistant materials in the solid-solution-strengthened superalloys family. Second, Haynes 230 is one of the most corrosion-resistant alloys at high temperatures. Third, we had prior bonding experience with this alloy. Finally, we were able to demonstrate excellent channel depth tolerances using sinker electrical discharge machining (EDM) ($\pm 0.7\%$) and photochemical machining (PCM) ($\pm 3.9\%$) using Haynes 230, as well as identify vendors that could scale these processes to a $1 \text{ m} \times 1 \text{ m}$ scale.

With this material as the basis, a conceptual rendering of a single unit-cell within the prototype is shown in Figure 2. Each unit-cell consists of a thin, flat, coversheet coated with a high absorptivity material (Figure 2a). The inside of the unit-cell consists of a flow passage containing a staggered array of micro-pins (detailed schematic shown in Figure 3). The flow length of a unit-cell is determined by the maximum allowable pressure drop within the device. As shown in Figure 2b, each unit-cell consists of two inlet headers (from the left and right), and a central outlet header. Supercritical CO_2 enters from both sides, is

Table 1: Dimensions of unit-cell and pin array.

Variable Name	Dimension	Value
t	Coversheet thickness	$450 \mu\text{m}$
L	Unit-cell base length	5 cm
W	Unit-cell base width	15 cm
D_{pin}	Pin diameter	$300 \mu\text{m}$
h_{pin}	Pin height	$150 \mu\text{m}$
S_L	Longitudinal pitch	$520 \mu\text{m}$
S_T	Transverse pitch	$600 \mu\text{m}$
S_D	Diagonal pitch	$600 \mu\text{m}$

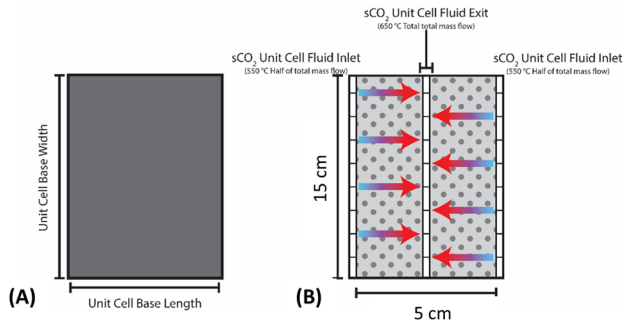


Figure 2: Schematic of unit-cell with representative dimensions (a) with bonded coversheet on and (b) coversheet removed showing internal pins and sCO₂ flow paths.

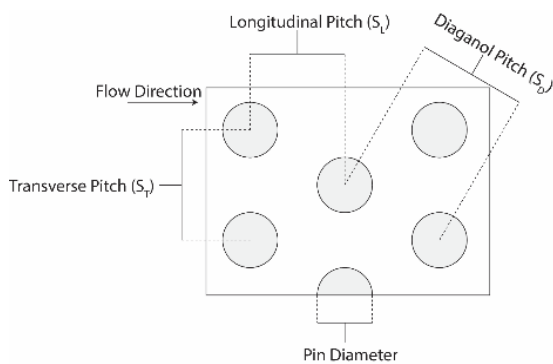


Figure 3: Detailed schematic of micro-pin array.

heated to the desired outlet temperature, and leaves through the middle. The dimensions for the unit-cell and staggered pin-array in the prototype device are provided in Table 1.

The prototype module consists of three unit-cells in parallel (Figure 4). Figure 4a shows a top view of the three-unit-cell prototype with the coversheet removed. Figure 4b shows the backside of this pin array with flow distribution headers and Figure 4c-d shows the cross section of the unit-cell and module headers with important dimensions. Flow enters through the module inlet header (in green) from the main receiver riser. The sCO₂ is distributed to the four unit-cell inlet headers (in blue), and then exits each unit-cell through the three unit-cell outlet headers (in red). Finally, flow from each unit-cell outlet header is collected in a module outlet header (in yellow), and returned to the main receiver downcomer. The dimensions for the prototype unit headers are shown in Table 2.

Table 2: Dimensions of unit-cell and module headers.

Header	W (mm)	L (mm)	D (mm)	t (mm)
(A) Unit-cell header	8.125	16.25	6.25	5
(B) Module header	22.7	22.7	12.7	5

Finally, penetrations were made through the micro-pin plate to allow sCO₂ to flow between the micro-pin array and the unit-cell inlet/outlet headers, shown conceptually in Figure 5. The

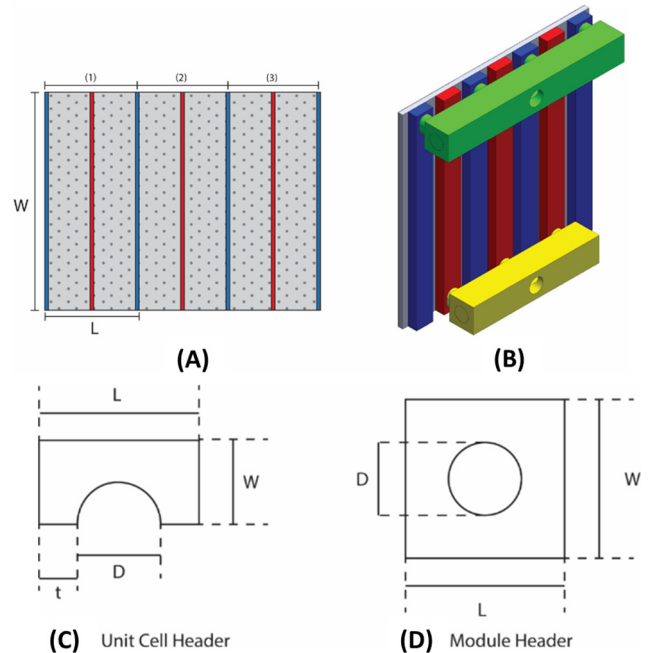


Figure 4: Schematic of three unit-cell prototype (a) with coversheet removed (b) unit cell and module headers shown and (c-d) header cross section with dimensions.

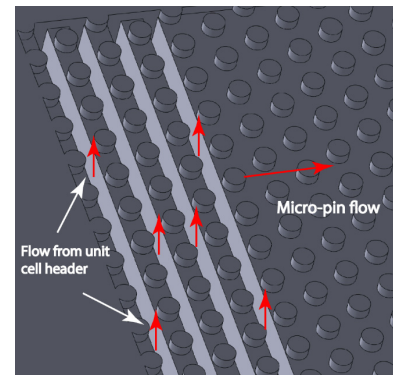


Figure 5: Rendering of the inlet/outlet slits for transition of flow from unit-cell headers to micro-pin array.

width of these slits was 0.20 mm, and the length was 10 mm. They were staggered from the top of the unit-cell to the bottom to enable flow to be well distributed.

RECEIVER FABRICATION APPROACH

A process flow diagram for the fabrication of the prototype receiver is shown in Figure 6. Raw material inputs are shown in green. First, a hot-rolled plate of Haynes 230 with a thickness of 6.35 mm was cut to size (~ 15 cm × 15 cm) and then the micro-pin array design was etched using a vendor proprietary photochemical etch process (Step 1 in Figure 6). An example of etched pin-array is shown in Figure 7. Then, the plate was sent to a second vendor for a wire EDM of the 0.2 wide mm slits (Step 2). A graphite punch was used to create a through hole to thread

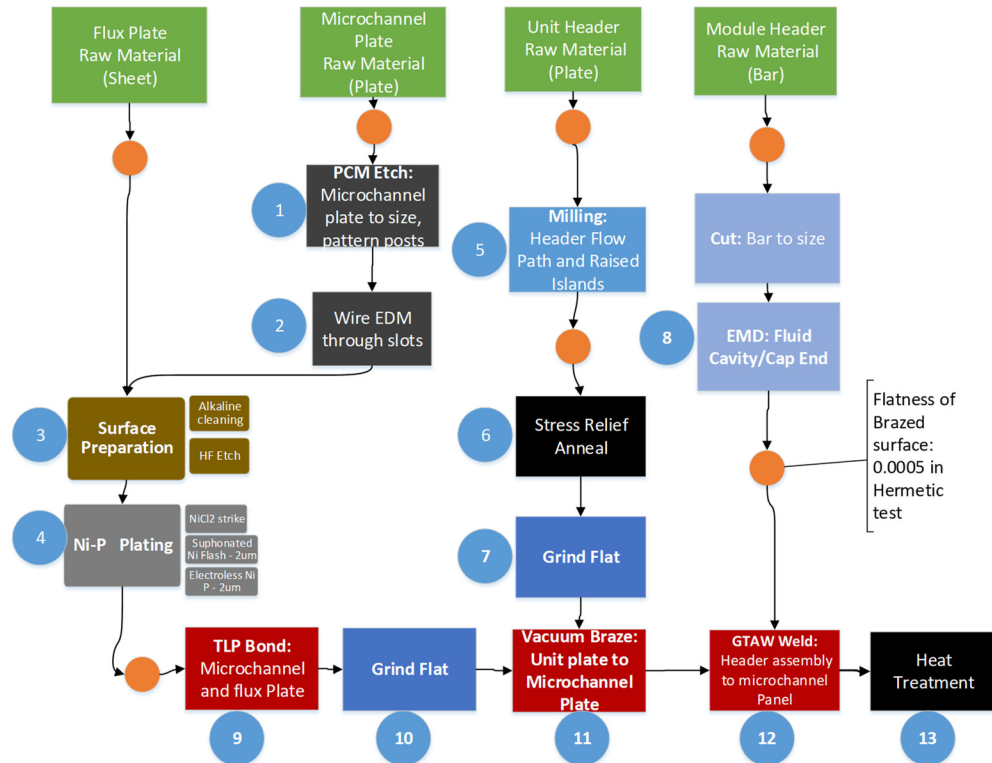


Figure 6: Process flow diagram for fabrication of prototype receiver.

the cutting wire. Each staggered slit required a new through hole to be made.

Then, a 450 μm thick sheet of cold-rolled Haynes 230 was cut to size for the receiver coversheet. The micro-pin plate and cover sheet bonding surfaces were prepared with an alkaline cleaning and hydrofluoric acid etch (3). The treated surfaces were then joined using a transient liquid phase bonding process (9). Here, the parts are subjected to a high temperature and pressure. The faying surfaces are plated with a material that contains a melting point depressant (in this case, phosphorous), causing the joint to liquefy at high temperature. Then, the melting point depressant diffuses into the base metal, resulting in an isothermal solidification of the joint. Initially, a NiCl strike was applied to help increase adhesion. Then, a 2 μm sulfonated layer of pure nickel was electrically deposited, followed by a 2 μm electroless mid-phosphorus layer (~6% P). This resulted in a phosphorous content of approximately 3% in the interlayer. The bonding temperature was 1150 $^{\circ}\text{C}$ at a vacuum pressure less than 1×10^{-5} torr for a dwell time of 4 hours. Once bonding was complete, the combined part was ground flat on the faying surface for the unit-cell headers.

In parallel, the unit-cell header plate was milled out of hot-rolled Haynes 230 plate to achieve the dimensions shown in Table 2, previously. Rather than individual parts as shown conceptually in Figure 4, a single plate was used that contained all the unit-cell headers with inlet/outlet ports (Figure 8). After machining, the part was stress relief annealed at 1200 $^{\circ}\text{C}$ for 1 hour (3 $^{\circ}\text{C}$ per minute ramp up/down), and ground flat. The unit-

cell header plate was then joined to the micro-pin plate via a vacuum brazing process (Table 3) using a 50 μm nickel based brazing foil containing boron as a melting point depressant (MBF-51 in [12]).

Finally, the module headers were machined from Haynes 230 bar and joined to the unit-cell header plate via a gas tungsten arc welding (GTAW) process. GTAW was also used to repair an external leak from the TLP process, and to join a set of Haynes 230 tubes for pressure testing. The entire part was shown to be hermetic to a shop air test of approximately 0.76 MPa. A photograph of the complete prototype receiver is shown in Figure 8.

Table 3: Vacuum brazing parameters.

Step	Description	Purpose
1	Ramp to 950 $^{\circ}\text{C}$ @ 5 $^{\circ}\text{C}$ per minute	
2	1 st Hold: 950 $^{\circ}\text{C}$ for 1.5 hours	Ensure part evenly heated
3	2 nd Hold: 1195 $^{\circ}\text{C}$ for 2.5 hours	Liquefy braze and diffuse away boron and silicon
4	Cool to 1100 $^{\circ}\text{C}$ (2 $^{\circ}\text{C}$ per min) in 1.5 mbar Argon	Solidify braze for diffusion hold
5	3 rd Hold: 1100 $^{\circ}\text{C}$ for 3.5 hours	Diffuse away any residual boron or silicon

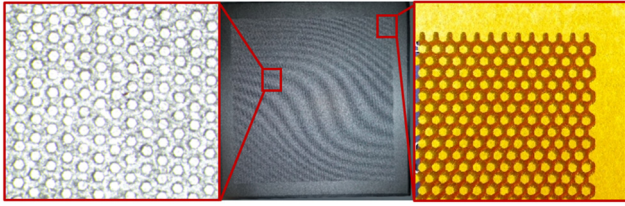


Figure 7: Example of etched pins.



Figure 8: Complete receiver prototype.

PROOF TESTING AND FAILURE ANALYSIS

Prior to installing the prototype on-sun, a room temperature proof test was conducted using the standards outlined in ASME Section VIII Div. 1 Hydrostatic Pressure Testing - Article UG-99(b). The hydrostatic test pressure was determined from Equation 1.

$$P = 1.3 \cdot MAWP \cdot \frac{\sigma_T}{\sigma_D} \quad (1)$$

where $MAWP$, σ_T , and σ_D are the maximum allowable working pressure/design pressure (20 MPa), the allowable stress at test temperature (20 °C), and the ASME maximum allowable stress at design temperature (720 °C). For Haynes 230 at these temperatures, the values of σ_T and σ_D were determined to be 207 MPa and 65 MPa, respectively [13]. This resulted in a room temperature required proof pressure testing of 82.8 MPa. The testing procedure is based on the ASME guidelines, summarized in Figure 9.

After confirming the unit showed no external leakage with air at 0.76 MPa, the unit was connected to a manual hydraulic pump and filled with hydraulic oil. The first step in the test required pressure to reach 33 MPa. The unit was ramped up to 33 MPa by first increasing pressure to 10 MPa, holding a minute, increasing pressure to 20 MPa, waiting a minute, and then increasing pressure to 33 MPa. During the last ramp to 33 MPa,

the unit failed at approximately 29 MPa. Failure occurred when the coversheet produced a bulge due to separation from the micro-pins (Figure 10). No external leakage occurred during the failure event.

The bulged area shown in Figure 10 was removed via laser cutting (Figure 11a), cleaned in an ultrasonic acetone bath, and sectioned using wire EDM (Figure 11b). We then conducted detailed scanning electron microscopy (SEM) to view failure sites and energy-dispersive X-ray spectroscopy (EDS) to evaluate elemental analysis of the failed areas. Analysis was conducted of the top coversheet, and the micro-pin plate in the failed region. This analysis revealed several potential failure modes that can be broadly categorized as (1) failures potentially relating to the transient liquid phase bonds between the micro-pins and 0.45 mm coversheet during post-processing, (2) failures related to manufacturing defects, (3) failures attributed to design. Each are described below, followed by some suggestions for mitigation of the failures that may be of use to the sCO₂ community fabricating high temperature/pressure heat exchangers based on printed circuit type architectures.

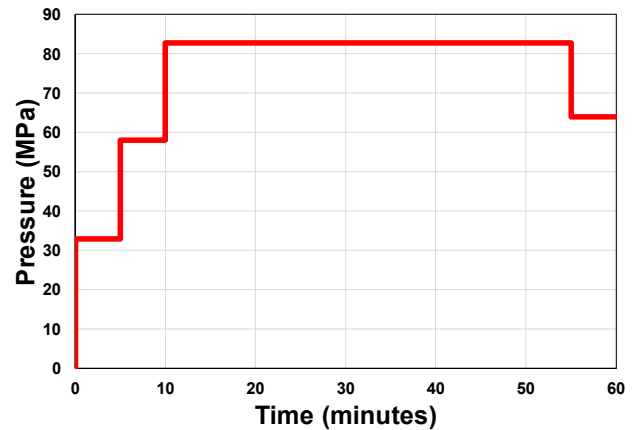


Figure 9: Proof pressure testing operating specifications.



Figure 10: Photograph of coversheet bulge failure.

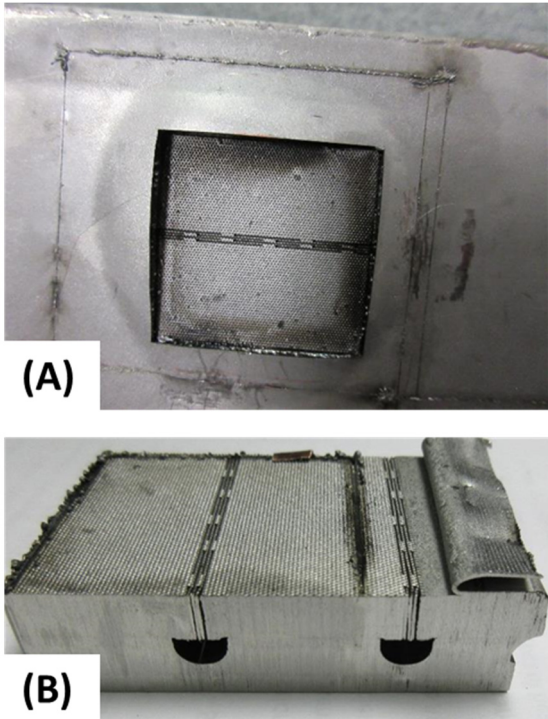


Figure 11: (a) Top view of coversheet showing bulge section removed and (b) side view of section micro-pin plate.

Failures Related to TLP Bond

In general, the SEM analysis showed that the fracture took place in the bond region in a ductile manner. Notably, the failure appears to be centered over the series of slits in the micro-pin array which function as fluid inlet/outlets (Figure 11a). Within the failed region, some pins were not adhered, or were poorly adhered to the top plate (Figure 12a-b). These “missing” bonded pins were sporadically located, and likely not the sole cause of failure. In regions where pins were partially adhered, aluminum oxide particles were found using EDS, causing a local brittle failure (Figure 12c). For pins that were well adhered, Al-oxide was found in the periphery of the bond, causing local brittle failure, despite a general ductile failure in the center (Figure 13). In both the well and poorly adhered pins, voids within the bonding region were detected (Figure 14). Finally, the profiles of both the adhered and poorly adhered pins show “liquid-like” wavy solidification features (see Figure 14) that are inconsistent with the original smooth photochemical etching process.

All of these findings support a hypothesis that failure was at least in part due to the TLP bond re-liquefying during the high temperature vacuum brazing and post-processing (heat treatment process). In this prototype, phosphorous was used as the melting point depressant based on prior work at Oregon State University. Phosphorous is much slower to diffuse than the more industry standard boron used in many TLP process. If all of the phosphorous did not diffuse out during the bonding process, then

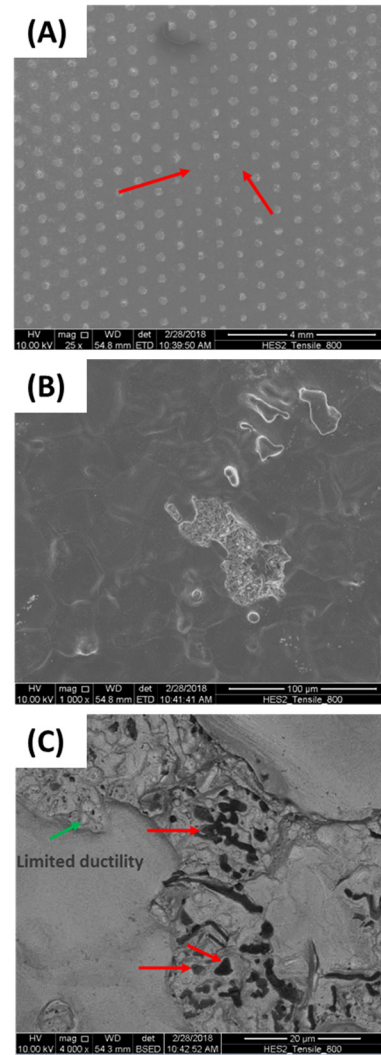


Figure 12: SEM of bottom side of coversheet showing (a) regions where not all pins were adhered (b) close up of “missing” pin area showing limited bonding and (c) backscatter image of “missing” pin area showing dark Al-oxide regions (red arrows) and areas of limited ductility (green arrow).

during the brazing or heat treatment process, the coversheet may lift off the pins or slide (article was not horizontal), causing the observed sporadic attachment and voids/inclusions. Furthermore, a liquefied bond would be much more susceptible to oxygen diffusion, resulting in the formation of Al-oxide within the bonding area of poorly adhered pins, and at the periphery of the well bonded

Failure Related to Manufacturing Defects

The fluid inlet/outlet slits are machined in the micro-pin plate using a wire-EDM process, as discussed above. The through hole for insertion of the wire is made with a graphite-based tool. SEM images of the pins near the slits show that some

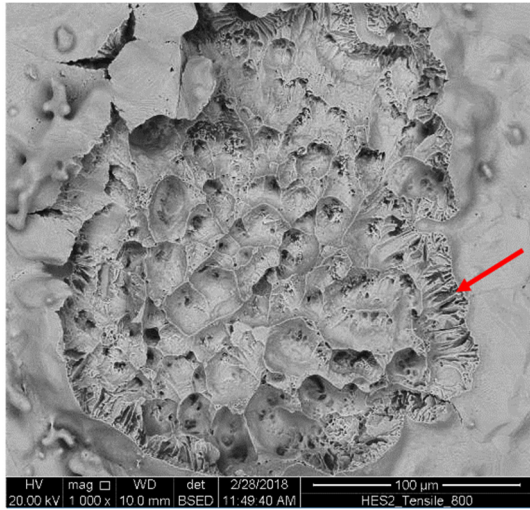


Figure 13: SEM of bottom side of coversheet showing failure of a well adhered pin with Al-oxide (dark spots) in bond periphery and local brittle failure.

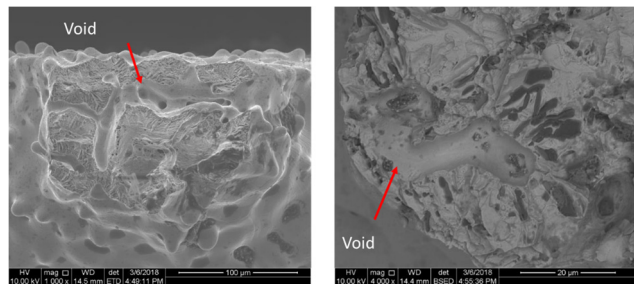


Figure 14: Observed voids in bond region of (left) poorly adhered pin and (right) well adhered pin.

pins are cut due to misregistration of the wire, reducing the cross section and bonding area (Figure 15). Furthermore, carbon contamination near the slits was observed (dark color in Figure 15b), attributed to the graphite hole punching tool. The carbon contamination was not removed by the cleaning process prior to electroplating and TLP bonding process, potentially altering the TLP bonding process. The probability of the contribution of both of these factors to the failure is increased due to the apparent initiation of failure in the region of the fluid inlet/outlet slits, shown in Figure 11a.

During the failure analysis there was some concern that the micro-pin array may have been over etched during the PCM process, yielding smaller than expected pins. This concern was due to the small pin cross sectional area observed in the failed regions as shown in Figure 15a. However, we analyzed the pin geometries in a region without failure by machining away the thin coversheet to reveal the pins, shown in Figure 16a. Here, the pin spacing and diameter are as expected (Table 1). Thus, the observed decreased area in the failed region is believed to be from necking of the pins during failure.

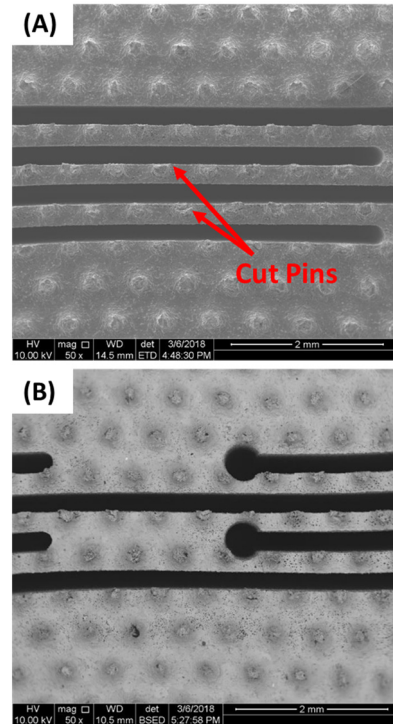


Figure 15: Image showing (a) cut pins and (b) potential carbon contamination (dark spots) in vicinity of wire EDM slit.

Failures Related to Design

We identified the inability of the design to accommodate manufacturing defects related to the TLP bonding and wire EDM processes as a key failure mode. The use of micro-pins versus continuous microchannels allows the device to be resilient to plugging. In a solar application, if even a single channel were plugged, a hot spot could develop leading to failure. To specify the geometry of the pin array design, the primary constraints were mechanical, manufacturing, and hydraulic.

The target lifetime of the solar receiver is >10,000 cycles. The type of failure observed in the proof test (i.e., coversheet delimiting from micro-pin array) was identified as the most critical potential failure mode to address. To develop a design to avoid this, elasto-plastic properties of TLP joined samples of Haynes 230 with patterned features similar to those of the prototype were obtained at room temperature and operational temperature of 760 °C. The data were then used to calibrate a FEA model of the joint, where the yield strength of the bond layer was iteratively changed and resulting force-displacement simulations compared to the data [9]. It was found that the joint materials' elastoplastic behavior was similar to that of the base material. Using these elastoplastic properties, FEA was performed for a range of micro-pin geometries (spacing and diameter) to detect the onset of plastic failure at 25 MPa and material properties at operation temperature (from [13]). The FEA model used to examine the deformation of the micro-pin included a bottom plate, pins, and a top plate, as well as a bonded region between the top plate and the pins. A pressure of 25 MPa

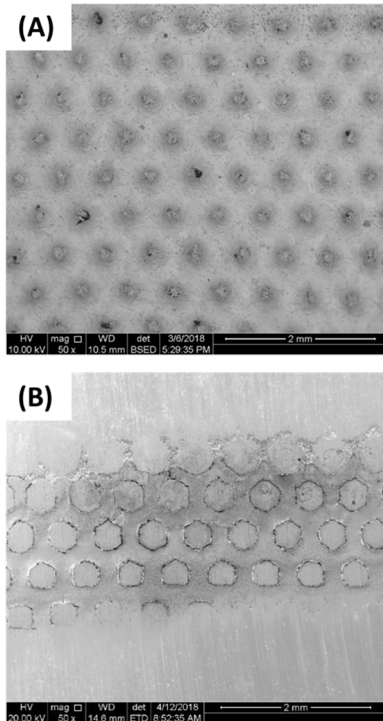


Figure 16: Image showing top view (a) of failed pin array with decreased pin diameter and (b) pin diameter in region without failure.

was applied to all interior surfaces. Potential designs were then limited to geometric combinations that would remain elastic. The avoidance of plastic failure would also prevent failure of the joint via low-cycle fatigue, i.e., > 10,000 cycle life.

When fabricating the pins with PCM, the pin-to-pin span/height ratio was approximately 2. This, combined with the mechanical model results specified the geometric limits of the pin array. With these limits, computational fluid dynamics simulations were used to evaluate the thermal hydraulic performance of the prototype unit-cells with different pin geometries and unit-cell flow length, as described in Hyder and Fronk [5]. These analysis considered axial conduction through coversheet, radiation and reflection losses for different optical coatings, and convection losses for different ambient conditions. The thermal analysis was confirmed with lab-scale experimental data from [14]. The design targets were a receiver efficiency > 90% (with assumed optical coating) and pressure loss less than 0.4 MPa, while heating 20 to 25 MPa sCO₂ from 550°C to 720°C. The pin-array dimensions reported in Table 1 met these targets with a mechanical safety factor > 1.2 at operating temperature using conservative mechanical properties of Haynes 230 [13].

However, over the 15 cm × 15 cm area of the prototype device, there are approximately 125,000 pins. Thus, even for highly controlled manufactured processes, there is a relatively high statistical likelihood that one or more pins may not be fabricated to tolerance, bonded correctly (Figure 12), and/or damaged during other fabrication process (Figure 15). The

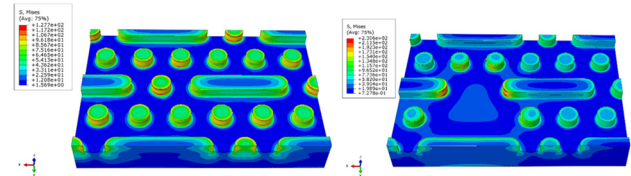


Figure 17: Image showing top view (a) of failed pin array with decreased pin diameter and (b) pin diameter in region without failure.

observed failure indicates that a more defect tolerant design of the pin array would increase the likelihood of prototype success. Many other sCO₂ recuperator and primary heat exchanger printed-circuit type designs fabricated with similar methods use micro channels with continuous walls rather than micro-pins. This increases the area available for bonding and increases the resilience of the device to manufacturing defects. However, this comes at the cost of decreased resilience to channel plugging and flow maldistribution, which is unacceptable for concentrated solar applications. Some alternatives are discussed below.

LESSONS LEARNED AND CONCLUSIONS

Fabricating high temperature and pressure heat exchangers is challenging and expensive, and the subject of multiple ongoing efforts across the world. The extreme operating conditions of the concentrated solar thermal environment make the problem even more challenging. This paper presented details on the design, fabrication, and identified failure modes in a printed-circuit type heat exchanger. From the challenges presented above, a few lessons learned can be of value to the sCO₂ community working with high-nickel content alloys.

Joining: One of the key failure mechanisms was related to the joining process. Joining of nickel-based alloys is widely studied in the literature. Generally, these studies are done with carefully controlled tensile test articles, and not with full components. As shown here, there can be difficulties when scaling proven laboratory processes to actual devices. Based on prior success of transient liquid phase bonding Haynes 230 with a Ni-P interlayer in 5 cm and 8 cm scale devices [15], the approach was adopted here, with approximately 3% P as a melting point depressant within the interlayer. Transient liquid phase bonding has the positive aspect that the bond region liquefies and can potentially fill some surface defects during the bonding process. However, due to the relatively slow diffusion of phosphorous into the base metal, there is some concern that the bond in the prototype device may have become liquid during other processes, causing degradation in the bond. Boron will diffuse faster than phosphorous, which would help ensure isothermal solidification of the joint during bonding. However, there is the possibility that because it diffuses so fast, uneven heating of large parts during the thermal ramp to the bonding temperature could cause the melting point depressant to non-uniformly diffuse out of some regions of the part before it is at the desired temperature.

To retire these risks, we have moved to a solid-state diffusion bonding process for Haynes 230. Here, the interlayer

and bond region will remain solid throughout the diffusion bonding process and, therefore, surface features have a more pronounced effect on porosity along the bond line. Based on the work of Kapoor et al. [16] for diffusion bonding of Haynes 230, we have identified process parameters (temperature, pressure, time) that will provide high percent bonded area without significant creep, permitting us to move forward with a solar receiver prototype design based on solid-state diffusion bonding. In our preliminary work exploring this approach, we are considering sub-scale prototypes either with or without a pure nickel-layer, with promising initial results in terms of joint yield strength and percent bonded area. Our second generation prototype will be fabricated using a diffusion bonding process.

Design: Another key lesson is to develop designs that are resilient to manufacturing defects, particularly when fabricating many small micro features. In our first prototype design, the failure of one pin potentially caused a cascade of failures resulting in “unzipping” of the bonded coversheet from the micro-pin array, as observed. In the failure analysis, some poorly bonded pins due were observed, although it was not possible to identify one single pin as the initiation of the failure. To mitigate this, we are considering designs consisting of arrays of pins and short bars (Figure 17). This type of design maintains resistance to plugging and blocking of the flow, while also increasing the area available for bonding. FEA analysis shows that this two feature design is more resilient to “missing” pins or bond area defects than a pure pin array. Work is ongoing to identify the best statistical distribution of defects to assess the resilience of the design.

In sum, we hope that the challenges, failure modes and lessons learned presented here can be used by others in the sCO₂ field to develop designs and fabrication strategies for their own applications that have a higher probability of success. Ultimately, this will decrease the time and cost in moving sCO₂ technology from the laboratory to the field.

NOMENCLATURE

D_{pin} pin height (μm)
 h_{pin} pin height (μm)
 L unit-cell base length (cm)
 $MAWP$ max allowable working pressure (MPa)
 P pressure (MPa)
 S_D diagonal pitch (μm)
 S_L longitudinal pitch (μm)
 S_T transverse pitch (μm)
 t coversheet thickness (μm)
 W unit-cell base width (cm)
 σ_D allowable stress at design temperature (MPa)
 σ_T allowable stress at test temperature (MPa)

ACKNOWLEDGEMENTS

This paper is based upon work supported by the U.S. Department of Energy, Office of Energy Efficiency and

Renewable Energy, Solar Energy Technologies Office, under Award Number DE-EE0007108.

REFERENCES

- [1] M. Mehos, C. Turchi, J. Vidal, M. Wagner, Z. Ma, C. Ho, W. Kolb, C. Andraka, and A. Kruienza, “Concentrating Solar Power Gen3 Demonstration Roadmap,” 2017.
- [2] M. Romero, R. Buck, and J. E. Pacheco, “An Update on Solar Central Receiver Systems, Projects, and Technologies,” *J. Sol. Energy Eng.*, vol. 124, no. 2, p. 98, 2002.
- [3] C. K. Ho and B. D. Iverson, “Review of high-temperature central receiver designs for concentrating solar power,” *Renew. Sustain. Energy Rev.*, vol. 29, pp. 835–846, 2014.
- [4] C. K. Ho, “Advances in central receivers for concentrating solar applications,” *Sol. Energy*, 2017.
- [5] M. B. Hyder and B. M. Fronk, “Simulation of thermal hydraulic performance of multiple parallel micropin arrays for concentrating solar thermal applications with supercritical carbon dioxide,” *Sol. Energy*, vol. 164, no. February, pp. 327–338, 2018.
- [6] K. R. Zada, M. B. Hyder, M. Kevin Drost, and B. M. Fronk, “Numbering-Up of Microscale Devices for Megawatt-Scale Supercritical Carbon Dioxide Concentrating Solar Power Receivers,” *J. Sol. Energy Eng.*, vol. 138, no. 6, p. 061007, 2016.
- [7] T. L’Estrange, “Experimental Characterization of a Supercritical Carbon Dioxide Microchannel Solar Thermal Receiver,” Cambridge University Press, Corvallis, OR, 2015.
- [8] M. Kapoor, Ö. N. Doğan, C. S. Carney, R. V. Saranam, P. McNeff, and B. K. Paul, “Transient-Liquid-Phase Bonding of H230 Ni-Based Alloy Using Ni-P Interlayer: Microstructure and Mechanical Properties,” *Metall. Mater. Trans. A*, vol. 48, no. 7, pp. 3343–3356, Jul. 2017.
- [9] W. H. Pratte, “Computational Modeling of a Diffusion Bonded Microchannel under High Pressure and Temperature,” Oregon State University, 2017.
- [10] C. Rymal, A. V. Apte, V. Narayanan, and K. Drost, “Numerical Design of a High-Flux Microchannel Solar Receiver,” in *Proceedings of the ASME 2013 7th International Conference on Energy Sustainability*, 2013, p. V001T11A012.
- [11] Ö. N. Doğan, C. Carney, R. P. Oleksak, C. R. Disenhof, and G. R. Holcomb, “High-Temperature Corrosion of Diffusion Bonded Ni-based Superalloys in CO₂,” in *The 5th International Symposium - Supercritical CO₂ Power Cycles*, 2016.
- [12] Metglas, “Amorphous Brazing Foil,” 2018. [Online]. Available: <https://metglas.com/wp-content/uploads/2018/10/Metglas-Brazing-Foil-Brochure-2018-FINAL.pdf>. [Accessed: 24-Apr-2019].
- [13] Haynes International, “Haynes ® 230 ® alloy,” 2017. [Online]. Available: <http://haynesintl.com/docs/default-source/pdfs/new-alloy-brochures/high-temperature->

- alloys/brochures/230-brochure.pdf.
- [14] T. L'Estrange, E. Truong, C. Rymal, E. Rasouli, V. Narayanan, S. Apte, and K. Drost, "High Flux Microscale Solar Thermal Receiver for Supercritical Carbon Dioxide Cycles," in *ASME 2015 13th International Conference on Nanochannels, Microchannels, and Minichannels*, 2015, p. V001T03A009.
- [15] V. Narayanan, B. M. Fronk, T. L'Estrange, and E. Rasouli, "Supercritical Carbon Dioxide Solar Thermal Power Generation—Overview of the Technology and Microchannel Receiver Development," 2019, pp. 333–355.
- [16] M. Kapoor, Ö. N. Doğan, K. Rozman, J. Hawk, A. Wilson, T. L'Estrange, and V. Narayanan, "Diffusion bonding of H230 Ni-superalloy for applicatoin in microchannel heat exchangers," in *The 5th International Symposium - Supercritical CO2 Power Cycles*, 2016.

MODELLING AND OPTIMISATION OF SUPERCRITICAL CARBON DIOXIDE TURBOMACHINERY

Ruan van der Westhuizen*

Stellenbosch University
Stellenbosch, South Africa
Email: rvanderwesthuizen@sun.ac.za

Johan van der Spuy

Stellenbosch University
Stellenbosch, South Africa

Albert Groenwold

Stellenbosch University
Stellenbosch, South Africa

Robert Dobson

Stellenbosch University
Stellenbosch, South Africa

ABSTRACT

In this work models of a centrifugal compressor and radial inflow turbine are presented. The models serve as a way to perform the initial design of the turbomachines for application in small- to medium-scale power cycles. The models are based on the classical mean-line velocity triangle approach which is supplemented with loss coefficients. Restrictive assumptions are not placed on the fluid and therefore the models can be used with supercritical carbon dioxide as will be explored in this work. In order to gain insight into the relationship between the geometrical specifications, thermodynamic operating conditions and performance characteristics of the turbomachinery, mathematical optimisation is performed for specific objectives under given constraints. The benefit of this is that the inevitable trade-offs between the design variables can be studied a priori, before any physical prototypes are built. Results are presented as Pareto plots between pairs of design variables. The importance of choosing an appropriate objective function and upper and lower bounds on the variables is discussed as well.

INTRODUCTION AND BACKGROUND

As a working fluid for power cycles, supercritical carbon dioxide (sCO₂) has many benefits. Above turbine inlet temperatures of 550°C, it can be shown that an sCO₂ Brayton cycle can achieve a higher thermodynamic efficiency than cycles that use other working fluids [1]. Furthermore, the performance of small sCO₂ Brayton cycles with simple layouts is comparable to much larger and more complicated steam Rankine cycle systems [1].

The performance of a Brayton power cycle is dominated by the performance of the turbomachinery [2]. Many variables have an influence on the performance of a turbomachine and it is a challenging engineering problem to find values for these variables that will lead to a well-designed machine.

New turbomachines have predominantly been designed by iterating on previous designs [3]. This is achieved through the use of basic theoretical principles and correlations that have been developed from empirical testing. Whilst this approach has proven to be technically successful and commercially viable for steam and gas turbomachinery, the sCO₂ turbomachinery industry is still relatively undeveloped. As a result, empirical correlations for sCO₂ turbomachinery are unavailable.

Another problem with this approach is that it is based on trial-and-error methods that are informed almost entirely by the knowledge and experience of the turbomachinery designer. Global optimisation is therefore not possible. Computational fluid dynamics (CFD) is a suitable alternative turbomachinery design tool and is amenable to more rigorous optimisation [4]; but the drawback of this approach is that CFD simulations are computationally expensive and unsuitable for system-level design and optimisation work.

The accuracy of CFD-derived performance analysis can be combined with the speed of gradient-based optimisation through the use of a *response surface model* (RSM) in which the effect of the design variables on the objective function of the optimisation are approximated [5]. Only a few CFD simulations are performed and the results of the objective function are then correlated to the design variables through a statistical regression analysis that yields a function or a neural network that yields an output value. The RSM then replaces the CFD in the optimisation process. RSM methods have been applied successfully to the optimisation of turbomachinery, including multi-objective (Pareto) optimisation [5, 6].

Despite the advantages of RSM methods, the accuracy of the results depends on the accuracy of the RSM approximation. Given the many variables involved in the analysis of turbomachinery, several CFD simulations are therefore still required in order to develop an accurate RSM.

The lack of suitable $s\text{CO}_2$ turbomachinery models that are both computationally inexpensive (i.e. do not require substantial CFD simulation work) and amenable to rigorous optimisation has resulted in the design of the turbomachinery receiving little to no attention during the initial design of $s\text{CO}_2$ power cycles. The machines are often modelled simply with a constant efficiency and with scant regard to their physical geometry. Although this may be satisfactory for elementary steady-state design work, it is obviously unsatisfactory for any detailed design work which requires matching of the cycle mass flow rate, proposed temperatures and pressures, and geometrical specifications with each other.

OBJECTIVES

The two common methods of designing and optimising turbomachinery (i.e. by iterating on previous designs or by using CFD simulations) have some drawbacks. This work presents an alternative approach which relies on mathematical models developed from standard theory. These models are required to meet three main objectives which are formalised as follows.

Firstly, the models should be developed as part of a larger power system model. Therefore, the interfaces (i.e. inlet and outlet) between the turbine or compressor stage and the rest of the system should be well-defined – both from a thermodynamic perspective and a geometrical perspective. The models must describe the design and performance of the turbomachines not only in isolation but also when integrated in a system.

Secondly, the models should be developed with robust mathematical gradient-based optimisation in mind as the primary application. This requires that the models consist entirely of a series of mathematical equations that capture the relationships between the variables of the machine.

Finally, given the lack of empirical data on $s\text{CO}_2$ turbomachines, it is conceivable that the current state-of-the-art of $s\text{CO}_2$ turbomachine modelling will be enhanced in the future by more accurate theory, procedures and correlations. In order to accommodate this, the models must be flexible and amenable to updates as required. Notwithstanding this, some applications may desire a faster computation time rather than the utmost modelling accuracy. As a result, the models must be based on the most elementary theoretical principles only. Any additional model complexity should augment rather than replace the basic principles.

MODELLING

The theoretical analysis of turbomachinery has been well-documented. Turbomachinery can be modelled reasonably accurately using only a few basic equations that can be found in most textbooks on turbomachinery (the interpretations of Aungier [3], Dixon and Hall [7], Korpela [8] and Japikse and Baines [9] are good examples). However, authors differ on the specifics of their notation and on the detail of their analyses. Furthermore, any model of a turbomachine must also take into consideration how that model is to be implemented because it will dictate the characteristics that the model should possess.

It is for these reasons that there are no universal analytical models for turbomachinery and it is worthwhile to present an introduction to the analytical turbomachinery models which are implemented in this work.

Consider a *stage* of a generic turbomachine, depicted schematically in Figure 1.

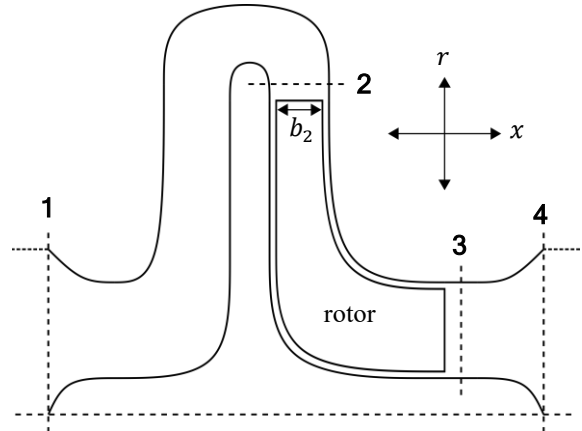


Figure 1: flow stations of a generic turbomachine stage

The stage consists of four main stations where the characteristics of the flow is analysed at. In a turbine, the flow is in the direction 1-2-3-4 and in a compressor the flow direction is reversed: 4-3-2-1. Sections 1-2 and 3-4 are stationary. In a turbine, 1-2 acts as a nozzle which accelerates the flow and 3-4 acts as a diffuser to slow the flow. In a compressor 4-3 is insignificant (and can be ignored) but 2-1 acts as a diffuser.

The *rotor* section between stations 2 and 3 is rotating and the transfer of momentum between the fluid and the blades occurs here.

A front view of the rotor section is depicted in Figure 2. Only one half of the blades are shown. The relevant blade dimensions are indicated. The outer radius of the disk r_2 is referred to as the *tip radius*. At station 3, the inner-most (smallest) radius r_{3h} is the *hub radius* whereas the larger radius r_{3s} corresponds to the *shroud radius*. The direction of rotation of the disk is also indicated in Figure 2: in the ω_T direction for a turbine and in the ω_C direction for a compressor.

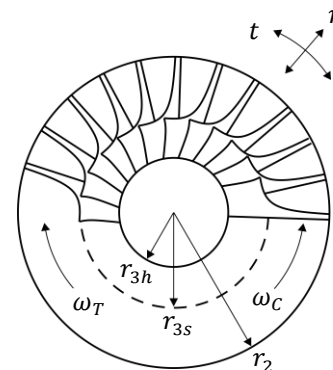


Figure 2: front view of a rotor disk

The geometry of a centrifugal compressor is very similar to the geometry of a radial inflow turbine and therefore common notation can be used. Assuming that the thickness of the blades is negligible, the radial flow area at station 2

$$A_{2r} = 2\pi r_2 b_2 \quad (1)$$

is the circumference of the disk multiplied by the blade width b_2 . At station 3 the axial flow area

$$A_{3x} = \pi(r_{3s}^2 - r_{3h}^2) \quad (2)$$

is the annulus between the shroud radius and the hub radius.

The mass flow rate

$$\dot{m} = \rho V_m A \quad (3)$$

is the product of the local density ρ , local absolute velocity V_m in the meridional (m) direction and area A normal to the flow. At station 2, the radial (r) direction is the meridional direction and at stations 1, 3 and 4 the axial (x) direction is the meridional direction. The flow can have a component in the tangential (t) direction at stations 2 and 3, but at stations 1 and 4 it is assumed that the flow has no tangential component. The conservation of mass is enforced as long as the mass flow rate is equal at all four flow stations.

A way to visualise the flow at stations 2 and 3 is to use a *velocity triangle*. A velocity triangle represents the relationship between the absolute velocity V , relative velocity R and blade velocity B .

The sign convention is as follows: the tangential direction is positive in the direction of blade rotation, and the meridional direction is positive in the direction of fluid flow. The angle that the absolute velocity vector makes with the meridional direction is denoted by α and the angle that the relative velocity vector makes with the meridional direction is denoted by β . With the positive meridional direction as reference, if the angle measurement is towards the positive tangential direction, then the angle is considered as positive. Conversely, if the angle measurement is towards the negative tangential direction, then the angle is considered as negative.

Figure 3 depicts a generic velocity triangle that can be used to analyse the flow at stations 2 and 3.

The flow direction is reversed in a compressor as compared to a turbine and the blades rotate in the opposite direction. However, the sign convention remains as previously defined and therefore the same velocity triangle can be used for both a turbine and a compressor.

A velocity triangle can be analysed using simple trigonometric rules that can be found from inspection.

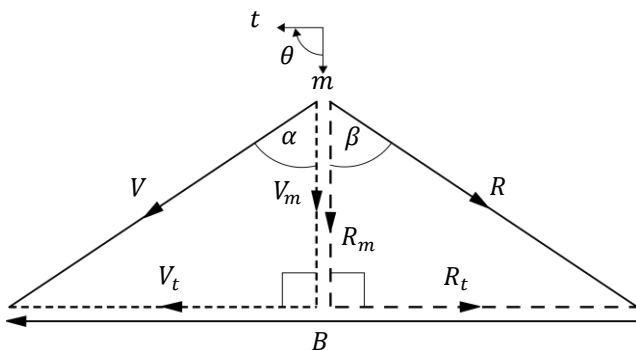


Figure 3: a generic velocity triangle

The relative velocity vector is defined as the vector subtraction of the blade velocity from the absolute velocity. Since the blade velocity only has a component in the tangential direction, this implies that

$$R_t = V_t - B \quad (4)$$

The blade speed

$$B = r\omega \quad (5)$$

can be calculated by multiplying the local radius by the angular velocity ω . At station 2, the tip radius r_2 is used and at station 3 the mean radius r_3 between the hub and shroud is used, where

$$r_3 = \frac{r_{3h} + r_{3s}}{2} \quad (6)$$

The conservation of momentum is taken into account by considering the resulting moment on the shaft

$$M = \dot{m}(V_{2t}r_2 - V_{3t}r_3) \quad (7)$$

The fluid power

$$\dot{W}_F = M\omega \quad (8)$$

can be determined by multiplying the moment by the angular velocity at which the shaft is rotating. However, this power is not equivalent to the power obtained from the conservation of energy (the first law of thermodynamics). Ignoring gravitational potential energy, the power obtained by applying the principle of the conservation of energy is

$$\dot{W} = \dot{m} \left[\left(h_2 + \frac{1}{2}V_2^2 \right) - \left(h_3 + \frac{1}{2}V_3^2 \right) \right] \quad (9)$$

The fluid power does not take into account the additional parasitic work terms such as leakage and windage, but the thermodynamic energy equation does [9]. The parasitic work

$$\dot{W}_P = |\dot{W} - \dot{W}_F| \quad (10)$$

is therefore the difference between the thermodynamic power and the fluid power.

The flow direction is defined in opposite directions for the compressor and turbine cases. This has the consequence that station 2 is always at a higher total enthalpy than station 3 and therefore the power rating is always a positive quantity regardless of whether a turbine or a compressor is under analysis.

The accurate modelling of sCO₂ thermodynamic properties is crucial for developing accurate sCO₂ turbomachinery models. A thermodynamic model of sCO₂ that is accurate across broad ranges of temperature and pressure cannot be based on simplifying assumptions such as the ideal gas or incompressible fluid assumptions.

Apart from evaluating lengthy and computationally expensive equations-of-state, the most accurate thermodynamic model can be achieved by interpolating from finely resolved tables of sCO₂ thermodynamic properties. Unfortunately, such an approach is also computationally expensive because a special interpolating function needs to be called with every iteration. An alternative approach is to use simple correlations of the form

$$x_3 = ax_1 + bx_2 + cx_1^2 + dx_1x_2 + ex_2^2 \dots \quad (11)$$

where the coefficients a, b, c, d, e, \dots are determined using a statistical regression analysis of the tabulated data.

This is valid because any thermodynamic property can be calculated if any two other properties are known [10]. It is therefore possible to state that a property x_3 can be expressed as a function of only two other properties x_1 and x_2 .

Equation 11 is an example of a second-order correlation, but the correlations can contain an arbitrary number of terms of any order. The more terms the correlations contain, in theory the more closely the properties will resemble the true properties of sCO₂ but the longer each calculation using the correlations will take. If fewer terms are used, then the properties that are calculated from the correlations will begin to deviate from the true properties of sCO₂ but the calculation speed will increase.

Another aspect to consider in the development of the turbomachinery models is the entropy generation or *losses* that occur throughout the stage. This is a fundamental part of accurately predicting turbomachine performance, but it is also the most challenging aspect to model.

There are numerous types of losses that occur throughout a turbomachine stage and there is no universal naming scheme nor is there a universally applicable loss model; in fact there are over 1.5 million possible loss model configurations [11]. Given the complexity of the physics encapsulated by the loss models, they are invariably based on empirically determined coefficients. However, as a result of the lack of empirical sCO₂ turbomachinery data, there are no loss coefficients that are specifically applicable to sCO₂ turbomachinery.

In the current models, three loss coefficients are employed. The first is the *rotor loss coefficient*

$$\zeta_R = \frac{h_0 - h_{0s}}{\frac{1}{2}R_2^2} \quad (12)$$

which represents the difference between actual total enthalpy achieved at the outlet of the rotor section and the total enthalpy that would have been achieved if the process was isentropic, as a fraction of the relative kinetic energy at the tip. The rotor loss coefficient applies to enthalpy values at station 2 in the case of a compressor and at station 3 in the case of a turbine.

The second loss coefficient is the *parasitic work coefficient*

$$\zeta_P = \frac{w_P}{\frac{1}{2}R_2^2} = \frac{\dot{W}_P}{\frac{1}{2}\dot{m}R_2^2} \quad (13)$$

which represents the parasitic work as a fraction of the relative kinetic energy at the tip of the rotor.

In the stationary sections of the turbomachinery (i.e. sections 1-2 and 3-4), the total enthalpy remains constant as a result of no shaft work and an assumption of negligible heat transfer. Only one additional loss factor – the *diffuser efficiency* – is necessary to characterise these sections. To derive the diffuser efficiency, consider the *pressure recovery coefficient* [9] of a diffuser

$$C_p = \frac{P_{out} - P_{in}}{P_{0,in} - P_{in}} \quad (14)$$

which represents the fraction of the kinetic available at the inlet to the diffuser that is converted into a static pressure rise. The ideal pressure recovery coefficient

$$C_{p,ideal} = 1 - (AR)^2 \quad (15)$$

is only a function of the area ratio AR . The ratio of the actual pressure recovery coefficient to the ideal pressure recovery coefficient is then defined as the *diffuser efficiency*

$$\eta_D = C_p / C_{p,ideal} \quad (16)$$

If the area ratio is defined as

$$AR = \frac{A_{small}}{A_{large}} \quad (17)$$

where A_{large} is the larger and A_{small} the smaller of the two flow areas of the section then the diffuser efficiency can be applied to a nozzle as well – the only difference is that the nozzle efficiency will exceed unity because the static pressure is reduced rather than raised [9].

The final factor to consider is *slip* which accounts for the fact that the flow at the tip is not perfectly guided by the blades of a compressor or by the inlet vanes of a turbine. Slip is incorporated into the models of this work by solving a third velocity triangle for each machine: in other words, a velocity triangle at station 3, a no-slip velocity triangle at station 2 and a velocity triangle at station 2 that includes slip. The two velocity triangles at station 2 can be linked through the *slip factor*

$$\sigma = \frac{V_{2t}}{V'_{2t}} \quad (18)$$

where V_{2t} represents the tangential velocity component with slip included and V'_{2t} represents the tangential velocity component without slip.

Although the turbomachinery models developed in this work are similar to the models developed by Da Lio et al. [12] and by Alshammari et al. [13], the computational implementation of the models is significantly different. Before the computational implementation is discussed however, it is necessary to define the concept of a mathematical optimisation problem.

MATHEMATICAL OPTIMISATION

A general constrained mathematical optimisation problem is formulated as [14]

$$\begin{aligned} &\text{minimise } f(\mathbf{x}) \text{ subject to} \\ &g_i(\mathbf{x}) \leq 0, i = 1, 2, \dots, m \\ &h_j(\mathbf{x}) = 0, j = 1, 2, \dots, r \\ &\text{with } \mathbf{x} = [x_1, x_2, \dots, x_n]^T \end{aligned} \quad (19)$$

The column vector \mathbf{x} contains the *design variables* of the problem. The problem has n design variables. These design variables represent the *design* of the system. A particular design can be compared with another design through the *objective function* $f(\mathbf{x})$.

The objective function is a function of one or more of the design variables and it has a scalar-valued solution. The objective function represents some kind of performance metric of the system and it is assumed that a smaller value of the objective function represents better performance. The best or *optimal* system design is therefore found when the objective function is minimised. If instead a performance metric should be maximised, then the objective function can simply be negated. All mathematical optimisation problems can therefore be treated as minimisation problems.

Not all system designs are valid designs. In order to restrict the design variables to yield a valid design, the problem is constrained by m inequality constraints $\mathbf{g}(\mathbf{x})$ and r equality constraints $\mathbf{h}(\mathbf{x})$. Each constraint is a function of one or more of the design variables.

COMPUTATIONAL IMPLEMENTATION

The scientific computing package MATLAB (version R2018b) by MathWorks includes an optimisation toolbox which has a built-in constrained optimisation algorithm called *fmincon* [15]. The user is required to specify the objective function $f(\mathbf{x})$ and a separate function which returns the vectors $\mathbf{g}(\mathbf{x})$ and $\mathbf{h}(\mathbf{x})$, which are the solutions to the constraints of the problem at some design \mathbf{x} .

The equality constraints of the turbomachinery optimisation problem are the model equations developed in this work.

The inequality constraints are used for incorporating factors such as checking that the flow is not choked, that the nozzle section has a converging area ratio and the diffuser sections a diverging area ratio, and that the design variables are within acceptable limits. In particular, the design limits for angles, velocity ratios and geometry ratios as reported by Korpela [8] are used in this work.

The constraints must be written such that all the terms are on the same side of the equation. A valid turbomachinery design (and solution) is therefore found if $\mathbf{g}(\mathbf{x}) \leq \mathbf{0}$ and $\mathbf{h}(\mathbf{x}) = \mathbf{0}$. For practical purposes however, a solution is considered valid as long as

$$\max(\mathbf{g}(\mathbf{x})) \leq t_c \approx 0 \quad (20)$$

and

$$\max(|\mathbf{h}(\mathbf{x})|) \leq t_c \approx 0 \quad (21)$$

where t_c is the *constraint tolerance* (0.001 in this work).

Given a starting point \mathbf{x}_0 , *fmincon* uses a gradient-based optimisation algorithm to attempt to minimise $f(\mathbf{x})$ whilst also satisfying Equations 20 and 21. It is the case that for most starting points the optimisation algorithm converges to an invalid solution or the solution converges to a local minimum rather than to the global minimum. It is therefore necessary to solve the problem a large number of times with different starting points throughout the design space. The *design space* is the set of all values of the design variables between their *lower bounds* $\hat{\mathbf{x}}$ and *upper bounds* $\hat{\mathbf{x}}$. All variables are given finite bounds.

MODEL CALIBRATION AND VERIFICATION

The loss coefficients introduced in Equations 12, 13 and 16 and the slip factor introduced in Equation 18 require numerical values before the turbomachinery models can be completed. Ideally, the coefficients would be found from empirical testing of sCO₂ turbomachines and correlated against dimensionless parameters such as specific speed or flow coefficient. However, such empirical data does not exist yet for sCO₂ turbomachinery. It is also conceivable that CFD simulations could be performed in lieu of experiments to find appropriate correlations. Indeed, any method that provides values for the three loss coefficients and the slip factor can be used to complete the models.

To demonstrate this, the commercial turbomachinery package CompAero [16] was used to find values for the loss coefficients and the slip factor. CompAero is a widely recognised compressor design tool and is based on the work of Aungier [3].

The software is clearly intended to work with gases and gas mixtures as working fluid and therefore its accuracy in predicting sCO₂ turbomachinery performance is untested.

However, even without support for sCO₂ CompAero is still a useful tool because it provides detailed information about the geometry and performance of the compressor and the thermodynamic properties are evaluated at all flow stations.

The following method was applied to find the values of the loss coefficients and the slip factor.

1. An arbitrary compressor was designed in CompAero, using CompAero's default values and the typical values suggested by Aungier [3]. Vapour CO₂ was used as the working fluid. The specifications of this compressor are given in the first part of Table 1 under the heading *Design specifications*.
2. The thermodynamic properties at the tip of the rotor and at the outlet of the stage, as well as the fluid work are recorded. These values are presented in the second part of Table 1 under the heading *Measurements used for calibration*.
3. In the compressor model of this work, the design specifications and the performance metrics are entered and treated as constant values whereas all the other variables including the loss coefficients and the slip factor are treated as free variables. The thermodynamic property correlations for sCO₂ in the model are replaced with thermodynamic properties for CO₂ in the vapour phase.
4. The model is solved numerically by running the optimisation algorithm for an arbitrary objective function. If a sufficient number of starting points are given, the optimisation algorithm finds a unique solution (within the constraint tolerance) for the compressor. The values for the loss coefficients and the slip factor can then be found from the models. In this way, the compressor model of this work is calibrated with the compressor model of CompAero. For the arbitrary design that was used for the calibration, the values for the loss coefficients and the slip factor are presented in the third part of Table 1 under the heading *Coefficients*.

Given the geometry of a turbomachine, its inlet conditions and two additional independent variables, then the operating condition of a turbomachine can be uniquely determined [7]. Once values for the loss coefficients and the slip factor are given as constant values to the model, then this condition becomes true for the models in this work.

Therefore, if only the values of the first and third part of Table 1 are supplied to the model, then the values of the second part as well as all the other thermodynamic properties, velocity components and flow angles can be uniquely determined.

Moreover, the model will give the same numerical values as the second part of Table 1, representing an error of zero with the CompAero design that has been used to calibrate the model. Since it is possible to achieve zero error only by adjusting the values for the loss coefficients and the slip factor, the models of this work can be considered as verified.

Table 1: design variables of an arbitrary compressor used for calibration of the model loss coefficients and slip factor

Design specifications	Value
Tip radius, r_2	74.5 mm
Hub radius, r_{3h}	26.1 mm
Shroud radius, r_{3s}	62.5 mm
Blade width, b_2	9.53 mm
Diffuser exit area, A_1	6 880 mm ²
Inlet total temperature, T_{03}	300 K
Inlet total pressure, P_{03}	130 kPa
Absolute flow angle at rotor inlet, α_3	0.00°
Physical blade angle at tip, β'_2	-35.1 °
Mass flow rate, \dot{m}	2.80 kg/s
Angular velocity, ω	55 000 rpm
Measurements used for calibration	Value
Tip total temperature, T_{02}	410 K
Tip total pressure, P_{02}	406 kPa
Stage exit total temperature, T_{01}	410 K
Stage exit total pressure, P_{01}	341 kPa
Fluid power, \dot{W}_F	275 kW
Coefficients	Value
Rotor loss coefficient, ζ_R	0.619
Parasitic work coefficient, ζ_p	0.0108
Diffuser efficiency, η_D	0.972
Slip factor, σ	0.808

Table 2: design variables and observed errors for an arbitrary compressor, using loss coefficients and slip factor calibrated to a different compressor

Design specifications	Value		
Tip radius, r_2	41.3 mm		
Hub radius, r_{3h}	14.5 mm		
Shroud radius, r_{3s}	27.0 mm		
Blade width, b_2	3.88 mm		
Diffuser exit area, A_1	1 580 mm ²		
Inlet total temperature, T_{03}	300 K		
Inlet total pressure, P_{03}	130 kPa		
Absolute flow angle at rotor inlet, α_3	0.00°		
Physical blade angle at tip, β'_2	-40.3°		
Mass flow rate, \dot{m}	0.36 kg/s		
Angular velocity, ω	80 000 rpm		
Results	CompAero	This work	Error
Tip total temperature, T_{02}	388 K	385 K	0.8%
Tip total pressure, P_{02}	375 kPa	370 kPa	1.3%
Stage exit total temperature, T_{01}	388 K	384 K	1.0%
Stage exit total pressure, P_{01}	284 kPa	321 kPa	13%
Fluid power, \dot{W}_F	28.0 kW	26.3 kW	6.1%

Although the values for the loss coefficients and slip factor presented in Table 1 produce zero error for that particular compressor design, it is to be expected that if a different compressor design is used with the same coefficient values then some error in the results will be observed.

In the first part of Table 2, the design specifications of another arbitrary compressor are given. The specifications have been entered as constant values in the compressor model of this work, together with the values of the loss coefficients and slip factor presented in the third part of Table 1. The model was solved numerically by running the optimisation algorithm for an arbitrary objective function. Again, several starting points are needed but the algorithm is able to find a unique solution for this compressor.

The results of the thermodynamic properties at the tip and at the stage outlet, and the fluid work from the model are compared with the values that CompAero has calculated they should be. Errors for the different results of between 0.8% and 13% are observed, with the greatest error observed for the stage outlet pressure.

Given an arbitrary compressor, the model can be calibrated to produce zero error. However, if the same calibrated model is applied to a different arbitrary compressor, some error is introduced. This confirms that a constant value for each loss coefficient and the slip factor cannot possibly be accurate for all compressor designs. It is necessary to replace the constant values with correlations against non-dimensional parameters developed from the results of CFD simulations or empirical tests of a wide variety of compressor designs. This is beyond the scope of the current work, but it should be clear that once such correlations are developed then they can easily be implemented in the models that have been presented.

Notice that the performance metrics used to calibrate the models are very general: total temperature and total pressure measurements are easy to measure on an experimental test bench and so is shaft power (CompAero only provides fluid power \dot{W}_F and not the required shaft power \dot{W} although in an experimental test the fluid power would not be known but the shaft power can easily be measured).

Therefore, regardless of whether experiments or CFD simulations are performed, the calibration method proposed in this work can be used to develop more generalised correlations for the loss coefficients and slip factor.

RESULTS

Two case studies will be presented which demonstrate the optimisation of a centrifugal compressor and a radial inflow turbine. In Table 3 the specifications of a typical sCO₂ compressor design case are presented.

Table 3: specifications of a typical compressor design case

Design specifications	Value
Stage inlet total temperature, T_{03}	335 K
Stage inlet total pressure, P_{03}	8.50 MPa
Absolute flow angle at rotor inlet, α_3	0.00°
Total-to-total pressure ratio, PR_0	2.50

The inlet temperature and pressure to the stage are close to (but not at) the critical conditions for CO₂, the flow enters the rotor section without incidence, and the required total-to-total pressure ratio is provided. The compressor designer is now tasked with finding the geometry of a compressor capable of achieving this pressure ratio at the stated conditions.

To assess the quality of candidate compressor designs, an objective function is required. A typical objective function might be to

- minimise the required shaft power \dot{W} ,
- minimise the required angular velocity ω ,
- maximise the mass flow rate \dot{m} throughput, or
- minimise the tip radius r_2 .

It is however unlikely that any of these objectives would be prioritised without consideration for the others, which therefore makes this a multi-objective optimisation problem. Multi-objective optimisation problems typically do not have a single global optimal solution and instead a range of optimal solutions exist which lie on the so-called *Pareto front*. Any point on the Pareto front is referred to as a *Pareto-optimal* point. Pareto-optimal points represent a solution which is optimal for at least one of the variables in the objective function.

Consider the results of the compressor optimisation on a plot of angular velocity against shaft power in Figure 4. Every point on the plot represents a valid solution or design that the designer is able to select – a *local minimum* of the optimisation problem. Most designs however are inferior and only the designs on the Pareto front should be considered. Every point on the Pareto front in Figure 4 represents a design which either minimises the shaft power at a particular angular velocity or minimises the angular velocity at a particular shaft power.

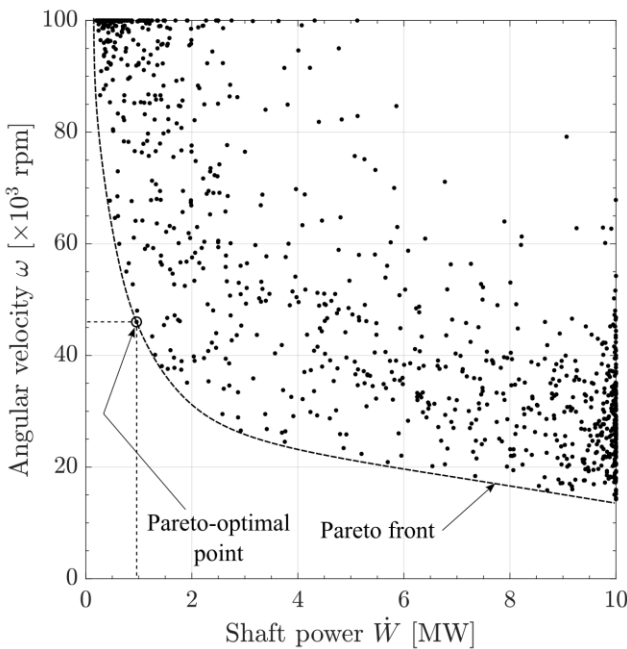


Figure 4: compressor angular velocity vs shaft power

The general trend that the Pareto front shows is that as shaft power is reduced, angular velocity must increase in order to sustain the required pressure ratio.

The large spread that is visible in the data shows that in general shaft power and angular velocity are poorly correlated for a compressor at a constant pressure ratio. The geometry of the compressor has a significant effect on the relationship between these two variables.

In comparison, the mass flow rate plotted against shaft power in Figure 5 shows a much smaller spread in the data, especially at lower power ratings. The conclusion of this is that mass flow rate is a much more dominant variable than angular velocity for a compressor at a constant pressure ratio. The Pareto-front in Figure 5 shows that there is a linear relationship between mass flow rate and shaft power as is to be expected: as the required mass flow rate increases the shaft power must increase proportionally. It is interesting to note however that at higher power ratings the influence of the compressor’s geometry plays a very significant role in determining the mass flow rate that can be achieved. If the Pareto-optimal design at a power rating of 10 MW is selected, then the mass flow rate can be as high as 220 kg/s; but if a poor design is selected then the mass flow rate can be up to 100 kg/s lower. At smaller power ratings, the influence of geometry is not as important in absolute terms, but since the achievable mass flow rates are lower the influence of geometry remains considerable.

The location of the Pareto-optimal point of Figure 4 on Figure 5 is indicated by the dotted-lines, which show the point to be close to or on the Pareto front in Figure 5 as well. The Pareto front in Figure 5 represents all designs which either maximise the mass flow rate at a given shaft power or minimise the shaft power at a given mass flow rate.

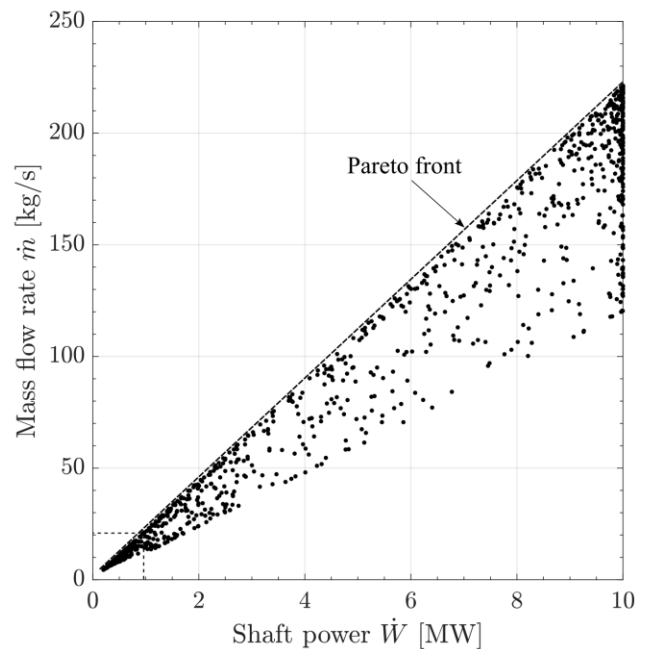


Figure 5: compressor mass flow rate vs shaft power

An even better correlation in the data can be seen if tip radius is plotted against angular velocity, as in Figure 6. The data shows a very narrow spread and the overall trend is very clear: in order to maintain a constant pressure ratio, as the compressor speed is reduced the tip radius has to increase. This relationship is only marginally affected by the other variables of the compressor's design.

However, even though the overall trend is clear, consider that if a tip radius of 30 mm is selected, the angular velocity can still be anywhere in the range of about 70 000 rpm to 100 000 rpm (and potentially even higher since 100 000 rpm was the upper bound on angular velocity for the optimisation) which is a very significant difference in practice. This highlights the importance of optimisation, as using a poor design could result in the compressor having to operate much faster than it needed to in order to achieve the required pressure ratio.

The Pareto front in Figure 6 shows the designs which either minimise tip radius at a given angular velocity or minimise angular velocity at a given tip radius.

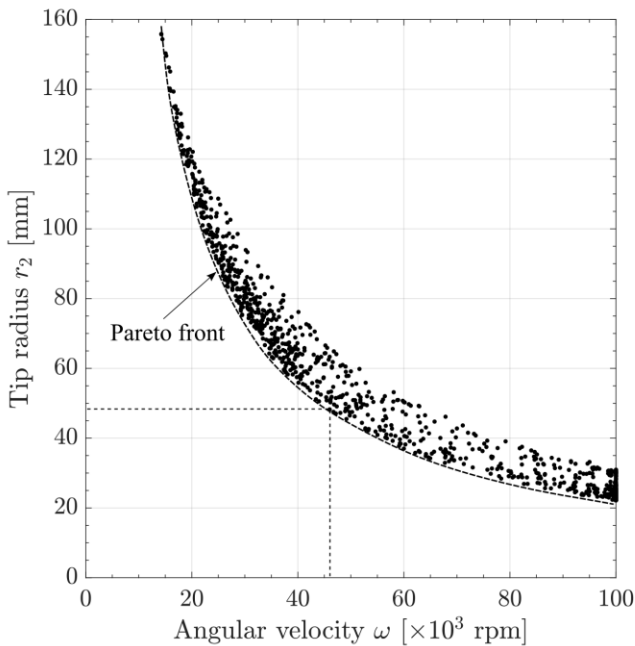


Figure 6: compressor tip radius vs angular velocity

The Pareto-optimal point of Figure 4 is shown in Figure 6 by the dotted lines and once again it lies on the Pareto front in Figure 6 as well. It is not a general rule that in a multi-objective optimisation problem that a point on one Pareto front would also lie on other Pareto fronts, but in this case it would appear as if a compressor design which is Pareto-optimal on the angular velocity vs shaft power plot is also Pareto-optimal on the mass flow rate vs shaft power plot and on the tip radius vs angular velocity plot.

In Table 4 selected results for the Pareto-optimal compressor design (identified in Figure 3) are provided.

Table 4: selected results of an optimised compressor design

Design results	Value
Tip radius, r_2	48.3 mm
Hub radius, r_{3h}	12.2 mm
Shroud radius, r_{3s}	32.0 mm
Blade width, b_2	4.83 mm
Mass flow rate, \dot{m}	21.2 kg/s
Angular velocity, ω	46 000 rpm
Shaft power, \dot{W}	958 kW

The second case study to be considered in this work concerns the design of a radial inflow turbine. In Table 5 the specifications of a typical sCO₂ turbine design case are given, including the stage inlet temperature and pressure. Additionally, the design is required to have no absolute tangential velocity component at the outlet of the rotor; and the rotor tip radius is required to be a specific value (an example of where this might be relevant specification is when a new rotor has to be designed to work with a previously designed volute/scroll section).

Table 5: specifications of a typical turbine design case

Design specifications	Value
Stage inlet total temperature, T_{01}	850 K
Stage inlet total pressure, P_{01}	25.0 MPa
Absolute flow angle at rotor outlet, α_3	0.00°
Rotor tip radius, r_2	75.0 mm

The task of the turbine designer is to find the geometry of a turbine that meets these specifications but also that

- maximises the generated shaft power \dot{W} ,
- minimises the angular velocity ω ,
- minimises the required mass flow rate \dot{m} , and/or
- maximises the total-to-static isentropic efficiency $\eta_{s,ts}$ (which is the ratio of the actual power produced to the power that would have been produced if the turbine was isentropic and if its diffuser reduced the flow velocity to zero)

Figure 7 shows the optimisation results of this case study, with angular velocity plotted against mass flow rate. Despite also being a multi-objective optimisation problem, in this case angular velocity and mass flow rate can both be minimised simultaneously – at zero flow. Clearly, this is an unpractical choice even though it is a valid solution based on the constraints of the problem and the specifications that were provided. As the flow and speed increase, the spread in the data also increases and two diverging fronts are created. On front 1 are the turbine designs which minimise angular velocity for a given mass flow rate and on front 2 are the turbine designs which minimise mass flow rate for a given angular velocity. These are *fronts* rather than *Pareto fronts* because on a Pareto front no global optimum exists and all solutions can be treated equally. In this case, a global optimum (for the relationship between angular velocity and mass flow rate) does exist but it lies at a point that does not represent a practical design; and a design that is selected on one of the fronts will be optimal for one metric but not for the other.

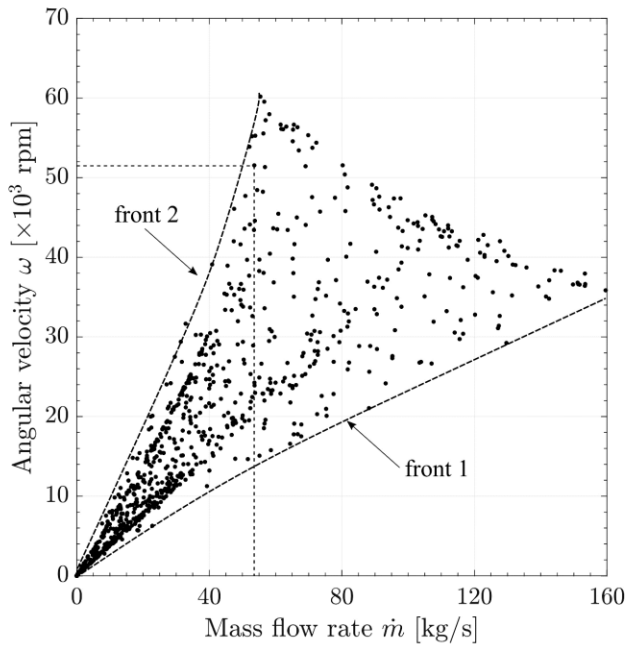


Figure 7: turbine angular velocity vs mass flow rate

A Pareto front can however be identified if power output is plotted against mass flow rate, as in Figure 8. The Pareto front corresponds to turbine designs in which the power output at a given flow rate is maximised or in which the mass flow rate for a given power output is minimised. The Pareto front is practically zero for low mass flow rates but rises sharply from about 20 kg/s. The front becomes almost vertical by the time it reaches a power output of 10 MW (the upper bound that was considered in this case) at a mass flow rate of 55 kg/s, indicating that beyond this point the Pareto-optimal power output is no longer dominated by the mass flow rate.

However, the large spread in the data is indicative that the other design variables of the turbine have a significant effect on the mass flow rate that is required to produce a particular power output. At 10 MW, the Pareto-optimal design requires 55 kg/s of mass flow through it, but a poor design can require a mass flow rate that is three times as much.

A Pareto-optimal turbine design is selected in Figure 8 and indicated by the dotted lines. This same design is also indicated by the dotted lines in Figures 7 and 9.

In Figure 9, the total-to-static isentropic efficiency of the turbine designs are presented. It can be seen that the efficiencies are very high and even the poor designs have efficiencies that exceed 85%. There are three reasons for this; the first is that the design limits for angles, velocity ratios and geometry ratios [8] proved to be effective for eliminating the worst designs. Secondly, constant loss coefficients were used which means – based on the definitions in Equations 12 and 13 – that simply by reducing the relative velocity at the tip the losses can be minimised. More accurate loss coefficients that are actually correlated against geometrical and flow parameters will ensure that the losses cannot be minimised by minimising a single term.

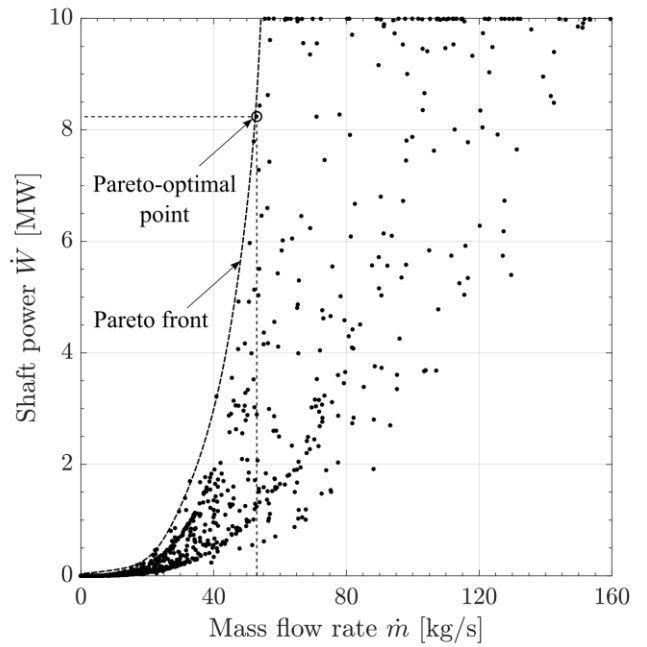


Figure 8: turbine shaft power vs mass flow rate

The third reason is that the allowable diffuser outlet area was very large (up to 1.6 m² was allowed, compared to blade dimensions which were restricted to a maximum of 0.5 m). As the area ratio of a diffuser increases, in general its ability to recover kinetic energy also increases. Therefore, the designs with high efficiencies typically have large diffusers as well.

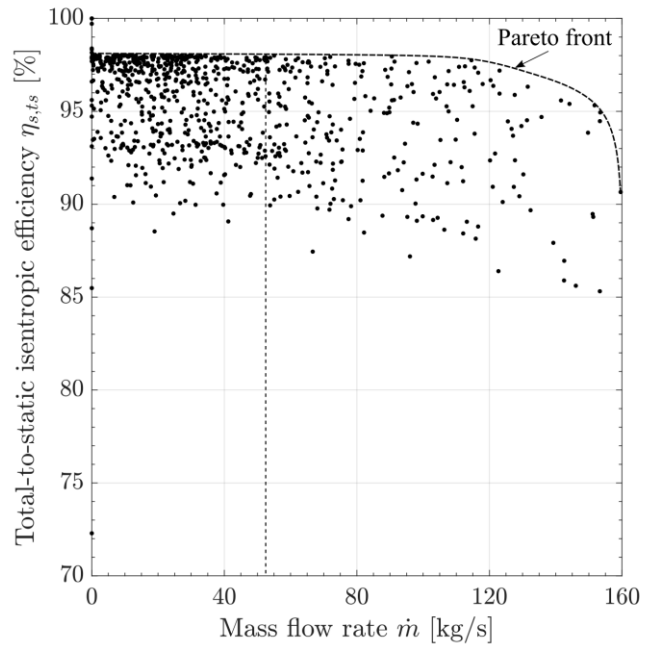


Figure 9: turbine efficiency vs mass flow rate

The Pareto front in Figure 9 (which indicates the designs that maximise efficiency for a given mass flow rate) is practically horizontal up to 120 kg/s. This shows that the highest efficiency can be achieved regardless of mass flow rate. However, the front drops at higher mass flow rates and this can be attributed to certain variables reaching their upper or lower bounds. For example, for some turbines at these high mass flow rates the diffuser exit area that is required for a high efficiency is larger than the given upper bound of 1.6 m².

In Table 6 selected results for the Pareto-optimal turbine design (identified in Figure 8) are provided.

Table 6: selected results of an optimised turbine design

Design results	Value
Hub radius, r_{3h}	16.1 mm
Shroud radius, r_{3s}	40.2 mm
Blade width, b_2	7.64 mm
Mass flow rate, \dot{m}	52.9 kg/s
Total-to-total pressure ratio, PR_0	1.83
Angular velocity, ω	55 000 rpm
Shaft power, \dot{W}	8.24 MW

APPLICATION

Once the general relationships between the major design variables of the turbomachines have been studied from the results above, it is up to the designer to select one of the designs or to change the given specifications or constraints and re-run the optimisation algorithm if the results are not satisfactory.

In this work, every compressor design is made up of 97 design variables; and every turbine design is made up of 111 design variables (the turbine requires more variables because section 4-3 is ignored for the compressor). The values of all these design variables for all the valid designs are stored on file. Once a candidate design is identified, then the designer can find the values for its other design variables from the file.

The choice of the design variables to specify and to plot on the graphs in this work is arbitrary and purely for the sake of demonstration. It is in fact possible to specify any combination of variables or to plot the results of any combination of design variables against each other. Once all of the equations of the models are expressed and the thermodynamic property correlations are added, the compressor model consists of 82 equality and 9 inequality constraints, and the turbine consists of 92 equality and 10 inequality constraints. These constraints and the choices of the upper and lower bounds on the variables influence which feasible designs are possible and what the design space that is available to the designer looks like. Therefore, choosing an optimal compressor or turbine design begins with properly defining the objective function(s) and choosing practical and realistic upper and lower bounds on the variables (a variable that is specified as a constant value has an equal upper and lower bound).

Ideally, the design space should be restricted as much as possible before running the optimisation algorithm.

In the turbine case study example, only a tip radius was specified but the required power rating, angular velocity or mass flow rate was not given. This led to the optimisation algorithm proposing unrealistically low mass flow rates as valid solutions. Whilst these are valid solutions indeed, it shows that optimisation is only useful insofar as the exact problem to be solved can be accurately identified.

CONCLUSION

Models for a centrifugal compressor and a radial inflow turbine have been developed based on the classical mean-line velocity triangle approach. The models can be used as an alternative to the proven CFD/RSM optimisation methods.

Restrictive assumptions were not made and correlations of fluid thermodynamic properties were generated from tabulated data. The loss coefficients and slip factor were calibrated against a compressor design from the commercial compressor design software CompAero. No difference was observed between the current compressor model and the CompAero model if the loss coefficients and slip factor were calibrated, but errors of up to 13% were observed if the same loss coefficients and slip factor were used to model another arbitrary compressor design.

Two typical design optimisation case studies were presented: one for a centrifugal compressor that was required to develop a fixed pressure ratio and one for a radial inflow turbine that was required to have a fixed tip radius. The results of the compressor case study showed that Pareto-optimal solutions could be identified on the angular velocity vs shaft power plot, the mass flow rate vs shaft power plot and the tip radius vs angular velocity plot. The results of the turbine case showed for a constant radius turbine minimising angular velocity and minimising mass flow rate are diverging objectives and Pareto-optimal solutions do not exist; although a global optimum exists at zero mass flow rate. Pareto-optimal solutions could be identified on the shaft power vs mass flow rate plot however, as well as on the efficiency vs mass flow rate plot. The high efficiencies in the latter plot highlighted the inaccuracies with using constant loss coefficients instead of correlations.

The models in this work can be applied equally well to other working fluids and the rather general results of this work are surely not applicable to sCO₂ only. The proposed methodology is however especially useful for sCO₂ turbomachinery optimisation because the industry is still in its infancy.

FUTURE WORK

Extensive CFD simulations or experiments on a wide variety of sCO₂ turbomachinery designs should be performed from which accurate and widely applicable correlations for the loss coefficients against non-dimensional flow parameters could be developed. These correlations could be developed using the methodology proposed in this work, and the constant coefficients applied as an example in this work should be supplemented with the developed correlations. Once such correlations have been developed, the presented models can be used additionally for off-design performance modelling, without the need for any changes to be made to the underlying computational implementation.

NOMENCLATURE

Letters

A	area (m ²)
AR	area ratio (-)
B	blade velocity (m/s)
b	blade width (m)
C_p	pressure recovery coefficient (-)
f	objective function
g	inequality constraint
h	enthalpy (J/kg); equality constraint
M	moment (Nm)
m	meridional direction
\dot{m}	mass flow rate (kg/s)
P	pressure (Pa)
PR	pressure ratio (-)
R	relative velocity (m/s)
r	radius (m); radial direction
T	temperature (K)
t	tolerance (-); tangential direction
V	velocity (m/s)
\dot{W}	power (W)
w	energy/work (J)
x	variable; axial direction
\tilde{x}	lower bound on variable
\hat{x}	upper bound on variable
x_0	starting point

Symbols

α	absolute flow angle (degrees)
β	relative flow angle (degrees)
ζ	loss coefficient (-)
η	efficiency (-)
θ	generic angle (degrees)
ρ	density (kg/m ³)
σ	slip factor (-)
ω	angular velocity (rad/s)

Subscripts

C	compressor
c	constraint
D	diffuser
F	fluid
h	hub
m	meridional direction
P	parasitic
R	rotor
r	radial direction
s	shroud, isentropic
T	turbine
t	tangential direction
ts	total-to-static
x	axial direction
0	total state
1	station 1
2	station 2 (tip)
3	station 3 (eye)
4	station 4

ACKNOWLEDGEMENTS

This work has been financially supported by the Solar Thermal Energy Research Group (STERG) based at Stellenbosch University.

REFERENCES

- [1] V. Dostal, M. J. Driscoll, and P. Hejzlar, "A Supercritical Carbon Dioxide Cycle for Next Generation Nuclear Reactors," *Technical Report MIT-ANP-TR-100*, 2004.
- [2] M. J. Hexemer and K. Rahner, "Supercritical CO₂ Brayton Cycle Integrated System Test (IST) TRACE Model and Control System Design," in *Supercritical CO₂ Power Cycle Symposium*, 2011.
- [3] R. H. Aungier, *Centrifugal Compressors: A Strategy for Aerodynamic Design and Analysis*. New York, NY: ASME Press, 2000.
- [4] Z. Li and X. Zheng, "Review of design optimization methods for turbomachinery aerodynamics," *Progress in Aerospace Sciences*, vol. 93, pp. 1–23, 2017.
- [5] M. C. Duta and M. D. Duta, "Multi-objective turbomachinery optimization using a gradient-enhanced multi-layer perceptron," *International Journal for Numerical Methods in Fluids*, vol. 61, pp. 591–605, 2009.
- [6] X. D. Wang, C. Hirsch, S. Kang, and C. Lacor, "Multi-objective optimization of turbomachinery using improved NSGA-II and approximation model," *Computer Methods in Applied Mechanics and Engineering*, vol. 200, pp. 883–895, 2011.
- [7] S. L. Dixon and C. A. Hall, *Fluid Mechanics and Thermodynamics of Turbomachinery*, 7th ed. Oxford, United Kingdom: Butterworth-Heinemann, 2014.
- [8] S. A. Korpela, *Principles of Turbomachinery*. Hoboken, NJ: Wiley, 2011.
- [9] D. Japikse and N. C. Baines, *Introduction to Turbomachinery*. Norwich, VT: Concepts ETI, Inc., 1994.
- [10] F. M. White, *Fluid Mechanics*, 7th ed. New York, NY: McGraw-Hill, 2011.
- [11] R. Persky and E. Sauret, "Loss models for on and off-design performance of radial inflow turbomachinery," *Applied Thermal Engineering*, vol. 150, pp. 1066–1077, 2019.
- [12] L. Da Lio, G. Manente, and A. Lazzaretto, "A mean-line model to predict the design efficiency of radial inflow turbines in organic Rankine cycle (ORC) systems," *Applied Energy*, vol. 205, pp. 187–209, 2017.
- [13] F. Alshammari, A. Karvountzis-Kontakiotis, A. Pesiridis, and P. Giannakakis, "Off-design performance prediction of radial turbines operating with ideal and real working fluids," *Energy Conversion and Management*, vol. 171, pp. 1430–1439, 2018.
- [14] J. A. Snyman, *Practical Mathematical Optimization*. Pretoria, South Africa: University of Pretoria, 2004.
- [15] The Mathworks Inc., "Matlab R2018b Documentation." 2018.
- [16] R. H. Aungier, "CompAero 2.00." Flexware, Grapeville, PA, 2011.

TRANSIENT RESPONSE OF SUPERCRITICAL CO₂ AXIAL TURBINE FOR KAIST MMR

In-woo Son

^a Department of Nuclear and Quantum Engineering,
Korea Advanced Institute of Science and Technology
373-1 Guseong-dong Yuseong-gu, Daejeon, 305-701,
Korea

Email: siw4139@kaist.ac.kr

Jin Young Heo

^a Department of Nuclear and Quantum Engineering,
Korea Advanced Institute of Science and Technology
373-1 Guseong-dong Yuseong-gu, Daejeon, 305-701,
Korea

Email: jyh9090@kaist.ac.kr

Bong Seong Oh

^a Department of Nuclear and Quantum Engineering,
Korea Advanced Institute of Science and Technology
373-1 Guseong-dong Yuseong-gu, Daejeon, 305-701,
Korea

Email: bongseongoh@kaist.ac.kr

Jeong Ik Lee

^a Department of Nuclear and Quantum Engineering,
Korea Advanced Institute of Science and Technology
373-1 Guseong-dong Yuseong-gu, Daejeon, 305-701,
Korea

mail: jeongiklee@kaist.ac.kr

ABSTRACT

The Supercritical CO₂ (S-CO₂) Brayton power cycle has the advantages of relatively high efficiency at moderate heat source temperature compared to a steam Rankine cycle or a helium Brayton cycle and compact components size. In nuclear energy industry, Small Modular Reactors have potentials in many aspects, flexibility of construction, and applicability for the distributed power source and reduced construction cost. Therefore, KAIST research team developed an S-CO₂ cooled Small Modular Reactor namely KAIST Micro Modular Reactor (MMR), using both advantages of S-CO₂ cycle and SMR. Currently, radial turbine is being used for the output of 12MWe in MMR. The original KAIST-MMR was designed to utilize radial turbine but the 12MWe power output of MMR can adopt axial turbine as well. Therefore, this paper explores the potential of improving both steady state performance and transient response by switching from radial type to axial type turbine. The implications of the transient analysis results show the advantages of using the axial turbine over the radial turbine because the axial turbine operates at relatively higher efficiencies for wider off-design ranges.

INTRODUCTION

The supercritical CO₂ (S-CO₂) cycle is attracting attention as it has the potential to replace the existing steam cycle in the process of developing the next generation nuclear power plants. In addition, the supercritical CO₂ cycle has a higher thermal efficiency than the steam Rankine cycle and the helium Brayton

cycle when the turbine inlet temperature is above 500 degree Celsius [1, 2]. It also has the advantage that the components of the cycle, such as turbines and compressors, are more compact than other cycles, making them well suited for small modular nuclear reactors. Fig. 1 compares the efficiency of a supercritical CO₂ Brayton cycle, a steam Rankine cycle, and a helium Brayton cycle [1].

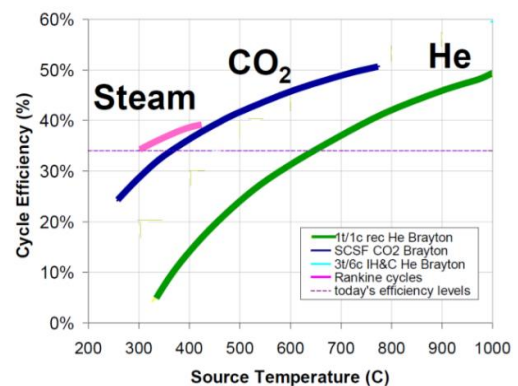


Fig. 1. Comparison of efficiency of S-CO₂ power cycle [1]

Recently, small modular reactor (SMR) technology has received worldwide attention, especially in developing countries. This is because it has the advantage in a region where power grid size is not large and distributed power generation can be more economical than the central power generation and distribution.

Based on these aspects, the KAIST research team developed a micro modular reactor (MMR) by combining two technologies:

SMR and gas turbine technologies [3]. MMR is sized such that it can be transported via truck and the layout of MMR is shown in Fig. 2. The design values of MMR are summarized in Table 1. These values were obtained from the design process of a nuclear system by using validated in-house codes. The design was conducted by using the following well-validated programs: KAIST-TMD [5] and KAIST-HXD [6].

The KAIST TMD code for the compressor was validated in the previous study [5]. In addition, for the same turbomachinery, equivalent conditions can provide a basis for comparing different working fluids [7]. Furthermore, sCO₂ turbine operates where the properties are behaving similar to an ideal gas. Therefore, the KAIST TMD code was validated using NASA's air radial turbine data, which is equivalent to sCO₂ conditions for a radial turbine case [8]. For the axial turbine, the loss set of the following reference was used [9]. In ref. [9], the author selected the GTHTR 300 design of JAEA [10], a direct cycle using helium gas, as a reference model to validate the axial turbine code. Thus, KAIST-TMD is validated in radial compressor, radial turbine, and axial turbine with the available data.

The KAIST-HXD code was developed by the KAIST research team using a new thermal hydraulic correlation for sCO₂ heat exchanger and the code is validated by a laboratory-scale PCHE test at the KAIST supercritical CO₂ pressurizing experiment (SCO2PE) facility [6].

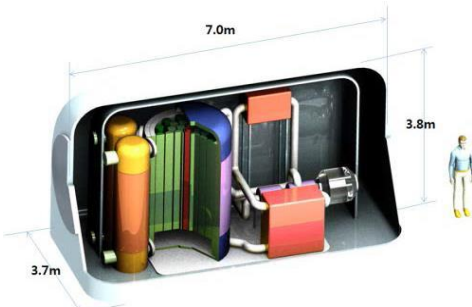


Fig. 2. Concept of KAIST-MMR [3]

Table 1. Summary of design results of MMR

Thermal power	36.2MWth	Net electric power	12MWe
Thermal efficiency	34.09%	Mechanical efficiency	98%
Mass flow rate	180.0kg/s	Total-to-total Pressure ratio	2.49
Turbine total-to-total efficiency	92%	Compressor total to total efficiency	85%
Generator efficiency	98%	Rotating speed	19,300rpm
Recuperator effectiveness	95%	Compressor inlet pressure	8.0MPa
Design point of recuperator	Hot side inlet : 440.7°C, 8.2MPa Cold side inlet : 142.1°C, 20.0MPa Temperature difference : 22-58°C		

DESCRIPTION OF KAIST-CCD, TMD, HXD CODE

KAIST-CCD

The KAIST-Closed Cycle Design (KAIST-CCD) code is based on MATLAB, and it is an in-house code developed by KAIST research team. Fig. 3 shows the main algorithm of the KAIST-CCD code. The monitored error value for the iteration is defined below.

$$Error = \frac{[heat\ input(n) - heat\ input(n-1)]}{heat\ input(n)} \quad (1)$$

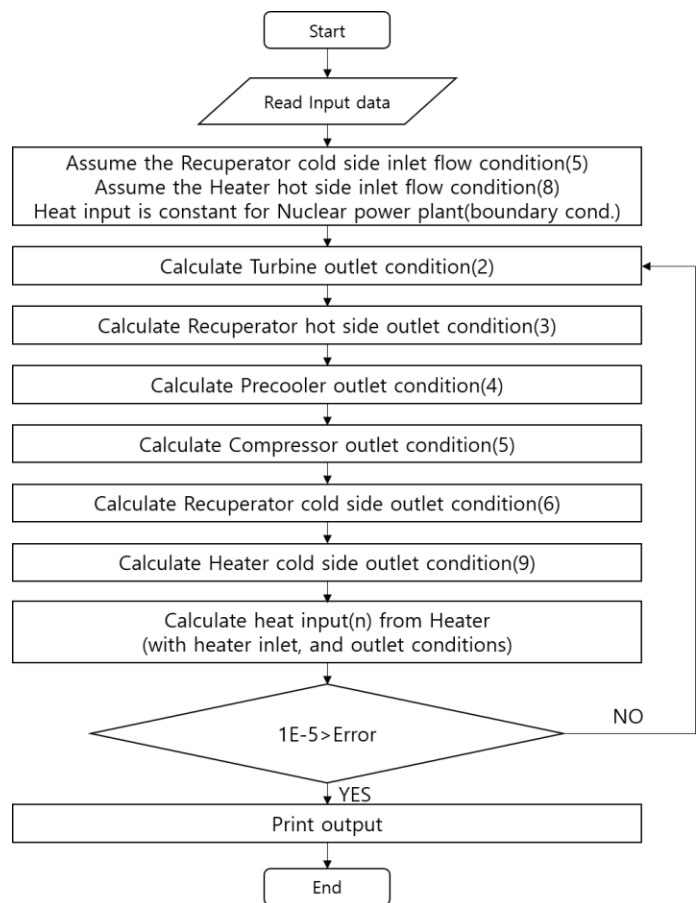


Fig. 3. Main algorithm of KAIST-CCD code for simple recuperated Brayton cycle [4].

Values of material properties such as enthalpy and entropy used in the code are provided by NIST-REFPROP (transport properties database) [11]. To illustrate how KAIST-CCD code works, the algorithm for the simple recuperated Brayton cycle analysis is shown in Fig. 3. The numbers in algorithm in Fig. 3 refer to the node numbers in Fig. 4. First, read input data: fluid type, cycle layout, Total heat received by the cycle, max, min temperature of the cycle, max pressure of the cycle, efficiency, flow split and pressure ratio of the components. Second, the

recuperator cold side inlet flow condition and the heater hot side inlet flow conditions are assumed. Next, the inlet and outlet conditions of each component are obtained using the models of the components and the assumed values. Finally, the heat input is obtained from the calculated condition values.

Since the heat source is prescribed, the error is estimated by comparing the prescribed heat source value to the calculated value. If the error is greater than or equal to 1E-5, the assumed values are updated to the calculated values.

Fig. 4 shows the nodes of the KAIST MMR for the KAIST CCD code. KAIST MMR is a system with a simple recuperated cycle as a power cycle and the shaft connects compressor and turbine to rotate at the same RPM. The CCD code is used to calculate the temperature, pressure, enthalpy, and entropy of each node. Therefore, the original MMR was optimized using KAIST-CCD when the turbine efficiency was changed.

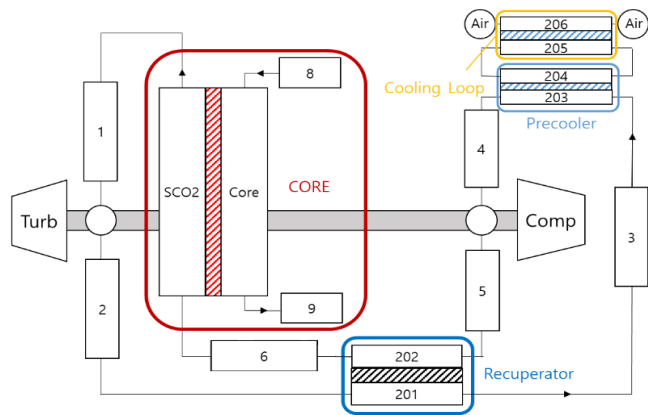


Fig. 4. Nodalization of MMR for CCD code

KAIST-TMD

The KAIST TurboMachinery Design (TMD) code is developed by the KAIST research team written in MATLAB environment. It can estimate the performance and geometry of turbines at the design point and the performance at various off-design points. The design method of KAIST-TMD code is briefly described in this paper and more detail can be found in [5].

Mass conservation (2) and Euler equations (3) are used for the design of turbomachineries based on 1-D mean line analysis because both equations can be applied regardless of the real or ideal gas.

$$\dot{m} = \rho(h_{st}, P_{st})AV \quad (2)$$

$$\Delta h_{turbine} = h_{o2} - h_{o1} = U_2 V_{\theta 2} - U_1 V_{\theta 1} \quad (3)$$

However, since all of the work of the turbomachinery is not produced in an isentropic process, losses have to be considered. Losses measure how far the actual process is from the ideal isentropic process. These losses can be defined with pressure loss

or enthalpy loss as shown in Fig. 5. A literature review has shown that pressure loss models can be easily applied to axial turbomachineries and enthalpy loss models can be applied to radial turbomachineries [12, 13]. Therefore, in KAIST-TMD, the pressure loss models are applied to the axial turbine and compressor, and the enthalpy loss models are used for the radial turbine and compressor design and analyses.

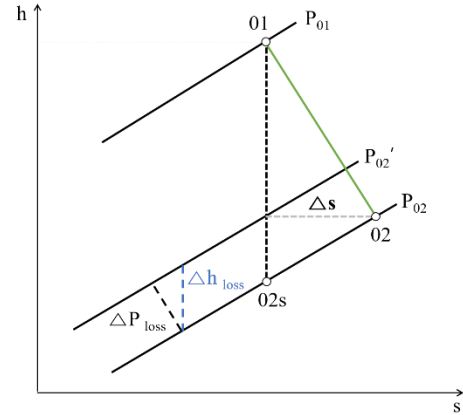


Fig. 5. h-s diagram of enthalpy and pressure loss model

Table.2 Summary of the loss model of each turbomachineries

Axial turbine	
Profile loss	Balje-Binsley [14]
Secondary loss	Kacker-Okaapu [15]
Tip clearance loss	Dunham-Came [16]
Radial compressor	
Incidence loss	Boyce [17]
Blade loading loss	Coppage et al. [18]
Skin friction loss	Jansen [19]
Clearance loss	Jansen [19]
Disk friction loss	Daily and Nece [20]
Mixing loss	Johnston and Dean [21]
Recirculation loss	Oh et al. [13]
Leakage loss	Aungier [22]
Radial turbine	
Incidence loss	Balje [23]
Rotor passage loss	Balje [23]
Clearance loss	Jansen [19]
Disk friction loss	Daily and Nece [20]

Using the models summarized above, a turbomachinery design in-house code, KAIST-TMD, was developed which is again written in MATLAB. The main code structure is shown in Fig. 6.

The main design variables are defined by the designer when designing the turbine with KAIST-TMD. Then the off-design values and the geometry values are calculated through the iteration process with the selected loss models suitable for the

selected turbomachinery. The property values are referred from REFPROP developed by National Institute of Standards and Technology (NIST) [11].

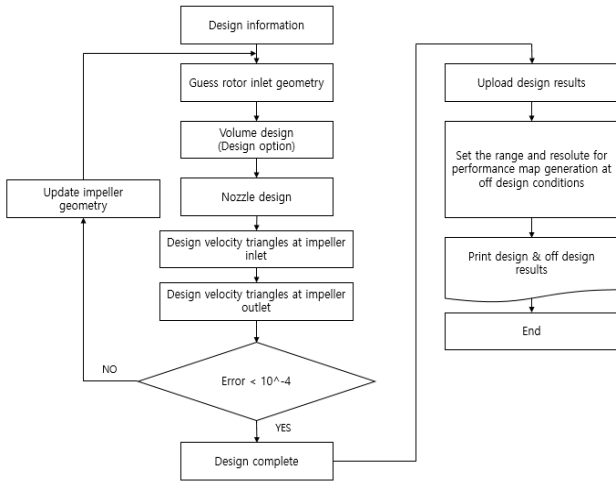


Fig. 6. Main algorithm of KAIST-TMD [5]

KAIST-HXD

The KAIST Heat eXchanger Design (HXD) code is based on MATLAB environment and was developed to design a printed circuit heat exchanger (PCHE) for the S-CO₂ power system applications. To overcome dramatic changes of properties of CO₂ near the critical point, the discretized design and analysis method is adopted in place of widely used conventional heat exchanger design methods such as LMTD method. In KAIST-HXD, the energy and momentum governing equations are solved numerically to calculate properties of CO₂ in finite number of volumes [6]. It performs analysis on the unit channel representing the entire heat exchanger. The total heat transfer for one control volume is calculated as follows.

$$Q = UA\Delta T = \frac{1}{\frac{1}{h'_{hot}A} + \frac{1}{t} + \frac{1}{h'_{cold}A}} \Delta T \quad (4)$$

To obtain pressure drop for one control volume, the friction factor must be determined. Friction pressure drop equation is as follows:

$$\Delta P = f \frac{l}{D_e} \frac{\rho V^2}{2} \quad (5)$$

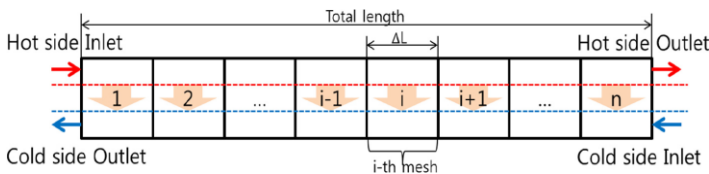


Fig. 7. Channel nodalization in KAIST_HXD [6]

Using the above equations, the inlet and outlet temperatures and pressures for one channel can be determined by the enthalpy change due to heat transfer and the pressure drop due to friction. The cold side can be calculated as above, but since the flow direction of the hot side is opposite to that of the cold flow (i. e. counter current), the calculation starts from the outlet of the cold side to the inlet. Therefore, the property of the cold side outlet should be assumed first. If the cold side inlet result obtained from the assumed cold outlet does not satisfy the cold inlet temperature calculated in the heat transfer equation and pressure boundary conditions, the new cold outlet temperature and pressure are assumed and the calculation is conducted again until the convergence conditions are met.

MOTIVATION OF AXIAL TURBINE DESIGNED UNDER THE CONDITION OF KAIST-MMR

The original MMR is designed to have an output of 12MWe, and the type of turbine satisfying these conditions is shown in Fig. 8 [24], which shows that both radial type turbine and axial turbine can be appropriate. In the previous MMR design, the design choice was using a single stage radial turbine.

TM Feature	Power (MWe)						
	0,3	1,0	3,0	10	30	100	300
TM Speed/Size	75,000 / 5 cm	30,000 / 14 cm	10,000 / 40cm	3600 / 1.2 m			
Turbine type	Single stage Radial		multi stage Axial				
	Single stage Radial	multi stage	single stage Axial	multi stage			
Bearings	Gas Foil		Hydrodynamic oil				
Seals	Adv labyrinth		Dry lift off				
	Magnetic		Hydrostatic				
Freq/alternator	Permanent Magnet			Wound, Synchronous			
	Gearbox, Synchronous						
Shaft Configuration	Dual/Multiple			Single Shaft			

Fig. 8. Component and technology options for S-CO₂ cycles [24]

The existing MMR radial turbine was designed at the boundary between the radial turbine and the axial turbine as shown in Fig. 8. In other words, it is designed to have the maximum capacity that can be covered by the single stage of radial turbine. If the capacity of the existing MMR becomes larger, the number of stages for the radial turbine has to increase or using axial turbine can be another choice. However, in the case of radial turbine, it is not recommended to increase the number of stages because the inter-stage flow path can induce large pressure drop, so an axial turbine can be more appropriate [25]. Before designing an axial turbine for the larger MMR, it is possible to evaluate the performance of an axial turbine compared to a radial turbine for existing MMR.

Therefore, the purpose of this paper is summarized as the following: 1. Design an axial turbine suitable for MMR. 2. Evaluate the potential for using an axial turbine for MMR by comparing off design performance with originally designed single stage radial turbine. The design is performed by using KAIST CCD and TMD codes. For the isolated grid application, timely transient response is imperative, therefore the newly designed MMR was evaluated with GAMMA + code and compared to the radial turbine based on MMR.

COMPARISON OF RADIAL AND AXIAL TURBINES

An axial turbine was designed to replace a radial turbine under the conditions of original MMR using KAIST-TMD code described above. Using the KAIST-TMD code, the following results were obtained.

A turbomachinery map was generated for the range of possible mass flow rates by raising the rpm from 60% to 120% of the design point for performance evaluation. The range of possible mass flow rates depends on the rpm. The minimum possible mass flow rate is 24% of the design point at rpm = 11,580 and the maximum possible mass flow rate is 126% of the design point at rpm = 17,370.

Table 3. The range of performance evaluation and design point of turbine

The range of the mass flow rate (min to max)	24-126%
The range of the rpm	60-120%
The rpm of design point	19300
The mass flow rate of design point	180kg/s

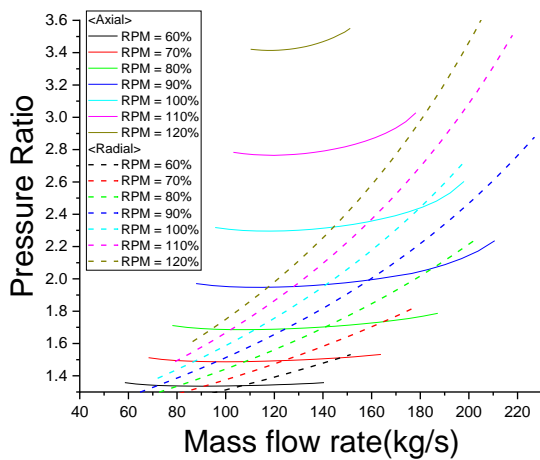


Fig. 9. Comparison of Pressure ratio map for MMR radial and axial turbines

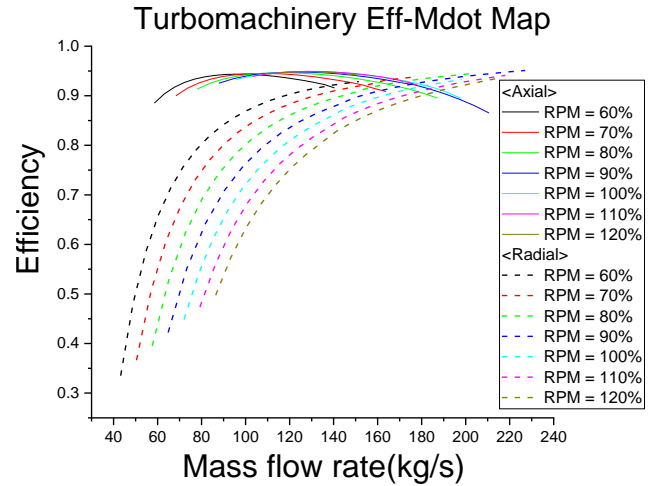


Fig. 10. Comparison of efficiency map for MMR radial and axial turbines

Figs. 9 and 10 show the pressure ratio-mass flow rate map and the efficiency-mass flow rate map of the axial turbine and the radial turbine. Results are generated from KAIST-TMD code. The performance map shown in Figs. 9 and 10 show that the slope is smooth compared to the radial turbine in both pressure ratio and efficiency for the axial turbine when the mass flow rate deviates from the design point. On the other hand, under the same conditions, the radial turbine shows a rapid change in efficiency and pressure ratio, which means that the axial turbine can operate in more stable performance than the radial under the off design operating conditions. In order to analyze these results, loss of radial turbine and axial turbine of KAIST-TMD code were obtained respectively.

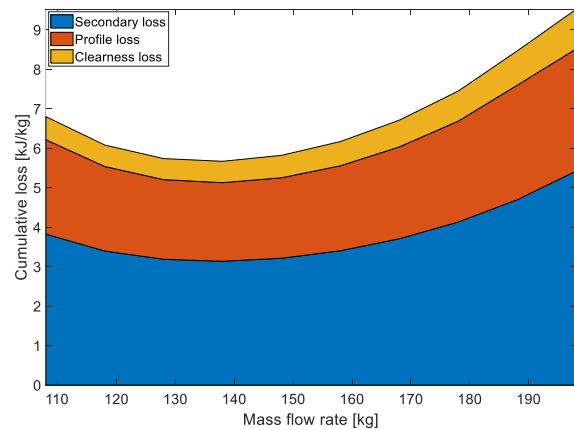


Fig. 11. The cumulative loss of the axial turbine – mass flow rate graph

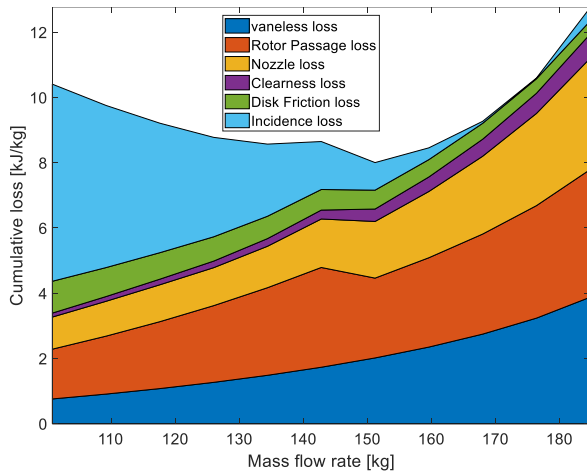


Fig. 12. The cumulative loss of the radial turbine – mass flow rate graph

The losses of radial turbine and axial turbine of KAIST TMD code were obtained as follows. Comparing Figs. 11 and 12, the overall cumulative loss for axial turbine is smaller than that of the radial turbines. Because the incidence loss for radial turbine which is generated during the off-design condition due to the mismatch of the direction of relative velocity of fluid at inlet and inlet blade angle is larger than that of the axial turbine. In addition, the incidence loss decreases with the approach to the design point, but since the vaneless space loss which occurs in a vaneless space between the impeller vane and the diffuser vane becomes larger as the mass flow rate increases, the efficiency of the radial turbine is higher than that of the radial turbine in the wide-range of off-design condition.

Therefore, these results show that the axial turbine has potentially better performance than the radial turbine under the off-design operation, and it is a motive to evaluate the potential of MMR using an axial turbine. As a result, the following design values were obtained and shown in Table 4.

Table 4. TMD code result of axial turbine MMR cycle

Number of stages	8
Turbomachinery work	21.53MW
Total-to-total-Pressure Ratio	2.44
Total-to-total efficiency	91.57%

Using the above results, the cycle was optimized by using KAIST-CCD code. It should be noted that the axial turbine for MMR developed conceptually in this paper is designed to be similar to the CSP turbine which is four stages axial turbine used in the Sunshot project. The developed turbine is for 10 MW power output CSP solution [26].

The CSP turbine was developed by aero design tools and full scale CFD tool was also used. A 4-stage design with 27000 RPM is selected due to the reduction of mechanical stress and the improvement of efficiency as shown in Fig. 13.



Fig. 13. Preliminary flow path layout of the 4-stage axial turbine [26]

Although it is designed with similar concepts, the CSP turbine produces 10 MW_e of power output with 27,000 rpm, four stages, while the axial turbine designed in this paper produces 12MW of power output with 19,300 rpm, 8 stages. From the viewpoint of the number of stages, it seems reasonable that the CSP turbine has better performance than the axial turbine designed in this paper. However, the CSP turbine has an rpm of 27,000, while the MMR axial turbine developed in this paper has an rpm of 19,300 due to the synchronized compressor. Therefore, if the rpm is increased to about 27,000, a turbine with four stage having similar performance can be produced by using KAIST_TMD code. This is left as future works for the further design optimization of the MMR.

OPTIMIZATION OF CYCLE FOR MAXIMIZING EFFICIENCY

In this paper, MMR using axial turbine was optimized under the original MMR condition by KAIST-CCD for selecting the highest efficiency. In other words, in case of MMR using axial turbine, the efficiency and pressure ratio of the turbine are changed from the input values of the original MMR using radial turbine and used as input values in the KAIST CCD code. The new input values of MMR using axial turbine are as follows.

Table 5. The input values of MMR using axial turbine for KAIST CCD

Thermal power	36.2MW _t h	Cycle layout	Simple brayton recuperation
Mechanical efficiency	98%	Total-to-total Pressure ratio	2.44
Turbine total-to-total efficiency	91.57%	Compressor total to total efficiency	85%
Generator efficiency	98%	Rotating speed	19,300rpm
Max Pressure	20Mpa	Recuperator effectiveness	95%
Max Temperature (Turbine inlet)	550 °C	Min Temperature (Compressor inlet)	60 °C

The T-S diagram obtained from the KAIST-CCD code and the property values such as temperature and pressure are shown in Table 6. T-S diagrams for new MMR with an axial turbine are shown in Fig. 14 to compare with the thermodynamic property values of original MMR with the radial turbine. The numbers in Fig. 14 correspond to the node numbers in MMR shown in Fig. 4, respectively.

Table 6. The optimization design value of new MMR using axial turbine

Mass Flow rate		182.15kg/s	
Point	Temperature(°C)	Pressure(Mpa)	
1	550	19.93	
2	440.72	8.17	
3	156.47	8.10	
4	60	8.01	
5	141.96	20	
6	388.48	19.98	
7	550	19.93	

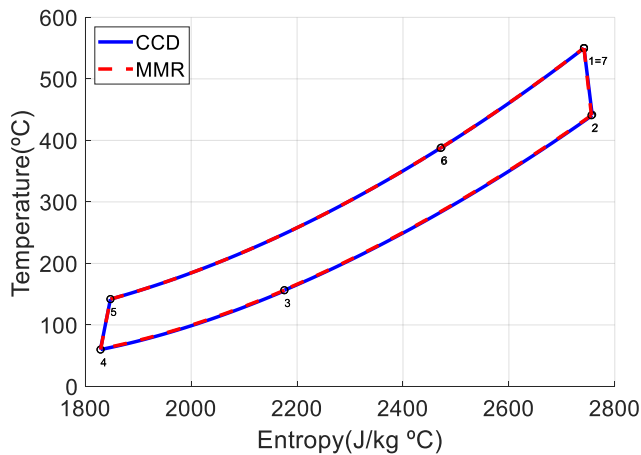


Fig 14. Comparison of T-s diagram of MMR and result of CCD code

As a result, it was confirmed that there is almost no difference in properties between two MMRs. This means that there is almost no difference in the T-s diagram between the cycle using the axial turbine with the best efficiency and that of the radial turbine. Therefore, since the GAMMA + code of original MMR using radial turbine is already constructed, only the turbine will be modified in the GAMMA+ transient simulation.

The KAIST research team modified GAMMA + code to become applicable to the original MMR. GAMMA+ code is originally developed for a gas cooled reactor transient analysis by KAERI. However the original GAMMA + code is designed to calculate the CO₂ properties with simple

correlation, but it was necessary to calculate the CO₂ property values near the critical point more accurately. The modified GAMMA + code used the REFPROP program developed by NIST to solve the above problems [11]. The REFPROP program accurately calculates the thermal and transport properties of various fluids, including CO₂. The modified GAMMA + code with NIST database for CO₂ properties near the critical point was validated using experimental data from SCO2PE [27].

As mentioned above, since the results obtained by using KAIST CCD code and the original value of MMR show no marked changes, GAMMA+ code of MMR can be adopted identically except for the turbine section, which are replaced by newly formed axial turbines. The design points under steady state of the main part of the cycle obtained by GAMMA + code is shown in Fig. 15.

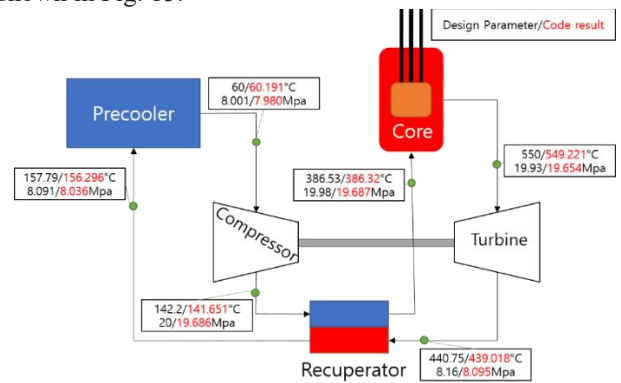


Fig 15. Comparison of design parameters and code result in the main part of the cycle

As shown in Fig. 15, the results of the code also show no dramatic changes compared to the original design points, but a slight difference of 0-0.3MPa occurs for the pressure. This seems to be due to the more precise consideration of the pressure drop using the Blasius ($Re < 30000$) & McAdams ($30000 < Re < 10^6$) correlations for pipe and Baik's correlation [6] for PCHE in GAMMA+ code, while KAIST_CCD does not accurately account for the pressure drop.

To compare the dynamic performance of the new MMR with the axial turbine and the original MMR with the radial turbine, it is assumed that a scenario simulating the load change and it is prescribed by MMR. The load varied from 100% to 70% and then back to 100%. This scenario starts at steady state ($t = 100$ s), during which the load drops from 100% to 70% ($t = 100-300$ s) for 200 seconds and rises from 70% to 100% for another 200 seconds ($t = 400-600$ seconds).

The results using both radial and axial turbines applied to the MMR system are shown Figs. 16 to 25. The load changed to the scenario mentioned above, and the result is shown in Fig. 16.

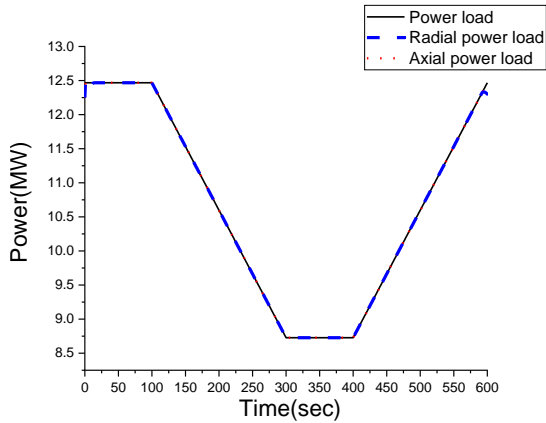


Fig. 16. Load of MMRs with Radial and Axial turbines

The results of the transient analysis show that thermal power of the MMR with an axial turbine are similar to those of the MMR with radial turbine as shown in Fig. 16, and the cycle efficiency of MMR with axial turbine comparable to the MMR with radial turbine in the off-design point in Fig. 18.

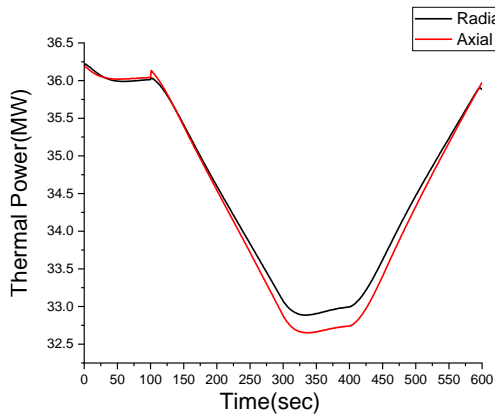


Fig. 17. Thermal power of MMR of Radial and Axial turbines

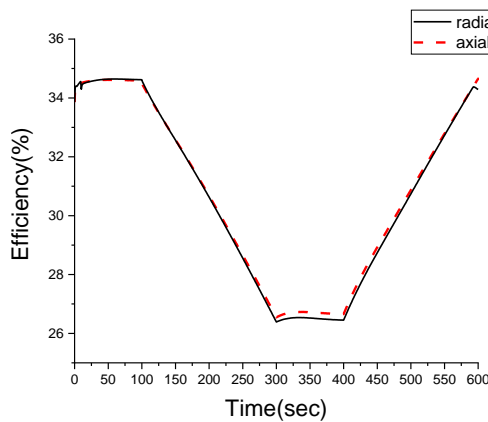


Fig. 18. Efficiency of MMRs with Radial and Axial turbines

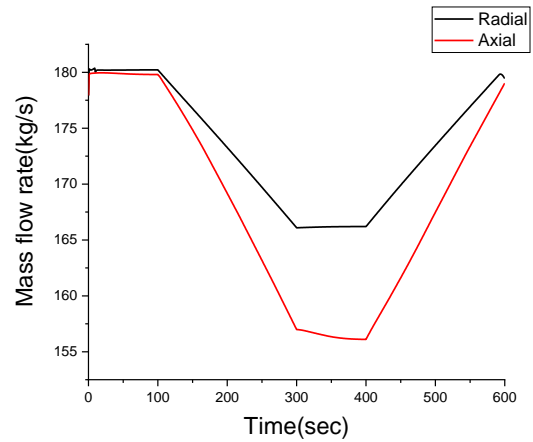


Fig. 19. Mass flow rate of MMRs with Radial and Axial turbines

Displayed from the efficiency maps of radial turbine and axial turbine in Fig. 10, the efficiency graphs of the axial turbine remain unchanged from the design efficiencies, whereas the graphs of the radial turbine drop abruptly as the mass flow rate decreases as shown in Fig. 19.

In Fig. 20, it can be seen that there is almost no difference between the radial and axial turbine works. This is because the same radial compressor was used and the thermal power and efficiency in axial and radial cases are similar, as shown in Figs. 16 and 17.

$$\dot{W}_{t,turbine} = \dot{Q}_{core}\eta_{thermal} + \dot{W}_{t,compressor} \quad (6)$$

Where $\dot{W}_{t,turbine}$ = Turbine work, $\dot{W}_{t,compressor}$ = Compressor work, \dot{Q}_{core} = Thermal power of MMR, $\eta_{thermal}$ = thermal efficiency of cycle.

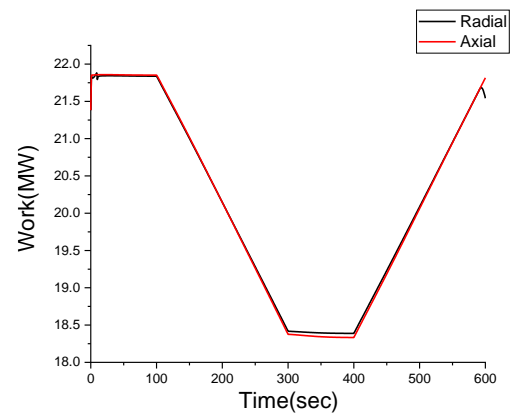


Fig. 20. Turbine work of MMRs with Radial and Axial turbines

The radial and axial turbine works are similar, but the mass flow

rate is relatively different. Therefore, the relationship between turbine work and mass flow rate has to be considered.

The formula for turbine work is:

$$\dot{W}_{t,turbine} = \dot{m}\Delta h_{turbine} \quad (7)$$

Where $\Delta h_{turbine} = h_{o2} - h_{o1} = U_2 V_{\theta 2} - U_1 V_{\theta 1}$, Enthalpy difference between the turbine inlet and outlet

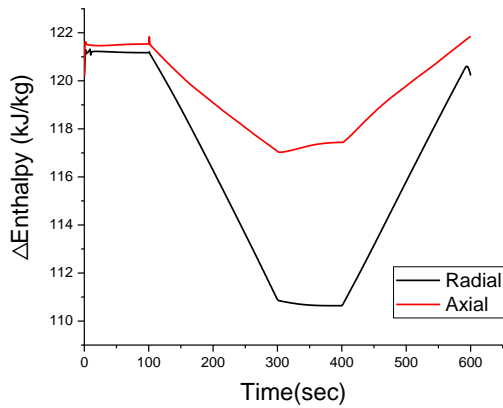


Fig. 21. Enthalpy change between the turbine inlet and outlet of MMR of Radial and Axial turbines

At the off-design point, the enthalpy difference ($\Delta h_{turbine}$) of the MMR with axial turbine is larger than that of the MMR with radial turbine as shown in Fig. 21 because the mass flow rate (\dot{m}) of the axial turbine is relatively reduced and turbine work of the axial and radial is no difference.

The implications of the results show the advantages of using the axial turbine over the radial turbine. Although the axial turbine operates at comparable efficiencies to radial turbine for off-design ranges, it retains its high $\Delta h_{turbine}$ compared to the radial turbine which consequently leads to having lower mass flow rate under a given turbine work. As a result, the specific work of the turbine is increased at lower load conditions when the axial turbine is adopted as shown in Fig. 21. The advantage will be amplified as the system capacity increases, and thus, the axial turbine will prove beneficial for larger size systems.

SUMMARY AND FUTURE WORKS

In this paper, an axial turbine was designed to replace the radial turbine of the KAIST MMR and the transition analysis was performed.

First, axial turbine was designed with KAIST_TMD code by using MMR design conditions for radial turbine system (turbine inlet temperature and pressure, turbine outlet pressure, rpm, mass flowrate) developed by KAIST research team. As a result, an

axial turbine with eight stages was designed which has a turbine work of 21.53 MW, a pressure ratio of 2.44, and a turbine efficiency of 91.57%.

Second, an optimization was performed with KAIST_CCD code using the newly designed system with axial turbine. As a result, the T-s diagram shows that there is almost no difference between the properties of the original MMR and the new MMR. Therefore, the code for performing the transition analysis with GAMMA+ code was created by using the operating conditions of the existing MMR, except for the newly developed axial turbine.

Third, in order to perform the transient analysis of MMR with axial turbine, GAMMA+ code is implemented at the scenario where load is changed from 100%-70%-100%. As a result, it was found that the efficiency of the MMR with axial turbine is comparable to the near design point and wider operating range of MMR is possible with axial turbine. Furthermore, axial turbine shows high specific work compared to the radial turbine which leads to having lower mass flow rate for the given turbine work. As a result, the specific work by the turbine can be increased at lowered load conditions when the axial turbine is adopted in the system.

In this study, the potential of the axial turbine was confirmed in terms of specific work under the off-design conditions when axial turbine or radial turbine is used. The axial turbine is more advantageous with respect to the specific work compared to the radial turbine under off-design conditions and these advantages will be amplified as the system becomes large. In addition, when the new system is bigger than the system of MMR, the advantages of axial turbine is maximized because axial turbine has better efficiency than the radial turbine for larger system.

Finally, the planned future works are to design the MMR with 4-stage axial turbine to operate at higher efficiency.

NOMENCLATURE

A	Surface area of the heat transfer [m ²]
A'	Flow area [m ²]
D	Diameter [m]
D _e	Equivalent diameter [m]
K	Form loss
P	Pressure [Pa]
Q	Thermal power [W]
R	Chemical reaction
T	Temperature [K]
U	Impeller tip speed [m/s]
V	Flow velocity [m/s]
Y	Mass fraction
W	Relative velocity [m/s]
W _t	Specific work [W/kg]
f	Friction factor

g	Gravitational acceleration [m/s ²]
h	Enthalpy [J/kg]
h'	Heat transfer coefficient [W/m ² K]
m	Mass flow rate [kg/s]
q	Specific heat [J/kg]
q''	Heat flux [W/m ²]
j	Diffusion flux [mol/m ² s]
t	Time [sec]
z	Height [m]
ρ	Density [kg/m ³]

Subscript	
o	Stagnation condition
s	Species
st	Static condition

REFERENCE

- [1] Steven A. Wright, Ross F. Radel, Milton E. Vernon, Gary, E. Rochau, Paul S. Pickard, "Operation and Analysis of a Supercritical CO₂ Brayton Cycle, Sandia National Laboratories, Sandia Report", SAND2010-0171.
- [2] White, C., "Analysis of Brayton Cycles Utilizing Supercritical Carbon Dioxide," National Energy Technology Laboratory, DOE/NETL-4001/070114 (2014).
- [3] S. G. Kim, et al., Conceptual System Design of a Supercritical CO₂ cooled Micro Modular Reactor, Proceedings of ICAPP, 2015.
- [4] M.S.Kim, Y.H.Ahn, B.J.Kim, J.I.Lee, "Study on the supercritical CO₂ power cycles for landfill gas firing gas turbine bottoming cycle.", Energy, 111(2016), pp. 893-909
- [5] J.K. Lee, J.I. Lee, Y.H. Ahn and H.J. Y, Design methodology of supercritical CO₂ brayton cycle turbomachineries, ASME Turboexpo, Copenhagen, Denmark, 2012
- [6] Seungjoon Baik, Seong Gu Kim, Jekyoun Lee, Jeong Ik Lee, "Study on CO₂-water printed circuit heat exchanger performance operating under various CO₂ phases for S-CO₂ power cycle application", Applied Thermal Engineering, 2017.
- [7] Kofskey, Milton G., and Donald E. Holeski. Cold performance evaluation of a 6.02-inch radial inflow turbine designed for a 10-kilowatt shaft output brayton cycle space power generation system. Vol. 2987. National Aeronautics and Space Administration, 1966
- [8] S.K.Cho. "Study on supercritical CO₂ radial turbine design methodology for decay heat removal system of sodium cooled fast reactor." (2016).
- [9] J.H.Kim. "A Review of Helium Gas Turbine Technology for High-temperature Gas-cooled Reactors". Nuclear Engineering and Technology, v. 39. no. 1, pp.21-30(2007)
- [10] Takizuka, Takakazu, et al. "R&D on the power conversion system for gas turbine high temperature reactors." Nuclear Engineering and Design 233.1-3 (2004): 329-346.
- [11] E.W. Lemmon, M.L. Huber, and M.O. McLinden, "NIST Standard Reference Database 23," NIST Reference Fluid Thermodynamic and Transport Properties –REFPROP, version, vol.9, p.55, 2010.
- [12] Ji Hwan Kim, Hee Cheon No. A Gas Turbine Code for Off-Design Performance and Transient Analysis of High-Temperature Gas-Cooled Reactors, 2008.
- [13] Hyoung Woo Oh, Myung Kyoong Chung. Investigation on the Design and Performance Analysis Methods of Centrifugal Turbomachines, 1998.
- [14] O.E. Balje and R.L. Binsley, Axial turbine Performance Evaluation. Part A - Loss-Geometry Relationship, Journal of Engineering for Power, Transactions of the ASME, pp. 341-348, 1968.
- [15] S.C. Kacker and U. Okapuu, A Mean Line Prediction Method for Axial Flow Turbine Efficiency, Journal of Engineering for Power, Transactions of the ASME, Vol. 104, pp. 111-119,1982.
- [16] Dunham, J., and P. M. Came. "Improvements to the Ainley-Mathieson method of turbine performance prediction." Journal of Engineering for Power 92.3 (1970): 252-256.
- [17] Boyce, Meherwan P, Centrifugal compressors : a basic guide, PennWell, 2003
- [18] Coppage, J. E., Dallenbach, F., Eichenberger, H. P., Hlavaka, G. E., Knoernschild, E. M. and Van Lee, N. Study of supersonic radial compressors for refrigeration and pressurization systems, WADC Report 55-257, 1956.
- [19] Jansen, W. A method for calculating the flow in a centrifugal impeller when entropy gradients are present, Royal Society Conference on Internal Aerodynamics (Turbomachinery),1967 (IME).
- [20] Daily, J. W. and Nece, R. E. Chamber dimension effects on induced flow and frictional resistance of enclosed rotating disks, Transactions of the ASME, J. Basic Engng, Vol. 82, pp.217-232, 1960.
- [21] Johnston, J. P. and Dean Jr, R. C. Losses in vaneless diffusers of centrifugal compressors and pumps. Analysis, experiment, and design, Transactions of the ASME, J. Engine for Power, Vol. 88, pp. 49-62, 1966.
- [22] Aungier, R. H., Mean streamline aerodynamic performance analysis of centrifugal compressors, Transactions of the ASME, J. Turbomachinery, Vol. 117, pp. 360-366, 1995.
- [23] Balje, O. E., A Contribution to the Problem of Designing Radial Turbomachines, Transactions of the ASME, Vol. 74, pp. 451, 1952
- [24] Siemicki James J., Anton Moiseyev, Robert L. Fuller, Steven A. Wright and Paul S. Pickard, "Scale Dependencies of Supercritical Carbon Dioxide Brayton Cycle Technologies and the Optimal Size for a Next-Step Supercritical CO₂ Cycle Demonstration", SCO₂ Power Cycle Symposium, 2011.
- [25] Philip P. Walsh, Paul Fletcher, "Gas Turbine Performance", Second Edition, pg 206- 215, 2004.
- [26] Chiranjeev Kalra, et al., Development of high Efficiency hot gas turbo-expander for optimized CSP supercritical CO₂ power block operation, The 4th International Symposium - Supercritical CO₂ Power Cycles
- [27] Bae, Seong Jun, et al. "Comparison of gas system analysis code GAMMA+ to S-CO₂ compressor test data." ASME Turbo Expo 2015: Turbine Technical Conference and Exposition. American Society of Mechanical Engineers, 2015.

DEVELOPMENT AND TESTING OF DRY GAS SEALS FOR TURBOMACHINERY IN MULTIPHASE CO₂ APPLICATIONS

Armin Laxander

EagleBurgmann Germany GmbH & Co. KG
Wolfratshausen, Germany

Andreas Fesl

EagleBurgmann Germany GmbH & Co. KG
Wolfratshausen, Germany

Benjamin Hellmig*

EagleBurgmann Germany GmbH & Co. KG
Wolfratshausen, Germany

Email:

benjamin.hellmig@eagleburgmann.com

ABSTRACT

Shaft seals have a substantial impact on turbomachinery performance. Due to minimized friction and low leakage rates, mechanical dry gas seals outpace other shaft sealing technologies in terms of efficiency when it comes to sealing gases at elevated pressures. Therefore, dry gas seals are standard equipment for most centrifugal compressors nowadays. Even in some pump applications, they have shown significant advantages for sealing liquid media. Dry gas seals are an important tool to optimize supercritical carbon dioxide (sCO₂) turbomachinery and therefore sCO₂ power cycles to the desired levels of efficiency.

The special characteristics of CO₂ are challenging for the safe operation of dry gas seals in CO₂ applications. E.g., we must avoid icing of CO₂, related to the Joule-Thomson effect when expanding CO₂ through the sealing gap, must be avoided. In addition, transitions between supercritical and liquid phase need to be carefully addressed.

EagleBurgmann is a manufacturer of dry gas seals and has constructed a CO₂ test loop for operating dry gas seals in a CO₂ environment, covering all non-solid phase conditions, i.e. gaseous, supercritical, liquid and liquid-gas. Moreover, dry gas seal designs, especially dedicated to operation in sCO₂ pumps and compressors have been developed.

The paper shall give insight into the seal and test loop design, the test campaign and results.

INTRODUCTION

Carbon dioxide and particularly supercritical CO₂ (sCO₂) plays a very important role in modern industrial processes, e.g. urea production, carbon capture and storage and enhanced oil recovery. Therefore, the need for sCO₂ turbomachinery will continue to grow in the future. In recent decades, supercritical CO₂ has gained even a lot more attention since it proves exceptionally attractive as a working fluid in power cycle applications. Numerous articles have been published describing the advantages of alternative power cycle technologies, being much more efficient and cost-effective compared to standard power generation, for example, the classical steam Rankine cycle [4, 5, 6].

Any process or power cycle efficiencies will be closely related to the employed sealing technology in turbomachinery equipment.

Dry gas seals are referenced in most of the above applications and are the standard choice due to their low leakage, friction losses, absence of wear and low power consumption. They are considered a substantial component for the development of efficient sCO₂ turbomachinery.

Apparently, in mere gaseous or supercritical applications a non-contacting dry gas seal will be the preferred design solution. It is less clear when multiphase conditions or phase transitions have to be managed by the seal. There are different approaches to encounter the demand for lowest possible CO₂ leakage [1].

The design solution presented in this paper entirely relies on a non-contacting operation mode in dynamic conditions, thus avoiding any uncertainties or issues with degrading seal performance due to worn or at least partially worn sliding faces.

Although designated as a dry gas seal, all kinds of non-solid CO₂ phase conditions must be reliably covered in order to guarantee operational safety. Cycle efficiency can be optimized when operating at the critical point. Yet, the risk of slipping into the two-phase region is quite high due to slight variations in pressure or temperature [10]. Prior to any industrial application, it is evidently recommended to prove operational safety of a new design in the entire range of pressures, temperatures and speeds in a CO₂ environment.

As to CO₂ commercial seal applications, there is only few published material available explaining in some detail the design, analytical methods and testing results, e.g. [1]. Detailed 3D CFD simulation results addressing the particular characteristics of CO₂ are usually restricted to the flow in the sealing gap, which has a prescribed constant shape [2]. These studies provide better understanding of physical effects in the sealing gap. However, since there is no thermal and mechanical coupling with the structural parts, methods and findings cannot be applied in industrial engineering work.

This paper focusses on describing a CO₂ multiphase seal design solution. The presentation encompasses design, numerical analyses and extensive testing results. Some essential functional principles in DGS technology, also application examples are given in [3]. Although the presented paper is a design solution for pump applications, the fundamental technology can also be employed in high-speed and high-pressure applications as required for compressors.

CO₂ MULTIPHASE SEAL

The CO₂ multiphase seal is basically a dry gas seal. Dry gas seals are gas lubricated mechanical seals, which are mounted between the impellers and the bearings of a pump, compressor or turbine shaft to seal the high-pressure process chamber against atmospheric conditions.

There are many references describing basic functional principles in theory and application related [7, 3]. At this point, only some major aspects related to the current application will be addressed.

The pressure requirements appearing in CO₂ industrial applications vary in a quite extensive range. The seal design follows the principles of a dry gas seal, but with the full intention to work with liquid, two-phase, gaseous and supercritical CO₂. The major seal design conditions are as follows:

- Pressure 0 ... 250 barg
- Material design temperature -50 ... 230°C
- CO₂ temperature in seal cavity -25 ... 160°C
- Maximum speed: 3600 rpm

It is common to employ a tandem seal arrangement as shown in Figure 1. The outboard seal, which has exactly the same design as the inboard seal, works primarily as a redundant seal. In the event of an IB seal failure, the OB seal still ensures safe operation. The biggest fraction release of the CO₂ leakage will

be via connection “B” into the vent. Only a small fraction of CO₂ leakage passes through the OB seal.

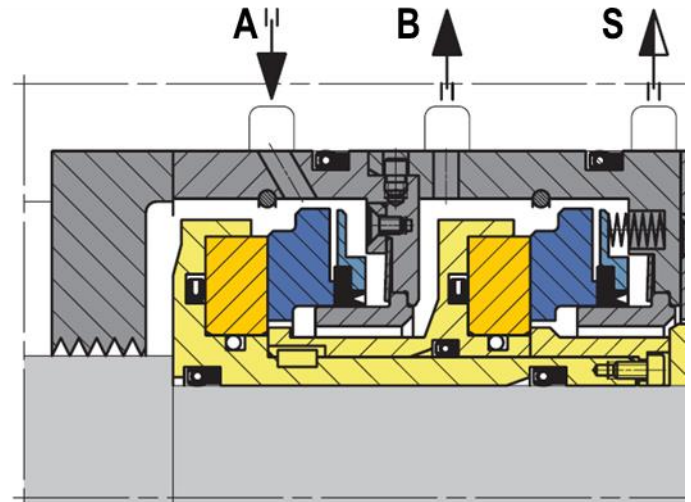


Figure 1: Multiphase seal in tandem arrangement (cross-section)

In the case of spatial restrictions or the abundance of the OB seal is acceptable, a single seal arrangement may be adopted. A single seal arrangement particularly requires well-defined conditions downstream of the IB sealing gap, e.g. the presence of humidity in conjunction with temperatures below 0°C can cause severe problems.

It is strongly recommended to always ensure a constant clean gas supply to the seal via connection “A” at all operating conditions, i.e. static and dynamic. The flow from the seal cavity back to the impeller through the process labyrinth prevents contaminated CO₂ reaching the sealing gap. For some of the tests described in the following, the single seal arrangement is realized by the simply disassembly of the outboard faces.

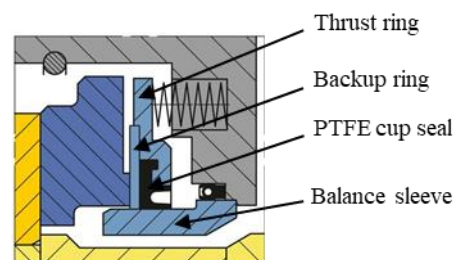


Figure 2: Dynamic secondary sealing unit (cross-section)

Figure 2 depicts some details of the secondary dynamic sealing unit. Backup ring and balance sleeve, both made of extremely stiff tungsten carbide, allow optimal control of the extrusion clearance between both parts in the entire pressure range. The specific design of the PTFE cup seals ensures minimum sliding forces combined with wear-free operation. Evidently, the operating contact pressure between the PTFE cup seal and the balance sleeve must still be sufficiently high to guarantee safe sealing against CO₂ leakage. Any secondary CO₂

leakage can severely affect the seal functionality, as will be demonstrated in the section presenting the experimental results.

Not only the high-pressure application range, but also the compromising effects of supercritical CO₂ prohibit employing elastomer secondary seals. All secondary seals exposed to CO₂ are PTFE based seals.

As base material for primary and mating ring, silicon carbide is selected. The particular material properties – very high Young’s modulus and very low *TEC/TC* ratio prove particularly appropriate for dry gas seal design solutions. Of course, a hard-hard combination of sliding faces requires a non-contacting, and thus wear-free operation throughout all dynamic operating conditions beyond the pertaining lift-off speed. Certainly, extensive preceding numerical simulation effort is required before entering final design, manufacturing and eventually testing.

Dry gas seals do need some kind of profiling on one of the rings to be able to establish a safe sealing gap throughout all operating conditions. These periodic face features may work either in both rotational directions or in only a single direction. All major seal suppliers have their own particular gas groove design and respective software tools to describe its specific 3D shape. The seal discussed in this paper has bidirectional grooves, cf. Figure 3.



Figure 3: EagleBurgmann U-type groove profiled seat. Due to the DF coating, the gas grooves hardly appear visible.

As a standard, the silicon carbide rings are coated with a DLC layer of a few micrometers. This is sufficient to protect the faces against wear in contact operation always occurring during start/stop sequences. The ultimate key feature of the CO₂ multiphase seal is the DiamondFace® coating on the sliding faces. DiamondFace® is an innovative microcrystalline diamond coating for mechanical seals. It is extremely hard and offers very high wear protection in case of fluid contamination, and excellent heat conductivity, maximum chemical resistance and low friction at low-speed contacting operation. Employing DF coating, the operating sealing gap height can again be reduced compared to standard dry gas seals, which is evidently beneficial

to the low-leakage design intent. Increased torque during start-up and shut-down is accounted for by specifically designed torque transmission features.

Dry gas seals with DiamondFace® coating have been utilized for many years in applications where gas phase transitions have to be accounted for, mostly ethane and/or ethylene applications. More than 150 DF coated seals have been successfully deployed in first installations of pumps or as replacement for poorly performing seals in existing applications [11].

CO₂ SPECIAL CHARACTERISTICS

The pressure-enthalpy diagram is most appropriate to describe the special characteristics of CO₂, cf. Figure 4. Whereas in the transcritical region, i.e. above the critical point, changes in physical properties are going rather smooth with pressure and temperature, these changes are locally substantial, in particular, inside the "dome", when moving towards and eventually crossing the liquid saturation line. The dome may be referred to as the region in the pressure-enthalpy diagram bounded by the two saturation lines, liquid and vapor. In the supercritical region, sCO₂ adopts properties midway between a gas and a liquid. Whereas dynamic viscosity is still on levels of gaseous fluids, the density is like that of a liquid.

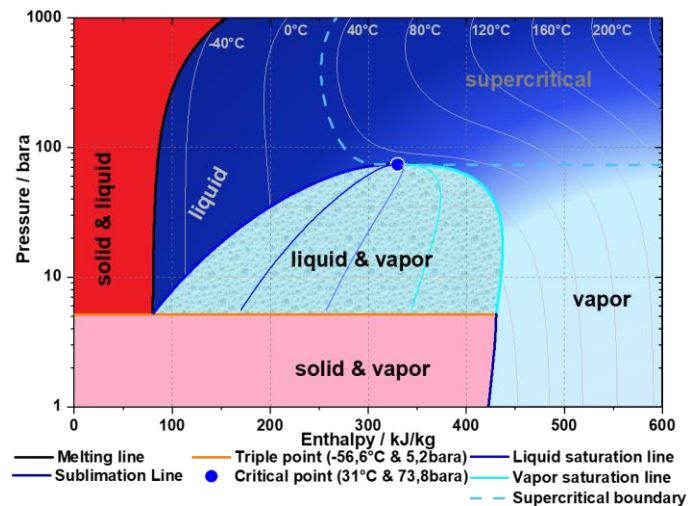


Figure 4: CO₂ pressure-enthalpy diagram.

Even in the liquid phase, also in the subcritical region, CO₂ retains certain properties more like of a gas. There is still a certain level of compressibility, which is not only important for operational efficiency in turbomachinery thermodynamic cycles but also provides some ease to numerical analysis. Regarding seal performance, the lower dynamic viscosity compared to liquid hydrocarbons and especially water will produce less frictional heat. Consequently, less thermally induced distortion of the rings is generated which benefits operational safety.

From a seal design point of view, the dry gas seal should always work as a transcritical system. This is, however, not realistic in most industrial applications. In fact, operating near the critical point in sCO₂ cycles offers various advantages and increases overall efficiencies. Although systems may be designed to avoid touching or crossing the dome when moving from one state to another, there is hardly entire control in a real process on major physical parameters, i.e. pressure and temperature. Deviations from the design point, e.g. slipping into the two-phase region, with all its unwanted implications, must be considered in dry gas seal design.

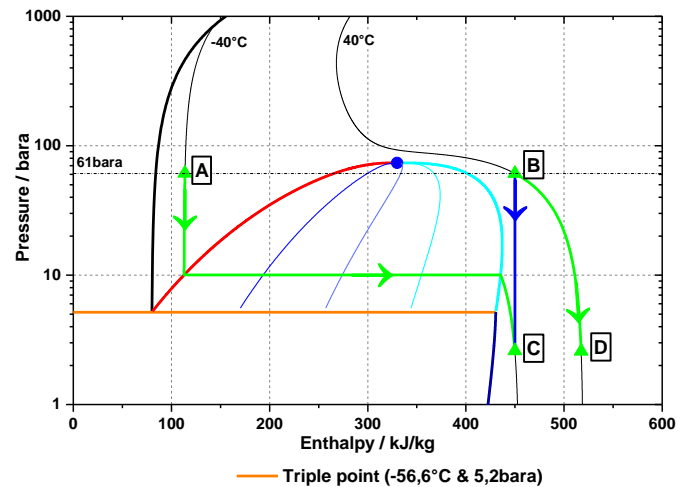


Figure 5: CO₂ expansion scenarios from 60 barg.

The temperature distribution in the vapor region is of even more importance. The difference between isothermal and adiabatic expansion is tremendous due to the very high Joule-Thomson coefficient. This is demonstrated by various expansion scenarios, as depicted in Figure 5. To end up at low pressure and minus 40°C, one may start at high pressure, 60 barg/-40°C and expand isothermally, A → C, or start from 60 barg/+40°C and expand adiabatically, B → C. Starting from 60 barg/+40°C, expanding to low pressure and +40°C is again an isothermal process. Whether expanding adiabatically or isothermally, or at least close to the ideal thermodynamic changes of state, respectively, is solely depending on the amount of leakage. Low leakage allows sufficient heat to be transferred from seat and seal face into the fluid, thus keeping the fluid temperature virtually unchanged. In the opposite extreme, if the amount of flow is high, the rate of heat transferred from the rings is not sufficient to compensate the temperature drop in the CO₂. Starting from lower temperatures than +40°C might even end up at the triple point including dry ice formation. For both scenarios – isothermal and isenthalpic expansion – test results will be presented.

As will be described in more detail in the following section, even isothermal expansion may not go entirely smooth when varying the cavity temperature, again referring to the 60 barg cavity pressure case. There will be some dependency on the

actual cavity temperature. In the pressure-enthalpy diagram, cf. Figure 5, the 60 barg line is aligned with the 22.7°C isothermal inside the dome where phase change takes place between gas and liquid. When approaching the boundaries from higher (right) or lower temperature (left), i.e. moving A and B closely towards the dome boundaries, resulting in noticeable changes in leakage behavior. This is obviously in conjunction with substantial changes of physical properties, in particular *HTC*, density and dynamic viscosity in the respective temperature range.

Consequential to all above considerations, the aim of any CO₂ seal design must be low leakage levels throughout the entire operating range. Thus, adverse effects on seal performance by the particular behavior of CO₂ can be largely avoided. It is also recommended to ensure always clean gas supply to the seal at all operating conditions, i.e. static and dynamic.

NUMERICAL ANALYSIS

Low duty mechanical seals may be designed by merely adopting basic analytical formulas and empirical rules, whereas dry gas seal design largely relies on computational analysis methods. Employing numerical design tools is utterly indispensable considering the strongly coupled physical effects of fluid dynamics, structural mechanics and thermodynamics.

In the course of theoretical investigations, it is important to gain as much information as possible about the seal performance to be expected. Ideally, subsequent test campaigns turn out only to be a design verification procedure, essentially confirming the design intent.

EagleBurgmann employs SealAnalysis [8], a coupled fluid-structure solver particularly designed for narrow gap flows for both, liquid and gaseous fluids. SealAnalysis, as a simulation kernel, is embedded in a wider software environment, which efficiently integrates all required individual tasks in the context of seal design and performance optimization.

It is absolutely necessary for CO₂ simulations to properly account for real gas effects in the equation of state. SealAnalysis employs tabulated physical properties calculated with REFPROP [9]. REFPROP, released by NIST, uses the Span and Wagner equation of state, a well-established model for CO₂, which fits well to experimental data particularly around the critical point.

Usually, there are separate solution algorithms each accounting for a specific thermodynamic state of the fluid, i.e. either liquid or gaseous. There are algorithms accounting also for phase transition problems, however, they often do not prove appropriate for dry gas seals with radially much larger extended sealing gaps compared to liquid seals. Yet, in contrast to water, for example, the particular properties of CO₂ allow to evade a possible numerical conflict. Due to the remaining compressibility in the liquid region, a pure gas solver can be employed to calculate seal performance even when moving through the gas-liquid into the liquid phase. Numerical stability and convergence to reasonable solutions is maintained. The

sonic transition phenomenon involving dynamic instabilities of the gas film as described in [12] is not considered relevant for the present application. Even at high cavity pressures PI the radial flow velocity is fairly low in the entire sealing gap and may reach sonic speed only at the gap outlet at nearly ambient pressure.

In the following, various results from numerical analyses will be discussed in detail. Figure 6 depicts the calculated CO_2 leakage in the entire operating range of the multiphase seal. The fluid condition of state varies between gaseous and supercritical.

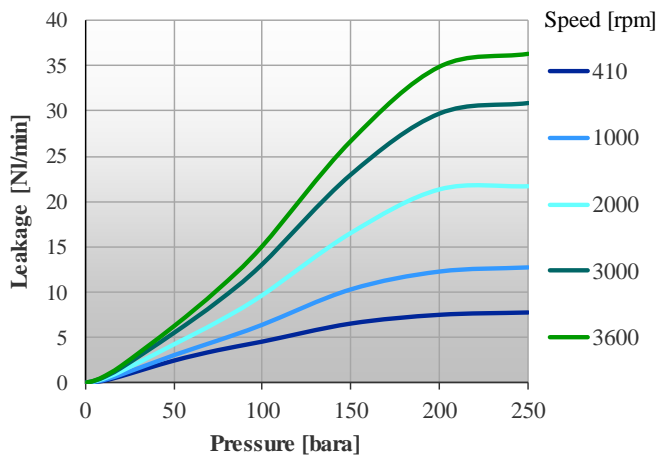


Figure 6: Predicted CO_2 leakage for a 113mm bidirectional seal assuming 100°C constant ambient temperature

TEST RIG

The test facility, located at the R&D center, allows switching with little expense between standard high-pressure dry gas seal testing and CO_2 testing, cf. Figure 7. In Figure 8 a severely reduced scheme of the CO_2 testing configuration is presented. The major parameters of the test rig are as follows

- Test gas: CO_2 , Air, N_2 , N_2 -He mix and He
- Shaft size: 50 ... 300mm
- Max speed: 20000 rpm
- CO_2 heating/cooling and circulation as closed loop
- CO_2 temperature control range: 20 ... 120 $^\circ\text{C}$
- CO_2 supply (max): 1000NI/min
- CO_2 max. testing pressure: 200 bar
- He max. supply pressure: 700bar

Temperature measurements can be added as needed. Leakages are measured for DE and NDE seal each. Due to spatial restrictions, thermocouples are sometimes placed on the balance sleeve instead of on the seal face, as done in the test configuration. Temperature differences between seal face and

balance sleeve are usually small. The seal size is 113mm, which refers to the inner diameter of the seat.

The CO_2 is circulated through the inboard cavities of DE and NDE seals. The integration of a heater and a cooler into this loop allows control the CO_2 inlet temperature. As recognized not until running the test campaign, the electrical heater reveals certain deficiencies concerning the CO_2 temperature control. Consequently, in some test sequences, in particular around the critical point, the CO_2 temperature jumped into a fluctuation mode, and it was hardly possible to stabilize the temperature again on a constant level.

The scheme in Figure 8 shows a tandem seal configuration with DE and NDE seals arranged face-to-face which accounts for thrust balance.



Figure 7: Test facility viewed from control room.

The temperature-controlled loop operation has only been applied to the tandem seal configuration according to Figure 8. The outboard seal in the tandem arrangement is supplied by the CO_2 backpressure, built up in the primary vent. The single seal tests, i.e. only inboard seals were mounted, were run as dead-end operation without heater or cooler. Purpose of this test series is to demonstrate the functionality of the seal under normal operating conditions without ‘well-protected’ inner seal cavity by pure CO_2 or N_2 , respectively. The sealing gap outlet is then exposed to possible humidity. Any malfunction, i.e. usually excessive leakage, may lead to ice formation and possible subsequent damage.

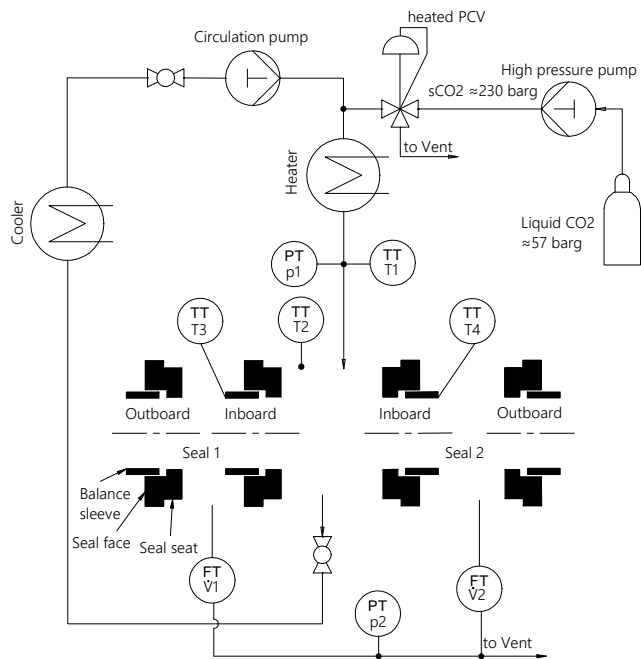


Figure 8: Simplified process & instrumentation diagram of CO₂ loop testing configuration.

TEST RESULTS AND ANALYSIS

In this paper, the focus is exclusively on pump seals. CO₂ pump seals often create more difficult challenges than compressor seals, which, at least, operate dynamically always in the gaseous or supercritical region. The design philosophy is quite similar; also, successful testing results exist.

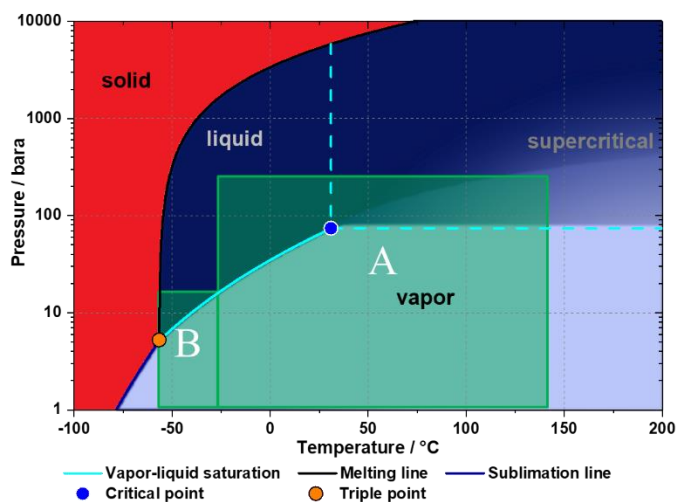


Figure 9: CO₂ testing range, A – standard performance testing, B – failure case.

In Figure 9 the scope of testing is depicted. Region A describes the standard performance testing range. The seal is subjected to phase transitions not only in the sealing gap, but also in the sealing cavity. Region B pertains to deliberately designed failure tests, primarily, to demonstrate the effect of adiabatic expansion and unacceptably high CO₂ leakage.

The test campaign is conducted to explore the seal behavior and seal performance in the described operation range. The results presented will confirm the seal design and demonstrate impressively predictive and analytic capabilities provided by numerical simulation.

As to the 113 seal, the maximum design pressure is 250barg, but the CO₂ maximum testing pressure is limited to 200barg (static) and 180barg (dynamic), respectively. A series of basic qualification tests with air as testing fluid preceded the CO₂ test campaign. After successful completion of the air pre-tests, a dedicated CO₂ test program has been set up.

Tandem seal - static tests:

- 60, 80 and 200barg with temperatures 0 ... 120°C
- 60barg long-term (18h), cooling down after dynamic run
- 200barg long-term (14h), cooling down after dynamic run

Tandem seal - dynamic tests:

- 60, 80 and 180barg with temperatures 20 ... 120°C, speed 3600rpm

Single seal - static tests:

- 60 and 200barg, ambient temperature, long-term (48h)
- 200barg long-term (14h), ambient temperature

Single seal - dynamic tests:

- 60 and 180barg with temperatures 0 ... 70°C, speed 3600rpm

The most interesting sequences of this extensive test campaign will be presented.

Static test without temperature control at 60barg

Testing a quite realistic scenario is looking at the pressurized system after a dynamic run at pressures lower than the critical point. The heater in the CO₂ loop is deactivated. The recordings in Figure 10 show seal cavity pressure, leakages of DE and NDE seals, temperatures in seal cavity and on balance sleeves. The plot starts right after a long 3600rpm run at 60barg and portrays the cooling down behavior of the seal over 18 hours. The seal temperatures are slightly below the cavity temperature, indicating that the expansion to ambient pressure is not entirely isothermal. The leakage trend with its peaks between 30°C and 20°C appears somewhat peculiar and suggests the requirement to explore such behavior.

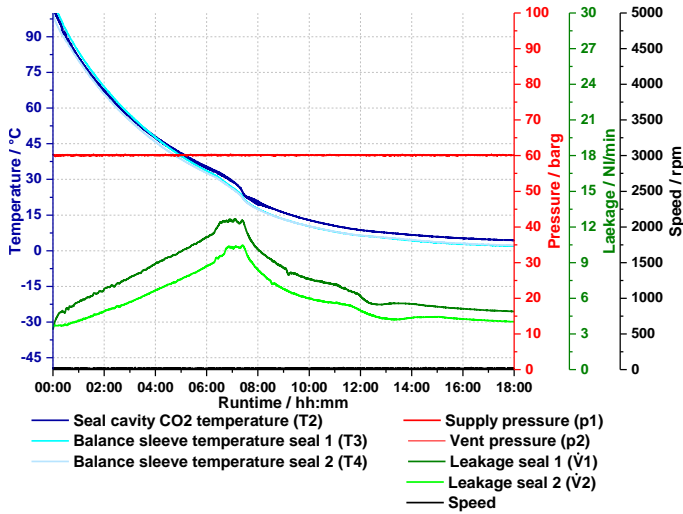


Figure 10: CO₂ static test, constant cavity pressure 60barg (*P*₁), temperature drop overnight from 100°C to 0°C.

The isobaric change of state in the experiment is reflected in the pressure-enthalpy diagram by a simple straight line A to B in Figure 11, starting in the vapor region, crossing the two-phase region aligned with the 22.7°C isotherm and ending as liquid CO₂.

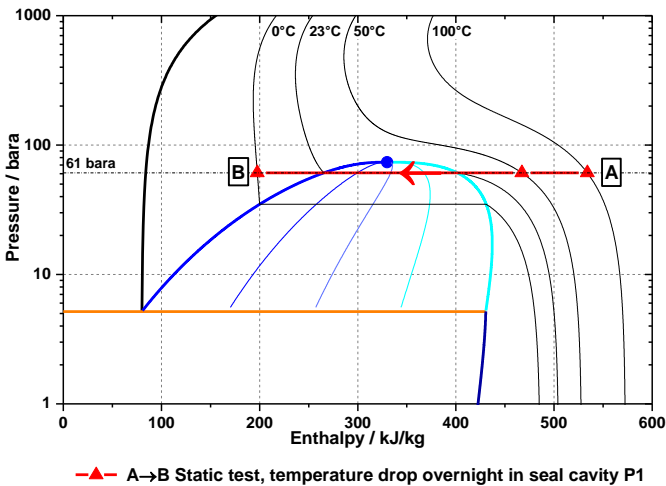


Figure 11: Static test depicted in pressure-enthalpy diagram, constant pressure 60barg, and temperature drop overnight from 100°C to 0°C (A → B).

To get better insight in effects close to the phase transition boundaries the time-dependent measured data from the static test are rearranged in a temperature-dependent plot, cf. Figure 12. Apparently, leakage is more sensitive when approaching the phase boundary from higher temperatures. Figure 12 now also includes the predicted leakage trend. The level of agreement of measured and calculated leakage proves amazingly good except

the continuous increase when coming from high temperature. The leakage peak in a narrow temperature interval now appears even more distinct. There are no further experimental data available to explain this particular leakage behavior. Additional information can only be provided by results from numerical analysis.

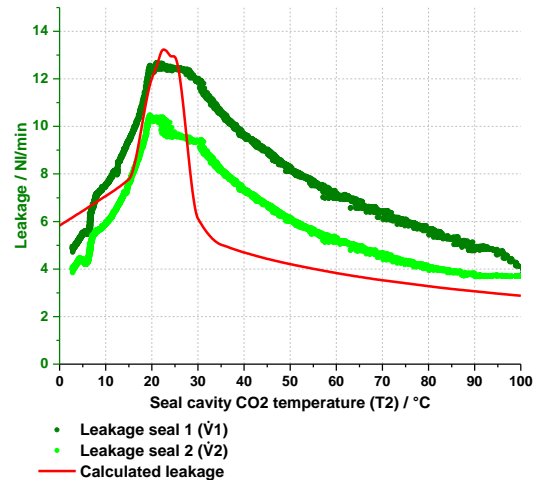


Figure 12: CO₂ static test, constant pressure 60barg, temperature drop overnight from 100°C to 0°C. Measured and calculated leakage as function of temperature.

It is most obvious to look at sealing gap heights because of the known relationship $\dot{V} \sim h^3$. Gap heights at outer and inner diameter of the sealing gap are shown in Figure 13. The relative change in the temperature range from 15°C to 30°C is in total agreement with the leakage trend depicted in Figure 12. The issue now gets to the question: why do the gap heights change in that specific temperature range? Just for comparison, also calculated gap heights for a Helium-Air mixture as test gas are added. Unsurprisingly, only a smooth tiny change can be observed.

It is not possible to provide an explanation for the local gap change without looking at the determining physical parameters driving the thermo-mechanical system, cf. Figure 14. In accordance with gap height and leakage trends, the first noticeable change beyond 15°C is observed for the calculated average heat transfer coefficient, which is decreasing from a more or less constant level below 15°C. The *HTC* essentially controls the heat exchanged between the silicon carbide rings and the seal cavity and thus the temperature distribution in the rings. Any change of internal temperature distribution will change the sealing gap shape, i.e. inner and outer gap height. Since the *HTC* is only provided as an average quantity over the entire surface of the rings, local effects cannot be resolved and described in detail. Density is closely related to the *HTC* and significantly drops across the liquid saturation line. As density drops, the Joule-Thomson coefficient rises. Changes in leakage are now expected to have a bigger effect on temperature distribution in the silicon carbide rings. This phenomenon is

clearly observed in Figure 13. Provided there is a very low leakage, the assumption of almost isothermal expansion is well justified. However, the trends in Figure 15 reveal how sensitive the system is. The larger positive $T_I - T_{FAV}$ trend indicates a lower average fluid temperature in the sealing gap compared to the cavity, i.e. the Joule-Thomson effect becomes clearly visible. The effect vanishes again with decreasing leakage.

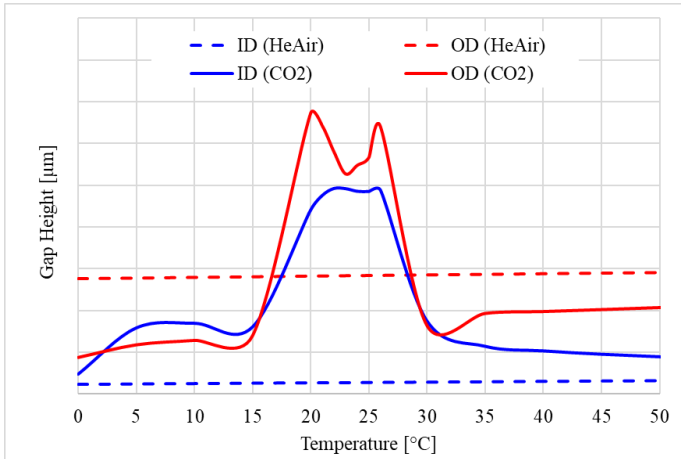


Figure 13: CO₂ static test, constant cavity pressure 60 barg (*PI*), temperature drop overnight from 100°C to 0°C. Calculated gap heights at inner and outer diameter as function of temperature. For comparison, also sealing gap heights for a simulation with a He-Air mixture are provided.

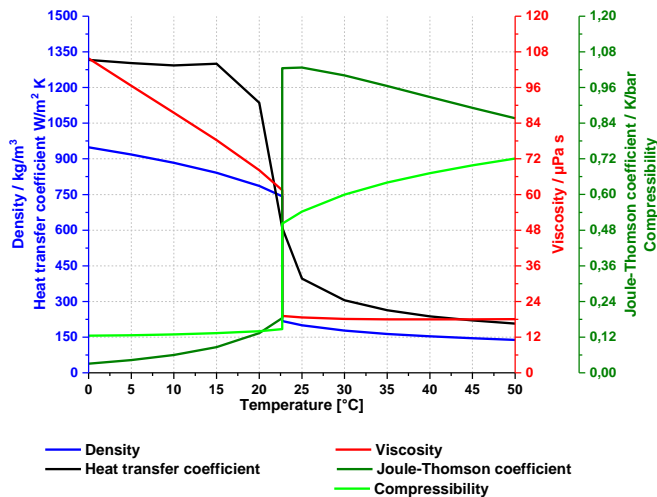


Figure 14: Determining physical parameters of CO₂ in sensitive temperature range at constant cavity pressure 60 barg (*PI*). Transition temperature is 22.7°C

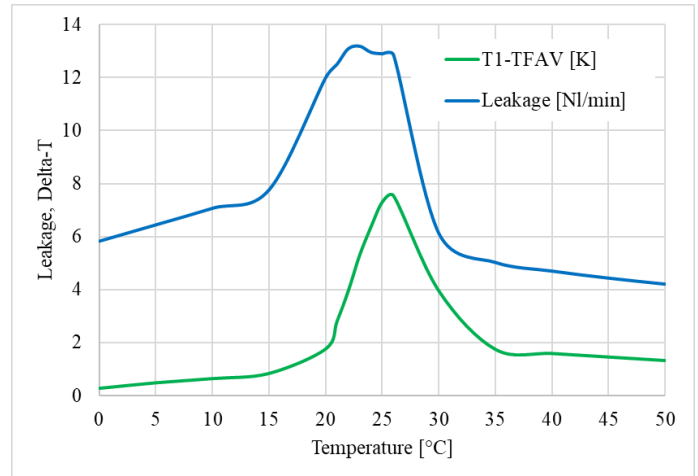


Figure 15: CO₂ static test, constant pressure 60 barg, temperature drop overnight from 100°C to 0°C. Calculated leakage and fluid temperature change as function of temperature.

Dynamic tests with temperature control at 80 barg and 180 barg

The seals run at 3600rpm and 80 barg, i.e. above the critical point. The CO₂ temperature control unit is now activated to test three distinct cavity temperature levels, i.e. 20°C (liquid CO₂, close to the dome), 50°C (supercritical, also close to the dome) and 120°C (supercritical).

The recordings in Figure 16 show seal cavity pressure, leakages of DE and NDE seals, temperatures in seal cavity and on balance sleeves. Whereas the 20°C liquid condition and 120°C supercritical condition perform rather unspectacular, simply as expected, the 50°C case causes considerable trouble for the temperature control unit. As mentioned above, the CO₂ temperature does now jump into a fluctuation mode between 45°C and 60°C. The seal reacts by mirroring the leakage to the cavity temperature. This test again clearly reveals the notable sensitivity of CO₂ when being close the critical point.

As above, the time-dependent measured data from the dynamic test are rearranged in a temperature-dependent plot, cf. Figure 17. It now becomes visible what is entirely concealed in the time-dependent plot: the leakage trends show exactly the same characteristics as in the static test, cf. Figure 10 and Figure 12. The only difference is that the leakages now peak at a single point, exactly at the critical temperature. This is immediately understandable by the fact that the process comes closest to the two-phase region exactly at the critical temperature, while in the 60 bar test both saturation lines are crossed, resulting in a plateau-like leakage maximum.

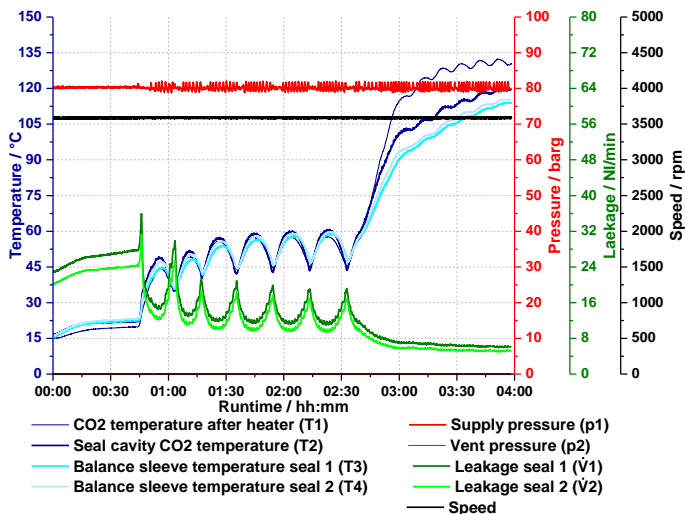


Figure 16: CO₂ dynamic test, constant cavity pressure 80 barg (*PI*), speed 3600 rpm. Cavity temperature control intent at three different levels.

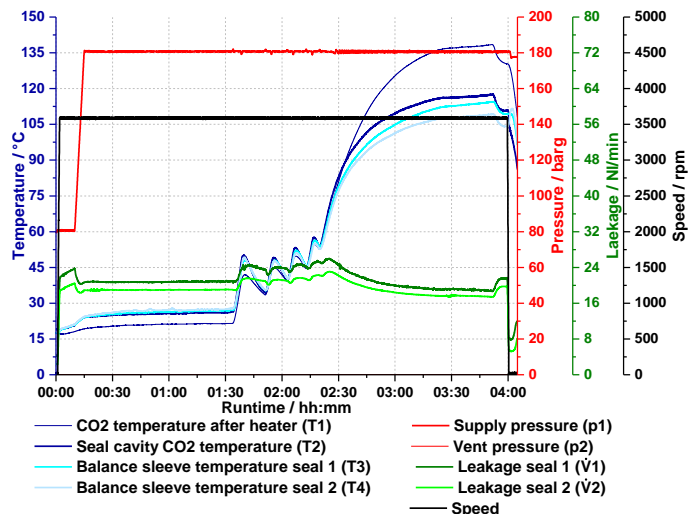


Figure 18: CO₂ dynamic test, constant cavity pressure 180 barg (*PI*), speed 3600 rpm. Cavity temperature control intent at three different levels.

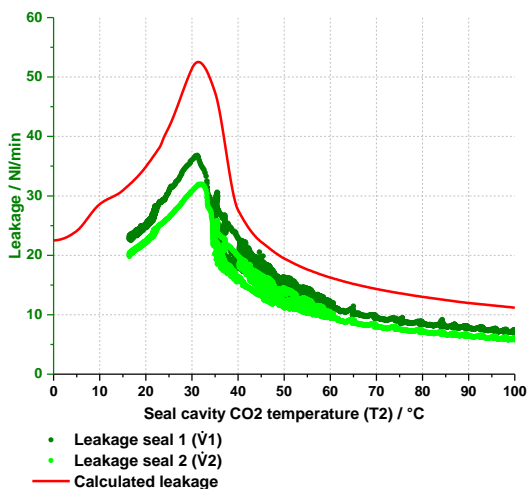


Figure 17: CO₂ dynamic test, constant cavity pressure 80 barg (*PI*), speed 3600 rpm, varying temperature. Measured and calculated CO₂ leakage as function of temperature.

Very similar results are achieved for the high-pressure dynamic test, cf. Figure 18 and Figure 19. The leakages again peak at a single point, now at 70°C. The same explanation as above applies, the process comes closest to the two-phase region at about 70°C.

The level of agreement of measured and calculated leakage proves outstanding good with respect to quality, a bit less with respect to quantity. As often, dynamic leakage predictions turn out to be higher than the measured ones.

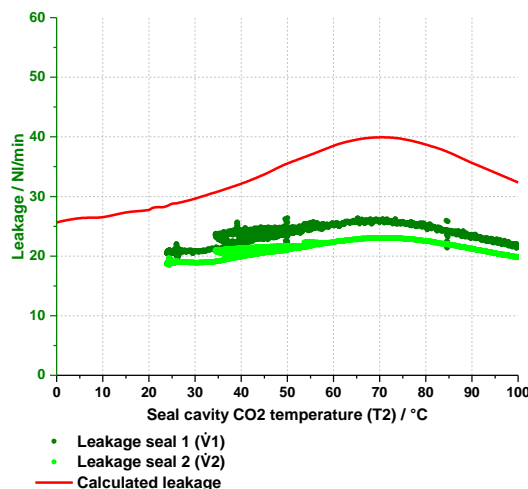


Figure 19: CO₂ dynamic test, constant cavity pressure 180 barg (*PI*), speed 3600 rpm, varying temperature. Measured and calculated CO₂ leakage as function of temperature.

Static test without temperature control at 200 barg

All previous test results presented in this paper apply to a tandem seal configuration and circulating CO₂. Two further test results are shown for a single seal configuration.

A long-term static test result for 200 barg is shown in Figure 20. Leakage and temperature trends very clearly indicate the upper limit of leakage up to which expansion is absolutely isothermal. Again, the term *isothermal* is used in a descriptive mode. It characterizes an observation in conjunction with very low CO₂ leakage. The temperature drop of CO₂ during expansion is instantaneously compensated by heat supply from structural parts. Thus, temperature is in dynamic equilibrium.

In general, the static seal performance can be considered quite satisfying, without any basic instabilities. However, there are two conspicuous leakage leaps. In fact, the reason for these events remains unclarified. A possible assumption refers to sudden or slow axial displacements of the shaft, starting from a pre-stressed position. Various similar events could be observed throughout the test campaign.

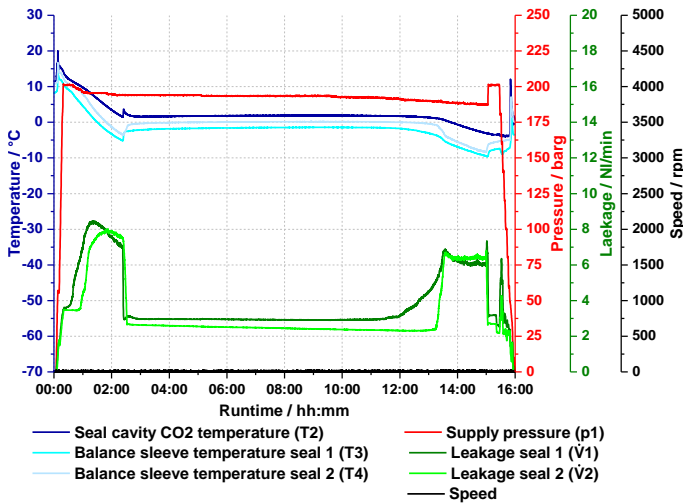


Figure 20: CO₂ static single seal test, initial pressure 200barg, no temperature control, dead-end operation.

Static test simulating a seal failure

As it is obvious from all previous remarks that CO₂ leakage, in particular static leakage, must remain low, by design of an additional static test, it was possible to deliberately demonstrate the effect of unacceptable high leakage either due to inappropriate seal design, malfunction of the seal, or failure of secondary sealing elements.

On both sides of the dry gas seal, DE and NDE, a bypass between stationary seal face and backup ring has been created by grinded tiny grooves in the backup ring, 35µm deep on the DE seal (seal 1) and 80µm deep on the NDE seal (seal 2), cf. Figure 2. The test result is shown in Figure 21. The temperatures in both seals immediately drop as pressure increases. Beyond 40 barg, the leakage rise and temperature drop is dramatic. Obviously, the initial local cooling spot, the grinded groove, does now significantly affect the distortion of seal faces, thus creating additional leakage. The NDE seal temperature has already reached the triple point. The temperature cannot drop any further. The sealing pressure was then limited to 60barg. For a certain period of time the system appeared to stabilize itself, yet, became unstable again. To avoid an entire breakdown and possible damages, the pressure was relieved. The expansion in the sealing gap from 60barg can be considered as adiabatic with a temperature drop indicated in the pressure-enthalpy diagram. Any heat available from the seal structural parts has been depleted. There is no heat remaining to compensate the adiabatic

cooling of the large mass flow through the sealing gap and bypass holes.

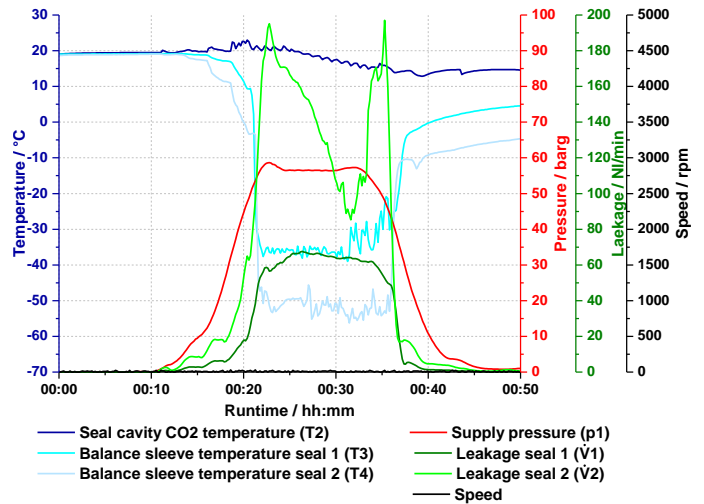


Figure 21: Seal failure simulation by specific experimental set-up.

The measured leakage peaks in the experimental seal failure simulation correspond quite well to a deliberately designed numerical test case where the sealing gap is tuned such that the ring temperature drops down to the triple point -56.6°C. This result again confirms the reliability of the CO₂ seal performance prediction.

SUMMARY & CONCLUSIONS

Process industry as well as power generation employing CO₂ as working fluid will certainly grow in the years and decades to come. Machinery rotating equipment requires efficient and reliable sealing devices. In this paper, a design solution for a multiphase CO₂ seal has been presented, which presumably covers most pressure requirements appearing in CO₂ industrial applications.

The seal, designed as dry gas seal, works with liquid, two-phase, gaseous and supercritical CO₂. The presented design solution does not require any additional heating of the high-pressure sealing cavity in order to avoid possible seal performance issues due to transitions into two-phase or even liquid regions.

A representative selection of test results has been shown, some of them explained by theoretical considerations and scrutinized by appropriate numerical simulation tools. The design intent – virtually isothermal expansion due to extremely low leakage, yet safe non-contacting dynamic operation – has been confirmed by many successful test results.

In addition, the solid numerical predictive capability particularly with CO₂ has been demonstrated in particularly close-to-critical CO₂ conditions and phase transitions. A deliberately designed failure test reveals the serious

consequences and emphasizes the paramount importance of the low leakage demand.

NOMENCLATURE

CFD	Computational fluid dynamics
DE	drive end
DF	DiamondFace®
DGS	dry gas seal
HLB	helium light bands
IB	inboard / product side
NDE	non drive end
NIST	National Institute of Standards and Technology
OB	outboard / atmospheric side
PTFE	Polytetrafluoroethylene
R&D	Research & Development
<i>HTC</i>	heat transfer coefficient (W/m^2-K)
<i>ID</i>	inner diameter of sealing face (mm)
<i>OD</i>	outer diameter of sealing face (mm)
<i>PI</i>	seal cavity pressure (bar)
<i>TC</i>	thermal conductivity ($W/m-K$)
<i>TEC</i>	thermal expansion coefficient ($1/K$)
<i>TFAV</i>	average fluid temperature in sealing gap (K)
<i>TI</i>	seal cavity temperature (K)

REFERENCES

- [1] Young L.A., Wondimu, B. (2014). The Development, Testing, and Successful Application of Arrangement 2 Seals for CO2 Pipelines. 43rd Turbomachinery & 30th Pump Users Symposia, Houston, Texas.
- [2] Fairuz Z.M., Jahn I. (2016), The influence of real gas effects on the performance of supercritical CO2 dry gas seals, Tribology International 102, 333-347
- [3] Tacon K., Twiss C., Mammadov V., Aslan-Zada F. (2014), Dry gas sealing solutions for high-pressure compressor applications, J Process Mechanical Engineering Vol. 228(3), 238-252
- [4] Allison T.C., Moore J.J., Wilkes J.C., Brun K. (2017). Turbomachinery Overview for Supercritical CO2 Power Cycles. 46th Turbomachinery & 33rd Pump Users Symposia, Houston, Texas.
- [5] Allam R., Scott M., Forrest B., Fetvedt J., Lu X., Freed D., Brown Jr. G.W., Sasaki T., Itoh M., Manning J. (2017), Demonstration of the Allam Cycle: An update on the

development status of a high efficiency supercritical carbon dioxide power process employing full carbon capture, Energy Procedia 114, 5948-5966

- [6] Ahn Y. et. al. (2015), Review of supercritical power cycle technology and current status of research and development, Nuclear Engineering and Technology Vol. 47, Issue 6, 647-661
- [7] Lebeck, Alan O., Principles and design of mechanical face seals, Vol. 294, New York: Wiley, 1991
- [8] Lebeck, Alan O. (2014) FSGS Face Seal with GaS Leakage and Performance Prediction, USER MANUAL, Mechanical Seal Technology Inc., Albuquerque
- [9] Lemmon, E. W. ; Huber, M. L. ; McLinden, M. O.: NIST Standard Reference Database 23: Reference fluid thermodynamic and transport properties - REFPROP 9.1, 2013
- [10] Poerner M., Musgrove G., Beck G., Nolen C.J. (2016), Understanding Wet Gas in a Supercritical Carbon Dioxide Cycle, The 5th International Symposium – Supercritical CO2 Power Cycles, March 28-31, San Antonio, Texas
- [11] EagleBurgmann seal solves problems associated with pumping light vaporous media (2015), Sealing Technology, Nov. 2015
- [12] Thatte a., Zheng X. (2014), Hydrodynamics and Sonic Flow Transition in Dry Gas Seals, Proceedings of ASME Turbo Expo, June 16-20, 2014, Düsseldorf, Germany

SUPERCRITICAL CARBON DIOXIDE/ALTERNATIVE FLUID BLENDS FOR EFFICIENCY UPGRADE OF SOLAR POWER PLANT

Marco Binotti*
Politecnico di Milano
Milano, Italy

Gioele Di Marcoberardino
University of Brescia
Brescia, Italy

Paolo Iora
University of Brescia
Brescia, Italy

Costante Invernizzi
University of Brescia
Brescia, Italy

Giampaolo Manzolini
Politecnico di Milano
Milano, Italy

ABSTRACT

The future of Concentrated Solar Power technology relies on significant cost reduction to be competitive against both fossil fuel power stations and renewable technologies as photovoltaics and wind. Most of the research activity on CSP focuses on supercritical CO₂ cycles to increase the solar plant efficiency together with a cost reduction. Recently, several research groups have started investigating the blending of CO₂ with small amounts of additives to boost the thermodynamic cycle performance. The potentialities of N₂O₄ and TiCl₄ were already demonstrated from theoretical point of view. The SCARABEUS project aims at developing and demonstrating CO₂ blends in concentrating solar power plant with maximum temperatures of 700°C, power cycle efficiency above 50% and cost of electricity below 96 €/MWh. The innovative fluid and newly developed components will be validated at a relevant scale (300 kW_{th}) for 300 h in a CSP-like operating environment.

INTRODUCTION

Concentrated Solar Power (CSP) plants are set to play an important role in the energy supply mix in the twenty first century. Unfortunately, the Levelized Cost of Electricity (LCoE) of CSP (currently about 150 €/MWh) has not attained the level targeted (100 €/MWh) except for few installations in exceptionally good locations. As of today, many ongoing research projects aiming at enhancing the efficiency of the power block (PB) and reducing the associated costs are based on supercritical CO₂ technology. However, relatively high ambient temperatures, typical in regions characterized by high solar irradiation, remain the Achilles heel of supercritical CO₂ cycles as the efficiency of these systems drops dramatically in warm environments where ambient temperature is close to or higher than the critical temperature of CO₂ (31°C), hence not allowing

to adopt condensation cycles with expectedly higher efficiencies. This issue stems as an intrinsic critical hurdle for the future commercialization of CSP plants, which may be difficult to overcome by any means with the technology currently in use or with standard supercritical CO₂ technology.

To address this limitation, the SCARABEUS project proposes a modified working fluid whereby carbon dioxide is blended with certain additives to enable condensation at temperatures as high as 60°C whilst, at the same time, still withstanding the required peak cycle temperatures.

The SCARABEUS project aims at developing and demonstrating an innovative power cycle based on blended CO₂ for CSP applications, yielding higher efficiency and lower cost. The application of supercritical CO₂ blends has the potential to increase the thermomechanical conversion efficiency from the current 42% to above 50%. In addition, capital expenditure (CAPEX) and operating expense (OPEX) can be reduced by 30% and by 35% respectively with respect to state-of-the-art steam cycles, thus exceeding the reduction achievable with standard supercritical CO₂ technology.

The primary objective of the SCARABEUS project is to demonstrate that using blended-CO₂ is the only route currently possible to meeting the very ambitious economic performance of next generation CSP plants. There are two main areas of research in this project: the first is the identification of the optimal additive which would reduce the size and increase the efficiency of the PB. The second is the development of tailored heat exchanger designs, particularly for the air-cooled condenser, to operate with the innovative fluid as these are key enabling components for the proposed technology. The project will demonstrate the innovative fluid and newly developed heat-exchangers at a relevant scale (300 kW_{th}) for 300 h in a CSP-like operating environment.

From preliminary analysis, it comes out that CO₂-N₂O₄ and CO₂-TiCl₄ mixtures as working fluids in PBs are promising thanks to

the high cycle efficiency, small turbomachinery and simple plant lay-out which bring about a substantial specific cost reduction. A simple regenerative cycle with the proposed innovative blends can reach a cycle efficiency as high as 48.6% for CO₂-N₂O₄ and 49.7% for CO₂-TiCl₄ compared to an efficiency of 48% for a complex recompression cycle with pure CO₂.

The SCARABEUS project scheduled work plan includes activities covering the whole value chain needed to prove thermodynamic, economic and environmental benefits of the proposed technology. It is broken down in seven work packages covering four years of work, starting on April 2019.

The consortium comprises 9 partners with the key complementary expertise, including 5 top level European universities, one innovative SME and three world leading companies.

CURRENT STATUS OF CONCENTRATING SOLAR POWER

CSP technology uses a series of mirrors to concentrate the direct solar radiation and to convert it into high temperature heat that is subsequently converted into electric power through a conventional power cycle. Currently there are about 5 GW of installed CSP plants mainly based on Parabolic Trough technology (3.7 GW) and on Solar Tower technology (0.6 GW). Parabolic trough collectors (PTC) use one-axis tracking systems and concentrate the radiation onto a receiver tube (linear concentrators) in which a heat transfer fluid (HTF) flows. The majority of the CSP plants based on PTC uses synthetic oil as HTF, thus limiting the maximum temperature slightly below 400°C. A standard re-heated steam cycle with maximum temperature around 370°C is thus the most commonly adopted power conversion technology with a net power block efficiency of about 37-38%. The use of solar salts as HTF in PTC is another interesting option that has been under development for several years and that will be applied in some of the new CSP plants in China. Solar salts can achieve temperatures up to 565°C guaranteeing a PB conversion efficiency of about 39-42%. Solar Tower (ST) systems use heliostat to concentrate the solar radiation onto a central receiver in which solar salts are used as HTF or in which steam is directly produced for the steam cycle. The first option (i.e. ST) is nevertheless preferred as it allows for the direct integration of high capacity thermal energy storage systems that enable a higher solar share or potentially continuous operation without fossil fuel backup. The standard PB conversion technology is also based on a steam cycle with similar performance as the previous ones.

Current and forecasts on CSP costs are reported in Table 1, showing how ST is expected to have the strongest LCOE reduction. The capacity factor represents the PB operating hours with respect to the yearly hours.

Table 1: Global weighted average CSP investment cost, capacity factor and LCOEs, 2015 and 2025 [1]

	Investment Cost (\$/kW)		Capacity Factor		LCOE (\$/kWh)	
	2015	2025	2015	2025	2015	2025
PTC	5550	3700	41%	45%	0.15-0.19	0.09-0.12
ST	5700	3600	46%	49%	0.15-0.19	0.08-0.11

The main driver to attain lower costs is the operating temperature, which can be combined with the use of supercritical cycles for further performance enhancement and cost reduction. Indeed, a higher operating temperature implies higher conversion efficiency of the PB which brings about a smaller area of the solar field (lower primary energy demand for the same electricity output). This would result in substantial capital cost reduction, as the solar field of a CSP power plant with thermal energy storage accounts for about 40-50% of the total capital cost [1]. Moreover, higher operating temperatures enable a higher temperature change across the thermal energy storage system, resulting in a much lower inventory of heat transfer fluid (molten salts in standard technology) and smaller footprint of the storage tanks (the storage size is on energy base, and consequently is inversely proportional to the temperature difference across the receiver).

The cost of the storage system, which accounts for between 10% and 15% of the total cost of the plant [1], can therefore be largely reduced.

SUPERCRITICAL CO₂ POWER CYCLES AND CO₂ BLENDS

Supercritical CO₂ systems have been extensively researched in recent years, both theoretically and experimentally. The potential of sCO₂ relies on the following features: (i) liquid or liquid-like (i.e. low compressibility) state of the working fluid during compression, which drastically reduces the associated work, and (ii) low expansion ratio of the cycle and low isentropic exponent of the working fluid (CO₂), which largely increase the potential to recuperate heat within the cycle. A number of experimental loops, based either on the Recompression and Simple Recuperated cycle layouts, have been constructed in the last ten years to demonstrate the feasibility of the concept [2-4]. The idea of blending the CO₂ to modify the critical properties of the working fluid dynamically has been explored in the past, mainly by Sandia National Labs in United States for low temperature heat sources [2]. Experiments performed by this institution confirmed that the addition of butane to the CO₂ increases the critical temperature with benefits for the cycle efficiency. On the contrary, adding SF₆ has the opposite effect (the critical temperature decreases). The proven concept was later protected under US Patent 20130033044A115 but, in spite of the evident interest in the concept and the successful

experimental demonstration, no further activity has been reported in recent years. Moreover, the experimental activity carried out by Sandia focused more on the compressor performance near the critical point, than to demonstrate the concept as a whole (i.e., the expected performance of the cycle using CO₂ blends at high heat rejection temperatures) nor the stability of the working fluid at the high temperatures that are sought in sCO₂ applications. Finally, the maximum temperature considered in this work was around 400 °C, as it aimed at geothermal and biomass applications only, and this is far from the temperatures achievable in ST plants.

Another innovative concept making use of CO₂ mixtures in sCO₂ power cycles at high pressure and temperature is the oxycombustion-based system developed by NetPower in collaboration with Toshiba, where a mixture of carbon dioxide and steam (plus traces of other gases) is expanded in the turbine [5]. Nevertheless, this concept was not aimed at modifying the critical point of the mixture but rather at achieving very high turbine inlet temperatures that would otherwise not be possible. Another important feature of the proposed technology is that it enables non-chemical, cost-effective carbon capture. Recently, Czech Technical University in Prague started to investigate the adoption of CO₂ blends as working fluid for temperatures up to 550°C [6]. The activity is theoretical and provides an estimation of the potential enhancement of the PB performance due to the presence of additives. Previous and on-going research activities in the area of CO₂ blends undertaken by various research groups worldwide are reported in the Table 2. From the table, two different lines of research can be outlined: blending with hydrocarbons (with limited operating temperature) and adoption of gases to increase the ideal gas effect.

There is just one activity, performed by Università degli Studi di Brescia and Politecnico di Milano [7,8], investigating the

adoption of blending fluids capable of increasing the critical temperature and withstanding temperatures up to 700°C. In the framework of this collaboration, two promising fluids have been identified for blending: TiCl₄ and N₂O₄. Titanium tetrachloride is a relatively low cost, non-carcinogenic fluid, with zero Global Warming Potential (GWP) and Ozone Depleting Potential (ODP), currently employed in high temperature industrial processes. In fact, it is remarkably stable, as also confirmed by a previous experimental thermal stability analysis carried out at temperatures up to 550 °C [9]. At room temperature, it appears as a colorless liquid. However, it reacts violently with water, even with the small amounts contained in humid air, to generate heat and corrosive gases containing hydrogen chloride. In the presence of water, it is also corrosive for many metals. However, all these unfavorable characteristics of TiCl₄, become less critical with high dilution with CO₂ [10].

Thermodynamic and transport properties of N₂O₄ have been calculated in the past years, [11–13]. Nitrogen dioxide and nitric oxide are considered greenhouses gases because they promote the formation of ozone, but it seems very unlikely that very reactive NO and NO₂ will reach the troposphere. N₂O₄ was also proposed as working fluid in Brayton cycles in the past years [14,15]. At ambient conditions, N₂O₄ is unstable and decomposes into NO₂ (nitrogen dioxide) which in turn can decompose into oxygen and nitric oxide (NO) depending on the pressure and temperature. In the following calculations it is always considered the system N₂O₄/NO₂/NO/O₂ at chemical equilibrium and, for simplicity, we will indicate it from now on as N₂O₄.

Table 2: Recent research activities on CO₂ mixtures with the main features

Research Institute	Years	Fluid	Temperature Range	Activity
UNIBS [16,17]	2012 2014	Mixtures of CO ₂ and hydrocarbons: benzene and toluene	400 °C	A thermodynamic analysis of supercritical and trans-critical cycles
UNIBS – POLIMI [7,8,18–20]	2016 2018	Binary mixtures of CO ₂ with Di-Nitrogen Tetroxide (N ₂ O ₄) and Titanium Tetrachloride (TiCl ₄)	400 °C to 700°C	Thermal stability tests up to 500 °C for TiCl ₄ . Thermodynamic modelling and overall cycle assessment
UNIBS [21]	2017	Mixtures of carbon dioxide and n-butane, sulphur hexafluoride, toluene	<350 °C	Thermodynamic evaluation of the performances of different Brayton cycles.
SANDIA[2]	2011 2013	Binary mixtures of carbon dioxide and Sulphur Hexafluoride (SF ₆) and different hydrocarbons.	50 °C to 160 °C	Experimental evaluation of the compressor performances with mixtures of carbon dioxide and SF ₆ and n-butane. A Patent.
KAIST [22]	2011	Binary mixture of CO ₂ and: argon, xenon, nitrogen, oxygen.	580 °C	Evaluation of performance of supercritical Brayton cycles for Sodium-cooled Fast Reactors
Czech TU in Prague [6]	2016 2017	Binary mixture of CO ₂ and: He, O ₂ , N ₂ , Ar, CH ₄ (methane), H ₂ S (Hydrogen Sulfide), CO	550°C	Thermodynamic evaluation of some Brayton cycles
Xian Jaotong University [23]	2018	Binary mixture of CO ₂ and hydrocarbons/organic fluids	<330°C	Parametric analysis and optimization based on thermodynamic and economic performance of the system

The power cycles were modelled calculated using Aspen Plus V9.0 [24] with the Peng-Robinson Equation-Of-State (EOS) [25] as CO₂-N₂O₄, CO₂-TiCl₄ and pure N₂O₄ cannot be modelled in RefProp EOS [26]. A k_{ij} equal to 0.0745 was assumed for TiCl₄ while equal to zero for N₂O₄ as discussed in previous works. Table 3 summarizes the main design parameters adopted for the cycles modelling. For further information, the reader can refer to the previous publication [7,8]

Table 3: Main assumptions for the power cycle simulation both at 700°C and 550°C maximum temperatures

Parameter	Value
Turbine inlet pressure (bar)	250
Minimum temperature (°C)	51
$\Delta p/p$ Hp/Lp side of regenerator	0.01/0.015
$\Delta p/p$ Primary Heat Exchanger	0.015
$\Delta p/p$ heat rejection Heat Exchanger	0.02
Compressor/Pump polytropic efficiency	0.89
Turbine isentropic efficiency	0.93
Mechanical/Electrical efficiency	0.99/0.99

A preliminary assessment was carried out in previous works [7,8] and the main results are reported in

Table 4 and Table 5.

Two different locations were considered, Seville and Las Vegas as they have different latitude and irradiation which both affect the solar plant performance and electricity production.

Results are reported in terms of energy and efficiency for the most relevant sections of the plant (i.e. the optical and thermal processes are not explicated as they are in common between all the cases and no development has been performed in these components.

E_{sun} stands for the solar energy available on the solar field;

E_{gross} is the gross electric energy generated by the PB neglecting heat rejection auxiliaries;

E_{netPB} is the net electricity generated by the power cycle;

E_{net} is the net electricity generated by the solar plant including the solar field auxiliaries' consumptions;

η_{net_PB} and $\eta_{overall}$ are the PB net electric and overall plant efficiencies.

Table 4: Yearly energy assessment for a solar plant placed in Seville and Las Vegas with maximum power cycle temperature equal to 550°C [7].

T_{max} 550°C	Seville (TES 8 hours)					Las Vegas (TES 10 hours)				
	Steam cycle	Pure CO ₂	N ₂ O ₄	N ₂ O ₄ +C O ₂	TiCl ₄ +CO ₂	Steam cycle	Pure CO ₂	N ₂ O ₄	N ₂ O ₄ +CO ₂	TiCl ₄ +C O ₂
E_{sun} [GWh]	609.1	609.1	609.1	609.1	609.1	807.6	807.6	807.6	807.6	807.6
E_{gross} [GWh]	115.4	115.7	116.9	122.8	123.6	143.9	146.2	147.3	155.1	156.2
E_{netPB} [GWh]	114.0	114.5	115.7	121.7	122.5	142.6	144.0	145.0	152.9	154.1
η_{net_PB} [%]	38.5	39.9	39.3	42.1	42.6	38.5	39.8	39.3	42.0	42.5
E_{net} [GWh]	112.7	111.3	114.4	119.5	119.6	140.9	139.5	143.4	149.9	150.0
$\eta_{overall}$ [%]	18.5	18.3	18.8	19.6	19.6	17.4	17.3	17.8	18.6	18.6

Table 5: Yearly energy assessment for a solar plant placed in Seville and Las Vegas with maximum power cycle temperature equal to 700°C [7].

T_{max} 700°C	Seville (TES 8 hours)				Las Vegas (TES 10 hours)			
	Pure CO ₂	N ₂ O ₄	N ₂ O ₄ +CO ₂	TiCl ₄ +CO ₂	Pure CO ₂	N ₂ O ₄	N ₂ O ₄ +CO ₂	TiCl ₄ +CO ₂
E_{sun} [GWh]	627.58	627.6	627.6	627.6	832.1	832.07	832.1	832.1
E_{gross} [GWh]	125.3	135.7	135.9	137.2	161.0	169.4	170.1	172.1
E_{netPB} [GWh]	124.3	134.7	135.0	136.2	159.2	167.4	168.2	170.3
η_{net_PB} [%]	48.3	46.0	47.8	48.5	48.1	46.1	47.8	48.5
E_{net} [GWh]	120.11	133.5	131.8	132.4	153.4	165.9	164	165.2
$\eta_{overall}$ [%]	19.14	21.3	21.0	21.1	18.4	19.9	19.7	19.9

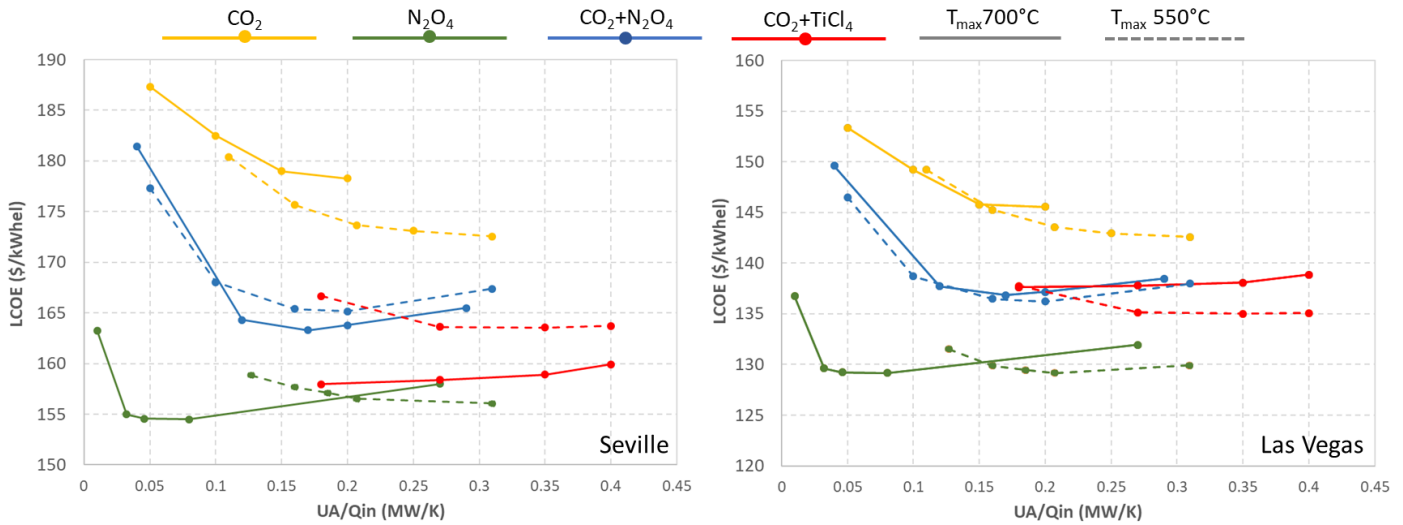


Figure 1. LCOE for the different working fluids and maximum temperatures in Seville and Las Vegas as function of the recuperative heat exchanger area [7]

Table 6: Power block specific costs for the different cases considered at different maximum temperatures together with the reference cases [7,8]

Maximum temperature 550°C – Solar salts as HTF					
	Steam cycle	Pure CO ₂	N ₂ O ₄	N ₂ O ₄ +CO ₂	TiCl ₄ +CO ₂
PB specific costs [\$/kW]	1400	1303.4	793.8	976.8	1043.0
Maximum temperature 700°C – Liquid Sodium as HTF					
	Steam cycle	Pure CO ₂	N ₂ O ₄	N ₂ O ₄ +CO ₂	TiCl ₄ +CO ₂
PB specific costs [\$/kW]	-	985.2	687.4	802.7	847.7

Table 5 pointed out that the cycle efficiency of the proposed innovative fluids can be as high as 47.8% for CO₂-N₂O₄ and 48.5% for CO₂-TiCl₄. Preliminary studies showed that these numbers can be improved by 1% assuming larger UA [7,8]. In addition, a simple regenerative cycle configuration can be adopted reducing the plant complexity. Table 6 summarizes the CAPEX of the PB for the different cases investigated outlining the potentialities to reduce the specific costs around 700\$/kW which corresponds to a reduction close to 50% and 20% with respect to conventional steam cycle and sCO₂ power blocks [27].

In terms of yearly electricity production (see

Table 4 and Table 5), the innovative fluids outperform the more conventional ones with an overall efficiency increase by 5%. The resulting LCOE (see Figure 1) which combines the thermodynamic and cost advantages of the innovative fluids is around 130 \$/MWh for a plant located in Las Vegas (US) and 155 \$/MWh for a plant located in Seville (US) compared to 147 \$/MWh and 184 \$/MWh of a steam cycle.

From the thermodynamic and economic results, CO₂-N₂O₄ and CO₂-TiCl₄ mixtures as working fluids in PB are promising

thanks to the high efficiency, small turbomachinery and simple plant lay-out which bring about a substantial specific cost reduction. However, the power cycle performance for the innovative cycles were based on simple thermodynamic models such as the Peng-Robinson equation of state, calibrated on a few available experimental data.

The SCARABEUS project will address these aspects combining theoretical modelling with experimental campaign.

THE SCARABEUS PROJECT

As mentioned in the introduction section, the primary objective of the SCARABEUS project is to demonstrate that using blended-CO₂ is the only route currently possible to meeting the very ambitious economic performance of next generation Concentrated Solar Power plants. Within SCARABEUS, a solar tower and an indirect cycle concept are considered: the heat transfer fluid (HTF) collects thermal power in the receiver and transfers it to the working fluid of the power cycle in dedicated heat exchangers. The indirect cycle concept is

selected because it does not require a new receiver development and enables the utilization of conventional thermal energy storage (TES) technologies. In this latter regard, it is noted that thermal energy storage is an essential feature to fully exploit the advantages of CSP over PV and wind energy technologies.

The first step of the project will be to identify the most promising candidate fluids (dopants) to be added to the CO₂. This phase will be based on a thorough literature review, starting from the relevant research activities summarized in Table 2, and on fluid compatibility analyses developed, both for the compounds already investigated and for new fluids that will be explored. Upon identification of the most promising candidates, a theoretical model to describe the thermo-physical properties of the working blends will be developed based on experimental data from literature and from the proprietary database of the applicants. The modelling will start from the simplest cubic equation of state formulation as Peng-Robinson [25] or Soave-Redlich-Kwong [28] with the calibration of mixing rules parameters passing through Volume Translated Peng Robinson (VTPR) or exploring predictive models as UNIQUAC Functional-group Activity Coefficients (UNIFAC) [29] or perturbed chain statistical associating fluid theory (PC-SAFT) [30] which accounts for species molecular structure and their interaction.

As already pointed out in previous research activities [8,10], the correct modelling of the thermo-physical properties behavior of the CO₂ blend is mandatory to accurately predict the fluid behavior around the critical point and the resulting cycle performance.

The theoretical description of these CO₂ blends will then be incorporated into a thermodynamic modelling environment to analyze the performance of the power plant. Simultaneously, dedicated experiments of CO₂-blends heat transfer properties will be carried out to perform and optimize the designs of the recuperative heat exchanger and air-cooled condenser. The complete performance model with an accurate characterization of the working fluid will enable the selection of the optimal CO₂ blends that yield the best performance of the PB. Based on this information, a more specific aerodynamic design, performance characterization and cost assessment of turbomachinery, recuperative heat exchanger and air condenser will be carried out. At the same time, a more refined performance model of the PB with the capability to simulate both design point and off-design behaviour of the SCARABEUS power plant with blended-CO₂ will be developed and, with this tool, an optimization of the entire plant will be performed (including solar field and thermal energy storage system).

One of the main outcomes of the modelling activities carried out in the project will be the specifications of the two working fluids yielding the best power plant performance. The thermal stability of these fluids will be investigated through dedicated experiments to ensure that decomposition at high temperature does not take place, neither in the short (immediate decomposition) nor in the long terms (after 2000 hours at high temperature). This will demonstrate the capability of the fluid to withstand temperatures up to 700°C in the presence of metallic

materials and lubricants. Additionally, vapor-liquid equilibrium measurements will be carried out to determine the Andrew's curve of the CO₂ blends. Afterwards, the Andrew's curve will be used to calibrate the thermodynamic models to verify the description of the behaviour of CO₂ blends, which is a necessary requirement to ensure the validity of the results provided by the performance models. In parallel, all the pieces of information produced by the project will be integrated in a thorough market analysis whereby the economic objectives of the project will be demonstrated. To this end, multi-variable cost estimators and financial models will be developed and integrated with the optimization tools.

Ultimately, resolving the outlined challenges leads to a lower cost of electricity (LCoE), yielding a technology that becomes cost competitive against photovoltaic systems and even fossil fuel technologies. The target LCoE to achieve this twofold objective is in the range between 50 and 100 €/MWh. Figure 2 summarizes the very large impact of SCARABEUS on the economic performance of CSP plants: 3500 €/kW_{el} CAPEX and 12 €/MWh_{el} OPEX (accounting for the contribution of the power block only) are the final economic targets of the project. Moreover, the drastic reduction of CAPEX and OPEX is even more pronounced if considered in the context of the current objectives of the SunShot initiative of the US Department of Energy [https://www.energy.gov/eere/solar/sunshot-2030], which is presently targeting 900 USD/ kW_{el} (CAPEX of the power block) and 2 USD/ MWh_{el} (OPEX of the power block, excluding fixed OPEX by capacity) for the next generation of sCO₂ power cycles to be deployed by 2030.

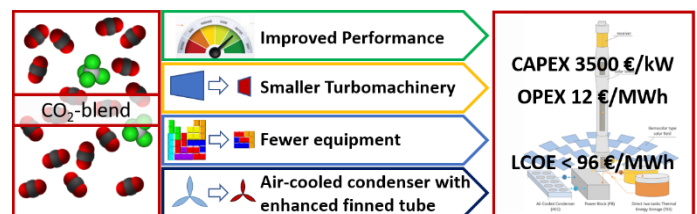


Figure 2. SCARABEUS approach and cost targets for a large scale solar tower plant

These ambitious objectives are tackled by SCARABEUS, a project conceived to bring about greater strides than would be obtained if steam turbine or combined gas/steam turbine technologies were used. This progress is built upon innovations on: (i) improvement of the PB performance, boosting the net heat to electricity efficiency to above 50%; (ii) reduction of the complexity of the PB since only one recuperator and one primary heat exchanger are necessary as opposed to more than ten heat exchangers typically adopted in a steam cycle; (iii) reduction of the size of turbomachinery compared to steam turbines of similar power output, bringing about large reduction in capital costs; (iv) innovation in heat exchanger design and manufacturing, aiming at the best compromise between thermal effectiveness and manufacturability.

THE SCARABEUS CONSORTIUM

Politecnico di Milano [31] will lead and coordinate the project and will be responsible for the dissemination of the project results. In addition, it will define the thermodynamic properties of the CO₂ mixture through vapour-liquid equilibrium measurements.

Technical University of Wien [32] has been working on sCO₂-cycles within the frame of two national projects where a transcritical sCO₂-test rig with a thermal power of 300kW thermal power has been constructed. This rig is currently operational and will be used in SCARABEUS.

Kelvion thermal solutions [33] has one of the world's largest product portfolios in the field of heat exchangers (plate, shell and tube and finned tubes heat exchanger; modular cooling tower systems) and will be responsible for the conceptual design and optimization of the air-cooled condenser and the recuperative heat exchanger.

Exergy [34] is an industrial company manufacturing turbomachinery and will work with City on design of the turbomachinery and will perform the associated cost analysis

University of Seville [35], one of the most active institutions in the field of supercritical carbon dioxide technology in Europe, will capitalize on its expertise in the area of sCO₂ cycle and turbomachinery design and optimization and of CSP technology (acquired through close collaboration with industry).

City University of London [36], has expertise in the design of turbomachinery including the effect of variable gas properties and will be responsible for the design and analysis of the turbomachinery components.

Quantis[37] will perform the technology assessment from a life cycle perspective (environmental life cycle assessment and life cycle costing).

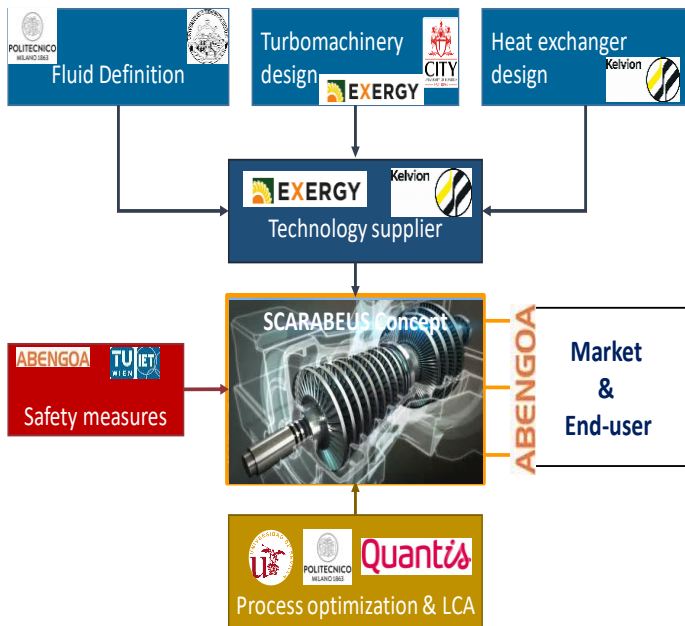


Figure 3. Value chain for the SCARABEUS project

Abengoa Energia [38] is one of the world leading companies in CSP, spanning its activities over the whole value chain: ownership, EPC, operation, servicing. The company will provide the end-user's perspective and will support the benchmarking of SCARABEUS in comparison to state-of-the-art commercial plants. They will also be responsible for the SCARABEUS technology exploitation

University of Brescia [39] has a laboratory for evaluating the stability of working fluids and holds a strong thermodynamic background on mixtures. They will support the assessment of the best candidate mixture as well as perform the corresponding stability tests.

The SCARABEUS value chain is summarized in Figure 3

CONCLUSIONS

This paper discussed the potentialities of the blended CO₂ as working fluids in power block. Previous work demonstrated that the adoption of CO₂-N₂O₄, CO₂-TiCl₄ can boost the efficiency above 49% assuming a maximum temperature equal to 700 °C while reducing the complexity and costs of the power section. SCARABEUS projects will start from these preliminary results and will demonstrate that the application of supercritical CO₂ blends can reduce the LCOE of a Concentrated Power plant below 100 €/MWh_{el}. The project will also demonstrate the innovative fluids at relevant scale for 300 hour in a CSP-like operating environment.

NOMENCLATURE

CAPEX	Capital Expenditure
CSP	Concentrated Solar Power
HTF	Heat Transfer Fluid
LCA	Life Cycle assessment
LCOE	Levelized Cost of Electricity
OPEX	Operating Expenditure
PB	Power Block
ST	Solar Tower
TES	Thermal Energy Storage
E_{sun}	Solar energy available on the solar field
E_{gross}	Gross electric energy generated by the power block
E_{netPB}	net electricity generated by the power cycle
E_{net}	net electricity generated by the solar plant;
η_{net_PB}	PB net electric efficiency.
$\eta_{overall}$	overall solar plant efficiency.

ACKNOWLEDGEMENTS

The SCARABEUS project has received funding from European Union's Horizon 2020 research programme under grant agreement N°814985.

Disclosure: The present publication reflects only the author's views and the European Union are not liable for any use that may be made of the information contained therein

REFERENCES

- [1] International Renewable Energy Agency (IRENA). Renewable Power Generation costs in 2017. 2018. doi:10.1007/SpringerReference_7300.

- [2] Conboy TM, Wright SA, Ames DE, Lewis TG. CO₂-Based Mixtures as Working Fluids for Geothermal Turbines. Albuquerque, New Mexico 87185 and Livermore, California 945: 2012.
- [3] barber Nichols sCO₂ cycle n.d. <https://www.barber-nichols.com/resources/performance-characteristics-operating-supercritical-co2-brayton-cycle>.
- [4] Cho J, Shin H, Ra HS, Lee G, Lee B, Baik YJ. Research on the Development of a Small-scale Supercritical Carbon Dioxide Power Cycle Experimental Test Loop. 5th Int. Symp. - Supercrit. CO₂ Power Cycles Symp., 2016, p. 1–18.
- [5] NetPower turbine n.d. <https://www.netpower.com/technology>.
- [6] Vesely L, Dostal V. Effect of multicomponent mixtures on cycles with supercritical carbon dioxide. In: ASME Turbo Expo 2017: Turbomachinery Technical Conference and Exposition G 2017; CUS 26 J 2017 through 30 J 2017; C 130041, editor. Proc. ASME Turbo Expo, 2017.
- [7] Binotti M, Invernizzi CM, Iora P, Manzolini G. Dinitrogen tetroxide and carbon dioxide mixtures as working fluids in solar tower plants. *Sol Energy* 2019;181:203–13. doi:10.1016/j.solener.2019.01.079.
- [8] Manzolini G, Binotti M, Bonalumi D, Invernizzi C, Iora P. CO₂ mixtures as innovative working fluid in power cycles applied to solar plants. Techno-economic assessment. *Sol Energy* 2019;181:530–44. doi:10.1016/j.solener.2019.01.015.
- [9] Bombarda P, Invernizzi C. Binary liquid metal–organic Rankine cycle for small power distributed high efficiency systems. *Proc Inst Mech Eng Part A J Power Energy* 2015;229:192–209. doi:10.1177/0957650914562094.
- [10] Bonalumi D, Lasala S, Macchi E. CO₂-TiCl₄ working fluid for high-temperature heat source power cycles and solar application. *Renew Energy* 2018;In press:1–13. doi:10.1016/j.renene.2018.10.018.
- [11] Svelha RA, Brokaw RS. Thermodynamic and Transport Properties for the N₂O₄ = 2NO₂ = 2NO + O₂ Systems. Cleveland Ohio: n.d.
- [12] Nesterenko VB., Bubnov VP. Calculation of Thermodynamic Functions of Chemically Reactive Gases. n.d.
- [13] Seshadri DN, Viswanath DS, Kuloor NR. Thermodynamic Properties of the System N₂O₄ = 2NO₂ = 2NO + O₂. *AICHe Journal* 1970;16:420–5.
- [14] Angelino G. Performance of N₂O₄ gas cycles for solar power applications. *Proc Inst Mech Eng* 1847-1982 (Vols 1-196) 1979;193:313–20. doi:10.1243/PIME_PROC_1979_193_033_02.
- [15] Kesavan K, Osterle J. Split-Flow Nuclear Gas Turbine Cycle Using Dissociating N₂O₄. In: Exhibit A 1982 IGTC and, editor. ASME Pap. 82-GT-181, April 18–22, 1982, London, England: 1982.
- [16] Invernizzi CM, Van Der Stelt T. Supercritical and real gas Brayton cycles operating with mixtures of carbon dioxide and hydrocarbons. *Proc Inst Mech Eng Part A J Power Energy* 2012;226:682–93. doi:10.1177/0957650912444689.
- [17] Lasala S, Bonalumi D, Macchi E, Privat R, Jaubert JN. The design of CO₂-based working fluids for high-temperature heat source power cycles. *Energy Procedia* 2017;129:947–54. doi:10.1016/j.egypro.2017.09.125.
- [18] Invernizzi CM, Iora P, Bonalumi D, Macchi E, Roberto R, Caldera M. Titanium tetrachloride as novel working fluid for high temperature Rankine Cycles: Thermodynamic analysis and experimental assessment of the thermal stability. *Appl Therm Eng* 2016;107:21–7. doi:10.1016/J.APPLTHERMALENG.2016.06.136.
- [19] Binotti M, Invernizzi C, Iora PG, Manzolini G. Innovative fluids for gas power cycles coupled with solar tower systems. *AIP Conf. Proc.*, vol. 2033, AIP Publishing LLC ; 2018, p. 070001. doi:10.1063/1.5067087.
- [20] Bradshaw RW, Goods SH. Corrosion Resistance of Stainless Steels During Thermal Cycling in Alkali Nitrate. *Sandia Rep* 2001:1–39.
- [21] Invernizzi CM. Prospects of Mixtures as Working Fluids in Real-Gas Brayton Cycles. *Energies* 2017;10:1649.
- [22] Jeong WS, Jeong YH, Lee JI. Performance of S-CO₂ Brayton Cycle with Additive Gases for SFR Application. *Supercrit. CO₂ Power Symp.*, Pittsburgh, Pennsylvania USA September 9 - 10, 2014: 2014.
- [23] Wu C, Wang S sen, Jiang X, Li J. Thermodynamic analysis and performance optimization of transcritical power cycles using CO₂-based binary zeotropic mixtures as working fluids for geothermal power plants. *Appl Therm Eng* 2017;115:292–304. doi:10.1016/j.applthermaleng.2016.12.077.
- [24] Aspen Plus - AspenTech. [Online]:[Www.AspentechCom/Products/Aspen-plusAspx](http://www.AspentechCom/Products/Aspen-plusAspx) 2011.
- [25] Peng DY, Robinson DB. NEW TWO-CONSTANT EQUATION OF STATE. vol. 15. 1976.
- [26] Lemmon E, Huber M, McLinden M. NIST standard reference database 23: reference thermodynamic and transport properties-REFPROP 2013.
- [27] Ho CK, Carlson M, Garg P, Kumar P. Technoeconomic Analysis of Alternative Solarized s-CO₂ Brayton Cycle Configurations. *J Sol Energy Eng* 2016;138:51004. doi:10.1115/1.4033573.
- [28] Ghanbari M, Ahmadi M, Lashanizadegan A. A comparison between Peng-Robinson and Soave-Redlich-Kwong cubic equations of state from modification perspective. *Cryogenics (Guildf)* 2017;84:13–9. doi:10.1016/j.cryogenics.2017.04.001.
- [29] UNIQUAC 2016. <https://ipfs.io/ipfs/QmXoyipizjW3WknFiJnKLwHCnL72vedxjQkDDP1mXWo6uco/wiki/UNIQUAC.html>.
- [30] Gross J, Sadowski G. Perturbed-chain SAFT: An equation of state based on a perturbation theory for chain molecules. *Ind Eng Chem Res* 2001;40:1244–60. doi:10.1021/ie0003887.
- [31] Politecnico di Milano n.d. www.polimi.it.
- [32] Technical University of Wien n.d. <https://www.tuwien.at/>.
- [33] Kelvion thermal solutions n.d. <https://www.kelvion.com/>.
- [34] Exergy n.d. <http://exergy-orc.com/>.
- [35] Universidad de Seville n.d. <http://www.us.es/eng>.
- [36] City University of London n.d. <https://www.city.ac.uk/>.
- [37] Quantis n.d. <https://quantis-intl.com/>.
- [38] Abengoa Energia n.d. <http://www.abengoa.com/web/en/negocio/energia/>.
- [39] University of Brescia n.d. <https://www.unibs.it/>.

ACCURATE AND PREDICTIVE MIXTURE MODELS APPLIED TO MIXTURES WITH CO₂

Andreas Jäger*

TU Dresden
Dresden, Germany

Email: andreas.jaeger@tu-dresden.de

Erik Mickoleit

TU Dresden
Dresden, Germany

Cornelia Breitkopf

TU Dresden
Dresden, Germany

ABSTRACT

Supercritical CO₂ as a working fluid offers distinct advantages for power cycles, such as a comparably low critical temperature and pressure. However, the favorable properties of supercritical CO₂ could potentially be enhanced by blending CO₂ with suitable additives. In order to find promising additives for CO₂, a theoretical screening seems to be most feasible, as extensive experimental studies would be very time-consuming. For this purpose, a mixture model is needed that on the one hand yields good predictive results and on the other hand should be as accurate as possible. Therefore, in this work the performance of the multi-fluid mixture model combined with UNIFAC and with different versions of COSMO-SAC is evaluated for mixtures containing CO₂. The results are compared to results calculated with accurate multi-fluid mixture models. It is demonstrated that the predictive results for phase equilibria as well as for homogeneous densities of the multi-fluid mixture model combined with UNIFAC and COSMO-SAC are superior to the results of the multi-fluid mixture model with standard mixing rules. However, it can also be seen that the parameters of UNIFAC and COSMO-SAC should be readjusted in order to further improve the results.

INTRODUCTION

Thermophysical properties of pure components and mixtures are important for the design and optimization of various processes in power and process engineering. The most accurate source of thermophysical property data are highly-accurate multiparameter equations of state. These equations of state are capable of representing all experimental data within the experimental uncertainty. The reference equation of state for carbon dioxide (CO₂) [1] is an example for such an equation of state.

If properties of mixtures are required, the multi-fluid mixture

model [2–4] can be used. This model allows for a very accurate representation of experimental data for mixtures, if the model parameters are fitted to experimental data. However, the predictive capabilities of this model are rather limited. Therefore, Jäger et al. [5,6] have developed a theoretically based departure function for the multi-fluid mixture model, which allows for the combination of the multi-fluid mixture model with the predictive excess Gibbs energy models UNIFAC and COSMO-SAC.

The basic idea of the UNIFAC model [7] is to describe the interactions of structural groups of molecules instead of modeling molecule-molecule interactions. In this way, the interactions of structural groups can be fitted to experimental data for well-studied mixtures and then be transferred to mixtures for which no experimental data exist. While UNIFAC is capable of describing fluid mixtures well and yields good predictive results, it also has some shortcomings. Many adjustable parameters need to be fitted to experimental data. Furthermore, it might happen that molecules cannot be subdivided into structural groups that exist in UNIFAC. In these cases, UNIFAC cannot be applied.

In order to overcome these shortcomings, the more predictive model COSMO-SAC [8], which only has a few substance-independent parameters, has been combined with the multi-fluid mixture model [6]. COSMO-SAC depends on quantum mechanical calculations, which need to be performed in order to calculate the screening charge densities on the molecular surface. Hence, COSMO-SAC considers the interactions of charged surface segments instead of modeling the interactions of structural groups of molecules.

Processes with supercritical CO₂ in thermal power generation offer some distinct advantages over currently used technologies, see, for example, Gampe et al. [9]. The favorable properties of supercritical CO₂ can potentially be further improved by considering mixtures of CO₂ with other substances as working

fluids instead of using CO₂ as a pure substance. As an example, the critical point can be shifted to other temperatures and pressures by mixing CO₂ with other substances. By this, the supercritical state could already be reached at lower temperatures and pressures compared to the critical temperature $T_c = 304.128$ K and critical pressure $p_c = 7.3773$ MPa of pure CO₂ (values taken from the reference equation of state for CO₂ by Span and Wagner [1]). Figure 1 shows parts of the vapor pressure curve of pure CO₂ calculated with the reference equation of state for CO₂ by Span and Wagner [1]. For comparison, Figure 1 shows parts of the bubble line and the dew line for a binary mixture of $x_{\text{CO}_2} = 0.9$ and $x_{\text{C}_2\text{H}_6} = 0.1$ calculated with the mixture model for CO₂ and C₂H₆ by Kunz and Wagner [4].

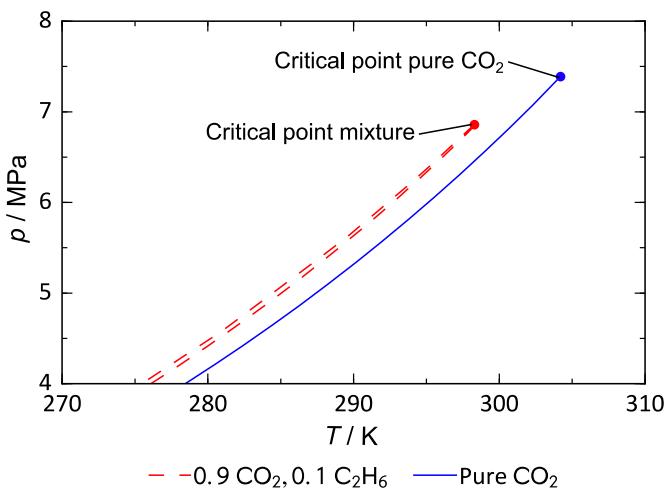


Figure 1: Calculated vapor pressure curve and critical point of pure CO₂ (solid blue line) in comparison to calculated dew and bubble lines and the mixture critical point of a binary mixture of 90% CO₂ with 10% C₂H₆ (dashed red line).

This indicates that the performance of power processes (thermal efficiency, net power etc.) could be optimized by finding suitable additives for CO₂. Since a lot of different substances can be considered as additives and various mixture compositions need to be investigated, an extensive experimental investigation for suitable additives does not seem feasible. Therefore, promising additives could be identified by a theoretical screening. For this purpose, mixture models will be needed which on the one hand allow for the use of reference equations of state (such as the reference equation of state for CO₂ by Span and Wagner [1]) and on the other hand can be used well predictively.

The multi-fluid mixture model originally proposed by Lemmon and Tillner-Roth [2] (which will be introduced in more detail in the next section) allows for the use of reference equations of state in order to model pure fluids. The model is also capable of representing experimental data for mixtures well if the adjustable parameters of the model are fitted to experimental data. However, the predictive capabilities of the multi-fluid mixture model are very limited, which has been shown by Jäger et al [5]

and will be discussed in more detail later in this work. Other equations of state with good predictive capabilities for modeling thermophysical properties of mixtures (vapor-liquid equilibria, liquid-liquid equilibria, excess enthalpies, etc.) are the well-known combinations of cubic equations of state with excess Gibbs energy models (g^E -models). Sophisticated examples for combinations of cubic equations of state with the g^E -model UNIFAC [7] are the predictive Soave-Redlich Kwong equation of state (PSRK) [10–12] and the volume-translated Peng-Robinson group contribution equation of state (VTPR) [13–15]. The disadvantage of these models is that only cubic equations of state can be used to model pure fluids and mixtures, which significantly limits the achievable accuracy. This is illustrated in Figure 2 by comparing highly-accurate experimental data on saturated liquid densities by Duscsek et al. [16] (overall combined standard uncertainty smaller than 0.015% for temperatures below 295 K. The uncertainty rises to 0.2% close to the critical temperature) to calculated saturated liquid densities from different models.

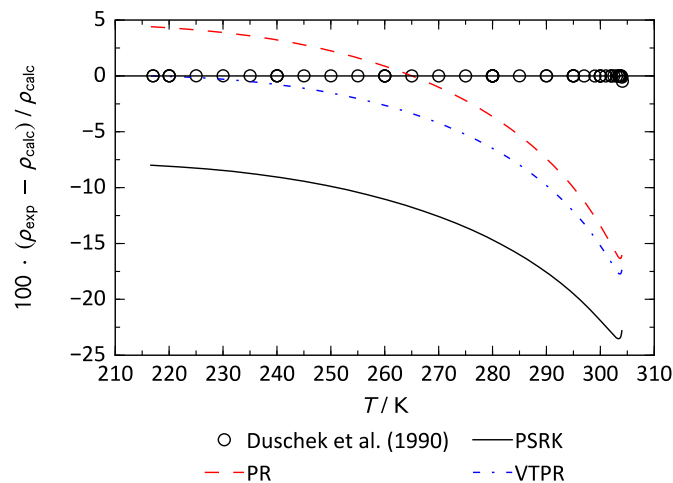


Figure 2: Deviations of experimental saturated liquid density data for CO₂ (symbols, Duscsek et al. [16]), of the PSRK (solid black line), of the PR (dashed red line), and of the VTPR (dash-dotted blue line) from the reference equation of state for CO₂ [1]. The reference equation for CO₂ is the zero line and deviations of the experimental data and the other models from the reference equation of state are displayed.

The reference equation of state for CO₂ is capable of representing the experimental data within the experimental uncertainty, while the PSRK, the original Peng-Robinson [17], and the Peng-Robinson with volume-translation applied at the triple point temperature of CO₂ yield maximum deviations from the experimental data of about -23.5%, -16%, and -18%, respectively (see Figure 2). Deviations of the PSRK and volume-translated Peng-Robinson to experimental data are especially high in the vicinity of the critical point of CO₂.

In order to overcome the shortcomings of the aforementioned models, we recently proposed a combination of the multi-fluid

mixture model with the g^E -models UNIFAC [5] and COSMO-SAC [6]. In this work, we extend this model by combining the multi-fluid mixture model with improved versions of the COSMO-SAC model, which consider different types of hydrogen-bonding interactions [18] and dispersive interactions [19]. Furthermore, the predictive capabilities of the combination of the multi-fluid mixture model with g^E -models with regard to the description of properties in the homogenous phase are investigated for the first time in this work.

MODEL DESCRIPTION

Lemmon and Tillner-Roth [2] proposed the multi-fluid mixture model in 1999. Subsequently, the model was further developed and applied to typical natural gas mixtures by Kunz and Wagner [4] and to typical mixtures relevant for carbon capture and storage (CCS) by Gernert and Span [20]. This model is an extended corresponding states model and reads

$$\alpha(\tau, \delta, \vec{x}) = \sum_{i=1}^N x_i [\alpha_{oi}^0(\rho, T) + \ln(x_i) + \alpha_{oi}^r(\delta, \tau)] + \sum_{i=1}^{N-1} \sum_{j=i+1}^N x_i x_j F_{ij} \alpha_{ij}^r(\tau, \delta). \quad (1)$$

The meaning of the symbols in Equation (1) is explained in the nomenclature. The reduced density δ can be written as

$$\delta = \rho / \rho_r \quad (2)$$

and the inverse reduced temperature is defined as

$$\tau = T_r / T. \quad (3)$$

The quantity ρ_r is the reducing density and the quantity T_r is the reducing temperature. These reducing functions are defined in the following way [4]:

$$T_r = \sum_{i=1}^N \sum_{j=1}^N x_i x_j \beta_{T,ij} \gamma_{T,ij} \frac{x_i + x_j}{\beta_{T,ij}^2 x_i + x_j} (T_{c,i} \cdot T_{c,j})^{0.5} \quad (4)$$

and

$$\frac{1}{\rho_r} = \sum_{i=1}^N \sum_{j=1}^N x_i x_j \beta_{v,ij} \gamma_{v,ij} \frac{x_i + x_j}{\beta_{v,ij}^2 x_i + x_j} \frac{1}{8} \left(\rho_{c,i}^{-\frac{1}{3}} + \rho_{c,j}^{-\frac{1}{3}} \right)^3. \quad (5)$$

The reducing temperature T_r contains the two adjustable parameters β_T and γ_T and the reducing density ρ_r contains the two adjustable parameters β_v and γ_v for each combination of components i and j . Typically, these four parameters of the mixture model are fitted to experimental data. If sufficient experimental data of good quality are available, additionally the binary departure function α_{ij}^r (see Equation (1)) can be established. This function does not have a fixed structure but consists of combinations of polynomial, exponential, and special terms that have to be determined during the fitting procedure, see [4]. If no experimental data exist for a mixture of interest, the multi-fluid mixture model according to Equation (1) can be used predictively by neglecting the binary departure function ($\alpha_{ij}^r = 0$) and applying standard mixing rules for the reducing functions, such as linear mixing rules for the reduced temperature

$$T_r = \sum_{i=1}^N x_i T_{c,i} \quad (6)$$

and the reduced density

$$\frac{1}{\rho_r} = v_r = \sum_{i=1}^N x_i v_{c,i} = \sum_{i=1}^N x_i \frac{1}{\rho_{c,i}}. \quad (7)$$

This predictive mixture model will be referred to as ‘‘LIN-MOD’’ in the following.

It has been demonstrated in our previous work [5,6] that the multi-fluid mixture model with linear mixing rules for the reducing functions (LIN-MOD) does not yield good predictive results for phase equilibria of binary mixtures. Therefore, we have proposed a combination of the multi-fluid mixture model with excess Gibbs energy models, which reads

$$\alpha(\tau, \delta, \vec{x}) = \sum_{i=1}^N x_i [\alpha_{oi}^0(\rho, T) + \ln(x_i) + \alpha_{oi}^r(\delta, \tau)] + \frac{\ln(1 + b\rho)}{\ln(1 + b\rho_{\text{ref}})} \left[\frac{g_{\text{GE}}^{\text{E,r}}}{RT} - \sum_{i=1}^N x_i [\alpha_{oi}^r(\delta_{\text{ref}}, \tau) - \alpha_{oi}^r(\delta_{i,\text{ref}}, \tau_i)] \right]. \quad (8)$$

with

$$\frac{1}{\rho_{\text{ref}}} = \sum_{i=1}^N x_i v_{s,i}^{\text{L}}(p_0), \quad (9)$$

with $v_{s,i}^{\text{L}}$ denoting the molar volume of the saturated liquid of component i at the reference pressure p_0 .

In this work, the residual excess Gibbs energy $g_{\text{GE}}^{\text{E,r}}$ is either calculated from UNIFAC [5,7] or different versions of COSMO-SAC [6,8]. While in our previous work [6] only the original version of COSMO-SAC [8] has been combined with the multi-fluid mixture model, in this article we investigate the performance of improved versions of COSMO-SAC [18,19] when combined with the multi-fluid mixture model. The combination of the multi-fluid mixture model with UNIFAC will be referred to as ‘‘UNI-MOD’’ and the combination with the original version of COSMO-SAC [8] will be referred to as ‘‘COS1-MOD’’. The combinations with the modification of COSMO-SAC considering different strengths of donor-acceptor surface segments [18] will be referred to as ‘‘COS2-MOD’’. Finally, the combination with the COSMO-SAC model considering dispersive interactions [19] will be referred to as ‘‘COS3-MOD’’.

For all calculations presented in this work, the reference equations of state for pure components have been used. For carbon dioxide (CO_2), the multiparameter equation of state by Span and Wagner was used [1]. For ethane (C_2H_6), the multiparameter equation of state by B ucker and Wagner was applied [21] and for methane (CH_4) the multiparameter equation of state by Setzmann and Wagner [22] was used. The database of Mullins et al. [23] containing COSMO calculations for 1432 components has been used to calculate sigma-profiles needed for

COS1-MOD, COS2-MOD, and COS3-MOD. For UNI-MOD, the UNIFAC parameters of the VTPR have been used.[13,14]. The multi-fluid mixture model (Equations (1) and (8)) is a fundamental equation formulated in the dimensionless Helmholtz energy α . Therefore, thermophysical properties can be calculated from this model by combining derivatives of the model with respect to its independent variables [4,24]. For example, the pressure can be calculated from this model in the following way

$$p = \rho RT \left(1 + \delta \left(\frac{\partial \alpha^r}{\partial \delta} \right)_{\tau, \tilde{x}} \right). \quad (10)$$

All of the described mixture models are implemented in the thermophysical property software TREND [25]. The necessary derivatives for the theoretically based departure function in combination with UNIFAC are supplied in the supplementary material of the article by Jäger et al. [5]. The required derivatives for the models “COS1-MOD”, “COS2-MOD”, and “COS3-MOD” have been calculated numerically by the central difference scheme. Phase equilibrium calculations have been performed in TREND [25] with the algorithms described by Gernert et al. [26] and Jäger [27].

PREDICTIVE RESULTS FOR PHASE EQUILIBRIA

In our previous works [5,6], we have investigated the representation of phase equilibria of binary mixtures of CO₂, ethane, propene, ethanol, and benzene over a broad temperature range. It was found that the combination of the multi-fluid mixture model with g^E -models yields better predictive results for phase equilibria than the multi-fluid mixture model with standard mixing rules (LIN-MOD). In this work, the predictive capabilities of the models will be evaluated exemplarily for a binary mixture of CO₂ + C₂H₆ on an isotherm of $T = 253$ K. Figure 3 shows the experimental vapor-liquid equilibrium (VLE) data of Nagahama et al. [28] (symbols) for a binary mixture of C₂H₆ + CO₂ in comparison to the multi-fluid mixture model with adjusted reducing function parameters by Kunz and Wagner [4] (solid blue line, no binary specific departure function was fitted for this binary mixture by Kunz and Wagner [4], i.e., $\alpha_{ij}^r = 0$). Furthermore, Figure 3 shows the results of the predictive multi-fluid mixture model with linear mixing rules according to Equations (6) and (7) without a departure function (dashed red line, LIN-MOD). It can be seen that the multi-fluid mixture model with adjusted parameters is capable of describing the azeotropic behavior of the binary mixture CO₂ + C₂H₆ correctly, while LIN-MOD is not capable of qualitatively correctly describing the behavior of this mixture. Note that Kunz and Wagner have adjusted the reducing function parameters for the binary mixture of CO₂ + C₂H₆ to experimental VLE data.

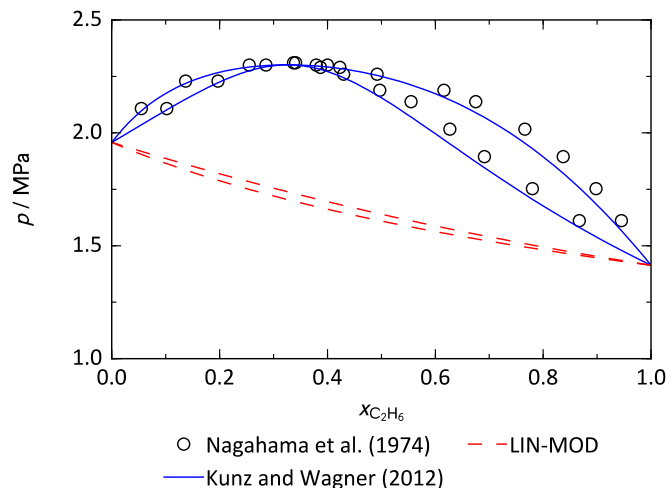


Figure 3: Experimental VLE data (symbols, Nagahama et al. (1974) [28]) for a binary mixture of CO₂ + C₂H₆ on an isotherm of $T = 253$ K and vapor-liquid equilibria calculated with the empirical multi-fluid mixture model by Kunz and Wagner [4] (GERG-2008, solid blue line) and with LIN-MOD (dashed red line).

COS3-MOD combines the multi-fluid mixture model with the improved version of COSMO-SAC considering dispersive interactions [19]. Hsieh et al. [19] proposed to consider the contribution to the activity coefficient due to dispersive forces with a one-constant Margules equation, depending on a molecular dispersion parameter $\varepsilon_{\text{molecule}}$. The dispersion parameters for methane and ethane ($\varepsilon_{\text{CH}_4}/k_B = \varepsilon_{\text{C}_2\text{H}_6}/k_B = 115.7023$ K) can be calculated from the atomic contributions provided by Hsieh et al. [19] in Table 2 of their article. The dispersion parameter for CO₂ can in principle also be calculated from these atomic contributions. However, Hsieh et al. [19] have not considered CO₂ in their fitting procedure and the resulting $\varepsilon_{\text{CO}_2}/k_B = 14.6531$ K does not yield good results for phase equilibria of mixtures with CO₂. Therefore, in this work $\varepsilon_{\text{CO}_2}/k_B$ has been manually adjusted (by trial-and-error) to the phase equilibria of the binary CO₂ + C₂H₆ mixture in order to obtain a value for $\varepsilon_{\text{CO}_2}/k_B$ which allows for a better representation of phase equilibria of mixtures of CO₂ with hydrocarbons. It was found that $\varepsilon_{\text{CO}_2}/k_B = 85$ K yields a good representation of phase equilibria for the binary mixture of CO₂ + C₂H₆.

Figure 4 shows the predictive results of the models UNI-MOD (using the VTPR parameters of UNIFAC, see [13,14]), COS1-MOD, COS2-MOD, and COS3-MOD. LIN-MOD is also shown for comparison.

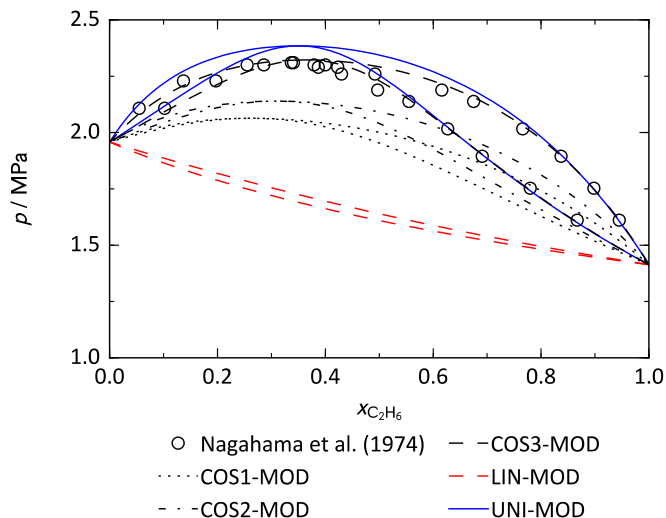


Figure 4: Experimental VLE data (symbols, Nagahama et al. (1974) [28]) for a binary mixture of $\text{CO}_2 + \text{C}_2\text{H}_6$ on an isotherm of $T = 253$ K and vapor-liquid equilibria calculated with the predictive models LIN-MOD (dashed red line), UNI-MOD (solid blue line), COS1-MOD (dotted black line), COS2-MOD (dashed-dotted black line), and COS3-MOD (dashed black line).

While LIN-MOD is not capable of representing the azeotropic behavior of the binary mixture of $\text{CO}_2 + \text{C}_2\text{H}_6$ correctly, all of the combinations of the multi-fluid mixture model with g^E -models predict the mixture behavior qualitatively correctly. UNI-MOD with VTPR parameters for UNIFAC ([13,14]) slightly overpredicts the bubble and dew point pressures as well as the pressure at the azeotropic point. A clear improvement can be seen for the different versions of COSMO-SAC combined with the multi-fluid mixture model. COS1-MOD qualitatively correctly describes the azeotropic behavior of the mixture, however, the calculated dew and bubble point pressures are underestimated by this model. COS2-MOD yields slightly better results than COS1-MOD. COS3-MOD describes the experimental data quantitatively well, however, note that $\varepsilon_{\text{CO}_2}/k_B$ has been adjusted by trial-and-error in order to improve the description of the experimental VLE data for this mixture. However, this demonstrates that the performance of COS3-MOD could be significantly improved by fitting the molecular dispersion parameters to experimental data.

PREDICTIVE RESULTS FOR DENSITIES

Predictive results of the combination of multi-fluid mixture models with g^E -models for properties in the homogeneous phase have not been investigated in our previous works. Therefore, here we present calculated densities in the homogeneous phase for different predictive and empirical models for the binary mixtures of $\text{CO}_2 + \text{CH}_4$ and $\text{CO}_2 + \text{C}_2\text{H}_6$. Accurate experimental density data in the homogeneous phase for these mixtures by Jaeschke et al. [29,30] are available and have been used for the

development of the GERG-2004 and GERG-2008 equation of state, see Kunz et al. [3] and Kunz and Wagner [4], respectively. Figure 5 shows relative deviations of the experimental density data by Jaeschke et al. [29,30] for a binary mixture of $\text{CO}_2 + \text{CH}_4$ on an isotherm of $T = 290$ K from calculated data with different models.

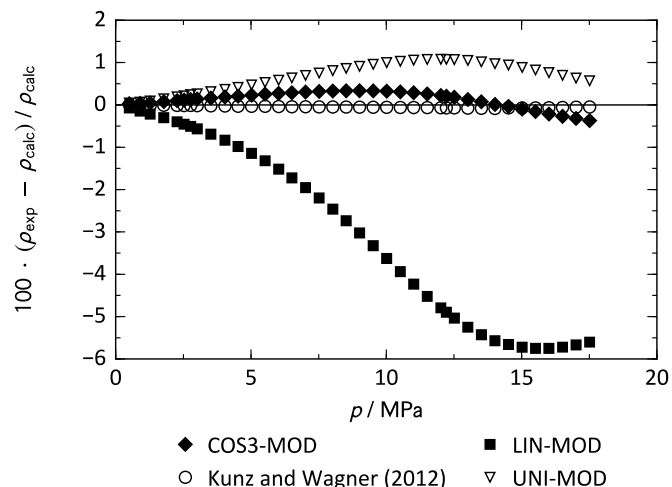


Figure 5: Relative deviations of experimental density data by Jaeschke et al. [29,30] for a mixture of $x_{\text{CH}_4} = 0.6855$ and $x_{\text{CO}_2} = 0.3145$ on an isotherm of $T = 290$ K from calculated results of the reference model by Kunz and Wagner [4] (GERG-2008), and calculated results of the predictive models LIN-MOD, UNI-MOD, and COS3-MOD.

The reference model of Kunz and Wagner (GERG-2008) which was fitted to the experimental data and contains an empirical departure function represents the data with the least deviation. The predictive model LIN-MOD deviates up to 6% from the data, while the predictive models UNI-MOD and COS3-MOD deviate significantly less from the data. In order to assess this in more detail, the average absolute relative deviations (AARD) for all models have been calculated. The AARD is defined according to

$$\text{AARD} = \frac{1}{N_p} \sum_{i=1}^{N_p} \left| \frac{\rho_{\text{exp},i} - \rho_{\text{calc},i}}{\rho_{\text{calc},i}} \right|, \quad (11)$$

with N_p being the number of data points. The AARDs of the different models for the experimental densities of Jaeschke et al. [29,30] are: $\text{AARD}_{\text{GERG-2008}} = 0.047\%$, $\text{AARD}_{\text{LIN-MOD}} = 2.993\%$, $\text{AARD}_{\text{UNI-MOD}} = 0.666\%$, and $\text{AARD}_{\text{COS3-MOD}} = 0.201\%$. Kunz and Wagner [4] estimate the combined standard uncertainty of the data to be 0.1 % in density. The GERG-2008 is capable of representing the experimental data within the measurement uncertainty. The predictive models do not represent the experimental data within the measurement uncertainty (which is to be expected); however, there are distinct differences between the performances of the predictive models. While LIN-MOD exhibits large deviations up to -6% , the

predictive models UNI-MOD and COS3-MOD deviate less from the experimental data and have a significantly lower AARD. In order to further investigate this phenomenon, deviations of these models to accurate experimental density data by Jaeschke et al. [29,30] for a binary mixture of CO₂ + C₂H₆ have been calculated. Figure 6 shows deviations of the experimental data in a temperature range from $T = 293.1$ K to $T = 313.1$ K from calculated data with different models.

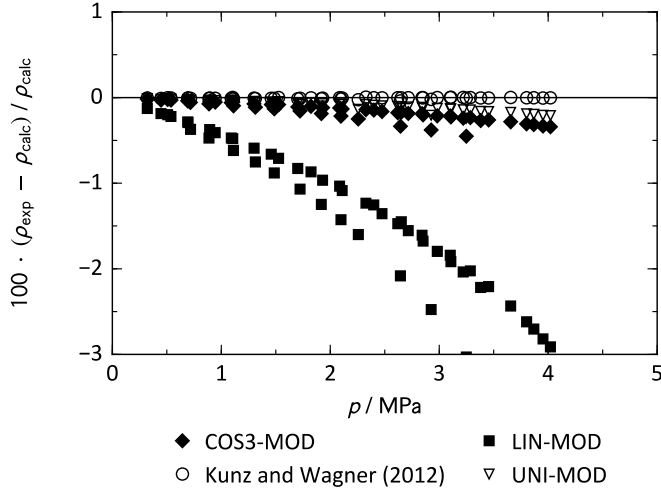


Figure 6: Relative deviations of experimental density data by Jaeschke et al. [29,30] for a binary mixture of $x_{C_2H_6} = 0.2267$ and $x_{CO_2} = 0.7733$ in a temperature range from $T = 293.1$ K to $T = 313.1$ K from calculated results of the reference model by Kunz and Wagner [4] (GERG-2008), and calculated results of the predictive models LIN-MOD, UNI-MOD, and COS3-MOD.

Again, the GERG-2008 represents the experimental data well. For this binary mixture, Kunz and Wagner fitted only the four parameters of the reducing functions (β_T , γ_T , β_v and γ_v) to the experimental data and have not developed an empirical departure function. The AARDs of the different models for the experimental densities of Jaeschke et al. [29,30] are: $AARD_{GERG-2008} = 0.007\%$, $AARD_{LIN-MOD} = 1.299\%$, $AARD_{UNI-MOD} = 0.0967\%$, and $AARD_{COS3-MOD} = 0.165\%$. Among the predictive models, again LIN-MOD deviates the most from the experimental data with deviations up to more than 3%. UNI-MOD and COS3-MOD represent the experimental densities significantly better.

CONCLUSIONS

In our recent work [5,6], we demonstrated that the combination of the multi-fluid mixture model with g^E -models yields good predictive results for the calculation of phase equilibria for various mixtures, while the multi-fluid mixture model with linear mixing rules for the reducing functions and without a departure function cannot be used well predictively. In this work, we extended our previous work by investigating the

model performance for mixtures with CO₂ with special focus on the representation of densities in the homogeneous phase. While in our previous work [6], only the original version of the COSMO-SAC model by Lin and Sandler [8] has been combined with the multi-fluid mixture model (COS1-MOD), in this work two improved models of COSMO-SAC [18,19] have been combined with the multi-fluid mixture model (COS2-MOD and COS3-MOD). It was found that COS2-MOD and COS3-MOD are capable of describing phase equilibria more accurately than COS1-MOD. Especially COS3-MOD could be significantly improved by fitting molecular dispersion parameters to experimental data.

For the investigated mixtures with CO₂, the combinations of the multi-fluid mixture model with UNIFAC and COSMO-SAC (UNI-MOD, COS1-MOD, COS2-MOD, and COS3-MOD) yield better predictive results regarding accurate experimental density data in the homogeneous phase. UNI-MOD and COS3-MOD represent the experimental densities by Jaeschke et al. [29,30] significantly better than LIN-MOD. However, the representation of experimental densities could still be improved, as the experimental data are not represented within the experimental uncertainties by the predictive models.

From these findings, it can be concluded that the combinations of multi-fluid mixture models with g^E -models yield good predictive results for properties of mixtures containing CO₂. Hence, these models could be employed to find suitable additives to CO₂ in order to improve the performance of power cycles with supercritical CO₂.

So far, the investigations have been restricted to mixtures of CO₂ with CH₄ and C₂H₆ for which accurate experimental data and multi-fluid mixture models exist. In future work, this study can readily be extended to mixtures of other components with CO₂.

NOMENCLATURE

Symbols

b	covolume of a cubic equation of state ($m^3 mol^{-1}$)
∂	partial derivative
F	parameter of the departure function (-)
i	index of summation
j	index of summation
k_B	Boltzmann's constant ($k_B = 1.380649 \cdot 10^{-23} J K^{-1}$)
N	number of components in the mixture
N_p	number of experimental points
p	pressure (Pa)
R	universal gas constant ($R = 8.3144598 J mol^{-1} K^{-1}$)
T	temperature (K)
x	mole fraction (-)
\vec{x}	vector of mole fractions (-)

Greek symbols

α	dimensionless Helmholtz energy (-)
β	model parameter (-)
δ	reduced density (-)
γ	model parameter (-)
ρ	molar density ($mol m^{-3}$)

τ reduced temperature (-)

Subscripts

c property at the critical point
calc calculated property
exp experimentally measured property
GE property calculated from an excess Gibbs energy model
i property of component *i*
j property of component *j*
o property of a pure fluid
r reducing property
s property at saturation (at vapor-liquid equilibrium)
ref property at reference pressure

Superscripts

0 ideal gas property
E excess property
L property of a liquid phase
r residual property

Chemical Formulas

CH₄ methane
C₂H₆ ethane
CO₂ carbon dioxide

Abbreviations

AARD average absolute relative deviation
CCS carbon capture and storage
COS1-MOD multi-fluid mixture model combined with COSMO-SAC by Lin and Sandler [8] using a theoretically based departure function.
COS2-MOD multi-fluid mixture model combined with COSMO-SAC by Hsieh et al. [18] using a theoretically based departure function.
COS3-MOD multi-fluid mixture model combined with COSMO-SAC by Hsieh et al. [19] using a theoretically based departure function.
COSMO-SAC conductor-like screening model - segment activity coefficient
LIN-MOD multi-fluid mixture model with linear mixing rules for the reducing functions and no departure function
PSRK predictive Soave-Redlich-Kwong equation of state
UNI-MOD multi-fluid mixture model combined with UNIFAC (with VTPR parameters) using a theoretically based departure function.
UNIFAC UNIQUAC Functional-group Activity Coefficients
VLE vapor-liquid equilibrium
VTPR volume-translated Peng-Robinson group contribution equation of state

REFERENCES

- [1] R. Span, W. Wagner, A New Equation of State for Carbon Dioxide Covering the Fluid Region from the Triple-Point Temperature to 1100 K at Pressures up to 800 MPa, *J. Phys. Chem. Ref. Data.* 25 (1996) 1509–1596. doi:10.1063/1.555991.
- [2] E.W. Lemmon, R. Tillner-Roth, A Helmholtz Energy Equation of State for Calculating the Thermodynamic Properties of Fluid Mixtures, *Fluid Phase Equilibria.* 165 (1999) 1–21.
- [3] O. Kunz, R. Klimeck, W. Wagner, M. Jaeschke, The Gerg-2004 Wide Range Equation of State for Natural Gases and Other Mixtures GERG TM15 2007, VDI-Verl., Düsseldorf, Germany, 2007.
- [4] O. Kunz, W. Wagner, The GERG-2008 Wide-Range Equation of State for Natural Gases and Other Mixtures: An Expansion of GERG-2004, *J. Chem. Eng. Data.* 57 (2012) 3032–3091. doi:10.1021/jc300655b.
- [5] A. Jäger, I.H. Bell, C. Breitenkopf, A theoretically based departure function for multi-fluid mixture models, *Fluid Phase Equilibria.* 469 (2018) 56–69. doi:10.1016/j.fluid.2018.04.015.
- [6] A. Jäger, E. Mickoleit, C. Breitenkopf, A Combination of Multi-Fluid Mixture Models with COSMO-SAC, *Fluid Phase Equilibria.* 476 (2018) 147–156. doi:10.1016/j.fluid.2018.08.004.
- [7] A. Fredenslund, R.L. Jones, J.M. Prausnitz, Group-Contribution Estimation of Activity Coefficients in Nonideal Liquid Mixtures, *AIChE J.* 21 (1975) 1086–1099.
- [8] S.-T. Lin, S.I. Sandler, A Priori Phase Equilibrium Prediction from a Segment Contribution Solvation Model, *Ind. Eng. Chem. Res.* 41 (2002) 899–913. doi:10.1021/ie001047w.
- [9] U. Gampe, J. Henoeh, G. Gerbeth, F. Hannemann, S. Rath, U. Hampel, S. Glos, Concept and preliminary design of a 600 °C+ sCO₂ test facility, in: *Proc. 2nd Eur. SCO₂ Conf.* 2018, Essen, Germany, 2018. doi:10.17185/dupublico/46084.
- [10] T. Holderbaum, J. Gmehling, PSRK: A Group Contribution Equation of State Based on UNIFAC, *Fluid Phase Equilibria.* 70 (1991) 251–265.
- [11] K. Fischer, J. Gmehling, Further Development, Status and Results of the PSRK Method for the Prediction of Vapor-Liquid Equilibria and Gas Solubilities, *Fluid Phase Equilibria.* 121 (1996) 185–206.
- [12] S. Horstmann, A. Jabłonec, J. Krafczyk, K. Fischer, J. Gmehling, PSRK group contribution equation of state: comprehensive revision and extension IV, including critical constants and α -function parameters for 1000 components, *Fluid Phase Equilibria.* 227 (2005) 157–164. doi:10.1016/j.fluid.2004.11.002.
- [13] B. Schmid, J. Gmehling, Revised Parameters and Typical Results of the VTPR Group Contribution Equation of State, *Fluid Phase Equilibria.* 317 (2012) 110–126. doi:10.1016/j.fluid.2012.01.006.

- [14] B. Schmid, A. Schedemann, J. Gmehling, Extension of the VTPR Group Contribution Equation of State: Group Interaction Parameters for Additional 192 Group Combinations and Typical Results, *Ind. Eng. Chem. Res.* 53 (2014) 3393–3405. doi:10.1021/ie404118f.
- [15] J. Ahlers, J. Gmehling, Development of an Universal Group Contribution Equation of State: I. Prediction of Liquid Densities for Pure Compounds with a Volume Translated Peng–Robinson Equation of State, *Fluid Phase Equilibria.* 191 (2001) 177–188. doi:10.1016/S0378-3812(01)00626-4.
- [16] W. Duschek, R. Kleinrahm, W. Wagner, Measurement and correlation of the (pressure, density, temperature) relation of carbon dioxide. II. Saturated-liquid and saturated- vapour densities and the vapour pressure along the entire coexistence curve, *J Chem Thermodyn.* 22 (1990) 841–864.
- [17] D.-Y. Peng, D.B. Robinson, A New Two-Constant Equation of State, *Ind. Eng. Chem. Fundam.* 15 (1976) 59–64. doi:10.1021/i160057a011.
- [18] C.-M. Hsieh, S.I. Sandler, S.-T. Lin, Improvements of COSMO-SAC for vapor–liquid and liquid–liquid equilibrium predictions, *Fluid Phase Equilibria.* 297 (2010) 90–97. doi:10.1016/j.fluid.2010.06.011.
- [19] C.-M. Hsieh, S.-T. Lin, J. Vrabec, Considering the dispersive interactions in the COSMO-SAC model for more accurate predictions of fluid phase behavior, *Fluid Phase Equilibria.* 367 (2014) 109–116. doi:10.1016/j.fluid.2014.01.032.
- [20] J. Gernert, R. Span, EOS–CG: A Helmholtz energy mixture model for humid gases and CCS mixtures, *J. Chem. Thermodyn.* 93 (2016) 274–293. doi:10.1016/j.jct.2015.05.015.
- [21] D. Bucker, W. Wagner, A Reference Equation of State for the Thermodynamic Properties of Ethane for Temperatures from the Melting Line to 675 K and Pressures up to 900 MPa, *J. Phys. Chem. Ref. Data.* 35 (2006) 205–266. doi:10.1063/1.1859286.
- [22] U. Setzmann, W. Wagner, A New Equation of State and Tables of Thermodynamic Properties for Methane Covering the Range from the Melting Line to 625 K at Pressures up to 1000 MPa, *J. Phys. Chem. Ref. Data.* 20 (1991) 1061–1155.
- [23] E. Mullins, R. Oldland, Y.A. Liu, S. Wang, S.I. Sandler, C.-C. Chen, M. Zwolak, K.C. Seavey, Sigma-Profile Database for Using COSMO-Based Thermodynamic Methods, *Ind. Eng. Chem. Res.* 45 (2006) 4389–4415. doi:10.1021/ie060370h.
- [24] R. Span, *Multiparameter Equations of State: An Accurate Source of Thermodynamic Property Data*, Springer, Berlin, Germany, 2000.
- [25] R. Span, R. Beckmüller, T. Eckermann, S. Herrig, S. Hielscher, A. Jäger, E. Mickoleit, T. Neumann, S.M. Pohl, B. Semrau, M. Thol, TREND. Thermodynamic Reference and Engineering Data 4.0, Lehrstuhl fuer Thermodynamik, Ruhr-Universitaet Bochum, Bochum, Germany, 2019.
- [26] J. Gernert, A. Jäger, R. Span, Calculation of Phase Equilibria for Multi-Component Mixtures Using Highly Accurate Helmholtz Energy Equations of State, *Fluid Phase Equilibria.* 375 (2014) 209–218. doi:10.1016/j.fluid.2014.05.012.
- [27] A. Jäger, *Complex Phase Equilibria of Gas Hydrates and Other Solid and Fluid Phases Modeled with Highly Accurate Equations of State*, Dissertation, Ruhr-Universität Bochum, 2016. <https://hss-opus.ub.ruhr-uni-bochum.de/opus4/frontdoor/index/index/docId/4546> (accessed April 12, 2019).
- [28] K. Nagahama, H. Konishi, D. Hoshino, M. Hirata, Binary vapor-liquid equilibria of carbon dioxide - light hydrocarbons at low temperature, *J Chem Eng Jpn.* 7 (1974) 323–328. doi:10.1252/jcej.7.323.
- [29] M. Jaeschke, A.E. Humphreys, *The GERG databank of high accuracy compressibility factor measurements*. GERG Technical Monograph 4 (1990), VDI-Verl., Düsseldorf, Germany, 1991.
- [30] M. Jaeschke, H.-M. Hinze, A.E. Humphreys, *Supplement to the GERG databank of high-accuracy compression factor measurements*. GERG TM7 1996. GERG Technical Monograph 7 (1996), VDI-Verl., Düsseldorf, Germany, 1997.

EFFECT OF IMPURITIES ON SUPERCRITICAL CO₂ COMPATIBILITY

Bruce A. Pint*

Oak Ridge National Laboratory
Oak Ridge, TN 37831-6156 USA
Email: pintba@ornl.gov

Kinga A. Unocic

Oak Ridge National Laboratory
Oak Ridge, TN 37831-6156 USA

James R. Keiser

Oak Ridge National Laboratory
Oak Ridge, TN 37831-6156 USA

ABSTRACT

Impurities may affect structural alloy compatibility in both indirect- and direct-fired supercritical CO₂ (sCO₂) cycles for high efficiency power generation with peak temperatures above 700°C. Using a new multi-pump gas control system, experiments with controlled impurity additions were compared to baseline results in research- or industrial-grade CO₂ at 750°C/300 bar. Low level impurities, 50 ppm O₂ and 50 ppm H₂O, were not found to affect mass change or reaction products after 2,500 h exposures. However, in RG sCO₂+1%O₂+0.25%H₂O, higher reaction rates were observed for both Ni- and Fe-based alloys, but especially Fe-based alloys were strongly affected by these high impurity levels. Analytical TEM was used to characterize the reaction products on alloy 625.

INTRODUCTION

Supercritical CO₂ (sCO₂) could be used as a working fluid for a variety of power generation applications because of its unique properties and relatively low critical point (31°C/74 bar) compared to water [1-4]. Subcritical CO₂ (43 bar) was used in the UK advanced gas cooled reactors (AGR), however, additives such as CH₄, were used to keep the O₂ partial pressure low to minimize graphite oxidation in the reactor core, which increased the C activity [5,6]. Thus, the AGR conditions are very different than those expected for sCO₂. While a range of peak temperatures is being considered for the various sCO₂ applications, CSP and fossil energy desire efficiencies over 50% and require >700°C for indirect-fired or closed cycles [7]. Direct-fired cycles also are targeting similar temperatures [4]. Most studies have shown relatively good compatibility for Ni-based structural alloys needed for >700°C applications in autoclaves using relatively high-purity CO₂ [8-17]. However, the role of impurities in sCO₂ compatibility has not been resolved, either for the low impurity levels in indirect-fired

cycles or the higher residual O₂ and H₂O from combustion in the direct-fired cycles [4]. (In addition, S and Cl could be present if coal-derived synthesis gas were combusted.) For example, O₂ additions have shown slightly negative effects [12,14] or little effect [15]. A recent publication provided an initial indication that pressure affects the role of impurities at 750°C/300 bar [17]. This paper provides additional characterization from that study and compares the results to a second experiment where low levels of O₂ and H₂O were intentionally added to simulate the highest impurity levels that might be found in IG CO₂. The structural alloys investigated included two advanced austenitic steels, an alumina-forming Ni-based superalloy (typically used for turbomachinery) and both SS and PS [18,19] Ni-based alloys identified by AUSC [20] for applications above 700°C. These impurity levels at 30 MPa increased the specimen mass change, particularly for the Fe-based alloys.

PROCEDURE

The alloys compared in this study and their measured compositions are shown in Table 1. Coupons (~12 x 20 x 1.5mm) were polished to a 600 grit finish and cleaned in acetone and methanol prior to exposure. All exposures used 500-h cycles at 750°C. Baseline exposures in laboratory air (~50% relative humidity) were conducted in a box furnace with heating for ~4 h and furnace cooling in air. For the 300 bar exposures, the experiments were conducted in an alloy 282 autoclave (~266 mm x 83 mm inner diameter) described previously [10,13]. Specimens were held on an alloy 282 sample rack and slowly heated to temperature over several hours (~2°C/min) in sCO₂, held at temperature ±2°C and then cooled in sCO₂ to room temperature by lowering the furnace and using a cooling fan on the autoclave. In all cases, the fluid flow rate was ~2 ml/min. Experiments were conducted in RG (4.1±0.7 ppm H₂O, <5 ppm O₂) and IG (18.8±16.9 ppm H₂O, <50 ppm O₂) CO₂ [17]. Two autoclaves were modified to use three pumps to deliver sCO₂,

* corresponding author(s)

Table 1: Chemical composition of the alloys measured by ICP and combustion analyses in mass% [17].

Alloy	Fe	Ni	Cr	Al	Other
25 SS	42.6	25.4	22.3	0.03	3.4W,3Cu,1.5Co,0.5Mn,0.5Nb
310HN	51.3	20.3	25.5	<	0.3Co,0.4Nb,1.2Mn,0.3Si,0.3N
625	4.0	61.0	21.7	0.1	8.8Mo,3.5Nb,0.2Ti,0.2Mn
230	1.5	60.5	22.6	0.3	12.3W,1.4Mo,0.5Mn,0.4Si
617B	1.2	54.6	22.3	1.0	11.9Co,8.2Mo,0.4Ti,0.04Mn
282 (#1)	0.2	57.1	19.6	1.6	10.6Co,8.6Mo,0.04Si,2.2Ti
282 (#2)	0.2	57.7	19.4	1.6	10.5Co,8.3Mo,0.05Si,2.1Ti
740	0.1	49.7	24.5	1.4	20.6Co,1.5Nb,1.4Ti,0.3Mn
247	0.07	59.5	8.5	5.7	9.8Co,10W,0.7Mo,3.1Ta,1.4Hf

< indicates below the detectability limit of 0.01%

CO₂-O₂ and H₂O [17]. Based on the gas flow rate, the O₂ level was calculated as 1.0±0.2% and the H₂O content as 0.25±0.05% for the high impurity experiment. For the low impurity experiment, 50ppm O₂ and 50 ppm H₂O were targeted.

For all experiments, specimen mass change was measured using a Mettler Toledo model XP205 balance with an accuracy of ±0.04 mg or 0.01 mg/cm². After exposure, samples were copper plated before being sectioned and mounted for light microscopy. Both oxide thickness and internal oxidation were measured using image analysis software with ~20-30 measurements taken for each specimen. Prior publications reported characterization using SEM and GDOES. Recent results using STEM/EDS are reported. The TEM specimens were prepared via the *in situ* FIB lift-out method on a Hitachi model NB5000 FIB-SEM. A W layer was deposited to protect the gas interface of the scale. The STEM imaging was carried out using a FEI model Talos F200X STEM with integrated EDS with four silicon drift detectors.

RESULTS AND DISCUSSION

Figure 1 shows mass change at 750°C/300 bar for the low impurity experiment with 50 ppm O₂ and 50 ppm H₂O additions to RG sCO₂ compared to a similar exposure in IG sCO₂. The mass change from 3-4 specimens in impure sCO₂ is shown using box and whisker plots where the whiskers show the minimum and maximum values. The lines connect the median values for each alloy. For clarity, only the dashed lines connecting the median values for 7-10 specimens in IG sCO₂ are shown. In most cases, only minor differences between the two environments were observed. The exception was the Fe-based alloy 25, which showed a higher initial mass gain in IG sCO₂. However, the subsequent rate of mass gain was very similar in the two environments. As observed previously [10,13,16,17], the mass gains were highest for the alloy 282 specimens because of the high level of Ti in this alloy (Table 1) which contains a high γ' fraction [18]. Previous work has shown that Ti accelerates the growth of the Cr₂O₃ scale [21,22]. Likewise, the mass gain for the 740 specimens was higher than that observed for alloy 625, which contains very little Ti, similar to alloy 25.

Figure 2 compares polished cross-sections of these alloys in the two environments. Consistent with the mass change data, little difference was observed in the reaction products between

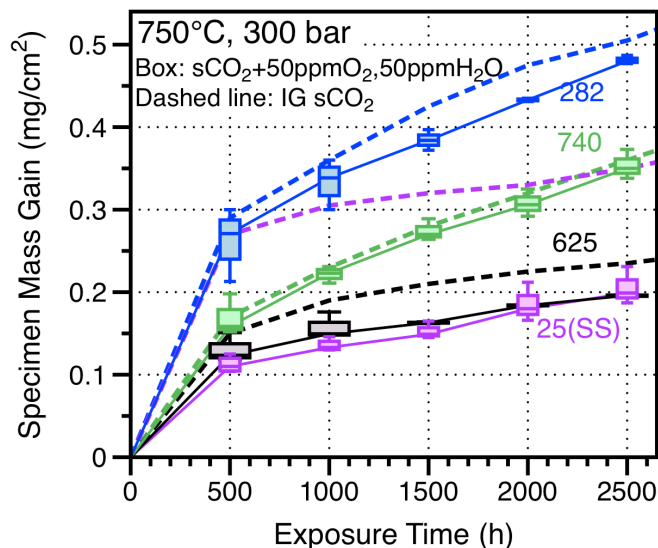


Figure 1: Specimen mass gain data for 500-h cycles at 750°C in 300 bar IG (dashed lines) and RG sCO₂ with 50ppm O₂ and 50ppm H₂O (solid lines). Box and whisker plots show data for 3-4 specimens exposed.

the two environments. Also consistent with the mass change data, the thinnest scales were observed for alloys 25 and 625 with very little internal oxidation. In contrast, the PS alloys showed thicker scales and similar internal oxidation in both environments. Previous TEM studies have shown both Ti and Al internally oxidized in 282 with Ti enriched in the scale at both the gas and metal interfaces [23].

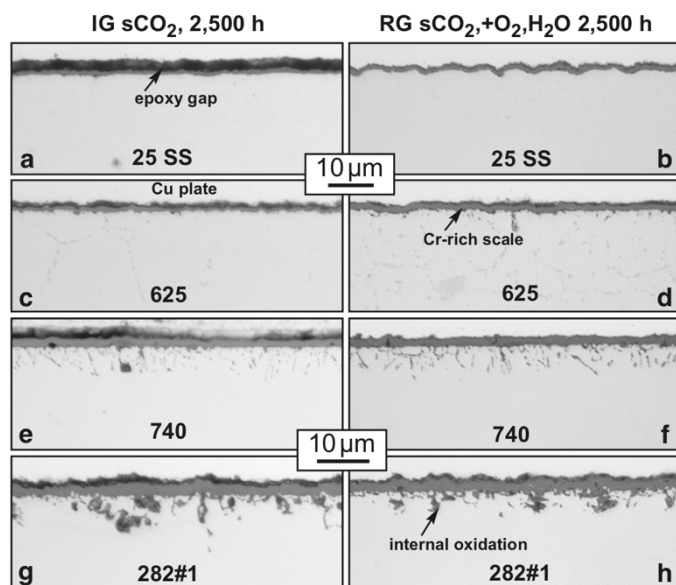


Figure 2: Light microscopy of polished cross-sections of specimens exposed for 2,500 h at 750°C/300 bar in IG sCO₂ and RG sCO₂ with 50 ppm O₂ and 50 ppm H₂O additions.

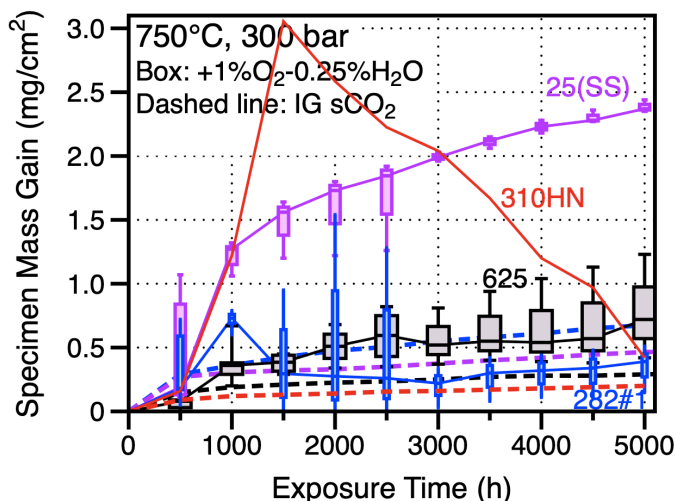


Figure 3: Specimen mass gain data for 500-h cycles at 750°C in 300 bar IG (dashed lines) and RG sCO₂ with 1% O₂ and 0.25% H₂O (solid lines). Box and whisker plots show data for 3-5 specimens exposed in the high impurity environment [17].

Similar to Figure 1, Figure 3 shows the mass change data at 750°C/300 bar for IG sCO₂ (dashed lines) and RG sCO₂ with 1%O₂ and 0.25%H₂O (solid lines and boxes) [17]. The mass gains were consistently higher for all of the materials but, particularly for the Fe-based alloys 25 and 310HN, there was a much larger increase and the drop in mass for 310HN suggested scale spallation. As all of the exposures were conducted for at least 2,500 h, Figure 4 tries to compare all of the mass change data for the four 300 bar exposures at 2,500 h [17]. As a baseline, the values are compared to a similar exposure in laboratory air. For many of the Ni-based alloys, the mass changes were very similar in all five environments. For the high impurity case, the largest mass gains were noted for the Fe-based alloys and for the alumina-forming superalloy 247.

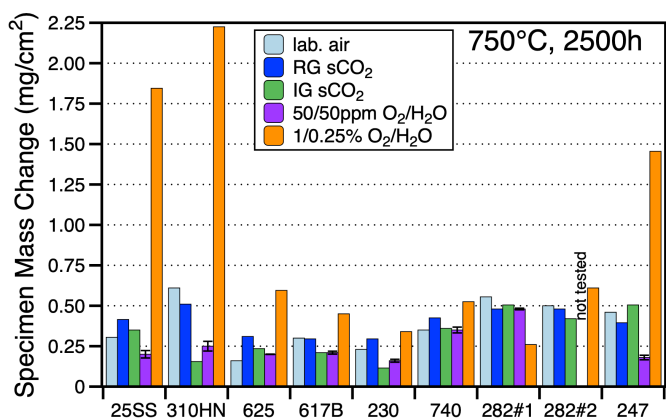


Figure 4: Median specimen mass gain values after 2,500 h exposures at 750°C in four different 300 bar environments compared to laboratory air exposures.

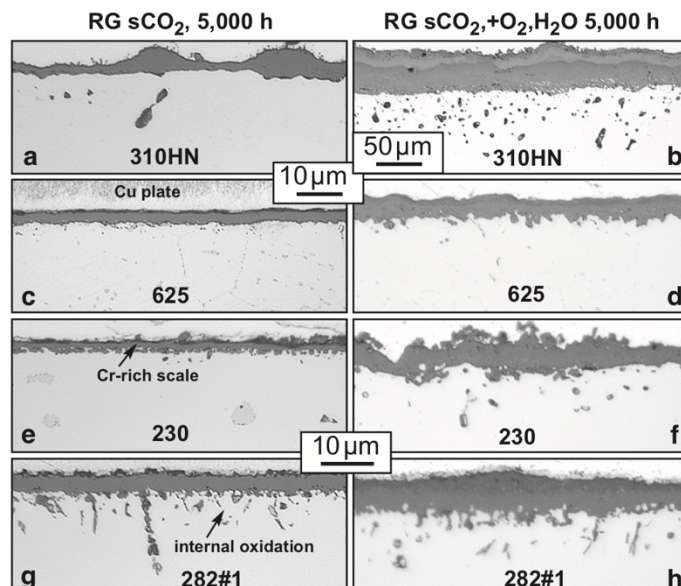


Figure 5: Light microscopy of polished cross-sections of specimens exposed for 5,000 h at 750°C/300 bar in RG sCO₂ and RG sCO₂+1%O₂+0.25%H₂O.

Figure 5 compares the reaction products in RG sCO₂ and sCO₂ with 1%O₂ and 0.25%H₂O after 5,000 h exposures. Characterization for alloys 247 and 25 after 2,500 h was studied in more detail and reported earlier [17]. Consistent with the mass change data, the oxide was thicker for all of the specimens with the addition of impurities. However, the major change for the 310HN specimen required a different magnification. SEM analysis of this specimen is in progress. For the Ni-based alloys, despite the increase, the oxide scales were still relatively thin. Figure 6 attempts to compare the scale thicknesses for each of the alloys after 5,000 h exposures in RG sCO₂ and RG sCO₂ with 1%O₂ and 0.25%H₂O. Similar to the mass change data, the results for alloys 25, 310HN and 247 are more significant.

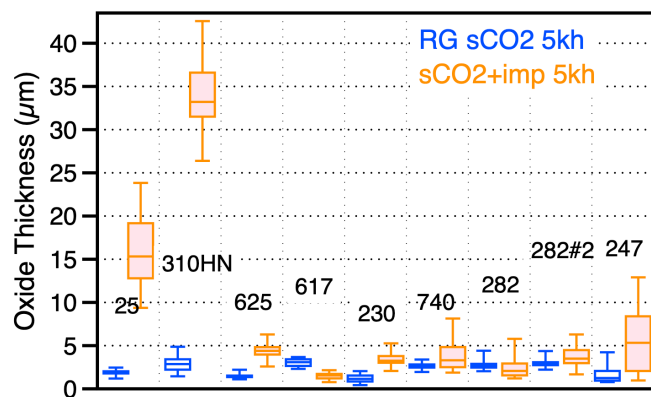


Figure 6: Box and whisker plots of the oxide scale thicknesses formed after 5,000 h at 750°C at 300 bar in RG sCO₂ (open boxes) and RG sCO₂+1%O₂+0.25%H₂O (shaded boxes).

Because of the thin reaction products formed on most of the alloys in these environments at 750°C, conventional characterization can be challenging. Therefore, analytical TEM was used to characterize the reaction products after exposure to the environments with intentional impurity additions. To build upon prior TEM work [23,24], alloy 625 was chosen for this analysis. The scale formed on alloy 282 was found to be extremely complicated and difficult to interpret because of the incorporation of Ti and Al into the reaction product [23]. Figure 7 shows an example of the scale formed after 1,000 h at 750°C in RG sCO₂ with 50 ppm additions of O₂ and H₂O. Similar to previous observations for alloy 625 after 1,000 h in IG sCO₂, the Cr₂O₃ scale contained a mixture of large and small grains [23]. Much larger Cr₂O₃ grains formed in laboratory air after a similar exposure. Also similar to previous observations, large Mo- and Nb-rich precipitates were observed at the metal-scale interface. These precipitates are typical for the oxidation of alloy 625 where Mo and Nb are rejected from the reaction front as Cr is selectively oxidized [25]. Figure 8 shows EDS maps of the same area as shown in Figure 7. Primarily a Cr-rich oxide scale was formed. The Mo- and Nb-rich precipitates are prominent in this particular location, Figures 8c and 8d. The void at the metal-oxide interface also has been widely observed after sCO₂ exposures [26]. The low level of impurities added to this experiment appears to have had very little effect on the reaction products which is consistent with the mass change in Figure 1 and the light microscopy of the thin reaction product in Figure 2.

In contrast, Figure 9 shows a similar BF-STEM image of the scale formed on an alloy 625 specimen after 1,000 h at 750°C in RG sCO₂+1%O₂+0.25%H₂O. The magnification is not the same in Figures 7 and 9. The average oxide thickness in the FIB

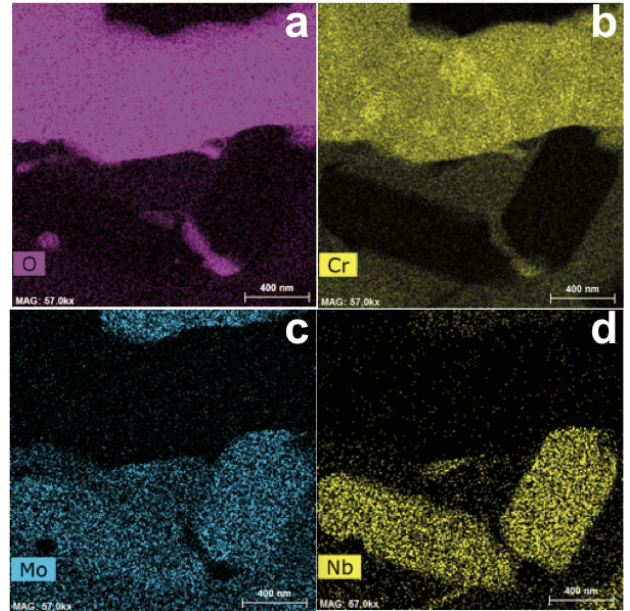


Figure 8: EDS elemental maps associated with the image in Figure 7 of the scale formed on alloy 625 after 1,000 h at 750°C in RG sCO₂ with 50 ppm additions of O₂ and H₂O, (a) O, (b) Cr, (c) Mo and (d) Nb.

TEM sections have increased from 0.8±0.06 μm with low impurity additions to 3.7±0.4 μm with high impurity levels. The EDS maps in Figure 10 indicate that the scale is enriched in Cr. However, the layer of Mo- and Nb-rich precipitates in Figure 7 appears to have been incorporated into the scale and in some

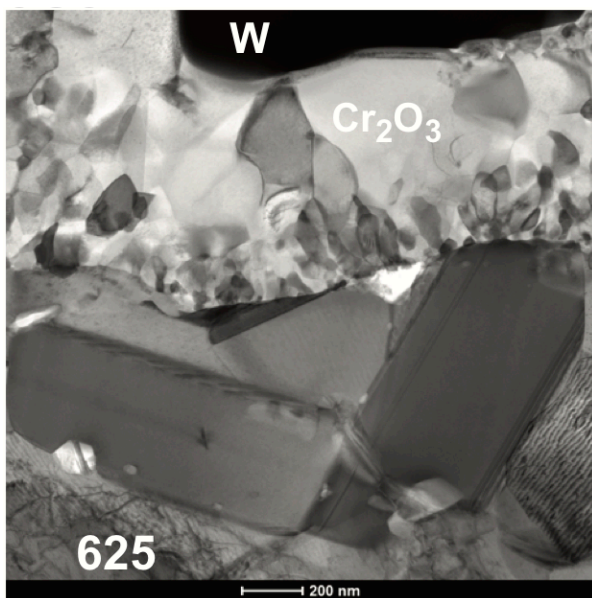


Figure 7: BF-STEM cross-sectional image of the scale formed on alloy 625 after 1,000 h at 750°C in 300 bar RG sCO₂ with 50 ppm additions of O₂ and H₂O.

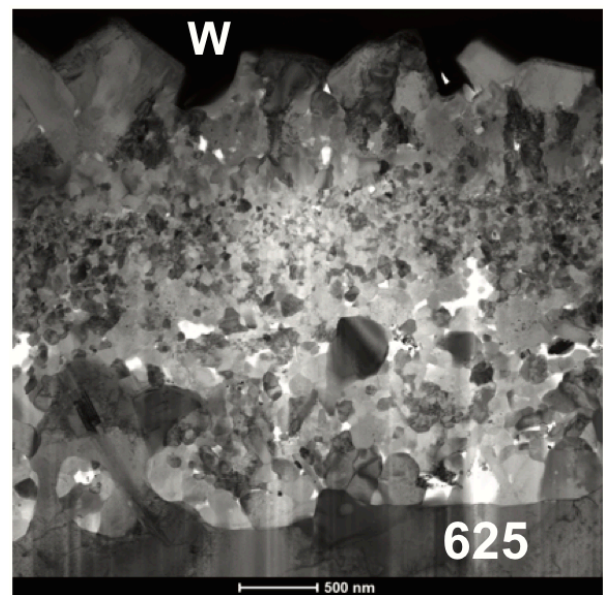


Figure 9: BF-STEM cross-sectional image of the scale formed on alloy 625 after 1,000 h at 750°C in 300 bar RG sCO₂ with additions of 1% O₂ and 0.25% H₂O.

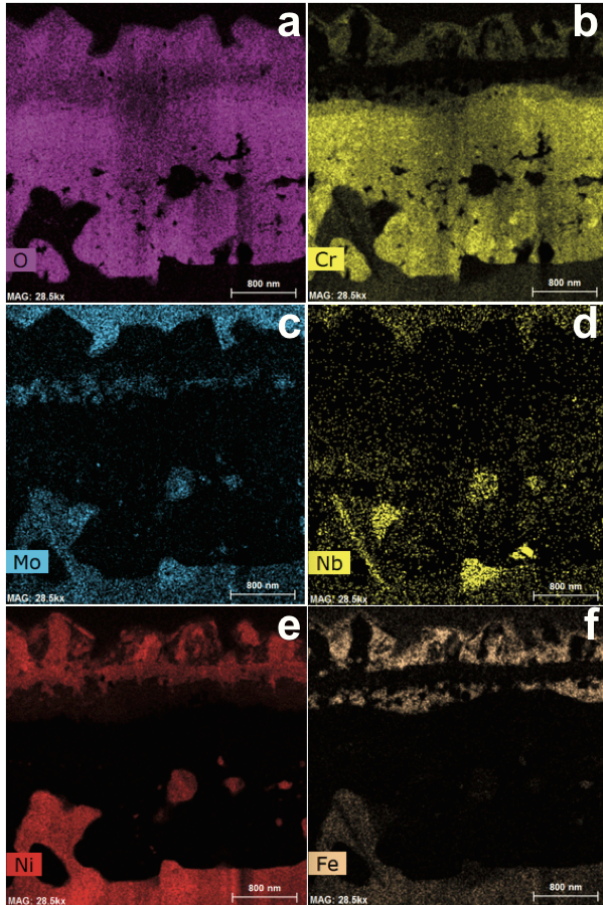


Figure 10: EDS elemental maps associated with the image in Figure 9 of the scale formed on alloy 625 after 1,000 h at 750°C in RG sCO₂+1%O₂+0.25%H₂O, (a) O, (b) Cr, (c) Mo, (d) Nb, (e) Ni and (f) Fe.

cases consumed by the reaction front. In addition, the outer part of the scale appears to be enriched in Ni and Fe. When a thicker scale is reported, it is not surprising to see oxidation of the base metal, often with the formation of an outer spinel-type MCr₂O₄ oxide layer. However, in this case the increased scale thickness is primarily due to a thicker Cr-rich layer with the Fe- and Ni-enriched layer being a relatively minor contribution. Because alloy 625 only contains only 4% Fe (Table 1), it is somewhat surprising to see Fe in the scale of a Ni-based alloy. It cannot be ruled out that the Fe may be from cross-contamination of the adjacent Fe-based alloy specimens in the autoclave experiment. Additional work is needed to rule out such a mechanism. No similar Fe enrichment was observed for the specimen shown in Figure 7 or after exposure in IG sCO₂ [23,24].

The strong effect of high levels of impurities at 750°C/300 bar on the Fe-based alloys suggests that similar studies should be conducted on Fe-based alloys at lower temperatures where they may be used to lower costs of the sCO₂ hardware. It is already clear that CO₂ restricts the use of steels to a larger degree than steam environments [27]. For example, while CSEF Grade 91

steel (Fe-9Cr-1Mo) is restricted to ~580°C in steam due to scale exfoliation issues [28], it is restricted to ~450°C due to internal carburization issues. Similar restrictions for steels might be further changed with the addition of impurities. For low impurity levels, the 50 ppm additions of O₂ and H₂O were selected to reflect the upper bound of impurities in IG CO₂. The minor effects of 50 ppm O₂ and H₂O additions suggests that these levels of impurities do not increase the oxidation rate at 750°C. This observation is consistent with the similar behavior of structural alloys in RG and IG sCO₂, Figure 4, despite the possibly higher levels of O₂ and H₂O in the latter. It could be speculated that the higher transient mass gain of the alloy 25 specimens in Figure 1 could be due to the higher impurity levels in IG sCO₂, but a similar increase was not observed when the O₂ and H₂O were intentionally added.

Considerable work remains to understand the mechanism by which these high impurity levels affect the reaction in sCO₂ and especially to isolate the roles of O₂ and H₂O. With the new experimental capability, it will now be possible to explore a wider range of impurity levels and determine the critical O₂ and H₂O levels where accelerated reaction rates are observed.

SUMMARY

For both direct- and indirect-fired supercritical CO₂ (sCO₂) cycles, impurities may be a concern. For indirect applications, comparison 500-h cyclic exposures were conducted at 750°C and 300 bar with RG and IG sCO₂ and the results were compared to RG sCO₂ with intentional additions of 50 ppm O₂ and 50 ppm H₂O. For both commercial Fe- and Ni-based structural alloys, mass changes and reaction products were unchanged with the impurity additions consistent with observed similarities between RG and IG sCO₂ experiments.

For higher impurity levels associated with direct-fired cycles, all of the alloys were somewhat affected by exposure to sCO₂+1%O₂+0.25%H₂O at 750°C/300 bar. The most significant effects were documented for the Fe-based alloys and the alumina-forming superalloy 247 after 5,000 h exposures. TEM characterization of the scales formed on 625 showed a much thicker Cr-rich oxide formed with the high impurity levels.

These results for high impurity levels are so different than prior results in ambient pressures that it is concluded that screening Fe-based alloys at a range of temperatures (400-700°C) is warranted to determine how impurities may affect sCO₂ compatibility at relevant pressures.

NOMENCLATURE

AUSC - U.S. Advanced Ultra-supercritical Steam Consortium
 BF – bright field
 CSEF – creep strength enhanced ferritic
 CSP – concentrating solar power
 EDS – energy dispersive x-ray spectrometer
 GDOES – glow discharge optical emission spectrometer
 FEI – electron microscope company
 FIB – focused ion beam
 ICP – inductively coupled plasma
 IG – industrial grade

PS – precipitation strengthened
RG – research grade
sCO₂ – supercritical carbon dioxide
SEM – scanning electron microscopy
SS – solid solution strengthened
STEM – scanning transmission electron microscopy
TEM – transmission electron microscopy

ACKNOWLEDGEMENTS

The authors would like to thank M. Howell, M. Stephens, T. M. Lowe, R. G. Brese and T. Jordan for assistance with the experimental work. Material was provided by Haynes International, Special Metals, Sandvik and Capstone Turbine, Corp. S. S. Raiman and R. Pillai provided helpful comments on the manuscript. This research was sponsored by the U.S. Department of Energy, Office of Fossil Energy, Crosscutting Technology Program and the Office of Energy Efficiency and Renewable Energy, Solar Energy Technology Program: SuNLaMP award number DE-EE0001556.

REFERENCES

- [1] V. Dostal, P. Hejzlar and M. J. Driscoll, "High-Performance Supercritical Carbon Dioxide Cycle for Next-Generation Nuclear Reactors," *Nuclear Technology*, 154 (3) (2006) 265-282.
- [2] H. Chen, D. Y. Goswami and E. K. Stefanakos, "A review of thermodynamic cycles and working fluids for the conversion of low-grade heat," *Renewable & Sustainable Energy Reviews* 14 (2010) 3059-3067.
- [3] B. D. Iverson, T. M. Conboy, J. J. Pasch and A. M. Kruiuzenga, "Supercritical CO₂ Brayton cycles for solar-thermal energy," *Applied Energy*, 111 (2013) 957-970.
- [4] R. J. Allam, M. R. Palmer, G. W. Brown Jr., J. Fetvedt, D. Freed, H. Nomoto, M. Itoh, N. Okita, C. Jones Jr., "High efficiency and low cost of electricity generation from fossil fuels while eliminating atmospheric emissions, including carbon dioxide," *Energy Procedia* 37 (2013) 1135-1149.
- [5] P. C. Rowlands, J. C. P. Garrett, L. A. Popple, A. Whittaker, A. Hoaskey, "The oxidation performance of Magnox and advanced gas-cooled reactor steels in high pressure CO₂," *Nuclear Energy* 25 (1986) 267-275.
- [6] Y. Gong, D. J. Young, P. Kontis, Y. L. Chiu, H. Larsson, A. Shin, J. M. Pearson, M. P. Moody and R. C. Reed, "On the breakaway oxidation of Fe₉Cr₁Mo steel in high pressure CO₂," *Acta Materialia*, 130 (2017) 361-374.
- [7] E. G. Feher, "The Supercritical Thermodynamic Power Cycle," *Energy Conversion*, 8 (1968) 85-90.
- [8] M. W. Dunlevy, "An Exploration of the Effect of Temperature on Different Alloys in Supercritical Carbon Dioxide Environment," M.Sc. Thesis, MIT, Cambridge, MA, 2009.
- [9] V. Firouzdor, K. Sridharan, G. Cao, M. Anderson and T. R. Allen, "Corrosion of a stainless steel and nickel-based alloys in high temperature supercritical carbon dioxide environment," *Corrosion Science* 69 (2013) 281-291
- [10] B. A. Pint and J. R. Keiser, "Initial Assessment of Ni-Base Alloy Performance in 0.1 MPa and Supercritical CO₂," *JOM* 67(11) (2015) 2615-2620.
- [11] R. I. Olivares, D. J. Young, P. Marvig and W. Stein, "Alloys SS316 and Hastelloy-C276 in Supercritical CO₂ at High Temperature," *Oxid. Met.* 84 (2015) 585-606.
- [12] J. Mahaffey, D. Adam, A. Brittan, M. Anderson and K. Sridharan, "Corrosion of Alloy Haynes 230 in High Temperature Supercritical Carbon Dioxide with Oxygen Impurity Additions," *Oxidation of Metals* 86 (2016) 567-580
- [13] B. A. Pint, R. G. Brese and J. R. Keiser, "Effect of Pressure on Supercritical CO₂ Compatibility of Structural Alloys at 750°C," *Materials and Corrosion*, 68 (2017) 151-158.
- [14] J. Mahaffey, A. Schroeder, D. Adam, A. Brittan, M. Anderson, A. Couet and K. Sridharan, "Effects of CO and O₂ Impurities on Supercritical CO₂ Corrosion of Alloy 625," *Metallurgical and Materials Transactions A* 49 (2018) 3703-3714.
- [15] S. C. Kung, J. P. Shingledecker, I. G. Wright, A. S. Sabau, B. M. Tossey, and T. Lolla, "Corrosion of Heat Exchanger Alloys in Open-Fired sCO₂ Power Cycles," in *Proceedings of the 6th International Symposium on Supercritical CO₂ Power Cycles*, Pittsburgh, PA, March 2018, Paper #5.
- [16] B. A. Pint and J. R. Keiser, "Effect of Pressure and Thermal Cycling on Long-Term Oxidation in Supercritical CO₂," NACE Paper C2019-12750, Houston, TX, presented at NACE Corrosion 2019, Nashville, TN, March 2019
- [17] B. A. Pint, J. Lehmusto, M. J. Lance and J. R. Keiser, "The Effect of Pressure and Impurities on Oxidation in Supercritical CO₂," *Mater. Corr.* (2019) DOI:10.1002/maco.201810652
- [18] L. M. Pike, "Development of a Fabricable Gamma-Prime (γ') Strengthened Superalloy," in *Superalloys 2008*, R. C. Reed et al. eds. TMS, Warrendale, PA, 2008, p.191-200
- [19] J. P. Shingledecker and G. M. Pharr, "Testing and Analysis of Full-Scale Creep-Rupture Experiments on Inconel Alloy 740 Cold-Formed Tubing," *J. Mater. Eng. Performance*, 22 (2013) 454-462.
- [20] R. Viswanathan, J. Shingledecker and R. Purgert, "Evaluating Materials Technology for Advanced Ultrasupercritical Coal-Fired Plants," *Power*, 154(8) (2010) 41-45.
- [21] P. J. Ennis and W. J. Quadackers, "Corrosion and Creep of Nickel-Base Alloys in Steam Reforming Gas," in *High Temperature Alloys, Their Exploitable Potential*, eds. J. B. Marriott, M. Merz, J. Nihoul and J. Ward, 1985, Elsevier, London, p.465-474.
- [22] M. P. Brady, B. A. Pint, Z. G. Lu, J. H. Zhu, C. E. Milliken, E. D. Kreidler, L. Miller, T. R. Armstrong and L. R. Walker, "Comparison of Oxidation Behavior and Electrical Properties of Doped NiO- and Cr₂O₃-Forming Alloys for Solid Oxide Fuel Cell Metallic Interconnects," *Oxidation of Metals*, 65 (2006) 237-61.
- [23] B. A. Pint, K. A. Unocic, R. G. Brese and J. R. Keiser, "Characterization of Chromia Scales Formed in Supercritical Carbon Dioxide," *Materials at High Temperature* 35 (2018) 39-49.

[24] B. A. Pint and K. A. Unocic, "The Effect of CO₂ Pressure on Chromia Scale Microstructure at 750°C," JOM 70 (2018) 1511-1519.

[25] A. Chyrkin, P. Huczowski, V. Shemet, L. Singheiser and W. J. Quadackers, "Sub-Scale Depletion and Enrichment Processes During High Temperature Oxidation of the Nickel Base Alloy 625 in the Temperature Range 900-1000°C," Oxid. Met. 75 (2011) 143-166.

[26] R. P. Oleksak, J. H. Tylczak, C. S. Carney, G. R. Holcomb and O. N. Dogan, "High-Temperature Oxidation of Commercial

Alloys in Supercritical CO₂ and Related Power Cycle Environments," JOM 70 (2018) 1527-1534.

[27] S. Sarrade, D Férona, F. Rouillard, S. Perrin, R. Robin, J.-C. Ruiz, H.-A. Turc, "Overview on corrosion in supercritical fluids," J. of Supercritical Fluids 120 (2017) 335-344.

[28] N. Nishimura, N. Komai, Y. Hirayama, and F. Masuyama, "Japanese experiences with steam oxidation on advanced heat-resistant steel tubes in power boilers," Materials at High Temperatures, 22, 3-10 (2005).

HEAT TRANSFER CHARACTERISTICS OF sCO₂ AND DYNAMIC SIMULATION MODEL OF sCO₂ LOOP

Gang Xiao*
Zhejiang University
Hangzhou, China
Email:

xiaogangtianmen@zju.edu.cn

Kaixiang Xing
Zhejiang University
Hangzhou, China

Jinyi Zhang
EDF R&D China
Beijing, China

Yann Le Moullec
EDF R&D China
Beijing, China

Pan Zhou
EDF R&D China
Beijing, China

Tianfeng Yang
Zhejiang University
Hangzhou, China

Mingjiang Ni
Zhejiang University
Hangzhou, China

Kefa Cen
Zhejiang University
Hangzhou, China

ABSTRACT

Supercritical CO₂ (sCO₂) Brayton cycle is a promising power generation technology with high efficiency, compact turbo-machineries and simple layout. Heat exchangers play an important role in sCO₂ Brayton cycle systems. Therefore it is important to have a comprehensive understanding on heat transfer characteristics of sCO₂ at various operation conditions, in order to better design the heat exchangers. A sCO₂ test loop is built to investigate the heat transfer characteristics of sCO₂, which consists of a test section for heat transfer (horizontal straight tube with an inner diameter of 8 mm), an electrical heater of 7.2kW, a heat recuperator of type coil tubes, a back-pressure valve, a CO₂ pump, a CO₂ cooler and a CO₂ storage tank. The test loop is designed to operate with pressure ranging from critical pressure to 15MPa, temperature ranging from critical temperature up to 600 °C, mass flow rate ranging from 20 to 70kg.h⁻¹. With this test loop, the heat transfer characteristics of sCO₂ under different conditions are measured and studied. These measurements are then used in the development of a new heat transfer correlations for sCO₂. Based on the developed correlation, a dynamic model has been built in Dymola and validated by experimental results. The experimental and simulation results show that: 1) The heat transfer coefficient (HTC) changes greatly for CO₂ at or near the critical point; 2) For sCO₂ at operation conditions far from the critical point, the wall-bulk temperature difference increases between the tube wall and sCO₂ flow with an increasing heating power, and the heat transfer coefficient is relatively stable. The experience gained by the experiment and simulation is then used to design a 150kWe sCO₂ Brayton cycle coupled with a solar solid particle receiver.

INTRODUCTION

Coupled the solar power with the sCO₂ Brayton cycle is one of the promising choices for future power generation. In recent years, many countries have completed the early work for sCO₂ Brayton cycle, such as USA, Korea, China and Japan at el.

The USA, who first suggested to use sCO₂ Brayton cycle in nuclear power system, takes the lead in developing sCO₂ power generation systems. Since 2011, DOE (Department of Energy) of USA started the SunShot Project (65 million dollars invested as research funding) and the Gen 3 Project (72 million dollars invested as research funding) for Supercritical CO₂ power cycle applied in solar thermal system. Sandia National Laboratory (USA) has been implementing and improving a supercritical CO₂ power generation test loop since 2005. Then, a 250kWe re-compression closed Brayton cycle is implemented using two turbine-alternator-compressor units consisting of gas foil bearings.[1] In addition, Bechtel Marine Propulsion Co. developed a 100 kWe supercritical CO₂ power generation cycle test loop using one turbo-generator and one turbo-compressor.[2] Korea Institute of Energy Research developed a 10 kWe-class simple Brayton cycle and an 80 kWe-class test loop for waste heat recovery.[3] Tokyo Institute of Technology (Japan) developed a 100 kWe sCO₂ experimental test loop.[4] Recently, researchers from Southwest Research Institute and General Electric Company (USA) successfully tested the axial sCO₂ turbine at temperature over 700 °C.

Zhejiang University started the research on sCO₂ power cycle since 2013. In order to have a comprehensive understanding about the heat transfer characteristics of sCO₂ from near ambient temperature to 600 °C, a test loop was built in 2017. Heat transfer experiments have been carried out in

2018. Based on the test loop, a dynamic model has been developed to explore the dynamic characteristic of a sCO₂ Brayton cycle. The steady state validation of the model has been done, while the dynamic validation with experiments will be finished in next 6 months.

The experience gained by the experiment and simulation is then used to design a 150kWe sCO₂ Brayton cycle coupled with a solar solid particle receiver. The selected cycle design to be implemented is a simple regenerative cycle, with a small-scale turbine and compressor. The inlet temperature and pressure of turbine are set to be 550°C and 20MPa respectively, and the efficiency of turbine is expected to be over 75%. The inlet temperature and pressure of compressor are set to be 35°C and 7.4MPa respectively, and the efficiency of compressor is expected to be about 75%. A 2MW regenerator is adopted to increase the compressor outlet sCO₂ flow temperature to 389°C at 20.1MPa, then with a particle/CO₂ heat exchanger as the main heater, the flow is heated up to 550°C before entering the turbine. This innovative system is going to be setup in 2019 and demonstrated in 2020 by Zhejiang University, located in a 1MW solar tower.

TEST LOOP IN ZHEJIANG UNIVERSITY

A sCO₂ test loop is developed in Zhejiang University as shown in Figure 1. The CO₂ flow from the gas source passes the filter, and is cooled to liquid phase in the cooling system. The liquid CO₂ flow rate is measured with a flow meter and then pressurized further by the pump. Here, a buffer tank is used to reduce the fluctuation, and a recuperator is used to preheat the liquid CO₂ stream with the exist stream of the sCO₂ from the straight tube test section. Then sCO₂ flow is heated to the designed inlet temperature in the four-stage heater, and flows through the test section. In this section, temperature and pressure of the sCO₂ flow are measured for the heat transfer characteristics investigation. The heat of the sCO₂ flow is reused in the recuperator. Then a heat exchanger is used to further cool down the sCO₂ flow for the safe operation of the back pressure valve. After the pressure is released, sCO₂ flows back to the source. The test loop can offer sCO₂ operating temperature and pressure at 50 ~ 550 °C, and 8~ 15 MPa respectively at the outlet of the test section.

CO₂ gas (99.99%wt) is used as the working fluid in experiments and the mass flow rate is controlled by a pump whose frequency ranges from 0 to 50 Hz. A mass flowmeter and thermocouples are used. The experiments have been carried out at 20~600 °C with the mass flow rate of sCO₂ ranged from 20 to 70 kg.h⁻¹ and pressure from 7 to 15 MPa.

HEAT TRANSFER EXPERIMENTS

Heat transfer experiments were carried out for sCO₂ from ambient temperature to 600°C, from 7MPa to 15 MPa. Fig. 2 shows the test section and the locations of the measuring points. The test section was basically a horizontal straight tube with an inner diameter of 8 mm (wall thickness of 3 mm), and it is heated uniformly by a copper column and six heat resistors. The maximum heating power is 7.2 kW. The test section was made

of Hac 276 alloy. The horizontal test section was 2.35 m long, and its heated section was 1.75 m. Fifteen K-type thermocouples were attached with 100 mm interval onto the outer surface of the tube to measure the wall temperatures. The test section was heat insulated by insulation cotton. Two pressure sensors and one pressure difference transducer are used to measure the pressure and pressure drop of the inlet and outlet. A straight tube is heated with a maximum heating power of 7.2 kW. Fifteen thermocouples are used to detect outwall temperature along the tube with an interval of 100 mm. The experiments were implemented at steady state. The accuracies and ranges of measuring devices are shown in Table 1. The thermocouples were calibrated by using thermometer, and the maximum error was less than 1.0%. The differences between the corrected value and the thermometer were less than 0.3 °C when thermometer readings were between 20 and 100 °C, respectively. The total uncertainty of the measuring temperature difference is 1.25%. The error in the electric heating power was 4.25%, considering the heat loss. The physical properties of CO₂ were calculated from the NIST package. Based on the calculated formulation, the maximum uncertainty of the heat transfer coefficient was estimated to be ±7.5%.

The tests were conducted with a change of the mass flux and the heat flux at a given pressure. In order to investigate the effects of the pressure on heat transfer, the experiments were carried out at several pressures: 7.6, 8.3, 9 and 11 MPa. Table 2 shows the range of the test conditions. The range of the Reynolds number based on the inlet condition is from 2×10⁴ to 1.1×10⁵. The working temperature of the test section is controlled from 30 to 600 °C, which is currently working temperature for the solar receiver.

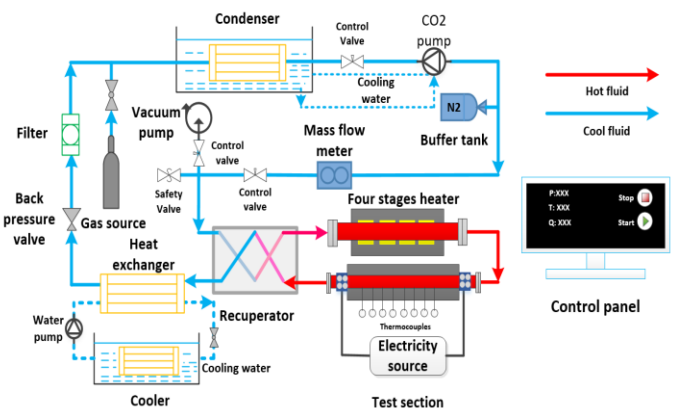


Figure 1: Layout scheme of the Test Loop.

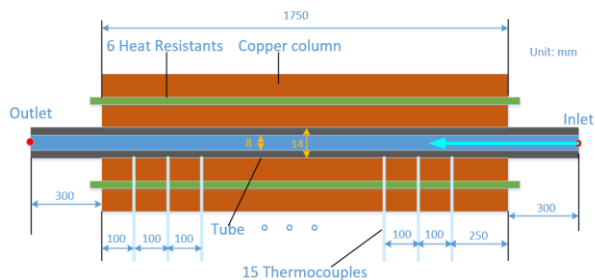


Figure 2: Test section and the locations of the measuring points.

Table 1 Range and accuracy of instruments.

Instruments	Range	Accuracy
Pressure difference transducer	100 kPa	0.1%
	500 kPa	0.1%
	1000 kPa	0.1%
Pressure transducer	10 MPa	0.1%
	25 MPa	0.1%
Thermocouple	220~1440 K	0.75%
Mass flow meter	0~300 hg.h ⁻¹	0.2%

Table 2 Parameters of the test conditions.

Fluid	CO ₂
Flow direction	Horizontal
Working Pressure (MPa)	7.6, 8.3, 9, 11, 15
Mass flow rate (kg/h)	20-60 kg/h
Inlet temperature, °C	30~450 °C
Heat flux q, kW/m ²	0~60
Reynolds number	2×10 ⁴ ~1.1×10 ⁵

EXPERIMENTAL RESULTS AND DISCUSSION

In Figure 4, several plots are shown for the mass flux from 34 kg/h to 60 kg/h, while the pressure is kept constant at 7.6 MPa, respectively. As the mass flux increases, the peak HTC increases. The HTC reaches the peak value near the pseudo-critical temperature. When fluid temperature (T_b) is higher than 373 K (100 °C), the HTC is quite stable as shown in Figure 5. As bulk fluid temperature increases, the HTC increases gradually.

Pressure effect is investigated by comparing the test results for 8.3 and 9.1 MPa. In Figure 6, the results show that higher pressure results in lower peak HTC. As the temperature reach the pseudo-critical point, the effect of pressure becomes outstanding, the HTC reach the peak. Especially in the vicinity of the critical pressure, the HTC is several times higher than HTC of conditions far away from pseudo-critical point, due to the steep variation of the physical properties there. In Figure 7, when fluid temperature is higher than 100 °C, the effect of pressure is not significant. As the pressure increases, the wall temperature decreases.

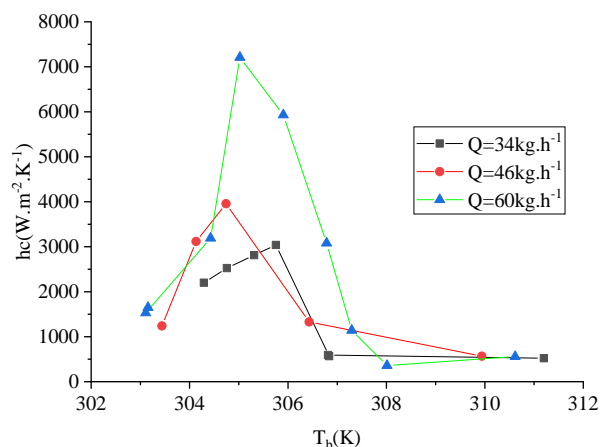


Figure 4: Effect of mass flux on the HTC (pseudo-critical state).

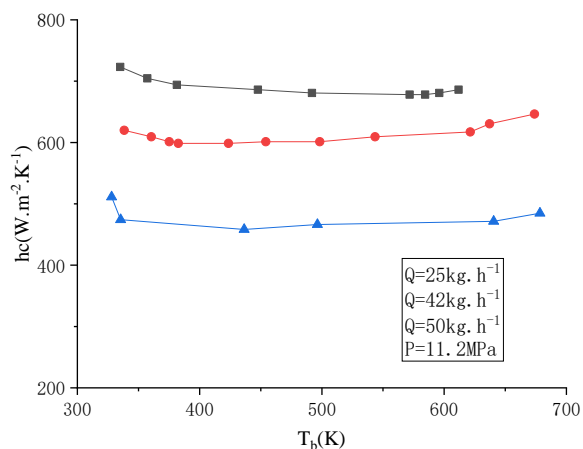


Figure 5: Effect of mass flux on the HTC (high temperature).

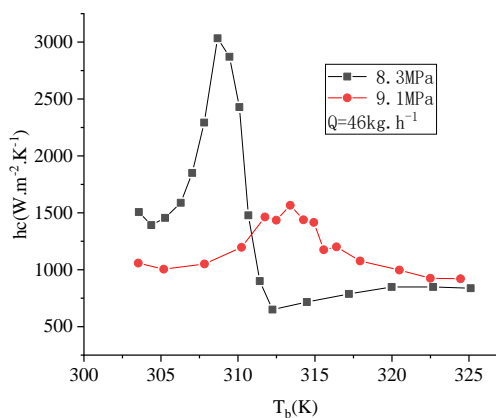


Figure 6: Effect of pressure on HTC (near pseudo-critical temperature).

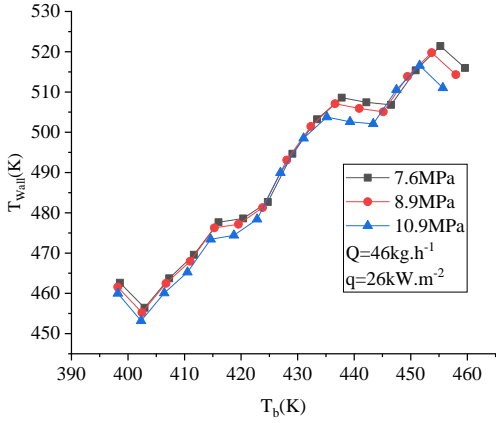


Figure 7: Effect of pressure on the wall temperature.

In order to evaluate the effect of the heat flux, an experiment was performed with the variation of heat flux while keeping the mass flow rate and pressure constant. Figure 8 shows the experimental results for a mass flux of 50 kg/h at a pressure of 11.2 MPa. The wall temperature is plotted along the tube length. The heat flux varies between 0 and 44 kW.m⁻². As the heat flux increases, the wall temperature increases. At high temperature, the effect of heat flux is ignorable, as shown in Figure. 9.

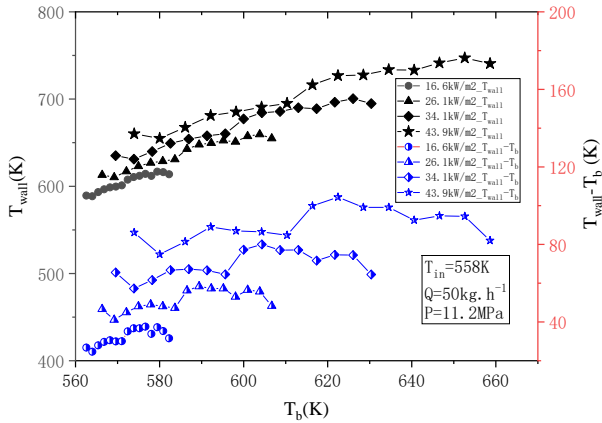


Figure 8: Effect of heat flux on the wall temperature difference.

In the literatures, many equations are available, such as Dittus-Boelte correlation, Gnielinski correlation, Jackson correlation[5], correlation from Liao & Zhao[6, 7], correlation from Kim[8, 9], correlation from Bae[5, 10, 11], et al. However, no correlation is suitable for our test loop experiments. Lee et al.[12] proposed that no simple correlation in terms of traditional dimensional parameters can be expected to give useful predictions except very limited ranges because of the strong coupling of heat transfer and fluid velocity. Here, three equations are used to compare with our experiment results at high temperature range, contains Gnielinski correlation,

Dittus-Boelter correlation and Jackson correlation. As shown in Figure 10, at high temperature range, Gnielinski correlation gives better evaluation of the HTC for straight tube than Jackson correlation. The average error between the experiment results and Gnielinski correlation is near 12% (over 20% for Jackson correlation). Near the pseudo-critical temperature (T_{pc}), the Jackson correlation is closer to the experiment result than Gnielinski correlation, as shown in Figure 11. However, the error between experiment results and Jackson correlation is larger than 30%. A new correlation is needed for this working conditions to evaluate the designed test loop.

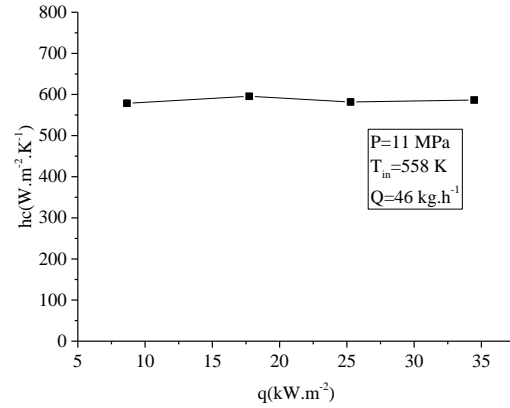


Figure 9: Effect of heat flux on HTC (at high temperature range).

Jackson[5] proposed a friction factor equation contained the Prandtl number, Reynolds number, density ratio and specific heat ratio. The Gnielinski correlation contains Reynolds number, the Prandtl number and the temperature difference facto. To get a better correlation, more factors should be considered. Therefore, the Nusselt number can be represented as a function of the following non-dimensional parameters:

$$Nu = \frac{hcD}{\lambda_{co2}} = f(Re_b, Pr_b, \frac{\rho_w}{\rho_b}, \frac{c_p}{c_{p,b}}, q^+, c_t) \quad (1.1)$$

$$q^+ = \frac{q\beta_b}{Qc_{p,b}} \quad (1.2)$$

$$c_t = \frac{T_b}{T_w} \quad (1.3)$$

Where Nu is the Nusselt number, Re is the Reynold number, Pr is the Prandtl number, hc is the THC, λ is the thermal conductivity, c_p is the specific heat, q^+ is the accelerate number, q is the heat flux ratio, c_t is the temperature factor, Q is the mass flux and β_b is volume expansion ratio.

Log-based non-linear curve fitting was employed to correlate the Nusselt numbers from our experiments, and a new heat-transfer correlation was constructed as follows:

$$Nu = 32.39 Re_b^{1.0084} Pr_b^{1.9876} \left(\frac{\rho_w}{\rho_b}\right)^{2.2123} \left(\frac{c_{p,w}}{c_{p,b}}\right)^{0.7389} q^{+0.9935} c_i^{6.1590} \quad (1.4)$$

The new correlation gives better result for this working conditions, especially the near the critical point as shown in Figure 13 and 14. The average error of the new correlation is near 5% at high temperature range.

Besides, the present correlation is compared with the Experiment results from Korean Atomic Energy Research Institute (KAERI)[11]. As shown in Fig. 14, the correlation can reflect the difference of HTC better than Dittus-Boelter correlation and Jackson correlation. However, this correlation cannot give a good prediction of the experiment results at that conditions. The mass flow rate and heat flux of the correlation is limited.

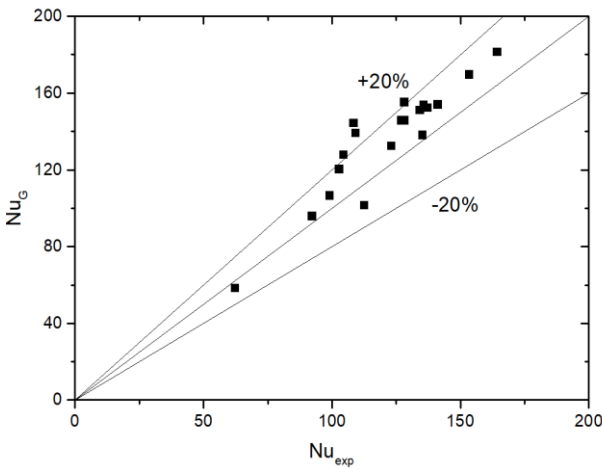


Figure 10: Comparison of HTC ($T_b/T_{pc} > 1.2$) (experiment results and Gnielinski correlation).

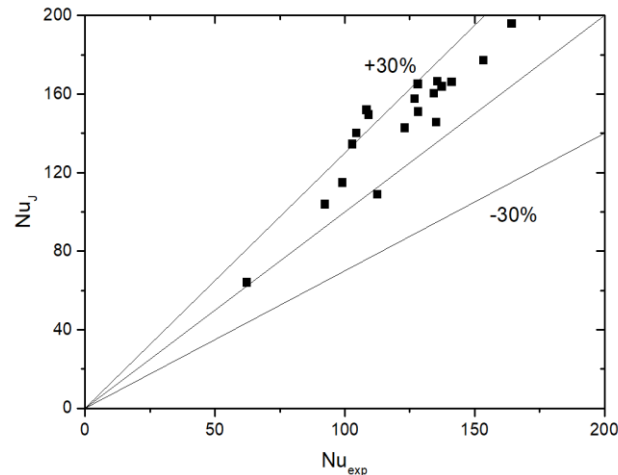


Figure 11: Comparison of HTC ($T_b/T_{pc} > 1.2$) (experiment results and Jackson correlation).

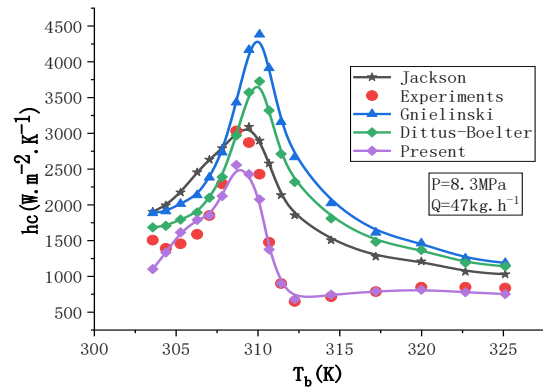


Figure 12: Comparison of HTC at 8.3 MPa ($T_b/T_{pc} < 1.2$) (experiment results, Gnielinski, Dittus-Boelter, Jackson and present correlation).

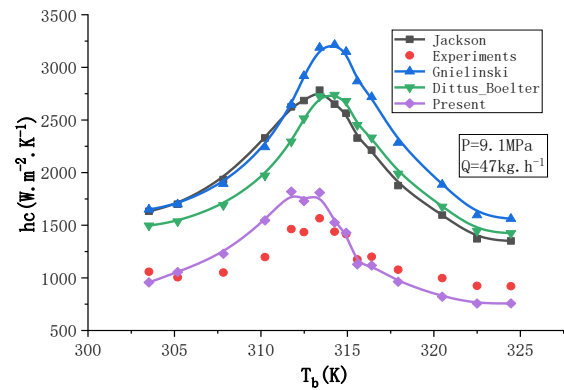


Figure 13: Comparison of HTC at 9.1 MPa ($T_b/T_{pc} < 1.2$) (experiment results, Gnielinski, Dittus-Boelter, Jackson, and present correlation).

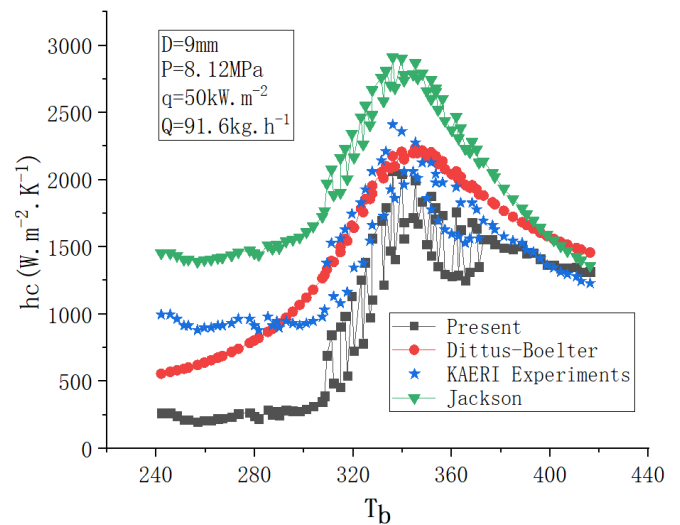


Figure 14: Comparison of HTC data from KAERI ($T_b/T_{pc} < 1.2$) (experiment results, Dittus-Boelter, Jackson, and present correlation).

DYNAMIC MODEL SIMULATION TOOL

For the sCO₂ Brayton cycle research, a dynamic model is built for this sCO₂ test loop in Dymola Software based on the dynamic modules library ThermoSysPro developed in EDF R&D. The thermodynamic properties of CO₂ is calculated by dynamic calling to NIST REFPROP in real time during simulation. The interface between Dymola and NIST REFPROP is done by MediaTwoPhaseMixture package developed by Henning Francke. The dynamic model is consists of a cooler, a four stages heater, a condenser, a recuperator, a back pressure valve, some control valves, a heating section and a three-plunger pump. In the test loop, back pressure valve is used to replace the turbine, while the friction coefficient change due to the open degree of the valve is regard as the load change during the operation. This dynamic model simulation is used to analyze the dynamic characteristics of different components.

In order to be consistent with the result of the experimental data, some modeling approach is considered. The following assumptions are made for this study:

- (1) Pressure losses in the mass flow meter, filter and sensors are replaced by singular pressure loss to reduce the complexity of the loop model for this study;
- (2) Expansion process is adiabatic.
- (3) Heat loss to the ambient air is estimated by constant heat exchanger coefficient.
- (4) The heat conduction between solid media is considered, while the heat conduction within CO₂ is ignored.

DYNAMIC MODEL INTRODUCTION

The pump is used to compress the liquid CO₂ from gas bottle pressure (around 5 MPa) to high working pressure (7~15 MPa) by plunger movement. It uses mechanical work to push the plunger, thus accelerating the liquid. Here we simplified the calculation of pump with constant isentropic efficiency. The relationship between the mass flow rate Q and the pump frequency, pressure ratio P_e is experimentally measured. A map is generated from a steady state situation for a certain temperature, pressure and frequency. The correlations are concluded as follow (according to the pump frequency from 20 to 50):

$$Q = \frac{30.934 - 4.2687Pe}{3600} \quad \text{for frequency}=20 \text{ HZ} \quad (1.5)$$

$$Q = \frac{45.503 - 5.8544Pe}{3600} \quad \text{for frequency}=30 \text{ HZ} \quad (1.6)$$

$$Q = \frac{57.802 - 6.21Pe}{3600} \quad \text{for frequency}=40 \text{ HZ} \quad (1.7)$$

$$Q = \frac{71.459 - 7.21Pe}{3600} \quad \text{for frequency}=50 \text{ Hz} \quad (1.8)$$

As shown in Figure 15, the correlation concluded for the mass flow rate is closed to the experimental result at different pressure ratios and frequencies. The maximum error of the mass flow correlation is $\pm 1.67\%$.

We defined the pressure ratio (Pe) as:

$$Pe = \frac{P_{in}}{P_{out}} \quad (1.9)$$

Where P_{in} is the pressure at the inlet, P_{out} is the pressure at the outlet.

The isentropic efficiency η is setting as constant ($\eta = 0.7$) to reducing the model complexity. Then the power can be calculated by equation:

$$W = Q(h_{out} - h_{in}) / (1 - \eta_f) \quad (1.10)$$

Where h is the enthalpy, η_f is the friction loss percentage. Here, η_f is 0.1.

The outlet enthalpy of the pump can be calculated by following equations and database:

$$\eta(h_{is} - h_{in}) = h_{out} - h_{in} \quad (1.11)$$

$$s_{out} = s = s_{in} \quad (1.12)$$

Where h_{is} is the isentropic enthalpy at the outlet calculated by the outlet pressure and outlet entropy. Other properties can be calculated by calling REFPROP based the outlet pressure and enthalpy.

Comparison between simulation result and experimental measure value is conducted, and the results are shown in Figure 16. The maximum outlet temperature error is $\pm 1\text{K}$ or $\pm 0.4\%$, within the measure error of thermocouples ($\pm 2.2\text{K}$ or $\pm 0.75\%$).

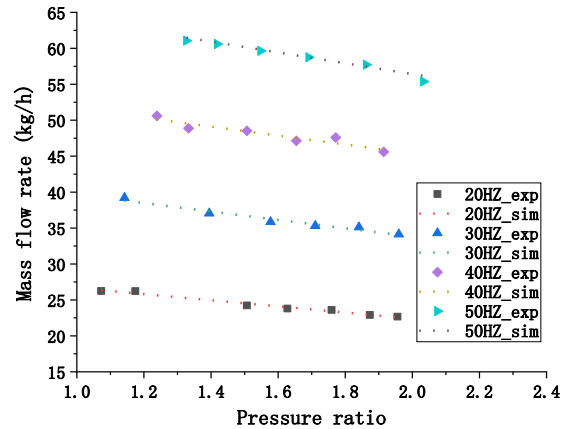


Figure 15: Mass flow map of the three-plunger pump.

Five heat exchangers are utilized in this test loop, including a recuperator, a cooler, a condenser, a four-stage heater and the heat section (test section). These heat exchangers consists of CO₂ pipe and relative wall boundary. The working conditions and pipe geometries are listed in Table 3.

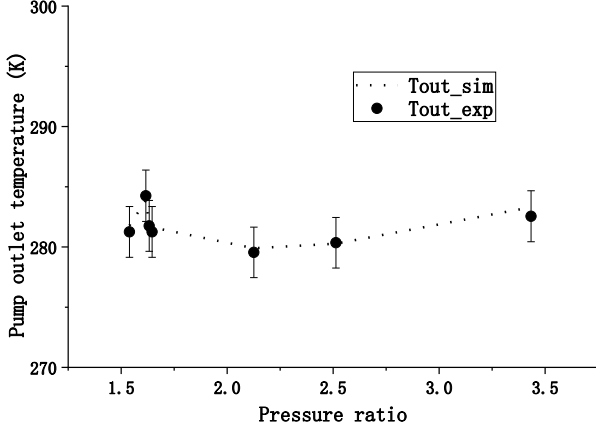


Figure 16: Pump outlet temperature comparison between experiments and simulation ($\eta=0.7$).

For a normal pipe, pressure loss equation is simplified as:

$$\Delta P_f = \frac{Q^2}{2\rho} K \quad (1.13)$$

Where K is the pressure drop coefficient, which can be calculated from the experiment results.

The mass flow model and heat transfer model for the dynamic pipe is shown in Figure 17. The dynamic pipe is divided into n sections. Temperature and pressure of each section is assumed uniform.

The energy equation for the fluid can be written as:

$$A\left(-\frac{dp[i+1]}{dt} + \rho[i] \cdot \frac{dh[i+1]}{dt}\right) dx = \quad (1.14)$$

$$Q[i] \cdot h_b[i] - h_b[i+1] \cdot Q[i+1] + dW_{1[i]}$$

Where h_b is the average specific heat capacity of flowing of the fluid, ρ is the density of the fluid, Q is the mass flow rate of the fluid, dW is the heat transfer to the pipe wall. The thermal conduction during two fluid area is ignored.

$$dW_1 = kds[i](Tp[i] - Tw[i]) \quad (1.15)$$

Where, k is the heat transfer coefficient of the CO₂ pipe, ds is the inner wall area per node, and dW_1 is calculated by the new correlation (1.2).

$$k = 32.39 \text{Re}_b[i]^{1.0084} \text{Pr}_b[i]^{1.9876} \left(\frac{\rho_w[i]}{\rho_b[i]}\right)^{2.2123} \quad (1.16)$$

$$\left(\frac{c_{p,w}[i]}{c_{p,b}[i]}\right)^{0.7389} q^+[i]^{0.9935} c_t[i]^{6.159} \lambda_{CO_2} / D$$

$$\text{Re}_b[i] = 4 \frac{Q[i] + Q[i+1]}{2 \cdot \pi i \cdot D \cdot \mu_b[i]} \quad (1.17)$$

$$c_t[i] = \frac{T_b[i]}{T_w[i]} \quad (1.18)$$

$$q^+[i] = \frac{qD}{c_{p,b}[i]T_b[i]\mu_b[i]\text{Re}_b[i]} \quad (1.19)$$

Where b means the bulk temperature, w means wall temperature, λ_{CO_2} is the thermal conductivity of CO₂, q is the heat flux density, Re is the Reynold number, Pr is the Prandtl number, c_t is the temperature factor and q^+ is the accelerate factor. The properties can be attained from the REFPROP database.

Table 3 Working condition for heat exchangers

Heat exchanger	Pipe diameter Inner/Outer (mm)	Pipe length	Wall condition
recuperator	6/10	12	Normal heat loss to ambient ($T_0=15^\circ\text{C}$)
heater	6/10	12×4	Heating power (500W*4) PID control; Normal heat loss to ambient ($T_0=15^\circ\text{C}$)
Cooler	4/6	6	Heat loss to cooling water ($T_0=0\sim 10^\circ\text{C}$)
Condenser	4/6	12	Heat loss to cooling water ($T_0=-5\sim 4^\circ\text{C}$)
Heat section	8/14	2	Heating power (0~7.2 kW); Normal heat loss to ambient ($T_0=15^\circ\text{C}$)

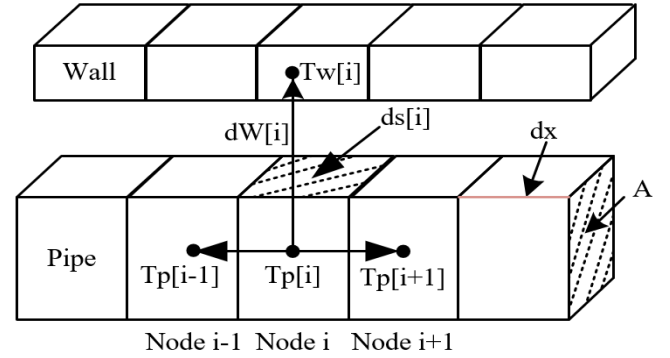


Figure 17: Heat transfer and mass flow model for dynamic pipe.

The mass balance equation for fluid is written as:

$$A dx \left\{ \left(\frac{d\rho}{d\rho}\right)_h [i] \frac{dp[i+1]}{dt} + \left(\frac{d\rho}{dh}\right)_p [i] \frac{dh[i+1]}{dt} \right\} = Q[i] - Q[i+1] \quad (1.20)$$

The wall is divided into n sections. Temperature and pressure of each section is assumed uniform. The heat transfer model for wall is shown in Figure 18.

The energy equations for solid at node i can be written as:

$$A\rho c_p \frac{dT_w[i]}{dt} dx = dW_2[i] + dW_1[i] + A\lambda(2T_w[i] - T_w[i-1] - T_w[i+1]) / dx \quad (1.21)$$

Where dW_2 is the energy transferred from the ambient, dW_1 is the energy transferred from the fluid. Thus, in the pipe, the equation of dW_2 and dW_1 are calculated as:

$$dW_2[i] = 2\lambda pi(Tw_2[i] - Tw[i]) / (\log(1 + \frac{e}{e+D})) dx \quad (1.22)$$

$$dW_2[i] = hc(2e + D) pi(T_0 - Tw[i]) dx \quad (1.23)$$

$$dW_1[i] = 2\lambda pi(Tw_1[i] - Tw[i]) / (\log(1 + e/D)) dx \quad (1.24)$$

Where hc is the heat transfer coefficient between wall and pipe fluid, T_{w1} is the temperature of the wall boundary at the ambient side, T_{w2} is the temperature of the wall boundary at the inner pipe wall side, e is the wall thickness, and D is the inner pipe diameter.

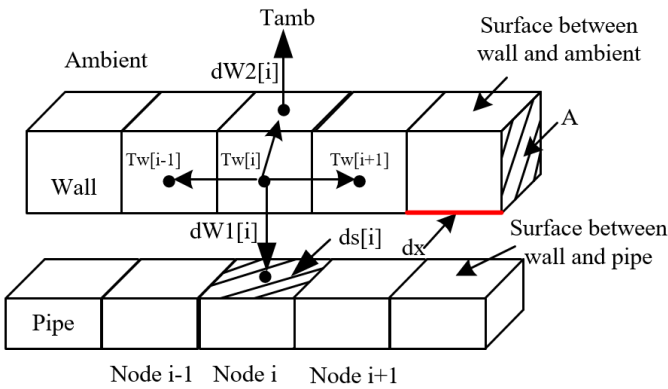


Figure 18: heat transfer model for the heat exchanger wall.

The recuperator is then modelled as two parallel pipes with a wall in between. The condenser and cooler are both modeled with a dynamic pipe and a cooling wall. The test section and four-stage heater are modeled with a dynamic pipe and a heating wall. The models' layout is shown in Figure 19.

The steady state validations of cooler and condenser are performed. The maximum errors of outlet pressure and outlet temperature between simulation and experiments for cooler are separately $\pm 0.1\%$ and $\pm 0.3\%$, as shown in Figure 20, while the measure errors of the temperature and pressure sensors are separately $\pm 0.75\%$ and $\pm 0.1\%$. The maximum errors of outlet pressure and outlet temperature between simulation and experiments for condenser are separately $\pm 0.03\%$ and $\pm 0.5\%$, while the measure errors of the temperature and pressure sensors are separately $\pm 0.75\%$ and $\pm 0.1\%$.

Validations of the heat section with the experimental results have been conducted for the influence of mass flow rate and working pressure. The maximum error of the outlet temperature and pressure are separately $\pm 1.6\%$ and $\pm 0.2\%$, as shown in Figure 21.

The back pressure valve is modified from the check valve by setting the pressure loss coefficient. The expanding process in back pressure valve is assumed to be isenthalpic. The pressure loss is calculated by equation (1.11).

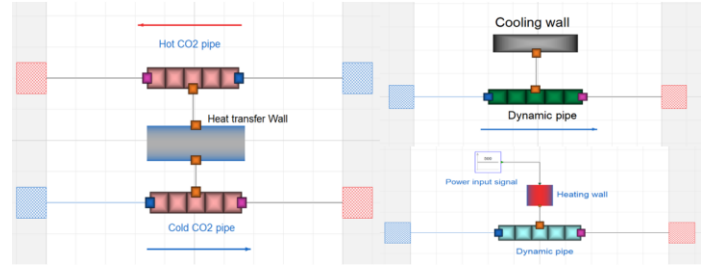


Figure 19: Layout of the heat exchangers: recuperator (left), cooler (right upper) and heater (right down).

The friction factor K is normal working at range between 10^{12} and 10^{14} . The control signal is used to change the friction factor:

$$K = signal \cdot 10^{12} \quad (1.25)$$

The signal is at the range of $0.01 \sim 100$, which means the open degree of the back pressure valve.

Control valve is used to control the fluid in this test loop. The specific enthalpy is assumed constant in the control valve. Here, the pressure drop is calculated by equation:

$$\Delta P C_v^2 = K \frac{Q^2}{\rho^2} \quad (1.26)$$

$$\Delta P = P_{out} - P_{in} \quad (1.27)$$

Where C_v is the flow coefficient, which is also used to calculate the pressure drop of the valve. The maximum $C_{v_{max}}$ is 5000 got from the valve producer. The pressure loss coefficient K is 1.733×10^{12} . Here, actual C_v is calculated as:

$$C_v = C_{v_{max}} signal \quad (1.28)$$

The signal here is also used to control the open degree of the valve, while 1 means opening and 0 means closed.

In addition, singular pressure drop model is used to simplify the non-standard pressure drop sections, such as filter and mass flow meter, and is calculated by the equation (1.11). Sensors models are used to get the state in the test loop during simulation.

The complete model is presented in Figure 21. The CO_2 flow from the volume is cooled to liquid phase in the condenser system. The liquid CO_2 flow rate (volumetric) is pressurized further by the pump and then measured with a flow meter. A recuperator is used to preheat the liquid CO_2 stream with the exist stream of the sCO_2 from the Straight Tube Test Section (STTS). Then sCO_2 flow is heated to the designed inlet temperature in the four-stage heater, and flows through the STTS. In this section, temperature and pressure of the sCO_2 flow are measured for the heat transfer characteristics investigation. The heat of the sCO_2 flow is reused in the recuperator. Then a heat exchanger is used to further cool down the sCO_2 flow for the safe operation of the back pressure valve. After released the pressure, sCO_2 flows back to the volume. The steady state validation of the model has been done, while the dynamic validation with experiments will be finished in next 6 months.

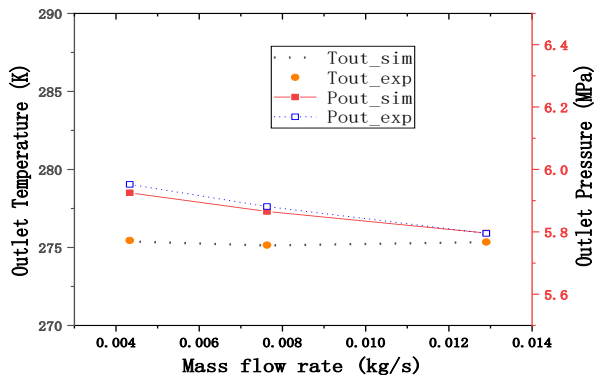


Figure 20: Comparison of the experiment and simulation result for cooler (outlet temperature and pressure).

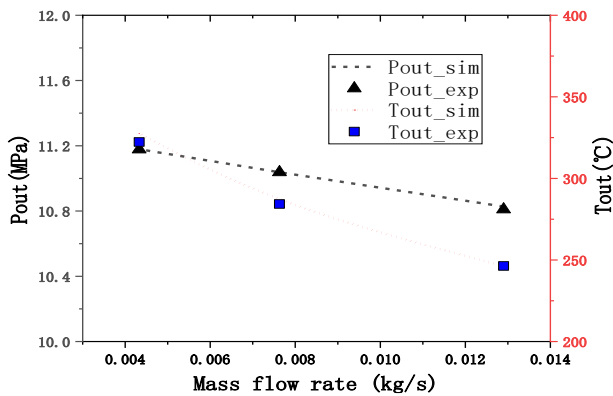


Figure 21: Comparison of the experiment and simulation result for heating section (outlet temperature and pressure).

150KWE SCO₂ BRAYTON CYCLE COUPLED WITH A PARTICLE RECEIVER

The experience gained by the experiment and simulation is then used to design a 150kWe sCO₂ Brayton cycle coupled with a solar solid particle receiver, as shown in Figure 22. The selected cycle design to be implemented is a simple regenerative cycle, with a small-scale turbine and compressor. The inlet temperature and pressure of turbine are set to be 550°C and 20MPa respectively, and the efficiency of turbine is expected to be over 75%. The inlet temperature and pressure of compressor are set to be 35°C and 7.4MPa respectively, and the efficiency of compressor is expected to be about 75%. A 2MW regenerator is adopted to increase the compressor outlet sCO₂ flow temperature to 389°C at 20.1MPa, then with a particle/CO₂ heat exchanger as the main heater, the flow is heated up to 550 °C before entering the turbine. This innovative system is going to be setup in 2019 and demonstrated in 2020 by Zhejiang University, located in a 1MW solar tower, as shown in Figure 23.

CONCLUSIONS

Zhejiang University has built a sCO₂ test loop since 2017. The heat transfer experiments have been done. The results show that: (1) existing correlations have significant error near the critical point; (2) at high temperature range, heat transfer characteristics of sCO₂ is quite stable. Base the experimental results, a new correlation is got, and used in the dynamic model developed in Dymola software. The steady state validation has been done. The error between simulation and experiments is smaller than 5%.

Then, in next 6 months, dynamic validation of the model will be completed. And the design experience will be used to design a 150 kWe sCO₂ simple Brayton cycle couple with the 2MW solar tower system built in Zhejiang University. The 150kWe test loop will be constructed in next two years.

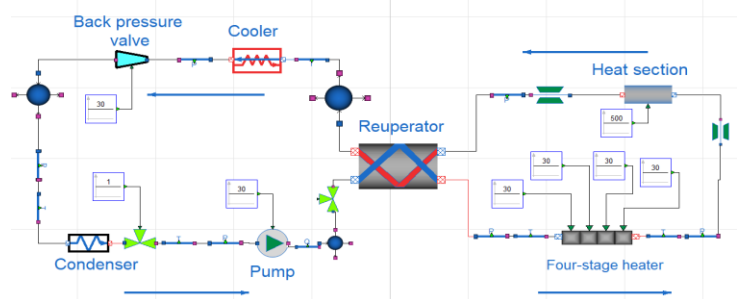


Figure 22: Complete model of the test loop.

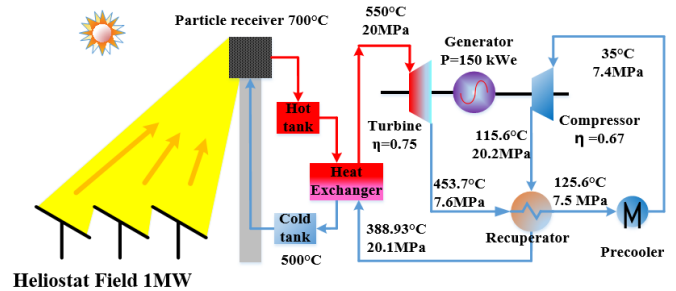


Figure 23: Layout of the 150kWe sCO₂ Brayton cycle.



Figure 24: Picture of the 1 MW Solar tower in Zhejiang University.

NOMENCLATURE

A	Area, m ²
Cv	Flow coefficient

c_p	Specific heat, kJ.kg^{-1}
c_t	Temperature factor
D	Diameter, m
DOE	Department of Energy
dx	Unit length, m
G	Mass flux, kg.h^{-1}
h	Enthalpy, kJ.kg^{-1}
hc	Heat transfer coefficient, $\text{W.m}^{-2}.\text{K}^{-1}$
HTC	Heat transfer coefficient, $\text{W.m}^{-2}.\text{K}^{-1}$
k	Heat transfer coefficient, $\text{W.m}^{-2}.\text{K}^{-1}$
K	Pressure drop coefficient
Nu	Nusselt number
P	Pressure
Pe	Pressure ratio
Pr	Prandtl number
q	Heat flux density, W.m^{-2}
q^+	Accelerate factor
Q	Mass flow rate, kg.s^{-1}
Re	Reynold number
t	Time, s
T	Temperature, K or $^{\circ}\text{C}$
W	Power, W
β	Volume expansion ratio, K^{-1}
λ	Thermal conductivity, W.m^{-2}
ρ	Density, kg.m^{-3}
μ	Dynamic viscosity, $\text{kg.s}^{-1}.\text{m}^{-1}$
Subscripts and superscripts	
0	Environment
1	Inner face
2	Outer wall face
b	Mass average value
D	Value obtained by Dittus-Boelter correlation
CO_2	Properties of CO_2
exp	Value obtained by experiments
f	Caused by friction
G	Value obtained by Gnielinski correlation
\bar{h}	Constant enthalpy
i	Node number
in	Inlet
is	isentropic
J	Value obtained by Jackson correlation
max	Maximum number
\bar{P}	Constant pressure
pc	Pseudo-critical
out	Outlet
w	Wall temperature
w1	Inner wall
w2	Outer wall

REFERENCES

- [1] Pasch J, Conboy T, Fleming D, Rochau G. Supercritical CO_2 Recompression Brayton Cycle: Completed Assembly Description. Sandia; 2012.
- [2] Cho J, Choi M, Baik Y-J, Lee G, Ra H-S, Kim B, et al. Development of the turbomachinery for the supercritical carbon dioxide power cycle. International Journal of Energy Research. 2016;40:587-99.
- [3] Cho J, Shin H-K, Ra H-S, Lee G, Roh C, Lee B, et al. Research on the development of a small-scale supercritical carbon dioxide power experimental test loop. The 5th International Symposium - Supercritical CO_2 Power Cycles. San Antonio, Texas 2016.
- [4] Utamura M, Hasuike H, Ogawa K, Yamamoto T, Fukushima T, Watanabe T, et al. Demonstration of Supercritical CO_2 Closed Regenerative Brayton Cycle in a Bench Scale Experiment. 2012:155-64.
- [5] Bae YY. Mixed convection heat transfer to carbon dioxide flowing upward and downward in a vertical tube and an annular channel. Nuclear Engineering and Design. 2011;241:3164-77.
- [6] Liao SM, Zhao TS. Measurements of Heat Transfer Coefficients From Supercritical Carbon Dioxide Flowing in Horizontal Mini/Micro Channels. Journal of Heat Transfer. 2002;124:413.
- [7] Liao SM, Zhao TS. An experimental investigation of convection heat transfer to supercritical carbon dioxide in miniature tubes. International Journal of Heat and Mass Transfer. 2002;45:5025-34.
- [8] Kim H, Kim HY, Song JH, Bae YY. Heat transfer to supercritical pressure carbon dioxide flowing upward through tubes and a narrow annulus passage. Progress in Nuclear Energy. 2008;50:518-25.
- [9] Kim DE, Kim M-H. Experimental investigation of heat transfer in vertical upward and downward supercritical CO_2 flow in a circular tube. International Journal of Heat and Fluid Flow. 2011;32:176-91.
- [10] Bae Y-Y, Kim H-Y, Kang D-J. Forced and mixed convection heat transfer to supercritical CO_2 vertically flowing in a uniformly-heated circular tube. Experimental Thermal and Fluid Science. 2010;34:1295-308.
- [11] Bae Y-Y, Kim H-Y. Convective heat transfer to CO_2 at a supercritical pressure flowing vertically upward in tubes and an annular channel. Experimental Thermal and Fluid Science. 2009;33:329-39.
- [12] Lee SH, Howell JR. Turbulent developing convective heat transfer in a tube for fluids near the critical point. Int J Heat Mass Transfer. 1998;41:14.

ACKNOWLEDGEMENTS

This work is supported by National Key Research & Development Program of China (2016YFE0124700).

EXPERIMENTAL INVESTIGATION OF HEAT TRANSFER AND PRESSURE DROP IN TUBES TO COOL CO₂ NEAR THE CRITICAL POINT

Andreas Wahl*

Institute of Nuclear Technology and
Energy Systems (IKE), Stuttgart, Germany
andreas.wahl@ike.uni-stuttgart.de

Rainer Mertz

Institute of Nuclear Technology and
Energy Systems (IKE), Stuttgart, Germany
rainer.mertz@ike.uni-stuttgart.de

Eckart Laurien

Institute of Nuclear Technology and
Energy Systems (IKE), Stuttgart, Germany
eckart.laurien@ike.uni-stuttgart.de

Jörg Straflinger

Institute of Nuclear Technology and
Energy Systems (IKE), Stuttgart, Germany
joerg.starflinger@ike.uni-stuttgart.de

ABSTRACT

In the frame of EU-project sCO₂-flex the design of a 25 MWe supercritical CO₂ (sCO₂) Brayton cycle will be developed. The system will be optimized to meet flexibility requirements, while reducing environmental impact and focusing on cost efficiency.

In the context of a sCO₂ Brayton cycle, the gas cooler is a key component to achieve a high overall efficiency. Close to the critical point, due to varying properties, heat transfer and pressure drop of carbon dioxide (CO₂) are difficult to predict. By performing experiments with the "SCARLETT" facility of the University of Stuttgart, expertise will be gained using CO₂ as working fluid in the pseudocritical region. The results of the fundamental experiments will be used for validation and improvement of correlations to develop heat exchangers working with high efficiency.

The heat transfer and pressure drop of carbon dioxide near the critical point cooled in a 2 mm diameter was investigated. The outer wall surface temperature is determined by soldering calibrated T-type thermocouples into the copper tube wall. Thermocouples are evenly distributed along the 1.2 m cooled length. The effects of the CO₂ mass flux of 400-1400 kg/m²s, inlet pressures of 7.7-8.5 MPa, bulk fluid temperatures of 10-85 °C and the flow orientation (upward, downward and horizontal) on the heat transfer and pressure drop were examined

INTRODUCTION

A sCO₂ Brayton cycle offers a number of benefits over competing power plant cycles. A high plant efficiency can be achieved due to the favourable fluid properties in the supercritical region. This is resulting in increased electricity production with the same fuel consumption [1]. The high gas density of sCO₂ allows to reduce the necessary compressor work and leads to a reduction in the overall size of the power plant [2]. The reduced size of turbomachinery, boiler and heat exchangers can be further translated into reduced capital costs.

The moderate value of its critical pressure (7.38 MPa) makes CO₂ more economical than water where the critical point is much higher (22.1 MPa). A low heat rejection temperature leads to power cycles with high efficiencies. The critical temperature of CO₂ (31 °C) contributes to that, however, it is not too low, to be cooled by the ambient temperature. CO₂ is a non-toxic and non-flammable natural working fluid ODP = 0 (ozone depletion potential) and GWP = 1 (global warming potential). It is available in sufficient quantities at reasonable costs. In environmental, cost and safety terms, CO₂ is regarded as an ideal natural refrigerant [3].

The properties of sCO₂ (Figure 1) lead to significant differences in the heat transfer characteristics [4]. This is caused by rapid changes of thermophysical properties close to the critical point. The understanding of heat transfer enhancement and deterioration phenomena during cooling in small diameter tube is crucial to develop new concept of compact heat exchanger for the Brayton cycle able to work with high efficiency, speed and reliability under high CO₂ pressure and low pinch point. The thermophysical properties change strongly with temperature and pressure.

As shown in Figure 1, for each pressure (77bar, 81 bar and 85 bar), the viscosity and density are strongly decreasing with increasing temperature. The isobaric heat capacity and thermal conductivity pass through a peak crossing the pseudocritical temperature. The pseudocritical temperature increases with increasing pressure [5]. Moreover, the distinct peaks are flattened.

In this study, the heat transfer and pressure drop in cooling conditions were measured at different CO₂ pressures, mass fluxes, temperatures and flow orientations. The effects of the parameters on the heat transfer were demonstrated. The measured pressure drop was compared with the prediction by taking in to account bulk, film and wall fluid properties.

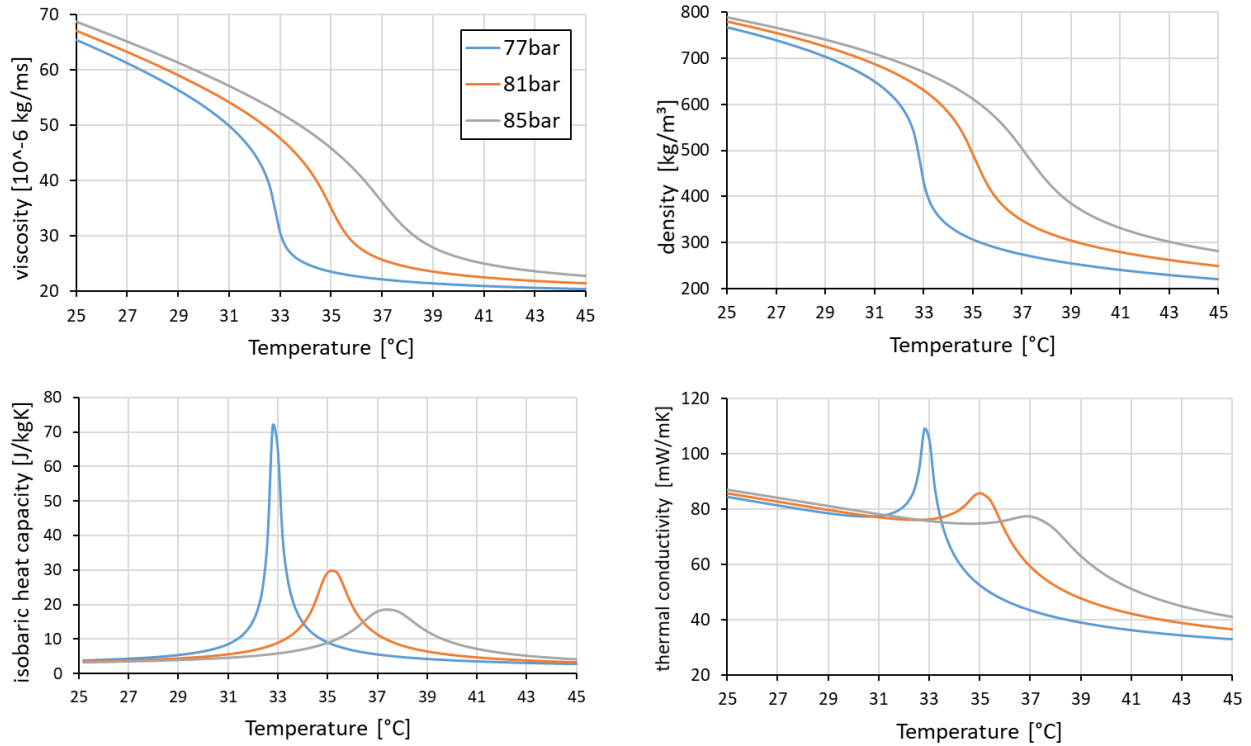


Figure 1: Properties of CO₂ vs temperature at different pressure [4]

STATE-OF-THE ART OF COOLING HEAT TRANSFER EXPERIMENTS

A number of researchers have experimentally investigated the heat transfer and pressure drop performance of CO₂ in tubes of different sizes and flow orientations. The research has been concentrated on tubes ranging from 0.5 to 10.7 mm in upwards, downwards and horizontal flow. Most of the work have been carried out in horizontal orientation.

Dang and Hihara [8] investigated the heat transfer and pressure drop in tubes with four different diameters ranging from 1 to 6 mm. The temperature of the outer tube wall was measured at 10 locations equally distributed along the 500 mm long tube-in-tube counter-flow heat exchanger. They found, that the Nusselt number increases slightly with increasing tube diameter. The comparison of the heat transfer coefficient over the bulk and film fluid temperature showed that the maximum is reached when the film temperature reaches the pseudocritical temperature. The film temperature is defined as:

$$T_f = \frac{(T_b + T_w)}{2} \quad (4)$$

The result is a modified Gnielinski equation [9] taking the film properties into account:

$$Nu_f = \frac{\left(\frac{f_f}{8}\right) (Re_b - 1000) Pr}{1,07 + 12,7 \sqrt{\frac{f_f}{8}} (Pr^{\frac{2}{3}} - 1)} \quad (5)$$

The Prandtl Number is defined with a variation in three different cases [8]. Due to large variations of thermophysical properties within a small temperature range, the heat transfer of supercritical fluid flow is strongly affected by heat flux and flow direction. Jackson and Hall [10] have developed a semi empirical parameter to characterize the influence of natural convection on turbulent vertical flows.

$$\frac{Gr}{Re^{2.7}} > 10^{-5} \quad (6)$$

In the case of cooling heat transfer, the turbulent upward flow leads to an intensification of heat transfer. The turbulent aiding mixed convection is present when the free and forced convection are in opposite direction. In the downward flow, a strong degradation of heat transfer is observed. In this case, the free and forced convection flows are in the same direction [11].

EXPERIMENTAL SET-UP

The test section applied here consists of a 1.5 m long cooper tube. The inner tube diameter is 2 mm and the outer tube diameter is 6 mm. The CO₂ flow can form a fully developed turbulent flow in the first 57 mm of the tube. At this point, a 1 mm hole is drilled through the tube wall to measure the pressure with relatively small impact on the flow. Additional 93 mm of uncooled tube length follows. The total cooled length of the tube is 1200 mm. The total length of the differential pressure measurement is 1386 mm, which contains an uncooled length of 186 mm (Figure 2).

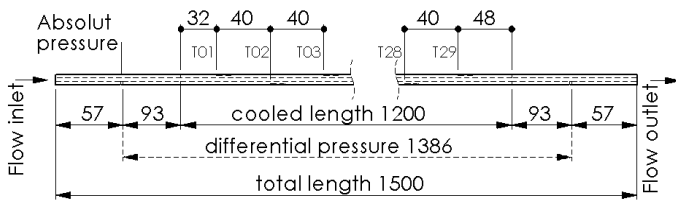


Figure 2: Detailed view of the test tube

T-type thermocouples are soldered into milled channels on the surface of the tube (Figure 3). The thermocouples are coated with stainless steel leading to high durability against corrosion. The heat conductance in the thermocouple wire could lead to a measurement error, thus the thermocouples have to be embedded a certain length inside the tube to eliminate this influence. The T-type thermocouples have a diameter of 0.5 mm. They are bended and laid in the milled channels (0.8x0.8x8mm depth/width/length).

The bending of the thermocouple leads to an asymmetry of the temperature measurement points in the cooled length. The first measurement position (T_{01}) is at 32mm of the cooled length. The spacing is equal along the tube with 40 mm between the measurement positions. The thermocouples were placed alternating on the top and on the bottom of the tube, to be able to investigate flow stratification. The solder alloy used to connect the tube with the thermocouples was a 96 % tin and 4 % silver mixture with implemented colophony. This material has a low temperature melting point (Solidus: 221 °C, Liquidus 238 °C), which does not exceed the temperature range of T-type thermocouples (-40 °C...+350 °C) and leads to a good thermal connection of the two components due to the high thermal conductivity.

The “outer tube” was designed to lead the thermocouples to the inner tube, deliver the cooling media in-and outflow, and close the annulus stream leak-tight .

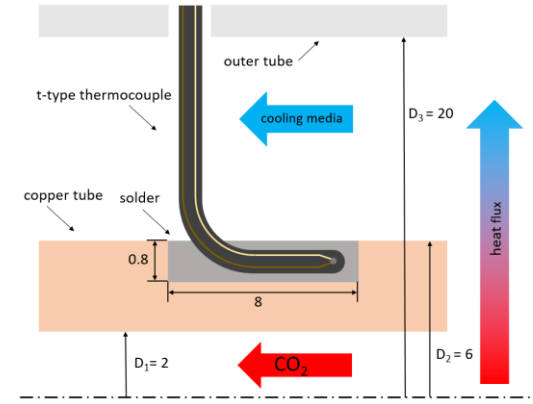


Figure 3: Detailed view of the thermocouple soldering in the tube surface (All dimensions in mm)

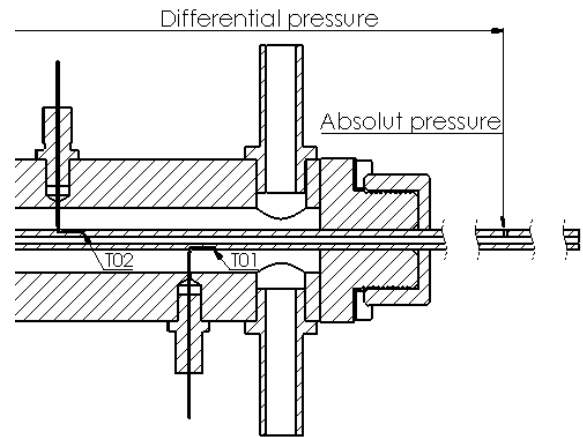


Figure 4: Flanging and cooling media supply into the test section

The flanges center the tube in the annulus. The size of the annulus is capable to deliver a high volume flux of cooling media (Figure 4). This intends to reduce the temperature difference in the flow, thus to support the inner tube with an isothermal cooling media. That could reduce the complexity and inaccuracies of the experiments.

The two before mentioned authors focused on the axially-averaged heat transfer. In Liao and Zhao’s [6] study, using a tube diameter of 2.1 mm and a 110 mm test section the heat transfer coefficient was averaged along a length to diameter ratio of 157. For Dang and Hihara’s [8] 2 mm tube, this value was 250. With the test facility presented in this work, the influence of CO₂ mass flow rate, CO₂ bulk fluid temperature, CO₂ pressure, volumetric cooling media flow and cooling media temperature can be investigated with a length to diameter ratio of 20, resulting in a higher resolution.

The SCARLETT test loop provides sCO₂ under defined boundary conditions. Figure 5 depicts the piping and instrumentation (P&I) diagram of the SCARLETT test loop, which is described as follows [12]. After evacuating the loop with a vacuum pump, the pressure vessels (1, 10) are filled with

CO₂ by a gas bottle. During normal operation, liquid CO₂ flows from the pressure vessel 1 through an electrical heated evaporator (2) and is slightly superheated. After leaving a demister unit (3), where remaining liquid CO₂ is separated from the flow, it enters a compressor (4), where it is compressed to a certain pressure and simultaneously heated by the compression.

Before entering a test section, there is a conditioning (5) of the sCO₂, which means that a defined temperature can be adjusted via cooling or heating the sCO₂ mass flow rate. In the test-section (6) different kind of experiments can be performed. After leaving the test section, the sCO₂ is cooled down in a gas cooler (7) followed by the expansion in an expansion valve (8). Before it enters the pressure vessel 2 (10) the CO₂ can be cooled down again in a condenser (9). Finally, it is pumped back from the pressure vessel 2 into the pressure vessel 1. The sCO₂ mass flow rate in the SCARLETT test loop can be adjusted from about 30 to 110 g/s. Lower mass flow rate in the test section can be achieved by bypassing with needle valves. It must be mentioned, that the achievable mass flow rate depends on the compressor performance map, which leads to less mass flow rate at higher pressures and vice versa. The sCO₂ temperature at the inlet of the test section can be varied from about 0 to 140 °C and the pressure from about 75 to 110 bar.

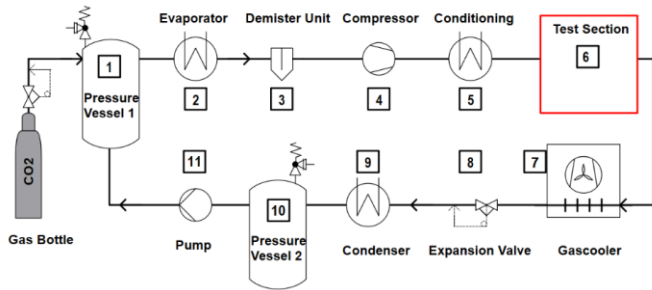


Figure 5: P&I diagram of the SCARLETT test loop.

DATA REDUCTION

All thermophysical properties were calculated using the Software REFPROP ver.9.0 [4]. The Reynolds numbers of the CO₂ flow are determined by measuring the CO₂ mass flow rate \dot{m}_{CO_2} by a Coriolis flowmeter. At the inlet, the dynamic viscosity (η_{CO_2}) of the flow can be calculated as a function of measured pressure (P_{CO_2}) and temperature (T_{CO_2}). Due to the varying thermophysical properties, the Reynolds number decreases drastically by crossing the pseudocritical temperature. Reynolds number at inlet conditions is calculated by:

$$Re_{CO_2} = \frac{4\dot{m}}{\pi d \eta} \quad (7)$$

The heat input \dot{Q} at each discretization step was defined by the calculated heat transfer coefficient htc_{cool} , the outer tube area $A_{t,o}$ and the temperature difference between wall and cooling media temperature.

$$\dot{Q} = htc_{cool} * A_{t,o} * (T_{t,o} - T_{cool}) \quad (8)$$

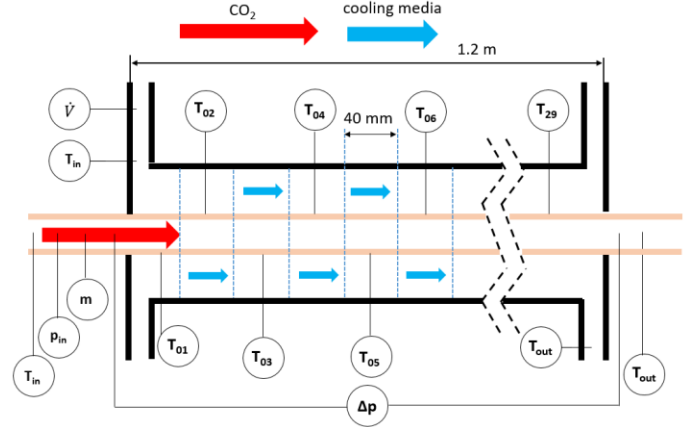


Figure 6: Schematic diagram of the test section including all measured quantities

The heat transfer coefficient of the cooling media flow in the annulus was estimated by the Nusselt correlation of Dirker [13]. htc_{cool} was assumed to be equal along the test section of 1200 mm. This assumption could lead to an overestimation of the CO₂ temperature along the tube by underestimating the heat flux in the entrance area of the cooling media flow. The described behaviour of the cooling media flow will be investigated in an additional test facility to implement a function of htc_{cool} over the length of the test section.

$$htc_{cool} = f(\dot{V}_{cool}, d_i, d_o, \text{fluid properties}) \quad (8)$$

The heat transfer through the copper tube \dot{Q} leads to a small difference between the inner ($T_{t,i}$) and outer ($T_{t,o}$) temperature of the tube wall by taking into account the thermal conductivity λ_{Cu} , the inner and outer diameter of the test tube (d_o , d_i), the length of the pipe section L . The inner tube temperature $T_{t,i}$ is equal to the wall temperature of CO₂ $T_{CO_2,w}$.

$$\dot{Q} = \frac{2 \pi L \lambda_{Cu}}{\ln(\frac{d_o}{d_i})} (T_{t,o} - T_{t,i}) \quad (9)$$

The heat transfer coefficient at the bulk temperature of CO₂ at every discretisation step was calculated by the heat \dot{Q} , the inner tube area A_i and the temperature difference between bulk and wall temperature.

$$htc_{CO_2} = \frac{\dot{Q}}{A_i * (T_{CO_2,b} - T_{CO_2,w})} \quad (10)$$

Both, CO₂ and cooling media temperatures are measured at the in- and outlet. Within the tube, the temperatures are calculated by the heat flux of the previous discretization step and the respective mass flux to determine the enthalpy of the flow. The heat exchanger is operated in co-current flow.

$$h_{CO_2/cool}(x+1) = h_{CO_2/cool}(x) \pm \frac{\dot{Q}(x)}{\dot{m}_{CO_2/cool}} \quad (11)$$

The procedure leads to 29 sets of the process parameters along the test section. Each thermocouple measurement is paired

with a cooling media and a CO₂ temperature. The calculation leads to a progress of the CO₂ bulk fluid temperature, which is the result of the earlier described assumptions, all parameters measured at the inlet and most significantly, the properties of CO₂.

UNCERTAINTY ANALYSIS

The uncertainty was mainly caused by the heat flux prediction by a uniform $h_{t_{cool}}$ along the test section and the temperature measurements. Prior to installation, the thermocouples were calibrated within a range of 5-60 °C by the use of a high accurate reference RTD (calibrated to 0.02 K). The resulting accuracy of the T-type thermocouples was ±0.1 K. The RTD's to measure both flows at in and outlet were ±0.3 K. The accuracy of the pressure transducer was 0.15 % of full range of 3/100 bar. The accuracy of the Coriolis-type mass flow meter was assumed to be 0.3 %. The volume flux of the cooling media was measured using an electromagnetic flow meter. The measurement data acquisition was used with a 40-channel Armature Multiplexer and a terminal block with temperature reference.

Additional to the measurement errors, the error of the manual soldering process has to be taken into account. For example, the manufacturing inaccuracies of the milled channels, the placing in the channel and the properties of the solder contribute to the assumed accuracy of the outer wall temperature of the cooper tube ($T_{t,o}$) of ±0.2 K.

$h_{t_{cool}}$ was assumed be constant along the test section with an accuracy of ±20 %. This value is a coarse estimation up to now. A 3-D flow simulation is planed to validate this assumption.

Due to the explained assumptions, the accuracy of the CO₂ temperature along the test section was assumed as ±0.5 K. From manufacturer certificate, the error of the inner and outer tube diameter was 0.05 mm. The heat conductivity of the cooper tube λ_{Cu} was assumed as 340 W/mK ±40 W/mK.

Table 1: Measured quantities and achieved accuracies

Meas. quantity	Symbol	Range	Unit	Accuracy
Volumetric flow	\dot{V}	0-2.5	l/s	±1%
Mass flow rate	\dot{m}	0-50	g/s	±0.3%
Pressure	P	0-100	bar	±0.15
Diff. pressure	ΔP	0-3000	mbar	±4.5
Thermocouples	T	5-60	°C	±0.1
RTD	T_{in}/T_{out}	0-100	°C	±0.3

RESULTS AND DISCUSSION

In this experimental study, the heat transfer was derived for different boundary conditions (Table 2). In Table 3, the measurement campaigns are summarized. The isothermal measurements were conducted with no cooling media flowing in the annulus.

Table 2: Experimental inlet conditions: horizontal cooling

CO ₂		
Temperature [°C]	Pressure [bar]	Mass flux [kg/m ² s]
37-85	77-85	400-1400
Cooling media		
Temperature [°C]	Volumetric flow [l/s]	
10-25	0.1-0.2	

Table 3: Measurement campaigns

condition	Flow direction	Number of experiments
isothermal	horizontal	91
cooled	horizontal	64
cooled	upwards	25
cooled	downwards	18

EXPERIMENTAL SYSTEM VALIDATION

The calculated results of the CO₂ heat output Q_{CO_2} are shown in Figure 7 as a function of the calculated cooling heat input \dot{Q}_{cool} in order to validate the experimental system. The results show that the heat transfer is mainly within range of ±20%. The uncertainties result from the temperature measurements. The small temperature difference (1-3 K) in the cooling media flow leads to a relatively high error of these values. In general, the calculated cooling media heat input is higher than the CO₂ heat output. At lower cooling media temperature, the behaviour seems to increase.

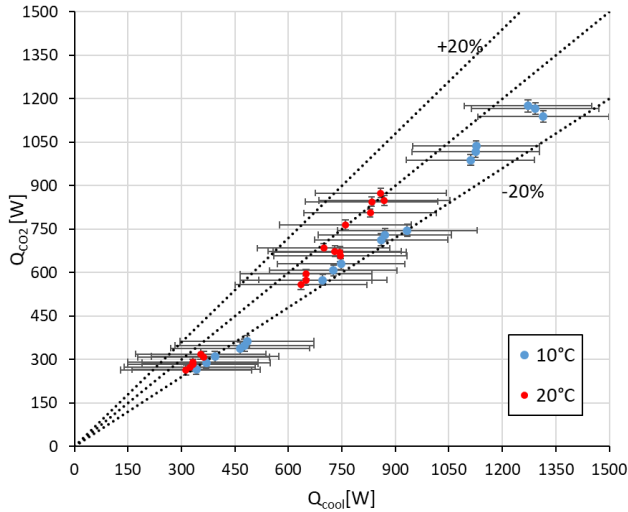


Figure 7: Energy balance: Q_{sCO_2} as a function of Q_{cool}

Figure 8 shows the result of a measurement point including error bars. htc_{CO_2} is displayed as a function of the bulk fluid temperature. The experimental conditions were $\dot{m} = 2.7 \text{ g/s CO}_2$, which is equal to a mass flux of $G = 860 \text{ kg/m}^2\text{s}$ for the inner tube diameter of 2mm. The volumetric cooling media flow rate was 0.1 l/s. The inlet conditions on the CO_2 side were 77 bar, $81.4 \text{ }^\circ\text{C}$ and $Re = 88400$. The inlet temperature of the cooling media was $10.2 \text{ }^\circ\text{C}$.

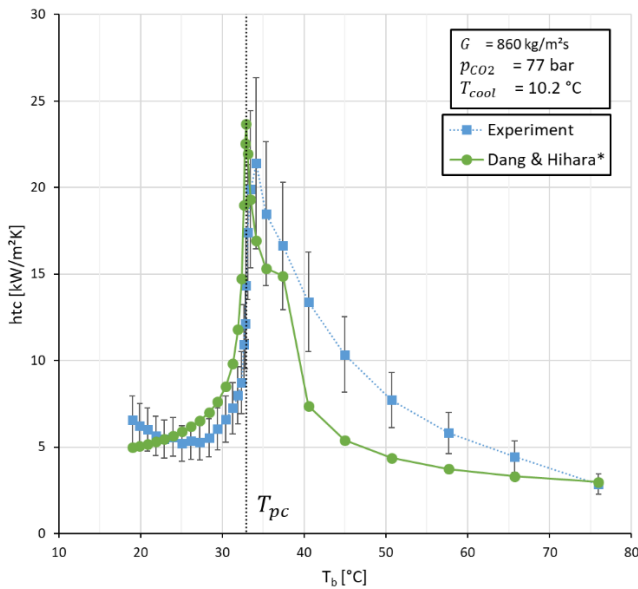


Figure 8: Heat transfer coefficient over bulk temperature at $\dot{m} = 2.7 \text{ g/s}$, $G = 860 \text{ kg/m}^2\text{s}$ and $p_{CO_2} = 77 \text{ bar}$

Due to the heat flux, CO_2 temperature is decreasing while cooling media temperature is increasing. The Reynolds number drops by the factor of 3. This is caused by the increase of viscosity. The results show a distinct peak close to the pseudo critical temperature (dashed line). The results are comparable with the predicted values of the Dang and Hihara [8] correlation.

EFFECT OF MASS FLUX

Figure 9a) presents the effect of mass flux at 415, 830 and $1370 \text{ kg/m}^2\text{s}$ (1.3, 2.6 and 4.3 g/s) for $p_{CO_2} = 85 \text{ bar}$ and $T_{cool} = 10 \text{ }^\circ\text{C}$. The heat transfer coefficient is shown as a function of T_b . The htc increases as the mass flux increases due to an increase in turbulent diffusion. As shown by Dang and Hihara [8], the maximum htc occurred at T_b slightly higher than T_{pc} .

In Figure 9 b) the heat flux q_{CO_2} is shown as a function of T_b . The heat flux is in total higher for increased mass flux. This is caused by the increased htc_{CO_2} , whereas T_{cool} and htc_{cool} were constant. The heat flux underwent a sharp decrease by crossing the pseudocritical temperature. At the first position of temperature measurement, q_{CO_2} is lower than the second position due to the lower temperature caused by heat conduction towards the flanging.

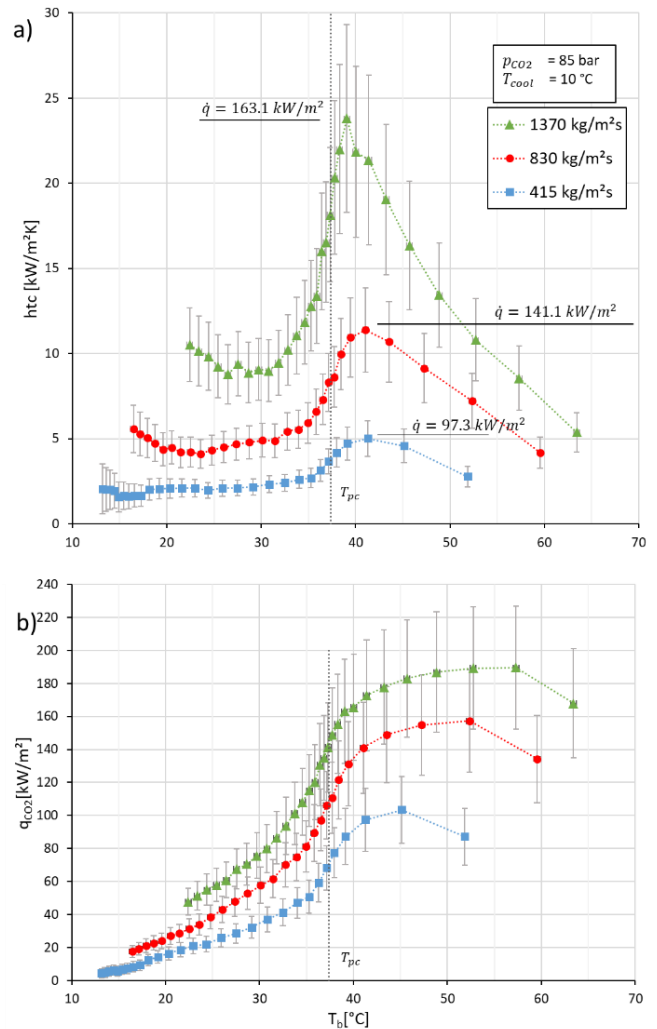


Figure 9: htc and heat flux over bulk temperature for different mass fluxes at $p_{CO_2} = 85 \text{ bar}$ and $T_{cool} = 10 \text{ }^\circ\text{C}$

In Figure 10 the htc is displayed at $p_{CO_2} = 81 \text{ bar}$ and $T_{cool} = 20 \text{ }^\circ\text{C}$ for different mass flux as a function of a) T_b and b) T_f . The peak in the heat transfer is located at the same bulk temperature for all mass fluxes. Depending on the film temperature, the temperature of the peak value seems to increase with increasing mass flux. This finding is contrary to Dang and Hihara's [8] work. It is to mention here that they showed this relation at a constant cooling heat flux of 12 kW/m^2 on a 4 mm tube. Further testing is necessary to achieve a better comparability. This will include higher temperature of the cooling media to achieve lower cooling heat flux.

The influence of the mass flux on the heat transfer coefficient increases near the critical temperature. When the mass flux was increased by a factor of 2, htc_{CO_2} increased by a factor of about 1.6 in the early stage of the cooling process whereas by a factor of about 3.3 near the critical point

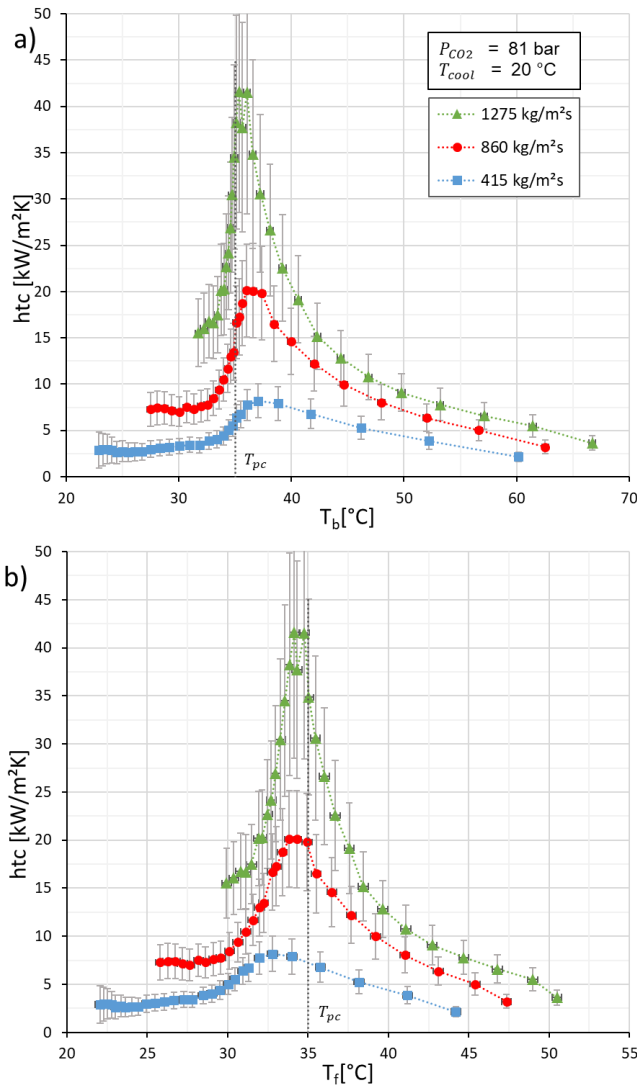


Figure 10: htc over bulk- and film temperature for different mass flux at $p_{CO_2} = 81 \text{ bar}$ and $T_{cool} = 10 \text{ }^\circ\text{C}$

EFFECT OF INLET PRESSURE

Figure 11 presents the htc of CO_2 for three different pressures ranging from 77 bar to 85 bar at $G = 860 \text{ kg/m}^2\text{s}$ and $T_{cool} = 10^\circ\text{C}$. For each pressure, the htc shows the same tendency in the gas like region. The htc increases continuously by approaching the pseudocritical temperature. In this stage, higher pressure has higher heat transfer coefficient due to the higher specific heat. The htc peak values are damped and moved to higher temperature with increased pressure. htc-values of 21, 15 and $12 \text{ kW/m}^2\text{s}$ are reached, respectively. This behaviour is related to the evolution of specific heat with temperature and pressure as shown in Figure 2. In the liquid-like region of the cooling process, the htc decreases for all pressures to the same level. In this stage, higher pressure has lower heat transfer coefficient due to the lower specific heat. The increasing tendency of the htc in the late stage of the cooling process, below $T_b = 25 \text{ }^\circ\text{C}$ in this case, is under investigation yet. In this temperature range, however, the measurement uncertainty increases as the CO_2 temperature approaches the cooling media temperature.

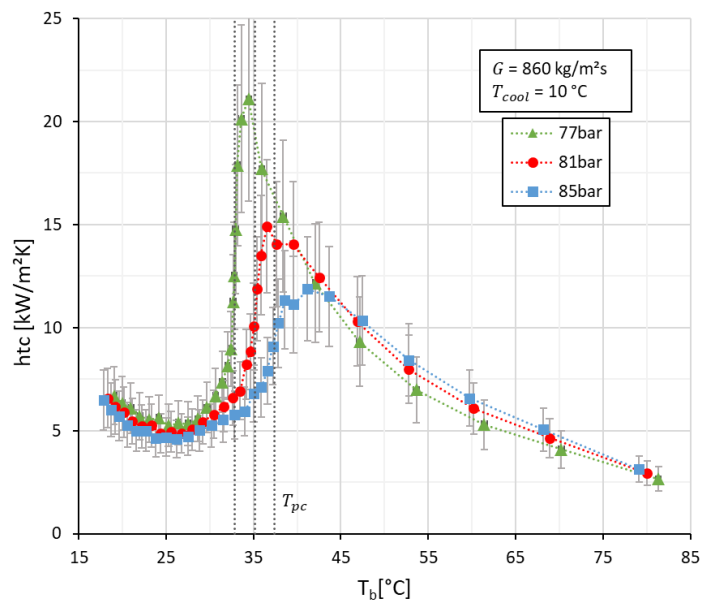


Figure 11: htc over bulk temperature for different pressures at $G = 860 \text{ kg/m}^2\text{s}$ and $T_{cool} = 10^\circ\text{C}$

EFFECT OF COOLING MEDIA TEMPERATURE

Figure 12 a) shows the htc at two different cooling media temperatures at $p_{CO_2} = 77 \text{ bar}$, $G = 860 \text{ kg/m}^2\text{s}$. $T_{cool} = 20 \text{ }^\circ\text{C}$ leads to slightly lower htc in the early stage of the cooling process whereas the peak value is significantly higher. In the late stage of the cooling process, the tendency is reversed: higher cooling media temperature leads to a higher htc.

In Figure 12 b) the wall temperature is displayed as a function of the bulk fluid temperature. $T_{cool} = 10 \text{ }^\circ\text{C}$ leads to a lower wall temperature, thus, the wall temperature is subcritical from the early stage of the cooling process. As T_b approaches T_{pc} , T_w is already far below T_{pc} , thus, the wall properties left the beneficial temperature range, which is close to the pseudocritical critical temperature.

At $T_{cool} = 20 \text{ }^\circ\text{C}$, the wall temperature reaches the pseudocritical temperature at $T_b = 48 \text{ }^\circ\text{C}$. As T_b reaches T_{pc} , T_w is close to T_{pc} . Thus, both T_b and T_w are in the temperature range of beneficial properties.

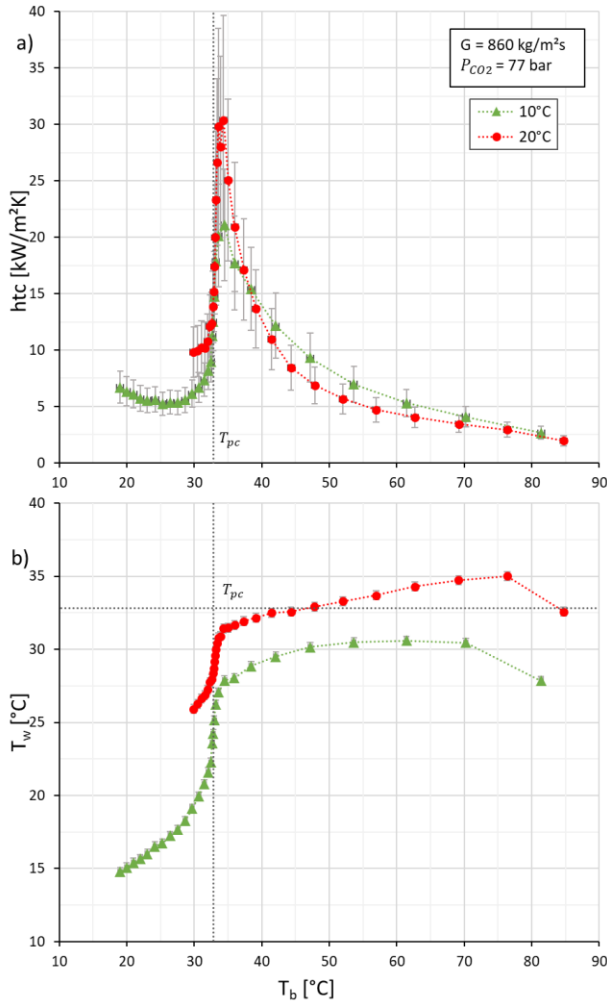


Figure 12: htc and Tw over bulk temperature for different cooling media temperature at $G = 860 \text{ kg/m}^2\text{s}$ and $p = 77\text{bar}$.

EFFECT OF FLOW DIRECTION

Figure 13 a) shows the htc for up- and downwards flow at $p_{CO_2} = 80 \text{ bar}$, $G = 415 \text{ kg/m}^2\text{s}$ and $T_{cool} = 25^\circ$. Figure 13 b) illustrates the mixed convection parameter $Gr/Re^{2.7}$. The horizontal dotted line displays the limit value defined by Jackson and Hall [10]. The mixed convection parameter increases in the gas like region towards a maximum value at the pseudocritical temperature. A sharp decrease is present in the liquid like region.

The mixed convection parameter at the presented configuration of $415 \text{ kg/m}^2\text{s}$, resulting in $Re_{CO_2,in} = 42000$ and $Re_{CO_2,out} = 13000$, is reaching the limit value near the pseudocritical point. However, does not exceed this value significantly. As the htc for up-and downwards flow show no significant difference, the limit value can be confirmed as far as, that at values up to 10^{-5} no influence present.

To reach higher values of the mixed convection parameter to investigate enhancement and degradation phenomena the mass flux has to be further reduced or the tube diameter has to be increased.

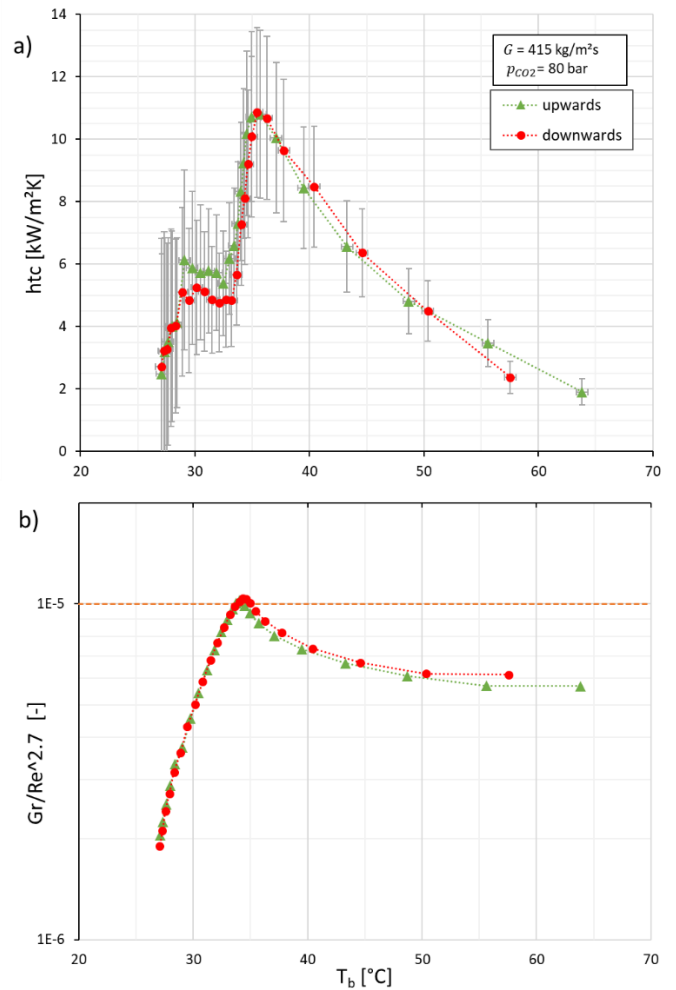


Figure 13: htc and $Gr/Re^{2.7}$ over bulk temperature for different flow orientations at $\dot{m} = 1.3 \text{ g/s}$ and $p = 80\text{bar}$.

PRESSURE DROP

Frictional pressure drop in fully developed turbulent single phase flow is calculated by taking into account the length of the test section l , mass flow rate \dot{m} , inner diameter d and the density ρ at the present pressure and temperature.

$$\Delta p = \zeta \frac{l \rho v^2}{2} = \frac{8}{\pi^2} \zeta \frac{l \dot{m}^2}{d^5 \rho} \quad (12)$$

The dimensionless friction factor ζ can be predicted as a function of Reynolds number Re and the relative roughness $\varepsilon = K/d$ with the roughness of the wall K [14].

$$\frac{1}{\sqrt{\zeta}} = -2 \lg \left[\frac{2.51}{Re \sqrt{\zeta}} + \frac{K/d}{3.71} \right] \quad (13)$$

The roughness of the tube was measured at three samples. The average value of $18.1 \mu\text{m}$ was taken into account to predict the friction factor. Figure 14 presents the friction factor of the uncooled flow in comparison with the presented prediction.

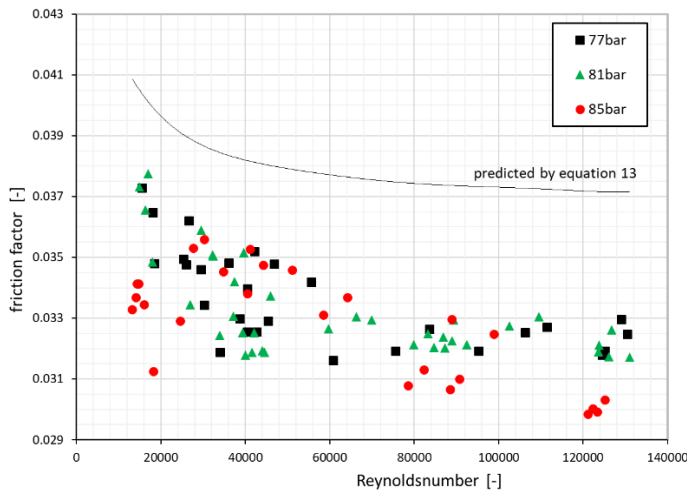


Figure 14: friction factor of the uncooled flow compared with the predicted value

The results show no significant difference for the three operation pressures. The evolution of the predicted value can be reproduced. At higher Reynolds number, the friction factor of rough pipes becomes constant, depending only on the pipe roughness as predicted by the moody chart [14]. The average deviation is 14%.

The prediction of the pressure drop under cooling conditions is shown in Figure 15. The predict was conducted by taking in to account the bulk, film or wall fluid properties. The prediction by the bulk fluid properties shows the highest error. The prediction with film and wall fluid properties show a much better agreement mainly within an error of 20%

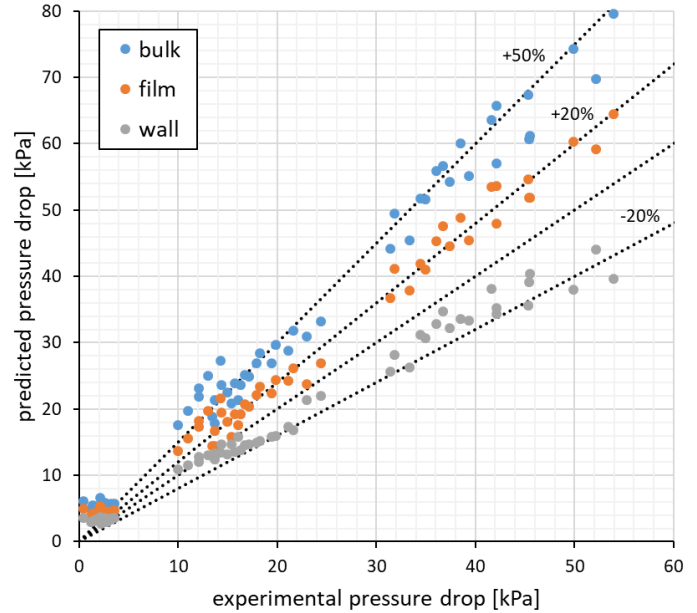


Figure 15: Experimental versus predicted pressure drop for different fluid

CONCLUSIONS

The cooling heat transfer of CO_2 near the critical point was investigated. Significant effects of mass flux, inlet pressure and cooling media temperature on the heat transfer were analysed. The mass flux showed significant effect especially near T_{pc} . The peak value of htc_{CO_2} appeared at T_b slightly higher than T_{pc} . Lower cooling media temperature caused stronger sub cooling, which leads to a lower peak value of htc_{CO_2} .

The influence of the flow orientation on the heat transfer coefficient is negligible within the investigated parameter range. However, the limit value of the mixed convection parameter was confirmed in this study. At $Gr/Re^{2.7} < 10^{-5}$ no difference between up and downwards flow is present.

The pressure drop in the isothermal experiments were predicted with an average error of +14%.

The prediction under cooling condition showed a much better agreement by taking into account the fluid conditions of the film and wall.

NOMENCLATURE

A	(m ²)	area of heat transfer
c_p	(J/kgK)	specific heat
g	(m/s ²)	acceleration of gravity
G	(kg/m ² s)	mass flux
Gr	(-)	Grashof number
h	(kJ/kg)	spec. Enthalpy
htc	(W/m ² K)	heat transfer coefficient
K	(m)	wall roughness
L	(m)	length of discretization
\dot{m}	(kg/s)	mass flow rate
Nu	(-)	Nusselt number
P	(bar)	pressure
Pr	(-)	Prandtl number
Q	(W)	heat
Re	(-)	Reynolds number
T	(°C)	temperature
v	(m/s)	velocity
V	(l/s)	volumetric flow

Greek symbols

Δp	(bar)	pressure drop
ε	(-)	relative roughness
η	(kg/ms)	dynamic viscosity
λ	(W/mK)	heat conductivity
ρ	(kg/m ³)	density
ζ	(-)	friction factor

subscripts

b	bulk
cool	cooling media
corr	correlation
CO ₂	carbon dioxide
Cu	copper
exp	experiment
f	film
in	inlet
out	outlet
t	tube
w	wall

ACKNOWLEDGMENT

This project has received funded by the European Union's Horizon 2020 research and innovation programme under grant agreement No 764690

REFERENCES

1. C. M. Mendez and G. Rochau, "sCO₂ Brayton Cycle: Roadmap to sCO₂ Power Cycles NE Commercial Applications -SAND2018-6187", *Albuquerque, New Mexico*.
2. V. Dostal; M. J. Driscoll; P. Hejzlar, "A Supercritical Carbon Dioxide Cycle for Next Generation Nuclear Reactors", *Advanced Nuclear Power Technology Program, MIT Center for Advanced Nuclear Energy Systems*, pp. 1–326 (2014).
3. S. B. Riffat; C. F. Afonso; A. C. Oliveira; D. A. Reay, "Natural refrigerants for refrigeration and air-conditioning systems", *Applied Thermal Engineering* 1, pp. 33–42 (1997).
4. E. W. Lemmon, M. L. Huber, M. O. McLinden, *REFPROP*, NIST SRD 23, United States of America (2010).
5. L. F. Cabeza; A. de Gracia; A. I. Fernández; M. M. Farid, "Supercritical CO₂ as heat transfer fluid: A review", *Applied Thermal Engineering*, pp. 799–810 (2017).
6. S. M. Liao and T. S. Zhao, "Measurements of Heat Transfer Coefficients From Supercritical Carbon Dioxide Flowing in Horizontal Mini/Micro Channels", *Journal of Heat Transfer* (3), pp. 413 (2002).
7. F. W. Dittus and L.M.K. Boelter, "Heat transfer in automobile radiators of the tubular type", *International Communications in Heat and Mass Transfer* 1, pp. 3–22 (1985).
8. C. Dang and E. Hihara, "In-tube cooling heat transfer of supercritical carbon dioxide. Part 1. Experimental measurement", *International Journal of Refrigeration* (7), pp. 736–747 (2004).
9. V. Gnielinski, "New equation for heat and mass transfer in turbulent pipe and channel flow", *International Chemical Engineering*, pp. 359–368 (1976).
10. J. D. Jackson and W. B. Hall, "FORCED CONVECTION HEAT TRANSFER TO FLUIDS AT SUPERCRITICAL PRESSURE", *Institution of Mechanical Engineers, Conference Publications* (1979).
11. A. Bruch; A. Bontemps; S. Colasson, "Experimental investigation of heat transfer of supercritical carbon dioxide flowing in a cooled vertical tube", *International Journal of Heat and Mass Transfer* (11-12), pp. 2589–2598 (2009).
12. W. Flaig; R. Mertz; J. Starflinger, "Design, control procedure and start-up of the sCO₂ test facility SCARLETT", *DuEPublico, 2nd European sCO₂ Conference 2018, 2nd European sCO₂ Conference 2018, Essen, Germany*, pp. 1–11 (2018).
13. J. Dirker and J. P. Meyer, "CONVECTION HEAT TRANSFER IN CONCENTRIC ANNULI", *Experimental Heat Transfer* 1, pp. 19–29 (2004).
14. Verein Deutscher Ingenieure, *VDI-Wärmeatlas* 11. ed., Springer Vieweg, Berlin (2013).

LARGE EDDY SIMULATION OF sCO₂ FLOW WITH A DISCONTINUOUS GALERKIN METHOD

Aldo Hennink*

Delft University of Technology
Department of Radiation Science
and Technology
Delft, The Netherlands
Email: a.hennink@tudelft.nl

Danny Lathouwers

Delft University of Technology
Department of Radiation Science
and Technology
Delft, The Netherlands

Martin Rohde

Delft University of Technology
Department of Radiation Science
and Technology
Delft, The Netherlands

Jan Leen Kloosterman

Delft University of Technology
Department of Radiation Science
and Technology
Delft, The Netherlands

ABSTRACT

We present large eddy simulations (LES) of heat transfer in sCO₂ at 8 MPa in a plane channel geometry with various temperature ranges. This presents a numerical challenge, as the density can vary by more than a factor 2. We use a pressure-based solver with a high-order discontinuous Galerkin discretization. The large eddy simulation is based on the Wall-averaged Local Eddy viscosity (WALE) model and a constant turbulent Prandtl number. We resolve the flow near the wall. Though our geometry allows for a structured grid, our numerical scheme is highly flexible with respect to unstructured meshes. We validate our LES with an isothermal flow, and with a simulation in a temperature range that is far from the pseudocritical line. The results for non-isothermal flow show that the LES can accurately predict the average velocity and temperature profiles, despite reducing the number of degrees of freedom by several orders of magnitude compared to the reference direct numerical simulation. This paper is a precursor to future work, in which we will present more extensive validation of the non-isothermal test case. Our results are a first step toward using a pressure-based discontinuous Galerkin solver for sCO₂ flows.

INTRODUCTION

There is a growing interest for using supercritical CO₂ in heat exchangers, but using such an innovative approach makes it harder to predict the efficiency based on previous experiments. Numerical simulations therefore seem an obvious approach, but unfortunately there are no reliable, affordable numerical models for heat transfer in supercritical CO₂. In this paper we investigate using a Large Eddy Simulation (LES) based on a discontinuous Galerkin (DG) method to predict the heat transfer in a heated infinite plane channel flow. Using an LES model greatly reduces the required computational resources compared to a more straightforward direct numerical simulation.

GOVERNING EQUATIONS

The governing equations for sCO₂ flow with heat transfer are

$$\begin{aligned}\frac{\partial(\rho h)}{\partial t} + \nabla \cdot (m h) &= \nabla \cdot (\lambda \nabla T), \\ \frac{\partial m}{\partial t} + \nabla \cdot (u m) &= \nabla \cdot \tau - \nabla p + F, \\ \frac{\partial \rho}{\partial t} + \nabla \cdot m &= 0,\end{aligned}$$

where t is the time, ρ is the density, u is the velocity, $m = \rho u$ is the mass flux, h is the specific enthalpy, λ is the thermal conductivity, T is the temperature, and p is the pressure. We can neglect effect of the pressure gradient on the Fourier heat flux:

$$-\lambda \nabla T \approx -\frac{\lambda}{c_p} \nabla h,$$

where c_p is the specific heat capacity [1]. The viscous stress tensor is

$$\tau = \mu \left(\nabla u + (\nabla u)^T - \frac{2}{3} (\nabla \cdot u) I \right).$$

That is, we leave out the bulk viscosity (or ‘volume viscosity’), as in all previous literature on supercritical fluids of which we are aware. There is no good experimental data for the bulk viscosity.

To close the system of equations, we calculate the material properties ρ , α , λ , μ , and T as a function of the computed specific enthalpy, evaluating the equations of state at a fixed thermodynamic pressure. In other words, we neglect the effect of turbulent pressure fluctuations on the material properties. This approach is valid because the pressure fluctuations are several orders of magnitude smaller than the absolute pressure.

We use the open-source CoolProp library to evaluate the material properties of CO₂ [2]. The data is based on [3] for the equation of state, [4] for the thermal conductivity (λ), and [5] for the dynamic viscosity (μ). The most important alternative to CoolProp is the proprietary REFPROP software library. There can be minor differences between CoolProp and REFPROP; in particular, the values for the thermal conductivity can differ by up to 1% [6]. We do not know which is more accurate, and we have not investigated this topic further.

CoolProp is too slow to be called directly in a high-performance CFD code, so we approximate all material properties with cubic B-splines. (See, e.g., [7].) We refine the B-splines locally as follows. We start with a very coarse approximation with only a few interpolation points. This spline interpolation is refined by looping over each segment, checking whether the segment deviates too much from the actual value, and adding an extra point if necessary. This refinement procedure is repeated until the maximum relative deviation at any point is at most 10^{-4} .

NUMERICAL METHOD

This section summarizes the numerical method. We only sketch the outlines of our approach.

Numerical schemes for fluid dynamics fall roughly into two broad categories. First, there are compressible solvers, which are used extensively for simulating high-Mach number flow. These methods can deal with strong density gradients and varying material properties. The problem is that they calculate a thermodynamic pressure from an equation of state. This thermodynamic relation is highly sensitive in supercritical CO₂: small changes in the density imply large changes in the pressure, which makes stable calculations infeasible with contemporary computational resources.

The second type of numerical methods is designed for incompressible flows. They usually assume a constant density, or postulate that the density gradients are small. These assumptions do not hold for sCO₂ in a heat exchanger. We have therefore modified an incompressible solver to deal with the strongly varying density gradients.

A pressure-correction method is used to march the solution forward in time [8]. This is a type of splitting scheme, meaning that we solve the transport equations one by one at each time step. We first march h forward in time, then update ρ as a function of h , and subsequently solve for the mass flux and pressure. We do not need to iterate within a time step: each equation is solved once. This is in line with most previous literature on the simulation of supercritical fluids in periodic, non-developing domains (e.g., [1]); flow in developing domains usually does require iteration (e.g., [9] and [10]). We also monitor the errors in the pressure-correction splitting scheme by calculating the difference between the discrete pressure vectors in two consecutive time steps; their relative difference is approximately 0.01 to 0.02 in the L_2 -norm.

We solve for the specific enthalpy (h), the mass flux (m) and the hydraulic pressure (p). This hydraulic pressure is only unique up to a constant; we do not compute the absolute pressure from an equation of state. The main challenges in developing the numerical scheme were connected to the strong density variations of the sCO₂, since most literature on incompressible fluids assumes a constant density. We adjusted the standard pressure-correction scheme to take the temporal derivative of the density into account.

In a discontinuous Galerkin method, the approximated quantity is modeled as a weighted sum of basis functions, each of which has support on one element in the mesh. The numerical solution is therefore generally discontinuous across element interfaces. We use a modal function set, meaning that the solution space in an element is the span of all polynomials up to a particular order. This is to be contrasted with a nodal DG method, where the function space within an element is the tensor product of one-dimensional Legendre sets. The polynomial bases for the unknowns are always of the same order.

We use a standard symmetric interior penalty method for the Fourier heat flux in the enthalpy equation [11], which is one of several discretizations of the diffusive terms in the transport equations. We include the spatial derivative of the density into this penalty method. The penalty parameter is based on [12]. We modified this discretization so that it could also be applied to the viscous stress in the momentum equations. This is similar to what is done for hyperbolic systems in compressible flows [13]. The Cartesian components of the mass flux are coupled implicitly, that is, we solve for all directions of the mass flux in a single linear system.

The convective terms for the density, enthalpy and momentum equations are all treated with the same upwind discretization, based on the Lax-Friedrichs flux.

SUBGRID-SCALE MODEL

We use a Wall-Averaged Local Eddy viscosity (WALE) LES model for the momentum equations, which prescribes an subgrid scale viscosity of

$$\nu_{SGS} = (C_w \Delta)^2 \frac{|\tilde{S}|_{Frob}^{d/3}}{|\tilde{S}|_{Frob}^5 + |\tilde{S}|_{Frob}^{d/2}},$$

where Δ is the LES filter width,

$$\tilde{S}_{ij} = \frac{1}{2}(\tilde{g}_{ij} + \tilde{g}_{ji}),$$

$$\tilde{S}_{ij}^d = \frac{1}{2}(\tilde{E}_{ij} + \tilde{E}_{ji}) - \frac{1}{3}\tilde{E}_{mn}\tilde{E}_{mn}\delta_{ij},$$

$$\tilde{E}_{ij} := \tilde{g}_{ik}\tilde{g}_{kj} \text{ and } \tilde{g}_{ij} := \partial\tilde{u}_i/\partial r_j.$$

Here \tilde{u} is the filtered (resolved) velocity, $r=[x,y,z]$ is the position vector, and $|\cdot|_{Frob}$ denotes the Frobenius norm of a matrix (i.e., the square root of the sum of the squares of the elements). See [14] and [15] for a motivation for this LES model.

A turbulent Prandtl number accounts for the subgrid-scale effects in the enthalpy equation. That is, the subgrid scale thermal conductivity is modeled as

$$\left(\lambda\right)_{SGS} = Pr_{SGS} \tilde{\rho},$$

where $\tilde{\rho}$ is the filtered (resolved) density. This removes small-scale structures in the enthalpy field, thereby making a numerical simulation feasible. We use a simple constant model, where Pr_{SGS} is fixed at a constant value. It is usually chosen in the range [0.3,0.9]. (See, e.g., [16].) In our case, setting $Pr_{SGS}=0.7$ removes enough small-scale effects to stabilize the numerical scheme. We do not investigate the effect of using other values. We suspect that an LES is less sensitive to the turbulent Prandtl number than a RANS calculation would be, because we believe that the primary goal of a subgrid model is not to model the physics accurately, but rather to stabilize the flow without overly distorting the large-scale structures. In fact, inaccurate subgrid models can yield accurate results, and vice versa. (See, e.g., [17]). Nevertheless, investigating the effect of the turbulent Prandtl number is certainly an interesting venue for other work.

IMPLEMENTATION

We developed an in-house computational fluid dynamics (CFD) code ‘DG Flows’ that implements our discontinuous Galerkin method. It is written in Fortran 2003/2008, and has been in development since late 2015. It has also been used to model the flow and heat transfer of molten salt, and to investigate experimental large-eddy simulation techniques.

We use the MPI-based PETSc software library to solve the linear systems that arise from the discretizations [18]. In particular, we use a conjugate gradient method with an incomplete Cholesky preconditioner for the pressure equation, and a GMRES method with an incomplete LU preconditioner for the enthalpy and momentum equations. The linear systems are solved up to a certain tolerance r_{tol} , meaning that the norms of the preconditioned residuals are at most r times the norm of the right-hand-side vector. We set $r_{tol}=10^{-6}$ for the enthalpy, the pressure, and the momentum equations.

To parallelize the calculation, the mesh is partitioned with the METIS software library, which is based on a multilevel recursive-bisection, multilevel k-way, and multi-constraint partitioning scheme [19]. We use a simple block-Jacobi scheme to distribute the linear solver over the processes.

RESULTS FOR PLANE CHANNEL FLOW

We test the numerical method and the LES model in a plane channel geometry. We show (i) an isothermal test case, (ii) a simulation with heat transfer at a temperature far from the critical point, and (iii) a simulation with heat transfer close to the pseudocritical point. In each case, the domain is $\Omega=[0,(4/3)\pi\delta]\times[-\delta,\delta]\times[0,2\pi\delta]$, where δ is the channel half-width. We impose no-slip boundary conditions at $y=\pm\delta$, and periodic boundary conditions in the x- and z-directions. The flow is in the z-direction. We add the constraint $\int_{\Omega} p dr = 0$ to ensure that the pressure is uniquely defined. We keep the body force in the flow direction (F_3) constant, so that the time-averaged wall shear stress ($\langle\tau_w\rangle=F_3\delta$) is known a priori. The friction velocity is $u_{\tau}=\sqrt{\langle\tau_w\rangle/\rho}$ and the Reynolds stress is $Re_{\tau}=\delta u_{\tau}/\nu$. We average the quantities of interest over time and in the x- and z-directions.

Isothermal Channel Flow

For the isothermal case we let $Re_{\tau}=180$, so that the results can be compared to the DNS data from [20], which was performed at $Re_{\tau}=178.13$. We use a second-order polynomial basis in the boundary elements, and gradually increase this to a fourth-order polynomial basis for elements in the bulk. We used 0.41M degrees of freedom per direction of the mass flux, whereas [20] used 4.0M. Figure 1 shows that the LES overpredicts the velocity by approximately 5%. Note that the bulk velocity is approximately proportional to Re_{τ} .

Channel Flow with sCO₂ far from Pseudocritical Point

The second test case is a heated plane channel flow with supercritical CO₂. We aim to reproduce the DNS data from [21], which was obtained with a compressible, DG-based solver at a Mach number of 0.2. They found that the turbulent pressure fluctuations are small at this Mach number, which justifies a comparison with our simulation with a low-Mach approximation, though there is of course a discrepancy in the material properties, which do not depend on the pressure in our simulation. The thermodynamic pressure is 8.0 MPa, and temperatures at the boundaries are fixed at $T=335\text{ K}$ at $y=-\delta$, and $T=345\text{ K}$ at $y=\delta$. This temperature range is far from the pseudocritical point. The bulk Reynolds number is defined as $Re_{\text{bulk}}=u_{\text{bulk}}\delta/v_{\text{ref}}$, where u_{bulk} is the bulk velocity, and v_{ref} is the kinematic viscosity at the thermodynamic reference point of (8.0MPa, 340 K). In [21] the body force is dynamically adjusted to keep the bulk Reynolds number constant at 2800 throughout the simulation.

Since we do not know a priori what body force will result in the desired bulk Reynolds number, we estimate the Darcy friction factor (c_f) with the Colebrook-White relation for smooth pipes:

$$\frac{1}{\sqrt{c_f}} = -2 \log_{10} \left(\frac{2.51}{Re_{\text{hydr}} \sqrt{c_f}} \right),$$

where Re_{hydr} is the Reynolds number based on the hydraulic diameter. This gives an estimate $c_f \approx 0.0300$, which is used in the Darcy-Weisbach equation to estimate the required volumetric force in the flow direction:

$$F_3 = c_f \frac{\rho}{2} \frac{u_{\text{bulk}}^2}{D_{\text{hydr}}},$$

where we evaluate the density at the thermodynamic reference point. The bulk Reynolds number was then checked *a posteriori*, showing that the body force needed to be increased by approximately 1% to achieve the desired bulk Reynolds number.

Figures 2, 3, and 4 compare the LES results with the DNS data in [21]. Figures 3 and 4 show a slight discrepancy in the thermodynamic properties, but this can be explained by the fact that we use a constant thermodynamic pressure to evaluate the density and temperature, that is, we do not take the effect of the pressure on T and ρ into account. Note that the error in the density at the boundaries is solely due to the low-Mach approximation, because our density is fixed by the boundary conditions for the temperature, whereas the density in the reference data can fluctuate with a varying pressure. Figure 4 shows a deviation of approximately 0.2% in density at the boundaries, which gives an indication of the error inherent in the low-Mach approximation. The error in the average density profile is not more than 0.2% anywhere else in the domain. Figure 2 shows that our LES predicts a slightly higher velocity near the hot wall, where the density is lower.

The velocity profile in the compressible DNS simulation is less asymmetrical. Nevertheless, the DNS data and the LES for the average velocity profile differ by only 3%, despite the fact that we use only 0.46M degrees of freedom, whereas [21] used 198M.

Channel Flow with sCO₂ That Includes the Pseudocritical Line

We also perform an LES of a heated channel flow in a temperature range that is close to the pseudocritical point. The thermodynamic pressure is 8 MPa, and the boundary conditions for the temperature are $T=311\text{ K}$ at $y=-\delta$, and $T=305\text{ K}$ at $y=+\delta$. Note that the thermal expansion ratio at this pressure is highest at $T=308\text{ K}$, so that the temperature range includes the pseudocritical line, and the material properties vary strongly. We use a constant body force F , such that $Re_{\tau}=180$ on average over the two boundaries. Unfortunately we do not have reference data with which to validate our results for this test case.

Figure 6 shows the average temperature profile. Compared to the simulation far from the pseudocritical point (Figure 3), the temperature is more homogeneous in the bulk of the fluid, indicating a better mixing, though the Reynolds number is the approximately same. Figure 7 shows that the density differs by more than a factor of between the two planes, which explains the strongly skewed velocity profile in Figure 5.

CONCLUSION

The results indicate that a large eddy simulation with a discontinuous Galerkin method can simulate turbulent flow of sCO₂ with heat transfer. This is achieved with far fewer degrees of freedom than a direct numerical simulation (DNS) would require, which opens the door to investigating the flows at moderate Reynolds numbers in engineering applications where DNS is still unattainable.

In future work we plan to validate our results for flow near the pseudocritical point. We will also investigate the efficacy of various LES models for heat transfer in supercritical fluids. In particular, it is not clear whether using a constant turbulent Prandtl number can accurately predict heat transfer deterioration. We also do not know how accurate the LES predictions are when a gravity force is included in the simulation.

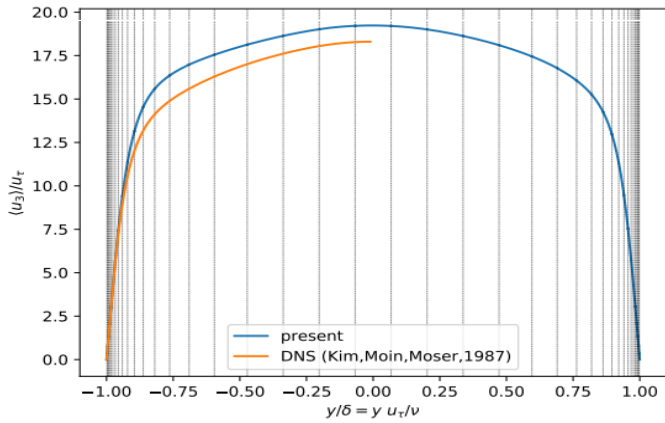


Figure 1: Average velocity profiles for the current LES and the DNS data from [20]. The gray vertical lines indicate the boundaries of the elements.

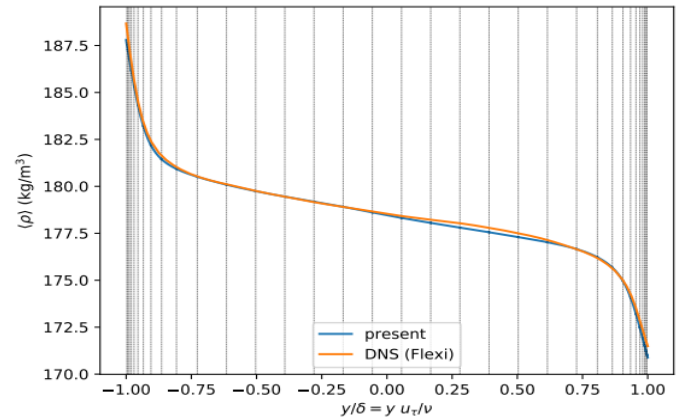


Figure 4: Average density profiles for the current LES and the DNS data from [21]. The gray vertical lines indicate the boundaries of the elements.

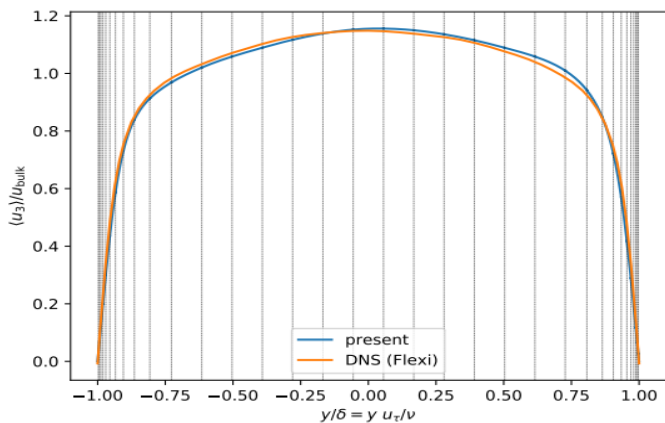


Figure 2: Average velocity profiles for the current LES and the DNS data from [21]. The gray vertical lines indicate the boundaries of the elements.

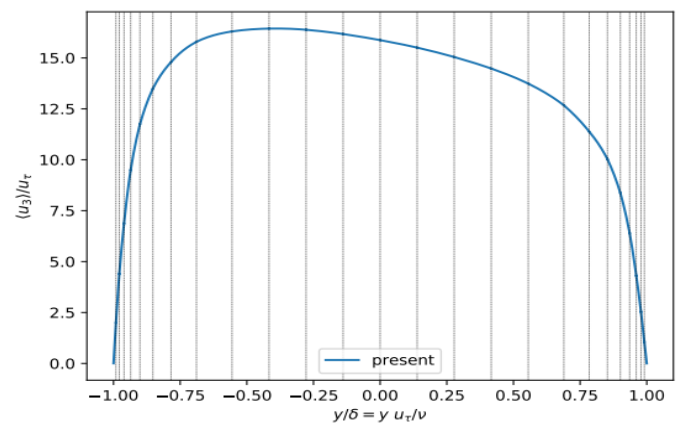


Figure 5: Average velocity profile for the LES near the pseudocritical point. The gray vertical lines indicate the boundaries of the elements.

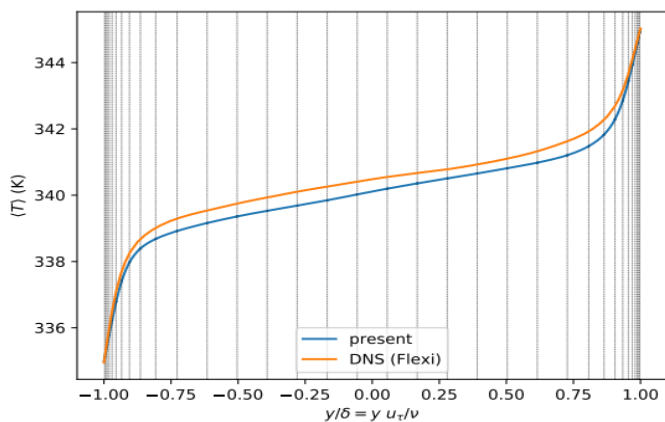


Figure 3: Average temperature profiles for the current LES and the DNS data from [21]. The gray vertical lines indicate the boundaries of the elements.

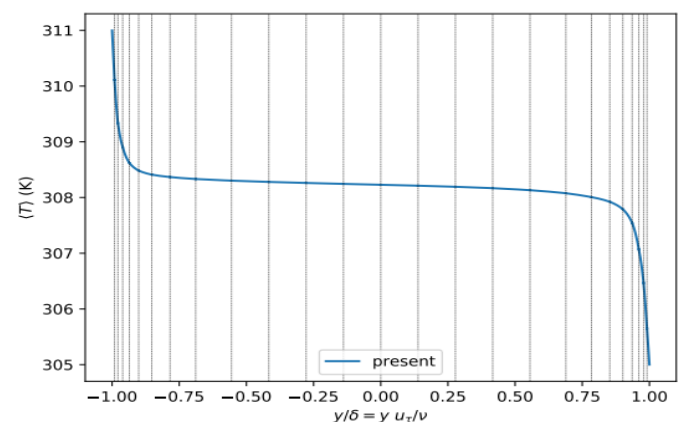


Figure 6: Average temperature profile for the LES near the pseudocritical point. The gray vertical lines indicate the boundaries of the elements.

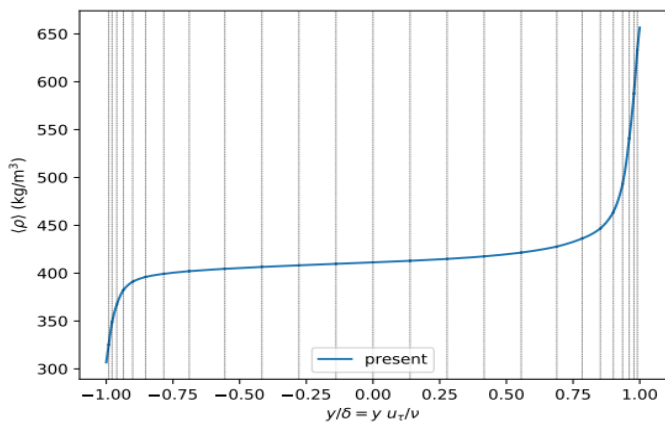


Figure 7: Average density profile for the LES near the pseudocritical point. The gray vertical lines indicate the boundaries of the elements.

ACKNOWLEDGEMENTS

This work was supported by the sCO₂-HeRo project that has received funding from the European research and training program 2014-2018 (grant agreement ID 662116).

This work was partially supported by the ENEN+ project that has received funding from the Euratom research and training Work Programme 2016 - 2017 - 1 #755576.

We thank the Institut für Kernenergetik und Energiesysteme (IKE) at the University of Stuttgart for providing the computational resources that were used for the simulation in Figures 5, 6, and 7.

We are grateful to Sandeep Pandey for providing the raw DNS data in [21].

REFERENCES

- 1: J. W. R. Peeters, 2016, Turbulence and turbulent heat transfer at supercritical pressure, PhD Thesis, Delft University of Technology, doi:10.4233/uuid:54f6098c-4c99-4129-8d8c-353a9411c0ae
- 2: Ian H. Bell, Jorrit Wronski, Sylvain Quoilin, Vincent Lemort, 2014, Pure and Pseudo-pure Fluid Thermophysical Property Evaluation and the Open-Source Thermophysical Property Library CoolProp, *Industrial & Engineering Chemistry Research* 53:6, pp. 2498-2508
- 3: R. Span, W. Wagner, 1996, A New Equation of State for Carbon Dioxide Covering the Fluid Region from the Triple Point Temperature to 1100 K at Pressures up to 800 MPa, *Journal of Physical and Chemical Reference Data* 25:6, pp. 1509-1596
- 4: G. Scalabrin, P. Marchi, F. Finezzo, R. Span, 2006, A Reference Multiparameter Thermal Conductivity Equation for Carbon Dioxide with an Optimized Functional Form, *Journal of Physical and Chemical Reference Data* 35:4, pp. 1549-1575
- 5: A. Fenghour, W. A. Wakeham, V. Vesovic, 2009, The Viscosity of Carbon Dioxide, *Journal of Physical and Chemical Reference Data* 27:1, pp. 31
- 6: CO₂ data page and validation, CoolProp, N. N., http://coolprop.sourceforge.net/dev/fluid_properties/fluids/CarbonDioxide.html#fluid-carbondioxide, retrieved on 2019-04-23

- 7: R. Bartels, J. Beatty, B. Barsky, 1996, *An Introduction to Splines for Use in Computer Graphics and Geometric Modeling*, Morgan Kaufmann
- 8: A. Segal, 2006, Finite element methods for the incompressible Navier-Stokes equations. Lecture notes for J. M. Burgerscentrum Research School for Fluid Mechanics, Delft Institute of Applied Mathematics
- 9: F. Ries, P. Obando, I. Shevchuck, J. Janicka, A. Sadiki, 2017, Numerical analysis of turbulent flow dynamics and heat transport in a round jet at supercritical conditions, *International Journal of Heat and Fluid Flow* 66:, pp. 172-184
- 10: H. Nematì, 2016, Direct numerical simulation of turbulent heat transfer to fluids at supercritical pressures, PhD Thesis, Delft University of Technology, doi:10.4233/uuid:b3fcb3a0-28b1-4335-a7a1-3fa1629e03d9
- 11: Douglas N. Arnold, Franco Brezzi, Bernardo Cockburn, L. Donatella Marini, 2001, Unified analysis of discontinuous Galerkin methods for elliptic problems, *SIAM Journal on Numerical Analysis* 39:5, pp. 1749-1779
- 12: Koen Hillewaert, 2013, Development of the discontinuous Galerkin method for high-resolution, large scale CFD and acoustics in industrial geometries, PhD thesis, Université catholique de Louvain,
- 13: Ralf Hartmann, 2008, Numerical Analysis of Higher Order Discontinuous Galerkin Finite Element Methods, Institute of Aerodynamics and Flow Technology DLR (German Aerospace Center)
- 14: F. Nicoud, F. Ducros, 1999, Subgrid-Scale Stress Modelling Based on the Square of the Velocity Gradient Tensor, *Flow, Turbulence and Combustion* 62:3, pp. 183-200
- 15: Ghader Ghorbaniasl, Chris Lacor, 2008, Sensitivity of SGS Models and of Quality of LES to Grid Irregularity, Quality and Reliability of Large-Eddy Simulations, pp. 155-166, Springer Netherlands
- 16: E. Garnier, N. Adams, S. Sagaut, 2009, *Large Eddy Simulations for Compressible Flows*, Springer Netherlands
- 17: A. W. Vreman, 1995, Direct and Large-Eddy Simulation of the Compressible Turbulent Mixing Layer, PhD Thesis, University of Twente,
- 18: PETSc web page, Satish Balay, Shrirang Abhyankar, Mark F. Adams, Jed Brown, Peter Brune, Kris Buschelman, Lisandro Dalcin, Alp Dener, Victor Eijkhout, William D. Gropp, Dmitry Karpeyev, Dinesh Kaushik, Matthew G. Knepley, Dave A. May, Lois Curfman McInnes, Richard Tran Mills, Todd Munson, Karl Rupp, Patrick Sanan, Barry F. Smith, Stefano Zampini, Hong Zhang, Hong Zhang, <http://www.mcs.anl.gov/petsc>, retrieved on 2019-04-23
- 19: George Karypis, Vipin Kumar, 1998, A Fast and High Quality Multilevel Scheme for Partitioning Irregular Graphs, *SIAM Journal on Scientific Computing* 20:1, pp. 359-392
- 20: J. Kim, P. Moin, R. Moser, 1987, Turbulence statistics in fully developed channel flow at low Reynolds number, *Journal of Fluid Mechanics* 177:, pp. 133
- 21: F. Fabian, S. Pandey, X. Chu, C.-L. Munz, E. Laurien, B. Weigand, 2018, High-fidelity direct numerical simulation of supercritical channel flow using discontinuous Galerkin spectral element method. *High Performance Computing in Science and Engineering*, Springer

CONFIGURATION OF A FLEXIBLE AND EFFICIENT sCO₂ CYCLE FOR FOSSIL POWER PLANT

Albannie CAGNAC*

EDF R&D

Chatou, France

Email: albannie.cagnac-1@edf.fr

Mounir MECHERI

EDF R&D

Chatou, France

Stefano BEDOGNI

EDF R&D

Chatou, France

ABSTRACT

As part of the sCO₂-Flex project, funded from the European Union's Horizon 2020 research and innovation program under grant agreement N° 764690, the consortium has set about developing a fossil fuel power cycle that allows both more flexibility and less emissions than currently operating power cycles. For this objective, the consortium has decided to work on a supercritical CO₂ (sCO₂) cycle in order to be able to gain in modularity in terms of size reduction, in efficiency because it is more efficient than a water-steam cycle, in flexibility because the design will be simplified and above all will take into account future constraints from the design stage.

EDF was responsible for providing the consortium with the most interesting fossil fuel cycle configurations from a flexibility and performance point of view. To this end, an iterative approach has been adopted and will be presented later in the paper.

First, 21 different cycle configurations were modelled in order to assess their impact on the performance for coal power plant application. Based on the expertise of the EDF R&D team, a selection of a few cycles has been made to be presented to different experts in order to determine: the industrial capacity to obtain equipment with the expected performance, the operability of this type of cycle according to these technical characteristics (the more complex a cycle will be to operate, the greater the risk of failure).

In a second step, all the current flexibility constraints were synthesized for the cycles in operation, as well as the influential factors to guarantee this flexibility (operating ramp of such a component, constraints related to the reliability of a component...). Then, on the basis of future energy mix scenarios and interviews with operators, we also drew insight about the future evolution of these constraints.

Finally, on the basis of the first selection of cycles and future flexibility constraints, cycle configurations were selected within

the consortium, taking into account also the potential industrial difficulties and costs for the development of components, in particular for the boiler, which is a key element for future markets for this type of cycle.

INTRODUCTION

Global electricity production has been undergoing major upheavals in recent years. The increase in production from renewable energies, most of which are fatal, and the political will to reduce greenhouse gas emissions are a difficult equation to solve. Indeed, if the reduction of gas emissions requires the closure of fossil power plants, the need to compensate for the intermittent production of renewable energies by ultra-flexible means of production argues in favor of maintaining these same plants. In addition, most of the world's electricity generation is still provided by fossil fuel power plants. It is this ambivalence that led the sCO₂-Flex project team to propose working on a completely new type of cycle adapted to a fossil power plant: a supercritical CO₂ Brayton cycle, designed to be more flexible and more efficient than current cycles.

WHY AN EFFICIENT AND FLEXIBLE CYCLE?

In recent years, global electricity production has undergone profound upheavals. Faced with the challenges of global warming, growing demand and economic challenges, electricity producers must be innovative in order to best meet society's requirements. Although renewable energies are growing rapidly, the majority of electricity in the world is produced by fossil fuel power plants, which emit high levels of greenhouse gases but contribute to the stability of the electricity grid through their flexibility. This flexibility has often improved at the cost of

making cycles more complex because they are designed to operate in base mode and not in flexible mode, making it more difficult for operators to operate (with an increased risk of failure) and a loss of efficiency due to the requirements of environmental regulations, imposing energy-intensive pollution control equipment. Based on this observation, our idea was to start from a completely new type of cycle to integrate all the elements necessary for flexibility and environmental requirements from the design stage and thus optimize performance and facilitate the operation of this cycle.

METHODOLOGY

From the previous literature and simulations [Le Moulec, 2013; Mecheri & Le Moulec, 2016], more than 21 supercritical CO₂ cycle configurations were first modelled. On the basis of the performances obtained on different technical characteristics (overall efficiency, boiler temperatures, efficiency of the different components, flow rate...) and expert reviews on the influential parameters of the current flexibility of a thermal cycle, we made a first selection of 6 cycle configurations considered as the most interesting for both efficiency and flexibility.

In a second step, it felt necessary to better understand what the future constraints related to flexibility would be in order to integrate them into the criteria for the selection of the best cycle configurations. To do this, we had to study the current cycle limits, anticipate future cycle operating chronicles and anticipate the constraints related to increasingly rapid and significant load variations.

In the last phase of our study, we shared the results of the first two phases in order to establish a choice between 3 configurations allowing the best compromise between performance and flexibility.

FIRST SELECTION OF CYCLES CONFIGURATIONS

More than 40 sCO₂ Brayton cycle architectures can be found in the literature [Crespi et al, 2017], but not all of them are compatible with the project framework. Indeed, the chosen cycle must fit coal boiler constraints (such as low temperature of the working fluid at the boiler inlet, low pressure drops for high flow rate, good heat integration for a high boiler efficiency...), be efficient and suitable for flexible operation loads.

Based on the knowledge given by previous simulation experiences [Le Moulec, 2013; Mecheri & Le Moulec, 2016] and literature review [Angelino, 1968; Crespi, 2017], we pre-selected 21 cycle configurations among the more than 40 possible ones. These configurations can be divided in 6 families of cycles (6 base form) with additional options. The list of these 21 cycles and the simplified process flow diagram of studied architectures' families are given in the following Table 1 and Figures 1 to 6.

Table 1: List of the 21 pre-selected configurations

FAMILY	ADDITIONAL OPTION	CYCLE NUMBER
1 - Recompression cycle	-	11
	One reheat	12
	Double reheat	13
	One intercooling	14
	Intercooling + reheat	15
	HTR bypass	16
2 - Partial cooling cycle	-	21
	One reheat	22
	Double reheat	23
	HTR bypass	24
3 - Pre-compression cycle	-	31
	One reheat	32
	Double reheat	33
	HTR bypass	34
4 - Turbine split-flow cycle	-	41
	One reheat	42
	LTR bypass	43
5 - Preheating cycle	-	51
	One reheat	52
	Double reheat	53
6 - Split-expansion cycle	-	61

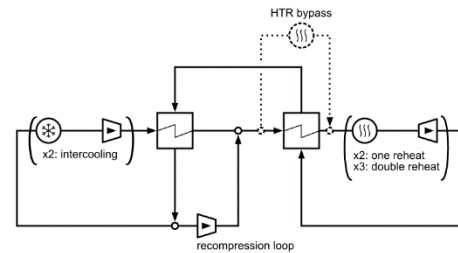


Figure 1: Recompression cycles Family

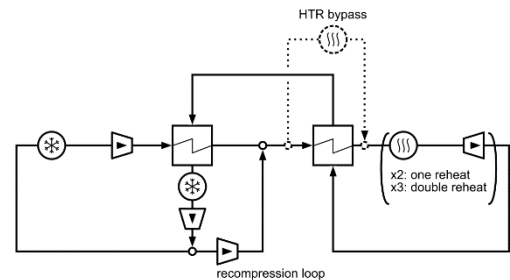


Figure 2: Partial cooling cycles Family

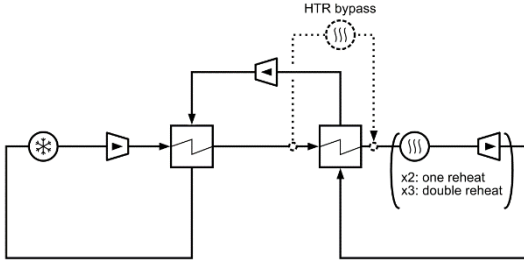


Figure 3: Pre-compression cycles Family

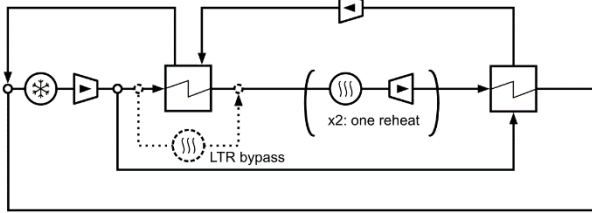


Figure 4: Turbine split flow cycles Family

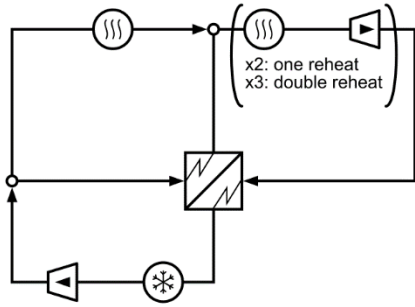


Figure 5: Preheating cycles Family

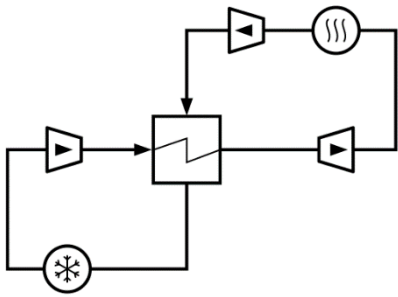


Figure 6: Split expansion cycle Family

To help us in the choice of several configurations, we decided to implement a sensitivity analysis on our selection of 21 cycle configurations. The $s\text{CO}_2$ Brayton cycle is very sensitive to many parameters [Dostal, 2004; Mecheri & Le Moullec, 2016]. In our study, the pressure drops, the maximum temperature/pressure and the cooling temperature impacts on the cycle performance (cycle net efficiency) were assessed regarding the setting displayed in the Table 2. These parameters and the new values were chosen after a first interview of experts.

Table 2 : Modified parameters for sensitivity analysis

MODIFIED PARAMETER	NEW VALUES
Heat exchanger and boiler pressure drops	HEx pressure drops = 0.1% of inlet pressure Boiler pressure drops = 0.1 MPa
Heat exchanger and boiler pressure drops	HEx pressure drops = 1% of inlet pressure Boiler pressure drops = 0.5 MPa
Boiler outlet maximal temperature	550°C (with compressor outlet pressure = 20 MPa)
Boiler outlet maximal temperature	700°C (with compressor outlet pressure = 30 MPa)
CO ₂ minimal temperature (cooling temperature)	30°C
CO ₂ minimal temperature (cooling temperature)	34°C

Once our 21 cycle configurations were known and the parameters of the sensitivity analysis determined with the help of the experts, we were able to carry out the modelling work for each of the configurations and their respective sensitivity analyses. We used the process modelling software AspenPlus® with RefProp (NIST) thermodynamic database to obtain the design point of each cycle architecture is based on a sensitivity analysis. This screening method enables to assess the best cycle performances (given the fixed constraints) but also to obtain the global heat and mass balance table which is important for the components' pre-design and design steps. The process simulation of cycle architectures is done regarding several assumptions and fixed parameters as defined below.

Table 3: Assumptions on fixed parameters

PARAMETER	UNIT	VALUE
Net cycle production	MWe	25
CO ₂ temperature at the heat sink outlet (MSCUSXXT2)	°C	33
Maximum CO ₂ temperature at the heater outlet (MSHSOXXT2)	°C	620
Maximum CO ₂ pressure at the main compressor outlet (MSCOMXXP2)	MPa	25.0
Compressors isentropic efficiency	%	80
Turbine isentropic efficiency	%	90
Pressure drops in the heater (MSHSOXX)	MPa	No reheat: 0.25
		One reheat: 0.2 + 0.1
		Two reheats: 0.2+0.1+0.1

		HTR/LTR bypass : 0.1+0.2
Pressure drops in the recuperators (MSRCUXX)	% of inlet pressure	0.5
Pressure drops in the heat sink heat exchanger (MSCUSXX)	% of inlet pressure	0.5
Maximum number of intercooling	1	
Auxiliary consumption	MWe	-
Boiler maximal efficiency	%	94
CO ₂ purity	%	100

RESULTS OF MODELLING AND SENSITIVITY ANALYSES

After modelling each of the 21 cycle configurations and performing the associated sensitivity analyses, we observed the impact of each of the parameters studied and established a list of 6 cycles configurations as offering the best compromise between performance and flexibility at the end of the first stage of our study. The conclusions associated with the effects of the parameters, as well as the 6 selected cycles, are presented below.

The first general conclusions concerning all studied architectures are:

- Effect of reheating: the reheating process consists in dividing the expansion step of the process and to send back the sCO₂ in the boiler to heat it again before finishing the expansion step. As a general statement, the CO₂ mass flow is reduced when the cycle efficiency increases at fixed electricity power production. In our study constraints, the electricity power production is fixed to be 25 MW_e: thus, the CO₂ mass flow decreases with the application of reheating process.
- Effect of intercooling: The intercooling consists in dividing the compression stage in two (or several) parts between which the CO₂ is cooled before finishing the compression stage. Intercooling enables to slightly increase the cycle efficiency (and thus the CO₂ mass flow rate at fixed electricity production) while ensuring at slightly lower CO₂ temperature at the boiler inlet.
- Effect of bypassing the recuperator: The high (or low) temperature recuperator bypass consists in extracting a fraction of the main CO₂ mass flow at the H (or L) TR inlet. This modification has a minor impact on the cycle performance and enables to reduce the minimal CO₂ temperature at the boiler inlet.

The main sensitivity analysis results are:

- As expected, the cycle pressure drops, and the boiler outlet temperature have high impact on the cycle efficiency. Cooling temperature and main compressor outlet pressure have lower impact of the cycle performance.
- As the electrical power production is fixed (25MW_e), better efficiency implies a lower CO₂ mass flow. Indeed, the efficiency improvement is mainly due to the amount of “recovered heat” in the recuperators, especially in the HTR. The cycle temperature balance is also impact by the pressure drops. Also, the “minimal boiler inlet temperature” is indeed impacted by the boiler outlet temperature: for a given cycle, higher boiler outlet temperature leads to higher turbine outlet temperature, thus, a higher “heat recovery” in the HTR and finally, a higher boiler inlet temperature.
- Cooling temperature variation study shows that the cycle performance will be affected by variability on the cooling temperature (flexibility).

Figure 7 illustrates the net cycle efficiency (in %) sensitivity with variation of the main compressor outlet pressure (MSCOM01P2 in MPa) for 3 different boiler outlet temperatures (MSHSOT2 in °C) for the cycle 11. It can be observed that, as predicted in [Dostal, 2004], the maximum cycle temperature has a stronger impact on the cycle next efficiency that the main compressor outlet pressure, which means that efforts to improve the net cycle efficiency must be concentrated to solve “high CO₂ temperature related issues” more than “high pressure related issues”. Of course, this conclusion is drawn regarding only the net cycle efficiency and should be balanced by considering other aspects (economic, flexibility...).

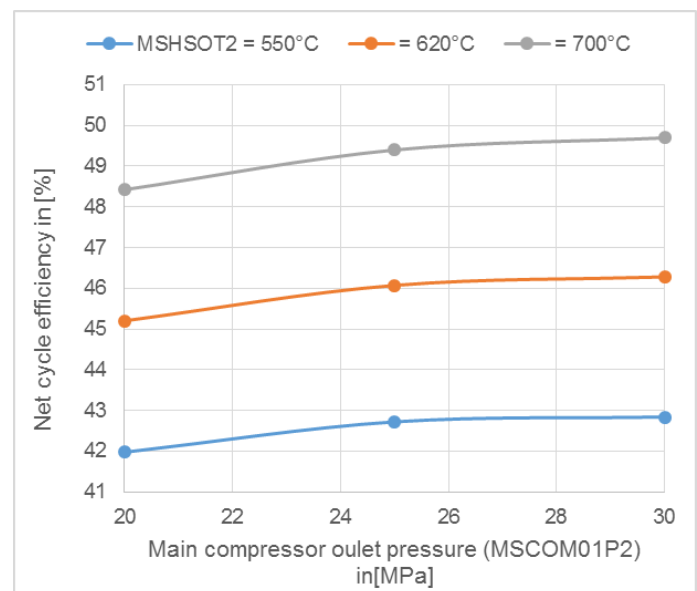


Figure 7: Cycle 11 (figure 1) net cycle efficiency (in %) as a function of the main compressor outlet pressure

(MSCOM01P2 in MPa) for 3 different boiler outlet temperatures (MSHSOT2 in °C).

FIRST SELECTED CONFIGURATIONS

Three families of configurations have performances that are too low compared to our initial requirements (efficiency around 40%, which is equivalent to the average efficiency of current power plants). These families are as follows:

- Preheating cycles,
- Turbine split-flow cycles,
- Split-expansion cycle.

Despite their unattractive performance, we presented these cycle configurations to various experts, who confirmed our choice to eliminate them for the rest of the process, noting also the possible difficulty of managing supercritical CO₂ during cycle operation, due to the different splits or by-passes of these configurations.

We have therefore selected from the three families of remaining configurations, the best cycles in terms of efficiency and technical constraints on the various components (for example, the boiler, an essential element for flexibility, cannot withstand a low temperature that is too high because the cycle could not withstand too many cold restarts).

The following table summarizes the 6 selected cycle configurations and the main associated technical characteristics.

Cycle number	Recompression cycles			Partial cooling cycles	Precompression cycles		
	11	12	13		23	31	32
Cycle net eff. (%)	46.08	48.38	48.97	42.77	42.99	45.22	45.72
Rejected Heat at the cooler (MWth)	28.54	26.37	26.02	33.50	32.38	29.94	29.54
Min boiler inlet temp. (°C)	439.3	514.6	541.2	467.7	453.9	528.0	555.4
Boiler eff. (%)	88,5	84,3	82,9	86,9	87,7	83,6	82,1
Total CO ₂ mass flow (kg/s)	239.5	221.6	217.6	200.1	279.4	264.4	260.6

ANALYSIS OF CURRENT AND FUTURE FLEXIBILITY CONSTRAINTS

After identifying 6 relevant cycles for the rest of our study, we focused on understanding current and future needs in terms of flexibility from the perspective of the fossil power plant operator. To this end, we have conducted interviews with experts, bibliographies of future regulations and simulations of future operating reports based on scenarios involving more renewable energies and therefore more restrictive for thermal power plant

operators in terms of load variations and number of start/stop times.

Load scenario for 2030 (50% of renewable energy):

The EU Reference Scenario is one of the European Commission's key analysis tools in the areas of energy, transport and climate action. It allows policy-makers to analyse the long-term economic, energy, climate and transport outlook based on the current policy framework. It is not designed as a forecast of what is likely to happen in the future, but it provides a benchmark against which new policy proposals can be assessed. National experts from all EU countries actively participate in its preparation.

The reference scenario is in phase with the European energy and environmental targets:

- 50% of renewable energy in the electricity mix (of which 27% is wind power),
- + 27% of energy performance.

Based on the EU 2016 reference scenario – energy trend for 2030 (EU REF 2016 - 2030), the European electricity mix has been estimated for 20 European countries in 2030. According to this estimation, 11 countries will still have coal-power plant production in 2030: Austria, Czech Republic, Finland, Germany, Hungary, Ireland, Italy, Netherland, Poland, Slovakia and Spain.

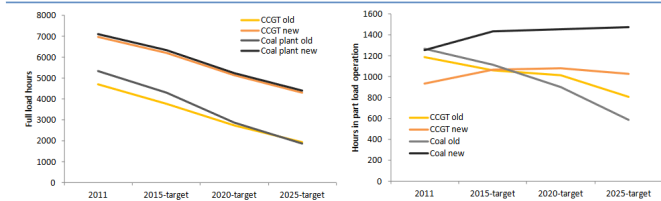
Next table summarizes the main figures about coal-power plant production estimation.

Table 4: EU coal fleet figures based on 2030 scenario

COUNTRY	NUMBER OF UNIT (COAL)	NUMBER OF START-UPS PER UNIT PER YEAR (AVERAGE)
Germany	20	25
Czech Rep.	18	19
Poland	13	27
Italy	6	26
Netherland	4	36
Finland	3	36
Austria	2	32
Spain	2	56
Ireland	2	57
Hungary	1	67
Slovakia	1	82

To identify the partial load operating share, we used public scenarios as well as prospective scenarios from network operators.

The following figure shows the evolution of the number of starts and part-load operation.



Source: IEA analysis.

Figure 8: Annual full load hours (left) and part-load operation time (right) for benchmark power plants under increasing RES shares (source: IEA analysis, 2014) (cf Annex)

The figure clearly shows that the main impact will be that both old and new fossil plants will reduce their full load operation in the future; in terms of part load, while old plants will again reduce their operation as they will not be able to compete due to low efficiencies, new ones with better flexibility performances will still be able to participate to the market increasing their part load operation, the price to pay being an increased number of startup/stops.

For sCO₂-Flex purposes, a single unit yearly operation profile is chosen, to be used as a reference for the simulations aiming at assessing the cycle’s capability to cope with future grid needs as well as the relevant efficiency figures (see Figure 8):

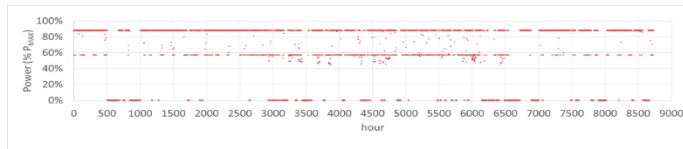


Figure 9: 2030 Reference Plant operation (cf Annex)

The chart is normalized on maximum power (P_{MAX}); the plant is supposed to participate to grid regulation, therefore a 12% power bandwidth is dedicated to such operation on both top and bottom ends of the operational power range: therefore the actual power never exceeds 88% P_{MAX} and seldom drops below 57% (minimum power being set at 45% P_{MAX}).

Such Reference Plant undergoes around 70 start-stop cycles, mostly hot and warm ones, meaning that the stops mainly last less than 48 hours.

Flexibility constraints

For this part of our study, the French Q600 power stations have been used as the reference for what has been defined as “most commonly used coal plants”; this may not be totally fair in terms of representativeness (average figures would probably be a better choice), nevertheless it allows to describe a real plant and to provide real and more coherent figures, resulting in more meaningful information.

The Q600 main parameters describing their capabilities in terms of flexibility (as it has been defined in the previous paragraphs) are listed in the table below:

Table 4: Q600 flexibility performances

PARAMETER	VALUE
Net continuous power output:	580 MW
Minimum continuous load:	280 MW
Load variation ramp:	+5 / -7 MW/min (+8% / -12% PNet)
Start-up time:	Cold start-up: 13h Warm start-up: 9h Hot start-up: 4.5h
Minimum up time after start-up:	8h
Primary Reserve power:	+ 40 MW @max power + 20 / -12 MW @min power
Secondary Reserve power:	± 60 MW @max power ± 20 MW @min power

In addition to the already mentioned minimum load, load ramp and start-up time, a few further parameters in Table 4 allow to have a better picture relevant to Q600 operational constraints:

- The minimum required time between two consecutive events of connection and disconnection from the grid (which results from the need to assure a proper sweeping of the combustion chamber and of the air preheaters);
- The allowances for primary and secondary regulation, which must be kept available for grid balancing (and which are paid for accordingly by the TSO).

For our question, load variation ramps and stop/start times are the important points that will allow us to determine if a supercritical CO₂ cycle can be more flexible than a conventional cycle. We have therefore tried to understand which elements of the cycle (component, operation,...) have an influence on these points.

In a conventional cycle, the start-up description is relevant to cold conditions; depending on the down time, some elements like the feed-water tank and the boiler have to be re-filled or not. All the heat exchangers (preheaters, superheaters and reheaters) are isolated and the turbine is under vacuum.

The first step is to restart the plant cooling loop, then to be sure of the water level inside the feed-water tank, needed to compensate for the water losses linked to the activation of the extraction pumps. The condenser is then put under vacuum and water circulates in the loop in order to be properly de-aerated, before starting to heat up. The boiler as well is filled with water, and some constraints must be taken into account during the heating process, in order to limit thermal stresses on the materials and components. In this phase the heat source is the auxiliary steam which comes either from an auxiliary boiler or from other sources available on site.

Before firing the boiler, some time is needed to rinse the inside of the tubes and sweep the outside (air side), in order to get rid of any particle which could have been left from the previous shut down; after that the burners are put in operation

and the boiler is fired; at first with auxiliary oil burners, then progressively by means of pulverized coal. The system is heated up again with some temperature rate constraints, while the turbine is being bypassed; the electric feed pumps are replaced by turbo pumps and the de-nitrification systems is activated.

When the proper steam grade is reached, the turbine inlet valve is opened and the turbine is progressively accelerated and heated.

The acceleration process consists in a sequence of speed increase at specific rates followed by short periods at constant speed in order to evenly heat up all the turbine elements and to eliminate all possible eccentricity issues. Furthermore, specific constraints on the temperature difference between steam and turbine organs are there, in order to avoid uneven thermal expansions, resulting in material stresses (or even in contacts between the rotor and the stator) as well as steam condensation on metal surfaces, generating water droplets which can be a cause of mechanical stress on the blades.

Once the turbine speed is stable at 3000 rpm and all the relevant parameters are ok, the alternator can be coupled with the grid, applying from the beginning some tenths of megawatts (normally 40) to avoid that any power flashback causes a grid disconnection.

In conclusion, both boiler and turbine of current coal power plants require time-consuming procedures during start-up in order to limit stress on these components (which could impact their residual lifetime). Considering the new sCO₂ cycle, which is the purpose of this project, some hypotheses can be made at general level, which will be further analysed in the future deliverables once the cycle architecture and the equipment are designed:

- sCO₂ boiler: most of the current coal-boiler constraints are expected to be still with new sCO₂ Boiler technologies, the only difference being the working fluid (the combustion should still be the same and the global geometry is not expected to be completely different from current technologies);
- sCO₂ turbine: it is expected to be much more compact than current steam turbines, therefore, problems related to thermal expansion will be different: the reduced dimensions of the equipment are likely to limit the differential expansion, but at the same time they cause an increased impact of leakage losses on turbine efficiency, which may lead to a reduced “rotor-stator” spacing, resulting in stricter tolerances in terms of differential expansion.

FINAL SELECTION OF CYCLES

On the basis of cycle modelling and our analysis of flexibility requirements, we therefore presented the 6 cycle configurations to experts in boilers, turbomachines, heat exchangers and thermal cycle operation to ask them to identify the 2 most relevant cycles to keep for the rest of the work of the sCO₂-Flex project. Their conclusions are as follows:

Constraints related to the project sCO₂-Flex objectives

- Performance

Regarding the performance constraint, the selection turns towards the most efficient cycles (family 1: recompression cycles). Cycle efficiency highly depends on its regenerative rate: highly regenerative cycles allow for high amount of recovered heat in the recuperators, thus requiring less heat input in the boiler for the same power output, leading to a cycle efficiency increase. A direct consequence is that high efficiency cycles have high CO₂ temperature at the boiler inlet (all other parameters being fixed).

Cycle 13 offers the best expected cycle performances. However, a double reheat cycle is more complex and challenging for the turbomachines; furthermore, CO₂ temperature at the boiler inlet is about 540°C, which is higher than 470°C and not recommended for boiler integrity.

- Flexibility and the control of the cycle

Complex and multipart cycle architectures can be difficult to control and regulate. From this point of view, the most flexible solution would probably have a simple cycle architecture (small number of recirculation loops or components are easier to control and regulate). However, as explained above, the cycle efficiency highly depends on its architecture (for example: recompression loop is highly recommended to have high cycle performances but it brings additional complexity). A compromise must be found between the cycle performance and the layout simplicity for better flexibility.

Constraints related to the main components

- Boiler

Coal boiler integrity depends on the cooling capacity of the working fluid (CO₂ in our case) to protect the boiler tubes and wall surfaces. The CO₂ temperature in the boiler must be securely and accurately controlled to ensure material protection.

Due to the corrosion problems of the materials, the fact that the heat exchange surfaces may be larger than for a steam boiler, as well as the fact that the temperature management of the sCO₂ will not be done in the same way as for a conventional boiler, we have decided to designate a new boiler model, in order to choose the most suitable materials to resist corrosion, put in place the necessary strategies to control the CO₂ temperature and integrate as much as possible the pollution control equipment

Our objective will then be to have a new boiler design with similar (or lower) cost and footprint than a conventional boiler.

- Turbomachinery

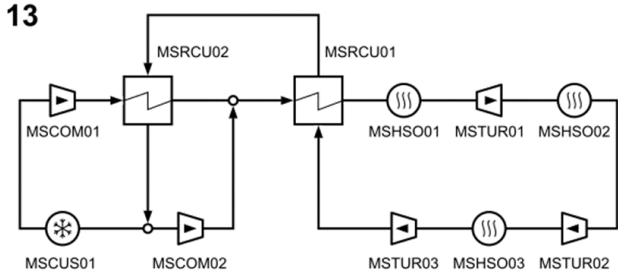
Concerning the turbomachines, two main aspects can be considered: i) the performance of each turbomachine (isentropic efficiency) and ii) the mechanical issues related to manufacturing process and the regulation/control at part load.

Depending on the cycle architecture, the design of the turbomachines changes (size, rotation speed, number of stages...). In this context changing the cycle architecture involve turbomachine efficiency and geometry variations at fixed power output. Thus, some architecture “families” are more interesting than others from the turbomachines point of view.

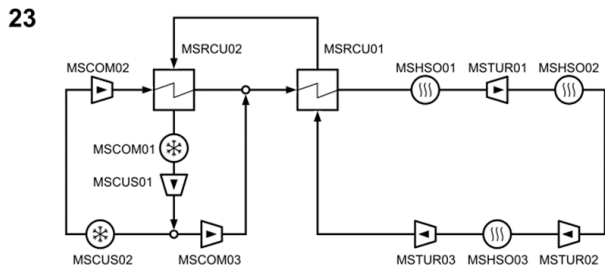
From the mechanical and manufacturing point of view, the most suitable group of cycle configuration is the “family” n°3, followed by the number n°2 and finally, the n°1 which represent complex turbomachines due to CO₂ temperature, pressure and flow rate conditions. It can be observed that this ranking is not favourable for the performance of the cycle. Here also, a compromise must be found between these two constraints

Finally, regarding all specified criteria, the 3 selected cycles for the next step of sCO₂-Flex project are the following:

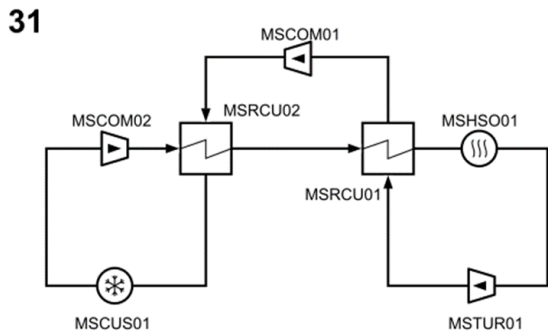
- Cycle 13 for cycle performance



- Cycle 23 for both boiler integrity and turbomachines (good turbomachine performances).



- Cycle 31 for simplicity, turbomachines and boiler integrity.



CONCLUSION

Our main objective for this study was to find several configurations of supercritical CO₂ cycles that would offer a compromise between performance and flexibility. One of our

main difficulties was to succeed in breaking free from the habits associated with conventional steam and water cycles. To do this, we first identified and modelled 21 cycle configurations, based on the scientific literature and our first work on supercritical CO₂ cycles. From the results of this step, we sought to determine what would be the main constraints related to flexibility with this type of cycle (constraints different from those known for water/steam cycles). We conducted a sensitivity analysis on the main influential parameters to determine their real impact. Then, based on several scenarios anticipating a strong increase in renewable energies in the European landscape (50% of electricity production), we established new annual reports on the operation of thermal power plants in order to establish hypotheses on load variations and the number of power plant shutdowns and start-ups.

Once all the results and assumptions were available, we were able to choose 3 interesting configurations for our project with operating and component experts.

During the rest of our project, we will work to optimize the most interesting configuration for both flexibility and performance. The selection among the 3 configurations will be made according to the developments of the turbomachines, exchangers, boiler as well as the optimization of the control-command.

NOMENCLATURE

HEX: Heat Exchanger
HTR: High temperature recuperator
LTR: Low temperature recuperator
MSCUSXX: Heat sinks of the cycle n°XX
MSHSOXX: Heat sources (heaters) of the cycle n°XX
MSCOMXX: Compressor of the cycle n°XX
MSTURXX: Turbine of the cycle n°XX
MSRCUXX: Recuperator of the cycle n°XX
TSO: Transmission System Operator
PR: Primary Regulation
SR: Secondary Regulation

ACKNOWLEDGEMENTS

This project has received funding from the European Union’s Horizon 2020 research and innovation programme under grant agreement N° 764690.

REFERENCES

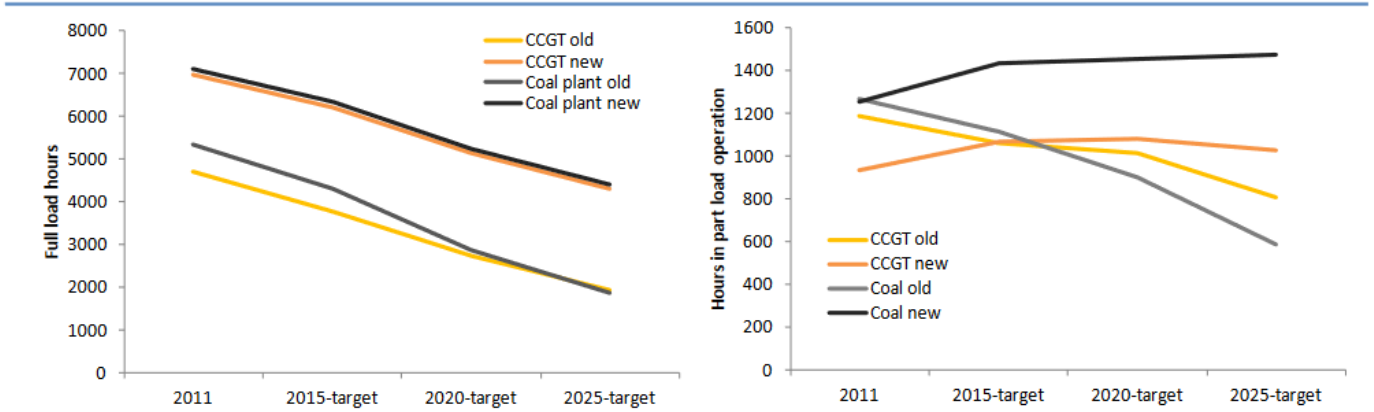
- [Angelino, 1968] Angelino G. Carbon dioxide condensation cycles for power production. *J Eng Gas Turb Power* 1968; 89(2): 229-237.
- [Crespi et al, 2017] Crespi F., Gavagnin G., Sanchez D., Martinez S.M. Supercritical carbon dioxide cycles for power generation: A review; *Applied Energy* 195 (2017) 152–183
- [Dostal, 2004] Dostal V. A supercritical carbon dioxide cycle for next generation nuclear reactors [Ph.D. thesis]. Department of Nuclear Engineering, Massachusetts Institute of Technology (MIT); 2004.

[Le Moullec, 2013] Le Moullec Y. Conceptual study of a high efficiency coal-fired power plant with CO₂ capture using a supercritical CO₂ Brayton cycle. *Energy* 2013; 49: 32-46.

[Mecheri & Le Moullec, 2016] Mecheri M., Le Moullec Y. Supercritical CO₂ Brayton cycles for coal-fired power plants; *Energy* 103 (2016) 758-771

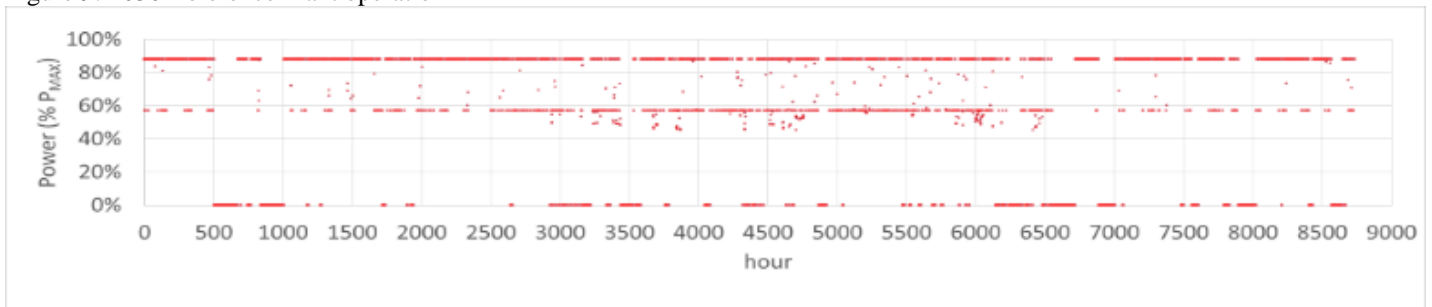
ANNEX

Figure 8: Annual full load hours (left) and part-load operation time (right) for benchmark power plants under increasing RES shares (source: IEA analysis, 2014)



Source: IEA analysis.

Figure 9: 2030 Reference Plant operation



**MODELLING AND PERFORMANCE ANALYSIS OF A SUPERCRITICAL CO₂
SYSTEM FOR HIGH TEMPERATURE INDUSTRIAL HEAT TO POWER
CONVERSION AT OFF-DESIGN CONDITIONS**

Matteo Marchionni
Brunel University London
Uxbridge, United Kingdom

Samira S. Saravi
Brunel University London
Uxbridge, United Kingdom

Giuseppe Bianchi *
Brunel University London
Uxbridge, United Kingdom
Email: giuseppe.bianchi@brunel.ac.uk

Savvas A. Tassou
Brunel University London
Uxbridge, United Kingdom

ABSTRACT

Industrial processes are currently characterized by thermal energy losses through high temperature exhausts or effluents (above 300°C) that, on a global scale, account for nearly 11.4% of their primary energy consumption, namely 12.1 EJ. For these high temperature exhausts, conventional waste heat to power conversion systems based on bottoming thermodynamic cycles are not very suitable since most of the state of the art working fluids are not able to perform safely and efficiently at high temperatures. Supercritical Carbon Dioxide (sCO₂) power systems allow to overcome these limitations because of the chemical and thermo-physical properties of the working fluid.

In order to provide insights on the behavior of sCO₂ systems, this paper presents the development of a one-dimensional numerical model of a low capacity (50 kW_e) simple regenerated system for medium to high temperature waste heat recovery applications. The unit is equipped with single-shaft radial turbomachinery and different heat exchanger technologies such as micro-tube, printed circuit, plate, etc. Flue gas and water are used as heat source and sink respectively. At nominal conditions, i.e. for a flue gas mass flow rate of 1.0 kg/s at 650°C, the unit operates at a cycle pressure ratio of 1.7, generating 50 kW_e with a thermal efficiency of 20%. The paper first discusses the modelling methodology, including turbomachinery and heat exchanger models implementation, and then assesses the steady-state performance of the unit at design and off-design operating conditions. From the simulations carried out operating maps of the unit have been obtained to form the baseline for the setting up of control strategies for the sCO₂ system. The results show that the system can generate up to 75 kW_e for a heat source mass flow rate of 1.2 kg/s and heat source temperature of 700°C.

INTRODUCTION

The increasing energy demand and the environmental concerns posed by the extensive use of fossil fuel, have steered research interest towards more sustainable power generation. In this context, a major challenge is the significant amount of thermal energy losses occurring in industrial processes. Indeed, on global scale, almost 30% of the primary energy consumption is rejected, through exhausts or effluents, into the environment [1]. To efficiently recover and re-use this thermal energy, heat to power conversion systems based on bottoming thermodynamic cycles represent one of the most promising technologies. Unlike those applications rejecting heat at low temperatures which benefit from commercially available solutions like the Organic Rankine Cycle (ORC) systems [2], the exploitation of exhausts and effluents at temperatures higher than 300°C still represents a technical challenge.

A promising technology for such applications is the Joule-Brayton cycle, using supercritical CO₂ (sCO₂) as working fluid, which allows to achieve higher efficiencies than ORCs due to the advantageous thermo-physical properties of the CO₂ near the critical point [3,4]. Many works are available in the literature on sCO₂ heat to power conversion systems. Theoretical investigations have been presented in references [5–8] to assess how different cycle architectures could improve system performance and economic figures. Numerical and experimental studies have also been performed on individual unit components such as heat exchangers, turbomachines and auxiliaries to overcome the technical challenges arising when CO₂ is used as a working fluid.

Kwon et al. [9] and Fu et al. [10] presented different numerical models of Printed Circuit Heat Exchangers (PCHES) to predict their off-design behavior when used as gas cooler or recuperator in sCO₂ Brayton power cycles, while Bae et al. [11]

proposed a new set of heat transfer and pressure drop correlations for these heat exchangers.

Several studies have also been carried out on $s\text{CO}_2$ turbomachinery. Various design methodologies have been developed for turbines [12,13], compressors [14–17] and auxiliaries such as bearings and seals [18,19], which in $s\text{CO}_2$ applications are of paramount importance to prevent leakage and to guarantee lubrication at high pressures and revolution speeds. Several computational models have also been implemented to predict their off-design performance [20–22], but few experimental analyses can be found. Experimental compressor and turbine performance maps have been presented only by Wright et al. [23], while experimental investigations of centrifugal compressors close to the CO_2 critical point have been reported by Utamura et al. [24] and Fuller and Eisemann [25].

Despite the intensive research from a purely theoretical point of view and from a component wise perspective, few works are available on the overall performance of small-scale power units (50–100 kW_e), particularly at off design conditions.

Lambruschini et al. [26] developed a model in Matlab Simulink of a 10 MW_e recompression Brayton cycle for power generation applications. Performance maps were used to predict the behaviour of turbomachines, while simple models (i.e. fixed heat transfer coefficient) were considered for the heat exchangers. Even though the dynamics of the system were investigated, more complex models are needed for heat exchangers in order to accurately predict the behaviour of the unit also in operating conditions far from the design point. A more detailed model developed in Dymola has been proposed by Zhang et al. in [27]. Performance maps were used to model the turbomachines while for the heat exchangers a finite volume approach was adopted. In particular, the local heat transfer coefficient for different operating conditions of the heat exchangers was predicted using heat transfer correlations. However, the heat exchanger models did not take into account the different heat exchanger technologies employed. Similarly, Luu et al. in [28] developed a model of a high capacity $s\text{CO}_2$ recompression cycle system for Concentrated Solar Power applications. Also in this work, the same approach has been used to model all the system heat exchangers, independently from the technology used.

The models reported in the literature not only refer to high capacity power units but also to layouts and component technologies that are specific to solar or nuclear power applications. In system models, heat exchangers are modelled independently from their typology and their specific geometrical and technological features. These assumptions may affect the validity of the overall performance predictions.

To fill the gap in the literature, in this work a more detailed model of a low capacity $s\text{CO}_2$ heat to power conversion system has been developed. The $s\text{CO}_2$ unit has been designed for Waste Heat Recovery (WHR) applications and therefore considers a simple regenerated layout due to its lower complexity and investment cost. The model implements performance maps for the turbomachines while each different heat exchanger is modelled considering its geometrical features and using

manufacturer’s data for calibration. The system performance has been investigated at design and off-design conditions. Amongst the main outputs, are performance maps for the whole system which can be used for control design purposes.

MODELLING METHODOLOGY

The model presented in this work refers to a 50 kW_e $s\text{CO}_2$ simple regenerated Brayton cycle unit for medium to high thermal grade WHR applications under construction at Brunel University London [29]. The facility employs flue gases as heat source and water as heat sink, either if other cooling sources can be used (i.e. air coolers). Both compressor and turbine are centrifugal machines, while plate, printed circuit and micro-tube heat exchangers are considered for the gas cooler, the recuperator and the primary heater respectively.

The model of the system has been developed in the commercial software platform GT-SUITE™. Figure 1 shows the model block diagram, where the uppercase captions point to the sub-models of each component, while the lowercase ones refer to the boundary and initial conditions of the model.

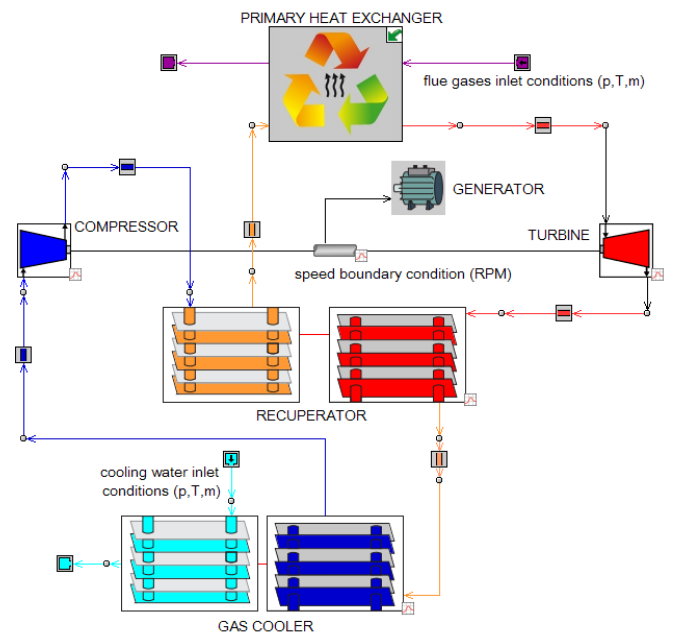


Figure 1: $s\text{CO}_2$ system model developed in GT-SUITE™.

The heat exchangers are modelled following a one-dimensional approach. According to their geometrical features, the hot and cold sides of the heat exchangers are approximated as one-dimensional (1-D) channels with an equivalent length and cross-sectional area. Both sides are therefore interconnected through convective connections to a thermal mass, which accounts for the thermal inertia of the heat exchanger and considers its real material properties. To account of the thermo-fluid property change, the channels and the thermal mass are discretized along the flow direction in a certain number of sub-volumes. Consequently, following the so called ‘staggered grid approach’ [30], the 1-D Navier-Stokes equations are numerically

solved to calculate the mass flow rates, pressures and total enthalpies of the hot and cold flows at the boundaries of the channels' sub-volumes. The other thermodynamic scalar quantities are computed through a dynamic-link library of the NIST Refprop database [31] and assumed constant in the whole sub-volume domain.

In order to solve the energy equation, the computation of the local heat transfer coefficients between the heat exchanger walls and the cold and hot channels respectively is required. For the refrigerant side (sCO₂ flow), the Gnielinski heat transfer correlation is employed [32] and calibrated against performance data provided by the manufacturers. For the non-refrigerant one (i.e. water or air), these data are used to calculate the best fitting coefficients of the Nusselt-Reynolds (Nu-Re) correlations for the equivalent 1-D networks. These correlations are then adopted to calculate the heat transfer coefficients [33].

Manufacturer data provide performance characteristics for different flow rates of the two working fluids to span a wide range of Reynolds numbers. This allows the prediction of the heat exchanger performance at off-design conditions. The pressure drops across the heat exchanger are computed using a modified version of the Colebrook equation [34]. A more detailed description of the modelling methodology can be found in [35,36].

The same modelling approach has been employed for the pipes connecting the different components, with the only difference that thermal losses are neglected. The inertia due to the mechanical shaft connecting the turbomachines and that of the generator are taken into account. Parasitic losses of the system ancillaries, such as the water cooling pump and the compressors required to extract the leakage flows from the generator cavity, have not been considered for the calculation of the system performance.

INTEGRATION OF TURBOMACHINERY MAPS

For the modelling of the turbomachines, performance maps have been used, generated by using three-dimensional Computational Fluid Dynamic (CFD) models. The compressor and turbine impeller geometries selected during the design stage are similar to the ones tested at the Sandia sCO₂ compression loop facility [23]. The number of vanes are equal (6+6, as shown in Figure 2) but the blade shape has been modified and the wheels dimensions scaled to achieve a higher efficiency. A wheel diameter of 57.12 mm has been selected for the turbine and 44.03 mm for the compressor. For the design and model of the turbomachines, different packages in ANSYS have been used (i.e. CCD, RTD and BladeGen).

To perform validation of the model, simulations have been carried out assuming the initial thermodynamic conditions of the CO₂ to be in the supercritical region. The inlet temperature has been set equal to 32.5°C, the inlet pressure 78.7 bar, and the design shaft speed has been set at 55,000 RPM. Compressor inlet operating conditions were determined to avoid the formation of liquid where the flow is accelerated locally.

ANSYS CFX 17.1 was employed to perform single-passage steady state calculations. The wheel's mesh has been generated

in ANSYS-TurboGrid, shown in Figure 2, together with the flow path of the compressor. An Automatic Topology and Meshing feature (ATM optimized) has been employed inside the impeller, with a mesh of approximately 10⁺⁶ nodes (Figure 2). The k-ε and total energy models have been used to take into account the flow turbulence and its compressibility, with total pressure and total temperature defined as inlet boundary conditions and the flow direction considered normal to the boundary. Outlet average static pressure has been chosen as outlet boundary condition.



Figure 2: ANSYS-TurboGrid Mesh and flow path for Supercritical CO₂ compressor.

To simulate the real gas effect, the Span-Wagner Equation of State model has been used to accurately generate the flow properties [37]. For this purpose, a Real Gas Property (RGP) format table has been created to implement the variable properties in the CFX code. The user-defined table includes CO₂ features such as specific heat ratio and density near the critical point, which fluctuates due to the phase change effect. These features have been created using the NIST Refprop 8.0 fluid property database. The generated property files have been combined with a MATLAB code to create a lookup table as an input of TASCflow RGP in ANSYS CFX 17.1.

Once validated, the model results have been used to obtain the turbomachinery performance data, which have been employed to generate the turbine and compressor performance maps in GT-SUITE™.

Figures 3 and 4 show the compressor operating and efficiency maps respectively. The maps are expressed in reduced data, meaning that the mass flow rate and revolution speed are scaled with the reference pressure and temperature considered to generate the data. Figure 5 and Figure 6 show instead the operating and efficiency maps of the turbine.

Each of these maps has been generated by maintaining constant the inlet thermodynamic conditions of the working fluid (pressure and temperature) and changing the outlet static pressure at different revolution speeds (at least five pressure ratios for each revolution speed are required to ensure an accurate interpolation of the operating curves). Beyond the speed range of the simulated working points, a linear extrapolation method is used to predict the performance of the turbomachines.

A small distortion is noticeable in these maps, which is particularly located in the surge line. This is due to the change in the pressure rise characteristics occurring between higher and lower rotational speeds. The pressure changes inside the

compressor stages for different speeds have been influenced by the supercritical CO₂ characteristics.

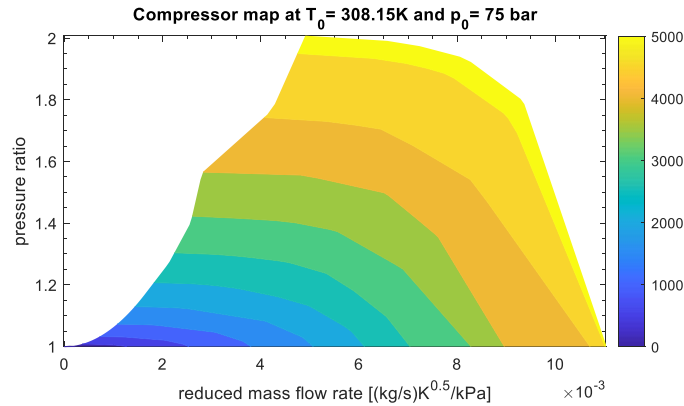


Figure 3: Compressor operating map generated for a reference temperature and pressure of 308.15K and 75 bar respectively (revolution speed expressed in reduced RPM [RPM/K^{0.5}]).

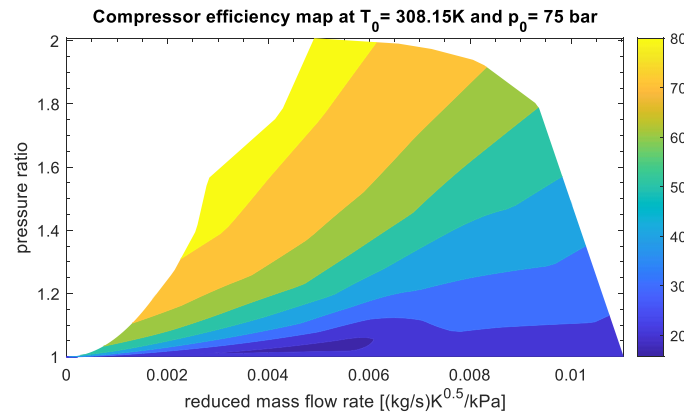


Figure 4: Compressor efficiency map generated for a reference temperature and pressure of 308.15K and 75 bar respectively (efficiency expressed in percentage units [%]).

The operation target for this compressor in the supercritical region approaches the critical point. This condition has positive effect on the choke line. In fact, the real gas properties of the CO₂ lead to a reduction of the choke margin in the compressor stage compared to the one typical of conventional machines using ideal gases [37].

RESULTS AND DISCUSSION

After the model validation stage, a series of simulations have been carried out to assess the steady-state performance of the sCO₂ system. The heat source and heat sink mass flow rates and inlet temperatures have been varied to analyze their effect on the unit, the net power output and thermal efficiency as well as on the temperature of the working fluid at the inlet of the turbine and the compressor, which are of important relevance to the cycle performance [8]. The revolution speed of the turbomachines has been maintained constant and equal to the design point for the whole set of simulations. Tables 1 and 2

summarize the nominal operating conditions of the system at the design point as well as the input and output quantities of the model.

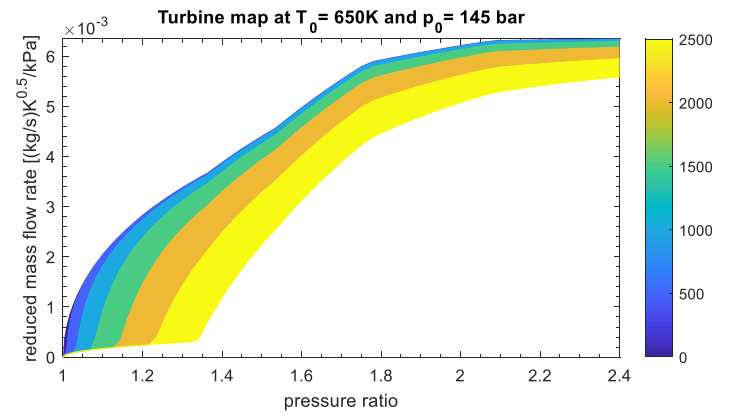


Figure 5: Turbine operating map generated for a reference temperature and pressure of 650K and 145 bar respectively (revolution speed expressed in reduced RPM [RPM/K^{0.5}]).

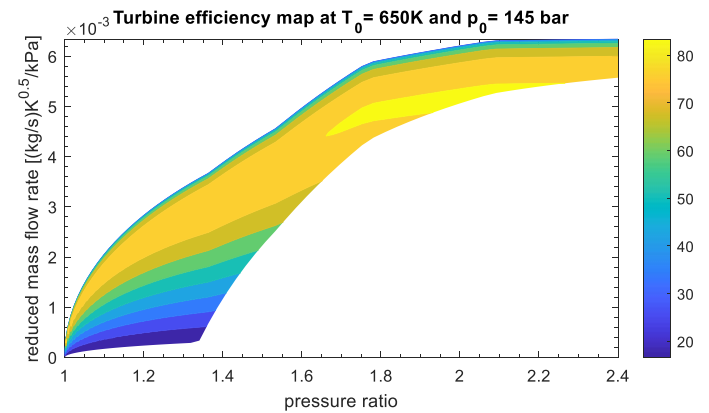


Figure 6: Turbine efficiency map generated for a reference temperature and pressure of 650K and 145 bar respectively (efficiency expressed in percentage units [%]).

Table 1 – Operating conditions of the sCO₂ unit at the design point

Supercritical CO ₂		Design	Model I/O
Mass flow rate	[kg/s]	2.1	Output
Highest pressure	[bar]	128	Output
Lowest pressure	[bar]	75	Output
Heat source: flue gas			
Mass flow rate	[kg/s]	1.0	Input
Inlet temperature	[°C]	650	Input
Inlet pressure	[bar]	1	Input
Cold source: Water			
Mass flow rate	[kg/s]	1.6	Input
Inlet temperature	[°C]	25	Input
Inlet pressure	[bar]	3	Input

Table 2 – Turbomachinery operating conditions at the design point

Compressor			
		Design	Model I/O
Revolution speed	[RPM]	86000	Input
Isentropic efficiency	[%]	75	Output
Inlet temperature	[°C]	36	Output
Turbine			
Revolution speed	[RPM]	86000	Input
Isentropic efficiency	[%]	80	Output
Inlet temperature	[°C]	400	Output
sCO ₂ unit			
Mechanical net power output	[kW]	50	Output
Overall efficiency	[%]	20	Output

Figure 7 shows how the power output of the sCO₂ unit changes following the variations of the heat load, namely the inlet temperature and mass flow rate. In this set of simulations, the inlet conditions of the heat sink have been maintained constant and equal to the design values. The cycle pressure ratio slightly changes depending on the heat load supplied at the heater. In particular, it can be seen that the map gives an indication of the limit conditions of the waste heat source for which the sCO₂ system is not able to generate power. It can be observed that for flue gas mass flow rates lower than 0.8 kg/s, the inlet temperature of the heat exchanger must be higher than 500°C in order to have a not null net power output. For lower temperatures, the compressor requires more power than the one generated by the turbine and consequently the net power output of the system is negative, around -15 kW (Figure 7). This is mainly due to the low design pressure ratio of the cycle, which together with the low divergence of the CO₂ isobaric lines, requires the achievement of high turbine inlet temperatures to reach a positive power output.

For this reason, high exhaust temperatures are needed to achieve high system power outputs. For instance, for a unitary exhaust mass flow rate, considering a flue gas temperature increase from 600°C to 850°C, the unit power output rises from 45 kW to 90 kW. If the same percentage change in the hot source mass flow rate occurs, for example at 650°C, the net outcome varies only from 50 kW to 62 kW.

The increase of the hot source mass flow rate, only leads to a slightly higher working fluid mass flow rate in the circuit to balance the higher thermal load available at the primary heater. Consequently, the thermal efficiency of the system remains almost constant and the power output gain is achieved thanks to the greater mass flow rate of CO₂ processed. On the contrary, a rise of the hot source temperature leads to a higher working fluid temperature at the turbine inlet, with a positive effect on the cycle thermal efficiency.

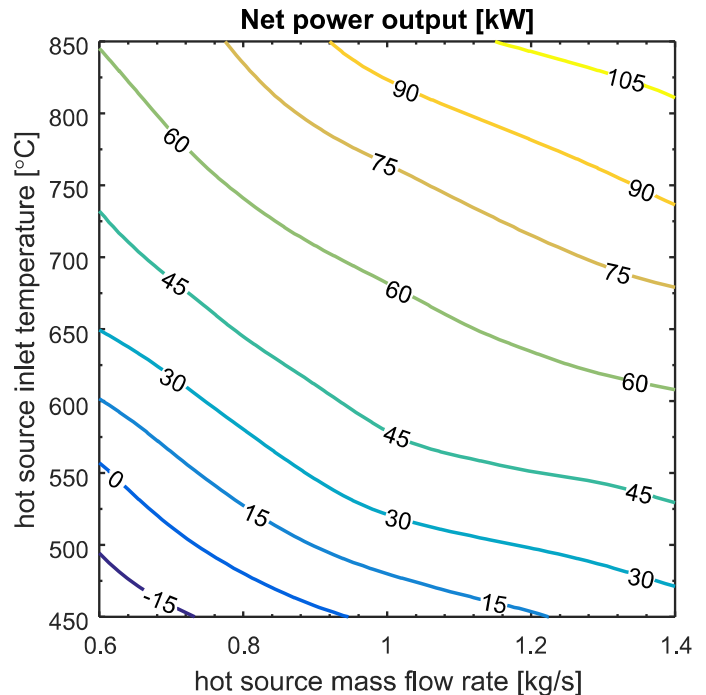


Figure 7: sCO₂ unit net power output as a function of the heat source inlet temperature and mass flow rate

Figure 8 confirms the abovementioned statement, showing a higher sensitivity of the cycle thermal efficiency to the hot source inlet temperature rather than its mass flow rate. In fact, a variation of the latter quantity from 0.8 kg/s to 1.2 kg/s at 650°C, leads to an efficiency rise of almost 12% (from 16% to 18%), against a 52% increase (from 10% to 22%) for the same percentage change of flue gas temperature (considering a 1.0 kg/s mass flow rate). An even higher efficiency (around 30%) can be achieved for an exhaust temperature of 850°C and a mass flow rate of 1.4 kg/s. A further increased efficiency can be obtained by increasing the design cycle pressure ratio, which would lead however to increased investment and operational costs due to higher-end materials and more expensive components, which is not desirable for WHR applications.

The efficiency of the cycle is also strongly influenced by the sCO₂ temperature at the turbine inlet. For the design adopted, the highest system power output and efficiency occur when a temperature at the turbine inlet of 650°C is reached (Figure 9), and are equal to 105 kW (Figure 7) and 30% (Figure 8) respectively.

For turbine inlet temperature lower than 275°C, occurring for a hot source mass flow rate and inlet temperature lower than 0.9 kg/s and 550°C respectively (Figure 9), the system is not able to generate net power output (Figure 7).

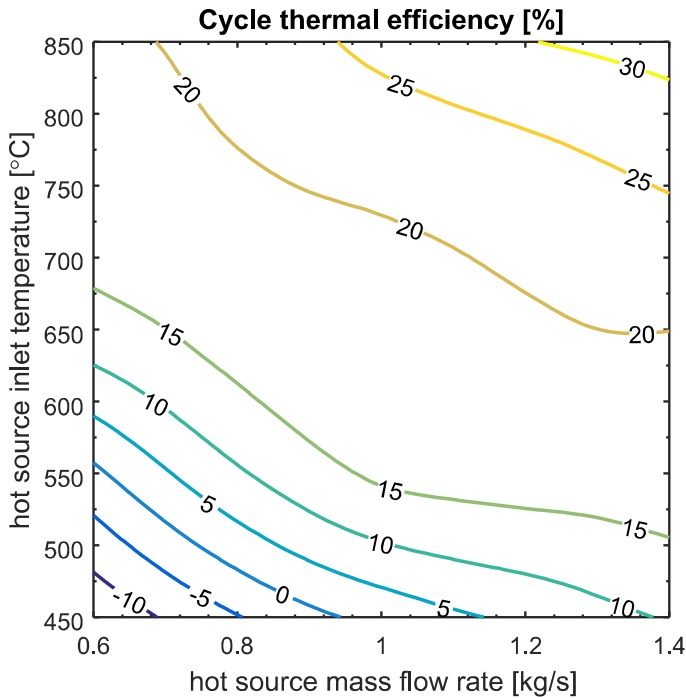


Figure 8: Variation of sCO₂ unit thermal efficiency with heat source inlet temperature and mass flow rate.

In particular, the results shown in Figure 9 suggest that it is possible to reduce the relevant temperature difference between the inlet temperature of the flue gases and the CO₂ at the turbine inlet by increasing the flue gas mass flow rate. For instance, if a hot source inlet temperature of 650°C is considered, increasing the hot source mass flow rate from 1 kg/s up to 1.4 kg/s can lead to a rise in the turbine inlet temperature from 400°C to 450°C, with a consequent increase in the power output from 50 kW to 63 kW (Figure 7) and of the thermal efficiency from 17% to almost 20% (Figure 8).

This increase in performance is due to the lower exergy loss occurring in the primary heater. Increasing the mass flow rate of the hot source counterbalances the higher thermal capacity of the CO₂. Then, a better matching of the temperature profiles of the two fluids in the heat exchanger can be achieved, leading to a higher exergy efficiency. A further solution would be the adoption of different cycle layouts designed to achieve better temperature profile matching. However, the higher investment cost due to the additional components required (i.e. heat exchangers, compressors and turbines), may increase the payback period of the heat to power conversion unit disproportionately.

A further positive effect on the system performance can also be achieved by reducing the inlet temperature of the cold source, as showed in Figure 10. Given a cooling fluid mass flow rate of 1.6 kg/s, a reduction of 20% in its inlet temperature can actually lead to a power output increase from 48 kW to 64 kW. Similarly, the same percentage variation of cold source mass flow rate, at an inlet temperature of 18°C, allows an increase in the system power output from 54 kW to 64 kW.

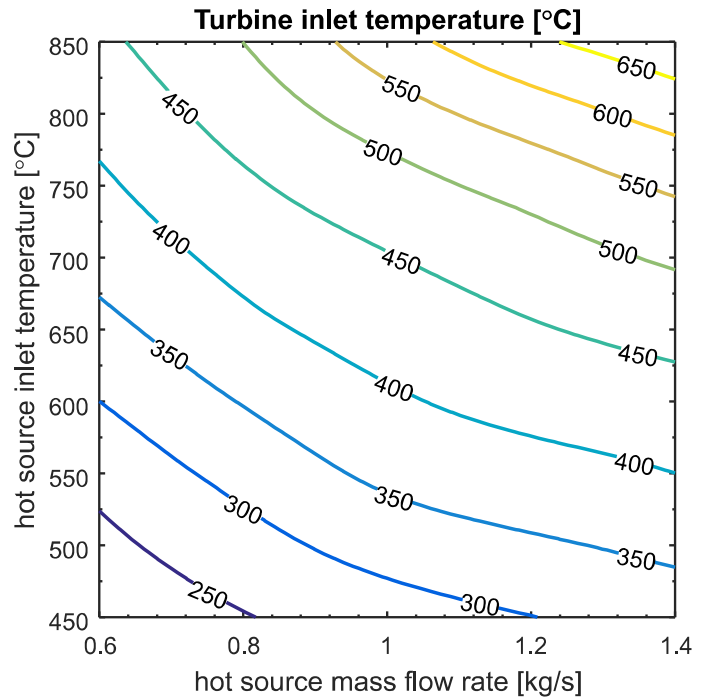


Figure 9: Variation of sCO₂ temperature at the turbine inlet with heat source inlet temperature and mass flow rate.

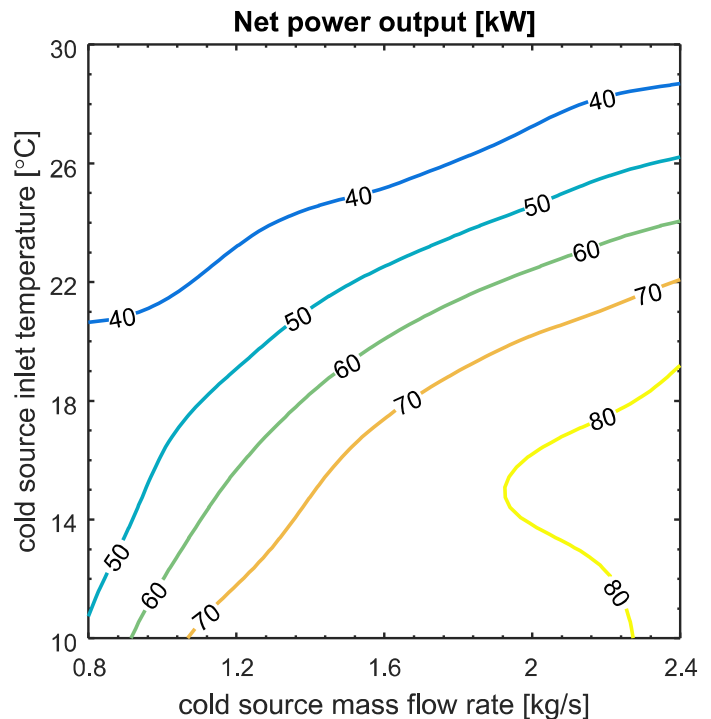


Figure 10: Variation of sCO₂ unit net power output with cold source inlet temperature and mass flow rate.

In particular, an increase of the cooling load allows to decrease the compressor inlet temperature of the CO₂, which gets closer to the critical point. At critical conditions, the CO₂

isothermal compressibility increases steeply, allowing a more efficient compression. The decreased compression power then leads to an increased system net power output and thermal efficiency.

The thermal efficiency gain achievable is shown in Figure 11. Considering a cold source mass flow rate of 1.6 kg/s, a decrease of its inlet temperature from 26°C down to 16°C leads to an increase in the cycle thermal efficiency from 9% to 21%. A higher efficiency value of 24% can be reached by increasing the cooling flow rate to 2.4 kg/s, and keeping its inlet temperature lower than 18°C. For higher cooling fluid temperatures the maximum efficiency is limited to 20%.

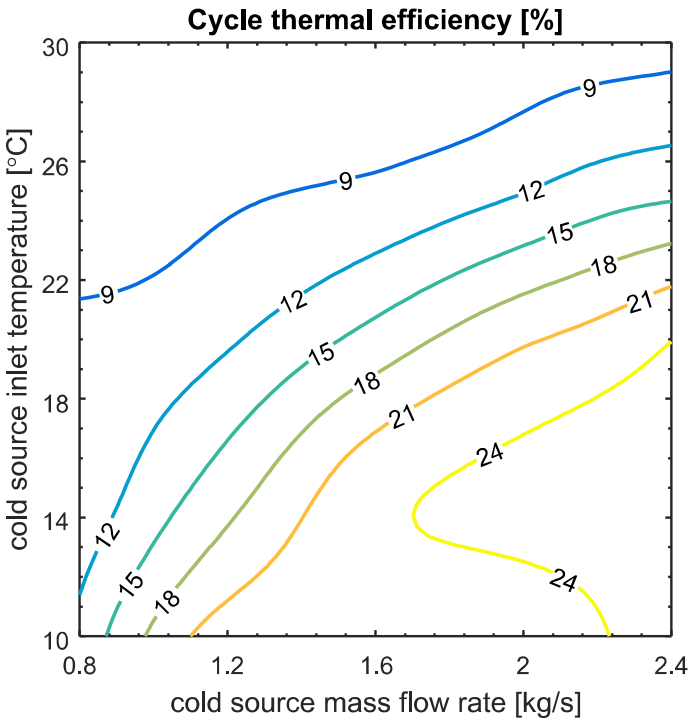


Figure 11: Variation of sCO₂ unit thermal efficiency with cold source inlet temperature and mass flow rate.

It can also be seen from Figures 10 and 11, that for mass flow rates higher than 1.6 kg/s and inlet temperatures lower than 20°C, less steep performance improvements can be observed. Considering for instance a cold source inlet temperature of 14°C and a variation of mass flow rate from 1.6 kg/s to 2.4 kg/s (Figure 10), the system power output increases only from 75 kW to 80 kW and the thermal efficiency from 23% to 24% (Figure 11).

The reason for this can be explained by referring to Figure 12, which shows the variation in the CO₂ temperature at the compressors inlet as a function of the cooling load available at the gas cooler. In the range of cold source inlet conditions considered, the compressor inlet temperature is constant and equal to 35°C. No further temperature reductions could be achieved even for increased cooling flow rate, due to the higher thermal capacity that the CO₂ assumes close to the critical point. This ensures a CO₂ temperature at the compressor inlet always

higher than the critical temperature which avoids condensation and dry conditions at the start of compression.

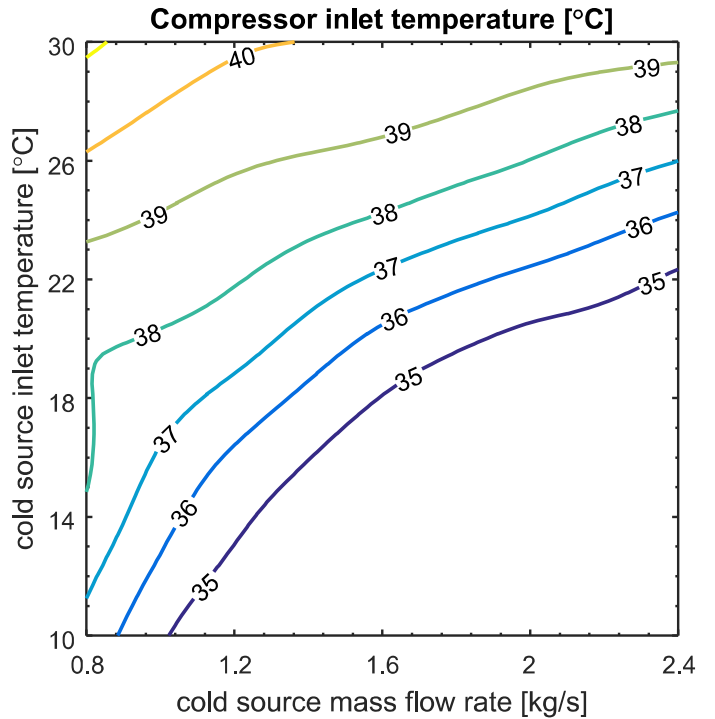


Figure 12: Variation of sCO₂ temperature at the compressor inlet with cold source inlet temperature and mass flow rate.

CONCLUSIONS

The aim of the research presented in this paper was to investigate the off-design performance of a low capacity sCO₂ heat to power conversion unit designed for medium to high thermal grade WHR applications. To model each component, performance data provided by manufacturers or obtained from more complex CFD models have been used. In particular, the operating maps of the radial compressor and turbine have been generated and presented.

Off-design steady state simulations were carried out to assess the effect of the hot and cold source inlet conditions on the unit performance as well as on the sCO₂ temperature at the inlet of the compressor and turbine. Performance maps of the sCO₂ unit have been generated and can be used in the design of control strategies for the system. In particular, the maps showed that the unit is not able to generate power if a heat source mass flow of 0.8 kg/s is used at a temperature lower than 500°C, due to the low sCO₂ temperature at the turbine inlet (275°C).

The temperature of the cold sink can have a significant influence on the unit power output and efficiency. For a fixed heat load and assuming a coolant mass flow rate of 1.6 kg/s, a decrease in the cooling fluid inlet temperature from 26°C to 16°C leads to an increase in the system power output and efficiency from 40 kW to 72 kW and from 9% up to 21% respectively. Moreover, the analysis showed that no condensation at the

compressor inlet occurs since the minimum temperature achieved is 35°C, which ensures safe operating conditions for the compressor over the whole range of cooling fluid inlet temperatures investigated.

NOMENCLATURE

CFD	Computational Fluid Dynamics
I/O	Input/Output
p_0	Reference pressure
RPM	Revolutions Per Minute
sCO ₂	supercritical carbon dioxide
T ₀	Reference temperature
WHR	Waste Heat Recovery

ACKNOWLEDGEMENTS

Aspects of the work have been funded by: i) European Union's Horizon 2020 research and innovation program under grant agreement No. 680599; ii) the Centre for Sustainable Energy Use in Food Chains (CSEF) of Brunel University London. CSEF is an End Use Energy Demand Centre funded by the Research Councils UK, Grant No: EP/K011820/1 and EPSRC project OPTEMIN (Optimising Energy Management in Industry) Grant No. EP/P004636/1. The authors would like to acknowledge the funders as well as contributions from Mr. Jonathan Harrison of Gamma Technologies during the model development. The paper all relevant data to support the understanding of the results. More detailed information and data, if required, can be obtained by contacting the corresponding author of the paper.

REFERENCES

[1] Forman C, Muritala IK, Pardemann R, Meyer B. Estimating the global waste heat potential. *Renewable and Sustainable Energy Reviews* 2016;57:1568–79. doi:10.1016/J.RSER.2015.12.192.

[2] Tchanche BF, Lambrinos G, Frangoudakis A, Papadakis G. Low-grade heat conversion into power using organic Rankine cycles – A review of various applications. *Renewable and Sustainable Energy Reviews* 2011;15:3963–79. doi:10.1016/j.rser.2011.07.024.

[3] Freund P, Bachu S, Simbeck D, Thambimuthu K. Annex I: Properties of CO₂ and carbon-based fuels. IPCC Special Report on 2005.

[4] Dostal V, Driscoll M, Hejzlar P. A supercritical carbon dioxide cycle for next generation nuclear reactors 2004.

[5] Turchi CS, Ma Z, Neises TW, Wagner MJ. Thermodynamic Study of Advanced Supercritical Carbon Dioxide Power Cycles for Concentrating Solar Power Systems. *Journal of Solar Energy Engineering* 2013;135:41007. doi:10.1115/1.4024030.

[6] Manjunath K, Sharma OP, Tyagi SK, Kaushik SC. Thermodynamic analysis of a supercritical/transcritical CO₂ based waste heat recovery cycle for shipboard power and cooling applications. *Energy Conversion and Management*

2018;155:262–75. doi:10.1016/j.enconman.2017.10.097.

[7] Kulhánek M, Dostál V. Supercritical Carbon Dioxide Cycles Thermodynamic Analysis and Comparison. *Proceedings of SCCO₂ Power Cycle Symposium 2011*:1–12.

[8] Marchionni M, Bianchi G, Tassou SA. Techno-economic assessment of Joule-Brayton cycle architectures for heat to power conversion from high-grade heat sources using CO₂ in the supercritical state. *Energy* 2018;148:1140–52. doi:10.1016/J.ENERGY.2018.02.005.

[9] Kwon JS, Bae SJ, Heo JY, Lee JI. Development of accelerated PCHE off-design performance model for optimizing power system operation strategies in S-CO₂ Brayton cycle. *Applied Thermal Engineering* 2019;159:113845. doi:10.1016/J.APPLTHERMALENG.2019.113845.

[10] Fu Q, Ding J, Lao J, Wang W, Lu J. Thermal-hydraulic performance of printed circuit heat exchanger with supercritical carbon dioxide airfoil fin passage and molten salt straight passage. *Applied Energy* 2019;247:594–604. doi:10.1016/J.APENERGY.2019.04.049.

[11] Bae SJ, Kwon J, Kim SG, Son I, Lee JI. Condensation heat transfer and multi-phase pressure drop of CO₂ near the critical point in a printed circuit heat exchanger. *International Journal of Heat and Mass Transfer* 2019;129:1206–21. doi:10.1016/J.IJHEATMASTRANSFER.2018.10.055.

[12] Shin H, Cho J, Baik Y-J, Cho J, Roh C, Ra H-S, et al. Partial Admission, Axial Impulse Type Turbine Design and Partial Admission Radial Turbine Test for SCO₂ Cycle. Volume 9: Oil and Gas Applications; *Supercritical CO₂ Power Cycles; Wind Energy, ASME; 2017, p. V009T38A019.* doi:10.1115/GT2017-64349.

[13] Taehan Kigye Hakhoe., 대한 기계 학회. Taehan Kigye Hakhoe nonmunjip. B = B Transactions of the Korean Society of Mechanical Engineers. Taehan Kigye Hakhoe; 1996.

[14] Pelton R, Allison T, Jung S, Smith N. Design of a Wide-Range Centrifugal Compressor Stage for Supercritical CO₂ Power Cycles. Volume 9: Oil and Gas Applications; *Supercritical CO₂ Power Cycles; Wind Energy, ASME; 2017, p. V009T38A031.* doi:10.1115/GT2017-65172.

[15] Shao W, Wang X, Yang J, Liu H, Huang Z. Design Parameters Exploration for Supercritical CO₂ Centrifugal Compressors Under Multiple Constraints. Volume 9: Oil and Gas Applications; *Supercritical CO₂ Power Cycles; Wind Energy, ASME; 2016, p. V009T36A008.* doi:10.1115/GT2016-56820.

[16] Monje B, Sánchez D, Savill M, Pilidis P, Sánchez T. A Design Strategy for Supercritical CO₂ Compressors. Volume 3B: Oil and Gas Applications; *Organic Rankine Cycle Power Systems; Supercritical CO₂ Power Cycles; Wind Energy, ASME; 2014, p. V03BT36A003.* doi:10.1115/GT2014-25151.

[17] Pasch J, Stapp D. Testing of a New Turbocompressor for Supercritical Carbon Dioxide Closed Brayton Cycles. Volume 9: Oil and Gas Applications; *Supercritical CO₂ Power Cycles; Wind Energy, ASME; 2018, p. V009T38A024.* doi:10.1115/GT2018-77044.

[18] Bidkar RA, Sevincer E, Wang J, Thatte AM, Mann A, Peter M, et al. Low-Leakage Shaft-End Seals for Utility-Scale Supercritical CO₂ Turboexpanders. *Journal of Engineering for Gas Turbines and Power* 2016;139:22503. doi:10.1115/1.4034258.

- [19] Du Q, Gao K, Zhang D, Xie Y. Effects of grooved ring rotation and working fluid on the performance of dry gas seal. *International Journal of Heat and Mass Transfer* 2018;126:1323–32. doi:10.1016/J.IJHEATMASSTRANSFER.2018.05.055.
- [20] Jeong WS, Kim TW, Suh KY. Computational Fluid Dynamics of Supercritical Carbon Dioxide Turbine for Brayton Thermodynamic Cycle. Volume 2: Fuel Cycle and High Level Waste Management; *Computational Fluid Dynamics, Neutronics Methods and Coupled Codes; Student Paper Competition, ASME*; 2008, p. 265–9. doi:10.1115/ICONE16-48240.
- [21] Saravi SS. An investigation into sCO₂ compressor performance prediction in the supercritical region for power systems. *Energy Procedia* 2019;161:403–11. doi:10.1016/J.EGYPRO.2019.02.098.
- [22] Pecnik R, Rinaldi E, Colonna P. Computational Fluid Dynamics of a Radial Compressor Operating With Supercritical CO₂. *Journal of Engineering for Gas Turbines and Power* 2012;134:122301. doi:10.1115/1.4007196.
- [23] Wright SA, Radel RF, Vernon ME, Rochau GE, Pickard PS. SANDIA REPORT Operation and Analysis of a Supercritical CO₂ Brayton Cycle. n.d.
- [24] Utamura M, Fukuda T, Aritomi M. Aerodynamic Characteristics of a Centrifugal Compressor Working in Supercritical Carbon Dioxide. *Energy Procedia* 2012;14:1149–55. doi:10.1016/J.EGYPRO.2011.12.1068.
- [25] Fuller, Robert L, Eisemann K. Centrifugal Compressor Off-design performance for supercritical CO₂. *Supercritical CO₂ Power Cycle Symposium, Boulder, Colorado*: 2011, p. 12.
- [26] Lambruschini F, Liese E, Zitney SE, Traverso A. Dynamic Model of a 10 MW Supercritical CO₂ Recompression Brayton Cycle. Volume 9: Oil and Gas Applications; *Supercritical CO₂ Power Cycles; Wind Energy, ASME*; 2016, p. V009T36A004. doi:10.1115/GT2016-56459.
- [27] Zhang J. The 6th International Supercritical CO₂ Power Cycles Symposium Dynamic modeling and transient analysis of a molten salt heated recompression supercritical CO₂ Brayton cycle. n.d.
- [28] Luu MT, Milani D, McNaughton R, Abbas A. Dynamic modelling and start-up operation of a solar-assisted recompression supercritical CO₂ Brayton power cycle. *Applied Energy* 2017;199:247–63. doi:10.1016/J.APENERGY.2017.04.073.
- [29] Bianchi G, Saravi SS, Loeb R, Tsamos KM, Marchionni M, Leroux A. Design of a high-temperature heat to power conversion facility for testing supercritical CO₂ equipment and packaged power units. *Energy Procedia* 2019;161:421–8. doi:10.1016/J.EGYPRO.2019.02.109.
- [30] T Gamma - Gamma Technologies Inc 2012. *GT-SUITE-Flow Theory Manual* 2012.
- [31] Lemmon, E. W., Marcia L. Huber and MOM. REFPROP, NIST Standard Reference Database 23, Version 8.0. 2007.
- [32] Pitla SS, Groll EA, Ramadhyani S. New correlation to predict the heat transfer coefficient during in-tube cooling of turbulent supercritical CO₂. *International Journal of Refrigeration* 2002;25:887–95. doi:10.1016/S0140-7007(01)00098-6.
- [33] Cipollone R, Bianchi G, Di Battista D, Fatigati F. Experimental and numerical analyses on a plate heat exchanger with phase change for waste heat recovery at off-design conditions. *Journal of Physics: Conference Series* 2015;655:12038. doi:10.1088/1742-6596/655/1/012038.
- [34] Colebrook CF, Blench T, Chatley H, Essex EH, Finnicome JR, Lacey G, et al. Turbulent flow in pipes, with particular reference to the transition region between the smooth and rough pipe laws. (include plates). *Journal of the Institution of Civil Engineers* 1939;12:393–422. doi:10.1680/ijoti.1939.14509.
- [35] Marchionni M, Bianchi G, Karvountzis-Kontakiotis A, Pesyridis A, Tassou SA. An appraisal of proportional integral control strategies for small scale waste heat to power conversion units based on Organic Rankine Cycles. *Energy* 2018;163:1062–76. doi:10.1016/J.ENERGY.2018.08.156.
- [36] Marchionni M, Bianchi G, Karvountzis-Kontakiotis A, Pesiridis A, Tassou SA. Dynamic modeling and optimization of an ORC unit equipped with plate heat exchangers and turbomachines. *Energy Procedia* 2017;129:224–31. doi:10.1016/J.EGYPRO.2017.09.146.
- [37] Baltadjiev ND, Lettieri C, Spakovszky ZS. An Investigation of Real Gas Effects in Supercritical CO₂ Centrifugal Compressors. *Journal of Turbomachinery* 2015;137:91003. doi:10.1115/1.4029616.

EXPERIMENTAL TESTING OF A 1MW sCO₂ TURBOCOMPRESSOR

Logan Rapp

Sandia National Laboratory
Albuquerque, NM, USA
Email: lmrapp@sandia.gov

David Stapp

Peregrine Turbine Technologies
Wiscasset, ME, USA

ABSTRACT

The Nuclear Energy Systems Laboratory (NESL) Brayton Laboratory at Sandia National Laboratories has been at the forefront of supercritical carbon dioxide (sCO₂) power cycle development since 2007 when internal R&D funds were used to investigate the stability of sCO₂ as a working fluid for power cycles. Since then, Sandia has been a leader in research and development of sCO₂ power cycles through government funded research and by partnering with industry to design and test components necessary for commercialization of sCO₂ Brayton cycles. Peregrine Turbine Technologies (PTT) is a small business working to commercialize sCO₂ power cycles with their proprietary thermodynamic cycles, heat exchangers, and turbomachinery designs. Under a Small Business Innovation Research (SBIR) program with the United States Air Force Research Laboratory, PTT has designed a novel motorless turbocompressor for sCO₂ power cycles. In 2017, Sandia purchased the first sCO₂ turbocompressor from PTT and installed it into the 1-MW thermal turbomachinery development platform at Sandia. PTT and Sandia have worked together to experimentally test the turbocompressor to the limits of the development platform (932 F @ 2500 psi). This report will detail the design of the turbomachinery development platform, the novel process used to start the turbomachinery, and the experimental results to date. The report will also look at lessons learned throughout the process of constructing and operating an experimental sCO₂ loop.

INTRODUCTION

In 2012, the NESL Brayton Lab at Sandia National Laboratories (SNL) completed the commissioning of a recompression closed Brayton cycle (RCBC) development platform (DP). The DP was used in both simple and

recompression configurations to investigate key technical issues related to the power cycle components as well as to validate analytical models of system performance. The experience and intellectual property accumulated over years of testing turbomachinery, heat exchangers, heat input, heat rejection systems, and support equipment for sCO₂ Brayton cycles has positioned the Brayton Lab at SNL as the premier facility for testing and development of Brayton power cycles.

In order to accelerate development and facilitate the commercialization of sCO₂ Brayton technology, the Brayton Lab sought industry collaboration. Through an evaluation of responses to solicitations to industry leaders, PTT was identified as the most promising company to achieve the goals of both the Brayton Lab and the DOE. PTT is a small business from Maine, USA which has the object of commercializing closed Brayton cycle (CBC) power generation systems. The first activity of the collaboration was the purchase of the first of a kind sCO₂ turbocompressor from PTT and the reconfiguration of the DP located at SNL for testing of the turbocompressor. The focus of this paper is the presentation of the preliminary testing and to highlight the important experimental results to date.

TEST OBJECTIVES

The turbocompressor, also referred to as the core, is designed to operate at 118,000 rpm, 1382 F (750C) turbine inlet temperature (TIT), and 6222 psi (42.9 MPa) compressor discharge pressure and is intended for use in a 1 MWe closed Brayton cycle engine also being developed by Peregrine. The Sandia DP where the core is installed limits the turbocompressor operation to approximately 2500 psi (17.2 MPa) with a TIT of 932 F (500 C). A P&ID of the system is shown in Figure 1 and of the secondary flows in Figure 2.

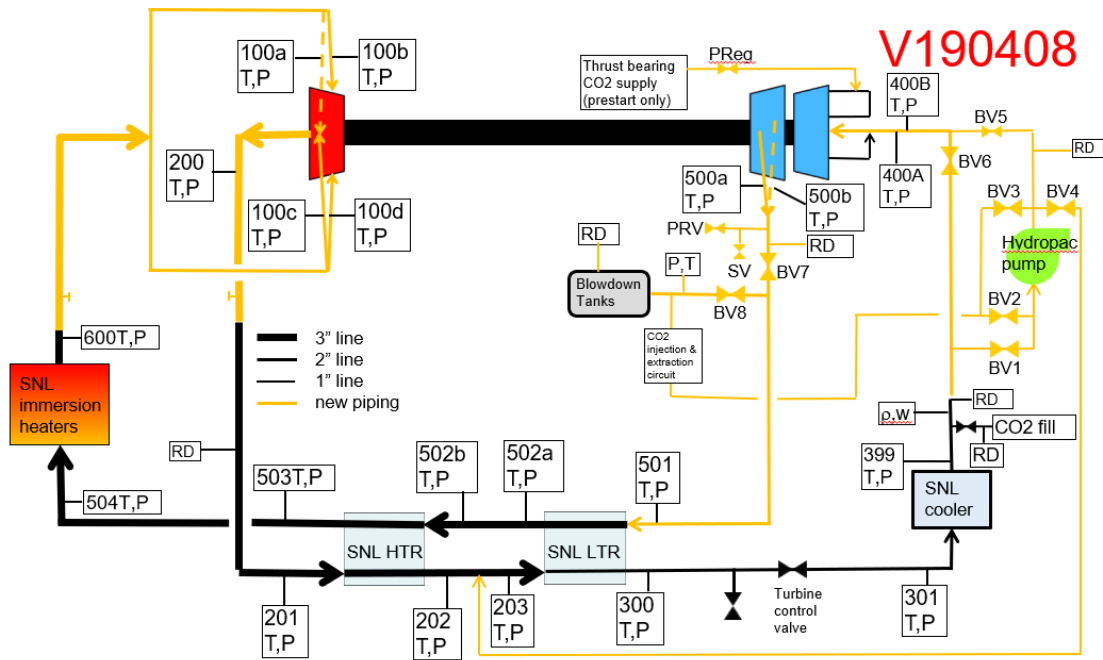


Figure 1: Development Platform piping and instrumentation diagram

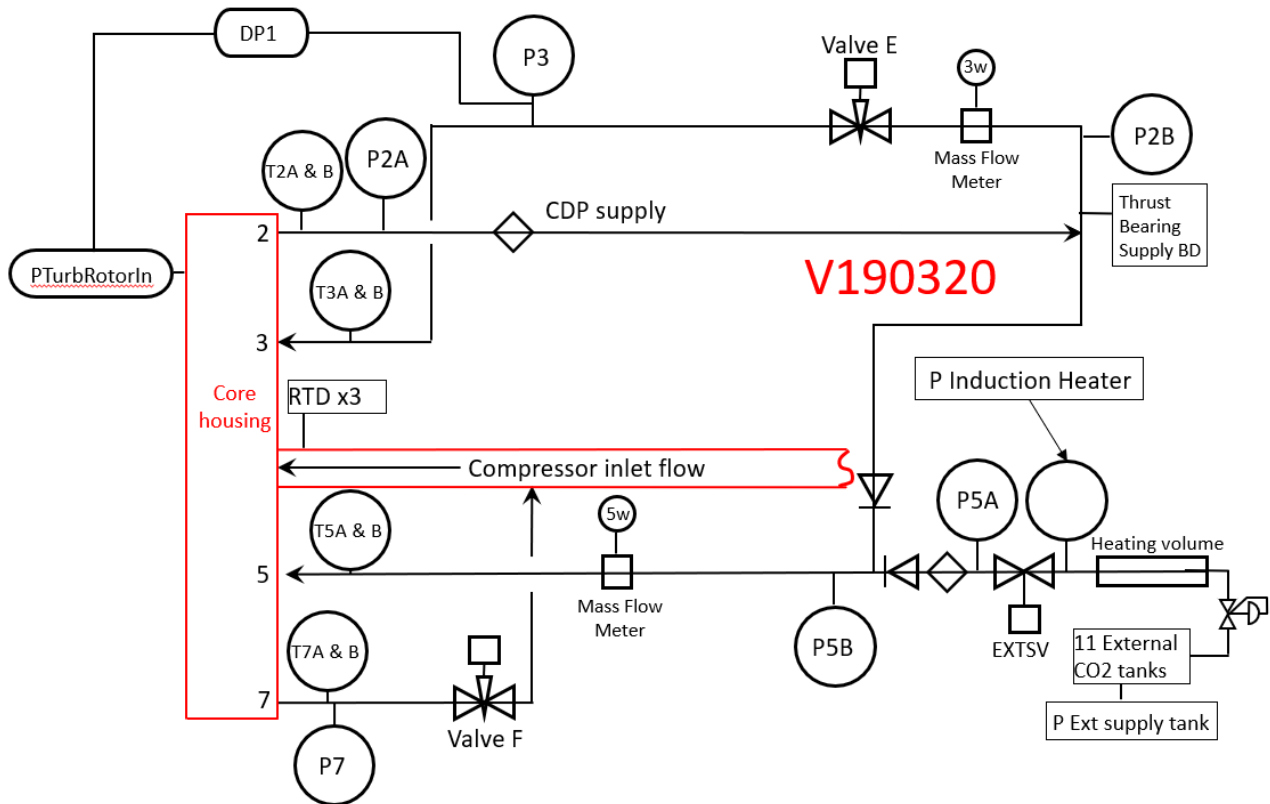


Figure 2: Secondary flows piping and instrumentation diagram

Further details regarding the various components of the DP can be found in [1].

While the conditions achievable in the DP do not meet the specified design-point operating conditions of the turbocompressor, they are sufficient to test and validate the performance of the machine during start up, steady state operation, and shut down. The original objectives identified at the beginning of the test campaign were listed as:

1. Demonstrate the successful start to steady state of the PTT core.
2. Demonstrate repeatable start and performance operations.
3. Demonstrate operations of core internal functions
 - a. Pressure activated leaf seals
 - b. Radial bearings
 - c. Thrust bearings
 - d. Secondary flows
4. Demonstrate compressor controllability via back pressuring and TIT manipulation
5. Map turbine and compressor performance over a range of conditions
 - a. Compressor inlet temperature
 - b. Compressor inlet pressure
 - c. Compressor pressure ratio
 - d. Turbine inlet temperature
 - e. Pressure loss effects
6. Support acoustical measurements for rotor speed

TESTING SUMMARY

To date, seven tests have been performed and data supporting objectives 1-4 has been successfully gathered. Objective 5 has just begun to be explored with the 8 hour long Test #7. The 6th objective is no longer applicable because an eddy current proximity probe was installed before Test #5 which is now used to measure both axial movement and rotational speed of the rotor. A summary of the tests performed is shown in Table 1.

Test Number	Test Date	Test Duration	TIT (°F)	Compressor Discharge Pressure (psi)	Max PR
1	8/9/2018	00:00:32	225	1240	1.2
2	10/10/2018	00:18:40	420	1400	1.25
3	11/14/2018	00:20:46	645	1750	1.59
4	3/1/2019	00:03:32	610	1460	1.26
5	3/6/2019	00:08:23	530	1510	1.3
6	4/4/2019	00:03:18	530	1510	1.28
7	5/7/2019	8:05:44	570	1475	1.27

Table 1: Summary of turbocompressor tests performed to date

Initially, the tests were limited in duration due to difficulties in balancing rotor thrust which resulted in thrust bearing

touchdown, axial rubs and subsequent failure of the turbine gas foil bearing. With several sets of test data in hand for data matching, secondary flow simulations gave additional insight into proper secondary flow and TCV valve settings in order to achieve complete thrust balance with no thrust bearing touchdown. Using this new information, the thrust bearing issue was resolved as of Test #4 and thrust balance was achieved as confirmed by proximity probe data. Tests #4-6 have experienced radial bearing failures after a period of stable running, which will be discussed in detail later. Test #7 demonstrated the successful operation of the radial bearings with an 8 hour test and controlled shut down.

TURBOCOMPRESSOR START

The Peregrine design is the first of its kind motorless sCO₂ high-performance turbocompressor. Because there is no motor to start the turbocompressor, an alternative starting method is employed. This method is referred to as the blowdown start because inventory tanks (labeled “Blowdown Tanks” in Figure 1) are charged to a higher pressure than the loop and then are used to blowdown through the primary heat exchanger and then into the turbine to start the turbocompressor. Before the system can be started, the loop must be preconditioned such that the compressor inlet is slightly above supercritical conditions and the turbine inlet is heated to near the TIT that is desired for the test. An external positive displacement compressor is used to circulate CO₂ for the preconditioning. Prior to the addition of the proximity probe the CO₂ was circulated at a flow rate to minimize the time required to precondition the loop. However, when the proximity probe was added it was discovered that this flow rate was sufficient to slowly spin the shaft. The spinning of the shaft during preconditioning may have caused damage to the radial foil bearings. Once this was discovered, later tests utilized a reduced flow rate for preconditioning to protect the radial bearings.

Once the system was preconditioned, the valve positions were changed to execute a start. As can be seen in Figure 1, BV7 is first closed and then BV8 is opened to start the blowdown. This causes mass to flow through the LTR, the HTR, and the heaters before flowing into the turbine inlet. Once the compressor discharge pressure is greater than the blow down pressure by a specified margin, BV7 opens and BV8 closes and the system begins operating on its own power. The required blowdown pressure to successfully start the turbocompressor was unknown and not easily calculated. Thus, for the first tests the blowdown pressure was set to a high pressure to ensure there was sufficient energy to start and subsequently lowered for later tests, all of which had successful starts. For Test #7 the blowdown pressure had to be increased which will be explained in greater detail in the Radial Bearing Failure section. The values of blowdown pressure can be seen in Table 2.

Test Number	Test Date	Blowdown Pressure (psi)
1	8/9/2018	1800
2	10/10/2018	1850
3	11/14/2018	1670
4	3/1/2019	1670
5	3/6/2019	1400
6	4/4/2019	1300
7	5/7/2019	1450

Table 2: Blowdown Pressures for successful starts

The blowdown process for the 11/14/18 test is shown in Figure 3. BV8 closes and BV7 opens when $P500A - P501 > dP_{min}$, where $dP_{min} = 20$ psi. This was done to ensure the pressure on the compressor discharge was high enough to prevent flow from the blowdown tanks from flowing back into the compressor discharge.

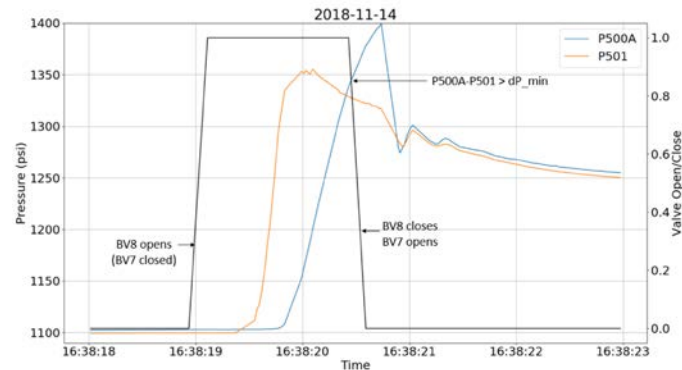


Figure 3: Blowdown start process - pressures and valve positions. Blowdown pressure = 1670 psi

This same process is shown for the 3/6/19 test in Figure 3, where the blowdown pressure was lowered to 1400psi from 1670psi.

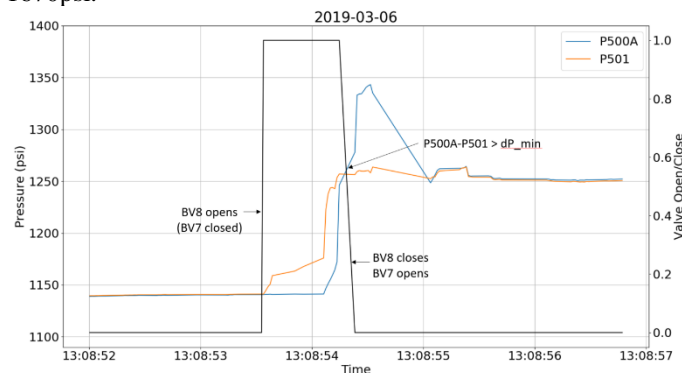


Figure 4: Blowdown start process - pressures and valve positions. Blowdown pressure = 1400 psi

As can be seen by comparing Figure 3 and Figure 4, the lower blowdown pressure reduced the pressure ramp rate of P501 from ~250psi to ~100psi. This decreases the severity of the blowdown event and reduces the possibilities that the radial

foil or thrust bearings could be damaged during the blowdown process.

THRUST BEARING ISSUES

In Tests #1-3, both the thrust bearing and the radial bearings experienced rubs/failures. Figure 5 shows the compressor inlet and discharge pressures plotted versus time with spikes in pressure circled in red. These spikes correspond to thrust bearing touchdown rubs, where the rub caused the rotor to slow down momentarily.

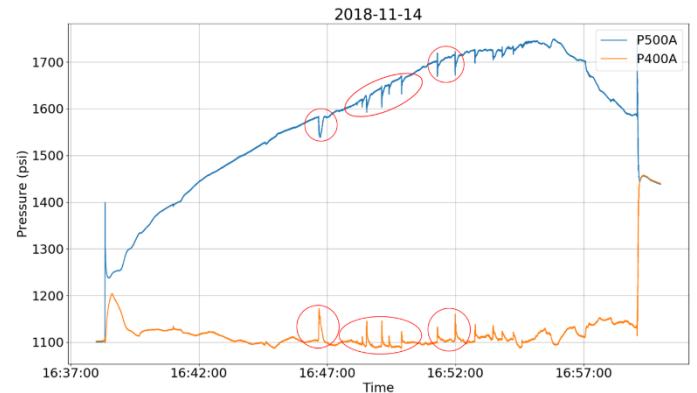


Figure 5: Compressor inlet and discharge pressure showing thrust bearing rubs

By adjusting the back pressure on the turbine using the turbine control valve (TCV) as well as adjusting the setting for Valve F in the secondary flows, the thrust balance on the rotor can be equilibrated. Valve F is part of the secondary flow control system and regulates the venting pressure on the aft side of the thrust disk of the rotor. This serves as a balance piston in the design and permits real-time adjustment of rotor thrust within a certain range. The testing on 2018-11-14 was performed with Valve F completely closed, so for the next test, both TCV and Valve F were opened using prescribed settings from the updated secondary flow analysis. Additionally, a proximity probe was added to monitor the axial movement of the shaft during the test. This allowed the proximity to be monitored and valve adjustments to be made in real time should the axial position start to change during a test. The plot of compressor inlet and discharge pressure for Test #5 is shown in Figure 6 and the proximity data is shown in Figure 7.

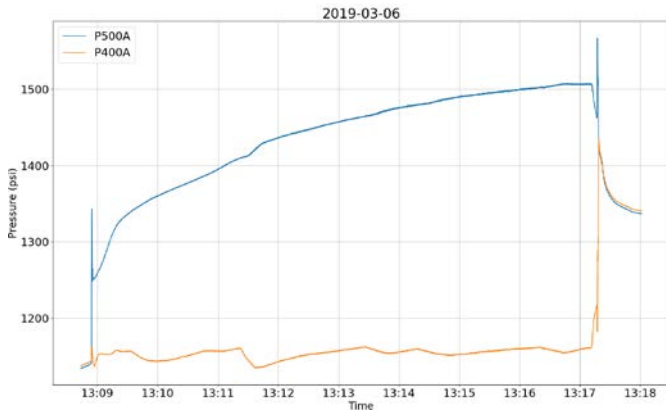


Figure 6: Compressor inlet and discharge pressure – thrust bearing issue resolved

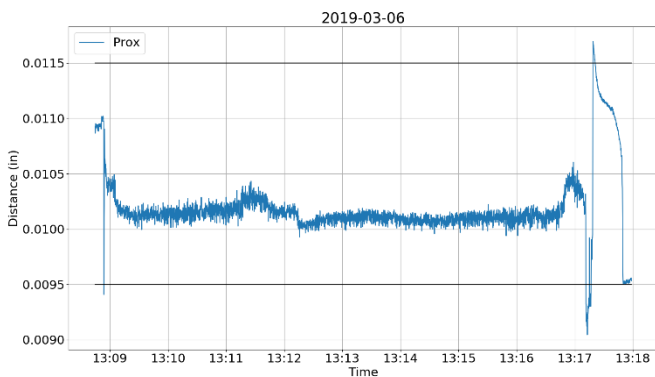


Figure 7: Proximity probe data for Test #5 showing axial position of the shaft with lines showing high and low proximity limits

As can be seen in Figure 6, there are no longer spikes in pressure due to a thrust bearing rub. Additionally, when the turbomachinery was disassembled after the test there was no indication of thrust bearing contact. In Figure 7, the horizontal lines indicate the minimum and maximum proximity before a rub would be expected; that is, at 0.0095in and 0.0115in, a thrust bearing rub would be expected. The proximity sensor data shows there was very little axial movement during the test. The initial drop in distance was due to the blowdown start and the position quickly recovers to approximately 0.0101in. The other dramatic change in proximity is during shutdown. The method used to shut down in Test #5 was closing BV7 and BV6 at the same time. This causes the shaft to stop spinning abruptly and thus some axial movement is expected during this event. The proximity probe data, as well as the lack of physical evidence of thrust bearing wear, gives confidence that the thrust balance problem has been resolved. However, the turbine end radial bearing continued to fail at some point during each test until the bearing design was improved for Test #7.

RADIAL BEARING FAILURE

The core features two radial gas bearings, one at the cold end near the low-pressure compressor and the other at the hot end near the turbine. With the exception of the last test, Test #7,

the aft (turbine side) radial bearing has failed and limited the duration of the test. While the root cause of those failures is still under investigation, presented here are some of the potential causes:

One hypothesis as to why the radial bearing is failing is the severe nature of the blowdown start. An attempt was made to reduce the severity of the blowdown by decreasing the blowdown pressure as described in the “Turbocompressor Start” section. Additionally, the valve which controls the blowdown start, BV8, was switched from a fast-acting valve to a slower actuated valve in attempt to further reduce the abrupt pressure change to the system.

In Tests #5 and #6, it was attempted to keep the test conditions such as starting turbine inlet temp and valve settings consistent and only change the blowdown pressure and valve actuation speed. In this way, if the bearing did not fail, then it might be reasonably concluded that the blowdown process was the culprit. However, the bearing did fail at a similar rotational speed in both tests. Plots of speed for Test #5 and #6 are shown in Figure 8 and Figure 9.

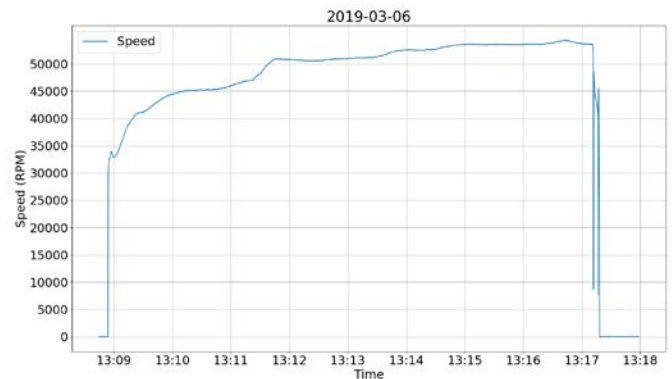


Figure 8: Rotor speed for Test #5

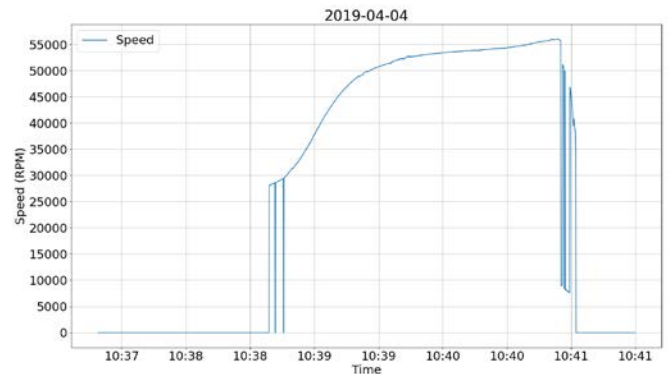


Figure 9: Rotor speed for Test #6

During Test #6, the proximity probe malfunctioned at the start of the test. This can be seen in the lack of data until approximately 10:38 in Figure 9. However, once the sensor began working the speed can be seen increasing until reaching approximately 56,000 rpm. Comparing Figure 8 and Figure 9, the plots show the bearing failed at approximately 55,000 rpm in both tests. Normally, this might indicate there is a critical speed

near 55,000 rpm that is causing instability of the shaft and failure of the bearing. However, the physical evidence of the bearing failure only shows yielded foils at a specific clocking of the bearing; that is, the foils are not yielded uniformly around the entire circumference of the bearing. If the failure was due to a critical speed instability of the shaft, the expected result would be yielded foils around the entire circumference of the bearing instead of only at a particular clocking. It should be noted that

rotordynamic analysis indicates that there are no mode crossings in the operating range above 35,000 rpm. This points to the failure being caused by a radial side load, which may be caused by non-uniform turbine inlet temperatures and/or flowrates.

The design of the PTT turbocompressor features 4 turbine inlets which are shown in Figure 10.

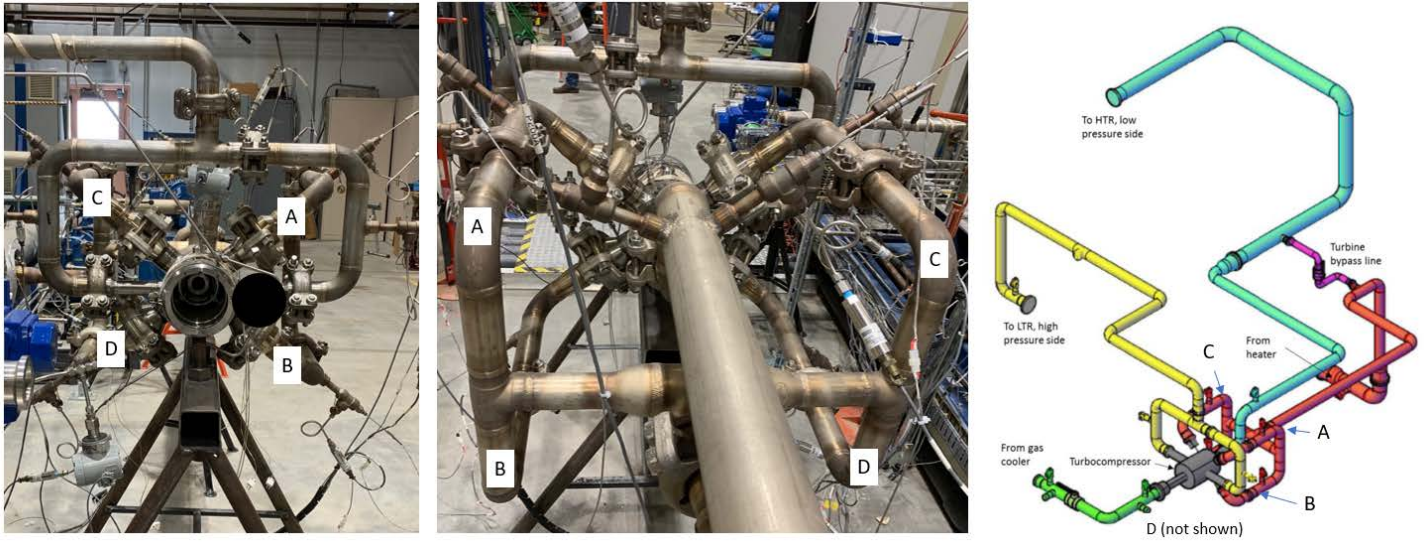


Figure 10: Left- Core case with compressor inlet and turbomachine cartridge removed. Center -Turbine inlets. Right-Isometric of piping around core

These inlets are designed to be symmetric and should have equal mass flow and temperature. However, during testing the legs appeared to be inconsistent in temperature, with variations as high as 50F. Figure 11 through Figure 15 show the TIT plots for Test #2-#6.

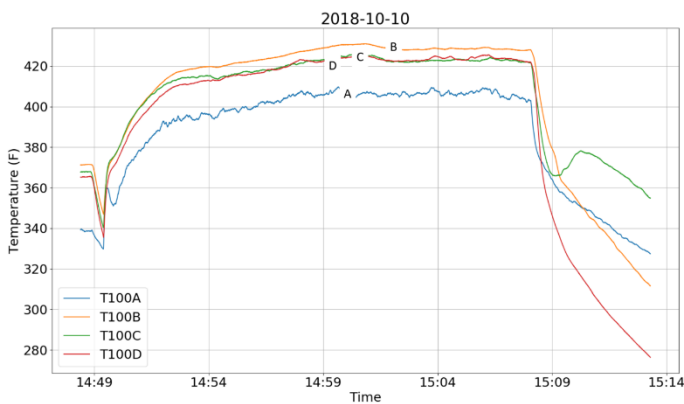


Figure 11: Turbine inlet temperature variations Test #2

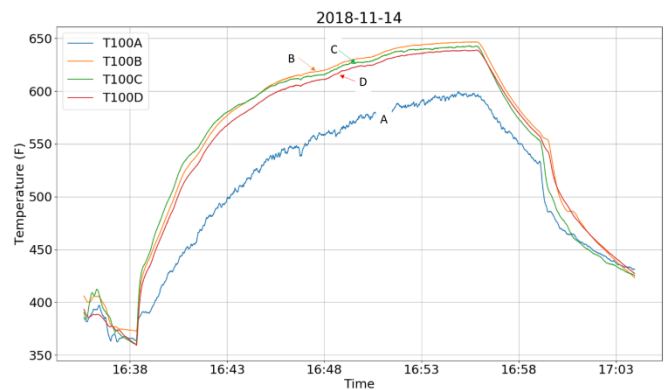


Figure 12: Turbine inlet temperature variations Test #3

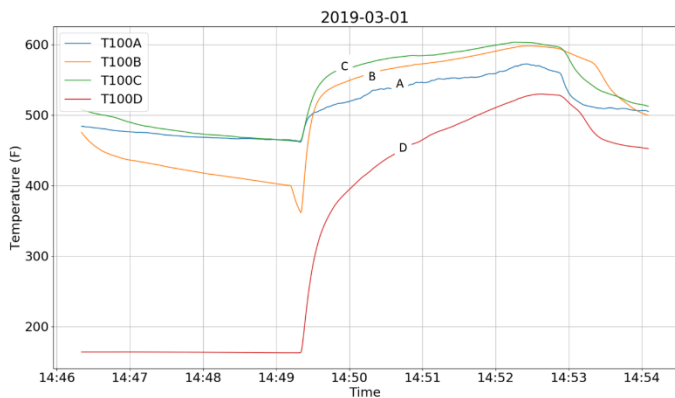


Figure 13: Turbine inlet temperature variations Test #4

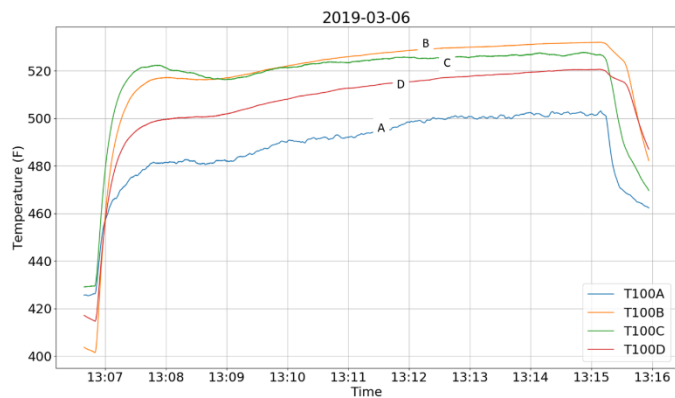


Figure 14: Turbine inlet temperature variations Test #5

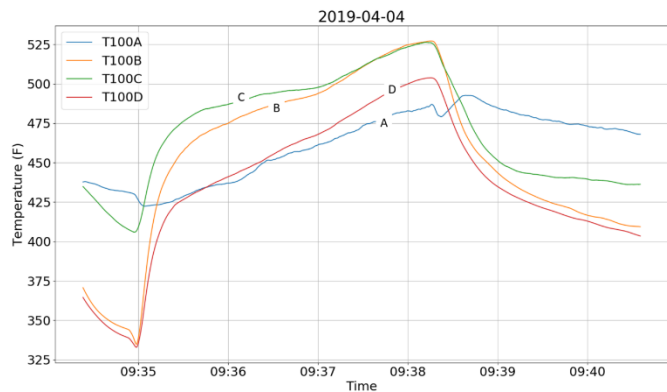


Figure 15: Turbine inlet temperature variations Test #6

As can be seen in the plots of TIT, leg “A” is often significantly cooler than the rest, and in later tests leg “D” is also cool. It is believed that Leg “D” in Test #4 had a cold, dense slug that did not have sufficient time to clear. The temperature can be seen to increase rapidly once the turbocompressor is started and the leg experiences a higher mass flow rate. The temperature profile of leg “A” shows a very jagged trace, which would indicate the instrument was not inserted into the flow adequately. When the lengths of the RTD’s were measured, they were found to be within ¼” inch of each other. However, the piping was not removed to physically see insertion depth of the instrument until after Test #6. When that was done, it was found that T100A was

not inserted correctly. The original placement of T100A is shown in Figure 16 on the left, and the new insertion depth is shown on the right.

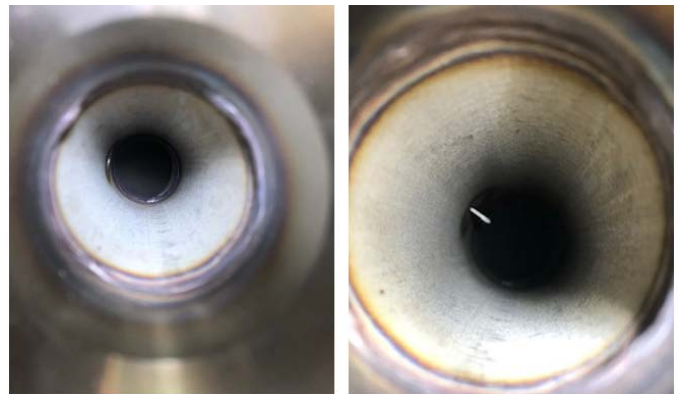


Figure 16: Insertion depth of T100A RTD; original insertion on left (not visible), new insertion shown on right.

As can be seen in Figure 16, the T100A was not inserted into the flow at all. Shown on the right in Figure 16 is the new RTD which was inserted to a depth to match the other three legs. A test was run without the turbocompressor in the loop in order to record the turbine inlet temperatures with the new T100A inserted to match the depth of the other legs. The results are shown in Figure 17.

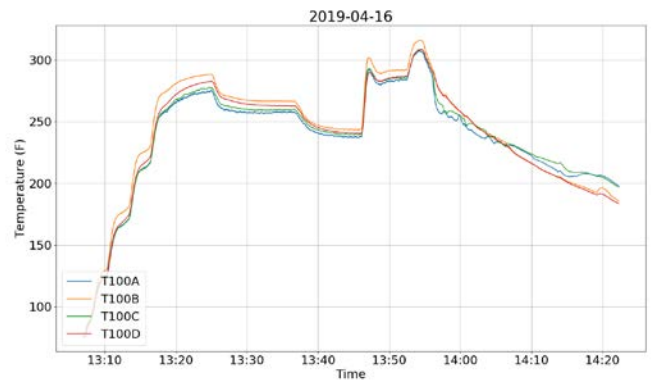


Figure 17: Turbine inlet temperatures with T100A replaced and inserted correctly into the flow

Figure 17 shows that the temperature discrepancy of T100A is no longer a problem. New RTDs were ordered and the existing T100A-D were replaced with closer detail paid to the insertion depth. Figure 18 shows the original and new insertion depths of T100A-D.

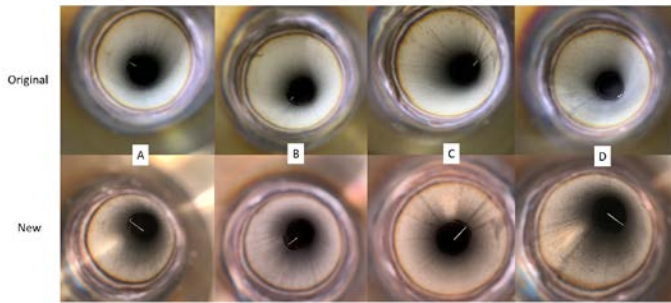


Figure 18: Original (top) and new (bottom) insertion depths of T100A-D

The next test of the turbocompressor demonstrated that the insertion depth of the RTDs was the issue and was resolved with the installation of new RTDs. Figure 19 shows the turbine inlet temperatures are in very good agreement with each other during Test #7.

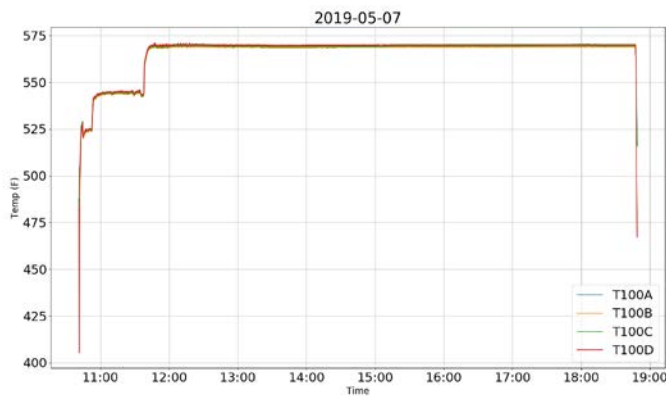


Figure 19: Turbine inlet temperatures with new insertion depth

With the insertion depth of the RTDs in mind, it is no longer believed that there is a significant temperature variation between the legs during the test. However, there does exist a temperature difference between the top and bottom legs at the start of the

turbocompressor due to stratification of the fluid due to temperature/density changes. This occurs during the time between ending the preconditioning of the system and the blowdown. If the cooler, denser fluid sinks to the bottom legs during this time and then is injected into the turbine during startup, this could cause an unbalanced radial load during the blowdown event. Perhaps this is sufficient to cause damage to the radial bearing which then fails later in the test.

It was decided to increase the length over diameter ratio of the aft radial bearing to increase the load capacity as well as the damping of the bearing. This resulted in the successful operation of the turbocompressor for 8 hours with a controlled shutdown. The speed vs time for Test #7 is shown in Figure 20 and the proximity data is shown in Figure 21. As can be seen in Figure 20, there were three unsuccessful start attempts before the turbocompressor was started successfully. The conditions for the attempted starts are shown in Table 3.

Start Number	Turbine Inlet Temp (F)	Blowdown Pressure (psi)	Outcome
1	460	1330	Unsuccessful
2	500	1360	Unsuccessful
3	525	1425	Unsuccessful
4	550	1450	Successful

Table 3: Conditions for attempted starts during Test #7

It is interesting to note the peak speed for each unsuccessful start attempt in Figure 20. It is clear that increasing the TIT and blowdown pressure impart more energy to the turbocompressor, but the conditions were not sufficient to achieve a successful start until the fourth attempt. It is believed that the stiffness and damping added by the new bearing increased the energy needed to start the turbocompressor. Further tests will explore the minimum TIT and blowdown pressure that is required for a successful start with the new aft radial bearing.

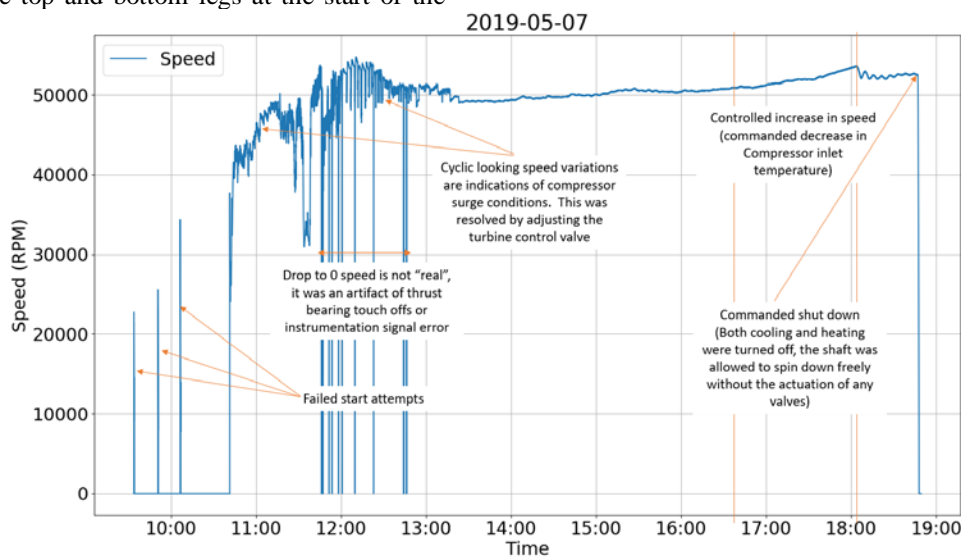


Figure 20 – Speed plot for Test #7

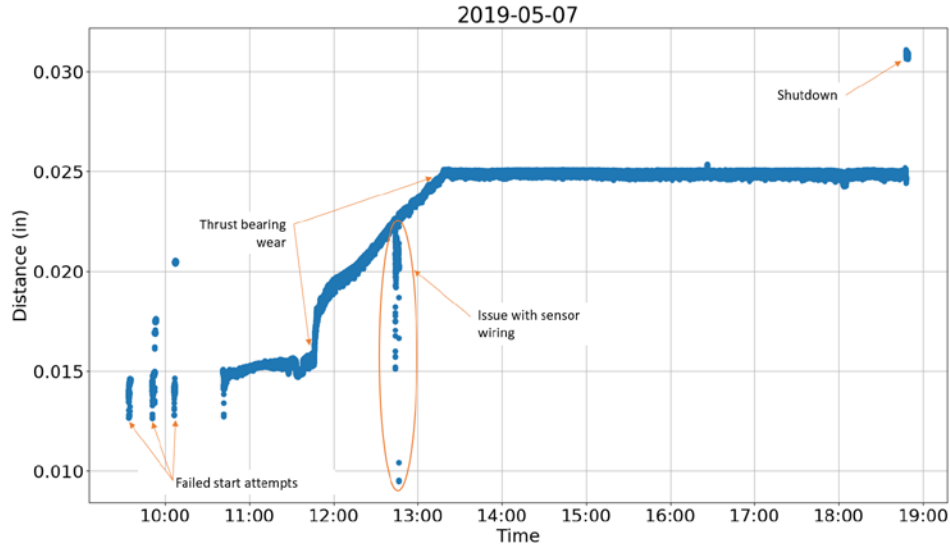


Figure 21 – Proximity probe plot for Test #7

After the successful start of the turbocompressor, it took some time to achieve steady state operation. As can be seen in Figure 21, there was very little axial movement for approximately the first hour of operation. However, during that time the operation was not steady state as the compressor was seeing surge conditions indicated by the fluctuations in speed in Figure 20. At approximately 11:45 the rotor began slowly moving in the aft direction and moved approximately 0.01 inches in the aft direction until it settled into an axial position of 0.025 inches. This movement was the result of a force unbalance and was corrected by adjusting the TCV and Valve F. The movement resulted in the wearing away of the thrust bearing which was evident in the post-test tear down of the turbocompressor. However, the ability of the thrust bearing to withstand wear and continue to perform acceptably is an impressive display of the robustness of the thrust bearing. In future testing, the valve positions will be adjusted more aggressively to attempt to arrest the movement of the shaft faster and prevent wear on the thrust bearing.

Now that the turbocompressor has been operated successfully for an extended duration of time and the ability to control the thrust balance is better understood, another test is planned to operate at higher inlet temperatures and corresponding compressor discharge pressure.

CONCLUSIONS

The SNL Brayton Lab has completed 7 tests of a new turbocompressor from Peregrine Turbine Technologies that is designed to process sCO₂ for a CBC operating at 1382 F, 6222 psi, and 12.1 lbm/s (750 °C, 42.9 MPa, and 5.5 kg/s) generating 1.0 MWe at nominally 45% thermal efficiency based on LHV of natural gas. The testing has demonstrated the successful startup using the blowdown method, resolved thrust bearing issues, and has resolved the issues with the aft radial bearing. Testing will continue and will focus on exploring the performance of the turbocompressor over a wide range of conditions and for longer

durations of time. Looking ahead, Peregrine Turbine Technologies is currently constructing a complete 1MWe power system which will use the turbocompressor currently being tested at SNL. Through a Cooperative Research And Development Agreement (CRADA), SNL and PTT are working to develop a test plan for testing the 1MWe unit at PTT facilities in Maine.

NOMENCLATURE

BV	Binary Valve
CRADA	Cooperative Research and Development Agreement
DP	Development Platform
HTR	High Temperature Recuperator
LTR	Low Temperature Recuperator
NESL	Nuclear Energy Systems Laboratory
MPa	mega-Pascal
P	Pressure
psi	pounds per square inch
PTT	Peregrine Turbine Technologies
RD	Rupture Disk
sCO ₂	Supercritical Carbon Dioxide
SNL	Sandia National Laboratories
T	Temperature
TIT	Turbine Inlet Temperature
TCV	Turbine Control Valve
w	mass flow

ACKNOWLEDGEMENTS

Sandia National Laboratories is a multimission laboratory managed and operated by National Technology & Engineering Solutions of Sandia, LLC, a wholly owned subsidiary of Honeywell International Inc., for the U.S. Department of Energy's National Nuclear Security Administration under contract DE-NA0003525. SAND2019-4801 C

REFERENCES

- [1] Pash J, Stapp D. Test of a New Turbocompressor for Supercritical Carbon Dioxide Closed Brayton Cycles. ASME. Turbo Expo: Power for Land, Sea, and Air, Volume 9: Oil and Gas Applications; Supercritical CO₂ Power Cycles; Wind Energy
- [2] Dostal V. A Supercritical Carbon Dioxide Power Cycle for Next Generation Nuclear Reactors. Massachusetts Institute of Technology, 2004.
- [3] Fleming D, Conboy T, Rochau G, Holschuh T, Fuller R. Scaling Considerations for a Multi-Megawatt Class Supercritical CO₂ Brayton Cycle and Path Forward for Commercialization 2015:1-8
- [4] Carlson M, Conboy T, Pasch J, Fleming D. Scaling Considerations for SCO₂ cycle heat exchangers. Proc. ASME Turbo Expo, 2014, p. 1-5

SUPERCRITICAL CO₂ POWER CYCLE PROJECTS AT GTI

Scott Macadam, PhD*

Institute Engineer
Gas Technology Institute (GTI)
Woodland Hills, CA, USA
smacadam@gti.energy

William W. Follett

Program Manager
Gas Technology Institute (GTI)
Woodland Hills, CA, USA
wfollett@gti.energy

Michael Kutin

Program Manager
Gas Technology Institute (GTI)
Woodland Hills, CA, USA
mkutin@gti.energy

Ganesan Subbaraman, PhD

Institute Fellow
Gas Technology Institute (GTI)
Woodland Hills, CA, USA
gsubbaraman@gti.energy

ABSTRACT

GTI (Gas Technology Institute) is leading several sCO₂ power cycle technology development projects. Three distinct projects are highlighted in this paper: (1) The 10 MWe Supercritical Transformational Electric Power (STEP) Pilot; (2) An indirectly heated coal/biomass-based Oxy-fired Pressurized Fluidized Bed Combustor (Oxy-PFBC); and (3) A novel high pressure oxy-combustor for direct-fired sCO₂ power cycles. All three projects have significant systems engineering, optimization, operations analysis, controls, and partnership/ collaboration requirements.

In the STEP Pilot Project, a team led by GTI, Southwest Research Institute (SwRI), and General Electric Global Research, along with the University of Wisconsin and Natural Resources Canada, is executing a project to design, construct, commission, and operate an integrated and reconfigurable 10 MWe sCO₂ Pilot Plant Test Facility located at SwRI's San Antonio, Texas campus. This project is a significant step toward commercialization of sCO₂ cycle based power generation and will inform the performance, operability, and scale-up to commercial power plants. The pilot plant design, procurement, fabrication, and construction are ongoing. By the end of this six-year project, the operability of the sCO₂ power cycle will be demonstrated and documented starting with facility commissioning as a simple recuperated cycle configuration initially operating at a 500°C turbine inlet temperature and progressing to a recompression closed Brayton cycle technology (RCBC) configuration operating at 715°C.

In the indirectly-heated Oxy-PFBC system, sCO₂ is heated via a set of hermetically-sealed heat exchangers embedded in a footerbubbling bed of solid fuel (coal and/or biomass) particles that are combusted in a mixture of oxygen and recycled CO₂ at about 8 bar. The resulting compact combustor lowers the capital cost, enables higher plant efficiencies and reduces CO₂ capture costs.

In the sCO₂ oxy-combustor project, GTI is designing a novel high-pressure oxy-combustor for direct-fired sCO₂ cycles. The design concept, which is derived from rocket engine injectors, has potential to offer performance improvements over more traditional gas turbine-derived combustors.

INTRODUCTION

The unique properties of supercritical CO₂ offer intrinsic benefits over steam as a working fluid in closed and semi-closed cycles to absorb thermal energy, to be compressed, and to impart momentum to a turbine.

The temperature and pressure threshold conditions required for supercritical CO₂ are nominally 31°C and 7.4 MPa. These conditions are easily achieved, and above these conditions is a supercritical fluid with higher density and incompressibility as compared to steam or air which results in much smaller turbomachinery (factor 10:1) for a given energy production level [1]. Given these attributes, sCO₂ power cycles can offer several benefits [1,2,3,4]:

- Higher cycle efficiencies due to the unique fluid and thermodynamic properties of sCO₂

- Reduced emissions resulting from lower fuel usage
- Compact turbomachinery, resulting in lower cost, reduced plant size and footprint, and more rapid response to load transients
- Reduced water usage, including water-free capability in dry-cooling applications
- Heat source flexibility

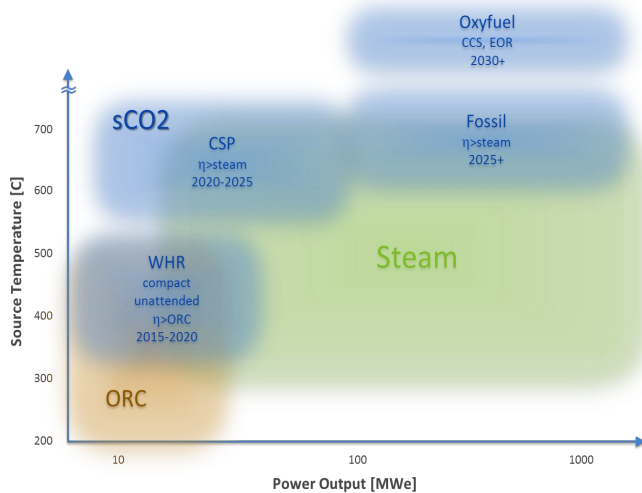


Figure 1 – sCO₂ Applications Map

These benefits can be achieved in a wide range of power applications including gas- and coal-fired power plants, bottoming cycles, industrial waste heat recovery, concentrated solar power, shipboard propulsion, biomass power plants, geothermal power, and nuclear power. Some of these applications are shown in Figure 1, which maps the sCO₂ application space relative to incumbent steam and Organic Rankine Cycle (ORC) options as a function of power output, and heat source temperature [2].

GTI (Gas Technology Institute) is leading several technology development projects that seek to advance the status of the sCO₂ power cycle technology across a range of potential applications. The STEP Project is a 10 MWe pilot demonstration indirect sCO₂ cycles that are directly applicable to WHR, CSP, and Fossil applications shown in Figure 1. The oxy-PFBC is a solid fossil fuel (and/or biomass) technology, while the direct cycle oxy-combustor project relates to Oxyfuel applications.

In leading these efforts, GTI is providing the necessary systems integration, optimization, and operability/controls required by all three projects. In addition, GTI is leading the partnership

coordination and development efforts required to successfully execute the projects.

More detailed descriptions of the three projects appear below.

1. STEP PROJECT

To facilitate the development and commercial deployment of the indirect sCO₂ cycle at elevated turbine inlet temperatures, pilot-scale testing is required to validate both component and system performance under realistic conditions at sufficient scale. The STEP (Supercritical Technology for Electric Power) project is a significant scale-up (to 10 MWe) of a fully integrated and functional electric power plant. Several technical risks and challenges will be mitigated in this project:

- Turbomachinery (aerodynamics, seals, durability)
- Recuperators (design, size, fabrication, durability)
- Materials (corrosion, creep, fatigue)
- System integration and operability (startup, transients, load following)

The STEP project will advance the state of the art for high temperature sCO₂ power cycle performance from Proof of Concept (TRL 3) to System Prototype validated in an operational system (TRL 7).

The objectives include:

- Demonstration of the operability of the Supercritical Carbon Dioxide (sCO₂) power cycle
- Verification of the performance of components including turbomachinery and recuperators
- Demonstration of the potential for producing a lower cost of electricity in relevant applications
- Demonstration of the potential for a thermodynamic cycle efficiency of greater than 50%
- Demonstration of a 700°C turbine inlet temperature or higher
- Validation of a recompression closed Brayton cycle (RCBC) configuration that can be used to evaluate system and components in steady state, transient, load following and limited endurance operation
- Reconfigurable facility to accommodate future testing:
 - System/cycle upgrades,
 - New cycle configurations such as cascade cycles and directly fired cycles,
 - New or upgraded components (i.e. turbomachinery, recuperators and heat exchangers)

Project Organization and Scope

GTI, SwRI, and GE-GR have formed a team to execute the STEP Demo project in line with program goals and objectives. This is a \$119 million private/public partnership with significant funding from the US Department of Energy (DOE). GTI is responsible for overall management of the project and is performing technology management, systems engineering, major component procurements, and will participate in testing in a test management role. SwRI is providing the host site for the test facility, and is responsible for the facility design engineering, and construction of test facility, and the supporting utility infrastructure. As host site, SwRI will manage the hardware installation and system assembly, perform facility commissioning, and execute test operations. GE-GR is providing the technical definition for the turbomachinery, the turbo-expander by GE-GR in collaboration with SwRI and the compression system by Baker Hughes, a GE Company (BHGE), as well as a first-of-a-kind sCO₂ turbine stop/control valve based on their line of valves for high-pressure steam turbines.

The combined team integrates the strengths of each individual organization and in aggregate, have completed or near to completing over two dozen sCO₂ technology related projects forming the building blocks for a successful STEP Demo [2,5,6,7,8,9,10].

A Joint Industry Program (JIP) team has also been formed to support the STEP Demo. This is an example of a consortium set up by GTI to provide both funding and guidance for the project. It includes a Steering Committee with the U.S. DOE, project partners GTI, GE, and SwRI, and funding members. Current members include Korea Electric Power Corporation (KEPCO), Southern Company Services, American Electric Power (AEP), and Natural Resources Canada (NRCAN). The Steering Committee ensures a collaboration process throughout the project life cycle.

The STEP Demo will be conducted in two major plant configuration phases as shown in Figures 2a and 2b. The initial system configuration will be the sCO₂ Simple Cycle, which comprises a single compressor, turbine, recuperator, and cooler.

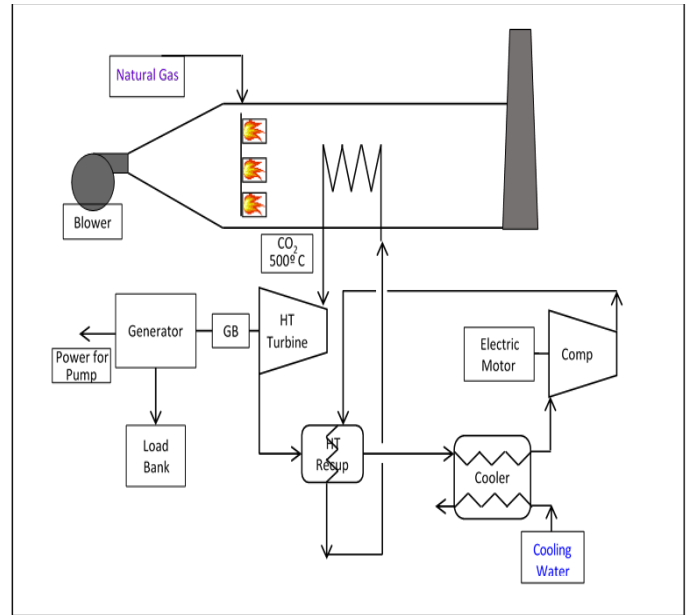


Figure 2a. Simple Cycle Configuration

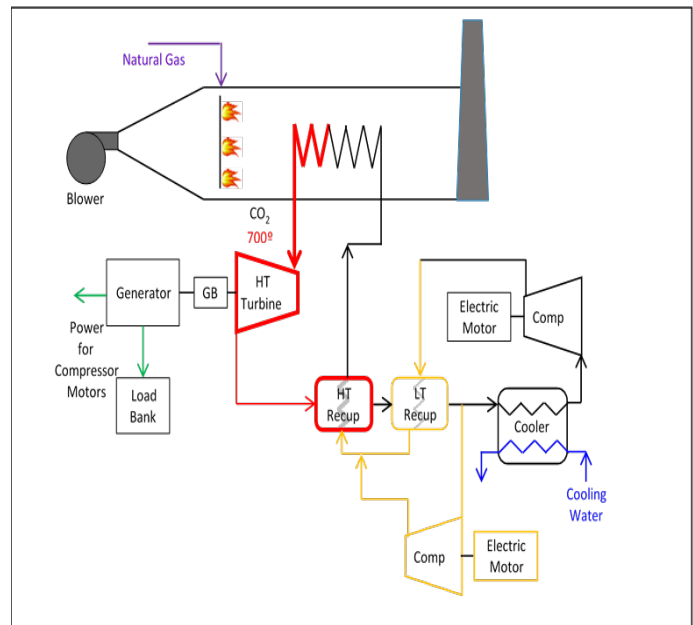


Figure 2b. Recompression Closed Brayton Cycle

A natural-gas fired heater that closely resembles a duct-fired Heat Recovery Steam Generator (HRSG) will supply heat. In Simple Cycle testing, sCO₂ fluid will be delivered to the turbine at approximately 500°C and 250 bar. This test configuration offers the shortest time to steady-state and transient data, while demonstrating controls and operability of the system, as well as performance validation of key components. In the second phase of testing, the system will be reconfigured to the Recompression Closed Brayton Cycle (RCBC). This is a high-efficiency cycle capable of achieving the >50% thermodynamic efficiency goal of the program. In this phase, a second (lower-temperature)

recuperator and a bypass compressor will be added. The turbine inlet temperature will be increased to the target level of 715°C.

Cycle Conditions - the different cases encompass the intended range of operating conditions for the facility. There are 2 Simple Cycle cases (max and min load) and 7 RCBC cases. The RCBC baseline case is the 10 MWe net cycle with a 715°C and 250 bar turbine inlet temperature and pressure condition. This RCBC baseline case sets the design requirements for the equipment, with the exception of the main cooler in which the simple cycle case was used. The remaining six RCBC cases are off-design conditions, varying sCO₂ cooler exit temperature, turbine inlet temperature, and the method with which the cycle power level is reduced.

Modeling – GTI has completed steady-state modeling of all design and off-design cases, for both Simple Cycle and RCBC testing. Information from this study have been used to develop specifications for key components. In addition, transient models developed by both GTI and GE-GR are tools to simulate start-up, trip, shutdown and transient cases.

The transient models provide support to the development of the controls system and test planning. Two different software tools are used to model transient behavior: Flownex and Numerical Propulsion System Simulation (NPSS). The main components of these models include main and bypass compressors, turbine, high and low temperature recuperators, cooler, heater, pipes and valves. The thermal mass and CO₂ fluid volume for each main component is based on vendor data or proven design practices. The validation of each main component with respect to steady state performance has been completed with vendor data. Due to

the availability of published experimental data, only the HTR component model has been validated with respect to transient performance.

Testing done in the STEP project will generate data to verify the steady state and transient modeling tool predictions and enable confidence in commercial system design. A snapshot of the Flownex simple cycle configuration model is shown in Figure 3.

The phased testing approach will address specific technical risks while minimizing added complexity at each phase. In this manner, programmatic risk will be minimized by reducing unnecessary complexity and applying lessons learned from prior phases to address technical challenges.

Schedule

The STEP project was launched in October 2016, and is a six-year effort with three distinct budget periods.

BUDGET PERIOD 1 - (ENDED FEBRUARY 2019)

Detailed Facility and Equipment Design (28 months)

- System analysis, P&IDs, Component Specs
- Design major equipment
- Procure heat source, cooling tower and long-lead items
- Materials and seal tests
- Start site construction

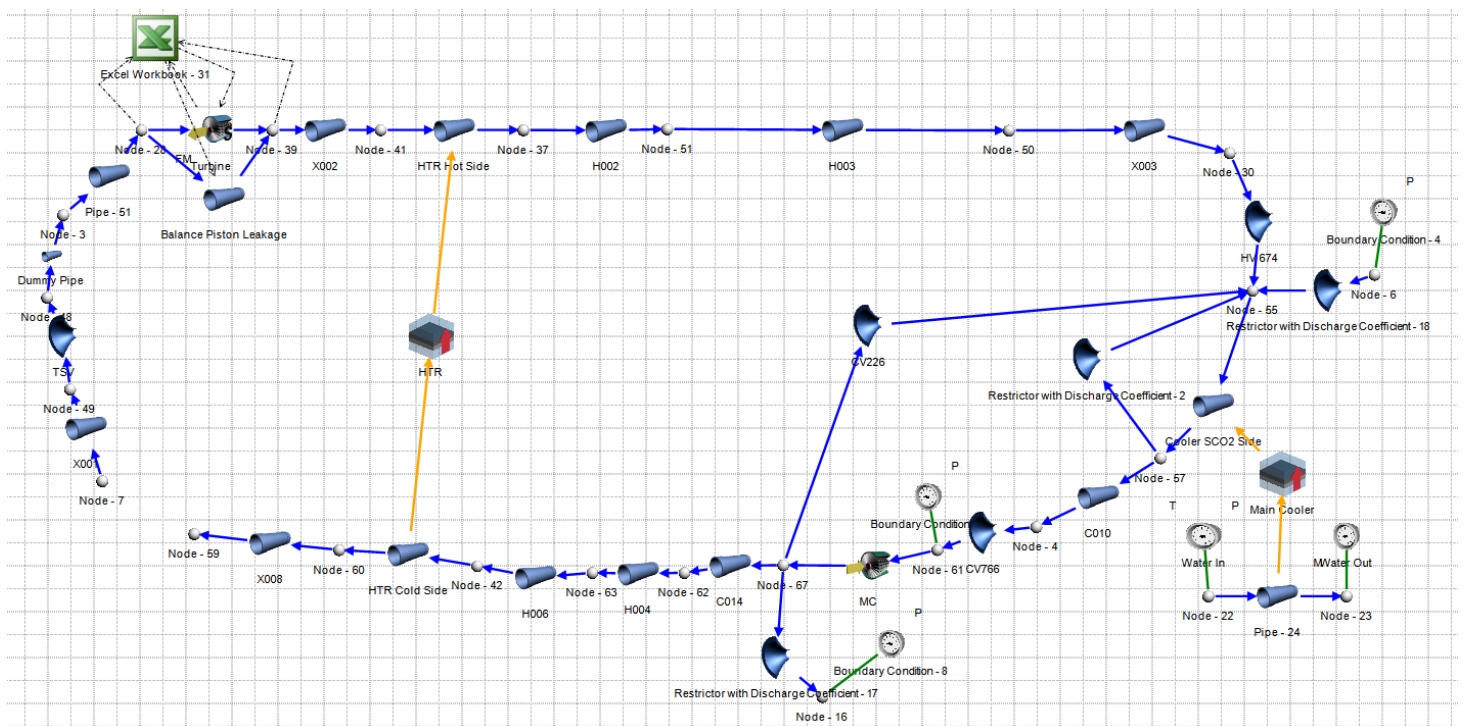


Figure 3– Flownex model concept

BUDGET PERIOD 2 - (ENDS JANUARY 2021)

Fabrication and Construction (24 months)

- Complete site construction and civil works
- Fabrication and installation of major equipment
- Commissioning and simple-cycle test

BUDGET PERIOD 3 - (ENDS SEPTEMBER 2022)

Facility Operation and Testing (20 months)

- Facility reconfiguration
- Test recompression cycle

Project Status

The project involves the design, procurement, and construction of components and their integration. This is supported by several technology development tasks involving the turbine, turbine stop valve, materials testing, and modeling.

Turbine Design - conceptual schematics of the 16 MW_e (gross) sCO₂ turbine, jointly designed by SwRI and GE, is shown in Figures 4 and 5. This effort advances an existing U.S. DOE-funded SunShot project in which SwRI and GE have fabricated and are currently testing a similar turbine [5, 9]. This SunShot project turbine was also designed for a turbine inlet temperature of 700°C but was successfully operated at reduced flow conditions, limiting power output to 1 MWe. The SunShot turbine is a 10 MWe frame size, the same as STEP but with a scaled gas path to 1 MWe to meet the existing flow loop capacity at SwRI. Despite the power reduction, with the same inlet temperature and scale, the SunShot turbine is risk reducing key technology concerns. Figure 4 is the conceptual view of the initial STEP turbine case design and associated stand, which was based on the prior Sunshot turbine design. Figure 5 is the current STEP turbine configuration, which incorporates advanced aerodynamics to reduce stage count from 4 to 3 and thus allows and even more compact turbine.

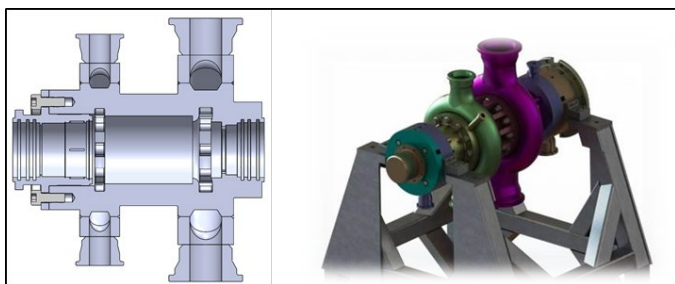


Figure 4 - Conceptual design of 10 MWe STEP sCO₂ Turbine

The STEP turbine will offer improvements over the SunShot turbine, including: increased casing and rotor life (100,000 hrs. vs 20,000 hrs.), shear ring retention rather than bolts, couplings on both shaft ends, and improved aerodynamic performance with an optimized volute flow area. The thermal management region will be enhanced based on lessons learned in the SunShot testing [11] and design enhancements developed under a related ARPA-E program [12]. Current STEP turbine design activities are focused on torsional train dynamics, rotor flow path preliminary design, and flow path mechanical and aeromechanical integrity.

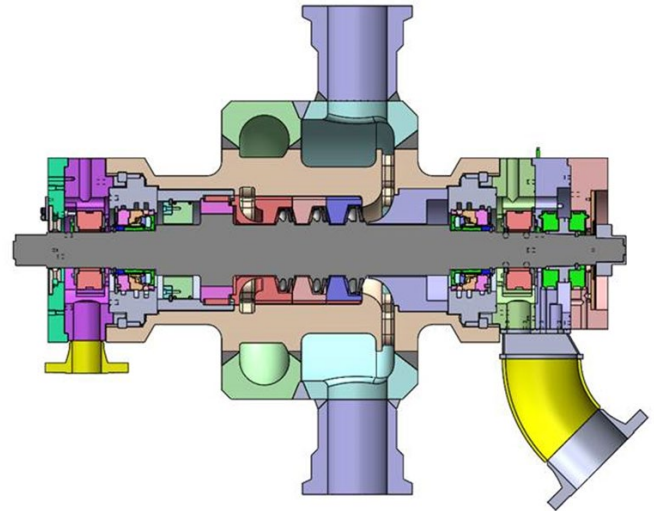


Figure 5 - 10 MWe STEP sCO₂ Turbine

Turbine Stop and Control Valve - GE has completed the design of the turbine control/stop valve that will be placed upstream of the turbine. The design is based on the existing commercial product line of steam valves, but with modifications to accommodate sCO₂ fluid and high operating temperatures, including novel stem seal materials (Figure 6). Specifically, the valve material leverages efforts under advanced ultra supercritical (AUSC) steam power development programs for industry leading high temperature, high-pressure materials and components [13, 14, 16]



Figure 6 – Turbine Stop Valve and Stem Testing at GE-GR

Compressor - The compressor is being provided by GE Oil & Gas Baker Hughes (Nuovo Pignone), and leverages an existing commercial product line as well as work undertaken in the DOE-funded APOLLO program [15]. The APOLLO program is risk reducing the compressor performance of a real gas near its critical point. The APOLLO program has designed and is currently constructing a STEP-scale compression system to validate the enhanced real gas capable design tools over the wide operating range of the RCBC cycle. The validation testing occurred in the first half of 2019, providing guidance to the BHGE team for inclusion into the STEP compression system.

Facility Design - The facility is at a greenfield site on the SwRI campus in San Antonio, Texas. SwRI has completed the building layout and general arrangement plan (Figures 7 & 8), along with initial analyses of the interconnecting piping system [16]. The Environmental Assessment was completed by an external specialist and has been approved by the DOE. Site groundbreaking took place in October 2018.

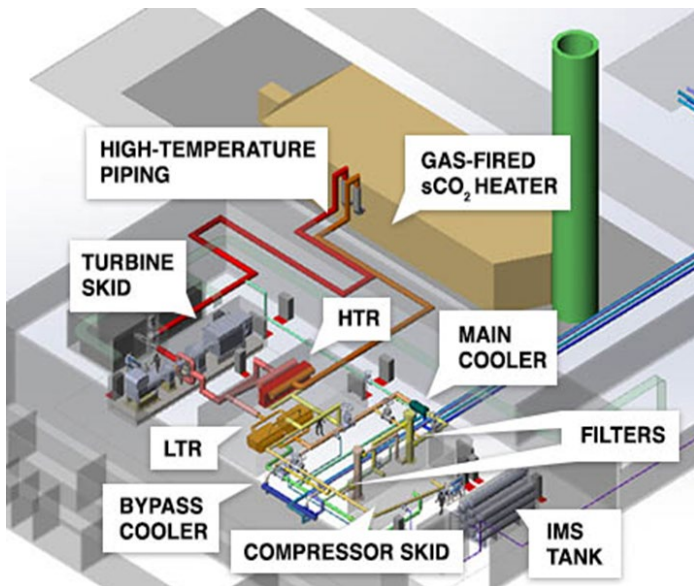


Figure 7 – Equipment general arrangement

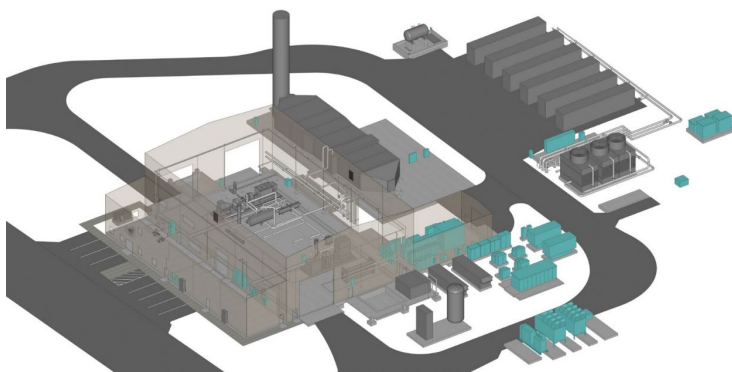


Figure 8 – Building and Site arrangement

Other Key Equipment - GTI has procured major hardware including the heater, compressor, recuperators, and cooling tower [16]. Optimus Industries LLC is under contract for the heater. It is a natural gas fired unit with a tube bundle and high temperature headers and piping fabricated out of Inconel 740H to accommodate the $>700^{\circ}\text{C}$, 250 bar sCO_2 conditions. Its arrangement is based upon a duct-fired Heat Recovery Steam Generator (HRSG) (Figure 9). The design is completed and is in production.

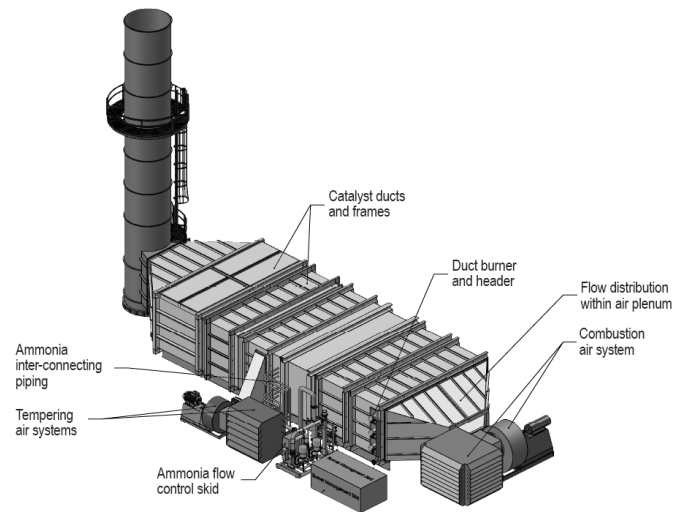


Figure 9 - Gas Fired Heater with 740H material for 715°C sCO_2

Recuperators - The heat exchangers include the High-Temperature Recuperator (HTR), Low-Temperature Recuperator (LTR), and coolers. All units are to be compact heat exchangers with high surface area/volume ratios. The HTR, LTR, and main cooler have been ordered from Heatric who will produce PCHE-type heat exchangers with thermal duties ranging between 13-49 MWth.

2. OXY-FIRED PRESSURIZED FLUIDIZED BED COMBUSTOR

GTI's Oxy-fired Pressurized Fluidized Bed Combustor (Oxy PFBC) is a highly integrated, innovative system designed to lower the capital and operating cost of clean power production. Pressurized combustion in oxygen eliminates the presence of nitrogen and other constituents of air, minimizing the generation of pollutants and enabling the economic capture of byproduct CO_2 . Oxy-PFBC is fuel-flexible, suitable for converting coal, petcoke, biomass or coal biomass blends into clean power.

GTI's Oxy-PFBC system was designed to minimize both the cost of the hardware and the levelized cost of electricity. It can be incorporated with a sCO_2 RCBC cycle for higher efficiency. One important feature of the Oxy-PFBC is the high power density combustor, which can eliminate hundreds of millions of dollars from the construction costs for a commercial scale

power plant. The compactness of the combustor is largely enabled by two key features: high pressure combustion which shrinks the reactor size, and heat exchanger tubes submerged in the fluidized bed which significantly reduces the heat exchanger size. Another key to reducing system cost is the CO₂ purification unit (CPU) which also operates at pressure to reduce size and cost. The combination of air separation unit and CPU is substantially less expensive than comparable amine-based post combustion capture clean up equipment.

Key benefits of the Oxy-PFBC technology:

- Pressurized for smaller, less costly combustor (1/3 the size, 1/2 the cost)
- Can be coupled with sCO₂ Brayton cycles for high plant efficiency
- Up to 98% CO₂ capture with coal, negative CO₂ emissions with biomass blends
- Produces purified CO₂ for chemical production or oil recovery
- Can produce steam for district heating or heavy oil recovery

GTI's Oxy-PFBC technology successfully completed component testing, and a 1 MW_{th} pilot scale plant was installed at the Natural Resources Canada facilities in Ottawa where it was tested in 2017. It also included a CO₂ Purification Unit (CPU). The 1 MW_{th} pilot testing achieved performance goals with the exception of carbon conversion. The combustor achieved oxy-combustion at the full target pressure of 8 bar.

Two key combustor performance goals that were achieved include exceeding the target sulfur capture in the combustor as well as exceeding the acid dewpoint target at full operating pressure. This validated assumptions about the pressures that can be achieved without acid gas condensation and the associated corrosion risks. The ability to achieve target operating pressures supports combustor cost assumptions. In addition, the CO₂ processing unit (CPU), demonstrated a new technology, the deoxidation (DeOxo) reactor. The CPU achieved all of its performance targets, while the DeOxo reactor demonstrated the ability to achieve 100 ppm or less of oxygen in the flue gas stream to meet CO₂ pipeline specs. The combustor experienced issues with numerous temperature sensors that were buried and insulated by bed material. This led to anomalous operating conditions which caused lower than expected carbon conversion and hardware damage.

The vision for the Oxy-PFBC and sCO₂ technologies is to combine them into a high efficiency, system for low cost carbon capture. The Oxy-PFBC and sCO₂ technologies are currently being developed independently, with a future strategy of combining and demonstrating them as a synergistic system. This is illustrated in the integrated roadmap shown in Figure 10. GTI's Oxy-PFBC and sCO₂ technologies both have multiple active programs continuing to advance the maturity of each in anticipation of a combined future demonstration.

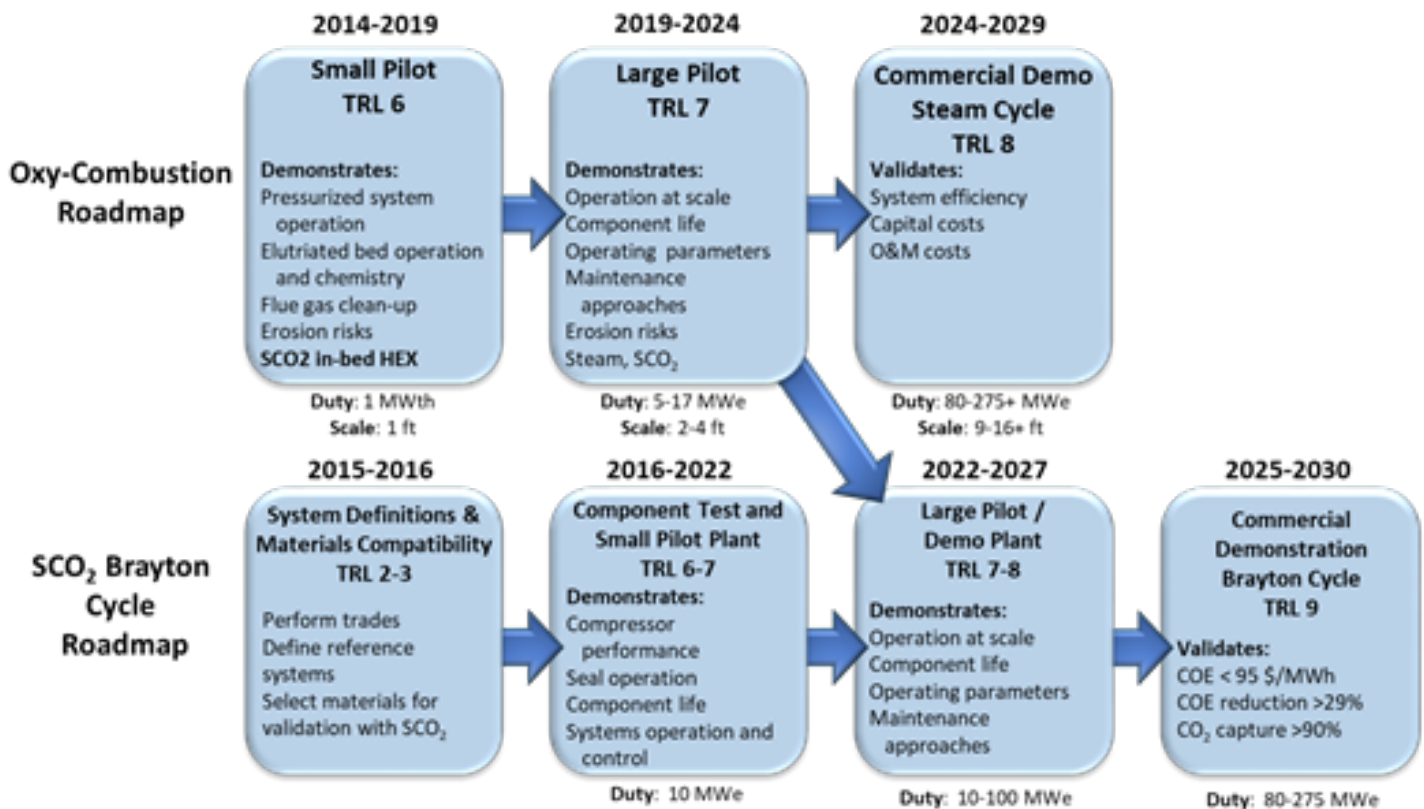


Figure 10 – Integrated oxy-PFBC and sCO₂ roadmap

3. OXY-COMBUSTOR FOR DIRECT sCO₂ CYCLES

GTI is also developing technology for direct-fired sCO₂ cycle applications. The direct sCO₂ cycle, shown in Figure 11, is characterized by high temperature and pressure turbomachinery that operates with sCO₂ working fluid that is heated above 1150°C at 300 bar in a pressurized oxy-combustor.

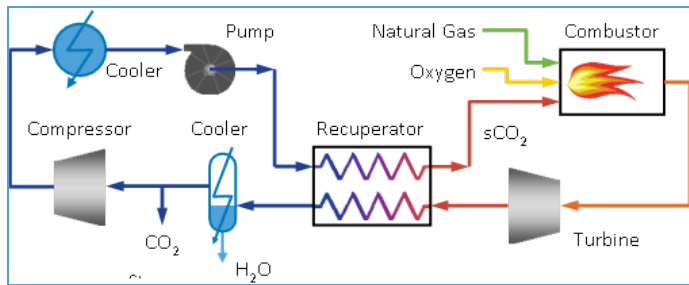


Figure 11 – Direct-fired sCO₂ cycle

The process conditions enable net cycle efficiencies from natural gas of over 50% (LHV basis) with near 100% CO₂ capture [17]. However, sensitivity analyses have shown that the overall cycle performance is dependent on combustor performance. For example, any products of incomplete combustion (CO, unburnt hydrocarbons) and excess O₂ degrade cycle efficiency [17].

This has highlighted a need for a high efficiency sCO₂ oxy-combustor that would generate low products of incomplete combustion at low excess O₂ levels. To address this need, GTI is leveraging its rocket engine combustor expertise and experience to design a novel sCO₂ combustor. This expertise was obtained with GTI's acquisition of Aerojet-Rocketdyne's energy division in 2015.

GTI has developed a conceptual design and is currently exploring opportunities with partners to further develop and test a prototype combustor.

SUMMARY

Supercritical CO₂ power cycles promise substantial cost, emissions, and operational benefits that apply to a wide range of power applications including coal, natural gas, waste heat, concentrated solar, biomass, geothermal, nuclear, and shipboard propulsion. GTI is engaged in several projects that seek to advance the state of the art of the technology.

Firstly, the STEP 10MWe program will demonstrate indirect fired sCO₂ cycles to known available materials limits (T>700C) in a fully integrated 10 WMe electric generating pilot. The project will enable the progression of technology readiness level from TRL of 3 level to a TRL of 7 and subsequent commercialization. The project is well underway. A strong team

is in place and is executing smoothly. GTI has also developed the oxy-PFBC technology that burns coal and/or biomass under pressurized oxy-combustion conditions to enable low-cost CO₂ capture. The technology is compatible with high temperature RCBC sCO₂ indirect cycles. This combination of high sCO₂ cycle efficiencies and relatively low oxy-PFBC capex has potential to lower levelized cost of electricity for power plants with near-zero CO₂ emissions. GTI is also developing a novel combustor for direct-fired sCO₂ cycles. This combustor, based on rocket engine concepts, has potential to improve combustor performance, improving overall cycle efficiencies for direct cycles.

A common theme between all three activities is the significant systems engineering, optimization, operations analysis, controls, and partnership/collaboration efforts required to successfully execute the projects.

REFERENCES

- [1] K. Brun, P. Friedman, R. Dennis, *Fundamentals and Applications of Supercritical Carbon Dioxide (sCO₂) Based Power Cycles*, Elsevier Ltd, 2017
- [2] D. Hofer, "Phased Development of a High Temperature sCO₂ Power Cycle Pilot Test Facility", 5th International Symposium Supercritical CO₂ Power Cycles, March 28-31, 2016, San Antonio, TX.
- [3] T. Held, "Transient Modeling of a Supercritical CO₂ Power Cycle and Comparison with Test Data", GT2017-63279, Proceedings of ASME Turbo Expo 2017: Turbomachinery Technical Conference and Exposition, June 26-30, 2017, Charlotte, NC
- [4] S. Patel, "Pioneering Zero-Emission Natural Gas Power Cycle Achieves First-Fire", Power Magazine, May 30, 2018
- [5] C. Kalra, D. Hofer, E. Sevincer, J. Moore and K. Brun, "Development of High Efficiency Hot Gas Turbo-Expander for Optimized CSP sCO₂ Power Block Operation", in 4th International sCO₂ Power Cycles Symposium, Pittsburgh, PA, 2014.
- [6] R.A. Bidkar, G. Musgrove, M. Day, C.D. Kulhanek, T. Allison, A.M. Peter, D. Hofer and J. Moore, "Conceptual Designs of 50-450 MWe Supercritical CO₂ Turbomachinery Trains for Power Generation from Coal. Part 2 Compressors", in The 5th International Symposium – Supercritical CO₂ Power Cycles, San Antonio, TX, 2016
- [7] R.A. Bidkar, E. Sevincer, J. Wang, A. Thatte, A. Mann, M. Peter, G. Musgrove, T. Allison, J. Moore, "Low Leakage Shaft-End Seals for Utility-Scale Supercritical CO₂ Turboexpanders",

Journal of Engineering for Gas Turbines and Power, ASME, 2017

[8] <http://energy.gov/eere/sunshot/concentrating-solar-power>

[9] J. Moore, et al, “Development of a 1 MWe Supercritical CO₂ Brayton Cycle Test Loop”, 4th International sCO₂ Power Cycles Symposium, Pittsburgh, PA, 2014

[10] DE-EE-0005804 “Development of a High Efficiency Hot Gas Turbo-Expander and Low Cost Heat Exchangers for the Optimized CSP Supercritical CO₂ Operation” DoE SunShot Award

[11] Moore, J.J., Cich, S., Day-Towler, M., Hofer, D., Mortzheim, J., “Testing of a 10 MWe Supercritical CO₂ Turbine” 47th Turbomachinery & 34th Pump Symposia, September 17-20, 2018.

[12] DE-AR-0000467 “Electrochemical Energy Storage with a Multiphase Transcritical CO₂ Cycle” DoE Advanced Research Projects Award.

[13] Purgert, R. et al, “Materials for Advanced Ultrasupercritical Steam Turbines”, Final Technical Report, DOE Cooperative Agreement: DE-FE0000234, Dec. 2015.

[14] J. Marion, F. Kluger, P.Sell, A. Skea, “Advanced Ultra-Supercritical Steam Power Plants”, Power GEN ASIA 2014, KLCC, Kuala Lumpur, Malaysia, September, 2014

[15] DE-EE-0007109 “Compression System Design and Testing for sCO₂ CSP Operation” DoE Concentrating Solar Power Advanced Projects Offering Low LCoE Opportunities (APOLLO) Award.

[16] J. Marion, M. Kutin, A. McClung, J. Mortzheim, and R. Ames, “The STEP 10 MWe sCO₂ Pilot Plant Demonstration”, GT2019-91917, Proceedings of ASME Turbo Expo 2019: Turbomachinery Technical Conference and Exposition, June 17-21, 2019, Phoenix, AZ

[17] Weiland N. et al, “Preliminary Cost and Performance Results for a Natural Gas-Fired Direct sCO₂ Power Plant”, 6th International sCO₂ Power Cycles Symposium, Pittsburgh, PA, 2018

THERMOECONOMIC MODELING AND ANALYSIS OF sCO₂ BRAYTON CYCLES

Mathias Penkuhn*

Technische Universität Berlin
Institute for Energy Engineering
Berlin, Germany
Email: mathias.penkuhn@tu-berlin.de

George Tsatsaronis*

Technische Universität Berlin
Institute for Energy Engineering
Berlin, Germany
Email: georgios.tsatsaronis@tu-berlin.de

ABSTRACT

Supercritical CO₂ (sCO₂) power cycles provide the possibility to significantly improve power generation from fossil fuels and renewable sources considering thermodynamic efficiency, economics, and flexibility. In the recent years, the increased attention for this technology led to numerous efforts to improve cycle efficiency considering several potential applications. Nevertheless, more complex cycle designs which provide the opportunity to increase the cycle efficiency have to be economically justified. However, due to the current state of research and development, and the prospective commercialization in the future, no final conclusions in terms of cycle design can be made because reliable economic data are not available.

The scope of the present study is the analysis and comparison of several generic sCO₂ Brayton cycle designs for power generation in terms of their economic feasibility. Due to the large number of highly uncertain or nonexistent economic parameters in case of sCO₂ Brayton cycles, an approach is used that reformulates the economic problem by introducing dimensionless numbers and exploiting thermo-economic similitude. It provides a first possibility to analyze the economic impact of employing different cycle improvement options like reheating, recompression, and intercooling using the simple recuperated cycle design as a reference. Finally, the possibility to further generalize the findings is discussed.

INTRODUCTION

Over the last decade, the application of supercritical CO₂ (sCO₂) for power generation has received substantial interest. The prospects of a high-efficiency, low-emission technology that at the same time features favorable economics and also provides higher operational flexibility [1] is driving extensive research and development activities worldwide.

Potential adoption of sCO₂ technology includes a variety of different applications [1–3], ranging from fossil-fuel [4–6], nuclear [7–9], and concentrated-solar [10–13] to waste-heat [14–16] based power generation. In contrast to conventional water-steam-based technologies [17], sCO₂ power cycles are generally characterized

by high-temperatures, high-pressure but low-pressure ratio, and highly-recuperative designs [18]. This leads to higher efficiencies in comparison to water-steam based power cycles operating at comparable conditions, and provides the possibility of considerably smaller turbomachinery [1].

The research activities have been directed to the identification of thermodynamically efficient power cycle designs. The compilation of Crespi et al. [18] shows a large variety of potential direct and indirect sCO₂ cycles for power generation. Some cycle designs, e.g., the recompression cycle which uses a split-compression design, and the Allam cycle have been identified as particularly promising designs. However, the most important question regarding the economic feasibility remains largely unanswered until today. Only limited data for economic studies [6, 16, 19, 20] is available and can be regarded as of highly uncertain quality. Therefore, despite the large amount of information on thermodynamically highly-efficient sCO₂ power cycle designs, it is not clear which designs actually bear the potential for long-term commercialization.

Based on experience, it is well-known that higher-efficiencies are often achieved by designing more complex systems incorporating established improvement options. However, this results in the conflicting aspects considering the demand for achieving high-efficiency at superior economic performance. In the present study on indirect (closed-cycle) sCO₂ power cycles considering different improvement options, the focus is put on developing a robust approach to analyze the different cycle designs regarding their thermo-economic potential. This is achieved by reducing the number of uncertain parameters using similitude theory. Based on the used approach, different cycles are compared and their potential application areas for high-efficiency and economically viable power generation are discussed.

SYSTEM DESCRIPTION

The recent gain in interest concerning the application of sCO₂ cycles for power generation resulted in the proposition of numerous different cycle designs [18]. The objective of most

* corresponding author(s)

studies on sCO₂ power cycles was the achievement of higher thermodynamic efficiencies. For that, a large subset of potential designs were derived using well-known principles for cycle improvement, e.g., intercooled compression (intercooling), reheating, and split-recompression which is also simply known as recompression. Therefore, the present study concentrates on the thermodynamic and economic improvement potential of the simple recuperated sCO₂ Brayton cycle considering the integration of the three different improvement options mentioned before.

Cycle Design

With a large set of possible sCO₂ power cycle designs being suggested in the literature [18], it is advantageous to use a hierarchical design approach to identify and order each cycle design according to its features. The early works of Gokhshtein and Dekhtyarev [21–23], Angelino [24, 25] and Feher [26] have identified the main features of a potential sCO₂ power cycle. Due to the particular properties of CO₂ which are different from that of water (H₂O), sCO₂ cycles are found to be configurations that exhibit a high-temperature, high-pressure but low-pressure ratio, and highly recuperative characteristic. The minimum configuration of such a power cycle consists of a compressor, turbine, heat exchangers for heat supply and removal, and a recuperator connecting the high-pressure and low-pressure parts. Heat recuperation is necessary and an advantageous option for improving the thermodynamic efficiency because of the low-pressure ratio with the turbine outlet temperature still being high and far away from the critical point of CO₂ (30.98 °C, 73.77 bar) around which the heat removal is carried out.

Based on the given considerations, a systematic sCO₂ power cycle design hierarchy is used that is shown in Figure 1. The reference design is the sCO₂ power cycle with recuperation, termed as Design (1), as depicted in Figure 2. This cycle is considered as the reference case with a single cooler for heat removal (E1), a recuperator (E2), and the single high-temperature heater (E3). Furthermore, the main compressor (C1A) which is connected by a shaft to the turbine (M1A) and the electric generator (G1).

The first improvement option investigated in this study, considers the integration of a reheating train (Design 2) which is used for increasing the specific expansion work, additionally using a high-temperature heater (E3B) and an expansion turbine (M1B). Another improvement option analyzed in this study is the integration of an intercooled compression train (Design 3) for minimizing the specific compression work requirement by splitting the main compressor into two sequential units (C1A, C1B) which are connected via the intercooler (E4). The last improvement option is the recompression option (Design 4) where the low-pressure stream exiting the recuperator is split into two streams bypassing the main compressor C1A using another compressor (C1C). Furthermore, this design requires the recuperator E2 to be split into a low-temperature and high-temperature thus enabling the transfer of a larger amount of specific heat in the recuperator for compensating the differences in sCO₂ properties.

For potentially achieving even higher efficiency sCO₂ power cycle designs, it is possible to further combine any improvement option with each other. However, such cycles exhibit an even higher complexity resulting in presumably more expensive designs.

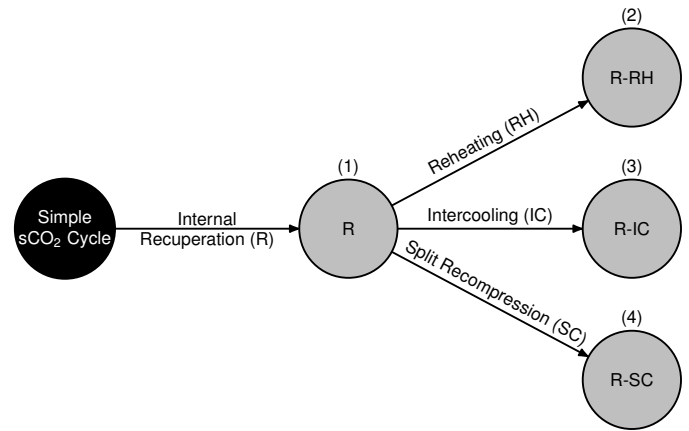


Figure 1: Hierarchical design of power cycles with different potential improvement options.

Cycle Simulation and Design Parameters

The comparison and benchmarking of different technologies, designs and options for power generation requires the use of best-practice guidelines, representing heuristics, and already available process data for modeling and simulation purposes. For the present study, AspenPlus is used for modeling and simulation. The thermodynamic properties are obtained using REFPROP [27, 28].

The different sCO₂ power cycle designs (Figure 2) are modeled and simulated using potentially viable design parameters according to [29], and [30]. Based on the full set of parameters given in Table 1, the main characteristics of the cycles of the present study are a compressor inlet pressure of 75 bar and an inlet temperature of 32 °C. On the other hand, the turbine inlet is specified by a pressure of 250 bar and a temperature of 600 °C. The size of the recuperator is limited either by a maximum effectiveness of 0.9 or a maximum outlet temperature of 400 °C on the cold side whichever applies to the specific cycle design. For the supply and removal of heat, models of generic heat sources and sinks are used that differ by their inlet and outlet temperatures, respectively.

METHODOLOGY

The present study employs conventional thermodynamic and economic methodologies for analyzing the different cycles. For conducting thermo-economic analyses both methodologies are combined which enables the evaluation of each cycles' performance considering the general conflict between thermodynamic and economic performance.

Thermodynamic Analysis

According to the general convention for quantifying the efficiency of single product power cycles, the overall thermodynamic efficiency η is defined as the ratio of net power generated and heat supplied as fuel to the cycle [17].

$$\eta = \frac{\dot{W}_{net}}{\dot{Q}_F} \quad (1)$$

It is however important to notice that a suitable framework [31, 32] for benchmarking different power cycles is required,

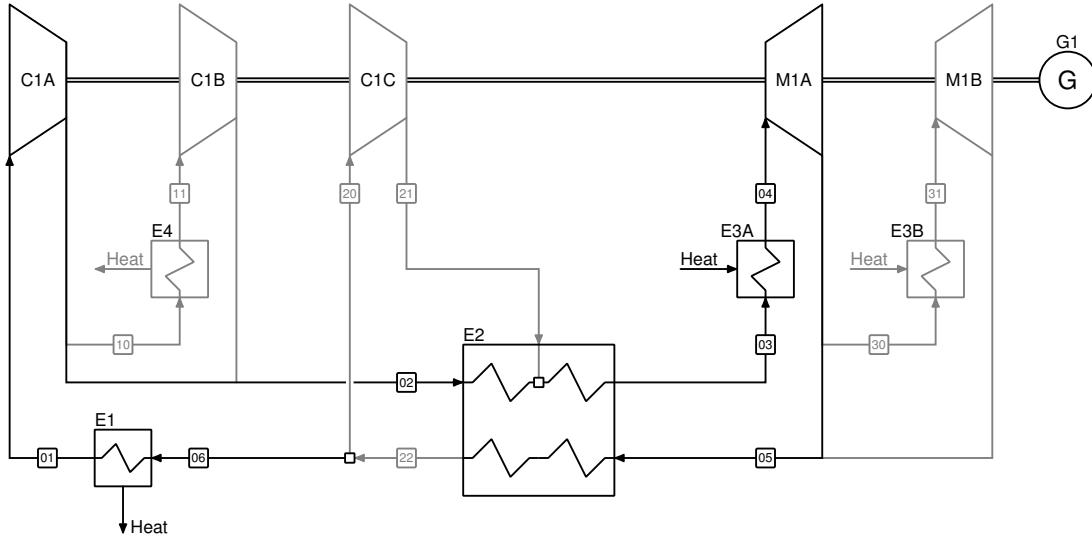


Figure 2: Flowsheet with superstructure showing all improvement options (in gray) of the simulated power cycles.

in particular regarding the site-specific environment conditions determining the heat sink temperature and characterizing the potential technology.

Economic Analysis

The evaluation, comparison, and cost optimization [33] of any energy-conversion system requires the comparison of annually recurrent monetary values, being related to capital investment, fuel costs, and expenses for operation and maintenance. As each of these cost components can vary significantly within the system's economic life, levelized values are used in the evaluation for the sake of comparability.

In the literature, different methodologies [34, 35] are found, sometimes with significant differences. The present study uses the total revenue requirement method (TRR method) [33] which employs well-established procedures. Based on data for the total capital investment and proper assumptions regarding economic, financial, and operating parameters, the systems economic performance can be determined.

In case of sCO₂ power cycles, the determination of total capital investment based on capital cost estimation for the cycle equipment is lacking substantial data. Therefore, it is only possible to use some generalized baseline data and to scale the capital cost C accordingly using a reference value, and a suitable cost attribute X , e.g., compressor and turbine power or heat exchanger area, and a scaling exponent n .

$$C = C_{\text{ref}} \cdot \left(\frac{X}{X_{\text{ref}}} \right)^n \quad (2)$$

In the literature, scaling exponents for different system components are available [33, 36]. Furthermore, in case of design studies, only capital cost data from prior estimates and systems is available which requires updating using cost indices [33].

Based on the total capital investment TCI , the expenses for fuel FC , and operation and maintenance OMC , it is possible to calculate the levelized total revenue requirement including factors

for discounting (CRF) and escalation ($CELF$) using an appropriate interest rate i_{eff} and constant escalation rates k during the system's economic life a .

$$TRR = CC_L + FC_L + OMC_L \quad (3a)$$

$$CC_L = CRF \cdot TCI = \frac{i_{\text{eff}} (1 + i_{\text{eff}})^a}{(1 + i_{\text{eff}})^a - 1} TCI \quad (3b)$$

$$FC_L = CELF \cdot FC_{\text{ref}} = \frac{k_{FC} (1 - k_{FC}^a)}{(1 - k_{FC})} CRF \cdot FC_{\text{ref}} \quad (3c)$$

$$OMC_L = CELF \cdot OMC_{\text{ref}} \quad (3d)$$

$$= \frac{k_{OMC} (1 - k_{OMC}^a)}{(1 - k_{OMC})} CRF \cdot OMC_{\text{ref}} \quad (3e)$$

Based on the overall system's economic parameters, it is possible to associate each system component with a cost rate \dot{Z}_k based on the system's annual time of full load operation τ and its share in capital investments x_k .

$$\dot{Z}_k = \dot{Z}_k^{\text{CI}} + \dot{Z}_k^{\text{OM}} \quad (4a)$$

$$\dot{Z}_k^{\text{CI}} = x_k \cdot \frac{CC_L}{\tau} \quad (4b)$$

$$\dot{Z}_k^{\text{OM}} = x_k \cdot \frac{OMC_L}{\tau} \quad (4c)$$

Employing the same considerations, it is also possible to quantify the cost rates for input streams with their respective cost rates \dot{C}_F .

$$\dot{C}_F = \frac{FC_L}{\tau} \quad (5)$$

The levelized cost rates are suitable input data for conducting a thermoeconomic analysis on the system's component level.

Thermoeconomic Analysis

For a conventional thermoeconomic analysis, the information provided by the economic analysis is used on the overall system

Table 1: Simulation parameters used for the analysis the sCO₂ power cycles based on literature data for benchmarking given by Weiland and Thimsen [29], and Crespi et al. [30].

Unit ID	Parameter	Value
M1 A/B	Turbine Inlet Temperature	600 °C
M1 A	Turbine Inlet Pressure	250 bar
M1 A/B	Turbine Isentropic Efficiency	90 %
M1 A/B	Turbine Mechanical Efficiency	99 %
C1 A/B/C	Compressor Inlet Pressure	75 bar
C1 A	Precompressor Inlet Pressure	50 bar
C1 A/B/C	Compressor Isentropic Efficiency	85 %
C1 A/B/C	Compressor Mechanical Efficiency	99 %
G1	Electric Generator Efficiency	99 %
E1, E4	Cooler Outlet Temperature	32 °C
E1, E4	Cooler Pressure Drop	15 kPa
E2	Maximum Recuperator Cold Side Outlet Temperature	400 °C
E2	Maximum Recuperator Effectiveness	0.9
E2	Recuperator Hot-Side Pressure Drop	280 kPa
E2	Recuperator Cold-Side Pressure Drop	140 kPa
E3 A/B	Primary Heat Exchanger Pressure Drop	200 kPa
E3 A/B	Primary Heat Exchanger Minimum Temperature Difference	50 K

level to relate input streams representing fuels and auxiliary streams with output streams associated with useful products.

In the present study, cost rates associated with heat and power streams are expressed as the product of their thermodynamic quantities for heat \dot{Q} and power \dot{W} , and their associated specific cost c per unit of energy.

$$\dot{C}_q = c_q \cdot \dot{Q} \quad (6a)$$

$$\dot{C}_w = c_w \cdot \dot{W} \quad (6b)$$

Considering the operation of the overall system at steady state, the cost balance is used to relate input and output streams expressing the total cost of the output streams as the sum of the input streams and cost streams associated with the monetary expenses.

$$\sum_{i=1}^n \dot{C}_{i,out} = \sum_{i=1}^n \dot{C}_{i,out} + \sum_{k=1}^n \dot{Z}_k \quad (7)$$

Based on the operation of a sCO₂ power cycle, Equation (7) contains terms for monetary expenditures related to the different system components \dot{Z} , for the energy streams related to heat supplied $\dot{C}_{q,1}$ and heat removed $\dot{C}_{q,2}$, i.e, coolant cost, and the cost rate \dot{C}_w for the net power output.

$$\dot{C}_w = \dot{Z} + \dot{C}_{q,1} + \dot{C}_{q,2} \quad (8)$$

Assuming that the coolant is available at negligible cost, Equation (8) can be simplified accordingly.

$$\dot{C}_w = \dot{Z} + \dot{C}_{q,1} \quad (9)$$

By associating the cost rates of heat supply and net power output in terms of fuel and product, the cost of electricity of the sCO₂

power cycle is generally related to the monetary expenses and its operation costs.

$$\dot{C}_P = \dot{Z} + \dot{C}_F \quad (10)$$

By splitting the cost rates of the net power output and the heat supply into its constituent terms, the specific leveled cost of electricity $c_{w,P}$ can be calculated [33].

$$c_{w,P} = \frac{\dot{Z}}{\dot{W}_{net}} + c_{q,F} \frac{\dot{Q}_F}{\dot{W}_{net}} \quad (11)$$

Based on the presented common procedure for economic and thermoeconomic analyses, the economic analysis is particularly subject to a large amount of highly uncertain data. This involves the cost estimation of the different components as well as the financial project parameters. For the analysis of sCO₂ cycle designs this is even more important due to of the low technology readiness level and the highly experimental nature of such technology.

However, in order to compare different sCO₂ power cycle designs, it is possible to employ similitude theory [37] as all the different cycles share a significant amount of common features. By choosing a reference cycle design, the different thermoeconomic parameters are effectively put into relation to each other and can be easily compared. By introducing the operating and economic characteristics of the reference cycle design, Equation (11) can be rewritten as:

$$\dot{C}_{w,P} \frac{\dot{C}_{w,P,ref}}{\dot{C}_{w,P,ref}} = \dot{Z} \frac{\dot{Z}_{ref}}{\dot{Z}_{ref}} + \dot{C}_{q,F} \frac{\dot{C}_{q,F,ref}}{\dot{C}_{q,F,ref}} \quad (12)$$

By reordering and applying of Equation (10), the following relationship is obtained:

$$\frac{\dot{C}_{w,P}}{\dot{C}_{w,P,ref}} = \underbrace{\frac{\dot{Z}_{ref}}{\dot{Z}_{ref} + \dot{C}_{q,F,ref}}}_{f} \frac{\dot{Z}}{\dot{Z}_{ref}} + \underbrace{\frac{\dot{C}_{q,F,ref}}{\dot{Z}_{ref} + \dot{C}_{q,F,ref}}}_{1-f} \frac{\dot{C}_{q,F}}{\dot{C}_{q,F,ref}} \quad (13)$$

The specific constants f and $1 - f$ quantify the contribution of carrying charges and fuel cost in case of the reference power cycle design, respectively. In addition, integration of Equations (6) into Equation (13) provides a direct relationship between the specific cost of electricity generated by the cycle, and its monetary expenses and fuel consumption.

$$\frac{c_{w,P}\dot{W}_{net}}{c_{w,P,ref}\dot{W}_{net}} = f \frac{\dot{Z}}{\dot{Z}_{ref}} + (1 - f) \frac{c_{q,F}\dot{Q}_F}{c_{q,F,ref}\dot{Q}_{F,ref}} \quad (14)$$

Finally, under the assumption that the net power output of each cycle is the same and that the specific cost of fuel are equal for all designs considered in this study as a first approximation, Equation (14) can be rewritten in terms of the power cycle efficiency η using Equation (1).

$$\frac{c_{w,P}}{c_{w,P,ref}} = f \frac{\dot{Z}}{\dot{Z}_{ref}} + (1 - f) \frac{\eta_{ref}}{\eta} \quad (15)$$

This equation finally shows the conflicting objective for thermo-economic improvement of power generation technologies in terms of monetary expenses, cycle complexity, and thermodynamic efficiency. Compared to a conventional thermoeconomic analysis, the amount of inherent uncertainty is significantly reduced due to the considerable reduction in parameters.

As the scope of the current study is the evaluation of different sCO₂ power cycle designs incorporating general improvement options, it is convenient to further identify the contribution and change for each power cycle component. The cost rate \dot{Z} of the overall power cycle is defined as the sum of the cost rates \dot{Z}_k of each component k .

$$\dot{Z} = \sum_{i=1}^n \dot{Z}_k \quad (16)$$

In case of the different sCO₂ power cycles considered in this study, the following components are effectively considered as a single item for the cost estimation procedure based on the flowsheet shown in Figure 2.

- Cooler E1/4: E1, E4;
- Recuperator E2: E2;
- Heater E3: E3A, E3B;
- Compressor C1: C1A, C1B, C1C;
- Turbine M1: M1A, M1B;
- Generator G1: G1

Under the premise that the different cycle designs are compared using the same financial and economic parameters as discussed above, the cost rate of each component can be related to that of the reference cycle design.

$$\frac{\dot{Z}}{\dot{Z}_{ref}} = x_{E1/4,ref} \frac{\dot{Z}_{E1/4}}{\dot{Z}_{E1/4,ref}} + x_{E2,ref} \frac{\dot{Z}_{E2}}{\dot{Z}_{E2,ref}} + x_{E3,ref} \frac{\dot{Z}_{E3}}{\dot{Z}_{E3,ref}} + x_{C1,ref} \frac{\dot{Z}_{C1}}{\dot{Z}_{C1,ref}} + x_{M1,ref} \frac{\dot{Z}_{M1}}{\dot{Z}_{M1,ref}} + x_{G1,ref} \frac{\dot{Z}_{G1}}{\dot{Z}_{G1,ref}} \quad (17)$$

Equation (17) thereby reduces to a form that allows for evaluation by using Equation (2) for each component. Therefore it is possible to account for different component designs and changes in

cycle parameters in terms of cost ratios and adjusted degression exponents. Assuming that the design of the different components does not change significantly, the cost estimation relationships are established using the heat transfer capacity UA for heat exchangers, and the power \dot{W} for compressors, turbines and generators.

$$\frac{\dot{Z}}{\dot{Z}_{ref}} = x_{E1/4,ref} \left(\frac{UA_{E1/4}}{UA_{E1/4,ref}} \right)^{n_{E1/4}} + x_{E2,ref} \left(\frac{UA_{E2}}{UA_{E2,ref}} \right)^{n_{E2}} + x_{E3,ref} \left(\frac{UA_{E3}}{UA_{E3,ref}} \right)^{n_{E3}} + x_{C1,ref} \left(\frac{\dot{W}_{C1}}{\dot{W}_{C1,ref}} \right)^{n_{C1}} + x_{M1,ref} \left(\frac{\dot{W}_{M1}}{\dot{W}_{M1,ref}} \right)^{n_{M1}} + x_{G1,ref} \left(\frac{\dot{W}_{G1}}{\dot{W}_{G1,ref}} \right)^{n_{G1}} \quad (18)$$

The degression exponents n_k used for cost estimation, and the share in cycle cost x_k of each cycle component are estimated using the baseline data given in Carlson et al. [20]. In case no absolute value for the reference system's cost is available, the share in cycle costs x_k for each component can be determined based on heuristics or estimated based on experience.

For the following analyses, Equations (15) and (18) can be used conveniently to evaluate the different sCO₂ power cycle designs considered in this study regarding their potential to provide an economically advantageous design.

RESULTS

For the thermodynamic and thermoeconomic study for comparing the different sCO₂ power cycle designs and improvement options, the following analyses are conducted for a reference cycle with a net power output of 100 MW.

Results of the Thermodynamic Analyses

The results of the simulations of the different sCO₂ power cycle designs are given in Table 2. The cycle designs differ significantly in massflow rates of the sCO₂ working fluid and operating temperatures of the recuperator, whereas the pressures are similar.

The simulation results concerning the main heat transfer equipment, compression and expansion equipment, and thermodynamic efficiency of the different cycles are presented in Table 3. The highest efficiency with 41.56 % is obtained for the recompression cycle design (4). The second highest efficiency is obtained for the intercooled cycle design (3) with an overall cycle efficiency of 36.87 %, and cycle design (2) with the reheating improvement option ranks third with an efficiency of 36.02 %. Finally, the simple recuperated cycle design (1), with an efficiency of 35.67 %, is the least efficient one. It is shown that each improvement option considered for this study indeed improves the thermodynamic efficiency of an sCO₂ power under the given parameterization.

Furthermore, it is interesting to notice that the different cycle parameters vary considerably with regard to the different improvement options. It can be seen in Table 3 that the largest amount of compression and expansion power is found for the intercooled cycle design (3) and recompression cycle design (4). Moreover, the amount of heat removed from the cycle is the smallest in case of the recompression cycle design (4). In contrast, the same cycle design also exhibits a significantly larger amount of heat transferred in the recuperator being comparable to the reheating

Table 2: Stream parameters of the different cycle simulations with a specified net power output of 100 MW

(a) Design (1): Simple Recuperated Cycle				(b) Design (2): Reheating Cycle			
Stream-No.	Temperature (°C)	Pressure (bar)	Massflow (kg/s)	Stream-No.	Temperature (°C)	Pressure (bar)	Massflow (kg/s)
1	32.00	75.00	864.1	1	32.00	75.00	818.4
2	100.13	253.40	864.1	2	100.13	253.40	818.4
3	341.02	252.00	864.1	3	400.00	252.00	818.4
4	600.00	250.00	864.1	4	600.00	250.00	818.4
5	457.14	77.95	864.1	5	526.43	77.95	818.4
6	135.83	75.15	864.1	6	142.76	75.15	818.4
				30	527.74	142.32	818.4
				31	600.00	140.32	818.4

(c) Design (3): Intercooled Compression Cycle				(d) Design (4): Recompression Cycle			
Stream-No.	Temperature (°C)	Pressure (bar)	Massflow (kg/s)	Stream-No.	Temperature (°C)	Pressure (bar)	Massflow (kg/s)
1	32.00	50.00	716.3	1	32.00	75.00	777.4
2	100.13	253.40	716.3	2	100.13	253.40	777.4
3	298.46	252.00	716.3	3	400.00	252.00	960.8
4	600.00	250.00	716.3	4	600.00	250.00	960.8
5	415.13	52.95	716.3	5	457.14	77.95	960.8
6	131.63	50.15	716.3	6	112.25	75.15	777.4
10	66.25	75.15	716.3	20	112.25	75.15	183.5
11	32.00	75.00	716.3	21	242.13	252.70	183.5
				22	112.25	75.15	960.8

Table 3: Main results of the reference case simulations with a specified net power out of 100 MW.

Cycle-Design	$\dot{Q}_{E1/4}$ (MW)	\dot{Q}_{E2} (MW)	\dot{Q}_{E3} (MW)	\dot{W}_{C1} (MW)	\dot{W}_{M1} (MW)	\dot{W}_{G1} (MW)	η (-)
(1)	177.58	316.82	280.34	36.14	137.15	100	35.67
(2)	174.87	360.63	277.59	34.23	135.24	100	36.02
(3)	168.33	223.78	271.26	44.91	145.92	100	36.87
(4)	137.52	379.76	240.59	51.49	152.50	100	41.56

cycle design (2). In case of the intercooled compression cycle design (3), the heat transferred in the recuperator is considerably smaller compared to the other designs.

Based on this observation, it is concluded that at higher turbine outlet temperatures, as in case of the reheating and recompression designs (2,4), the amount of heat transferred in the recuperator is significantly increased in order to achieve high cycle efficiencies. In contrast, the amount of heat transferred in the intercooled cycle design (3) is significantly smaller based on the potential for reduced turbine outlet pressures and temperature. Based on these findings, the operating parameters of the recuperator are thus considered the most important feature for an sCO₂ power cycle design.

Results of the Thermo-economic Analyses

Thermo-economic analyses are conducted in order to identify the economic feasibility of each cycle design.

A major advantage of the methodology used for the thermo-economic analysis is the possibility to determine the maximum

allowable ratio of monetary expenses for each cycle design in comparison to the reference cycle design (1) for obtaining equal specific cost of electricity. The results are shown in Figure 3. Based the characteristics of each design, it can be concluded that in case the thermo-economic factor approaches unity, the specific cost of heat become negligible, and the ratio of the cost rates of the different cycle becomes unity representing the theoretical limiting case. On the other hand, the characteristics for smaller thermo-economic factors, correctly allows for the identification of the well-known conflict between higher thermodynamic efficiencies and increased capital investment. Whereas the difference in cost rates between the reference case and the reheating and intercooling cycle designs (2, 3) is generally small, the difference is generally larger in case of the recompression cycle design (4).

Based on the available general relationship between thermodynamic efficiency and monetary expenditures, the detailed thermo-economic analyses for the 100 MW sCO₂ power cycle designs are conducted. The results are presented in Table 4. Based on the calculation of the design parameters for each cycle component

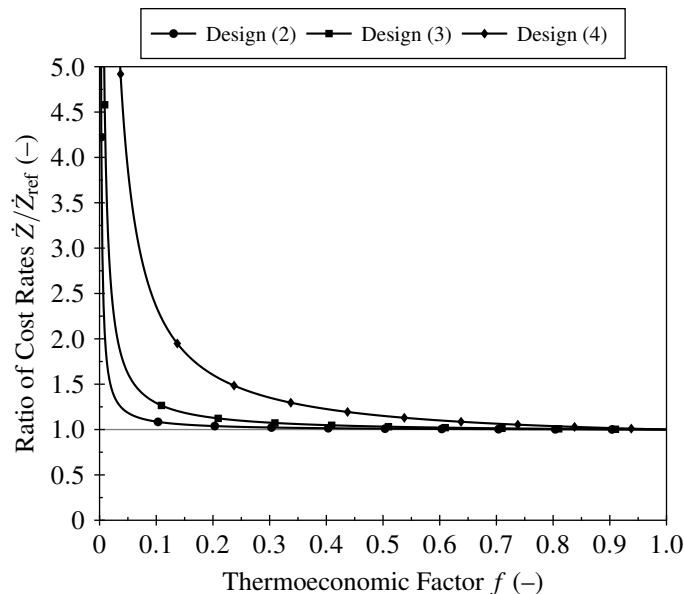


Figure 3: Isolines determining the maximum ratio of cost rates \dot{Z}/\dot{Z}_{ref} for the overall cycle design resulting in the same specific cost of electricity $c_{w,p}/c_{w,p,ref} = 1$ as for the reference design (1).

determining its size and cost, the economic scaling laws using a suitable degression coefficient are applied, and the resulting ratio of each cycle design's actual cycle cost rate in comparison to the reference cycle cost rate is determined.

It is shown in Table 4 that the cost rate ratios for the reheating and intercooling design (2,3) are comparable. In contrast, the same ratio is much higher in case of the recompression design (4). Based on the determined cost distribution for each cycle, it can be seen that the main cost drivers are the recuperator, compressor and turbine component costs. The share in overall cycle cost is significantly larger for the recuperator in case of the recompression cycle compared to the reference case. The same results are found for the compression and turbine components. In case of the intercooling compression cycle design (3), the cost share of the recuperator is significantly smaller compared to the reference case, whereas the compression and turbine components become more important. Considering the results of the reheating cycle design (2), it is concluded that the cost shares are basically the same as for the reference cycle design (1).

Based the ratio of cost rates determined for the different cycle designs, it is possible to identify the actual ratio of the levelized cost of electricity for each power cycle design. The results are shown in Figure 4. It is seen that the reheating cycle design (2) provides a small general benefit over the full range of the thermo-economic factor. In contrast, the ratio of levelized cost of electricity for the intercooling compression cycle design (3) is larger than unity for thermo-economic factors larger than 0.6 and becomes favorable for thermo-economic factors smaller than 0.6, obtaining an even smaller ratio than the reheating cycle design for thermo-economic factors smaller than 0.4. In case of the recompression cycle design (4), favorable results are only obtained for thermo-economic factors smaller than 0.25.

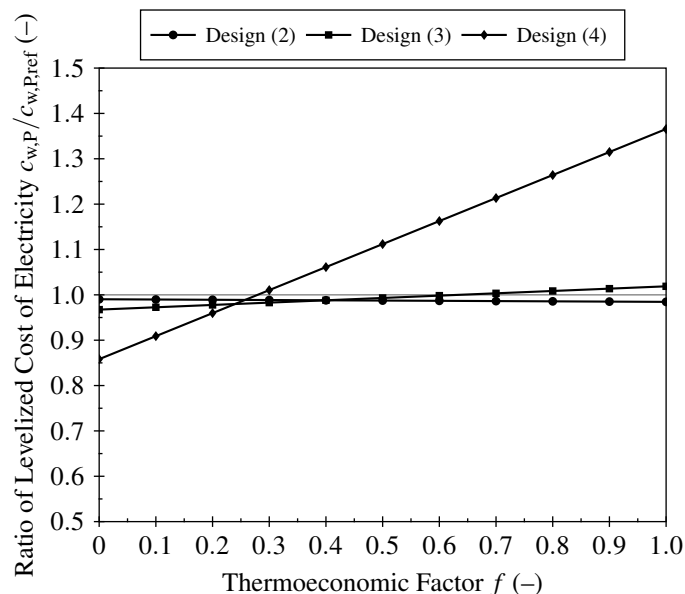


Figure 4: Actual ratio of levelized cost of electricity for the sCO₂ power cycle designs considered in this study.

The results of this study can be explained mostly by the scaling relations for estimating each component cost. Due to the unfavorable degression exponents for the heat exchanger components, a significant increase in heat exchange capacity UA is highly detrimental for the cycles economic performance. This can only be compensated by the increased efficiency in case of very expensive heat generation technologies and fuels. On the other hand, with more favorable degression exponents, an increase in compression and expansion equipment can be economically justified if significantly higher efficiencies can be realized.

CONCLUSIONS

Supercritical CO₂ power cycles have a high potential for substituting conventional technologies for power generation. However, as economic data is still limited and highly uncertain, a new approach for the thermo-economic evaluation of sCO₂ power cycle design has been introduced and applied for comparing the economic viability of a simple recuperated cycle design and three different options for improving the cycle efficiency. The approach presented in this study has significantly reduced the number of parameters required for the evaluation of the different cycle designs.

The results for a particular system study, using a benchmarking parameterization, have shown that an increase in heat exchanger capacity is economically not justified because of an unfavorable cost degression in case of the heat exchangers. On the other hand, larger compressor and turbine components can be economically justified if a higher efficiency is realized. Furthermore, it has been shown that the economic viability of a sCO₂ cycle design generally depends on the specific technology that is used for heat supply.

Based on the promising simplicity of the new approach, a

Table 4: Thermo-economic results of the simulations with a specified net power output of 100 MW.

Design Parameter	n (–)	x_k (–)	Design (1)		Design (2)		Design (3)		Design (4)	
			Parameter (kW/K; MW)	\dot{Z}/\dot{Z}_{ref} (–)						
$UA_{E1/4}$	0.9500	0.045	3354.1	0.05	3184.4	0.04	4299.0	0.06	2988.8	0.04
UA_{E2}	0.9500	0.180	4646.5	0.18	4678.5	0.18	3440.4	0.14	11981.8	0.44
UA_{E3}	1.0000	0.180	5606.8	0.18	5551.8	0.18	5425.2	0.17	4811.8	0.15
\dot{W}_{C1}	0.7865	0.270	36.1	0.27	34.2	0.26	44.9	0.32	51.5	0.36
\dot{W}_{M1}	0.6842	0.225	137.1	0.23	135.2	0.22	145.9	0.23	152.5	0.24
\dot{W}_{G1}	1.0000	0.100	100.0	0.10	100.0	0.10	100.0	0.10	100.0	0.10
Cycle		1.000		1.00		0.98		1.02		1.34

larger set of sCO₂ power cycle designs will be investigated in the future considering actual technologies for heat generation. In combination with sensitivity and optimization studies on the cycle parameters, the suggested approach is able to provide a systematic and robust basis for the design of sCO₂ power cycles. Moreover, the integration with an exergoeconomic analysis is going to provide even more significant results by revealing the actual cost formation process within each power cycle.

NOMENCLATURE

C	Cost (\$)
\dot{C}	Cost rate (\$/s)
\dot{W}	Power (MW)
\dot{Q}	Heat stream (MW)
UA	Heat transfer capacity (kW/K)
\dot{Z}	Cost rate (\$/s)
c	Specific costs (\$/kJ)
f	Thermo-economic factor (–)
n	Degression coefficient (–)
x	Fraction (–)

Superscripts and subscripts

CI	Capital investment
F	Fuel
L	Levelized
OM	Operation and maintenance
P	Product
k	Component
ref	Reference
q	Heat
w	Power

REFERENCES

- [1] Brun, K., Friedman, P. and Dennis, R., (eds.) *Fundamentals and Applications of Supercritical Carbon Dioxide (sCO₂) Based Power Cycles*. Woodhead Publishing (2017).
- [2] Zhu, Q. “High-efficiency Power Generation – Review of Alternative Systems.” Technical Report No. CCC/247, International Energy Agency (IEA). 2015.
- [3] Brewer, J. and Shelton, W. “Supercritical CO₂ Power Cycles – Literature Survey.” Technical report no., U.S. Department of Energy. 2012.
- [4] Le Moullec, Y. “Conceptual Study of a High Efficiency Coal-fired Power Plant with CO₂ Capture Using a Supercritical CO₂ Brayton Cycle.” *Energy* Vol. 49 (2013): pp. 32–46. DOI: 10.1016/j.energy.2012.10.022.
- [5] Mecheri, M. and Le Moullec, Y. “Supercritical CO₂ Brayton cycles for coal-fired power plants.” *Energy* Vol. 103 (2016): pp. 758–771. DOI: 10.1016/j.energy.2016.02.111.
- [6] Weiland, N. T. and White, C. W. “Techno-Economic Analysis of an Integrated Gasification Direct-Fired Supercritical CO₂ Power Cycle.” *Fuel* Vol. 212 (2018): pp. 613–625. DOI: 10.1016/j.fuel.2017.10.022.
- [7] Ahn, Y., Bae, S. J., Kim, M., Cho, S. K., Baik, S., Lee, J. I. and Cha, J. E. “Review of Supercritical CO₂ Power Cycle Technology and Current Status of Research and Development.” *Nuclear Engineering and Technology* Vol. 47, No. 6 (2015): pp. 647–661. DOI: 10.1016/j.net.2015.06.009.
- [8] Dostal, V., Hejzlar, P. and Driscoll, M. J. “High-Performance Supercritical Carbon Dioxide Cycle for Next-Generation Nuclear Reactors.” *Nuclear Technology* Vol. 154, No. 3 (2006): pp. 265–282. DOI: 10.13182/nt154-265.
- [9] Dostal, V., Hejzlar, P. and Driscoll, M. J. “The Supercritical Carbon Dioxide Power Cycle: Comparison to Other Advanced Power Cycles.” *Nuclear Technology* Vol. 154, No. 3 (2006): pp. 283–301. DOI: 10.13182/nt06-a3734.
- [10] Garg, P., Kumar, P. and Srinivasan, K. “Supercritical Carbon Dioxide Brayton Cycle for Concentrated Solar Power.” *The Journal of Supercritical Fluids* Vol. 76 (2013): pp. 54–60. DOI: 10.1016/j.supflu.2013.01.010.
- [11] Turchi, C. S., Ma, Z., Neises, T. W. and Wagner, M. J. “Thermodynamic Study of Advanced Supercritical Carbon Dioxide Power Cycles for Concentrating Solar Power Systems.” *Journal of Solar Energy Engineering* Vol. 135, No. 4 (2013): p. 041007. DOI: 10.1115/1.4024030.
- [12] Iverson, B. D., Conboy, T. M., Pasch, J. J. and Kruiuzenga, A. M. “Supercritical CO₂ Brayton Cycles for Solar-Thermal Energy.” *Applied Energy* Vol. 111 (2013): pp. 957–970. DOI: 10.1016/j.apenergy.2013.06.020.
- [13] Binotti, M., Astolfi, M., Campanari, S., Manzolini, G. and Silva, P. “Preliminary Assessment of sCO₂ Cycles for Power Generation in CSP Solar Tower Plants.” *Applied Energy* Vol. 204 (2017): pp. 1007–1017. DOI: 10.1016/j.apenergy.2017.05.121.
- [14] Chen, H., Goswami, D. Y. and Stefanakos, E. K. “A Review of Thermodynamic Cycles and Working Fluids for the Conversion of Low-grade Heat.” *Renewable and Sustainable*

- Energy Reviews* Vol. 14, No. 9 (2010): pp. 3059–3067. DOI: 10.1016/j.rser.2010.07.006.
- [15] Huck, P., Freund, S., Lehar, M. and Peter, M. “Performance Comparison of Supercritical CO₂ Versus Steam Bottoming Cycles for Gas Turbine Combined Cycle Applications.” *Proceedings of the 5th International Symposium – Supercritical CO₂ Power Cycles*. 2016.
- [16] Wright, S. A., Davidson, C. S. and Scammell, W. O. “Thermo-Economic Analysis of Four sCO₂ Waste Heat Recovery Power Systems.” *Proceedings of the 5th International Symposium – Supercritical CO₂ Power Cycles*. 2016.
- [17] Haywood, R. W. *Analysis of Engineering Cycles – Power, Refrigerating and Gas Liquefaction Plant*, 4th ed. Pergamon Press (1991). DOI: 10.1016/B978-0-08-040738-8.50002-5.
- [18] Crespi, F., Gavagnin, G., Sánchez, D. and Martínez, G. S. “Supercritical Carbon Dioxide Cycles for Power Generation: A Review.” *Applied Energy* Vol. 195 (2017): pp. 152–183. DOI: 10.1016/j.apenergy.2017.02.048.
- [19] Ho, C. K., Carlson, M. D., Garg, P. and Kumar, P. “Technoeconomic Analysis of Alternative Solarized s-CO₂ Brayton Cycle Configurations.” *Journal of Solar Energy Engineering* Vol. 138, No. 5 (2016): p. 051008. DOI: 10.1115/1.4033573.
- [20] Carlson, M. D., Middleton, B. M. and Ho, C. K. “Technoeconomic Comparison of Solar-driven sCO₂ Brayton Cycles Using Component Cost Models Baselined with Vendor Data and Estimates.” *Proceedings of the ASME 2017 – 11th International Conference on Energy Sustainability*. ES2017-3590: p. V001T05A009. 2017. DOI: 10.1115/es2017-3590.
- [21] Gokhshtein, D. P. “The Problem of Increasing the Efficiency and Power of Gas-Turbine Power Plants.” *Thermal Engineering* Vol. 7, No. 12 (1960): pp. 33–38.
- [22] Dechtjarow, W. L. “Über Leistung und Wirkungsgrad bei CO₂-Dampfkraftanlagen.” *Archiv für Energiewirtschaft* Vol. 15, No. 20 (1962): pp. 809–819.
- [23] Gokhshtein, D. P., Dekhtyarev, V. L. and Kozorez, A. I. “Future Designs of Thermal Power Stations Operating on Carbon Dioxide.” *Thermal Engineering* Vol. 18, No. 4 (1971): pp. 36–38.
- [24] Angelino, G. “Perspectives for the Liquid Phase Compression Gas Turbine.” *Journal of Engineering for Gas Turbines and Power* Vol. 89, No. 2 (1967): pp. 229–237. DOI: 10.1115/1.3616657.
- [25] Angelino, G. “Carbon Dioxide Condensation Cycles for Power Production.” *Journal of Engineering for Gas Turbines and Power* Vol. 90, No. 3 (1968): pp. 287–295. DOI: 10.1115/1.3609190.
- [26] Feher, E. G. “The Supercritical Thermodynamic Power Cycle.” *Energy Conversion* Vol. 8, No. 2 (1968): pp. 85–90. DOI: 10.1016/0013-7480(68)90105-8.
- [27] Lemmon, E. W., Huber, M. L. and McLinden, M. O. “NIST Reference Fluid Thermodynamic and Transport Properties – REFPROP.” Technical Report No. NIST Standard Reference Database 23, U.S. Department of Commerce. 2013.
- [28] White, C. W. and Weiland, N. T. “Evaluation of Property Methods for Modeling Direct-Supercritical CO₂ Power Cycles.” *Journal of Engineering for Gas Turbines and Power* Vol. 140, No. 1 (2017): p. 011701. DOI: 10.1115/1.4037665.
- [29] Weiland, N. and Thimsen, D. “A Practical Look at Assumptions and Constraints for Steady State Modeling of sCO₂ Brayton Power Cycles.” *Proceedings of the 5th International Symposium – Supercritical CO₂ Power Cycles*. 2016.
- [30] Crespi, F., Gavagnin, G., Sánchez, D. and Martínez, G. S. “Analysis of the Thermodynamic Potential of Supercritical Carbon Dioxide Cycles: A Systematic Approach.” *Journal of Engineering for Gas Turbines and Power* Vol. 140, No. 5 (2017): p. 051701. DOI: 10.1115/1.4038125.
- [31] Jordal, K. “Benchmarking of Power Cycles with CO₂ Capture – The Impact of the Selected Framework.” *International Journal of Greenhouse Gas Control* Vol. 2, No. 4 (2008): pp. 468–477. DOI: 10.1016/j.ijggc.2008.04.009.
- [32] Chou, V. H., Kearney, D., Turner, M. J., Woods, M. C., Zoelle, A. and Black, J. B. “Quality Guidelines for Energy System Studies: Process Modeling Design Parameters.” Technical Report No. DOE/NETL-341/051314, U.S. Department of Energy. 2014.
- [33] Bejan, A., Tsatsaronis, G. and Moran, M. J. *Thermal Design and Optimization*. Wiley (1996).
- [34] Rubin, E. S., Booras, G., Davison, J., Ekstrom, C., Matuzewski, M., McCoy, S. and Short, C. “Toward a Common Method of Cost Estimation for CO₂ Capture and Storage at Fossil Fuel Power Plants.” Technical report no., Electric Power Research Institute (EPRI). 2013.
- [35] Zoelle, A., Turner, M. J., Chou, V. H. and Fisher, J. C. “Quality Guidelines for Energy System Studies: Performing a Techno-Economic Analysis for Power Generation Plants.” Technical Report No. DOE/NETL-341/020915, U.S. Department of Energy. 2015.
- [36] Turner, M. J., Pinkerton, L. L. and Black, J. B. “Quality Guidelines for Energy System Studies: Capital Cost Scaling Methodology.” Technical Report No. DOE/NETL-314/013113, U.S. Department of Energy. 2013.
- [37] Kline, S. J. *Similitude and Approximation Theory*. Springer (1986). DOI: 10.1007/978-3-642-61638-9.

**PROBABILISTIC TECHNIQUE FOR SOLVING COMPUTATIONAL PROBLEM:
APPLICATION OF ANT COLONY OPTIMIZATION (ACO) TO FIND THE BEST sCO₂
BRAYTON CYCLE CONFIGURATION**

Mounir MECHERI*

EDF R&D

Chatou, FRANCE

Email: mounir.mecheri@edf.fr

Qiao ZHAO

EDF R&D

Chatou, FRANCE

ABSTRACT

This paper studies the potential of a probabilistic technique to solve complex problems such as thermodynamic cycle layout optimization. The Ant Colony Optimization (ACO) algorithm has been used to find an optimal configuration of a supercritical CO₂ Brayton Cycle (sCO₂-BC) for a specified application (coal power plant).

This optimization is done by coupling an existing **process simulation software** (ProSimPlus) and an existing **optimization solver** (MIDACO). In this study, more than a 1000 cycle configurations have been analyzed regarding performance, costs and the value of the Levelized Cost Of Electricity (LCOE).

Main results show that the optimal sCO₂-BC configuration depends on the optimization criteria (objective function).

INTRODUCTION AND CONTEXT

Since the beginning of sCO₂-BC studies, many theoretical works led to general recommendations to achieve best performances for several applications (nuclear, coal, concentrated solar, biomass, geothermal, waste heat) [1, 2, 3].

These recommendations are the results of a time-consuming optimizations (mainly by performing sensitivity analysis) of a high number of possible cycle configurations due to a high number of parameters and variables (heat source and heat sink temperatures, pressure ratios, CO₂ mass flows and split ratios, heat exchanger pinch temperatures) to combine with a high number of possible sCO₂-BC configurations as shown in Appendix A (number of intercooling, number of reheat, number of recompression loop, boiler configuration...) [5].

Furthermore, optimizing only the cycle efficiency leads to complex cycle architectures using several turbomachines (reheats, intercooling) and large heat exchangers, which reduces the benefits of having simple and compact cycles [5, 6, 7, 8]. In other words, maximizing the cycle efficiency leads to performant but more expensive cycles with larger footprint, reducing their competitiveness compared to existing power technologies [8, 9].

In this context, the economic should be considered within the optimization problem in addition to performance criteria. However, taking the economic into account increases the number of optimization parameters, variables and constraints, leading to complex and non-linear problems to solve [4, 10].

The “sensitivity analysis” screening method (manual optimization) is unsuitable to solve such problems because it only covers a restricted number of possible solutions and increases the risk of missing the optimal solution. Furthermore, compare to manual optimization, a computer is able to cover a very high number of calculations within a reasonable timeframe.

However, to solve the described optimization problem, the computer must be able to automatically modify the sCO₂-BC configuration as well as the corresponding operating parameters to be optimized. This paper is describing the methodology that enables automatic cycle configuration (and parameters) modification within a commercial process simulation software.

OBJECTIVES

The main objective of this paper is to use an existing optimization technique (Ant Colony Optimization) within

commercial process simulation software to help finding the optimal sCO₂-BC configuration for a specified application.

To do so, the method relies on the concept of “superstructures” (i.e. multi-path process flow systems). Superstructures enable to easily generate a very high number of cycle configurations within a single process flowsheet. Then, the optimization solver is able to automatically switch from one to another configuration during a process simulation routine [4].

METHODOLOGY

The optimization methodology used in this paper and developed in [4] is based on the following routine:

For a given sCO₂-BC configuration:

- 1) The process simulation is performed by the chosen **process simulation software** for a given set of parameters;
- 2) Variation of the operating condition within boundaries specified by the user (e.g. variation of the maximum cycle temperature between 200°C and 500°C...) is performed by the **optimization solver**;
- 3) The comparison of the cycle performances and costs for every tested case (cycle configuration + operating conditions) enables to find the optimal solution.
- 4) Finally, the sCO₂-BC configuration is automatically¹ switched by the **optimization solver** and the routine goes back to step 1) above. More details about the methodology are given in next paragraphs.

Superstructure for automatic flowsheet generation

The first challenge of this methodology is to enable automatic switch of sCO₂-BC configurations in the process simulation software. One solution is to use “path switches” (Figure 1) in the process flow diagram: they enable to select different configurations just by changing the switch position.

The switch position is represented by an integer variable (for example, “1” for the upper position and “2” for down position in a “2 paths” switch) as depicted in Figure 1. This integer variable becomes an optimization variable that the optimization solver is free to change, as explain in the “Optimization details” section below. In these conditions, the solver can automatically generate different cycle architectures.

¹ The specificity of the ACO optimization is its ability to automatically select “population” (here cycle configuration) regarding both history and random principle [4, 7] as explained in “Optimization details” section in this paper.

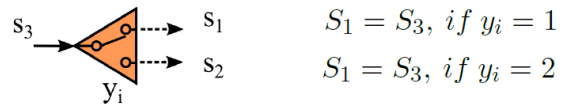


Figure 1: example of a “2 path” switch with its integer decision variable (y_i)

In this study, the global flowsheet is using several switches (“2 or 3 paths” switches) enabling a high number of possible cycle configurations, using different components (or units). This global flowsheet is called a “superstructure”. Next figure is showing an example of a very simple superstructure with 3 different units using a reactant “A” to create two products “C” and “D”:

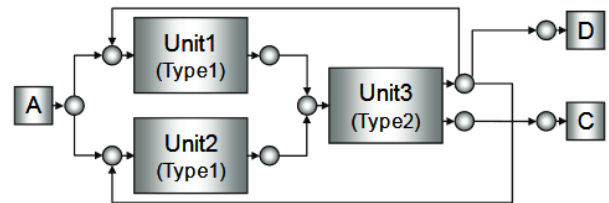


Figure 2: Example of a Superstructure process flow [11]

In the case of sCO₂-BC configuration optimization, the superstructure can be divided in 3 main parts:

- i. the cooling and compression part (dealing with the number a recompression loop and the number of intercooling),
- ii. the heat source and electricity production part (dealing with the number of reheat and the boiler configuration),
- iii. and the heat integration part (dealing with the number of recuperators).

The Figure 3 illustrates a simple superstructure of a sCO₂-BC with three “2 paths” switches.

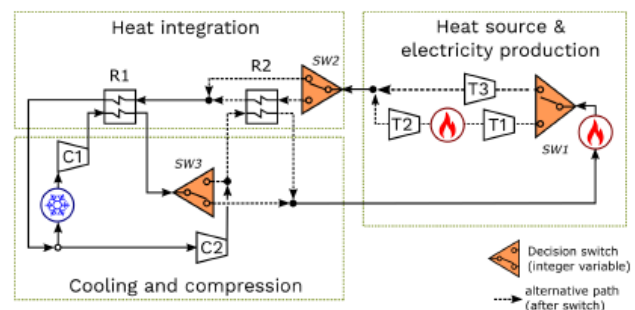


Figure 3: Simple superstructure of sCO₂ Brayton cycle [4]

An example of the optimal configuration of the superstructure shown in Figure 3 is given in Appendix B.

Non-linear optimization problem

Using integer variables in the optimization process leads to strongly non-linear and non-convex problems. These problems cannot be solved with classical/basic optimization methods such as gradient method.

In this study, Mixed Integer Nonlinear Programming (MINLP) approach is used combined with a meta-heuristic optimization technique: Ant Colony Optimization (ACO).

The ACO algorithm is a probabilistic technique used for solving computational problems [12]. Further details regarding this technique are given in [12]. The ACO solver used in this study is MIDACO Solver [13].

Problem definition and Pareto front

To solve an optimization problem, the user needs to define the objective function(s), the constraints/boundaries, the fixed parameters and the optimization variables (i.e. variable that can be varied by the optimization solver to reach objectives).

For example:

- the objective function can be to maximize the cycle efficiency (or to minimize the cost of electricity production),
- the constraints and boundaries can be the minimal and maximal allowable temperatures and pressures due to materials constraints, or the heat exchanger temperature pinch, the amount of heat available in the boiler...),
- the fixed parameters can be equipment data (e.g. the turbomachinery efficiency),
- the optimization variables can be some operating parameters such as pressure ratios, temperature, flow rates... and other integer/real variables such as the “switch path number”...

The MIDACO solver enables “multi-objective” optimization, which means that several criteria (for example, both “maximization of performance” and “reduction of cost of electricity”) can be sought by the optimizer solver.

The use of “multi-objective” optimization leads to a “Pareto front” (situation where improving one objective is degrading another objective).

Communication between the process simulation software and the solver

As explained, one objective of this work is to use a commercial process simulation software to ease the construction of the superstructure. In this study, the software ProSimPlus is used [14].

ProSimPlus has its own optimization module but is also able to interact with external solvers. ProSimPlus sends simulation results (for a given set of variables) to the MIDACO solver (MINLP Optimization) which analyzes them and proposes another sCO₂-BC configuration (or operating conditions) to test (see Figure 4).

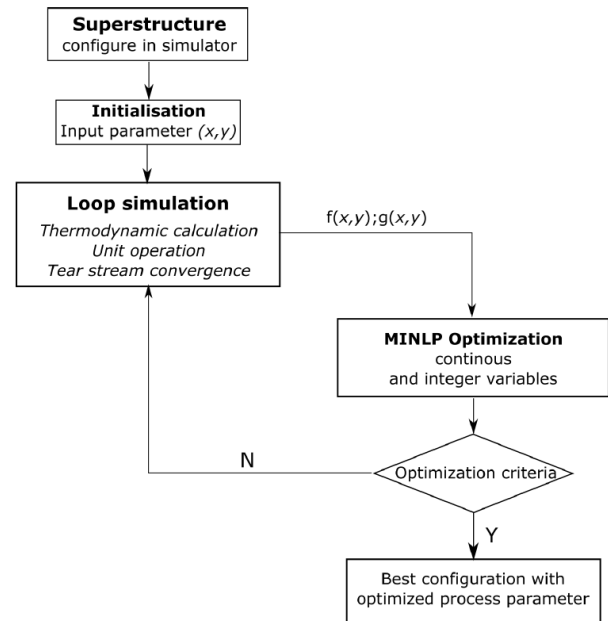


Figure 4: Program structure of simulator-based superstructure optimization [4]

Optimization details: concept of seed

The randomness of the initial ant colony population in the MIDACO Solver is controlled by a pseudo-random number generator called “seed” (the seed determines the sequence of pseudo-random numbers sampled by the generator) [15].

Changing the “seed value” in MIDACO Solver lead to a different result and prevent the optimizer of being trapped in a local optimum sector (see the iterations of a “4 seeds” optimization example in Figure 5).

The impact of the seed selection normally varies with the complexity of the problem. In general, the more complex the problem, the bigger the influence of the seed can be [4, 7].

For difficult problems, it is therefore often a more promising strategy to execute several short runs of MIDACO Solver with different random seeds, rather than performing only one very long run [15].

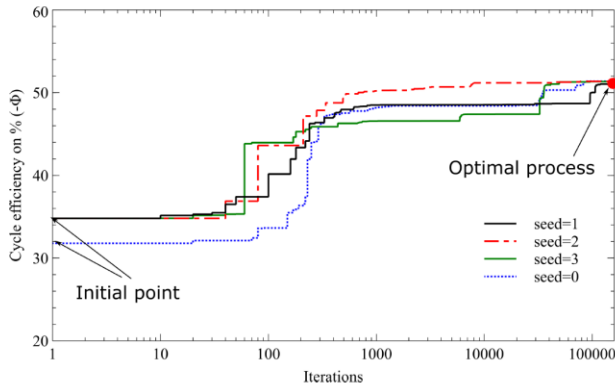


Figure 5: Optimization progress of four runs with different random seeds [4]

Optimization details: “feasible path” vs “unfeasible path”

Simulation convergence of complex processes (with recycling loops) can be very challenging. To ease convergence, the process simulation software creates “tear streams”. In this case, some recycling loops are cut and the software takes care of equalizing parameters from one side to the other side of the tear-streams.

There are two ways to use optimization module with tear steams. The “feasible path” mode, which means that the software is handling the equalization of tear-stream at each calculation (ensuring convergence of each calculation but is very long).

The “unfeasible path” mode, where the tear-streams are handled by the optimization solver as “optimization parameter” (enabling to avoid convergence of useless configurations).

In this study, “feasible path” leads to locals optimum and is then not compatible with the problem to solve as shown in Figure 6.

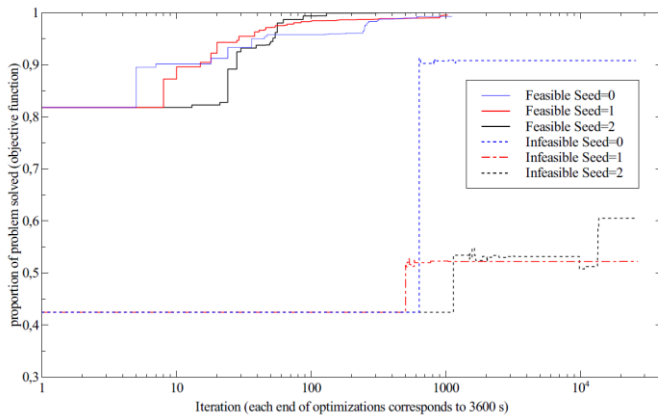


Figure 6: Relative performance comparison between “Feasible Path” approach and “Infeasible Path” approach [4].

Optimization details: optimization progress

Evolution of created populations evolves with time (i.e. number of iteration). Generation of a high number of populations coming from different seed enables to show the optimization progress (in colonies and seeds but also, globally) as shown in an example of cycle efficiency optimization in Figure 7.

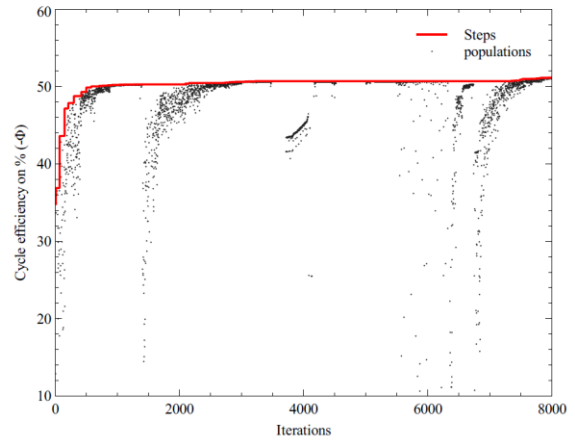


Figure 7: Optimization progress of sCO₂ Brayton cycle [4]

PROBLEM DEFINITION

Superstructure used in this study [4]

The final superstructure used in this study is plotted in Appendix C. It is composed of 3 “two-path” switched and 2 “three-path” switch, enabling to test more than 1000 sCO₂-BC configurations. For each cases, the solver can modify all parameters and variables within the given boundaries .

Objective functions [4]

In order to show the importance on the objective function, the problem has been solved in two steps:

- a) First, the problem has been set with only one objective function: maximization of the cycle efficiency
- b) Then, the problem is solved with multi-objective method. Three objectives have been chosen:
 - i. maximization of the cycle efficiency,
 - ii. minimization of the investment costs (CAPEX) and,
 - iii. minimization of the Levelized Cost of Electricity (LCOE).

In the MIDACO Solver, it is possible to weight every objective in order to avoid conflicting situations (e.g. maximizing the efficiency implies higher costs, which is in opposition with minimizing the CAPEX). In this study, the dominating weight has been set on the LCOE objective. The implementation of the economics in the problem is very important because it enables to release some technical constraints (or boundaries) initially set to avoid unrealistic solutions.

For example, the minimum “pinch temperature” of recuperators is initially fixed to 10 K in the “mono-objective” optimization otherwise its theoretical optimal value for best performance tends to zero (i.e. heat exchanger with infinite exchange surface), which has no industrial meaning.

However, in “multi-objective” optimization, it is not necessary to put a lower limit for the “pinch temperature” value because one objective is to reduce costs (efficient heat exchangers with low temperature pinch value are expensive).

Next tables are showing “assumptions”, “constraints” and “optimization variables” of the optimization problem (see considered superstructure in the appendix C).

Assumptions on fixed variables and equipment data [4]

Next table shows the fixed variables and equipment data for the optimization problem.

Parameter	Value
Turbine inlet temperature	620 °C
Turbine inlet temperature after reheating	620 °C
CO ₂ flowrate before main cooling	6 000 kg/s
Minimum pinch temperature value (mono-objective optimization)	10
Turbine isentropic efficiency	90 %
Compressor isentropic efficiency (-)	89 %
Pressure drop in every component (% of inlet pressure)	1 %

Optimization variables and their bounds [4]

Next table shows the optimization variables and their bounds for the final superstructure (depicted in appendix C):

Optimized continuous variables	Bounds
Main compressor pressure inlet (MPa)	[3.3 - 10]
Main compressor pressure outlet (MPa)	[3.3 - 30]
Secondary compressor pressure outlet (MPa)	[3.3 - 30]
Secondary compressor pressure outlet (MPa)	[3.3 - 30]
CO ₂ temperature at the heat sink outlet (°C)	[31.2 - 100]
Split flow for second recompression loop	[0 - 0.5]
Split flow for third recompression loop	[0 - 0.5]
Split flow for fourth recompression loop	[0 - 0.5]
Temperature of the cold side outlet of the first recuperator (°C)	[31.2 - 620]
Temperature of the hot side outlet of the second and third recuperator (°C)	[31.2 - 620]
Pressure ratio of the second, the third and the fourth turbines	[1 - 5]
Flow fraction passing to the seventh turbine	[0 - 0.5]
Flow fraction of CO ₂ preheated by flue gases	[0 - 0.5]

Optimized integer variables	Values
Switch 1	1, 2 or 3
Switch 2	1, 2 or 3
Switch 3	1 or 2
Switch 4	1 or 2
Switch 5	1 or 2

Main assumption regarding calculation of the Levelized Cost Of Electricity (LCOE)

The LCOE of considered cycles is calculated with the following equation:

$$LCOE = \frac{CAPEX \times f_a + OPEX}{P_e \times \text{Hour}_{year}}$$

where:

- CAPEX is the capital expenditure of main components (recuperators, heat sink, turbines, compressors and the boiler with its gas treatment unit) taking into account the piping, Instrumentation and Control, land, civil and transportation;
- OPEX is the operational expenditure including Operation & Maintenance and coal price;
- f_a the discount factor (taking into account the discount rate (8%) and the plant lifetime (40 yr));
- P_e the electrical power output of the power plant;
- Hour_{year} , the plant availability (7884 h/yr);

RESULTS

As explained, the problem has been solved with a mono-objective function first (maximization of performance) and then with a multi-objective function.

The Figure 8 depicts the convergence of the mono-objective problem (with 4 different seeds and 100 000 iterations). Results shows that the best configuration (according to given hypotheses, boundaries and constraints) is a “2-reheat double-recompression” cycle (Figure 9) and achieve a net cycle efficiency of ~52%.

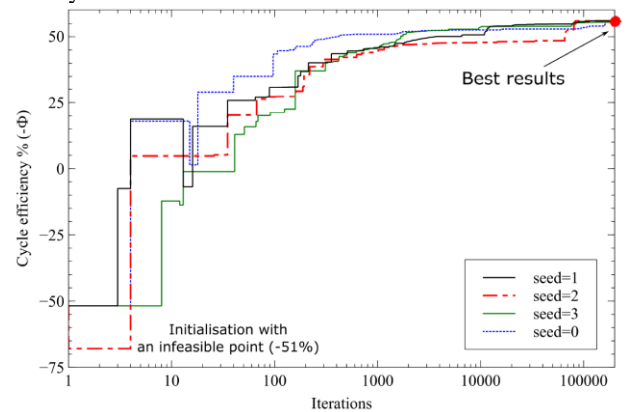


Figure 8: Energy performance optimization progress of four runs with different random-seeds [4]

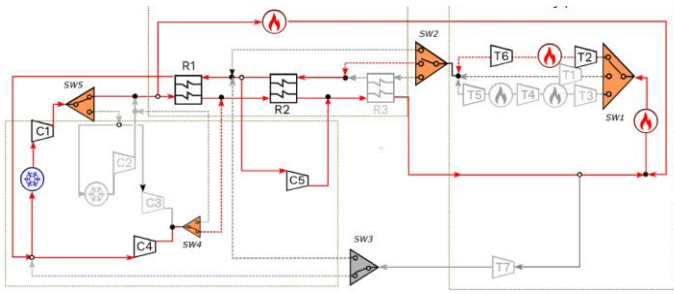


Figure 9: “Energy performance” optimization result: a “2-reheat double-recompression” cycle [4]

This cycle configuration is unusual, using a third compressor to compress a fraction of the CO₂ mass flow at the high-temperature recuperator’s hot stream outlet to re-inject it just at the boiler inlet. This configuration uses a high number of turbomachineries and some optimization variables logically reach their lower/higher bounds (e.g. maximal temperature and pressure of the cycle...).

In order to be compared with the multi-objective solution, the LCOE of this mono-objective solution has been estimated (~61 \$/MWh). Table 1 is comparing main results between mono-objective and multi-objective optimization.

While using the multi-objective problem (and thus releasing some equipment constraints such as the temperature pinch value of recuperators), the result is different as shown in the following section.

Pareto front and “multi-objective” optimization result

The Figure 10 shows the evolution of the optimization process (each gray dots represents a calculated configuration). The star represents the initial point (i.e. the mono-objective solution described in the first paragraph of the “Results” section).

Efficiency and CAPEX are respectively represented in “x” and “y” axis. The third dimension of the graph is represented by color (LCOE). It is interesting to see that the mono-objective solution (star) is located on a front (due to pinch constraint) at high cost (because reducing cost was not an objective at this moment).

Then, some new populations start finding new configurations (due to addition of economic criteria and the release of the pinch constraint). An example of the search history and a 3D plot of the Pareto font are given in the appendix D.

The Multi-objective solution enables to reach higher performance at lower cost electricity. This is due to fact that releasing constraints enables to reach higher performances.

Then, the economic functions enable to gauge/weigh the cost impact of this increment of performance.

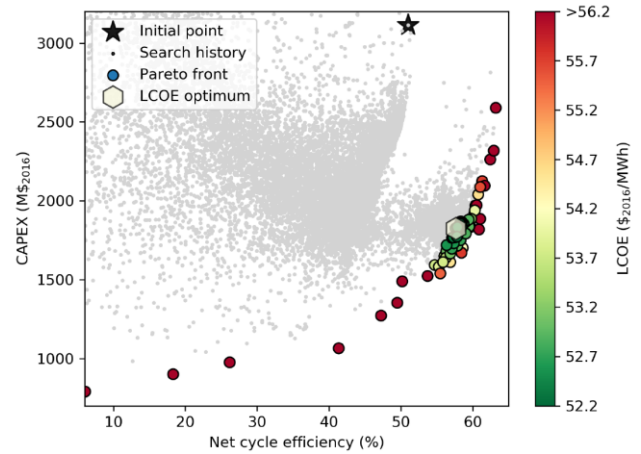


Figure 10: Investment cost versus plant efficiency versus LCOE (color axis) at different generation [4]

Finally, the best multi-objective solution is a “single-reheat with one intercooling” configuration (Figure 11) reaching a net cycle efficiency of ~57%² for a LCOE of ~52 \$/MWh. For a 1GWe base load power plant (i.e. producing during more than 8000h/yr), it represents a save of about 68 M\$/yr.

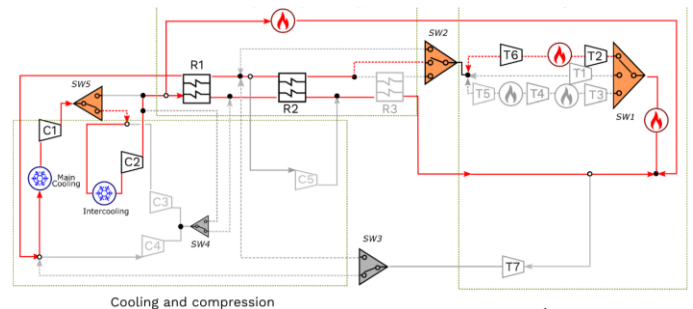


Figure 11: Techno-economic multi-objective optimization result: a “single-reheat with one intercooling” cycle [4]

Table 1: comparison between mono and multi objective optimization results

Optimization	Net cycle eff.	CAPEX	LCOE
Mono-objective	51%	3,124 M\$	61 \$/MWh
Multi-objective	57% ²	1,826 M\$	52.3 \$/MWh

² This better performance compared to “mono-objective” optimization is due to the fact that the “pinch temperature” constraint of 10 K has been relaxed in the “multi-objective” calculation. Then, the optimizer selects the best compromise between the performance and the cost of the heat-exchangers. In this case, it appears that it is worth paying extra-cost of very performant heat-exchanger (with low “pinch temperature” value) for having both a lower LCOE and higher performance. R1 pinch is equal to 5K while R2 pinch reaches 20K.

CONCLUSION AND PERSPECTIVES

The objective of coupling a commercial process simulation software with the probabilistic optimization technique ACO (Ant Colony Optimization) to solve complex multivariable computational problems (selection of the best sCO₂-BC configuration and its best operating conditions in the case of electricity production) has been successfully reached. This solution offers more flexibility in the optimum research compared to “sensitivity analysis” method and does not need graphical/visual comparison to find the best option.

The study shows that the definition of a non-linear optimization problem has an impact on the results of the final solution. For example, in this study, the best economic cycle configuration (multi-objective) differs from the energetic (mono-objective) solution. Indeed, the theoretical best configuration would have an infinite number of reheat (or number of intercooling) and heat exchangers with an infinite surface.

Also, it shows that some restrictions initially establish to contain the technical optimization in realistic options (for example: fixing the minimal recuperator temperature pinch value to 10K) have no real meaning while considering multi-objectives optimization with economic objective. Thus, relaxing some initial “conservative” technical constraints can lead to more efficient or/and cheaper solutions.

This work relies on several assumptions and hypothesis (cost correlations, equipment data) that need to be refined for more accurate results. Also, this study has been focusing on the global methodology and the application to a complex case. Then, more efforts must now be made to improve and consolidate this tool by including uncertainties in the process calculation, by reducing the computational time required for the optimization itself and by improving the construction of the superstructure.

NOMENCLATURE

ACO: Ant Colony Optimization
CAPEX: CAPital EXpenditure
OPEX: OPerational EXpenditure
LCOE: LevLized Cost Of Electricity
LRGP : Laboratoire Réactions et Génie des Procédés
sCO₂-BC: supercritical CO₂ Brayton Cycle

ACKNOWLEDGEMENTS

The results of this study are extracted from the PhD of Qiao ZHAO done in EDF and LRGP from 2015 and 2018 [4].

REFERENCES

- [1]: Feher E.G. – The supercritical thermodynamic power cycle; *Energy Convers Manag*, 8 (2) (1968), pp. 85-90
- [2]: Angelino G. – Carbon dioxide condensation cycles for power production; *ASME; J. Eng. Power*; 1968.
- [3]: Dostal V., Driscoll M.J., and Hejzlar P. – A supercritical carbon dioxide cycle for next generation nuclear reactors. PhD thesis, MIT, 2004.
- [4]: [Zhao Q.](#) – Conception and optimization of supercritical CO₂ Brayton cycles for coal-fired power plant application; Université de Lorraine, 2018. English. NNT: 2018LORR0080 http://docnum.univ-lorraine.fr/public/DDOC_T_2018_0080_ZHAO.pdf
- [5]: Crespi F., Gavagnin G., Sanchez D., Martinez S.M. Supercritical carbon dioxide cycles for power generation: A review; *Applied Energy* 195 (2017) 152–183
- [6]: Serrano I.P, Linares J.I., Cantizano A., Moratilla B.Y – Enhanced arrangement for recuperators in supercritical CO₂ Brayton power cycle for energy conversion in fusion reactors; *Fusion Engineering and Design*; Volume 89, Issues 9–10, October 2014, Pages 1909-1912; <https://doi.org/10.1016/j.fusengdes.2014.03.083>
- [7]: Wang L., Pan L.M, Wang J, Chen D., Huang Y., Hu L. – Investigation on the temperature sensitivity of the S-CO₂ Brayton cycle efficiency, *Energy*, Volume 178, 2019, Pages 739-750, ISSN 0360-5442, <https://doi.org/10.1016/j.energy.2019.04.100>
- [8]: Marchionni M., Bianchi G., Tsamos K.M., Tassou S.A – Techno-economic comparison of different cycle architectures for high temperature waste heat to power conversion systems using CO₂ in supercritical phase; 1st International Conference on Sustainable Energy and Resource Use in Food Chains, ICSEF 2017, 19-20 April 2017, Berkshire, UK
- [9]: Discroll M.J. – Supercritical CO₂ Plant Cost Assessment; Center for Advanced Nuclear Energy Systems MIT Nuclear Engineering Department; September 2004 <http://citeseerx.ist.psu.edu/viewdoc/download?doi=10.1.1.502.4874&rep=rep1&type=pdf>
- [10] Khadse A., Blanchette L., Kapat J., Vasu S., Hossain J., Donazollo A. – Optimization of Supercritical CO₂ Brayton Cycle for Simple Cycle Gas Turbines Exhaust Heat Recovery Using Genetic Algorithm; *Journal of Energy Resources Technology* Copyright VC 2018 by ASME JULY 2018, Vol. 140 / 071601-1
- [11]: Henao C.A., A superstructure Modeling Framework For Process Synthesis Using Surrogate Models; University Of Wisconsin-Madison; 2012;
- [12]: M. Dorigo, T. Stützle, Ant Colony Optimization: Overview and Recent Advances. M. Gendreau and Y. Potvin, editors, *Handbook of Metaheuristics*, 2nd edition. Vol. 146 in

International Series in Operations Research & Management Science, pp. 227--263. Springer, Verlag, New York, 2010.
https://rd.springer.com/chapter/10.1007%2F978-1-4419-1665-5_8

[13]: MIDACO Solver <http://www.midaco-solver.com/>

[14]: ProSimPlus; Steady-State Process Simulation and Optimization [accessed April 2019]:
http://www.prosim.net/bibliotheque/File/Brochures/Brochure_PSP-En-2018-compressed.pdf

[15]: User manual of MIDACO-Solver; [accessed april 2019]
http://www.midaco-solver.com/data/other/MIDACO_User_Manual.pdf

APPENDIX A: CLASSIFICATION OF FEW INDIVIDUAL PROCESS MODIFICATIONS [4]

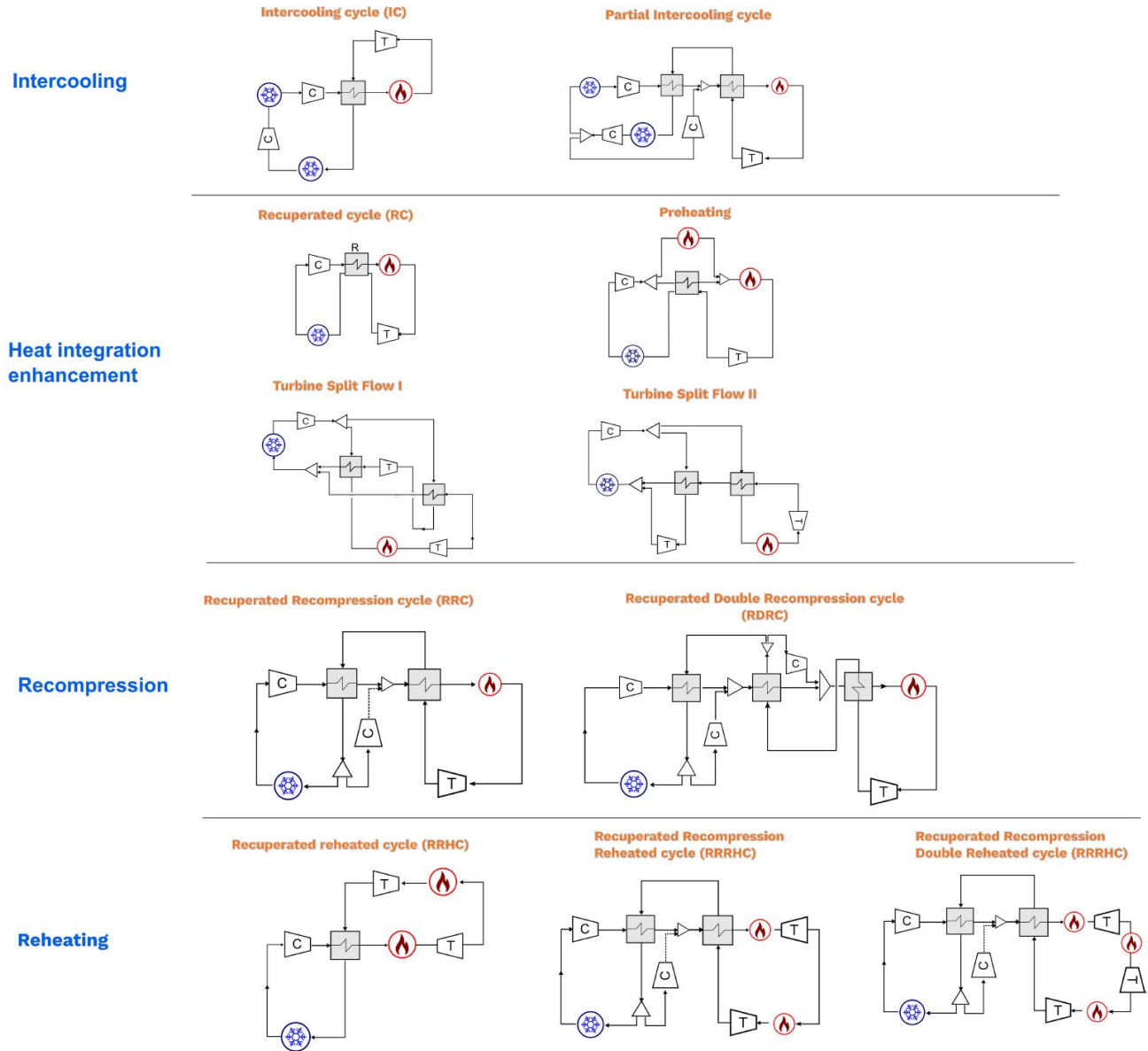
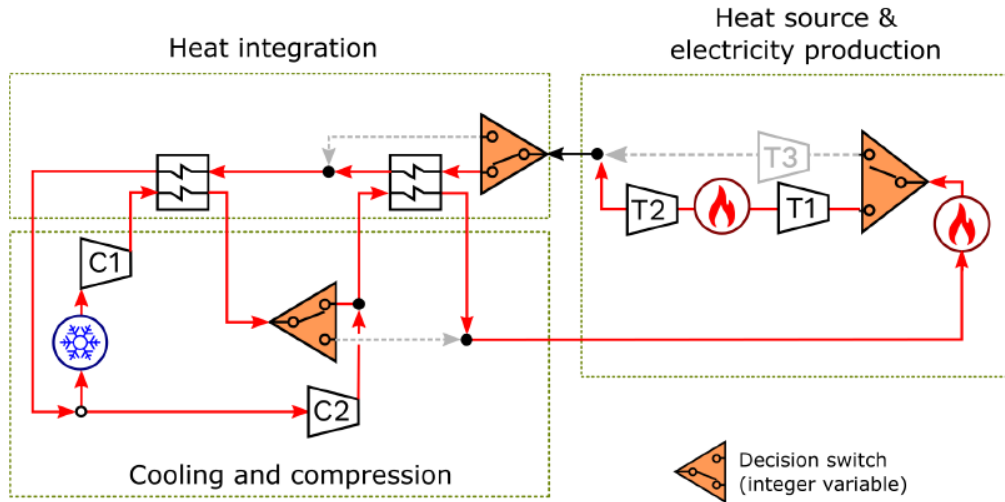
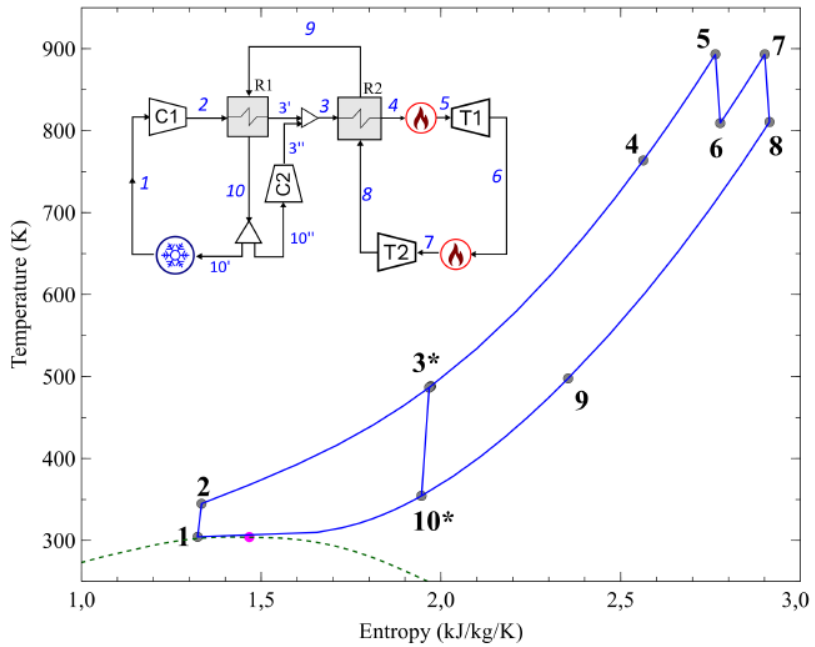


Figure 12: Classification of a few individual process modifications of sCO₂ Brayton cycle [4]

APPENDIX B:



a) optimal process $y=\{1,1,1\}$ in superstructure



b) Temperature-Entropy diagram of optimal process

Figure 13: Process synthesis result: optimal flowsheet for the simple superstructure of sCO₂ Brayton cycle [4]

APPENDIX C:

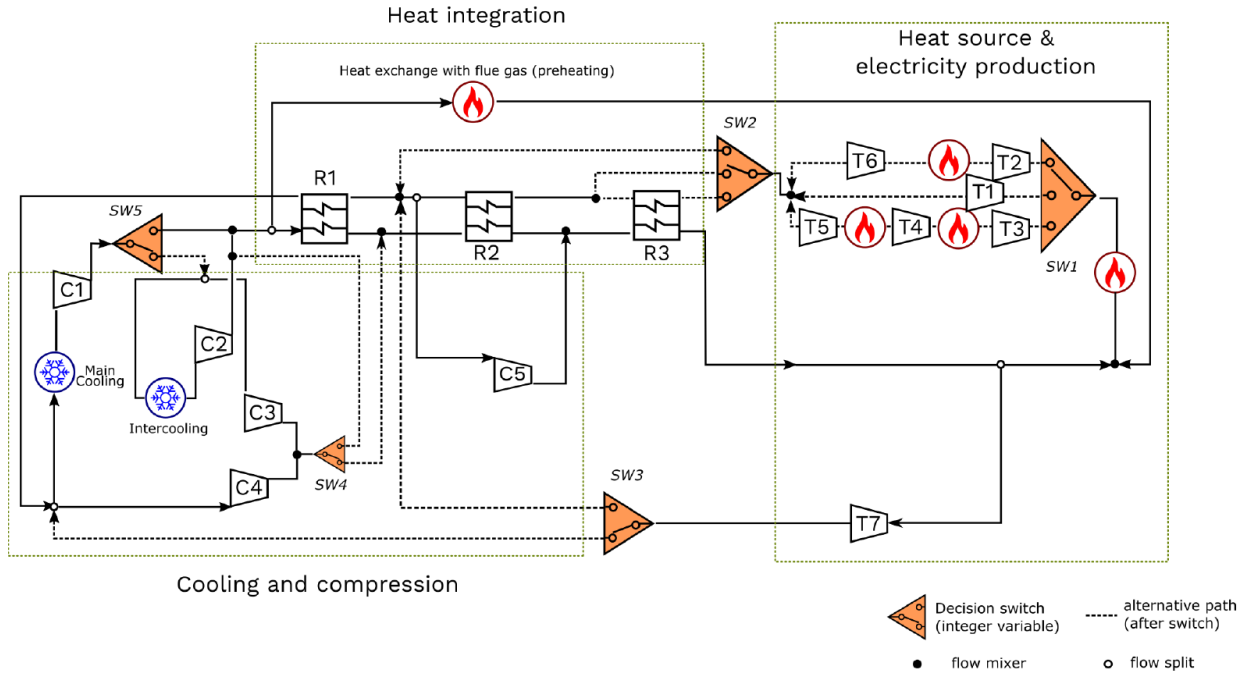
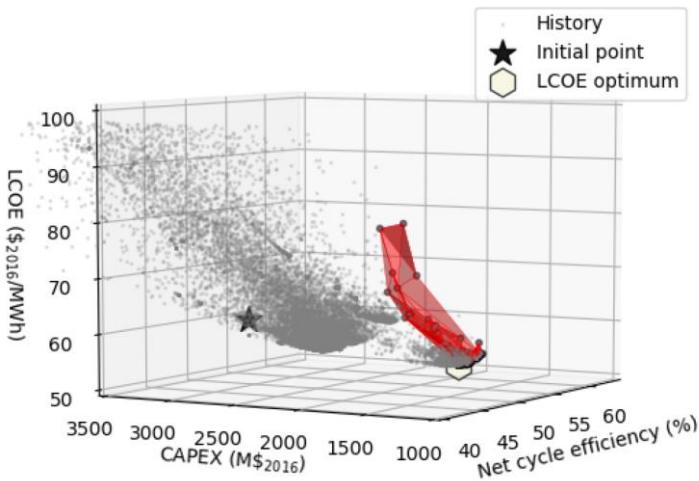


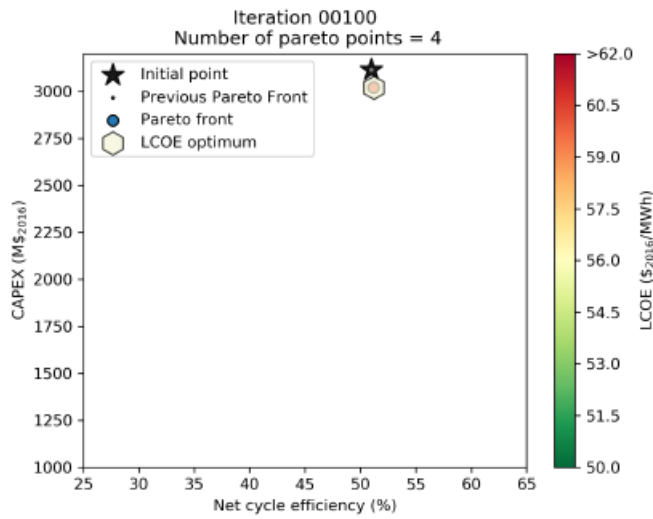
Figure 14: Superstructure for sCO₂ Brayton cycle ($2^7 \times 3^2 = 1152$ structural alternatives) [4]

APPENDIX D:

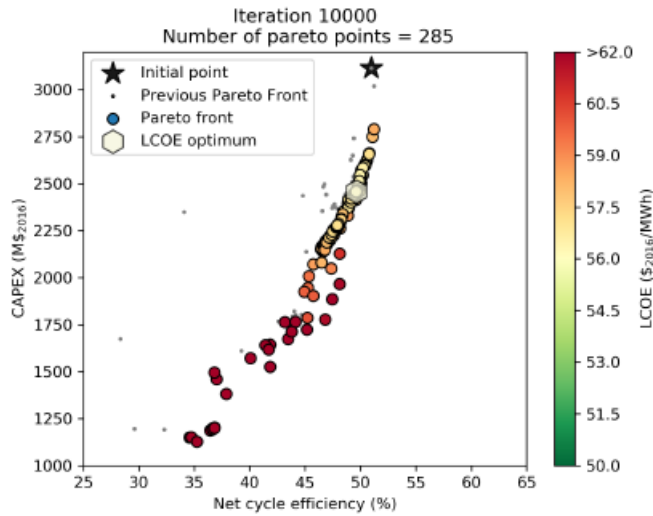


Content	Unit	Initialization (Case B)	Best result
Cycle efficiency (with penalty introduced by flue gas)	%-pts	50.94	57.62
Net power plant efficiency LHV ($\eta_{plant} = \eta_{boiler} \times \eta_{cycle} \times \eta_{alt} \times \eta_{aux}$)	%-pts	45.98	52.01
Production electricity	MWh/year	9 453 871	6 659 504
CAPEX total	\$/MWh	25.69	21.31
OPEX total	\$/MWh	35.16	30.95
LCOE	\$/MWh	60.86	52.26

Figure 15: 3D representation of optimization iteration process. Axis are the three objective functions: LCOE, CAPEX and net cycle efficiency) and Techno-economic results of energy-optimal process and LCOE-optimal process [4]

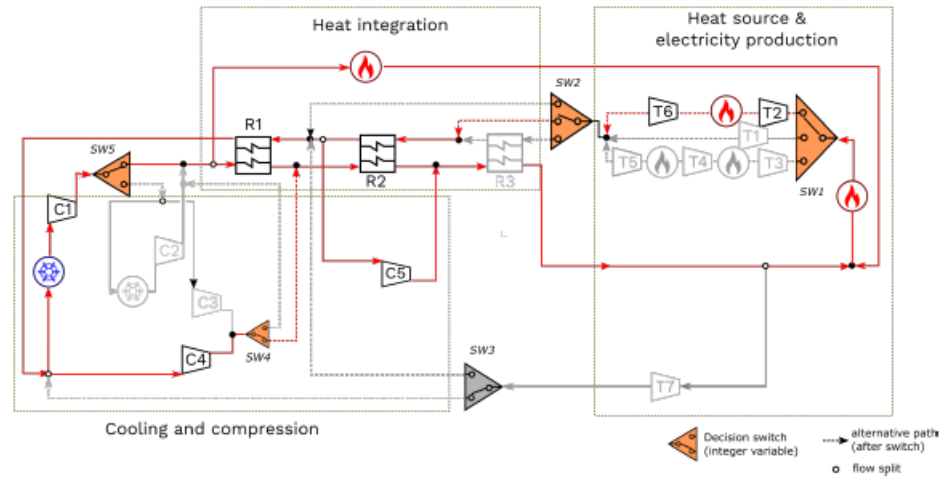


Iteration 100



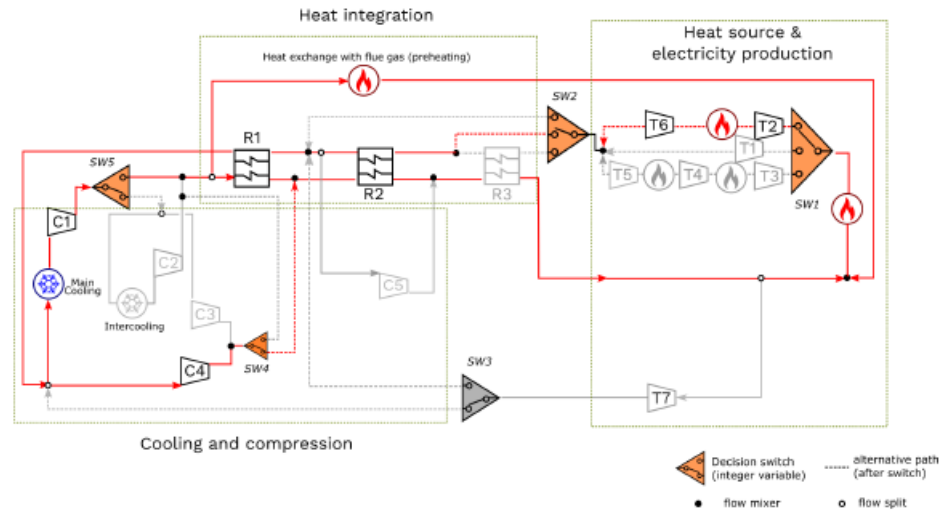
Iteration 10000

APPENDIX E:



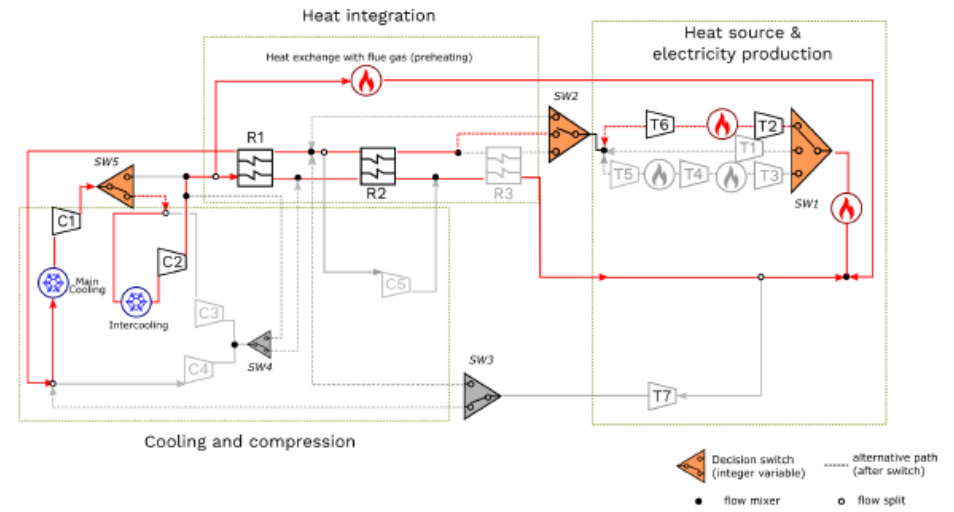
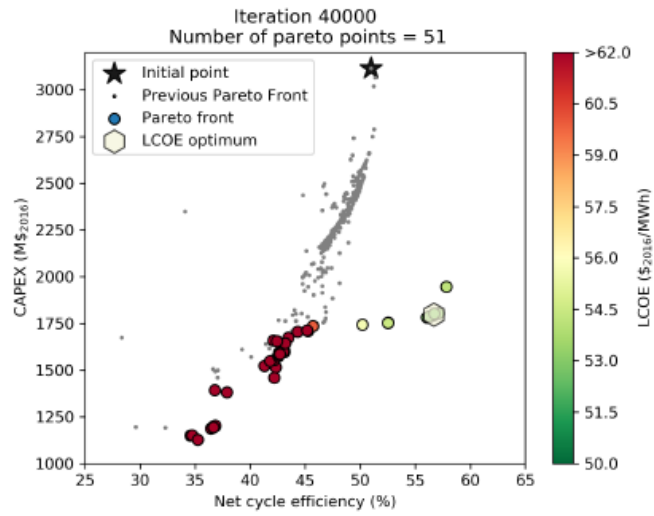
$$y = \{3, 2, 1, 1, 1\}$$

single reheating double recompression configuration



$$y = \{3, 2, 1, 1, 1\}$$

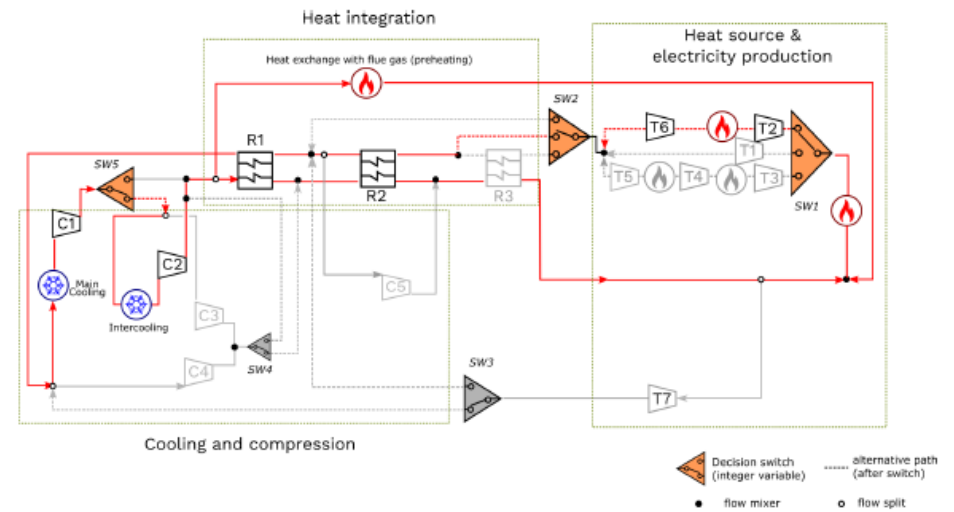
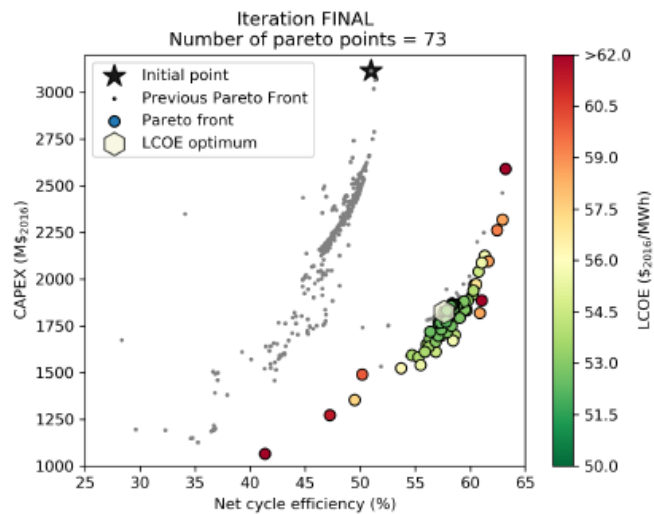
single reheating single recompression configuration



Iteration 40000

$$y = \{3, 2, 1, 1, 2\}$$

single reheating intercooling configuration



Iteration 65800

$$y = \{3, 2, 1, 1, 2\}$$

single reheating intercooling configuration

Figure 16: Evolution of Pareto front on function of iteration as well as instantaneous best process configuration [4]

COOLING SYSTEM COST AND PERFORMANCE MODELS FOR ECONOMIC sCO₂ PLANT OPTIMIZATION WITH RESPECT TO COLD sCO₂ TEMPERATURE

Sandeep R. Pidaparti
KeyLogic
Pittsburgh, PA, U.S.A.

Charles W. White
KeyLogic
Fairfax, VA, U.S.A.

Andrew C. O'Connell
KeyLogic
Pittsburgh, PA, U.S.A.

Nathan T. Weiland*
National Energy Technology Laboratory
Pittsburgh, PA, U.S.A.
nathan.weiland@netl.doe.gov

ABSTRACT

Several studies have shown that the efficiency of sCO₂ power cycles can be significantly improved by reducing the cold sCO₂ temperature, which increases the sCO₂ density at the inlet to the compressor and reduces its specific power requirement. Due to the near-ambient CO₂ critical temperature of 31 °C, the effects of ambient temperature on sCO₂ plant performance are far more significant than for steam Rankine cycles, thus cooling systems tailored to sCO₂ cycle operation are necessary to realize the benefits that are possible through sCO₂ cold temperature management.

To this end, cost and performance models for four different types of sCO₂ cooling systems are presented in this work. These systems cover direct and indirect (via water) cooling of the sCO₂ working fluid, as well as wet and dry cooling techniques to approach ambient wet and dry bulb temperatures, respectively. The heat and mass transfer modeling of these systems are briefly reviewed along with the cost scaling algorithms that have been developed from a combination of literature, cost modeling software, and vendor quotes.

The results of these efforts are a set of sCO₂ cooling system spreadsheet modeling tools that are available for download by the sCO₂ community. The cooling system models can be used by cycle designers to weigh the benefits and drawbacks of various cooling systems in terms of equipment cost, auxiliary power requirements, and water usage. Detailed modeling and capital cost estimation of these cooling systems as a function of ambient conditions and assumed temperature approaches also allows for optimization of the cold sCO₂ temperature to minimize the overall cost of electricity (COE) for a given plant location, accounting for the increased cooling equipment cost required to achieve this temperature. Preliminary economic optimization using these spreadsheet models shows that cooling system optimization improves indirect sCO₂ plant efficiency by 3-4 percentage points, and reduces COE by up to 8%, demonstrating the value and utility of this approach.

INTRODUCTION

A significant feature of the sCO₂-based power cycle is its operation close to the CO₂ critical point (31 °C, 7.37 MPa) towards the cold side of the cycle. For most sCO₂ power cycles, the benefits of reducing the cold sCO₂ heat rejection temperature are particularly advantageous. In this regime, lowering the CO₂ temperature increases its density significantly, reducing the specific power required for compression. Further, lowering the cold sCO₂ temperature allows for an increase in the low temperature recuperator (LTR) effectiveness and also makes the low-grade heat recovery process a more attractive option. Both effects can improve the efficiency of a power plant based on the recompression Brayton cycle (RCBC): the former by directly increasing the power cycle efficiency and the latter by increasing the quantity of heat harvested by the cycle. For similar reasons, the addition of main compressor intercooling typically improves the specific power of a recompression cycle, reducing the sCO₂ mass flow, and thus the required cycle size and cost, for a given power output [1].

To realize the benefits of reduced sCO₂ cycle cold end temperatures, detailed study of the power cycle cooling system is required. Given the close proximity of the CO₂ critical temperature to ambient conditions, sCO₂ cycle cooling system design plays an important role in determining the cold-end cycle performance. However, the capital cost of cooling capacity additions grows exponentially as the sCO₂ cold temperature approaches the design ambient temperature, thus an economic optimum exists that balances the efficiency benefits of cold sCO₂ cycle temperature reductions against the added cooling system expense. Modeling tools for performing such analyses for sCO₂ power cycles are unavailable in the literature, but would allow cycle designers to select the cooling system type, size and operating parameters to economically optimize the plant's interaction with the ambient heat sink.

The objective of this paper is to describe, demonstrate, and make available to the sCO₂ community a set of compact and easy

to use spreadsheet-based models for quantifying the technical (auxiliary power requirement and water usage) and economic (capital and operating costs) performance of four cooling technologies that could be considered for use in sCO₂ power cycle applications. These cooling technologies are:

1. Conventional wet cooling with an evaporative cooling tower.
2. Indirect dry (ID) cooling which uses water-cooled heat exchangers for the sCO₂ power cycle coolers and an air-cooled heat exchanger (ACHE) to reject the cycle waste heat from water to air.
3. Direct dry cooling where each sCO₂ power cycle cooler is an air-cooled heat exchanger directly cooling the CO₂.
4. Adiabatic cooling technology in which the sCO₂ coolers are again air-cooled heat exchangers but the air is cooled below the ambient dry bulb temperature by evaporating water.

These four technologies were selected because they span the gamut of the primary air- and water-cooled technologies that have been considered for the sCO₂ power cycles to date. The models are intended to assist sCO₂ cycle designers in solving three key design questions: at what temperature should the CO₂ coolers be operated for a given ambient temperature, which cooling technology is best for a given application, and what operating conditions are optimal for a given application. To accomplish this, the models give reasonable cooling system designs, complete with techno-economic performance estimates, regardless of the application's geographic location or ambient conditions. This further enables the cycle designer to weigh the capital and operating cost of the selected cooling system against the performance benefits to the sCO₂ cycle.

To provide some context for the discussion below, the modified sCO₂ RCBC shown in Figure 1 is used as a demonstration case for the cooling system economic optimization.

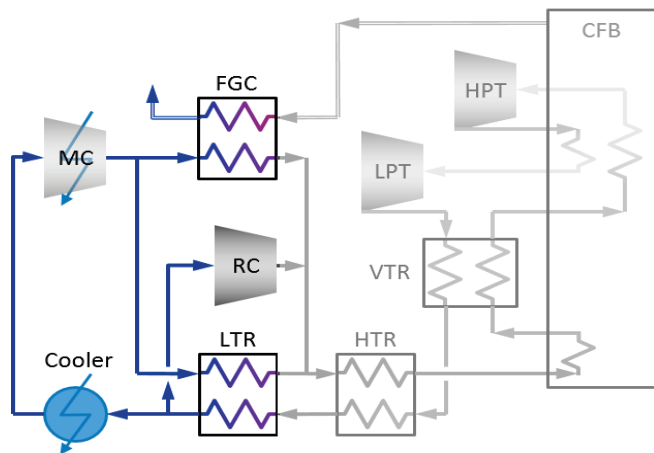


Figure 1: Recompression sCO₂ power cycle

This cycle was modeled using Aspen Plus® (Aspen) in a prior study in which an oxy-coal circulating fluidized bed (CFB) was the primary heat source [1]. From the CFB, the heated CO₂ passes through a turbine (HPT) with one stage of reheat (LPT).

The low-pressure CO₂ is then cooled by passing through three stages of recuperators: a very high temperature recuperator (VTR), a high temperature recuperator (HTR), and an LTR. These recuperators in turn heat the high-pressure CO₂ delivered to the CFB. Other cycle types with and without the VTR or reheat have been investigated [1], however, the hot end of the power cycle is shown in gray scale in Figure 1 to focus attention on the subject of this paper - the low temperature portion of the cycle.

After exiting the LTR, the majority of the CO₂ passes through a cooler before being compressed to the peak cycle pressure in the intercooled main compressor (MC) while the rest of the CO₂ enters the recycle compressor (RC). After exiting the MC, the majority of the CO₂ enters the cold side of the LTR where it is partially heated and then mixes with the effluent from the RC. A slipstream of the CO₂ from the MC is heated in a flue gas cooler (FGC) or low temperature economizer before also mixing with the LTR cold side outlet stream.

The original study of the modified RCBC in Figure 1 examined the cost and performance of a baseline coal-fired oxy-CFB power plant with carbon capture [1]. The results showed that the sCO₂ plant offered a significantly higher efficiency and lower cost of electricity (COE) than a plant employing a Rankine cycle at operating conditions similar to the sCO₂ plant. The results also showed that a single stage of intercooling for the main compressor offered both higher overall plant efficiency (0.4 – 0.6 percentage points) and a 1.8 – 2.7% lower COE compared to the baseline configuration. More significant improvements in efficiency (0.6 – 1.6 percentage points) are reported in cases where the pressure ratio between intercooled main compressor stages is optimized [2].

The cold sCO₂ temperature considered in this study was 35 °C, though a preliminary investigation of cold sCO₂ temperatures ranging from 20 – 40 °C for this plant was recently performed [3, 4]. The results show that the plant efficiency increases by about 1 percentage point per 5 °C reduction in cold sCO₂ temperature, accounting for corrections to manage internal pinch points in the FGC, LTR, and cooler for cases with condensing CO₂ and/or main compressor intercooling. A similar efficiency improvement trend with reduction in cold sCO₂ temperature was also encountered in a study of a recompression Brayton cycle plant without CO₂ capture [5, 6].

Several other studies have explored the benefits of reducing the sCO₂ cooler temperature. An early study by Wright *et al.* [7] projected a 4-5 percentage point increase in plant efficiency for a nuclear light water reactor with an sCO₂ power cycle, by moving to condensing cycle operation. An experimental portion of this study proved the feasibility of this concept by demonstrating condensed CO₂ operation of a radial compressor and gas cooler that were designed for gas phase operation near the CO₂ critical point. A later study on sCO₂ power cycles for air-cooled sodium fast reactor nuclear applications showed improvement in cycle performance as the compressor inlet temperature is decreased, as well as variability in performance with compressor inlet pressure [8]. Similar studies in the nuclear application space have shown that an optimal compressor inlet pressure exists for maximizing efficiency as the compressor inlet

temperature is varied. This optimal pressure is typically at [9] or slightly above the pseudo-critical pressure for CO₂ [10].

Pidaparti *et al.* [11] showed the importance of selecting optimum water conditions for the cooling tower to minimize overall plant capital cost for RCBC. Studies comparing the economics of air versus water-cooling have also appeared in the literature. Pidaparti *et al.* performed a detailed study of the economic benefits of air-cooling for the sCO₂ Brayton cycle and found that with a suitable CO₂-to-air cooler design, air-cooling is economically competitive with water-cooling [10]. Held *et al.* performed a comparative analysis of wet cooling versus air cooling for a notional 10 MWe sCO₂ cycle and found that air-cooling will generally be more economically advantageous [12]. Hruska *et al.* performed a life cycle earnings optimization on an air-cooled sCO₂ power cycle compared to a Rankine cycle and found that for the same sized air-cooled heat exchanger, the sCO₂ Brayton cycle can achieve lower heat rejection temperatures than the steam Rankine cycle, which corresponds to higher cycle efficiencies and overall higher life cycle earnings [13].

While some of these studies have presented descriptions of the models and methodologies used to perform their analyses, none have published the actual models. Further, while reliable cost models for dry sCO₂ coolers have recently become available [14], they do not account for variations in cooling system design and operating parameters. The primary contribution of the present study is the development and publication of cost and performance models for four separate cooling system types, which can be used for economic optimization of any sCO₂ plant type with respect to cycle heat rejection to the atmosphere.

COOLING SYSTEM MODELS

This section describes the technical basis of the performance and cost models for all four cooling technologies explored in this study, as well as for water/sCO₂ heat exchangers, where applicable. The cooling technology models, and technical details on their operation and use, can be found in Reference [15]. Wherever possible, the models are compared to data from either commercial software packages or from vendors for validation. All the models operate in design mode only, and do not predict cooling system performance under off-design conditions.

Wet Cooling Tower Performance and Cost Model

The simplest of the cooling technology models in this study uses water/sCO₂ heat exchangers for each of the sCO₂ process coolers and an evaporative wet cooling tower to reject the heat absorbed by the water to the atmosphere. Figure 2 is a schematic diagram for a forced draft wet cooling tower. The warm water exiting the sCO₂ process coolers is collected and fed to the top of the cooling tower where it falls by gravity through a section of packing. Induced draft fans at the top of the tower draw ambient air into the tower through louvers and across the wet packing. As the air passes over the packing, a portion of the water is evaporated, cooling the remaining water. The cooled water is collected at the base of the tower and returned to the CO₂ process coolers via a circulating water pump.

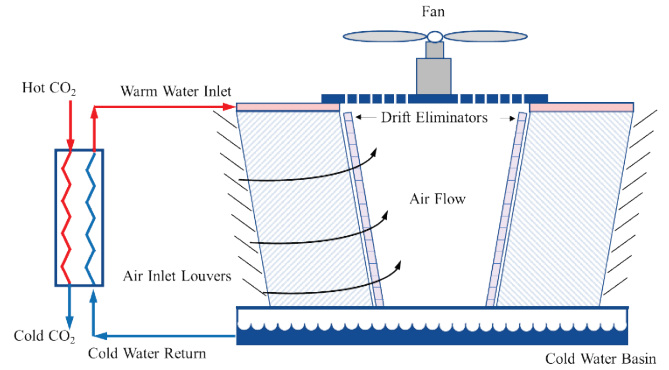


Figure 2: Schematic of the wet cooling tower technology

The central element of the wet cooling tower model is the energy balance that equates the cooling demand of the cooling water with the heat duty of the tower which is the sum of the sensible heat absorbed by the humid air as it passes through the tower plus the latent heat of the evaporated water. The inputs to the model are those typically used to design a wet cooling tower, namely the ambient air conditions (pressure, dry bulb temperature and percent relative humidity or wet bulb temperature), the cold end approach temperature (cold water return temperature minus ambient air wet bulb temperature), the temperature drop (or range) of the water stream, and the inlet water flow rate or total cooling duty. The total water flow rate, m_w , and total cooling duty, Q , are related by:

$$m_w = \frac{Q}{\text{Range} \cdot C_{p_w}}$$

where C_{p_w} is the average heat capacity of the water. The total amount of water evaporated is obtained from the solution to the overall mass and energy balance and this in turn determines the required air flow rate based on a calculated humidity ratio of the air exiting the tower assuming a hot end approach temperature of 4.7 °C and an assumed relative humidity of 100 percent.

The required fan power is calculated from the required air flow rate, ambient pressure, fan head (default 0.124 kPa) and mechanical efficiency (default 80%). The required power for the circulating water pump is calculated from the total water flow rate, pump head (default 0.254 MPa) and mechanical efficiency (default 80%). The total water loss from the cooling tower is calculated as the sum of the evaporation rate, the blowdown flow rate calculated from the cycles of concentration (default 4) and the entrained water loss or drift loss (default 0.001% of the total water flow rate) [14]. This model has been commonly used in NETL systems studies over the past two decades.

The cooling tower cost algorithm is based on the Zanker correlation, which was presented in a paper by Leeper [15, 16]. This equation estimates the cooling tower construction cost in 1967 dollars with reasonable accuracy based on the total cooling duty, the cooling water range, the cold end approach temperature, and the design ambient wet bulb temperature. Therefore, the Zanker correlation captures the cost impact of various cooling tower design parameters while also accounting for the ambient

conditions available to the tower. Validation of the cost model was performed using the software packages STEAM PRO and PEACE from Thermoflow [17], as shown in Figure 3. In performing the validation, it was determined that the modified Zanker correlation below, incorporating power law scaling for the cooling duty and the cold end approach temperature, results in greater accuracy:

$$\$_{1967} = \frac{Q^0 * \left(\frac{Q}{Q^0}\right)^{0.8426}}{C * A^0 * \left(\frac{A}{A^0}\right)^{0.4376} + 39.2R - 586}$$

In the modified Zanker correlation, $\$_{1967}$ is the cooling tower construction cost in 1967\$, Q is the cooling duty, Q^0 is the reference case cooling duty (3,465 MMBtu/h), A is cold end temperature approach, A^0 is the reference case cold end approach temperature (8.52 °F), R is the cooling water range (°F), and C is given by the following equation:

$$C = \frac{279}{[1 + 0.0335 * (85 - T_{wb})^{1.143}]}$$

where T_{wb} (°F) is the design wet bulb temperature. Cost estimates were converted to 2011\$ using the Chemical Engineering Plant Cost Index (CEPCI) [18].

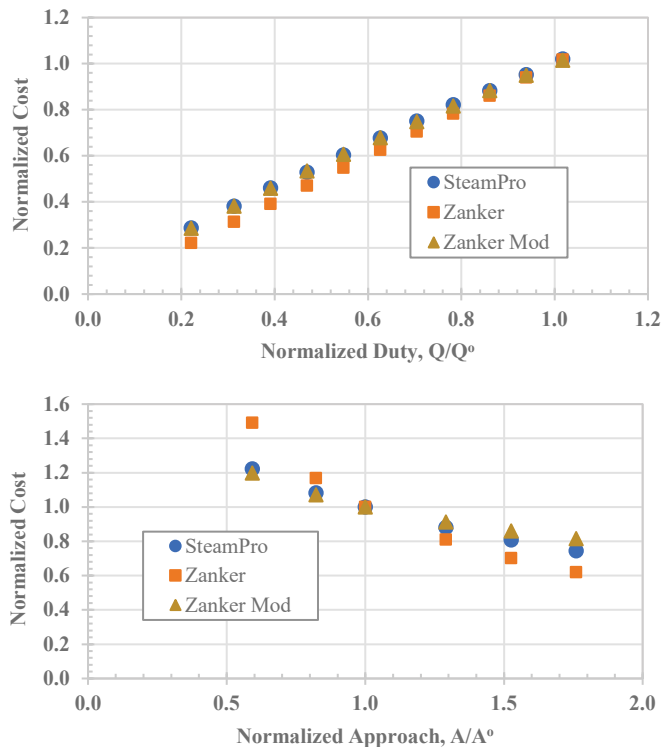


Figure 3: Normalized Cost vs Normalized Duty (top) and Normalized Approach (bottom) for a wet cooling tower

The developed model covers a single cooling tower that is assumed to fulfill the total cooling duty requirements of the

plant. The cooling tower approach temperature is assumed to be limited to a minimum of 2.8 °C (5 °F) at the recommendation of cooling tower manufacturers [14].

In the study by Held *et al.* [12], it is noted that the evaporation processes in the wet cooling tower concentrates water impurities, which ultimately may lead to fouling of the water-side of the cycle cooler. If a microchannel heat exchanger is used for the water/sCO₂ cooler, then an intermediate high purity water cooling loop is recommended to avoid difficulties with cleaning the intricate flow passages of these heat exchangers. This study assumes a microtube or similar water/sCO₂ heat exchanger that is more easily cleaned on the water side, avoiding the need for a secondary heat transfer loop.

Indirect Dry Cooling Performance Model

The schematic of an air-cooled heat exchanger (ACHE) bay and associated water/sCO₂ cooler is presented in Figure 4. As depicted in the schematic, a process fluid (water in this case) to be cooled flows through the finned tube heat exchanger bundle (often consisting of multiple rows of tubes and bundles), while fans blow a cold crossflow of air over these bundles. To meet the required cooling duty several such bays can be employed.

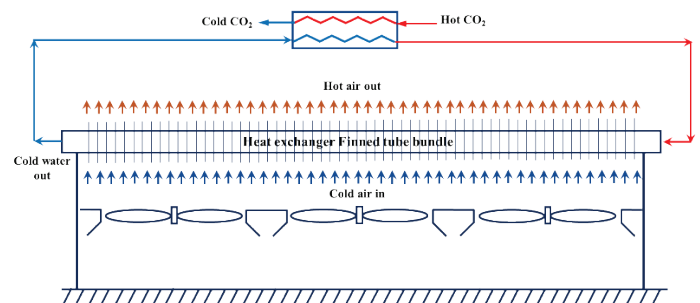


Figure 4: Schematic of the indirect dry cooling technology

The performance model is based on Example 8.1.1 from the textbook by Kröger [19]. The key output variables of the performance model are the number of required bays and the auxiliary fan power consumption to meet the required cooling duty under specified process conditions. The adjustable inputs in the model are cooling duty, CO₂ and water fluid parameters (inlet temperature and pressure, outlet temperature), and ambient dry bulb temperature and pressure. The model iteratively calculates the required air flow rate (and fan power), average air outlet temperature, average process fluid flow rate per bay, and the number of required bays.

The implicit energy balance and draft equations are solved iteratively for the main outputs. Closure of the energy balance equations is provided using the ϵ - NTU relationship. The ϵ - NTU is feasible and sufficiently accurate for fluids that have only small variation in thermo-physical properties over the temperature range of interest. Effectiveness (ϵ) of the cross-flow heat exchanger bay is calculated assuming that both the fluids are unmixed. To calculate the NTU , air-side and water-side heat transfer coefficients are needed. The air-side heat transfer coefficient and pressure drop are calculated by assuming that the

tube bundle geometry is the same as the one specified in Example 8.1.1 from the Kröger textbook [19]. The water-side heat transfer coefficient is calculated from the Dittus-Boelter equation, with water properties calculated based on the integrated value between the water inlet and outlet temperatures.

Table 1 shows the design basis and cost estimate for a reference ACHE used as the indirect dry cooler in this application. The cost estimate was prepared by Black & Veatch [20]. This reference indirect dry cooling system cost was converted to 2011\$ using the CEPCI [18] and used to determine the bare erected cost (BEC) of a single bay assuming linear scaling. Since the indirect dry model calculates the number of bays required as a primary output, the BEC for any indirect dry cooling configuration is taken as the required number of bays multiplied by the per-bay BEC.

Table 1: Design basis and cost estimate for reference ACHE

Parameter	Value (English Units)	Value (SI Units)
Duty	1820 MMBtu/h	533.4 MW _{th}
Cooling water flow rate	184,000 gpm	41,791 m ³ /h
ACHE water inlet temp	89 °F	31.7 °C
ACHE water outlet temp	69 °F	20.6 °C
ACHE outlet temperature approach	10 °F	5.6 °C
Bays required	68	
BEC, \$1,000 ₂₀₁₇	80,272	

The approach of using a single per-bay cost value was validated using the results from a series of sensitivity analyses performed in STEAM PRO. Figure 5 shows the cost and number of cells/bays versus the cooling duty, the dry bulb temperature, and the temperature approach. The estimates for the cost and number of cells are from STEAM PRO while the number of bays is scaled from the Black & Veatch reference case. The plots show good agreement between the SteamPro data and the Black & Veatch data. The maximum deviation occurs for an approach below 5.6 °C (10 °F).

In this model, the bay size is governed by the effective frontal area of one tube, which results in modular bay cooling duties between about 15 and 25 MW, depending on approach temperature and range parameters. Approach temperatures below 2.8 °C (5 °F) are not recommended by STEAM PRO, and limits on the range are generally unspecified.

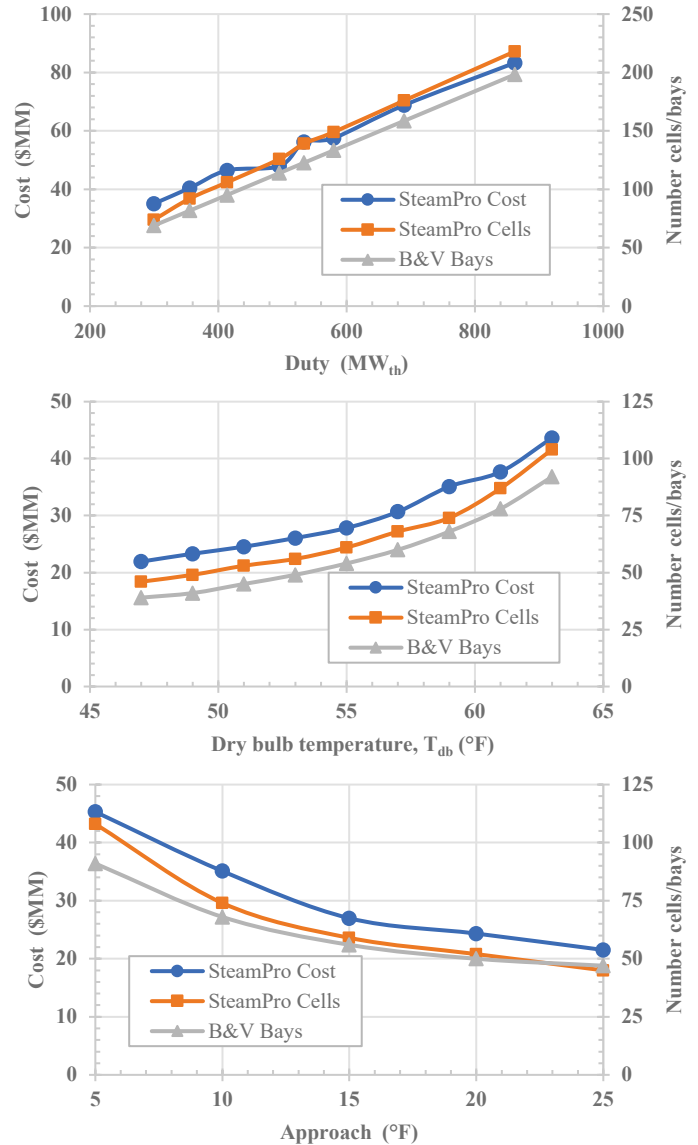


Figure 5: Cost and number of ACHE cells/bays vs. cooling duty, dry bulb temperature and approach temperature

Water-sCO₂ Heat Exchangers

To allow a complete cooling system assessment for the processes using a wet cooling tower or the indirect dry cooling technology, models were developed for the water/sCO₂ coolers required in these systems. For the oxy-CFB indirect sCO₂ cycle system analyzed in this paper, two water/sCO₂ coolers are required, one for the main sCO₂ cooler and the other for the intercooler used in the main CO₂ compressor. Both coolers are modeled as counter-current flow heat exchangers. The thermo-physical properties for both CO₂ and water are calculated using the Span-Wagner equation of state [21] by linking the model to REFPROP [22]. Due to the nonlinear variations in the properties for CO₂, the model discretizes the coolers into 100 segments in the direction of flow. The temperatures and conductance (UA) at each zone are calculated from the energy balance and heat

transfer relations. The minimum temperature approach was determined from an economic optimization to minimize the overall COE. The capital cost model for the water/sCO₂ coolers is identical to that used for the power cycle's low temperature recuperator; \$0.294/(W/K) on a 2011 dollar year basis [15].

Direct Dry Cooling Performance and Cost Models

The schematic of the direct dry CO₂ cooler bay modeled in this study is shown in Figure 6. As depicted in the schematic, CO₂ flows inside finned tube bundles with multiple rows of tubes and passes. The induced draft fans located at the top of the cooler draw cold air over the tube bundles in a crossflow arrangement. Details of the modeled tube bundles are provided in Table 2.

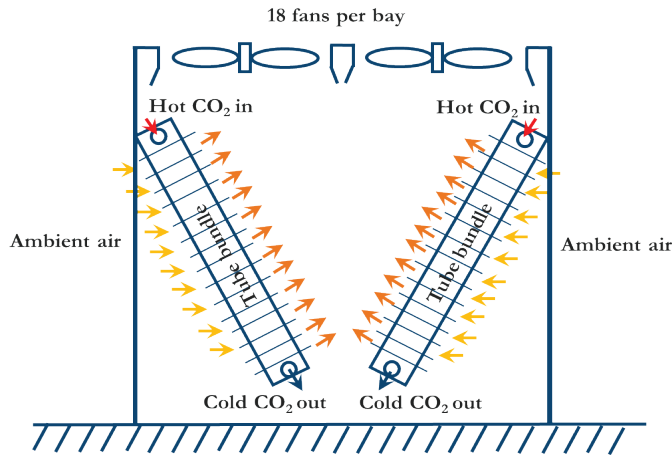


Figure 6: Schematic of the direct dry CO₂ cooler

Table 2: Geometric dimensions of the modeled plate fin-and-tube heat exchanger

Parameter	Value
Tube outer diameter (mm)	12
Tube wall thickness (mm)	0.7
Tube inner diameter (mm)	10.6
Finned tube length (m)	11.385
Tube arrangement pattern	Staggered
Fin thickness (mm)	0.15
Number of tube bundles	2
Number of tubes per row	64
Number of tube passes	3
Number of tubes per pass	2

The performance model is based on Example problems from the Kröger textbook [19]. The adjustable inputs in the spreadsheet are cooling duty, CO₂ operating conditions (inlet temperature and pressure, outlet temperature), air flow rate and ambient dry bulb temperature and pressure. The key output variables of the performance model are the number of required bays and the auxiliary fan power consumption.

The implicit energy balance and draft equations are solved iteratively for the main calculated outputs. Closure to the energy balance equations is provided using the ϵ - NTU relationship.

The ϵ - NTU relationship is derived under the assumption of constant properties. This assumption is not valid for CO₂ near the critical point due to the rapidly varying thermo-physical properties in this region. The cooler bay tube bundle is discretized into multiple sub-sections to account for the variation of thermo-physical properties of CO₂. For each sub-section the properties are assumed to be constant and the ϵ - NTU relationship is applied to each sub-section.

The effectiveness (ϵ) of each sub-section is calculated using the ϵ - NTU relationship for cross flow heat exchangers with both fluids unmixed. The air-side heat transfer coefficient and pressure drop across the tube bundle are calculated using the correlations published by Wang *et al.* [23]. For the CO₂-side, a separate set of correlations are used for condensing and non-condensing cases [19]. The CO₂-side heat transfer coefficient and pressure drop for the non-condensing cases are calculated using the Gnielinski correlation [24], while those for the condensing cases are calculated using correlations published by Cavallini *et al.* [25]. According to Cavallini *et al.*, the condensation heat transfer coefficient is either dependent or independent of the difference between the saturation temperature and the wall temperature. Since the wall temperature is unknown *a priori* an iterative algorithm is used to determine the condensation heat transfer coefficient. The frictional pressure drops for the condensing cases are calculated using the correlation of Friedel [26]. The thermo-physical properties for both CO₂ and air are calculated using the Span-Wagner equation of state [21] by linking the Excel spreadsheet to REFPROP [22].

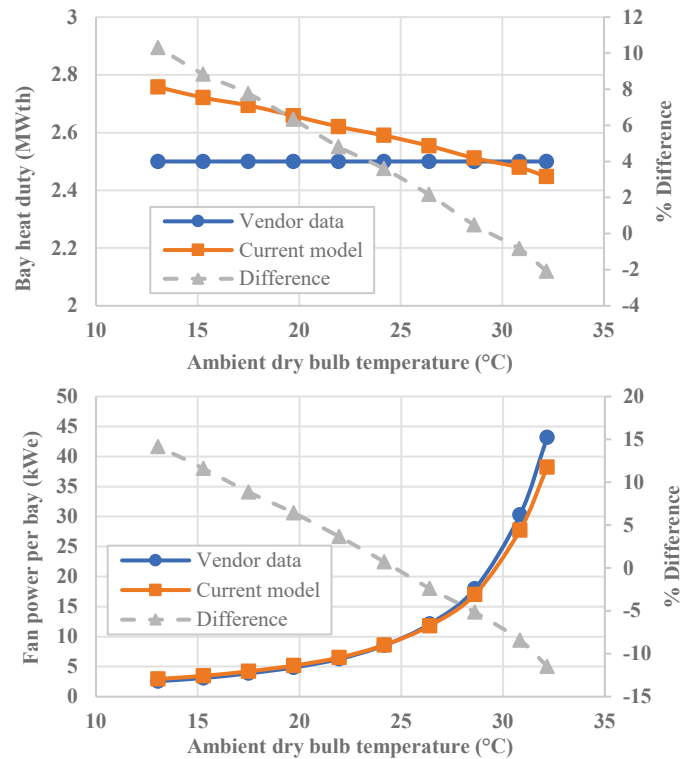


Figure 7: Direct dry cooler bay heat duty (top) and fan power consumption (bottom) as a function of ambient temperature

The performance model was validated against data provided by Guentner, a CO₂ cooler vendor. Figure 7 compares the calculated bay heat duty and fan power consumption from the model and the vendor data. The model was able to predict the vendor data for bay heat duty and fan power consumption within $\pm 10\%$ and $\pm 15\%$ respectively. This accuracy is quite good since the model doesn't fully replicate the vendor tube bundle.

The equipment capital cost of the direct dry cooler is scaled linearly with the number of cooler bays calculated from the performance model. The cost of each cooler bay is determined from the vendor quote. The equipment capital cost is converted to 2011\$ using the CEPCI [18]. No further validation of the linear cost model is performed due to lack of reliable data.

Adiabatic Cooling Performance and Cost Model

When the ambient temperatures are high the performance of dry coolers suffer due to approach to the dry bulb temperature. "Adiabatic" cooling systems are used in the CO₂ refrigeration industry to enhance the performance of CO₂ coolers during hot ambient conditions. The schematic of the adiabatic CO₂ cooler bay modeled in this study is shown in Figure 8. The construction of the adiabatic cooler bay is identical to that of direct dry cooler bay from Figure 6, with the addition of pre-cooler pads prior to the tube bundles. These pre-cooler pads are wetted with water when the ambient dry bulb temperature is above a certain set point. As the air is drawn over the wet cooling pads, the air is humidified and cooled to approach the wet bulb temperature. The modeled tube bundles are the same as those of the direct dry cooler from Table 2.

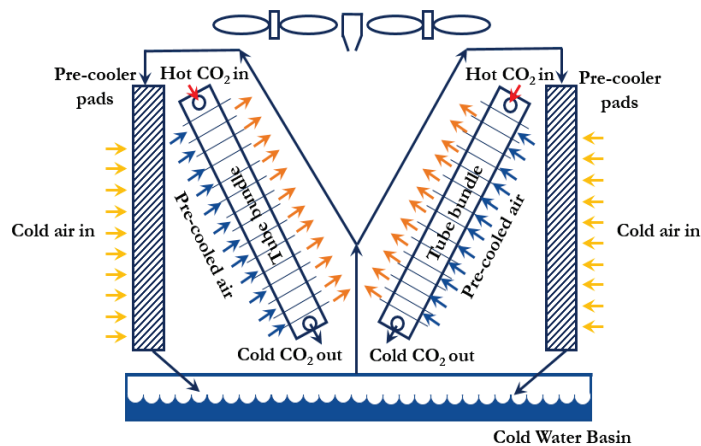


Figure 8: Schematic of the adiabatic cooling technology

The performance model for the adiabatic cooler is broken into two separate models that are executed in series; one for the pre-cooler pad and one for the tube bundle. The pre-cooler pad model solves the simplified mass and energy balance equations between the air and water film in the direction of air flow [27]. The outputs of the pre-cooler pad model are the air outlet temperature, humidity ratio and water consumption rate.

The pre-cooler pad efficiency (approach to wet-bulb temperature), heat transfer coefficient and the pressure drop

across the pad depends on the air flow rate and type of the cooling pad. It is assumed that the pad is constructed out of corrugated cellulose paper and the correlations published by S. He *et al.* [27] are used. The outputs from the pre-cooler pad model are provided as inputs to the direct dry cooler bay performance model described in the previous section.

The performance model is validated against data provided by Guentner for their adiabatic CO₂ coolers. Figure 9 compares the calculated bay heat duty, fan power consumption and water consumption between the current model and the vendor data. The model was able to predict the vendor data within $\pm 10\%$. Again, the accuracy is quite good considering that the pre-cooler pad model and tube bundle model don't fully replicate the vendor design.

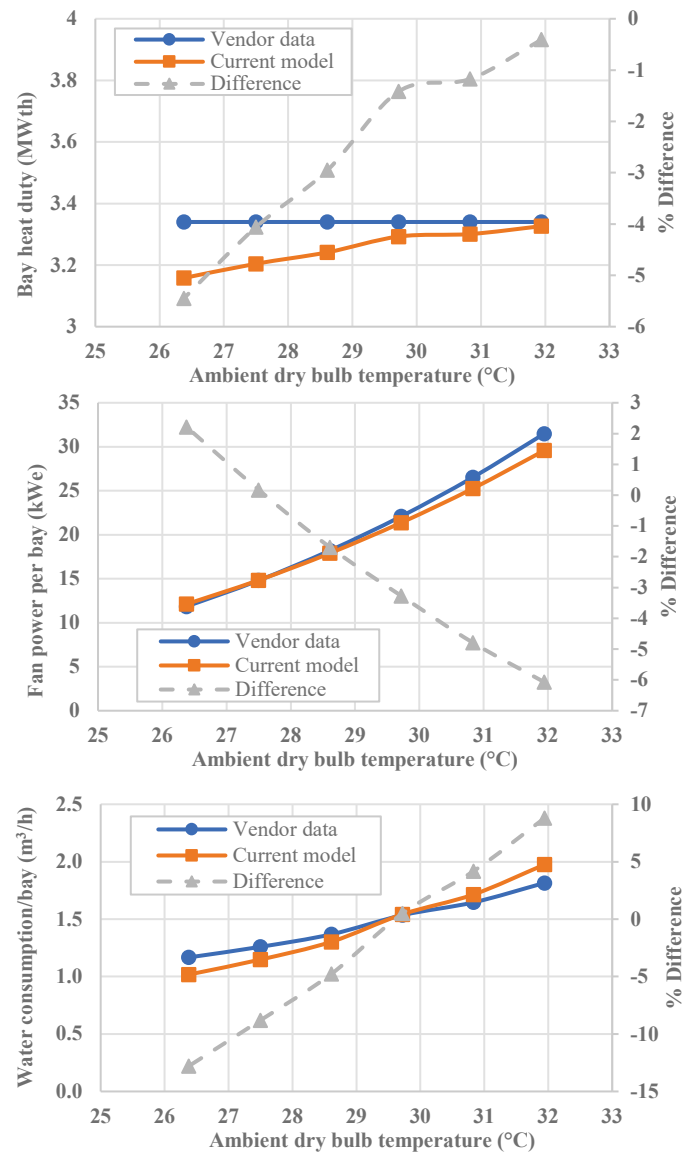


Figure 9: Adiabatic cooler bay heat duty (top), fan power consumption (middle) and water consumption rate (bottom) as a function of ambient dry bulb temperature.

The validated performance model can be used to calculate the number of cooler bays, auxiliary fan power and water consumption as a function of the CO₂ process conditions, cooling duty, ambient air conditions and volumetric flow rate of air.

The equipment capital cost of the adiabatic cooler is scaled linearly with the number of cooler bays calculated from the performance model. The cost of each cooler bay is determined from the vendor quote. The equipment capital cost is converted to 2011\$ using the CEPCI [18].

RESULTS AND DISCUSSION

Figure 1 shows a simplified schematic of the RCBC used in this study. A more detailed process flow diagram depicting all of the major plant components as well as a state point table is provided in Reference [1]. As the present work is primarily focused on process sensitivities around the low temperature components of the cycle, the presence or operation of higher temperature cycle components affects the study results only in that they establish a baseline plant efficiency against which these sensitivities are compared.

In modeling the sCO₂ cycle in Aspen, the exit temperatures in the recuperators are determined using design specifications within the model that target a minimum temperature approach at 5.6 °C (10 °F). Similar design specifications are applied to the flue gas and CO₂ coolers.

As a default, the main CO₂ compressor has a single stage of intercooling, although the Aspen model allows a greater number of intercooling stages to be used so that the optimal number of intercooling stages can be determined. In all cases, the intercooler outlet temperature is set equal to the main CO₂ cooler outlet temperature, and the intercooler pressure drop is set to 0.014 MPa (2 psid) for water-cooled cases and 0.14 MPa (20 psid) for air-cooled cases to account for longer sCO₂ pipe runs to the coolers. The isentropic efficiencies and pressure ratios for each compression stage are approximately equal.

The superheat and reheat units, depicted in Figure 1 internal to the CFB, constitute the primary heat exchanger, with each heating the high-pressure sCO₂ stream to the turbine inlet temperature of 760 °C. Two economizers are included in the power cycle to recover additional heat from the flue gas, with the FGC in Figure 1 serving as the flue gas cooler which recovers low quality heat from the flue gas in parallel with the LTR.

Table 3 lists the major assumptions and specifications applied to the RCBC.

Table 3: sCO₂ Brayton cycle model parameters

Parameter	Value
Turbine inlet temperature (°C)	760
Compressor outlet pressure (MPa)	34.6
Intercooler pressure drop (MPa)	0.14 or 0.014
Turbine isentropic efficiency	0.927
Compressor isentropic efficiency	0.85
Cycle pressure drop (MPa)	0.41
Minimum temperature approach (°C)	5.6

Although the focus of this paper is on the cooling system, the following sections show results for the whole plant. The Aspen model yields the performance estimates for the balance of plant components, such as the air separation unit and the CO₂ purification unit. Cost scaling algorithms were used to estimate the capital costs for the non-cooling system components. Details about these performance and cost models along with the methodology used to estimate COE are provided in Reference [1].

The Aspen plant model was run for cooler temperatures of 20, 25, 30, 35, and 40 °C, and the compressor inlet pressure (CIP) that maximizes the cycle and plant efficiency was calculated [4]. It was found that the optimal CIP is slightly higher than the saturation pressure or pseudo-critical pressure, consistent with other studies from literature [10]. The optimal CIP and the maximum cycle efficiency for the five cooler outlet temperatures are summarized in Table 4, where it can be seen that the cooler pressure drop (ΔP_{cooler} of 0.014 MPa vs 0.14 MPa) has no significant effect system performance.

Table 4: Optimal compressor inlet pressure and maximum cycle efficiency as a function of cooler exit temperature

CO ₂ cooler temperature (°C)	$\Delta P_{cooler}=0.014$ MPa		$\Delta P_{cooler}=0.14$ MPa	
	Optimal CIP (MPa)	Maximum η_{cycle} (%)	Optimal CIP (MPa)	Maximum η_{cycle} (%)
20	5.86	57.24	5.86	57.24
25	6.55	56.68	6.55	56.67
30	7.45	55.99	7.38	55.92
35	8.34	55.20	8.27	55.20
40	9.31	54.46	9.24	54.39

Although the maximum cycle efficiency increases with decreasing cooler outlet temperature, the capital cost of CO₂ coolers and auxiliary fan power consumption are expected to increase at the same time. Therefore, one would expect a natural trade-off between the efficiency and COE depending on the type of cooling technology and selected parameters for the cooling technology. The four cooling technology performance and cost models described in the previous sections were applied to explore such trade-offs and determine the optimum cold sCO₂ temperature. All presented results assume an ambient pressure of 101.325 kPa, and air dry and wet bulb temperatures of 15 °C and 10.82 °C respectively, corresponding to 60% relative humidity.

Wet cooling tower model results

Figure 10 shows example composite T-Q diagrams for the entire sCO₂ cooling system for the 25 °C (condensing) and 40 °C (noncondensing) cooler temperature cases. In the case of wet cooling technology, cooling tower range ($Range = T_{wi} - T_{wo}$) and approach to the wet bulb temperature ($T_{wct,app} = T_{wo} - T_{wb}$) are the two independent cooling technology parameters that influence the auxiliary power consumption, capital cost and water consumption rate. The sCO₂ temperatures are fixed by the cycle model, as is the air wet bulb temperature and the hot end air/water approach temperature. For condensing CO₂ cases, 1-D

modeling of the water/CO₂ cooler ensures that a temperature cross does not exist at the point where CO₂ first condenses.

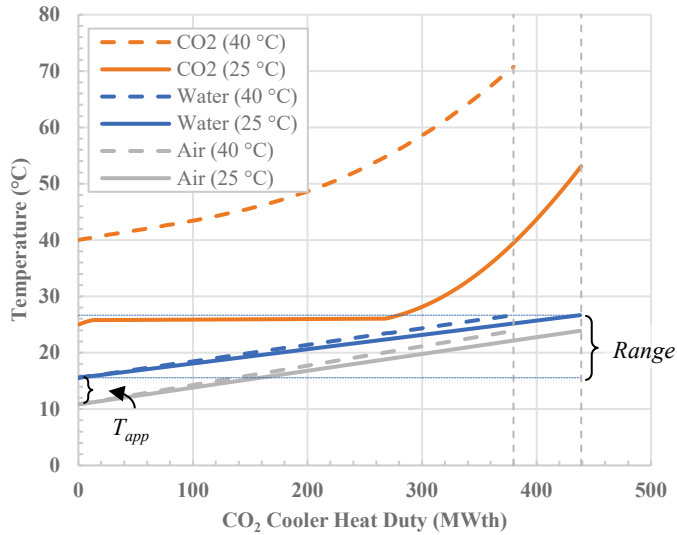


Figure 10: Composite T-Q diagram for the sCO₂ cooling system at 25 °C and 40 °C

Figure 11 shows the COE (without CO₂ transport & storage [T&S] costs) and plant efficiency as a function of cooling tower range and temperature approach for the sCO₂ cooler outlet temperature of 25 °C. For a fixed temperature approach of 2.8 °C (5 °F), the cooling tower range was varied from 5 °C (9 °F) to 20 °C (36 °F). Increasing the cooling tower range impacts the plant efficiency and COE in the following ways: 1) the plant efficiency increases due to a reduction in cooling tower fan and cooling water pump power consumption, 2) the capital cost of water/CO₂ coolers increases due to reduced driving forces and consequently higher heat transfer area requirements, and 3) the capital cost of the cooling tower decreases according to the modified Zanker correlation described earlier. The net impact of these opposing trends on the plant's COE yields a minimum value at a particular value of the cooling tower range (~15.3 °C in this example case).

For the optimum range of ~15.3 °C (27.5 °F), the cooling tower temperature approach was varied from 0 to 11.1 °C (20 °F). Decreasing the cooling tower approach temperature impacts the plant efficiency and COE in the same way as increasing the range as discussed above, except that this leads to a decrease in the water/CO₂ cooler cost due to increased driving forces. The net impact on the plant is that COE attains a minimum value at a low value of cooling tower temperature approach (0.7 °C in this example case). However, as indicated earlier, 2.8 °C was chosen as the minimum cooling tower temperature approach based on recommendation by cooling tower manufacturers. Colder CO₂ cooler temperature cases also optimize to this 2.8 °C temperature approach, though the plant efficiency increases with decreasing temperature approach in these cases. Table 5 shows the optimum values of cooling tower temperature approach and range for each of the cooler exit temperatures. Note that the cooling tower range impacts plant

efficiency and COE more than the cooling tower approach temperature, since it affects both water consumption and cooling tower size.

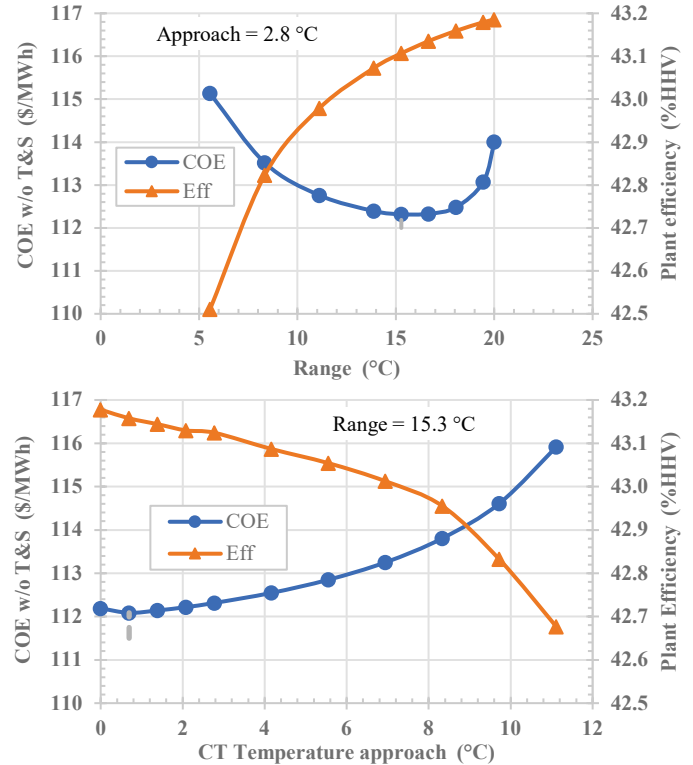


Figure 11: Variation of plant efficiency and COE with respect to cooling tower range and approach temperature.

Table 5: Optimum values of wet cooling tower (WCT) range and temperature approach for each cooler exit temperature

CO ₂ cooler temperature (°C)	Optimum WCT approach (°C)	Optimum WCT range (°C)
20	2.8	8.9
25	2.8	15.6
30	2.8	24.4
35	2.8	27.8
40	2.8	27.8

Indirect dry cooling technology model results

In the case of indirect dry cooling technology, the ACHE water range ($Range = T_{wi} - T_{wo}$) and approach to the dry bulb temperature ($T_{app} = T_{wo} - T_{db}$) are the two independent cooling technology parameters that influence the auxiliary power consumption and capital cost. These are analogous to the parameters shown in Figure 10 except T_{app} is the approach to the higher dry bulb temperature. As with the wet cooling tower, the sCO₂ temperatures are fixed by the cycle model, and the inlet air dry bulb temperature is fixed. The hot end air/water approach temperature varies due to the crossflow nature of the ACHE cooler.

Figure 12 shows the COE and plant efficiency as a function of the ACHE range and temperature approach for a cooler outlet temperature of 25 °C. For a fixed ACHE temperature approach

of 2.8 °C (5 °F), the ACHE range was varied from 2.2 °C (4 °F) to 13.3 °C (34 °F). Increasing the ACHE range impacts the plant efficiency and COE as follows: 1) the plant efficiency increases due to reduction in ACHE auxiliary fan power consumption, 2) the capital cost of the water/CO₂ coolers increases due to reduced driving forces and consequently higher heat transfer area requirements, and 3) the capital cost of the ACHE decreases. Due to these opposing trends, the net impact on the plant is that the COE attains a minimum value for a particular value of the ACHE range (approximately 11.1 °C in this example case).

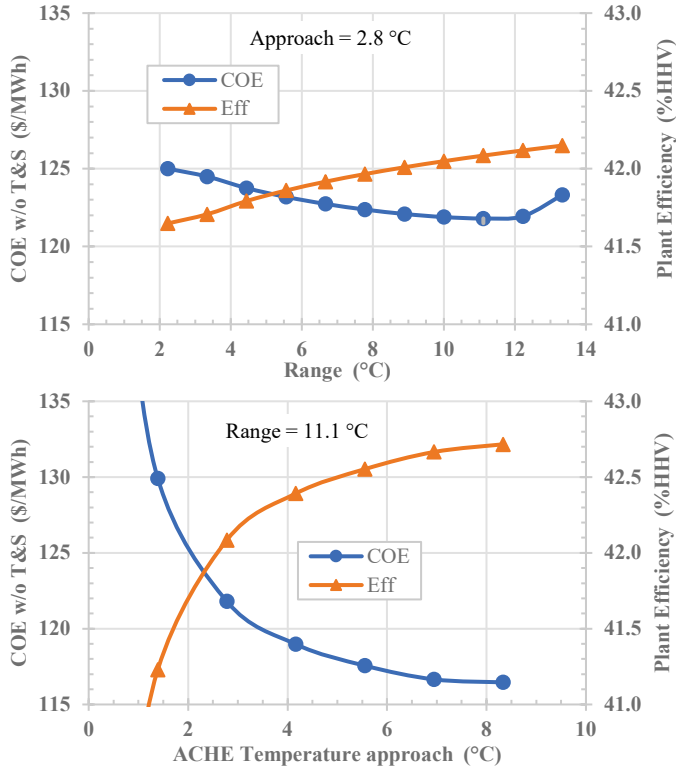


Figure 12: Variation of plant efficiency and COE with respect to indirect dry cooler (ACHE) range and approach temperature

For the optimum range of 11.1 °C (20 °F), the ACHE cooler temperature approach was varied from 0.7 °C (1.3 °F) to 8.3 °C (14.9 °F). Increasing the ACHE temperature approach impacts the plant efficiency and COE in the same manner as increasing the ACHE range, with the minimum COE occurring for larger values of the ACHE temperature approach.

Table 6: Optimum values of Indirect dry (ACHE) temperature approach and range for each the cooler exit temperature

CO ₂ cooler temperature (°C)	Optimum ACHE temp. approach (°C)	Optimum ACHE range (°C)
20	4.5	0.37
25	7.9	1.39
30	12.0	3.35
35	16.3	4.75
40	20.1	9.70

Table 6 shows the optimum values of ACHE temperature approach and range for each of the cooler exit temperatures. Note that the optimal cooling system parameters are not general, and only apply to the modeled plant using the economic assumptions applied in its analysis.

Direct dry cooling technology model results

In the case of direct dry cooling technology, the volumetric flow rate of air is the only parameter that influences the cooling duty, auxiliary power consumption, and the capital cost. Figure 13 shows the COE and plant efficiency as a function of the volumetric flow rate of air per bay for a cooler outlet temperature of 25 °C. Increasing the volumetric flow rate of air decreases plant efficiency due to increases in the dry cooler auxiliary fan power consumption, while the number of required cooler bays to meet the design specifications decreases resulting in lower capital cost of the CO₂ coolers. Due to these opposing trends, the COE attains a minimum value for a particular value of air flow rate (approximately 90 m³/s in this example case).

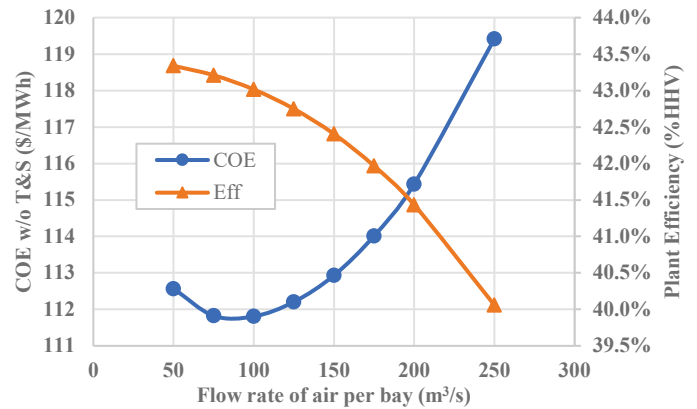


Figure 13: Variation of plant efficiency and COE with respect to flow rate of air per bay for the direct dry cooler

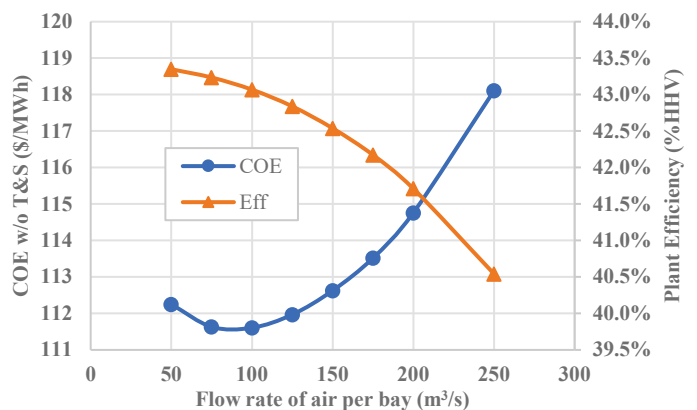


Figure 14: Variation of plant efficiency and COE with respect to flow rate of air per bay for the adiabatic cooler

A similar set of conclusions can be drawn for adiabatic cooling technology as well as depicted in Figure 14. However, in

the case of adiabatic cooling technology the water consumption rate increases with the air flow rate.

Plant COE Optimization Results

Based on the sensitivity analyses presented in the previous sections, the optimum cooling technology parameters are determined for each of the CO₂ cooler temperatures and all four cooling technologies. Figure 15 presents the optimized plant efficiency and COE as a function of CO₂ cooler outlet temperature. Notably, the plant efficiency is shown to improve by 3.0 – 3.5 percentage points, and the plant COE is reduced by as much as 8%, by decreasing the CO₂ cooler temperature from 40 to 20 °C, depending on the cooling technology.

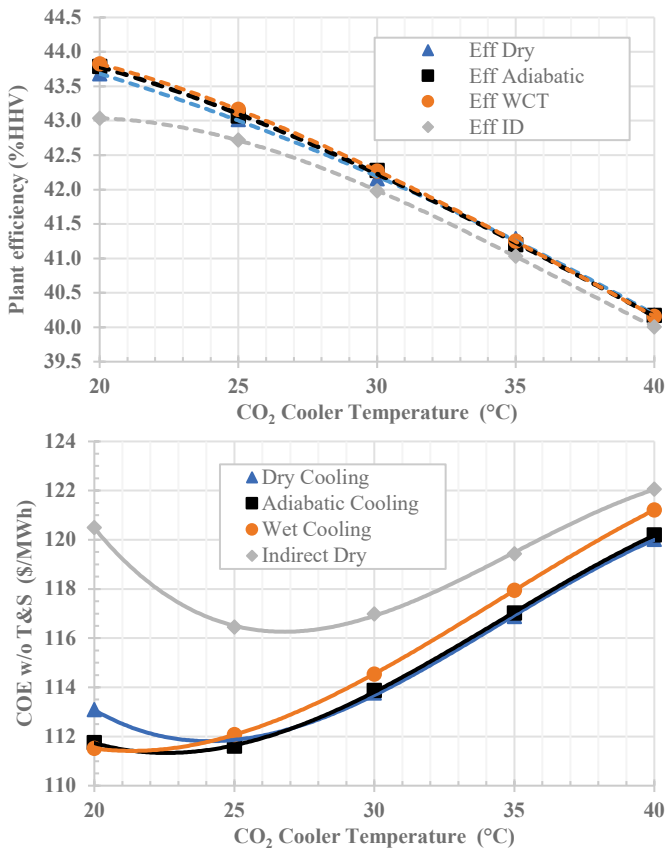


Figure 15: Optimized COE and plant efficiency as a function of cooler outlet temperature for all four cooling technologies

Out of the four cooling technologies, indirect dry cooling technology yields the lowest plant efficiency and highest COE for all the CO₂ cooler temperatures. For CO₂ cooler temperature above 25 °C, both the direct dry cooling and adiabatic cooling technologies offered nearly the same plant efficiency and COE. Moreover, the COE is lowest for the direct dry cooling and adiabatic cooling technologies (relative to other cooling technologies) for CO₂ cooler temperature above 25 °C. The COE of the direct dry cooling technology attains a minimum value for CO₂ cooler temperature of ~25 °C. As the CO₂ cooler temperature decreases below ~25 °C, the COE of the direct dry

cooling technology starts to increase due to increases in the capital cost of the CO₂ coolers. It is interesting to note that the COE of the adiabatic cooling technology continues to decrease with CO₂ cooler temperature unlike the direct dry cooling technology.

For the lowest value of the CO₂ cooler temperature investigated (20 °C), the COE of adiabatic cooling and wet cooling tower technologies are similar. However, the water consumption rate in the case of adiabatic cooling technology is significantly lower (689 m³/h for adiabatic cooling vs 1,146 m³/h for wet cooling tower). This reduced water consumption makes the adiabatic cooling technology more attractive in hot and dry regions where the water resources are typically scarce. Moreover, unlike the wet cooling tower, adiabatic cooling technology offers the flexibility to operate in dry cooling mode when allowed by low ambient temperatures.

An important point to note is that the optimized results presented here are valid only for the ambient conditions selected. In case of higher/lower ambient temperatures, the optimum cooler temperature will change accordingly for each of the cooling technologies.

CONCLUSIONS & FUTURE WORK

This paper describes the development of performance and cost models for four cooling technologies of interest to indirect sCO₂ power cycle designers, covering both direct sCO₂ cooling and indirect cooling through a water intermediate fluid, as well as wet and dry cooling technologies for approach to ambient wet and dry bulb temperatures, respectively. The models are applicable for any ambient conditions and can thus be used for plant site selection analyses or studies of the expected performance of the system under different climate scenarios. The spreadsheet models are publicly available to the sCO₂ research community to assist in economic optimization of sCO₂ plant designs [15]. While not intended to cover all available cooling technologies, these models do provide a representative cross-section of the various cooling types, all developed with a uniform set of assumptions to allow one to weigh the benefits and drawbacks of each cooling technology type.

Each of the cooling technology models were applied to a pre-existing RCBC model with an oxy-CFB primary heat source to demonstrate their utility in cold-end cycle optimization. Sensitivity analyses show the performance and cost impacts of variations in the design range and approach temperature as well as the air flow rate through the cooling bay for the dry cooling and adiabatic cooling technologies. These sensitivity analyses show the interplay between the overall plant efficiency and COE and generally identify the point of minimum COE.

Finally, a comparative analysis of all four technologies was conducted over a range of CO₂ cooler outlet temperatures between 20 °C and 40 °C. The sCO₂ plant efficiency is shown to improve by 3.0 – 3.5 percentage points, and the plant COE is reduced by as much as 8%, by decreasing the CO₂ cooler temperature from 40 to 20 °C, depending on the cooling technology. This highlights the importance and impact of cooling

system thermal integration for sCO₂ power cycles, and the utility of the spreadsheet models in helping cycle designers develop commercially competitive indirect sCO₂ power systems.

Between the cooling technologies studied, indirect dry cooling has the lowest plant efficiency while wet cooling yields the highest efficiency, with dry cooling and adiabatic cooling only slightly lower. The differences in the impact of CO₂ cooler temperature on efficiency increase as the cooler temperatures approach ambient conditions. The variations in the COE between the four cooling technologies are even more striking. Indirect dry cooling yields the highest COE at all CO₂ cooler temperatures. At the lowest CO₂ cooler temperatures, wet cooling and adiabatic cooling yield the lowest COE while above ~25 °C, direct dry and adiabatic cooling give the lowest COE. Each cooling technology shows a minimum in COE, generally for CO₂ cooler temperatures between 20 °C and ~27 °C.

Work is currently underway to enable use of these spreadsheet cooling models for semi-closed direct sCO₂ power cycles, where the working fluid includes water, oxygen, and other sCO₂ impurities. Future work on the cooling technology models is expected to focus on further improvements in the accuracy of performance and cost estimates through additional vendor data and to increase the number of adjustable design variables for the cooling technologies. These models will be applied to future direct and indirect sCO₂ techno-economic analyses to optimize cooling system designs as a function of plant site ambient conditions, including seasonal temperature variability.

NOMENCLATURE

A	- WCT cold end temperature approach
ACHE	- Air-cooled heat exchanger
BEC	- Bare erected cost
C	- Zanker correlation coefficient
CEPCI	- Chemical Engineering Plant Cost Index
CFB	- Circulating fluidized bed
CIP	- Compressor inlet pressure
COE	- Cost of electricity
FGC	- Flue gas cooler
gpm	- Gallons per minute
HHV	- Higher heating value
HTR	- High temperature recuperator
ID	- Indirect dry
kWe	- Kilowatt electric
LTR	- Low temperature recuperator
m	- Mass flow rate
MC	- Main compressor
MWe	- Megawatt electric
MWth	- Megawatt thermal
NETL	- National Energy Technology Laboratory
NTU	- Number of transfer units
oxy	- Oxygen
Q	- Heat duty
R	- Range
RC	- Recompression (bypass) compressor

RCBC	- Recompression Brayton cycle
REFPROP	- Reference Fluid Thermodynamic and Transport Properties Database
sCO ₂	- Supercritical carbon dioxide
T _{ACHE,app}	- ACHE temperature approach
T _{db}	- Dry bulb temperature
T-Q	- Temperature-heat duty
T&S	- Transportation & storage
T _{wb}	- Wet bulb temperature
T _{WCT,app}	- Wet cooling tower temperature approach
T _{wi}	- Inlet water temperature
T _{wo}	- Outlet water temperature
UA	- Conductance
VTR	- Very high temperature recuperator
WCT	- Wet cooling tower
ε	- Heat exchanger effectiveness

ACKNOWLEDGEMENTS

The authors wish to thank Richard Dennis (NETL) for his support for this project. The authors also wish to thank Wally Shelton, Travis Shultz (NETL), Mark Woods (KeyLogic) and Eric Lewis, Dale Keairns (Deloitte Consulting, LLP) for their technical assistance and input. Finally, the authors would like to thank Ian Runsey (Guentner), Jamison Ditthardt (Guentner), Tim Leach (Guentner) for providing the vendor data for the dry and the adiabatic cooling technologies. This work was completed under DOE NETL Contract Number DE-FE0004001.

REFERENCES

- [1] National Energy Technology Laboratory (NETL), "Techno-economic Evaluation of Utility-Scale Power Plants Based on the Indirect sCO₂ Brayton Cycle," DOE/NETL- 2017/1836, Pittsburgh, PA, September 2017.
- [2] Y. Ma, M. Liu, J. Yan and J. Liu, "Thermodynamic study of main compression intercooling effects on supercritical CO₂ recompression Brayton cycle," *Energy*, vol. 140, pp. 746-756, 2017.
- [3] National Energy Technology Laboratory (NETL), "Indirect sCO₂ Cycle Cooling Integration for Improved Plant Performance and Cost," DOE/NETL-2018/####, Pittsburgh, PA, January 2018.
- [4] N. Weiland, C. White and A. O'Connell, "Effects of Cold Temperature and Main Compressor Intercooling on Recuperator and Recompression Cycle Performance," in *2nd European Supercritical CO₂ Conference*, Essen, Germany, August 30-31, 2018.
- [5] C. White, W. Shelton, N. Weiland and T. Shultz, "sCO₂ Cycle as an Efficiency Improvement Opportunity for Air-fired Coal Combustion," in *The 6th International Supercritical CO₂ Power Cycles Symposium*, Pittsburgh, PA, March 27-29, 2018.

- [6] National Energy Technology Laboratory (NETL), "Supercritical Carbon Dioxide (sCO₂) Cycle as an Efficiency Improvement Opportunity for Air-Fired Coal Combustion," Pittsburgh, PA, February 2019.
- [7] S. A. Wright, R. F. Radel, T. M. Conboy and G. E. Rochau, "Modeling and Experimental Results for Condensing Supercritical CO₂ Power Cycles," Sandia National Laboratories, Albuquerque, 2011.
- [8] T. M. Conboy, M. D. Carlson and G. E. Rochau, "Dry-Cooled Supercritical CO₂ Power for Advanced Nuclear Reactors," *Journal of Engineering for Gas Turbines and Power*, vol. 137, pp. 012901-1, 2015.
- [9] J. J. Sienicki, A. Moisseytsev and Q. Lv, "Dry Air Cooling and the sCO₂ Brayton Cycle," in *Proceedings of the ASME Turbo Expo 2017*, Charlotte, NC, 2017.
- [10] S. R. Pidaparti, P. J. Hruska, A. Moisseytsev, J. J. Sienicki and D. Ranjan, "Technical and Economic Feasibility of Dry Air Cooling for the Supercritical CO₂ Brayton Cycle Using Existing Technology," in *5th International Symposium - Supercritical CO₂ Power Cycles*, San Antonio, Texas, March 28-31, 2016.
- [11] S. R. Pidaparti, A. Moisseytsev, J. J. Sienicki and D. Ranjan, "Counter flow induced draft cooling tower option for supercritical carbon dioxide Brayton cycle," *Nuclear Engineering and Design*, vol. 295, pp. 549-558, 2015.
- [12] T. J. Held, J. Miller and D. J. Buckmaster, "A Comparative Study of Heat Rejection Systems for sCO₂ Power Cycles," in *The 5th International Symposium - Supercritical CO₂ Power Cycles*, San Antonio, Texas, March 28-31, 2016.
- [13] P. J. Hruska, G. F. Nellis and S. A. Klein, "Methodology of Modeling and Comparing the Use of Direct Air-Cooling for a Supercritical Carbon Dioxide Brayton Cycle and a Steam Rankine Cycle," in *5th International Symposium - Supercritical CO₂ Power Cycles*, San Antonio, Texas, March 28-31, 2016.
- [14] N. T. Weiland, B. W. Lance and S. R. Pidaparti, "sCO₂ Power Cycle Component Cost Correlations from DOE Data Spanning Multiple Scales and Applications," in *ASME Turbo Expo 2019*, Phoenix, Arizona, 2019.
- [15] National Energy Technology Laboratory, "Cooling Technology Performance and Cost Models for sCO₂ Power Cycles," NETL, Pittsburgh, 2019. <https://www.netl.doe.gov/energy-analysis/details?id=3199>
- [16] SPX Cooling Technologies Inc., *Cooling Tower Fundamentals 2nd Edition*, Overland Park, Kansas: SPX Cooling Technologies Inc., 2009.
- [17] A. Zanker, "Cooling Tower Costs from Operating Data," in *Calculation and Shortcut Handbook*, New York, McGraw-Hill Book Co., 1967, pp. 47-48.
- [18] S. A. Leeper, "Wet Cooling Tower: 'Rule-of-thumb' Design and Simulation," Idaho National Engineering Laboratory, EGG-GTH-5775, pp 10-11, 1981.
- [19] Thermoflow, *STEAM PRO and PEACE software modules version 27.0*, Southborough, MA: info@thermoflow.com, 2017.
- [20] Chemical Engineering, "The Chemical Engineering Plant Cost Index," 2019. [Online]. Available: <https://www.chemengonline.com/pci-home>.
- [21] D. G. Kröger, *Air-cooled heat exchangers and cooling towers (Vol. 2)*, PennWell Books, 2004.
- [22] National Energy Technology Laboratory (NETL), "Air Cooled Heat Exchanger (ACHE) Design Final Presentation," Pittsburgh, PA, 2017.
- [23] R. Span and W. Wagner, "A New Equation of State for Carbon Dioxide Covering the Fluid Region from the Triple-Point Temperature to 1100 K at Pressures up to 800 MPa," *J. Phys. Chem. Ref. Data*, vol. 25, no. 6, pp. 1509-1596, 1996.
- [24] National Institute of Standards and Technology (NIST), *NIST Reference Fluid Thermodynamic and Transport Properties - REFPROP*, U.S. Department of Commerce, 2007.
- [25] C.-C. Wang, K.-Y. Chi and C.-J. Chang, "Heat transfer and friction characteristics of plain fin-and-tube heat exchangers, part II: Correlation," *International Journal of Heat and mass transfer*, vol. 43, no. 15, pp. 2693-2700, 2000.
- [26] V. Gnielinski, "New equations for heat and mass transfer in turbulent pipe and channel flow," *Int. Chem. Eng.*, vol. 16, no. 2, pp. 359-368, 1976.
- [27] A. Cavallini, D. D. Col, L. Doretti, M. Matkovic, L. Rossetto, C. Zilio and G. Censi, "Condensation in horizontal smooth tubes: a new heat transfer model for heat exchanger design," *Heat transfer engineering*, vol. 27, no. 8, pp. 31-38, 2006.
- [28] L. Friedel, "Improved friction pressure drop correlation for horizontal and vertical two-phase pipe flow.," *Proc. of European Two-Phase Flow Group Meet., Ispra, Italy*, 1979.
- [29] S. He, Z. Guan, H. Gurgenci, K. Hooman, Y. Lu and A. M. Alkhedhair, "Experimental study of film media used for evaporative pre-cooling of air," *Energy conversion and management*, vol. 87, pp. 874-884, 2014.

STUDY OF AUTONOMOUS CONTROL SYSTEM FOR S-CO₂ POWER CYCLE

Bong-Seong Oh
KAIST

Daejeon, Republic of Korea
Email: bongseongoh@kaist.ac.kr

Jeong Ik Lee*
KAIST

Daejeon, Republic of Korea
Email: jeongiklee@kaist.ac.kr

ABSTRACT

Various control strategies for supercritical carbon dioxide cycle (S-CO₂ cycle) have been developed. A combination of bypass and inventory controls is regarded as one of the most important and efficient strategy. When only an inventory control is actuated, the system pressure changes significantly to maintain velocity and temperature at approximately constant level. Hence, an off-design performance of turbomachinery is comparable to on-design performance so that inventory control could allow S-CO₂ cycles to maintain high thermal efficiency during part load operating conditions. Nevertheless, an inventory control alone is expected to have issues of delayed response, compressor surge and unexpected system shut down. Therefore, a bypass control should compensate the slow response time of an inventory control even though the bypass control results in undesirable cycle performance at off-design operating conditions. A quantitative assessment of inventory control for an S-CO₂ cycle has been rarely conducted because non-ideal thermodynamic properties of S-CO₂ make the assessment of appropriate inventory for the selected operating conditions to be difficult. In this paper an S-CO₂ cycle performance inventory tanks are modeled to assess various control schemes in terms of response and efficiency.

INTRODUCTION

Supercritical CO₂ cycles (S-CO₂ cycles) are regarded as a promising power cycle because S-CO₂ cycles have many advantages in a practical application. High thermal efficiency, low volume to power ratio, mild environment for keeping integrity of turbomachinery blade are the expected advantages of the cycle [1-4]. Thanks to small volume and high efficiency of S-CO₂ cycles, KAIST has developed an S-CO₂ cooled fully modularized Small Modular Reactor, namely KAIST Micro Modular Reactor (MMR), to provide energy to a remote region for 20 years without refueling [5].

An important feature for the MMR is to be equipped with autonomous control. In the previous work, a part load simulation of MMR was implemented and it showed that MMR core is autonomously regulated without a reactivity control.

Two controllers used in the system are inventory and turbine bypass controls to adjust the system to demand from grid [6]. However, the inventory control was assessed based on the infinite inventory tank previously. In this paper, the effect of having finite volume inventory tank will be first evaluated. Various control schemes are compared to find the most proper scheme in terms of fast response and part load efficiency as well.

KAIST MMR

MMR is designed to supply electricity to a remote region and can be transported by ship, train and vehicle. The heat is rejected to ambient air so that it can be independent from the site location. MMR is composed of a single unit including reactor core, power conversion system and all other supporting systems in a double wall containment for good transportability. For compactness of the system, the layout of MMR is simple recuperated cycle. The following figure represents a conceptual picture of MMR.



Figure 1: Conceptual picture of MMR

INVENTORY CONTROL

For closed Brayton cycles including S-CO₂ cycles, turbine bypass, inventory, turbine throttle and turbine inlet temperature controls are conventionally used to follow a load following condition [7-9]. Among these control strategies, inventory control is known as the most efficient control [10, 11] but the

inventory control is not expected to be used for rapid load changes because gas transfer from and to the operating inventory is normally a very slow process [12]. To compensate its slow characteristic time, turbine bypass control is operated in case of a drastic load change situation. However, turbine bypass valve makes efficiency of closed Brayton cycles to be inferior as shown in Figure. 2.

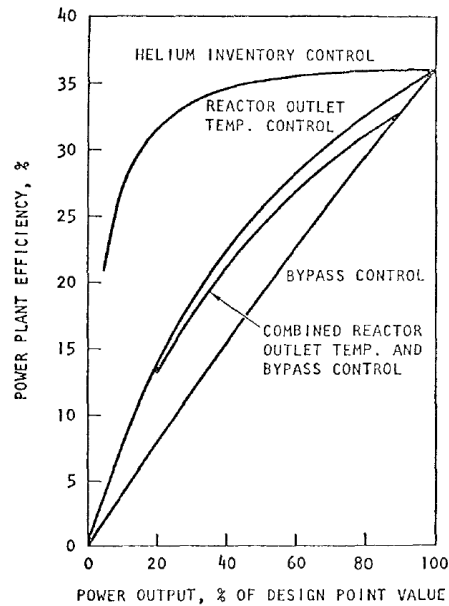


Figure 2: Part-load efficiency for the various control modes [10]

PART LOAD OPERATION RESULTS WITH INFINITE VOLUME OF INVENTORY TANKS

In this part, various control scheme which is indicated in Table I with infinite volume of inventory tanks will be analyzed and part load results will be presented when infinite volume is applied. The grid load is reduced from 100% to 25% and it will be increased again from 25% to 100% with $\pm 5\%$ per minute rate of grid load change [9].

Table I. Control scheme options of MMR

<p><Control scheme 1></p>	<p><Control scheme 2></p>
<ul style="list-style-type: none"> - Turbine bypass (1) - Discharging: Compressor outlet (2-2) - Feeding: Precooler inlet (2-1) 	<ul style="list-style-type: none"> - Turbine bypass (X) - Discharging: Compressor outlet (2-2) - Feeding: Precooler inlet (2-1)
<p><Control scheme 3></p>	<p><Control scheme 4></p>
<ul style="list-style-type: none"> - Turbine bypass (X) - Discharging: Compressor outlet (2-2) - Feeding: Compressor outlet (2-1) 	<ul style="list-style-type: none"> - Turbine bypass (1) - Discharging: Compressor outlet (X) - Feeding: Compressor outlet (X)

Commonly, a single inventory tank, whose pressure is in between maximum and minimum pressures of a cycle, is located between the compressor outlet and the precooler inlet. The layout is shown in control scheme 1, which is the most general control scheme of closed gas Brayton cycles. Since mass transfer can occur naturally due to pressure difference between inventory tank and the cycle, control scheme 1 is advantageous in the aspect of simplicity and fast response when load is decreased. However, control scheme 1 leads to a delayed response in case of increase in load. The reason is that the system inventory should also increase when the load is increased. In control scheme 1, inventory is increased at the compressor inlet which can cause an instantaneous rise of compressor mass flow rate compared to the turbine. Consequently, compressor work exceeds turbine work at the beginning of inventory charging [13]. If charging rate is slow enough, turbine and compressor gradually reach the balance and the cycle will approach to a new stable state but if not the system will be unstable so that the system can shut down. It can be confirmed in right figure of Figure 3. The dashed slopes in the figure represents demanded load and solid line means the actual current load. As shown the figure, when inventory is supplied at compressor inlet, there is a large distinction between demand load and current load. Hence, application of control scheme 1 is not proper in order to have fast response control system for both increase and decrease in power.

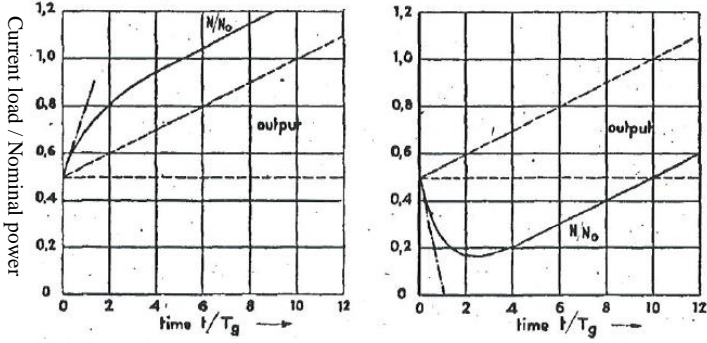


Figure 3: Net power when introducing inventory into compressor outlet (left) and compressor inlet (right) [13]

It can be also confirmed that control scheme 1 is not suitable for the load increase condition in case of MMR system as shown in Figure 4.

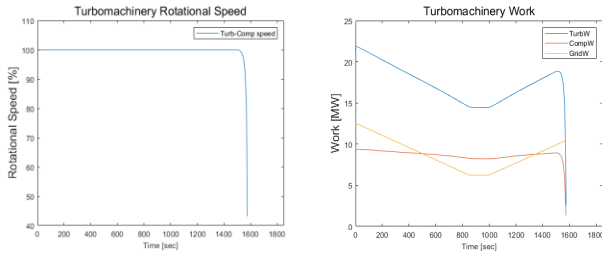


Figure 4: turbine speed (left) and grid demand and net power (right) with control scheme 1

Control scheme 2 is identical with control scheme 1 except there is no turbine bypass control. In case of control scheme 1, turbine bypass control compensates slow response of inventory charging but control scheme 2 does not have turbine bypass control at all. As a result, control scheme 2 makes MMR system to be very unstable even at 10% load reduction as shown in Figure 5.

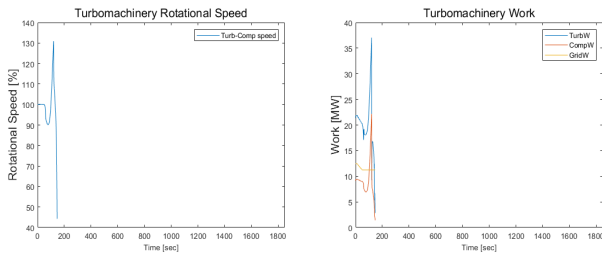


Figure 5: Turbine speed (left) and grid demand and net power (right) with control scheme 2

Control scheme 3 requires two inventory tanks and both tanks are located at compressor outlet. One tank is pressurized more than the compressor outlet pressure to charge inventory through compressor outlet line and the other is pressurized less than compressor outlet pressure to discharge inventory. When this scheme is applied, delayed response problem which occurs in case of load increase can be resolved. Since inventory charging

and discharging are conducted at the compressor outlet, compressor work does not exceed turbine work during inventory control. Especially, the response time of this control scheme is quick enough to regulate turbine rotational speed with only inventory control so that the turbine bypass control can be eliminated from the control scheme. This control scheme was firstly devised by Salzmann et al. [14]. As shown in Figure 6, control scheme 3 shows superior performance compared to control schemes 1 or 2.

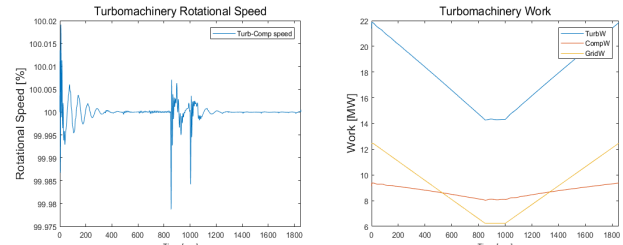


Figure 6: Turbine speed (left) and grid demand and net power (right) with control scheme 3

Control scheme 4 represents that the control scheme is equipped with only bypass control. Due to nature of bypass control, it shows the fastest response than other control schemes.

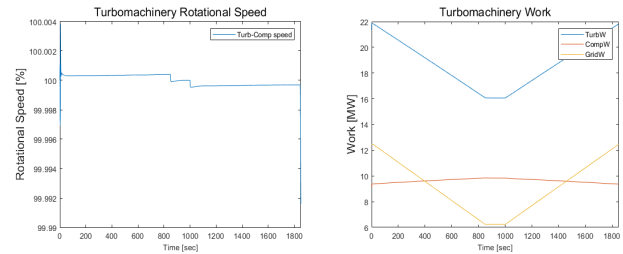


Figure 7: Turbine speed (left) and grid demand and net power (right) with control scheme 4

CONCEPTUAL DESIGN OF INVENTORY TANK

Previous results are calculated with an assumption that infinite volume exists in inventory tanks. However, inventory tanks indeed have finite size. Therefore, upper and lower limit of MMR part load along to inventory volume, initial pressure and temperature will be assessed by adopting thermodynamic equilibrium states between MMR loop and inventory tank.

Upper and lower limit of conventional closed gas cycle's load range with given initial mass of inventory tank and loop can be obtained from the following equation [15].

- Lower limit (load decrease)

$$x_L = \frac{1 + M_1 / M_o}{1 + yM_1 / M_o} \quad (1)$$

- Upper limit (for a further load increase)

$$x_U = \frac{1 + M_1 / M_o}{1 + \frac{y}{\omega} M_1 / M_o} \quad (2)$$

M_0, M_1 : Initial mass of gas respectively in the loop and in the transfer tank

y : Ratio of the cycle HP to the initial pressure of the tank

ω : Pressure ratio of the closed gas cycle

The equations (1)~(2) are derived based on the pressure equilibrium with isothermal process after inventory tank is connected to the primary loop. To obtain the lower or upper limit at given inventory tank condition, some assumptions are made.

1. Ideal gas of Equation of State
2. Isothermal process between tank and loop
3. High pressure is proportional to current part load operation

$$\left(x = \frac{P_{high}(t)}{P_{high,o}} = \frac{W_{net}(t)}{W_{net,o}} \right)$$

4. Turbomachinery pressure ratio is constant during part load condition

In case of finite inventory tank design for S-CO₂ cycles, the previous assumptions should be demonstrated whether they are reasonable or not. The first assumption cannot be applied to an S-CO₂ inventory tank because CO₂ has abrupt property changes near the critical point. The second assumption is still used to analyze the S-CO₂ system because the temperature difference between loop and tank can result in thermal stress and two phase flow problem. As a result, initial temperature of inventory tank should be identical with point where inventory tank is connected to the loop. From the comparison results of three control schemes, CO₂ inventory should be charged or discharged at the compressor outlet as proven in control scheme 3. The initial temperature of low pressure and high pressure inventory tank should be determined as 142°C which is the outlet temperature of MMR compressor at the design point. The third assumption can be also applied to S-CO₂ part load condition. Figure 8 represents equilibrium pressure of GAMMA+ code at compressor outlet with respect to part load condition after an infinite volume of inventory tank is connected. The figure shows that almost linear dependence between part load and equilibrium pressure until 20% so that the part load operation using finite volume of inventory tank will be limited to 20% part load as a lower boundary. Therefore, current part load can be estimated from the current equilibrium pressure of compressor outlet.

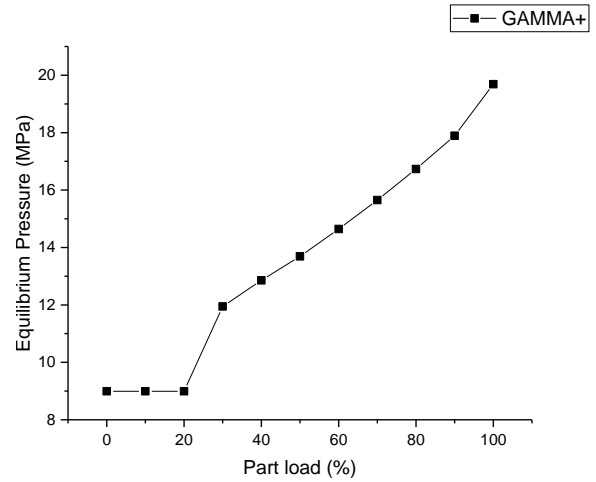


Figure 8: Equilibrium pressure after inventory tank is connected

The final assumption is partially proven in S-CO₂ systems as shown in Figure 9. The figure shows almost constant pressure ratio of compressor with respect to part load condition when infinite volume of inventory is applied. In short, except the first assumption, other three assumptions can be applied to S-CO₂ cycles.

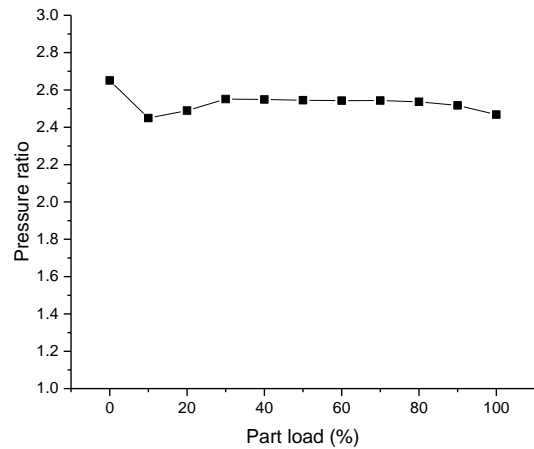


Figure 9: Pressure ratio of compressor along to part load condition

Compared to equation (1) and (2), equilibrium state of MMR loop with inventory tanks cannot be expressed in a single equation. Instead of formulating equation, calculate equilibrium state can be calculated from NIST database. Figure 10 shows the flow chart how the equilibrium pressure of MMR is obtained. This calculation process is implemented in MATLAB.

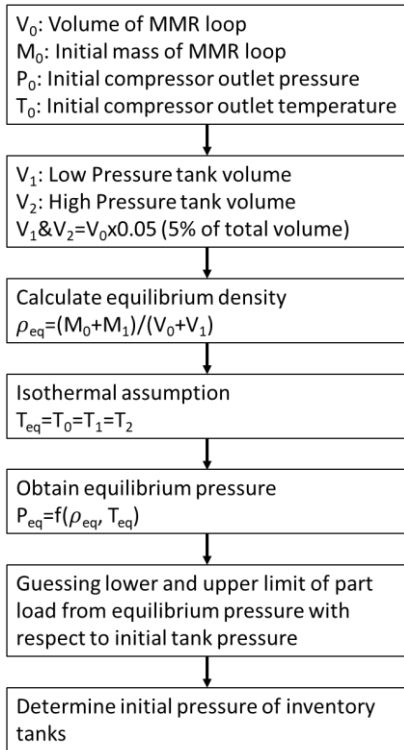


Figure 10: Flow chart to obtain equilibrium pressure of S-CO₂ cycle

Basically, there are three parameters (Initial pressure, temperature and volume of inventory tank) for deciding equilibrium condition. In case of MMR system, transportability is the prior factor so that volume has to be constrained and then initial temperature is determined as the compressor outlet temperature to minimize thermal stress as mentioned earlier. Thus, only initial pressure is the parameter to confirm whether the finite inventory tank can have capability: 100-25-100% load change with $\pm 5\%$ per minute rate.

At first, LP tank's volume for discharging inventory is constrained for 5% of total external volume of MMR which is 7m for axial length and 3.9m for diameter (83.6m³). Therefore, the equilibrium pressure results with respect to initial pressure of inventory tank. The calculation is based on 4.19m³ volume of inventory tank and an isothermal condition was assumed as shown in Figure 10. The small discrepancy is due to LP inventory tank is not going through isothermal process. Nevertheless, the MATLAB code shows reasonable predictions on the equilibrium pressure.

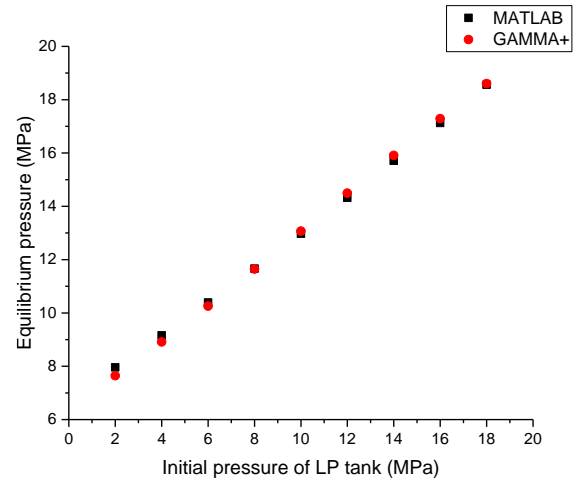


Figure 11: Equilibrium pressure with respect to initial pressure of LP tank

From Figure 11, initial pressure of LP tank should be less than 2MPa to receive the excessive inventory for reducing load down to 25% level. According to Figure 8, MMR has 20% part load at around 8MPa of equilibrium pressure. On the other hand, the HP tank for charging inventory to the loop should recover the equilibrium pressure from 25% part load condition (8MPa) to 100% full load condition (20MPa). At the first calculation, 30MPa for an initial pressure of HP tank and 4.19m³ showed marginal equilibrium pressure about 21MPa as shown in Figure 12. The marginal equilibrium pressure can cause slow response when load is increased because pressure difference between inventory tank and loop becomes small.

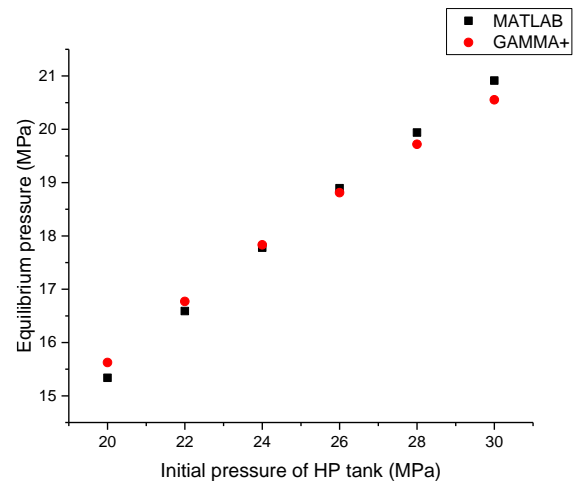


Figure 12: Equilibrium pressure with respect to initial pressure of HP tank

To resolve the marginal equilibrium pressure problem, increasing initial pressure can be a solution but too high initial pressure of inventory tank can require strong structure material.

Hence, instead of increasing initial pressure of HP tank, increasing volume of HP tank can lead to more reasonable enhancement. From MATLAB calculation, 8.36m³ volume and 30MPa initial pressure showed 24MPa equilibrium pressure. As a result, HP tank is decide to have 8.36m³ volume. 30MPa for initial pressure and 142°C for initial temperature.

PART LOAD OPERATION RESULTS WITH FINITE VOLUME OF INVENTORY TANKS

From the part load simulation with infinite volume of inventory tanks, it can be seen that only control scheme 3 is available to meet the part load requirement. First, part load results (100-25-100% with 5%/min rate) with control scheme 3 using finite volume of inventory tanks will be presented.

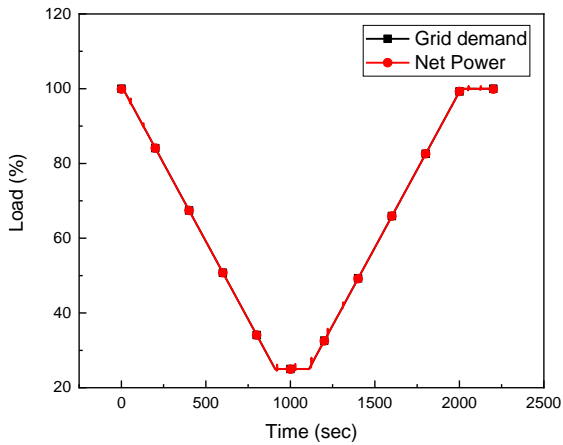


Figure 13: Grid load and net power results applying control scheme 3 with finite inventory tanks

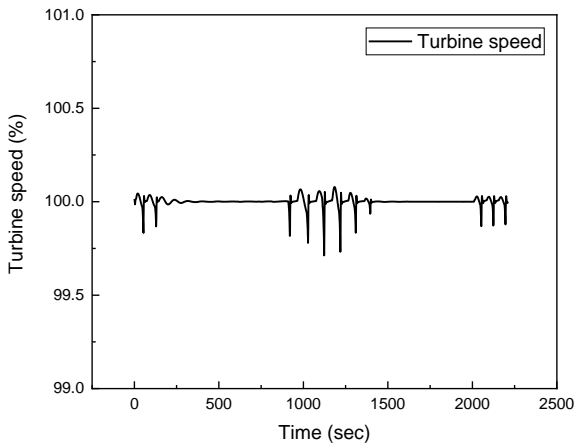


Figure 14: Turbine rotational speed result applying control scheme 3 with finite inventory tanks

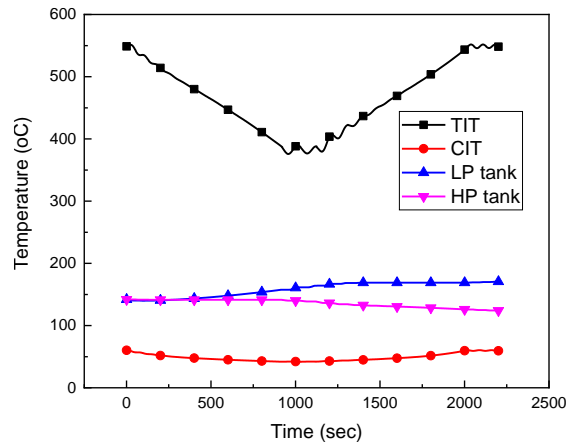


Figure 15: Temperature results applying control scheme 3 with finite inventory tanks

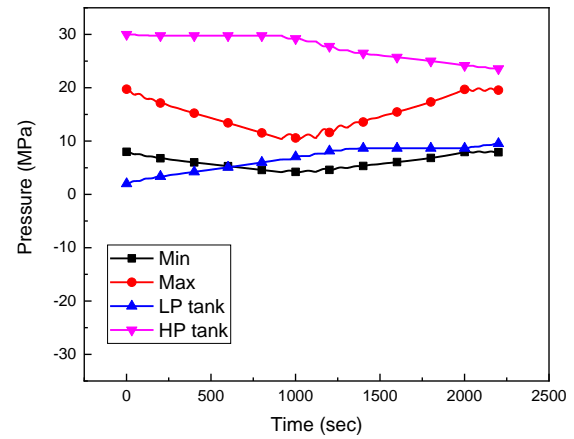


Figure 16: Pressure results applying control scheme 3 with finite inventory tanks

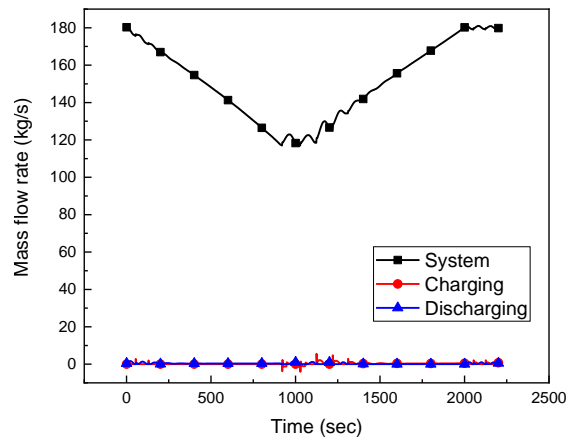


Figure 17: Mass flow rate results applying control scheme 3 with finite inventory tanks

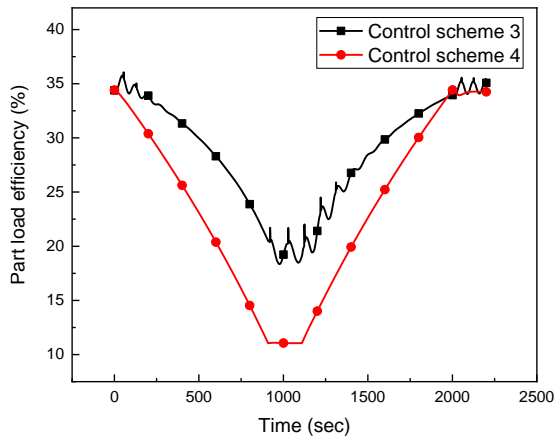


Figure 18: Part load efficiency of control scheme 3 and 4

Part load results with control scheme 3 using finite inventory tanks show some oscillations in the value, which can result from that control scheme 3. Nevertheless, this control scheme has potential to have fast response because transferred mass flow rate is small as indicated in Figure 17. By optimizing controller gains, it could be equipped with fast response. In Figure 15, temperatures of inventory tanks are not varied substantially, so that isothermal process assumption seems to be reasonable. In Figure 16, when load is decreased LP pressure is increased for receiving inventory from the loop and when load is increased HP pressure is decreased for providing inventory to the loop. In terms of part load efficiency, from Figure 18, it is noticeable that control scheme 3 is the most efficient control scheme than other schemes.

CONCLUSIONS

MMR has been designed to provide electricity to a remote region by adopting transportable nuclear system concept. Autonomous regulation is another requirement of MMR because it will be operated in a remote region. From this demand, various control schemes are evaluated in terms of response and efficiency. Based on the part load results using infinite volume of inventory tank, initial thermodynamic states of inventory tanks can be determined and the finite inventory tanks are again applied to the three control schemes.

The results showed that among four control schemes control scheme 1 and 2 are inadequate due to its slow response. Especially, control scheme 3 has the highest part load efficiency because no bypass control is adopted but its response time is not so fast. Furthermore, inventory controller's parameters such as valve area, and variable controller's gains will be studied to treat fast transient demand.

NOMENCLATURE

x_L : Lower limit
 x_U : Upper limit
 M_0 : Initial mass of MMR loop
 M_1 : Initial mass of inventory tank
 y : Ratio of the cycle HP to the initial pressure of the tank
 ω : Pressure ratio of the closed gas cycle
 P_{High} : Current Pressure at compressor outlet
 $P_{High,0}$: Nominal Pressure at compressor outlet
 W_{net} : Current Net Power
 $W_{net,0}$: Nominal Net Power
 P_0 : Initial compressor outlet pressure
 P_1 : Initial pressure of inventory tank
 T_0 : Initial compressor outlet temperature
 T_1 : Initial temperature of inventory tank
 V_1 : Volume of inventory tank
 ρ_{eq} : Equilibrium density between loop and tank
 T_{eq} : Equilibrium temperature between loop and tank
 P_{eq} : Equilibrium pressure between loop and tank

REFERENCES

- [1] V. DOSTAL, M.J. DRISCOLL, P. HEJZLAR. (2004). A supercritical carbon dioxide cycle for next generation nuclear reactors. USA: Massachusetts Institute of Technology, MIT-ANP-TR-100.
- [2] G. ANGELINO. (1968). Carbon dioxide condensation cycles for power production. *Journal of Engineering for Power*, 90 287-295.
- [3] E.G. FEHER. (1968). The supercritical thermodynamic power cycle. *Energy Conversion*, 8 85-90.
- [4] Y. AHN, S.J. BAE, M. KIM, S.K. CHO, S. BAIK, J.I. LEE, J.E. CHA. (2015). Review of supercritical CO₂ power cycle technology and current status of research and development. *Nuclear Engineering and Technology*, 47 647-661.
- [5] S.G. KIM, H. YU, J. MOON, S. BAIK, J.I. LEE, Y. KIM, Y.H. JEONG. (2016). A concept design of supercritical CO₂ cooled SMR operating at isolated microgrid region. *International Journal of Energy Research*, n/a-n/a.
- [6] B.S. OH, Y.H. AHN, H. YU, J. MOON, S.G. KIM, S.K. CHO, Y. KIM, Y.H. JEONG, J.I. LEE. (2017). Safety evaluation of supercritical CO₂ cooled micro modular reactor. *Annals of Nuclear Energy*, 110 1202-1216.
- [7] A. MOISSEYTSSEV, J.J. SIENICKI. (2007). Development of a plant dynamics computer code for analysis of a supercritical carbon dioxide Brayton cycle energy converter coupled to a natural circulation lead-cooled fast reactor. pp. Medium: ED.
- [8] N.A. CARSTENS, D.M. DRISCOLL, D.P. HEJZLAR, D.J. CODERRE. (2007). *Control Strategies for Supercritical Carbon Dioxide Power Conversion Systems*. USA: Massachusetts Institute of Technology, 213502891-MIT.
- [9] X. YAN. (1990). Dynamic analysis and control system design for an advanced nuclear gas turbine power plant. Massachusetts Institute of Technology.
- [10] F. OPENSHAW, E. ESTRINE, M. CROFT. (1976). Control of a gas turbine HTGR. ASME 1976 International Gas Turbine and Fluids Engineering Conference, American Society of Mechanical Engineers, pp. V01BT02A032-V001BT002A032.
- [11] K.P. KUMAR, A. TOURLIDAKIS, P. PILIDIS. (2004). Performance Review: PBMR Closed Cycle Gas Turbine Power Plant. *Nuclear Technology*.
- [12] R. COVERT, J. KRASE, D. MORSE. (1974). Effect of various control modes on the steady-state full and part load performance of a direct-cycle nuclear gas turbine power plant. ASME 1974 Winter Annual Meeting: GT Papers, American Society of Mechanical Engineers, pp. V001T001A002-V001T001A002.
- [13] F. SALZMANN. (1947). Regulation Theory for Thermal Power Plants Employing a Closed Gas Cycle. *Trans. ASME*, 69 329.
- [14] F. SALZMANN. (1950). Method of and apparatus for control of thermal power plants of the closed circuit type. Google Patents.
- [15] D. BITSCH, J. CHABOSEAU. (1970). Paper 11: POWER LEVEL CONTROL OF A CLOSED LOOP GAS TURBINE, BY NATURAL TRANSFER OF GAS BETWEEN THE LOOP AND AUXILIARY TANKS. *Nuclear gas turbines*, Thomas Telford Publishingpp. 111-115.

THERMO-ECONOMIC HEAT EXCHANGER OPTIMIZATION FOR ELECTRO-THERMAL ENERGY STORAGE BASED ON TRANSCRITICAL CO₂ CYCLES

Luis Sanz Garcia*, Emmanuel Jacquemoud and Philipp Jenny
MAN Energy Solutions Zurich AG
Zurich, Switzerland
Email: luis.sanz-garcia@man-es.com

ABSTRACT

The Electro Thermal Energy Storage (ETES) based on thermodynamic cycles using transcritical CO₂ was first developed by ABB corporate research [1]. The target being to set up a large-scale site-independent electricity storage system. The system has been reviewed and developed further by MAN-ES to an energy management system capable of storing not only electricity, but heat and cold as well.

The paper first presents the basic thermodynamic cycle layout, characterized by its heat pump and heat engine concept. Special attention is paid to the high-pressure (i.e. high-temperature) side of the system, where the rapid changes of sCO₂ in heat capacity result in additional modeling complexity. The major challenge lays in the design of heat exchanger (HEX) that provides the best trade-off between cost and performance. On top of that, the novelty of using the same heat exchanger(s) for both charging and discharging cycles on high and low pressure sides of the cycles represents an interesting solution to improve the performance to cost ratio of the entire system. However, this comes at the expense of potential oversizing of the heat exchanger(s). The paper presents the steady state model developed to simulate both thermodynamic cycles. Using a constrained optimization approach, the solver is guided towards solutions where the required heat exchanger surface for both cycles is similar. The consequences of using the same heat exchanger for both cycles are presented for different ETES configurations, allowing identifying significant investment cost reductions and in some cases even improving the entire system's performance. A significant reduction of up to 50% heat exchanger cost can be reached. Additionally, 14% of plant cost for a given round-trip efficiency can be obtained for certain system configurations.

INTRODUCTION

The need to meet the high expectations governments have set regarding reduction of greenhouse gases (GHG) has

substantially increased the interests in large-scale energy storage systems capable of coping with the fluctuating nature and unpredictability of renewable energy [2-4]. The current established technologies based on rotating turbomachinery to face this growing need are Pumped Hydroelectric Storage (PHS) and Compressed Air Energy Storage (CAES). These technologies are however constrained by the topology of the site in which they are installed. The Electro Thermal Energy Storage (ETES) developed in its first stages by ABB corporate research [1] allowed to store large amounts of electricity without relying on any geological constraint. The main thermodynamic performance indicator for electrical storage systems is the so-called roundtrip efficiency (η_{RT}) given by Equation 1.

$$\eta_{RT} = \frac{\text{electric energy provided during discharging}}{\text{electric energy consumed during charging}} = \frac{E_{out}}{E_{in}} \quad (1)$$

Going one step further, the system could also be conceived for heating and cooling applications. The temperature ranges (0°C – 180°C) of the ETES system allows to consider it as a tri-generation energy management system, providing heat, cold and electricity on demand to various process industries or large scale utilities. A schematic representation of a typical ETES plant is presented in Figure 1.



Figure 1. Schematic representation of the tri-generation energy management system: MAN ETES

Performance indicators defined to characterize the efficiency of cooling and heating applications are hot and cold coefficients of performance (COP) defined by Equations 2 and 3 respectively.

$$COP_{hot} = \frac{Hot_{DH}}{E_{in}} \quad (2) \quad COP_{cold} = \frac{Cold_{DC}}{E_{in}} \quad (3)$$

Previous studies of ETES based on transcritical CO2 cycles

The basic layout of the ETES process and component design as well as the preliminary economic study was firstly presented in [1]. CO2 (R744 in refrigerant nomenclature) was selected working fluid due to its suitable thermo-physical properties, high energy density and low critical point ($T_c = 31.1 \text{ }^\circ\text{C}$, $P_c = 73.8 \text{ bar}$). A heat pump (HP) in which the CO2 is compressed by a compressor (COMP) beyond the critical point characterizes the charging cycle. Making use of HEXs, the sCO2 is cooled down and afterwards expanded to a sub-critical state using a work-recovery expander (EXP) instead of a throttling valve to improve the COP of the heat pump (HP). An isothermal evaporation closes the cycle. The discharging cycle on the hand has a similar configuration as a heat engine (HE). A pump (PUMP) will pressurize the fully-condensed subcritical CO2 up to a supercritical state. Making use of the stored heat during the charging cycle, the sCO2 will be heated up and afterwards expanded through power turbines (TURBs) that will drive the generator to provide electricity to the grid. An isothermal condensation of the subcritical CO2 will close the cycle. Typical state point diagrams of both cycles are found in Figure 2.

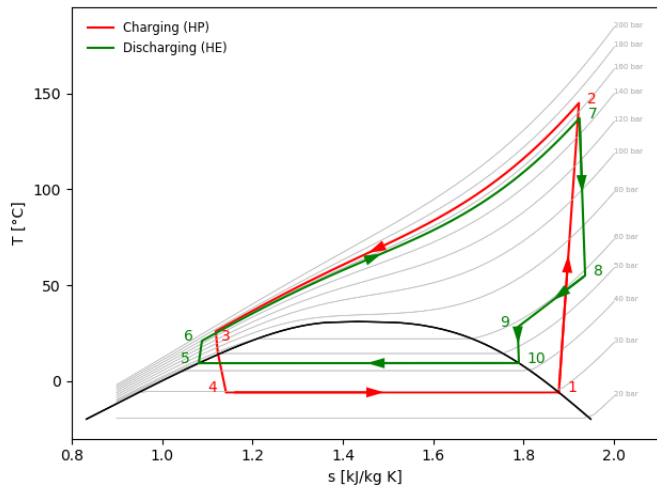


Figure 2. Temperature-entropy diagram of the ETES transcritical CO2 cycles

The possible storage technologies were also studied in [1], where it became obvious that the cold side of the cycle should use a phase changing material in order to make use of an isothermal storage. Ice was selected as cold storage material due to its wide use in the industry as well as its low price. On the hot side of the system, the gliding nature of the temperature profile of sCO2

(see Figure 2) led to select sensible heat storage in order to reduce the exergy losses between charging and discharging cycles. The excellent heat transfer properties of water combined with its low cost and temperatures in which the ETES system operates made it the ideal medium. The number of hot tanks as well as different cycle configurations was further studied in [5-6], where a maximum $\eta_{RT} = 62.3\%$ was obtained using a Pinch Analysis approach.

The importance of investment costs is another crucial aspect to consider in detail when it comes to building such a system when selecting the system's intensive and extensive parameters. Using the most promising cycle configurations from [5-6], the optimal trade-off between thermodynamic performance and investment costs of the entire system were analyzed in [7]. In order to estimate equipment costs, sizing factors of each component (HEX surface, shaft power, etc) were assumed as the main cost drivers based on interpolation data from selected equipment suppliers.

Use of same heat exchanger for charging and discharging cycles

Taking advantage of the fact that charging and discharging cycles never operate at the same time, the cost-reduction potential of using the same components for both cycles should be considered. As mentioned in [7], using the HEXs between CO2 and storage media for both cycles becomes particularly interesting and has significant impact on total plant cost (CAPEX). This solution requires the flow to be reversed on both sides of the HEX with the target and main challenge to match the required area (A_{HEX}) for the charging case with that of the discharging. Considering that A_{HEX} is calculated as shown in Equation 4, the only component-specific parameter is the overall heat transfer coefficient (k), since Q_{HEX} and MTD (Equation 5) are provided by the process streams boundary conditions. Please note the use of MTD throughout this study instead of the traditional $LMTD$ in order to consider heat exchanges with non-constant thermal capacities process streams. Assuming a total HEX heat duty Q_{HEX} , a constant k through the entire HEX and discretizing the component into n segments of the same duty Q_i , the MTD is calculated as presented in Equation 5.

$$A_{HEX} = \frac{\dot{Q}_{HEX}}{k \cdot MTD} \quad (4) \quad \frac{\dot{Q}_{HEX}}{MTD} = \sum_{i=1}^n \left(\frac{\dot{Q}_i}{LMTD_i} \right) \quad (5)$$

In [7], all of the HEX between CO2 and storage medium were dimensioned assuming $k = 1600 \text{ W m}^{-2} \text{ K}^{-1}$, considered to be an average value for sCO2-water HEX [8]. Assuming the same k represents a modelling simplification advantage. However, the deltas found between predicted and real A_{HEX} result in strong over/under dimensioned HEXs that will not provide the expected

outlet temperatures. Indeed, k depends on a variety of parameters of different nature as shown in Equation 6.

$$\frac{1}{k} = \frac{1}{h_{hot}} + \frac{l_{wall}}{\lambda} + \frac{1}{h_{cold}} \quad (6)$$

The nature of these parameters is diverse:

- HEX: geometry, material, wall thickness, etc.
- Streams properties: thermal conductivity, viscosity, heat capacity, temperature, pressure, etc.
- Pressure drop through the channels.

The relevance of each of these parameters will vary as discussed later on in this paper.

The fact that k depends on so many parameters makes it necessary to calculate this value for each specific HEX both on charging and discharging cycles. Equation 7 summarizes the challenge of using the same HEX for both cycles.

$$A_{ch} = A_{dch} \Rightarrow \frac{\dot{Q}_{ch}}{k_{ch} \cdot MTD_{ch}} = \frac{\dot{Q}_{dch}}{k_{dch} \cdot MTD_{dch}} \quad (7)$$

In other words, the model's goal will be to approximate as much as possible both HEX surfaces by a combination of \dot{Q}_i , MTD_i and k_i for each cycle. The heat duty ratio ($\dot{Q}_{dch}/\dot{Q}_{ch}$) between charging and discharging depends mainly on the process intensive and extensive parameters, namely the charging and discharging times (t_{ch} and t_{dch} respectively) as well as charging and discharging power.

Additionally, the ratio between both pressure drops through the HEX ($\vartheta = \Delta P_{dch} / \Delta P_{ch}$) must also be estimated. For a given geometry, ϑ depends mainly on the different friction coefficients and velocities of the streams. Parameters such as mass flow ratio (δ), viscosity and density of the streams play therefore a crucial role in the value of ϑ .

This paper first defines realistic models for the prediction of k and ϑ . By means of constrained optimization the different HEXs surfaces are matched for both charging and discharging operations. Finally, the results allow to see the advantages in terms of cost to performance ratio of using the same HEX for both cycles for different cycle configurations and ETES boundary conditions. A comparison using different HEX is performed as well as benchmark configuration.

HEAT EXCHANGERS OPERATING CONDITIONS

There are two main sorts of HEX used for the ETES cycles, namely the low and high-pressure HEX. The type of technology used for each group of HEX is different since they operate at different operating conditions.

Low-pressure side heat exchanger

This HEX is the so-called *COLD HEX*. The main purpose of this heat exchanger in the ETES process is:

- Produce ice during charging cycle by evaporating CO₂ in subcritical state (4 → 1 in Figures 2)
- Melt ice during discharging cycle by condensing CO₂ in subcritical state (10 → 5 in Figures 2)

The heat exchange between CO₂ and ice storage is done by means of an ethylene glycol-water loop. Throughout this paper, a 25% ethylene glycol in water by mass brine ($\phi_{glyc} = 25\%$) is considered. During charging, the brine would cool down by evaporating the CO₂ and afterwards heated up by freezing the water inside the ice storage tank. On the other hand, during discharging, the brine would be heated up by the condensing CO₂ and afterwards cooled down by melting the ice formerly stored during charging cycle. Figure 3 shows a typical enthalpy – temperature of an ETES COLD HEX. Figure 3 is a clear example of the philosophy behind this paper, where $\dot{Q}_{dch} > \dot{Q}_{ch}$ is compensated by smaller temperature differences in the charging case with respect to the discharging.

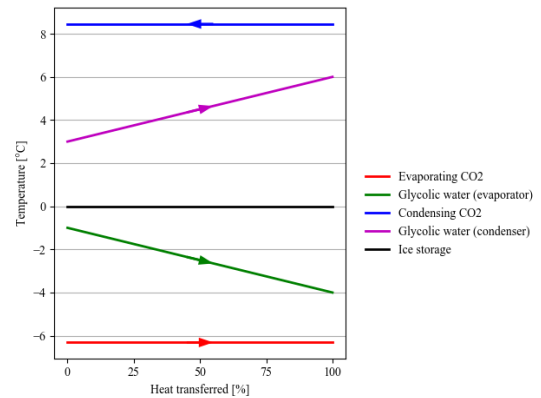


Figure 3. COLD HEX thermal profiles for charging and discharging cycles

The operating conditions of this HEX are bounded by maximum condensing pressure of CO₂. Assuming a maximum saturating pressure $p_{sat} = 50$ bar ($T_{sat} = 14.28$ °C), semi-welded HEX were considered to provide the best performance-to-cost ratio.

The duty of the HEX is determined by both the saturation temperature (i.e. pressure) and the vapor quality x at which the CO₂ enters and exits the HEX. Limitations are however imposed in order to guarantee the integrity and performance the turbomachinery upstream and downstream of the HEX. For instance, in the discharging (i.e. condensing) cycle the CO₂ enters at saturated vapor ($x=1$) and will exit at saturated liquid ($x=0$). In the charging cycle (i.e. evaporating), the quality at the outlet of the evaporator is fixed at saturated vapor ($x = 1$) to avoid

droplets at the COMP inlet. On the other hand, the inlet of the evaporator is a degree of freedom of the process depending solely on the EXP characteristics (see Figures 1, 2). An upper bound value of $x = 0.4$ was imposed to be realistic and this will be assumed throughout this study.

High-pressure side heat exchanger(s)

These HEXs are the so-called *HOT HEX*. The main purpose of these heat exchangers is:

- Heat up water in the hot storage tanks by cooling sCO₂ downstream the COMP (2 → 3 in Figures 1,2)
- Use the hot water to heat up sCO₂ upstream of the TURB (6 → 7 in Figures 1,2)

The first major challenge when it comes to defining the boundary conditions and design of these HEXs relies on the fact that the working fluid through these HEXs is CO₂ at supercritical conditions. As a consequence, the variation in heat capacity c_p during isobaric cooling (2 → 3 Figure 2) or heating (6 → 7 Figure 2) of sCO₂ requires special attention in order to reduce as much as possible the exergetic irreversibilities between charging and discharging cycles. Although early studies of the system suggested the use of only 2 tanks with different temperatures [1], later studies pointed out the performance enhancement opportunity of adding intermediate tanks that would follow the curves for both charging and discharging cycles [5-7]. A schematic representation of the multiple storage tank principle is shown in Figure 4. The ideal water thermal profile would have the same temperature difference between charging and discharging profiles. The only way of achieving this would be with an infinite number of tanks that would be able to adapt to the change in c_p of the sCO₂ by changing the water mass flow from one tank to the subsequent one. A realistic water thermal profile will count with a finite number of tanks n_{tanks} , would be divided into $n_{tanks} - 1$ segments, each of them with a different thermal capacity ($C_w = c_{p,w} \cdot m_w$) of the water. The optimum n_{tanks}

is a compromise between exergy losses and CAPEX of the ETES system. Figure 2 shows how the change in “shape” of the isobars becomes more significant approaching the triple point. The lower the HOT HEX pressure level (i.e. closer to triple point) the more sensitive c_{CO_2} and thus more penalizing since a higher number of tanks is required to follow the sCO₂ thermal profile compared to the subcritical CO₂ exchange, where the pinch point ΔT_{pp} was found at the extremities of the HEX, the change in c_p during isobaric heat exchange can lead to ΔT_{pp} in the middle of the HEX (see Figure 5).

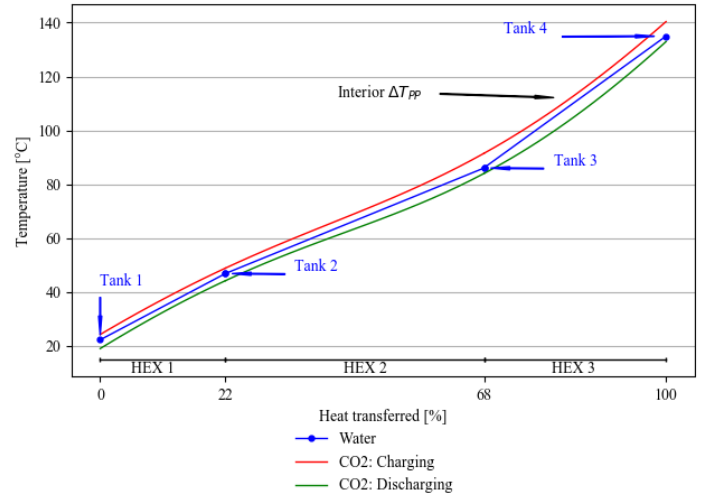


Figure 5. HOT HEX thermal profiles for charging and discharging cycles in a 4-tank ETES configuration

The main challenge of the high pressure side is then to determine the temperature of the tanks as well as the heat duty assigned to each of the HEX. This duty is determined by the volume flow leaving and entering each of the tanks. To guarantee the tanks filling and emptying at the same rate, the same ratio of water volume flow δ_{H_2O} through each of the HEX should be kept as shown in Equation 8 below. Since the water side of the HEX is

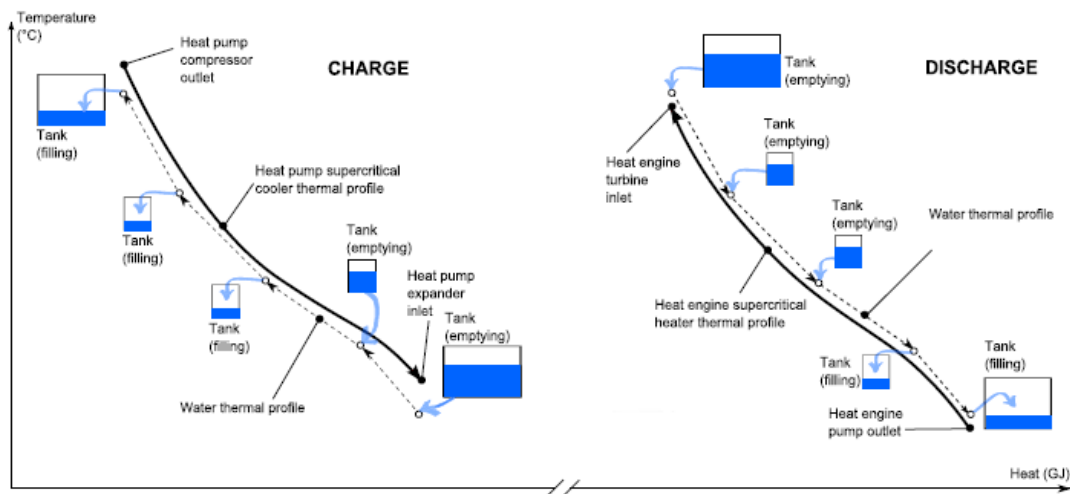


Figure 4. Multiple hot storage tanks principle for a 5-tank ETES configuration [7]

at the same operating conditions in both cycles, the ratio of volume flows is equivalent to δ .

$$\delta_{H2O} = \left(\frac{\dot{v}_{ch}}{\dot{v}_{ach}} \right)_i = \left(\frac{\dot{m}_{ch}}{\dot{m}_{ach}} \right)_i \quad \forall i = 1, \dots, n_{HEX} \quad (8)$$

The type of HEX was selected both on the operating conditions of the sCO₂ (80-270 bar, 10 – 200 °C) and the requirement of having small ΔT_{pp} between both streams to reduce exergetic losses. Among the potential technologies that could cope with this criteria, printed circuit heat exchangers (PCHE) was considered to provide the best compromise between performance and footprint compared to other traditional solutions such as shell and tube HEX.

ETES CYCLE OPTIMIZATION MODEL

The complexity of selecting the numerous parameters defining the ETES requires the development of models capable of simulating and predicting the sizing and performance of all key components constituting the system. The retained ETES configuration is usually selected after an optimization of performance against cost. Therefore, the prediction of cost and performance integration of each key components is fundamental to allow for the best cycle definition. Moreover, the models shall permit the required sensitivity to modification of thermodynamic cycle parameters such as mass flows, temperatures and pressures. To address this challenge, a steady-state ETES model has been developed in python [9] capable of carrying out single/multi-objective and multi-variable optimization. It is based on a sequential calculation solver, so the design is achieved starting from a fixed point and proceeds solving mass and energy balances sequentially component by component following the flow and defining for each of them boundary conditions and applying design rules and component limitation. NIST REFPROP [10] is used to calculate the thermodynamic and transport properties of the different fluids involved in the system. The nature of the software makes the choice of degrees of freedom a crucial step to achieve a feasible and meaningful design. It is characterized by an objective function subject to a set of constraints (linear and non-linear) that the optimizer should satisfy to come to feasible ETES configurations. The general formulation of a constrained optimization problem is presented in Equation 9:

$$\begin{aligned} \min_x & \left(f(x) + \sum_i Pen_i(x) \right) \\ \text{subject to} & \quad b_j \leq g_j(x) \leq c_j \quad \forall j = 1, \dots, n_{constr} \quad (9) \\ & \quad l_b \leq x \leq u_b \\ & \quad x_k \in \mathbb{R} \quad x_l \in \mathbb{Z} \end{aligned}$$

Under this formulation, for a set of decision variables x the optimizer will try to minimize the objective function $f(x)$. The decision variables can be either real (x_k) or integers (x_l) and are limited within an upper and lower bound (u_p and l_b respectively). By including the sum of penalties $Pen(x)$ in the minimization

problem, the optimizer is guided towards feasible solutions by penalizing any violations on constraints. The value of the penalty is proportional to the violation. A weighting factor is also imposed in order to address differences in the magnitudes of each penalty as well as to address the severity of this penalty (more critical constraint violations will have greater weighting factors). Two are the main types of penalties applied to the ETES optimization problem:

- Cycle unfeasibility: one or both cycles are not closed.
- Component limitation: the calculated solution leads to an unfeasible component (either rotating machinery or HEX)

Thermodynamic modelling

The independence of each individual component of the system allows to prioritize the complexity of the components based on their sensibility to modification of input boundary conditions.

Turbomachinery modelling

For the purposes of this paper, a zero-dimensional model for turbomachinery key components was applied and considered as accurate enough. The assumed isentropic efficiencies (η_{is}) of these machines are shown in Table 1. The generators and motors were assumed to have an efficiency of 99% from electric to mechanical power and vice versa.

Machine	Isentropic efficiency (η_{is})
COMP	81%
EXP	90%
TURB	92%
PUMP	86%
Auxiliary Pumps	85%

Table 1. Assumed turbomachinery isentropic efficiencies

Heat exchanger modelling

The major modelling complexity relies in the challenge of using the same HEX for both cycles, which made it necessary to address the HEX modelling with more care than for the rotating machinery. The use of zero-dimensional models as done in [5-7] can lead to large discrepancies after comparison with realistic supplier data in A_{HEX} (defined by k). A strict technical approach would be to develop a comprehensive geometrical model of each HEX as done in [11]. However, the lack of detailed geometrical information as well as the current necessity of rapid computational time led to choose a mid-way solution. One-dimensional models for both HOT and COLD HEX was considered to be accurate enough to cope with the sensitivity of all relevant input parameters.

For each HEX, a set of parameters is required to calculate k (i.e. A_{HEX}). Given the differences in both conditions and type of HEX used, COLD and HOT HEX were treated separately. First of all,

the parameters (both intensive and extensive) having the biggest influence on k and ΔP_{HEX} were identified. On a second step, the impact of each of these parameters on k and ΔP_{HEX} was determined using polynomial regression models based on HEX suppliers' data for different operating conditions. The quality of the approximation of these models is determined by the adjusted Coefficient of Determination (CoD_{adj}) [12]. The higher variety of modeled HEX designs the higher the CoD_{adj} . Additionally, the importance of each variable on the estimation of the output is given by the Coefficient of Importance (CoI) [12]. Table 2 shows the results of the approximation models used to estimate k .

	CO2 state	Variables	CoI	CoD _{adj}		
HOT HEX	Supercritical	$\Delta P_{\text{H}_2\text{O}}$	81%	94.9%		
		ΔP_{CO_2}	49%			
		λ_{CO_2}	26%			
		μ_{CO_2}	25%			
		$c_p \text{ CO}_2$	25%			
		$\lambda_{\text{H}_2\text{O}}$	20%			
		$\mu_{\text{H}_2\text{O}}$	19%			
		MTD	0%			
COLD HEX	Subcritical evaporating	ΔP_{glyc}	77%	97.2%		
		MTD	65%			
		T_{CO_2}	47%			
		ΔT_{glyc}	24%			
		x_{in}	3%			
		x_{out}	2%			
		ϕ_{glyc}	0%			
	Subcritical condensing	ΔP_{glyc}	76%	96.3%		
		MTD	61%			
		ΔT_{glyc}	42%			
		T_{CO_2}	7%			
		ϕ_{glyc}	3%			

Table 2. Regression models for estimating k

The higher complexity of estimating k between sCO₂ and H₂O is evidenced by the higher number of parameters required for HOT HEX compared to the COLD HEX. Additionally, average values of μ , λ on both sides (sCO₂ and H₂O) are included in the regression model. Furthermore, the significant changes in c_p of sCO₂ are also accounted for by including an average of this parameter throughout the entire HEX in the approximation. ΔP from both sides is also considered given its impact on the turbulence. In the COLD HEX, ΔP_{CO_2} is neglected given the negligible value for a semi-welded plate HEX during evaporation and condensation. The large differences in convective heat transfer h (see Equation 6) between subcritical evaporating and condensing CO₂ led to determine different parameters to determine k_{COND} and k_{EVAP} . Finally, MTD is considered in both types of HEX to account for the engineer's design methodology for each specific HEX. As a general design rule, for smaller MTD , higher ΔP values are necessary to increase

k . The conducted regression studies showed higher values of CoD_{adj} when considering this parameter.

The relevance of ΔP in k estimation becomes clear in Table 2, being the parameter having the greatest impact of all for the three regression studies. The selection of optimal HEX design is closely linked to ΔP : while high values of ΔP results in higher pumping power (i.e. smaller η_{RT}), it also increases drastically k (i.e. smaller A_{HEX} , thus smaller CAPEX). The optimal ΔP is then a compromise between cost and performance and its optimal value is selected based on ETES system boundary conditions such as price of electricity. The approach chosen to estimate ΔP_{HEX} leads to more accurate results for the COLD HEX, since operating conditions do not vary that much between the different operating cases and easily predicted on the HEX supplier side. ΔP_{glycol} is determined as a function of the velocity and density of the brine. Maximum absolute errors up to 5% can be expected for both evaporating and condensing cases. Based on supplier data, the negligible values of ΔP_{CO_2} combined with the complexity associated with phase-changing pressure drops led to impose a constant value for both evaporating and condensing cases.

The large changes in operating conditions for the HOT HEX led to take another approach to estimate ΔP_{CO_2} and $\Delta P_{\text{H}_2\text{O}}$. In this case, the HEX is assumed to be design for a specific ΔP_{HEX} for each of the two streams (water and CO₂). The charging case is considered as the limiting case. If the same HEX is used for both cycles, the ΔP_{HEX} on both sides for the discharging case will no longer be imposed, but calculated and proportionally based on the ΔP_{HEX} applied on the charging case. A new equation is therefore required to determine ϑ on both sides of the HEX. If different HEX are used for both cycles, ϑ is obviously not calculated and ΔP_{dch} is specified before the calculation. A summary of the approximation of ϑ as well as the importance of the parameters influencing its value is available in Table 3. The dependency of μ on ΔP via Reynolds number is accounted for in both functions. Since $\theta_{\text{H}_2\text{O}} = 1$ for every HOT HEX, the $\mu_{\text{H}_2\text{O}}$ was selected to estimate $\vartheta_{\text{H}_2\text{O}}$ instead of θ as done for ϑ_{CO_2} .

	Variables	CoI	CoD _{adj}
Water	$\delta_{\text{H}_2\text{O}}$	92%	98.8%
	$\mu_{\text{H}_2\text{O}}$	31%	
CO ₂	δ_{CO_2}	96%	97.4%
	θ_{CO_2}	40%	

Table 3. Regression models for estimating ϑ for HOT HEX

The high values of CoD_{adj} obtained for both k and ϑ estimation confirm the one-dimensional model as accurate enough for the implementation into the ETES process simulation and optimization routine.

Economic modelling

In order to reach a meaningful thermo-economic optimization analysis, the associated component costing model of the plant are of equal importance as the performance models. For this paper, the purchasing cost of the different components included in the system are calculated based on characteristic sizing factor (A_{HEX} , shaft power, volume of storage tanks, etc.). To properly address the cost against performance trade-off, it is crucial to count on reliable data regarding equipment costs. The numerous exchanges with suppliers of the various components allows to have consolidated up-to-date data to estimate with a relatively low uncertainty. Additional costs related to engineering, civil work and procurement are assumed to be a fixed percentage of the total equipment cost.

Modelling approach using same heat exchanger

The current steady state model of the ETES system is conceived to provide after each iteration for a given set of decision variables:

- Process state conditions at inlet and outlet of each component
- Cycle performance (η_{RT} , COP_{hot} , COP_{cold})
- Cost and size of equipment

A_{HEX} for charging and discharging are firstly calculated independently from one another. By applying a constraint where a maximum oversizing is allowed between charging and discharging cases, the optimizer should try in the next iteration to reduce that penalty. The addition of this new constraint reduces the number of non-penalized solutions, resulting in longer computational times (i.e. number of evaluations) to obtain optimal ETES systems. Since this penalty is applied to each HEX, increasing the number of tanks (i.e. HOT HEX) reduces the number of non-penalized solutions and ultimately longer computational time is required by the optimizer to find optimal ETES systems. Maximum oversizing of 15% for both HOT and COLD HEX was considered to be an adequate compromise between computational time and accuracy of the solution inside the conventional design margin applied by suppliers. The penalty assigned to an oversizing higher than the abovementioned value is proportional to the committed violation.

RESULTS AND DISCUSSION

The benefits of using the same HEX are evaluated comparing different ETES configurations and system boundary conditions. This evaluation is carried out launching 36 single-objective optimization runs which target being to maximize η_{RT} . ETES designs with thermal export are not evaluated in this study, therefore COP_{hot} and COP_{cold} are not included in the objective function. To evaluate a broad spectrum of ETES configurations, the following four parameters are imposed for each of the runs:

- Using same and different HEX (x2)

- Different number of hot storage tanks: 2 and 5 (x2)
- Different minimum allowed ΔT_{PP} inside HEX: 1, 2 and 4 K (x3)
- Different β : 0.25, 0.5, 1 (x3)

The considered optimization variables are:

- Evaporation temperature [$^{\circ}C$]
- COMP outlet pressure [bar]
- Condensation temperature [$^{\circ}C$]
- Pressure difference between COMP and PUMP outlet pressures [bar]
- δ_{CO2} [-]
- δ_{H2O} for HOT HEX [-]
- Heat distribution among HOT HEX [-]
- Hot storage tank temperatures [$^{\circ}C$]

A total of 8 optimization variables is considered for the simplest case with only 2 tanks. Two additional optimization variables must be considered (heat distribution and tank temperature) should be considered by adding an additional tank. As extensive variables, all optimization runs are characterized by a charging power $P_{ch} = 8.5$ MW during 8 hours.

Additionally, a summary of the optimization set-up for the different runs is presented in Table 4. To guarantee more reliable optimization results, the smaller the number of non-penalized solutions, higher number of iterations are imposed as stopping criteria. This results in longer computational times for cases using the same HEX as well as cases with higher number of hot storage tanks.

Approach	Number of storage tanks	Number of iterations	Population size
Same HEX	2	3500	50
	5	5000	
Different HEX	2	2000	
	5	3500	

Table 4. Single-objective optimization run set-ups

Figure 6 offers good summary of the cost and performance of the different optimization runs, separating the results into cases using the same and different HEX. The CAPEX of the different solutions is displayed as the cost reduction opportunity of each of the solutions with respect to the most expensive of all. The results of Figure 6 confirm that the covered spectrum of ETES configurations is quite broad, varying both in cost and performance. Looking closely at the solutions using the *different HEX* approach, six types of solutions can be clearly identified, one per each combination of n_{tanks} (x2) and minimum allowed ΔT_{PP} (x3). Since no component is shared between both cycles, the optimum ETES system in terms of performance does not depend on β , which defines the size of the discharging cycle key

components. Therefore, for a given η_{RT} , the CAPEX is reduced as β increases when using different HEX on both cycles.

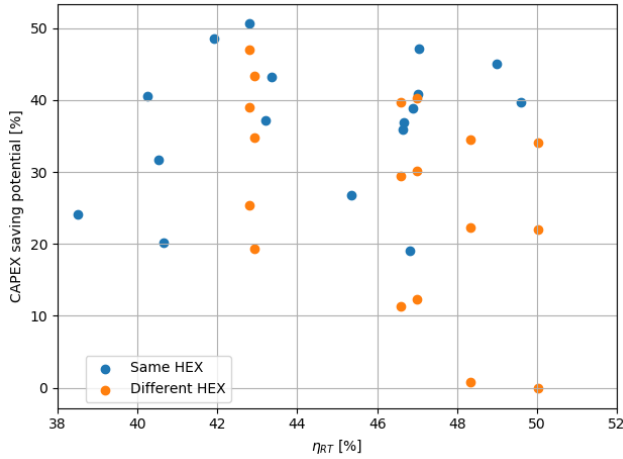


Figure 6. CAPEX saving potential against η_{RT} using same and different HEX for several ETES configurations with $t_{ch} = 8h$ and $P_{ch} = 8.5 MW$

To better understand the benefits derived from using the same HEX approach, solutions with similar configurations (n_{tanks} , ΔT_{PP} and β) should be compared separately since each of them have different costs and performances. CAPEX per discharged electrical energy provides the thermo-economic performance of the ETES system. The difference of this value is compared in Figures 8 and 9 for the different variables defining the considered ETES configurations. Maximum ETES plant cost per discharging electricity of up to 14% are expected as a result of using the same HEX for both cycles. The identification of the most promising cases is carried out by evaluating each of the three parameters individually.

Minimum allowed pinch point (ΔT_{PP})

Unlike n_{tanks} and β , which play an important role in the costing of other key ETES components, ΔT_{PP} only impacts the cost and performance of the HEX. This is evidenced by the greater influence of this parameter on CAPEX saving potential per discharged electricity shown in Figures 7 and 8. Since the impact of HEX cost is directly proportional to the inverse of MTD (see Equation 4), smaller ΔT_{PP} result in more expensive HEX and a higher portion of the total plant cost is assigned to this component. The results of Figure 7 and 8 allow to confirm the higher thermo-economic benefit of the *same HEX* approach for ETES configuration with smaller ΔT_{PP} .

Time ratio (β)

Contrary to *different HEX* approach, if the HEXs are used for both charging and discharging operations, β plays a crucial role in thermodynamic performance of the system. Configurations with small values of β area characterized by high discharging

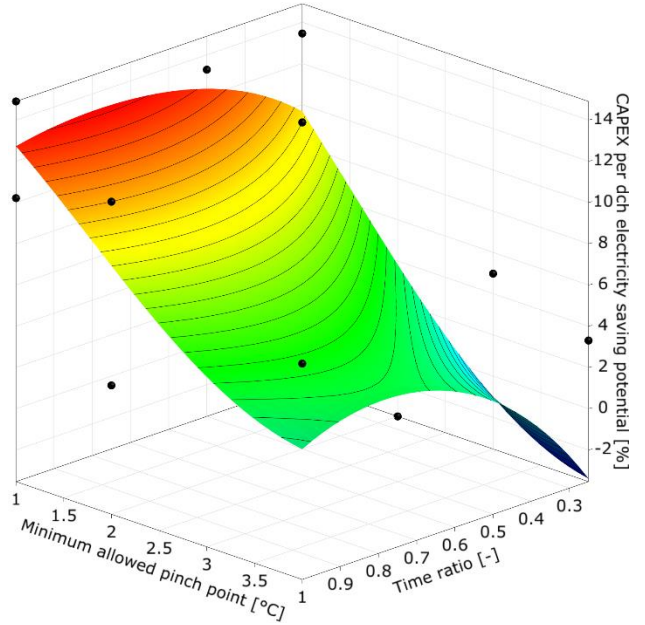


Figure 7. Response surface of CAPEX saving potential per discharged electrical energy as a function of minimum allowed ΔT_{PP} and β

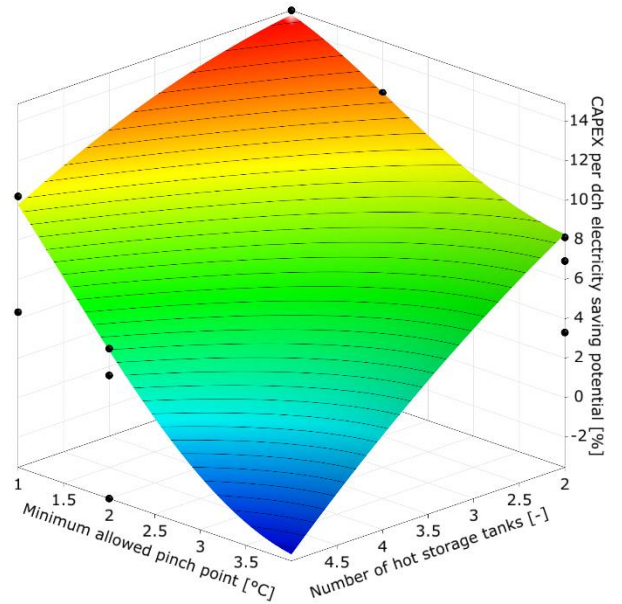


Figure 8. Response surface of CAPEX saving potential per discharged electrical energy as a function of minimum allowed ΔT_{PP} and n_{tanks}

cycle sizes (i.e. high δ) to compensate for the small t_{dch} . Since δ determines Q_{ch}/Q_{dch} , the MTD of the smallest duty is reduced to find solutions with minimum HEX oversizing. A smaller value of β results in:

- Closer charging and discharging thermal profiles (see Figure 5) leading to fewer exergetic losses take place in the HEXs.

- Higher ΔP due to higher δ on both sides of the HEX

The compromise between these two parameters determines greatly the benefits of using the same HEX approach compared to using two separate components. For the assigned boundary conditions of the optimization runs conducted in this paper, high values of β yield higher thermo-economic performances (see Figure 7).

As seen in Figure 7, the impact of β is smaller than ΔT_{PP} on cost savings per discharging electricity since β also impacts the cost of other equipment, mainly TURB and PUMP. This results in smaller CAPEX reduction when one of the HEX is removed from the cycle.

Number of hot storage tanks (n_{tanks})

ETES configurations with small n_{tanks} reduces the number of total HEX and thus the contribution of this component to total plant cost. On the other hand, the exergetic losses due to the changes in c_p of the CO₂ in the supercritical region increase when n_{tanks} decrease since the water thermal profile is unable to follow the CO₂ charging and discharging profiles (see Figure 5).

The thermo-economic impact of n_{tanks} using the *same HEX* approach is shown in Figure 8. The results show more promising results for ETES configurations with smaller number of hot storage tanks. These results are however highly influenced by the complexity of finding global minima by the optimizer and thus number of iterations (see Table 4). Higher potential η_{RT} for similar CAPEX are expected for configurations with higher n_{tanks} when increasing the number of iterations.

CONCLUSIONS

The methodology to use the same HEX for charging and discharging process cycles applied to the ETES system and its various configurations was firstly presented. By means of constrained optimization, maximum A_{HEX} difference of 15% appears to lead to a satisfactory compromise between computational time and the prediction of realistic HEX performance.

The importance of k and ΔP on both cost and performance of the overall system confirms the importance of implementing accurate estimations for both parameters. The dependency of k on ΔP on both sides of the HEX is to be carefully considered as shown in Tables 2.

A series of single-objective optimization runs were conducted to evaluate the thermo-economic advantage of using the same HEX for both charging and discharging cycles in steady-state conditions. From a cost perspective, the higher the contribution of HEX on total ETES plant cost, the more interesting becomes to use the same component for both cycles. On the other hand, from a performance perspective, the increase of cycle

complexity limits the number of possible ETES solutions for given set of system boundary conditions. Among the considered parameters that define the ETES system, ΔT_{PP} proved to be most decisive when evaluating the possibility of using the same HEX for both cycles. Smaller values of ΔT_{PP} represent the most promising cases, given the greater portion of the cost allocated for the HEXs. Additionally, β values between 0.6 and 1 show great potential of applying the same HEX approach in an ETES system. Maximum CAPEX per discharged electricity reductions of 14% are expected for ETES configurations with $n_{\text{tanks}} = 2$, $\beta = 0.7$ and minimum allowed $\Delta T_{PP} = 1K$. For particular ETES configurations, favorable thermo-economic are reached by using different HEX for both charging and discharging cycles. Nevertheless, the reduction in footprint as a result of using the same component should be considered, making it crucial to use the same HEX for both cycles to obtain the most compact ETES plant possible.

The behavior of the HEXs in transient and off-design operating conditions should be considered in a further step for a more comprehensive assessment and to eventually identify other component limitations still unknown at this stage.

NOMENCLATURE

A_{HEX}	Heat Exchanger Surface
CAPEX	Capital Expenditure
COMP	Compressor
COP_{hot}	Hot Coefficient of Performance
COP_{cold}	Cold Coefficient of Performance
h	Convective heat transfer
ρ	Density
μ	Dynamic Viscosity
θ	Dynamic Viscosity Ratio for a specific HEX (discharging/charging)
ETES	Electro-Thermal Energy Storage
EXP	Hydraulic Expander
HE	Heat Engine
HEX	Heat Exchanger
HP	Heat Pump
k	Overall Heat transfer coefficient
δ	Mass flow ratio (discharging/charging)
$LMTD$	Logarithmic Mean Temperature Difference
\dot{m}	Mass flow
MTD	Mean Temperature Difference
OPEX	Operating Expenses
TURB	Power Turbine
$Pen_i(x)$	Penalty i for a set of input parameters x
ΔT_{PP}	Pinch Point of Heat Exchanger
ΔP_i	Pressure drop inside Heat Exchanger i
ϑ	Pressure drop ratio in heat exchanger (discharging/charging)
PUMP	CO ₂ Pump
φ_{glyc}	Composition of ethylene glycol in water by mass brine

η_{RT}	Round-trip Efficiency
λ	Thermal Conductivity
t_{ch}	Charging time
t_{dch}	Discharging time
β	Ratio between discharging and charging times (t_{dch}/t_{ch})
v	Volumetric flow

ACKNOWLEDGEMENTS

The writers would like to recognize the support and preliminary studies carried out by ABB which have set the baseline for the further development of the ETES system.

REFERENCES

- [1] M. Mercangöz, J. Hemrle, L. Kaufmann, A. Z'Graggen, and C. Ohler. Electrothermal energy storage with transcritical CO₂ cycles. *Energy*, 45(1):407 – 415, 2012.
- [2] Connolly D, Lund H, Mathiesen BV, Pican E, Leahy M. The technical and economic implications of integrating fluctuating renewable energy using energy storage. *Renewable Energy* 2012;43:47-60.
- [3] Kaldellis JK, Zafirakis D. Optimum energy storage techniques for the improvement of renewable energy sources-based electricity generation economic efficiency. *Energy* 2007;32(12):2295-305.
- [4] Lund H, Mathiesen BV. The role of carbon capture and storage in a future sustainable energy system. *Energy* 2012;44(1):469-76.
- [5] Morandin M, Maréchal F, Mercangöz M, Buchter F. Conceptual design of a thermo-electrical energy storage system based on heat integration of thermodynamic cycles e Part A: Methodology and base case. *Energy* 2012; 45: 375-85.
- [6] Morandin M, Maréchal F, Mercangöz M, Buchter F. Conceptual design of a thermo-electrical energy storage system based on heat integration of thermodynamic cycles e Part B: Alternative system configurations. *Energy* 2012; 45:386-96.
- [7] Morandin M, et al., Thermo-economic design optimization of a thermo-electric energy storage system based on transcritical CO₂ cycles, *Energy* (2013), <http://dx.doi.org/10.1016/j.energy.2013.05.038>
- [8] Yoon SH, Kim JH, Hwang YW, Kim MS, Min K, Kim Y. Heat transfer and pressure drop characteristics during the in-tube cooling process of carbon dioxide in the supercritical region. *International Journal of Refrigeration* 2003;26(8):857e64.
- [9] Python Software Foundation. Python Language Reference, version 3.6. Available at <http://www.python.org>
- [10] Lemmon EW, Huber ML, McLinden MO. NIST Standard reference Database 23: reference fluid thermodynamic and transport Properties-REFPROP, Version 9.1, National Institute of Standards and technology. Gaithersburg: Standard Reference Data Program; 2010.
- [11] Baik, Y.; Heo, J.; Koo, J.; Kim, M. The effect of storage temperature on the performance of a thermoelectric energy storage using a transcritical CO₂ cycle. *Energy* 2014, 75, 204–215
- [12] Montgomery, D. C. and G. C. Runger (2003). *Applied Statistics and Probability for Engineers* (Third ed.). John Wiley & Sons.

DuEPublico

Duisburg-Essen Publications online

UNIVERSITÄT
DUISBURG
ESSEN

Offen im Denken

ub | universitäts
bibliothek

This text is made available via DuEPublico, the institutional repository of the University of Duisburg-Essen. This version may eventually differ from another version distributed by a commercial publisher.

DOI: 10.17185/duepublico/48871

URN: urn:nbn:de:hbz:464-20190925-112151-4



This work may be used under a Creative Commons Attribution 4.0 License (CC BY 4.0) .